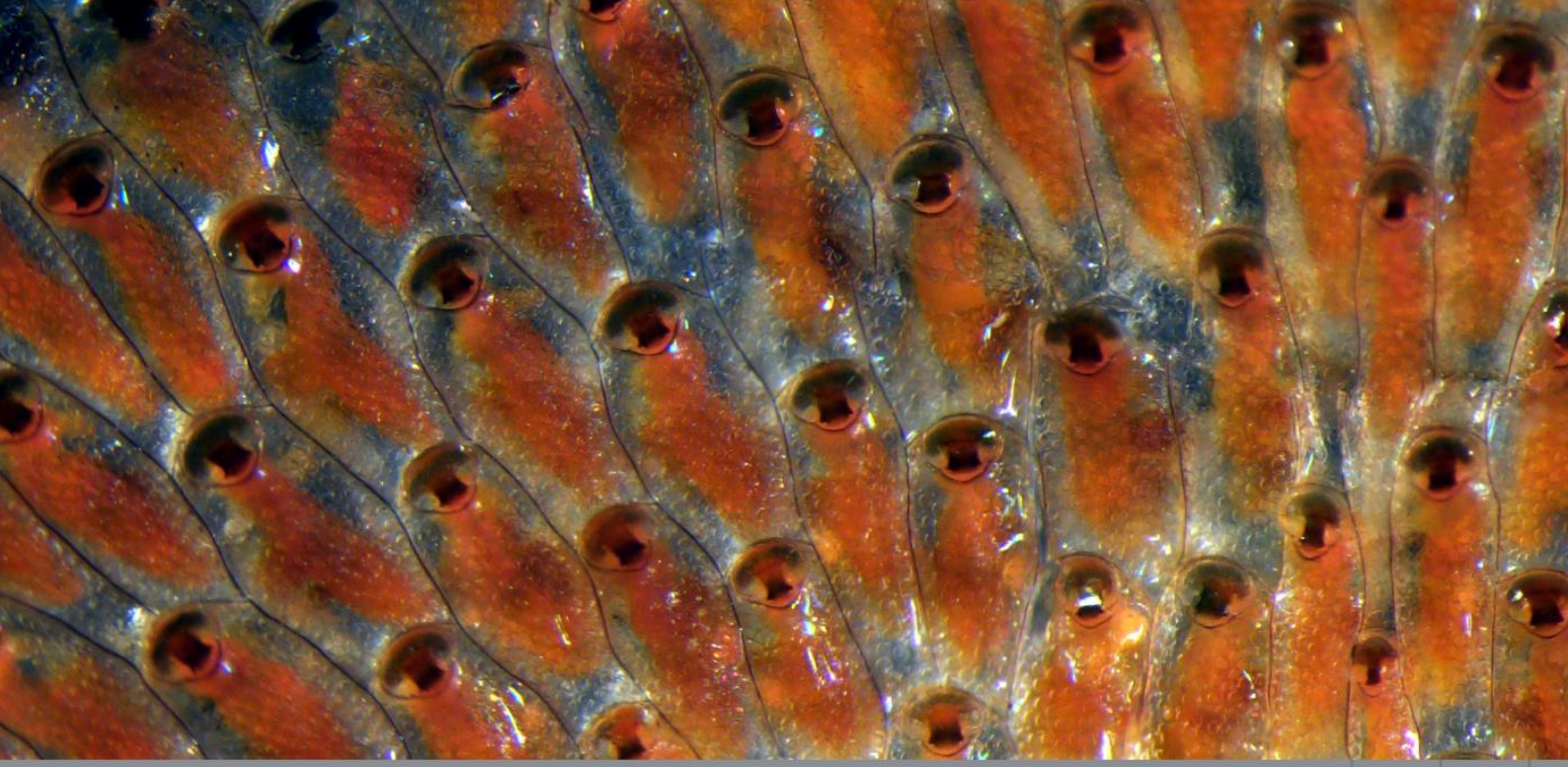


17th Multinational Congress on Microscopy

17MCM

Portorož, Slovenia
7 - 12 September, 2025

17th Multinational Congress on Microscopy
17 MCM
Book of Abstracts

Uredniki: Kristina Žagar Soderžnik, Rok Kostanjšek, Barbara Šetina Batič, Polona Mrak, Nada Žnidaršič, Samo Hudoklin, Blaž Belec, Sašo Šturm, Miran Čeh, Elena Tchernychova, Melanija Hadolin [editors]

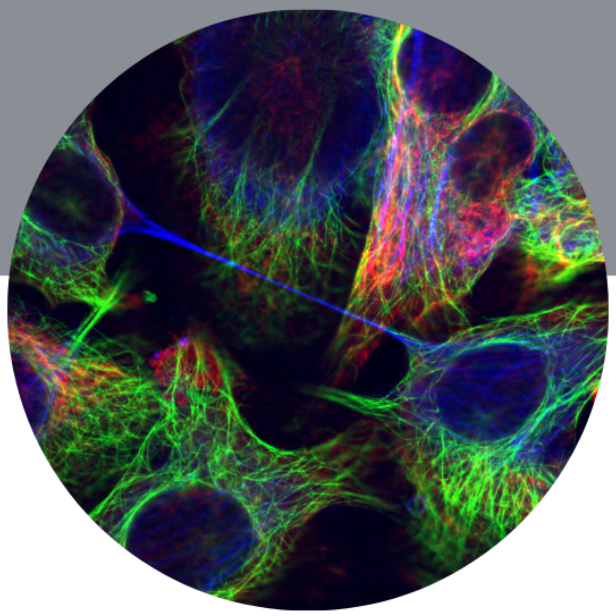
Založnik: Slovensko društvo za mikroskopijo / Slovene Society for Microscopy [publisher]

Ljubljana, 2025

https://17mcm.si/

CIP- Kataložni zapis o publikaciji
Narodna in univerzitetna knjižnica, Ljubljana

17th Multinational Congress on Microscopy: book of abstract: 7.-12. September 2025, Portorož / urednik Kristina Žagar Soderžnik… [et al.]. spletni vir – Ljubljana: Slovensko društvo za mikroskopijo, 2025
ISBN 978-961-94264-4-9
COBISS.SI-ID 247005187



17th Multinational Congress on Microscopy

17MCM

Portorož, Slovenia

7 - 12 September, 2025

Book of Abstracts

Editors:

Kristina Žagar Soderžnik, Rok Kostanjšek, Barbara Šetina Batič, Polona Mrak, Nada Žnidaršič, Samo Hudoklin, Blaž Belec, Sašo Šturm, Miran Čeh, Elena Tchernychova, Melanija Hadolin

Publisher:

Slovene Society for Microscopy

Sponsors and exhibitors

Sponsors

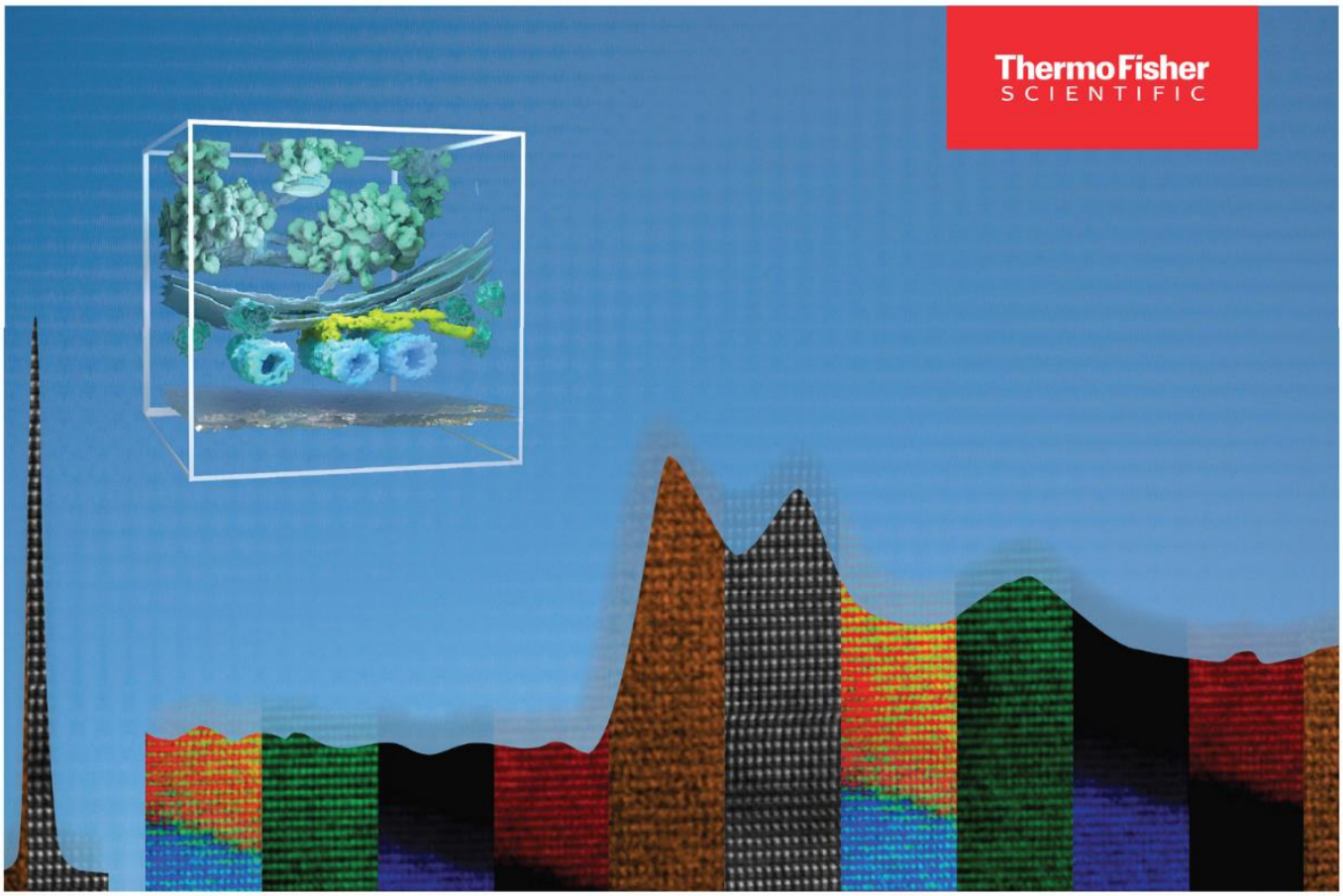


Exhibitors



Content

Plenary lectures	1
IM1 Spectroscopy and hyperspectral imaging of hard and soft matter	11
IM2 Innovations and synergies in correlative microscopy	32
IM3 Quantitative imaging in SEM/STEM, electron diffraction, 4D-STEM and ptychography	44
IM4 Advances in single particle analysis (SPA) and cryo-electron microscopy	69
IM5 Development of sample preparation methods, instrumentation, workflows, and data solutions for volume electron microscopy	79
IM6 Electron optics and beam shaping for electron microscopy	91
IM7 In-situ and environmental microscopy	104
IM8 Machine learning and data analysis in microscopy: advances and open-source solutions	115
LS1 Advances in multiscale fluorescence imaging and image processing	136
LS2 Volume electron microscopy in life sciences and tissue engineering	147
LS3 Structure and function of cells and organelles	160
LS4 Microscopy in pathology and regenerative medicine	196
LS5 Cell dynamics and high-resolution fluorescence microscopy	235
LS6 From a whole organism to sub-cellular imaging: correlative microscopy and multimodal imaging	246
LS7 Advances in sample preparation in biomedical research and beyond	268
LS8 3D functional imaging of materials and biological samples	282
MS1 Ceramics, ceramic composites and geological materials	300
MS2 Polymers, soft, and organic materials	336
MS3 Metals and alloys	347
MS4 0D, 1D and 2D materials	380
MS5 Magnetic, ferroelectric, and spintronic materials	407
MS6 Thin films, heterostructures, coatings, surfaces and interface	428
MS7 Advanced materials for energy storage and conversion	479
MS8 Advanced functional materials	506
Exhibitor presentations	525
IMPRESS Special session	539
Lunch workshops	562
Index of Authors	570



From cryo-tomography to (S)TEM EELS

Visit our booth to discover how transformative advances in electron microscopy for biology and materials science can accelerate your research.

Learn more at **thermofisher.com/electronmicroscopy**

thermo scientific

For research use only. Not for use in diagnostic procedures. For current certifications, visit thermofisher.com/certifications
© 2025 Thermo Fisher Scientific Inc. All rights reserved. All trademarks are the property of Thermo Fisher Scientific and its subsidiaries unless otherwise specified.

Plenary lectures

Type of presentation: Plenary

Microscopy-based analysis of biomimetic 2D and 3D *in vitro* models for preclinical studies

Mateja Erdani Kreft[a], Aleksandar Janev[a], Larisa Tratnjek[a], Urška Dragin Jerman[a], Nataša Resnik[a], Tadeja Kuret[a], Daša Zupančič[a], Taja Železnik Ramuta[a], Tanja Višnjar[a], Uroš Cerkvenik[a], Luka Predojević[b], Marjanca Starčič Erjavec[b], Gaja Markovič[a], Žiga Sardoč[a], Alen Punčuh[a], Eva Boc[a], Mark Grm[a], Andreja Erman[a], Samo Hudoklin[a], Rok Romih[a], Peter Veranič[a]

[a]*Institute of Cell Biology, Faculty of Medicine, University of Ljubljana, Slovenia*

[b]*Department of Biology, Biotechnical Faculty, University of Ljubljana, Slovenia*

Contact email: mateja.erdani@mf.uni-lj.si

Introduction: Biomimetic 2D and 3D *in vitro* models are indispensable tools for investigating tissue physiology and pathology [1–18], offering reliable, reproducible, and ethically acceptable alternative to animal models. In urology, such models are particularly relevant for studying bladder cancer [5–14] as well as bacterial [15, 16] and interstitial cystitis [17, 18]. Microscopy-based approaches are essential for validating the architecture of *in vitro* models, characterising their structural and molecular features, and investigating key mechanisms involved in disease progression, drug action, and intercellular communication.

Methods: We employed a variety of microscopy approaches, including light and electron microscopy, correlative microscopy, freeze-fracture replica immunolabelling and live-cell imaging, and 3D reconstruction techniques to assess the structural and functional properties of biomimetic *in vitro* models [1–18]. *In vitro* models were constructed using normal human, porcine, or mouse urinary bladder epithelial (urothelial) cells, as well as non-invasive papilloma and muscle-invasive cancer urothelial cells. The models were exposed to various conditions to assess their relevance to bladder cancer pathology, or were subjected to uropathogenic bacteria, oxidative stress, and inflammatory stimuli to mimic disease states such as bacterial and interstitial cystitis. To enhance biomimicry and explore the therapeutic potential of the human amniotic membrane (hAM), we either incorporated hAM into the models as a biological scaffold or applied hAM-derived preparations for therapeutic testing.

Results: Biomimetic *in vitro* models successfully recapitulated the key characteristics of human urothelium, including cellular organisation, barrier integrity, and disease-specific responses. In interstitial cystitis *in vitro* model, hAM treatment significantly reduced inflammation and oxidative stress while promoting epithelial differentiation and restoring tight junction integrity. Bladder cancer *in vitro* models revealed a potential role for tunnelling nanotubes in facilitating intercellular communication between cancerous and normal urothelial cells, potentially contributing to the spread and recurrence of the disease. Additionally, hAM demonstrated regenerative potential for the normal urothelium and showed promise as an antimicrobial and anticancer agent.

Discussion and Conclusions: By integrating advanced microscopy techniques, we demonstrated that 2D and 3D in vitro models can mimic both normal and diseased human tissue architecture. This approach highlights the essential role of combining tissue engineering with advanced microscopy techniques in preclinical research, enabling in-depth analysis of disease mechanisms and the evaluation of potential therapies.

References:

[1] M. E. Kreft et al., *Biol Cell* **2010**, 102(11), 593-607
[2] T. Višnjar et al., *Histochem Cell Biol* **2012**, 137(2), 177–86
[3] M. E. Kreft, H. Robenek, *PLoS One* **2012**,7(6), e38509
[4] U. D. Jerman et al., *Tissue Eng Part C Methods* **2014**, 20(4), 317–27

[5] T. Višnjar et al., *Sci Rep* **2017**, 7(1), 12842
[6] T. Ž. Ramuta et al., *Cell Transplant* **2018**, 27(1), 77–92
[7] M. E. Kreft et al., *Histochem Cell Biol* **2022**, 158(3), 229–240
[8] A. Janev et al., *Front Bioeng Biotechnol* **2021**, 9, 690358
[9] U. D. Jerman et al., *Int J Mol Sci* **2021**, 22(11), 5565
[10] N. Resnik et al., *Front Cell Dev Biol* **2022**, 10, 934684
[11] T. Potrč et al., *Nanoscale* **2023**,15(19), 8611-8618
[12] A. Janev et al., *Sci Rep* **2023**,13(1), 19227
[13] T. Kuret et al., *Sci Rep* **2025**, 15(1), 12975
[14] G. Markovič et al., *Radiol Oncol* **2025** (*in press)*
[15] T. Ž. Ramuta et al., *Biomedicines* **2021**, 9(2), 218
[16] L. Predojević et al., *Microorganisms*. **2022**, 10(4), 783
[17] T. Kuret et al., *Front Immunol* **2022**, 13, 960667
[18] T. Kuret et al., *Front Immunol* **2025 (***under revision)*

Type of presentation: Plenary

Atomistic structure of interfaces: Where theory and experiment meet

Aleksander Rečnik[a]

Vesna Ribić[a], Vanja Jordan[a], Sandra Drev[a], Matej Komelj[a]

[a]*Department for Nanostructured Materials, Jožef Stefan Institute (Ljubljana), Slovenia*

Contact email: aleksander.recnik@ijs.si

Introduction. Electron microscopy is a prime tool for studying interfaces in materials. With integrated diffraction, imaging and spectroscopy methods it provides direct insight into the translation state, local reconstruction, presence of foreign atomic species and bonding at and across the interfaces. Complete 3D information on the interface structure with dopant distributions can be obtained at the atomic scale when an interface is examined from complementary projections. With the advancements in technology the ability for microscope–assisted probing of different physical aspects of interfaces is growing and providing a valuable data for material's design. Beyond experimental possibilities, theoretical *ab initio* calculations, on the other hand, are becoming a powerful tool capable of predicting and reproducing experimentally observed non–periodic features, such as interfaces, at even a greater detail. In this talk we show how electron microscopy–based structure data can be leveraged and enhanced with quantum–chemical calculations to extract quantum–level structural properties directly from interfaces.

Materials and methods. Different synthetic and natural samples were used in the study of interfaces. Samples with perfectly coherent and pure interfaces, coherent interfaces with foreign elements, and fully incoherent and impure interfaces are used to demonstrate the power of combined theoretical and experimental methods in solving interface structures. From the experimental part, electron diffraction and high–resolution transmission electron microscopy (HRTEM) in complementary projections were used to identify a translation state of crystals across the interface. This provides the first and the most essential piece of information for structure design. Each interface is then studied by atomic–resolution imaging and spectroscopy methods basically including annular bright–field (ABF), high–angle annular dark–field (HAADF) scanning transmission electron microscopy (STEM), HRTEM, electron energy–loss spectroscopy (EELS) and energy–dispersive x–ray spectroscopy (EDS). All experimental data is gathered and used to reconstruct atomistic model of the interface. The model is tested through image simulations in different crystallographic projections to confirm whether all structural elements indeed correspond to observations. Any experimental detail is helpful in order to reduce the number of model variants for quantum–chemical calculations. Experimentally based interface models are then designed for *ab initio* calculations. For this purpose, the models must be constructed as periodic [1]. The basic structure optimization approaches involve force–field calculations and density functional theory (DFT) calculations where experiment–based interface structures are relaxed to their thermodynamically stable states. Total energies can be used for comparison of interface stability in case of multiple variants. The obtained models can then be used to predict various physical properties of studied interfaces, including which interface would from spontaneously under specific growth conditions [2].

Results. Examples, starting from simple deformation twins in mineral aragonite ($CaCO_3$), chemically induced twins in chrysoberyl (Be_2AlO_4) and spinel (Mg_2AlO_4), inversion boundaries in doped ZnO, to incoherent interfaces observed in hydrothermally grown rutile (TiO_2) will be presented to demonstrate the broad applicability of the combined experimental and theoretical approach in interface studies. The case studies demonstrated here make a bridge between two scientific communities, theoreticians and experimentalists, to work hand in hand in solving fundamental materials science problems.

Superstructure reflections or diffraction artifacts? In TEM, electron diffraction is the primary tool for phase identification. However, we often observe diffraction conditions that are not permitted by the space group and complicate phase interpretation. These effects are result of dynamic scattering, which ignites certain forbidden reflections. Moreover, in some materials, we observe additional reflections, that appear as superstructure reflections. These are the result of the so–called double diffraction that

may occur when the object contains overlapping epitaxial or twin domains. In such case the diffracted beams from upper domain act as incident beam for lower domain. Depending on lattice superposition, this can generate false diffraction conditions, much like superstructure reflections. Thus an utmost care must be taken when interpreting such diffraction patterns. The main obstacle to quantify these effects is that the inclined interfaces, which generate double diffraction are nonperiodic objects that can not be directly used in continuum–based calculations, and thus the simulation of dynamic scattering through inclined interfaces is not possible. Using a practical example of polysynthetically twinned aragonite we demonstrate a novel method that works around this problem and makes the simulation of dynamic double diffraction possible for any given crystallographic projection. The method is useful for advance calculations of diffraction patterns that may experimentally be observed.

Where to put the atoms? Our next example is demonstration how quantum–chemical calculations can be employed to fully resolve the atomistic structure of an interface where the translation between bulk crystals is known. This is often the case with lower cost–range microscopes having a lesser resolution. Here we demonstrate how conventional 200 kV Jeol 2100 TEM equipped with thermoionic source of electrons with a point–to–point resolution of 0.19 nm can be used to solve the twin boundary structure in chrysoberyl. Owing to light elements the material behaves as a weak phase object up to reasonable thickness so that translation state could be identified. But not the interface. With the use of atomistic modeling and DFT structure refinement local arrangement of Be atoms could be projected, and twin structure, that could not be reconstructed based on coarse contrast features, was solved [1].

What is missing? Sometimes chemistry of interfaces is not that trivial as it seems at first glance. This is shown on the example of twins in natural spinel. Through careful examination of lattice images and composition of twin boundary, using Jeol 2010F microscope, it appeared that Mg atoms that should be present on interfacial tetrahedral sites were missing. The question arose whether the sites are empty, or occupied by something so light that can not be detected. Empty sites could be excluded as they would generate an extreme charge balance problem, and such an interface would not be stable. On the other hand, a light element, such as Be, would be a good candidate for multiple reasons. According to DFT calculations Be generates a more stable twin interface than Mg, it elegantly solves the apparent charge balance problem, and is common in the *hcp* sequences of taaffeite (Be, Mg) polytypes. A speculative conclusion [2] was soon supported by the synthesis of spinel twins with the addition of BeO [3], and a decade later, we have been able to detect and image Be on spinel twin using HAADF–STEM by a new Jeol ARM. This study demonstrates how can we overcome the gap and use the old–time microscopes with the impaired resolution capability, supported by crystal chemistry–based structure modeling and quantum–chemical calculations to predict a yet unobserved structural feature from the interface.

So many variants, what is the most stable one? The next example demonstrates the power of quantum–chemical calculations to predict most stable interface structures. In the original quantitative HRTEM study of Sb–doped inversion boundaries (IBs) in ZnO a local stacking of Aβ−Bα−AβC−γA−αC (IB_2) was identified in two crystallographic projections [4]. However, contrary to experimental observation, DFT screening of IB stacking variants constructed on known stacking faults in originating wurtzite structure indicated that the model with Aβ−Bα−AβC−γB−βC stacking (IB_3) should be the most stable one for Sb–doping [5], and not the one reported in the originating study. Does the new structure exist, are DFT calculations wrong? These are the questions that will be answered in the presentation.

What makes it shifted? With the advancement in microscopy resolution and associated techniques, our boundaries move further into the unknown. In our study of hydrothermal growth of rutile TiO_2 under acidic conditions we discovered unusual shifts between the fibers. For long time there was no answer for this unnatural behavior that makes the adjacent fibers alternatively stretched and compressed under some hidden force. Weak contrast features in the inter–fiber space resolved in HAADF–STEM images suggested the presence of some molecular species that could be responsible for this phenomenon. DFT calculations showed that when water is placed between non–shifted fibers nothing happens, but when it is placed in shifted inter–fiber space, as observed in our samples, it immediately dissociates! So, the water is the hidden force that made the unusual shifts between the fibers [6].

References: [1] Drev *et al.* (2015) Am Mineralogist **100**/4. [2] Daneu *et al*. (2007) Phys Chem Min **34**. [3] Drev *et al*. (2013) CrystEngComm **15**. [4] Rečnik *et al*. (2001) J Am Ceram Soc **84**/11. [5] Ribić *et al*. (2020) Acta Materialia **199**. [6] Ribić *et al*. (2024) Advanced Materials **36**/4.

Type of presentation: Plenary

Bridging structure and function: Advancing CLEM workflows for organelle-level imaging

Judith Klumperman[a]

[a]*Center for Molecular Medicine, University Medical Center Utrecht, The Netherlands*

Contact email: j.klumperman@umcutrecht.nl

Fluorescence microscopy (FM) enables rapid navigation through biological samples and offers a highly sensitive toolkit for functional imaging and protein localization. Electron microscopy (EM), in turn, provides ultrastructural detail, revealing critical structural context. Correlative Light and Electron Microscopy (CLEM) merges these strengths of FM and EM into a powerful imaging approach that integrates molecular function and form at the single-cell or organelle level. As the application of CLEM grows, new methods are emerging worldwide to enhance its accuracy, sensitivity, and throughput. Our lab focuses on advancing CLEM methodologies through optimized sample preparation, as well as collaborative development of hardware and software tools. Biologically, we are interested in the endo-lysosomal system and its roles in health and disease, to which we apply our CLEM pipelines.

One of our CLEM pipelines is based on immuno-EM, using ultrathin cryosections (Tokuyasu method), in which sections are labeled with both fluorescent and gold-conjugated antibodies. These are sequentially imaged by FM and transmission EM. This "on-section" CLEM approach is ideal for identifying rare events ("needle in a haystack") in complex biological systems and for assigning ultrastructural context to fluorescent signals. By increasing the precision of on-section FM–EM correlation, we enabled to use fluorescence alone to locate structures in EM—even for targets such as lipids, for which no direct EM probes exist. By increasing the throughput of on-section CLEM, we facilitated correlation of hundreds of fluorescent signals within a single sample, allowing quantitative localization studies of a wide diversity of molecular targets.

A second CLEM pipeline allows for integrating live-cell imaging with EM. Because EM requires chemical fixation, dynamic processes observed by FM are typically studied in different samples than those used for EM. Consequently, our understanding of organelles is based on averages of dynamic data (by FM) and averages of ultrastructural data (by EM), without direct correlation between these data sets. To bridge this gap, we developed a live-cell CLEM method that enables tracking of individual organelles from live imaging through volume-EM approaches such as focused ion beam scanning EM (FIB-SEM) and array tomography. This allows direct correlation of dynamic behavior, molecular identity, ultrastructure, and spatial context of single organelles.

Our current work focuses on advancing volume-EM techniques for CLEM. In my presentation, I will provide an overview of the CLEM methodologies developed in our lab and illustrate these with examples from our own research, as well as collaborative projects.

Type of presentation: Plenary

Electron wave shaping and its applications from ghost imaging and ptychography to quantum state tomography

Vincenzo Grillo[a]

[a]*CNR-NANO, Modena, Italy*

Contact email: Vincenzo.grillo@nano.cnr.it

BACKGROUND AND AIMS

It has been 15 years since the first idea of electron vortex beam and beam shaping has been put forward. From static holograms to electrostatic tuneable and programmable phase plates, it has been a long journey with different improvement and problem solving. In this presentation I will review the ideas for beam shaping and the challenge into bringing toward applications.
These include new imaging modes inspired by light optics that join ptychography and computational ghost imaging. I will further show a new imaging ideas based on the first lock-in modulation of the beam and that can give us access to new quantities like vertical magnetic field or frequency enhanced imaging.
However, to me the most important success of beam shaping is the creation of the first Orbital Angular Momentum spectrometer. I and my group have recently shown the possibility to do the first OAM-resolved EELS spectroscopy (OAM_EELS) of core atomic transitions.
Using this as a tool I can demonstrate quantum state tomography that is recovering the density matrix of the scattered electron through many projective measurements, a cornerstone of quantum optics and metrology.
The angular momentum basis or reduced dimensionality conditions (systematic beam) can help us to carry out quantum state tomography of inelastic scattering in a relatively compact way while still maintaining all the advantages with respect to traditional EELS spectroscopy.
As a conclusion and prospect, I will discuss "quantum post-selection" based on controlled beam shaping and entanglement as this will enable to create new excitation state of a materials.

METHODS

Figure a-d shows the instruments of beam shaping advancements: a) innovative MEMS design b) OAM sorter configuration c) example of OAM EELS result d) example of on bord circuitry on MEMS.

RESULTS

In Figure e-g I show some of the most recent results like e) computational ghost imaging reconstruction now including also some input from ptychography f) Density matrix reconstruction in the OAM basis. g) lock-in differential imaging. This imaging depending on the applied MEMS can be found to enhance a particular bandpass frequency but also to be useful in magnetic measurements.

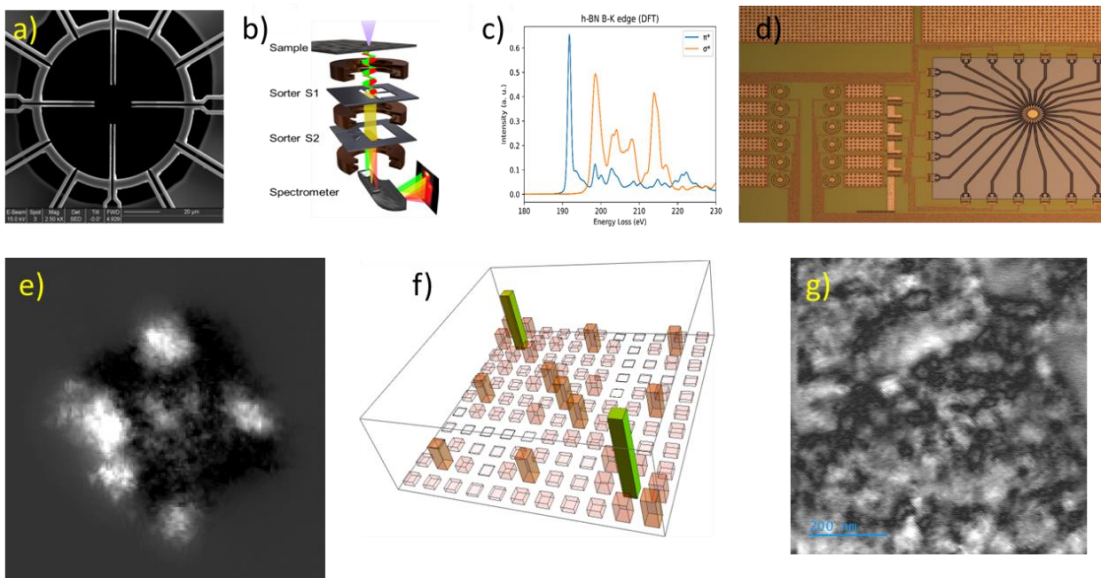


Figure 1: Methods of beam shaping: a) MEMS technology b) OAM-sorter spectroscopy configuration c) example of OAM EELS spectra d) On board electronics. Results: e) example of computational ghost image reconstruction f) example of density matrix reconstruction g) example of lock-in based differential beam shaping

CONCLUSIONS

The beam shaping is still a work in progress but permits to innovate imaging and complement the most advanced idea in microscopy. I believe that Quantum state tomography will be in future the method of electron to better extract EELS information of complex systems.

References

[1] Tavabi, A.H., Rosi, P., Bertoni, G. et al. Demonstration of angular-momentum-resolved electron energy-loss spectroscopy. Nat Commun **16**, 6601 (2025)

Type of presentation: Plenary

Enterovirus genome release and delivery

Pavel Plevka[a], Aygul Ishemgulova[a], Liya Mukhamedova[a], Zuzana Trebichalská[a], Lenka Šmerdová[a], Dominik Hrebík[a], David Buchta[a], Karel Škubník[a], Tibor Füzik[a], Jiří Nováček[a]

[a]*CEITEC, Masaryk University, Brno, Czech Republic*

Contact email: pavel.plevka@ceitec.muni.cz

Enteroviruses, the causative agents of diseases ranging from the common cold to poliomyelitis, are one of the largest groups of non-enveloped viruses. To initiate infection, most enteroviruses enter cells by receptor-mediated endocytosis. However, it remains unknown how enterovirus particles release their genomes and ensure that the virus RNA reaches the cytoplasm. We show that the expansion of enterovirus RNA genomes, induced by acidic pH in endosomes, triggers the opening of enterovirus particles. The exit of the RNA from the enterovirus particle results in a loss of a few adjacent capsid-protein pentamers. The opening in the capsid, which is more than 120 Å in diameter, enables the release of the genome without the need to unwind its putative double-stranded RNA segments. Furthermore, we used cryo-electron tomography of infected cells to show that endosomes containing enteroviruses deform, break open, and release the virus particles into the cytoplasm. Endocytosis of very-low-density lipoprotein, the natural substrate of rhinovirus 2 receptor, results in disruption of endosomes similar to that of enterovirus-containing endosomes. In combination, our results show that enterovirus receptor binding and endocytosis activate a cellular membrane remodelling pathway that disrupts the virus-containing endosomes and thus releases the virus particles and genomes into the cytoplasm.

IM1 Spectroscopy and hyperspectral imaging of hard and soft matter

Type of presentation: Invited

IM1-IN-1 Beyond phonon spectroscopy: recent advances in high-resolution electron energy-loss spectroscopy

Quentin Ramasse[a,b], Demie Kepaptsoglou[a,c]

[a]*SuperSTEM Laboratory, (Daresbury), United Kingdom*

[b]*Schools of Chemical and Process Engineering & Physics and Astronomy, University of Leeds, (Leeds), United Kingdom*

[c]*School of Physics, Engineering and Technology, University of York, (York), United Kingdom*

Contact email: qmramasse@superstem.org

By pushing the energy resolution of state-of-the-art scanning transmission electron microscopes (STEMs) below 10meV while maintaining atomic-sized probes, and in combination with a step change in detection technology, the chemical and electronic structure of a wide range of materials systems can be directly determined with unprecedented detail, across the energy scale from the core-loss to the vibrational spectroscopy regimes. Phonons can now be routinely studied at atomic resolution [1], along with their momentum-space dispersion [2], and related to local atomic structure and chemistry, for instance leading to insights into thermal transport in thermoelectric oxides, as will be shown here in the case of Nb and Al-doped TiO_2 'thick' films, which exhibit peculiar crystallographic-shear structures, line defects which are thought to contribute to the exceptional thermoelectric behaviour of these materials [3,4]. All experiments were carried out using a monochromated Nion UltraSTEM MC at 60kV acceleration voltage. The instrument is equipped with an ultra-high-resolution ground-potential monochromator, a Nion IRIS spectrometer and a Dectris ELA hybrid-pixel detector for EELS, and can routinely reach energy resolutions of 7meV or better.

There are now early theoretical and experimental hints that beyond phonon spectroscopy, excitations such as magnons, the periodic oscillations of the spin of charge carriers in ferro- and antiferro-magnets, can be detected in the STEM, perhaps even at atomic resolution [5]. Magnons occupy the same meV-range spectral window as phonons. The promise of detecting magnons spectroscopically in a STEM, and to follow the phonon spectroscopy blueprint towards studies of their dispersion and their atomic-scale modifications, is therefore tantalizing. With spin-based architectures becoming a cornerstone of quantum technology, studying magnons at the nanoscale is a key challenge for spintronics. Here, we show that bulk THz magnons can be excited and detected at the nanoscale using STEM [6]. We demonstrate nanoscale momentum-resolved measurements on (anti-)ferromagnetic materials (NiO and yttrium iron garnet, YIG). The experiments reveal the unambiguous signature of magnons in NiO (Figure 1), and magnon-polaron bands in YIG. The experiments are in excellent agreement with theoretical EELS calculations using parameters that reflect the experimental conditions, particularly the sample temperature, and magnetic environment.

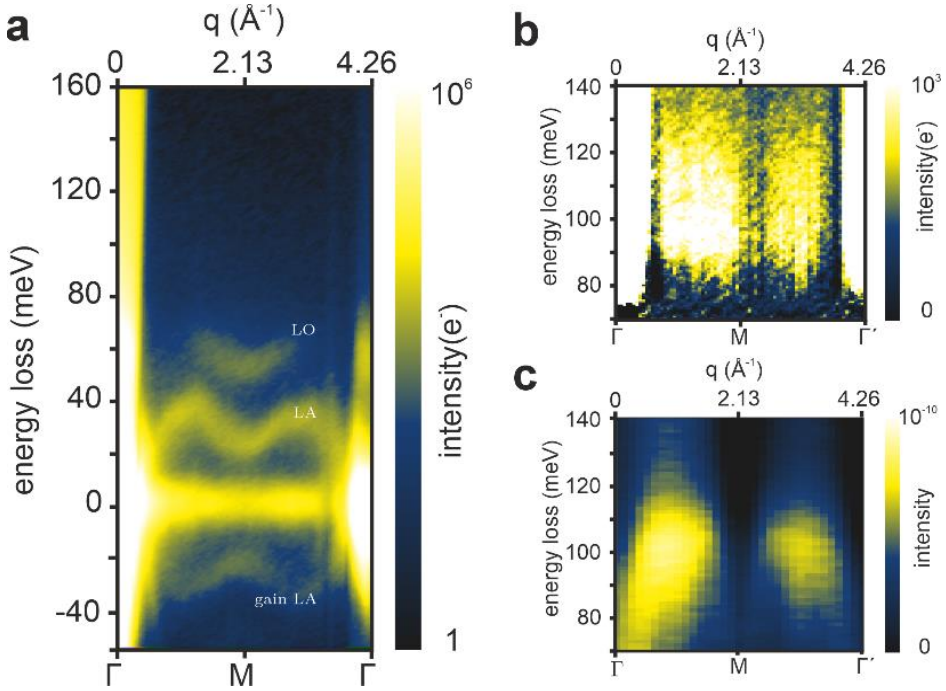


Figure 1: **a.** ω-**q** EELS map along the Γ → M **q**-path of NiO, showing the dispersion of the NiO LA / LO phonon branches, as well as the LA gain branch. **b** Experimental background-subtracted and **c** calculated ω-**q** EELS maps showing the dispersion of the magnon bands (adapted from [6]).

References:

1. F.S. Hage *et al.*, *Science* **2020**, 367, 1124-1127.
2. F.S. Hage *et al.*, *Science* **2018**, 4, eaar7495.
3. X. Liu *et al.*, *ACS Appl. Mater. Interfaces* **2021**, 13, 57326-57340.
4. X. Liu *et al.*, *ACS Appl. Mater. Interfaces* **2023**, 15, 5071-5085.
5. K. Lyon *et al.*, *Phys. Rev. B* **2021**, 104, 214418.
6. D. Kepaptsoglou *et al.*, *Submitted* **2025**, https://arxiv.org/abs/2410.02908v4.

Type of presentation: Invited

IM1-IN-2 Recent advances in STEM spectroscopy using synchronized electron and photon beams

Odile Stephan[a], Yves Auad[a], Florian Castioni[a], Malo Bezard[b], Heyu Wang[a], Xiaoyan Li[a], Jean-Denis Blazit[a], Luiz Tizei[a], Mathieu Kociak[a]

[a]*Universite Paris-Saclay-CNRS, France*

[b]*Sorbonne Universite-CNRS, France*

Contact email: odile.stephan@universite-paris-saclay.fr

The field of nano-optics using free electron beams in an electron microscope is blooming, with applications from plasmons, phonons or excitons mapping at near atomic resolution, to quantum optics. These results have been boosted by constant disruptions in EM technology – monochromation, fs sources of pulsed electrons, high efficiency light injection and detection system in the EM - and theory – introduction of optics or concepts of optics in the realm of EM, such as EMLDOS or quantum statistics, to name a few. In particular, the combination of free electrons and light has recently been utilized to achieve a remarkable level of simultaneous spatial and spectral resolution and for accessing new physical information. The new detectors such as the Timepix3 direct electron detector, which provides sub-10 ns time resolution, occur as real game changers. Event-based hyperspectral acquisition schemes [1] offer an alternative approach to pulsed electron beam technology for synchronizing photon and electron beams or conducting coincidence experiments.

We will present an overview of these recent developments.

- Firstly, we will discuss time-correlated experiments based on coincidence measurements between inelastic electron scattering and photon emission events. Cathodoluminescence excitation (CLE) spectra (so called as the counterpart to photoluminescence excitation (PLE) spectroscopy) are constructed with EELS events that are time-correlated with a photon emission [2]. Such measurements have been shown to provide a measure of the excitations' decay time [3]. Here, we will focus on polarized CLE experiments, which enable the selection of photon polarization states to investigate chirality and polarization effects at the nanometer scale in plasmonic nanostructures.

- Secondly, we will show how Electron Energy-Gain Spectroscopy that allies the spectral resolution of a pump laser to the spatial resolution of a free electrons beam is the perfect tool to probe photonic modes in high-quality factor photonic cavities, which cannot be resolved with common EM spectroscopic techniques. In such experiments, micro-eV spectral resolution is achieved to realize nanoscale mapping of photonic modes with quality factors as high as 10^4, relying on mode matching of a tightly focused laser beam to whispering gallery modes [4].

- Finally, we will present a novel pump−probe photon−electron method for mapping temperature dynamics with unprecedented spatial and temporal resolutions [5]. By combining focused laser-induced heating and synchronized time-resolved monochromated EELS, we will demonstrate the ability to follow temperature changes at the nanometer and nanosecond scales and how such an approach opens new opportunities for investigating transient thermal phenomena in nanoscale materials.

References:
[1] Y. Auad et al, Ultramicroscopy 239, 113539 (2022)
[2] N. Varkentina, Y. Auad, et al, Science Advances 8 (40), eabq4947
[3] N. Varkentina, Y. Auad, et al, Appl. Phys. Lett. 123, 223502 (2023).
[4] Y. Auad et al, Nature Comm. 14, 4442 (2023)
[5] F. Castioni et al., Nano Lett. 25, 1601 (2025)

Type of presentation: Oral

IM1-O-1 First demonstration of angular-momentum-resolved electron energy-loss spectroscopy

Giovanni Bertoni[a], Enzo Rotunno[a], Amir H. Tavabi[b], Paolo Rosi[a], Luca Belsito[c], Alberto Roncaglia[c], Stefano Frabboni[a], Gian Carlo Gazzadi[a], Ebrahim Karimi[d], Peter Tiemeijer[e], Rafal E. Dunin-Borkowski[b], Vincenzo Grillo[a]

[a]*Istituto Nanoscienze, CNR, (Modena), Italy*

[b]*ER-C, Forschungszentrum Jülich, (Jülich), Germany*

[c]*Istituto per lo Studio dei Materiali Nanostrutturati, CNR, (Bologna), Italy*

[d]*Department of Physics, University of Ottawa, (Ottawa), Canada*

[e]*Thermo Fisher Scientific, (Eindhoven), the Netherlands*

Contact email: giovanni.bertoni@cnr.it

Introduction: Rotational symmetry plays a fundamental role in determining selection rules for atomic transitions probed by electron energy-loss spectroscopy (EELS). In this study, we demonstrate the first experimental realization of orbital angular momentum-resolved EELS (OAM-EELS) using a transmission electron microscope (TEM) equipped with a custom-designed electrostatic OAM sorter [1]. The experiment focuses on the B K-edge of hexagonal boron nitride (h-BN), a system characterized by π* and σ* antibonding orbitals with distinct angular momentum projections. By coupling energy dispersion with OAM analysis, our approach allows direct access to the angular character of electronic transitions.

Methods: The experimental configuration utilizes a pair of electrostatic phase elements (S1 and S2) placed after the sample to perform a log-polar conformal transformation [2], converting the OAM phase into a measurable linear coordinate (Fig. 1a,b). A 300 kV TEM with a convergence semi-angle $\alpha = 5.4$ mrad was employed to minimize angular aberrations of the device. The resulting two-dimensional spectrum encodes both information of energy-loss on the horizontal axis and OAM on the vertical axis. To retrieve the intrinsic OAM spectral components $c_m(E)$, we performed a deconvolution of the point spread function (psf) derived from the zero-loss peak measured in vacuum, and incorporated a model-based MLLS fitting to obtain $I(E,\ell) = \sum_m c_m(E)\Gamma_m(\ell)$. The OAM profiles of the sorter $\Gamma_m(\ell)$ are modelled on 1s Bloch wave approximation for elastic propagation and by including inelastic scattering.

Results: The extracted 2D spectrum $I(E,m) = \sum_m c_m(E)$ (Fig. 1c) reveals distinct profiles for π* and σ* transitions with onset at ~192 eV and ~198 eV, respectively. The π* feature is centered at 0 ħ, while the σ* feature has maxima at ±1 ħ, in agreement with dipole selection rules (Fig. 1d,e). A comparison of our simplified model based on 1s Bloch wave approximation with multislice simulations confirms the role of delocalization in broadening the experimental OAM spectra $\Gamma_m(\ell)$. A Monte Carlo modelling of the inelastic scattering events demonstrates that off-axis atomic excitations contribute incoherently to $\Gamma_m(\ell)$ (Fig. 2a), leading to an intrinsic spread beyond the expected discrete values, and predicting a variance in the OAM profile $\sigma_\ell \geq \frac{\hbar}{2}\sqrt{1+\sigma_p^2/\sigma_x^2}$, depending on the probe and exit-wave function spatial extensions, well reproduced in the experiment (Fig. 2b).

Discussion and Conclusions: Our analysis shows that the observed OAM broadening stems principally from intrinsic delocalization of inelastic scattering and secondly on technological limitations in the current sorter fabrication. By estimating the OAM uncertainty, we quantitatively account for the spread in the OAM distribution $\Gamma_m(\ell)$. Further improvements in sorter design and optimization for large convergence will enhance spatial and angular resolution. Importantly, this technique enables post-selection of specific angular momentum channels, offering unprecedented access to symmetry-resolved spectroscopy at the nanoscale. Applications extend to orbital mapping, magnetic dichroism (EMCD)

[3], and multipolar transition analysis, potentially transforming our ability to interrogate local electronic structure with atomic resolution [4].

Acknowledgments: Supported by EU Horizon: IMPRESS (No. 101094299), ESTEEM3 (No. 823717), Q-SORT (No. 766970), SMART-electron (No. 964591), and Italian MUR IR0000027 iENTRANCE@ENL.

References:

1. Tavabi, A. H. et al. *Phys. Rev. Lett.* **2021,** 126, 094802.
2. McMorran, B. J. et al. *New J. Phys.* **2017**, 19, 023053.
3. Rotunno, E. et al. *Phys. Rev. B* **2019,** 100, 144416.
4. Submitted for publication, preprint: https://doi.org/10.21203/rs.3.rs-4606043/v1

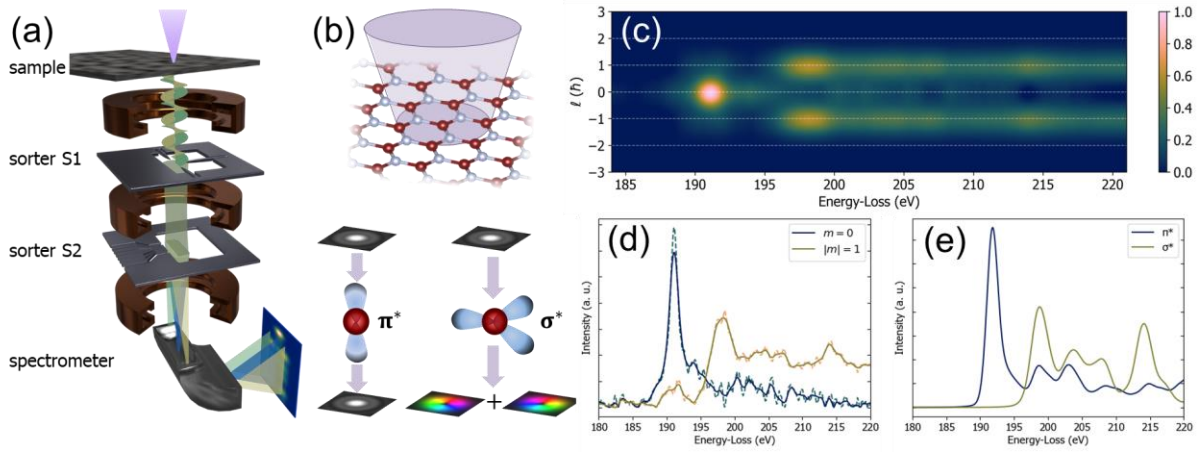


Figure 1: Experimental setup for OAM-EELS. (a) Schematic diagram to realize OAM-EELS double dispersion, (b) sketch of electron beam illumination on h-BN at $\alpha = 5.4$ mrad and the electron wavefunction after single scattering on boron, (c) experimental $I(E,m) = \sum_m c_m(E)$ after model-based fitting to remove delocalization and psf of the sorter, (d) experimental EEL spectra for $m = 0$ and $|m| = 1$ (dashed lines are raw results, full lines are smoothed curves), (e) corresponding spectra obtained from ab-initio DFT calculations.

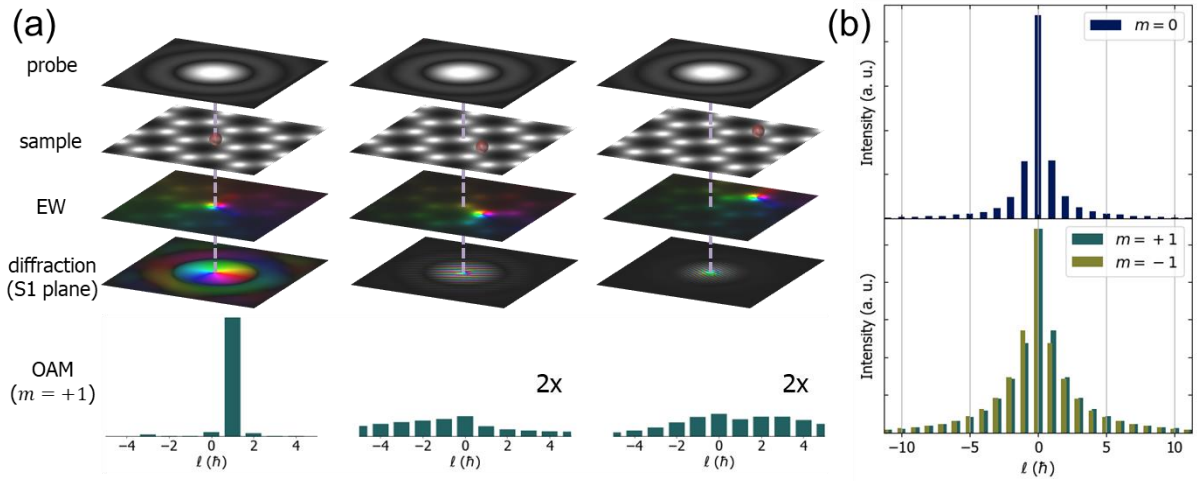


Figure 2: Numerical model for simulating scattering delocalization. (a) Effect of probe size and scattering delocalization for $m = +1$ for a B atom on the optical axis of the OAM sorter (left column) and for two B atoms off-axis. Each B atom in the illuminated area emits its own inelastically-scattered wave. In the far field, the phase of the off-axis atoms is distorted, (b) the OAM sorter records an incoherent sum of their contributions as seen in the simulated OAM profiles $\Gamma_m(\ell)$ for $m = 0$ and $m = \pm 1$ ($\alpha = 5.4$ mrad).

Type of presentation: Oral

IM1-O-2 Investigation of Electron Scattering in Ultrathin Films Using Time-of-Flight Spectroscopy

Ivo Konvalina[a], Aleš Paták[a], Lukáš Průcha[a], Jakub Piňos[a], Michal Štulpa[a], Tomáš Fořt[a], Ilona Müllerová[a], Eliška Materna Mikmeková[a]

[a]*Institute of Scientific Instruments of the Czech Academy of Sciences, (Brno), Czech Republic*

Contact email: konvalina@isibrno.cz

A detailed understanding of electron scattering mechanisms, especially at very-low energies, is essential for improving electron spectroscopy techniques and developing advanced materials for next-generation electronic devices. However, accurate inelastic mean free path (IMFP) data at lower energies remain scarce. In this study, we investigate electron scattering in ultrathin elemental films, focusing on transmission and reflection modes. Our approach combines experimental measurements using a newly developed time-of-flight (ToF) spectrometer [1] with computational methods based on density functional theory (DFT) simulations, which we have validated on a graphene sample [2].
The ToF spectrometer, integrated into an ultra-high vacuum scanning low-energy electron microscope (UHV SLEEM), enables imaging and acquisition of low-energy loss data. Measurements on nanometer-thin foils require precise sample preparation, which we achieve through chemical vapor deposition (CVD) of graphene followed by magnetron sputtering to create well-defined ultrathin foils. We compare experimental electron energy-loss spectra (EELS) obtained via ToF spectroscopy with theoretical energy-loss functions (ELFs) derived from DFT calculations.
Preliminary results on a 6 nm gold foil sample reveal the expected energy loss peaks at approximately 2.4 eV, attributed to the surface plasmon, and around 24 eV for the interband transitions. These findings demonstrate the potential of our combined experimental and computational approach to refine IMFP data and deepen our understanding of electron interactions in nanostructured materials.

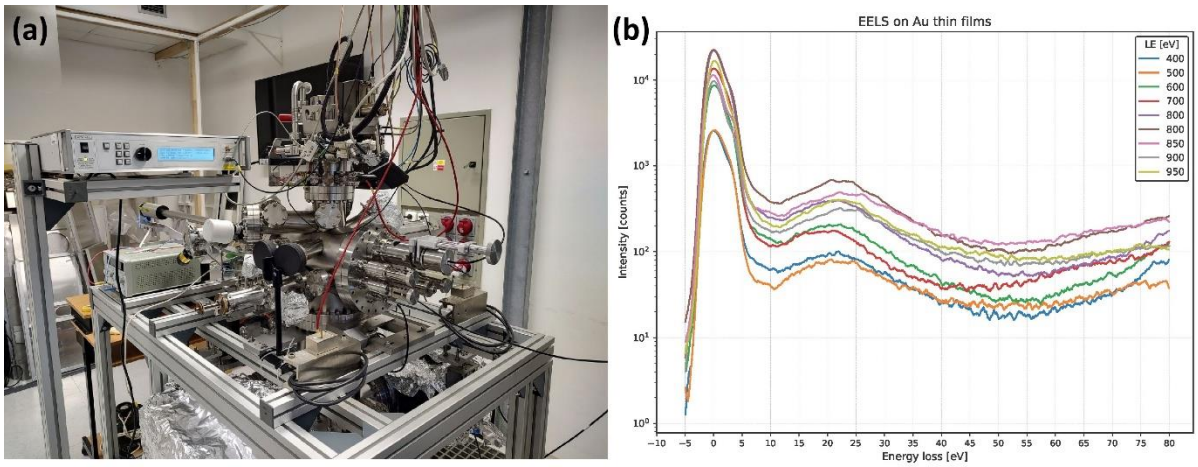


Figure 1: UHV SLEEM/ToF device (a), experimental EELS for an Au film (b).

Acknowledgement:
The research was supported by the Technology Agency of the Czech Republic, grant number TN02000020 together with institutional support RVO:68081731. With support of Strategy AV21, program Breakthrough Technologies for the Future – Sensing, Digitisation, Artificial Intelligence and Quantum Technologies.

References:

1. I. Konvalina, et al., *Nanomaterials* **2021**, 11, 2435
2. A. Paták, et al., *Phys. Rev. B* **2025**, 111, 125113

Type of presentation: Oral

IM1-O-3 Perspectives of ultrafast hyperspectral imaging in Scanning Electron Microscopy

Abbas Kosari Mehr[a,b], Erfan Afshnar[a,b], Madiha Khan[a,b], Ritik Tanwar[a,b], Mohamed Zaghloul[a,b], Wenzheng Cao[a,b], Anjam Khursheed[a], Silvia Maria Pietralunga[b,c], Alberto Tagliaferri[a,b]

[a]*Politecnico di Milano, (Milano), Italy*

[b]*Center for Nano Science and Technology - IIT, (Milano), Italy*

[c]*Istituto di Fotonica e Nanotecnologie, (Milano), Italy*

Contact email: alberto.tagliaferri@polimi.it

Scanning Electron Microscopy (SEM) is commonly associated with rapid and effective morphological imaging of bulk sample at nanoscale, which alone makes it a pervasive tool present in a large variety of experimental laboratories and all at once limits SEM's role to a complementary characterization tool. The last years mark the introduction in SEM of high performant energy selective filtering in the SEM's electron energy and time, with resolutions down to few meV and below ps. These advances have the potential to open bulky specimens and surface properties to analytical and dynamical imaging capabilities similar, and complementary, to what scanning and traditional TEM have already demonstrated for thin samples. SEM struggles however to demonstrate the hyperspectral imaging capabilities of electronic, structural and collective excitations imaging in nanostructured devices and bulky specimens that may be expected from these technical figures of merit.

In this talk, I will comment on the perspectives of the novel hyperspectral and dynamical imaging capabilities appearing in the SEM scenario, based on experimental results in recent years. I will then discuss possible approaches to merge in a multidimensional SEM microscopy some of the present frontier filtering capabilities: energy, time, and momentum. Several of these advanced filters can operate simultaneously in a tabletop SEM instrument, possibly in operando conditions. This approach has the potential of granting to small laboratories the nanoscale surface mapping of electronic band structure and collective phenomena into advanced materials and devices, which are presently tackled only at large scale facilities or by destructive approaches.

Type of presentation: Oral

IM1-O-4 Spin Resonance Spectroscopy meets Transmission Electron Microscopy

Philipp Haslinger[a]

[a]*Atominstitut, USTEM, TU Wien*

Contact email: Philipp.haslinger@tuwien.ac.at

Coherent spin resonance methods such as nuclear magnetic resonance and electron spin resonance spectroscopy have led to spectrally highly sensitive, non-invasive quantum imaging techniques. Here, we will present a spin resonance spectroscopy approach developed for transmission electron microscopy [1,2] and will explain different techniques to sense with electrons for microwave manipulated spin states of the sample. This could enable state-selective observation of spin dynamics on the nanoscale and indirect measurement of the environment of the spin systems, providing information on, for example, atomic structure, local chemical composition and neighbouring spins.

[1] P. Haslinger, S. Nimmrichter, and D. Rätzel, *Spin Resonance Spectroscopy with an Electron Microscope,* Quantum Sci. Technol. **9**, 035051 (2024).

[2] A. Jaroš, J. Toyfl, A. Pupić, B. Czasch, G. Boero, I. C. Bicket, and P. Haslinger, *Electron Spin Resonance Spectroscopy in a Transmission Electron Microscope,* arXiv:2408.16492 (2024).

Type of presentation: Poster

IM1-P-1 Cathodoluminescence spectroscopy study of plasmonic emissions in different Bi_2Se_3 systems

Blaž Belec[a], Thanveer Thajudheen[a], Sandra Gardonio[a], Mattia Fanetti[a], Matjaž Valant[a]

[a]*Materials Research Laboratory, University of Nova Gorica, Slovenia*

Contact email: blaz.belec@ung.si and mattia.fanetti@ung.si

Topological insulators (TIs), with Bi_2Se_3 as a representative, have attracted the attention of researchers as promising candidates for plasmonics in the UV-visible [1]. Investigating plasmonic effects at the nanoscale remains challenging due to the limitations of conventional optical and electron-based techniques, such as dark-field microscopy (DFM), near-field scanning optical microscopy (NSOM), and transmission electron microscopy coupled with electron energy loss spectroscopy (TEM-EELS). As a powerful alternative, cathodoluminescence (CL) spectroscopy in a scanning electron microscope (SEM) provides sub-particle spatial resolution while enabling direct correlation with morphological and compositional properties, making it an effective tool for exploring plasmonic phenomena in Bi_2Se_3-like systems [2,3]

In this study, we employ CL spectroscopy coupled with SEM to investigate emissions in various Bi_2Se_3 systems: pristine nanoparticles, coated nanoparticles, Cr-doped nanoparticles, and bulk Bi_2Se_3. Our findings reveal edge-localized emission in the visible range (~400 nm), independent of nanoparticle size, surface modifications, or chemical doping. Furthermore, this emission is also observed at the step edges of bulk Bi_2Se_3single-crystal. By ruling out alternative mechanisms such as bandgap transitions, excitons, and surface plasmons, we attribute this emission to wedge Dyakonov modes, arising from the hyperbolic optical nature of Bi_2Se_3. These results deepen our understanding of light-matter interactions in TI and highlight the potential of Bi_2Se_3systems for plasmonic and photonic applications [4].

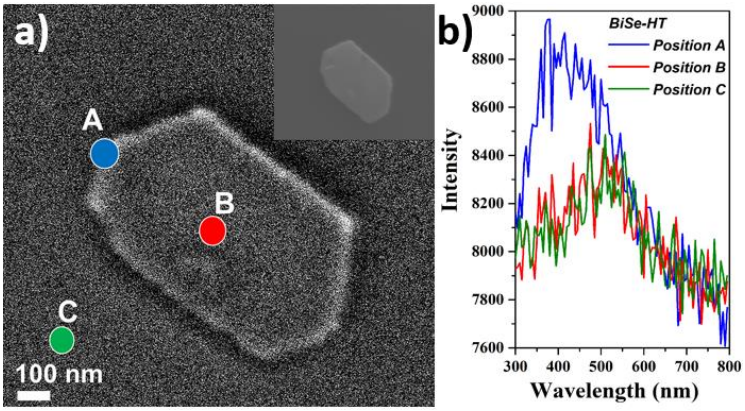


Figure 1: a) Panchromatic CL image with b) corresponding emission spectra obtained by positioning the incident beam on hydrothermally synthesized Bi_2Se_3 *(BiSe-HT)* nanoplatelet as indicated by the coloured dots in a).

References:

1. Ou, J.-Y.; So, J.-K.; Adamo, G.; Sulaev, A.; Wang, L.; Zheludev, N. I. Ultraviolet and Visible Range Plasmonics in the Topological Insulator Bi1.5Sb0.5Te1.8Se1.2. Nat Commun **2014**, 5 (1), 5139

2. Kociak, M.; Stephan, O. Mapping plasmons at the nanometer scale in an electron microscope, Chem. Soc. Rev. 2014, 43, 3865

3. Zhao, M, et al., Visible Surface Plasmon Modes in Single Bi_2Te_3 Nanoplate. Nano Lett., 2015, 15(12)

4. Thajudeen, T.; Belec, B.; Gardonio, S.; Fanetti, M.; Valant, M. Exploring plasmonic emission in Bi_2Se_3 cathodoluminescence spectroscopy, *March 2023, submitted*

Type of presentation: Poster

IM1-P-2 Low-energy Core-loss EELS as a Dose-effective Approach for Elemental and Oxidation State Mapping

Mario Pelaez-Fernandez[a,b,c], Daniel del-Pozo-Bueno[d,e], Maya Marinova[f], Adrien Teurtrie[a], Marta Estrader[e,g], Germán Salazar-Alvarez[h], Raul Arenal[b,c], Hugues Leroux[f], Francesca Peiró[d,e], Sonia Estradé[d,e], Francisco De la Peña[a]

[a]*Unité Matériaux et Transformations (UMET UMR 8207), U. Lille (Villeneuve d'Ascq), France*

[b]*Instituto de Nanociencia y Materiales de Aragon (INMA), CSIC-U. Zaragoza (Zaragoza), Spain*

[c]*Laboratorio de Microscopias Avanzadas, Universidad de Zaragoza (Zaragoza), Spain*

[d]*LENS-MIND, Departament d'Enginyeria Electrònica i Biomèdica, U. Barcelona (Barcelona), Spain*

[e]*Institute of Nanoscience and Nanotechnology (IN2UB), U. Barcelona (Barcelona), Spain*

[f]*Univ. Lille, FR 2638-IMEC-Institut Michel-Eugène Chevreul, F-59000 (Lille), France*

[g]*Department of Inorganic and Organic Chemistry,U. Barcelona (Barcelona), Spain*

[h]*Department of Material Science and Engineering, Ångström Lab, U. Uppsala (Uppsala), Sweden*

Contact email: mariopf@unizar.es

STEM-EELS ability for oxidation state quantification by analysing the fine structure of the elemental ionization edges has been [1] and continues to be [2] a pillar of EELS-related research. In the last decade, oxidation state mapping at the atomic level [3] has become common. Meanwhile, advances in data analysis have enabled 3D oxidation state mapping through tomographic reconstruction of EELS oxidation maps tilt-series [4].

To date, most methods of oxidation state analysis involve ionization edges with onset energies above 100 eV. For example, the standard method for iron oxidation state analysis is based on the fine structure of the Fe-$L_{2,3}$ ionization edges at ~708 eV. However, the small ionization cross-section of these ionization edges presents serious experimental challenges for beam-sensitive samples.

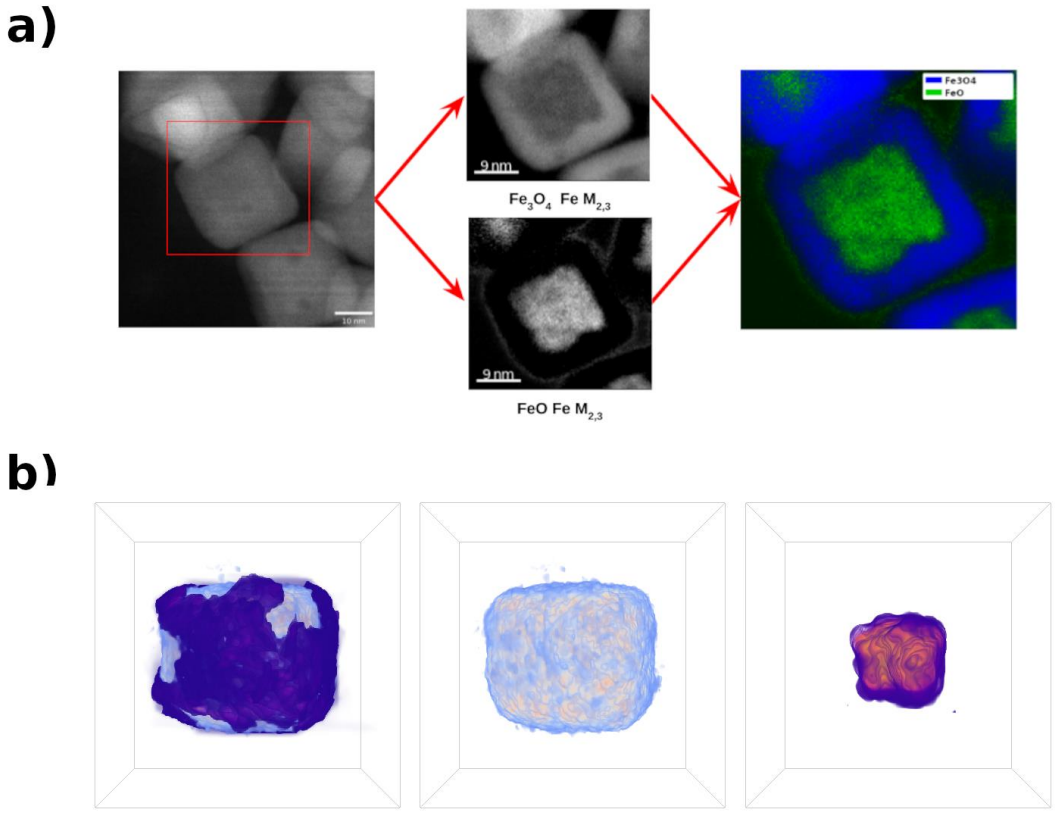
The recent development of Direct Electron Detectors (DEEs), much more sensitive than their traditional counterparts, has brought with it a new myriad of possibilities in both traditional microscopy and EELS. Within this context, the high dynamic range provided by these new detectors is being used to inquire into EELS edges that could not be properly exploited before.

While most of these novel EELS analyses focus on high- energy core-loss EELS edges, this work explores another possibility rendered by hybrid pixel DEEs: performing quantitative EELS analysis using the lower energies of core-loss edges, in other words, performing Low-Energy Core-Loss Electron Energy-Loss Spectroscopy (LE-CLEELS).

We demonstrate this approach by performing EELS-bonding tomography on previously studied beam-sensitive FeO/Fe_3O_4 core-shell nanocubes[4]. These tomographic EELS studies have exploited the Fe-$M_{2,3}$ ionization edges, situated at an energy of 54 eV.

EELS spectrum images were acquired on an FEI TITAN Themis 300 S/TEM with a dwell time of 1 ms and a pixel size ranging from 0.2 nm for single maps to 0.4 for tomography studies. EELS maps were taken at 9 different angles ranging from -70 to 70 degrees for these tomographic studies, and a four-dimensional datacube was created by stacking all diffeent spectrum images. The four-dimensional datacube was then analyzed using a combination of SVD decomposition, blind source separation, and curve fitting EELS quantification, using comparison maps between the Fe-$M_{2,3}$ edge and Fe-$L_{2,3}$ edges as a ground truth for the distribution of the different oxidation states and the calibration of the Fe-$M_{2,3}$ edges.

The results of our study (see Figure 1) demonstrate successful tomographic reconstruction enabled by the significantly enhanced signal-to-noise ratio (SNR) of the Fe-$M_{2,3}$ edges. Upon quantification, we found that an electron dose 50 times lower was required compared to the commonly used Fe-$L_{2,3}$ edges. Moreover, the improved SNR allowed us to achieve substantially higher resolution than in previous studies of these materials, enabling the mapping of a 1–2 nm-thick reduced layer at the very edge of our core–shell particles.



This work challenges the conventional notion that EELS is mostly suited to the chemical analysis of light elements. This also highlights the potential of LE-CLEELS for low- dose analysis, opening new possibilities for advanced materials characterization on beam-sensitive materials.

Figure 1: Results on the 2D and 3D mapping of the FeO and the Fe_3O_4 oxidation states in the Fe-$M_{2,3}$ EELS edges. a) Successful 2D mapping of the different oxidation states in a core-shell nanoparticle. b) tomographic reconstruction of the three different layers in the nanoparticle, from left to right: a reduced thin layer around the nanoparticle, the Fe_3O_4 shell and the FeO core.

Acknowledgments

MPF thanks the support of the Spanish Ministry for Science and Universities for its support via the "Ayudas para la recualificación del sistema universitario Margarita Salas".

References:

1. L. A. J. Garvie, P. R. Buseck, *Nature*, **1998**, 396, 667–670.
2. D. del-Pozo-Bueno, F. Peiró. S. Estradé, *Ultramicroscopy*, **2021**, 221, 113190.
3. A. Gloter *et al*, *Mater. Sci. Semicond. Process.*, **2017**, 65, 2–17.
4. P. Torruella *et al*, *Nano Lett.*, **2016**, 16, 5068–5073.

Type of presentation: Poster

IM1-P-3 Irradiation-induced point defects in optical fibers investigated by cathodoluminescence microscopy and spectroscopy

Mattia Fanetti[a], Antonino Alessi[b,c], Imene Reghioua[d,e] , Allan Travailleur[b], Sylvain Girard[d]

[a]*Univerza v Novi Gorici, 5270 Ajdovščina, Slovenia*

[b]*LSI, CEA/DRF/IRAMIS, CNRS, Ecole Polytechnique, Institut Polytechnique de Paris, 91128 Palaiseau, France*

[c]*Department of Physics and Chemistry Emilio Segré, University of Palermo, 90123 Palermo, Italy*

[d]*Laboratoire Hubert Curien, CNRS, Université Jean Monnet, 42000 St-Etienne, France*

[e]*current affiliation: STMICROELECTRONIS, 38920 Crolles, France*

Contact email: mattia.fanetti@ung.si

Silica-based optical fibers (OF) are widely exploited in telecommunication applications. When used in harsh radiation environment (e.g. in nuclear power plants, space, accelerators), the irradiation can affect the OF optical (transmission, emission) and structural properties. In fact, exposure to irradiation (either with high energy electrons, or UV, or X-rays, or γ-rays, or swift ions, etc.) may result in the generation of point defects in Silica, resulting in strong decrease or alteration of transmission properties (e.g. [1]). The identification of point defects, as well as the characterization of their concentration, distribution and irradiation-dependence is of crucial importance for an effective use of OF in harsh environment.

Cathodoluminescence (CL) spectro-microscopy, coupled with Scanning Electron Microscopy, is an effective tool to study the defect nature and distribution in OFs [2]. In fact, some of the defects in Silica have known emission peaks in the ultraviolet and visible ranges, such as Oxygen Deficient Center II (ODCII) at 4.4 eV and 2.7 eV, and Non-Bridging Oxygen Hole Center (NBOHC) at 1.91 eV. If a dopant is present, additional emission peaks are detectable, such as for example the Germanium Lone Pair Center (GLPC), which displays a peak at 3.1 eV in the Ge-doped silica. The advantage of CL investigation is the possibility of characterizing the emission spectra at a selected point with a lateral resolution of below 1 μm which is not possible by means of other standard spectroscopy techniques (e.g. photoluminescence). Moreover, when performed in a SEM apparatus, CL spectro-microscopy can be straightforwardly combined with SEM imaging and EDX spectroscopy, which allows the coupling of emission properties with morphology and compositional information (Fig.1).

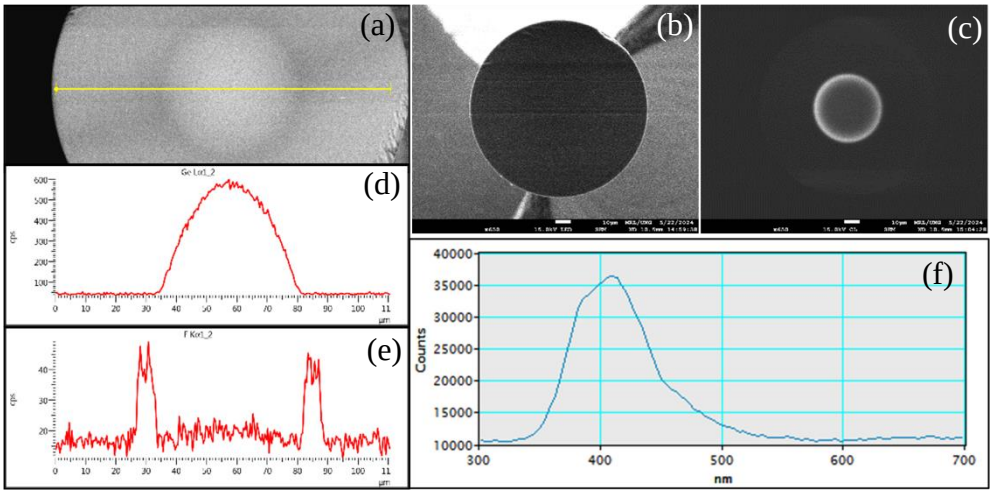


Figure 1: cross-sectioned multimode OF imaged with: back-scattered electrons (a), secondary electrons (b), cathodoluminescence panchromatic map (c), together with a CL spectrum acquired in the core (f). Below (a), the compositional EDX profiles of germanium (d) and fluorine (e).

Finally, the effect of the e-beam irradiation experienced by the OF during the CL measurement can be investigated by itself. Indeed, upon the 5-15 keV electron irradiation of typical CL measurement conditions, some point defects can be bleached, others can be generated, while others are not affected by this kind of irradiation. Based on these phenomena, the investigation of the kinetic of CL emission vs irradiation dose can provide further information on the defect's nature and role in the affecting the optical properties [3].

In this contribution, selected CL-based investigations applied to the characterization of point defects will be shown, in particular in cases where the defects are generated by ionizing radiation. Both pure-silica core and Ge-doped OFs have been irradiated with X-rays, γ-rays and electron, and the irradiation induced defects are characterized by CL and correlated with the transmission and optical properties.

Concerning Ge-doped fibers, pristine, UV and γ-irradiated specimens have been investigated by CL. UV and γ-irradiation modify the Ge defect density, which is not necessarily correlated with the Ge-doping concentration. Moreover, by controlled exposure to electron beam irradiation in the SEM apparatus, we could verify that the electron irradiation decreases the GLPC intensity (*bleaching*) [2]. The effect of Oxygen loading, which should decrease the density of GLPC, is also investigated [4].

Regarding pure-silica core OFs, the investigation aims in identifying the defect(s) responsible for the significant attenuation in transmission properties observed under irradiation [5] and still not fully understood [6]. A SEM/EDX/CL characterization of these OFs will be presented and discussed in the contribution.

Acknowledgments: this work is contributed by Slovenian Research Agency (bilateral ARIS-CEA project NC-24005)

References:
[1] A. Alessi et al., *J. Appl. Phys.* **2015**, 118, 085901.
[2] I. Reghioua et al., *IOP Conf. Ser.: Mater. Sci. Eng.* **2017**, *169*, 012006.
[3] I. Reghioua et al., J. Luminesc. **2016**, *179*, 1–7.
[4] I. Reghioua et al. *Appl. Sci.* **2022**, *12*, 3916.
[5] A. Morana et al., *Sensors* **2020**, *20*, 7254
[6] S. Girard et al., *Optical Materials: X* **2022**, *16*, 100191

Type of presentation: Poster

IM1-P-4 EDXS Quantification in the TEM: How Can Ray Tracing Help?

Michael Oberaigner[a], Nikolaus Grogger[b], Judith Lammer[a], Daniel Knez[b], Georg Haberfehlner[b], Gerald Kothleitner[a,b], Werner Grogger[a,b]

[a]*ZFE, Graz Centre for Electron Microscopy, Graz, Austria*

[b]*FELMI, Graz University of Technology, Graz, Austria*

Contact email: werner.grogger@felmi-zfe.at

Introduction

During the last two decades, energy-dispersive X-ray spectrometry (EDXS) has received a major boost in terms of detection sensitivity with the introduction of silicon drift detectors (SDD). These detectors can be manufactured in large sizes almost without loss of energy resolution and may be combined in multi-detector systems comprising 2 or more detectors. As a consequence, very large solid angles up to 4 sr (corresponding to more than 30% of all emitted characteristic X-rays) may be reached, allowing for single atom sensitivity [1–4]. However, due to the huge size of these detectors, the geometric situation in the TEM has changed considerably, with effects on the quantitative evaluation of the spectra. The conventional procedure of tilting the specimen towards the EDXS detector in order to increase the take-off angle and thereby minimizing the absorption in the specimen, does not work anymore. In particular, detector shadowing has started to play an important role in the absorption process between the X-ray's generation site and the EDXS detector. Not only the absorption of (low-energy) X-rays in the specimen, but also the absorption by different parts of the specimen holder need to be considered for quantitative EDXS work using such systems [5,6].

Methods & Results

In our work we have taken up this topic and developed a Python-based software tool called *edXTrace*, which can model the described absorption effects using a ray tracing approach. The tool is very flexible as it can work with any detector-specimen geometry, arbitrary detector sizes and shapes as well as different specimen holders and specimen shapes. At first, a scene is created in *edXTrace* (Figure 1), which contains detectors, specimen and specimen holder (including all individual parts like washers, clamps etc.). For all items, which are part of the absorption path, their positions and sizes need to be set and 3D model files as well as their chemical composition need to be provided.

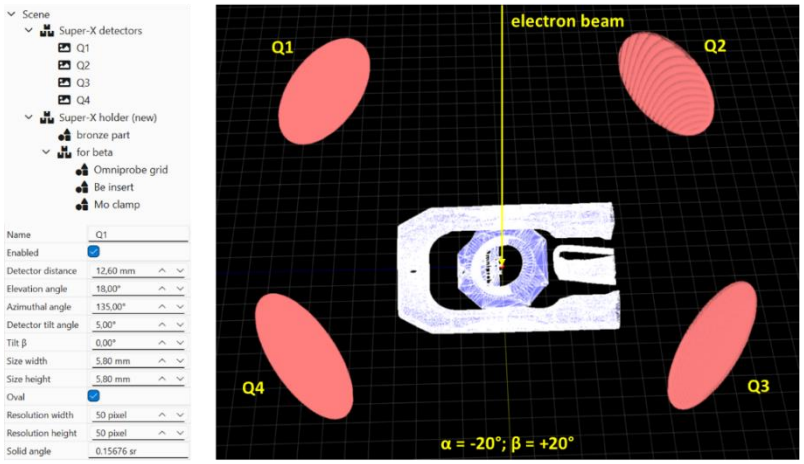


Figure 1: Graphical user interface of edXTrace: left: setup of scene and each item's properties (position, size, material etc.); right: real-time representation of scene including detectors, specimen holder, and grid. The specimen tilt (α = -20°; β = +20°) is towards detector Q4.

Once the scene containing all relevant parts is defined, *edXTrace* can compute the amount of shadowing for each detector for a chosen X-ray energy (Figure 2). It should be noted that not only the absorption in the specimen, but also the absorption on the way from the specimen to the detector depends on the

energy of the X-ray quantum. The colors in Figure 2 give quantitative information about the number of X-rays hitting the detectors. Additionally, a built-in solid angle calculation routine provides accurate values for the detector's effective solid angle regardless of the shape and size of the detector. *edXTrace* can also provide quantitative correction data for each spectrum, so that the line intensities can be converted as if there was no absorption at all. This "absorption correction" will correct for the absorption by all parts of the specimen holder (main holder, inserts, washers, clamps, grids etc.) and can also be applied for the absorption in the specimen. The entire output is easily accessible via the generated HDF5 file. In addition, images (e.g., Figure 2) can also be created, which offer a simple way to visualize the shadow cast by the detector qualitatively.

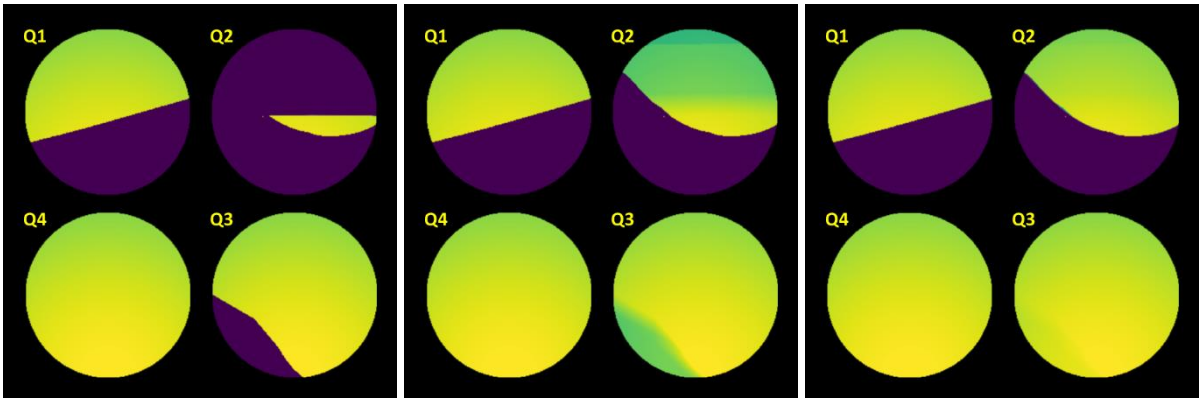


Figure 2: Shadow images of the four detectors shown in Figure 1; left: for O-K_α X-rays (0.52 keV); center: for Cu-K_α X-rays (8.04 keV); right: for Ba-K_α X-rays (32.05 keV); yellow: full illumination, violet: no illumination.

The energy dependency of shadowing can be nicely seen in Figure 2: For the highest energy X-rays (Ba-K, right) only the bronze part of the main specimen holder is absorbing. As the X-ray's energy decreases, other items – in particular the Be insert holding the specimen – will also contribute and change the shadow images (left and center; Q2 and Q3). The Be insert is completely opaque for O-K X-rays illuminating only a tiny area of detector Q2, which is located opposite the point at which the sample is looking (Figure 2, left, Q2).

Discussion & Conclusions

We developed *edXTrace*, which is intended to be an indispensable tool for enhancing the accuracy of quantitative X-ray analysis in TEMs with large area and/or multiple detector systems. It integrates nicely into the X-ray quantification workflow, as its output is directly useable for correcting intensities in order to reliably yield correct results. The use of *edXTrace* with regard to quantitative analysis and the errors that arise when the described effects are neglected will be demonstrated using a NiO specimen. Future enhancements could include the incorporation of the X-ray production process and the absorption properties of the detector assembly (window, contact and dead layer, crystal thickness). The software will be provided for public download.

Acknowledgments

The authors acknowledge funding from "ESTEEM3" (*European Union's Horizon 2020 research and innovation program* under grant agreement No 823717) and "IMPRESS" (*European Union's Horizon Europe framework program for research and innovation* under grant agreement No 101094299). Views and opinions expressed are however those of the authors only and do not necessarily reflect those of the European Union or the European Research Executive Agency (REA). Neither the European Union nor the granting authority can be held responsible for them.

References

1. H. von Harrach et al., *Microsc. Microanal.* **2009**, *15*, 208–209.
2. H.S. von Harrach et al., *J. Phys. Conf. Ser.* **2010**, *241*, 012015.
3. N.J. Zaluzec, *Microsc. Microanal.* **2021**, *27*, 2070–2074.
4. N.J. Zaluzec, in: *Proc. EMAG 2021*, Royal Microscopical Society, **2021**.
5. W. Xu et al., *Ultramicroscopy* **2018**, *184*, 100–108.
6. J. Kraxner et al., *Ultramicroscopy* **2017**, *172*, 30–39.

Type of presentation: Poster

IM1-P-5 Advanced EELS techniques in catalyst analysis

Daniela Ramermann[a], Michael Poschmann[a], Christoph Göbel[a], Wenchao Wan[a], Elisabeth H. Wolf[a], Saskia Heumann[a], Holger Ruland[a], Walid Hetaba[a]

[a]*Max Planck Institute for Chemical Energy Conversion, (Mülheim an der Ruhr), Germany*

Contact email: walid.hetaba@cec.mpg.de

Analytical transmission electron microscopy (TEM) is a very versatile toolbox that gives access to morphological and electronic structure properties as well as the elemental composition of the investigated materials. Especially in catalysis research the set of techniques available within analytical TEM are highly valuable to investigate structure-function relationship of the studied materials. Using a combination of the Gatan Continuum S spectrometer and the special inert transfer setup [1] in our Talos F200X microscope with high-level analysis methods, additional information on various catalyst materials can be gained.

To improve the results of an oxidation state analysis of catalyst materials, we replaced the commonly applied method of cross-section models with the use of well-defined reference spectra. While EELS reference databases [2,3] are a useful, but not exhaustive, source of reference spectra, measuring high-quality reference materials gives a complete and reliable dataset tailored to the specific studied materials. Here we show the results of investigation of a Cu/ZnO based methanol synthesis catalyst [4] using commercially available Cu, Cu_2O, CuO, Zn, ZnO, and Al_2O_3 reference samples for the oxidation state analysis. After thorough investigation of the reference samples and acquisition of EELS references, very accurate spatially resolved oxidation state maps were acquired (figure 1).

For some materials, accessing elemental edges at higher energy losses is beneficial or even necessary to perform a thorough analysis. In this work we show a Co-based NH_3 reformation catalyst as an example, for which we performed a spatially resolved oxidation state analysis using the Co-K edge. Alignment of the microscope and spectrometer for these energies is not a standard procedure anymore and needs to be performed carefully [5]. However, we were able to analyse the differences between bulk and surface spectra of the Co-based catalyst (figure 2). The results show the capability to investigate elemental edges at high energy losses using a standard analytical TEM setup, which are usually only accessible in a synchrotron.

We show that sophisticated EELS analysis as well as investigating previously inaccessible elemental edges can become an important addition to TEM capabilities for special investigations within the analysis workflows in catalysis research or materials science.

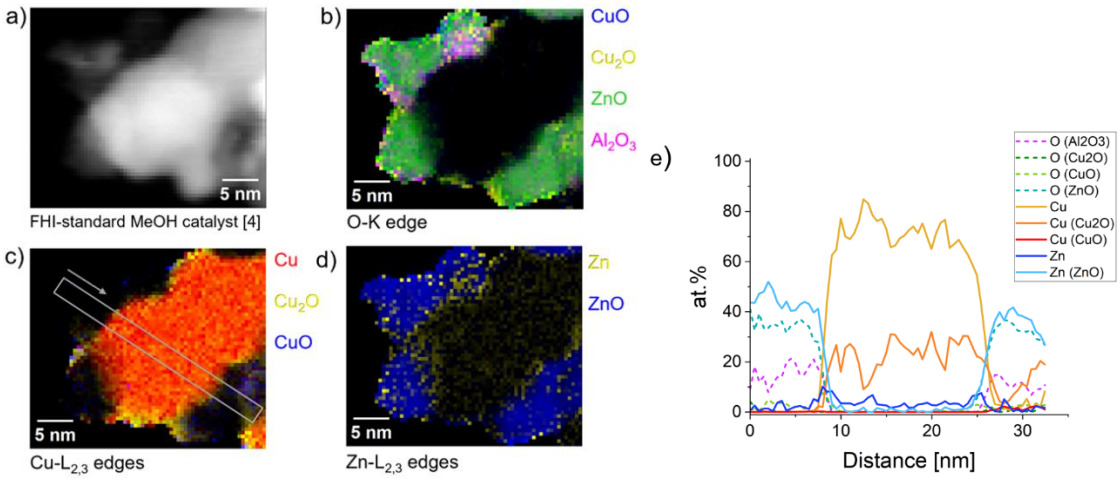


Figure 1: (a) HAADF image of a methanol synthesis catalyst. Oxidation state maps using the fit results of the (b) O-K edge, (c) Cu-$L_{2,3}$ edge and (d) Zn-$L_{2,3}$-edge. (e) Line profile quantifying the results.

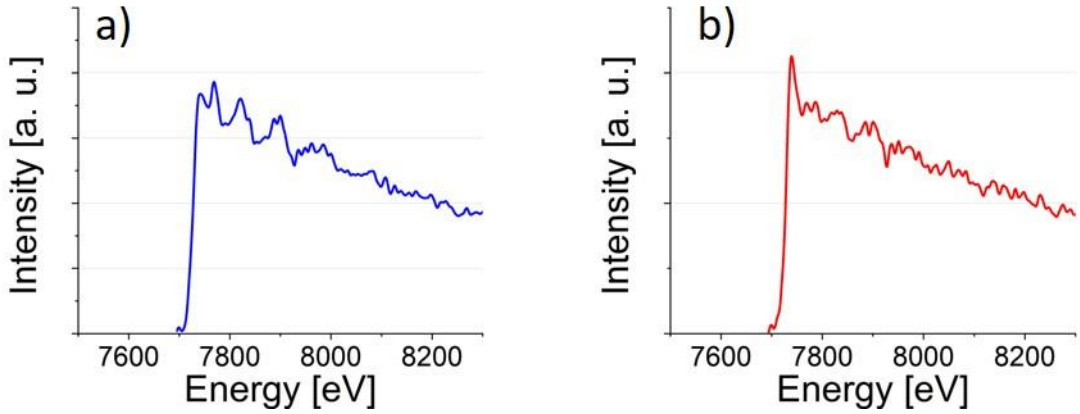


Figure 2: Co-K edge acquired (a) in the bulk and (b) at the surface of a catalyst particle.

References:

1. Hetaba et al., *BIO Web Conf. (EMC 2024)* **2024**, *129*, 03008.
2. Ewels et al., *Microscopy and Microanalysis* **2016**, *22*, 717-724.
3. https://eels.info/atls
4. Schumann et al., *ChemCatChem* **2014**, *6*, 2889-2897.
5. MacLaren et al., *Advances in Imaging and Electron Physics* **2019**, *210*, 299-355.

Type of presentation: Poster

IM1-P-6 Raman tweezers for the analysis of secondary microplastics generated by degradation of surgical masks in water

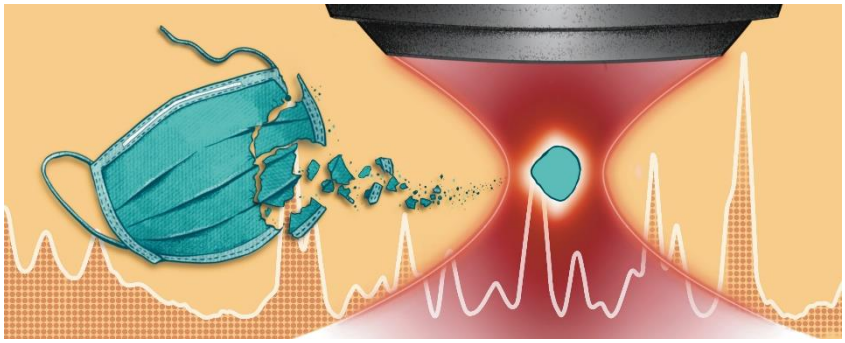
Martin Kizovský[a], Silvie Bernatová[a,b], Antonino Foti[b], Maria Grazia Donato[b], Zdeněk Pilát[a], Jan Ježek[a], Ota Samek[a], Pietro G. Gucciardi[b], Alessandro Magazzù[b], Pavel Horký[c], Martin Šiler[a], Onofrio M. Maragò[b], Pavel Zemánek[a]

[a]*Czech Academy of Sciences, Institute of Scientific Instruments, Královopolská 147, 61200 Brno, Czech Republic.*

[b]*Consiglio Nazionale della Ricerche, Istituto per i Processi Chimico-Fisici, Viale F. Stagno D'Alcontres 37, I-98158 Messina, Italy.*

[c]*Mendel University in Brno, Animal Nutrition and Forage Production Research, Zemědělská 1, 61300 Brno, Czech Republic.*

Contact email: martink@isibrno.cz



The COVID-19 pandemic has underlined the role of plastics as an irreplaceable material to society, proving an inexpensive and widely available feedstock for single-use medical equipment, groceries and commerce packaging[1]. In 2021, an estimated 89 million surgical masks were required each month[2]. These masks are non-recyclable and, as the most of single-use plastic items, either end up in landfills or are released directly into the environment, including oceans, freshwater, soil and air[3]. The transport from land to oceans is usually caused by aeolian processes and aquatic runoffs of mismanaged plastic waste[4]. Weathering of plastics causes break down into microplastics (MPs)[5] and nanoplastics (NPs)[6]. MPs range from 1 µm to 5 mm in diameter. NPs are generally addressed as objects smaller than 1 µm[7].
This study presents a combination of optical tweezers and Raman spectroscopy – Raman Tweezers (RT) – for the detection and chemical identification of secondary MPs. Tightly focused laser passed through a microscope objective allows for simultaneous micromanipulation and chemical analysis of MPs in aquatic environment[8]. The origin of the MPs in this study was from mechanical degradation of surgical face masks followed by UV-induced photodegradation.

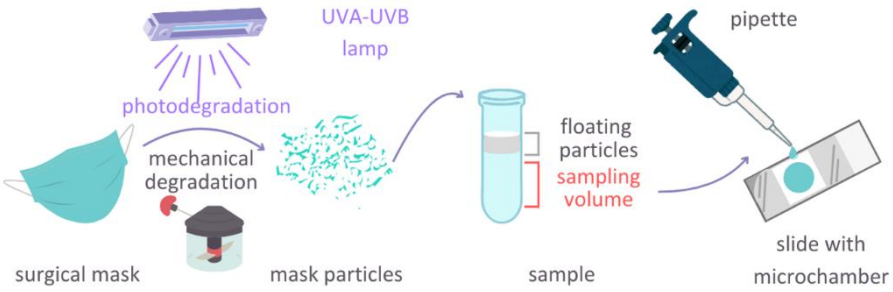


Fig. 1: Process of the MPs preparation.

RT enabled to optically trap and acquire Raman spectra of freely floating fragments down to approximately 760 nm inside a glass microchamber. Also, fragments of up to tens of µm deposited at the bottom of the microcell were identified. The size and the Raman response of the generated MPs was correlated. The main chemical compound of the MPs from surgical masks was identified as polypropylene. More interestingly, several of the analyzed fragments also contained a pigment, phthalocyanine, that serves as a UV and antimicrobial protective substance.

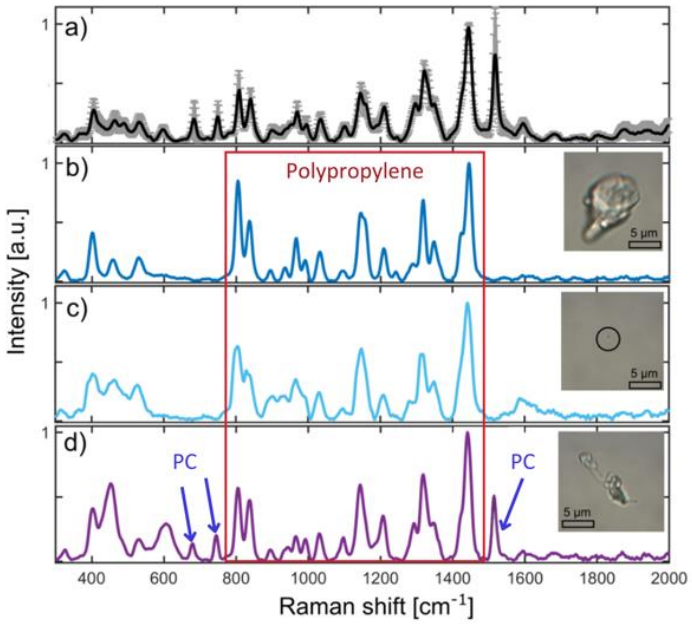


Fig. 2: Raman spectra of the analyzed MPs.

This study introduces RT as a tool to analyze size and chemical composition of sub-20 µm secondary MPs, directly in water, at the single particle level, with a minimal or no requirement for the pretreatment of the samples. The presented RT setup also offers the potential to be modified into a portable version, which would enable on-site analyses of MPs.

References:

[1] Prata, J. C. et al. *Environ. Sci. Technol.* **2020**, *54* (13), 7760–7765.
[2] Joseph, B. et al. *Advanced Industrial and Engineering Polymer Research* **2021**, *4* (3), 199–208.
[3] Ellis, L. D. et al. *Nat Catal* **2021**, *4* (7), 539–556.
[4] Mellink, Y. et al. *Front. Environ. Sci.* **2022**, *10*.
[5] Gerritse, J. et al. *Scientific Reports* **2020**, *10* (1), 10945.
[6] Gigault, J. et al. *Nat. Nanotechnol.* **2021**, *16* (5), 501–507.
[7] Mariano, S. et al. *Front. Toxicol.* **2021**, *3*, 636640.
[8] Gillibert, R. et al. *Environ. Sci.: Nano* **2022**, *9* (1), 145–161.

Acknowledgement:

This project is financed from the state budget by the Technology Agency of the Czech Republic in the frame of the National Centres of Competence (TN02000020/Centre of Advanced Electron and Photonic Optics), and by the Czech Academy of Sciences (RVO: 68081731). Electron microscopy and Raman spectroscopy analysis provided at Core Facility Electron microscopy and Raman spectroscopy, ISI CAS, Brno, CR, is supported by MEYS CR (LM2023050 Czech-BioImaging). This study is based upon work from COST Action PRIORITY (CA20101), supported by COST (European Cooperation in Science and Technology). We acknowledge support from the European Union (NextGeneration EU) through the SAMOTHRACE Project (grant number ECS00000022) of the Ministero dell'Università e della Ricerca (MUR)-Piano Nazionale di Ripresa e Resilienza (PNRR) and PRIN2022 projects PLASTACTS project (grant number 202293AX2L) and PRIN2022 SEMPER project (grant number 20227ZXT4Z). The authors express their gratitude to the funding agency (Technology Agency of the Czech Republic) for their support in financing the research related to the project number SS06020224.

Type of presentation: Poster

IM1-P-7 Quantum state secondary electron emission spectroscopy in low voltage scanning electron microscope for probing Valence band

Abbas Kosari Mehr[a], Mohamed Zaghloul[a], Ritik Tanwar[a], Wenzheng Cao[a], Madiha Khan[a], Erfan Afshar[a], Silvia Maria Pietralunga[b], Anjam Khursheed[a], Alberto Tagliaferri[a]

[a]*Politecnico di Milano, Physics department, Milan, Italy*

[b]*CNR Istituto di Fotonica e Nanotecnologie, Milan, Italy*

Contact email: abbas.kosari@polimi.it

Introduction

Probing the surface and near-surface valence band (VB) with nanoscale lateral resolution is essential for advancing surface science and related technologies. However, conventional spectroscopic tools lack the resolution to achieve this goal. Scanning Electron Microscopy (SEM), known for its nanoscale imaging capabilities, can be paired with Secondary Electron Emission Spectroscopy (SEES) in the low-energy range (below 50 eV). When operated under low-voltage excitation conditions (<3 kV), the approach offers high signal yield and rapid data collection, making it suitable for nanoscale material mapping and VB analysis [1]. Despite these advantages, analyzing spectral data at low kinetic energies remains challenging due to a strong background signal from secondary electron cascades. Currently, no comprehensive model describes the full secondary electron (SE) emission process and its fine energy structure.

Objectives

This work aims to develop an experimental approach for characterizing the valence band of materials using SEM equipped with a specialized electron energy analyzer. It explores how the detailed features in experimental spectra relate to the occupied and unoccupied quantum states of the VB and introduces a theoretical model connecting the valence band Density of States (DOS) to the observed SE spectral response.

Materials & Methods

An ultra-high vacuum scanning Auger microscope (SAM) integrated with a Cylindrical Mirror Analyzer (CMA) was modified with custom entrance optics for detecting low-energy electrons. Experiments were conducted on highly oriented pyrolytic graphite and various metals at primary beam energies below 3 kV. To minimize surface contamination, we performed measurements in an ultra-high vacuum (UHV) environment with controlled electron exposure. Data interpretation was guided by the Fermi Golden Rule and perturbation theory, using ab initio calculated DOS as input.

Results

The acquired spectral data demonstrated high reproducibility. Spectra recorded at various primary electron (PE) energies retained consistent fine structures, indicating robustness across conditions. The energy positions and intensity patterns of spectral features closely matched predictions from the proposed model, showing promising agreement.

Conclusion

This study confirms that SEES measurements can be reliably reproduced and semi-quantitatively modeled, offering insight into the quantum states of the valence band under UHV conditions. The approach opens new possibilities for examining valence band DOS in complex materials and devices.

References

[1] Han, W., et al. "Quantitative material analysis using secondary electron energy spectromicroscopy." Sci Rep 10, 22144 (2020).

IM2 Innovations and synergies in correlative microscopy

Type of presentation: Invited

IM2-IN-1 Applications of Correlative Light Electron Microscopy (CLEM) and Volume Electron Microscopy in Cancer Biology

Galina V. Beznoussenko[a], Alexander A. Mironov[a]

[a]*Department of Cell Biology, IFOM ETS—The AIRC Institute of Molecular Oncology, Via Adamello, 16, 20139 Milan, Italy.*

Contact email: galina.beznusenko@ifom.eu

Introduction

Correlative microscopy has become the widely used field, integrating different approaches and combining of the capabilities of in vivo fluorescence video microscopy with the high-resolution power of electron microscopy (EM). This approach is based on the association of these two techniques. An individual intracellular structure can be monitored *in vivo*, typically using markers fused with green fluorescent protein (GFP), and a ‘‘snapshot’’ of its three-dimensional (3D) ultrastructure and tomographic reconstruction can then be captured at any chosen point in its life cycle. Rapid translocations or shape changes of specific intracellular organelles, such as intracellular traffic, cell migration, among others. To understand how such functions, including budding transport carrier, mitotic spindle development, micronuclei formation, the fusion and detachment of membrane compartments, are organized and executed *in vivo*, it is necessary to apply the degree of spatial resolution afforded by EM. However, conventional EM provides only an average image of the structure of interest and typically examines ultrathin sections, limiting the ability to achieve a full 3D view.

Methods

Electron microscopic examination, immune EM gold labelling based on pre-embedding and correlative light-electron microscopy (CLEM) were performed as previously described (Beznoussenko et al., 2015; 2023).

Results

By combining correlative microscopy, electron tomography, and in vivo models, we reported that ATR-defective cells exhibit altered nuclear plasticity and YAP delocalization (Kidiyoor GR, 2020). Chromosomal instability generates micronuclei-aberrant extranuclear structures that catalyze the acquisition of complex chromosomal rearrangements present in cancer. Using Correlative Light Electron Microscopy (CLEM) and serial electron tomography, we have shown that micronuclei (MN) undergo and catastrophic nuclear envelope collapse, which exposes DNA to the cytoplasm. The proximity of micronuclei to mitochondria leads to oxidation-driven homo-oligomerization of p62, which limits endosomal sorting complex required for transport (ESCRT)-dependent micronuclear envelope repair by triggering autophagic degradation (Martin S., at al., 2024). The frequent observation of micronuclei in tumors suggests that they are not merely passive elements but may actively contribute to tumor progression. The mislocalization of Emerin is associated with a molecular signature linked to poor prognosis in prostate cancer patients and is enriched in metastatic samples. It also corresponds with increases in the migratory and invasive potential of tumor cells, especially in a collagen-rich microenvironment (Popeda M., 2024).

Conclusions

Thus, using CLEM and volume electron microscopy was shown that micronuclear formation, nuclear envelope collapse, Emerin mislocalisation are key factors in cancer progression. These findings highlight how structural and molecular changes at the cellular level contribute to tumor aggressiveness and poor prognosis, providing potential targets for future cancer research and therapy.

References

1. Kidiyoor GR, Li Q, Bastianello G, Bruhn C, Giovannetti I, Mohamood A, **Beznoussenko GV**, Mironov A, Raab M, Piel M, Restuccia U, Matafora V, Bachi A, Barozzi S, Parazzoli D, Frittoli E, Palamidessi A, Panciera T, Piccolo S, Scita G, Maiuri P, Havas KM, Zhou ZW, Kumar A, Bartek J,

Wang ZQ, **Foiani M.** ATR is essential for preservation of cell mechanics and nuclear integrity during interstitial migration. Nat Commun. 2020 Sep 24;11(1).
2. Martin S, Scorzoni S, Cordone S, Mazzagatti A, Beznoussenko GV, Gunn AL, Di Bona M, Eliezer Y, Leor G, Ben-Yishay T, Loffreda A, Cancila V, Rainone MC, Ippolito MR, Martis V, Bedin F, Garrè M, Vaites LP, Vasapolli P, Polo S, Parazzoli D, Tripodo C, Mironov AA, Cuomo A, Ben-David U, Bakhoum SF, Hatch EM, Ly P, Santaguida S. A p62-dependent rheostat dictates micronuclei catastrophe and chromosome rearrangements Science. 2024 Aug 30;385(6712).
3. Popęda M, Kowalski K, Wenta T, Beznoussenko GV, Rychłowski M, Mironov A, Lavagnino Z, Barozzi S, Richert J, Bertolio R, Myszczyński K, Szade J, Bieńkowski M, Miszewski K, Matuszewski M, Żaczek AJ, Braga L, Del Sal G, Bednarz-Knoll N, Maiuri P, Nastały P. Emerin mislocalization during chromatin bridge resolution can drive prostate cancer cell invasiveness in a collagen-rich microenvironment. Exp Mol Med. 2024 Sep;56(9):2016-2032. doi: 10.1038/s12276-024-01308-w. Epub 2024 Sep 2.
4. Beznoussenko G.V., Mironov A.A. (2015) Correlative video-light-electron microscopy of mobile organelles. Methods Mol Biol 2015;1270:321-46.
5. Mironov AA, Beznoussenko GV. Algorithm for Modern Electron Microscopic Examination of the Golgi Complex. Methods Mol Biol. 2023;2557:161-209..

Type of presentation: Invited

IM2-IN-2 Correlative Light-Electron Microscopy: A Precision Tool for Unraveling Complex Cellular Processes in Health and Disease

Roman S. Polishchuk[a]

[a]*Telethon Institute of Genetics and Medicine, Pozzuoli, Italy*

Contact email: polish@tigem.it

Correlative Light-Electron Microscopy (CLEM) has evolved into a powerful approach that synergistically integrates the dynamic imaging capabilities of fluorescence microscopy with the ultrastructural resolution of electron microscopy. Over the past two decades, CLEM has transitioned from a niche methodology into a mainstream strategy in cellular research. This talk will highlight how CLEM enables researchers to tackle specific and challenging questions in both fundamental biology and human pathology.

We will trace the development of CLEM from its early implementations to modern applications that leverage GFP-based video microscopy and cutting-edge techniques such as electron tomography and FIB-SEM. Particular emphasis will be placed on its use in studying membrane trafficking events and elucidating phenotypes associated with transient structures transporting proteins and lipids along the biosynthetic pathway.

Recent advances have expanded CLEM's relevance to biomedical research, including investigations into the formation of replication organelles during SARS-CoV-2 infection and the intracellular trafficking of the copper transporter ATP7B in Wilson disease. These case studies exemplify the versatility of CLEM in addressing both fundamental and translational research questions by enabling the dissection of complex biological mechanisms—from genetic disorders to viral pathogenesis.

Type of presentation: Oral

IM2-O-1 Correlative microscopy: Uncovering the role of vacancies and contamination on the mechanical stiffness of defect-engineered graphene

Wael Joudi[a,b] , Rika Saskia Windisch[c], Alberto Trentino[a,b] , Diana Propst[a,b] , Jacob Madsen[a], Toma Susi[a], Clemens Mangler[a], Kimmo Mustonen[a], Florian Libisch[c] and Jani Kotakoski[a,]

[a]*University of Vienna, Faculty of Physics, Boltzmanngasse 5, 1090 Vienna, Austria*

[b] *University of Vienna, Vienna Doctoral School in Physics, Boltzmanngasse 5, 1090 Vienna, Austria*

[c]*Institute for Theoretical Physics, Faculty of Physics, Technical University of Vienna, Wiedner Hauptstrasse 8-10, 1040 Vienna, Austria*

Contact email: wael.joudi@univie.ac.at

The two-dimensional elastic modulus E^{2D} of defective graphene is correlated to its vacancy density and vacancy type distribution, enabled by an interconnected ultra-high vacuum system including all instruments used [1]. The graphene surface is cleaned at a mm scale by laser light illumination. The vacancies are introduced into the exposed atomic lattice by irradiating pristine graphene with low energy (< 200 eV) Ar ions. The atomic structure of the irradiated graphene is imaged via aberration-corrected medium angle annular dark field (MAADF) scanning transmission electron microscopy (STEM). Specifically, in a semi-automated process, areas in the order of 10^4 nm² are imaged at atomic resolution and then analysed by a convolutional neural network in terms of atomic structure. Throughout multiple samples we find a total of 5865 vacancies and assign them to their corresponding types. The vacancy type distributions reveal single and double vacancies to be the most abundant. Subsequent atomic force microscopy nanoindentation measurements reveal a steep decrease of E^{2D} with increasing vacancy density. This is in contrast to what has been observed in Ref. [2]. We link this drastic drop in stiffness to vacancy-induced corrugation, which is observable in atomic resolution STEM images (Fig. 1(a)). According to atomistic simulations (Fig. 1(b)), these corrugations are caused by vacancies with two or more missing atoms, while single vacancies have no visible impact on the morphology. Based on this, we present an analytical model describing the decrease of E^{2D} as a function of the areal density of vacancies with at least two missing atoms. Lastly, we demonstrate that the opposite effect similar to Ref. [2], can be achieved by not removing the surface contamination prior to the irradiation, which also in our measurements leads to a similar increase of E^{2D}.

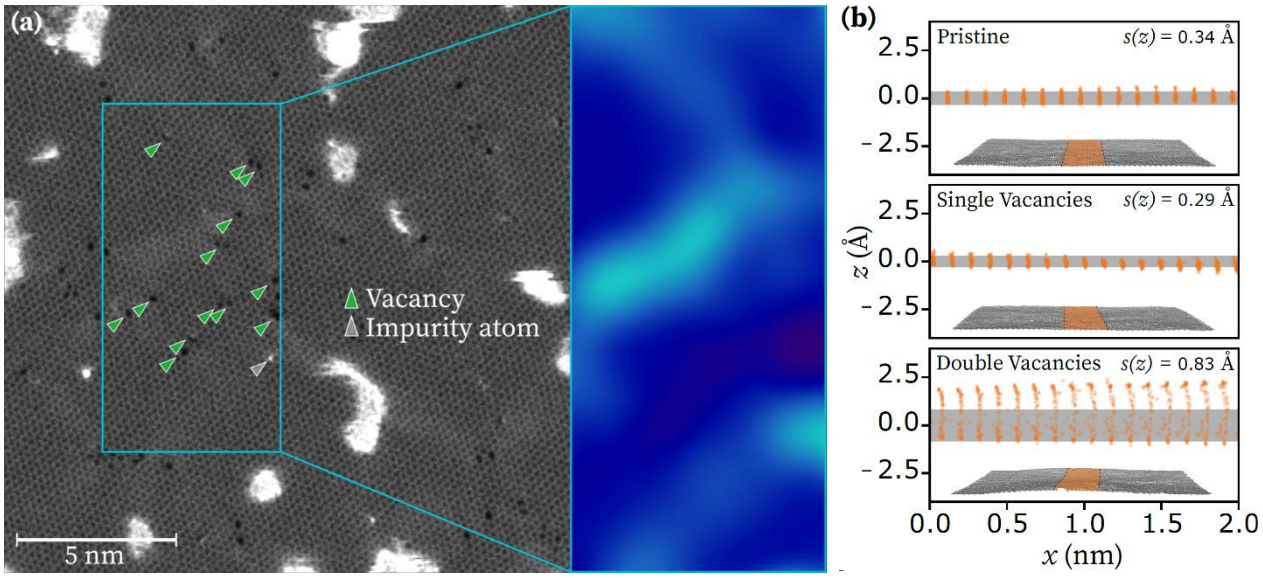


Figure 3: (a) MAADF STEM image of irradiated graphene, where the corrugation is visible as small intensity gradients across the graphene lattice. The magnification of the area within the turquoise box with Gaussian blur highlights the morphological roughness. (b) Cross-sectional view of simulated

structures of graphene containing no vacancies (pristine), single vacancies and double vacancies. The orange dots represent carbon atoms within a 2x12 nm² cutout (orange area within the inset), while the grey overlay corresponds to their standard deviation $s(z)$ in terms of vertical position z. Each inset displays the corresponding complete 12x12 nm² structure. From Ref. [3]

Reference

1. C. Mangler et al., Microscopy and Microanalysis 28 (S1), 2940 (2022)
2. G. López-Polín et al., Nature Physics 11, 26 (2015)
3. W. Joudi et al., arXiv (2025), https://arxiv.org/abs/2412.05194

Type of presentation: Oral

IM2-O-2 Multimodal cryo-FIB-SIMS imaging on frozen-hydrated lamella of biological tissues

Antje Biesemeier[a], Tatjana Taubitz[a,b], Zahraa Berro[a,c], Jean-Nicolas Audinot[a], Tom Wirtz[a] and Olivier De Castro[a]

[a]*Advanced Instrumentation for Nano-Analytics (AINA), Luxembourg Institute of Science and Technology (LIST), Belvaux, Luxembourg*

[b]*Department of Structural Biochemistry, Max Planck Institute of Molecular Physiology, Otto-Hahn-Str. 11, 44227 Dortmund, Germany*

[c]*Doctoral Programme in Systems and Molecular Biomedicine of the DSSE, University of Luxembourg, 4365 Belval Esch-sur-Alzette, Luxembourg*

Contact email: antje.biesemeier@list.lu

Correlative high-resolution morphological and chemical analyses in biological systems typically rely on the usage of a number of different analytical instruments: e.g. a combination of light and electron microscopes together with chemical analysis tools with or without imaging capabilities (e.g. mass spectrometry or energy dispersive x-ray microanalysis). Respective sample transfers and finally subsequent data processing and correlation are time-consuming and oftentimes quite challenging. Special care has also to be taken regarding the actual sample preparation needs for the analysis in vacuum to avoid compositional changes. Therefore, cryo-investigations are nowadays the state-of the art in biological electron microscopy, as they allow close-to native sample preservation and minimizing structural or chemical changes. However, the limited availability of cryo-compatible instruments for correlative morphological and chemical analyses at highest spatial resolution and concerns regarding contaminating or even damaging the frozen-hydrated sample during sample-transfer, here as a result of ambient temperature and humidity, remain.

Our group recently developed a prototype focused ion beam based secondary ion mass spectrometry workstation (FIB-SIMS) dedicated for multimodal *in situ* imaging and chemical analysis of biological samples in a close to native cryogenic state [1, 2. The chemical imaging platform is combining the relevant key capabilities, i.e. high spatial resolution (< 1 nm for secondary electron imaging), < 15 nm for secondary ion mass spectrometry (SIMS)), chemical sensitivity (down to ppm), dynamic range of masses up to m/z 500 and isotopic selectivity. It is based on a gas field ion source microscopy platform (based on ZEISSS NanoFab) and modified to also allow investigation of sensitive and frozen-hydrated samples in the cold (<-141°) and thin samples via transmitted beam imaging.

An exemplary set of samples is shown to underline the beneficial use of cryogenic temperature FIB-SIMS analysis obtained from beam-sensitive samples investigated both at RT and at < -140° C as well as the first mass-resolved correlative SE-STIM-SIMS analysis on frozen-hydrated lamella for A549 cancer cells.

Funding: This project has received funding from the European Union's Horizon 2020 Research and Innovation Programme under grant agreement No. 720964 and by the Luxembourg National Research Fund via the project INTER/DFG/19/13992454 and FNR/CORE/ C21/BM/15754743

References:

1. O. De Castro et al., *Anal. Chem.* **2021**, *93*, 14417–14424.
2. O. DeCastro et al. *Micr Microanal*, **2023**, *29*, Suppl. 1, 1, 785–786.

Type of presentation: Oral

IM2-O-3 Investigating Magnetic Domain Wall Pinning in Nanowires via Correlative X-ray and Electron Transmission Microscopy

Núria Bagués[a], Laura Álvaro-Gómez[b], Claudia Fernández-González[a], Lucía Gómez-Cruz[b], Ana Arché-Núñez[a], Waqas Khaliq[a], Lucía Aballe[a], Lucas Pérez[b,c], Sandra Ruiz-Gómez[a],

[a]*ALBA Synchrotron Light Source Facility, Cerdanyola del Vallès, Spain*

[b]*Universidad Complutense de Madrid, Madrid, Spain*

[c]*IMDEA Nanociencia, Madrid, Spain*

Contact email: nbagues@cells.es

Domain wall (DW) motion in 3D magnetic nanowires is highly sensitive to local variations within the material, such as microstructural defects or local compositional changes [1-3]. These variations can act as pinning sites, restricting DW movement and affecting their dynamics. Understanding and controlling DW pinning mechanisms is crucial for a precise manipulation of DWs in 3D magnetic nanowires, an essential requirement for their integration into spintronic devices.

In this work, we investigate the correlation between DW pinning and chemical and structural variations in permalloy cylindrical nanowires. To achieve this, we correlate X-ray Transmission Microcopy (TXM) and Transmission Electron Microscopy (TEM) of the same nanowires. The nanowires were synthesized via template-assisted electrodeposition using nanoporous alumina templates [4], with chemical modulations intentionally introduced to explore their role as engineered pinning sites for DWs. The nanowires were then placed on a custom-designed substrate compatible with both imaging techniques. First, TXM was used to visualize current-driven DW motion and identify pinning sites. Subsequently, the same locations were analysed using TEM to investigate potential structural and compositional variations.

TXM results revealed consistent DW pinning at the intentionally introduced chemical modulations. However, additional pinning sites were observed outside these regions, in areas where the nanowires were expected to have a homogeneous composition. To characterize these pinning sites in detail, we performed Scanning (S)TEM combined with Energy Dispersive X-ray Spectroscopy (EDS) to analyse chemical variations across the nanowires. STEM-EDS confirmed the locations of the chemical modulations and verified a homogeneous elemental composition across the rest of the nanowires. This finding, together with STEM images, suggest that the additional pinning sites may be linked to variations in crystallinity or grain size. Recently, we performed nano-beam electron diffraction mapping (4D-STEM) to detect potential crystallographic variations. Data analysis is ongoing, and while a detailed evaluation is still in progress, initial observations point to a correlation of local variations in crystallinity or grain structure with the unintentional pinning sites.

This study provides valuable insights into the interplay between chemical and structural variations and DW motion. By refining our understanding of pinning mechanisms, this work contributes to the development of more efficient and reliable domain wall-based three-dimensional spintronics devices.

Acknowledgments: NB, AAN, WK and SRG acknowledge funding by MCIN with funding from European Union NextGenerationEU (PRTR-C17.I1) and by Generalitat de Catalunya.

References:

1. M. Schöbitz et al., *The Journal of Physical Chemistry C,* **2023**, 127(5), 2387-2397
2. S. Ruiz-Gomez et al., *Nanoscale. 12,* **2020,** 17880
3. L. Álvaro-Gómez et al., *Phys. Rev. B,* **2022**, 106, 054433
4. Ruiz-Gomez et al., *Micromachines*, **2022**, 13, 1223

Type of presentation: Oral

IM2-O-4 Urban particulate matter and human health: correlative microscopy methods and simulated tissues modeling

Giulia Pia Servetto[a], Alessandra Passarella[a], Matilde Mora[a], Ruggero Vigliaturo[a,b]

[a]*Department of Earth Sciences, University of Torino, (Torino), Italy*

[b]*Interdepartmental Centre for Studies on Asbestos and Other Toxic Particulates "G. Scansetti", University of Torino, (Torino), Italy*

Contact e-mail: giuliapia.servetto@unito.it

Urbanization and the intensification of anthropogenic activities contribute to elevated concentrations of particulate matter (PM) in urban environments. This increase in PM concentrations poses an amplified risk of human exposure, including the potential accumulation of the finest fraction of PM (nanoparticles with aerodynamic diameter up to 100 nm - NPs) in the brain. The present study integrates multiple imaging techniques, such as electron microscopy and optical fluorescence microscopy, to characterize urban PM from Casale Monferrato (Italy). Additionally, biosimulant modeling approaches, including pre- and post-interaction studies through simulated brain tissues, are employed to evaluate the potential physicochemical transformations of exogenous NPs within a biochemical environment.

Samples were collected from 14 locations in Casale Monferrato. Investigation of pre-interaction samples were conducted using SEM-EDXS, and optical fluorescence microscopy. The dimensional distribution measured on SEM images showed particles with an average diameter of ~12.295 μm with different morphologies. The main heavy metal detected through EDXS investigations is Fe. Optical fluorescence microscopy acquisitions identified fluorescent particles (which could be either organic matter, plastics or fluorescent minerals) in each sample. Preliminary results indicate that a significant concentration of the urban PM analyzed can be inhaled, with a fraction that could potentially accumulate into the brain tissues. To examine the possible transformations of NPs upon exposure to the brain environment, dissolution experiments were conducted using simulated brain tissues developed in our laboratory. To simulate the human brain, 1% agarose hydrogel was used. The simulated tissues were exposed to <100 nm NPs (previously filtered from the starting samples) for 168 hours, after which the NPs were extracted and analyzed. NPs in post-interaction samples were characterized identically to those in pre-interaction samples.

The proposed imaging approach combining simulated tissues, SEM-EDXS, and optical fluorescence microscopy for urban PM characterization provides valuable insights into the mineralogical and chemical composition of airborne particles transforming into complex simulated biosystems. This approach contributes to a more comprehensive understanding of potential human exposure pathways, thereby advancing knowledge of the environmental and health-related implications of urban PM pollution. Indeed, the integration of these imaging techniques facilitated a multi-scale analysis, yielding comprehensive information of both pre- and post- interaction samples. For instance, optical fluorescence microscopy allowed for a better understanding of the localization and actual presence of C-containing species, which were hard to locate by SEM-EDXS because of the sample preparation using C-tape and C-sputtering. Furthermore, this methodological approach enabled the assessment of the dimensional distribution of the measured particles at various magnifications (i.e. 4×, 40×, 400×, and 4000×).

Type of presentation: Poster

IM2-P-1 All-Micro (ALLiance to boost cross-border innovation through MICROscopy): an ITA-SLO cross-border Network for Sustainable Microscopy

Mattia Fanetti[a], Simone Dal Zilio[b], Gregor Kapun[c], Gabriele Baj[d]

[a]*Materials Research Laboratory, Univerza v Novi Gorici, Ajdovščina, Slovenia*

[b]*Istituto Officina dei Materiali CNR-IOM, Trieste, Italy*

[c]*Nanocenter - Center odličnosti nanoznanosti in nanotehnologije, Ljubljana, Slovenia*

[d]*Centro Interdipartimentale Microscopia Avanzata CIMA, Università di Trieste, Trieste, Italy*

Contact email: mattia.fanetti@ung.si

The use of advanced optical and electron microscopy facilities is often limited to highly specialized organizations and individuals, which in many cases are not accessible (and not even known) by those externals stakeholders (industry, researchers, …) potentially interested in using these tools to support their creativity and competitiveness. Moreover, the significant costs associated with high-end state-of-the-art equipment and constant technological advancements are an obstacle to the transition of advanced microscopy methods from academic or fundamental research towards practical applications in industry and services.

The aim of ALL-MICRO project is the establishment of a cross-border laboratory network, within the Interreg ITA-SLO program area, where advanced optical and electron microscopy facilities are connected together and interfaced with the industrial and economic regional fabric.

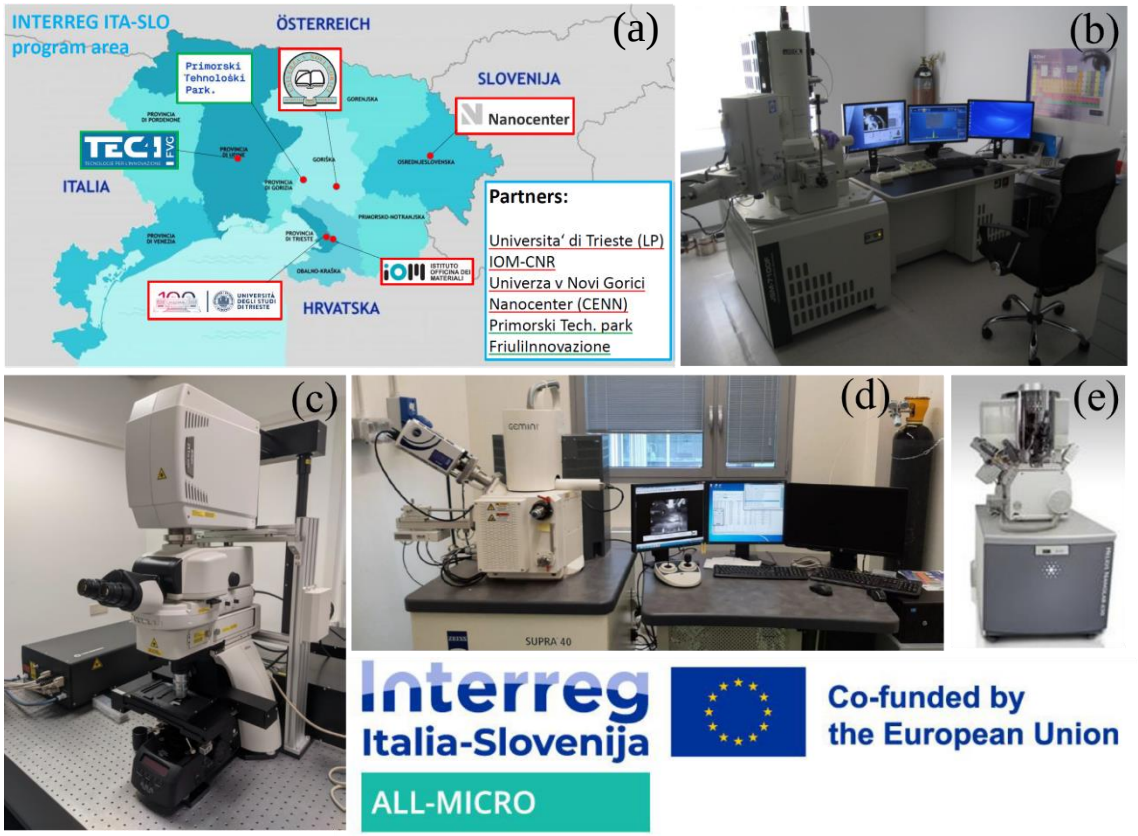


Figure 1: the Interreg ITA-SLO area, with the locations of ALL-MICRO partners (a), four examples of facilities belonging to the network: SEM+CL laboratory at University of Nova Gorica (b), multiphoton

optical microscope at University of Trieste (c), SEM laboratory at IOM-CNR (d), dual-beam FIB-SEM at Nanocenter (e).

ALL-MICRO is a two-years project (from April 2024 to April 2026) co-financed by European Regional Development Fund (ERDF) under the Interreg VI-A Italia-Slovenia program. The project involves four microscopy laboratories hosted in regional institutes (Fig.1a): University of Trieste, Istituto Officina dei Materiali - CNR-IOM (Trieste), University of Nova Gorica (Ajdovščina) and Nanocenter (Ljubljana).

The facilities involved in the project includes: optical and confocal microscopy, Scanning Electron Microscopy (+ microanalysis (EDX), + Cathodoluminescence spectro-microscopy), Transmission Electron Microscopy (+ EDX), Raman spectro-microscopy, Focused Ion Beam (+ cryo-stage), Scanning Tunneling Microscopy, Atomic Force Microscopy, and several facilities for sample preparation (coating, cross-sectioning, staining, …).

The project activities include: 1) exchange of knowledge and mutual training of experts of the four microscopy centers; 2) execution of demonstrative experiments proposed by the companies and 3) organization of cross-border microscopy courses for scientists (i.e. PhD student and Post-DOC) and technicians.

Two technology transfer actors are also within the partnership: TEC4I FVG Friuli Innovazione (Udine, Italy) and Primorski Tehnoloski Park (Šempeter pri Gorici, Slovenia). Their fundamental role is in fostering an effective connection between the ALL-MICRO laboratory network and the industrial environment. First, they will identify and engage potential external users interested in exploring the opportunities presented by the new microscopy techniques. Second, they will support the interaction by providing places, expertise and tools for knowledge exchange and project developing, with the idea to create an environment where the collaboration between laboratories and economic tissue is catalysed.

The outcome of the project is the creation of a network of tightly collaborating advanced microscopy laboratories, with empowered technical capability and a smart and sustainable use of the resources. Moreover, the joint effort in engaging external users results in a more effective interaction with the industrial and research actors in the region.



Figure 2: Some examples of cross-training activities. UniTS staff trains other ALL-MICRO experts on confocal microscopy image processing (a), beginning of SEM training session at UNG (b), UNG staff shows to other ALL-MICRO expert the TEM apparatus (c), Nanocenter staff trains other ALL-MICRO experts on FIB.

Aknowledgements: ALL-MICRO is financed by the Interreg VI-A Italy-Slovenia Programme.

Type of presentation: Poster

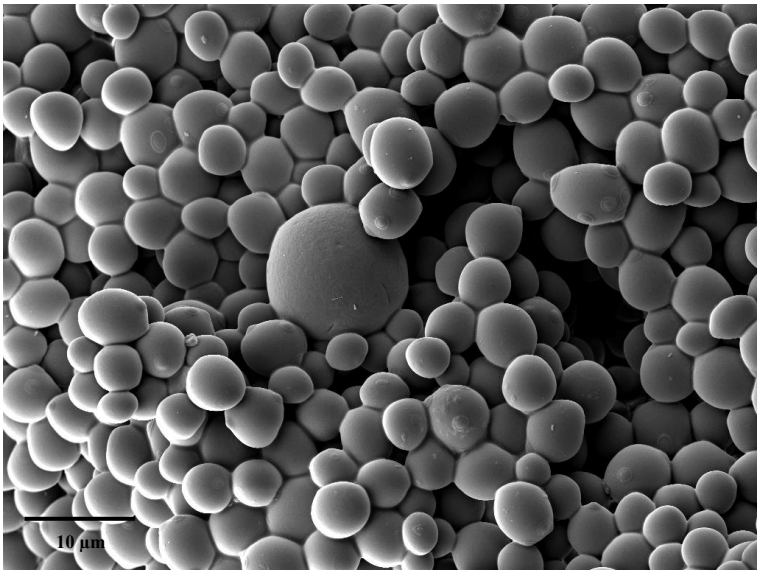
IM2-P-2 Fast and Frozen: Visualising a wide spectrum of specimens using Cryo-SEM combined with an on-site freeze fracture system

Dominique Pernitsch[a], Kerstin Hingerl[a], Melisa Malovcic[a], Dagmar Kolb[a,b]

[a]*Core Facility Ultrastructure Analysis, Center for Medical Research, Medical University of Graz, Graz, Austria*
[b]*Division of Cell Biology, Histology and Embryology, Gottfried Schatz Research Center, Medical University of Graz, Graz, Austria*

Contact email: kerstin.hingerl@medunigraz.at

Abstract
The main goal in the electron microscopic field of life sciences remains preserving the ultrastructure from biological samples as native as possible. A crucial technique against this issue proved to be cryogenic fixation, which is growing in significance in research communities over the years. This boom is primarily focused on samples suitable for TEM microscopes. Yet, how should someone proceed if their research question demands SEM procedures?
We, the team of the Core Facility Ultrastructure Analysis at the Medical University of Graz, would like to present the various range of applications of our Quorum PP3010T Cryo-SEM Preparation System, which is attached to our Zeiss Sigma 500.
The Cryo-SEM system comprises of two dewars for cooling, a preparation desk containing a slusher pot for the freezing process, a transfer device and a prep chamber, which is connected with the microscope chamber. Thus, we have the potential to plunge freeze, transfer the frozen samples under cold vacuum conditions into the preparation chamber, freeze fracture, sublime and sputter coat samples on location. Having such a fast and simple freeze fracture device beside our SEM makes investigating the samples simple and supports the effort of preparing them close to their natural state.
As a result, the spectrum of applications for our Cryo-SEM is remarkable and encompasses human, animal, plant and food samples as well as microorganisms. Moreover, one of the Cryo-SEM's biggest advantages is the ability to prepare even samples that cannot be processed using room temperature SEM methods so far. Saliva, gels or foams are finally viable for examining in an electron microscope. Armed with the above insights and perspectives, it is obvious how the Quorum PP3010T Cryo-SEM Preparation System has become a core component of our methodological portfolio.



Cryo-SEM image of Saccharomyces cerevisiae

IM3 Quantitative imaging in SEM/STEM, electron diffraction, 4D-STEM and ptychography

Type of presentation: Invited

IM3-IN-1 Developments in 4D-STEM and Ptychography: From Series Registration to Live Compression

Benedikt Haas[a], Sarah Flöter[a], Anton Gladyshev[a], Marcel Schloz[a], and Christoph T. Koch[a]

[a]*Department of Physics and Center for the Science of Materials Berlin, Humboldt-Universität zu Berlin, Germany*

Contact email: haas@physik.hu-berlin.de

Momentum-resolved scanning transmission electron microscopy, mostly called 4D-STEM, is a powerful acquisition technique allowing to collect large amounts of information from down to sub-atomic dimensions that has become a mature and widely used method [1]. 4D-STEM data sets can be used, depending on the acquisition geometry, for a plethora of analyses: from structural characterization over strain measurements to phase microscopy. Ptychography is such a phase microscopy principle based on 4D-STEM data from overlapping regions, that has gained a lot of interest as it can efficiently use the wealth of information to gain novel information about the sample, e.g. super-resolution [2] or 3D information [3].
However, 4D-STEM has several drawbacks that we will address here: drift and errors in probe positions inherent to STEM acquisition and the large size of data sets and thus problems in handling and analyzing them. Here, we demonstrate solutions and show how ptychography and other analysis techniques can benefit. We will also demonstrate how to acquire energy-resolved 4D-STEM data and what it might be used for. In the end, we will compare ptychography, as an increasingly popular phase microscopy technique, with the conventional TEM phase technique in-line holography using synthetic data and show that ptychography is often but not always superior.

Errors in probe positions that are inherent to STEM and can arise due to drift but also more fundamentally from hysteresis and noise in the scan coils. For STEM imaging, the acquisition of multiple frames and subsequent registration of the data has been successfully used in the past to remedy these problems. We have extended this principle to 4D-STEM by acquiring a series of 4D-STEM data sets and non-rigidly registering accompanying images (or ones created from the 4D data). The found distortions can then be compensated by applying the shifts to each image that corresponds to one pixel in reciprocal space independently. The series of now registered 4D maps that can be summed for a high fidelity 4D data set allowing for significantly better data analyses [4] and we will demonstrate examples. This method also enables the registration of 4D-STEM series where a parameter, such as the defocus, has been varied. We show that such a defocus 4D-STEM series (a 5D dataset) leads to improved 3D information if the ptychographic reconstruction is adapted to make use of it [5].
The richness of 4D-STEM data is not only boon but also bane as the large data size complicates handling, analysis and storage. We demonstrate live processing of 4D-STEM [6] to get direct feedback in an ongoing data acquisition in the form of configurable masks applied to the detector frames (virtual dectors). They not only enable imaging such as annular dark-field but also more complex information, e.g. center-of-mass (COM) data (through gradient masks). As some types of analyses, such as COM, can already be delivered by the live processing, the raw data might not be needed and can be discarded before ever saving it to a hard drive, which leads to a drastic compression of typically several thousandfold. This leads to the question whether the data can be represented in an elegant basis that allows for strong compression while keeping high fidelity of the data. Investigating the performance of different bases for ptychography shows that down to only 15 values per scan position can yield good reconstructions [7] even with sparse STEM sampling (1 Å) and large beam footprint exceeding the unit cell size in the case of an adapted basis set obtained from the Gram-Schmidt algorithm. We will show a comparison of different bases and their performance.
We show that it is also possible to obtain energy-resolved 4D-STEM data. Starting with a typical single-focus electron energy-loss spectroscopy (EELS) setup, the detector frames of a 4D-STEM acquisition then contain one energy and one momentum axis. The momentum space contained within the entrance aperture is projected onto a line by the focusing of the EELS. Using the abovementioned registration

scheme, it is then possible to register a series where the diffraction plane was rotated. In the simplest case, two orthogonal projections can be used, sufficient to calculate COM, but tomographic reconstruction of the momentum plane from multiple projections is also possible. The resulting 5-dimensional data then has combined information of energy-loss and momentum-transfer at atomic resolution [8] and can contain information about orbital angular momentum, giving insight into the local electronic structure, bonding asymmetries, and symmetry-breaking effects such as chirality or crystal field splitting at the atomic scale.
As electron ptychography is quickly becoming more widespread, it seems useful to compare it to other phase microscopy techniques where interest seems to fade. We have conducted a comparison of ptychography, in the form of the extended ptychographic iterative engine (ePIE) [9] as implemented in abTEM [10], and in-line holography based on the iterative wave-function reconstruction (IWFR) algorithm [11] to compare reconstructions of thin samples (up to a few nm). Synthetic data was generated using abTEM for three types of samples (Si wedge, Si with defect, graphene) at two high tensions (30 kV and 200 kV) and for various doses. We analyze the resolution and the phase shifts using several metrics. While ptychography consistently outperforms in-line holography in terms of spatial resolution, we show that for very low doses (10^2 e/Å^2) in-line holography can yield better reconstructions, especially at higher beam energy.

Registering and live-processing of 4D-STEM data remedies main drawbacks of the technique and offers new possibilities for analyses. Energy-resolving 4D-STEM literally opens a new dimension for 4D-STEM and enables new insight into materials at the atomic level.
A comparison between in-line holography and ptychography shows that while ptychography is rightly a very actively used and researched technique with high spatial resolution, under certain conditions such as low doses in-line holography can outperform it.

Acknowledgements
The authors thank Kristiane Elsner for sample preparation, Lewys Jones for help with data registration and Andreas Mittelberger for his involvement in developing live processing.

References:

1. C. Ophus, *Micr. Microanal.*, **2019**, 25, 563–582.
2. Z. Chen et al., *Science* **2021**, 372, 826-831.
3. H.G. Brown et al., *Microsc. Microanal.* **2022**, 28, 1632-1640.
4. C. O'Leary, B. Haas et al., *Microsc. Microanal.* **2022**, 28, 1417-1427.
5. M. Schloz et al., *Microsc. Microanal.* **2025**, 31, ozae110.
6. B. Haas et al., *Microsc. Microanal.* **2021**, 27, 994-997.
7. A. Gladyshev et al., *arXiv* **2022**, arXiv:2211.07372.
8. B. Haas, C.T. Koch, *Microsc. Microanal.* **2022**, 28, 406-408.
9. A. Maiden et al., *Optica* **2017**, 4, 736-745.
10. J. Madsen, T. Susi, *Open Res. Eur.* **2021**, 1, 1-29.
11. L.J. Allen et al., *Ultramicroscopy* **2004**, 100, 91-104.

Type of presentation: Invited

IM3-IN-2 Low-Dose 4D STEM for Cross-Disciplinary Materials Characterisation

Lothar Houben[a], Shahar Seifer[b], Michael Elbaum[b]

[a]*Department of Chemical Research Support,Weizmann Institute of Science, Rehovot, Israel*

[b]*Department of Chemical and Biological Physics,Weizmann Institute of Science, Rehovot, Israel*

Contact email: lothar.houben@weizmann.ac.il

While 4D STEM has seen significant advances in high-resolution imaging under high electron fluence, such approaches are fundamentally limited when applied to radiation-sensitive materials. Our work focuses on low-dose 4D STEM methodologies tailored for beam-sensitive systems such as biological specimens and organic matter. Recognising the limitations of conventional techniques like ptychography under low signal-to-noise conditions, we develop alternative image reconstruction algorithms from scanning diffraction data that are robust to low-count statistics. The example of 4D STEM cryo-tomography from a defocussed scan across a cryo-sample of T4-bacteriophages is shown in Figure 1. Our bright-field reconstruction scheme is closely related to the tilt-corrected bright-field approach [1], but work with the defocused probe to reduce the dose rate and simplifies the computation of the upscaled bright-field image. These 4D STEM bright-field methods, incorporated into tomographic reconstruction workflows, are beneficial for thick biological samples, where traditional TEM phase contrast imaging is limited.

In parallel, we explore low-dose scanning nanodiffraction for diffraction-based imaging and crystallographic mapping. This inherently dose-efficient approach is employed to study organic, biogenic and bioinspired material, and cryogenically preserved organic systems. To support this, we develop computational strategies for diffractive signal interpretation and integrate analytical information to build a comprehensive understanding of complex material systems. Figure 2 presents the analysis of scanning nanobeam diffraction data of bioinspired

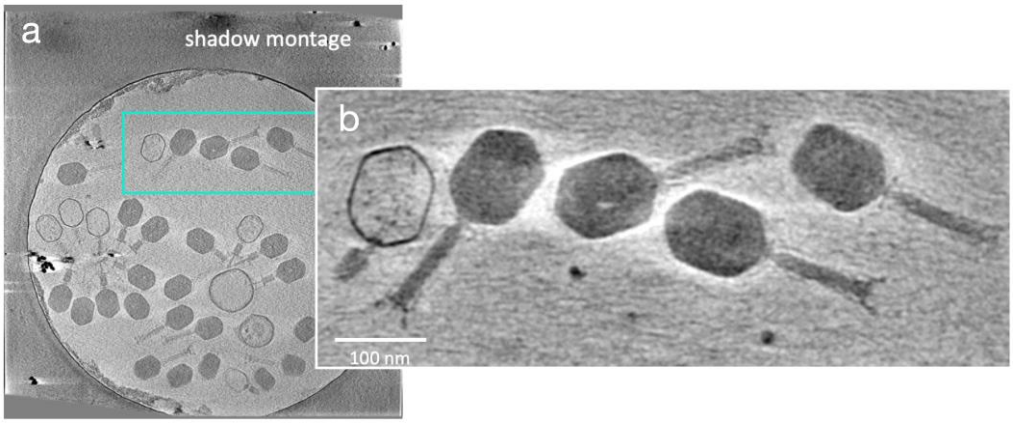


Figure 1: Slice of a 3D reconstruction of 4D STEM data of a T4-bacteriophage cryo-sample. The upscaled in-focus data (a) was obtained from tilt series of diffraction data in a 4D STEM scan of a defocussed low-dose probe. (b) Magnified view with details of the phage including the head containing the genetic material and tail for attachment and DNA delivery.

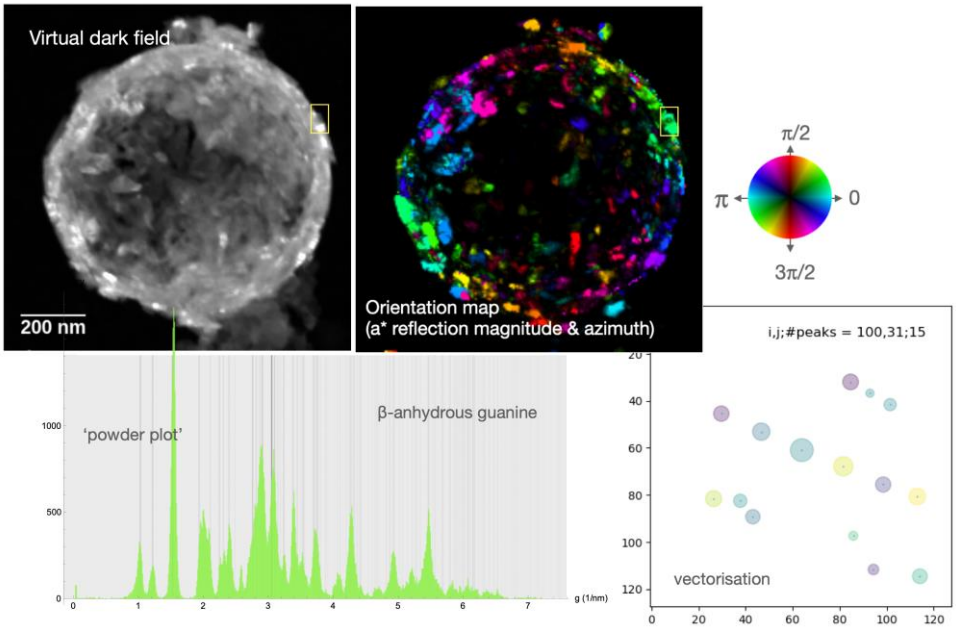


Figure 2.: Orientation and phase mapping of bio-inspired crystalline core-shell guanine spherulites from 4D STEM nanobeam diffraction data sets. Data reduction produces a sequence of feature vectors for signal representation and efficient computation, one for each diffraction frame. Here, the feature vector is a set of Bragg reflections with their spacings, polar angle and intensity. Orientation maps or 'powder plots' are representations of the feature vector set. (hkl) orientation maps are extracted by filtering the feature vector set l for the respective lattice spacings. The powder plot and the a* map in this example was processed from data taken on an EMPAD hybrid pixel detector with 128x128 diffraction frame pixels at 200 kV acceleration voltage with a semi-convergence angle of 0.2 mrad. The measurements were done at room temperature with a primary beam current of 4 pA and a pixel dwell time of 2 ms, resulting in a total fluence of about 6 $e^{-}/Å^{2}$.

guanine spherulites [2], with a one-shot 4D STEM exposure crystallographic phase and orientation habit of the architecture of molecular crystals are resolved with high precision. This work demonstrates how low-dose 4D STEM can be extended beyond conventional imaging to enable cross-disciplinary characterisation of challenging materials.

References:

1. Y. Yu, M. Colletta, K.A. Spoth, D.A. Muller, L.F. Kourkoutis, *Microscopy and Microanalysis* **2022**, 28 (S1), 1192–1194.
2. L. Alus, L. Houben, N. Shaked, A. Niazov-Elkan, I. Pinkas, D. Oron, L. Addadi, *Advanced Materials* **2024**, 36, 2308832.

Type of presentation: Oral

IM3-O-1 Advanced STEM of Point Defect Clusters in Doped STO

Elena Unterleutner[a], Philipp Brunner[b], Wolfgang Sprengel[b], Ferdinand Hofer[a,c], Gerald Kothleitner[a,c], Daniel Knez[a]

[a]*Institute of Electron Microscopy and Nanoanalysis, Graz University of Technology, (Graz), Austria*

[b]*Institute of Materials Physics, Graz University of Technology, (Graz), Austria*

[c]*Graz Centre for Electron Microscopy (ZFE), (Graz), Austria*

Contact email: elena.unterleutner@felmi-zfe.at

Introduction

Atomic-scale defect detection in complex oxides such as $SrTiO_3$ (STO) is crucial for optimizing their functional properties. The controlled introduction of dopants and vacancies enables precise tuning of electronic and magnetic behavior, making detailed knowledge of their structural and electronic configurations essential. In this study, we present a comprehensive approach that refines the entire workflow, from advanced sample preparation to sophisticated data analysis, for reliable point defect characterization using aberration-corrected scanning transmission electron microscopy (STEM).

Methods

To develop and optimize defect characterization techniques, we investigate STO doped with low concentrations of Ta. The atomic-scale distribution and defect structures introduced by doping are analyzed by correlating information from integrated differential phase contrast (iDPC) and high-angle annular dark-field (HAADF) imaging, as well as positron annhilation spectroscopy (PAS).

Multislice (MS) simulations are employed to optimize experimental parameters, while precise sample preparation techniques, including wedge polishing, ensure optimal imaging conditions. Extremely thin samples (<18 unit cells) were prepared, and their thickness was verified using position-averaged convergent beam electron diffraction (PACBED) to enable direct comparison with MS simulations. The primary focus of this study is to investigate the point defects comprised of O and Sr vacancies associated to adjacent Ta dopants. By integrating simultanous HAADF and iDPC imaging, we systematically examine the spatial correlation between Ta dopants, Sr vacancies, and oxygen vacancies in doped STO.

Results

Our findings, illustrated in Figures 1 and 2, confirm the presence of Ta dopants in STO using HAADF imaging. The results further suggest a correlation between Ta incorporation and the formation of Sr vacancies (Figure 1). Additionally, iDPC-based oxygen vacancy detection indicates a potential link between O vacancies, Sr vacancies, and Ta dopants (Figure 2).

Discussion and conclusions

These results contribute to the ongoing development of robust, quantitative approaches for defect analysis in complex oxides. Current efforts focus on refining data analysis techniques to establish a reliable defect characterization framework, which can be extended to other complex oxide material systems. By systematically optimizing both experimental and analytical methods, this study advances atomic-scale defect quantification, paving the way for improved control over functional properties in doped oxides.

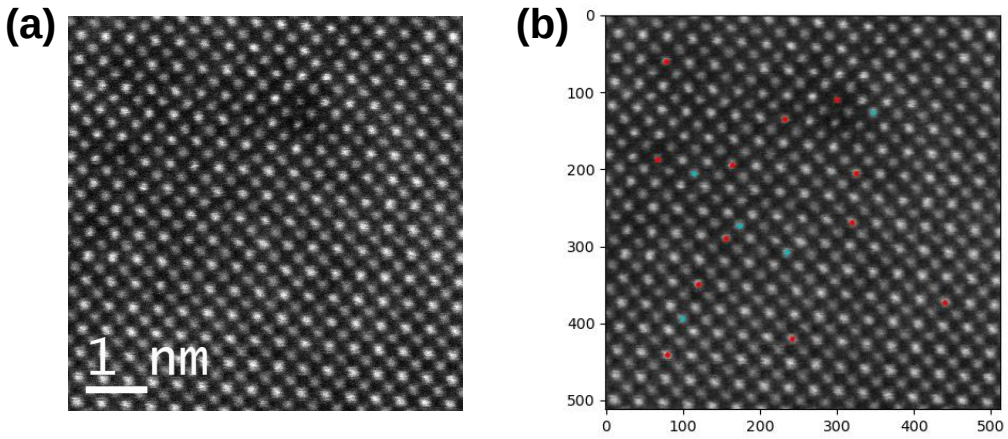


Figure 1: STEM HAADF image of STO:Ta (a), same image with deviating columns marked. Columns with too low intensity in red (Sr vacancies) and columns with too high intensity in cyan (Ta dopants) (b). Scale corresponds to 1 nm.

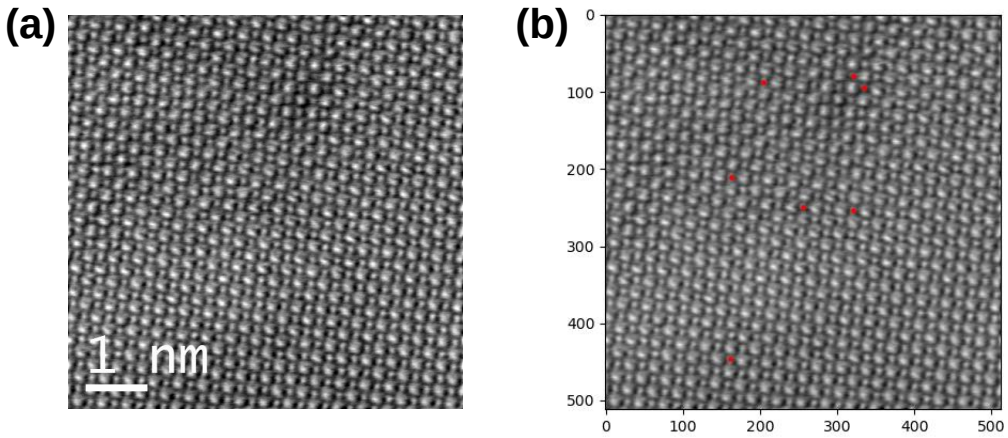


Figure 2: STEM iDPC image of STO:Ta (a), same image with columns with too low intensity marked in red (O vacancies) (b). Scale corresponds to 1 nm.

Type of presentation: Oral

IM3-O-2 Electric Field and Pair Distribution Function mapping by Precession Scanning Electron Diffraction (4D-SPED) in TEM

Athanassios S Galanis[a], Alejandro Gomez-Pereza[a], Joaquim Portillo[a], Evangelos Grivas[a], Partha Pratim Das[a], Martijn Fransen[a], Jaume Gázquez-Alabart[b], Roger Guzman[b], Gervasi Herranz[b], Manuel Bibes[c], Janine Guckelhorn[b], Gyanendra Singh[b], Sergi Plana-Ruiz[d], Stavros Nicolopoulos[a]

[a]*NanoMEGAS SPRL (Brussels) Belgium*

[b]*ICMAB-CSIC, Campus UAB, Bellaterra, (Barcelona) Catalonia, Spain*

[c]*Laboratoire Albert Fert, CNRS, Thales, Université Paris Saclay, Palaiseau, France*

[d]*SRCIT, Universitat Rovira i Virgili, (Tarragona) Catalonia, Spain*

Contact email: tgalanis@nanomegas.com, sergi.plana@urv.cat, partha@nanomegas.com

Introduction

Material characterization is key to understanding structural, electronic, and functional properties. While techniques like X-ray diffraction or optical methodologies provide valuable insights, advanced TEM methods offer enhanced capabilities. 4D-Scanning Precession Electron Diffraction (4D-SPED) is a well-established technique in TEM for orientation and phase mapping (commercially known as ASTAR) [1], as well as for strain analysis [2] at nanometer scale resolution. By leveraging precession to reduce the dynamical effects of electron scattering [3], the quality of these maps is significantly improved. In this context, this work expands the applications of 4D-SPED to two modern characterizations: the mapping of electric field (EF) to probe the charge distribution in electronic, optical, and electromechanical materials, and ePDF mapping, which is particularly useful for studying amorphous, nanocrystalline, and disordered systems, with applications in semiconductor materials, amorphous glass, amorphous solid dispersions and polymers [4].

Materials and Methods

EF studies: The use of beam precession for EF mapping is interesting because it helps to reduce the diffraction contrast produced by dynamical scattering inside the transmitted beam. Usually, a center of mass (COM) algorithm is used to detect the beam deflection caused by Coulomb forces on the sample, enabling calculation of the apparent electric field on the sample. The uniformization of the transmitted beam intensity by the precession movement helps to disentangle the structure contribution from the physical properties, resulting in more accurate analysis. As a case study, the apparent EF at an interface of STO doped with 1% Ca and AlO is shown with and without the use of beam precession by employing a fully automated software through a COM algorithm [5].

ePDF Mapping: Data collection of a semiconductor material with multiple amorphous layers was performed using beam scanning combined with beam precession (4D-SPED). The data were analyzed using newly developed, fully automated software dedicated to ePDF mapping analysis. This software processes the diffraction data by determining the center of each pattern, calculating 1D profiles, and computing the ePDF.

Results and Discussion

EF studies: The deflection of the central beam in the data series was calculated using a novel, straightforward software employing a Center of Mass algorithm. The calculated beam deflection is presented as a color map that corresponds to the direction of the transmitted beam shift—and consequently, to the electric field direction. The apparent electric field and potential is calculated along an area of interest (data not shown). At the AlO-CaSrTiO interface, the emergence of a 2D electron gas can be directly and clearly identified in the precessed data. In contrast, the non-precessed data shows poor results, mainly due to the high dynamical effects and strong contrast in the transmitted beam, which prevents the COM algorithm from accurately calculating the center of mass.

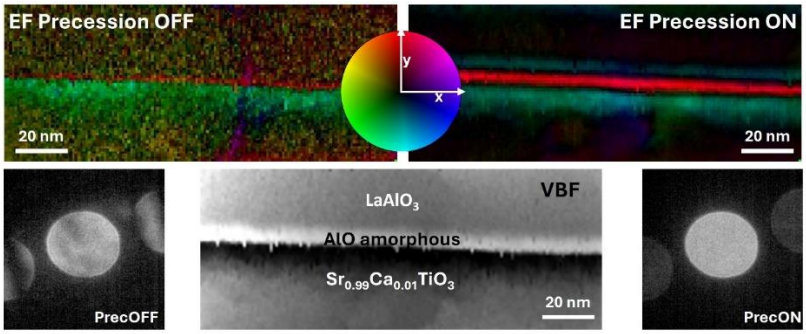


Figure 1: Electric Field maps by 4D-Scanning ED, without (left) and with Precession of 0.8° (right). The colors are related to the direction of the EF according to the reference color wheel (middle up). Representative diffraction pattern (bottom) from the same pixel of the scanned area, without (left) and with precession (right). Sample structure is shown within the Virtual Bright Field image (middle bottom).

ePDF Mapping: The ePDF was automatically computed for every pixel/step of the precessed electron diffraction data series using the ePDF Mapping data analysis software. The computed ePDFs were used to determine the Pearson correlation function, enabling a rapid assessment of similarities and differences across the scanned area. Additionally, peak positions, widths, and heights of the ePDF profiles were analyzed to identify structural variations. For the semiconductor material, the study reveals that the scanned area primarily consists of two distinct layers: an amorphous silicon nitride (Si_3N_4) layer (indicated by yellow pixels, see Fig. 2-Left) and an amorphous silicon oxide (SiO_2) layer (indicated by green pixels; see Fig. 2-Left). In the amorphous Si_3N_4 layer, the first peak position in the experimental ePDF is 1.65 Å, which is very close to the Si–N distance in crystalline Si_3N_4 (1.68 Å). In the amorphous SiO_2 layer, a slightly shorter bond distance was observed (first peak at 1.56 Å) compared to the standard Si–O distance in crystalline quartz (approximately 1.61 Å), possibly may be due to the addition of a small amount of carbon.

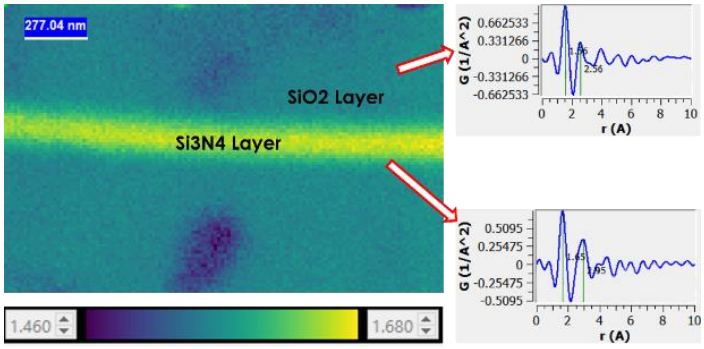


Figure 2: Left - Color map showing the variation of peak positions (Å) in the scanned area, highlighting layers of Si_3N_4 and SiO_2 and Right: Representative ePDF (blue curve) from these layers, with vertical green lines indicating the first two peak positions and their numerical values—1.56 and 2.56 Å for the SiO_2 layer, and 1.65 and 2.95 Å for the Si_3N_4 layer—in the experimental ePDF.

Conclusions

We present the development of two novel software tools for processing 4D-SPED data for electric field and electron pair distribution mapping in TEM. A case study for each method is presented, each using a single semiconductor material of high interest. This work highlights the necessity of applying precession during 4D-STEM experiments to enhance data quality and ensure reliable, robust results.

References

[1] E.F. Rauch *et al*. *Zeitschrift für Kristallographie* **2010**, *225*, 103
[2] A. D. Darbal *et al*. *Microsc. Microanal.* **2014**, *20*, 1066
[3] R. Vincent and P. Midgley, *Ultramicroscopy* **1994**, *53*, 271
[4] Y. Rakita et al. *Acta Materialia* **2023**, *242*, 118426
[5] L. Bruas *et al. J. Appl. Phys.* **2020**, *127*, 205703
[6] V. S. Chejarla et al, *Small Methods 2023*, 2300453

Type of presentation: Oral

IM3-O-3 Exploring perovskites at the atomic level by 4DSTEM: Experimental & Simulation

Meryem Lachhab[a,b], Maxime Vallet[c], Charles Paillard[d], Goran Dražić[a,e], Brahim Dkhil[c] and Mojca Otoničar[a,b]

[a]*Electronic Ceramics Department, Jožef Stefan Institute, Ljubljana, Slovenia*

[b]*Jožef Stefan International Postgraduate School, Ljubljana, Slovenia*

[c]*Université Paris-Saclay, CentraleSupélec, CNRS-UMR8580, Laboratoire SPMS, 91190 Gif-sur-Yvette, France*

[d]*Department of Physics, University of Arkansas, Fayetteville, Arkansas 72701, United States*

[e]*Department of Materials Chemistry, National Institute of Chemistry, 1000 Ljubljana, Slovenia*

Contact email: meryem.lachhab@ijs.si

Understanding lattice distortions and their influence on strain and charge distribution at the nanoscale is essential for establishing structure-property relationships in materials. In this study, we utilize four-dimensional scanning transmission electron microscopy (4D-STEM) to analyse unstrained perovskite structures at the atomic scale by collecting conversion beam electron diffraction (CBED) patterns and measuring the center-of-mass (CoM) shifts [1]. By analysing defect-free lattice regions, we aim to establish a reference dataset for non-distorted strain-free diffraction patterns.

Lead-free ferroelectric perovskite; $BiFeO_3$ (BFO); was sintered using the cold sintering process (CSP) to obtain a dense microstructure at 650 MPa applied pressure and relatively low temperatures, 300 °C [2]. We then performed 4D-STEM experiments on BFO and $SrTiO_3$ (STO; single crystal STO as a non-ferroelectric cubic reference material) using a Double-Corrected Monochromated Spectra 300 S/TEM at variable camera lengths, convergence semi-angles and pixel sizes to investigate their impact on the CBED CoM shift measurements and final spatial resolution. The diffraction data were analysed using py4DSTEM [3], and abTEM was used to simulate the CBED from model structures of the same materials for comparison with experimental results [4]. Differences between experimental and simulated data were observed, highlighting the need for parameter optimization in both experimental and computational workflows.

By combining experimental STEM techniques with simulations, this research provides valuable insights into the structure-property behaviour of ferroelectric perovskites. Our findings present a baseline for future investigations into how CSP-induced defects influence the properties of lead-free perovskites, contributing to the development of environmentally sustainable ceramics through low-temperature processing.

The authors would like to thank Vinko Sršan and Victor Regis for their help with the simulations.
The Slovenian Research and Innovation Agency (ARIS) is acknowledged for funding the research under Programme P2-0105-1, Project J2-50077, bilateral project BI FR/Proteus, and young researchers funding

References:

1. Colin Ophus, *Microscopy and Microanalysis*, Volume 25, Issue 3, June **2019**, pp. 563 – 582.
2. S Salmanov, M Otoničar, *Journal of the European Ceramic Society,*Vol 45, Issue 1, January **2025**.
3. Benjamin H Savitzky, Colin Ophus, *Microscopy and Microanalysis*, Vol 27, no 4, August **2021**, pp. 712–743.
4. Madsen J and Susi Z, *Open Research Europe*, Vol 1, no 24, **2021**.

Type of presentation: Poster

IM3-P-1 Evaluating Electron Radiation Damage Mitigation in Graphene Liquid Cell

Min Chevalier Kwon[a], Pavel Filipčík[b], Willy Stehl[a], Jan Pieter Abrahams[a,b]

[a]*Biozentrum, University of Basel, 4056 Basel, Switzerland*

[b]*Paul Scherrer Institut (PSI), Laboratory of Nanoscale Biology, CH-5232 Villigen PSI, Switzerland*

Contact email: min.chevalierkwon@unibas.ch

We want to visualise individual biomolecules at high resolution in their active, native, and dynamic state, using transmission electron microscopy (TEM). EM requires the samples to be placed in a vacuum, and electron beam damage limits the resolution that can be achieved. The current state-of-the-art is cryo-EM: flash-frozen samples are studied at liquid nitrogen temperatures. We are exploring a different approach, in which we encapsulate biological materials between graphene sheets in graphene liquid cells (GLCs). It has been reported that graphene and/or retaining the liquid state can improve the lifetime of biological samples in the EM at room temperature [1]. We aim to evaluate electron radiation damage in biological samples encapsulated in GLCs. Here, we investigated the diffusion rates of fluorescent dyes and biomolecules in GLCs using fluorescence correlation spectroscopy (FCS) and TEM, and performed elemental analysis of ferritin in GLCs using electron energy loss spectroscopy (EELS). Our results show the successful encapsulation of liquid by observing Brownian diffusion in these confined environments by TEM and FCS, and further confirmed the presence of water by detecting an oxygen peak in GLCs by EELS.

Reference:
[1] Keskin, S., & de Jonge, N. (2018). Reduced radiation damage in transmission electron microscopy of proteins in graphene liquid cells. Nano letters, 18(12), 7435-7440.

Acknowledgement:
This research was supported by the Swiss National Science Foundation.

Type of presentation: Poster

IM3-P-2 Selective defect creation in 2D hexagonal boron nitride via low-energy Ar^+ irradiation

Shrirang Chokappa[a], Manuel Längle[a], Vladimir Zobac[a], Toma Susi[a], and Jani Kotakoski[a]

[a]Faculty of Physics, University of Vienna, (Vienna), Austria

Contact email: shrirang.chokappa@univie.ac.at

In recent years, point defects in hexagonal boron nitride (hBN) have received increasing attention for being an excellent host for single photon emitters (SPE) at room temperature [1,2]. It has been predicted that carbon atom substitutions in a boron site beside a nitrogen vacancy (C_BV_N) in hBN are the most likely emission source [4]. SPEs are a growing research area that have potential applications in quantum communications, information and simulations as well as photonics [3], and introduces the question of whether defect creation in hBN can be controlled. The aim of this study was to explore the possibility of selectively creating one type of vacancy, either boron or nitrogen, in two dimensional monolayer hBN. Here, we prepare monolayer hBN samples using an electrochemical delamination method for hBN transfer from copper foil to TEM grids, and subject them to low-energy Ar^+ irradiation.

According to simulations using time dependent density functional theory molecular dynamics (TDDFT-MD), the energy of an Ar^{+1} ion in a head-on collision with nitrogen requires 34.5 eV to successfully knock it out from the hBN lattice, and requires 45.5 eV to successfully knock out a boron atom, indicating the possibility of selective defect creation. In this experimental study, hBN samples were irradiated with four different ion energy profiles centred at: 0 eV (physically this means an irradiation with the higher energy spread (σ) of the beam-profile), 40 eV, 60 eV and 150 eV, and using our interconnected ultra-high vacuum system [5], the irradiation effects were directly imaged via scanning transmission electron microscopy (STEM) without exposing the samples to ambient conditions. Large area semi-autonomous STEM image acquisition [6] was performed to acquire hundreds of images of hBN before and after irradiation. Pre-irradiation data was used to assess the intrinsic defect concentration in hBN and post-irradiation data was used to analyse the irradiation induced vacancy type and concentration for each of the energies. The intrinsic defect concentration was found to be ca. 0.06 nm^{-2} with ca. 44% single vacancies (ca. 55% boron and 45% nitrogen), ca. 37.5% double vacancies and the rest being more complex vacancies. The ion-induced vacancy concentration was found to be ca. 0.20 nm^{-2}. Interestingly, for 0 eV we found ca. 60% single vacancies (ca. 92% boron and 8% nitrogen), for 40 eV ca. 72% single vacancies (ca. 81% boron and 19% nitrogen), for 60 eV ca. 68.5% single vacancies (ca. 91% boron and 9% nitrogen), and for 150 eV ca. 60.7% single vacancies (ca. 62% boron and 38% nitrogen). These results demonstrate a high selectivity for boron single vacancies across the range of ion energies with the 150 eV irradiation being an outlier to the trend, known to be because of a different irradiation setup resulting in different irradiation parameters. This work showcases the possibility of selectively creating one type of vacancy, primarily boron single vacancies [7], in hBN with the range of Ar^+ ion energies used here, but the underlying mechanism behind the vacancy creation is yet to be understood and is not in line with the expected results from the simulation work.

References:
1. Tran et al., Nature Nanotech. 11, 37-41 **(2016)**
2. Grosso et al., Nature Comms. 8, 705 **(2017)**
3. Liu et al., Nano Mat.Science 3, 291-312 **(2021)**
4. Tawfik et al., Nanoscale 9, 13575-13582 **(2017)**
5. Mangler et al., Micro. and Microanal. 28 S1, 2940-2942 **(2022)**
6. Mittelberger et al., Micro. and Microanal. 23 S1, 809-817 **(2017)**
7. Längle et al., arXiv:2404.07166 **(2024)**

Type of presentation: Poster

IM3-P-3 Combining 3D electron diffraction and nanotexture analysis for the characterization of meteorite's impact ejecta

Paola Parlanti[a], Muriel Veron[b], Luigi Folco[c], Enrico Mugnaioli[c], Mauro Gemmi[a]

[a]*Istituto Italiano di Tecnologia, Center for Materials Interfaces, (Pontedera), Italy*

[b]*Université Grenoble Alpes, SIMaP, (Grenoble), France*

[c]*Università di Pisa, Dipartimento di Scienze della Terra, (Pisa), Italy*

Contact email: paola.parlanti@iit.it

Kamil is an impact crater that was produced by the impact of a small iron meteorite (Kamil Gebel) in southwestern Egypt. The meteorite fragmented with the impact with the target, generating thousands of fragments which are mixtures of meteorite and target materials, as well as smaller particles. Among the smaller particles, Fe-Ni oxide spherules (few hundreds um size) are particularly abundant in the crater's soil [1]. By means of 3D electron diffraction (3D ED) and nanotexture analysis, we characterize three Kamil Fe-Ni spherules, classified based on their Nickel content [2], in order to identify new mineralogical phases and ultimately unveiling their mechanism of formation.

Starting from three Kamil spherules embedded in resin, with a Focus Beam Scanning Electron Microscope (FIB-SEM) we firstly cut three lamellae for Transmission Electron Microscopy (TEM) analysis across the regions of interest. Each thin section was then analysed according to the workflow: 1) TEM/STEM imaging to investigate section's morphology; 2) TEM Energy Dispersive Spectroscopy (EDS) microanalysis to elucidate chemical composition of the different structures in the section; 3) 3D ED analysis, a single crystal diffraction technique [3], focused on the different sub-micrometric crystals in the material, and identification of their structures; 4) texture and phase analysis through Precession Assisted Crystal Orientation Mapping (PACOM) method [4], to visualize the orientation of the phases, which would elucidate their process of formation; 5) High-resolution TEM imaging, to provide clearer insights into the relationships between those phases.

The three spherules selected in this work were previously [2] classified based on the average Nickel content as: *i*) very high Ni, *ii*) high Ni, *iii*) intermediate Ni. Depending on their Ni content, these spherules show details being fingerprints of their formation processes. 3D ED allowed us to identify trevorite ("spinel Fe rich") and bunsenite ("Ni rich") crystals (respectively, blue and green in Figure 1) in the three sections. The HR TEM analysis, combined with PACOM orientation mapping, showed that trevorite and bunsenite are coherent inside the same grain. We could also visualize an amorphous interstitial material in the three sections, which resulted being formed by two components: a) small SiO_x droplets, or/and b) P-Fe rich amorphous material. The combination of PACOM and EDS analysis could allow us to discriminate these two amorphous phases in the section *i* (Figure 1, top right panel, pink and black colours – "amorphous SiO_2" and "amorphous P rich", respectively). Interestingly, the second amorphous material, the P-Fe rich, appears to be crystallized in the olivine crystal form with a high P content in the *iii* section (yellow phase Figure 1, bottom right panel). Also, metallic Ni nuggets (red phase in Figure 1, right column) were found in the *ii* and *iii*, but not in the *i*.

Taken together, these results suggest that the Fe-Ni-P meteorite's material strongly oxides and mixes together with the Si from the target. Then, with the cooling, oxidised Fe and Ni crystallize into trevorite and bunsenite oxides, while the remaining Fe mixes with the Si-P-rich liquid, which can either remain amorphous or crystallize into olivine. The remaining Ni in the liquid instead form the metallic Ni nuggets, which appear to be interspersed in the P rich material (either amorphous or olivine). This broad investigation of the nanoscale mechanism of formation of the Fe-Ni spherules was possible thanks to the combination of 3D ED, EDS, HR TEM, and PACOM.

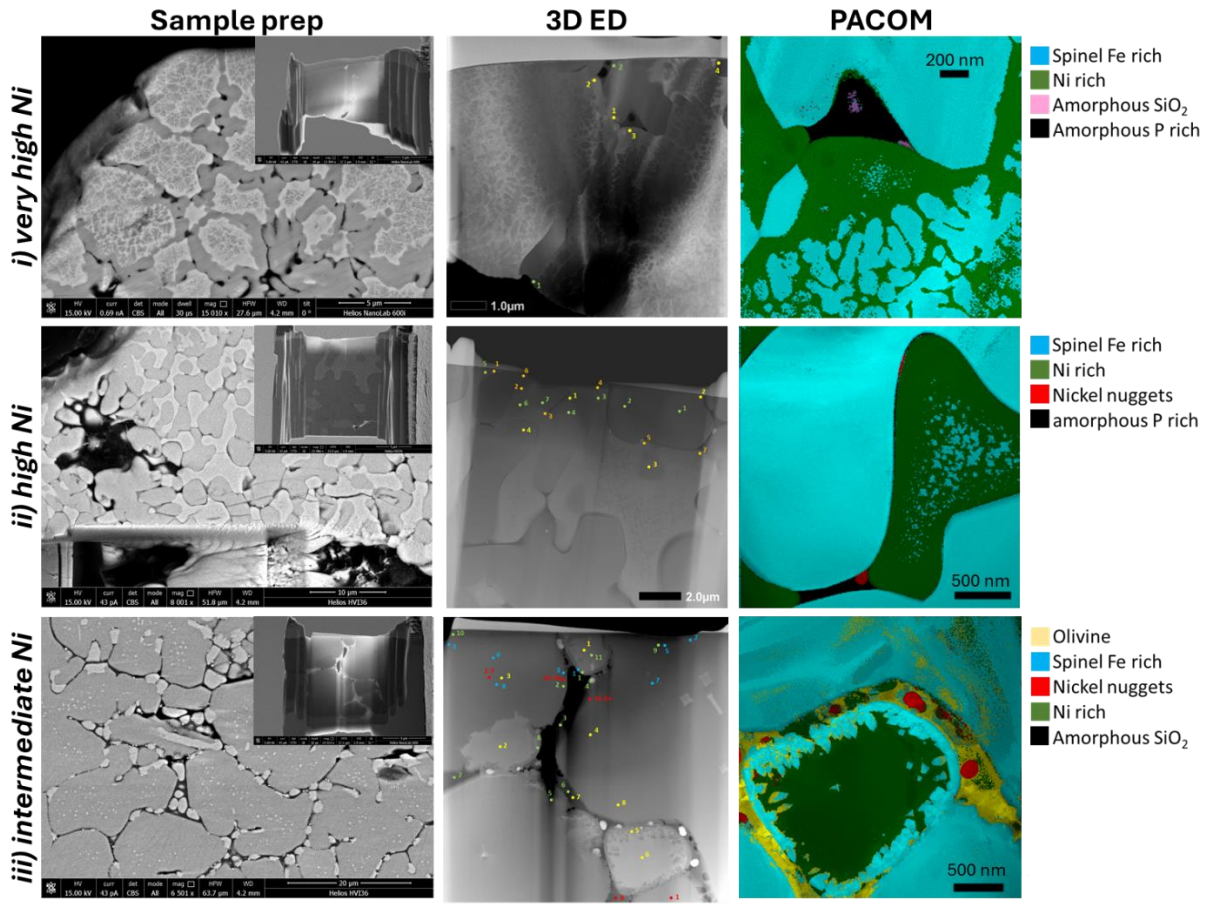


Figure 1: Characterization of Kamil Gebel's impact ejecta: workflow overview. Three impact ejecta, classified according to their average Ni content, were firstly cut in thin sections for TEM using a FIB-SEM (panels in the left column). After extensive EDS analysis of the three samples, 3D ED was performed on different crystals (middle column: see coloured dots in the STEM images, indicating the locations where 3D ED data were collected), in order to identify the different phases being in the material. Phase/orientation mapping was then carried out on different locations of the three lamellae. In the right column, representative images of phase mapping and the list of the identified phases are shown.

References:

1. L. Folco et al., *Meteorit. Planet. Sci*. **2015**, 50, 382-400.
2. L. Folco et al., *Geochim. Cosmochim. Acta*. **2022**, 335, 297-322
3. M. Gemmi et al., *ACS Cent. Sci*. **2019**, 5, 1315-29.
4. E.F. Rauch, M. Véron, *Mater. Charact*. **2014**, 98, 1-9.

Type of presentation: Poster

IM3-P-4 Automated processing of powder electron diffraction patterns

Pavlina Sikorova[a], Miroslav Slouf[b], Radim Skoupy[a,c], Ewa Pavlova[b], Vladislav Krzyzanek[a]

[a]*Institute of Scientific Instruments of the CAS, Brno, Czech Republic*

[b]*Institute of Macromolecular Chemistry of the CAS, Prague, Czech Republic*

[c]*Biozentrum, University of Basel, Basel, Switzerland*

Contact email: pavlinasik@isibrno.cz

Introduction: The newly introduced 4D-STEM-in-SEM techniques allow a modern SEM microscope to function as a user-friendly powder electron diffractometer, among other applications [1]. We have developed an open-source Python package named STEMDIFF (https://pypi.org/project/stemdiff), which reduces 4D-STEM datasets from SEM microscopes to 2D powder electron diffraction patterns [1]. Powder electron diffraction patterns can be compared with theoretically calculated powder X-ray diffraction patterns to identify the expected crystal structures in a sample. This is a straightforward process that can be routinely performed even by users without extensive crystallographic knowledge. However, fully automating crystal structure identification requires software capable of determining the center of any diffraction pattern. This contribution presents and compares several algorithms for efficient automated or semi-automated center determination in electron diffractograms.

Methods: We have developed the automated center determination within our open-source Python package named EDIFF (the package itself is under development [2]). The center determination is in *ediff.center* module of the whole package. The basic center detection method ('manual') relies on semi-automatic center detection, where the user first defines three points on the diffraction pattern from which a circle is calculated, and its center coincides with the center of the diffractogram. The remaining methods are fully automated: the 'intensity' method determines the center by calculating the intensity or mass distribution within an array, the 'hough' method employs the Hough transform to detect circular features, making it particularly effective for diffraction patterns with concentric intensity distributions, and the 'phase' method identifies the center of symmetry in a diffraction image through a combination of weighted intensity averaging and phase cross-correlation [3].
Refinement of the detected center coordinates is also available, either by manual shifting using the keyboard or automatically based on image properties (intensity sum or variance)—both contributing to precise center location determination.
After identifying the center location, the radial distribution is computed and visualized using the presented package. Background subtraction can be applied to the profile to improve compatibility with previously calculated XRD profiles. The processed data overlay is then used as a crucial step in crystallographic analysis.

Results: The EDIFF package, actively being developed by all co-authors of this contribution, is designed as an intuitive, user-friendly Jupyter Notebook [4]. This notebook serves as a template, enabling users to process arbitrary 2D-diffractogram by simply following a predefined workflow. The workflow has been successfully tested on various 2D diffraction patterns from TEM and 4D-STEM-in-SEM. In this contribution, we focus on the *ediff.center* module, which determines the key parameter for further processing – the diffractogram center coordinates.
The 'safe choice' is the interactive 'manual' method that can be successfully applied to any diffractogram regardless of its properties—subject to the necessary user input. The 'intensity' method is a suitable choice for 4D-STEM-in-SEM only, as there is no beam stopper obscuring the true maximum intensity/mass in the image. The advantage over the 'manual' method is that it is fully automatic. The Hough transform overcomes the problems with incomplete circular patterns and allows automatic detection as well. However, it works only for circular diffraction patterns. Phase cross-correlation has proven effective across different types of diffraction data, successfully identifying the center in both

polycrystalline and single-crystal patterns. Its robustness makes it a reliable method for diverse crystallographic analyses, regardless of the sample's structural characteristics. Example outputs are in Figure 1.
Additionally, some misdetections are corrected through refinement methods. Users can choose between manual adjustments, which allow for precise control but introduce the risk of human error, or automatic refinement, which enhances accuracy based on pre-defined criteria, but may fail to converge to the true center if the initial detection is significantly off.

Discussion and conclusions: Despite being originally developed for data from 4D-STEM-in-SEM, EDIFF effectively processes diffraction patterns acquired by other modalities, making it a versatile tool for crystallographic analysis across different microscopy platforms.
The future steps involve expanding the package's capabilities by developing tools for image enhancement—such as beam stopper removal, artifact, noise and background removal. Consequently, this would extend its applicability to a broader range of diffraction data, including more complex crystal structures and challenging imaging conditions. These advancements will further solidify EDIFF as a versatile tool for crystallographic analysis.

Acknowledgements: This research was supported by the project TN02000020 (TACR). We also acknowledge the Core Facility Electron Microscopy and Raman Spectroscopy, supported by the Czech-BioImaging large RI project (LM2023050 funded by MEYS CR).

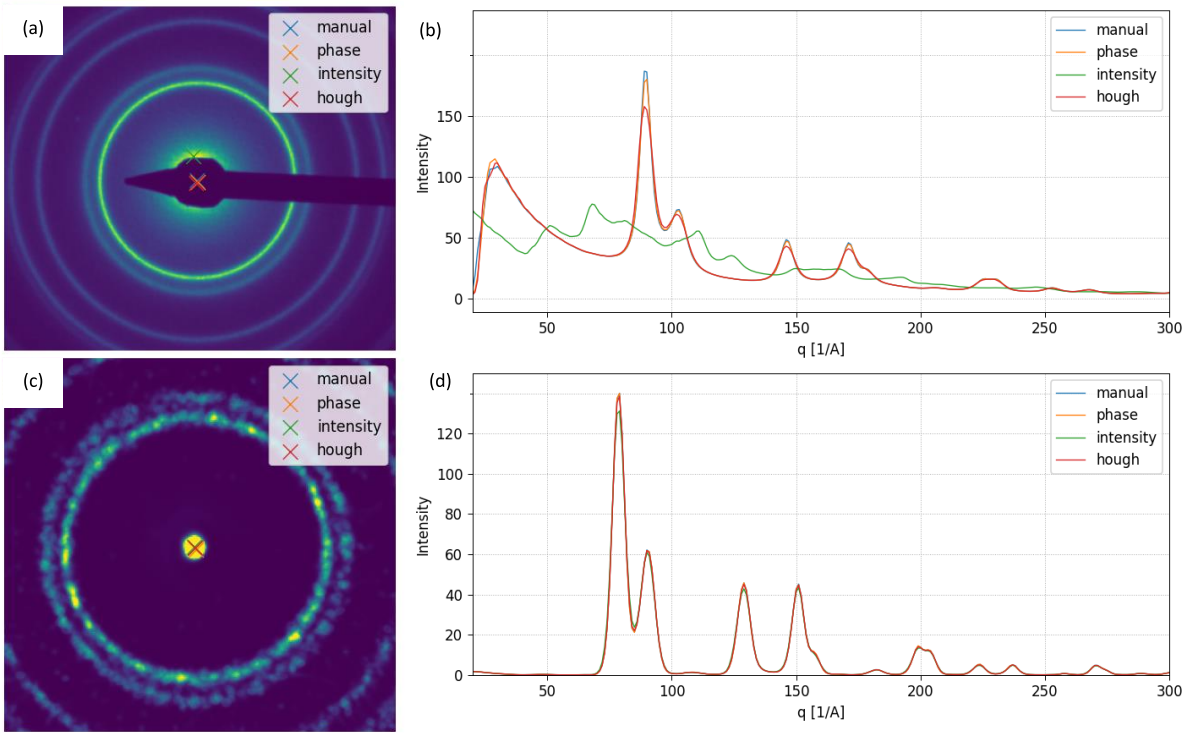


Figure 1: Comparison of center detection methods applied to Au nanoislands using TEM/SAED (a, b) and 4D-STEM-in-SEM (c, d), shown in both 2D images (a, c) and their corresponding 1D profiles (b, d). Due to the presence of the beam stopper in (a), the *intensity* method fails, while the other methods perform comparably. For the 4D-STEM data, all methods perform well, with their 1D profiles being nearly identical, aside from slight differences in peak intensities

References:

1. M. Slouf, *Materials* **2021**, *14(24)*, 7550.
2. M. Slouf, *Microscopy and microanalysis* **2025**, under review.
3. LP René de Cotret, *Adv Struct Chem Imaging* **2018**, *4(1)*, 11
4. https://docs.jupyter.org/en/latest/

Type of presentation: Poster

IM3-P-5 Electron ptychography experiment design with *PtychoScopy*

Radim Skoupy[a,f], Elisabeth Muller[a], Timothy J. Pennycook[b], Manuel Guizar-Sicairos[c,d], Emiliana Fabbri[e], and Emiliya Poghosyan[a]

[a]*PSI Center for Life Sciences, Villigen PSI, Switzerland*

[b]*EMAT, Department of Physics, University of Antwerp, Belgium*

[c]*École Polytechnique Fédérale de Lausanne (EPFL), Switzerland*

[d]*PSI Center for Photon Science, Villigen PSI, Switzerland*

[e]*PSI Center for Energy and Environmental Sciences, Villigen PSI, Switzerland*

[f]*Present Adress: EPFL and University of Lausanne, Switzerland*

Contact email: radim.skoupy@epfl.ch

Electron ptychography is a rapidly growing computational imaging technique with many applications due to its superior image contrast, simultaneous sensitivity to heavy and light elements, high dose efficiency, ability to correct for aberrations through illumination recovery and single sign contrast transfer function [1-2]. Despite its advantages, it suffers from drawbacks of hardware due to the need for fast detectors, as well as time-consuming large data processing. Some of these drawbacks can be avoided with a clever and careful experimental design, resulting in a reduction of data redundancy (here understood as data above the level required for proper image reconstruction) as well as a better reconstruction of an investigated sample. The sweet spot can be found by a wise choice of parameters and a prior understanding of a sample. To simplify the task, we present a straightforward way to design electron ptychography data acquisition settings using the Python-based tool *ptychoScopy* [3-4].

The acquisition design process can be divided into three parts, corresponding to the areas of a scanning transmission electron microscope from top to bottom: probe, scan and detection. With *a priori* knowledge of the sample, the appropriate beam energy and probe angle can be selected so that the spatial frequencies of the sample match the contrast transfer function. For low dose experiments, a defocused beam can be used to increase the electron beam diameter on a sample and to allow sufficient interbeam position overlap for proper reconstruction with generous scanning step size. The detection part is then highly dependent on the chosen camera length as it changes the maximum angle collected by a detector as well as its angular sampling. It also changes the probe window where illumination is characterised during the reconstruction process and the size of the reconstructed pixels. Finally, the beam dwell time (equal to the detector pixel time) has an impact on the total dose and the individual detector pixel coverage angle through any binning that may be required for higher frame rates. This brief description is shown graphically in Fig. 1, together with the position of the very important control loops as incorporated in the *ptychoScopy* tool.

In summary, a high-quality data acquisition design can help overcome many of the drawbacks of electron ptychography, resulting in optimal contrast transfer, planned electron dose, and the ability to reconstruct high-quality images without the need for time-consuming post-acquisition reciprocal-space upsampling [5]. This opens up the technique to a wider audience with less experience and provides an opportunity to skip the initial inappropriate parameter combination from the very first day.

Acknowledgement:
The authors acknowledge funding from the SNSF project (206021_177020) for co-financing the TEM ARM-200F (PSI) and PSI Research Grant 2021 for financing this work (R.S.).

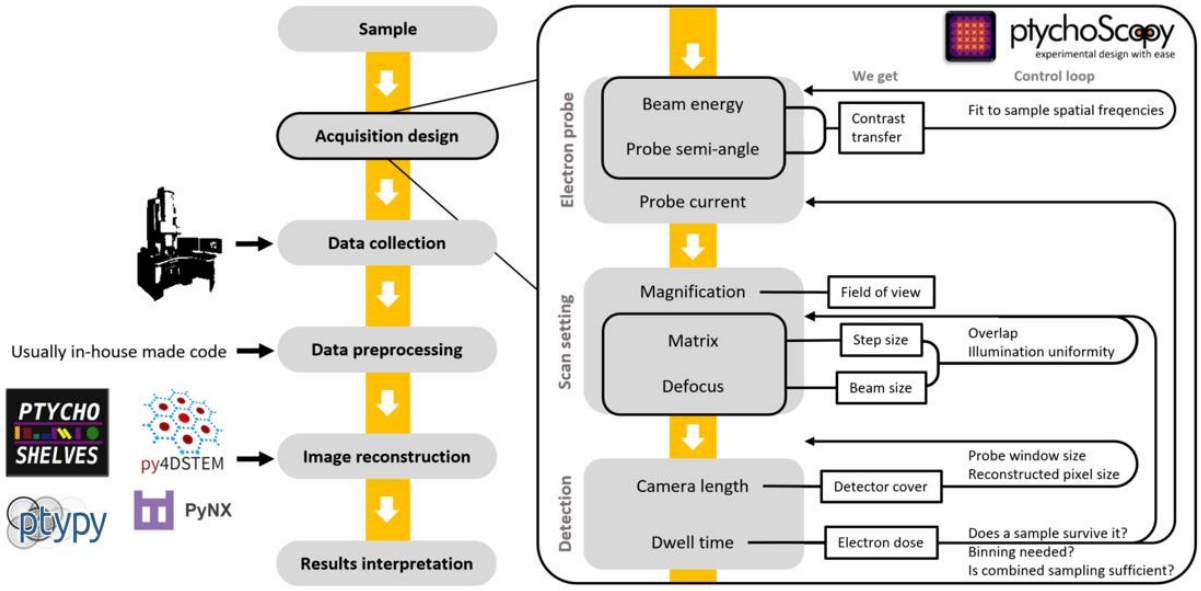


Figure 1: Experimental pipeline for electron ptychography with a detailed flowchart of the acquisition design step as it is covered by ptychoScopy.

References:

1. M. Guizar-Sicairos & J. R. Fienup, *Opt. Express* **2008,** 16, 7264–7278.
2. A. M. Maiden & J. M. Rodenburg, *Ultramicroscopy* **2009**, 109, 1256–1262.
3. R. Skoupy, E. Muller, T. J. Pennycook et al., *Scientific Reports* **2025**, 15, 24959.
4. R. Skoupy, D. Grando Stroppa, M. Guizar-Sicairos et al., *Microsc. Microanal* **2024,** 30S1, 1846–1847.
5. J. C. da Silva & A. Menzel, *Opt. Express* **2015**, 23, 33812.

Type of presentation: Poster

IM3-P-6 4D-STEM/PNBD: A semi-automated powder electron diffraction in SEM microscopes

Miroslav Slouf[a], Pavlina Sikorova[b], Ewa Pavlova[a], Vladislav Krzyzanek[b]

[a]*Institute of Macromolecular Chemistry, Czech Academy of Sciences, Praha, Czech Republic*

[b]*Institute of Scientific Instruments, Czech Academy of Sciences, Brno, Czech Republic*

Contact email: slouf@imc.cas.cz

Introduction and methods: We describe recent improvements of our method named 4D-STEM/PNBD (powder nanobeam diffraction in four-dimensional scanning transmission electron microscopy). The method can change an SEM microscope equipped with a 2D-array STEM detector to a user-friendly powder electron diffractometer. The whole process of obtaining and interpreting powder electron diffraction pattern in SEM consists of three steps, which are illustrated in Fig. 1 and described below:

1. Collection of 4D-STEM dataset with a quasi-parallel scanning beam from a region of interest in the specimen. This step is easy with modern hardware (an SEM equipped with an array detector) and software (a graphical user interface of modern microscopes). The resulting dataset may be huge (several gigabytes of data), but its collection is easy and reasonably fast (from tens of seconds to a few minutes).
2. Conversion of the huge and complex 4D-STEM dataset to a single 2D-powder electron diffraction pattern, by combining the individual nanobeam diffraction patterns (NBD). This step is surprisingly challenging, as we have to maximize signal-to-noise ratio by clever algorithms such as multiparameter filtering of the individual NBDs. However, the 4D-STEM → 2D-diffractogram conversion can be automated by means of our open-source program package STEMDIFF (https://pypi.org/project/stemdiff).
3. Final processing of 2D powder electron diffraction pattern, which is quite easy even for a non-crystallographer, comprising three sub-steps: (i) conversion of the experimental 2D-difractogram to 1D-diffraction profile, (ii) calculation of theoretical powder X-ray diffraction pattern of the expected crystal structure, and (iii) comparison of the 1D experimental and theoretical diffraction profiles. If the two profiles overlap, we have successfully identified the investigated nanocrystalline material. The 2D-diffractogram → 1D-profile conversion and processing are automated in our open-source EDIFF package (https://pypi.org/project/ediff).

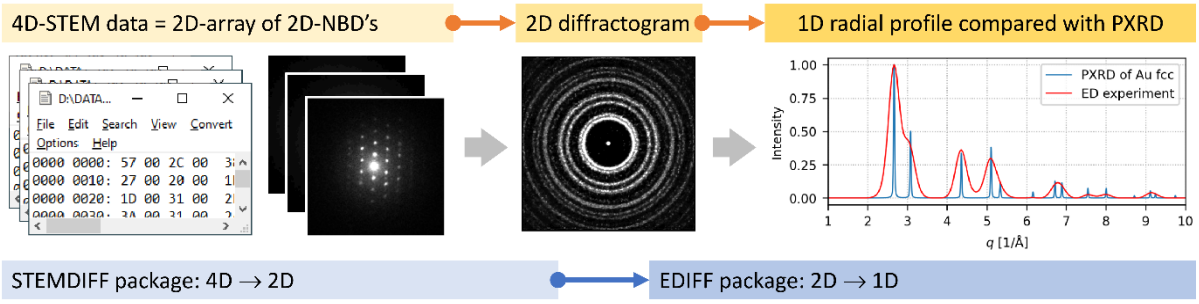


Figure 1: Principle of 4D-STEM/PNBD method: the conversion of a 4D-STEM dataset to a powder electron diffraction pattern and its comparison with theoretically calculated X-ray diffractogram.

Results and discussion: This contribution includes a live demo, demonstrating that the recent improvements of both packages (STEMDIFF and EDIFF) enable fast, user-friendly, semi-automated

processing of 4D-STEM datasets. Thanks to some behind-the-scenes processing tricks, such as estimating the shape of primary beam followed by 2D-PSF deconvolution of the individual NBDs, the 4D-STEM/PNBD results can be even better than those from standard TEM/SAED experiments, as documented in Fig. 2.

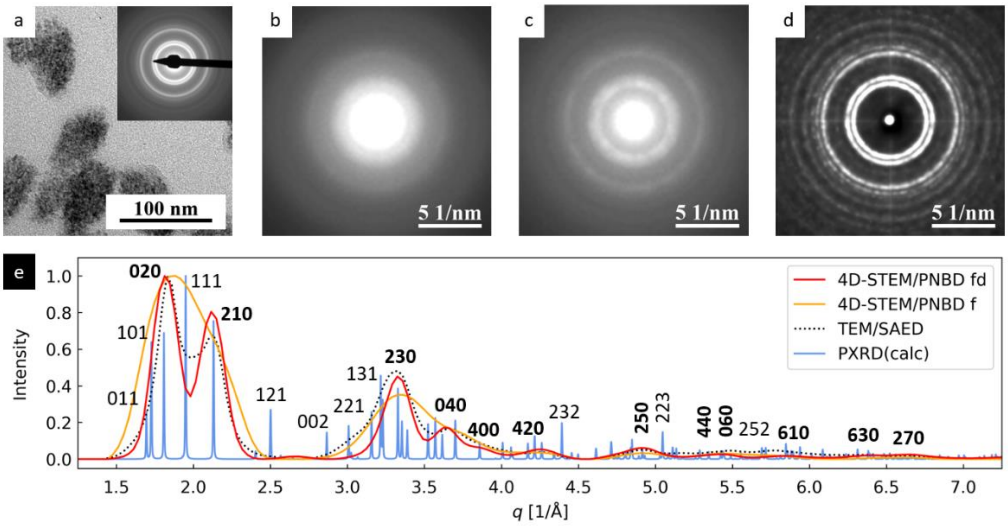


Figure 2: 4D-STEM/PNBD results for TbF_3 nanocrystalline aggregates: (a) morphology of the nanoparticles observed by TEM/BF and their diffraction pattern obtained by a standard TEM/SAED method; (b) 4D-STEM/PNBD diffractograms calculated by the summation of *all* NBD's, (c) 4D-STEM/PNBD diffractograms calculated by the summation of *filtered* NBD's; (d) 4D-STEM/PNBD diffractogram calculated by summation of *filtered and deconvoluted* NBD's; (e) comparison of 1D radially averaged diffraction profiles from 4D-STEM/PNBD (orange and red lines represent summation of *filtered*, and *filtered-and-deconvoluted* NBD's), diffraction profile from TEM/SAED (black dotted line), and theoretically calculated diffraction pattern of TbF_3 nanocrystals (blue line). The higher intensities of some diffractions (marked with blue font) result from a preferred orientation of the nanocrystals (zone axis [001]).

Conclusions: In a common SEM microscope, we can use several *imaging* modes (such as SE, BSE, and STEM imaging) and *spectroscopic* modes (such as EDX or cathodoluminescence). Nevertheless, traditional SEM microscopes do not offer a simple *diffraction* mode that could be used as an equivalent to the standard TEM/SAED (selected-area electron diffraction) technique. The 4D-STEM/PNBD method can fill this gap. It provides simple, fast and user-friendly way how to obtain and analyse powder electron diffraction patterns in SEM. The only requirement is an SEM microscope equipped with a 2D-array STEM detector, which is quite easy to add to a modern SEM. The advantage of powder electron diffraction patterns consists in the fact that their analysis is quite straightforward, even for common SEM users without deep crystallographic knowledge. Moreover, our open-source STEMDIFF and EDIFF packages can be used as intuitive templates to process powder electron patterns from both TEM and SEM microscopes.

Acknowledgements: Technology agency of the Czech Republic, program NCK2, project TN02000020.

Type of presentation: Poster

IM3-P-7 Contrast Optimization Aided by Machine Learning Applied to Virtual 4D-STEM Images

Daniel G. Stroppa[a,b], Roberto dos Reis[c,d]

[a]*DSTL GmbH, Switzerland*

[b]*DECTRIS AG, Switzerland*

[c]*Department of Materials Science and Engineering, Northwestern University, USA*

[d]*NUANCE Center, Northwestern University, USA*

Contact email: daniel.stroppa@dstl.ch

Scanning Transmission Electron Microscopy (STEM) has revolutionized imaging due to its high spatial resolution and easy interpretation due to varied contrast mechanisms. The enhanced flexibility in terms of scattering range detection in comparison with STEM is one of the reasons that led to the increased interest in 4D-STEM [1]. Supported by the recent evolution of pixelated detectors, 4D-STEM currently allows for the recording of the complete electron scattering range at speeds commensurate with traditional STEM experiments [2]. With the possibility of flexible reconstruction of virtual STEM images with arbitrary detector shapes, contrast optimization for sample regions with different scattering cross-sections is envisioned. This study focus on the optimization of contrast in virtual 4D-STEM images, employing both user-guided and machine-learning (ML) optimization approaches.

Reference samples from semiconductor devices and supported catalysts were measured with fast 4D-STEM under experimental conditions mirroring standard STEM imaging practices, with 1024x1024 scan positions and 10 us dwell time. The resultant datasets comprised 10^6 diffraction patterns with 96x96 pixels each, presenting a great challenge for manual contrast optimization due to the vast data volumes and nuanced contrast differences within the areas of the specimens.

In this current study, we develop a computational framework designed to automate the enhancement of contrast in similar regions within 4D-STEM data. Our methodology integrates the advanced deep learning architecture, ResNet101 [3], for feature extraction, followed by Principal Component Analysis (PCA) for dimensionality reduction, and the application of hierarchical clustering techniques. The utilization of ResNet101, distinguished for its deep residual learning capabilities, is strategically chosen to adeptly capture the nuanced, hierarchical features inherent in 4D-STEM datasets. The initial phase of our analysis involves processing the 4D-STEM diffraction patterns through the ResNet101 model, which has been pre-trained on extensive image datasets. This step is instrumental in extracting comprehensive high-dimensional feature vectors with essential attributes of each pattern. Following feature extraction, we employ PCA to transform the high-dimensional feature space into a lower-dimensional one, effectively reducing the computational complexity while preserving the variance critical for subsequent analysis. This dimensionality reduction is crucial for enhancing the tractability and interpretability of the dataset, allowing for a focused examination of the significant variances among diffraction patterns. The analysis concludes with hierarchical clustering, an agglomerative method that iteratively merges data points based on their similarity. This method is selected for its adaptability in uncovering the inherent groupings within the data, thereby facilitating an intuitive understanding of similarities across the dataset.

This integrated approach that merges deep learning-based feature extraction, PCA, and hierarchical clustering presents a robust strategy for automatically enhancing the contrast of similar regions within 4D-STEM data. [4]

References:

1. C. Ophus, Microsc. Microanal. 25-3 (2019) 563-582. DOI: 10.1017/S1431927619000497
2. M. Wu *et al.*, J. Phys. Mater. 6 (2023) 045008. DOI: 10.1088/2515-7639/acf524

3.He, K., Zhang, X., Ren, S., & Sun, J. (2015). Deep Residual Learning for Image Recognition. CoRR, abs/1512.03385. Available at: http://arxiv.org/abs/1512.03385
4. This work made use of the EPIC facility of Northwestern University's NUANCE Center, which has received support from the SHyNE Resource (NSF ECCS-2025633), the IIN, and Northwestern's MRSEC program (NSF DMR-2308691). This research was supported in part through the computational resources and staff contributions provided for the Quest high-performance computing facility at Northwestern University which is jointly supported by the Office of the Provost, the Office for Research, and Northwestern University Information Technology.

Type of presentation: Poster

IM3-P-8 Surface and sub-surface defect analysis in semiconductors by Secondary Electron Emission Spectroscopy and local charge transport mapping

Ritik Tanwar[a], Wenzheng Cao[a], Abbas Kosari Mehr[a], Erfan Afshar[a], Madiha Khan[a], Raffaele Giani[b], Anjam Khursheed[a], Giovanni Isella[b], Silvia Maria Pietralunga[a,c], Alberto Tagliaferri[a]

[a]*Dipartimento di Fisica, Politecnico di Milano, Piazza Leonardo da Vinci 32, 20133 Milano, Italy.*

[b]*L-NESS, Physics Department, Politecnico di Milano, via Anzani 42, 22100, Como, Italy.*

[c]*CNR-lstituto di Fotonica e Nanotecnologie, Milano, Italy.*

Contact email: ritik@polimi.it

Semiconductor defects, on one side, undermine functionality and reliability of devices, on the other side, defects may offer the possibility to be engineered to develop peculiar quantum-like effects. In both cases high resolution, non-destructive means of characterisation are necessary. Prevailing semiconductor defect characterisation techniques are destructive, like TEM, or lack nanometric spatial precision for localised defect investigation. To address this, we explore Electron Beam-Induced Current (EBIC) for defect characterization within scanning electron microscopy (SEM). However, EBIC's limited spatial resolution restricts nanoscale defect investigation. Here, we propose secondary electron emission spectroscopy (SEES) to overcome this limitation. SEES correlates secondary electron spectra with valence band density of states[1]. Defects perturb the local electronic structure, necessitating detailed probing of these modifications, could potentially be viable with SEES. Integrating SEES with bulk-sensitive EBIC offers a comprehensive framework to study defect-induced charge transport and emission mechanisms.

The investigated Ge-Si photodiodes serve as a model heterostructure for EBIC and SEES measurements, where epitaxial strain-induced dislocations emerge at the interface and grow into the bulk germanium[2]. These dislocations act as electrically active centers, mediating carrier recombination, and generation, thereby influencing device performance. We adopted a commercial SEM, integrating it with a custom-designed secondary electron energy analyzer, employed to acquire SEES spectra. The experimental apparatus can be configured as an add-on for commercial SEMs.

Dislocation mapping in Ge-Si p-i-n diodes via EBIC revealed their electrical activity. SEES was performed on test samples to calibrate the energy analyzer. Future work includes room-temperature and low-temperature SEES for dislocation contrast, alongside low-temperature EBIC measurements using a custom-designed cooling stage for concurrent surface and bulk characterization. Ultimately, this work seeks to establish SEES as a viable nanoscale defect analysis technique by benchmarking it against EBIC, thereby assessing its reliability in resolving defect-induced electrical activity with nanometer spatial precision.

[1] Han W et al. Sci Rep. 2020;10(1):22144.
[2] Osmond J et al. Thin Solid Films. 2008;517(1):380-382.

Type of presentation: Poster

IM3-P-9 Sub-Angstrom Resolution at below 40 $e^-/Å^2$ with Electron Ptychography

Zeyu Wang[a], Biao Yuan[b], Xiaoyan Wu[c], Timothy J. Pennycook[b], Giorgio Divitini[a]

[a]*Electron Spectroscopy and Nanoscopy, Istituto Italiano di Tecnologia, Genova, Italy*

[b]*EMAT, University of Antwerp, Antwerp, Belgium*

[c]*School of Physical Science and Technology & Shanghai Key Laboratory of High-Resolution Electron Microscopy, ShanghaiTech University, Shanghai, China*

Contact email: zeyu.wang@iit.it

Ptychography has proven its ability to achieve ultra-high spatial resolution, reveal light elements, and explicitly account for dynamical effects in scanning transmission electron microscopy (STEM). By making use of almost all scattered electrons, ptychography also offers extremely high dose efficiency, that can even outperform conventional TEM with greater robustness to temporal incoherence [1]. Recently a resolution record for low dose ptychography of 1.96 Å was set at 98 $e^-/Å^2$ with the beam sensitive metal organic framework (MOF) MOSS-6 [1]. While this material has a large lattice spacing other materials such as the organic halide perovskite $CH_3NH_2PbI_3$ ($MAPbI_3$) require a resolution better than 1.96 Å to resolve their denser crystal structure and have even lower dose tolerances than 98 $e^-/Å^2$.

In this work, we demonstrate experimental sub-angstrom resolution ptychography at an electron dose of only ~36 $e^-/Å^2$, with ultrathin $MAPbI_3$. This is a particularly relevant material as so far, the clearest images of the halide perovskites have been acquired with annular dark field (ADF) STEM due to the material damaging significantly faster in conventional TEM than STEM. While the heavy Pb containing columns show up strongly in the Z-contrast ADF signal, the dose efficiency of ADF is overall relatively poor and light columns such as those of the MA molecules are difficult to detect. This is especially problematic with a very thin material such as a few units cell thick ultrathin $MAPbI_3$, in which the ADF signal is weaker than in a thicker sample. Indeed, with our three-unit cell thick sample the MA columns are essentially invisible in the ADF.

By using an event driven direct electron detection Timepix3 camera we can acquire 4D STEM at speeds equivalent to 2,000,000 frames per second [3], enabling a 500 ns dwell time. This very rapid scan speed, especially for 4D STEM, makes it possible to collect high-quality dose fractionated ultra-low dose data with a focused probe and very little drift. In addition to the low dose, it seems likely that repeated rapid scans with a focused probe all the sample to handle higher doses compared to more continuous exposure as in TEM. Dose fractionation allows us to build up signal until damage occurs, removing drift between the individual scans.

An advantage of 4D STEM is being able to compare multiple methods with the same dataset. For our ~36 $e^-/Å^2$ ultra-low dose data the bright field (BF) and annular bright field (ABF) do not appear significantly stronger than the ADF images. Parallax imaging also appears similarly noisy, although with sufficient area averaging it can show the MA columns, which the BF and ABF do not, at least with the amount of averaging we tried. iCoM performs significantly better, showing the MA columns without area averaging and less overall noise, although the raw images display the low frequency noise typical of iCoM and iDPC. All the types of ptychography we tested clearly show the MA columns, including SSB, WDD, ePIE, LSQML and multislice LSQML.

The key to achieving sub-Ångstrom resolution at this ultralow dose however is the use of the multislice method, which was only possible to converge using our newly introduced soft-threshold sparse constraint inspired by the L_1-minimization problem in compressive sensing theory [4]. While we used this constraint in both single slice and multislice LSQML, the single slice results look almost identical to ePIE results, and do not reach as high a resolution as the multislice results. This suggests that properly

accounting for dynamic effects is necessary to reach the highest resolution even for such a thin sample as our ~3 nm thick $MAPbI_3$.

Furthermore, despite how thin the material is, contrast reversals appear on the heavy Pb-I columns in all the single slice ptychography results. In thicker samples, these can often be removed by focusing the probe to the midplane of the sample, but this is not an option with an ultrathin material. In such cases one can use our phase offset method of contrast reversal correction [5] to remove the "donuts" due to the contrast reversals. However, the fact that using the multislice method removes them without the need for any correction step is strong evidence that such contrast reversals are indeed resulting from dynamical effects, and therefore that multislice ptychography can potentially offer more quantitatively accurate results than corrected single slice results. While multislice ptychography is in general more computationally intensive than its single slice counterparts, we note that the multislice LSQML is significantly faster than single slice ePIE for our results, in which we used six slices in the multislice calculations. This is due to the LSQML method generally converging much faster than ePIE for such low dose data with very sparse individual diffraction patterns, which we believe is likely due in large part to the batch nature of the LSQML algorithm.

Compared to direct ptychography methods such as SSB, the iterative methods are all much slower but do appear sharper. This could potentially be due in part to the frequency weightings used, and applying alternative transfers such as a noise normalized frequency weighting [6] to SSB and WDD might help. However, it also seems likely that the greater clarity of the iterative methods is in part because they include additional signals from scattering outside the bright field disk, which the direct methods do not normally make use of. While the intensity of the scattering within the BF disk is much higher, scattering to higher angles remains significant, containing enough electrons to form ADF images even at the ultra-low doses, especially when lower angles are included as in low angle ADF.

By achieving sub-Ångstrom resolution even at the ultralow dose of ~36 $e^-/Å^2$ even with an ultrathin material by using multislice ptychography we significantly broaden the range of materials and orientations that can be resolved in beam sensitive materials.

References

[1] T.J. Pennycook, *et al*., Ultramic., **196**, (2019) 131.
[2] G. Li, *et al.*, Nat. Commun., **16**, (2025) 914.
[3] D. Jannis, *et al.*, Ultramic., **233**, (2022) 113423.
[4] Z. Wang, *et al.*, J. Am. Chem. Soc., **147**, 21 (2025) 18025–18032.
[5] C. Hofer, *et al.*, Ultramic., **258**, (2024) 113922.
[6] C. O'Leary, *et al.*, Ultramic., **221**, (2021) 113189.

IM4 Advances in single particle analysis (SPA) and cryo-electron microscopy

Type of presentation: Invited

IM4-IN-1 Use of cryo-EM to study filamentous plant viruses and their virus-like particles

Marjetka Podobnik[a]

[a]*National Institute of Chemistry, Ljubljana, Slovenia*

Contact email: marjetka.podobnik@ki.si

Potyviruses are one of the largest genera of plant viruses that infect a wide range of crops. They cause significant yield losses (up to 50 %, in severe cases even 90 %) and reduce crop quality, jeopardising global food security. Potyviral genomes encode eleven proteins. Most of them have been reported to multitask, which is enabled by their multi-(sub)domain structures and a relatively high level of intrinsic structural disorder. This also applies to the only structural protein, the coat protein (CP), which forms a filamentous and flexible capsid around the genomic positive-sense single-stranded RNA.

Potyviruses evolve rapidly due to their high mutation rate and ability to recombine. 214 species are currently documented (https://ictv.global/taxonomy). As they infect numerous plant species, potyviruses are a multifaceted threat. However, there is still a lack of information on the molecular factors and mechanisms that control the infection cycle of potyviruses. Understanding the molecular background of virus biology and evolution is crucial for predicting and dealing with existing and emerging strains that could circumvent existing resistance and helps in the development of broad-spectrum resistance strategies for different crops.

In my research group, we use cryo-EM as an essential tool to study the structural organisation of potyviruses and their VLPs as well as other molecular systems involved in virus infection. By integrating methodological approaches from structural biology, biochemistry, biophysics, bioinformatics and *in planta* experiments, we investigate the role of intrinsic structural plasticity of viral proteins for their multifunctional nature and try to unravel their mechanisms of action. I will also discuss the value of the high-resolution structures of VLPs for understanding the biology of potyviruses and their potential for applications in nanobiotechnology.

Type of presentation: Invited

IM4-IN-2 Enabling High-Resolution Cryo-FIB-SEM Volume Imaging through Specialized Serial Acquisition

Pavel Křepelka[a], Jana Moravcová[a], Jiří Nováček[a]

[a]*CEITEC, Masaryk University, (Brno), Czech Republic*

Contact email: pavel.krepelka@ceitec.muni.cz

Cryo-volume electron microscopy (CVEM) is a rapidly developing technique for three-dimensional visualization of cells and tissues in near-native frozen states. Compared to conventional volume electron microscopy, which relies on dehydration and heavy metal staining that can introduce artifacts and compromise ultrastructural fidelity, cryogenic approaches simplify preparation, minimize structural distortions, and preserve fluorescence signals for correlative workflows. An additional advantage is the compatibility of CVEM with cryo-tomography. However, imaging unstained vitrified material at cryogenic conditions has been limited by low sensitivity, anisotropic resolution, and charging-related artifacts.

Here, we present an automated CVEM workflow that overcomes these limitations. Proposal imaging geometry maximizes secondary electron yield, enhances contrast, and reduces charging artifacts. Shallow-angle O^+ plasma milling with spot-geometry compensation improves vitrified ice ablation efficiency while preserving smooth, artifact-free surfaces. We systematically optimized electron dose and plasma milling conditions and measured the electron dose required for superior image quality. To enhance reproducibility and usability, we developed acquisition-control software with advanced features including low-dose focusing, real-time resolution measurement, and automated workflow assistance. A dedicated post-processing pipeline enabling reconstruction of unstained cells and tissues with structural preservation down to ~15 nm in all dimensions.

We demonstrate the performance and versatility of this approach on diverse biological specimens, including INS-1E beta cells, COS-7 cells, oocytes, and muscle tissue. The results highlight the capability of CVEM to deliver ultrastructural detail with reduced artifacts, robust reproducibility, and broad applicability. Together, these advances establish CVEM as a powerful and routine method for high-resolution, correlative, and comprehensive studies of cellular and tissue architecture.

Type of presentation: Oral

IM4-O-1 From MDa to kDa – across the scale cryoEM SPA analysis of biological molecules.

Artur P. Biela[a]

[a]*NSRC SOLARIS, Jagiellonian University, Kraków, Poland*

Contact email: artur.biela@uj.edu.pl

Cryo-electron microscopy has gained considerable attention and has proven to be a powerful tool in structural biology. For the past years, scientists worldwide tried to push the boundaries of the technique and used it in their research projects to solve structures of all kinds of biological molecules. Here, in this presentation, I would like to show that size does matter, but there is a way to overcome this issue. Starting from large protein assemblies like synthetic cages of paradoxical geometry derived from bacterial enzyme, virus-like particles of different shapes and sized (both: spherical and rod-like) being in the MDa range (*Figure 1*), going down to relatively small multimeric enzymes in complexes with their partners (both: proteins and small molecules), and finally finishing at sub 30-kDa particles like free tRNA molecule, being the smallest molecule so far reconstructed with cryoEM. Despite the broad range of molecular masses, we were able to show some important features of the molecules investigated like the symmetry of the assemblies, paradoxical arrangements of the building blocks, draw some rules about the symmetry breaking, describe the composition of the complexes, decipher the mechanism of their action, get to know the nature of the crucial bonds or even the influence of the introduced modifications on the structure's rigidity (to some extend)(*Figure 2*).

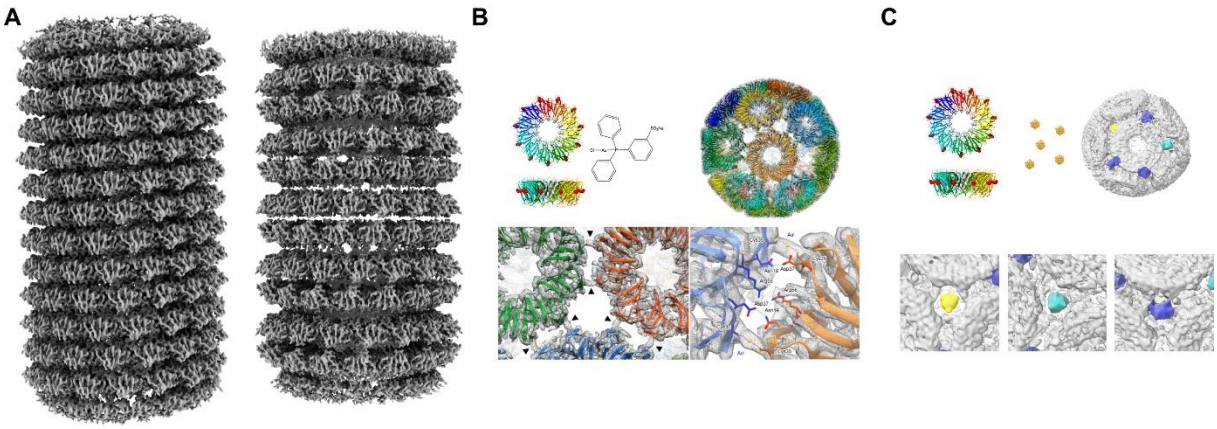


Figure 4. (A) an overview on two polymorphic structures of the modified TMV coat protein assemblies (B) synthetic protein cage made with toroidal-shaped protein and held by Au(I) bridges (C) synthetic protein cage made with toroidal-shaped protein andheld by gold nanoparticles (AuGNPs)

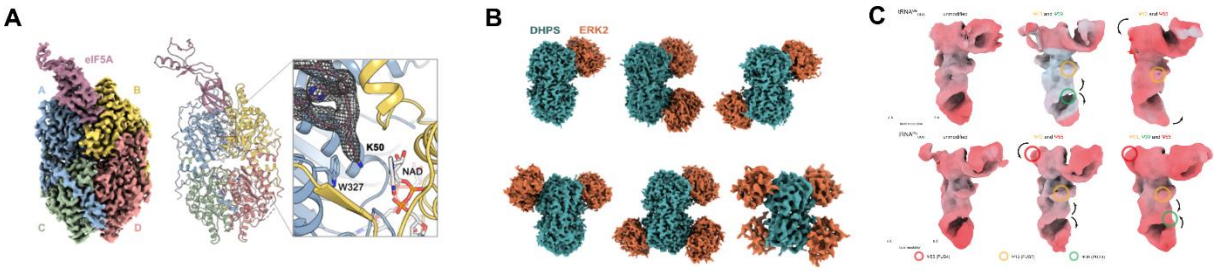


Figure 5. (A) reconstruction of a DHS-eIF5A complex with zoom onto active site (B) different stoichiometry complexes of DHS and its biding partner ERK2 (C) set of structures of free tRNA molecules showing modification sites and thier influence on the flexibility/ridigity

References:

1. Malay, A.D., et al, *Nature* **2019,** 569, 438-422
2. Majsterkiewicz, K., et.al, *Nano Letters*, **2022**, 22, 8, 3187-3195
3. Wątor, E., et al, *Nature Comm*, **2023**, 14, 1698
4. Becker, A.E., et al, *Cell Reports*, **2024**, 43, 114831
5. Biela, A.D., et al, *EMBO Journal*, **2025**, in press
6. Abu-Baker, I., et all, *under review*

Type of presentation: Oral

IM4-O-2 A closer look at the protein-lipid complex of actinoporin pores

Gašper Šolinc[a], Marija Srnko[a], Ana Crnković[a], Marjetka Podobnik[a], and Gregor Anderluh[a]

[a]*National Institute of Chemistry, Ljubljana, Slovenia*

Contact email: gasper.solinc@ki.si

Pore-forming proteins (PFPs) disrupt normal membrane function by forming pores thus compromising membrane integrity. PFPs are usually produced as soluble monomers that bind to various membrane components. After binding, they oligomerize and undergo conformational changes to form transmembrane pores. These pores are lined by either α-helical clusters or β-barrels[1]. Actinoporins are a well-studied α-PFP family originally discovered in sea anemones. They bind specifically to membranes containing sphingomyelin (SM), which is required for oligomerization, while the presence of cholesterol in the membrane enhances their activity. The only known structure of the actinoporin pore is that of fragaceatoxin C (FraC) [2] from the strawberry anemone (*Actinia fragacea*). We explored the structure of the pore of actinoporin homologue Fav from the mountainous star coral (*Orbicella faveolata*) using cryo-electron microscopy (cryo-EM).

Pores of recombinantly expressed Fav were prepared on lipid vesicles of various lipid compositions (Fig. 1a). For high-resolution characterization, using single particle analysis pores were isolated from the vesicles with detergents (Fig. 1b-d).

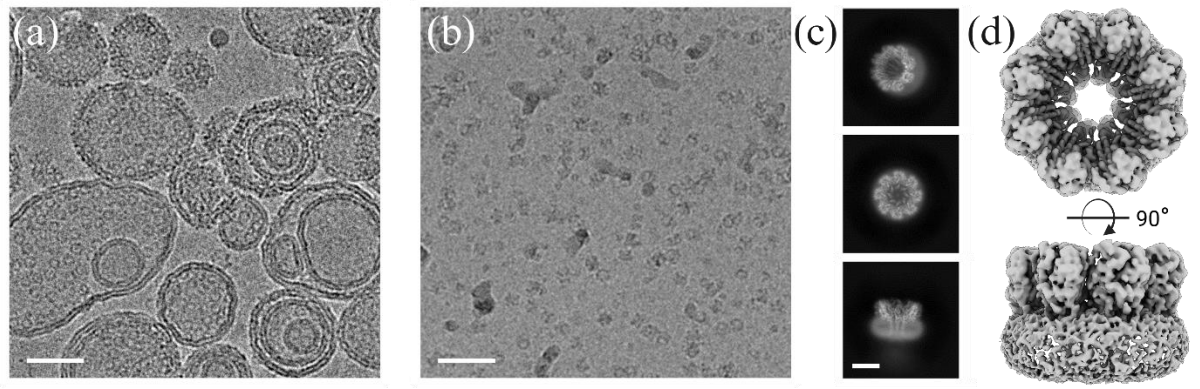


Figure 1: **Cryo-EM analysis of Fav pore**. Representative micrographs of Fav pores on lipid vesicles (a) and of solubilized Fav pores (b). Scale bar is 50 nm. (c) 2D class averages of Fav pores. Scale bar is 5 nm. (d) Cryo-EM map of octameric fav pore at two angles.

Cryo-EM maps reveal numerous lipids associated with the Fav pore (Fig. 2a), representing lipids in the upper leaflet of the membrane surrounding the pore. When cholesterol was present in the membranes used to prepare pores, more lipids are associated with the pore (Fig. 2b). Among there lipids are densely packed cholesterol molecules under the pore cap. We also observed phospholipids, which we categorized into three groups based on their position and role (Fig. 2c). Receptor lipids are located in the membrane binding region. Structural lipids are located between two protomers and interact with both. Bridging lipids, located at the complex's outer edge, have only limited interactions with the protein, but stabilize the pore by forming an interaction bridge between two protomers.

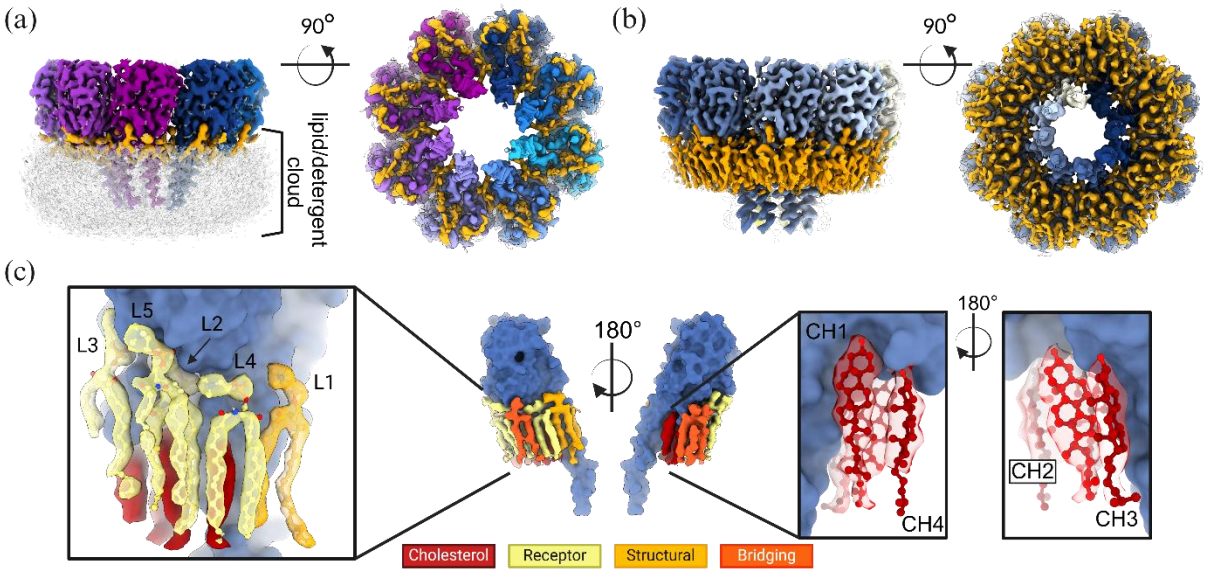


Figure 2: **The structure of the Fav pore**. A side and a bottom view of cryo-EM map of octameric Fav pore extracted from membranes without (a) and membranes with (b) cholesterol. Each protomer is coloured with a distinct colour, and regions of the map corresponding to well-defined lipids are shown in orange. (c) Surface representation of a Fav pore promoter with parts of the map corresponding to lipids associated with it shown at two different angles. Some lipids are highlighted.

Our findings provide detailed insight into protein-lipid interactions and underscore the diverse and essential roles that membrane lipids play in protein pores. Beyond the specific case of Fav pores these insights can be applied in the study of other membrane proteins, many of which may rely on lipid interactions for their function and stability.

References:

[1] M. D. Peraro, F. G. van der Goot, *Nat. Rev. Microbiol.* **2015**, *advance on*, 77–92.
[2] K. Tanaka, J. M. M. Caaveiro, K. Morante, J. M. González-Manãs, K. Tsumoto, *Nat. Commun.* **2015**, *6*, DOI 10.1038/ncomms7337.
[3] G. Šolinc, M. Srnko, F. Merzel, A. Crnković, M. Kozorog, M. Podobnik, G. Anderluh, *Nat. Commun.* **2025**, DOI 10.1038/s41467-025-58334-z.

Type of presentation: Poster

IM4-P-1 SOLARIS Cryo-EM Facility at SOLARIS National Synchrotron Radiation Centre, Kraków, Poland

Paulina Indyka[a], Michał Rawski[a], Marcin Jaciuk[a,b], Grzegorz Ważny[a,c], and Artur Biela[a]

[a] *National Synchrotron Radiation Centre SOLARIS, Jagiellonian University, Kraków, Poland*

[b]*Malopolska Centre of Biotechnology, Jagiellonian University, Gronostajowa 7A, 30-387 Kraków, Poland*

[c]*Doctoral School of Exact and Natural Sciences, Jagiellonian University, Kraków, Poland*

Contact email: paulina.indyka@uj.edu.pl

SOLARIS Cryo-EM Facility at the SOLARIS National Synchrotron Radiation Centre is a modern and extensive research unit operating since 2019 in Krakow, Poland. *Our priority research area revolves around the field of structural biology, where the usual goal is to understand the spatial structure of biologically relevant organic and inorganic molecules, and to understand their dynamics and interactions.*
We provide access to two high-end cryo-electron microscopes dedicated determining structures of biomacromolecules: Krios G3i (300 kV), and Glacios (200 kV), both ThermoFisher Scientific.
In experiments, we use single particle analysis (SPA), cryo-electron tomography (cET) and microcrystal electron diffraction (MicroED) techniques allowing to analyse specimens at near-atomic resolution.
Figure 1. d*emonstrates the research capabilities available at the SOLARIS* Cryo-EM Facility.

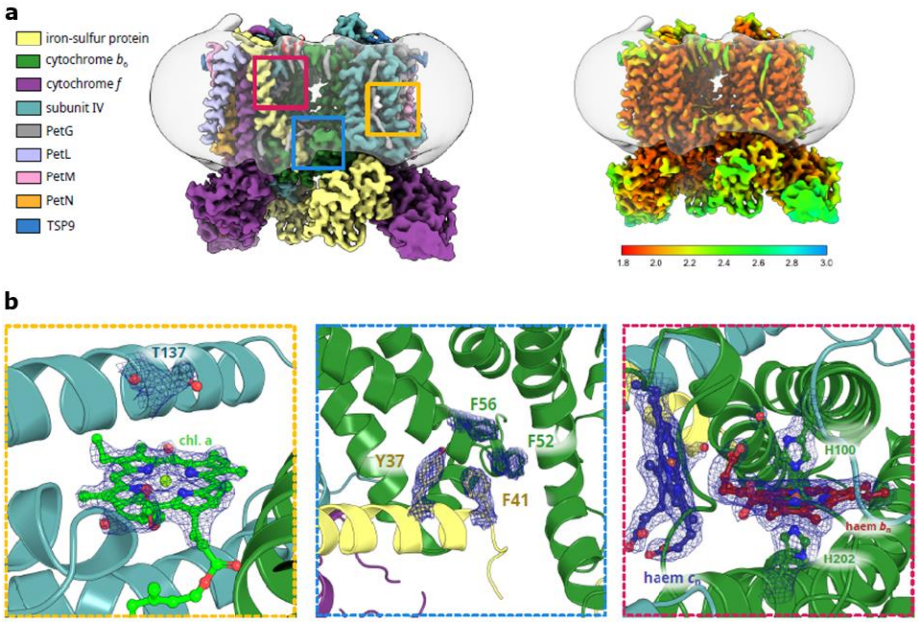


Figure 1. An overview of the structure of cytb6f and cofactor. **a**, 1.9 Å cryo-EM of DPQ-incubated cytb6f with color-coded subunits (left) and local resolution map coloured by resolution range (right); **b**, close-up view of selected 1.9 Å map regions with remarkable resolution of amino-acid sidechains and cofactors. The colours of the frames correspond to regions marked by squares in **a**.

S. Pintscher, R. Pietras, B. Mielecki, M. Szwalec, A. WójcikAugustyn, P. Indyka, M. Rawski, Ł. Koziej, M. Jaciuk, G.Ważny, S. Glatt,and A.Osyczka, Molecular basis of plastoquinone reduction in plant cytochrome b6f, *Nature Plants*

Type of presentation: Poster

IM4-P-2 Activities of the cryo-EM facility at the National Institute of Chemistry, Slovenia

Matic Kisovec[a], Marjetka Podobnik[a]

[a]*National Institute of Chemistry, (Ljubljana), Slovenia*

Contact email: matic.kisovec@ki.si

The field of cryo-electron microscopy (cryo-EM) has undergone rapid development and significant technical improvements in recent decades. Advances in sample preparation, microscope hardware, direct electron detectors and data analysis have heralded the so-called 'resolution revolution'. Cryo-EM with its three main methodological approaches, single particle analysis (SPA), tomography (cryoET) or microcrystal electron diffraction (MicroED), has become a powerful tool to gain structural insights into individual biological molecules, their complexes, cellular organelles, whole cells, tissues, viruses and synthetic nanoparticles, as well as peptides and even small organic molecules, at atomic or near-atomic resolution.

The cryo-EM facility at the National Institute of Chemistry was established in 2019 and remains the only one in the region. It includes the 200 kV Glacios™ cryogenic transmission electron microscope, which can be used to perform SPA, cryo-ET and MicroED experiments. The samples are vitrified by plunge- freezing (Vitrobot) and the Falcon 3C and Ceta-D detectors enable the acquisition of high-quality data. HPC (High Performance Computing) infrastructure is available for data storage and analysis.

The cryo-EM facility is part of the Centre for Molecular Interactions and Structural Biology based at the Department of Molecular Biology and Nanobiotechnology. Cryo-EM Facility is open to internal and external users, and we actively collaborate with various academic and industrial partners.

I will present several successful structural projects that have been completed in recent years, from plant viruses to virus-like particles [1,2], pore-forming proteins [3,4], extracellular vesicles [5,6] and more.

References:

1. A. Kežar, et al. *Science Advances*, **2019**, eaaw3808.
2. L. Kavčič, et al. *Commun Chem*, **2024**, 7, 1–19.
3. G. Šolinc, et al. *Biochemical and Biophysical Research Communications*, **2023**, 674, 44–52.
4. G. Šolinc, et al. *Nat Comm*, **2025**, in press.
5. A. Romolo, et al. *International Journal of Molecular Sciences*, **2022**, 23, 15801.
6. D. Božič, et al. *International Journal of Molecular Sciences*, **2021**, 22, 12772.

Type of presentation: Poster

IM4-P-3 Optimization of macromolecule imaging in Cryo-EM method

Grzegorz Ważny[a,b], Michał Rawski[a], Artur Biela[a], Sebastian Glatt[c]

[a]*SOLARIS National Synchrotron Radiation Centre, Jagiellonian University, Cracow, Poland*

[b]*Doctoral School of Exact and Natural Sciences, Jagiellonian University, Cracow, Poland*

[c]*Malopolska Centre of Biotechnology, Jagiellonian University, Cracow, Poland*

Contact email: grzegorz.wazny@uj.edu.pl

Total electrons dose (electrons per angstrom square) is a critical parameter in single particle cryo-EM. A higher dose allows to a higher signal to noise ratio, but also causes a bigger beam-induced motion. Too high dose can destroy the most sensitive parts of observed particles. It is generally known how to determine the dose for proteins and DNA to obtain high resolution, but for RNA dose issues and radiation damage are not clearly understood. In my PhD research, I will try to find answers for a few essential questions about the resistance of nucleotides to beam radiation and optimize the data collection method. To reach these aims, I've collected a data set on a Krios microscope for human type Ribosome and E coli Ribosome with a dose of 160 electrons per angstrom square (160 frames) and 80 electrons per angstrom square (80 frames) accordingly. Next, I sliced each micrograph for a sequence of frames. This procedure delivered information of the impact of dose on the degree of particle destruction as well as how beam-induced motion changes the final reconstruction resolution. Additionally, these results show the possibility of optimizing the data collection method in SPA cryo-EM.

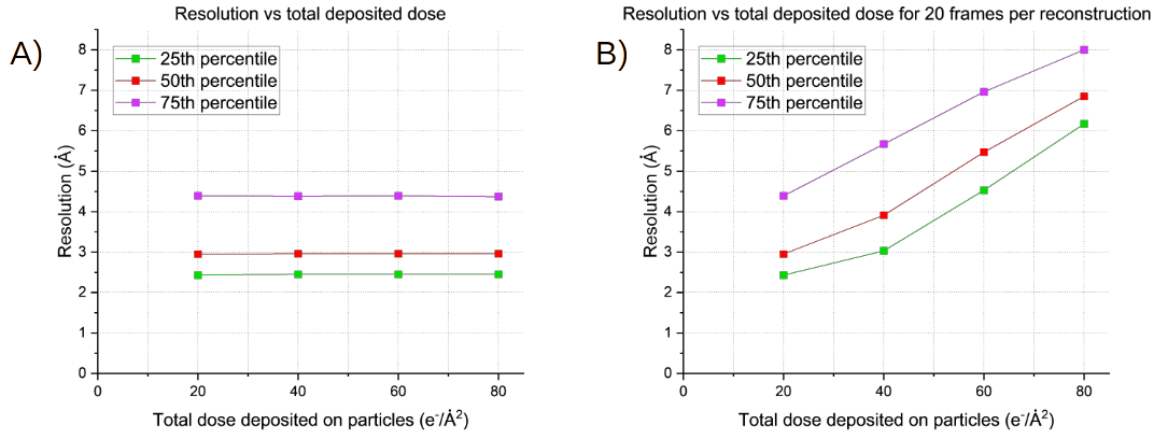


Figure 6: a) Resolution vs total deposited dose on particles: (A) for different frames per reconstruction, (B) for 20 frames per reconstruction.

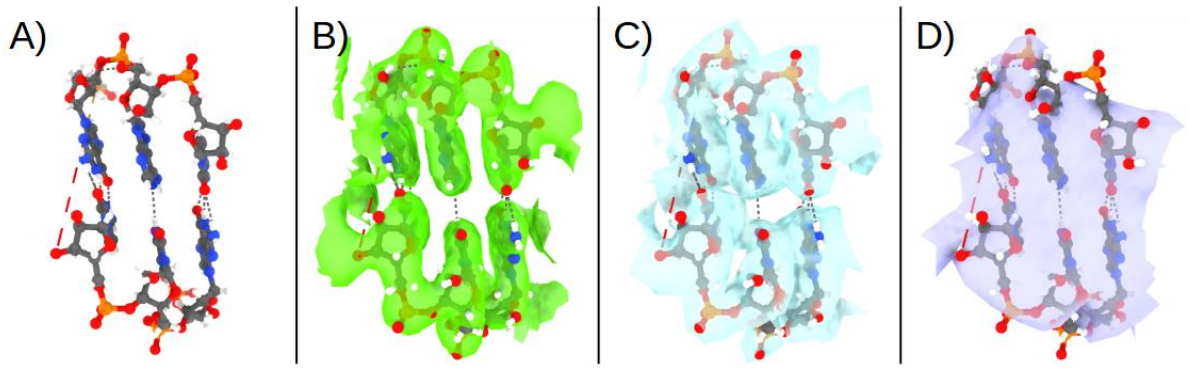


Figure 7: (A) Part of a model of *E.Coli* ribosome representing pairs of nucleotides. Part of a potential map with fitted in it a part of the model shown in figure A: potential map obtained from frames 1-20 (B), potential map obtained from frames 21-40 (C), potential map obtained from frames 41-60 (D).

IM5 Development of sample preparation methods, instrumentation, workflows, and data solutions for volume electron microscopy

Type of presentation: Invited

IM5-IN-1 Novel embedding resins for volume EM with enhanced resistance to e-beam damage

Miroslav Slouf[a], Ewa Pavlova[a], Beata Strachotova[a], Adam Strachota[a], Vladislav Krzyzanek[b], Jana Nebesarova[c,d]

[a]*Institute of Macromolecular Chemistry CAS, Heyrovskeho nam. 2, 162 06 Prague 6, Czech Republic*

[b]*Institute of Scientific Intruments CAS, Kralovopolska 147, 612 64 Brno, Czech Republic*

[c]*Institute of Parasitology, Biology Centre CAS, Branisovska 31, 37005 Ceske Budejovice, Czech Republic*

[d]*Faculty of Science, Charles University, Vinicna 7, 128 00 Prague 2, Czech Republic*

Contact email: slouf@imc.cas.cz

Volume electron microscopy (Volume EM, vEM) is one of the key current trends in the investigation of the ultrastructure of biological samples. Traditional techniques have been relying on 2D-imaging of ultrathin sections in TEM microscopes. Modern vEM methods (FIB-SEM, SBF-SEM, and AT-SEM) are based on 3D-reconstructions of SEM datasets.

A crucial step before a SEM measurement of a biological material is the selection of a sample preparation method to ensure fixation of its sensitive structure. One well-established approach consists in the embedding of samples in synthetic polymer resins. Commercially available embedding resins have been developed and perfected for traditional techniques that employ TEM microscopes, which work with high-energy electrons and thin specimens. The performance of these resins in SEM microscopes, which work with low-energy electrons and thick specimens, is much worse. The commercial embedding resins in vEM frequently suffer from charging and e-beam damage.

To solve the above-described problem, we have developed two types of polymer resins with enhanced resistance to electron beam damage: (a) commercial resins modified with different types of chemical stabilizing agents and (b) novel resins based on more e-beam-resistant polymers. All details of our modification cannot be revealed at the moment (patent pending), but the results clear and promising:

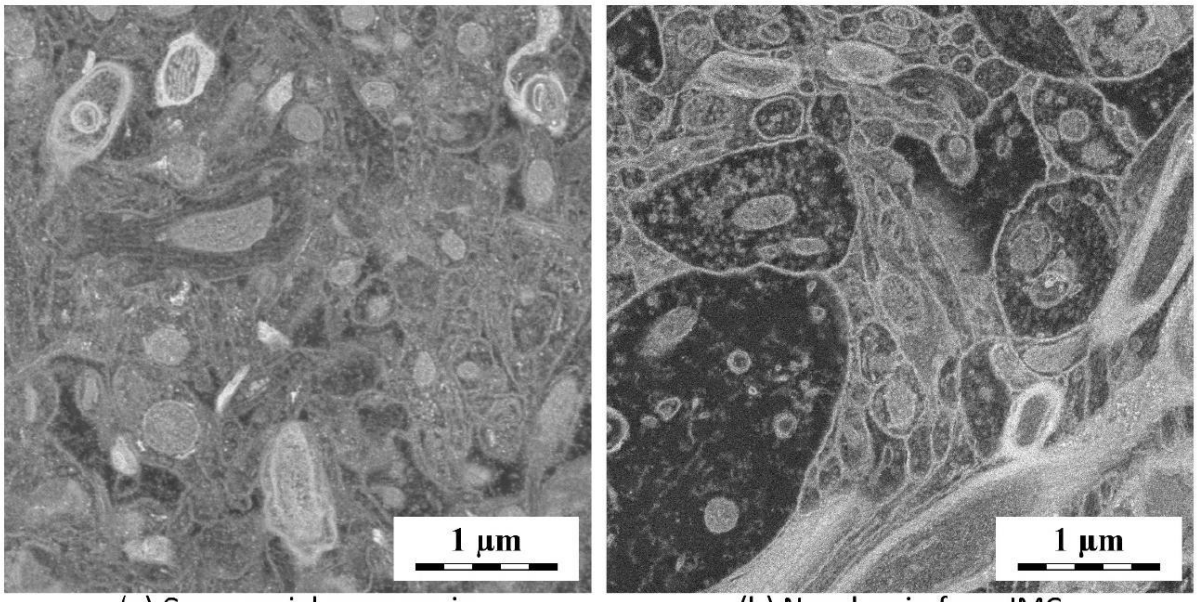
- The carbon-based commercial resins modified with chemical stabilizing agents show significantly lower charging in comparison with non-modified resins (Fig. 1). The greatest advantage is that the modified resins can be applied in exactly the same way like the non-modified resins. The typical concentration of the stabilizing agent is 5 wt.%, which does not influence the curing, mechanical properties, and cuttability significantly.
- The silicon-based novel resins exhibit even better performance that the carbon-based modified resins in the sense that the charging is minimized. The lower surface charge results in higher contrast (Fig. 2). The current disadvantage (which can be mitigated in the future) consists in a different, slightly more demanding resin preparation protocol.

Our experimental data have demonstrated that both the modified carbon-based resins and the newly developed silicon-based resins outperform the commercially available embedding resins as far as the modern SEM applications are concerned. Micromechanical properties and cuttability of the conventional and new resins were comparable. In the presentation, we will show multiple real-life applications comparing the same samples embedded in conventional and new resins. The tested samples come mostly from biology (mouse brain, liver, and kidney tissues), but also from materials science (magnetic polymer microspheres).

Acknowledgement: Technology Agency of the Czech Republic, project TN02000020.

Sample and radiation dose		Charging during BSE imaging			Image quality	
Resin type	Dose	None	Partial	Strong	Acceptable	Bad
Pure	1 e/nm^2	4% (1)	33% (10)	63% (19)	37% (11)	63% (19)
Stabilized	1 e/nm^2	0% (0)	81% (26)	19% (6)	81% (26)	19% (6)
Pure	20 e/nm^2	23% (7)	17% (5)	60% (18)	40% (12)	60% (18)
Stabilized	20 e/nm^2	46% (15)	41% (13)	13% (4)	87% (28)	13% (4)
Pure	200 e/nm^2	30% (9)	17% (5)	53% (16)	47% (14)	53% (16)
Stabilized	200 e/nm^2	53% (17)	28% (9)	19% (6)	81% (23)	19% (6)

Figure 1: Charging of selected biological specimen (mouse brain tissue) embedded in a standard carbon-based resin (Resin type: Pure) and the carbon-based resin with our chemical stabilizing agent (Resin type: Stabilized). The charging was evaluated at three doses which are typical of low, medium and high magnification during vEM microscopy (SEM microscope, no sputtering, accelerating voltage 3 kV). All samples were embedded in the same epoxy resin (Hard Plus Resin 812). For the stabilized samples, the resin contained 5 wt.% of chemical stabilizing agent. The comparison comprised 62 samples: 30 pure samples and 32 stabilized samples. The numbers in the table give percentage (%) and number of samples (in round brackets) with the given type of charging.



(a) Commercial epoxy resin (b) Novel resin from IMC

Figure 2: SEM/BSE micrographs comparing the cut sections of OsO_4-stained mouse brain tissue embedded in: (a) commercial epoxy resin and (b) our novel silicon-based resin T4D1(EpD,5%). The real width, total dose, accelerating voltage and all other experimental conditions during data collections were as similar as possible (a high-resolution FEGSEM microscope MAIA3, TESCAN, Czech Republic; accelerating voltage 3 kV). We note higher sharpness and higher contrast achieved with the novel resin, which could be attributed to lower charge on the surface of the silicon-based resin.

Type of presentation: Invited

IM5-IN-2 The combination of high-resolution diffraction techniques in the scanning electron microscope for statistical relevant description of crystal defects and resulting properties in metals and alloys

Stefan Zaefferer[a], Shao-Pu Tsai[b], Peter Konijnenberg[c], Koundinya NTBN[d], Parimala Banavath[e]

[a]*Max Planck Institute for Sustainable Materials, (Düsseldorf), Germany*

[b]*National Taiwan University, (Taipeh), Taiwan*

[c]*Research Centre Juelich & RWTH Aachen, (Juelich & Aachen), Germany*

[d]*Indian Institute of Technology Jodhpur, (Jodhpur), India*

[e]*Indian Institute of Technology Madras, (Chennai) India*

Contact email: s.zaefferer@mpi-susmat.de

The properties of crystalline materials (metals and alloys, ceramics, rocks and minerals) critically depend on the type, amount, and spatial or temporal distribution of lattice defects. By lattice defects we mean dislocations, stacking faults or anti-phase boundaries, grain and phase boundaries, small precipitates and elastic stress fields. Usually, lattice defects are inhomogeneously distributed in the microstructure and observations by high-resolution methods, in particular TEM or APT, may not properly reflect this distribution. As a consequence, structure-property relations are difficult to derive from high-resolution measurements, and conclusions on materials behaviour may be questionable.
Modern techniques in scanning electron microscopy (SEM) for the characterization of microstructure, crystal structure, crystallographic texture and chemical composition allow – to a certain extent – to close the gap between statistically robust observations and high resolution measurements. These techniques include high-accuracy and high speed electron backscatter diffraction (EBSD), controlled electron channelling contrast imaging (cECCI) and low-kV energy-dispersive x-ray spectroscopy (EDS).

For **EBSD** a number of innovative analysis techniques, including spherical indexing or general image matching allow a very significant improvement in indexing robustness, orientation accuracy and spatial resolution. This will be illustrated by means of texture and microstructure measurements on very heavily (>90 %) cold rolled samples of electrical steel samples and transformation-annealed DP steel samples.

3D EBSD by means of robotic serial sectioning and high-speed EBSD mapping enables the crystallographically complete 5-parameter characterization of grain boundaries. We illustrate this approach by an investigation on the corrosion behaviour of grain boundaries in stainless steels.

cECCI allows direct observation of dislocations, stacking faults and other defects with almost TEM-quality and resolution but on large bulk samples. These capabilities will be demonstrated by means of dislocation observations around nano-indents in initially non-charged and hydrogen-charged microstructure of stainless steel.

A further powerful technique that is, however, not considered here is **low-kV EDS**, which allows to measure the chemical composition of precipitates with a spatial resolution of >50 nm and a good sensitivity for light elements on large samples.

Combination of two or more of these techniques allows a statistically meaningful characterization of defects. In this way it is possible to bridge the scale between nano-or-micrometer characterization of defects and macroscopic behaviour of materials. This approach calls for application of machine learning algorithms that are trained by large number of microstructural observations. This enables the prediction of macroscopic properties (e.g. fracture toughness of hydrogen embrittled materials or texture evolution based on shear band formation) of new samples/materials based on a few microstructural images.

Type of presentation: Poster

IM5-P-1 EDIC; A new method to enhance reliability of structure determination, using electron diffraction data correction

Erzsébet Dodony[a,b], István Dódony[n.a.], György Sáfrán[b]

[a]*Hungarian Research Network, Center for Energy Research, Institute of Technical Physics and Materials Science, Thin Film Physics Laboratory, (Budapest), Hungary*

[b]*Department of Material Physics, Eötvös Loránd University, (Budapest), Hungary*

Contact email: erzsebet.dodony@ek.hun-ren.hu

Introduction:
Advancements in nanotechnology have made it essential to understand materials at the atomic scale. Among the various techniques available, transmission electron microscopy (TEM) is particularly effective for this purpose. Electron diffraction (ED) patterns play a crucial role in determining material structures. However, ED patterns require intensity corrections to account for the geometric relationship between the Ewald sphere and the reciprocal lattice. To obtain intensity data which is better suited for structure determination, we have developed a method to account for the effect of the Ewald sphere upon the diffracted intensities and reestablishes the $I_{hkl} \propto |F_{hkl}^2|$ proportionality.

Methods and Results:
The structure factors (F_{hkl}) describe the atomic arrangement within a crystal, hence knowing their value ensures succesfull crystal structure solution. The base of all structure solution methods using electron diffracton intensity data is, that the measured intensities are proportional with the square of the structure factor ($I_{exp,hkl} \propto |F_{hkl}^2|$), which is not true in experimental conditions. To aid more precise structure determination using diffracted intensities we developed a method, to counteract the effect of the Ewald sphere upon diffracted intensities.
The experimental intensities of the elongated spike shaped reflections - which sit on the reciprocal lattice plane - are determined by, where the Ewald-sphere intersects them. As the Ewald-sphere bends away from the reciprocal lattice plane and intersects the reflections further away from the plane, we measure smaller and smaller intensities compared with the theoretical (structure factor proportional) values (**Figure 1**). In order to get back the theoretical values best suited for crystal structure determination, we have to correct the experimental data for this effect.

In 1992, J.M. Cowley [1] laid the groundwork by defining the effect of the Ewald-sphere on theoretical intensities ($I_{hkl} = F_{hkl}^2$) to calculate expected experimental intensities ($I_{exp,hkl}$), see **Equation 1**, where $E_{w,hkl}$ is the Ewald function defined by Cowley.

$$I_{exp_{hkl}} \propto |F_{hkl}|^2 * (E_{w_{hkl}})^2 = |F_{hkl}|^2 * \left(\frac{sin\frac{\pi\lambda t}{2d_{hkl}^2}}{\frac{\pi\lambda t}{2d_{hkl}^2}} \right)^2 = |F_{hkl}|^2 * \left(\frac{sin\frac{\pi\lambda t d^{*2}_{hkl}}{2}}{\frac{\pi\lambda t d^{*2}_{hkl}}{2}} \right)^2 , Eq.1$$

, where $I_{exp,hkl}$ is the experimental diffracted intensity at coordinates hkl (Miller-index), F_{hkl} is the structure factor of the crystal calculated at coordinates hkl, $E_{w,hkl}$ is the value of the Ewald function calculated at coordinates hkl, λ is the electron wavelength, t is the thickness of the specimen, d_{hkl} is the interplanar distance between the family of (hkl) planes and d^*_{hkl} is the reciprocal lattice point at coordinates hkl. Therefore, to obtain a $|F_{hkl}|^2$ proportional intensity data set, we multiply the $I_{exp,hkl}$ with the inverse $(E_{w,hkl})^2$ value. We call the process Electron Diffraction Intensity Correction (EDIC) and the function for aligned crystals $C^0_{hkl} = 1/(E_{w,hkl})^2$ is called EDIC correction function.

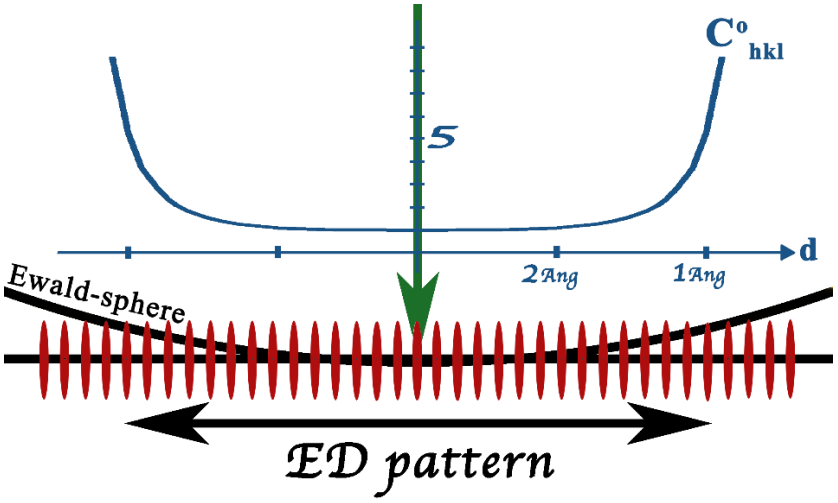


Figure 1 Schematic of the relationship between the Ewald-sphere with reflections on the reciprocal lattice plane, as well, the C^0_{hkl} EDIC correction function calculated for a 10nm thick crystal up to a value of 9. As the Ewald-sphere bends away from the reciprocal lattice plane we detect smaller and smaller experimental intensities compared to their theoretical (structure factor square proportional) value.

The C^o_{hkl} correction function can be applied to only diffraction intensity datasets obtained from an oriented crystal. In experimental work it occurs that the pattern exposed is slightly misoriented, so we extended the method of correction to such cases as well. In misoriented cases the Ewald-sphere dips bellow the reciprocal lattice plane, hence a different correction function is needed. By examining the new geometry, we defined the C^{tilt}_{hkl} function for correcting misaligned cases to F_{hkl}^2 proportional intensities (**Equation 2**), adequate for crystal structure solution.

$$|F_{hkl}|^2 \propto I_{exp_{hkl}} * C^{tilt}_{hkl} = I_{exp_{hkl}} * \left(\frac{\frac{\pi\lambda t}{2}\sqrt{\frac{1}{\lambda^2} - \left(\frac{1}{\lambda} - \left|\sqrt{\frac{1}{\lambda^2} - d^{*2}_{hkl}} - \sqrt{\frac{1}{\lambda^2} - d^{*2}_{dist}}\right|\right)^2}}{sin\left(\frac{\pi\lambda t}{2}\sqrt{\frac{1}{\lambda^2} - \left(\frac{1}{\lambda} - \left|\sqrt{\frac{1}{\lambda^2} - d^{*2}_{hkl}} - \sqrt{\frac{1}{\lambda^2} - d^{*2}_{dist}}\right|\right)^2}\right)} \right)^2 , Eq.2$$

,where d^*_{dist} is the distance (in 1/Å) between the direct beam and the center of the Laue zone.

Manual application of these corrections is time-consuming, especially for crystals with large unit cells and hundreds of reflections. Therefore, a computer program (EDIC) has been developed to automate the correction process. The program allows rapid intensity correction of experimental ED samples, thus allowing the determination of unknown structures from experimental intensity data sets with higher accuracy.
We tested the method both on simulated and experimental datasets, and have found drastic improvement in reliability factors, after correction, showing better fit to theoretical - F_{hkl}^2 proportional intensities. For the experimental electron diffraction of $NiSi_2$ R-factor decreased from R=0,36 to R=0,098 showing the adequacy of the method.

Discussion and conclusions:
When determining a crystal structure from experimental electron diffraction data, it is important to recognize that the measured intensities may deviate from the ideal F_{hkl}^2 proportional intensities. Using uncorrected intensities can lead to inaccurate structural models. To address this issue, we have developed both a method and associated software to correct the intensities of reflections in experimental selected area electron diffraction (SAED) patterns. The corrected dataset, which is proportional to $|F_{hkl}|^2$, provides a more reliable basis for accurate crystal structure determination. The method was extended to misaligned crystals also, which opened a door to the possibility to apply corrections to Precession Electron Diffraction data (PED) in the future, further increasing the importance of the method in solving crystal structures.

References:

1. J.M. Cowley, *Oxford Univ.Press.*, **1992**, ISBN 9780198555582J
2. E. Dodony, I. Dódony, G. Sáfrán, *Micron*, **2024**, 183, 103649

Type of presentation: Poster

IM5-P-2 The Power of FIB-SEM for Visualizing the Internalization of 2D Materials In Vitro

Damjana Drobne[a], Špela Saje[a], Francesco Tatti[b], Sara Novak[a]

[a]*University of Ljubljana, Biotechnical faculty, Department of Biology, Ljubljana, Slovenia*

[b]*Thermofisher, Eindhoven, Netherlands*

Contact email: damjana.drobne@bf.uni-lj.si

Focused Ion Beam-Scanning Electron Microscopy (FIB-SEM) combines precise FIB milling with conventional scanning electron microscopy (SEM) to reveal the surface morphology and subsurface features. One of the most cutting-edge applications of FIB/SEM on fixed and dried biological samples is its use as High-Resolution 3D Imaging that enables site-specific milling followed by visualization of subsurface morphological characteristics with nanometer precision. This is particularly useful for studying cellular architecture and tissue organization. Unlike cryo-FIB, dried samples do not require vitrification or cryogenic handling, making the preparation process more straightforward and accessible. In addition, dried samples are more stable over time, allowing for extended studies without the risk of contamination or degradation.

In the study presented here we have used SEM and FIB-SEM to visualize graphene oxide (GO) internalized by two cell types *in vitro*, i.e. A549 and Beas-2B cell lines. **The aim** of this study was to investigate the cellular uptake dynamics, distribution, and potential ultrastructural alterations induced by GO exposure, providing insights into its interactions with different cell types. We have used FIB/SEM SCIOS 2 from Thermofisher Scientific to assess if GO is internalised by cells exposed to graphene oxide (GO) for 24 hours. To this end, cells were seeded onto glass coverslips, allowed to adhere, treated with GO in suspension, and incubated for 24 hours before being fixed for SEM analysis.

The results indicate that the uptake of graphene oxide (GO) by A549 cells is more pronounced compared to Beas-2B cells, as illustrated in Figure 1.

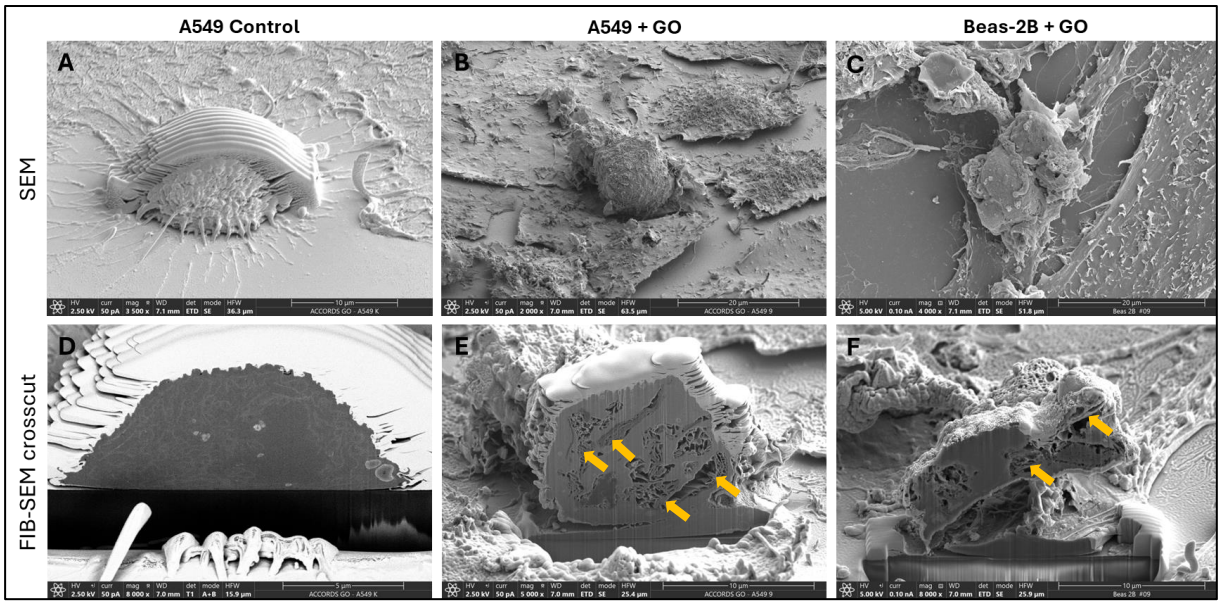


Figure 1. SEM (A-C) and FIB-SEM (D-F) images of A549 (A, B, D, E) and Beas-2B (C, F) cells cultured on glass coverslips and treated with low-oxidized graphene oxide. Untreated A549 cells (A,D) imaged by SEM (A) and FIB-SEM (D) exhibit typical morphology. A549 (B, E) and Beas-2B (C, F) cells exposed to low-oxidized GO interact closely with the material; cross-sections reveal

possible internalized material. Arrows are pointing to GO material. Scale bars and imaging conditions are indicated within each image.

We present evidence that FIB/SEM plays a vital role in bridging surface-level investigations conducted via Scanning Electron Microscopy (SEM) with the high-resolution ultrastructural analyses enabled by Transmission Electron Microscopy (TEM). By integrating focused ion beam milling with advanced electron imaging, FIB/SEM provides exceptional clarity in visualizing internalized material within cells in vitro, offering valuable insights into cellular interactions and uptake mechanisms.

ACKNOWLEDGEMENT Study was supported by project ACCORDs that received funding from the European Union's Horizon Europe Framework Programme under grant agreement No 101092796. We thank also Slovenian Research and Innovation Agency (ARIS; J1-50014; J1-2482, P1-0184, P1-0153) and the Infrastructural Centre for Microscopy of Biological samples (MRIC UL, I0-0022-0481-08) at the Biotechnical faculty University of Ljubljana.

References:

Drobne, D. (2013). 3D Imaging of Cells and Tissues by Focused Ion Beam/Scanning Electron Microscopy (FIB/SEM). In: Sousa, A., Kruhlak, M. (eds) Nanoimaging. Methods in Molecular Biology, vol 950. Humana Press, Totowa, NJ. https://doi.org/10.1007/978-1-62703-137-0_16

Drobne D, Novak S, Erman A, Dražić G. New Opportunities for FIB/SEM EDX in Nanomedicine: Cancerogenesis Research. Biological Field Emission Scanning Electron Microscopy. 2019 Apr 8;2:533-43.

Type of presentation: Poster

IM5-P-3 Micro-computerized tomography for evaluation of dental stud attachment wear

Tadej Mirt[a], Tine Malgaj[a], Klemen Leopold[a], Urban Bogataj[b], Rok Kostanjšek[b], Peter Jevnikar[a]

[a]*Medical faculty, Department for Prosthodontics, University of Ljubljana, Slovenia*

[b]*Biotechnical faculty, Department of Biology, Chair of Zoology, University of Ljubljana, Slovenia*

Contact email: tine.malgaj@mf.uni-lj.si

Objectives:
The study aimed to evaluate the surface wear of novel stud attachments for the retention of mandibular implant-supported prosthesis using a micro-computerized tomography (m-CT).

Methods: A prospective randomized controlled study compared the wear properties of a novel Novaloc attachment system to the conventional Locator system. Twenty edentulous patients requiring overdentures were included, and 20 implant-supported mandibular prostheses were randomized into two groups: Locator (n=9) or Novaloc (n=11). At annual follow-ups, the abutments were unscrewed and extraorally recorded using m-CT. After the image reconstruction and segmentation, mesh surface models of the abutment at each time point were obtained. The root mean squared error (RMSE), maximum distance, volume change, and percentage of worn surface (Spct) in the region of interest (ROI) were measured for each model at the initial and subsequent time points. To evaluate the wear pattern, the Shape Index (SI) – a measure of local curvature – was calculated for each mesh point. The Mann-Whitney U test was used to analyze the differences in m-CT measurements between both experimental groups ($P<0.05$).

Results: After 2 years, both groups exhibited minimal surface changes. In the Novaloc group, the wear of one abutment was clinically observed. However, no significant differences were found between the groups ($P>0.05$). The RMSE was between 2 and 4 μm for most samples, while for the abutment with clinically observed wear, the RMSE exceeded 8 μm, with a maximum deviation of 28 μm. The Spct of the ROI ranged from 0 to 3% and increased to 7% with a volume loss of 0.079 mm3 in the case of clinically observed abutment wear.

Conclusions: After 2-years of clinical service, the Novaloc attachment system showed comparable wear properties to the conventional Locator system.

Type of presentation: Poster

IM5-P-4 Effects of different preparation methods and detector use on SEM imaging of bacterial flagella

Marko Radenković[a], Ivana Milošević[a], Elizaveta Pavlova[a], Éva Tóth[b,] Hajnalka Jankovics[b]

[a]*BioSense Institute - Research and Development Institute for Information Technologies in Biosystems, Novi Sad, Serbia*

[b]*Bio-Nanosystems Laboratory, Research Institute of Biomolecular and Chemical Engineering, University of Pannonia, Veszprém, Hungary*

Contact email: marko.radenkovic@biosense.rs

Introduction:
High-resolution scanning electron microscopy (SEM) has undergone significant advancements in electron sources and detection techniques, allowing for the detailed visualization of supramolecular and subcellular structures. SEM can now achieve resolutions of 1 nm for biological samples, though this requires careful and appropriate preparation. A common method for imaging nonconductive samples involves coating them with conductive materials such as gold (Au), platinum (Pt), or carbon (C). While this approach is effective for obtaining high-resolution images, it can obscure fine morphological details. In this study, two different preparation procedures for bacterial flagella (the organelles responsible for locomotion) were compared with focus on flagella's morphology.

Methods:
Flagella of *Salmonella sp* (Lignières, 1900) Typhymurium were obtained from Research Institute of Biomolecular and Chemical Engineering (University of Pannonia, Hungary). Two sample preparation methods were employed, both utilizing gold-coated polyvinylchloride (PVC) surfaces as substrates.
In the first approach, a suspension of flagella in buffer solution (20 mM HEPES, 150 mM NaCl, 1 mM TCEP) was placed on the substrate and allowed to settle for 15 minutes. After that the sample was rinsed with MilliQ water to remove salt.
The second method involved chemical fixation and dehydration. Flagella suspension was mixed with 2% glutaraldehyde (GA) in 10 mM phosphate-buffered saline (PBS) and incubated for 1 hour at room temperature. Then the fixed flagella were deposited onto the substrate and left to adhere for 15 minutes. Then the substrate with flagella were treated with graded ethanol–water series: 10%, 20%, 30%, 40%, 50%, 60%, 70%, 80%, 90% and 96% with each series lasting for 1 minute.
After drying, the flagella prepared by both methods were analyzed using an Apreo 2C High-Resolution Scanning Electron Microscope (HRSEM, Thermo Fisher Scientific, USA). Imaging was performed at a low accelerating voltage (1 kV) and probe current (50–100 pA), using In-Lens Secondary Electron Detector and the Everhardt-Thornley Detector (ETD) [1].

Results:
The first preparation method was significantly faster than the second, however, the flagella were barely visible and appeared two-dimensional, detectable only with the In-Lens Secondary Electron Detector (Figure 1A) at low voltage and a working distance of 2 mm. In contrast, the second method yielded higher-resolution images, revealing flagella's three-dimensional structure (Figure 1B). While both methods are suitable for statistical analyses, such as evaluation the number or length of flagella, as well as their width, only the second method provided sufficient detail for morphological analysis.

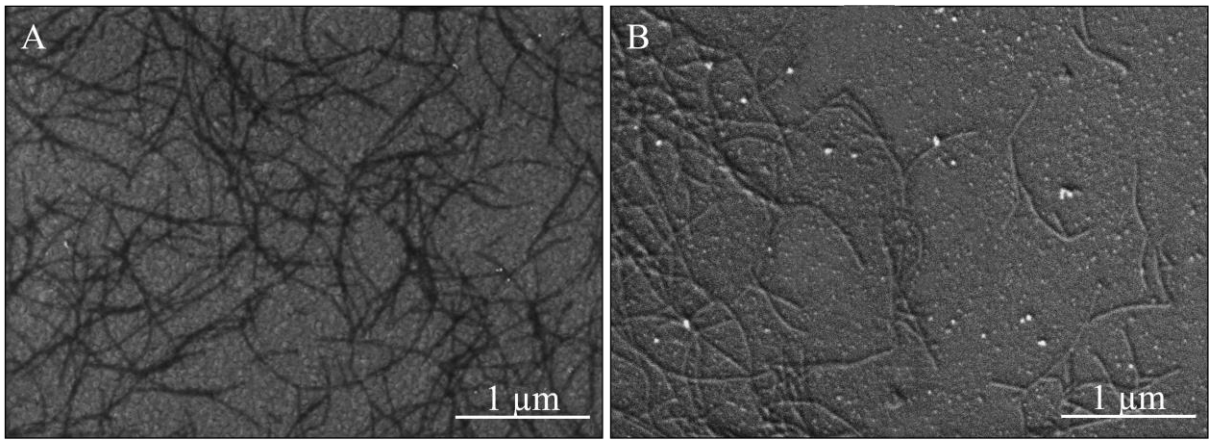


Figure 1: A- Flagella prepared by the first method (In-Lens Secondary Electrons detector); B- Flagella prepared by the second method (Everhardt-Thornley detector).

Discussion and Conclusions:
This study highlights the importance of tailoring sample preparation protocols to the specific analytical goals of SEM imaging, ensuring that the chosen method aligns with the desired balance between efficiency and detail.

Acknowledgements
The authors gratefully acknowledge the financial support of the Ministry of Science, Technological Development, and Innovation of the Republic of Serbia (Grants No. 451-03-66/2025–03/200358)

References:
1. B. J. Griffin, *Scanning*, **2011**, *33: 162-17*

Type of presentation: Poster

IM5-P-5 High throughput micro-combinatorial study of microstructure and materials properties of binary and ternary

György Gyula Sáfrán[a], Daniel Olasz[a], Ildikó Cora[a], Miklós Serényi[a]

[a]Hungarian Research Network, EK, MFA, Hungary

Contact email: safran.gyorgy@ek.hun-ren.hu

This work describes the principles and applications of the microcombinatorial technique for high throughput thin films characterisation and presents the scientific results obtained by its application. The patented microcombinatorial technique has proven to be a very useful research tool in transmission electron microscopy (TEM) and materials science. It involves the production on a single substrate, by magnetron sputtering, of a sample with laterally varying properties, containing either a complete two- or three-component thin film system, e.g. including all possible combinations of material A, material B and the whole proportions of A to B. This allows to efficiently test and develop new materials with specific properties. One of its applications is the study of thin films and coatings by TEM and other analytical methods, where the micro-combinatorial technique can be used to efficiently produce and test complete databases or 'libraries' of materials of varying composition, hardness, thickness and other parameters. This method has proven to be very effective in optimising materials for semiconductor devices, optoelectronics and photovoltaic cells, and hard coatings. Such systems already investigated in the whole concentration range: e.g. Si-Ge, Hf-O-N, Si-O-N, Mg-Si, Al-Cu, Y-Ti-O, etc. The most important result obtained using microcombinatory is the first publication in the literature of a complete phase map of a complete thin film system (Y-Ti-O), similarly to the phase diagrams of solids.

IM6 Electron optics and beam shaping for electron microscopy

Type of presentation: Invited

IM6-IN-1 Optical Near-field Electron Microscopy

Thomas Juffmann[a]

[a]*University of Vienna, Austria*

Contact email: thomas.juffmann@univie.ac.at

We present experimental results on optical near-field electron microscopy, a novel super-resolution microscopy technique for the study of interfaces (1). The technique is based on imaging optical near-fields using the electro-optics of a low energy electron microscope. We demonstrate that this technique can reach a resolution better than 30nm, and show proof-of-principle applications in plasmonics, electrochemistry, and biophysics.

(1) R. Marchand, R. Šachl, M. Kalbáč, M. Hof, R. Tromp, M. Amaro, S. J. van der Molen and T. Juffmann, Optical Near-Field Electron Microscopy, Phys. Rev. Applied 16, 014008 (2021)

Type of presentation: Invited

IM6-IN-2 Electron Optics and Beam Shaping with a Special View on EELS

Axel Lubk[a,b], Johannes Schultz[a], Jörg Fink[a], Giulio Guzzinati[c]

[a]*Leibniz Institute for Solid State and Materials Research Dresden, Dresden, Germany*

[b]*Institute of Solid State and Materials Physics of TU Dresden, Dresden, Germany*

[c]*CEOS GmbH, Heidelberg, Germany*

Contact email: a.lubk@ifw-dresden.de

Introduction:

Electron energy loss spectroscopy (EELS) in the transmission electron microscope (TEM) is concerned with the determination of a wide variety electronic excitations in solids, ranging from collective low energy modes, such as phonons and plasmons, to high-energy single particle excitations, such as inner shell electron excitations. Herein, the versatility of the electron optics of a TEM allows both tailoring the illumination in the sample plane, e.g., by focusing to a spot, as well as the selection of the recorded signal, e.g., by recording momentum-resolved in the far field. This amounts to pre- and postselecting the quantum states of the scattered electrons and offers a multifacetted view on the non-local dielectric response of matter, which is difficult to obtain with other spectroscopy methods (e.g., employing x-rays).

Methods:

In this contribution, we will provide a short overview on the physical content of EELS in terms of response functions with a focus on momentum-resolved EELS and 4D STEM EELS. As an example we consider surface and bulk plasmonic responses in metals, e.g., the relation of plasmonic resonances to band renormalization and local field effects. Subsequently, state-of-the-art electron optics of TEM EELS is briefly introduced including the novel CEOS heart monochromator[1] and sector magnet energy filters, again with a focus on low-loss momentum-resolved EELS and 4D STEM EELS modes.

Discussion and conclusions:

Two case studies are considered, demonstrating current possibilities of TEM EELS employing different pre- and postselection modes. The observation of hybridized 2D plasmons in the layered (strange) metal Sr_2RuO_4[2] and of surface plasmons on rod-shaped and split-ring resonator shaped Al nanoparticles[3]. In Sr_2RuO_4, outside the classical range of electron-hole excitations, well-defined plasmons are observed. The optical (acoustic) plasmon due to in-phase (out-of-phase) 2D charge oscillations of neighbouring layers exhibits a quadratic (linear) positive dispersion. It is possible to describe the range of optical plasmon excitations in a mean-field random phase approximation without taking correlation effects into account. In metallic nanostructures, localized surface plasmons give rise to transient electromagnetic fields. The field component parallel to the propagation direction of the STEM probe gives rise to its energy loss, whereas the two perpendicular components deflect the beam. All three components are probed with the 4D STEM EELS setup, yielding insight into the spatial distribution of the surface plasmons and their non-local interaction.

These results (together with many others, namely those employing some sort of angular-momentum pre- or postselection) highlight the possibilities of electron optical beam shaping (either in the pre- or postscattering channel) in combination with EELS in state-of-the-art TEM for topical problems in solid state physics.

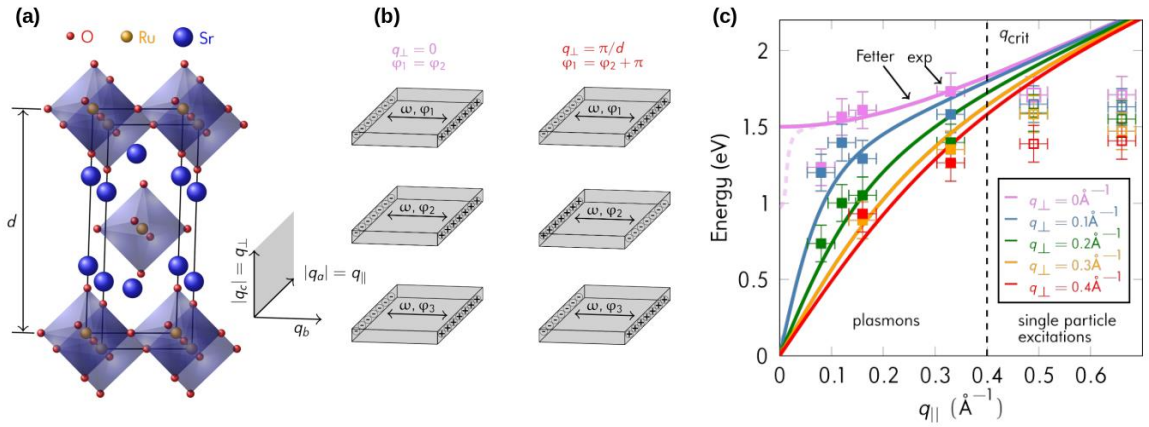


Figure 1: Coupled (hybridized) 2D plasmon modes in Sr_2RuO_4 (a,b) probed by momentum resolved TEM EELS (c). The coupled 2D plasmons oscillating with a fixed phase difference between 0 and ⊓ in adjacent RuO_2 layers (b) give rise two a family of acoustic and optical plasmon modes visible in momentum-resolved EELS (c). Solid lines correspond to theoretic plasmon dispersion relations.

Acknowledgments:

The authors acknowledge funding from the HORIZON EUROPE framework program for research and innovation under grant agreement n. 101094299.

References:

[1] Börrnert, F., Uhlemann, S., Müller, H. et al., A novel ground-potential monochromator design *Ultramicroscopy* **53**, 113805 (2023)

[2] Schultz, J., Lubk, A., Jerzembeck, F. *et al.* Optical and acoustic plasmons in the layered material Sr2RuO4. *Nat Commun* **16**, 4287 (2025).

[3] Krehl, J., Guzzinati, G., Schultz, J. *et al.* Spectral field mapping in plasmonic nanostructures with nanometer resolution. *Nat Commun* **9**, 4207 (2018)

Type of presentation: Oral

IM6-O-1 Entanglement in Bragg Scattering

Stefan Löffler[a], Stefan Nimmrichter[b], Dennis Rätzel[c], Philipp Haslinger[a], Peter Schattschneider[a]

[a]*TU Wien, Austria*

[b]*Universität Siegen, Germany*

[c]*Universität Bremen, Germany*

Contact email: stefan.loeffler@tuwien.ac.at

The transmission electron microscope (TEM) is a ubiquitous tool for material characterization. One of its core features is its supreme spatial resolution down to the sub-Angstrom range, owing to the electron beam's short wavelength. The dominant method of interaction between the electron beam and the sample is the long-ranged Coulomb interaction, which gives rise (among other things) to the well-known Bragg scattering in crystalline samples. Therefore, at its core, Bragg scattering is a quantum-mechanical process, which we can describe by a unitary transformation acting on the joint quantum state of electron and sample. Given that such a unitary transformation can entangle the two systems [1,2], the question naturally arises in what way this affects the Bragg scattering signal.

In this work, we present a full quantum-mechanical treatment of Bragg scattering based on a density matrix that describes the joint quantum state of the electron and of the atoms in the sample. Unlike the traditional description as scattering of the probe electron's wavefunction in a fixed external potential that is treated as a perturbation in a one-electron model, the density matrix allows us to describe changes in the combined electron-scatterer wavefunction, e.g., upon Bragg scattering.

We show that the electron beam and the sample do become entangled and that the purity of the electron beam state after tracing out the sample states decreases as a function of the overlap between different sample states. This can have measurable consequences, e.g., reducing the contrast of the lattice fringes in high-resolution images [3]. However, in the limit of an increasingly heavy rigid lattice, our model approaches the standard treatment of a single probe electron in a fixed external potential.

Another interesting aspect that can be studied in the density-matrix formulation of Bragg scattering is time dependence. When the sample can be considered to be in a single, freely evolving quantum state, this state naturally broadens over time. This, in turn, affects the interaction with the electron beam, leading to a change in purity depending on the evolution time after the preparation of the sample state. With latest-generation ultra-fast TEMs, it should be possible to detect and exploit these changes, giving rise to a new way for studying quantum decoherence with a TEM. In fact, it was recently proposed to exploit the entanglement between an electron and a levitated nanocrystal sample as a means to bring the sample's centre of mass into a quantum superposition state [4].

The full quantum description of Bragg scattering not only broadens our horizon and allows deeper insights into the quantum mechanical scattering occurring inside a TEM, it also paves the way for novel quantum metrology. At the same time, it confirms inherited convictions that in the limit of heavy rigid lattices, "classical TEM" works as we have come to expect.

References:
1. P. Schattschneider, S. Löffler, *Ultramicroscopy,* **2018**, 190, 39-44.
2. P. Schattschneider, S. Löffler, H. Gollisch, R. Feder, *Ultramicroscopy,* **2020**, 241, 146810
3. S. Löffler et al., in preparation
4. S. Nimmrichter, D. Rätzel, I. Bicket, M. Seifner, P. Haslinger, arXiv:2502.13821, **2025**

Type of presentation: Oral

IM6-O-2 Miniaturized Magnetic Multipoles for Ultrafast Beam Shaping in the Transmission Electron Microscope

Johannes Schultz[a], Max Herzog[a], Axel Lubk[a,b]

[a]*Leibniz Institute for Solid State and Materials Research Dresden, Dresden, Germany*

[b]*Institute of Solid State and Materials Physics of TU Dresden, Dresden, Germany*

Contact email: j.schultz@ifw-dresden.de

The authors have requested that the abstract not be published.

Type of presentation: Oral

IM6-O-3 Electron Beam Shaping with a MEMS Phase Plate via Current-Controlled Electrostatic Potential

Payam Habibzadeh Kavkani[a], Paolo Rosi[b], Vincenzo Grillo[b], Marco Beleggia[a]

[a]*University of Modena and Reggio Emilia, Italy*

[b]*CNR-NANO S3, Modena, Italy*

Contact email: payam.habibzadehkavkani@unimore.it

Keywords: Electron beam shaping, phase plate, electron microscopy, aberration corrector

Electron beam shaping is increasingly critical in advanced electron microscopy, supporting novel imaging, spectroscopy, and material characterization. Central to these developments are phase plates, electron-optical elements capable of precisely modulating both the phase and amplitude of the electron wavefunction [1]. By forming specific beam profiles, such as vortex beams, these devices boost nanoscale sensitivity to magnetic and structural properties and facilitate orbital angular momentum (OAM) measurements via dual-phase plate systems [2, 3]. Such functionalities arise from interactions with carefully tailored electric or magnetic potentials, demonstrating that careful control of electron phase shifts can enhance resolution and enable advanced imaging techniques.

While electrostatic phase plates offer real-time tuning via voltage control, they remain limited by electrode configurations and biasing channels, complicating the generation of finely tuned or gradient-like fields. To address these challenges, we present a Current-Controlled Electrostatic Phase Plate that leverages multi-material Micro-Electro-Mechanical Systems (MEMS) technology to establish a continuous, tunable potential gradient without relying on numerous discrete electrodes. Rooted in Maxwell's equations, this approach supports advanced beam-shaping scenarios—such as vortex beam generation and aberration correction and provides real-time tunability for high-precision electron beam control.

We employed COMSOL Multiphysics (Electrocurrent module) to simulate and design the chip. Post-processing with Python scripts, including a multislice algorithm, determined the total phase shifts. Gradient-based optimization refined applied potentials and electrode geometries, ensuring alignment with analytically derived phase requirements for threefold astigmatism correction (Fig. 1) and vortex beam generation (Fig. 2). The devices were then fabricated on silicon-on-insulator (SOI) wafers, fully compatible with electrically biased TEM holders. Simulation results confirm that the Current-Controlled Electrostatic Phase Plate creates a continuous potential gradient while reducing the required number of electrodes, matching theoretical phase profiles for targeted beam shaping.

These findings highlight the significant promise of MEMS-based Current-Controlled Electrostatic Phase Plate in overcoming electrostatic limitations by enabling tunable, continuous potential gradients. Ongoing experimental validations demonstrate robust performance in astigmatism correction, vortex beam generation, and advanced imaging. This versatile platform thus extends electron microscopy’s capabilities, opening new avenues in nanotechnology, materials science, and beyond.

[1] M. Malac et al., "Phase plates in the transmission electron microscope: operating principles and applications," J. Microsc., vol. 70, no. 1, pp. 75–112, 2021. doi:10.1093/jmicro/dfaa070.
[2] A. H. Tavabi et al., "Generation of electron vortex beams with over 1000 orbital angular momentum quanta using a tunable electrostatic spiral phase plate," Appl. Phys. Lett., vol. 121, no. 7, p. 073506, 2022. doi:10.1063/5.0093411.
[3] G. Pozzi et al., "Design of electrostatic phase elements for sorting the orbital angular momentum of electrons," Ultramicroscopy, vol. 208, p. 112861, 2020. doi:10.1016/j.ultramic.2019.112861.

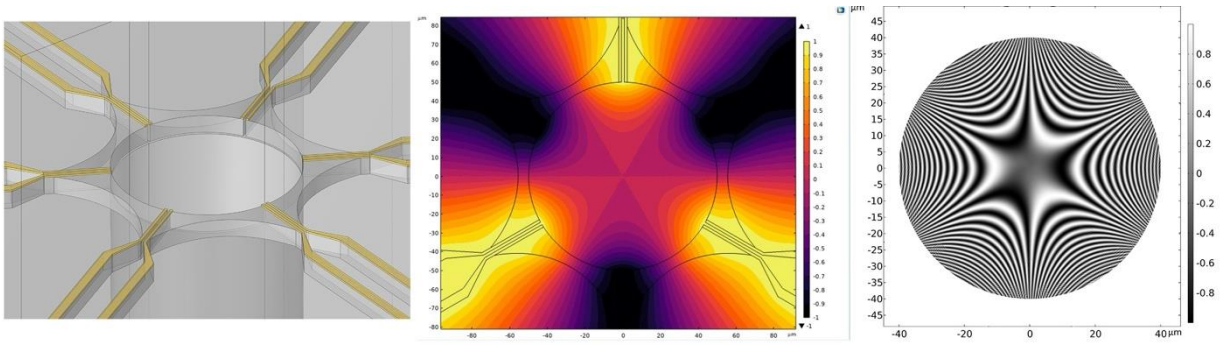


Figure 1: Tunable Current-Controlled Electrostatic Phase Plate for Three-Fold Astigmatism Correction. Gradient-based shape-optimized device (left), electric potential distribution (middle), and corresponding phase profile (right).

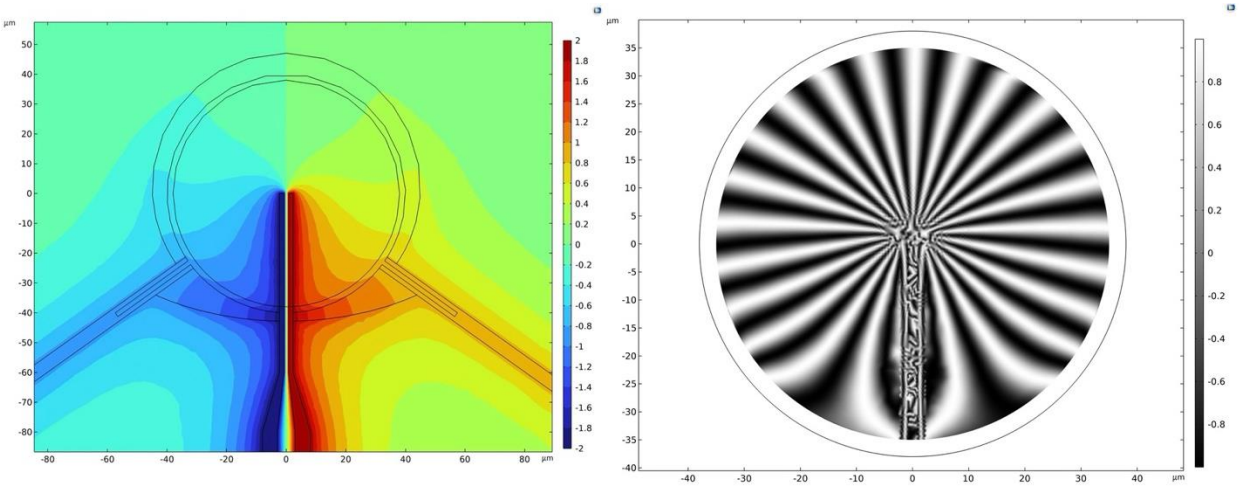


Figure 2: Tunable 4-Biased Current-Controlled Electrostatic Phase Plate for the Generation of Vortex Beams. Electric potential distribution (left) and corresponding phase profile (right).

Type of presentation: Poster

IM6-P-1 Towards spatially coherent low-energy electron and ion beams

Matias Eriksson[a], Prosenjit Majumder[a], Robert Fickler[a]

[a]*Physics Unit, Photonics Laboratory, Tampere University, Tampere, Finland*

Contact email: matias.eriksson@tuni.fi

In recent years, structured matter waves have attracted significant attention, particularly in the realm of structured electrons. Spatially coherent field-emission electron sources are already well understood and widely used, enabling coherent manipulation of the electron beam wavefront. The innovations within the field have enabled many intriguing applications of structured electrons in electron microscopy and spectroscopy, and many ongoing developments aim to further exploit structured electrons for use in quantum experiments and advanced microscopy schemes [1].

We are working towards an experimental setup with a tunable low-energy field emission and gas field ion emission source for structuring electron-, and ultimately ion beams. A cryogenically cooled nanotip field emission / gas field ion emission source together with a 1-1.5 m-long free propagation region enables the generation of a transverse-spatially coherent electron/ion beam, where we expect coherence lengths exceeding multiple micrometers for ions, sufficient for beam structuring using nanofabricated electrostatic elements. The initial plan is to explore the physics of low-energy vortex electrons and ions generated using electrostatic chopsticks as a minimally intrusive and tunable shaping element [2]. A custom-built vacuum chamber is used for full access to the beamline, where along standard electrostatic deflectors and lenses, we will place magnetic shields along the entire beamline to ensure minimal disruption by ambient magnetic fields.

The first successful implementation of a spatially coherent ion source will open a new field of coherent ion research, with many interesting experimental possibilities ranging from exploring fundamental physics within the framework of composite charged wave systems, to developing new techniques for advances in e.g. ion microscopy, utilizing the orders of magnitude lower wavelengths and electric and magnetic properties of the structured ions.



Figure 1: A combined field emission and gas field ion emission source.

References:

1. Harris, J., Grillo, V., Mafakheri, E., Gazzadi, G. C., Frabboni, S., Boyd, R. W., & Karimi, E. (2015). Structured quantum waves. *Nature Physics*, *11*(8), 629–634. https://doi.org/10.1038/nphys3404

2. Tavabi, A. H., Larocque, H., Lu, P.-H., Duchamp, M., Grillo, V., Karimi, E., Dunin-Borkowski, R. E., & Pozzi, G. (2020). Generation of electron vortices using nonexact electric fields. *Physical Review Research*, *2*(1), 013185-. https://doi.org/10.1103/PhysRevResearch.2.013185

Type of presentation: Poster

IM6-P-2 Development and Application of an Aberration Calculation Program for Electron Lenses Based on Differential Algebra

Zhicheng Liu[a], Shikai Zhu[a], Xu Liu[a,*], Bin Qin[a]

[a]*State Key Laboratory of Advanced Electromagnetic Technology, School of Electrical and Electronic Engineering, Huazhong University of Science and Technology, Wuhan 430074, Hubei, China*

Contact email: lxhustliu@hust.edu.cn

1. Introduction

The primary goal of this research is to develop an aberration calculation program for electron lenses using the differential algebra (DA) method. This program aims to evaluate the linear focusing parameters and high-order aberration coefficients (up to fifth-order) of electromagnetic compound lenses, which are critical for improving the resolution and performance of electron microscopy systems, including both scanning electron microscopy (SEM) and transmission electron microscopy (TEM).

2. Methods

The program is implemented in Python and integrates with the finite element software POISSON SUPERFISH. The DA method is employed to compute the transfer map of electron trajectories, enabling the calculation of Gaussian optical properties and aberration coefficients without deriving analytical expressions for derivatives. The program uses adaptive Gaussian wavelet superposition algorithm to fit axial electromagnetic field distributions [1], ensuring high precision in field value fitting. The Fourth-Order Runge-Kutta method (RK4) is utilized for solving particle trajectories. The specific algorithm implementation framework is shown in Figure 1. The program's accuracy is validated by cross-comparing results with previous studies on Glaser magnetic lenses [2], Schiske electrostatic lenses [3], and combined electromagnetic lenses [4].

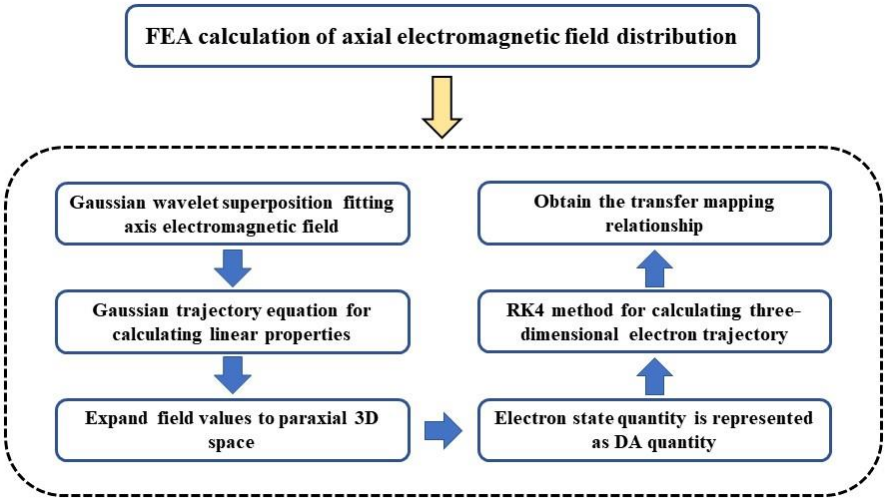


Figure 1: DA algorithm framework.

3. Results

The program successfully calculates the first-order optical properties and high-order aberration coefficients for various electron lenses. The adaptive Gaussian wavelet superposition fitting method balances computational efficiency and accuracy, with the relative error of the axial magnetic field integral of the magnetic lens being on the order of 10^{-4}. The results show that the program can compute aberration coefficients up to the fifth order, providing a comprehensive tool for electron optical system design.

4. Discussion and conclusions

By integrating DA with finite element simulations, the program provides a powerful tool for reducing spherical and chromatic aberrations, which are critical for achieving high resolution in electron

microscopy. The program's adaptability allows for modifications based on specific requirements, facilitating its application in machine learning and digital twin technologies for electron microscopes. Future work will focus on further refining the program's efficiency and expanding its capabilities to include more complex lens configurations and higher-order aberration analyses. This research represents a significant step toward automating and optimizing the design of electron optical systems, with potential applications in advanced microscopy and materials science.

References:

1. Z. Liu, *Ultramicroscopy.* 2006, 106, 220-232.
2. Y. Kang, T. Tang, Y. Ren, et al., *Optik.* 2007, 118, 158-162.
3. M. Cheng, T. Tang, Y. Zhenhua, *Optik.* 2001, 112, 250-254.
4. Z. Liu, *Nucl. Instrum. Methods Phys. Res. A.* 2004, 519, 154-161.

Type of presentation: Poster

IM6-P-3 Aberration correctors and their benefits in SEM

Martin Vodička[a], Ondřej Sháněl[a], Radovan Vašina[b]

[a]*Institute of Physical Engineering, Brno University of Technology, Brno, Czech Republic*

[b]*Thermo Fisher Scientific, Brno, Czech Republic*

Contact email: 216935@vutbr.cz

Electron microscopy is a field with a history that spans nearly a century, accompanied by numerous challenges and stringent technological demands. The initial setback occurred in 1936 when Otto Scherzer demonstrated that static, rotationally symmetric, electromagnetic lenses with zero charge along the axis invariably exhibit positive spherical (Cs) and chromatic (Cc) aberration [1]. So far, many aberration correctors have been proposed but only those violating the axil symmetry have been commercialized yet only for transmission electron microscopes [2], [3]. Aberration corrector for scanning electron microscope (SEM) is still mainly academic field [4]. The main reason is high cost and complexity of the system. We are to investigate the resolution limits of aberration corrected SEM and outline the benefits of different aberration corrector types. In the following we will focus on comparison of these parameters:

1. Ultimate resolution
2. System stability, tunability and complexity
3. Product cost

To calculate the probe size, we use the root power sum method introduced by Barth and Kruit [5]. Figure 1. presents probe size containing 50% of total current (d50). In specific set of conditions, it shows the reduction in probe size as Cs and Cc are decreased. For a given system operating within specific operating parameters, it indicates the most advantageous correction strategy (red arrows). The Cs and Cc contributions to d50 vary according to the operational regime. Specifically, at high landing energies, the Cs aberration predominates, while at low landing energies (less than 1 keV), the Cc aberration becomes decisive. The selection of corrector function is contingent on the specific use case.

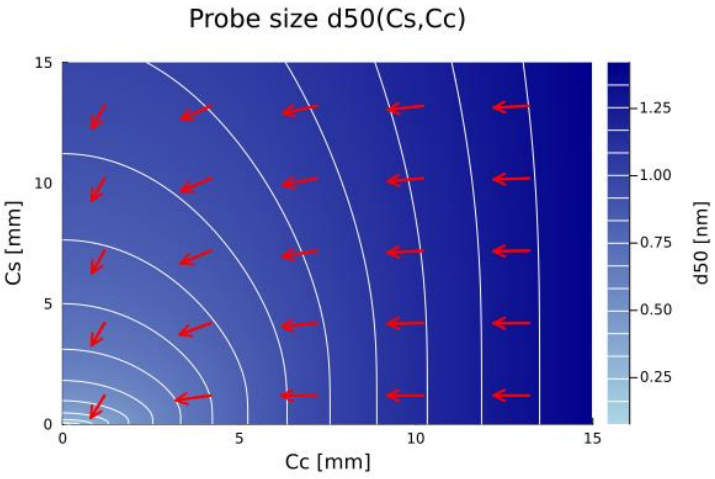


Figure 8 Dependence of d50 on Cs and Cc for typical SEM conditions (Ip = 100 pA, *dU = 0.63* eV, *U = 30* kV, *Br = 2e8* A $sr^{-1}m^{-2}$ V^{-1}*)*

Comparison of system stability (Sta), tunability (Tun), complexity (Com) and product cost for different types of correctors is summarized in Table 1.

Table 1 Comparison of various types of aberration correctors

Corrector type	Cs	Cc	Sta	Tun	Com	Cost	Pros	Cons
Quadrupole-octupole	+	+	↑	↑↑↑	↑↑↑↑	$$$$	Proven	Size, mass
Hexapole	+	-	↑	↑↑	↑↑↑	$$$$	Proven	Size, mass
Mirror	+	+	↑↑	↑↑	↑↑↑↑	$$	Axial symmetry, proven	Unconventional design, tolerances
Foil (Phase plate)	+	+	↑↑↑	↑	↑	$	Axial symmetry	Contamination, absorption, charging

Resolution enhancement is pivotal for the study of material structures, composition, defects, and interfaces with unprecedented precision. The advantages of aberration correction extend beyond the

mere reduction of the beam spot size. Cs correction facilitates the aperture angle to be increased, thereby enhancing the total current in the beam and leading to an improved signal-to-noise ratio. The enhancement of signal quality enables in-situ and 3D analysis with low-voltage operation that minimises beam-induced damage. Furthermore, when Cs is fully corrected, the necessity for a short focal length to achieve high resolution is mitigated, enabling larger pole piece gaps, a feature that is particularly advantageous for a wide variety of experiments with large field of view requirements. The broad range of applications of these aberration-corrected SEMs is likely to be significant in both academic and industrial laboratories.

References:

1. Scherzer, O. Zeitschrift für Physik. **1936**, vol. 10. doi: 10.1007/BF01349606.
2. Krivanek, O.L. et al. Ultramicroscopy. **1999**, vol. 78. doi:10.1016/S0304-3991(99)00013-3
3. Haider, M. et al. Ultramicroscopy. **1998**, vol. 75. doi:10.1016/S0304-3991(98)00048-5
4. Zach, J. et al. Nucl. Instrum. **1995**, Vol. 363. doi:10.1016/0168-9002(95)00056-9
5. Barth, J.E. et al. Optik **1996,** Vol. 101(3). ISSN: 0030-4026

IM7 In-situ and environmental microscopy

Type of presentation: Oral

IM7-O-1 Atomic-Scale Dynamics of Ni Catalysts Revealed by Operando TEM in Dry Reforming of Methane

Milivoj Plodinec[a,b], Claudiu Colbea[a,b], Hannah Nerl[c]

[a]*Scientific Center for Optical and Electron Microscopy, ETH Zürich, Switzerland*

[b]*Department of Chemistry and Applied Biosciences, ETH Zürich, Switzerland*

[c]*Humboldt University, Institute of Physics, Germany*

Contact email: mplodinec@ethz.ch

The utilization of CO_2 as a feedstock for chemical synthesis and fuel production represents a critical step toward achieving a sustainable, carbon-neutral economy. A key challenge in this domain is the development of efficient and selective catalysts capable of effectively converting CO_2 into valuable products. [1] Nickel (Ni) nanoparticles have emerged as highly promising catalysts for CO_2 conversion due to their notable catalytic activity and selectivity. However, the atomic-scale mechanism underlying CO_2 conversion over Ni nanoparticles remains poorly understood. [2] This study employs operando transmission electron microscopy (TEM) to directly observe the dynamic behavior of Ni nanoparticles during the dry reforming of methane (DRM).

Ni nanoparticles were sputter-deposited onto a microelectromechanical systems (MEMS)-based nanoreactor. [3] Operando TEM experiments were conducted using an aberration-corrected JEOL GRAND ARM Vortex TEM operating at 300 kV, integrated with a DENSsolutions Climate gas system and a HIDEN quadrupole mass spectrometer (QMS) 3F PIC for real-time gas analysis. Before initiating the DRM reaction, the Ni nanoparticles underwent a reduction treatment at 500°C in an H_2:He gas mixture (1:4 ratio). Subsequently, DRM was performed at 1 bar total pressure using a gas mixture of CH_4 and CO_2 at temperatures ranging from 500°C to 900°C.[3]

The operando TEM imaging revealed significant changes in the size, shape, and structure of Ni nanoparticles during the catalytic reaction (Fig. 1a). After the initial reduction treatment in a gas mixture of H2 and He, the average size of the Ni nanoparticles was ~10 nm (StdDev: 4nm). Next, the mixture of CH4 and CO2 was introduced into the nanoreactor. A stepwise increase in temperature to 850°C followed. When reaching 500-550°C, the Ni nanoparticles began switching from a slightly oxidized state to a metallic (active) state. Upon further temperature increase to 850°C, the Ni nanoparticles started to change morphology by oscillating between a more rounded and a faceted shape, forming well-defined (111) and (100) facets, achieving a highly active and selective catalyst state. Furthermore, while initially maintaining their shape and size, significant redispersion of the Ni nanoparticles was observed after 900 s. Once present, the redispersion was progressive over time (Fig. 1a). This could be attributed to the formation of intermediate volatile species, such as Ni(CO)x and NiOx. The simultaneously recorded MS data (Fig. 1b) suggests that the redispersion of Ni nanoparticles negatively affected catalyst activity, leading to deactivation.

In summary, the operando TEM imaging revealed that the Ni nanoparticles underwent significant changes in size, shape and structure, including nanoparticles redispersion during the high catalytic catalyst activity at 850°C. These dynamic changes suggest that the reaction mechanism is complex, involving multiple steps and intermediate species. The insights gained from this study may guide the design of more efficient and selective catalysts for DRM. Overall, the operando TEM experiments provided a unique window into the atomic-scale dynamics of Ni nanoparticles during DRM.

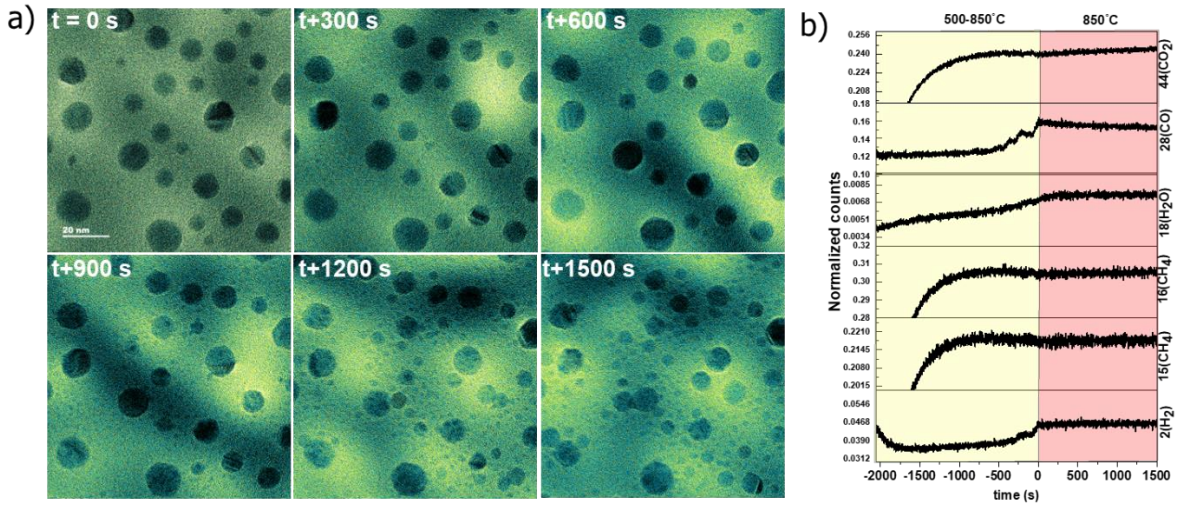


Figure 1. By correlating activity with structural information through operando TEM, the active Ni catalyst nanoparticles were directly visualized during dry reforming of methane. a) High resolution TEM images showing shape and size evolution of Ni nanoparticles at 850°C in DRM. b) Corresponding MS data showing CO_2 and CH_4 conversion and their selectivity to CO and H_2 with a stepwise temperature increase: 500-850°C. (Reaction conditions CO_2:CH_4 = 1:1, pressure 1000 mbar, temperature ramp 5 °C/min)

[1] Homs, N., Toyir, J. and De la Piscina, P.R., 2013. Chapter 1-Catalytic Processes for Activation of CO_2,
[2] Jang, W.J., Shim, J.O., Kim, H.M., Yoo, S.Y. and Roh, H.S., 2019. Catalysis Today, 324, pp.15-26
[3] Plodinec, M., Microscopy and Microanalysis, 28(S1), (2022), p. 146–148,

Type of presentation: Oral

IM7-O-2 Advancements in Plasma Microcell Integration for *in situ* TEM Experiments

Ulrich Schürmann[a], Niklas Kohlmann[a], Luka Hansen[b], Holger Kersten[b], Lorenz Kienle[a]

[a]*Department of Materials Science, Kiel University (Kiel), Germany*

[b]*Institute for Experimental and Applied Physics, Kiel University (Kiel), Germany*

Contact email: usc@tf.uni-kiel.de

Introduction

In situ transmission electron microscopy has become an increasingly important field. Direct observation and analysis of the fabrication and modification of nanostructured materials and surfaces are crucial for both fundamental plasma physics and materials science. Plasma processes, while offering a highly suitable approach for modifying nanostructures, have received little attention so far and are not yet established as part of the standard toolkit for *in situ* studies. Typically, plasma treatment and subsequent material analysis are carried out as two separate steps, requiring a sample transfer from the plasma environment into the electron microscope. To eliminate this separation, a microplasma cell - based on the concept proposed by Tai et al. [1] - was selected and further developed to enable *in situ* plasma treatment directly within the TEM.

Methods

For the integration of the *in situ* plasma cell, we used a modified sample holder provided by Hummingbird. The design of the cell was optimized to ensure vacuum-tightness and reproducibility. Gold coated silicon nitride window grids (used as electrodes) separated with Kapton spacers form the plasma chamber and are built in a ceramic housing and sealed with O-rings and low vapor pressure epoxy. Due to the single-use design, each cell can be tested for functionality and vacuum integrity prior to its insertion into the TEM. TEM investigations were performed using a JEOL JEM-2100. In addition, to address the challenge of sample transfer without breaking the vacuum, we established an Identical Location TEM (ILTEM) process using a Gatan vacuum transfer holder in combination with an FEI Tecnai F30 microscope. This approach allows the same sample positions to be analysed in the TEM both before and after *ex situ* plasma treatment [2].

Results

The *in situ* microplasma cell can be integrated into most standard TEM sample holders. Achieving a stable plasma requires careful selection of the cell geometry and all relevant discharge parameters, making the design process both critical and challenging. On the one hand, factors such as the type of gas, its purity, and the pressure must be optimized, while on the other hand, these need to be combined with a vacuum-tight cell design that remains transparent to the electron beam. A stable atmospheric pressure DC normal glow microplasma discharge was first characterized outside the TEM holder to ensure it met the necessary stability and size requirements for *in situ* TEM integration. Electrical and optical diagnostics confirmed operation within the normal glow discharge regime [3]. First results for *ex situ* plasma treatment of transition metal dichalcogenide (TMDC) materials via ILTEM will be present.

Discussion and Conclusion

This work presents the current design status and the potential impact of a plasma microcell for TEM integration. Additionally, the authors provide an outlook on the adaptation of plasma treatment experiments to the microcell environment, along with recent results related to the ILTEM approach.

Acknowledgments

The authors thank the Deutsche Forschungsgemeinschaft (DFG, German research foundation) for funding (KI 1263/17-1, KE 574/8-1).

References

1. K. Tai, T.J. Houlahan Jr., J.G. Eden, S.J. Dillon, *Scientific Rep.* **2013**, *3*(1), 1325.
2. N. Kohlmann, L. Hansen, O. Lupan, U. Schürmann, A. Reimers, F.Schütt, R. Adelung, H. Kersten, L. Kienle, *ACS Applied Materials & Interfaces* **2021**, *13*(51), 61758 - 61769.
3. L. Hansen, N. Kohlmann, U. Schürmann, L. Kienle, H. Kersten, *Plasma Sources Science and Technology* **2022**, *31*(3), 035013.

Type of presentation: Oral

IM7-O-3 Electron beam enlargement modelling in the environmental scanning electron microscope at the low gas temperature

Redouane Belkorissat[a]

[a]*Department of Computer Science, Ibn Khaldoun University Tiaret, Algeria*

Contact email: belkhorissat_r@proton.me

Analyzing a sample using the environmental scanning electron (ESEM) microscopy is often confronted to a set of constraints due to the presence of gas during the passage of the primary electron beam. Indeed, the electrons beam gas atom scattering will deviate one fraction of the primary electrons beam from their initial axis direction and will forming a nearly cone shape around the initial electrons beam impact point with the sample surface. This cone shape is called the skirt of electrons, and the detected signal to noise ratio in the ESEM is more important if the electrons skirt radius is reduced. Many parameters affecting the change of the electron skirt radius are considered theoretically and experimentally. Among them, the electron beam energy (E), the working distance (WD), gas pressure (P) and gas type **[1].** The effects of all these parameters were only studied under room ambient temperature.

Recently, when the low temperature method (LTM) for water vapor gas is applied in ESEM analysis of biological samples with their native states, the gas temperature can be decreased from room temperature to (-20 °C) for gas pressure ranging from 10 Pa to 200 Pa. Therefore, this parameter effect on the electrons skirt radius must be elucidated for different gas pressure.

In this study, the effect of water vapor gas temperature on the electron skirt radius is calculated for two water vapor gas pressures (of 100 Pa and 10 Pa). This was done via a new calculation program based on Monte Carlo method **[2]** and by selecting the elastic or inelastic collision processes, when monitoring the electron trajectories for the considered ESEM conditions.

The obtained results showed a decrease of the un-scattered electron-beam fraction when decreasing the gas temperature. On the other hand, this change is very low at 10 Pa gas pressure (The unscattered electrons beam fraction variation of 2% is obtained). This obtained results can be explained to the decrease of the electrons atoms scattering probability, resulted from the decrease of the water vapor molecules concentration when the gas temperature is increased).

The present improved Monte Carlo calculation of electron-gas interaction allowed us to obtain the minimum of beam skirt radius with change of un-scattered electron fraction at low scattering conditions. The obtained results showed that both the vapor gas pressure and temperature can affect the beam skirt radius.

References:

[**1].** Danilatos G D, Fondations of environmental scanning electron microscope Advances in electronics and electron physics. 1988, 71: 109-250.

[2] Joy D C, Monte Carlo Modeling for Electron Microscopy and Microanalysis, OUP: NY, 1995.

Keywords: ESEM; Monte Carlo simulation; electron-gas interaction; skirt

Type of presentation: Poster

IM7-P-1 InCAEM: A Singular Infrastructure for Advanced Energy Materials Research

Núria Bagués[a], Lucía Aballe[a], Jordi Arbiol[b1,b2], Ana Arché-Núñez[a], Rodrigo Arilla del Caño[c], Esther Barrena[c], Caterina Biscari[a], Karol Y. Bustos[c], Joan Casas[a], Alba Cazorla[c], Emigdio Chávex-Ángel [b2], Hui Chen[b2], Marc G. Cuxart[b2], Martin Børstad Eriksen[d], Antoni Garcia de Herreros[a], Alba Garzón Manjón[b2], Anna Gribbon[b2], David Llorens[b2], Daniel Martín-Jiménez[c], Ana Belén Martínez [a], Gonzalo Merino[d], Aitor Mugarza[b1,b2], Josep Nicolás[a], Carmen Ocal[c], Joaquín Otón[a], Rogger Palacios-Rivera[c], Seyedeh Leila Panahi[a], Marc Raventós[a], Gemma Rosas[a], Sandra Ruiz-Gómez[a], Talha Mehtab Shaikh[b2], Sergio Vicente [a], Muhammad Waqas Khaliq[a], Yongchao Zhang[b2]

[a]*ALBA Synchrotron Light Source Facility, Cerdanyola del Vallès, Spain*

[b1]*ICREA Institució Catalana de Recerca i Estudis Avançats, Barcelona, Spain*

[b2]*Catalan Institute of Nanoscience and Nanotechnology (ICN2) CSIC and BIST, Barcelona, Spain*

[c]*Materials Science Institute of Barcelona (ICMAB-CSIC), Barcelona, Spain*

[d]*Scientific Information Port (PIC) IFAE and CIEMAT, Barcelona, Spain*

Contact email: nbagues@cells.es

The *In Situ* Correlative Facility for Advanced Energy Materials (InCAEM) project aims to establish a unique, open-access research infrastructure dedicated to advanced energy materials science. Launched in October 2022 and led by four partner institutions — ALBA, ICN2, ICMAB, and PIC-IFAE — the facility is expected to be fully operational by the end of 2025. It will integrate cutting-edge instrumentation, infrastructure, and specialized personnel to support state-of-the-art research addressing key challenges outlined in the European Green Deal.

Among the new instruments to be installed at ALBA synchrotron are a high-resolution (scanning) transmission electron microscope (STEM) for *in situ* experiments and several scanning probe microscopes (SPM), with different capabilities and operation from ultra-high vacuum to gas and liquid environments. Additionally, advanced data infrastructures will be implemented at ALBA and PIC-IFAE to support *in situ* and *ex situ* data processing. In parallel, efforts are also underway to adapt existing beamlines for correlative experiments and develop multi-modal pipelines and experimental workflows.

By integrating operando sample environments with complementary characterization tools and advanced data analysis, InCAEM will enable true multi-modal, multi-length-scale characterization of functional materials. This will support the development of sustainable materials for applications such as batteries, electric vehicles, and solar cells. While STEM and SPM provide high spatial resolution and diverse contrast mechanisms, X-ray-based techniques offer efficiency and highly specific chemical, structural, electronic, and magnetic insights, allowing the study of larger fields of view, thicker samples, and faster processes.

This presentation will introduce the InCAEM project and highlight the opportunities it offers to the scientific user community. We will focus on showcasing new STEM capabilities being installed at the Joint Electron Microscopy Center at ALBA (JEMCA), including a double-aberration-corrected STEM and *in situ* S/TEM holder systems with the ability to operate in gas or liquid environments. We will also present the progress in the adaptations being developed for various ALBA beamlines, enabling electron and X-ray microscopy and spectroscopy correlative workflows.

Acknowledgments: InCAEM is part of the Advanced Materials programme within the Planes Complementarios programme, launched and funded by the Ministry of Science and Innovation (MCIN) with the support of NextGeneration EU funds (PRTR-C17.I1) and by Generalitat de Catalunya.

Type of presentation: Poster

IM7-P-2 Ecosystemic Transformation of Water Mining – RE-VESTIC INSPIRE PepePolymers®

Pepe Betancort[a], José Antonio Da Silva[b]

[a]*Global3CCS*

[b]*Avesar*

Contact email: pepe.betancort@global3ccs.com

This paper presents a real-world product certification system developed in the Canary Islands (an EU outermost region), designed to transform brine from desalination into traceable, value-added product systems. The approach is based on the in-situ application and certification of polymeric materials under real conditions, enabled by connected sensors and remote-control tools such as Graco OnSite®.

Methods

The ECODESIGN3CCS® system integrates human-led supervision with modular hardware and software to monitor and validate the structural, thermal, and environmental performance of polymer-based coatings and reinforcements. Data collection is automated yet fully traceable, incorporating product application, workforce training, and lifecycle assessment into a single operable platform.

Results

Validated through several pilot deployments—including a technical assistance proposal for McAllen, Texas—the system proved adaptable to extreme conditions and promising for integration into local green economies. Certified operators, primarily women, formed reliable field teams responsible for executing and verifying every stage of the application process.

Audiovisual demonstrations of ECODESIGN3CCS® in real-world scenarios are available at:
• https://www.youtube.com/watch?v=FJQ17_plNIY
• https://youtu.be/ESNHbBqH0qc?si=CljgFpi3HMGzoNnD

Discussion and Conclusions

Beyond its technical reliability, ECODESIGN3CCS® introduces a new paradigm: certification as a territorial, human-driven infrastructure. By shifting scientific verification from laboratory conditions to real operational environments, the system broadens the scope of interoperability in line with the goals of the IMPRESS Special Session.

Our recent Non-Disclosure Agreement (NDA) with the Arenales Neighborhood and Solidarity Association (AVESAR) strengthens this localized approach. It empowers families and community agents to actively participate in product validation and environmental data collection processes. This neighborhood pact enhances the social component of our system while enabling a more just and inclusive implementation of the Digital Product Passport in vulnerable urban areas, proving that traceability can also serve as a tool for urban equity.

Type of presentation: Poster

IM7-P-3 Novel Nano Channel Chip for In Situ TEM Liquid Cell Analysis and Particle Trapping Without Manual Preassembly of Chip

Mervan Ramadan[a], Emil Christian Stillhoff Jensen[a], Niccolò Bottauscio[a], Murat Nulati Yesibolati[b]

[a]*Insight Chips ApS, (Kongens Lyngby), Denmark*

[b]*Technical University of Denmark (DTU), (Kongens Lyngby), Denmark*

Contact email: mervan@insightchips.com

Liquid cell transmission electron microscopy (TEM) enables the characterization of liquid samples and suspended nanoparticles, offering insights into dynamic processes at the nanoscale. However, traditional liquid cells require manual preassembly, which can be time-consuming and is always prone to variability in the liquid thickness and bulging. We present the Nano Channel Chip, developed by Insight Chips, a novel liquid cell that eliminates manual preassembly while providing precise control over liquid thickness and effective particle trapping for enhanced in situ TEM analysis. The liquid thickness can be chosen depending on the sample and experimental requirements, allowing for reproducible in situ liquid TEM characterisation.

The Nano Channel Chip, produced by Insight Chips ApS, features user-selectable nanochannels with a depth of 125 nm and a trap region where the liquid thickness is 10 nm to capture nanoparticles during in situ flow. Polystyrene particles (30 nm) and silver nanoplates (70 nm) were used as test samples. The samples were introduced using a TEM flow holder (Insight Chips ApS) connected to a syringe and a collecting reservoir. The syringe was manually pressed to flow samples through the Nano Channel Chip, with particles trapped at the height-step trap while liquid continued through the Nanochannels and a bypass to the holder outlet. Imaging was performed at DTU Nanolab using a Tecnai 20 TEM equipped with a TVIPS 4K camera.

The Nano Channel Chip successfully trapped 30 nm polystyrene particles and 70 nm silver nanoplates in the TEM's Field of View (FOV) in front of the 10 nm trap region during continuous liquid flow. The bypass system allowed safe in situ flow without disrupting the imaging process, demonstrating the chip's reliability for dynamic experiments.

The Nano Channel Chip offers significant advantages over traditional liquid cells by eliminating manual preassembly and providing precise, reproducible liquid thickness control via nanochannels. The integrated trap design enhances the ability to capture and study nanoparticles in situ in the FOV, making it a powerful tool for high-resolution TEM studies and statistical analysis of nanoparticles. Future work will focus on exploring applications with a broader range of nanomaterials and liquid dynamics. This innovation has the potential to streamline liquid-phase TEM workflows and advance the study of dynamic nanoscale processes.

We acknowledge DTU Nanolab for providing access to the Tecnai 20 TEM and technical support.

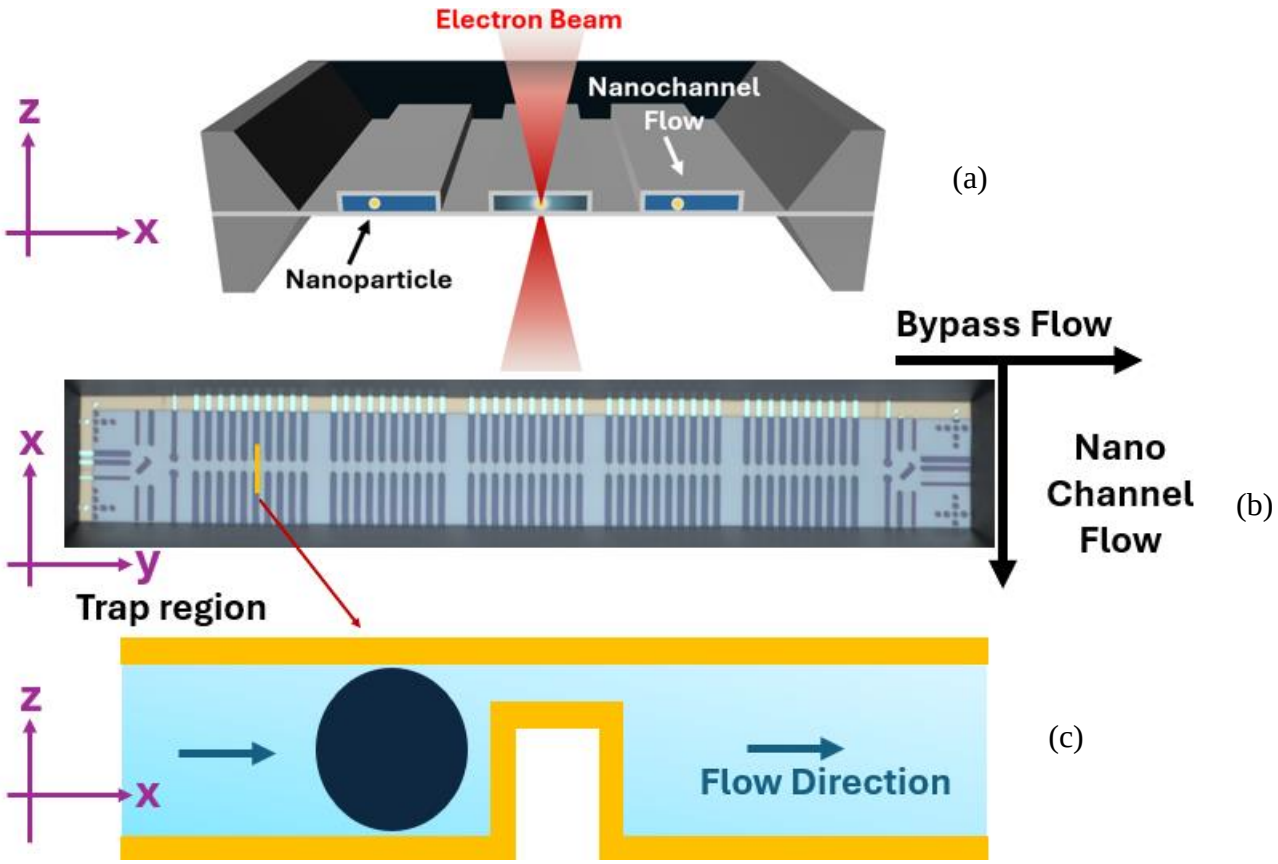


Figure 1: Illustration of the Nano Channel Chip. Illustration of Nanochannels exposed to electron beam (a), Optical image of the Nanochannels that are in the in FOV of the TEM (b), Sketch of Trap region of the Nanochannels illustrating the trapping mechanism (c).

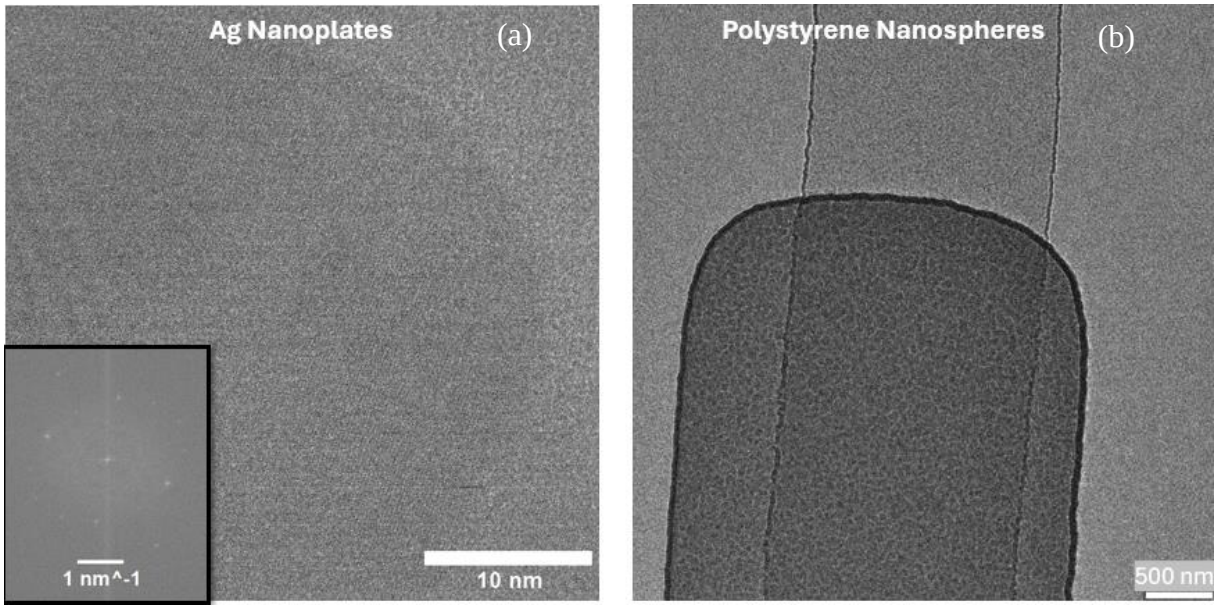


Figure 2: TEM images of trapped particels. 70 nm Ag nanoplate (from NanoCompsix) imaged with atomic rows shown together with the FFT (a), 30 nm Polystyrene nanospheres (from Sigma-Aldrich) trapped and imaged (b).

Type of presentation: Poster

IM7-P-4 Characterization of Carbon Black Produced via Methane Pyrolysis Using Environmental TEM

Lukas Weidler[a]

[a]*Energy Engineering, Division of Energy Science, Luleå University of Technology, (Luleå), Sweden)*

Contact email: lukas.weidler@ltu.se

Introduction: Carbon black plays a crucial role in applications ranging from rubber reinforcement—74 % of the carbon black produced is used in the tire industry[1]—to energy storage. It is a bulk chemical typically produced from fossil raw materials. In this work, Carbon Black (CB) produced via Methane Pyrolysis (MP) at different production temperatures, a potentially more sustainable source, is investigated. However, the oxidation behaviour of MP-CB at the nanoscale remains largely unknown. Environmental Transmission Electron Microscopy (ETEM) is employed to characterize MP-CB and compare its behaviour with that of industrial carbon black.

Methods: MP-CB was produced by RISE ETC in Piteå, Sweden, using a lab-scale drop tube furnace reactor. ETEM experiments were conducted with a Hitachi HF3300S microscope (located in Lund, Sweden; operating at 300 kV), equipped with gas injection and heating capabilities. MP-CB samples were deposited on MEMS-based heating chips and exposed to an oxygen atmosphere (approximately 1 Pa) at temperatures up to 1000 °C. Two experimental procedures were carried out: (1) static imaging during controlled oxidation pauses, followed by video recording at a constant temperature; and (2) video recording during continuous heating (30 °C/min). The resulting image sequences were optimized using Python scripts and analysed to track structural changes and the overall dynamics of the oxidation process.

Results: Videos from experimental procedure (2), recorded at a magnification of 100 kx, provided an overview of the oxidation behaviour of MP-CB between 500 °C and 1000 °C. The MP-CB samples, produced at temperatures ranging from 1200 °C to 1700 °C, exhibited a trend of increasing reactivity with higher production temperatures. However, samples produced closer to 1700 °C deviated from this trend, showing reduced reactivity despite the higher production temperature. Experimental procedure (1) revealed four distinct combustion modes observable under the microscope: (i) surface burning, (ii) internal burning, (iii) particle fragmentation, and (iv) foam-mode. The first two modes were most prominently visible.

Discussion: These results provide direct insights into the oxidation mechanisms of MP-CB and demonstrate the effectiveness of ETEM in visualizing dynamic processes at the nanoscale under reactive conditions. The findings contribute to a deeper understanding of the thermal stability of carbon materials, which is critical for high-temperature applications. Furthermore, the results highlight that the manufacturing temperature significantly influences the stability of MP-CB, leading to variations in its properties. Future work will focus on correlating these in situ observations with macroscopic Thermogravimetric Analysis (TGA) data and exploring the effects of different production temperatures and atmospheric compositions. The long-term goal is to tailor MP-CB properties to match those of conventionally manufactured industrial CB, using self-produced samples.

Acknowledgements: This work was supported by RISE Research Institutes of Sweden for sample production, with special thanks to Henrik Wiinikka. The ETEM experiments were made possible with the support of the microscopy team at Lund University, Sweden, including Daniel Madsen, David Wahlqvist, and Martin Ek.

References:

1. The Impact of Sustainability on Carbon Black to 2044 [Internet]. [cited 2025 Jul 29]. Available from: https://www.smithers.com/services/market-reports/materials/the-future-of-carbon-black-to-2023?utm_source=chatgpt.com

IM8 Machine learning and data analysis in microscopy: advances and open-source solutions

Type of presentation: Invited

IM8-IN-1 Convolutional neural networks for scanning transmission electron microscopy image analysis: Towards automated analysis of large volume datasets

Diana Propst[a,b], Wael Joudi[a,b], Manuel Längle[a], E. Harriet Åhlgren[a,c], Jacob Madsen[a], Clara Kofler[a,b], Barbara M. Mayer[a], David Lamprecht[a,d], Gerlinde Habler[e], Clemens Mangler[a], Viera Skakalova[a,f], Lado Filipovic[d], Toma Susi[a], Jani Kotakoski[a]

[a]*University of Vienna, Faculty of Physics, Austria*

[b]*University of Vienna, Vienna Doctoral School in Physics, Austria*

[c]*University of Helsinki, Physics Department, Finland*

[d]*Technical University of Vienna, Institute for Microelectronics, Austria*

[e]*University of Vienna, Department of Lithospheric Research, Austria*

[f]*Slovak Academy of Sciences, Institute of Electrical*

Contact email: diana.propst@univie.ac.at

The use of convolutional neural networks has become prevalent in recent years, with the emergence of new open source tools and decrease in their computational cost. For microscopy imaging, traditionally the analysis of recorded data has been performed either manually or with the help of various algorithms, such as the commonly used thresholding and Fourier transforms. Neural network methods provide here a new attractive alternative, offering the advantage of not needing to know in advance how to formulate an algorithm to discern specific features in an image. In the case of scanning transmission electron microscopy, atomic resolution imaging enables the investigation of material features on the smallest scale. However, this requires high volumes of data to make a reliable statement on the statistical distribution of these features throughout the sample. Thus, a research objective in this field can easily demand up to thousands of images. With such a large dataset, one often encounters the following situation: The data has been recorded under varying conditions leading to image-to-image variations within the recorded data. Therefore, not only does the analysis have to address the sheer number of resulting images, often making manual methods impossible, it also needs to be robust against the aforementioned variations, making algorithmic methods tedious. In this presentation, approaches to overcome this challenge using convolutional neural networks to automate the workflow will be illustrated on two examples: impurity atoms in doped diamond and defect-engineered single-layer hexagonal boron nitride and graphene, using atomically resolved annular dark field scanning transmission electron microscopy images. Besides demonstrating the advantages of this method that enables novel, efficient approaches to image analysis, the scope of its applicability and remaining challenges will also be discussed.

Type of presentation: Oral

IM8-O-1 *ViFoSe*, an user-friendly open-source post-processing tool for foreground segmentation in time-lapse videos.

Filippo Piccinini[a,b], Abdelaziz Mohamed Abdelrahman[c], Luca Rinaldi[c], Michele Sarneri[c], Jae-Chul Pyun[d], Misu Lee[e,f], Bongseop Kwak[g], Bosung Ku[h], Nicola Normanno[a], Gastone Castellani[b,i]

[a] *IRCCS Istituto Romagnolo per lo Studio dei Tumori (IRST) "Dino Amadori", Meldola (FC), Italy.*

[b] *Department of Medical and Surgical Sciences (DIMEC), University of Bologna, Bologna, Italy.*

[c] *Department of Electrical, Electronic, and Information Engineering "Guglielmo Marconi", University of Bologna, Cesena (FC), Italy.*

[d] *Department of Materials Science and Engineering, Yonsei University, Seoul, Republic of Korea.*

[e] *Division of Life Sciences, College of Life Science and Bioengineering, Incheon National University, Incheon, Republic of Korea.*

[f] *Institute for New Drug Development, College of Life Science and Bioengineering, Incheon National University, Incheon, Republic of Korea.*

[g] *College of Medicine, Dongguk University, Goyangsi, Gyeonggi-do, Republic of Korea.*

[h] *Central R&D Center, Medical and Bio Decision (MBD) Co., Ltd., Suwon, Republic of Korea.*

[i] *IRCCS Azienda Ospedaliero-Universitaria di Bologna S.Orsola, Bologna, Italy.*

Contact email: filippo.piccinini@irst.emr.it; f.piccinini@unibo.it.

Introduction: Time-lapse videos are commonly acquired in microscopy and outdoor imaging to study the behaviour of objects of interest (OOIs) under different stimuli. However, in most cases, the relevant information pertains only to the OOIs, considered as the foreground (FG, e.g. moving cells), while the background (BG, e.g. an inorganic scaffold) is often irrelevant. Several algorithms have been proposed in the literature for FG segmentation in 2D images [1]. Additionally, with the recent proliferation of tools designed to facilitate remote meetings (e.g., Microsoft Teams, Zoom, Google Meet, Skype, etc.), FG segmentation algorithms have also gained popularity in video applications. Today, a wide range of algorithms is available, spanning from post-processing to real-time solutions, accommodating dynamic/static cameras and/or BG, and catering to both general and case-specific scenarios [2]. However, no freely available tool allows users to test different automatic solutions while also providing manual corrections for missed detections or false inclusions. Essentially, a freely available, comprehensive solution for FG segmentation across all possible scenarios is still lacking. In this work, we propose *Video Foreground Segmentation* (*ViFoSe*), a user-friendly, open-source, post-processing tool for FG segmentation in time-lapse videos (**Figure 1**). *ViFoSe* is developed in *MATLAB* (The MathWorks, Inc., MA, USA) and it has a very intuitive graphical user interface (GUI). It includes several automatic algorithms, but its key feature is the set of options provided for easily correcting missed or incorrect detections.

Methods: First, we conducted a review analysis of the algorithms described in the scientific literature and the tools developed for major operating systems (e.g., *Windows*, *macOS*, *Android*) to understand the limitations and opportunities of the available solutions. Then, videos under controlled conditions were acquired using two different cameras to create a representative dataset for testbed. Specifically, we began by considering common real-world scenarios with a static camera and static BK, including: (*a*) a single OOI always visible; (*b*) multiple OOIs always visible; (*c*) a single OOI not always visible; (*d*) multiple OOIs not always visible. Then, the analysis has been extended to all possible variations involving a dynamic camera and/or dynamic BK.

Results: The experiments conducted demonstrate *ViFoSe*'s ability to correctly segment OOIs, even when they cross each other or are partially hidden behind BG elements, in cases with a static camera and static BK (**Figure 2**). Thanks to the implementation of SURF, gradient correlation, and phase

correlation algorithms [3], *ViFoSe* can also segment FG in videos acquired with a slightly dynamic camera. In these cases, the videos are first stabilized aligning the single frames [4], and then the common part across all frames is cropped and processed using the same algorithms designed for videos acquired with static cameras. However, poor results were obtained when analysing videos with a dynamic BG (e.g., moving cells in hydrogels with debris or outdoor videos recorded in windy conditions).

Discussion and conclusions: In this work, we presented *ViFoSe*, a user-friendly, open-source, post-processing tool for FG segmentation in time-lapse videos. The experiments conducted demonstrated its ability to segment FG in various scenarios, except in cases with dynamic BG. As future work, we aim to extend *ViFoSe*'s capabilities to real-time applications. The *MATLAB* source code, standalone applications for *Windows*, *macOS*, and *Linux*, user documentation, video tutorial, and the extensive testbed dataset are available upon request.

Acknowledgments: F.P. and G.C. acknowledge the support received from the MAECI Science and Technology Cooperation Italy–South Korea Grant Years 2023–2025 by the Italian Ministry of Foreign Affairs and International Cooperation (CUP project: J53C23000300003); J.-C.P. and M.L. from the National Research Foundation (Funding No.: 2022K1A3A1A25081295); N.N. from the Italian Ministry of Health and the contribution of "Ricerca Corrente" within the research line "Appropriateness, outcomes, drug value and organisational models for the continuity of diagnostic therapeutic pathways in oncology"**.**



Figure 1: *ViFoSe'*s main GUI includes three panels: one for visualizing the input original video, one for the binary (e.g., black and white) foreground masks, and one for the output rendered video.

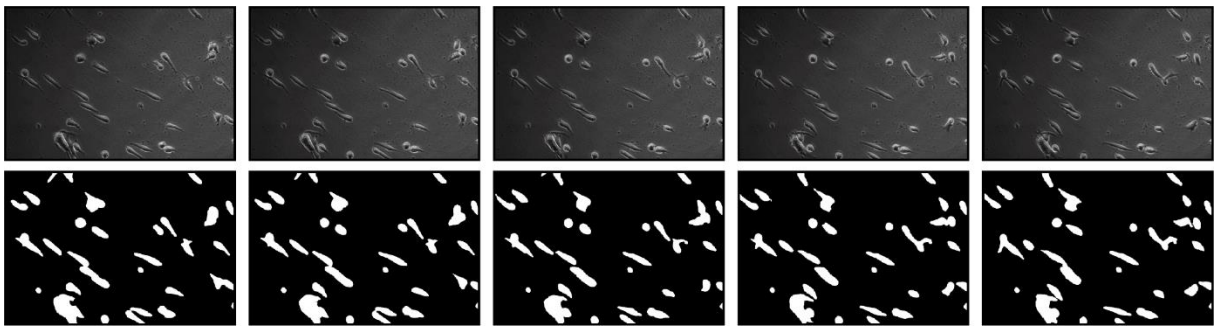


Figure 2: Foreground segmentation. First row: Randomly selected frames from an input video acquired with a brightfield widefield microscope. Second row: Corresponding foreground masks obtained.

References:

1. A. Archit, *et al*. Segment Anything For Microscopy. *Nature Methods*. **2025**, 1-13.
2. T. Vicar, *et al*. Cell Segmentation Methods For Label-Free Contrast Microscopy: Review And Comprehensive Comparison. *BMC Bioinformatics*. **2019**, 20, 1-25.
3. F. Piccinini, *et al*. Automated Image Mosaics By Non-Automated Light Microscopes: The MicroMos Software Tool. *Journal of Microscopy*. **2013**, 252(3), 226-250.
4. F. Piccinini, *et al*. Data Science for Health Image Alignment: A User-Friendly Open-Source ImageJ/Fiji Plugin for Aligning Multimodality/Immunohistochemistry/Immunofluorescence 2D Microscopy Images. *Sensors*. **2024**, 24(2), 451.

Type of presentation: Oral

IM8-O-2 Optimization of SEM Instrumental Parameters for Enhanced Imaging Applying Machine Learning

Behnaz Abbasgholi-NA[a], Marco Prenassi[b], Emanuele Panizon[b], Tommaso Rodani[b], Simone Dal Zilio[a]

[a]*Istituto Officina dei Materiali CNR-IOM (Trieste), Italy*

[b]*AREA Science Park (Trieste), Italy*

Contact email: asbaghi@iom.cnr.it

The scanning electron microscope (SEM) is one of the most versatile instruments available for characterizing the micro- and nanostructural properties of solid samples. A major reason is the high resolution that can be achieved when examining bulk objects which makes SEM indispensable in various fields ranging from materials science to biology.

Although scanning electron microscopy (SEM) is a well-established technology, there is still room for improvement in both imaging quality and automation. The goal is to achieve an optimal balance between ease of use and performance while minimizing hardware complexity and instrumentation costs, which remain a key advantage of SEM. In this context, the implementation of advanced algorithmic methods for automating acquisition settings is essential to enhance efficiency and reproducibility in analyses. Given the versatility of SEM and its application to a wide range of materials and samples, we have developed a generalized approach that is not limited to a specific sample type, maximizing adaptability and effectiveness across various experimental settings. Instrumental SEM parameters should be carefully optimized for high-quality SEM imaging. The key parameters that influence image quality can be recognized as: Electron beam parameters including acceleration voltage, beam current, and spot size; Geometrical and imaging parameters, which encompass working distance, aperture size, magnification, focus, and stigmation. Detection and image acquisition settings cover detector type, scan speed (dwell time), and drift correction. Sample preparation and environmental conditions include sample coating and chamber pressure.

Optimization of the acquisition parameters is crucial for obtaining high-quality images and accurate data. Operator-based adjusting of these parameters presents several challenges, including the interdependence of settings, the risk of sample damage, time-consuming operations, and operator skill dependencies. Moreover, the sample dependency of the acquisition parameters becomes crucial due to the wide range of possible applications of SEM characterization. These difficulties underscore the importance of automation in optimizing operations of SEM settings, making the process more efficient, consistent, and less prone to error. We developed an algorithm-based approach that can identify the optimum conditions for accelerating voltage, working distance, and aperture size for each type of sample.
SEM experiments on target sample are conducted based on a full-factorial design in which parameters are varied simultaneously, to explore also the cross-correlation of the considered parameters. To assess image quality, we needed a suitable metric. Since the reference image—obtained under optimum conditions—served as the goal of our investigation, we chose a no-reference image quality metric. The acquired images were analyzed using this metric. A polynomial regression model—a type of supervised learning—was employed as a baseline to determine the optimal operating conditions within the selected SEM parameter space. By predicting the no-reference image quality metric for any given setting, the model guides the identification of parameter adjustments that minimize NIQE (thus maximizing image quality). Given the small training set, at each new image acquisition, the predicted NIQE is compared with the computed value, and the model is updated with every new data point, continuously refining its predictions and enabling fully autonomous optimization while significantly reducing operator intervention. This approach not only streamlines the SEM imaging process but also significantly reduces

the time required for each imaging session by automating the optimization of key parameters. The proposed algorithm promises to enhance the efficiency of SEM operations, minimize operator intervention, and ensure more consistent, accurate, and faster sample characterization across a wide range of applications.

References:

1. Goldstein, J. I., Newbury, D. E., Michael, J. R., Ritchie, N. W., Scott, J. H. J., & Joy, D. C. (2017). *Scanning electron microscopy and X-ray microanalysis*. springer.
2. Mittal, A., Soundararajan, R., Bovik, A. C. *IEEE Signal Processing Letters* **2013**, 22(3): 209–212.
3. Cho, Y. Cho, J. Park, J. Wang, J. Jeong, S. Lee, J. Hwang, Y. Kim, J. Yu, J. Chung, H. Park, H. *Communications Engineering* **2024**, 3(1):82.

Type of presentation: Oral

IM8-O-3 Mitigating beam damage during FIB-SIMS imaging: a new methodology using alternative FIB scans

Andrés Miranda Martínez[a], Olivier De Castro[a], Sayantan Sharma[a,b], Olivier Bouton[a], Tom Wirtz[a], Santhana Eswara[a]

[a]*Advanced Instrumentation for Nano-Analytics (AINA), Luxembourg Institute of Science and Technology (LIST), Belvaux, Luxembourg*

[b]*University of Luxembourg, 2 Avenue de l'Université, Esch-sur-Alzette L-4365, Luxembourg*

Contact email: sayantan.sharma@list.lu

Secondary ion mass spectrometry (SIMS) is a surface analysis technique that identifies characteristic secondary ions generated when a sample is bombarded by a primary ion beam. This technique can detect all elements in the periodic table including hydrogen and lithium. It offers excellent sensitivity, high dynamic range and even isotope selectivity. As a result, SIMS is widely utilized for chemical analysis across various fields of materials research.

In this context, our group at Luxembourg Institute of Science and Technology has developed various focused ion beam (FIB)-SIMS instruments over the years by incorporating magnetic sector-based SIMS systems on different FIB platforms [1-3]. The integration of SIMS capabilities into FIB instruments offers several advantages, including high-resolution chemical imaging and direct correlation of SIMS data with other imaging or analytical techniques within the same instrument such as secondary electron (SE), back-scattered electron imaging or energy dispersive X-ray spectroscopy. However, the resolution in FIB-SIMS imaging is constrained by beam damage and shot noise. Beam damage leads to structural alterations of the samples, while shot noise affects the signal-to-noise ratio (SNR), introducing artifacts in the image [4]. To overcome these limitations while ensuring high-resolution imaging, new scanning techniques can be explored.

In this contribution, we present the development of a novel methodology that addresses these challenges by minimizing the ion dose delivered to the sample through use of alternative illumination and acquisition protocols. The implementation of this method was carried out on a high-vacuum dual beam FIB-scanning electron microscope (SEM) instrument consisting of an electron beam column, a gallium liquid metal ion source-based FIB column and equipped with a magnetic sector SIMS system [3]. A custom-built acquisition system, controlled by an acquisition card, was used here to manage FIB control and data acquisition through a LabVIEW program. Additionally, Python algorithms were used for determining the specific locations to be scanned, optimizing the acquisition process.

As a demonstration of our alternative scanning methodology, SIMS images were obtained from a FeTi alloy sample using different scan patterns. The secondary ion images of the titanium isotopes obtained using different scan patterns are shown in Figure.1. Furthermore, as mentioned in the previous section, a Python based adaptive sampling technique was also implemented. This technique uses a fast, low-dwell-time scan followed by a targeted high-dwell-time scan on selected pixels, identified using dedicated Python scripts [5]. This combined approach significantly reduces acquisition time and dose while improving the SNR in the resulting image.

The developed methodology enables high resolution imaging with lower beam dose and increased acquisition speed. This can significantly enhance use of FIB-SIMS for investigation of beam sensitive samples such as biological or organic samples and 2D materials, or to capture transient events.

The authors acknowledge funding from the European Union's Horizon Europe research and innovation program under Grant Agreement No. 101104032 (OPINCHARGE).

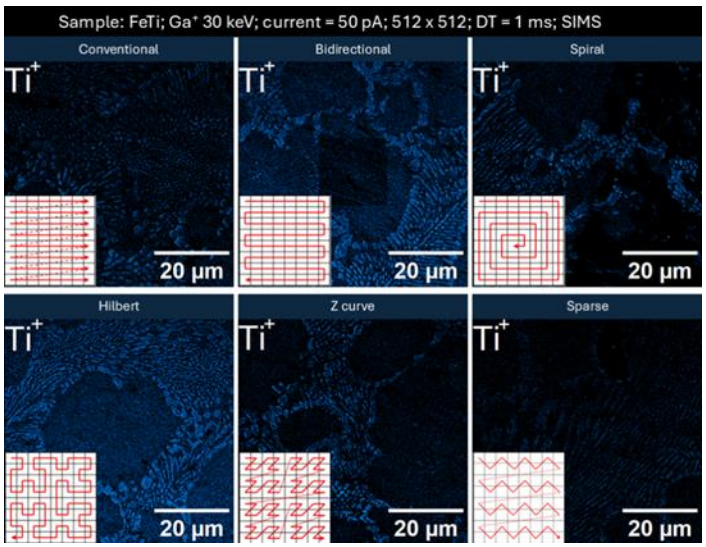


Figure 1: Example of SIMS images (ΣTi isotopes) obtained with different scan patterns from a FeTi sample

References:

1. J.-N. Audinot et al., Reports on Progress in Physics 84 (2021)
2. O. De Castro et al., Analytical Chemistry 93 (2021)
3. O. De Castro et al., Analytical Chemistry 94 (2022)
4. D. Nicholls et al., Ultramicroscopy 233 (2021)
5. T. Dahmen et al., Microscopy and Microanalysis, 25 S1 (2019)

Type of presentation: Oral

IM8-O-4 Automated Thickness Determination from 4D-STEM Data by CNNs

Michael Oberaigner[a], Alexander Clausen[b], Dieter Weber[b], Gerald Kothleitner[a,c], Rafal E. Dunin-Borkowski[b], and Daniel Knez[c]

[a]*Graz Centre for Electron Microscopy, Graz, Austria*

[b]*Ernst Ruska-Centre for Microscopy and Spectroscopy with Electrons, Forschungszentrum Jülich, Jülich, Germany*

[c]*Institute of Electron Microscopy and Nanoanalysis, University of Technology, Graz, Austria*

Contact email: michael.oberaigner@felmi-zfe.at; daniel.knez@felmi-zfe.at

Introduction

Determining sample thickness along the beam direction is critical for many TEM characterization techniques. The position averaged convergent beam electron diffraction method (PACBED) has proven to be a very precise thickness determination for thin specimens. Nevertheless, the required visual inspection of experimental PACBED patterns with simulations is error prone, subjective and time consuming. Although, Xu and LeBeau [1] have shown the automatization of this process by convolutional neural networks (CNN), the high computational cost and the required knowledge about machine learning or multislice modelling can prevent the usage of this technique for the broader community. To address these challenges, we have developed a prototype for a server-based approach to simulate PACBEDs, train CNNs and predict sample thicknesses. This prototype incorporates pre-trained models that can be accessed by the user via a web service directly from the data acquisition and analysis software.

Methods

The prototype performs the following three steps to analyse PACBEDs [2]:

1. Simulation: A training dataset of PACBEDs is generated by multislice simulations. The user is required to input a CIF-file and a parameter space, including a high tension, and ranges of convergence angle, mistilt and thickness. The final model is only valid within these boundaries.
2. Training: The CNN models consist of a pre-trained Xception model, as feature extractor and fully connected layers for classification. The simulated dataset is used to train CNN models for predicting the scale (size of the PACBEDs), mistilt and thickness.
3. Prediction: The training dataset and the trained models are stored in the database and can be accessed through any Python-capable device. The server returns the thickness and mistilt prediction including a validation plot to compare the estimated PACBED with the measured PACBED.

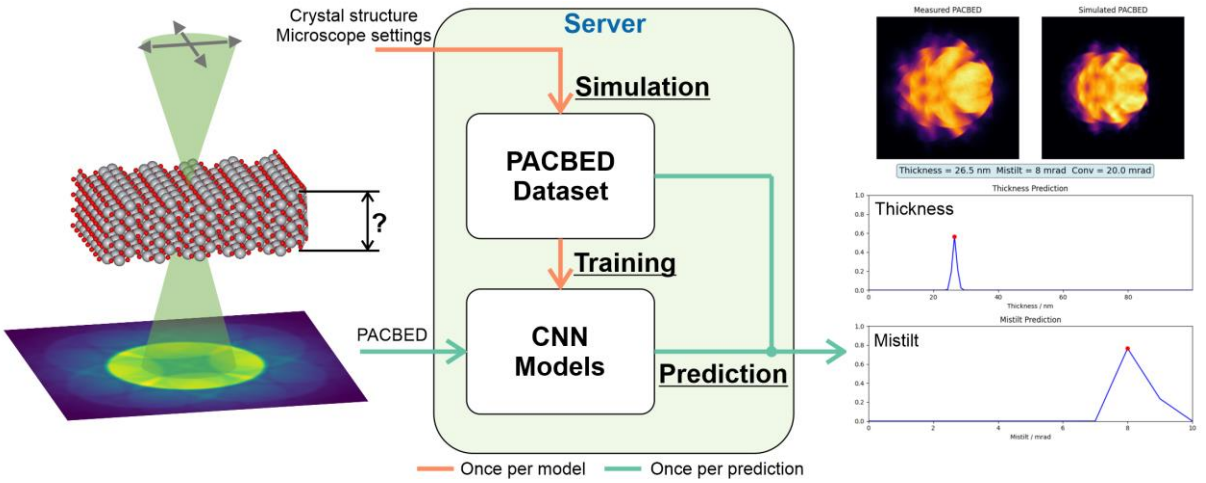


Figure 2: Server-based prototype for predicting the thickness and mistilt by analysing PACBEDs with CNNs including a validation plot as feedback.

Results

Whilst the prototype is not currently accessible via the internet, it is already proving useful for applications within a local network, as it allows thickness determination during a microscope session. Furthermore, given its capacity to predict hundreds of patterns within a minute, thickness and mistilt maps can be generated from 4D-STEM data. For instance, Figure 2 presents thickness and mistilt maps derived from a beryl experiment.

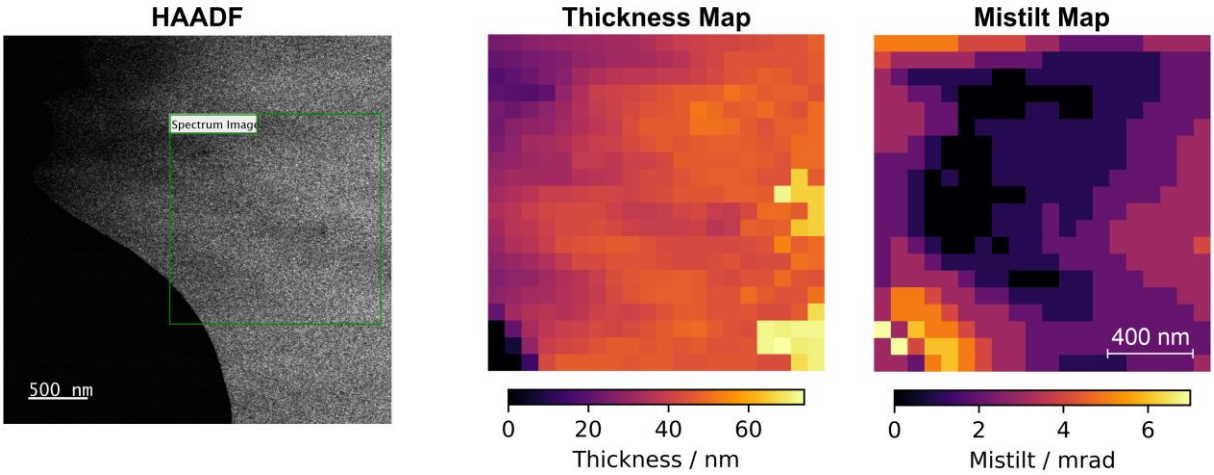


Figure 2: Generation of a thickness and mistilt map from a 4D-STEM dataset of beryl at high tension of 300 kV and convergence angle of 7 mrad.

Discussion and conclusions

Before this prototype will go online, security aspects have to be considered, for example per-user limits, especially for training and simulation. While the prototype returns a validation plot to compare the predicted PACBED with the experimental PACBED, a more sophisticated solution for mispredictions has to be implemented. Nevertheless, the efficiency of this approach not only enhances accessibility but also enables the rapid generation of large-scale thickness maps, significantly expanding the capabilities of PACBED-based analysis in STEM.

Acknowledgments

We acknowledge funding from the European Union under grant no. 101094299 (IMPRESS) and FWF under grant no. I4309-N36.

References:

[1] W. Xu and J. M. LeBeau, *Ultramicroscopy*. **2018**, 188, 59–69

[2] M. Oberaigner et al., *Microscopy and Microanalysis*. **2023**, 29, 427–436

Type of presentation: Oral

IM8-O-5 Enhanced Low-Loss EELS Analysis through Hybrid Unsupervised and Supervised Machine Learning

Vanessa Costa-Ledesma[a], Daniel del-Pozo-Bueno[a], Catalina Coll[b], Josep Nogués[b,c], Borja Sepúlveda[d], Laura Bocher[e], Mathieu Kociak[e], Javier Blanco-Portals[a], Francesca Peiró[a,c], Sònia Estradé[a]

[a]*LENS-MIND, Department of Electronics and Biomedical Engineering and Institute of Nanoscience and Nanotechnology (IN2UB), University of Barcelona (UB), Barcelona, Spain*

[b]*Catalan Institute of Nanoscience and Nanotechnology (ICN2), CSIC and BIST, Campus UAB, Bellaterra, Barcelona, Spain*

[c]*Catalan Institution for Research and Advanced Studies, ICREA Academia, Barcelona, Spain*

[d]*Instituto de Microelectrónica de Barcelona (IMB-CNM, CSIC), Bellaterra, Barcelona, Spain*

[e]*Laboratoire de Physique des Solides (LSP), Microscopie électronique STEM, Orsay, France*

Contact email: vcostale7@ub.edu

Spatially-resolved electron energy loss spectroscopy (EELS) in scanning transmission electron microscopy (STEM) is a powerful tool for nanoscale characterization of optical, electronic, and structural properties. However, analysing low-loss EELS signals, crucial for understanding nanophotonic resonances, remains challenging due to overlapping resonances, proximity to the intense zero-loss peak, and poor signal-to-noise ratios. Here, we propose a highly efficient machine learning approach combining dimensionality reduction with unsupervised and supervised algorithms to enhance the extraction and interpretation of spatially localized spectral features in low-loss EELS data. Applied to silicon/gold hybrid nanopillars, our methodology accurately identified and mapped complex plasmonic, Mie, and hybrid resonances, closely matching results from finite-difference time-domain (FDTD) simulations. This robust and versatile approach significantly simplifies low-loss EELS data analysis, paving the way for advanced characterization of complex nanostructured materials.

Introduction

Spatially-resolved electron energy loss spectroscopy (EELS) within a scanning transmission electron microscope (STEM) offers high-resolution insights into optical, electronic, and structural characteristics at the nanoscale. Despite significant advancements, interpreting low-loss EELS signals remains challenging due to overlapping resonances, proximity to the zero-loss peak, and inherently low signal-to-noise ratios. In this work, we propose and validate a hybrid unsupervised-supervised machine learning (ML) methodology aimed at enhancing analysis and spatial classification of low-loss EELS data, demonstrating its effectiveness through nanophotonic resonance mapping.

Methods

EELS-STEM measurements were performed on silicon/gold (Si/Au) nanopillars fabricated via colloidal lithography, composed of a silicon pillar (200 nm diameter, 2 μm length) capped with an Au nanodisc (75 nm thickness). Spectral images were acquired using a monochromated NION HERMES STEM (60 keV, 15-25 meV energy resolution, 10 ms per pixel). The proposed ML methodology involves dimensionality reduction and clustering combined with a supervised algorithm. Results were cross-validated through finite-difference time-domain (FDTD) simulations.

Results

Applying the proposed ML strategy allowed efficient denoising, identification, and automated spatial classification of complex low-loss EELS spectra. The method successfully identified plasmonic, hybrid, and dielectric (Mie) resonances, accurately mapping their spatial distribution across the nanopillars. The experimental results exhibited strong agreement with FDTD simulations, confirming the ability of the method to separate closely overlapping resonance modes and correctly classify them spatially.

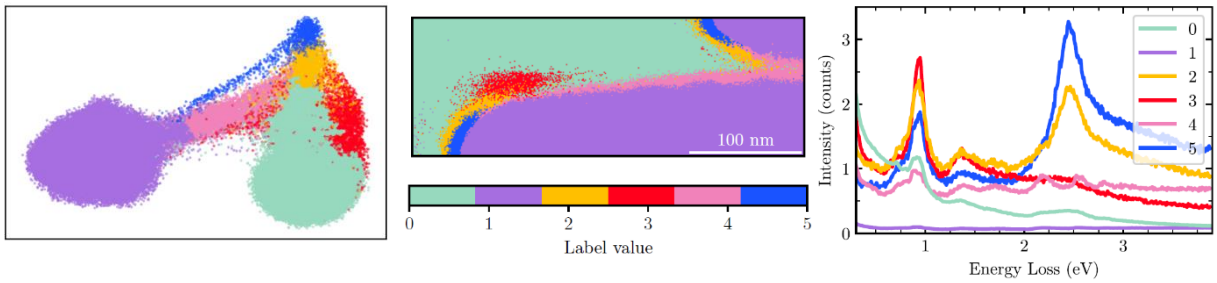
Discussion and Conclusions

The developed ML-based method demonstrates remarkable robustness and precision in handling complex EELS datasets. It significantly improves the interpretability of low-loss EELS spectra, accurately extracting detailed spatial resonance maps. The simplicity, automation, and effectiveness of this approach offer substantial advantages over conventional analytical strategies, thereby greatly facilitating the study of advanced nanophotonic systems. Future work will extend this methodology to other types of collective excitations and nanostructured systems, further exploring its versatility and broader applicability.

Acknowledgments

This work has been supported by Spanish Project PDC2021-121366-I00 (MCIN/AEI/10.13039/501100011033, EU NextGenerationEU/PRTR), PID2022-138543NB-C21, PID2022-138588OB-C31 and PID2022-138588OB-C32 (MCIU/AEI), Generalitat de Catalunya (2021SGR00242, 2021SGR00651), ELECMI - ICTS Electron Microscopy for Materials Science and ESTEEM3 programs. F.P. acknowledges ICREA Academia funding. B.S. acknowledges María de Maeztu Grant CEX2023-001397-M (MICIN/AEI). ICN2 is supported by CERCA and Severo Ochoa Excellence programs (CEX2021-001214-S).

The references are marked with square brackets, with the sequential reference number – [1] and referred at the end of the document.



References:

[1] J. Blanco-Portals, F. Peiró, S. Estradé, Microsc. Microanal. 28 (2022), 109–122.

[2] J. Nelayah, M. Kociak, O. Stephan, F. J. García de Abajo, M. Tencé, L. Henrard, D. Taverna, I. Pastoriza-Santos, L. M. Liz-Marzán, C. Colliex, Nat. Phys. 3 (2007), 348–353.

[3] V. Flauraud, D. T. Alexander, O. J. F. Martin, J. Brugger, ACS Nano 11 (2017), 3485–3495.

Type of presentation: Poster

IM8-P-1 Dimensional calibration of high resolution instrumentation at nanoscale

Ingo Busch[a], Peer Barlen, Lars Daul[a], Michelle Fernandez Scarioni

[a]Physikalisch-Technische Bundesanstalt, Braunschweig, Germany

Contact email: Ingo.Busch@ptb.de

Introduction

An accurate calibration of high resolution microscopes, such as scanning probe microscopes (SPM) or electron microscopes, is a fundamental requirement for a appropriate scientific application providing reliable measurement data [1]. Only with a careful and reliable calibration with traceability to the International System of Units (SI), necessary quality ratings, comparability and international exchange of data can be achieved. Hence, the calibration process is crucial to scientific workflow and quality management in industrial processes[2].

However, it is concerning that a significant proportion of instruments utilised in nanotechnology applications are either uncalibrated or possess incorrect or incomplete calibration. A survey of SPM revealed a concerning situation[3]. When comparing certified samples, the results from participants indicate that only a small fraction of instruments are well calibrated, with many instruments being used in the setup of the SPM as delivered by the manufacturer at installation time. For the rest of the SPM a calibration was carried out but was either unsuccessful or incomplete. The survey results indicated that the reliability of the instrument operation was contingent on the accuracy of the measured data. To address this issue, the use of crystalline standards with direct traceability to the SI is recommended.

Methods

An analysis of the factors contributing to this noteworthy calibration rate reveals three primary elements influencing nanoscale calibration:

1) Availability of calibration standards
2) Cost of certified standards
3) Complexity of application of standards and data refinement

The application of crystalline standards based on crystalline Silicon give options to address these points. Crystalline standards are using the lattice parameter of Silicon as natural ruler for the SI unit of meter. In fact, with the redefinition of the SI in 2019, the lattice parameter of Silicon has become a secondary realisation of the SI unit “Meter” for length up to 100 nm [4]. Hence, traceability of such standards is a build-in feature of such standards and reduces cost and effort for calibration.

For the manufacture of crystalline standards structure creation by self-organisation is applied to pre-structured Silicon chips. Classical lithographic processing is applied to create specific patterns on the chip with lateral dimensions of 50 µm to 250 µm, approximately. The structures are created by reactive ion etching in a SiO_2 layer of 300 nm thickness, removing the SiO2 in the specific regions. In the following process the sample is annealed in ultra high vacuum with temperatures up to approximately 1280°C. During this annealing within the patterns the self-organisation process is induced, leading to a recrystallisation of the surface layer, recreating the Silicon structure up to the surface.

At the end of the annealing three types of structures are created, giving a traceable length representation useable for the calibration of the z-axis of microscopes. Crystalline patterns with sub-nanometer step height are formed. The step hight is given by the lattice parameter of Silicon. For the (111) lattice plane, used in these experiments, a constant step height of h = 0.314 nm is created.
Three different types of basic pattern are created:

1) Atomical flat surface,
2) Amphi theater structure,
3) Staircase Structure,

which can be used for the calibration of the z-axis of SPM or microscopes in general.

Results

The benefits of crystalline standards regarding to uncertainty of the step hight calibration and minimal step hight of calibration artefacts (resolution) given by the lattice parameter, has been demonstrated before in single experiments, leading to the secondary representation of the unit meter in the redefinition of the SI in 2019. Both, uncertainty and resolution could be reduced by more than a factor of 10 compared to the standards available before.

With the new production facility at PTB the transfer of these calibrations approach from the lab to the applications is now under development. Fig. 1 shows a SPM image of a crystalline standard prototype in staircase structure.

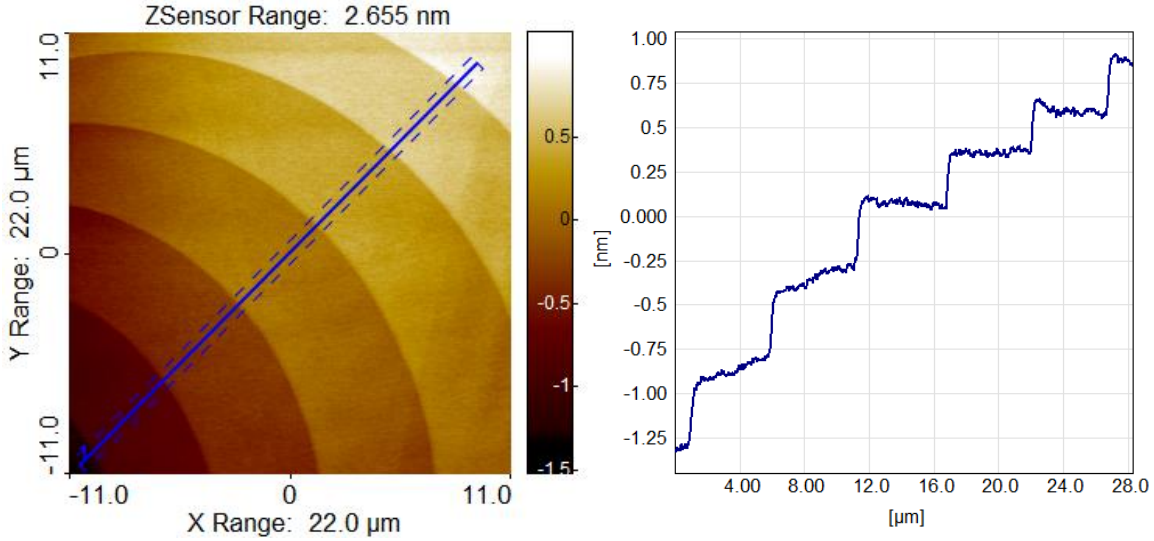


Figure 1: SPM image of a staircase structure with seven atomical flat terraces of the Si crystal in (111) orientation (left). On the right side a cross section through the crystalline steps averaged over 39 lines is displayed. In z-direction a distance of $h = 7 \times d_{111} = 2.20$ nm is covered (d_{111} is the lattice parameter for the (111) plane.

To serve the demand for large number of calibration standards, needed to calibrate almost all high resolution microscopes on a regular basis, new sample layout has been developed and tested, a direct current heating for sample annealing is implemented to enable upscaling the number of samples processed in parallel. By fine tuning the processing parameter furthermore the yield of the process has been optimized.

Conclusion

Crystalline standards are very promising candidates to increase the very low rate of calibrated SPM in application, since they are pushing the limits of uncertainty and resolution downward, while lowering the cost of calibration at the same time. Setup of new production facilities at PTB opens options for introducing high quality standards for reliable calibration of instruments at massively reduced costs.

Acknowledgement

This work was performed in the project Crystalline surfaces, self assembled structures and nano-origami as length standards in (nano)metrology (CRYSTAL), which is jointly funded by the EMRP participating countries within EURAMET and the European Union.

References

1. R.J. Emerson IV, T.A. Camesano, Ultramicroscopy 106 (2006) 413-422
2. Martyn Sené, Ian Gilmore, Jan-Theodoor Janssen, *Metrology is the key to reproducing results*. Nature vol. 547 (2017) 397-399
3. A Yacoot A et al 2020 *How accurate is your atomic force microscope? A comparison of dimensional measurements made using different AFMs*. Microscopy and Analysis 34 (6):S4-S9
4. Mise en practique, BIPM; https://www.bipm.org/documents/20126/41489670/CCL-GD-MeP-3.pdf/5240b431-730f-3daf-4d8a-be590de99cdb?version=1.12&t=1667554482952&download=true

Type of presentation: Poster

IM8-P-2 Convolutional neural network for machine vision in electron and optical microscopy for correlative analysis

Andrea Cicconardi[a,b], Alessio Gagliardi[c], Giorgio Divitini[a]

[a]*Istituto Italiano di Tecnologia (IIT), Genova, Italy*

[b]*Università degli studi di Genova, Genova, Italy*

[c]*TUM School of Computation, Information and Technology, Munich, Germany*

Contact email: andrea.cicconardi@iit.it

Introduction

Optical and electron microscopy (OM and EM) and spectroscopy present complementary strengths and weaknesses. Differences include spatial resolution, spectral resolution, sample damage and excitation intensity, as well as different sets of constraints for the sample (hydration, thickness, etc.) [1][2].

To exploit synergies between OM and EM, specific correlating workflows need to be developed. Variations in resolution, signal-to-noise ratio, and other nuances of each technique present challenges that need to be overcome to have generally applicable workflow, understanding physical phenomena underpinning the collected signal and interpret them with high spatial resolution can be complex.

In this context, deep learning (DL), particularly convolutional neural networks (CNN), offers a powerful tool to analyse images from single and multiple sources, highlighting correlations and extracting information from different techniques. The approach we demonstrate enables the creation of a multidimensional representation where each material (whether a 2D material, bulk material, or nanomaterial) is associated with extracted properties.

This method has the potential to enhance data correlation and interpretation, providing new insights into material behaviour at the microscopic level. Furthermore, it allows for the improvement of resolution in OM, reconstructing the shape and the properties of a specific material (i.e., defects in a flake of a 2D material).

Methods

We adopt a convolutional neural network (CNN), implemented with Python programming language, in order to classify and combine information from experimental techniques.

- Micro-PhotoLuminescence (PL) – (Renishaw inVia Raman microscope)
- Scanning Electron Microscopy - CathodoLuminescence (SEM-CL) – (Attolight Allalin SEM-CL)
- Electron Energy Loss Spectroscopy (EELS) – (Thermo Fisher Spectra 300 S/TEM)
- Ellipsometry

Preliminary Results

As a proof of concept, we analysed MoS_2 flakes, which feature thickness-dependent variations in electronic properties for a thickness below a few monolayers. Specifically, its bandgap transitions from indirect in the bulk form to direct in a monolayer. We acquired hyperspectral maps from different regions with varying thickness, aiming to investigate excitonic phenomena through CL and PL (Fig.1A-B).

The excitonic peaks can be observed in EELS and ellipsometry as well, and data collection for these techniques is ongoing.[3]

To explore the potential of machine learning in this context, we trained a U-Net — a specialised convolutional neural network (CNN) architecture [4] — on high-angle annular dark field (HAADF) images containing a collection of nanocrystals. Nanocrystals were chosen for an initial investigation, rather than flakes, since representative images with hundreds of features can be acquired rapidly. The goal was to reconstruct the images and quantify the crystals within them. Although these are preliminary

results, they provide insight into how CNNs could assist in classifying the optical and electronic properties associated with the studied materials (Fig. 1C).

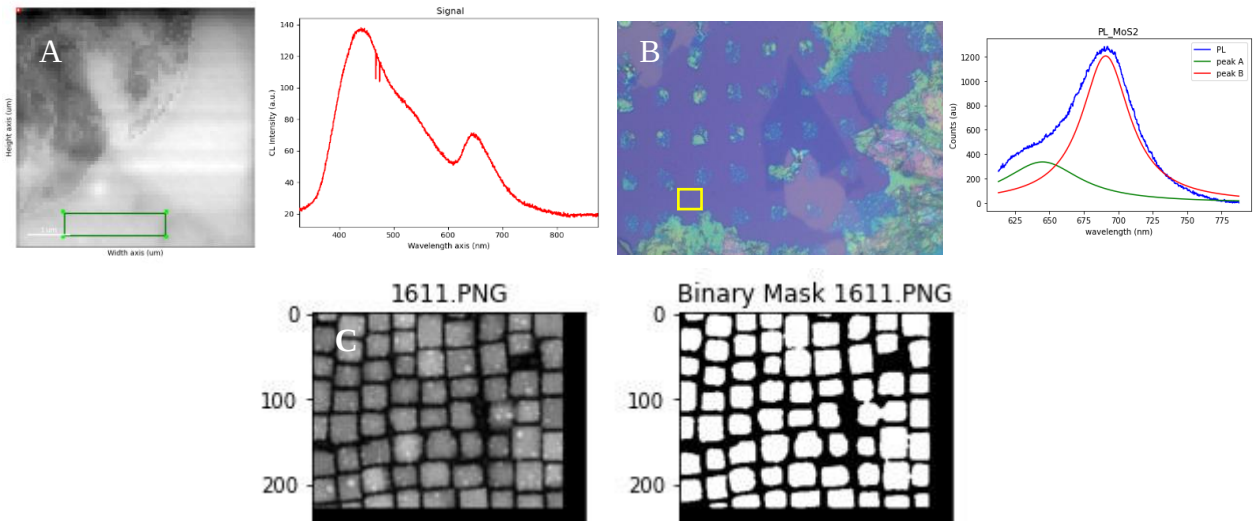


Figure 1: (A) CL hyperspectral map of a MoS2 monolayer (green rectangle) and the corresponding average spectrum. (B) Micro-PL image with the measured luminescence spectrum (yellow rectangle); the two fitted Lorentzian curves show the exciton peaks, visible also in the CL spectrum. (C) Result of the U-Net binary mask to identify features in an ensemble of nanocrystals.

Discussion and conclusions

This research aims to bridge the gap between OM and EM by integrating deep learning techniques to increase the overall achievable spatial resolution and to maximise information output by leveraging complementarity of the two techniques. By correlating the high-resolution data from EM to inform and improve OM images, we can gain valuable insights into the local properties of materials. The use of a robust and validated approach, such as CNN, could lead to more in-depth studies of materials, facilitating advancements in various applications, from nanotechnology to materials engineering. Through careful implementation and evaluation of the proposed methodologies, this study aspires to contribute to the field and inspire further exploration of integrated imaging techniques.

References:

1. Born, M. and Wolf, E. (1999) *"Principles of Optics: Electromagnetic Theory of Propagation, Interference, and Diffraction of Light."* Cambridge University Press, London. http://dx.doi.org/10.1017/CBO9781139644181
2. D. B. Williams and C. B. Carter, *"Transmission Electron Microscopy: A Textbook for Materials Science,"* 2nd Edition, Springer, New York, 2009. https://doi.org/10.1007/978-0-387-76501-3
3. Ilka Kriegel et al. *"Light-Driven Permanent Charge Separation across a Hybrid Zero-Dimensional/Two-Dimensional Interface"*, The Journal of Physical Chemistry C 2020 124 (14), 8000-8007, DOI: 10.1021/acs.jpcc.0c01147
4. Olaf Ronneberger, Philipp Fischer, Thomas Brox, *"U-Net: Convolutional Networks for Biomedical Image Segmentation"*, 2015, arXiv:1505.04597

Type of presentation: Poster

IM8-P-3 EELS spectrum analysis using Bayesian estimation

Hayato Saeki[a], Satoshi Ogawa[a,b], Makoto Kuwahara[a,b]

[a] *Graduate School of Engineering, Nagoya University, Japan*

[b] *Institute of Materials and Systems for Sustainability, Nagoya University, Japan*

Contact email: saeki.hayato.z9@s.mail.nagoya-u.ac.jp

Introduction: Electron Energy Loss Spectroscopy (EELS) is widely used in various fields, including elemental and electronic state analysis. The spectra obtained by EELS are divided into zero-loss, low-loss, and core-loss peaks according to energy. These each peaks provide distinct physical information. Therefore, when one analyses a specific peak, it is necessary to eliminate background arising from other peaks by techniques such as fitting and peak deconvolution. However, fitting of EELS spectrum using unimodal basis functions (e.g. Gaussian), especially for low-loss regions, relies heavily on the analyst's experience. Furthermore, least-squares fitting methods, such as the commonly used Levenberg-Marquardt algorithm, tend to converge to local minima close to the given initial values, which means fitting accuracy dependent on the initial value selection. In order to avoid dependence on the analyst's experience and initial value selection, this study focuses on Bayesian estimation and attempts to analyse EELS spectra using a replica-exchange Monte Carlo method [1, 2] to comprehensively explore the parameter space.

Analytical Methodology: In this analysis, the replica-exchange Monte Carlo method is iteratively applied to various parameters of the model function for fitting, such as the Gaussian full width at half maximum, to generate the probability distribution of their existence. The optimal parameters are then obtained through Maximum A Posteriori (MAP) estimation. The replica-exchange Monte Carlo method involves creating multiple replicas with varying shapes by altering the inverse of the noise variance of the posterior distribution derived from Bayes' theorem. These replicas are then subjected to parallel Metropolis algorithm optimization to explore the optimal values. The Metropolis algorithm allows for the exploration of a wide range of values by probabilistically accepting candidate points even when they deviate from the optimal value. Furthermore, by employing the replica-exchange method, the states between replicas are exchanged at a certain probability, facilitating escape from local minima, thereby enabling efficient and comprehensive exploration. After repeated iterations of this exploration, the best replica is selected from each set of replicas based on a comparison of Bayesian free energies [3], and the optimal values for various parameters are obtained from the posterior distribution of the selected replica.

Results: In this study, we have conducted an analysis of STEM-EELS spectra from Au nanoparticles synthesized using the solution plasma process [4] and dispersed on an amorphous carbon support film. Initially, we performed an analysis for the EELS spectrum in the region of the supporting membrane, as shown in Figure 1, to determine the background component. We have used model functions composed of a pseudo-Voigt function [5] for the fitting of zero-loss peak and various other functions (such as a Voigt function, a pseudo-Voigt function, convolution of a Gaussian function and a sigmoid function, etc.) for the fitting of plasmon-loss peaks. Subsequently, for the EELS spectrum at the center of the Au nanoparticles, we have performed the analysis using the former background component and a model function composed of a summation of multiple peaks. An example of the fitting results is shown in Figure 2. As shown in Figure 2, the method employing replica-exchange Monte Carlo method successfully separates the spectra of the supporting membrane and Au nanoparticles. Furthermore, the optimal number of peaks for each fitting was determined by comparing the Bayesian free energies between models for both the background and the Au spectrum [1,2].

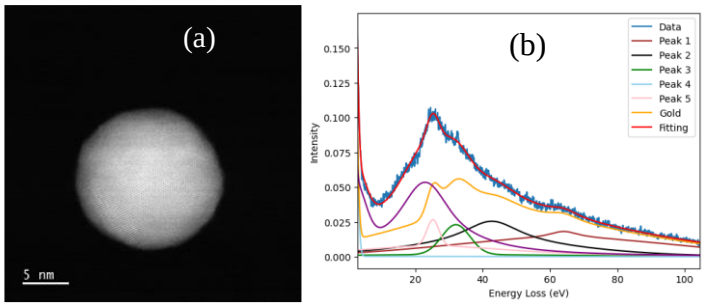


Figure 1: STEM image of Au Nano-particle (a) and example of plasmon-loss peak fitting with pseudo-Voigt functions (b).

References:

1. K. Nagata et al., *Neural Networks*., **2012**, 28, 82-89.
2. S.Tokuda et al., *J.phys.Soc.Jpn.*, **2017**, 86, 024001.
3. G. Suzuki et al., *J Electron Spectrosc Relat Phenom*., **2024**, 274, 147450.
4. O. Takai, *Pure Appl. Chem*., **2008**, 80, 9, 2003-2011.
5. B. D. Levin et al., *Microsc. Microanal*., **2019**, 25, 674-675.

Type of presentation: Poster

IM8-P-4 A Deep Learning Approach to Drift Correction in Atomic-Scale STEM Imaging

Vinko Sršan[a,b], Marjan Stoimchev[b,c], Dragi Kocev[c], Sašo Džeroski[c], Sašo Šturm[a,b,d]

[a]*Jožef Stefan Institute, Department for Nanostructured Materials, Jamova cesta 39, 1000 Ljubljana, Slovenia,*

[b]*International Postgraduate School Jožef Stefan, Jamova cesta 39, 1000 Ljubljana, Slovenia,*

[c]*Department of Knowledge Technologies, Jožef Stefan Institute, Jamova cesta 39, 1000 Ljubljana, Slovenia,*

[d]*Department of Geology, Faculty of Natural Sciences and Engineering, University of Ljubljana, Aškerčeva Cesta 12, 1000 Ljubljana, Slovenia*

Contact email: vinko.srsan@ijs.si

The scanning transmission electron microscope (STEM) is becoming a pivotal tool in material characterization at the atomic scale. Due to advances in aberration correction, deep sub-Angstrom resolution is achievable. Imaging in STEM is performed by rastering the sharp electron probe over the region of interest, where at each probe position a diffraction pattern is being recorded. The fundamental limitation of such an operation lies in two temporal components, namely the fast scan axis and slow scan axis, that are mutually perpendicular. In the case of sample drift, a slight movement of the sample due to thermal drift or sample stage instability, the resulting image can be deformed along a long scan axis. On the other hand, instabilities of scanning coils may increase noise levels or jittering artefacts even along the fast axis of the scan. All of these disturbances can result in undesired image artefacts that may alter underlying physical information or make it inaccessible.

To date, a multitude of methods have been developed to remove artefacts from the STEM images, yet there is no single solution that successfully corrects all artefacts simultaneously. In order to introduce a simple and robust solution for the correction of images that are distorted both by simple and complex artefacts, we propose a deep learning approach for flow estimation. The flow estimation for drift correction yields a displacement map of individual pixels, offering understanding how different regions of the image were influenced by the drift, while simultaneously allowing reversal of drift-induced pixel displacements. The model was trained on, 30960 simulated image pairs, where each pair includes an image with the drift and an image without the drift. The drifts included in the dataset exhibited a large variety of magnitudes and geometries. After training, the model was tested on 32400 image pairs that were not included in the training dataset. The model showed strong robustness while reconstructing drifts that correspond to atomic-scale images of materials that were not included in the training dataset. Finally, the structural similarity index metric was calculated to be 0.85, showing high robustness in the correction of noisy images.

Acknowledgements: This work has been supported by the Slovenian Research Agency through the P2-0084 research program and J7-4637 project.

Type of presentation: Poster

IM8-P-5 Delivering state of the art imaging data science to aid research and development at Johnson Matthey

Aakash Varambhia[a], Tom Ellaby[a], Zaeem Najeeb[a], Dogan Ozkaya[a]

[a]*Johnson Matthey Technology Centre, Blounts Court Road, Sonning Common, United Kingdom*

Contact email: aakashm.varambhia@matthey.com

Johnson Matthey (JM) is a global leader in sustainable technologies, employing advanced scientific methods to tackle critical challenges in energy, chemical synthesis, and automotive sectors. Central to our strategy is the development of innovative digital tools accessible via our dedicated internal App Store, a pioneering initiative within the chemicals industry designed to democratise access to advanced analytical capabilities across JM.

This presentation highlights the transformative impact of JM's App Store, which provides specialised, web-based applications for microscopy and materials characterisation. These applications, built on robust front-end frameworks in Python, streamline workflows in image segmentation, visualisation, particle metrology, and data preparation for advanced simulations. The App Store significantly enhances collaborative potential by offering seamless, concurrent access to powerful analytical tools without the need for extensive local installations, thereby reducing time to deployment and accelerating the pace of research and innovation within JM.

A key feature of this platform is its integration with high-performance Python libraries, enabling efficient handling and processing of large datasets across multiple research domains, including Hydrogen Technologies, Clean Air, and Fuel Cell development. Examples such as the particle sizing application, routinely utilised across JM for nanoparticle analysis, illustrate the platform's capability to provide accessible, high-quality data analytics to support critical decision-making processes.

Looking forward, our research is pioneering the integration of machine learning models with real-time microscopy data acquisition. This approach represents a paradigm shift towards predictive materials design, offering profound implications for sustainable technology advancement.

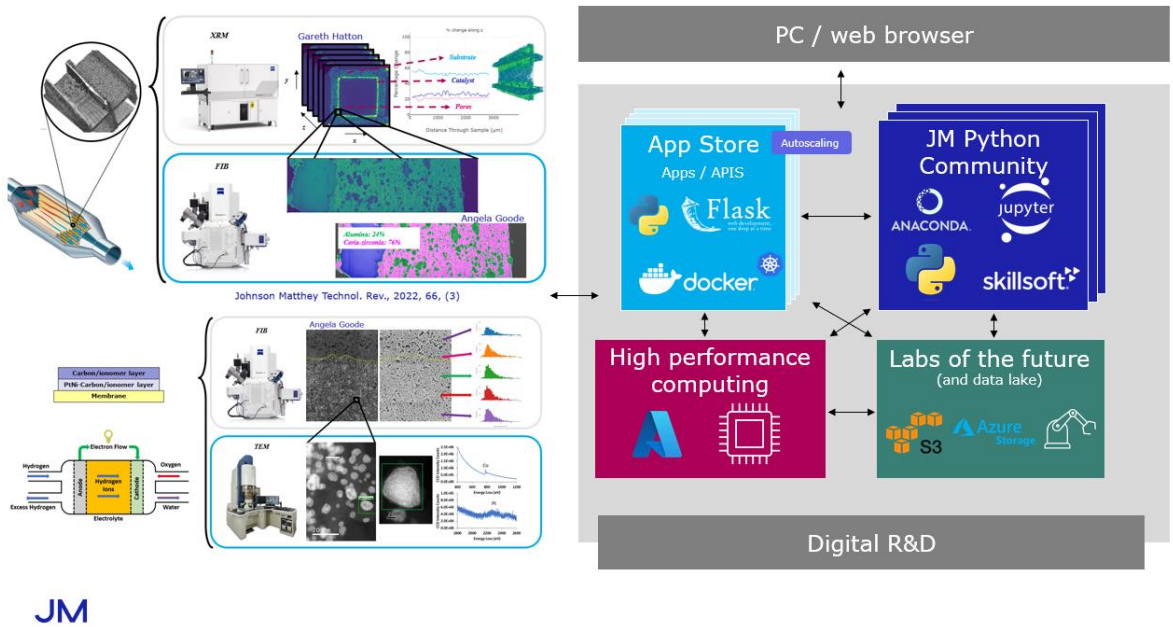


Figure 1. How the Appstore sits at the intersection of microscopy instrumentation, modelling and data science at Johnson Matthey

Type of presentation: Poster

IM8-P-6 Fractal modelling and fracture mechanics of urban particle populations in biological tissues

Ruggero Vigliaturo[a,b], Giulia Pia Servetto[a], Alessandra Passarella[a], Sara Di Felice[a]

[a]*Department of Earth Sciences, University of Torino, (Torino), Italy*

[b]*Interdepartmental Centre for Studies on Asbestos and Other Toxic Particulates "G. Scansetti", University of Torino, (Torino), Italy*

Contact email: ruggero.vigliaturo@unito.it

The mineralogical landscape of the brain is determined by the presence of biogenic minerals, and the accumulation of anthropogenic exogenous mineral phases that can access the body following different pathways. Both biogenic minerals and exogenous minerals are likely to have an active role in multiple neurodegenerative diseases which are likely to cause million of deaths in 2050.

The access of exogenous particles to the human brain is determined by their dimensional range and distribution. In this work, we are proposing to apply a fractal model and fracture mechanics for determine the likelihood of a certain particle population to access different regions of the human brain.

By means of fracture mechanics, heterogeneous nanominerals population can be described with a low number of parameters. These parameters can be used to set references on which it is possible to describe several bio-interaction pivotal features such as: adhesion, surface forces and possible reaction path of surfaces. The final aim is an attempt to describe this particle population as a single entity with disparate properties. For this purpose, we have dimensionally studied multiple nanomineral particles population which are representative of urban particulate matter. Preliminary results show that using a best fit probability distribution, combined with fracture mechanics theory, it is possible to fully describe many properties of the particles population as a whole, in particular those properties with an influence on the interaction with the biosphere and the localization in a target tissue.

LS1 Advances in multiscale fluorescence imaging and image processing

Type of presentation: Invited

LS1-IN-1 Advancing Super-Resolution Imaging: Integrating Fluorescence Lifetime, Scanning Microscopy, and Energy Transfer Techniques for Isotropic Nanoscale Bioimaging

Jörg Enderlein[a]

[a]*Institute of Physics – Biophysics, Georg August University, Friedrich-Hund-Platz 1, 37077 Göttingen, Germany*

Contact email: jenderl@gwdg.de

Recent advancements in super-resolution microscopy have enabled unprecedented insights into the spatial organization of cellular structures. In this talk, I will present a series of methodological innovations that synergistically integrate fluorescence-lifetime single-molecule localization microscopy (FL-SMLM) [1,2], image scanning microscopy (ISM) [3,4], and metal- or graphene-induced energy transfer (MIET/GIET) imaging [5–7]. These approaches collectively offer isotropic three-dimensional resolution at the nanometer scale, multiplexed imaging capabilities, and robustness against chromatic aberrations.

First, I will discuss our work on **MIET and GIET microscopy**, which exploit distance-dependent quenching phenomena near metallic or graphene interfaces to determine the axial position of single emitters with sub-10 nm accuracy. The combination of MIET with dSTORM or DNA-PAINT provides truly isotropic 3D resolution, extending the reach of localization microscopy into the axial dimension without interferometric complexity.

Second, I will highlight the development of **fluorescence lifetime DNA-PAINT (FL-PAINT)**, a technique that enables multi-target super-resolution imaging through fluorescence lifetime multiplexing without fluid exchange. By utilizing orthogonally designed imager strands conjugated to fluorophores with distinct lifetimes, we achieve simultaneous imaging of multiple targets in the dense intracellular environment.

Lastly, I will introduce our latest development of **fluorescence-lifetime image scanning microscopy SMLM (FL-iSMLM)**, which achieves a near twofold enhancement in lateral resolution by integrating a single-photon detector array into a confocal laser scanning microscope. This method combines the localization precision of ISM with the multiplexing power of fluorescence-lifetime detection, enabling sub-5 nm resolution in fixed cells while simultaneously allowing discrimination of targets based solely on their fluorescence lifetimes.

References

[1] J. C. Thiele, D. A. Helmerich, N. Oleksiievets, R. Tsukanov, E. Butkevich, M. Sauer, O. Nevskyi, and J. Enderlein, Confocal Fluorescence-Lifetime Single-Molecule Localization Microscopy, ACS Nano **14**, 14190 (2020).

[2] J. C. Thiele, O. Nevskyi, D. A. Helmerich, M. Sauer, and J. Enderlein, Advanced Data Analysis for Fluorescence-Lifetime Single-Molecule Localization Microscopy, Front. Bioinform. **1**, 740281 (2021).

[3] C. B. Müller and J. Enderlein, Image Scanning Microscopy, Phys. Rev. Lett. **104**, 198101 (2010).

[4] N. Radmacher, O. Nevskyi, J. I. Gallea, J. C. Thiele, I. Gregor, S. O. Rizzoli, and J. Enderlein, Doubling the resolution of fluorescence-lifetime single-molecule localization microscopy with image scanning microscopy, Nat. Photon. **18**, 1059 (2024).

[5] A. I. Chizhik, J. Rother, I. Gregor, A. Janshoff, and J. Enderlein, Metal-induced energy transfer for live cell nanoscopy, Nature Photon **8**, 124 (2014).

[6] A. Ghosh, A. Sharma, A. I. Chizhik, S. Isbaner, D. Ruhlandt, R. Tsukanov, I. Gregor, N. Karedla, and J. Enderlein, Graphene-based metal-induced energy transfer for sub-nanometre optical localization, Nat. Photonics **13**, 860 (2019).

[7] J. C. Thiele, M. Jungblut, D. A. Helmerich, R. Tsukanov, A. Chizhik, A. I. Chizhik, M. Schnermann, M. Sauer, O. Nevskyi, and J. Enderlein, Isotropic Three-Dimensional Dual-Color Super-Resolution Microscopy with Metal-Induced Energy Transfer, Science Advances **8**, 14190 (2021).

Type of presentation: Oral

LS1-O-1 Immersive Virtual Reality System for Mice Combined with 3D-Targeted Photostimulation as a Prototype for Visual Restoration

Gergely Szalay[a,b], Linda Judak[a,b], Gergely Dobos[c], Plauska Andrius[b], Chakrabarti Abhrajyoti[b], Gabor Juhasz[b], Pal Maak[d], Katalin Ocsai[b,e], Balazs Tarjan[b,f], Huba Szebik[b], Aron Szepesi[a,b], Andras Feher[b], Mate Veres[b], Balazs Rozsa[a,b,g]

[a]*Laboratory of 3D Functional Network and Dendritic Imaging, Institute of Experimental Medicine, Budapest, Hungary*

[b]*BrainVisionCenter Research Institute and Competence Center, Budapest, Hungary*

[c]*Bay Zoltán Nonprofit for Applied Research, Budapest, Hungary*

[d]*Doctoral School, Semmelweis University, Budapest, Hungary*

[e]*Department of Algebra and Geometry, Institute of Mathematics, Budapest University of Technology and Economics, Budapest, Hungary*

[f]*Department of Atomic Physics, Budapest University of Technology and Economics, Budapest, Hungary*

[g]*Faculty of Information Technology and Bionics, Pázmány Péter Catholic University, Budapest, Hungary*

Contact email: szalay.gergely@koki.mta.hu

Our recently developed mouse head-mounted virtual reality device (Moculus) allows binocular depth perception and full visual immersion. This precisely controlled environment, combined with real-time three-dimensional acousto-optical (AO) imaging, has uncovered detailed circuit substrates engaged during rapid visual learning. Using this approach, during a visual discrimination task, we found that both control and reinforcement-associated visual cue coding neuronal assemblies undergo transient expansion in response to reinforcement feedback, reaching near-saturation activation level. This enhanced computational capability facilitates competition among neuronal assemblies encoding behaviorally relevant information.

For the long-term goal of cortical stimulation based visual restoration, this expanded representation of specific visual cues provides an excellent candidate for neural interfacing, as it offers a large set of potential targets capable of generating visual-like perception.

In this talk we will demonstrate how Moculus technology, combined with high-speed voltage imaging, targeted photostimulation and real-time motion correction, enables the design of a prototype for artificial visual perception. The increased temporal resolution of two-photon voltage imaging allows the detection of complex spatiotemporal activity patterns underlying visual perception. Using AO-based photostimulation we can artificially regenerate this pattern, while real-time motion correction ensures precise targeting even in awake, behaving animals.

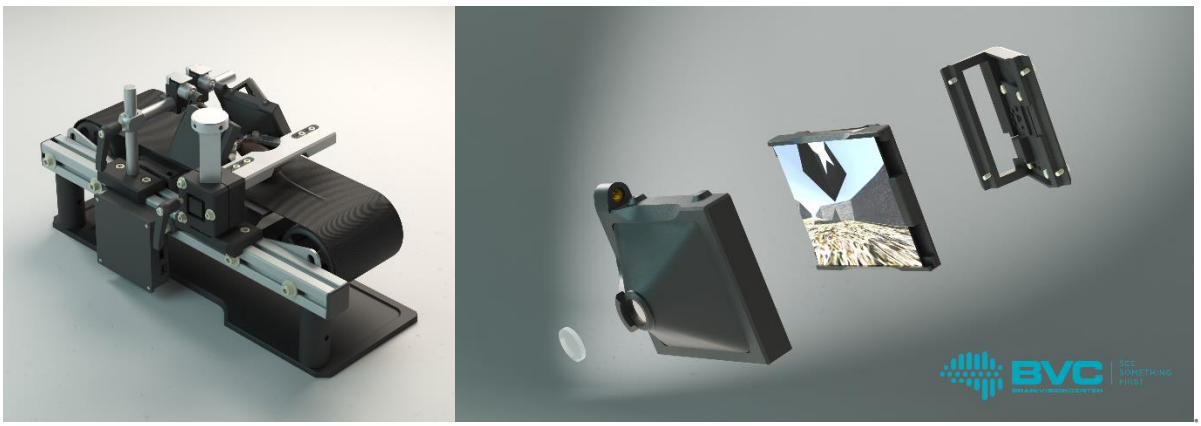


Figure 1. – 3D rendered images of the MouseVR system. **Right**: full system with the treadmill detecting the animal running speed. **Left**: optical design of the Moculus' screens.

Type of presentation: Oral

LS1-O-2 Micropipette-Based Single-Cell Isolation from Live Spheroids

Mariachiara Stellato[a], Viktor Pal[b], Akos Diosdi[b, c], Maria Harmati[b], Daniel Remondini[a], Nicola Normanno[d], Gastone Castellani[e, f], Filippo Piccinini[d, e], Peter Horvath[b, c]

[a]*Department of Physics and Astronomy "Augusto Righi" (DIFA), University of Bologna, Italy.*

[b]*Synthetic and System Biology Unit, HUN-REN Biological Research Centre (BRC), Szeged, Hungary.*

[c]*Single-Cell Technologies Ltd, Szeged, Hungary.*

[d]*IRCCS Istituto Romagnolo per lo Studio dei Tumori (IRST) "Dino Amadori", Meldola (FC), Italy.*

[e]*Department of Medical and Surgical Sciences (DIMEC), University of Bologna, Italy.*

[f]*IRCCS Azienda Ospedaliero-Universitaria di Bologna S.Orsola, Bologna, Italy.*

Contact email: filippo.piccinini@irst.emr.it; f.piccinini@unibo.it.

Introduction: 3D multicellular spheroids are a well-established and widely used model to study tumours *in vitro*. Unlike 2D cell cultures, they can mimic *in vivo* conditions, thus providing a reliable tool for better understanding drug responses and tumorigenesis [1]. In recent years, single-cells isolation from 3D spheroid as gained traction as a technique able to give useful insight about cells inside tumours. Conventional methods like enzymatic digestion and mechanical dissociation require complete sample destruction [2-5]. In this work, we propose a new technology to perform *in vitro* single-cell isolation from spheroids using a micromanipulator, that will be integrated with an automatic method for cell selection and isolation. This technique allows to extract living single cells from the aggregate while keeping both the cell and the spheroid alive.

Methods: To develop this technique, we tested borosilicate micropipettes with an inner diameter ranging between 3 and 20 µm created with a PC-10 pipette puller (Narishige, Tokyo, Japan) using borosilicate capillaries (World Precision Instruments, Sarasota, USA). We created spheroids monocultures using HeLa Kyoto EGFP-alpha-tubulin/H2B-mCherry cervical cancer cells (Cell Lines Service, Eppelheim, Germany). To generate spheroids with various sizes, cells were seeded into u-DISH 35mm, Bioinert (Ibidi) and incubated for 24 h at 37 °C and 5% CO_2. Then, spheroids were embedded into TrueGel3D hydrogel (Sigma-Aldrich) and used for single cell isolation. This cell line was selected due to its fluorescence properties, enabling the identification of dividing cells we aimed to collect in this project. For imaging, the Leica LMD-6 multichannel microscope (Leica, Wetzlar, Germany) was used, both in brightfield and fluorescence mode.

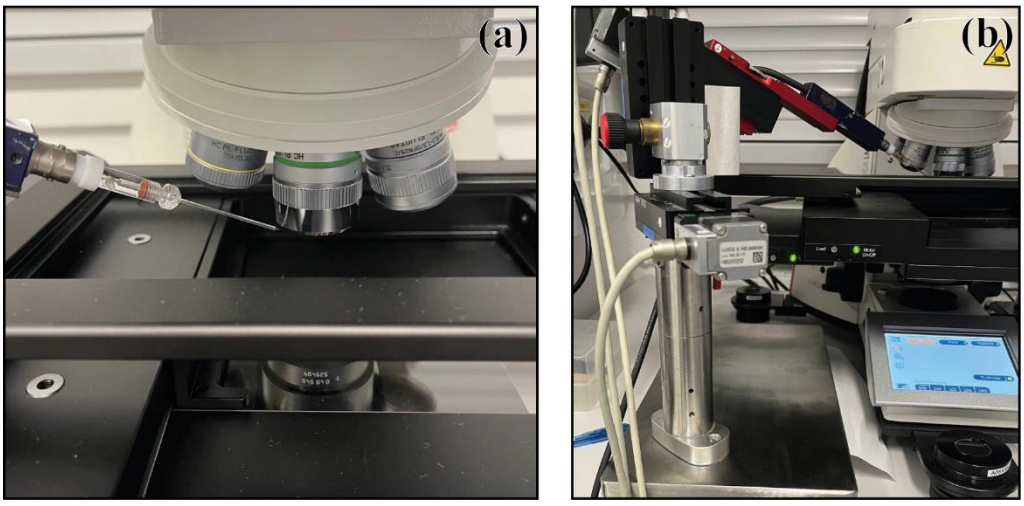


Figure 1: Single-cell isolation technology setup. Close up of the glass pipette positioned under the 20× objective (a). Robotic arm used to control the pipette for the single-cell isolation (b).

Spheroids were observed under a 20× (0.4 NA drv) magnification objective. The cells to be isolated were selected from the microscopy images and then approached with the pipette using a SM-5 robotic arm (Luigs & Neumann, Ratingen, Germany) manually controlled (**Figure 1**). To avoid the pipette filling with the hydrogel, a continuous positive pressure of 280 mBar was applied. Once the pipette attaches to the single cell, a negative pressure of -500 mBar is applied to create a seal, detach the cell from the spheroid and remove it with the glass pipette. To aid the detachment, local enzymatic digestion is performed. The collected single cell can be further analysed.

Results: Using this technique, we were able to consistently select and isolate single cells of interest from the outer region of spheroids embedded into hydrogel. The obtained cells are viable and can be further analysed (**Figure 2**).

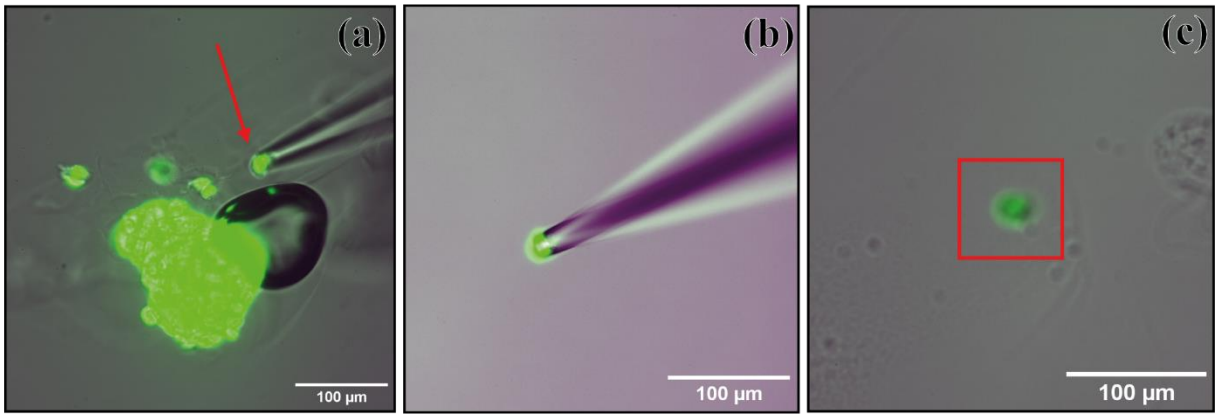


Figure 2: Single-cell isolation example. The selected single cell (red arrow) is detached from the spheroid with a borosilicate pipette (a). The pipette holding the isolated single cell is removed from the spheroid culture (b). The single cell (red square) is released in a new holder with different culture media. (c).

Discussion and conclusions: This protocol represents an initial step toward isolating single cells while maintaining the viability of both the spheroid and the extracted cell. This can lead to reliable and repeatable studies for drug testing and tumor studies and paves the way for the single-cell-based downstream analyses of selectively isolated target cells from 3D cultures. Up to this point, only cells from the outer layer of the spheroid were selected successfully. Two are the main future steps. First, consistently select and isolate cells from the inner layers of the spheroids to have better insights in the spheroid's behavior as a tumor model. Secondly, completely automatize the process to make it fast and reproducible.

Acknowledgments: N.N. acknowledges the support received from the Italian Ministry of Health and the contribution of "Ricerca Corrente" within the research line "Appropriateness, outcomes, drug value and organisational models for the continuity of diagnostic therapeutic pathways in oncology"; G.C. and F.P. from the MAECI Science and Technology Cooperation Italy–South Korea Grant Years 2023–2025 by the Italian Ministry of Foreign Affairs and International Cooperation (CUP project: J53C23000300003).

References:

1. M. Stellato, *et al.* Radiomic analysis of 3D spheroids using 2D brightfield images. *Biomedical Signal Processing and Control.* **2025**, *103*, 107366.
2. C. Brasko, *et al.* Intelligent image-based in situ single-cell isolation. *Nature Communication*, **2018**, 9, 226.
3. D. Li, *et al.* Complete disassociation of adult pancreas into viable single cells through cold trypsin-EDTA digestion. *J. Zhejiang Univ. Sci. B*, **2013**, 14, 596-603.
4. T. Sun, *et al*. Observation of the effects of different enzyme digestion time and enzyme digestion methods on the extraction of primary renal tubular epithelial cells from Sprague–Dawley suckling mice. *Biochem Genet*, **2024**, 63(1), 906-916.
5. K. Koos, *et al.* Automatic deep learning-driven label-free image-guided patch clamp system. *Nature Communication*, **2021**, 12, 936.

Type of presentation: Oral

LS1-O-3 Optimizing Microscopy Methodologies for Xylogenesis: Advances and Challenges in Wood and Phloem Formation Analysis

Angela Balzano[a], Luka Krže[a], Maks Merela[a]

[a]*University of Ljubljana, Biotechnical Faculty, Department of Wood Science and Technology, Rožna dolina, Cesta VIII/34 1000 Ljubljana, Slovenia*

Contact email: Angela.Balzano@bf.uni-lj.si

Xylogenesis, the process of wood formation, is of fundamental importance for understanding the growth dynamics of trees and their responses to environmental changes. Microscopy is essential to follow the differentiation of xylem and phloem cells, but methodological challenges remain, especially in Mediterranean hardwood species due to their complex xylem anatomy, irregular growth patterns, high wood density. To cope with these challenges, our research optimises microscopic techniques by integrating epifluorescence, brightfield and polarised light microscopy with refined sample preparation protocols, including key improvements in embedding and sectioning.

We emphasise the importance of paraffin embedding, precise alignment and optimised cutting techniques to maintain specimen integrity and avoid artefacts that could compromise anatomical analyses. Fluorescence imaging of slides stained with Safranin Red & Astra Blue significantly improves the detection of lignification progress, enhances the visualisation of differentiation stages and facilitates the identification of cambial activity, secondary wall deposition and programmed cell death. In addition, we are addressing the challenges associated with distinguishing stages of cell maturation, adapting methods for heterogeneous wood tissue and ensuring high quality thin sections for accurate microscopic observation.

By refining microscopy methods and sample preparation techniques, adapting methodologies to species-specific wood structure we are improving the accuracy of xylogenesis studies and providing deeper insights into tree physiology, adaptive strategies and the effects of environmental stress on wood formation. These advances contribute to the development of improved imaging and analysis techniques that support quantitative wood anatomy and ecophysiological research.

Type of presentation: Oral

LS1-O-4 Automated quantitative fluorescence microscopy and image feature analysis for *in vitro* detection of adverse effects

Blaž Režonja[b], Martina Štampar[a], Alja Štern[a], Špela Rozman[b], Aleksandar Janev[c], Mateja Erdani Kreft[c], Bojana Žegura[a]

[a]*National Institute of Biology, Ljubljana, Slovenia*

[b]*Biotechnical faculty, University of Ljubljana, Slovenia*

[c]*Institute of Cell Biology, Faculty of medicine, University of Ljubljana, Slovenia*

Contact email: blaz.rezonja1@gmail.com

Introduction:
With the increasing number of chemicals requiring safety evaluation, there is a strong need for physiologically relevant and reliable research techniques and models to assess their genotoxic potential and associated adverse health effects. In recent years, advanced 3D cell-based systems have been developed to more accurately model biological processes in living cells and organs. In this context, hepatic spheroids serve as an alternative to animal models, offering enhanced structural, physiological, and metabolic properties suitable for a wide range of applications, including (geno)toxicity studies [1]. High-content automated quantitative fluorescence microscopy, with its diverse modalities and rapidly advancing image analysis capabilities, has become a powerful tool for fast and cost-effective toxicological assessment. This is particularly beneficial for high-multiplex, spatial, or time-dependent studies [2]. However, notable gaps remain in microscopy-based approaches for studying (geno)toxicity-related stress in 3D cells models. Given the complexity of cellular responses to xenobiotics, a combination of high-throughput scanning and high-content imaging—such as automated microwell plate and glass slide readers—is required to generate comprehensive datasets on cellular parameters following xenobiotic exposure [3]. This study aimed to evaluate and optimize an automated quantitative fluorescence microscopy approach using the Cytation 5 Microplate Reader (Agilent BioTek) alongside quantitative image analysis to investigate cellular responses of two polycyclic aromatic hydrocarbons (PAH)found in polluted air [4]. The findings will be further validated using laser scanning confocal microscopy (Leica Stellaris 8) to ensure accuracy and confirm cellular responses.

Methods:
In vitro 2D and 3D (spheroid) models formed from the hepatocellular carcinoma HepG2 cell line were used for (geno)toxicity screening, integrating confocal microscopy and quantitative image analysis. The 2D cultures were seeded on glass slides and in 96-well plates and cultured for 24h under standard conditions (37°C, 5% CO_2). In contrast, spheroids were formed in AggreWell plates and cultured under dynamic conditions (37°C, 5% CO_2) in bioreactors within the ClinoStar system (CelVivo) for 21 days, with media changed every 48h. For optimization and method validation, well-characterized genotoxic agents – benzo(a)pyrene, etoposide, tert-butyl hydroperoxide – each with known mechanisms of action, were tested in both 2D and 3D models. This step ensured that fluorescence signal detection in treated cells corresponded to specific toxicological effects, confirming the robustness of the imaging approach for identifying (geno)toxic compounds. After optimization, the models were exposed to the PAH chemicals, benzo[b]fluoranthene (BBF) and benzo[g,h,i]perylene (BGP), both individually and in binary mixtures. Following treatment, protocols were optimised for fixation (4% paraformaldehyde) and staining, including permeabilization, blocking, and labelling with primary and secondary antibodies for both 2D and 3D models, to ensure high-quality imaging. The 2D cells were directly seeded into black 96-well plates and on slides, while spheroids were embedded in 0.5% agarose and transferred into black 96-well plates or sectioned into 5 mm paraffin slices for analysis using the Cytation 5 and laser scanning confocal microscopy (LSCM), respectively (Fig. 1). Multiple biomarkers were evaluated using selected antibodies to evaluate key endpoints, including cell viability (Ki67), DNA damage (γH2AX, p-H3, PARP1), oxidative stress (PEX14, Nile Red staining), mitochondrial morphology (MitoBrilliant), and cytoskeletal morphology changes (DM1A, CK18). The resulting images were analysed using Gen5

(Agilent BioTek), LAS X (Leica Microsystems), ImagePro (Media Cybernetics), and ImageJ, employing a combination of semi-automated image segmentation, fluorescence colocalization, and quantitative analysis. Statistical analysis and visualization were performed using RStudio (Posit) with the Tidyverse package and GraphPad Prism 8.



Figure 1: Main methodological steps and equipment. HepG2 spheroid culturing and PAH exposure under dynamic conditions (a), automated high-content imaging of 2D slides and 96-well plates (b) and laser scanning confocal microscopy (c).

Results & Discussion:

The results revealed distinct differences in responses between the 2D and 3D models across the tested endpoints, aligning with existing literature data on toxicological effects. Additionally, the results confirm that automated quantitative fluorescent microscopy (Cytation 5) is a **highly effective approach for automated image acquisition of toxicology endpoints**, particularly when integrated with semi-automated computational image analysis. Furthermore, it establishes high-throughput immunofluorescent imaging as a **key methodology in modern toxicology**, supporting the **3R concept (Replace, Reduce, Refine)** by minimizing animal testing while providing detailed insights into cellular responses to xenobiotics. Future work will be focused on optimizing a broader range of biomarkers for automated high-content imaging, in-depth analysis of the resulting data, and further developing automated imaging workflows for confocal microscopy.

Acknowledgments:

This study was supported by the Slovenian Research and Innovation Agency [Research Core Funding No. P1-0245, P3-0108] and the HE projects Twinning for Excellence to strategically advance research in carcinogenesis and cancer [CutCancer; g.a. No. 101079113] and HE project Evidence Driven Indoor Air Quality Improvement [EDIAQI; g.a. No. 101057497].

References:

1. Štampar M., Sedighi Frandsen H., Rogowska-Wrzesinska A., Wrzesinski K., Filipič M., & Žegura B., Science of The Total Environment, **2021**, 755, 143255, doi: 10.1016/j.scitotenv.2020.1432557
2. Stossi F., Singh P. K., Safari K., Marini M., Labate D., & Mancini M. A., Biochemical Pharmacology, **2023**, 216, 115770, doi: 10.1016/j.bcp.2023.115770
3. Nikitaki Z., Pariset E., Sudar D., Costes S. V., & Georgakilas A. G, Cancers, **2020**, 12(11), 3288, doi: 10.3390/cancers12113288
4. Patel A. B., Shaikh S., Jain K. R., Desai C., & Madamwar D., Frontiers in Microbiology, **2020**, 11, 562813, doi: 10.3389/fmicb.2020.562813

Type of presentation: Poster

LS1-P-1 Quantifying Electron Radiation Damage in Biological Samples: Insights from Fluorescence Analysis

Amatassalam Ben Meriem[a,b], Jan Pieter Abrahams[a,b]

[a]*Basel University, Department of Structural Biology & Biophysics, Biozentrum, Basel, Switzerland*

[b]*Paul Scherrer Institute, Laboratory of Nanoscale Biology, Viligen, Switzerland*

Contact email: amatassalam.benmeriem@unibas.ch

Electron microscopy has shown a great potential in structure elucidation and imaging of biological samples due to the strong interaction of electrons with matter. However, as a major drawback, this radiation drastically affects and breaks the bonds within the studied sample. Electron radiation damage is an irreversible phenomenon. Thus, preserving the native state of a protein while reaching high resolution remains a significant challenge. In this study, we aim to quantify electron radiation damage during diffraction data collection, by establishing the relationship between the reduction of intrinsic properties and the increase in structural diversity through decay of Bragg peaks. Experimental parameters such as the energy, total dose of electrons applied and the preservation method, will be systematically examined.

Additionally, we seek to optimize crystallization strategies to obtain thinner specimens ranging from tens to hundreds of nanometers, enabling high-quality diffraction datasets. This pilot experiment is focused on a specific class of proteins usually considered to track cellular behaviour and tag molecules: fluorescent proteins. To facilitate real-time analysis of radiation damage, we are extending our transmission electron microscope (TEM) with an in-column fluorescence microscope. This setup allows us to correlate the decay of fluorescence intensity with the loss of resolution in Bragg peaks as a function of radiation damage.

By establishing this platform, we aim to robustly optimize data collection parameters to minimize radiation damage in biological samples. This research will contribute to the development of advanced techniques for preserving the structural integrity of biological specimens under electron radiation, facilitating high-resolution imaging and structure determination in the field of structural biology.

LS2 Volume electron microscopy in life sciences and tissue engineering

Type of presentation: Invited

LS2-IN-1 Shedding Light on the Molecular Mechanisms of Skin Pigmentation

Duarte Barral[a]

[a]*iNOVA4Health, NOVA Medical School, Faculdade de Ciências Médicas, Universidade NOVA de Lisboa; Lisboa, Portugal*

Contact email: duarte.barral@nms.unl.pt

Skin pigmentation is sustained by the photopigment melanin, which protects against the genotoxic effects of ultraviolet radiation. In the skin epidermis, melanin is produced by melanocytes, in melanosomes, and transferred to keratinocytes, where it is processed and forms supra-nuclear caps. Despite the crucial role of melanin secretion, transfer and processing by keratinocytes for skin pigmentation, the pathways involved remain controversial and poorly characterized. We have been studying these processes by characterizing the pathways and regulators involved, and described that melanin is transferred through exo/phagocytosis of melanocores, as well as the molecular machinery involved. We have also characterized melanin processing within keratinocytes and found that it resides in weakly acidic and weakly degradative compartments, named melanokerasomes. We also gathered evidence that melanokerasomes represent a lysosomal-derived storage compartment that has exited the lysosome cycle, allowing melanin to persist for long periods and exert its photoprotective effects. These studies provide a better understanding of the skin pigmentary system and shed light on how skin phototype is determined, as well as how basal and facultative pigmentation are regulated.

Type of presentation: Invited

LS2-IN-2 Array Tomography: A flexible and accessible approach to volume electron microscopy

Jemima Burden[a]

[a] *University College London, (London), United Kingdom*

Contact email: j.burden@ucl.ac.uk

Just as context and perspective deepen our understanding of everyday situations, they are equally vital in biological research. Whether the focus is cancer biology, neurodegeneration, cell and developmental biology, tissue engineering, or drug discovery, answering complex questions often demands a multidimensional view. Volume electron microscopy (vEM) offers precisely that: a powerful suite of techniques enabling high-resolution, three-dimensional ultrastructural imaging across 100s micron-scale volumes. When combined with correlative light or X-ray imaging for precise targeting, vEM opens doors to investigations that were previously out of reach. In this talk, I will present our accessible approach to vEM, sharing examples from a range of research areas to highlight its flexibility, transformative potential, and practical impact across disciplines.

Type of presentation: Oral

LS2-O-1 Beyond Apoptosis: Unravelling Thapsigargin-Induced Non-Apoptotic Cell Death Pathways in Immune- and Cancer Cells

Philip Steiner[a], Korollus Melek[b], Ancuela Andosch[c,d], Lena Wiesbauer[a], Anna Madlmayr[a], Hubert Kerschbaum[c] and Susanna Zierler[a,e]

[a]*Institute of Pharmacology, Faculty of Medicine, Johannes Kepler University Linz, Linz, Austria*

[b]*Institute of Biochemistry and Molecular Medicine, University of Bern, Bern, Switzerland*

[c]*Department of Biosciences and Medical Biology, Paris Lodron University Salzburg, Salzburg, Austria*

[d]*Core Facility Imaging, Center for Medical Research, Faculty of Medicine, Johannes Kepler University Linz, Linz, Austria*

[e]*Walther Straub Institute of Pharmacology and Toxicology, Ludwig-Maximilians-Universität München, Munich, Germany*

Contact email: philip.steiner@jku.at

Introduction:
The sarco/endoplasmic reticulum Ca^{2+}-ATPase (SERCA) inhibitor Thapsigargin (TG) has been an important tool in research on intracellular Ca^{2+} dynamics. In addition, its potential, along with related derivative compounds, as an anticancer therapeutic has sparked considerable interest [1]. While the prevailing hypotheses attribute TG-induced cell death to caspase-dependent apoptosis [2], our investigation reveals an alternative form of programmed cell death. This study challenges the conventional understanding, shedding light on previously unrecognized mechanisms of TG-mediated cell death.

Methods:
Our comprehensive methodology integrated advanced imaging and analytical techniques to elucidate TG's impact on immune- and cancer cells. We utilized both 2D and 3D transmission electron microscopy (TEM), coupled with morphometric analysis, to provide high-resolution ultrastructural insights. This was complemented by live-cell laser scanning microscopy (LSM) featuring real-time fluorescence imaging. Additionally, we employed cell death assays to characterize the cellular response to TG exposure.

Results:
Contrary to expectations, TG exposure did not induce hallmark apoptotic features like nuclear fragmentation or apoptotic body formation. Instead, our observations revealed a distinct morphological signature characterized by perinuclear space ballooning, extensive cellular vacuolization, mitochondrial enlargement and degradation and structural aberrations in the ER (Fig. 1 a-b). Crucially, cell death assays corroborated these findings, confirming a caspase-independent mechanism of programmed cell death following TG treatment.

Discussion and conclusions:
Our findings suggest that TG induces a form of cell death more consistent with autosis, a non-apoptotic process, rather than classical apoptosis. This conclusion is supported by the observed ultrastructural features, particularly extensive vacuolization and perinuclear space ballooning. These results challenge the prevailing paradigm of TG-induced caspase-dependent apoptosis in innate immune- and cancer cells, revealing instead an alternative cell death pathway. This mechanistic insight is pivotal for the potential development of TG as an anticancer therapeutic. Moreover, our study underscores the critical importance of comprehensive characterization of cell death mechanisms in biomedical research, highlighting the complexity of cellular responses to pharmacological modulation.

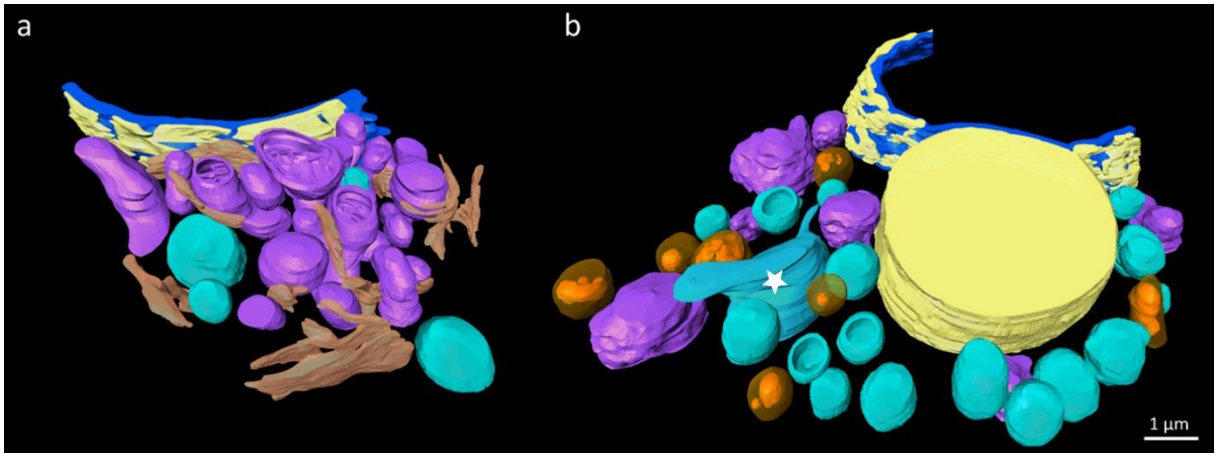


Figure 1: 3D ultrastructural comparison of control and TG-treated cell sections of RBL-1 cells. (a) 3D TEM tomogram of an untreated RBL-1 cell, displaying normal morphology and distribution of cellular components: mitochondria (purple); ER (melon); vesicles (mint); nucleus (blue); perinuclear space (yellow). (b) 3D TEM tomogram of an RBL-1 cell 30 minutes post-exposure to 2 µM TG, revealing significant ultrastructural alterations: mitochondria are enlarged, reduced in number and with irregular surface morphology; ER is no longer observable in thick tomography sections; vesicles increase in number, with infrequent irregular shapes (asterisk); enhanced cellular vacuolization; increased presence of autophagolysosomes (orange); ballooning of the perinuclear space. Scale bar (1 µm) applies to both tomograms.

References:

1. J.T. Isaacs, W.N. Brennen, S.B. Christensen, S.R. Denmeade, *Molecules*. **2021**, 26 (24)
2. A. Jaskulska, A.E. Janecka, K. Gach-Janczak, *Int J Mol Sci*. **2020**, 22 (1)

Type of presentation: Oral

LS2-O-2 Membrane Segmentation in Volumetric Electron Microscopy Data

Manca Žerovnik Mekuč[a], Tin Pren[a], Samo Hudoklin[b],
Alexander A. Mironov[c], Rok Romih[b], Matija Marolt[a], Ciril Bohak[a]

[a]*Faculty of Computer and Information Science, University of Ljubljana, (Ljubljana), Slovenia*

[b]*Institute of Cell Biology, Faculty of Medicine, University of Ljubljana, (Ljubljana), Slovenia*

[c]*FIRC Institute of Molecular Oncology, (Milan), Italy*

Contact email: ciril.bohak@fri.uni-lj.si

Introduction: Understanding the structure and function of cellular compartments—especially their 3D organization—is essential in molecular biology. Advances in microscopy now allow detailed reconstruction of cells from rich volumetric datasets. However, a key challenge is the segmentation of these large volumes. Most existing methods rely on supervised deep learning models trained on organelle-specific annotations, which limits generalizability. In contrast, we propose a membrane-centric approach. Since many cellular structures are enclosed by membranes with similar visual features, we created a dataset annotated for membranes and not for individual organelles. We then used this dataset to test several state-of-the-art segmentation methods. Our results show that a single model trained on membrane data can effectively delineate multiple compartments, suggesting a scalable strategy for broader segmentation tasks.

Methods: We used volumetric data from electron tomography of urinary bladder tissue, focusing on umbrella cells. To train the models, we manually annotated a subset of the data to serve as ground truth for segmentation. We compared five state-of-the-art methods chosen for their relevance to membrane or electron microscopy segmentation: CDeep3M [1], a cloud-enabled pipeline for 3D EM data; Ilastik [2], an interactive tool that uses classical machine learning; SAM [3], a zero-shot segmentation model from Meta AI adapted to our volumes; μSAM [4], a SAM variant tuned for high-resolution microscopy; and nnU-Net [5], a self-configuring framework widely used in biomedical segmentation. Each method was evaluated for its ability to segment membranes in the tomographic volumes, aiming to identify models that generalize across diverse membrane-bound compartments.

Results: We evaluated all models on a held-out test set. CDeep3M and Ilastik did not provide satisfactory membrane segmentations, while SAM and its microscopy-adapted variant, μSAM, also underperformed. In contrast, nnU-Net showed the best generalization and accuracy in the segmentation of membrane-bound compartments. Figure 1 compares the 2D results of all methods, while Figure 2 shows a 3D reconstruction from nnU-Net, highlighting its ability to capture membrane structures with high accuracy.

Discussion and conclusions: Our results show that a fully supervised, state-of-the-art model—nnU-Net—can successfully segment membranes enclosing a variety of intracellular compartments. Rather than relying on organelle-specific features, this approach focuses on learning the general visual features of membranes, which enables the detection of membrane-bound structures even if they were not explicitly included in the training set. This membrane-centric strategy reduces the need for extensive, compartment-specific annotations and provides better scalability and transferability compared to traditional supervised methods. Encouraged by these findings, our ongoing work is expanding our training datasets to include diverse electron microscopy modalities, such as FIB-SEM, as well as a wider range of voxel sizes and magnifications. Our goal is to develop a generalist membrane segmentation model that performs robustly under different imaging conditions and in different biological samples, including those not seen during training. Such a tool would support large-scale, automated analysis of complex cellular structures and provide valuable benefits to microscopy and cell biology research.

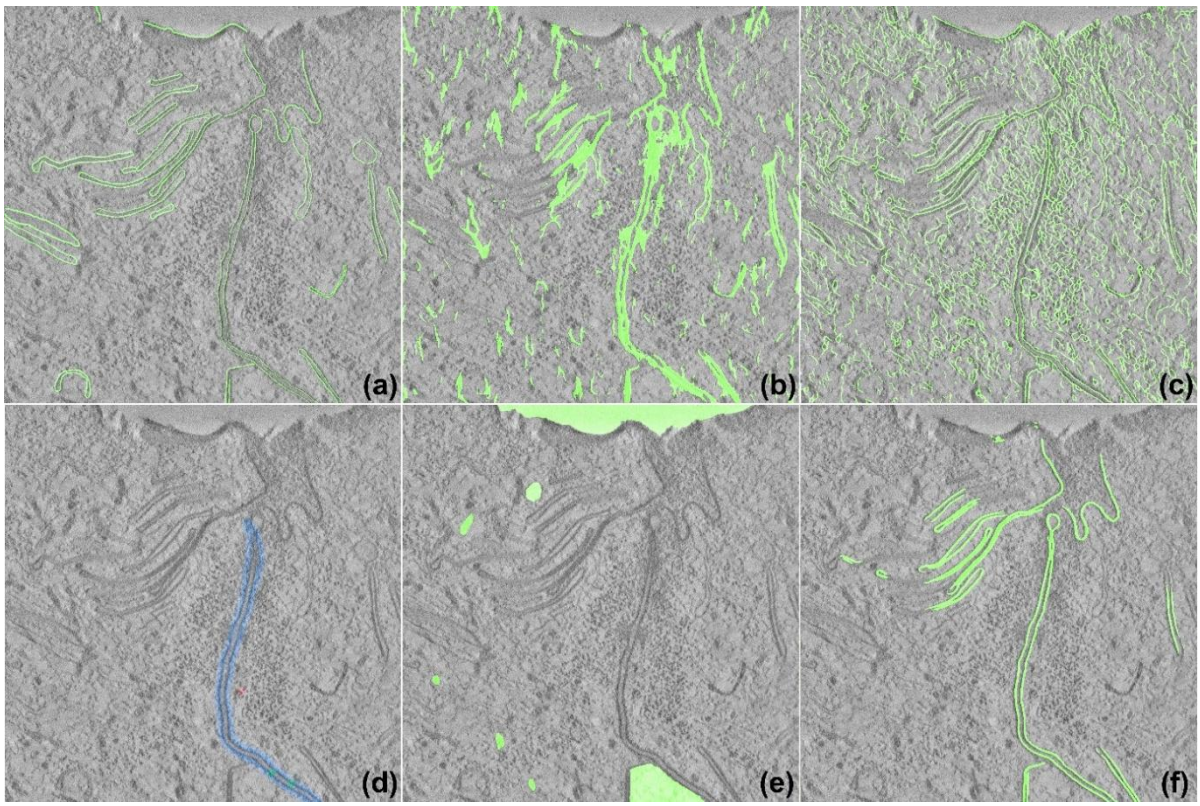


Figure 1: Comparison of segmentation results from different methods on a representative 2D slice. (a) Input electron tomography image with manually annotated ground truth, (b) CDeep3M, (c) Ilastik, (d) SAM, (e) μSAM, (f) nnU-Net.

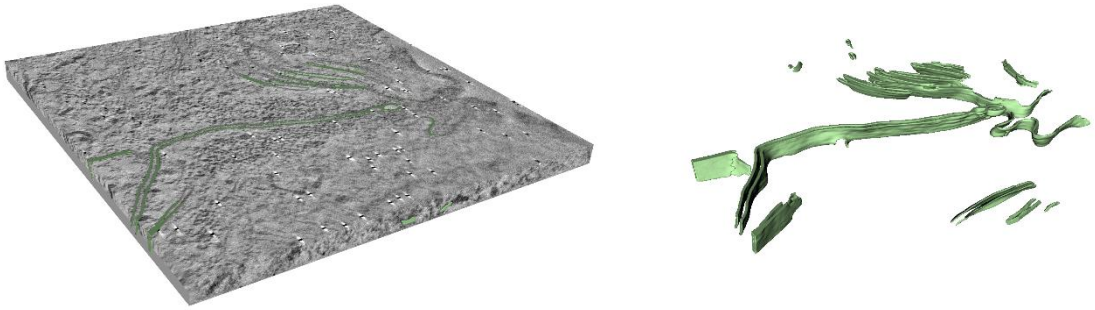


Figure 2: Example of 3D segmentation results using the best-performing method, nnU-Net. (left) Input electron tomography volume, and (right) nnU-Net segmentation output.

Acknowledgments: The work was supported by the Slovenian Research Agency research project J2-50221 – Cell visualization of unified microscopic data and procedurally generated sub-cellular structures (2024 – 2027) and Innovation Agency research core funding no. P3-0108.

References:

1. M. Haberl, et al., *CDeep3M—Plug-and-Play cloud-based deep learning for image segmentation.* **2018**, Nature methods, 15.9: 677-680.
2. S. Berg, et al., *Ilastik: interactive machine learning for (bio) image analysis.* **2019**, Nature methods, 16.12: 1226-1232.
3. A. Kirillov et al., *Segment anything*. **2023**, Proceedings of the IEEE/CVF international conference on computer vision. 2023.
4. A. Archit, et al., *Segment anything for microscopy.* **2025,** Nature Methods, 2025, 1-13.
5. F. Isensee, et al., *nnU-Net: a self-configuring method for deep learning-based biomedical image segmentation.* **2021**, Nature methods, 18.2: 203-211.

Type of presentation: Oral

LS2-O-3 Volume electron microscopy of intracellular compartments in the urinary bladder epithelium

Samo Hudoklin[a], Bruno Humbel[b], Feng-Xia (Alice) Liang[c], Manca Žerovnik Mekuč[d], Ciril Bohak[d], Matija Marolt[d], Tim Zaveršek[a], Rok Romih[a]

[a]*Institute of Cell Biology, Faculty of Medicine, University of Ljubljana, (Ljubljana), Slovenia*

[b]*Electron Microscopy Facility, University of Lausanne, (Lausanne), Switzerland*

[c]*Dep. of Cell Biology, Langone's Microscopy Laboratory, New York University, (New York), USA*

[d]*Faculty of Computer and Information Science, University of Ljubljana, (Ljubljana), Slovenia*

Contact email: samo.hudoklin@mf.uni-lj.si

Introduction: Volume electron microscopy (vEM) provides crucial information about the distribution and spatial interactions of intracellular compartments within the cells, which helps us to better understand their functions in health and disease. Several vEM methods (e.g., electron tomography – ET, focused-ion beam—scanning electron microscopy – FIB-SEM, serial block-face—scanning electron microscopy – SBF-SEM) are available that differ in mechanical requirements, sample preparation, and in volume-to-resolution aspects.
Urinary bladder epithelium (urothelium) is a highly specialized 3-layered tissue that provides blood-urine permeability barrier and is frequently used as a research model to study polarized membrane trafficking [1]. During urothelial differentiation, membrane compartments (e.g. Golgi apparatus – GA) in superficial urothelial cells are reorganized, which leads to the assembly of ER-derived transmembrane proteins termed uroplakins into urothelial particles, and hundreds of particles into urothelial plaques [2]. Two urothelial plaques line a urothelium characteristic fusiform vesicle, which transport plaques to the apical plasma membrane, where they provide a molecular basis for the permeability barrier.
Our aim was to define spatial relationships between intracellular compartments involved in the formation and transport of urothelial plaques using vEM methods.

Methods: Urinary bladders of adult mice were cryo-fixed with an EM CPC metal mirror or EM ICE high-pressure device (both Leica), freeze-substituted in AFS (Leica) with 2% OsO_4 in acetone, and embedded in Epon. ET was performed on 300 nm thick serial sections with a Tecnai 20 (FEI), running at 200 kV. Tomograms covered angles from +65˚ to -65˚ in 1˚ steps. FIB-SEM analysis was done in Helios NanoLab 650 (FEI). The dimensions of pixels were x=5.49 nm, y=5.49 nm, z=15.0 nm. For SBF-SEM samples were fixed in 4% FA + 2% GA in 0.1 cacodylate buffer, followed by incubations in ferrocyanide reduced OsO_4, thiocarbohydrazide-OsO_4 liganding and subsequent uranyl acetate and *en bloc* lead aspartate staining following the protocol of Deerinck *et al* [3]. Manual segmentation and modelling were done with IMOD software. For the purpose of developing automatic segmentation pipelines and their evaluation, intracellular compartments were manually annotated in 5 FIB-SEM sub-volumes of size 256×256×256 voxels. Convolutional neural network-based protocols for automatic segmentation of mitochondria, GA, FVs, and endolysosomes from FIB-SEM data and the annotated training dataset (UroCell) we published on Github [4].

Results: Results of ET showed that GA contains an extensive tubule-vesicular cis- and trans-GA network surrounding large GA cisternae [5]. Fusiform vesicles were flattened and positioned individually or in stacks [6]. Direct tubular contacts between GA cisternae and FVs were not observed. Using FIB-SEM, larger volumes of tissue were analysed, and connections between the GA stacks were observed. However, manual segmentation of organelles in volumetric data becomes unfeasible within a reasonable time due to the high number of sections and numerous compartments present in each one. To overcome this problem, protocols for the automatic segmentation of multiple organelles were developed and compared with other publicly available protocols [4, 7]. Segmentation metric for mitochondria and endolysosomes showed Dice similarity coefficient 0.942 and 0.882, respectively. SBF-SEM was used to provide ultrastructural overview of the urothelium ranging from basal to

superficial cell layer. First, we had to adapt the protocol of sample preparation by additionally introducing heavy metals to the sample [3] to reduce the charging and to increase the contrast during imaging. Segmentation revealed that the number of mitochondria is the lowest in the basal cells and the highest in the superficial urothelial cells. Mitochondria in intermediate cells were frequently seen in proximity to the endoplasmic reticulum. In superficial cells, mitochondria often contained lipid-resembling inclusions in the matrix.

Discussion and conclusions: In this study, we implemented three vEM methods to investigate the urinary bladder's epithelium. The data revealed that the number of intracellular compartments – such as GA, FVs, mitochondria, and endolysosomes – that contribute to the formation of urothelial plaques, as well as the complexity of their interactions, increases as cells differentiate from less-differentiated basal cells to the terminally differentiated superficial cells. However, after obtaining the raw vEM data, the biggest challenge is finding reliable, user-friendly software for automatically segmenting large volumetric datasets. There is a strong need for such software that would allow researchers to efficiently analyse large amounts of volumetric data both qualitatively and quantitatively in a short time.

Acknowledgments: This research was funded by the Slovenian Research and Innovation Agency research core funding no. P3-0108. The work was also supported by the Slovenian Research Agency research project J2-50221 – Cell visualization of unified microscopic data and procedurally generated sub-cellular structures (2024 – 2027).

References:

1. M.E. Kreft, S Hudoklin, *Protoplasma* **2010**, 246(1-4)
2. X.R. Wu, X.P. Kong, *Kidney Int* **2009**, 75(11)
3. T.J. Deerinck, E.A. Bushong, *NCMIR methods for 3D EM **2010***
4. M. Žerovnik Mekuč, C. Bohak, *Comput Biol Med* **2020**, 119
5. S. Hudoklin, K. Jezernik, *Plos One* **2011**, 6(8):e23636.
6. S. Hudoklin, K. Jezernik, *Plos One* **2012**, 7(3):e32935
7. M. Žerovnik Mekuč, C. Bohak, *Comput Methods Programs Biomed* **2022**, 223:106959

Type of presentation: Oral

LS2-O-4 Some neurons are better connected than others in locust's network of visual interneurons

Gerd Leitinger[a], Erin Cocks[b], Snjezana Radulovic[a], Robert Reimer[a], F. Claire Rind[b]

aMedical University of Graz, Gottfried Schatz Research Center, Austria

bNewcastle University, Newcastle upon Tyre, United Kingdom

Contact email: gerd.leitinger@medunigraz.at

Two neurons on either side of the locusts' brain, the lobula giant movement detectors LGMD1 and LGMD2, reliably signal impending collisions. They are connected with each facet of the compound eye by trans-medullary afferent neurons that signal increases or decreases in light levels. Uniquely, each afferent has synaptic output with the LGMD and with neighbouring afferents, in a reciprocal arrangement. Although it is known that each afferent neuron links a defined space on the dentritic tree with a defined facet, only two full length reconstructions of these neurons have been publishes so far[1], so the detailed branching and connectivity pattern of the afferent neurons remains unknown. In order to understand the functioning of the LGMD's neural circuits, we 3-D reconstructed the terminal arbours of 90 afferent neurons connected with the LGMD2. We used either serial block face scanning electron microscopy or automated tape collection ultramicrotomy for this purpose.
We found that some – appr. 10 % - of the afferent neurons differed significantly from the others, these neurons were termed «hubs » and had a signficiantly larger terminal arbour. Moreover, the « hubs » were in synaptic contact with a larger number of individual neigbours, and had significantly more synapses onto the LGMD2 than their counterparts. This signifies that signal strength is increased for certain neurons at the cost of resolution.

Sponsored by the Austrian Science Fund FWF, grant 10.55776/P32058

Keywords
Locust giant movement detector, serial block face SEM, ATUM Tome SEM

Reference:
[1] Wernitznig S *et al.*, J Comp Neurol 2022, 530:518

Type of presentation: Poster

LS2-P-1 The sexually dimorphic retina of a butterfly, from microspectrophotometry to connectomics

Monika Kos[a], Kentaro Arikawa[b], Andrej Meglič[c], Marko Ilić[a], Primož Pirih[d], Uroš Cerkvenik[a], Gregor Belušič[a]

[a]*University of Ljubljana, Biotechnical Faculty, Ljubljana, Slovenia*

[b]*The Graduate University for Advanced Studies SOKENDAI, Hayama, Japan*

[c]*University Eye Clinc, Ljubljana, Slovenia*

[d]*Paris Lodron University, Salzburg, Austria*

Contact email: gregor.belusic@bf.uni-lj.si

The silver-washed fritillary Argynnis paphia is a nymphalid butterfly with sexually dimorphic retinal mosaic. The females have the photoreceptors maximally sensitive in the ultraviolet (UV), blue (B) and green (G), whereas the males have an additional, red-sensitive (R) photoreceptor type. The R class is based upon a G-absorbing opsin, filtered through a red screening pigment. The R photoreceptors electrically inhibit a male-specific class of G photoreceptors, thus forming a green-red colour-opponent neural channel. The structure and function of the colour filter and the inhibitory synapses have remained unknown. We localized the water-soluble red pigments and measured their absorbance in semithin sections of compound eyes, fixated with gaseous formaldehyde. To identify the synapses, a stack of serial sections of the retina, obtained using a SBF-SEM microscope, was segmented with the aid of AI. Distinct synapse-like structures could be readily observed between the processes of G and R cells. Additionally, the stack yielded an excellent view of the tracheolar tapetum. Together, the anatomical data allow for a quantitative optical and electrical modeling of the primary processes that are the basis for colour vision.

Type of presentation: Poster

LS2-P-2 Ultrastructure and gene expression in tomato flower pedicel abscission zone

Magda Tušek Žnidarič[a], Maja Zagorščak[a], Živa Ramšak[a], Katja Stare[a], Marko Chersicola[a], Maruša Pompe Novak[a,b], Aleš Kladnik[c], Marina Dermastia[a]

[a]*Department of Biotechnology and Systems Biology, National Institute of Biology (Ljubljana), Slovenia*

[b]*School of Viticulture and Enology, University of Nova Gorica (Vipava), Slovenia*

[c]*Department of Biology, Biotechnical Faculty, University of Ljubljana (Ljubljana), Slovenia*

Contact email: marusa.pompe.novak@nib.si

Introduction

Abscission is a highly coordinated physiological process that enables plants to detach specific organs in response to developmental signals, hormonal regulation, and environmental stimuli. This event takes place within a specialized region known as the abscission zone (AZ) [2]. The process of cell separation is initiated by the degradation of the middle lamella, followed by cell wall disintegration and the subsequent formation of a protective barrier [3]. During abscission, vesicle-mediated transport facilitates the release of essential proteins and metabolites, which are directed toward the cell wall and middle lamella of differentiating AZ cells. In the AZ of the flower pedicel, vesicle trafficking is closely associated with a significant upregulation of genes involved in vesicle transport. Furthermore, the proximal AZ of the pedicel exhibits distinct structural features, including endoreduplicated nuclei and the presence of cytoplasmic paramural bodies, along with an array of membrane-bound vesicles containing electron-dense material [4,5,6], which may be associated with non-conventional protein secretion pathways [7]. Despite its essential role in plant development and reproduction, the molecular mechanisms underlying abscission remain insufficiently understood.

This study investigates the molecular and ultrastructural mechanisms underlying abscission in tomato flower pedicels, with a specific focus on chloroplast vesiculation. The research examines the structural degradation of chloroplasts in the AZ and links these morphological changes to differential gene expression patterns. The study particularly highlights the involvement of Senescence-Associated Gene 12 (SAG12) and Chloroplast Vesiculation (CV) in vesicle-mediated degradation pathways. Understanding these processes may provide new insights into plant senescence and organ separation, with potential applications in agriculture and plant biotechnology [1].

Methods [1]

The research utilized a combination of ultrastructural, histological, and molecular approaches to analyze chloroplast vesiculation in tomato flower pedicels. Tomato plants (*Solanum lycopersicum*) were cultivated under controlled conditions, and abscission was induced by removing flowers. Transmission electron microscopy (TEM) was employed to examine chloroplast ultrastructure and vesicle formation at different time points post-abscission induction. Laser microdissection enabled precise spatial sampling of AZ tissues for gene expression analysis. Quantitative PCR (qPCR) was conducted to assess the differential expression of key vesiculation-related genes, including SAG12, CV, CURT1A, CURT1B and CURT1C. Additionally, transcriptomic data from prior studies were reanalyzed to identify regulatory networks involved in vesiculation. The impact of ethylene on vesicle formation was evaluated by treating detached flower clusters with 1-methylcyclopropene (1-MCP), a known ethylene inhibitor [1].

Results [1]

The study revealed significant alterations in chloroplast ultrastructure following abscission induction. TEM analyses showed vesicles budding from thylakoid membranes and accumulating within the chloroplast stroma. The volume density of vesicles increased significantly, while thylakoid volume decreased, indicating a correlation between vesiculation and chloroplast degradation. Gene expression

analysis demonstrated that SAG12 and CV were strongly upregulated, suggesting their involvement in autophagy-independent chloroplast degradation. In contrast, CURT1A, which is associated with thylakoid membrane organization, was significantly downregulated. Ethylene inhibition via 1-MCP treatment delayed vesicle formation, further implicating ethylene in the regulation of these processes. Differential expression of photosynthesis-related genes, particularly those involved in the light reactions, underscored the functional consequences of chloroplast restructuring during abscission [1].

Discussion and Conclusions [1]

The discovery and confirmation of chloroplast vesiculation have significantly advanced our knowledge of chloroplast structure and function. Although initially regarded as artifacts, these vesicles have been consistently detected in various plastid types across both wild-type and mutant plants under different physiological conditions, underscoring their biological relevance. This research highlights their possible involvement in abscission, a fundamental process in plant growth and adaptation to environmental changes. Investigating the functional implications of chloroplast vesiculation within the context of abscission could provide novel insights into its contributions beyond membrane remodeling. A more comprehensive understanding of its involvement in organ separation may facilitate the identification of new molecular targets with potential applications in agricultural and biotechnological strategies [1].

Acknowledgments

The authors would like to thank Amnon Lers for his many years of friendship, fruitful collaboration, and for introducing us to the field of tomato abscission. This work was supported by the infrastructural center “Microscopy of Biological Samples” (MRIC UL, I0-0022-0481-08) located at the University of Ljubljana, Biotechnical Faculty. This work was supported by the Slovenian Research and Innovation Agency (ARIS) with grants J1-5444 and P4-0165 and a fellowship for young researchers to M.C.

References

1. Žnidarič, M., Zagorščak, M., Ramšak, Ž., Stare, K., Chersicola, M., Novak, M., Kladnik, A. and Dermastia, M. 2025. Chloroplast Vesiculation and Induced Chloroplast Vesiculation and Senescence-Associated Gene 12 Expression During Tomato Flower Pedicel Abscission. *Plant Direct* 9: e70035. https://doi.org/10.1002/pld3.70035
2. Patterson, S. E., J. L. Bolivar-Medina, T. G. Falbel, et al. 2016. Are We on the Right Track: Can Our Understanding of Abscission in Model Systems Promote or Derail Making Improvements in Less Studied Crops? *Frontiers in Plant Science* 6: 1268.
3. Roberts, J. A., K. A. Elliott, and Z. H. Gonzalez-Carranza. 2002. Abscission, Dehiscence, and Other Cell Separation Processes. *Annual Review of Plant Biology* 53: 131–158.
4. Bar-Dror, T., M. Dermastia, A. Kladnik, et al. 2011. Programmed Cell Death Occurs Asymmetrically During Abscission in Tomato. *Plant Cell* 23: 4146–4163.
5. Dermastia, M., A. Kladnik, T. Bar-Dror, and A. Lers. 2012. Endoreduplication Preferentially Occurs at the Proximal Side of the Abscission Zone During Abscission of Tomato Leaf. *Plant Signaling & Behavior* 7: 1106–1109.
6. Chersicola, M., A. Kladnik, M. T. Žnidarič, et al. 2017. 1-Aminocyclopropane-1-Carboxylate Oxidase Induction in Tomato Flower Pedicel Phloem and Abscission Related Processes Are Differentially Sensitive to Ethylene. *Frontiers in Plant Science* 8: 464.
7. Wang, X., K. P. Chung, W. Lin, and L. Jiang. 2018. Protein Secretion in Plants: Conventional and Unconventional Pathways and New Techniques. *Journal of Experimental Botany* 69: 21–37.

LS3 Structure and function of cells and organelles

Type of presentation: Invited

LS3-IN-1 Fruit fly nephrocytes: Versatile tools to study the endolysosomal system

Dávid Hargitai[a,b], Anikó Nagy[a,b], Virág Balogh[a,b], Iván Bodor[a,b], Péter Lőrincz[a,b]

[a]*Department of Anatomy, Cell and Developmental Biology, Eötvös Loránd University, Budapest, Hungary*

[b]*HAS-ELTE Momentum Vesicle Trafficking Research Group, Eötvös Loránd University, Budapest, Hungary*

Contact email: peter.lorincz@ttk.elte.hu

Lysosomes are the final destination for autophagic and endocytic degradation. Once considered mere cellular waste bags, they are now recognized as highly dynamic organelles essential for cellular homeostasis. Two primary pathways deliver cargo for lysosomal degradation: autophagy and endocytosis, and these ensure the degradation and recycling of intra- and extracellular material, respectively. Drosophila has long served as a powerful model for studying lysosome-related processes. The larval fat body is a well-established system for autophagy research, extensively used over the past two decades. While endocytosis has also been studied in flies, a standardized —comparable to the fat body in autophagy research— had been lacking.

Drosophila larval nephrocytes function as key regulators of haemolymph composition through filtration and endocytosis. Their highly infolded plasma membrane forms a network of lacunae, whose entrances are sealed by slit diaphragms. Haemolymph is filtered across the basement membrane and nephrocyte diaphragm, and particles smaller than ~10-11 nm that pass through are selectively endocytosed. This continuous endocytic activity makes nephrocytes an excellent system for investigating the endolysosomal pathway. Any disruption in the endolysosomal system leads to striking alterations in the appearance of the endosomal compartments. Furthermore, the depth of the lacunar channels is regulated by the balance between endosomal uptake and recycling, making nephrocytes a valuable tool not only for studying endolysosomal degradation but also endosomal recycling.

In my presentation, I will provide an overview of this remarkable cell type and share our latest findings obtained using nephrocytes as a model.

Type of presentation: Invited

LS3-IN-2 Insights into the surface properties of microalgae using atomic force microscopy (AFM)

Tea Mišić Radić[a]

[a]*Ruđer Bošković Insitute, Zagreb, Croatia*

Contact email: tmisic@irb.hr

Atomic force microscopy (AFM) is a technique that enables three-dimensional imaging of living cells in their native state and physiological environment with nanometer resolution. In addition, the ability of AFM to measure interaction forces in the piconewton range enables the characterization of surface properties such as elasticity, viscoelasticity, hydrophobicity and adhesion. Although AFM is increasingly used in the study of biological systems, it has not yet established itself in the study of microalgae. Microalgae, as important primary producers in the ocean, form the basis of the marine food web and play an important role in maintaining the ecological balance of marine ecosystems. One of the pioneering AFM studies on microalgae focused on diatoms and revealed fine structural details of their frustules without the need to alter the samples. While diatoms continue to dominate AFM-based microalgae research, the technique has also been applied to other microalgal classes. In addition to morphological characterization at the single cell level, AFM has also been used to study the surface properties of microalgal cells, with cell elasticity being the most commonly studied parameter. Overall, the ability of AFM for multiparametric characterization, either alone or in combination with complementary techniques, offers considerable potential to answer numerous unresolved questions in microalgae research.

Type of presentation: Oral

LS3-O-1 Recognition of a new exctracellular vesicle release mechanism

Tamás Visnovitz[a], Dorina Lenzinger[a], Lilla Lankovics[a], István Dudás[a], Tünde Bárkai[a], Krisztina V Vukman[a], Kelsey Fletcher[a], Csaba Cserép[b], Ádám Dénes[b], Péter Lőrincz[c], Gábor Valcz[a], Edit I Buzás[a,d,e]

[a] *Semmelweis University, Department of Genetics, Cell- and Immunobiology, (Budapest) Hungary*

[b] *Laboratory of Neuroimmunology, HUN-REN Institute of Experimental Medicine, (Budapest) Hungary*

[c] *ELTE Eötvös Loránd University, Department of Anatomy, Cell and Developmental Biology, (Budapest) Hungary*

[d] *HUN-REN-SU Translational Extracellular Vesicle Research Group, (Budapest) Hungary*

[e] *HCEMM-SU Extracellular Vesicle Research Group, Hungary (Budapest) Hungary*

Contact email: visnovitz.tamas@semmelweis.hu

Introduction: Extracellular vesicles (EVs) are phospholipid bilayer enclosed structures in the extracellular space with critical roles in cellular homeostasis and intercellular communication. The small extracellular vesicles (sEVs), which are 50–200 nm in size and typically of endosomal origin, have been extensively studied. [1]. However, the mechanisms of sEV biogenesis remain incompletely understood. Emerging evidence suggests that EV biogenesis is more complex than predicted previously [2]. Our findings demonstrate that various cell types, such as tumorous HT29, HepG2, non-tumorous HEK293, HEK293T-PalmGFP, cardiac (HL-1, H9c2) cell lines and primary suspension type bone marrow derived mast cells release multivesicular large extracellular vesicles (MV-lEVs). Furthermore, the presence of these MV-lEVs was confirmed in kidney, spleen, liver and heart tissues [3, 4].

Methods: The unique, MV-lEV-mediated sEV release pathway was discovered using a wide range of state-of-the-art microscopic techniques. High-resolution confocal microscopy (Leica SP8, Evident FV4000) and super-resolution nanoscopy (Zeiss Elyra SIM2, Nikon-CrestOptics DeepSIM, and Abberior Facility Line STED microscope) were employed on both fixed and live cells. Transmission electron microscopy (TEM) techniques with or without immunogold labelling were also applied. These microscopy studies were further supported by molecular techniques (including gene silencing, protein analysis) and high-resolution flow cytometry.

Results: Our findings demonstrate that all tested cell types release MV-lEVs containing intraluminal vesicles (ILVs) to the extracellular space (Fig.1a). Unlike conventional exosome release or ectosome shedding, these MV-lEVs release the ILVs as sEVs into the extracellular space through a "torn bag" mechanism upon rupture of their outer membrane Fig.1a). The observed MV-lEVs were identified as secreted amphisomes containing ILVs from both multivesicular bodies and autophagosomes (Fig.1b). The external membrane of the budding MV-lEVs is clearly derived from the plasma membrane (Fig.2g), therefore we termed the released MV-lEVs 'amphiectosomes'. By super-resolution nanoscopy, we captured consecutive stages of the intracellular amphisome formation, including fragmentation of the LC3-positive autophagosome-derived membrane and ILV formation (Fig2b-f). Amphiectosome secretion was found to be an active process, distinct from any other known extracellular vesicle release pathways. Surprisingly, while under steady state conditions, exocytosis-dependent exosome release was not observed by TEM, it was significantly induced by A23187 Ca^{2+} ionophore.

Discussion and conclusions: Our findings indicate that the release of sEVs by the "torn bag" mechanism represents a fundamental and widespread pathway for sEV secretion in non-stressed, steady-state mammalian cells, while sEVs are released primarily via exocytosis under stress conditions. This novel "torn bag" mechanism of EV secretion is distinct from the well-established exocytosis-driven exosome secretion pathway.

Acknowledgments: The research was funded by the NVKP_16-1-2016-0004, OTKA K120237, K135637, Advanced 150767 and FK 138851, EKA 2022/045-P101, LP2022-13/2022, LP2022-5/2022, VEKOP-2.3.2-162016-00002, VEKOP-2.3.3-15-2017-00016, the Higher Education Excellence Program (FIKP), TKP2021-EGA-23, RRF-2.3.121-2022-00003, 2019-2.1.7-ERA-NET-2021-00015, EU's Horizon 2020 (No. 739593), NAP2022-I-1/2022 and János Bolyai Research Scholarship of the Hungarian Academy of Sciences. The authors would like to thank the ZEISS Microscopy Customer Center Team, Auro-Science, UniCam, Györgyné Vidra and Györgyi Balogh for their help and advises.

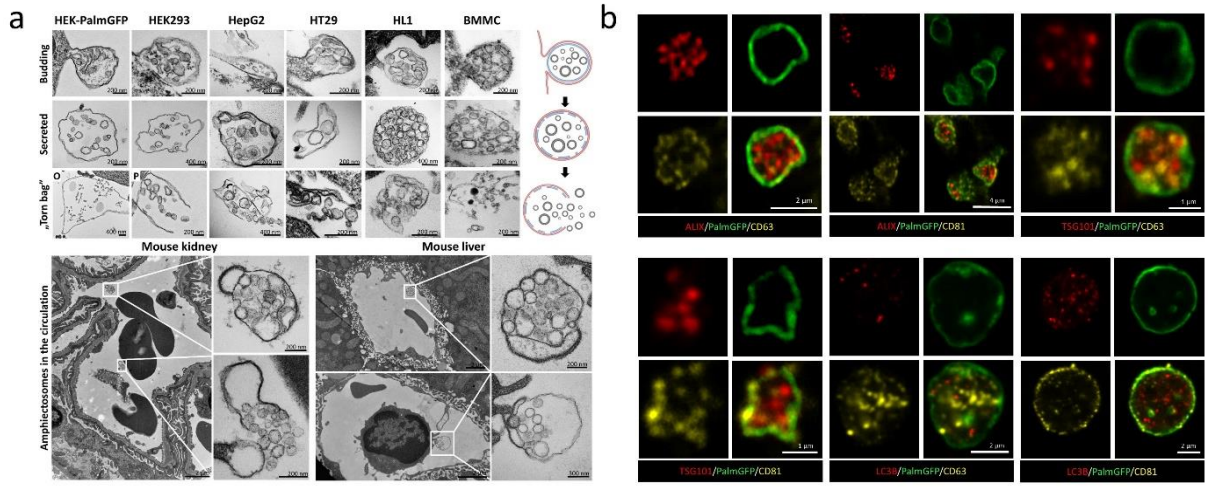


Figure 1 Detection of the release of large, multivesicular EVs by transmission electron microscopy (a) and confocal microscopy (b). Based on Visnovitz, et al., 2025.

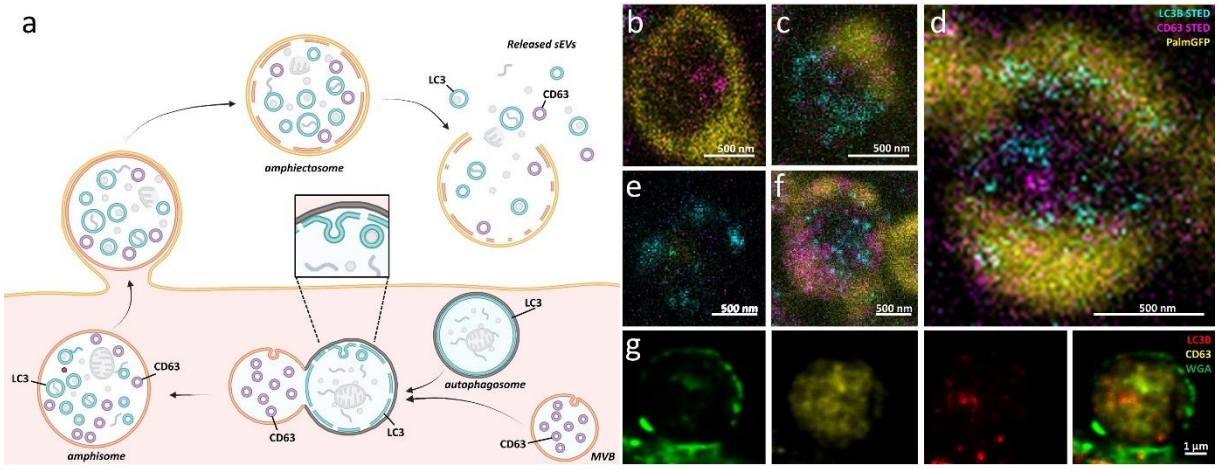


Figure 2: Amphiectosome release. Based on our data, a model of amphiectosome release was generated (a). Steps of amphisome formation including LC3 positive ILV formation by super-resolution (STED) microscopy (b-f). MVB (b), an autophagosome with Palm-GFP negative membrane (e), fusion of an autophagosome and an MVB (c), formation of LC3B positive ILVs in an amphisome (f) and a mature amphisome (e) were detected. The plasma membrane origin of amphiectosomes was verified by fluorescently labelled WGA applied *in vitro* (g). Based on Visnovitz, et al., 2025.

References:

1. J.A. Welsh, et al., *Journal of Extracellular Vesicles* **2024,** 13(2): p. e12404.
2. E.I. Buzas *Nat Rev Immunol.* **2023,** 23(4): p. 236-250.
3. G. Valcz, et al., *Journal of Extracellular Vesicles* **2019,** 8(1): p. 1596668.
4. T. Visnovitz, et al., **2025,** *eLife* 13:RP95828.

Type of presentation: Oral

LS3-O-2 Nanoalgosomes as observed by scanning and cryogenic transmission electron microscopes

Anna Romolo[a], Jelena Danilović Luković[b], Venkata S.R. Jampani[c], Lars Gedda[d], Katarina Edwards[d], Matej Hočevar[e], Apolonija Bedina Zavec[f], Matic Kisovec[f], Aleš Iglič[g], Veronika Kralj-Iglič[a]

[a]*University of Ljubljana, Faculty of Health Sciences,* (*Ljubljana*), *Slovenia*

[b]*University of Belgrade, Institute for Multidisciplinary Research,* (*Belgrade*), *Serbia*

[c]*Institute J.Stefan,* (*Ljubljana*), *Slovenia*

[d]*Uppsala University, Department of Chemistry – Ångström, Physical Chemistry,* (*Uppsala*), *Sweden*

[e]*Institute for Metals and Technology,* (*Ljubljana*), *Slovenia*

[f]*National Institute of Chemistry,* (*Ljubljana*), *Slovenia*

[g]*University of Ljubljana, Faculty of Electrical Engineering,* (*Ljubljana*), *Slovenia*

Contact email: veronika.kralj-iglic@zf.uni-lj.si

Introduction: Microalgae are important actors in creation of the atmosphere and are due to their ability to adapt and survive in harsh environments also potential modulators of space. It is of interest to study their properties and interactions within the microalgal society which includes also other microorganisms. Although previously observed, microalgae EPs (called nanoalgosomes) have recently been systematically studied [1,2]. Here, scanning electron images and cryogenic transmission electron images of microalgae, extracellular particles (EPs) found in microalgae cultures and EPs isolated from conditioned media of different microalgae species are presented. We observed *Hematococus pluvialis, Phaeodactylum tricornutum* and *Tetraselmis chuii* by using scanning electron microscopy (SEM) and cryogenic electron microscopy (cryoTEM).

Methods: Cultures of *Hematococus pluvialis*, *Phaeodactylum tricornutum* CCAP 1052/1A ,and *Tetraselmis chuii* CCAP 66/21b were from the Culture Collection of Algae and Protozoa (CCAP) of SAMS (Oban, Scotland). The medium for *Phaeodactylum tricornutum* and *Tetraselmis chuii* was prepared by adding edible salt and enrichment solution to the sterilized water. The medium for *Hematococus pluvialis* was prepared according to the CCAP procedure [3]. Microalgae were grown in borosilicate bottles, in respirometer under controlled light, gas and temperature condition, or in natural ambient with controlled temperature. *Tetraselmis chuii* was treated by osmotic schock which caused shedding off of the flagellae. EP were isolated from the suspension containing collected flagellae. A sample of conditioned medium was taken for imaging. Also, EPs were isolated by differential ultracentrifugation. For SEM with contrast, samples were loaded onto Cellulose Ester filters and incubated in 2% OsO_4 for two hours. Then the osmium was removed and the samples were dehydrated in a graded series of ethanol, treated with hexamethyldisilazane, air-dried, sputtered with Au/Pd (PECS Gatan 682) and examined with a JSM-6500F Field Emission Scanning Electron Microscope (JEOL Ltd., Tokyo, Japan). For minimally invasive preparation of the sample, the aluminum stands that enter the SEM chamber were covered with nano-thin film of cyanoacrylate polymer, which created hydrophobic surface. We mounted a few microliters of unfixed sample onto this surface and let it dry in air. The samples were observed under the Thermo Fisher Scientific Apreo 2 with EDS/EBSD, LOW vacuum mode SEM. We imaged *T. chuii* nanoalgosomes with two cryo-TEM microscopes: (i): C-flat™ 2/2, 200 mesh holey carbon grids (Protochips, Morrisville, NC, USA) were glow-discharged at 60s, 20 mA, air atmosphere, positive polarity (GloQube ® Plus, Quorum, Laughton, UK). We applied 3 µL of sample to the grid. Then, the sample was blotted and vitrified in liquid ethane on Vitrobot Mark IV (Thermo Fisher Scientific, Waltham, MA, USA). Vitrobot conditions were as follows: 100% relative humidity, blot force: 2, blot time: 7 s and 4 °C. Samples were visualized under cryogenic conditions. We used a 200 kV Glacios microscope with Falcon 3EC detector (Thermo Fisher Scientific, Waltham, MA, USA).

(ii): a 300 mesh carbon grid was prepared with a holey polymer film and glow discharged. The sample containing nanoparticles in suspension was applied to the grid at 25°C in high humidity, blotted, and vitrified in liquid ethane. Samples were visualized under cryogenic conditions using a 80 kV Zeiss TEM Libra 120 transmission electron microscope with BioVision Pro-SM slow scan CCD.

Results: We have observed different types of nanoalgosomes in samples with different microalgae species. Nanoalgosomes from *P. tricornutum* and *H. pluvialis* were numerous in conditioned medium. The size of these EPs were homogeneous within the species and nanoalgosomes had globular shape. Nanoalgosomes isolated from the *T. chuii* flagellae suspension had largely rod-like shape. CryoTEM revealed the ultrastructure of these shapes indicating that they are hairs and scales detached from the flagellae.

Discussion and conclusions: The advantage of SEM is to observe nanoalgosomes directly in the conditioned medium thus avoiding isolation procedure that can be detrimental to EPs in the sample. Cryo-TEM is however superior to determine the identity of the particles in the sample by providing their ultrastructure, however, cells and larger fragments should be removed prior to the observation. Combination of both, SEM and cryo-TEM is optimal. Preparation of the sample for SEM on the cyanoacrylate polymer surfaces and its examination in low vacuum yielded quality images at considerably shorter preparation time (about 1 hour) comparing to the method requiring fixation, staining and drying (one to two working days).

Acknowledgments: The authors acknowledge the financial support from the Slovenian Research and Innovation Agency core founding No. P1-0099, P2-0232, P3-0388, P1-0391, and IO-0003, projects No. N1-0400, J2-4427, J2-4447, and J3-60063, the University of Ljubljana interdisciplinary preparative project Nanostructurome 802-12/2024-5, and by the Science Fund of the Republic of Serbia, Grant No. 7078– BioSynthClust

1. Adamo, G.; Fierli, D.; Romancino, D. P.; et al. Nanoalgosomes: Introducing Extracellular Vesicles Produced by Microalgae. *J. Extracell. Vesicles* **2021**, *10*, e12081.
2. Picciotto, S.; Barone, M. E.; Fierli, D.; et al. Isolation of Extracellular Vesicles from Microalgae: Towards the Production of Sustainable and Natural Nanocarriers of Bioactive Compounds. *Biomater. Sci.* **2021**, *9*, 2917–2930.
3. Bischoff, H. W.; Bold, H. C. Phycological Studies IV. Some soil algae from Enchanted Rock and related algal species. *U. Texas Pub*. **1963**, No. 6318.

Type of presentation: Oral

LS3-O-3 Immunolocalisation of mechanosensory proteins PIEZO and TRPV4 in the urinary bladder urothelium: which method to believe?

Rok Romih[a], Maja Deutsch[a], Dominika Peskar[a], Andreja Erman[a]

[a]*Institute of Cell Biology, Faculty of Medicine, Ljubljana, Slovenia*

Contact email: rok.romih@mf.uni-lj.si

Introduction: The urinary bladder undergoes repeated cycles of filling and voiding. The degree of tension in the bladder wall must be sensed and transduced to the nervous system, otherwise the bladder dysfunction ensues. Many studies suggest that membrane cation channels PIEZO and transient receptor potential vanilloid (TRPV) channels are activated by mechanical stretch, which in turn enables the release of ATP and NO from the cells [1]. However, there is still a controversy regarding the localisation of different classes of sensory proteins in the urinary bladder wall. Here, we focused on the epithelium of the bladder wall, the urothelium. We tested various antibodies against PIEZO1, PIEZO2 and TRPV4 and used various microscopic approaches.

Methods: Mouse urinary bladders were prepared for immunofluorescence on frozen sections (IF-Fr), "en face" immunofluorescence (en face IF) and immuno-electron microscopy (iEM). For IF-Fr, the bladder halves were fixed with 4% formaldehyde, embedded in OCT medium, cut, and immunolabelled with primary antibodies and secondary antibodies labelled with Alexa Fluor 488. For en face IF, bladders were cut into 2 x 2 mm pieces, fixed and immunolabeled as for IF-Fr. The cell nuclei were stained with DAPI. IF-Fr and en face IF samples were imaged with a fluorescence microscope (AxioImager Z.1, Zeiss) and confocal microscope (Zeiss LSM 900; Zeiss), respectively. For iEM, bladders were cut into 1 mm^3 pieces, fixed in 2% formaldehyde plus 0.05% glutaraldehyde, dehydrated in graded alcohols with lowering the temperature to -50 °C and embedded in Lowicryl HM20. Ultrathin sections of bladder tissue were labelled with primary antibodies and then with secondary antibodies conjugated to 12 nm gold, counterstained and analysed by transmission electron microscope (TEM). Polyclonal primary antibodies against PIEZO1 were from Novus Biologicals (NBP2-75617) and Proteintech (15939-1-AP, 28511-1-AP), against PIEZO2 from Novus Biologicals (NBP1-78624) and Proteintech (26205-1-AP), while primary antibodies against TRPV4 were from Abcam (ab39260) and LS Bio (LS-C94498).

Results: PIEZO1 was detected in the urothelium with both Proteintech antibodies. IF-Fr showed a strong reaction in basal and intermediate urothelial cells (Figure 1a), while en face IF reaction was weaker and mainly limited to the plasma membranes of urothelial cells (Figure 1b). PIEZO2 was detected in the urothelium only with Proteintech antibody. The IF-Fr immunoreaction was similar to that of PIEZO1 (Figure 1c). On the other hand, the reaction with the en face IF was stronger although some nonspecific labelling was observed, as evidenced by the presence of fluorescence in the cell nuclei (Figure 1d). TRPV4 labelling with antibodies from Abcam was mostly confined to the plasma membranes of basal and intermediate urothelial cells and basolateral plasma membrane of superficial urothelial cells (Figure 2a). With iEM, gold nanoparticles were detected only on the plasma membranes, but the number of gold particles was low (Figure 2b).

Discussion and conclusions: We have shown that an appropriate selection of antibodies in combination with various microscopic methods detect the mechanosensory proteins PIEZO1, PIEZO2 and TRPV4 in the plasma membranes of the basal and intermediate cells of normal mouse urinary bladder urothelium. TRPV4 is clearly detected on the basolateral plasma membranes of the superficial (umbrella) cells. In our study, this localisation is not clearly confirmed in the case of either PIEZO channel. Detection of cation channels studied here is in agreement with their proposed function. Namely, their activation by bladder stretching can lead to the rise of cytoplasmic Ca^{2+} concentration, which elicits the release of chemical mediators from cells [1]. Mediators then bind to receptors of cells in the lamina propria (LP), particularly on the afferent nerve endings, which transmit information to the central

nervous system. In the future, we plan to investigate these mechanoreceptors in interstitial cystitis/bladder pain syndrome (IC/BPS). IC/BPS is a chronic bladder disorder characterized clinically by recurring episodes of pelvic pain and increased urination frequency, significantly impairing patients' quality of life [2]. We hypothesise that alterations of expression and localisation of PIEZO1, PIEZO2 and TRPV4 in the urothelium play an important role in in the dysfunction of urinary bladder, related to IC/BPS.

Acknowledgments: The study was supported by the ARIS grant P3-0108.

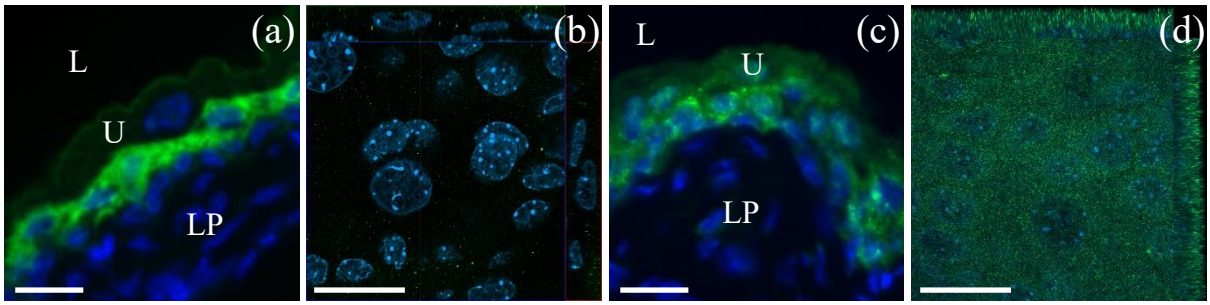


Figure 1: PIEZO1 (a, b) and PIEZO2 (c, d) are seen in basal and intermediate urothelial cells (green fluorescence). Immunofluorescence on frozen sections with vertical view of the urothelium (a, c). Immunofluorescence on tissue piece with "en face" view of the mouse urothelium (b, d). Bars: 20 µm.

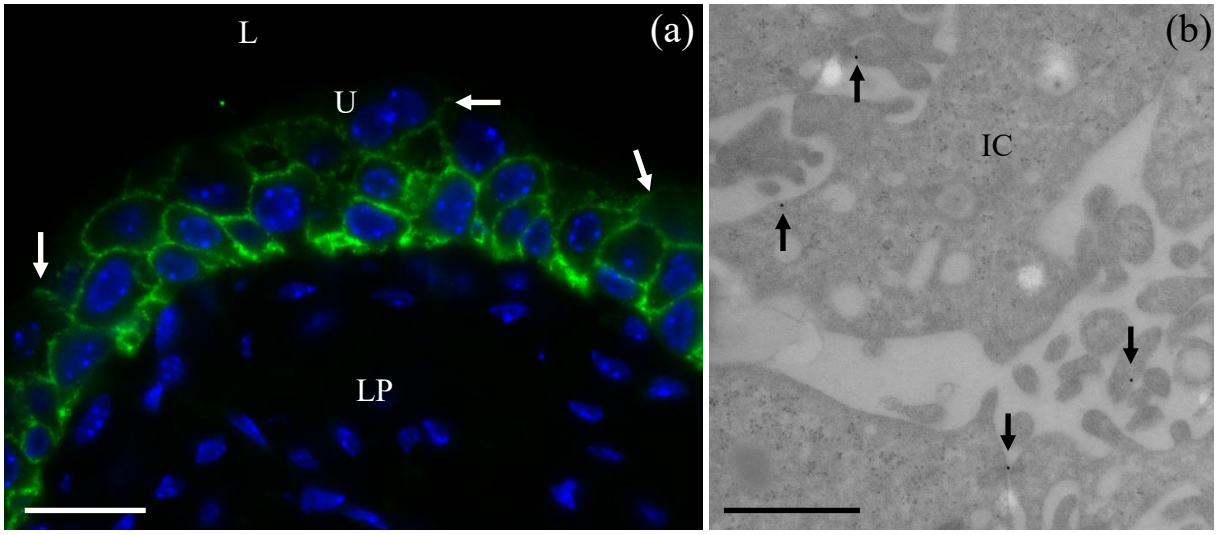


Figure 2: TRPV4 is seen in plasma membranes of urothelial cells in frozen section (a) and in ultrathin section (b). Arrows show the labelling of basolateral plasma membranes between adjacent umbrella cells (a) and the localization of gold particles on the plasma membranes of the intermediate urothelial cells. L = bladder lumen, U = umbrella cell, LP = lamina propria, IC = intermediate cell. Bars: 20 µm (a), 500 nm (b).

References:

1. Mutafova-Yambolieva VN, *Purinergic Signal.* **2024**, *https://doi.org/10.1007/s11302-024-10063-6.*
2. Jiang YH, *Int J Mol Sci.* **2023**, 24(1):820.

Type of presentation: Oral

LS3-O-4 Mysteries of crustacean armour: a combined approach to scale formation

Ana Žuran[a], Miloš Vittori[a]

[a]*University of Ljubljana, Biotechnical Faculty, Department of Biology, Ljubljana, Slovenia*

Contact email: ana.zuran@bf.uni-lj.si

Terrestrial isopods (Oniscidea) are a group of crustaceans that have successfully adapted to life on land, in part due to their finely structured and mineralised exoskeletal cuticle. The cuticle is a complex extracellular matrix deposited by the epidermis during development and moulting in adults [1]. In many species, the outermost cuticular layer, called the epicuticle, forms various structures such as scales and other surface ornaments, often with a complex 3D architecture. Although these structures influence the surface properties of the cuticle and may play an important role in the conquest of different terrestrial habitats [2, 3], the cellular mechanisms underlying their formation are still unknown. The aim of this study was to decipher the mechanisms of epicuticular scale formation on the dorsal surface of the species *Porcellio scaber* and *Armadillidium pallasii* during moult.

For the analysis, dorsal plates (tergites) of *P. scaber* and *A. pallasii* specimens at different stages of cuticle deposition during preparation for moult [4] were dissected, chemically fixed with aldehydes, decalcified, and post-fixed with OsO_4. Scanning electron microscopy was used to observe the 3D architecture of the scales, while their ultrastructure was analysed in relation to the ultrastructure of the underlying epidermal cells using transmission electron microscopy.

The fully formed scales of *P. scaber* and *A. pallasii* have distinctly different architectures, but our results show that they are formed by a similar mechanism. The deposition of the epicuticle and scales begins at the earliest premoult stage in both species. Initially, the epidermal cells that deposit the cuticle form finger-like projections on the apical surface that outline the edges of the new scales and serve as a scaffold for scale deposition. While more material is deposited, the scales gradually take shape. As they approach their final form, the cellular projections are likely to retract as they are no longer evenly distributed across the cross-section of the scales. Once the deposition of the next cuticular layer, i.e. the exocuticle, begins, the new scales are already fully formed and are indistinguishable from the scales on the surface of the old cuticle.

Our results reveal an intricate cellular mechanism responsible for the formation of complex surface structures in terrestrial crustaceans and provide valuable insights into evolutionary adaptations in arthropods. Furthermore, preliminary results indicate that this mechanism is driven by cytoskeletal reorganisation. Our future efforts will therefore focus on fluorescence visualisation of cytoskeletal elements during scale formation.

Acknowledgments:
This work has been supported by the infrastructural center "Microscopy of biological samples", (MRIC UL, I0-0022-0481-08) located at the University of Ljubljana, Biotechnical faculty, and the Slovenian Research and Inovation Agency (ARIS, P1-0184, scheme for young researchers).

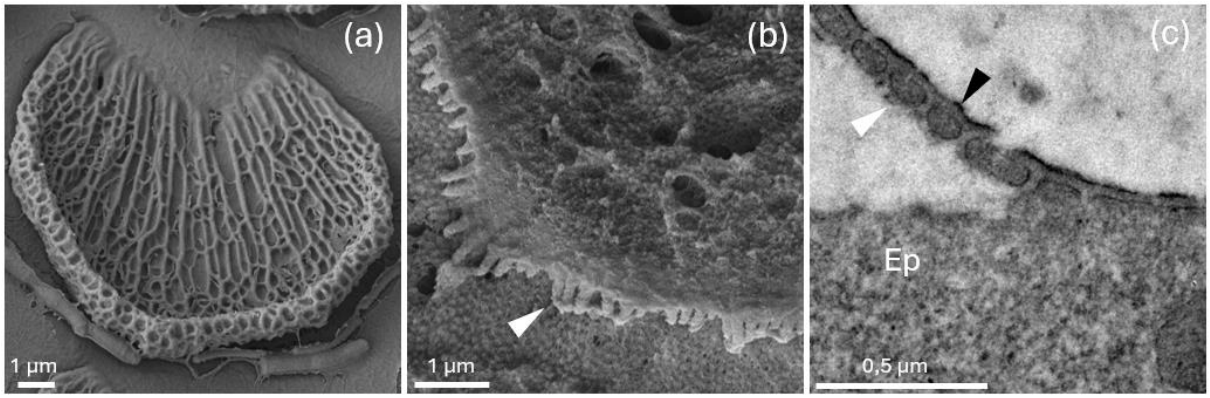


Figure 1: Formation of an epicuticular scale on the dorsal surface of the isopod species *P. scaber*. A fully formed scale in a freshly moulted specimen (a). Scanning (b) and transmission electron micrograph (c) of a scale in the initial stage of cuticle deposition: cell projections (white arrowheads) are visible on the apical surface of the epidermis (Ep) on which the epicuticle/scale (black arrowhead) is deposited.

References:

1. S. Sfenthourakis, S. Taiti, *Zookeys*, **2015**, *515*, 13–25.
2. H. Schmalfuss, *Zoomorphologie*, **1978**, *91*, 263–274.
3. M. Vittori, I. Gantar, *Arthropod Struct. Dev*, **2020**, *58*, 100968.
4. P. Zidar, D. Drobne, J. Štrus, *Crustaceana*, **1998**, *71*, 646-654.

Type of presentation: Poster

LS3-P-1 Protective effect of ferulic acid in monosodium glutamate-induced kidney injury: alight and transmission electron microscopical study

Merve Acikel Elmas[a], Gokcen Ozgun [b], Anil Can [b], Seda Sezer [a c], Serap Arbak [a]

[a]*Acibadem Univ., School of Medicine, Dept. of Histology and Embryology, (Istanbul), Turkiye*

[b]*Acibadem Univ., Institute for Health Sciences, Dept. of Medical Biotechnology, (Istanbul), Turkiye*

[c]*Okan University, School of Medicine, Dept of Histology and Embryology, (Istanbul), Turkiye*

Contact email: arbaks@yahoo.com

Introduction: Monosodium glutamate (MSG), used as a flavour enhancer, can cause harmful effects in different organs, including liver, kidney and central nervous system [1]. MSG is known to cause kidney injury by generation of reactive oxygen species leading to damage of lipids, proteins, and DNA through generation of free radicals. Ferulic acid (FA), as a strong antioxidant, is claimed to ameliorate the harmful effect of biomolecules by suppressing/regulating the production of reactive species and the oxidative stress [2].

The aim of this study was to investigate the therapeutic effect of ferulic acid which is known to have antioxidant and anti-inflammatory properties on MSG-induced experimental kidney injury using histopathological and ultrastructural methods.

Methods: In this study, male Wistar albino rats (7 weeks old, 160-200g) were used and kept in a laboratory environment with a temperature of 22±2°C and a standard light/dark (12/12 hours) cycle throughout the experimental period. Rats were randomly divided into 5 groups (n:8/group). Control group was administered with 1 ml of distilled water by gavage every day during the experiment for 38 days. Rats in the DMSO+FA group were administered 1 ml of dimethyl sulfoxide (DMSO) for 28 days and FA solution (25mg/kg, dissolved in DMSO) by gavage in the last 10 days of the experiment. To induce an MSG-induced kidney injury, MSG solution (600 mg/kg, dissolved in DMSO) was orally given to the rats (MSG group) for 28 days. MSG+DMSO group was treated by MSG solution (600 mg/kg, dissolved in DMSO) by gavage for 28 days and 1 ml of DMSO was given by gavage on the last 10 days of the experiment. MSG solution (600 mg/kg) for 28 days and then FA solution (25 mg/kg) on the last 10 days of the experiment were given orally to the rats in the treatment group (MSG+FA). At the end of the experiment the rats were sacrificed under anesthesia. Tissue samples from the kidney tissues were processed for light and transmission electron microscopical evaluations. Paraffin sections were stained with Hematoxylin-eosin (H&E) and Periodic acid-Schiff reaction (PAS). Renal injury, based on tubular and glomerular degeneration, inflammatory cell infiltration, and vasocongestion has been scored light microscopically by using a scale ranging from 0 to 3 (0: none; 1: mild; 2: moderate; and 3:severe) for each criterion. Glomeruli and renal tubules were ultrastructurally investigated by using convential transmission electron microscopical tissue processing methods.

Results: The light microscopical examinations revealed prominent renal tissue injury in MSG and MSG +DMSO groups, with degenerated glomeruli, vacuolization in renal tubular cells and decreased PAS positivity of basal membranes of both glomeruli and proximal and distal convoluted tubules. These degenerations were mildly observed in MSG+FA group, suggesting a ameliorating effect of FA. Ultrastructural investigations at transmission electron microscopical level revealed similar findings as in light microscopy with a prominent amelioration in MSG+FA group whereas MSG and MSG +DMSO groups displayed severe damage mostly at basal membranes of glomeruli and renal tubules.

Conclusion: Regarding the light and transmission electron microscopical results,, we could suggest that administration of ferulic acid to the rats in this experimental model of MSG-induced kidney degeneration contributed significantly to the amelioration of the kidney parenchymal damage by decreasing the oxidative stress through regulating the formation of reactive oxygen species.. We could conclude that ferulic acid reduces nephrotoxic damage induced by MSG and has healing properties for kidneys.

References:

1. A. Sharma, J of Biomedical Sci. **2015**, 22, 93.
2. V. Erseçkin, K. Irak, S. Yildirim, N. Mert, Drug Chem Toxicol. **2022**, 45(2), 663-669.

Type of presentation: Poster

LS3-P-2 Ultrastructural changes of the injured renal tissue in the cage-reared rainbow trout Oncorhynchus mykiss (Walbaum, 1792)

Marina Ugrin[a], María Fernandez Godoy[b], Ivana Restović[c], Jerko Hrabar[d], Nives Kević[e] and Ivana Bočina[e]

[a]*Ph.D. study of Biophysics at the Faculty of Science, University of Split, Split, Croatia,*

[b]*Faculty of Sciences, University of Málaga, Málaga, Spain*

[c]*Faculty of Humanities and Social Studies, University of Split, Split, Croatia*

[d]*Institute of Oceanography and Fisheries, Split, Croatia*

[e]*Faculty of Science, University of Split, Split, Croatia*

Contact email: bocina@pmfst.hr

Introduction: Fish, commonly used as bioindicators in ecotoxicology, are particularly sensitive to environmental pollutants due to their aquatic lifestyle [1]. Pollutants and toxicants often accumulate in metabolic organs such as the liver and kidney, leading to histological damage [2]. In cage-reared fish, specific environmental and feeding conditions influence their susceptibility to kidney injuries. Cage-reared fish are fed artificial diets designed to promote commercial growth and are confined to limited spaces, making them vulnerable to infections and environmental stressors. To mitigate these risks, preventive treatments, including antibiotics and chemicals, can exacerbate kidney damage in these fish [3].

Methods: Kidney tissues from 40 samples of four different growth stages of cage-reared rainbow trout were used to determine morphological changes. A haematoxylin- eosin staining revealed changes in renal glomeruli and tubules. Transmission electron microscopy (TEM) was used to confirm changes and to assess the severity of these changes on the ultrastructural level.

Results: TEM analysis (Fig.1) revealed apoptotic changes in the glomeruli, an anomalous Bowman's capsule and glomerular basement membrane, as well as, fragmented nuclei with condensed chromatin, and irregularly shaped podocytes with a significant loss of foot processes. Significant ultrastructural changes were particularly evident in the proximal and distal tubules, which exhibited altered mitochondrial morphology, vacuole formation, and apoptotic cells, further confirming structural damage in the renal tissue.

Conclusion: TEM analysis revealed key ultrastructural alterations associated with nephropathy, in glomeruli and particularly in the renal tubules of cage reared rainbow trout, suggesting that environmental conditions, as well as, preventive treatments and feeding habits of cage-reared fish could seriously affect kidney tissues. Future studies should involve expression patterns of nephropathic markers in injured renal tissue of the cage-reared fish.

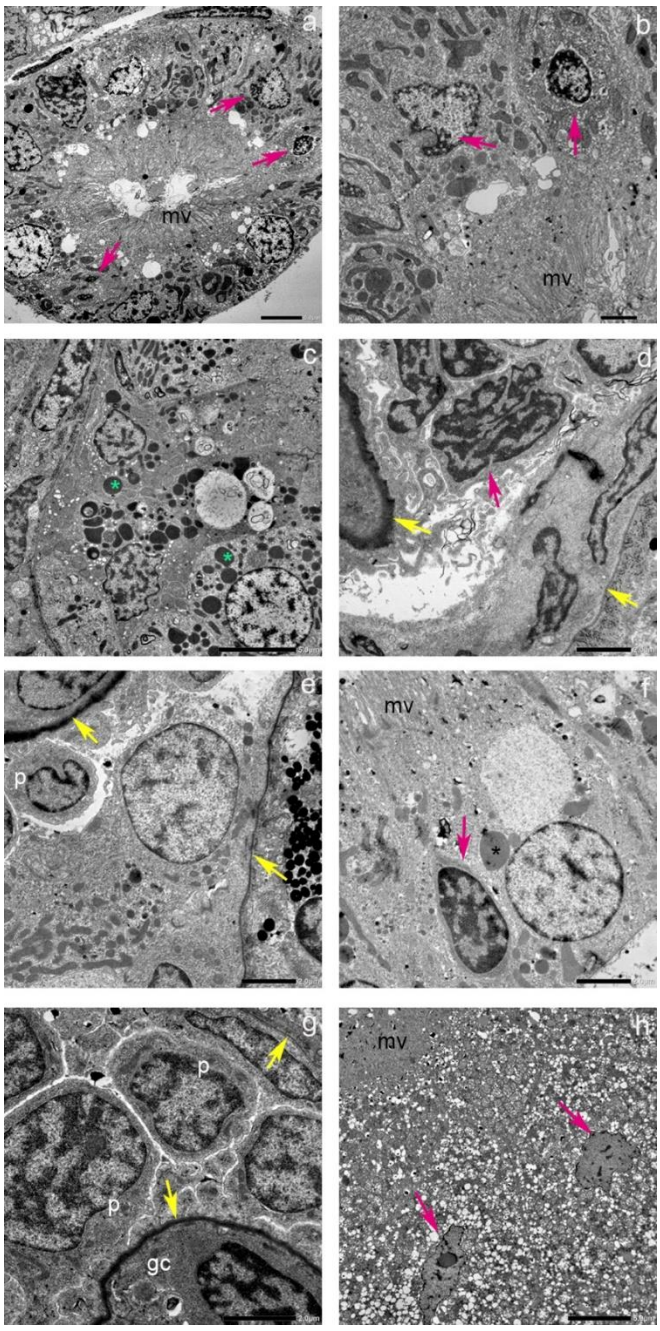


Figure 1. A cross sections throughout the kidney tissue in four growth stages of rainbow trout *Oncorhynchus mykiss*. (a,b) – growth stage I; (c,d) – growth stage II; (e,f) – growth stage III; (g,h) – growth stage IV. Pink arrows – apoptotic cells and nuclei; yellow arrows – capsular and glomerular basement membranes; gc – glomerular capillary; p – podocytes; mv – microvilli; asterix – lipid droplets.

References:

1. O.B. Okwuosa, J.E. Eyo, E.E. Omovwohwovie, *IRE Journals* **2019**, *2*, 354-368.
2. M.M.P. Camargo, C.B.R. Martinez, *Neotrop. Ichthyol.* **2007**,*5*, 327-336.
3. M. I. Abubakar, I. Adeshina I, I. Abdulraheem, S. Abdulsalami, *Acta Biol.* **2019**, *26*,19-30.

Type of presentation: Poster

LS3-P-3 Histopathology of the gills of farmed common carp (*Cyprinus carpio*): a bioindication method

Aleksandra Dobričić[a], Zoran Marković[a], Božidar Rašković[a]

[a]*Faculty of Agriculture, University of Belgrade, (Belgrade), Serbia*

Contact email: aleksandra.dobricic@agrif.bg.ac.rs

Introduction: Freshwater ecosystems have experienced a progressive deterioration in water quality in recent decades, primarily due to anthropogenic activities. Conventional approaches to detect pollutants by analytical methods are often resource-intensive and time-consuming, while the impact on the organisms inhabiting aquatic ecosystems is difficult to assess. In contrast, bioindicators offer an alternative for monitoring environmental pollutants and can serve as an early warning mechanism. An ideal biological indicator should have characteristics such as wide distribution and abundance, strong indicative capacity and thorough scientific characterisation [1]. In Teleostei, the gills serve as the main organ for gas exchange between the bloodstream and the aquatic environment. Structurally, the gills consist of four pairs of gill arches, each bearing two rows of protruding gill filaments (primary lamellae). Secondary lamellae extend from the primary lamellae, which substantially increase the entire respiratory surface area. The primary lamellae are lined with stratified epithelium that harbours specialised cells, with mucous and chloride cells being the most abundant. The surface of the secondary lamellae is covered with pavement cells. Due to their large surface area and constant direct contact with the surrounding water, gills are highly susceptible to damage by pollutants, even at low concentrations, making them a reliable and sensitive biological indicator for environmental monitoring [2].

Methods: In this study, the gill histology of common carp (*Cyprinus carpio*) reared in semi-intensive culture in ponds was used as a bioindicator of aquatic pollution. The water in the carp farms in Serbia usually comes from nearby rivers and is not treated before being transferred into the ponds. Fish sampling was conducted during three seasons in 2024 (spring, summer and autumn) in four fish farms, —three of which were supplied by river water (Tisza, Tamis and Danube) and one by an artesian well in a fish farm at the University of Belgrade. One-year-old common carp were anesthetized with clove oil followed by spinal cord severance. The second gill arch from the left side of the fish was excised for histological examination, fixed in 4% buffered formalin for 48 hours and subsequently transferred to 70% ethanol for storage until further processing. Histological staining of the tissue was performed with haematoxylin and eosin (H&E). Gill tissue alterations were assessed using the methodology developed by Bernet *et al*. [3], which classifies histopathological changes into five different reaction patterns. Each pattern comprises a series of alterations that affect either specific functional components of the gills or the organ as a whole. The defined reaction patterns are as follows: (1) Circulatory disturbances (e.g., hemorrhage, hyperemia, aneurysms and intercellular edema); (2) regressive changes (including architectural and structural disorganization, plasma and nuclear alterations, deposits, atrophy and necrosis); (3) progressive changes (such as hypertrophy and hyperplasia); (4) inflammatory responses (characterised by exudate formation, activation of the reticuloendothelial system and cellular infiltration); and (5) neoplastic changes (including benign and malignant tumour formations). Each observed alteration is assigned an importance factor from 1 to 3, indicating its pathological significance — from minor to irreversible damage. In addition, a semi-quantitative scoring system is used to assess the severity and extent of each alteration on a scale of 0 to 6, with 0 indicating the absence of pathological changes and 6 indicating the presence of severe, diffuse lesions in the tissue.

Results: Preliminary histopathological examination of the gills revealed several significant alterations indicating environmental stress and exposure to pollutants. Among the most frequently observed changes were mainly those of the first category (in terms of importance factor) such as marked hyperemia and vascular stasis. Hyperplasia of both the mucosal cells and the primary epithelium (Fig. 1) was consistently present in all samples analysed. Oedema of the primary lamellae was also present.

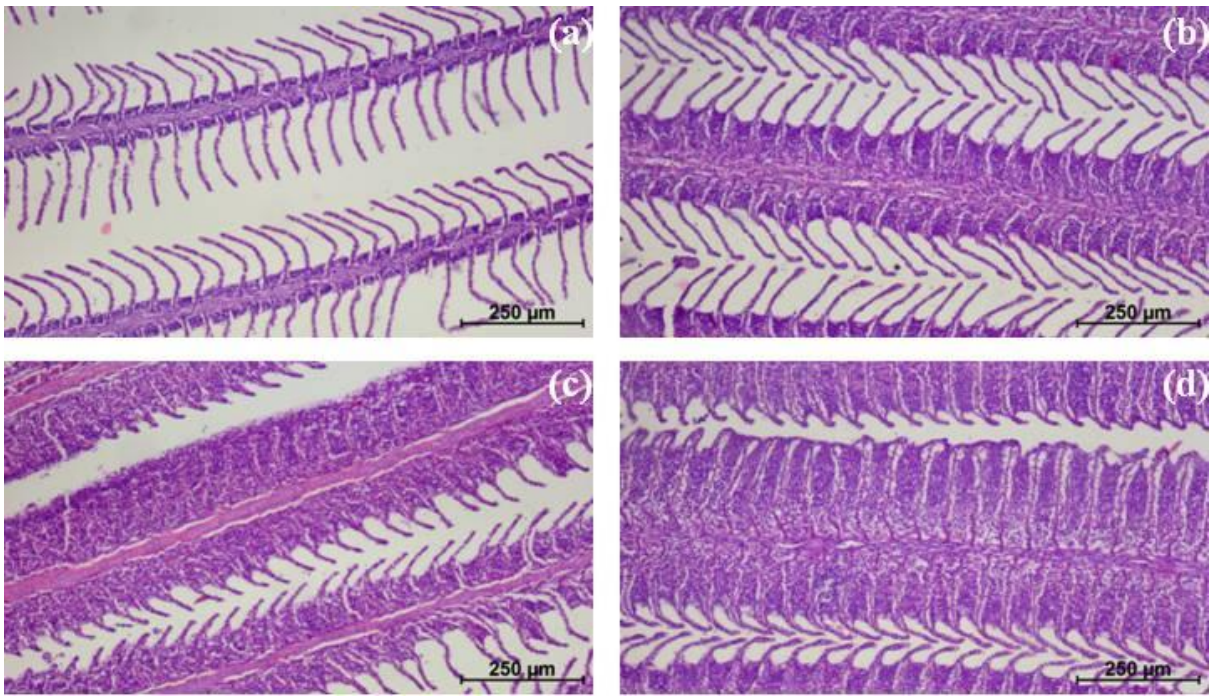


Figure 1: Illustration of the semi-quantitative scoring system used in the study: (a) normal primary lamella; (b) mild hyperplasia of the primary epithelium. (c) moderate hyperplasia of the primary epithelium (d) complete fusion of the primary lamella.

The presence of parasites was detected in almost all gill samples, but showed a variable distribution. The most frequently found parasites were Trematodes and ciliated protists from the family *Trichodinidae*. Although less common, the presence of aneurysms, hemorrhages and telangiectasias was noted.

Discussion and conclusions: Discussion and conclusions: The two main reaction patterns of the observed histopathological alterations were circulatory disturbances and progressive alterations. Circulatory disturbances usually occur during hypoxia, when gas exchange and/or blood flow in the gill apparatus is impaired [4]. On the other hand, the mechanism behind fish gill hyperplasia is based on the increasing diffusion distance between blood and surrounding water. This is usually a sign of chronic exposure to water pollutants (mostly heavy metals and pesticides) and the result is a reduction in fish respiration [5]. Both alterations are reversible, as fish gills are known to remodel quickly [5]. The quantification of the extent and intensity of the histopathological changes allowed a correlation between the scores and the water quality parameters in different fish farms. This method served as a good and reliable bioindicator of water pollution and is in line with other studies using a similar methodology [6].

Acknowledgments: This research was funded by the Ministry of Education, Science and Technological Development of the Republic of Serbia, grant number 451-03-137/2025-03/200116.

References:

1. S. Gouda, H. Hesham, A. Taha, *Egypt. J. Aquat. Biol. Fish.* **2024**, *28*, 1209-1235.
2. E. Strzyzewska, J. Szarek, I. Babinska, *Vet. Med.* **2016**, 61, 123-132.
3. D. Bernet, H. Schmidt, W. Meier, P. Burkhardt-Holm, T. Wahli, *J. Fish Dis.* **1999**, *22*, 25-34.
4. L. Zhao *et al. Aquat. Toxicol.* **2020**, *224*, 105514.
5. C.F. Sales *et al., Fish Shellfish Immunol*. **2017**, *68*, 10-18.
6. B. Rašković *et al., Cent. Eur. J. Biol.* **2013**, *8*, 975-985.

Type of presentation: Poster

LS3-P-4 In search of specific markers of telocytes in mouse urinary bladder by fluorescence microscopy and transmission electron microscopy

Manca Jernejc[a], Andreja Erman[b]

[a]*University of Ljubljana, Biotechnical Faculty, Department of Biology, Ljubljana, Slovenia*

[b]*Institute of Cell Biology, Faculty of Medicine, University of Ljubljana, Ljubljana, Slovenia*

Contact email: andreja.erman@mf.uni-lj.si

Introduction: Telocytes (TCs), previously known as interstitial Cajal-like cells, are a type of interstitial cells, found in various organs of the human and animal body, including the urinary bladder. Their role is not yet fully understood, while their morphology is well described. TCs have a small oval body with a nucleus surrounded by very little cytoplasm. The structures that distinguish them from other interstitial cells are their extremely long, thin cellular extensions, called telopodes [1]. With these, TCs form large 3D networks that are crucial for communication with surrounding cells such as fibroblasts, endothelial cells, blood vessels, muscle cells and nerve endings as well as for intercellular signaling under both physiological and pathological conditions [1, 2]. TCs are an interesting subject of research as many features regarding their function and morphology are still undiscovered. Moreover, it is speculated that there are several subtypes of telocytes that are organ- and even site-specific in terms of their structure, immunophenotype and function. The aim of this study was to analyze the expression of molecular markers, specific for TCs in the mouse urinary bladder and to identify potential telocyte subtypes in this organ.

Methods: We performed immunofluorescence on cryosections and immunogold labeling on ultrathin sections of mouse urinary bladders. For identification and characterization of TCs, TEM was used as the ”gold standard”, while for immunophenotypic analysis of TCs, fluorescence microscopy (FM) and transmission electron microscopy (TEM) were used.

Results: Based on the results obtained so far, we identified telocytes among the interstitial cells in the lamina propria and determine four specific molecular markers (connexin 43 (Cx43), ectonucleoside triphosphate diphosphohydrolase 2 (ENTPD2), endothelial nitric oxide synthase (eNOS), and CD34) that allow differentiation between TCs and fibroblasts in the mouse urinary bladder (Figure 1).

Discussion and conclusion: In the future, we would like to distinguish subtypes of TCs in the lamina propria of the mouse urinary bladder based on colocalization of specific markers. Further studies should be conducted to find other molecular markers and functions of TCs to expand the knowledge of these fascinating cells in the normal and pathologic urinary bladder.

Acknowledgments: This work was funded by the Slovenian Research and Innovation Agency (ARIS) grant P3-0108.

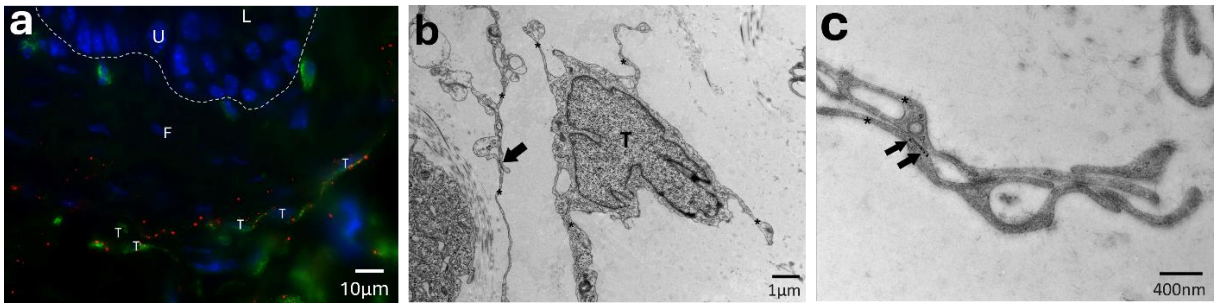


Figure 1: Representative micrographs of telocytes under the fluorescence microscope (a) and the transmission electron microscope (b, c). (a) Positive immunoreaction against CD34 (green fluorescence)

and Cx43 (red fluorescence) in bodies and telopodes of telocytes (T). The cell nuclei are labeled with the fluorescent dye DAPI (blue fluorescence). The dashed line represents the basal lamina. (b) TEM micrograph of a telocyte (T) with a nucleus in a small, polygonal cell body and with four telopodes (asterisks). In close proximity are two telopodes (asterisks) of adjacent TCs connected by gap junctions (arrow). (c) The result of immunogold labeling of Cx43 with clearly visible gold nanoparticles (two arrows) at the site of the gap junctions connecting two parallel telopodes (asterisks). L-lumen of the urinary bladder; U- urothelial cell, F-fibroblast (in image a).

References:
1. LM. Popescu, M. Faussone-Pellegrini, *J. Cell. Mol. Med.* **2010**, 14, 729-740.
2. CE. Condrat, MG. Barbu, DC. Thompson, CA. Danila, AE. Boboc, N. Suciu, D. Crețoiu, SC. Voinea, *Tissue Barriers in Disease, Injury and Regeneration*. **2021**, 1-41.

Type of presentation: Poster

LS3-P-5 Visualizing the algal response on polystyrene particles: A focus on EPS production

Komazec Bruno[a], Balen Biljana[a], Dimitrov Nino[b], Peharec Štefanić Petra[a]

[a]*Division of Molecular Biology, Department of Biology, Faculty of Science, University of Zagreb, Horvatovac 102a, 10000 Zagreb, Croatia*

[b]*Croatian Institute of Public Health, Rockefellerova 7, 10000 Zagreb, Croatia*

Contact email: bruno.komazec@biol.pmf.hr

Polystyrene nanoparticles (PS-NPs) are widely used in various commercially available products due to their exceptional properties. By functionalizing their surface with different chemical groups, they obtain additional specific properties, which makes them particularly valuable in various industries. Due to their frequent use, large quantities of PS-NPs are released into the environment, where they enter aquatic ecosystems directly or indirectly via rainwater, where algae are among the most abundant organisms. In order to investigate the impact of differently functionalized PS-NPs on the alga *Chlorella vulgaris*, we treated algal cells with PS-NPs, PS-NH_2-NPs and PS-COOH-NPs for 72 hours at a final concentration of 40 mg L^{-1}, which corresponds to the upper limit of exposure to polystyrene monomers in humans. The uptake of polystyrene particles into the cells and the retention in the extracellular polymeric substances (EPS) layer around the algal cells was analysed by pyrolysis-coupled mass spectrometry (Py-GC-MS). Morphological and ultrastructural changes of the cells as well as the localization of PS-NPs in the EPS were investigated by transmission electron microscopy (TEM). Visualization of the EPS was also performed by light microscopy using the fluorescently labelled lectin ConA, while quantification of the increase in EPS content was performed using a microtiter plate reader. Py-GC-MS analysis showed that after all treatments, more particles were retained on the EPS layer than the amount of internalized particles. Among the various treatments, the PS-COOH-NPs accumulated the least on EPS and at the same time penetrated the algal cells the least, which is probably due to their surface charge. TEM analysis under native conditions confirmed that all particles used bind to EPS, although it is notable that PS-NH_2-NPs predominantly bind to the cell wall itself. Fluorescence microscopy showed that all treatments with polystyrene nanoparticle induced EPS production around the algal cells, which was additionally quantified using a microtiter plate reader. Furthermore, TEM examination shows that all treatments induced significant ultrastructural changes in the cells, mainly in the form of plasmolysis, although a slight impairment of the integrity of the thylakoid membranes of the chloroplasts can also be seen. In conclusion, all treatments had a negative effect on the structural integrity of the algal cells and triggered increased EPS synthesis, probably with the aim of keeping the majority of the particles outside the cells and reducing their phytotoxic effect on the algae.

Type of presentation: Poster

LS3-P-6 Insight into the particle-based nature of mucilage as a response of *Chlorella sorokiniana* cell to manganese excess

Jelena Danilović Luković[a], Isidora Santrač[a], Anna Romolo[b], Valentina Ćurić[a], Darja Feizpour[c], Aleš Iglič[d], Veronika Kralj-Iglič[b]

[a]*University of Belgrade, Institute for Multidisciplinary Research, (Belgrade), Serbia*

[b]*University of Ljubljana, Faculty of Health Sciences, (Ljubljana), Slovenia*

[c]*Institute for Metals and Technology, (Ljubljana), Slovenia*

[d]*University of Ljubljana, Faculty of Electrical Engineering, (Ljubljana), Slovenia*

Contact email: veronika.kralj-iglic@zf.uni-lj.si

Introduction: *Chlorella sorokiniana* is a green microalga species with a wide variety of applications in biotechnology, food, and the pharmaceutical industry. The mechanism of its interaction with manganese and cooper has been studied [1,2] and showed that the first line of defense in manganese excess was bioimmobilization by production of polyphosphate-enriched mucilage [2]. Microalgae are a source of extracellular vesicles/nanoparticles that enable intercellular communication and hold promise for life sciences technology [3]. Herein, we aimed to observe the nanoparticles' presence in extracellular matrix/mucilage produced by *C. sorokiniana* before and after the treatment with a sublethal dose of manganese using transmission electron microscopy (TEM).
Methods: Microalgal aliquots of control (untreated; collected at 0h) and cultures were treated for 4 days with $MnCl_2$ (in a dose of 1 mM). The samples were washed with medium and applied to carbon formvar-coated 200 mesh grids. The imaging was performed using Talos F200i (Thermo Fisher Scientific, Waltham, MA, USA).
Results: Small grey, slightly irregularly shaped nanoparticles with a diameter between 60 and 120 nm, and pale grey particles with electron-dense ring, with average diameter 30 to 60 nm, were observed in the control group (Figure 1B,C). Round electron-dense nanoparticles with larger diameter (200-400 nm) were found in both investigated groups (Figure 1A-F). The metal-treated microalgae produced notable quantities of mucilage with uniform pale grey roundish nanoparticles inside (180-200 nm in diameter) (Figure 1D,E).
Discussion and conclusions: Based on our TEM observations, *C. sorokiniana* produces extracellular nanoparticles that are caught in mucilage as a response to manganese exposure. The sizes of the nanoparticles observed vary depending on the treatment, with the metal excess leading to the production of mucilage containing nanoparticles of around 180-200 nm. These observations align with the broader understanding that microalgae can interact via nanoparticles, including metal-based ones, and can even be used for the synthesis of nanoparticles [4]. Further characterization using techniques like energy-dispersive X-ray spectroscopy could help determine the elemental composition of these nanoparticles and mucilage [5]. Also, further studies employing analytical methods would provide a deeper understanding of the nature and potential metal content of microalgae-derived nanoparticles.

Acknowledgments: The authors acknowledge the financial support from the Slovenian Research Agency core founding No. P2-0132, P2-0232, P3-0388, IO-0006, projects No. J2-4427, J2-4447, J3-60063, the University of Ljubljana interdisciplinary preparative project Nanostructurome 802-12/2024-5, and by the Science Fund of the Republic of Serbia, Grant No. 7078– BioSynthClust

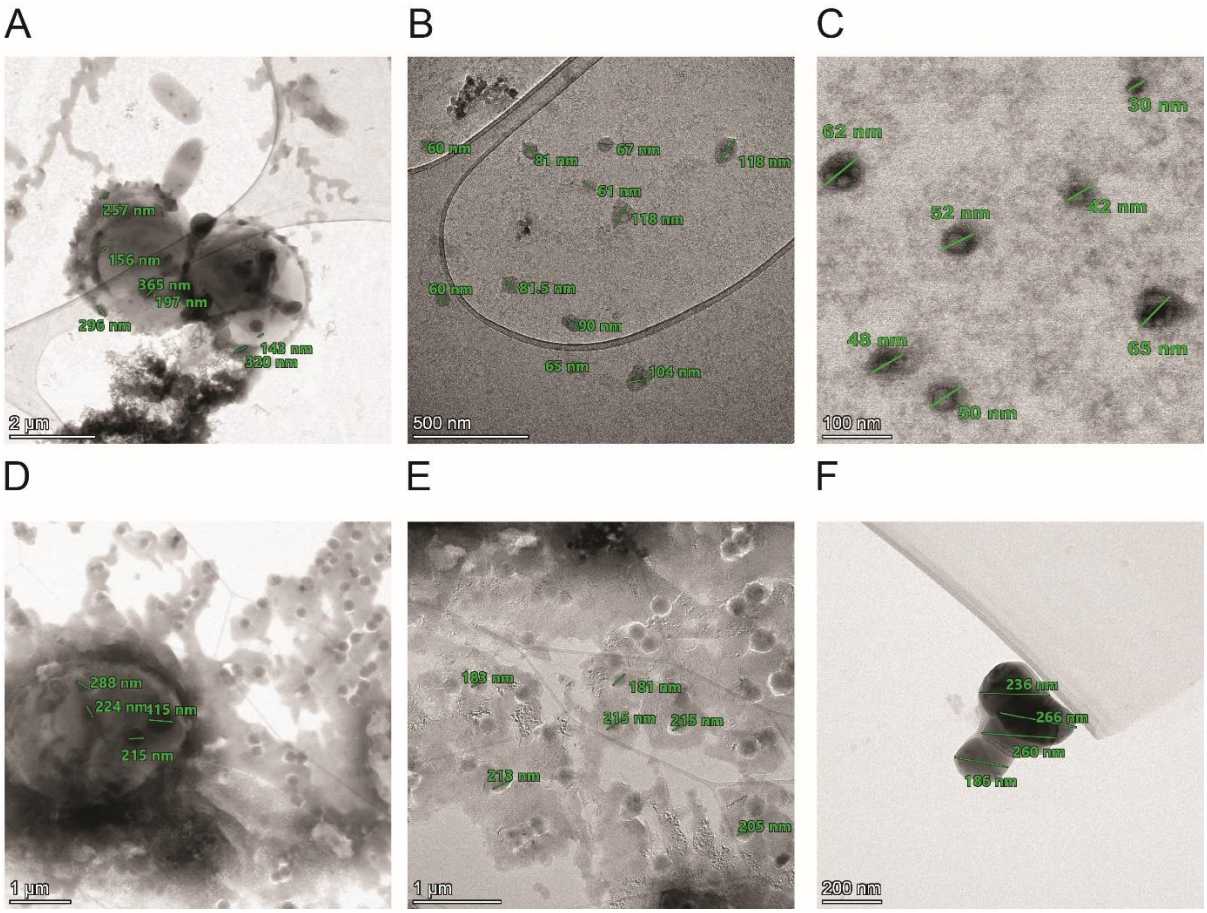


Figure 1A-C: control sample of *C. sorokiniana* culture; A: microalgae, B,C: extracellular particles; D-E: sample treated with 1 mM Mn^{2+} for four days. D: microalgae E,F: extracellular particle. Note the mucilage in panels D and E. Different magnifications were used for practical reasons.

References:

1. Vojvodić, S.; Stanić, M.; Zechmann, B.; Dučić, T.; Žižić, M.; Dimitrijević, M.; Spasojević, I. Mechanisms of Detoxification of High Copper Concentrations by the Microalga *Chlorella sorokiniana*. *Biochem. J.* **2020**, 477 (19), 3729–3741.
2. Vojvodić, S.; Dimitrijević, M.; Žižić, M.; Dučić, T.; Aquilanti, G.; Stanić, M.; Spasojević, I. A Three-Step Process of Manganese Acquisition and Storage in the Microalga *Chlorella sorokiniana*. *J. Exp. Bot.* **2023**, 74 (3), 1107–1122.
3. Picciotto, S.; Barone, M. E.; Fierli, D.; Aranyos, A.; Adamo, G.; Božič, D.; Bongiovanni, A. Isolation of Extracellular Vesicles from Microalgae: Towards the Production of Sustainable and Natural Nanocarriers of Bioactive Compounds. *Biomater. Sci.* 2021, **9** (8), 2917–2930.
4. LewisOscar, F.; Vismaya, S.; Arunkumar, M.; Thajuddin, N.; Dhanasekaran, D.; Nithya, C. Algal Nanoparticles: Synthesis and Biotechnological Potentials. *Algae-Organisms for Imminent Biotechnology* **2016**, *7*, 157–182.
5. Aminullah, A. Y.; Sukarni, S.; Prasetiyo, A.; Zakaria, Y.; Permanasari, A. A.; Puspitasari, P. Elemental Compositions Analysis of Arthrospira Platensis-Activated Carbon Blend Using Energy-Dispersive X-Ray Spectroscopy. *IOP Conf. Ser. Earth Environ. Sci.* **2021**, *847*(1), 012027. DOI: 10.1088/1755-1315/847/1/012027.

Type of presentation: Poster

LS3-P-7 Light and Transmission Electron Microscopy Complement Functional Genomics Screening in *Chlamydomonas reinhardtii* to Reveal Novel Mechanisms of Susceptibility to Herbicide Paraquat

Tim Godec[a,g], Carissa R Bleker[a], Katja Stare[a], Tjaša Lukan[a], Valentina Levak[a,g], Magda Tušek Žnidarič[a], Tina Kosjek[b], Milena Horvat[b], Katarina P van Midden[c], Francesco Trenti[d], Graziano Guella[d], Kristina Sepčič[e], Maruša Kerenčič[f], Tina Eleršek[f], Anže Županič[a]

[a]*National Institute of Biology, Department of Biotechnology and Systems Biology (Ljubljana) Slovenia*

[b]*Jožef Stefan Institute, Department of Environmental Sciences (Ljubljana) Slovenia*

[c]*University of Ljubljana, Faculty of Chemistry and Chemical Technology (Ljubljana) Slovenia*

[d]*University of Trento, Department of Physics (Trento) Italy*

[e]*University of Ljubljana, Biotechnical Faculty (Ljubljana) Slovenia*

[f]*National Institute of Biology, Department of Genetic Toxicology and Cancer Biology (Ljubljana) Slovenia*

[g]*Jožef Stefan International Postgraduate School (Ljubljana) Slovenia*

Contact email: valentina.levak@nib.si

Functional genomics screening is a powerful approach to elucidate the molecular mechanisms underlying the toxicity of environmental pollutants. In this study, we employed functional genomics techniques to investigate the mechanisms of toxicity for herbicide paraquat, using the model organism *Chlamydomonas reinhardtii*. Through a comprehensive analysis of knockout mutants, we identified several candidate genes that conferred either tolerance or susceptibility to the herbicide. We discovered potential transporter candidates, one of which was further validated by measuring paraquat accumulation using mass spectrometry. Transiently expressed in *Nicotiana benthamiana*, this transporter was found to colocalize with endoplasmic reticulum and plasmalemma. Additionally, we identified genes involved in fatty acid elongation, and their knockouts displayed increased tolerance to paraquat. Lipidomic analysis of one of these mutants revealed significant differences in galactolipids, which prompted us to examine the xylakoid membranes using transmission electron microscopy. Our observations did not show structural variations between the mutants and the wild type when they were not exposed to paraquat. Contrastingly, wild type treated with paraquat showed significant changes in ultrastructure that lead to cell death while the mutant retained the intact ultrastructure (Figure 1), suggesting that xylakoid membranes resisted functionality of paraquat's target, Photosystem I. Furthermore, the mutant exhibited slower growth under light conditions, indicative of compromised photosynthesis. Collectively, our findings highlight the utility of functional genomics in *Chlamydomonas reinhardtii* for uncovering new mechanisms of toxicity in ecotoxicology studies.

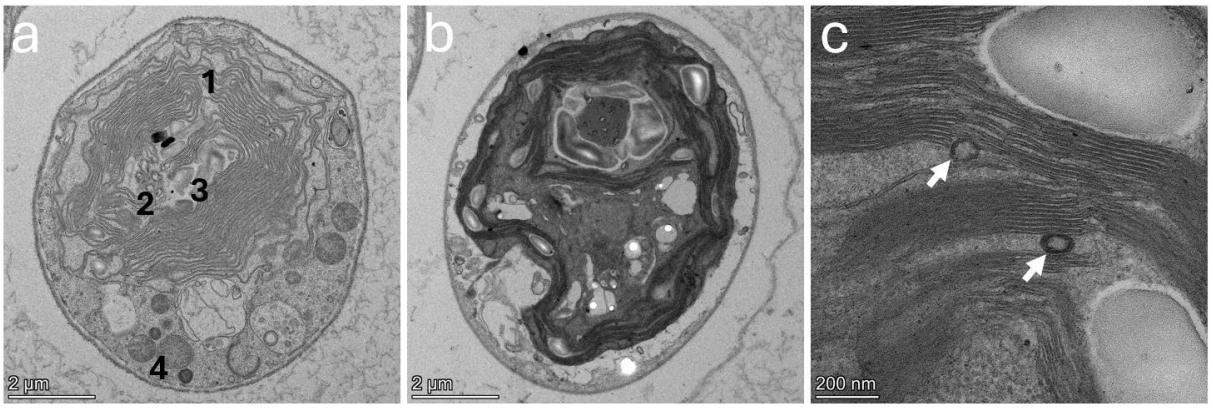


Figure 1: *Chlamydomonas reinhardtii* treated with 1600 nM paraquat. a) wild type showed diminished electron density of the whole cell, extension of plasmalemma towards the cell wall, collapse of the chloroplast, specifically loss of integrity of thylakoids (1) and pyrenoid organization (2), lower content of starch (3) and dilatation of mitochondria (4) while b) Cre08.g373050 mutant showed preserved phenotype, comparable to nontreated control. c) Cre08.g373050 mutant contained higher frequency of vesicles in chloroplast (pointed with arrows) regardless of paraquat treatment.

Type of presentation: Poster

LS3-P-8 Cytotoxicity Assessment of Functionalized Graphene-Based Composites

Špela Saje[a], Veno Kononenko[a], Matej Hočevar[b], Damjana Drobne[a], Alexander Doolin[c], Sara Novak[a]

[a]*University of Ljubljana, Biotechnical faculty, Ljubljana, Slovenia*

[b]*Institute of Metals and Technology, Ljubljana, Slovenia*

[c]*Haydale Ltd. Ammanford, Wales, United Kingdom*

Contact email: sara.novak@bf.uni-lj.si

Introduction: The continued development of nano-, advanced, smart materials and their commercial success require that feasible and cost-effective strategies are developed that include safe and sustainable-by-design (SSbD) production. Graphene family materials are already being used in commercial products. In the frame of the ACCORDs project, a holistic, reliable, and practical characterization framework is being developed, that correlates material characterisation methods with the toxicity of 2D materials and thus developing predictive strategies to ensure their safe and sustainable use. Graphene is currently used in the aviation industry to dissipate the energy from lightning strikes and prevent damage. Carbon fibre composites are increasingly being used in the construction of aircraft because they significantly reduce weight, save fuel, and reduce emissions. By adding electrically conductive graphene into the resin component, electrical conductivity is increased by 600%. Company HAYDALE LTD (UK) a partner in ACCORDs project, produced composite materials, masterbatches in an epoxy resin system with raw graphene material, ammonia functionalized and fluorine functionalized graphene. In the presented study cell adhesion on differently functionalized composite materials was tested, morphological changes of attached cells were evaluated and the cytotoxicity was tested.

Methods: A549 cells were seeded onto composite samples in 24-well plates and incubated for 24 hours to allow cell adhesion and proliferation. To evaluate density and viability of adhered cells, differential staining using acridine orange (for visualisation of all adhered cells) and propidium iodide (for visualisation of dead cells) was performed. Stained samples were observed using fluorescence microscopy. After imaging, samples were washed with PBS and fixed overnight in modified Karnovsky fixative. Following fixation, samples were post-fixed twice in 1% osmium tetroxide, with thiocarbohydrazide treatment applied in between. Samples were than dehydrated through graded ethanol series and hexamethyldisilazane. Air dried samples were mounted on holders and sputter-coated with gold/palladium for imaging with scanning electron microscopy (SEM). For cytotoxicity assessment, samples were transferred to new plates and incubated with resazurin for 3 hours, after which the fluorescence intensity of formed resorufin was measured using a spectrofluorimeter.

Results: Cells adhered and proliferated on all the composite samples. There are no observable differences in cell adhesion or viability on differently functionalized graphene composites. SEM images showed that cells adhered to the composite surfaces and were forming intercellular connections with neighbouring cells. In all tested composites cell morphology was not affected. Fluorescence imaging and resazurin assay results were in agreement, indicating that cell viability on the composites was comparable to that on the control surface.

Conclusions:
Our results indicate that raw graphene material, ammonia functionalized and fluorine functionalized graphene did not influence cell attachment, cell viability nor morphology of cells. The graphene-based composite materials supported good cell adhesion and proliferation, with no detectable cytotoxic effect.

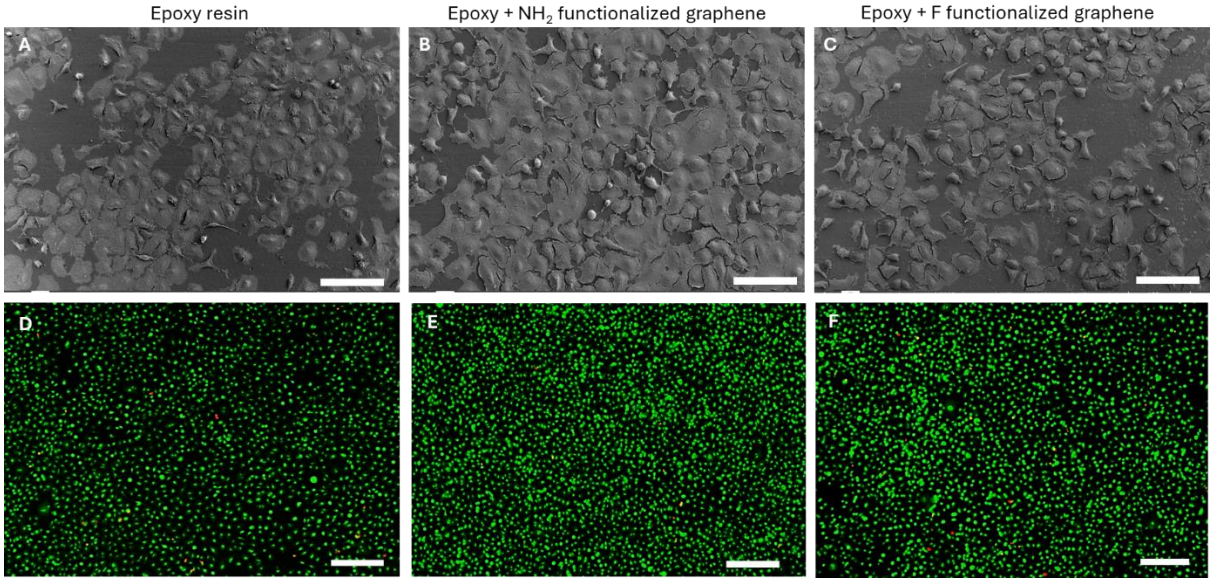


Figure 1: Scanning electron microscopy (SEM) images (A–C) and fluorescence microscopy images (D–F) of A549 cells seeded on three composite material surfaces. A/D = epoxy resin, B/E = epoxy resin + ammonia functionalized graphene, and C/F = epoxy resin + fluorine functionalized graphene. SEM images were acquired at 200× magnification. In fluorescence microscopy (D–F) nuclei of all cells are stained green, nuclei of dead cells are stained red. Scale bar = 100 μm.

Type of presentation: Poster

LS3-P-9 Optimization of Sample Preparation and Scanning Electron Microscopy Imaging for the Investigation of *Trebouxia* Flagellate Cells

Davide Porrelli[a,b], Enrico Boccato[a], Fabio Candotto Carniel[a], Claudio Ametrano[a], Mauro Tretiach[a]

[a] *Department of Life Sciences, University of Trieste, Trieste, Italy*

[b] *Interdepartmental Center for Advanced Microscopy, University of Trieste, Trieste, Italy*

Contact email: dporrelli@units.it

Introduction: *Trebouxia* species are the most frequent unicellular microalgae found as photobionts of lichens; despite this, their life cycle is still poorly understood, particularly the biological processes involving the flagellate cells and the sexual reproduction. In the frame of a project aimed at investigating the behaviour of flagellate cells in real time with light microscopy, this work focused on optimizing the sample preparation protocols and the sample imaging with the Scanning Electron Microscope (SEM), to characterize the morphology of the flagellate cells, trying to adapt an imaging technique already used in other green algae to this genus [1,2].

Methods: *Trebouxia decolorans*, *T. gelatinosa*, *T. vagua* and *T. angustilobata* were grown on solid *Trebouxia* medium and subcultured every 3 weeks. Cells were pelleted by centrifugation and the samples were fixed with Karnovsky's fixative and then stained with OsO_4. Samples were then dehydrated using an optimized protocol of supercritical CO_2 (with the critical point drier Emitech K850X) to preserve their structure. A carbon coating was performed to make the sample conductive and to allow to use the backscattered electrons for the analysis. The imaging was performed using the Gemini300 Zeiss SEM, equipped with an InLens Secondary Electron detector, an Energy selective Backscattered detector and a retractable 6 segment annular BackScattered Detector; the analyses were performed at a working distance of 5 mm, with an acceleration voltage of 5 kV.

Results: the fixation and dehydration protocols allowed to obtain samples in which the morphology and the structure of the flagellate cells was not altered, and to investigate and characterize their presence. Moreover, the post-fixation step using OsO_4 was fundamental to stain the intracellular lipid vesicles that characterize the flagellate cells (Figure 1), which were visible using the backscattered electrons even if the samples were not sectioned and the entire cells were analysed. Another set of samples stained with Nile Red and analysed with fluorescence microscopy (Figure 2), confirmed the presence of the lipid vesicles.

Discussion and conclusions: several attempts have been made to investigate the structure of the flagellate cells. The first approach, consisting in the environmental Scanning Electron Microscopy analysis, failed due to the structural instability of the analysed cells, which were collapsing in the environmental conditions, altering their morphology. Attempts to optimize a fixation and dehydration protocol, based on the use of stepwise soakings in solutions of ethanol/deionized water followed by solutions of hexamethyldisilazane/ethanol, also failed to preserve the structure of the flagellate cells and prevent their collapsing. Eventually, the use of an optimized protocol with the critical point drier, applied on the pellets of cells succeeded, ensuring the preservation of the flagellate cells structure. The staining performed using OsO4 allowed to confirm the presence and to analyse the lipid vesicles within the flagellate cells, thanks to the affinity of this molecule to the lipid molecules as reported for Transmission Electron Microscopy analyses [3] and for block-face Scanning Electron Microscopy analyses [4-6]. The dehydration protocol, together with the post-fixation with OsO_4 and the imaging with backscattered electrons, resulted in a high detailed imaging analysis of these type of cells and could pave the way for a more thorough approach for the investigation of the biological processes of these species.

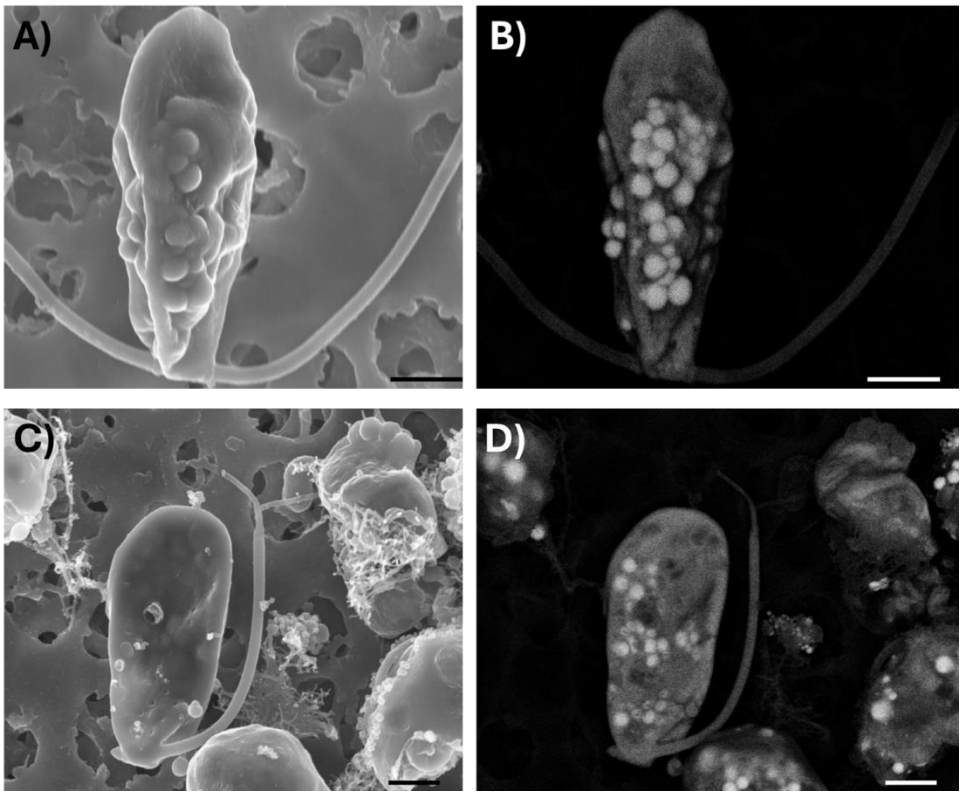


Figure 1. SEM photomicrographs of elongate flagellate cells of *Trebouxia angustilobata* undergoing cell fusion. Comparison between images acquired with secondary electron (A and C) and backscattered electrons (B and D). Scale bars = 1 μm.

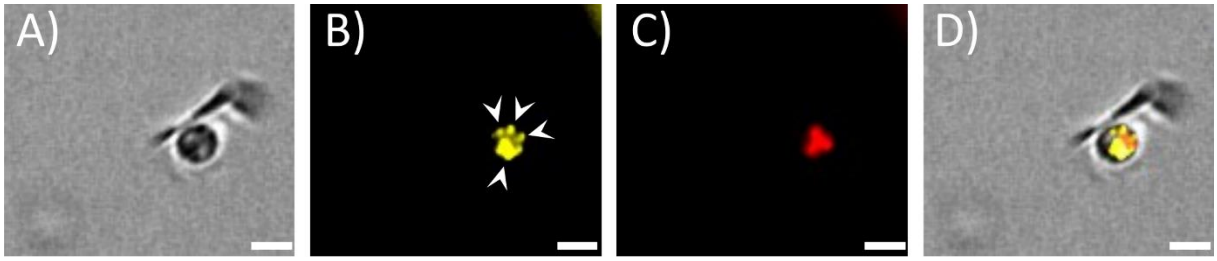


Figure 2. Flagellate cells of *Trebouxia decolorans* under epifluorescence microscopy observed through the brightfield (A), the fluorescence of the Nile red staining (B, yellow) the autofluorescence of the chlorophyll *a* (Chl*a*F; C, red), and all signal merged (D). Scale bars = 5 μm.

References

1. R. Innami, S. Miyamura, M. Okoshi, T. Nagumo, K. Ichihara, T. Yamazaki, S. Kawano, *Commun. Biol.* **2022**, *5*, 1–12.
2. Y. Mogi, Y. Kagami, K. Kuwano, S. Miyamura, T. Nagumo, S. Kawano, *J. Phycol.*, **2008**, *44*, 1290–1299.
3. V. Bello, G. Mattei, P. Mazzoldi, N. Vivenza, P. Gasco, J. M. Idee, C. Robic, E. Borsella, *Microsc. Microanal.* **2010**, *16*, 456–461.
4. S. J. Antreich, C. Permann, N. Xiao, G. Tiloca, A. Holzinger, *Fron. Plant Sci.* **2024**, 1358974.
5. R. A. Mukhamadiyarov, L. A. Bogdanov, T. V. Glushkova, D. K. Shiskova, A. E. Kostyunin, V. A. Koshelev, A. R. Shabaev, A. V. Frolov, A. N. Stasev, A. A. Lyapin, A. G. Kutikhin, *Front. Cardiovasc. Med.* **2021**, *8*, 739549.
6. M. T. Núñez-López, G. Del Rosario-Hernández, L. López-Gómez, P. Mestres-Ventura, *Eur. J. Anat.* **2018**, *22*, 471–481

Type of presentation: Poster

LS3-P-10 Unveiling tunnelling nanotubes in urothelial spheroids and bladder cancer biopsy samples

Nataša Resnik[a], Larisa Tratnjek[a], Daša Zupančič[a], Karmen Wechtersbach[b], Jera Jeruc[b], Mateja Erdani Kreft[a], Peter Veranič[a]

[a]*Institute of Cell Biology, Faculty of Medicine, University of Ljubljana, Slovenia*

[b]*Institute of Pathology, Faculty of Medicine, University of Ljubljana, Slovenia*

Contact email: natasa.resnik@mf.uni-lj.si

Introduction: Tunnelling nanotubes (TNTs) are membrane structures that facilitate long-distance cell-to-cell communication between various cell types, playing roles in both health and disease [1]. TNTs facilitate the uni- or bidirectional transfer of cellular components such as proteins, organelles, signalling molecules and nucleic acids (miRNA, mRNA) [1]. Their presence in cancer cells has been associated with increased resistance to therapy, enhanced metastatic potential, and the spread of pro-survival signals [2]. In conventional 2D mono- and co-cultures of cancer and normal urothelial cells, TNTs appear as thin, nanometer-scale membranous structures that extend across the flat surface to connect cells [3]. **The main issue is that the relatively artificial and static nature of 2D cultures restricts the complexity of cell interactions and may not fully replicate tissue conditions.** While 2D cultures offer accessibility and ease of study, 3D models, known as spheroids, better mimic in vivo conditions, making them more relevant for studying TNT functions in physiological and pathological contexts, particularly in cancer research [4]. To date, TNTs have not been examined in urothelial 3D in vitro models or in human biopsy samples. Our aim was therefore to investigate TNTs in spheroids, 3D in vitro models of urothelial cells, as well as in human urothelial tumours.

Methods: In vitro: Human muscle-invasive T24 bladder cancer cells and normal urothelial SV-HUC-1 cells were seeded in low-attachment plates. Cells were allowed to self-assemble into 3D spheroids for 3 and 7 days, forming non-compact and compact spheroids, respectively. The spheroids were processed for cryosectioning, followed with fluorescence immunolabelling, or entire spheroids were processed for scanning electron microscopy. In vivo: Paraffin-embedded sections of human urothelial carcinoma were immunolabelled. Sections were examined with fluorescence and confocal microscopy, and whole spheroids with scanning electron microscopy.

Results: Scanning electron microscopy revealed that TNTs connect cells across a wide extracellular space in non-compact urothelial spheroids. The physiological relevance of TNTs was further supported by their presence in urothelial carcinoma, where, similar to spheroids, they were predominantly found in regions with wide extracellular spaces. In both urothelial spheroids and biopsy samples, TNTs contained α7-nicotinic acetylcholine receptors, mitochondria, and microtubules, as demonstrated by immunofluorescence.

Discussion and conclusions: We demonstrated that TNTs are present in non-compact spheroids of both cancer and normal urothelial cells, as well as in human urothelial carcinoma, highlighting their potential role in cell-to-cell communication within the tumour microenvironment. This result, revealed through various microscopic techniques, underscores the crucial role of microscopy in TNT investigation. Further studies are needed to determine whether the frequency of TNTs varies based on the normal to cancer urothelial cell ratio in co-culture spheroids, as well as in response to treatment and cancer progression.

References:

1. Pinto, G.; Brou, C. et al., C. *Trends Cancer* **2020**, *6*, 874-888
2. Matejka, N.; Reindl, J. *Radiat Oncol* **2019**, *14*, 218
3. Resnik, N.; Baraga, D. et al., *Front Cell Dev Biol* **2022**, *10*, 934684
4. Pulze, L.; Congiu, T. et al., *Int J Mol Sci* **2020**, *21*, 5400

Type of presentation: Poster

LS3-P-11 Does endoplasmic reticulum stress contribute to the damage of trophoblast cells caused by Bisphenol A?

Fatma Beyza Sag[a], Zehra Sezer[a,b], Elif Guzel Meydanli[a,b]

[1]*Department of Histology and Embryology, Cerrahpasa Faculty of Medicine, Istanbul University-Cerrahpasa, Istanbul, TÜRKİYE*

[2]*Health Biotechnology Joint Research and Application Center of Excellence, 34220, Esenler, Istanbul, TÜRKİYE*

Contact email: beyzasag@istanbul.edu.tr

Introduction: Bisphenol-A (BPA) is an endocrine-disrupting chemical found in various synthetic materials, as well as in the environment. It can enter the human body through different pathways [1]. BPA has been linked to negative effects on trophoblast cells, which are crucial for placental formation, potentially leading to pregnancy-related issues such as pre-eclampsia and fetal developmental disorders, as well as other health problems [2]. Studies have suggested that the endoplasmic reticulum (ER) stress mechanism may be involved in the damage caused by BPA[3], but its specific role in affecting the placenta is still not fully understood. This study aimed to explore the connection between ER stress and the impact of BPA on trophoblast cells.

Methods: In this study, BeWo cells were used and stimulated with forskolin to induce syncytial formation. After that, the cells were exposed to 0.003 μM, 3 μM, 30 μM and 300 μM BPA during two different times as 48 and 72 hours. After the experiment is terminated, the role of BPA mediated ER stress on trophoblast cells were examine by analyze the proteins levels of GRP78, p-IRE1, p-PERK and ATF6. In addition, the effects of BPA on differentiation and secretion capacity, apoptosis and cell viability of trophoblast cells were also examined and the results were compared with ER stress data. In this study, Western blot, immunohistochemistry, ELISA, and CCK-8 analyzes were be performed.

Results: Our findings revealed for the first time that ER stress played an important role in the effect of BPA on human trophoblast cells. Additionally, we suggest that BPA-induced apoptosis in trophoblast cells might be linked to ER stress.

Discussion and Conclusion: This study is the first to demonstrate that BPA induces ER stress and activates key unfolded protein response signaling proteins, including GRP78, p-IRE1, p-PERK, and ATF6 in BeWo cell line at varying concentrations and durations. These findings suggest that BPA, which has been implicated in pregnancy-related pathologies such as preeclampsia and fetal developmental disorders, may exert its effects via ER stress mechanisms. This study provides important insights into how BPA impacts trophoblast cells and may help in understanding the pregnancy-related issues associated with BPA exposure. In conclusion, the results highlight the need for more comprehensive studies to better understand the mechanisms by which ER stress impacts trophoblast function and viability.

Acknowledgement: This research was funded by the Scientific and Technological Research Council of Turkey (TÜBİTAK Project No: 121S021).

References:

1. Michałowicz, J. Bisphenol A - Sources, toxicity and biotransformation. *Environ Toxicol Pharmacol* 37, 738–758 (2014).
2. Rolfo, A. *et al.* Fetal–maternal exposure to endocrine disruptors: Correlation with diet intake and pregnancy outcomes. *Nutrients* 12, 1–19 (2020).
3. Kim, S. H., Kang, D. W., Kwon, D. & Jung, Y. S. Critical role of endoplasmic reticulum stress on bisphenol A-induced cytotoxicity in human keratinocyte HaCaT cells. *Environ Toxicol* 39, 4091–4104 (2024).

Type of presentation: Poster

LS3-P-12 The Adaptation of Mitochondrial Dynamics to Hormonal Changes in the Endometrium and Placenta

Zehra Sezer[a], A. Umit Kayisli[b], İsmail Cepni[c], Timucin Timuroglu[d], Elif Guzel Meydanli[a]

Department of Histology and Embryology, Cerrahpasa Faculty of Medicine, Istanbul University-Cerrahpasa, Istanbul, Turkiye [a]

Department of Obstetrics and Gynecology, Morsani College of Medicine, University of South Florida, Tampa, FL, USA [b]

Department of Obstetrics and Gynecology, Cerrahpasa Faculty of Medicine, Istanbul University-Cerrahpasa, Istanbul, Turkiye [c]

Department of Obstetrics and Gynecology, Medicana Kadıkoy Hospital, Istanbul, Turkiye [d]

Contact email: zehra.sezer@iuc.edu.tr

Introduction: Successful implantation and pregnancy depend on the transformation of endometrial stromal cells (ESCs) into decidual cells (DCs), a process known as decidualization . This process begins in the mid-secretory phase of the menstrual cycle and continues into early pregnancy (first trimester; FP) [1], [2]. Decidualization involves extensive cellular remodeling, which is thought to require mitochondrial quality control mechanisms, including fusion, fission, and mitophagy. However, the regulatory influence of steroid hormones on these mitochondrial processes remains poorly understood. Importantly, inadequate decidualization is a major contributor to implantation failure, recurrent miscarriage, and early pregnancy loss, even in the presence of a viable embryo [3]. Therefore, this study aimed to investigate the physiological and hormone-mediated regulation of mitochondrial fusion, fission, and mitophagy throughout the menstrual cycle and pregnancy.

Methods: Mitochondrial dynamics and mitophagy markers were analyzed in endometrial stromal cells (ESCs) of endometrial tissues across different menstrual cycle phases: early (EP) and late (LP) proliferative phases, as well as early (ES), mid (MS), and late (LS) secretory phases in vivo. Similarly, decidual cells (DCs) were evaluated in placental tissues from the first trimester (FP) and term pregnancy (TP). Immunohistochemistry (IHC) was performed to assess the expression of mitochondrial fission markers (Drp1, Fis1, MFF), fusion markers (MFN2, OPA1), and mitophagy markers (Pink1, Parkin). Stromal-specific analysis of immunoreactivity was conducted using the HSCORE method. To investigate hormone-dependent regulation, ESCs isolated from the endometrium in EP phase and DCs isolated from FP and TP tissues were cultured and treated in vitro with 17β-estradiol (E2), medroxyprogesterone acetate (P4), or a combination of both. Protein expression levels of mitochondrial markers were evaluated by Western blot analysis. Additionally, transmission electron microscopy (TEM) was employed to examine mitochondrial morphology and assess dynamic changes in ultrastructure.

Results: In vivo immunohistochemical analysis demonstrated that mitochondrial fission was significantly increased in EP-ESCs, as evidenced by elevated Drp1 and MFF expression ($p<0.04$), while in FP- and TP-DCs, fission was predominantly regulated by Drp1 and Fis1 ($p<0.02$). P4 treatment in vitro further enhanced Drp1 expression in both ESCs and FP-DCs ($p<0.03$), indicating a P4-dependent mechanism of fission activation. Mitochondrial fusion markers, MFN2 and OPA1, were significantly upregulated in LP-ESCs and FP-DCs ($p<0.001$), but their expression did not significantly change following E2 or P4 treatment ($p>0.05$), suggesting a hormone-independent regulation. Pink1 and Parkin, key mitophagy markers, exhibited increased expression in FP- and TP-DCs ($p<0.001$), with P4 and E2+P4 treatments significantly enhancing Pink1 levels in FP-DCs ($p<0.001$), while Parkin expression was most notably elevated after combined hormone treatment in both ESCs and DCs ($p<0.002$). TEM analysis supported these findings, revealing reduced mitochondrial number ($p<0.001$), length ($p<0.004$),

and branching ratio ($p<0.006$) in DCs compared to ESCs, consistent with increased mitochondrial turnover via fission and mitophagy during decidualization.

Discussion and Conclusions: This study demonstrates that mitochondrial fusion, fission, and mitophagy are tightly regulated processes that support ESC proliferation, differentiation, and pregnancy maintenance. While P4 regulates Drp1-mediated fission, the combined action of E2 and P4 influences mitophagy in a cell-type-specific manner, highlighting distinct hormonal control over mitochondrial remodeling. In vivo findings revealed enhanced mitochondrial dynamics in DCs, whereas ultrastructural analyses indicated reductions in mitochondrial number, length, and branching, suggesting that fission and mitophagy are dominant in mitochondrial turnover during ESC-to-DC differentiation. The activation of mitophagy in FP-DCs may balance mitochondrial remodeling and mitigate oxidative stress, reinforcing its critical role in early pregnancy adaptation. These findings underscore the physiological importance of mitochondrial dynamics and mitophagy in decidualization, providing insights into potential therapeutic targets for reproductive disorders.

Acknowledgments: Endometrial and term placenta samples were collected from patients at Cerrahpaşa Medical Faculty, while first-trimester placenta samples were obtained from Medicana Hospital, following informed consent. Ethical approval for these procedures was granted from the Ethics Committee of Istanbul University-Cerrahpasa, Cerrahpasa Faculty of Medicine (Decision No: 41421735-302.14.02-75595). This study was supported by the Istanbul University-Cerrahpaşa Scientific Research Projects Coordination Unit (IUC-BAP, Project No: 35075).

References:

1. A. Owusu-Akyaw, K. Krishnamoorthy, L. T. Goldsmith, and S. S. Morelli, “The role of mesenchymal-epithelial transition in endometrial function,” *Hum Reprod Update*, vol. 25, no. 1, pp. 114–133, **2018**, doi: 10.1093/humupd/dmy035.
2. J. P. Carrascosa, J. A. Horcajadas, and J. M. Moreno-Moya, “The Molecular Signature of the Endometrial Receptivity: Research and Clinical Application,” *Reproductomics: The -Omics Revolution and Its Impact on Human Reproductive Medicine*, pp. 279–301, Jan. **2018**, doi: 10.1016/B978-0-12-812571-7.00016-2.
3. T. Garrido-Gomez *et al.*, “Defective decidualization during and after severe preeclampsia reveals a possible maternal contribution to the etiology,” *Proc Natl Acad Sci U S A*, vol. 114, no. 40, pp. E8468–E8477, Oct. **2017**, doi: 10.1073/PNAS.1706546114.

Type of presentation: Poster

LS3-P-13 Characterization of red blood cells changes during storage by atomic force microscope

Francesca Terracciano[a], Xavier De La Torre[a], Francesco Donati[a], Francesco Botrè[a].

[a]Laboratorio Antidoping, FMSI, Rome, Italy

Contact email: f.terracciano@labantidoping.it

Autologous blood transfusions (ABT) are illicit, "blood doping" practices, consisting in the reinfusion of whole blood, or of red blood cells (RBCs) concentrates, generally corresponding to 5-10% of the total circulating volume. Once reinfused, the levels of haemoglobin increase, with an enhanced capacity of oxygen delivery to tissues, thus improving performance, especially in endurance sports disciplines [1].
To date, there is still no reliable direct method to detect ABT. Suspect of ABT abuse may be indirectly revealed by the non-physiological variations in certain reference haematological parameters, monitored individually and longitudinally in the haematological module of the "Athlete Biological Passport". However, the results of this analysis may be influenced by various confounding factors [2].
Our previous studies proposed a promising multi-parametric, analytical strategy to detect ABTs by monitoring RBCs modifications occurring during storage, focusing specifically on alteration of the expression of surface markers, oxidative state, senescence biomarkers, and vesiculation [3]. Besides these biochemical markers, specific cellular parameters may be examined as diagnostic targets to discriminate the *ex-vivo* storage conditions of a blood sample [4].
Therefore, this work proposes a new analytical procedure for the detection of advanced forms of doping aimed at characterizing the alterations of the RBCs occurring during the "*ex-vivo*" blood storage to determine whether these changes make stored RBCs distinguishable after reinfusion [5].
In particular, the project focused on the potential offered the atomic force microscope (AFM), that enables the three-dimensional visualization and characterization of the properties of various materials, as well as to simultaneously evaluate alterations in morphological, rheological and surface expression parameters of biological samples [6,7].
At first, a validation phase of a sequential pretreatment protocol for RBCs analysis was developed and optimized, allowing to scan RBCs surface while keeping their morphology unchanged and ensuring as minimal manipulation as possible in compliance with doping purposes. All blood samples were analysed with the atomic force microscope Park NX-12 and the "SmartScan" software.
Subsequently, by analysing RBCs stored at 4°C, which is the maximum storage period established by blood banks according to WHO recommendations, it was possible to recognize the four main categories of morphological aging (erythrocytes, intermediates, echinocytes and spheroids), to determine their progressive reduction/increase and their dependence on the type of hemopreservative used.
Results showed that RBCs complete the transition into spherocytes in 21 days whereas the same process is slowed down in the presence of hemopreservatives, with conversion completed at 40 days (Fig. 1).
As a final step, given the ethical limitations in evaluating the proposed approach on real samples, the study involved the simulation of an "*ex-vivo*" autologous transfusion, mimicked by adding 10% of blood stored for 40-45 days to fresh blood. An increase in the proportion of echinocytes was observed in the *ex-vivo* transfused samples, which remained detectable even under stressing experimental conditions designed to mimic the recipient circulatory stream.
Altogether, these preliminary results demonstrate that it is possible to map morphological changes occurring during blood storage at a nanoscale resolution and that they are irreversible and detectable in *ex-vivo* transfusions, suggesting that the AFM approach might be feasible for anti-doping purposes.
Moreover, these data lay the groundwork for a more extensive analysis of RBC storage lesions, which will be directed at coupling morphological analysis with changes in expression of surface biomarkers

and changes in rheological properties of RBCs in order to develop a robust multiparametric procedure to detect blood transfusions.

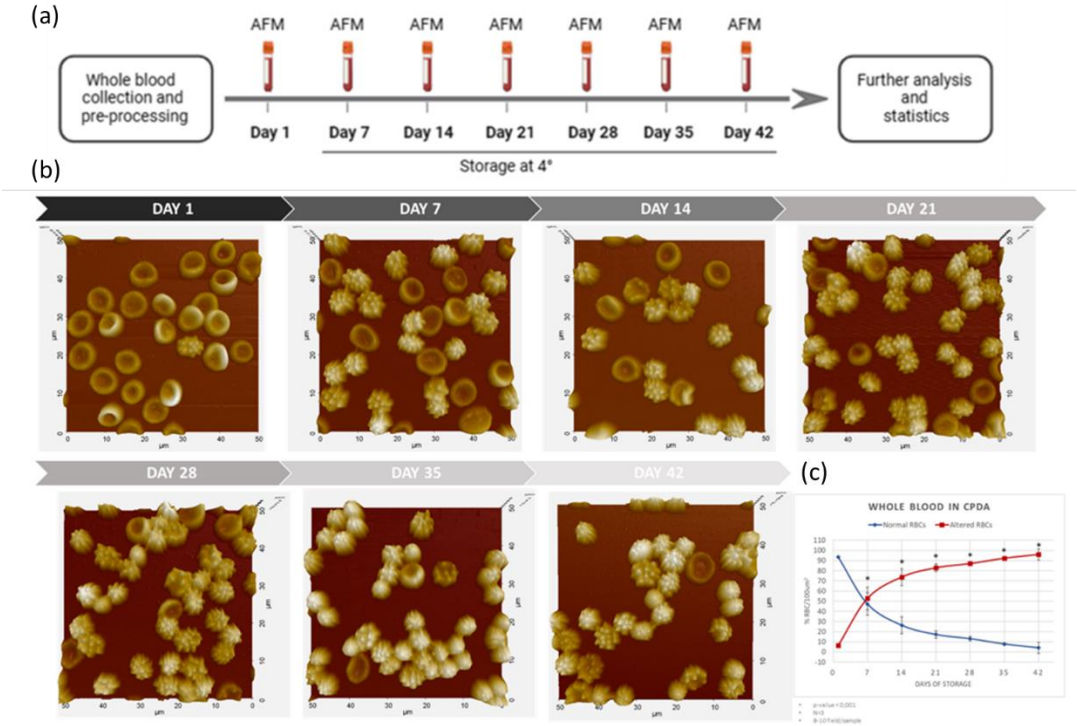


Figure 1: AFM analysis of stored RBCs. Graphical representation of the experimental strategy used (a); Representative 50μm^2 fields of RBCs at different storage time points (b); Percentage of RBC subtypes per field (8-10 fields/sample, N=3) and statistical analysis (t-test vs day 0; *p-value < 0.001) (c).

References:

1. S.A. Solheim, J. Bejder, A. Breenfeldt Andersen, J. Mørkeberg, N.B. Nordsborg. Autologous blood transfusion enhances exercise performance-strength of the evidence and physiological mechanisms. *Sports Med Open*. **2019**, 5(1), 30.
2. B. Krumm, J.J. Saugy, F. Botrè, F. Donati, R. Faiss. Indirect biomarkers of blood doping: A systematic review. *Drug Test Anal*. **2024**, 16(1), 49-64.
3. G.M. Biasini, F. Botrè, X. De La Torre, F. Donati. Age-markers on the red blood cell surface and erythrocyte microparticles may constitute a multi-parametric strategy for detection of autologous blood transfusion. *Sports Med Open*. **2023**, 9(1), 113.
4. M. Grau, E. Zollmann, J. Bros, B. Seeger, T. Dietz, J.A. Noriega Ureña, A. Grolle, J. Zacher, H.L. Notbohm, G. Suck, W. Bloch, M. Schumann. Autologous blood doping induced changes in red blood cell rheologic parameters, RBC age distribution, and performance. *Biology (Basel)*. **2022,** 11(5), 647.
5. S.C. Voss, M. Jaganjac, A.M. Al-Thani, J.C. Grivel, C.M. Raynaud, H. Al-Jaber, A.S. Al-Menhali, Z.A. Merenkov, M. Alsayrafi, A. Latiff, C. Georgakopoulos. Analysis of RBC-microparticles in stored whole blood bags – a promising marker to detect blood doping in sports? *Drug Test Anal*. **2017**, 9(11-12), 1794-1798.
6. A.S. Kamruzzahan, F. Kienberger, C.M. Stroh, J. Berg, R. Huss, A. Ebner, R. Zhu, C. Rankl, H.J. Gruber, P. Hinterdorfer. Imaging morphological details and pathological differences of red blood cells using tapping-mode AFM. *Biol Chem*. **2004**, 385(10), 955-60.
7. V. Sergunova, S. Leesment, A. Kozlov, V. Inozemtsev, P. Platitsina, S. Lyapunova, A. Onufrievich, V. Polyakov, E. Sherstyukova. Investigation of red blood cells by atomic force microscopy. *Sensors (Basel)*. **2022**, 22(5), 2055.

Type of presentation: Poster

LS3-P-14 Distribution of Golgi matrix proteins GRASP65 and GRASP55 during early urothelial regeneration

Tim Zaveršek[a], Aleksandar Janev[a], Samo Hudoklin[a], Rok Romih[a]

[a]*University of Ljubljana, Faculty of Medicine, Institute of Cell Biology, (Ljubljana), Slovenia*

Contact email: tim.zaversek@mf.uni-lj.si

Introduction. Golgi reassembly-stacking proteins, GRASP55 and GRASP65 help organizing the Golgi apparatus (GA) into a cis-to-trans cisternal orientation and individual GA stacks into GA ribbons [1-3]. In terminally differentiated superficial urothelial cells, GA participates in processing tissue-specific transmembrane proteins called uroplakins and their organization into urothelial plaques [4, 5]. Urothelial plaques are delivered to the apical plasma membrane via fusiform vesicles (FVs), where they contribute to the blood-urine permeability barrier [6]. If urothelium is reversibly damaged e.g. by chemotherapeutics, such as cyclophosphamide (CP), regeneration of the tissue involving differentiation of urothelial cells and rearrangements of GA can be followed [7]. The aim of our study was to investigate the distribution of GRASP55 and GRASP65 during the early stages of urothelial regeneration *in vivo* and *in vitro* and their correlation with uroplakins and urothelial plaques.

Methods. For the *in vivo* model of urothelial regeneration, Sprague Dawley rats were treated with an intraperitoneal injection of CP (100 mg/kg) and euthanised with carbon dioxide at days 3 and 14 after treatment. The urinary bladders were prepared for histological, ultrastructural and immunofluorescence (IF) analyses. Paraffin sections were stained with haematoxylin and eosin for histology analysis. IF analysis was performed using antibodies against GA markers (GRASP55: Proteintech, 10598-1-AP; GRASP65: Invitrogen, PA3-910) on non-sectioned urothelium viewed from the apical side (*en face* method) and against uroplakins (kind gift of prof. Tung-Tien Sun, New York University) on frozen sections. For transmission electron microscopy (TEM), samples were chemically fixed with 4% FA + 2% GA in 0.1M cacodylate buffer and postfixed with 1% OsO_4, dehydrated and embedded in Epon. For the *in vitro* model of urothelial regeneration, SV-HUC-1 cell culture was grown on glass slides until confluence. A wound healing assay was performed using a pipette tip to introduce a scratch to the culture, and afterwards the cell migration to the denuded area was observed after 15 hours. The cell culture was then chemically fixed with 4% FA for subsequent IF analysis of GRASPs or with 4% FA + 2% GA and postfixed with 1% OsO_4 and prepared for TEM. Ultrathin sections were observed with CM100 TEM (Philips) running at 80kV.

Results. CP caused focal injuries of rat urothelium, seen as missing layers of urothelial cells, locally with exposures of basal lamina. On day 3, hyperplastic urothelium was seen, which on day 14 returned to nearly normoplastic organisation with large superficial cells resembling the controls. In the apical cells of the controls, IF analysis showed GRASP55 and GRASP65 as linear fragments that formed a network throughout the basal portion of cytoplasm (Fig. 1a, d). In controls, strong immunolabelling of uroplakins was seen (Fig. 1g), with numerous FVs in the cytoplasm (Fig. 1j) and urothelial plaques in the apical plasma membrane of superficial cells. On day 3 after CP injection, GRASP55 was diffusely distributed throughout the cytoplasm, while GRASP65 formed discreet spots (Fig. 1b, e). Uroplakin staining was weak and FVs in cytoplasm were scarce, while apical plasma membrane contained microvilli and individual urothelial plaques (Fig. 1h, k). On day 14 after CP injection, GRASP55 remained diffused throughout the cells (Fig. 1c). On the other hand, IF staining of GRASP65 was still concentrated into discreet spots or longer fragments (Fig. 1f) and occasionally formed a network closer to the one in control cells. On day 14, uroplakin staining was positive in superficial cells and their cytoplasm contained numerous FVs (Fig. 1l). Apical plasma membrane was covered with urothelial plaques.

In vitro, a scratch assay induced cell migration to the site of injury. Immunofluorescent labelling of GRASPs was diffused throughout the cytoplasm in mitotic cells, whereas it formed a network of fragments next to or around the nucleus in most other cells (Fig. 1 m, n). Migrating cells were present at the edge of the denuded area.

Discussion and conclusions. In this work we have shown the redistribution of Golgi matrix proteins GRASP55 and GRASP65 during early phases of urothelial regeneration. In the *in vivo* model, GRASP redistribution coincides well with reorganisation of GA distribution from simple to complex the that has already been described and correlates with the beginning of urothelial plaques formation in the differentiating urothelial cells. *In vitro* scratch assay of a confluent cell culture is as a model for cell migration, mirroring epithelial-mesenchymal transition. *In vivo* and *in vitro* results combined point into direction that the complex network of GA, which is present in differentiated superficial cells and depends on GRASPs, must be disassembled in cells involved in urothelial regeneration after injury. This disassembly is necessary to enable epithelial-mesenchymal transition, which facilitates cell migration to the injury site. Once the cells have filled the damaged area, mesenchymal-epithelial transition occurs, GRASPs are reassembled, and uroplakin formation is restored, re-establishing the blood-urine permeability barrier. Therefore, results suggest that GRASPs play a crucial role in both terminally differentiated specialized cells and in regenerating cells after injury.

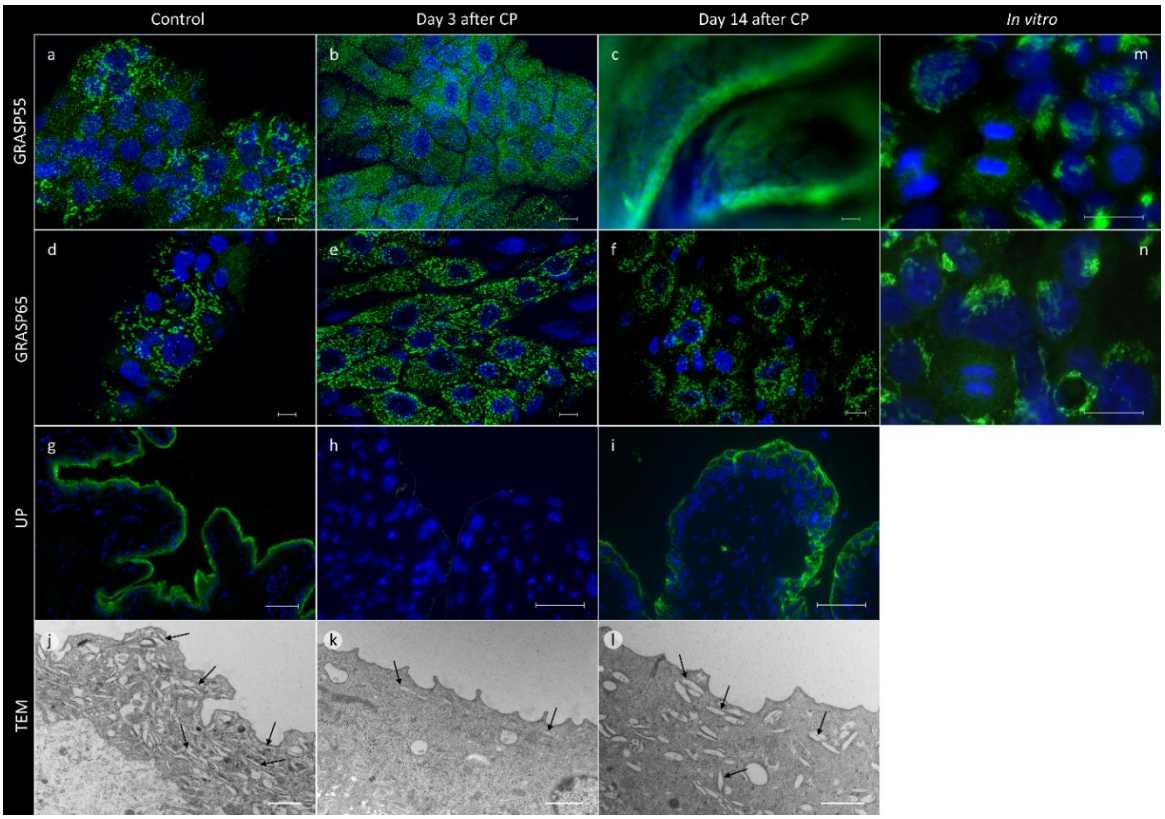


Figure 1: Immunofluorescence labelling of GRASP55, GRASP65, uroplakins (UP) and ultrastructure of urothelial cells *in vivo* and *in vitro*. Control urothelium (a, d, g, j), urothelium 3 days (b, e, h, k) and 14 days (c, f, i, l) after cyclophosphamide (CP) injection. *In vitro*: SV-HUC-1 cells (m, n). Bars: 10 µm (a, b, d-f), 30 µm (c, g-i), 1 µm (j-l), 20 µm (m, n).

References:

1. Zhang, X., Y. Wang, *Trends Biochem Sci*, **2020**. 45(12): 1065-1079.
2. Bekier, M.E., 2nd, et al., *Mol Biol Cell*, **2017**. 28(21): 2833-2842.
3. Feinstein, T.N. and A.D. Linstedt, *Mol Biol Cell*, **2008**. 19(7): 2696-707.
4. Hudoklin, S., et al., *PLoS One*, **2011**. 6(8): e23636.
5. Visnjar, T., et al., *Sci Rep*, **2017**. 7(1): 12842.
6. Kreft, M.E., et al., *Protoplasma*, **2010**. 246(1-4): 3-14.
7. Hudoklin, S., D. Zupancic, and R. Romih, *Cell Tissue Res*, **2009**. 336(3): 453-63.

LS4 Microscopy in pathology and regenerative medicine

Type of presentation: Invited

LS4-IN-1 An ultrastructural perspective on cell death with a focus on atherosclerosis

Ida Daniela Perrotta[a]

[a]*University of Calabria, Department of Biology, Ecology and Earth Sciences – Centre for Microscopy and Microanalysis (CM2), 87036 Rende, Cosenza ITALY*

Contact email: ida.perrotta@unical.it

Keywords: Cell death, Atherosclerosis, Electron Microscopy

Cell death is an important physiological process that occurs in multicellular organisms, whose roles extend from embryonic development, tissue homeostasis, and aging to the regulation of immune responses and prevention of autoimmunity. An imbalance in the natural process of cell death in our body (either too little or too much) can wholly or partially induce many disease states, including neurodegenerative diseases, ischemic damage, atherosclerosis and many types of cancer [1, 2]. Cell death was once believed to occur primarily through apoptosis or necrosis. Over the past few decades, with the increasing scientific knowledge more sophisticated phenomena came on the scene and novel forms of cell death have been identified. Cell death strategies can be categorized into two main groups: an uncontrolled and accidental form of cell death (ACD), generally caused by a traumatic injury, and a programmed cell death (PCD), a highly regulated and controlled process of cellular suicide that involves the activation, expression, and regulation of a series of genes. In mammalian cells, PCD may take the form of apoptosis or of non-apoptotic PCD that include autophagy, methuosis, paraptosis, and ferroptosis [3-5]. Necrosis is an unregulated and non-programmed passive mode of ACD due to a failure in plasma membrane permeability that disrupts the plasma membrane and releases cellular components while mitotic catastrophe is a type of oncosuppressive cell death mechanism that inhibits proliferation of cells undergoing aberrant mitosis. Since the potential modulation of cell fate represents a relevant therapeutic goal, the research focuses on the analysis of cell death processes, characterizing their similarities and differences, to achieve targeted strategies. At present, the different intracellular pathways to carry out the death sentence have been extensively studied and various elements of the underlying molecular machinery have been identified [6, 7]. The field of cell death presents many opportunities for microscopists, but unfortunately cell death researches rarely includes ultrastructural findings from transmission electron microscopy (TEM). TEM with its high resolving power can provide unequivocal nanoscale information that permits to examine the fine ultrastructural details within the cell, the alteration of cytoplasmic organelles and subcellular structures, the nuclear reorganization, and the loss of membrane integrity that ultimately lead to a clear discrimination between the different types of cell death programs and that very often cannot be explored with other experimental approaches. This lecture presents a gallery of original TEM images and provides an ultrastructural description of the way/s by which cells can die with particular focus on human atherosclerosis. Future works in this area will provide important new insights offering also innovative therapeutical opportunities.



Figure 1. Representative EM images of three classical forms of cell death – necrosis, apoptosis, and autophagy.

References:

1. E. Lee, C.H. Song, S.J. Bae, K.T. Ha, R. Karki. *Exp Mol Med*. **2023**, 55, 1632-1643.

2. M. Li, Z.W. Wang, L.J. Fang, S.Q. Cheng, X. Wang, N.F. Liu. *Cell Death Dis*. **2022**, 18, 467.
3. S. Shen, Y. Shao, C. Li. *Cell Death Discov*. **2023**, 9, 284.
4. W. Park, S. Wei, B.S. Kim, B. Kim, S.J. Bae, Y.C. Chae, D. Ryu, K.T. Ha. *Exp Mol Med*. **2023**, 55, 1573-1594.
5. I. Vitale, L. Galluzzi, M. Castedo, G. Kroemer. *Nat Rev Mol Cell Biol*. **2011**, 12, 385-392.
6. L. Galluzzi, I. Vitale, S. Aaronson et al. *Cell Death Differ*. **2018**, 25, 486-541.
7. S. Wang, S. Guo, J. Guo, Q. Du, C. Wu, Y. Wu, Y. Zhang. MedComm (2020). **2024**, 5, e693.

Type of presentation: Invited

LS4-IN-2 Expression of GABA-A receptors in brain tumors

Ivan Capo[a], Jovana Drljaca Lero[b], Aleksandra Popovic[c], Aleksandar Milenkovic[d,e], Ivan Milenkovic[f]

[a]*Department of Histology and Embryology, Faculty of Medicine, University of Novi Sad, Serbia*

[b]*Department of Pharmacy, Faculty of Medicine, University of Novi Sad, Serbia*

[c]*Department of Physiology, Faculty of Medicine, University of Novi Sad, Serbia*

[d]*Faculty of Medicine, University of Novi Sad, Serbia*

[e]*Clinic for Otorhinolaryngology, Military Medical Academy, Belgrade, Serbia*

[f]*Department of Neurology, Medical University Vienna, Austria*

Contact email: ivan.capo@mf.uns.ac.rs

Glioblastoma is the most common primary brain tumor and the most aggressive high-grade glioma, with an extremely poor prognosis and very little therapeutic progress in the last decade. The increase in glioma malignancy correlates with a decrease in GABA-A receptor expression, and if GABA (γ-aminobutyric acid) shows negative effects on cell proliferation and/or migration, GABA-A receptor agonist drugs would represent potential antitumor drugs.On this occasion, we will present the specificities of human glioblastoma in terms of GABA-A receptor expression as well as expression in cell-line xenograft (CLX) model on rats. With special emphasis, the effect of temozolomide on the expression of GABA-A subunits will be presented, as well as the importance of GABA-A antagonists in the mentioned animal model (CLX - U87 cell line).

Type of presentation: Oral

LS4-O-1 Navigating the Human Protein Atlas to map the composition of extracellular matrix proteins in normal and cancer tissues

Jaroslaw Bryk[a], Yun Wah Lam[b]

[a]*Department of Physical and Life Sciences, University of Huddersfield, UK*

[b]*Department of Health Sciences, Hong Kong Metropolitan University, Hong Kong*

Contact email: wywlam@hkmu.edu.hk

In solid tumours, cancer cells exist within a dynamic microenvironment where extracellular matrix (ECM) proteins, play crucial roles in tumour progression, metastasis, and drug resistance. Despite their clinical importance, a systematic characterisation of ECM proteins remains challenging, as their insolubility often hinders accurate detection by traditional proteomic technologies. Immunohistochemistry (IHC) allows the in-situ localisation of proteins within the context of tissue architecture and is ideal for the biochemical characterisation of tumour microenvironment, yet its compatibility with unbiased proteomics is limited by a lack of high-quality image databases and computational tools for automated analysis. Currently, computational methods for quantifying DAB-stained regions of tissue sections, such as Fiji, requires pre-defined colour matrices and manual adjustments, which limit reproducibility and throughput. We developed a novel computational pipeline, Hue-based Quantification (HUE-Q), to automate DAB quantification that works by isolating haematoxylin-stained regions using hue-defined pixel masking. The HUE-Q pipeline showed a strong correlation compared to Fiji (R=0.86) and with approximately 150 times higher throughput. Using HUE-Q, we mined the IHC staining intensity in the Human Protein Atlas (HPA), the world's largest publicly available IHC image repository. We analysed ~290,000 IHC images of 1,141 antibodies against 685 ECM proteins in 43 normal human organs and 5 cancer tissues. Our data reveal an extraordinary level of tissue specificity in ECM expression, including specific changes of ECM composition in the TME. To our knowledge, this is the largest repository of ECM expression in human to date and will have a broad impact on cancer research, from the use of ECM in cell culture experiments to the identification of ECM drug targets for cancer therapies.

Type of presentation: Oral

LS4-O-2 The First Identification of Telocyte Cells in the Human Ovarian Stroma: Morphological and Immunophenotypical Characterization

Merjem Purelku[a], Ceren Cebi[b], Sait Sukru Cebi[b], Sennur Ilvan[c], Ismail Cepni[b], Gamze Tanriverdi[d]

[a]*Bahcesehir University, School of Medicine, Department of Histology and Embryology, Istanbul, Turkiye*

[b]*Istanbul University - Cerrahpasa, Cerrahpasa Medical Faculty, Obstetrics and Gynecology Department, Turkiye*

[c]*Istanbul University - Cerrahpasa, Cerrahpasa Medical Faculty, Pathology Department, Turkiye*

[d]*Istanbul University - Cerrahpasa, Cerrahpasa Medical Faculty, Histology and Embryology Department, Turkiye*

Contact email: merjem.purelku@gmail.com

Background:
Telocytes (TCs) are a newly recognized type of interstitial cell, previously referred to as interstitial Cajal-like cells (ICLCs). Defined by their distinctive long, slender telopodes and secretory vesicles, TCs have been identified in multiple organs, including several within the female reproductive system. However, their presence in the human ovary has not been clearly demonstrated or characterized until now. Given the complexity of stromal cell populations in the ovary and the regulatory roles TCs play—ranging from tissue homeostasis and immune surveillance to angiogenesis and stem cell guidance—investigating their presence may reveal important aspects of ovarian physiology and pathology.
Aim:
This study aimed to determine the existence and distribution of telocytes within the human ovarian stroma, utilizing immunohistochemistry, double immunofluorescence, and transmission electron microscopy (TEM), alongside immunogold labeling.
Methods:
Ovarian tissue samples were collected from women aged 18–65 undergoing total hysterectomy and bilateral salpingo-oophorectomy (THBSO) for benign uterine conditions, excluding those with prior chemotherapy. After standard tissue processing, telocytes were identified using immunohistochemistry with CD34 and further characterized via double immunofluorescence staining with CD34/c-kit, CD34/vimentin, CD34/PDGFR-β, and CD34/α-SMA. Ultrastructural analysis was performed using TEM, and immunogold labeling with CD34 was applied for precise telocyte confirmation.
Results:
Telocyte cells were identified in the ovarian stroma based on their distinct morphology and immunophenotype. They exhibited strong CD34 positivity and co-expressed PDGFR-β and vimentin, while showing weak positivity for α-SMA. In contrast, fibroblasts were CD34-negative but strongly positive for vimentin and PDGFR-β, whereas pericytes were CD34-negative and strongly positive for α-SMA and PDGFR-β. This allowed clear distinction between TCs, fibroblasts, and pericytes. TEM analysis revealed telocytes as cells with small bodies and extremely long, thin processes located around blood vessels and throughout the stroma. Immunogold labeling using CD34 further supported their accurate identification.
Conclusion:
Our findings confirm the presence of telocyte cells in the human ovarian stroma and distinguish them from other stromal cell types. This study contributes novel insights into the cellular composition of the ovary and highlights the potential functional roles of TCs in reproductive health and disease.
Keywords: Human ovary, Telocytes, Immunofluorescence, TEM

Type of presentation: Oral

LS4-O-3 Morphological and Mechanical Characterization of Major Ampullate Spider Silk Fibers in Liquid Environments: Insights from SEM and Single-Fiber Tensile Testing

Leon Ploszczanski[a], Gerhard Sinn[a], Karolina Peter[a], Aida Naghilou[b], Sarah Stadlmayr[b], Christine Radtke[b], Helga C. Lichtenegger[a]

1: Institute of Physics and Materials Science, BOKU University, Universität für Bodenkultur Wien, Austria

2: Plastic and Reconstructive Surgery, Medical University Vienna/Vienna General Hospital, Vienna, Austria

Contact email: leon.ploszczanski@boku.ac.at

Spider silk has been established as one of nature's most fascinating materials, used in applications such as fishing and wound healing for centuries [1, 2]. In recent years, it has attracted vivid attention due to its unique strength, toughness, and elasticity. One of the more remarkable applications of spider silk in medicine is its use for nerve growth and nerve regeneration [3-10]. Schwann cells, which are crucial for the nerve regenerative process, have been shown to adhere to spider silk and migrate along it without any inflammatory response or physiological pH changes [11]. Despite the regenerative performance of different spider silks being studied, very little attention has been paid to the interface between Schwann cells and spider silk and its correlation to material and surface properties. Systematic studies combining mechanical, morphological, chemical, and structural investigations of spider silk together with an assessment of its nerve regenerative potential are still rare [13, 14].

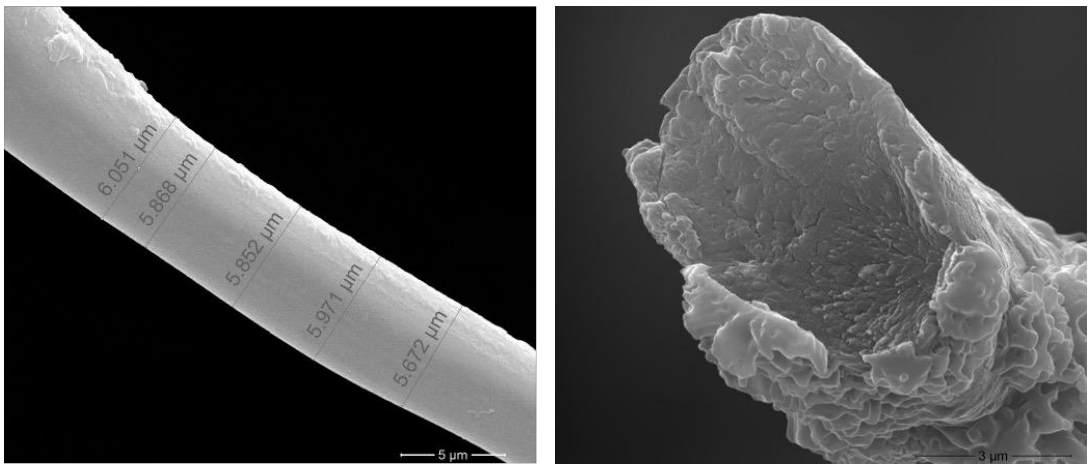
This study focuses on major ampullate (MA) silk from *Nephila edulis*, aiming to characterize its performance under physiologically relevant conditions. Specifically, the research investigates the morphological and mechanical performance of single MA silk fibers when submerged in solutions with various properties to simulate different biological, hydrating, and dehydrating scenarios. The major ampullate gland dragline silk is collected on reels and glued onto a plastic sample holder with cyanoacrylate superglue. For measurement, the thin side supports of the holder are removed prior to immersion into the liquid, so that only the single fiber is under tension.

The study employs light microscopy to measure the width of the immersed silk fibers before tensile testing and scanning electron microscopy (SEM) to observe surface modifications post-tensile testing. A novel aspect of this research is the ability to pull single MA silk fibers immediately after immersion in the solution, allowing for real-time assessment of their mechanical properties. The tensile tests have been performed on an Asmec nano indenter in tensile mode, and electron micrographs for post-mortem analysis of the fiber are recorded with a FEI Quanta 250 FEG ESEM in high vacuum conditions, after Au sputter coating. The first tests with the modified nano indenter were successful and proved the concept of repurposing the indenter to a micro tensile stage. Video capturing of the tensile test in situ is possible, allowing the straining of the fiber to be watched while conducting the experiment and collecting stress/strain data with the nano indenter control software.

By examining the interactions between silk fibers and different types of solutions, the research aims to elucidate the critical factors that influence silk's structural integrity and mechanical performance. Understanding these interactions is essential for optimizing the use of spider silk in medical applications, particularly for NGCs [12].

Overall, this study contributes to the increasing knowledge on spider silk as a biomaterial, advancing the field of regenerative medicine.

References:
1. Newman, J. and C. Newman, Oh what a tangled web: the medicinal uses of spider silk., https://doi.org/10.1111/j.1365-4362.1995.tb01600.x
2. Römer, L. and T. Scheibel, The elaborate structure of spider silk., https://doi.org/10.4161%2Fpri.2.4.7490
3. Allmeling, C., et al., Spider silk fibres in artificial nerve constructs promote peripheral nerve regeneration., https://doi.org/10.1111/j.1365-2184.2008.00534.x
4. Allmeling, C., et al., Use of spider silk fibres as an innovative material in a biocompatible artificial nerve conduit., https://doi.org/10.1111/j.1582-4934.2006.tb00436.x
5. Hennecke, K., et al., Bundles of spider silk, braided into sutures, resist basic cyclic tests: potential use for flexor tendon repair. PloS one, 2013. 8(4): p. e61100-e61100.
6. Kuhbier, J.W., et al., Interactions between spider silk and cells--NIH/3T3 fibroblasts seeded on miniature weaving frames. PloS one, 2010. 5(8): p. e12032-e12032.
7. Kuhbier, J.W., et al., First investigation of spider silk as a braided microsurgical suture. Journal of Biomedical Materials Research Part B: Applied Biomaterials, 2011. 97B(2): p. 381-387.
8. Radtke, C., et al., Spider Silk Constructs Enhance Axonal Regeneration and Remyelination in Long Nerve Defects in Sheep. PLOS ONE, 2011. 6(2): p. e16990.
9. Schäfer-Nolte, F., et al., Biomechanics and biocompatibility of woven spider silk meshes during remodeling in a rodent fascia replacement model. Annals of Surgery, 2014. 259: p. 781–792.
10. Wendt, H., et al., Artificial Skin – Culturing of Different Skin Cell Lines for Generating an Artificial Skin Substitute on Cross-Weaved Spider Silk Fibres. PLOS ONE, 2011. 6(7): p. e21833.
11. Radtke, C., Natural Occurring Silks and Their Analogues as Materials for Nerve Conduits. International journal of molecular sciences, 2016. 17(10): p. 1754.
12. Semmler, M., et al., Silk-in-silk nerve guidance conduits enhance regeneration in a rat sciatic nerve injury model., https://doi.org/10.1002/adhm.202203237
13. Naghilou, A., et al., Correlating the secondary protein structure of natural spider silk with its guiding properties for Materials Science and Engineering., https://doi.org/10.1016/j.msec.2020.111219
14. Peter, K., et al., Exploring the Unique Properties and Superior Schwann Cell Guiding Abilities of Spider Egg Sac Silk., ACS Appl. Bio Mater., 2025, 8, 1307−1319



Post-testing and inner structure micrograph of Dragline MAG silk of *Nephila edulis*

Type of presentation: Oral

LS4-O-4 Periodontal and bone regeneration with magnesium barrier membranes: an *in vitro* study

Domen Kanduti[a,b], Aleksandar Janev[c], Boris Gašpirc[a,b], Anton Sculean[d], Mateja Erdani Kreft[c], Peter Veranič[c], Nataša Resnik[c]

[a]*Department for Oral Diseases and Periodontology, Faculty of Medicine, University of Ljubljana, Slovenia*

[b]*Department for Oral Diseases and Periodontology, University Medical Centre Ljubljana, Slovenia*

[c]*Institute of Cell Biology, Faculty of Medicine, University of Ljubljana, Slovenia*

[d]*Department of Periodontology, School of Dental Medicine, University of Bern, Switzerland*

Contact email: domen.kanduti@mf.uni-lj.si, natasa.resnik@mf.uni-lj.si

Introduction: Periodontitis is chronic inflammatory disease that affects the supporting tissues around teeth. If untreated, it leads to tooth loss. In its severe form it affects more than 1 billion people worldwide. Periodontal treatment nowadays consists of not only preventing inflammatory and immune response of the tissue and its further loss but also to regenerate lost periodontal tissues [1]. The regeneration of periodontal tissues depends on the cells that first colonize the root surface. In 1976, Melcher described that the cells that first colonize the tooth or root surface determine the nature and quality of the tissue that will be formed, and therefore the reparation or regeneration of the tissues [2, 3, 4]. According to the specifics of periodontal wound healing, the concept of guided tissue regeneration has been developed. For complete tissue regeneration, barrier membranes are an important element in regenerative treatment as they allow separation of bone and soft tissue components of periodontal defect. They can be used with or without bone graft, depending on the bone defect anatomy [3, 4]. Nowadays magnesium-based bio-alloys emerged, promising favourable degradation rates, enhanced biocompatibility and favourable effect on bone regeneration and bone healing [5, 6]. One of the key requirements of any biomaterial is its biocompatibility. This study was designed as *in vitro* study comparing biocompatibility of magnesium membranes versus standard collagen membranes, which are currently considered as the "gold standard" in the field of regenerative periodontology. Cell attachment, adhesion, morphology, and matrix mineralization were assessed using light and scanning electron microscopy, while transcriptomic profiling was employed to identify gene expression changes.

Methods: All experiments were performed *in vitro* using murine osteoblasts MC3T3-E1 cell line as a model. The cells were grown for 3 weeks without membrane (control group), with collagen (Coll) membranes (Collprotect® membrane), and with magnesium (Mg) membranes (NOVAMag® membrane, both membranes from Botiss biomaterials GmbH, Zossen, Germany). Then cells with membranes or without were parallelly processed for light and scanning electron microscopy, and mRNA was isolated for mRNA sequencing.

Results: Light microscopy and scanning electron microscopy revealed that osteoblasts around Mg membranes exhibited similarly interconnected and organized cell networks as osteoblasts around Coll membranes and in the absence of membranes.
The Mg membranes appeared to better support biomineralization, as density of mineralized particles was the highest in samples with Mg membranes, as shown by scanning electron microscopy (Figure 1) and mRNA profiling, which revealed upregulated expression of genes associated with osteogenic differentiation.

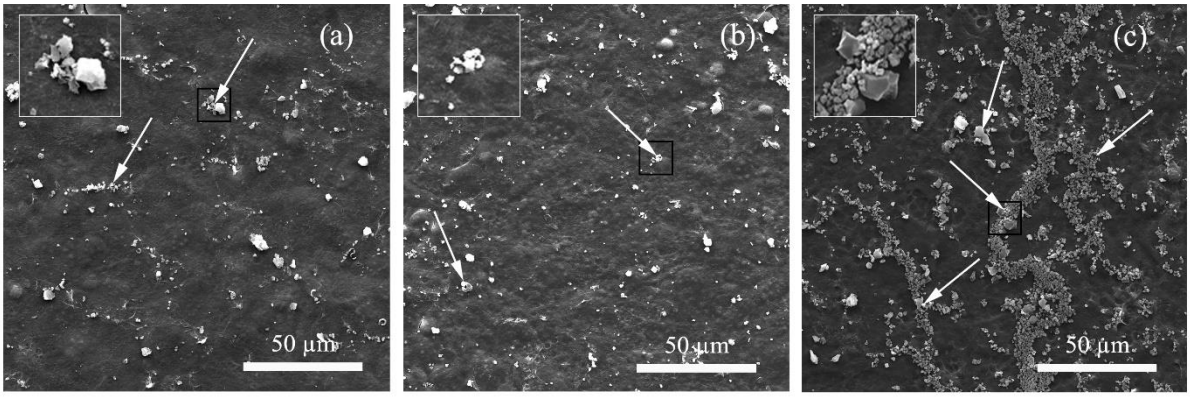


Figure 1: Osteoblasts, grown on a membrane-free surface (a), around Coll membrane (b), and around Mg membrane (c), are tightly connected as revealed by scanning electron microscopy. Mineralized particles (indicated by arrows and enlarged in white-framed insets) are most densely distributed in the matrix above the osteoblasts surrounding the Mg membrane. White-framed insets show 3× magnifications of black-framed regions.

Discussion and conclusions: In regenerative periodontology, the use of biocompatible, osteoinductive, and resorbable regenerative materials has a beneficial effect on treatment outcome and reduces the possibility of postoperative complications [3, 4]. In addition to appropriate mechanical properties, Mg membranes have favourable osteoinduction and osteogenic differentiation properties [5, 6] compared to Coll membranes due to Mg^{2+} release. Our microscopy and transcriptomic analyses revealed that the Mg membrane promotes extracellular matrix mineralization and upregulation of key genes involved in osteogenic differentiation, without exhibiting cytotoxic effects. These results highlight the great potential of Mg membranes for bone tissue engineering applications.

REFERENCES:

1. Dentino A, Lee S, et. al., Periodontol 2000. **2013**, 61, 16-53.
2. Melcher AH, J Periodontol. **1976**, 47, 256-260.
3. Sculean A, Chapple LCI, et. al., Periodontol 2000. **2015**, 68, 7-20.
4. Sculean A, Nikolidakis D, et. al., Periodontol 2000. **2015**, 68, 182-216.
5. Zhou Y, Zhang A, et. al., ACS Biomater Sci Eng. **2024**, 10, 3514-3527.
6. Zhang J, Tang L, et. al., Adv Healthc Mater. **2019**, 8, e1901030.

Type of presentation: Poster

LS4-P-1 Investigation of the Therapeutic Effects of Allium cepa Extract on Ovaries and Uterus in Chronically Administered DHEA Rats by Apoptotic Pathways

Said Bahadır Aslan[a], Hakan Şahin[a], Yasemin Ersoy Çanıllıoğlu[b], Gözde Erkanlı Şentürk[a]

[a]*Istanbul University- Cerrahpasa, Cerrahpasa School of Medicine, Department of Histology and Embryology, Istanbul, Turkiye*

[b]*Bahcesehir University, School of Medicine, Department of Histology and Embryology, Istanbul, Turkiye*

Contact email: said.aslan@iuc.edu.tr

Dehydroepiandrosterone (DHEA), a steroid hormone synthesized by the adrenal glands and the liver, serves as a crucial precursor in the biosynthesis of both androgens and estrogens. Currently, DHEA finds applications across diverse medical and physiological domains, including the management of sexual dysfunctions, the attenuation of menopausal symptoms, body weight regulation, and the potential enhancement of athletic performance. Within this context, existing literature has explored the metabolic and endocrine influences of DHEA administration on the ovaries and uterus. Allium cepa (AC), commonly known as onion, is characterized by a rich array of nutritional components and bioactive phytochemicals. These include flavonoids and flavonol glycosides, alongside phenolic and organosulfur compounds. This compositional profile confers upon AC a spectrum of biological activities, notably encompassing antioxidant, anti-inflammatory, and enzyme inhibitory properties. With a long history of use in traditional medicine and a significant role in dietary intake, AC has been the subject of numerous investigations into its effects on various disease states. The present study aimed to investigate the morphological alterations occurring in the ovarian corpus luteum and the uterine surface epithelium, stroma, and glands of rats subjected to chronic administration of DHEA and DHEA+AC by investigating apoptotic pathways. Findings were derived from immunohistochemical analysis and semi-thin section examination conducted at the light microscopy level. For ovarian tissues, statistical analysis revealed a significant increase in Bcl-2 expression in the DHEA+AC treatment group compared to both the control and DHEA groups. In uterine tissues, a statistically significant elevation in phospho-AKT levels was observed in the surface epithelium of both the DHEA and DHEA+AC groups relative to the control group. Furthermore, the glandular epithelium of the DHEA+AC group demonstrated a statistically significant increase in the levels of Bcl-2 and NFkB compared to the control group. A statistically significant increase in stromal phospho-AKT levels was also noted in the DHEA+AC group compared to the control. Additionally, histopathological examination of the corpus luteum in the DHEA-treated group revealed the presence of basophilic stained cells alongside the typical luteal cells. These results suggest that AC may exert its effects on ovarian and uterine tissue through various apoptotic pathways in DHEA-administered rats.

Key Words: Dehydroepiandrosterone, Allium cepa, Ovary, Uterus, Apoptotic pathways

Type of presentation: Poster

LS4-P-2 Virome of the invasive signal crayfish and its correlation with histopathological changes of the hepatopancreas

Katarina Bačnik[a], Tobia Pretto[b], Ana Bielen[c], Sandra Hudina[d], Denis Kutnjak[a]

a National Institute of Biology (Ljubljana), Slovenia

b Istituto Zooprofilattico Sperimentale delle Venezie (Legnaro, padova), Italy

c Faculty of Food Technology and Biotechnology, University of Zagreb (Zagreb), Croatia,

d Faculty of Science, University of Zagreb (Zagreb), Croatia

Contact email: katarina.bacnik@nib.si

Host-associated microbial communities, including viruses, can play important roles during biological invasions by either preventing or facilitating the establishment or spread of the introduced species through effects on population demography and inter-species interactions. The knowledge about the presence and role of viruses in association with invasive alien species has been scarce so far. Using high-throughput sequencing (HTS) we have previously characterized the virome of one of the most successful invasive species of freshwater invertebrates in Europe, the signal crayfish (*Pacifastacus leniusculus*), identifying novel and divergent signal crayfish associated RNA viruses along its invasion range [1]. Some of the viruses present in invasive host may cause histopathological changes of the tissues, such as previously observed high prevalence of idiopathic necrotizing hepatopancreatitis of the signal crayfish in the Korana River in Croatia [2].

To assess the histopathological changes and correlate them with the diversity and prevalence of known and novel viruses, we sampled signal crayfish individuals in September 2024 at four different locations in Korana River and its affluents. We used hepatopancreas tissue to calculate organosomatic condition indices, to isolate RNA for shotgun HTS followed by virome characterization and to assess the occurrence of qualitative (severity of observed changes) and quantitative (frequency of observed changes) histopatological factors. Additionally, tissue blocks of selected hepatopancreas samples with observed pathological changes were used to prepare ultrathin sections stained with uranyl acetate for examination under transmission electron microscopy (TEM).

Hepatopancreas virome analysis, using state-of-the-art in-house established shotgun metagenomics pipeline, identified known and novel viruses from different taxonomic groups. Using TEM we observed ultrastructurally different epithelial cell types with many cell organelles and plenty of lipid globules. The contribution of various intrinsic (condition index, histopathological scores, possible observation of viral particles using TEM) and extrinsic (crayfish population density) factors to composition of signal crayfish viromes along the invasion range will be presented.
The results of this study will gain new knowledge on the effects of viral infections on the signal crayfish health and invasion success.

References:
1. K. Bačnik, D. Kutnjak, S. Černi, A. Bielen, S. Hudina, *Viruses*, **2021**, 13, 11, (2259)
2. A. Bekavac, P. Dragičević, Z. Dragun, A. Beck, I. Maguire, D. Ivanković, Ž. Fiket, R. Gračan, S. Hudina. *J. Fish Dis.* **2021**, 1–16.

Type of presentation: Poster

LS4-P-3 Molecular switch from Laminin beta 2 to Laminin beta 1 chain in brain microvasculature supports endothelial sprouting and is associated with increased blood brain barrier permeability

Serguei I. Bannykh[a], Katherine S. Bannykh[a], Antonio C. Fuentes-Fayos[a], Joshua J. Breunig[a]

[a]*Cedars-Sinai Medical Center, (Los Angeles), USA)*

Contact email: serguei.bannykh@cshs.org

Introduction:
Blood-Brain-Barrier (BBB) plays a pivotal role in maintaining cerebral function. Given its fundamental physiologic significance a certain redundancy and overlap in its key components is expected. From a cellular prospective there is a well-established role of endothelial cells (EC), pericytes (PC) and astrocytes. On a molecular side the constituents of BBB are mostly found among intercellular junction proteins. Here we identify that an alteration in expression of basal membrane protein laminin α and ß isoforms are critical components facilitating microvascular remodelling and permeability.

Methods: We performed a correlative analysis of post-gadolinium enhanced magnetic resonance imaging (MRI) of the brain, immunohistochemical (IHC), in-situ hybridization (ISH), transmission electron microscopic (TEM) and bioinformatic analysis of single cell RNA sequencing (scRNA-seq) databases of 1131 neuroectodermal tumours and controls. Bioinformatic analyses were performed using 47 external single-cell datasets of 3 adult brains as normal samples [1] and 44 brain tumor samples (4 low-grade glioma, 22 newly diagnosed GBM, and 18 recurrent GBM [2, 3], total cell count: 319 152. Scanpy v1.9 was used to merge, filter, and analyze the single-cell data. Samples were individually filtered by percentage of mitochondria genes (≤0.05), read counts (≤17500), number of genes (4500≤ ≥750) and doublet score (≤0.04). After the filtering, the total cell count was: 65 079, total gene count: 3193. Harmony was used to normalize all the data previous to the analyses to avoid bias between samples and datasets. Leiden algorithm and UMAP were used to establish the clusters of the samples. To characterize the clusters, marker genes (pval_cutoff = 0.0001, log2fc_min = 1.5) were ranked using t-tests and Wilcoxon rank-sum tests. This selection of lineage-specific markers was done in concordance with previously reported. Plotly (v5.18.0) was used to plot the data generated in these analyses.

Results: Normal brain shows intact BBB, with no evidence of post gadolinium enhancement (PGE) on MRI (Fig 1). By using IHC we detect that normal brain microvasculature (MV) contains no laminin ß1 (LAMB1) chain of heterotrimeric laminin protein. Instead, brain MV shows prominent deposition of laminin ß2 (LAMB2), which is also located at the other site of BBB: glial limitans. In conditions of increased MV remodelling, such as stroke, inflammation, and especially high-grade gliomas (HGG) brain MRI highlight pathology with local PGE. In such conditions, IHC detects a loss of LAMB2 labelling and its replacement by LAMB1. Loss of LAMB2 parallels an appearance of PGE on brain MRI. ISH corroborates IHC data and shows at least 100-fold increase in LAMB1 copy numbers/per MV cell in cases of HGG. This up-regulation of LAMB1 is fully abrogated by treatment with vascular endothelial growth factor (VEGF) inhibitor bevacizumab, its replacement by LAMB2 and disappearance of PGE on MRI. scRNA-seq identify quiescent EC and PC as the main source of LAMB2 in the normal brain and confirmed that LAMB1 is expressed by immature EC in HGG.
Discussion and conclusions: Our study shows that brain MVC produce LAMB2 which is continuously deposited along the sites of intact BBB. Remodelling of MV is accompanied by PGE on MRI, loss of LAMB2 and acquisition of LAMB1, which is mediated by VEGF. Genes for human LAMB1 & 2 are located on 7q22 and 3p21 and encode for proteins of 1,786 and 1,798 aminoacids, respectively, with most of the difference between two proteins is within a stretch of extra 12 aminoacids in N-terminus in LAMB2. In silico analysis predicts a completely different set of interactive proteins, which might account for their non-overlapping functions and explain the role of LAMB1 in support of endothelial sprouting and LAMB2 is maintaining of intact BBB.

Acknowledgments. The authors were supported by DoD grant HT9425-23-1-0269, NIH grant R33CA236687, American Cancer Society grant RSG-16-217-01-TBG.

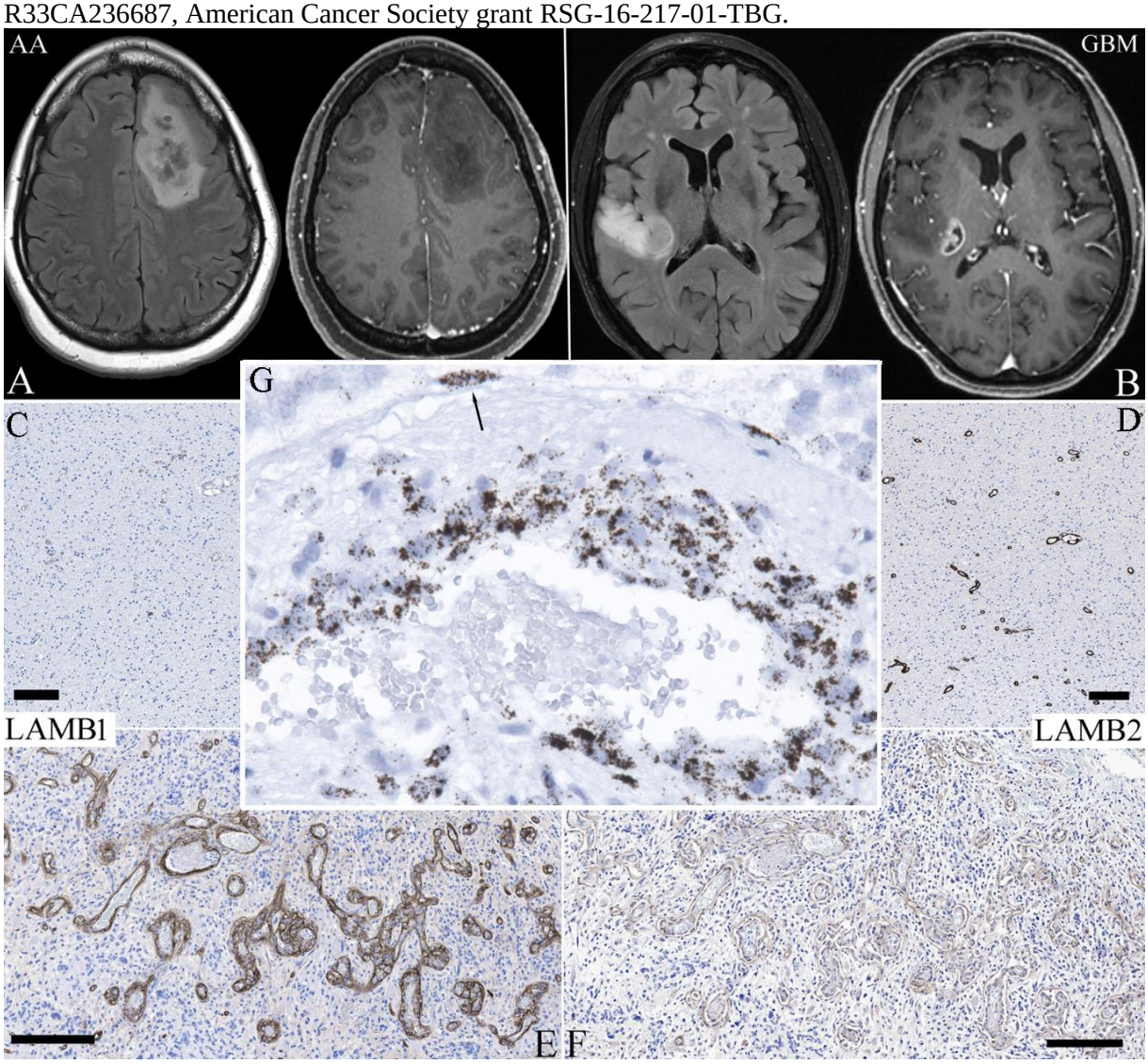


Figure 1: MRI, IHC, ISH showing a summary of contrasting findings of low and high grade gliomas. A and B are representative MRI FLAIR (left) and T1 PGE (right in a pair) of IDH1 mutant CNS WHO grade 3 (AA) and IDH1 wild type CNS WHO grade 4 (GBM). C-F: Corresponding IHC images from the above patients stained with abs against LAMB1 (C, E) & LAMB2 (D, F). The IHC images depict serial sections. G: ISH for LAMB1 of the above case of GBM. Arrow point to a presumed glial cell of glia limitans.

References:

1. Winkler EA, Kim CN, Ross JM, Garcia JH, Gil E, Oh I, et al. A single-cell atlas of the normal and malformed human brain vasculature. Science. 2022;375(6584):eabi7377. Epub 2022/01/28. doi: 10.1126/science.abi7377.
2. Abdelfattah N, Kumar P, Wang C, Leu JS, Flynn WF, Gao R, et al. Single-cell analysis of human glioma and immune cells identifies S100A4 as an immunotherapy target. Nat Commun. 2022;13(1):767. Epub 2022/02/11. doi: 10.1038/s41467-022-28372-y.
3. Crouch EE, Joseph T, Marsan E, Huang EJ. Disentangling brain vasculature in neurogenesis and neurodegeneration using single-cell transcriptomics. Trends Neurosci. 2023;46(7):551-65. Epub 2023/05/21. doi: 10.1016/j.tins.2023.04.007.

Type of presentation: Poster

LS4-P-4 The Effects of Amylin on Aggression in Wistar Rats Exposed to the Resident-Intruder Paradigm

Gafur Rakici[a], Duygu Neccar[b], Gozde Erkanli Senturk[b], Oguzhan Ekici[a], Sila Guvenir Seven[a], Gonul Simsek[a]

[a]*Department of Physiology, Cerrahpasa Faculty of Medicine, Istanbul University-Cerrahpasa, Istanbul, Turkey*

[b]*Department of Histology and Embryology, Cerrahpasa Faculty of Medicine, Istanbul University-Cerrahpasa, Istanbul, Turkey*

Contact email: gozde.erkanlisenturk@iuc.edu.tr

Aggression can be seen together with substance addiction, psychiatric diseases and other health problems and can turn into violence. Our study investigated the effect of amylin on aggression centers in the central nervous system and its possible therapeutic effects.

Two experiments were carried out on rats divided into four groups. In Experiment 1, saline was applied to one group of rats, while intraperitoneal amylin was administered to the other group. In Experiment 2, intraperitoneal amylin was administered to both groups. In Experiment 2, saline was administered to one group of rats through a cannula attached to the Area Postrema (AP), and amylin antagonist was administered to the other group. After rats in all groups were housed in cages with ovariectomized females for a week, they were exposed to the Resident Intruder Paradigm with another male rat that was younger and weaker than them for 10 minutes, and the behaviors were recorded. The brain of rats were examined with immunohistochemical and behavioral tests. In Experiment 1, it was determined that amylin significantly reduced Medial Amygdala (MeA) activation and aggression behavior. In Experiment 2, it was observed that immunoreactivity increased in the Bed Nucleus of Stria Terminalis (BNST), Ventrolateral of the Ventromedial Hypothalamus (VMHvl) and MeA nuclei of rats administered amylin antagonist to the AP. Findings indicate that amylin has an antiaggressive effect and that its antiaggressive effects may occur through AP.

Keywords: Aggression, Islet Amyloid Polypeptide, Social Behavior, AC 187

Type of presentation: Poster

LS4-P-5 Brain Decellularization Process in Transgenic Alzheimer Rat Model

Ahmet Ozturk[a], Selenay Furat[a], Canan Ozturk[a], Can Kilic[a], Gokhan Duruksu[a], Seda Halbutogullari[a], Yusufhan Yazir[a]

[a]*Kocaeli University, (Kocaeli), TÜRKİYE*

Contact email: selenay.furat@hotmail.com

Introduction: Alzheimer's disease is a neurodegenerative disease characterized by a decrease in daily vital activities and impaired cognitive abilities, accompanied by neuropsychiatric symptoms and behavioral changes. The main pathological findings in this disease are the accumulation of abnormally amyloid beta (Aβ) plaques outside the cell and the formation of neurofibrillary tangles with the phosphorylation of tau proteins accumulated inside the cell. We aimed to investigate the role of brain extracellular matrix (ECM) age in Alzheimer's Disease 'independently of cellular aging'. Our study is a 3D cell culture model created to understand how brain ECM age changes Alzheimer's pathogenesis. For this purpose, first step includes the creation of young and old ECM platforms.

Methods: At this stage, brain extracellular matrices (dbECMs) were produced by decellularization of the brains taken from donors. dbECMs were obtained from both healthy (inbred Fischer 344 rats) and transgenic Alzheimer's (inbred TgF344-AD rats created with Fischer344 strain) young (6 months old) and old (16 months old) rats. The decellularization process were performed by modifying previous studies [1]. Samples were incubated for half an hour in cold PBS containing 1% antibiotic and antimycotic solution. Then, they were frozen and thawed at -80 °C for 4 hours and this process were repeated 4 times. Then, they were sterilized with the help of an orbital shaker using 1% Triton X-100 (4 hours), distilled water (30 minutes), 4% deoxycholate (4 hours), distilled water (30 minutes), and 0.1% peracetic acid in 4% ethanol (2 hours) and the decellularization process were completed. Brain ESMs obtained from donors with Alzheimer's phenotype were treated with IDE (Insulin degrading enzyme) to destroy any amyloid beta plaques that may remain after decellularization. In this way, it was ensured that the extracellular matrix obtained from Alzheimer's models were not contain amyloid beta aggregates. Immunoflourescense staining was performed to demonstrate amyloid beta expression in healthy, transgenic and decellularised brain tissues, and histochemical staining was performed to demonstrate successful decellularization.
Results: Transgenic rat brains (young and old) showed increased expression of amyloid beta compared to healthy ones. Nuclear staining was not detected in H&E staining in decellularized brain tissues.

Discussion and conclusions: Detailed investigations in these models will be transformed into data describing how ECM age affects Alzheimer's pathogenesis. The experimental model we will create to investigate the roles of ECM age in Alzheimer's disease has a structure that can be modified and used for many diseases that occur during the aging process.

Keywords: Alzheimer, Decellullarization, Aging, Brain, Extracellular matrix

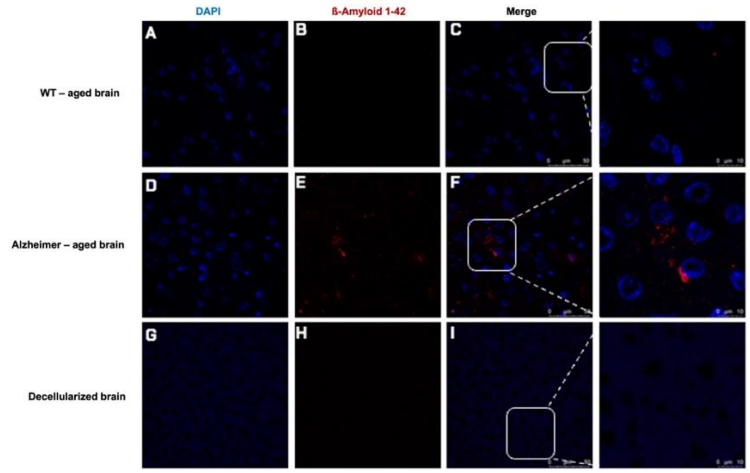


Figure 1: Amyloid-β staining of wild type, transgenic Alzheimer and decellurized rat brain tissues.

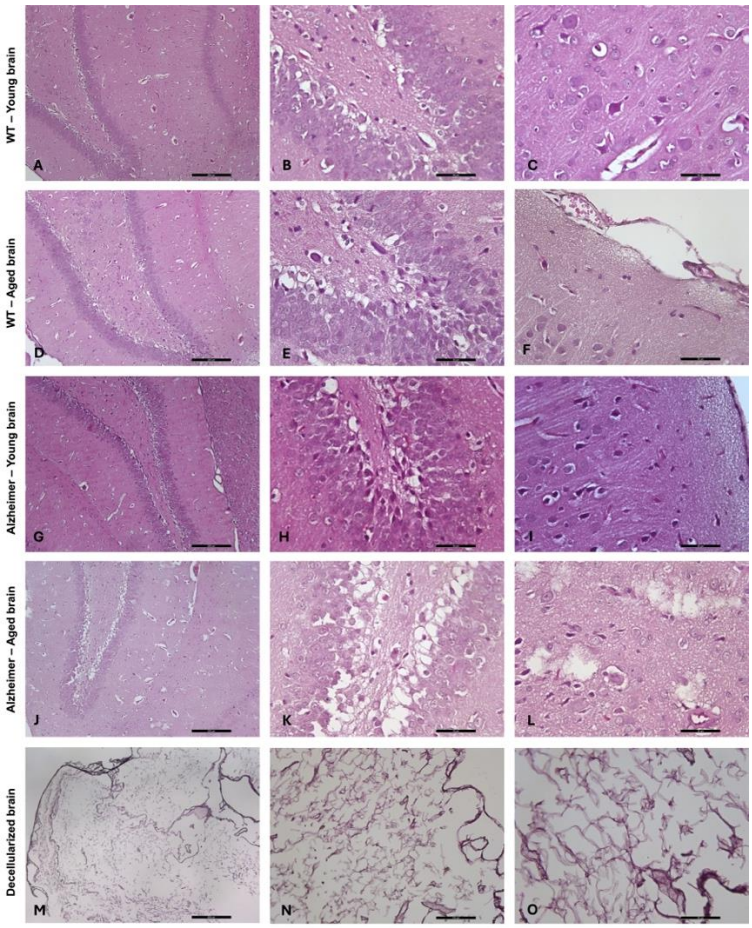


Figure 2: H&E staining of wild type, transgenic Alzheimer and decellurized rat brain tissues.

References:

1. Lin, Q., Wong, H. L., Tian, F. R., Huang, Y. D., Xu, J., Yang, J. J., Chen, P. P., Fan, Z. L., Lu, C. T., Zhao, Y. Z. **2017**. "Enhanced neuroprotection with decellularized brain extracellular matrix containing bFGF after intracerebral transplantation in Parkinson's disease rat model". International journal of pharmaceutics, 517(1-2), 383–394.

Type of presentation: Poster

LS4-P-6 Chemotherapy-induced metabolic changes in glioblastoma stem and differentiated cells in a context of the tumor microenvironment

Simona Katrin Galun[a], Urban Bogataj[b], Metka Novak[a], Klementina Fon Tacer [cd], Miloš Vittori[b], Cornelis J.F. Van Noorden[a], Barbara Breznik[a]

[a]*National Institute of Biology, Department of Genetic Toxicology and Cancer Biology, (Ljubljana), Slovenia*

[b]*University of Ljubljana, Biotechnical Faculty, Department of Biology, (Ljubljana), Slovenia*

[c]*Texas Tech University School of Veterinary Medicine, (Amarillo), Texas, USA*

[d]*Texas Center for Comparative Cancer Research, Texas Tech University, (Amarillo), Texas, USA*

Contact email: simonakatrin.galun@nib.si

Introduction: Glioblastoma (GBM) is one of the most aggressive primary brain tumors with a poor survival prognosis. Standard therapy for GBM treatment includes surgery, radiotherapy, and chemotherapy. The latter is in the form of the cytotoxic agent temozolomide (TMZ) which functions by attaching alkyl groups to DNA, resulting in cellular damage. A major obstacle in the treatment of GBM is its resistance to TMZ, which is largely attributed to the presence of glioblastoma stem cells (GSCs). These cells exhibit significant plasticity, which includes mechanisms such as activating DNA repair processes to counteract the damage induced by TMZ and utilizing ABC transporters to expel the cytotoxic substance. The ability of GSCs to resist therapy is closely linked to the tumor microenvironment (TME), where cancer cells interact with surrounding non-cancerous cells, exchanging soluble molecules, metabolites and organelles. The TME can influence GSCs, prompting them to adopt different metabolic pathways for energy production, supporting their resistance to cytotoxic agents. Mitochondria consequently play an important role, by altering their function and inducing metabolic changes that help cancer cells to survive under cytotoxic stress, thereby contributing to resistance to TMZ [1,2,3].

Methods: To better understand the effect of TMZ on GSC metabolism in a context of the tumor microenvironment, we compared changes in cellular metabolic viability and the ultrastructural characteristics of mitochondria in two GSC and two differentiated GBM cell lines. The cell lines were exposed to conditioned media of endothelial cells and treated with TMZ. To evaluate the mitochondrial ultrastructure, we utilized transmission electron microscopy. Cellular metabolism was assessed using a metabolism-based cell viability assay and extracellular flux analysis using Seahorse assay.

Results: We observed distinct differences in the mitochondrial ultrastructure and cell metabolism between GSCs and differentiated GBM cells. In GSCs, mitochondria predominantly appeared normal and structurally intact, with the presence of some mitochondria with abnormal ultrastructural alterations (Fig 1d). Most of GSCs contained electron-dense mitochondria with narrow cristae (Figure 1a), which are associated with high OXPHOS activity. The Seahorse assay confirmed that GSCs primarily rely on OXPHOS for ATP production and are more quiescent. In contrast, the ultrastructure of mitochondria in differentiated GBM cells was highly variable. However, a consistent observation was the presence of defective mitochondria (Figure 1c, d), which corelate with impaired OXPHOS activity. Additionally, we observed electron-dense mitochondria with dilated cristae (Figure 1b) corresponding with reduced OXPHOS activity. In accordance with ultrastructure results, the Seahorse assay indicated that differentiated GBM cells depend more on glycolysis for ATP production.
After exposure of GSCs and differentiated GBM cells to conditioned media of endothelial cells, that represents a part of the perivascular niche in TME, we observed significant changes in mitochondrial ultrastructure. This led to predominance of normal mitochondria in both GSCs and differentiated GBM cells, suggesting a direct influence of selected part of TME on mitochondrial ultrastructure and potentially their function.

When conditioned media of endothelial cells was combined with TMZ treatment, cell viability and mitochondrial ultrastructure in GSCs remained unaffected. In contrast the viability of differentiated GBM cells decreased, but the mitochondrial ultrastructure was not affected.
Moreover, we noticed the plasticity of GBM cells in a context of changing mitochondrial ultrastructure under different environmental conditions. Namely, growth and other factors, such as epidermal growth factor (EGF), fibroblast growth factor (FGF), heparin sulfate, hydrocortisone hemisuccinate, ascorbic acid and fetal bovine serum in the culture media, shift mitochondrial ultrastructure towards normal. In both GSCs and differentiated GBM cells, we observed mitochondria with electron-dense matrix with narrow and dilated cristae (Figure 1a, b), demonstrating the GBM cell adaptive response to environmental changes [4,5].

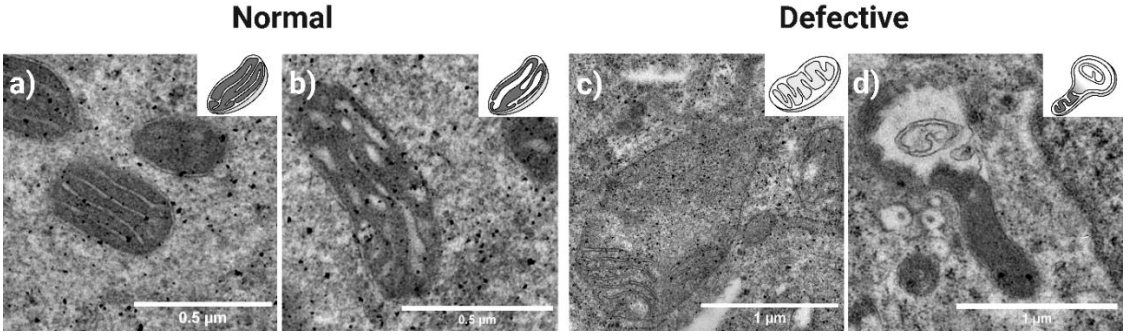


Figure 1: Mitochondrial ultrastructure. Mitochondria were classified into two following types: normal and defective. Normal mitochondria are defined as mitochondria with electron-dense matrix with narrow cristae indicating metabolism with a high OXPHOS rate (a) and mitochondria with electron-dense matrix with dilated cristae indicating metabolism with a lower OXPHOS rate (b). Defective mitochondria are defined as mitochondria with electron-lucent matrix and cristae reduced in size and numbers indicating metabolism without OXPHOS (c) and mitochondria with abnormal ultrastructural alterations (swollen with membrane swirls) indicating damage and stress in mitochondria (d) [4].

Discussion and conclusions: We showed that GSCs exhibit high degree of plasticity enabling them to rapidly adapt to therapeutic pressures and survive. The differential response observed between GSCs and differentiated GBM cells to the combination of conditioned media of endothelial cells and TMZ treatment, reveals a unique protective mechanism that selectively preserves GSCs viability and mitochondrial function. Underscoring their superior adaptive capabilities and suggesting that the perivascular niche may provide protective signals that specifically benefit GSCs during chemotherapeutic stress. The results provide a basis for further studies related to the role of mitochondria in GSCs chemotherapeutic resistance and plasticity.

Acknowledgments: This work was supported by the Slovenian Research and Innovation Agency (ARIS) grants (P1-0245 (B.B., M.N.), J3-4504 (M.N.), BI-US/22-24-007 (B.B), J3-2526 (C.J.F.V.N.), BI-US/24-26-022 (M.N.), Young Researcher grant (SKM; 59639), by University Infrastructural Centre "Microscopy of Biological Samples" at the Biotechnical Faculty, University of Ljubljana (M.V.), Texas Tech University start-up (to K.F.T.), Cancer Prevention and Research Institute of Texas Scholar Award RR200059 (to K.F.T.), the Foundation for Prader–Willi Syndrome Research Grant 22-0321 and 23-0447 (to K.F.T.), Fulbright Fellowship Scholar (B.B.) and European Union's Horizon project Twinning for excellence to strategically advance research in carcinogenesis and cancer (CutCancer; 101079113) (B.B. and M.N.).

References:
1.C. Bernhard et al., *Int. J. Mol. Sci.* **2023**, *24*, 9137.
2. E. J. Kim et al., *Oncol. Rep.* **2017,** *39*, 411-416.
3. N. Lomeli et al., *Mitochondrion* **2020**, *52*, 56–66.
4. U. Bogataj et.al., *bioRxiv* **2025**, 2025.02.17.638633.
5. S.K. Galun, *RUL* **2024**, 576.385.5:615.28(043.2).

Type of presentation: Poster

LS4-P-7 Adiposoft-based analysis of visceral adipose tissue in ovariectomized rats treated with alendronate, hop extract, and their combination, stained with picrosirius red

Edi Rođak[a,b], Robert Grgac[a], Lucija Hudek[c], Nada Oršolić[d], Tatjana Belovari[a], Nikola Bijelić[a]

[a]*Department for Histology and Embryology, Faculty of Medicine Osijek, University of Osijek, J. Huttlera 4, 31000 Osijek, Croatia*

[b] *Department of Medicine, University of Connecticut Health Centre, 263 Farmington Ave., Farmington, CT 06030, USA*

[c]*Faculty of Medicine Osijek, University of Osijek, J. Huttlera 4, 31000 Osijek, Croatia*

[d]*Department of Animal Physiology, Faculty of Science Zagreb, University of Zagreb, Rooseveltov trg 6, 10000 Zagreb, Croatia*

Contact email: rgrgac@mefos.hr

Introduction. Osteoporosis is the most common metabolic bone disorder in the modern population, typically resulting from reduced estrogen levels. Ovariectomy is a well-established method for modelling osteoporosis in experimental animals. Among osteoporosis treatments, bisphosphonates (e.g. alendronate) are one of the most commonly used medication classes. Recently, phytoestrogens from hops and other sources have gained attention in research, showing promising results. Obesity and metabolic syndrome have increased in recent decades, potentially impacting osteoporotic patients in various ways. One of the side effects of ovariectomy in rats is weight gain, especially an increase in visceral adipose tissue. We investigated whether treatment with alendronate, hop extract and their combination affects the morphology of adipocytes of visceral (perigonadal) adipose tissue of ovariectomized rats.

Methods. A total of 70 female 6-month-old Wistar rats were used in this study. The animals were divided into 7 groups of 10. One group underwent a sham operation, while bilateral ovariectomy was performed on the remaining animals. Ovariectomized animals were further divided into six groups: an untreated group, a group treated with low-dose alendronate, a group treated with high-dose alendronate, a group treated with hop extract, a group treated with low-dose alendronate + hop extract, and a group treated with high-dose alendronate + hop extract. Animals were euthanized, and organs, including perigonadal adipose tissue, were harvested and fixed in 4% paraformaldehyde. Tissue samples were sectioned and stained using the picrosirius red (PSR) method. Additionally, two groups (sham-operated and ovariectomized untreated) were stained with hematoxylin-eosin to validate the use of PSR-stained slides in Adiposoft. Digital images of the samples were processed in Fiji software (Fiji Is Just ImageJ) using the Adiposoft plug-in.

Results. A comparison of measurements obtained using PSR and HE staining methods revealed no significant differences. Adipocyte diameter and average adipocyte area were smaller in the hop extract groups, particularly compared to low alendronate and low alendronate + hop extract groups. The number of adipocytes per square millimeter was significantly higher in the hop extract group compared to the previously mentioned two groups, as well as the high alendronate + hop extract group.

Discussion and conclusions. Hop extract and alendronate appear to have a moderate effect on adipocyte morphology. In our study, total body fat, total visceral fat, and adipocyte mitotic activity were not measured. Therefore, it is difficult to determine whether adipocyte proliferation occurred or if changes were limited to lipid droplet size within the cells. Further research is needed to clarify this. PSR staining can be used with the Adiposoft plug-in as an alternative to hematoxylin-eosin staining with the same settings.

Acknowledgments. The authors would like to acknowledge the help of Hopsteiner company by generously donating hop extract XanthoFlav™ for research purposes.

Type of presentation: Poster

LS4-P-8 Investigating the antitumor effects of quercetin on human colorectal adenocarcinoma cells: An *in vitro* study

Basak Isildar[a]

[a]*Balıkesir University, Faculty of Medicine, Histology and Embryology Department, Balıkesir, Turkiye*

Contact email: basakisildar@gmail.com

Introduction: Colorectal cancer is one of the most widespread cancers in the human population. Due to its high prevalence and significant adverse effects on health, new treatment strategies are needed. In this context, interest in identifying effective bioactive compounds with anticancer potential is increasing [1]. Quercetin is a key flavonol in human diets and is abundant in fruits and vegetables. Studies have shown quercetin exhibits anticancer activity by decreasing cell proliferation and inducing apoptosis and autophagy [2]. However, its exact mechanisms remain to be fully understood and require further investigation.

Methods: In order to study the therapeutic effects of quercetin on colorectal cancer, an *in vitro* experimental model was created and SW480, human colorectal adenocarcinoma cells were used. The effective dose was determined through a 3-(4,5-Dimethylthiazol-2-yl)-2,5-Diphenyltetrazolium Bromide (MTT) cytotoxicity assay, testing concentrations ranging from 0 to 200 μM. Based on the results, 150 μM was selected for further analysis. To assess cellular energy metabolism, mitochondrial membrane potential and lactate levels were evaluated. Apoptosis was evaluated using cleaved caspase-3 immunohistochemical staining, while autophagy was assessed through beclin-1 expression. The results were evaluated statistically.

Results: A concentration of 150 μM quercetin (24 h), which reduced cell viability to approximately 40%, was selected for mechanistic analyses, as it allowed investigation of apoptotic and metabolic responses without causing excessive cell death. The analyses reveal that quercetin achieves this effect on SW480 cells by modulating energy metabolism and thus inducing apoptosis and autophagy. Dose-dependent cytotoxicity results are shared in Fig. 1 and representative micrographs of immunocytochemical analyses are shared in Fig. 2.

Discussion and conclusions: These findings suggest that quercetin may serve as a promising therapeutic agent for colorectal cancer by targeting cellular energy metabolism and activating cell death pathways.

Keywords: Colorectal cancer, quercetin, apoptosis, autophagy

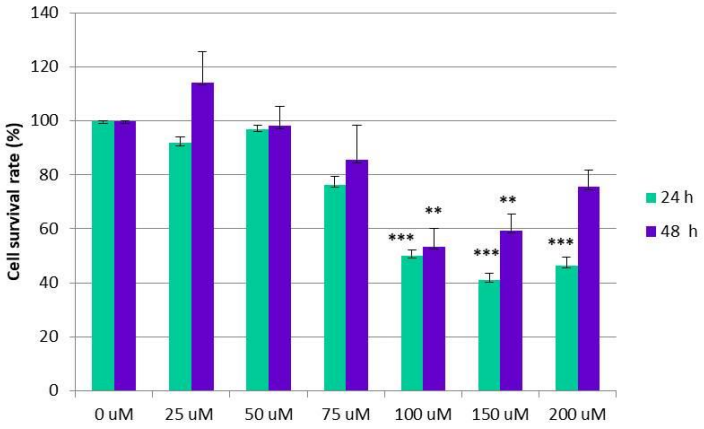


Figure 9: Dose-dependent cytotoxicity results of quercetin on SW480 cells, ***p < 0.001 vs. 0, 25, 50 µM (24 h) and 0, 25, 50 µM (48 h), **p < 0.01 vs. 0, 25, 50 µM (24 h) and 0, 25, 50 µM (48 h).

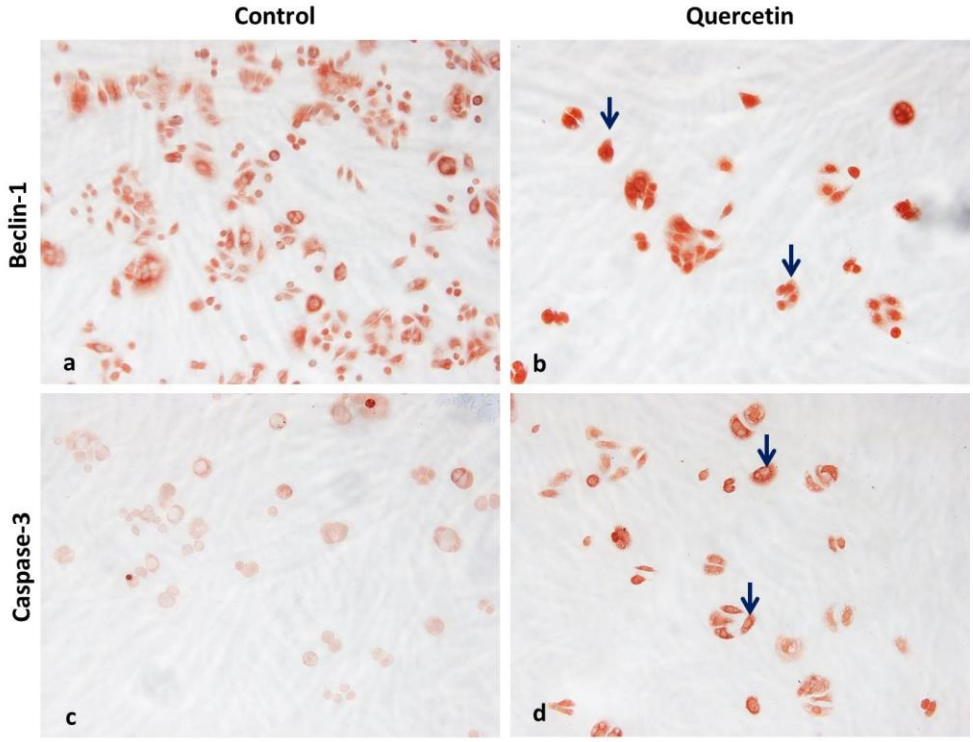


Figure 10: Representative micrographs of immunocytochemical analyses. Arrows: Cells showing strong expression.

References:

1. Dekker, E., Tanis, P. J., Vleugels, J. L. A., Kasi, P. M., & Wallace, M. B. (2019). Colorectal cancer. Lancet (London, England), 394(10207), 1467–1480. https://doi.org/10.1016/S0140-6736(19)32319-0
2. Reyes-Farias, M., & Carrasco-Pozo, C. **2019**. The Anti-Cancer Effect of Quercetin: Molecular Implications in Cancer Metabolism. International journal of molecular sciences, 20(13), 3177. https://doi.org/10.3390/ijms20133177

Type of presentation: Poster

LS4-P-9 The effect of a novel SARS-CoV E Protein Inhibitor on ultrastructure of Murine Hepatitis Virus-Infected L-929 Cells

Mojca Janc[a,b], Nina Kobe[a,b], Živa Lengar[a], Polona Mrak[c], Magda Tušek Žnidarič[b], Valentina Levak[a,b], Maruša Pompe Novak[a], Polona Kogovšek[a]

[a] *National Institute of Biology, Department of Biotechnology and Systems Biology (Ljubljana), Slovenia*

[b] *Jozef Stefan International Postgraduate School (Ljubljana), Slovenia*

[c] *University of Ljubljana, Biotechnical faculty, Department of Biology, (Ljubljana), Slovenia*

Contact email: mojca.janc@nib.si

Introduction: The severe acute respiratory syndrome coronavirus 2 (SARS-CoV-2) can easily be recognized as one of the most influential viruses of the last 10 years. The continuous evolution and mutation of the virus into new variants has posed significant challenges to existing antiviral treatment strategies. This underscores the urgent need to identify potential drug targets and develop effective therapeutics. Once a novel antiviral compound has been identified and initial antiviral properties are assessed, in-depth biological characterization is required.

Methods: In this study, we examined the effects of a novel SARS-CoV-2 E protein inhibitor, identified through an *in silico* approach (unpublished), at the ultrastructural level. For this purpose, L-929 mouse cells were infected with murine hepatitis virus (MHV, strain A59), a known SARS-CoV-2 surrogate, and treated with the novel inhibitor. Simultaneously, negative and positive controls were included in the examination, namely uninfected and untreated cells as a negative control and infected and untreated cells as a positive control. To observe the ultrastructural effects of the inhibitor on uninfected cells, we examined also uninfected and treated cells. The cells from eight cell cultures samples (duplicates of individual treatments) were harvested 48 hours after infection, fixed in glutaraldehyde, postfixed in osmium tetroxide, dehydrated in ethanol and infiltrated in resin. Using an ultramicrotome, semithin and ultrathin sections were prepared from resin block. The semithin sections were stained with toluidine blue. The ultrathin sections were collected on TEM grids and later stained with uranyl acetate and lead citrate. The grids were then examined with a Thermo Scientific TALOS L120C transmission electron microscope, operating at 100 kV, and micrographs were recorded with Ceta 16M camera.

Results: In the infected cells, both untreated and treated, viral particles were observed both inside the cells, grouped in vesicles, and outside the cells, adhered to the cell membrane or as free viral particles between the cells. The difference in ultrastructure between infected and uninfected cells indicated that viral infection triggered cytoplasmic vacuolization, rearrangement of endoplasmic reticulum, viral particles accumulations, called viral factories, and mitochondrial swelling. In the uninfected cells treated with inhibitor we observed increased number of vesicles with myelin-like structures.

Discussion and conclusions: Preliminary results showed that in the samples of treated and infected cells a lower amount of the infected and lysed cells was observed compared to the positive control, which imply the antiviral effect of the tested inhibitor. These ultrastructural observations are in line with the results of the cell-based infectivity assay, that was performed simultaneously.

Type of presentation: Poster

LS4-P-10 Antiviral Efficacy of Electrolysed Saline (EOS) Against Both Enveloped and Non-Enveloped Viruses: A TEM Study

Marko Kolenc[a], Haris Munjaković[b,d], Tina Mikuletič[a], Irena Šest[a], Tina Triglav[a], Andrej Steyer[c], Katja Seme[a], Aleš Fidler[e,f], and Rok Gašperšič[b,d]

[a]*Institute of Microbiology and Immunology, Faculty of Medicine, University of Ljubljana, Slovenia*

[b]*Department of Oral Medicine and Periodontology, University Clinical Centre Ljubljana, Slovenia*

[c]*Public Health Microbiology Department, National Laboratory of Health, Environment, and Food, Ljubljana, Slovenia*

[d]*Department of Oral Medicine and Periodontology, Faculty of Medicine, University of Ljubljana, Slovenia*

[e]*Department of Endodontic and Restorative Dentistry, Faculty of Medicine, University of Ljubljana, Slovenia*

[f]*Department of Endodontic and Restorative Dentistry, University Clinical Centre Ljubljana, Slovenia*

Contact email: marko.kolenc@mf.uni-lj.si

Introduction

Dental spray is widely recognized as a potential vector for viral transmission. High-speed dental instruments generate aerosolized spray, comprising cooling liquid and oral fluids, which can remain airborne for extended durations. This airborne dispersion increases the risk of infection, as viruses have been detected in saliva, gingival crevicular fluid, and various respiratory secretions. The objective of this study was to evaluate the antiviral efficacy of electrolysed saline (EOS), predominantly composed of hypochlorous acid (HOCl), as a virucidal agent against both enveloped and non-enveloped viruses. EOS was compared with other antimicrobial agents commonly used in clinical dentistry.

Methods

A suspension assay was conducted to assess the reduction in viral load following exposure to the antimicrobial agents. The reduction in viable virus was quantified using titration, and the 50% Tissue Culture Infectious Dose (TCID50/mL) was determined.

Virus samples from the suspension assay were ultracentrifuged at 100,000×g (Airfuge; Beckman Coulter, Indianapolis, USA) to concentrate viral particles onto formvar-coated grids. Negative staining was performed using 2% phosphotungstic acid. Transmission electron microscopy (TEM) analysis was conducted using a JEM-1400 Plus (JEOL, Tokyo, Japan) at 120 kV. Human adenoviruses (HAdVs) and herpes simplex virus type 1 (HSV-1) were identified based on their characteristic morphology and dimensions. The extent of structural damage to the viral capsid or envelope was evaluated based on the specific antiviral treatment applied.

Results

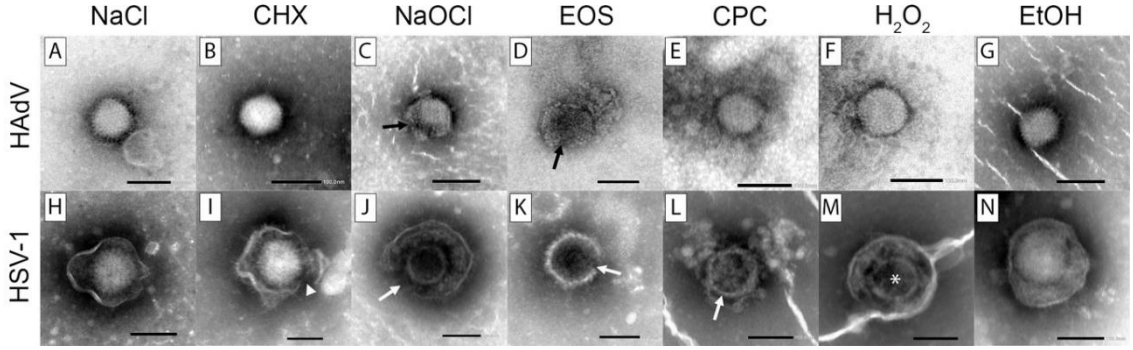


Figure 1: presents electron micrographs of HAdV (panels A–G) and HSV-1 (panels H–N) after a 1-minute exposure period. Panels A and H serve as negative controls. Minimal morphological alterations were observed in HAdV samples treated with CHX, CPC, H2O2, or EtOH (panels B, E, F, and G), with only minor size variations compared to the control. However, treatment with NaOCl and EOS (panels C and D) resulted in substantial degradation of the viral nucleocapsid.

For HSV-1, exposure to EtOH (panel N) did not induce significant morphological changes relative to the negative control. In contrast, CHX treatment (panel I) led to visible damage to the viral envelope, while H2O2 exposure (panel M) caused pronounced nucleocapsid degradation. The most extensive structural damage was observed following treatment with NaOCl, EOS, and CPC (panels J, K, and L), characterized by severe envelope disruption and significant nucleocapsid degradation.

Discussion

EOS demonstrated a potent antiviral effect, significantly reducing the infectivity of both enveloped and non-enveloped viruses. Notable morphological changes were observed in both viral types following EOS treatment. EOS achieved a viral load reduction exceeding 4 log (99.99%), confirming its strong virucidal activity. These findings underscore the potential of EOS as an effective antiviral agent for use in clinical dentistry and other healthcare settings where infection control is paramount.

Acknowledgments

This study was supported by grants from the Slovenian Research and Innovation Agency (ARIS) P3-0293 and P3-0083.

References

1. Munjaković H, Mikuletič T, Zayed N, Kolenc M, Manevski D, Triglav T, Steyer A, Teughels W, Seme K, Fidler A, Gašperšič R. Electrolyzed Saline Prevents Virus Transmission in Dental Procedures: An In Vitro Study. J Dent Res. **2025**.
2. Fidler A, Steyer A, Manevski D, Gašperšič R. Virus Transmission by Ultrasonic Scaler and Its Prevention by Antiviral Agent: An In Vitro Study. J Periodontol. **2021**.

Type of presentation: Poster

LS4-P-11 Post mortem degradation of ferritin and its significance for determining the iron content of the human brain

Stefan Ropele[a], Luca Schmid[a], Michael Stöger-Pollach[b], Sowmya Sunkara[a], Snjezana Radulovic[a], Walter Goessler[c], Gerd Leitinger[a]

aMedical University of Graz, Gottfried Schatz Research Center, Austria

bTechnical University of Vienna, University Service centre for TEM, Austria

cUniversity of Graz, Analytical Chemistry, Austria

Contact email: gerd.leitinger@medunigraz.at

There are several ways of visualizing iron in the human brain. Most of the iron is stored in ferritin's iron core, and these cores can be visualized on iron (L-) maps using energy filtered transmission electron microscopy. MRI allows iron quantification by applying R_2* mapping. R_2* is strongly dependent on the paramagnetic properties of ferritin. However, the relationship between magnetic configuration of the iron core in ferritin is still incompletely understood and could influence the accuracy of iron quantification using MRI. It is generally believed that most of the signal from R_2* mapping is picked up from the iron cores of ferritin, and not from cytoplasmic iron.

We aimed to use small brain samples of human donors in order to relate the R_2* signal with numbers of ferritin and total iron content. For this, we combined iron mapping using electron microscopy with R_2* mapping using quantitative fMRI, and determined the total iron content using mass spectrometry. The number of ferritin cores was determined from iron maps of postmortem brain samples from six deceased human subjects. The mean iron content of adjacent human samples were obtained using mass spectrometry, and quantitative MRI at 3 Tesla was used for R_2* mapping of the same samples. Analyses focused on three gray matter regions: the frontal cortex, putamen, and globus pallidus. The post mortem intervals of the human donors had ranged from 6 to 24 hours. We demonstrated that autolysis led to a rapid degradation of ferritin iron cores, with fewer than one-third remaining detectable via EFTEM after 24 hours postmortem. The degradation followed a single-exponential decay pattern, suggesting that approximately 94% of the total brain iron is stored in ferritin in fresh tissue. However, R_2* relaxation rates did not follow this degradation pattern but instead correlated strongly with total iron content as measured by mass spectrometry. This signifies that R_2* mapping-derived magnetic susceptibility for iron appeared to be independent of the structural and magnetic organization of the ferritin iron core and shows a linear relationship with total iron content.

grant sponsor: FWF, grant 10.55776/P29370; ethics votum Medical University of Graz, 28-549 ex 15/16

Type of presentation: Poster

LS4-P-12 Proferroptotic response to nutrient deprivation and sorafenib treatment in hepatocellular carcinoma cells – a microscopic study

Milica Markelić[a], Vesna Otašević[b], Nevena Savić[b], Tamara Saksida[b], Anđelija Gudelj[b], Ana Stančić[b], Ksenija Veličković[a], Jelena Krstić[c]

[a]*University of Belgrade - Faculty of Biology, (Belgrade), Serbia*

[b]*Institute for Biological Research "Siniša Stanković", National Institute of Republic of Serbia, University of Belgrade, (Belgrade), Serbia*

[c]*Gottfried Schatz Research Center, Medical University of Graz, (Graz), Austria*

Contact email: milica.markelic@bio.bg.ac.rs

Nutrient deprivation (ND) is already recognised as a potential adjuvant therapy for cancer treatment. In the recent study by Krstic *et al* [1], a positive correlation between ND-induced sensitisation of hepatocellular carcinoma (HCC) cells to sorafenib (Sfb), a drug used to treat HCC, and p53 status was demonstrated. This indicates the essential role of p53 in the priming HCC cells for regulated cell death (RCD). Preliminary microscopic data indicated a possible involvement of ferroptosis, an iron-dependent RCD characterised by the accumulation of lipid peroxides, in this process. Therefore, we wanted to find out whether ferroptosis plays a role in the removal of HCC cells depending on p53 status.

To this end, p53 wild-type (p53 WT) and p53 knockout (p53 KO) HepG2 cells were grown in growth medium (GM) or in starvation medium (SM) and treated with Sfb (10 μM) or with the ferroptosis inducer RSL-3 (3 μM) for 6 hours. The morphological signs of ferroptosis and the immunopositivity of the main regulator of ferroptosis-related signalling pathways, nuclear factor erythroid 2-related factor 2 (Nrf2) and ferritin heavy chain 1 (FTH1), which is involved in the sequestration of iron, were analysed microscopically. In addition, western blotting of the Nrf2 downstream antiferroptotic proteins - glutathione peroxidase 4 (GPX4) and cystine glutamate antiporter (xCT) - and of FTH1 was performed. The level of lipid peroxidation was determined by analysing the oxidation of Bodipy 581/591 C11 using flow cytometry.

The results showed activation of the proferroptotic pathway by ND, as reduced nuclear translocation of Nrf2 was detected, followed by lower levels of GPX4, xCT and FTH1 (Figure 2). Microscopically, this was followed by increased accumulation of lipids and lipofuscin. However, the extent of lipid peroxidation was not altered. The effects of RSL-3 were similar to those of ND, but in combination of those two a significant increase in lipid peroxidation was observed. The proferroptotic effects of Sfb were weak, as it only inhibited GPX4 protein expression and slightly increased lipid peroxidation. However, in combination with ND, an accumulation of lipids/lipofuscin and a tendency to accumulate lipid peroxides was observed, which was supported by the inhibition of the Nrf2/GPX4/xCT axis.

These results suggest an involvement of ferroptosis in the clearance of HCC cells during ND in combination with Sfb. The proferroptotic effect of RSL-3, ND and Sfb is p53-dependent, as no reduction of GPX4 and xCT was detected in the p53 KO HepG2 cells. This could at least partially explain the resistance of p53 KO HCC to these treatments.

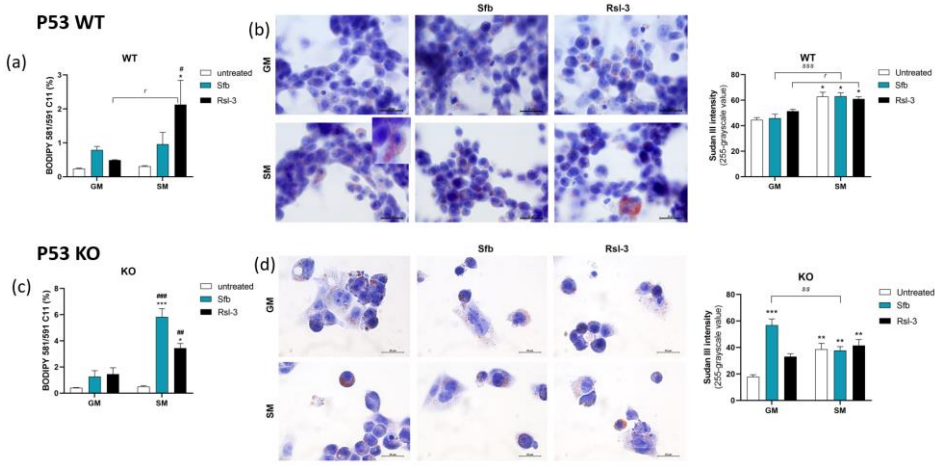


Figure 1: Lipid peroxidation and accumulation of lipids/lipofuscin in p53 WT and p53 KO HepG2 treated with sorafenib (Sfb) or RSL-2 ferroptosis inducer. (a, c) Percentage of cells with oxidized Bodipy C11; (b, d), Sudan III detection of lipids and lipofuscin inside HCC (scale bar – 20 μm, magnification – x40) and quantification of cellular level of lipids/lipofuscin. Statistical significance in comparison to: *untreated cells in GM, #untreated cells in SM, sSfb-treated cells in GM, rRsl-3-treated cells in GM

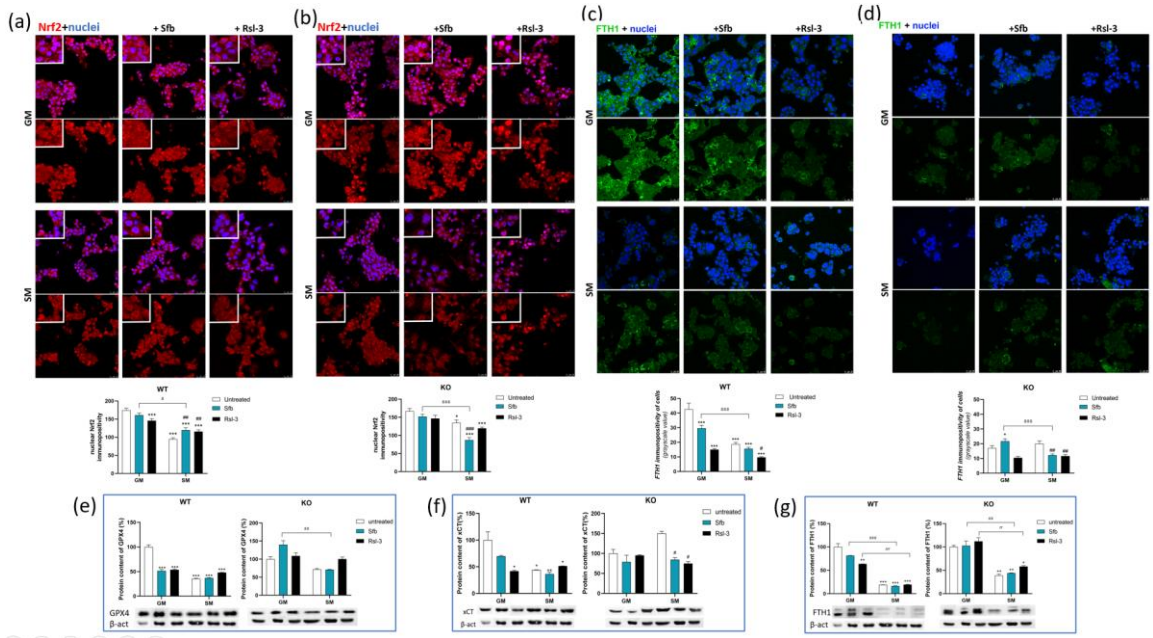


Figure 2: Detection of ferroptosis-related proteins. Immunofluorescence detection of (a, b) Nrf2 and (c, d) FTH1 in p53 WT and p53 KO HepG2 cells treated with Sfb or RSL-3 and grown in normal (GM) or starvation medium (GM), (scale bar – 50 μm, magnification – x63), followed by the quantification of nuclear immunopositivity to Nrf2, and the quantification of cellular positivity to FTH1. Protein levels of (e) GPX4, (f) xCT and (g) FTH1. Statistical significance in comparison to: *untreated cells in GM, #untreated cells in SM, sSfb-treated cells in GM, rRsl-3-treated cells in GM

Acknowledgements: This study was a part of the project of bilateral cooperation of Serbia and Austria (337-00-577/2021-09/29) and was supported by the Ministry of Science, Technological Development and Innovations of Serbia: 451-03-137/2025-03/ 200178, 451-03-136/2025-03/ 200007.

References:

1. J. Krstic, I. Reinisch, K. Schindlmaier, M. Galhuber, Z. Riahi, *et al. Sci Adv.* **2022**;8(3), eabh2635. Fasting improves therapeutic response in hepatocellular carcinoma through p53-dependent metabolic synergism.

Type of presentation: Poster

LS4-P-13 Effect of endometrial environment on chromatin abnormalities of sperm

Duygu Neccar[a], Zehra Sezer[a], Sercin Karahuseyinoglu[b], Cetin Demirdag[c], İsmail Cepni[d], Elif Guzel Meydanli[a]

[a] *Cerrahpasa Medical Faculty, Istanbul University-Cerrahpasa, Istanbul, Turkey.*

[b] *Koc University Medical Faculty, Koc University, Istanbul, Turkey.*

[c] *Cerrahpasa Medical Faculty, Istanbul University-Cerrahpasa, Istanbul, Turkey*

[d] *Cerrahpasa Medical Faculty, Istanbul University-Cerrahpasa, Istanbul, Turkey*

Contact email: duygu_d86@hotmail.com, duygu.neccar@iuc.edu.tr

Introduction: In the chromatin condensation process, the replacement of histones with transition proteins (TPs) and TPs with protamines in round spermatids provides the maturation of sperm chromatin structure. In this process, the first chaperone identified of TPs, HSPA2 protein, plays a role both by accompanying TPs and facilitating the binding of proteins involved in chromatin packaging [1]. The deficiency of one or more of these proteins involved in sperm chromatin packaging causes incomplete, i.e. abnormal, chromatin condensation in sperms. Accordingly, demonstrating that sperm chromatin maturation can occur in an in vitro environment outside the male genital system has led us to consider the potential effect of the endometrium on abnormal chromatin structure sperm before fertilization. It that it was shown that exosomes significantly provided chromatin repair in sperm as a result of incubation of semen samples taken from dogs with exosomes isolated from conditioned medium (CM) of adipose tissue-derived mesenchymal cells, has been enforced our hypothesis [2]. In this study, based on the assumption that human uterosomes and/or endometrial cells-CM (EC-CM) contain HSPA2, our hypothesis is 'EC-CM, obtained from human ECs and confirmed to contain uterosomes, will repair abnormal chromatin structures in sperm'.

Methods: EC were isolated from endometrial tissues taken from fertile women (n=8). They were incubated with serum-free DMEM/F12 medium supplemented with 0.5% Insulin-Transferrin-Selenium, 10^{-8} M estrogen, 10^{-7} M progesterone at 37°C for 24 h. At the end of the period, EC-CM was collected and was centrifuged with ultracentrifuge for uterosome isolation. At the end of ultracentrifugation, the part containing uterosomes was determined as a pellet, and the part without uterosomes was determined as a supernatant (SNT). The presence of uterosomes in the pellet was detected by TEM and Western Blot. The semen samples were taken from men (n=20), were evaluated using aniline blue (AB) staining. Sperm samples with an AB-positive immature sperm ratio ≥20% were incubated with EC-CM, SNT, and Ham (control) for 15 min, 1 h, and 4 h. Sperm chromatin abnormalities were detected by employed to AB and CMA3 staining. HSPA2 protein expression was analyzed in EC-CM, uterosomes and SNT using the Western blot to determine the localization of HSPA2. Then, the presence and quantity of HSPA2 protein in the sperm nucleus were assessed using immunofluorescence (IF) analysis in the experimental groups.

Results: For AB, 1 h and 4 h of incubation, a significant reduction in the immature sperm ratio was detected in the EC-CM group compared to the control group (p=0,007, p=0,001). The results obtained using CMA3 staining exhibited a pattern similar to those observed with AB staining. CMA3 analysis demonstrated a statistically significant reduction in the proportion of immature sperm in the groups incubated with EC-CM for 1 h and 4 h compared to the control group (p=0.011, p=0.002). In the western blot analysis for HSPA2, it was revealed distinct bands in EC-CM and uterosomes whereas no band formation was observed in the SNT. These findings showed that HSPA2 in EC-CM is primarily associated with uterosomes rather than existing freely in the SNT. In the IF assessment of HSPA2, it was revealed a statistically significant increase in HSPA2 expression only in the group incubated with EC-CM for 1 hour compared to both the control and SNT groups (p<0.001).

Discussion and conclusions: In conclusion, this study demonstrated that EC-CM significantly reduces the immaturity ratio associated with sperm chromatin abnormalities. It was clearly shown that uterosomes, due to their membrane-bound structure, play a central role in the mechanism by which EC-CM exerts its effects on sperm with abnormal chromatin structure, whereas the soluble factors present in EC-CM do not contribute to this effect. Moreover, HSPA2 protein was identified as a key mediator of the uterosomal mechanism, and was found exclusively within the uterosomes of EC-CM. These findings suggest that, during sperm transit through the uterus, uterine fluid may influence not only physiological but also structural processes in sperm via the uterosomes it contains.

Acknowledgments: This research was approved by the Clinical Trials Ethics Committee of Istanbul University-Cerrahpasa, Cerrahpasa Faculty of Medicine (Ethics Approval No:100223). This study was supported by the Istanbul University-Cerrahpaşa Scientific Research Projects Coordination Unit (IUC-BAP, Project No: 35102) and TUBITAK (Project No: 121S358).

Keywords: Endometrial cells, sperm chromatin abnormality, HSPA2, conditioned medium, uterosome

Reference

1. J. Govin *vd.*, "Post-meiotic shifts in HSPA2/HSP70.2 chaperone activity during mouse spermatogenesis", *Journal of Biological Chemistry*, c. 281, sy 49, ss. 37888-37892, 2006, doi: 10.1074/jbc.M608147200.
2. A. Y. Qamar, X. Fang, M. J. Kim, ve J. Cho, "Improved post-thaw quality of canine semen after treatment with exosomes from conditioned medium of adipose-derived mesenchymal stem cells", *Animals*, c. 9, sy 11, ss. 1-13, 2019, doi: 10.3390/ani9110865.

Type of presentation: Poster

LS4-P-14 Human Serum Albumin Nanoparticles as a Drug Delivery System to Enhance Temozolomide Efficacy in Glioblastoma Cell Line

Hakan Sahin[a], Oguz Yucel[b], Eren Yildirim[b], Said Bahadir Aslan[a], Serkan Emik[b], Gulten Gurdag[b], Gamze Tanriverdi[a], Gozde Erkanli Senturk[a]

[a]*Department of Histology and Embryology, Cerrahpasa Faculty of Medicine, Istanbul University-Cerrahpasa, Istanbul, Turkey*

[b]*Department of Chemical Engineering, Faculty of Engineering, Istanbul University-Cerrahpasa, Istanbul, Turkey*

Contact email: hakan.sahin@iuc.edu.tr

Glioblastoma is the most aggressive type of brain cancer. Temozolomide (TMZ) is widely used in glioblastoma treatment. Although TMZ treatment has improved patient survival rates, resistance to the drug often limits its effectiveness, leading to cancer recurrence despite intensive treatment. Nanoparticle (NP) systems offer a promising strategy for delivering various active substances to target tissues and organs. Human serum albumin (HSA) is a biocompatible, biodegradable, and non-immunogenic protein that can serve as an NP carrier by binding to active substances, making it a suitable candidate for clinical applications. In this study, TMZ-loaded HSA NPs were applied to C6 (rat glioblastoma) and T98G (human glioblastoma) cell lines. Our findings demonstrated that TMZ-loaded HSA NPs significantly reduced cell survival compared to TMZ treatment alone supported by MTT (3-[4,5-dimethylthiazol-2-yl]-2,5 diphenyl tetrazolium bromide) and histologic analysis. These results indicate that encapsulating TMZ in HSA NPs enhances its therapeutic effectiveness against glioblastoma in vitro. These findings highlights the potential of NP-based drug delivery systems to overcome chemotherapy resistance in glioblastoma, suggesting that albumin-based formulations could be further explored as a promising approach for improving TMZ efficacy in clinical studies.

Keywords: Nanoparticles, Human Serum Albumin, Glioblastoma

Type of presentation: Poster

LS4-P-15 Therapeutic effects of H_2S donors on ferroptosis-mediated liver damage in C57BL/6 mice – a microscopic study

Nevena Savic[a], Ksenija Velickovic[b], Milica Markelic[b], Marko Miler[a], Andjelija Gudelj[a], Vesna Martinovic[a], Ilijana Grigorov[a], Milos Filipovic[c], Ana Stancic[a], Vesna Otasevic[a]

[a]*Institute for Biological Research "Siniša Stanković", National Institute of Republic of Serbia, University of Belgrade, (Belgrade), Serbia*

[b]*University of Belgrade - Faculty of Biology, (Belgrade), Serbia*

[c] *School of Molecular Biosciences, College of Medical Veterinary and Life Sciences, University of Glasgow, (Glasgow), UK*

Contact email: nevena.savic@ibiss.bg.ac.rs

Today, it is well known that diabetes (DM)-induced liver damage includes different types of cell death such as apoptosis, necrosis, autophagy and pyroptosis [1]. Recently, our group discovered that hepatocytes [2], as well as pancreatic β-cells [3], in diabetic condition are prone to ferroptosis, a regulated cell death initiated by iron-driven lipid peroxidation. Besides well-described oxidative imbalance in DM, it is less known that DM is also characterized by decreased level of hydrogen-sulfide (H_2S) in peripheral tissues and the circulation [4]. Although H_2S has antiferroptotic properties, its role in DM-induced liver damage remains unclear. This study aimed to examine the antiferroptotic effects of three H_2S/reactive sulfur species (RSS) donors in the diabetic liver.

DM was induced in male C57BL/6 mice with one i.p. STZ injection (150 mg/kg). Two months after DM induction, synthetic H_2S donors: (1) direct H_2S donor – GYY4137, (2) polysulfide donor – Sodium sulfide (Na_2S_4) and (3) persulfide donor – cysteine-3-sulfide (Cys-S3) were i.p. administered, for one month. After treatments ended, mice were sacrificed, afterwards blood and liver were collected and processed for further biochemical, microscopical and molecular analyses.

As shown in Figure 1, treatment with H_2S donors led to amelioration of diabetes-induced increase in glycemia, glycosuria and ALT level. In accordance with the improvement of biochemical parameters, morphological and morphometric analysis of liver revealed reduced fibrosis and less DM-induced hypertrophy and binucleation of hepatocytes in groups treated with GYY and Cys-S3.

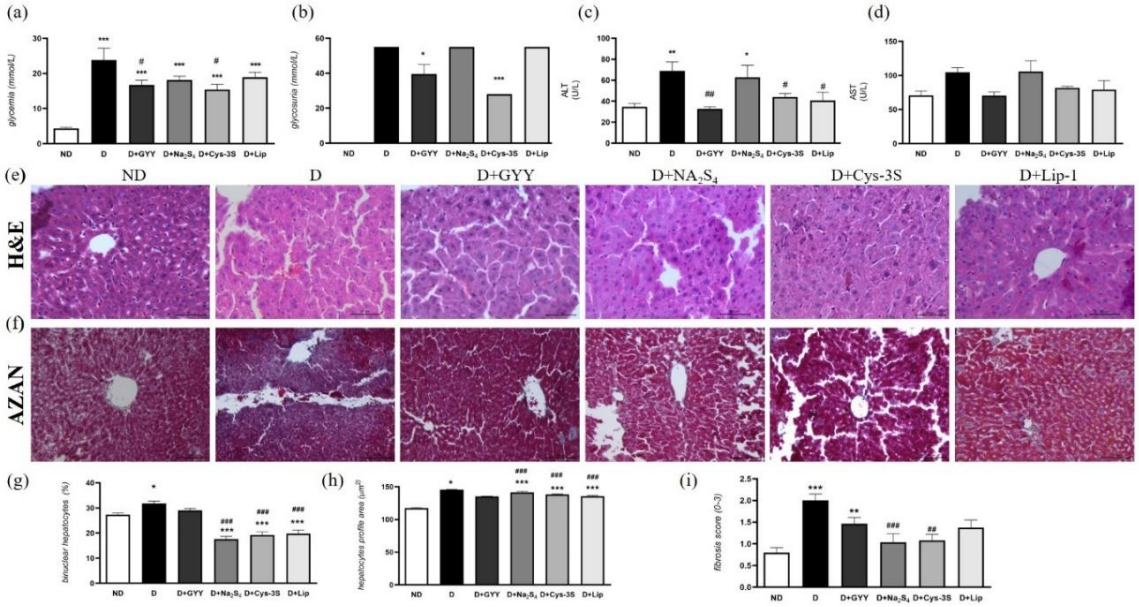


Figure 1: Biochemical and morphological parameters. Glucose level in serum (a) and urine (b), serum ALT (c) and AST (d) activity. H&E (e) and AZAN (f) staining of liver. Quantification of binucleation (g), profile area (h) of hepatocytes, and level of fibrosis in liver (i).

Regarding the signs of ferroptosis – free iron and lipofuscin accumulation (Figure 2; quantification – 2b and 2c) were significantly decreased in Na_2S_4 and Cys-S3 treated groups, while Cys-S3 also decreased DM-induced lipid peroxidation (lowered 4-HNE immunopositivity, Figure 2d). Regarding immunopositivity of the main enzyme involved in the removal of lipid peroxides in the membrane, GPX4, a tendency to return to control levels was observed in the hepatocytes of mice treated with Na_2S_4 and Cys-S3 (Figure 2e).
These findings highlight the potent antiferroptotic effects of H_2S donors and point to a novel strategy for preventing or treating diabetes by modulating ferroptosis through H_2S signalling.

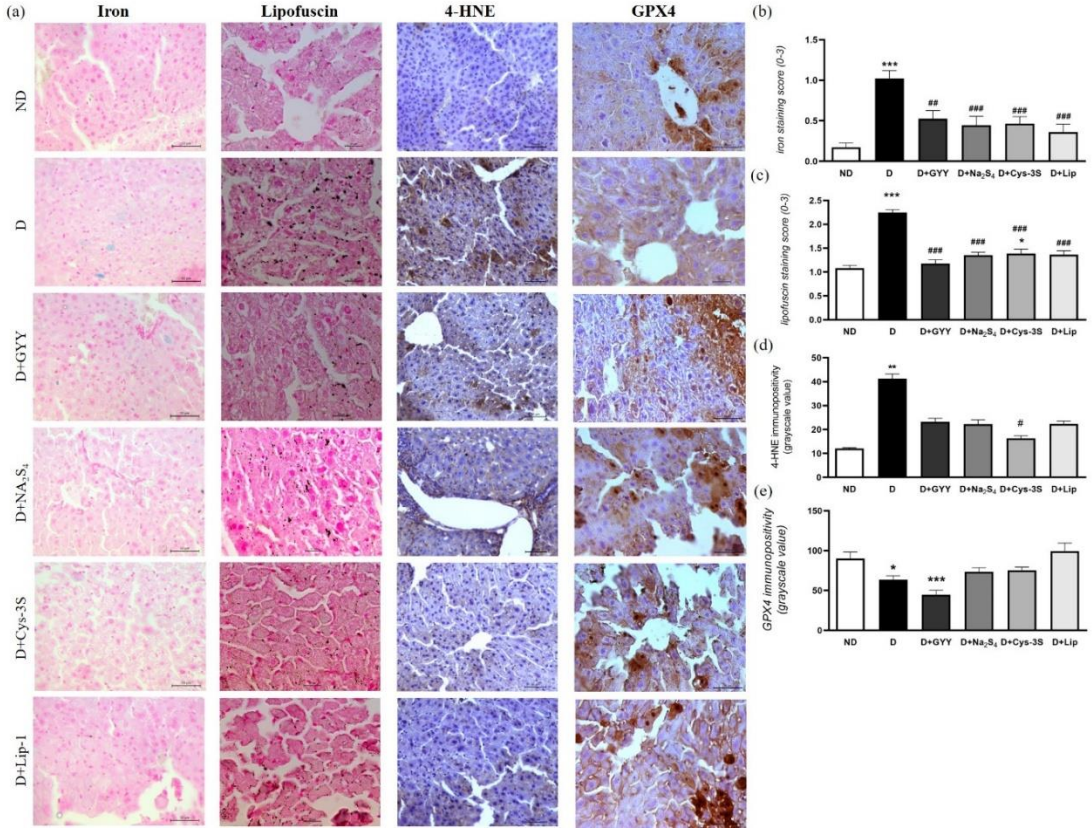


Figure 2: Detection of iron, lipofuscin; immunohistochemically detection of 4-HNE, GPX4 (a) and their quantification (b, c, d and e, respectively).

References:

1. Rojas, Joselyn, et al. "Pancreatic beta cell death: novel potential mechanisms in diabetes therapy." Journal of diabetes research 2018.1 (**2018**): 9601801.
2. Stancic, Ana, et al. "Ferroptosis as a Novel Determinant of β-Cell Death in Diabetic Conditions." Oxidative Medicine and Cellular Longevity 2022.1 (**2022**): 3873420.
3. Stancic, Ana, et al. "Involvement of ferroptosis in diabetes-induced liver pathology." International Journal of Molecular Sciences 23.16 (**2022**): 9309.
4. Jain, Sushil K., et al. "Low levels of hydrogen sulfide in the blood of diabetes patients and streptozotocin-treated rats causes vascular inflammation?." (**2010**): 1333-1337.

Aknowledgments:
Ministry of Education, Science and Technological Development of the Republic of Serbia (Contract No. 451-03-66/2024-03/ 200007). This research was supported by the Science Fund of the Republic of Serbia, #GRANT No. 6677, "Targeting ferroptosis in diabetes and diabetic complications by hydrogen (per)sulfide" – DiaSulFer.

Type of presentation: Poster

LS4-P-16 Microscopy techniques to evaluate the cytotoxic effect induced by copper complexes on glioblastoma cells

Sofia Migani[a,b], Giuseppina Bozzuto[a] Marisa Colone[a], Maria Luisa Dupuis[a], Annarica Calcabrini[a], Miriam Caviglia[a,b], Jo' Del Gobbo[b], Maura Pellei[b], Carlo Santini[b], Maria Beatrice Morelli[c], Annarita Stringaro[a]

[a] *National Center for Drug Research and Evaluation, Italian National Institute of Health, Viale Regina Elena, 299, 00161 Rome, Italy*

[b] *School of Science and Technology, Chemistry Division, University of Camerino, via Madonna delle Carceri (ChIP), 62032 Camerino (MC), Italy*

[c] *School of Pharmacy, Immunopathology and Molecular Medicine Unit, University of Camerino, via Madonna delle Carceri 9, 62032 Camerino (Italy)*

Contact email: annarita.stringaro@iss.it

Introduction: Glioblastoma (GBM) is a highly proliferative and poorly differentiated primary brain tumor. The current standard of care includes surgery, radiotherapy, and systemic therapy, mainly based on temozolomide (TMZ) chemotherapy. However, despite recent advances in these multimodal approaches, the prognosis for GBM patients remains poor, primarily due to the development of TMZ resistance and tumor recurrence. Therefore, there is an urgent need to identify less toxic and more effective therapeutic alternatives [1].
In this context, metal-based compounds have emerged as promising pharmaceutical agents for cancer diagnosis and treatment. Among them, copper complexes are particularly interesting candidates, as copper is an essential element involved in cellular growth and development, and metal-based therapeutics using endogenous metals may exhibit reduced toxicity [2].

Methods: In this study, the bis(pyrazol-1-yl)acetic acid was conjugated to the bioactive molecule amantadine and used as supporting ligand for the synthesis of novel Cu(I) and Cu(II) complexes. The lipophilic triphenylphosphine (PPh_3) and the hydrophilic 1,3,5-triaza-7-phosphaadamantane (PTA) were used as co-ligands to stabilize copper in its +1 oxidation state and to modulate the solubility of the related complexes. The antitumor activity of the synthesized Cu(I) and Cu(II) complexes was evaluated against U87 and LN18 human glioblastoma cell lines. Cell viability studies were performed by MTT assay. The most promising cytotoxic effects were observed for the Cu(I) complexes containing the PPh_3 co-ligands. Apoptosis induction and cell cycle analysis were evaluated by flow cytometry. Moreover, to explore the mechanism of action and the morphological alterations associated with cell death, Scanning Electron Microscopy (SEM), Fluorescence Microscopy (IF), and Confocal Laser Scanning Microscopy (CLSM) were employed.

Results: Viability assays in U87 and LN18 glioblastoma cell lines showed that the copper complexes with PPh_3 ligands, owing to their increased lipophilicity, exhibited the strongest cytotoxic activity. Notably, their micromolar IC_{50} values were lower than those of cisplatin.
Treatment with these copper compounds at their respective IC_{50} concentrations led to an increase in the percentage of Annexin V-positive cells and caused alterations in cell cycle profiles. These cytometry results suggest the induction of apoptotic cell death. According to cytotoxicity studies, SEM and FI micrographs acquired 24 hours after treatment with the copper compounds showed that both showed a reduced number of adherent cells and morphological features indicative of cellular distress, such as rounding and alterations in cytoskeletal architecture.

Discussion and conclusions: These preliminary results suggest that copper complexes, particularly those bearing PPh_3 ligands, may be promising as potential therapeutic agents for

glioblastoma. To overcome the potential systemic toxicity, further studies are needed to develop nanoformulations capable of delivering these compounds selectively to tumor cells.

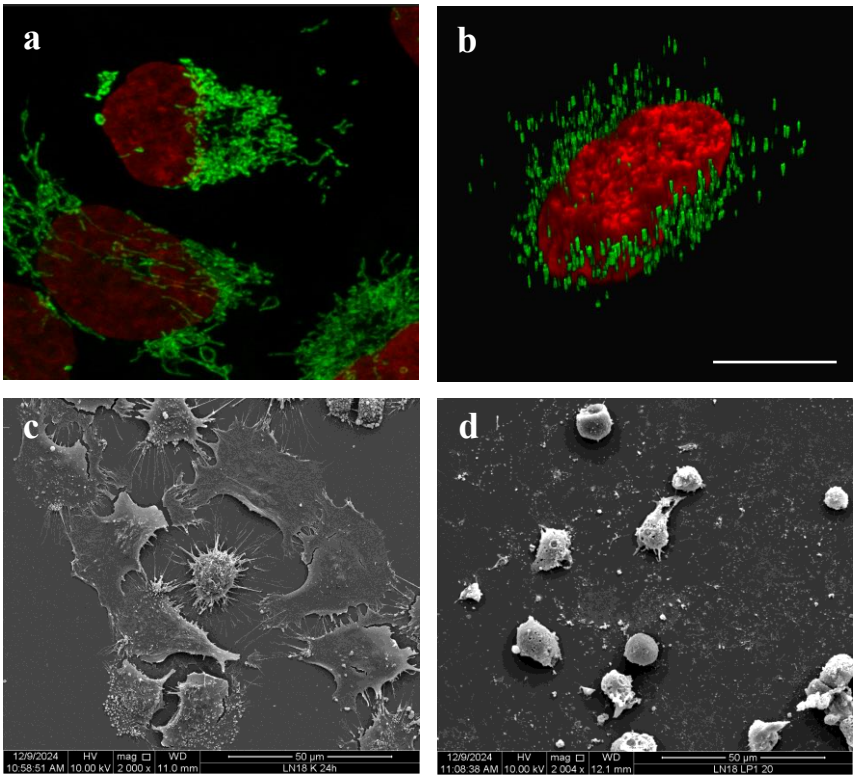


Figure 1. Laser scanning confocal microscopy micrographs of LN18 cells: (a) untreated LN18 cells; (b) LN18 cells treated for 24 h with IC_{25} (1.75 μM) of $[Cu(L^{Ad})(PPh_3)_2]PF_6$. Mitochondria (green signal) and nuclei (red signal) were labelled with MitoTracker® probe and PI, respectively. Scale bar: 10 μm. Scanning electron microscopy micrographs of LN18 cells: (c) untreated LN18 cells; (d) LN18 cells treated for 24h with IC_{25} (1.75 μM) of $[Cu(L^{Ad})(PPh_3)_2]PF_6$.

References

1. A. Serafino, E.K. Krasnowska, S. Romanò, A. De Gregorio, M. Colone, M.L. Dupuis, M. Bonucci, G. Ravagnan, A. Stringaro § M.P. Fuggetta, Int. J. Mol. Sci. **2024**, 25(19), 10572.
2. C. Santini, M. Pellei, V. Gandin, M. Porchia, F. Tisato, C. Marzano, *Chem. Rev.* **2014,** *114* (1), 815-862.

Type of presentation: Poster

LS4-P-17 Revealing Disparities in Macropinocytosis Between Bladder Cancer and Normal Urothelial Cells: Implications for Targeted Therapy

Larisa Tratnjek[a], Aleksandar Janev[a], Nataša Resnik[a], Mateja Erdani Kreft[a]

[a]*Institute of Cell Biology, Faculty of Medicine, University of Ljubljana, Slovenia*

Contact email: natasa.resnik@mf.uni-lj.si

Introduction: Cancer cells use macropinocytosis, a non-specific endocytic pathway that facilitates the uptake of extracellular substances, to survive under restrictive conditions, support unrestricted growth in a hostile tumor microenvironment and to develop resistance to treatments that target anabolic pathways. This adaptation results from hypoxia and nutrient deprivation in rapidly growing malignant tumors, leading to necrotic cell death at the core of solid tumors [1]. Cancer cells ingest necrotic debris via macropinocytosis and utilize amino acids, fatty acids, sugars, and nucleotides for biosynthesis [2,3]. The importance of macropinocytosis in cancer is further emphasized by its unique presence in certain cancer cells compared to normal cells of the same type, creating opportunities for selective targeting [4-8]. Several strategies have been proposed to exploit macropinocytosis for potential anticancer therapies, including inhibition of macropinocytosis to starve tumors, stimulation to increase drug uptake, and hyperstimulation to induce methuosis – non-apoptotic cell death resulting from large fluid-filled vacuoles derived from macropinosomes that cause membrane rupture and cell death. This study aimed to assess the potential of macropinocytosis to discriminate between bladder cancer and normal urothelial cells and to explore whether targeting macropinocytosis could selectively decrease the viability of bladder cancer cells.

Methods: Macropinocytosis was analysed in 2D and 3D monoculture and co-culture *in vitro* models, composed of muscle invasive T24 bladder cancer cells and normal urothelial cells (NPU and SV-HUC-1) using a fluid-phase marker, 70 kDa tetramethylrhodamine (TRITC)-dextran. The effect of inhibiting and (hyper)stimulating macropinocytosis on the viability of bladder cancer and normal urothelial cells was examined utilizing ethyl-isopropyl amiloride (EIPA) and silmitasertib (CX-4945), respectively. Fluorescence and confocal microscopy were employed to evaluate macropinocytotic uptake in the *in vitro* models. Sample preparation of 3D models for microscopic analysis included cryosectioning and paraffin-embedded tissue sectioning. The distinction between cancer and normal urothelial cells in co-culture *in vitro* models was based on the expression of E-cadherin in normal cells and N-cadherin in cancer cells, as identified by immunolabeling. Transmission electron microscopy was used to examine methuosis.

Results: Bladder cancer cells exhibited significantly higher macropinocytosis-mediated uptake compared to normal urothelial cells. This difference was consistently observed in both 2D and 3D monoculture and co-culture *in vitro* models. Inhibition of macropinocytosis decreased the viability of bladder cancer cells, while silmitasertib treatment increased macropinocytosis in bladder cancer cells but not in normal urothelial cells. Hyperstimulation induced extreme vacuolization and cell death in bladder cancer cells.

Discussion and conclusions: The difference in macropinocytosis between bladder cancer and normal urothelial cells highlights a unique vulnerability that could be selectively targeted for therapeutic intervention. The use of various microscopic techniques was essential in revealing these differences, allowing for precise observation of macropinocytosis in both cell types. Our preliminary results support the potential of manipulating macropinocytosis - either through inhibition or (hyper)stimulation - as a promising therapeutic strategy for bladder cancer, due to its selective effects on cancer cells.

References

1. S. Y. Lee et al., *Oxid Med Cell Longev* **2018**, 3537471.

2. V. Jayashankar and A. L. Edinger, *Nat Commun* **2020**, 11, 1121.
3. Z. Qiu et al., *Front Pharmacol* **2022**, 13, 919819.
4. J. J. Kamphorst et al., *Cancer Res* **2015**, 75, 544-53.
5. S. Song et al., *Front Oncol* **2020**, 10, 570108.
6. M. Colin et al., *Cancers* (Basel) **2019**, 11(3):411.
7. N. Resnik et al., *Histochem Cell Biol* **2023**, 160, 435-52.
8. N. Kostevšek et al., *RSC Adv* **2018**, 8(26), 14694-14704.

Type of presentation: Poster

LS4-P-18 Revealing LRAT and NeuroD1 Colocalization in human urothelial cancer cells in vivo using proximity ligation assay

Daša Zupančič[a], Karmen Wechtersbach[b], Jera Jeruc[b], Maruša Mišmaš Zrimšek[a], Nataša Resnik[a]

[a]*Institute of Cell Biology, Faculty of Medicine, University of Ljubljana, (Ljubljana), Slovenia*

[b]*Institute of Pathology, Faculty of Medicine, University of Ljubljana, (Ljubljana), Slovenia*

Contact email: dasa.zupancic@mf.uni-lj.si

Introduction: Urinary bladder cancer (BC) is a widespread disease that is the fifth most common cancer in the European Union [1,2]. In most cases, BC originates from the urothelium and has a recurrence rate of 50–70% [2]. In addition to invasive urothelial carcinomas such as high-grade urothelial carcinoma, which invades the lamina propria (T1, HG), there are several non-invasive urothelial neoplasms among urothelial tumours, including urothelial papilloma (UP), papillary urothelial neoplasm of low malignant potential (PUNLMP), non-invasive papillary urothelial carcinoma of low-grade (Ta, LG), non-invasive papillary urothelial carcinoma of high-grade (Ta, HG) and urothelial carcinoma in situ (Tis) [3]. Several epidemiologic studies have shown that a diet rich in vitamin A reduces the risk of bladder cancer [4]. Vitamin A is an essential nutrient and refers to a group of retinoids, with retinol, retinal and retinoic acid being the most biologically active forms, which have effects on embryonic development, proliferation, differentiation and apoptosis of various cell types [5]. Our previous study using a vitamin A-enriched diet in mice with BC induced by BBN (N-butyl-N-(4-hydroxybutyl)nitrosamine) showed significant upregulation of *LRAT* and *NeuroD1* [7]. Their products, lecithin-retinol acyltransferase (LRAT) esterifies retinol to retinyl esters for storage [6], and NeuroD1, a neurogenic differentiation factor 1, acts as a transcriptional activator and contributes to the regulation of various cell differentiation pathways and plays a role in nucleocytoplasmic transport [8]. We have shown that LRAT was translocated from the cytoplasm to the nuclei of urothelial cells during early bladder carcinogenesis in mice treated with BBN [7]. In addition, LRAT was immunolabeled to a higher degree in superficial bladder tumours than in invasive bladder tumours [9]. In the urothelium of normal mice, LRAT was localized in the cytoplasm of urothelial cells. Therefore, our research focuses on the association between NeuroD1 and LRAT. In this preliminary study, we aimed to analyse whether LRAT and NeuroD1 are colocalized in the nuclei of different human bladder tumour biopsy specimens using double immunolabelling and Proximity Ligation Assay (PLA).

Methods: We used paraffin-embedded sections of urothelial tumours from the archives of the Institute of Pathology, Faculty of Medicine, University of Ljubljana. The study was conducted in accordance with the Declaration of Helsinki and approved by the Slovenia National Medical Ethics Committee, approval number 0120-23/2021/10. We used the samples from 8 patients: 5 from patients with urothelial tumours (1 with PUNLMP, 1 with UP, 1 with Ta, LG, 1 with Ta, HG, and 1 with T1, HG) and 3 samples of normal urothelium. All patients who participated in the study underwent transurethral resection of the urinary bladder (TURB) at the Department of Urology, University Medical Center Ljubljana. The paraffin sections were first stained with hematoxylin and eosin and examined by a pathologist specialized in urinary tract pathology for diagnosis. Subsequently, double immunofluorescence and the PLA method with rabbit anti-LRAT and mouse anti-NeuroD1 were performed. Immunofluorescence was performed according to the standard protocol and the PLA method was performed using the NaveniTriFlexTM Cell MR Kit (Navinci) according to the manufacturer's instructions. Images were acquired using a fluorescence microscope and a confocal microscope.

Results: Double immunolabelling showed association of LRAT and NeuroD1 in the nuclei and cytoplasm of urothelial cells from normal urothelium, PUNLMP, UP, Ta, LH, Ta, HG and T1, HG samples. The PLA assay confirmed that LRAT and NeuroD1 were present in the nuclei and cytoplasm of urothelial cells in close proximity, i.e. 20-100 nm according to specification, in all samples (Figure 1).

Discussion and conclusions: Our results show that the enzyme LRAT is not only present in the cytoplasm of normal and cancer urothelial cells, but also in the nuclei. Furthermore, we have shown that the transcriptional activator NeuroD1 is also expressed in the nuclei and cytoplasm of normal urothelial

cells and cancer samples of different stages. We hypothesize that LRAT and NeuroD1 exert anti-cancer effects in BC through their joint action in the nuclei of cancer urothelial cells. To further investigate this hypothesis, we will confirm the colocalization of LRAT and NeuroD1 using immunoelectron microscopy. In addition, we will analyse the anti-cancer effect using 2D and 3D in vitro models.

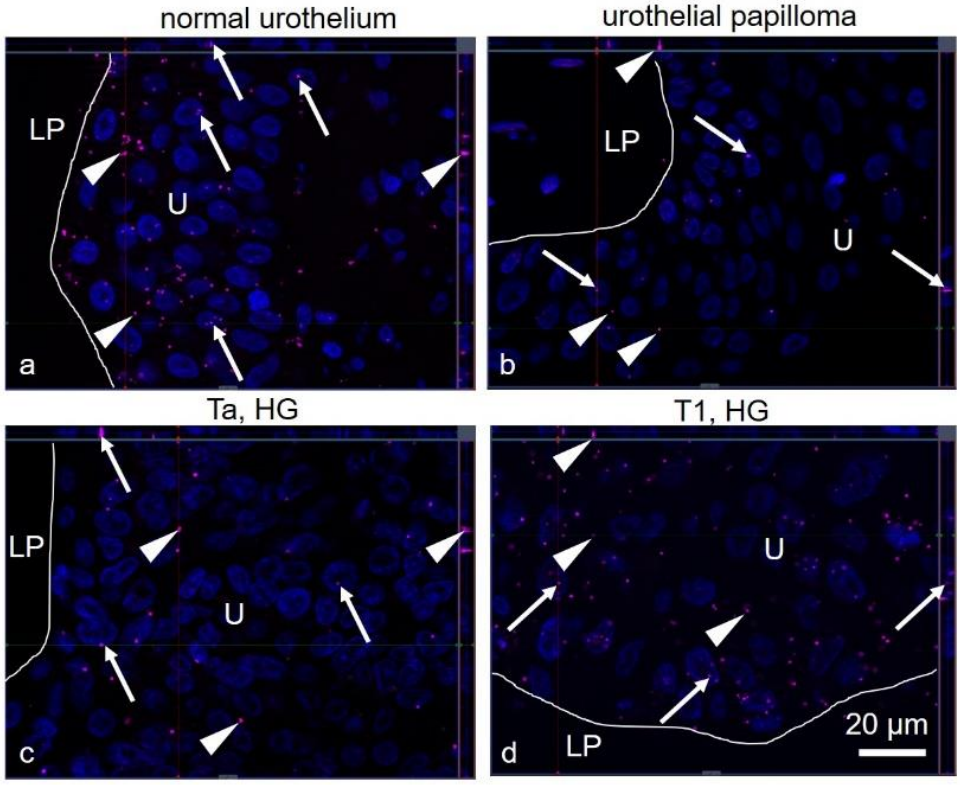


Figure 1: PLA method on paraffin sections of normal bladder urothelium and bladder tumours showing nuclear and cytoplasmic colocalization of LRAT and NeuroD1. Normal urothelium with positive PLA reaction (magenta signal) in the nuclei (white arrows) and cytoplasm (white arrowhead) of the urothelial cells (a). Urothelial cells of a urothelial papilloma (b), a high-grade non-invasive papillary urothelial carcinoma – Ta, HG (c) and a high-grade invasive papillary urothelial carcinoma – T1, HG (d) with PLA-positive reaction (magenta signal) in the nuclei (white arrows) and in the cytoplasm (white arrowhead) of the urothelial cell. The nuclei are stained blue with DAPI, the white line represents the position of the basal lamina, U – urothelium, LP – lamina propria.

Acknowledgments: The authors would like to thank Nada Pavlica Dubarič for her technical assistance and all colleagues at the Institute of Cell Biology (UL, MF). We are grateful for financial support from the Slovenian Research and Innovation Agency ARIS, grant numbers P3-0108, Z3-50118 and P3-0003.

References:

1. F. Bray, M Laversanne, *CA Cancer J Clin* **2024**, *74*, 229-263.
2. A. Richters, K.K.H. Aben, *World J Urol* **2020**, *38*, 1895-1904.
3. G.J. Netto, M.B. Amin, *Eur Urol* **2022**, *82*, 469-482.
4. C.M. Steinmaus, S. Nunez, *Am J Epidemiol* **2000**, *151*, 693-702.
5. E. Doldo, Costanza, G. *Biomed Res Int* **2015**, *2015*, 624627.
6. A. Carazo, K.Macáková, *Nutrients* **2021**, *13*.
7. D. Zupancic, J. Korac-Prlic, *Cancers (Basel)* **2020**, *12*.
8. R. Mehmood, N. Yasuhara, *Exp Cell Res* **2009**, *315*, 1639-1652.
9. S. Boorjian, S.K. Tickoo, *Clin Cancer Res* **2004**, *10*, 3429-3437.X.

LS5 Cell dynamics and high-resolution fluorescence microscopy

Type of presentation: Invited

LS5-IN-1 *Dictyostelium discoideum* IQGAP proteins IqgC and IqgD - siblings or distant relatives

Anja Čizmar[a], Darija Putar[a], Maja Marinović[a], Lucija Mijanović[a], Igor Weber[a], Jan Faix[b], Vedrana Filić[a]

[a]*Ruđer Bošković Institute, Zagreb, Croatia*

[b]*Institute for Biophysical Chemistry, Hannover Medical School, Hannover, Germany*

Contact email: vedrana.filic@irb.hr

Introduction: IQGAPs (*IQ-motif containing GTPase-activating proteins*) are large multidomain proteins that bind different binding partners. They serve as scaffolds that modulate various signalling pathways, e.g. Ras-Raf-MEK-ERK and PI3K-Akt [1]. A structural feature of IQGAPs is the presence of adjacent GRD (*GAP-related domain*) and RGCt (*RasGAP C-terminal*) domains in the C-terminal half of the protein. According to this structural signature, the protist *Dictyostelium discoideum* has four IQGAP-related proteins: DGAP1, GAPA, IqgC and IqgD. However, with the exception of IqgD, the IQGAPs of *D. discoideum* are significantly shorter and do not contain any other functional domains that are present in the N-terminal half of members of the IQGAP family of higher eukaryotes [2]. GRD is homologous to the catalytic domain of RasGAPs (*Ras GTPase-activating proteins*), proteins that facilitate the hydrolysis of GTP at the active site of Ras GTPases, thereby deactivating them. However, unlike RasGAPs, IQGAPs have lost their GAP activity due to mutations of critical amino acids in GRD and no longer interact with Ras proteins. Instead, they interact with the GTPases Cdc42 and Rac1 from the Rho family and are involved in the remodelling of the actin cytoskeleton. *D. discoideum* DGAP1 and GAPA are similar to their mammalian counterparts; they have also lost their GAP activity, they do not bind Ras GTPases, they bind Rac1 GTPases and are involved in actin cytoskeleton remodelling [3,4]. We analysed the functions of IqgC and IqgD. Unexpectedly, the amino acid sequence of IqgC suggested that its GRD may have conserved catalytic activity, and we confirmed that IqgC is indeed a functional RasGAP [5]. IqgD, on the other hand, is the only *D. discoideum* IQGAP that possesses an N-terminal CHD (*calponin homology domain*) and could bind directly to F-actin.

Methods: The coding DNA sequences of *iqgC* and *iqgD* were amplified from the cDNA of the axenic *D. discoideum* strain AX2 and cloned into a suitable expression vector. Confocal microscopy was used to investigate the subcellular localisation of fluorescently labelled IqgC and IqgD in living cells. Polyclonal antibodies against both proteins were developed by immunisation of rabbits. The interactions with potential binding partners were tested in the yeast two-hybrid system and in co-IP and pull-down assays. They were also confirmed in living cells by BiFC (*bimolecular fluorescence complementation*) and confocal microscopy. The GAP activity of IqgC was tested using a luminescence-based assay. To investigate the functional significance of the individual domains, truncated protein variants were constructed and corresponding point mutations were introduced. To investigate the biological role of IqgC and IqgD, knockout clones were generated by homologous recombination. *IqgC*- and *iqgD*-null cells were confirmed by PCR, Southern and western analyses. Various functional assays were performed with wild-type, knockout and overexpressing cell lines.

Results: IqgC localises to macropinocytic cups and macropinosomes and, to a lesser extent, to phagocytic cups and phagosomes [5]. It colocalises with the probe for active Ras at macropinosomes. IqgD shows similar localisation to macroendocytic cups, however it is also recruited throughout the cell cortex where it colocalises with the probe for active Rac1 GTPases and the probe for F-actin (unpublished). The yeast two-hybrid assay showed that IqgC interacts with a Ras family GTPase, RasG, while it does not interact with Rac GTPases, which constitute *D. discoideum* Rho family. On the contrary, IqgD interacted with the Rac1 GTPases of the Rho family, but not with the tested Ras GTPases. The interaction of IqgC and RasG was further characterised biochemically and using BiFC method. We showed that IqgC binds to the active form of RasG and acts as its GAP, and that this interaction is mediated via its GRD [5,6]. Since RasG is critical for efficient macropinocytosis in *D. discoideum*, we examined macropinocytosis in the absence of its negative regulator IqgC and showed that IqgC suppresses fluid uptake [5,6]. It also negatively regulates phagocytosis of large particles.

The interactions of IqgD with the GTPases Rac1A, Rac1B and Rac1C were confirmed in living cells using the BiFC method. IqgD binds all three Rac1 GTPases only in their active form. However, image analysis showed subtle differences in the BiFC signal distribution with respect to the interacting GTPase. Thus, the interactions between IqgD and Rac1A or Rac1B appear to be stronger in the retracting cortical regions, whereas Rac1C appears to have the same affinity for IqgD in the retracting and protrusive structures such as the macropinocytic cups. Interestingly, the protein lacking GRD was localised in the protrusive structures, while the protein lacking RGCt was found exclusively in the retracting cortex. BiFC experiments performed with these truncated variants of IqgD showed that both domains are required for interaction with Rac1. Since IqgD contains CHD, which is known to interact with F-actin, we next examined the localisation of IqgD without CHD and showed that this truncated protein is cytosolic. The same loss of cortical localisation was observed for full-length IqgD when cells were exposed to latrunculin. We conclude that the cortical localisation of IqgD depends on an intact cell cortex and is mediated via its CHD. To further investigate the cellular function of IqgD, we attempted to generate *iqgD*-null cells. The predicted recombination event at the *iqgD* locus was confirmed by PCR and Southern blot. Unexpectedly, western blot showed the presence of the protein. Subsequent analyses revealed the presence of an additional locus containing the coding sequence of *iqgD*, but without introns. Our attempts to inactivate this alternative gene at an unknown genomic locus were unsuccessful. Therefore, we phenotypically characterised the *iqgD*-L1-null (knockout at locus 1) cells. There was no difference in growth rate in suspension, macropinocytosis efficiency and macropinosome size between *iqgD*-L1-null and wild-type cells. However, growth on solid agar in the presence of bacteria was significantly slowed. Curiously, this was not caused by reduced phagocytosis of bacteria, as judged by the clearance of bacteria from the suspension. We are currently conducting further experiments to determine the underlying cause.

Discussion and conclusions: Our results show that IqgC and IqgD, although sharing domain architecture with DGAP1 and GAPA, have unique biological functions. IqgC stands out because, unlike IQGAPs from *Dictyostelium* or mammals, it is a genuine RasGAP with conserved catalytic activity towards the Ras GTPase. On the other hand, similar to DGAP1 and GAPA, IqgD interacts with Rac1 GTPases and not with Ras. IqgD is the largest IQGAP of *D. discoideum* that contains an N-terminal extension with CHD in addition to the GRD-RGCt domains and is thus most similar to human IQGAPs. Interestingly, DGAP1 and GAPA are localised in the posterior retracting cortex and IqgC in anterior macropinocytic cups, while IqgD adopts both localisations, much like F-actin. Our results suggest that IqgD is a Rac1 effector that interacts with F-actin via its CHD. Nevertheless, further experiments are required to substantiate this hypothesis and to reveal the effect of IqgD on the actin cytoskeleton.

Acknowledgments: This work has been supported by the Croatian Science Foundation under the project IP-2020-02-1572.

References:

1. L. Thines, F.J. Roushar, A.C. Hedman, D.B. Sacks, *J. of Cell Biol.* **2023**, *222*, e202205062.
2. K.B. Shannon, *Int. J. of Cell Biol.* **2012**, *2012*, 1–14.
3. H. Adachi, Y. Takahashi, T. Hasebe, M. Shirouzu, S. Yokoyama, K. Sutoh, *J. Cell Biol.* **1997**, *137*, 891–898.
4. J. Faix, C. Clougherty, A. Konzok, U. Mintert, J. Murphy, R. Albrecht, B. Mühlbauer, J. Kuhlmann, *J. Cell. Sci.* **1998**, *111*, 3059–3071.
5. M. Marinović, L. Mijanović, M. Šoštar, M. Vizovišek, A. Junemann, M. Fonović, B. Turk, I. Weber, J. Faix, V. Filić, *Proc. Natl. Acad. Sci. U.S.A.* **2019**, *116*, 1289–1298.
6. D. Putar, A. Čizmar, X. Chao, M. Šimić, M. Šoštar, T. Ćutić, L. Mijanović, A. Smolko, H. Tu, P. Cosson, I. Weber, H. Cai, V. Filić, *Open Biol.* **2024**, *14*, 230372.

Type of presentation: Invited

LS5-IN-2 Noradrenaline and Cannabinoid Regulation of Astrocyte Energy Metabolism Revealed by FRET Nanosensors

Marko Kreft[a,b,c], Katja Fink[b,c], Nina Vardjan[b,c], Kaja Belko Parkel[b], Robert Zorec[b,c]

[a]*Department of Biology, Biotechnical Faculty, University of Ljubljana, Ljubljana, Slovenia*

[b]*Laboratory of Neuroendocrinology-Molecular Cell Physiology, Institute of Pathophysiology, Faculty of Medicine, University of Ljubljana, Ljubljana, Slovenia*

[c]*Celica Biomedical Center, Ljubljana, Slovenia*

Contact email: Marko.Kreft@bf.uni-lj.si

Astrocytes are central to maintaining brain homeostasis, actively contributing to neurotransmission and providing metabolic support to neurons. Positioned between blood vessels and neurons, they facilitate glucose uptake and store glycogen as a readily mobilizable energy source. Glycogen turnover in astrocytes is tightly regulated by hormonal and neurochemical signals, including insulin, noradrenaline (NA), and endocannabinoids (eCBs). In this study, we investigated how NA and eCB signaling modulate astrocytic energy metabolism, focusing on intracellular glucose and lactate dynamics, calcium signaling, and glycogen utilization.

Primary cultured rat astrocytes were analyzed using genetically encoded Förster Resonance Energy Transfer FRET-based nanosensors for real-time measurements of cytosolic glucose and lactate, along with cytochemical assays for glycogen content. FRET is a non-invasive optical technique that detects molecular interactions or conformational changes based on energy transfer between two fluorescent proteins in close proximity. In this study, FRET-based genetically encoded nanosensors enabled real-time monitoring of intracellular glucose and lactate levels in single live astrocytes by measuring changes in fluorescence emission ratios. Specific agonists targeting CB1 and CB2 receptors were applied to assess cannabinoid effects. Both CB1 and CB2 activation significantly elevated intracellular glucose and lactate levels, indicative of enhanced aerobic glycolysis. Interestingly, CB2 receptor stimulation evoked a stronger metabolic response and more pronounced glycogen degradation, pointing to receptor-specific pathways for energy mobilization. These effects were accompanied by robust calcium signaling, suggesting a coordinated regulation of metabolism and gliotransmission. Together, our results highlight the role of astrocytic CB1 and CB2 receptors not only in neuromodulation but also as key regulators of cellular energy allocation. The capacity of cannabinoid signaling to drive glycogenolysis and glucose utilization underscores its relevance to brain energetics, particularly in disorders such as Alzheimer's disease, increasingly viewed as "type 3 diabetes" due to impaired glial metabolism.

To further dissect the involved pathways, we applied targeted metabolic inhibitors under NA stimulation. The glycolytic blocker 2-deoxy-D-glucose (2-DG) reduced lactate production by inhibiting glucose entry into glycolysis. The glycogen phosphorylase inhibitor 1,4-dideoxy-1,4-imino-D-arabinitol (DAB) suppressed glycogen breakdown, while 3-nitropropionic acid (3-NPA) inhibited oxidative phosphorylation via succinate dehydrogenase blockade. Our results reveal that NA-induced lactate elevation depends critically on D-glucose uptake and glycogen degradation. This indicates that glucose entering glycolysis primarily transits through the glycogen shunt and contributes to both lactate production and oxidative phosphorylation when mitochondrial function is intact. These findings underscore the metabolic flexibility of astrocytes in response to neuromodulatory cues and highlight the interplay between energy storage and utilization.

References:

1. K. Fink, J. Velebit, N. Vardjan, R. Zorec, M. Kreft, *J Neurosci Res.* **2021**,99, 1084-1098.
2. M. Muhič, N. Vardjan, H.H. Chowdhury, R. Zorec, M. Kreft, *J Biol Chem.* **2015**;290, 11167-11176.

Type of presentation: Oral

LS5-O-1 Exploring Plectin's Function in Migration of Astrocytes and Glioblastoma Through Confocal Microscopy

Maja Potokar [a,b], Maja Žugec[a], Jernej Jorgačevski[a,b], Robert Zorec[a,b]

[a]*Faculty of Medicine, University of Ljubljana, Ljubljana, Slovenia*

[b]*Celica Biomedical, Ljubljana, Slovenia*

Contact email: maja.potokar@mf.uni-lj.si

Introduction: Glioblastoma (GBM) is the most aggressive form of brain tumour, characterized by rapid cell proliferation, invasiveness, and resistance to therapy. GBM arise in the subventricular zone adjacent to the lateral ventricles, and in the subcortical white matter and then spread along the blood vessels and axons to the surrounding brain tissue. The strategies of GBM to spread throughout the central nervous system (CNS) are poorly understood. Recent studies have shown that alterations in aquaporin 4 (AQP4) and intermediate filament (IF) proteins play a crucial role in the pathology of GBM. IF proteins are linked via plectin (PLEC), a major cytolinker that occurs in multiple isoforms, important for regulating cytoskeletal dynamics, but its specific role in GBM remains unclear [1].
Astrocytes are the most abundant glial cells in the CNS, and they express PLEC in large quantities. Neural stem cells-derived astrocytes give rise to GBMs and during GBM transformation they undergo significant changes in cytoskeletal organization and distribution of membrane proteins [2]. PLEC is a key scaffolding protein, which has been shown to influence the structural integrity of different cell types, modulating cellular migration, but the role of PLEC in astrocyte and GBM migration has not been investigated. Given the hypothesized role of AQP4 in invasiveness of glioma, exploring its relationship with PLEC is crucial for deciphering the molecular mechanisms underlying GBM progression. In this study we examined the correlation between PLEC and AQP4 expression in GBM tissue, the effects of PLEC deficiency on AQP4 distribution, and assessed impact of PLEC on astrocyte migration.

Methods: To investigate the role of PLEC in astrocytes and GBM we used primary and immortalized astrocytes of mice and human origin, human GBM cell lines and human GBM samples. Using a combination of transcriptomic analysis and immunohistochemistry, immunohistochemistry, and live-cell imaging with a confocal microscope we analysed organization of cytoskeleton and protein localization at the plasma membrane. Cells were cultured on poly-D-lysine- and laminin-coated glass coverslips, fixed with 4% formaldehyde, and permeabilized with 0.1% Triton X-100 before immunolabelling with primary antibodies against PLEC, AQP4, and cytoskeletal components, followed by Alexa Fluor-conjugated secondary antibodies. For immunohistochemistry, formalin-fixed, paraffin-embedded human GBM tissue slices were deparaffinized, rehydrated, and subjected to heat-mediated antigen retrieval prior to blocking and antibody staining. Fluorescently labelled samples were imaged using a Zeiss LSM 800 confocal microscope with a 63×/1.4 oil immersion objective, using excitation wavelengths of 405 nm, 488 nm, and 561 nm, with emission spectra collected through bandpass filters. Z-stack imaging at 0.5-µm intervals enabled high-resolution visualization of intracellular structures, while 1-µm intervals were used for human GBM tissue slices. Live-cell imaging of astrocyte migration was performed using a wound-healing assay, in which cells were seeded in 35-mm culture dishes and time-lapse imaging was performed at 4-hour intervals over 28 hours. Image stacks were skeletonized to assess filament orientation and density, and to gain insight into the influence of PLEC on cytoskeletal dynamics. Image analysis was performed using Fiji software, quantifying protein colocalization, fluorescence intensity, cytoskeletal organization and speed of migrating astrocytes.

Results: Analysis of GBM RNA transcriptome datasets revealed a significant correlation between PLEC and AQP4 expression in astrocytoma and GBM samples. Immunohistochemical staining of human GBM tissue sections confirmed this correlation, with PLEC and AQP4 showing higher colocalization in GBM samples with low proliferative index cases, which are more invasive, suggesting a role of PLEC in glioma progression.

In addition, immunolabeling of mouse and human primary astrocytes and immortalized cells (astrocytes and GBM) showed that immortalized cells have more plasmalemmal AQP4 aggregates. PLEC deficiency led to a significant reduction of plasmalemmal AQP4 aggregates, suggesting the hypothesis that PLEC is involved in positioning of AQP4 within the plasma membrane. In PLEC-deficient astrocytes, actin filaments (AFs) were retracted from the plasma membrane and exhibited increased bundling, while vimentin filaments (VFs) were distributed closer to the plasma membrane and appeared less organized. These structural alterations suggest that PLEC plays a crucial role in maintaining cytoskeletal integrity and plasmalemmal abundance of AQP4 aggregates by coordinating the interactions via AFs.
Additionally, live-cell imaging of astrocyte migration using the wound-healing assay demonstrated that PLEC deficiency impaired cell motility. PLEC-deficient astrocytes migrated significantly slower than their wild-type counterparts, with a significantly prolonged time required to close 50% of the wound gap. This reduced migration speed was partially rescued by the overexpression of specific PLEC isoforms, particularly P1c, which was also demonstrated to be the predominant isoform associated with plasmalemmal AQP4 aggregates**.**

Discussion and conclusions:
This study highlights the role of PLEC in GBM by demonstrating its correlation with AQP4 and its influence on organization of cytoskeleton and cell migration of astrocytes. Confocal microscopy revealed that PLEC deficiency leads to a reduction of plasmalemmal AQP4 aggregates and altered AF and VF distribution, impairing astrocyte motility. The predominant PLEC isoform associated with AQP4, P1c, also had the greatest impact on restoring migration speed. The greater peripheral localization of PLEC in GBM cells in comparison with primary astrocytes and the increased presence of PLEC at the cell surface in GBM cells suggest its potential as a biomarker and therapeutic target. These findings provide new insights into the mechanisms of GBM progression and open up avenues for targeted therapeutic interventions.
Acknowledgments: The authors thank Prof. Dr. Simon Horvat and Urška Hostnik for the development and implementation of a rapid genotyping test for neonatal F2 crossbred offspring, and Katja Skulj for the maintenance and breeding of transgenic PLEC knockout lines.

References:

1. M. Žugec, B.Furlani, M.J. Castañon, B. Rituper, I. Fischer, G. Broggi, R. Caltabiano, G.M.V. Barbagallo, M. Di Rosa, D.Tibullo, R. Parenti, N. Vicario, S. Simčič, V.M. Pozo Devoto, G.B. Stokin, G. Wiche, J. Jorgačevski, R. Zorec, M. Potokar, *Journal of Biomedical Science*. **2024**, *31*, 11-22
2. E.J. van Bodegraven, J.V. van Asperen, P.A.J. Robe, E.M Hol. *Glia*. 2019;67,1417–1433

Type of presentation: Poster

LS5-O-2 Live Imaging of Calcium and Hormonal Crosstalk in Potato: Insights into Endophyte-Mediated Immune Enhancement

Katja Fink[a], Tjaša Mahkovec Povalej[a], Katja Stare[a], Tjaša Lukan[a], Kristina Gruden[a]

[a]*Department of Biotechnology and Systems Biology, National Institute of Slovenia, Ljubljana, Slovenia*

Contact email: katja.fink@nib.si

Plants rely on complex signaling networks to defend themselves against pathogens, with interactions between microbial communities playing a crucial role in shaping immune responses. Our study focuses on understanding how endophytic bacteria, such as *Bacillus subtilis* and *Paenibacillus sp*., enhance potato immune response against pathogens like potato virus Y (PVY). Although the precise mechanisms remain unclear, these endophytes are known to modulate plant immunity, potentially by activating specific hormonal signaling pathways. By monitoring calcium fluxes and hormone-related signals (JA, ET, and SA) in plant cells, we aim to clarify the link between endophyte-induced immune effects and plant signal transduction mechanisms. Using transgenic potato plants expressing fluorescent sensors for stress-responsive hormones and calcium, we will assess immune responses in both leaves and roots under biotic stress conditions. We monitor these signals in real time in intact plant tissues by employing live confocal microscopy at the cellular level. We are adjusting imaging protocols to enhance signal stability over extended periods, allowing us to track intracellular calcium dynamics and expression of hormone-dependent genes with high spatial and temporal precision.

We suggest that this approach is suitable to uncover spatial and temporal dynamics of calcium signaling and hormonal interactions with minimal disturbance of plant physiology. The results of this methodological approach will contribute to a deeper understanding of plant immune responses and provide new insights into the molecular basis of endophyte-mediated defense enhancement, with potential applications in sustainable crop protection strategies.

Keywords: Endophytic bacteria, Plant immune response, Calcium signaling, Hormonal interactions, Confocal microscopy

Type of presentation: Poster

LS5-P-1 Unraveling the Noncanonical Mitochondrial Import Signals of NME6 – a Member of the NME/NDPK Family

Maja Herak Bosnar[a], Lea Vrbančić[a], Bastien Proust[a], Nikolina Škrobot Vidaček[a], Maja Jazvinšćak Jembrek[a], Valentina Štimac[a], Iva Marija Tolić[a], Maja Šutić[a]

[a]*Ruđer Bošković Institute, (Zagreb), Croatia*

Contact email: mherak@irb.hr

Introduction: Nucleoside diphosphate kinases (NDPKs or NME) are a family of evolutionarily conserved enzymes with crucial roles in various biological processes, including suppression of metastasis. The 10 human NME genes are divided into two groups based on phylogenetic analysis and exon-intron structure. Proteins encoded by Group I genes (NME1-4) are highly homologous and all exhibit NDPK activity in their hexameric form. They transfer the terminal phosphate from d(NTP)s to d(NDP)s via a high-energy phospho-histidine intermediate. In contrast, group II NME proteins (NME5-9) are more diverse among themselves and differ significantly from Group I proteins [1]. The NDPK activity of most Group II members remains unresolved, and overall, there is a lack of data regarding their cellular functions. Recent studies have provided new insights into the structure and function of the NME6 protein. Our group discovered that NME6 exists in two isoforms within the cell and localizes specifically in the mitochondrial matrix, probably adjacent to the mitochondrial inner membrane [2]. In mitochondria, NME6 colocalizes with the GTPase RCC1L and is involved in mitochondrial RNA maturation, ribosome assembly, and translation. Furthermore, it has been shown that the specific interaction between NME6 and RCC1L is necessary for the NME6's NDPK activity, distinguishing NME6 from group I NME proteins [3,4]. Although NME6 is localized in mitochondria it lacks the canonical mitochondrial targeting signal (MTS) at its N-terminus. Therefore, our current research focuses on identifying crucial signals within the NME6 protein sequence that facilitate its mitochondrial import.

Methods: On the basis of *in silico* analysis using TargetP and iMTS-L predictors to identify potential internal mitochondrial targeting regions, we designed and generated GFP-fused deletants and mutants of NME6 [5]. The localization of these GFP-tagged NME6 constructs was studied imaging of live cells (HeLa and MDA-MB-231T) by confocal microscopy to pinpoint the regions essential for mitochondrial matrix localization. Further, we are using STED (stimulated emission depletion) microscopy to directly see the fine details of NME6 localization within mitochondria and define the. This will be addressed by dual color STED between NME6 and markers of submitochondrial compartments.

Results and discussion: Our experiments, so far, revealed that the main mitochondrial import signal lies in the first 7 amino acid residues on the N-terminus of NME6. Moreover, we have proved that the positive charges, mainly arginine residues (internal mitochondrial sequences, iMTS) within the NME6 sequence grossly contribute to its undisturbed entry into mitochondria. Our preliminary data using STED excluded the presence of NME6 at the outer mitochondrial membrane and confirmed a partial colocalization signal with the inner membrane but further experiments are needed to confirm our findings.

Acknowledgments: This work was supported by the Croatian Science Foundation under the project number IP-2022-10-7420

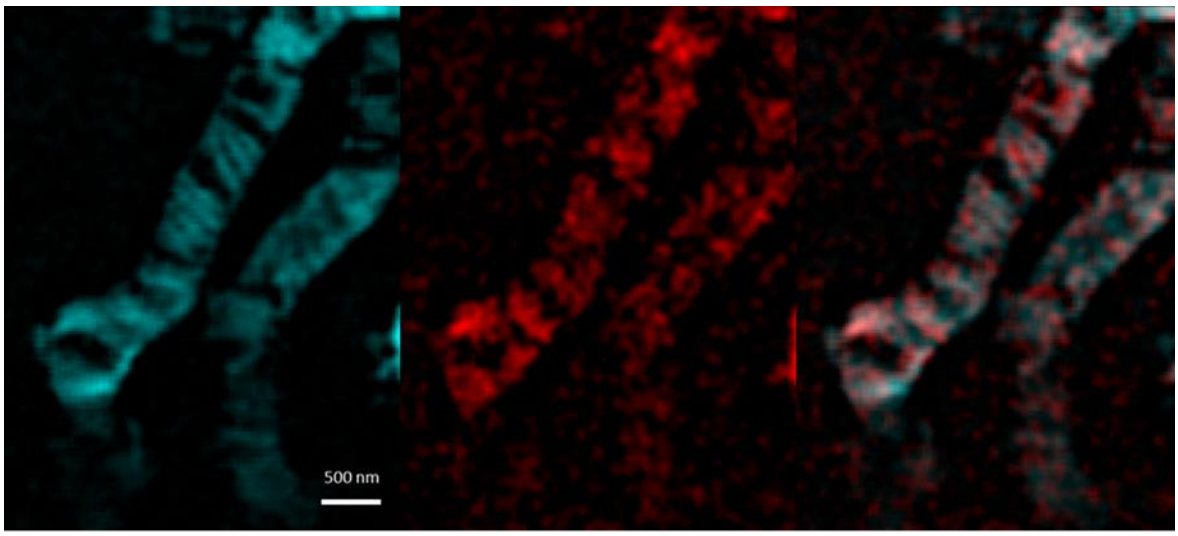


Figure 1: Live cells dual-color STED. Human HeLa cells coloured with inner membrane mitochondrial dye PKMO (cyan) transfected to express NME6 (red, SNAP-sir-647). The overlay shows abundant colocalization (white). Resolution goes down to 75nm on the presented image.

References:

1. M. Boissan, S. Dabernat, E. Peuchant, U. Schlattner, I. Lascu, ML Lacombe. *Mol. Cell. Biochem.* **2009,** *329*, 51-62.
2. B. Proust, M. Radić, N. Škrobot Vidaček, C. Cottet, S. Attia, F. Lamarche, L. Ačkar, V. Godinić Mikulčić, M. Tokarska-Schlattner, H. Ćetković, U. Schlattner, M. Herak Bosnar. *Cell Biosci.* **2021**,*11*, 195.
3. N. J. Kramer, G. Prakash, R.S. Isaac, K. Choquet, I. Soto, B. Petrova, H.E. Merens, N. Kanarek, L.S. Churchman, *Nat. Cell Biol.* **2023**, *25*, 1575-1589.
4. N. Grotehans, L. McGarry, H. Nolte, V. Xavier, M. Kroker, Á.J. Narbona-Pérez, S. Deshwal, P. Giavalisco, T. Langer, T.N. MacVicar. *EMBO J.* **2023,** *42* ,e113256.
5. K. Schneider, D. Zimmer, H. Nielsen, J. M. Herrmann, T. Mühlhaus. *Biol. Chem.* **2021**, *402*, 937-943.

Type of presentation: Poster

LS5-P-2 Effect of decellularized placenta-derived ecm molecules on in vitro angiogenesis

Simal Yaren Sahin[a,b], Halime Kenar[a,b,c]

[a]*Biomaterials Center, Acibadem Mehmet Ali Aydinlar University, Turkiye*

[b]*Department of Biomaterials, Graduate School of Natural and Applied Sciences, Acibadem Mehmet Ali Aydinlar University, Turkiye*

[c]*Department of Biomedical Engineering, Faculty of Engineering and Natural Sciences, Acibadem Mehmet Ali Aydinlar University, Turkiye*

Contact email: halime.kenar@acibadem.edu.tr

Introduction

Angiogenesis, the formation of new blood vessels from pre-existing ones, is an important fundamental process in tissue engineering, particularly for the development of thick and metabolically active constructs. In vitro reconstitution of endothelial capillary-like networks is often achieved using co-culture systems combined with extracellular matrix (ECM)-based biomaterials. Among these, ECM molecules derived from decellularized tissues have gained prominence due to their ability to retain native matrix components and bioactive factors. Decellularized placenta-derived ECM molecules have been identified as particularly rich in pro-angiogenic cues, including collagen, fibronectin, laminin, and bound growth factors [1]. These ECM molecules have been shown to support endothelial cell adhesion, migration, and network formation in vitro without the need for added angiogenic supplements. Concentration dependent effect of decellularized placenta-derived ECM molecules on endothelial cells' capillary-like structure formation capability was investigated in this study through confocal microscopy.

Methods

Human placental disc was decellularized through use of Triton X-100 and SDS and digested with pepsin to obtain ECM in a soluble form. Ibidi µ-Slide (18 Well Glass Bottom) was coated with different concentrations of decellularized human placenta-derived ECM molecules (dPL) and with CellMatrix (ATCC) as a control group. CellMatrix was prepared at 2% (v/v) in DMEM/F12, while dPL was diluted in DMEM/F12 to final concentrations of 0.1 mg/mL, 0.3 mg/mL, and 0.6 mg/mL. Each coating solution (100 µL) was incubated at 37 °C for 1 hour. After incubation, coating solutions were removed and human primary coronary artery endothelial cells (ATCC PCS-100-020) and human primary neonatal skin fibroblasts (ATCC PCS-201-010) were seeded on each coated surface at a 5:1 ratio (endothelial cell:fibroblast, total of 3000 cells per well). The co-cultures were maintained for 30 days in DMEM:EGM2 (1:1 v/v) medium supplemented with 6% FBS. At the end of the culture period, cells were fixed with 4% formaldehyde, permeabilized with 0.1% Triton X-100 and blocked with 3% BSA. Primary antibodies targeting CD31 and Vimentin were applied overnight at 4 °C, and after washing with PBS, fluorescently labelled secondary antibodies (Alexa Fluor 488 and Alexa Fluor 594) were added and samples incubated for 1 hour at 37 °C. The immunostained cells were then countersatined with DAPI and examined using confocal microscopy.

Results

Endothelial network morphology demonstrated distinct patterns across the groups. Minimal cell adhesion was observed on the 0.1 mg/mL dPL coated glass surface. On the 0.3 mg/mL dPL coated surface, endothelial cells formed branched and interconnected structures resembling capillary networks. In the 0.6 mg/mL dPL group, endothelial cells were organized in big clusters, which were not interconnected. An increase in endothelial cell coverage was observed with rising dPL concentration. On the CellMatrix coated surface, capillary-like structures with total coverage similar to the 0.3 mg/mL dPL group, but displaying finer and less branched networks, were detected.

Discussion

The use of decellularized human placenta-derived ECM was found to modulate endothelial network formation in a concentration-dependent manner. In particular, the 0.3 mg/mL dPL group supported the formation of interconnected and branched endothelial capillary-like structures, whereas the 0.6 mg/mL dPL group resulted in more compact clusters representing the very early stage preceding capillary network formation [2]. In comparison, CellMatrix coating allowed for the development of capillary-like networks, with similar coverage to the 0.3 mg/mL dPL group, but being finer and less branched. The observed differences suggest that placenta-derived ECM may provide more biologically active cues, potentially different placental ECM proteins, glycosaminoglycans and growth factors than standard ECM products like CellMatrix. In the 0.1 mg/mL dPL group, minimal cell adhesion was observed, indicating that a threshold concentration is required to support cellular attachment and even cell distribution. The presence of fibroblasts in all conditions likely contributed to ECM deposition, facilitating capillary network maturation in accordance with dPL ECM concentration.

Conclusion

ECM composition and density are critical parameters in guiding angiogenic responses in vitro. Results of the study support the use of placenta-derived ECM as a tunable platform for vascularized tissue engineering applications.

References:

1. A. Roy, M. Mantay, C. Brannan, S. Griffiths. *Biomed Res Int.* **2022**, 6751456.
2. A. Freiman, Y. Shandalov, D. Rozenfeld, E. Shor, S. Segal, D. Ben-David, S. Meretzki, D. Egozi, S. Levenberg. *Stem Cell Research & Therapy* **2016**, 7, 5.

LS6 From a whole organism to sub-cellular imaging: correlative microscopy and multimodal imaging

Type of presentation: Invited

LS6-IN-1 Advanced Microscopy Approaches Unveil Plectin as a Key Regulator of Focal Adhesions in Astrocytes

Jernej Jorgačevski[a,b], Borut Furlani[a], Robert Zorec[a,b], Maja Potokar[a,b]

[a]*Faculty of Medicine, University of Ljubljana, Ljubljana, Slovenia*

[b]*Celica Biomedical, Ljubljana, Slovenia*

Contact email: jernej.jorgacevski@mf.uni-lj.si

Introduction: Astrocytes are essential for central nervous system (CNS) homeostasis, supporting synaptic plasticity, neurovascular interactions, and metabolic processes. Their structural integrity relies on cytoskeletal components, including intermediate filaments (IFs) such as vimentin and glial fibrillary acidic protein, which interact with other cytoskeletal networks through linker proteins such as plectin. Plectin, a versatile cytolinker, is highly expressed in astrocytes and plays a crucial role in cytoskeletal organization [1].
Focal adhesions (FAs) mediate the interactions of astrocytes with the extracellular matrix and are vital for processes such as migration and mechanosensing. Plectin has been implicated in FA dynamics, but its specific role in astrocytes remains unclear [2]. Given that reactive astrogliosis, a response to CNS injury, is associated with cytoskeletal reorganization and increased FA formation, understanding plectin's function is crucial. In this study, we have investigated how plectin regulates FA dynamics, cytoskeletal organization, and mechanical properties of astrocytes, revealing its role in physiological and pathological conditions.

Methods: Experiments were conducted on primary ($Plec^{+/+}$ and $Plec^{-/-}$) and immortalized ($Plec^{+/+}p53^{-/-}$and $Plec^{-/-}p53^{-/-}$) mouse astrocytes cultured in standard feeding medium or serum-free neurobasal medium [1]. FA proteins and cytoskeletal components, including vinculin, plectin, α-tubulin, vimentin, and actin filaments, were visualized through immunocytochemical labelling. Alternatively, cells were transfected using plasmid DNA encoding for fusion proteins between fluorescent proteins and various plectin isoforms, Vinculin-Venus, and Paxillin-EGFP.
Microscopy techniques included confocal laser scanning microscopy (LSM 980), structured illumination microscopy (SIM; ELYRA PS.1, Zeiss), and stimulated emission depletion microscopy (STED; STEDYCON, Abberiror Instruments). Time-lapse imaging was used to analyse FA turnover, while fluorescence recovery after photobleaching (FRAP) was used to measure vinculin and paxillin mobility. Atomic force microscopy (AFM; Nanowizard II, JPK Instruments) was used to assess cellular mechanical properties, including Young's modulus and viscoelasticity [3]. Additionally, the intracellular plectin levels were quantified using ELISA. The results were analysed using Fiji and Python-based image processing [1].

Results: SIM and STED microscopy revealed that plectin localizes to FAs in astrocytes, where its distribution is polarized and depends on FA maturation. Time-lapse confocal microscopy showed that plectin deficiency reduces the number of FAs and impairs FA turnover by lowering the rate of assembly and increasing the rate of degradation. FRAP demonstrated altered vinculin and paxillin mobility in plectin-null astrocytes.
SIM measurements confirmed that plectin-deficient astrocytes exhibit a disrupted vimentin network with reduced connectivity and increased filament bundling. Quantitative analysis of cytoskeletal interactions using confocal microscopy and image processing software revealed reduced colocalization of FAs with vimentin in plectin-null cells. AFM measurements indicated that plectin-deficient astrocytes exhibit reduced stiffness, particularly in peripheral regions, and altered viscoelastic properties.
In a serum-induced model of reactive astrogliosis, confocal microscopy and ELISA quantification showed increased number and size of FAs and increased plectin expression.

Discussion and conclusions:
Our findings highlight the role of plectin in astrocyte cytoskeletal dynamics. Using advanced microscopy approaches, we show that plectin orchestrates interactions between IFs, actin filaments, and

FAs, regulating key processes such as morphological differentiation, FA turnover, cytoskeletal organization, migration, and cell mechanics. High-resolution imaging demonstrates how plectin-mediated cytoskeletal remodelling enables astrocytes to dynamically adapt their structure and function in both physiological and pathological conditions. These insights not only deepen our understanding of the role of plectin in astrocyte biology but also position it as a potential therapeutic target for disorders associated with abnormal astrocyte behaviour, including neurodegenerative diseases and glioblastoma [4].

Acknowledgments: The authors thank Primož Runovc for his help with the experiments, prof. dr. Simon Horvat and Urška Hostnik for developing and implementing a rapid genotyping assay for neonatal F2 crossbred offspring, and Katja Skulj for maintaining and breeding of transgenic plectin knockout lines.

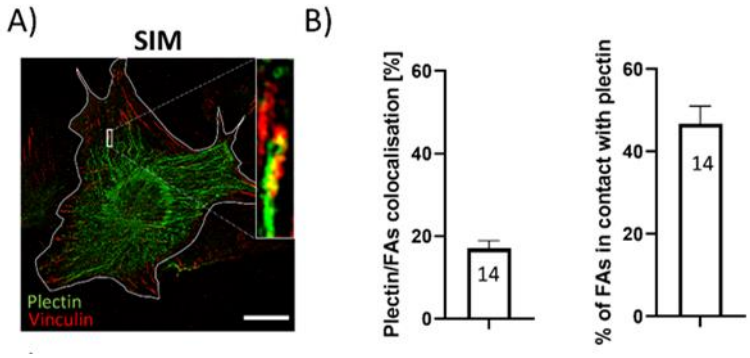


Figure 1: Plectin colocalizes with FAs in mouse astrocytes. A) SIM micrograph of a primary mouse astrocyte, immunolabelled for vinculin (red) and plectin (green). The inset shows an enlarged FA with partial overlap of both signals. B) Quantitative analysis supports these observations. The left graph shows the percentage of plectin overlapping with the FA signal, while the right graph displays the percentage of FAs that are in contact with plectin. The numbers in the columns indicate the total number of cells analysed.

References:

1. M. Žugec, B. Furlani, M.J. Castañon, B. Rituper, I. Fischer, G. Broggi, R. Caltabiano, G.M.V. Barbagallo, M. Di Rosa, D. Tibullo, R. Parenti, N. Vicario, S. Simčič, V.M. Pozo Devoto, G.B. Stokin, G. Wiche, J. Jorgačevski, R. Zorec, M. Potokar, *J Biomed Sci.* **2024**, *31*, 1-22.
2. M. Gregor, S. Osmanagic-Myers, G. Burgstaller, M. Wolfram, I. Fischer, G. Walko, G.P. Resch, A. Jörgl, H. Herrmann, G. Wiche, *FASEB J.* **2014**, *28*, 715-29.
3. M. Lisjak, M. Potokar, B. Rituper, J. Jorgačevski, R. Zorec, *J Neurosci.* **2017**, *37*, 10748-56.
4. B. Furlani, M. Potokar, V.M. Pozo Devoto, G. Wiche, R. Zorec, J. Jorgačevski, doi: *https://doi.org/10.1101/2025.01.14*.

Type of presentation: Invited

LS6-IN-2 Merging Electrons with Other Modalities

Jiří Týč[a]

[a]*Biology Centre Czech Academy of Sciences, (České Budějovice) Czech Republic*

Contact email: jiri.tyc@paru.cas.cz

In the quest to understand biological complexity, resolution alone is no longer enough. Electron microscopy offers unmatched structural detail, but to fully interpret biological systems, we increasingly combine it with complementary modalities — a strategy known as multimodal imaging. This enables not only precise localization of regions of interest, but also the acquisition of compositional and functional information across scales.

This talk will focus on multimodal and hierarchical imaging strategies anchored in electron microscopy, outlining key principles and practical workflows for integrating EM with correlative light microscopy (CLEM), X-ray imaging, energy-dispersive X-ray spectroscopy (EDX), and Raman microspectroscopy. Special attention will be given to how these combinations extend EM's interpretive power — and how they help reveal biological structures and processes that would remain hidden to any single method alone.

Type of presentation: Invited

LS6-IN-3 Open Access to Imaging Excellence and Opportunities for Imaging Core Facility Staff – Updates from Euro-BioImaging and Global BioImaging

Johanna Bischof[a]

[a]*Euro-BioImaging ERIC*

Contact email: johanna.bischof@eurobioimaging.eu

Euro-BioImaging offers all scientists open access to a large portfolio of imaging instruments, expertise, training opportunities, and data management services. The technologies offered by Euro-BioImaging can be accessed at Euro-BioImaging Nodes, which comprise more than 200 internationally renowned imaging facilities distributed across Europe. They cover the whole spectrum of biological and biomedical imaging. In addition to access to cutting-edge instruments, the Euro-BioImaging Nodes provide expertise, guidance and training on all aspects of the imaging experiment.

Euro-BioImaging has a strong commitment to Open Science, working with image data repositories such as the BioImage Archive and EMPIAR, providing tools for image analysis and management in ome.zarr, as well as offering image analysis and support with data FAIRification.

For the technical experts at imaging core facilities, Euro-BioImaging provides a cross-European network, platform for exchange of experience and collaboration, as well as opportunities for training and skill-building through the EVOLVE project.

Global BioImaging is an international network of imaging infrastructures and communities spanning the globe with 13 partner networks, representing imaging scientists in core facilities in more than 60 countries. Recognizing that scientific, technical and data challenges are universal rather than restricted by geographical boundaries, it brings together imaging facility operators and technical staff, scientists, managers and science policy officers from around the globe, to network, exchange experiences and build capacity internationally.

Global BioImaging provides training courses for imaging scientists on facility management and image data topics. The GBI working groups focus on a range of different topics of interest, from Image Data and Impact Assessment to Career Paths and Training, and provide opportunities for international networking and policy-making through regular publication of international recommendations.

Through the Wellcome Trust funded Imaging4All program, Global BioImaging also offers researchers in low- and middle-income countries the opportunity to participate in imaging trainings and to access imaging core facilities for their research anywhere in the world.

Type of presentation: Oral

LS6-O-1 Volume Electron Microscopy Methods for Investigating Nitrogen Handling and Cellular Vision in Microscopic Algae

Eva Durinova[a], Jana Pilatova[b,c], Jiri Miksatko[a], Ambarneil Saha[d], Alexander Pattison[d], Tomas Ostatnicky[c], Peter Mojzes[c], Peter Ercius[d], Crysten Blaby-Haas[b,e]

[a]*Faculty of Science, Charles University, Prague, Czech Republic*

[b]*Molecular Foundry, Lawrence Berkeley National Laboratory, Berkeley, California, USA*

[c]*Faculty of Mathematics and Physics, Charles University, Praha, Czech Republic*

[d]*National Center for Electron Microscopy, Lawrence Berkeley National Laboratory, Berkeley, California, USA*

[e]*Joint Genome Institute, Lawrence Berkeley National Laboratory, Berkeley, California, USA*

[*]*Contributed equally*

Contact email: eva.durinova@natur.cuni.cz

Recent advancements in volume electron microscopy (vEM) have enabled biologists to visualize well-preserved organic structures with exceptional resolution, making these methods increasingly vital for studying complex biological systems. Among the various techniques—such as focused ion beam and serial block-face scanning electron microscopy (FIB-SEM and SBF-SEM), array tomography, and electron tomography—each offers distinct advantages, though some have limitations. Combining these methods based on the specimen's specific characteristics is often essential for obtaining the most informative results.

In this study, we investigated *Effrenium voratum* (Symbiodiniaceae, Dinoflagellata, Alveolata, SAR), a unicellular marine eukaryote related to symbionts of corals, anemones, and clams. We focused on a challenging biogenic crystalline material localized in two compartments: vacuoles with metabolic functions [1,2] and the eyespot, which plays a key role in cellular vision [3,4]. In conventional TEM sections, crystals often drop out due to their brittle mechanical properties, making vEM techniques crucial for preserving intact crystal structures.

To explore the structural and optical properties of the eyespot, we employed serial section electron tomography and FIB-SEM. While electron tomography offers excellent resolution in the nm to sub-nm range, its limited section depth (200–300 nm per slice) restricts the volume that can be imaged. FIB-SEM was used to overcome this constraint, enabling whole-cell scanning at a resolution of 3×4×20 nm.

The chemical identity of the biocrystals, initially believed to be formed by uric acid, has been debated [3]. Here, we provide direct evidence that these crystals consist of β-polymorphic anhydrous guanine using in situ Raman microscopy, alongside primary structural techniques such as 3D electron diffraction and 4D scanning transmission electron microscopy (4D STEM).

We demonstrate that guanine crystals support nitrogen metabolism during nutrient limitation, a condition observed in coral reefs [1]. Additionally, the exceptional optical properties of guanine crystals suggest their role in cellular optical functions [5]. Our results provide new insights into the arrangement of guanine crystals within the cell, allowing us to determine the eyespot's size, location, and orientation, along with initial findings on its formation process. The eyespot in *E. voratum* consists of multiple crystalline layers of guanine with a high refractive index (1.83), separated by cytoplasmic layers with a lower refractive index (1.34)—each approximately 70 nm thick. Our detailed 3D reconstruction of the eyespot arrangement was used to predict its reflectance spectra via finite-difference time-domain optical simulations, establishing a functional link to the eyespot's role in microbial phototaxis—the ability to navigate marine environments.

Reference

1. Mojzeš P, Gao L, Ismagulova T, Pilátová J, Moudříková Š, et al. (2020) Guanine, a high-capacity and rapid-turnover nitrogen reserve in microalgal cells. Proc Natl Acad Sci USA 51: 32722-32730.
2. Pilátová J, Pánek T, Oborník M, Čepička I, Mojzeš P (2022) Revisiting biocrystallization: purine crystalline inclusions are widespread in eukaryotes. ISME J 9: 2290-2294.
3. Yamashita H, Kobiyama A, Koike K (2009) Do uric acid deposits in zooxanthellae function as eye-spots? PLoS One 7: 1-9.
4. Horiguchi T, Kawai H, Kubota M, Takahashi T, Watanabe M (1999) Phototactic responses of four marine dinoflagellates with different types of eyespot and chloroplast. Phycological Res: 101-107.
5. Jantschke A, Pinkas I, Hirsch A, Elad N, Schertel A, Addadi L, Weiner S (2019). Anhydrous β-guanine crystals in a marine dinoflagellate: Structure and suggested function. J Struct Biol 207: 12-20.

Type of presentation: Oral

LS6-O-2 Semi-automated Classification of Nanoparticle Signals from Opposite Surfaces of Ultrathin Sections in Low-Voltage STEM

František Kitzberger[a], Pavlína Sikorová[b], Jakub Opelka[c], Miroslav Šlouf[d]

[a]*Laboratory of Electron Microscopy, Institute of Parasitology, Biological Centre CAS, České Budějovice, Czech Republicđ*

[b]*Institute of Food Science and Biotechnology, Brno Universirty of Technology, Brno, Czech Republic*

[c]*Institute of Entomology, Biological Centre CAS, České Budějovice, Czech Republic*

[d]*Institute of Macromolecular Chemistry, CAS, Prague, Czech Republic*

Contact email: frantisek.kitzberger@paru.cas.cz

The simultaneous detection of immunogold labelling, which is applied to both surfaces of ultrathin sections, doubles the number of biomolecules that can be detected and localized by a low-voltage scanning transmission electron microscopy (LV-STEM); STEM-in-SEM [1].

The principle consists in that each immunogold marker exhibits two different intensity profiles, depending on its position on top vs. bottom surface. Nevertheless, manual classification of these intensity profiles tends to be user-dependent, time-consuming and error-prone. Our solution is to use semi-automated, computer-assisted detection and classification of the markers.

Recent methodological improvements have enabled the clear visualization of ultrastructure solely using backscattered electron (BSE) signals, entirely eliminating the need for simultaneous STEM detection. However, this enhancement introduced complexities in distinguishing signals from nanoparticles localized on the top versus the bottom surfaces of ultrathin sections.

Motivated by these methodological advances, we have developed an open-source Python package, which can be used in the form of a user-friendly Jupyter notebook in order to facilitate unbiased, semi-automated detection and classification of nanoparticles based on their intensity profiles. In its current version, the notebook supports manual annotation of nanoparticle signals, providing foundational datasets necessary for subsequent machine learning integration. Future development will incorporate automated Gaussian profile fitting, high-throughput and fully-automated classification. Ultimately, this workflow is expected to streamline quantitative analyses, reducing human bias and enhancing reproducibility in LV-STEM imaging studies.

Acknowledgement: This work was supported by Czech-BioImaging large RI project (LM2023050) and TACR (TN02000020).

References:
[1] DOI: 10.1016/j.jsb.2024.107014

Type of presentation: Poster

LS6-P-1 Morphological features of *Himantoglossum calcaratum* (Beck) Schltr. subsp. *calcaratum* (Orchidaceae) pollinarium

Marina Mačukanović-Jocić[a], Svetlana Aćić[a], Ivan Šoštarić[a], Vladan Đorđević[b]

[a]*University of Belgrade, Faculty of Agriculture, (Belgrade), Serbia*

[b]*University of Belgrade, Faculty of Biology, (Belgrade), Serbia*

Contact email: acic@agrif.bg.ac.rs

Introduction: The pollinarium morphology of *Himantoglossum calcaratum* subsp. *calcaratum* (Orchidaceae, Orchidoideae) was examined by both, light stereomicroscope and scanning electron microscopy (SEM), as a contribution to the pollen atlas of Serbian apiflora. The genus *Himantoglossum* comprises 11 taxa, i.e., nine species and two subspecies, distributed in North Africa, Europe, Asia Minor, the Caucasus, Israel, and southwestern Iran [1]. Five taxa of this genus are represented on the Balkan Peninsula: *H. adriaticum* H. Baumann, *H. calcaratum* (Beck) Schltr. subsp. *calcaratum*, *H. calcaratum* subsp. *jankae* (Somlyay, Kreutz & Óvári) R. M. Bateman, Molnar & Sramkó, *H. comperianum* (Steven) P. Delforge, and *H. robertianu*m (Loisel.) P. Delforge. The only representatives of this genus in Serbia (*H. calcaratum* subsp. *calcaratum* and *H. calcaratum* subsp. *rumelicum*) belong to the section Caprinum. Ochid species *Himantoglossum calcaratum* (Beck) Schltr. subsp. *calcaratum* is a Balkan endemic taxon, distributed in Serbia, Montenegro, Bosnia and Herzegovina, Albania and North Macedonia. A spontaneously growing specimens of *H. calcaratum* subsp. *calcaratum* (Balkan Lizard Orchid) found in the canyon of the Uvac river, located in southwestern Serbia (temperate biome), was used for pollinarium analysis.

Methods: Pollinaria were sampled from Balkan Lizard Orchid plants at anthesis. Each open flower of the inflorescence was manually emasculated using fine pin, simulating the behaviour of a co-adaptive pollinator, in order to extract the entire, intact pollinarium. Pollinaria were placed in a labelled envelope and transported to the laboratory for examination under a stereomicroscope and SEM microscope. For SEM analysis, fresh pollinaria were mounted on metal stubs, coated with gold using a BAL-TEC SCD 005 Sputter Coater (100 s at 30 mA), and examined with a JEOL JSM-6390LV scanning electron microscope at an accelerating voltage of 10–15 kV. Measurements were performed on a sample of 15 pollinaria for each morphological character. Pollinarium structure was also observed using a using Nikon SMZ18 stereo zoom microscope with Nikon DS-Fi1 35 mm camera attached.

Results: The pollen dispersal unit of *H. calcaratum* subsp. *calcaratum* orchid is a club-shaped pollinarium with an average length of 3521.25±222.76 μm (SEM) (Figs. 1A, B). The pollinarium comprises of sectile pollinium (1629.33±139.84 μm in length and 1453.33±80.31 μm in width) (Figs. 1A, B), a shiny and flexible caudicle (1894.5±43.85 μm long) and a sticky viscidium. The caudicle acts as a stalk, and the viscidium is a sticky structure that helps attach the pollinia to a pollinator. The sectile pollinium consists of subunits called massulae (Figs. 1C, D) that are connected at the base by sticky materials. Each massula (mean length: 317.89 ± 22.48 μm) exhibits a roughly trapezoidal prismatic form (Fig. 1D) and consists of agglutinated pollen tetrads (Fig. 1E). SEM analysis revealed that the exine surface displays rugulate ornamentation (Fig.1F). All pollen grains within a tetrad are inaperturate.

Discussion and conclusions: The study provides new insights into the pollinarium morphology of Balkan endemic species *Himantoglossum calcaratum* subsp. *calcaratum* native to Serbia. In addition, the pollinia of the Balkan Lizard Orchid exhibit a basal extension called caudicle, that merges into a sticky viscidium, similar to previous studied Orchidoideae species [2].

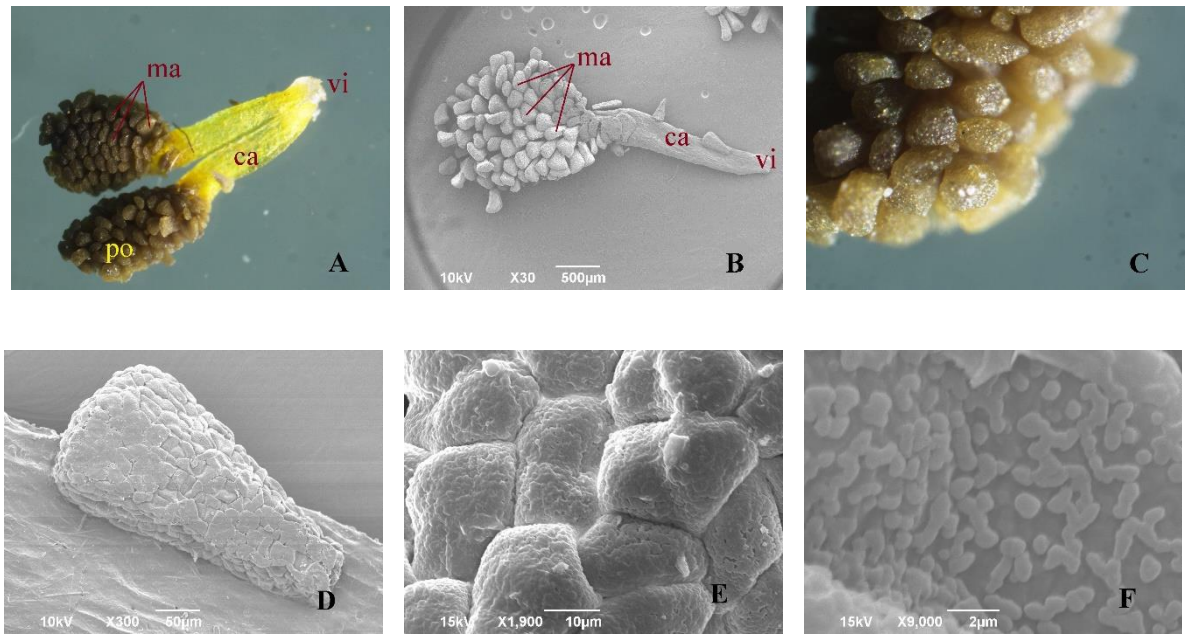


Figure 1: **A**: Overview of two pollinaria, each consisting of a massulate pollinium (po), caudicle (ca), and viscidium (vi); **B**: pollinarium (SEM); **C**: a few massulae (ma) forming the pollinium; **D**: a single detached massula formed by multiple pollen tetrads; **E**: the outward-facing surface of the massula revealing several agglutinated tetrads; **F**: detail of exine surface showing rugulate ornamentation. **A, C**- stereomicroscope images (**A**- 3x; **C**- 10x); **B, D-F** - SEM micrographs.

References:

1. POWO. "Plants of the World Online. Facilitated by the Royal Botanic Gardens, Kew, **2025,** published on the Internet; https://powo.science.kew.org/
2. C. Purgina, F. Grímsson, M. Weber, S. Ulrich, *Rev. Palaeobot. Palynol*., **2024,** 331, 105211.

Type of presentation: Poster

LS6-P-2 Bridging Light and Electron Microscopy: R221 Resin for CLEM in Microbes and Plants

Andrea Cheradil[a], Julia Buchner[a], Matthias Ostermeier[b], Andreas Klingl[a]

[a]*Plant Development & Electron Microscopy, Biocentre LMU Munich, Planegg-Martinsried, Germany*

[b]*Department of Molecular Plant Science, Biocentre LMU Munich, Planegg-Martinsried, Germany*

Contact email: a.cheradil@campus.lmu.de

The authors have requested that the abstract not be published.

Type of presentation: Poster

PS6-P-3 Czech-BioImaging: National imaging platform open to all scientists

Pavel Hozak[a]

[a]*Institute of Molecular Genetics of the Czech Academy of Sciences, Prague, Czech Republic*

Contact email: hozak@img.cas.cz

Innovative imaging technologies allow us to study hidden biological processes in cells, tissues, and whole organisms thanks to technological development. Imaging became one of the crucial elements of research in biological and medical fields.

Czech-BioImaging is a national research infrastructure for biological and medical imaging. It has been in operation since 2016 and is the only advanced research platform performing cell and molecular imaging for research in the Czech Republic. It also represents three National Euro-BioImaging ERIC Nodes providing technical and scientific excellence to international researchers by the integration of multiple imaging technologies together with image processing and analysis tools in an open-access mode.

Sixteen core facilities involved in the Czech-BioImaging are providing open access to most advanced imaging technologies to users from both academic, medical and private sectors. The distributed character allows access to a portfolio of technologies to many users at different locations covering the major cities in the Czech Republic.

Czech-BioImaging provides users with the technical background and necessary expertise and guidance from experiment design to analysis and interpretation of acquired data for project solutions, especially in cell and molecular biology, genetics, physiology, parasitology, tumor biology, neuroscience, developmental biology and pathology. Czech-BioImaging portfolio includes advanced light and fluorescence microscopy, super-resolution microscopy, electron microscopy, correlative light and electron microscopy, sample preparation, various anatomical and molecular methods in preclinical and medical imaging, and image data analysis.

The technological and methodological foundation of Czech-BioImaging significantly improves biomedical research in the Czech Republic. Due to the extensive expertise and long-time experience, Czech-BioImaging is also heavily involved in organization of various hands-on courses, workshops, annual conference, and many other awareness-raising activities. Owing to many methodological publications, it has become a partner of instrumentation manufacturers.

Acknowledgement: National Infrastructure for Biological and Medical Imaging – Czech-BioImaging is funded by the Ministry of Education, Youth and Sports of the Czech Republic (project No. LM 2023050 and Infrastructure project "Modernisation of the VVI Czech-BioImaging" CZ.02.01.01/00/23_015/0008205.

Type of presentation: Poster

LS6-P-4 Internal anatomy of parasitic acantocephalans in endangered underground amphibian analyzed by a combination of microCT and FESEM

Rok Kostanjšek[a], Grega Benko[a]

[a]*Department of Biology, Biotechnical Faculty, University of Ljubljana, Ljubljana, Slovenia*

Contact email: rok.kostanjsek@bf.uni-lj.si

Introduction: Acanthocephalans are obligatory endoparasites that require two hosts to successfully complete their life cycle. They attach to the intestinal wall of vertebrates (final hosts) and release their eggs into the intestinal lumen and subsequently into the environment, where the eggs are ingested by arthropods (intermediate hosts). These are then preyed upon by their final hosts, allowing a new generation of acanthocephalans to reach their site of sexual reproduction. *Acanthocephalus anguillae* is a widely distributed European freshwater parasite, typically cycling between fish and the crustacean *Asellus aquaticus*. Recently, however, the parasite was discovered in the gut of an endangered cave amphibian, also known as proteus or olm (*Proteus anguinus*), and in a population of exclusively cave-dwelling crustaceans [1], indicating the first known case of a multiple-host parasitism in a subterranean environment. Fully achieved reproductive capacity of these parasites is usually demonstrated by their ability to produce and release fully mature eggs into the digestive system of their final host. Although mature eggs can be identified by their characteristic elongated shape, morphological analysis in our case was considerably challenged by the limited amount of available biological material (i.e. potentially adult female parasites attached to the intestinal wall of highly endangered and rare host). To overcome this challenge, we used a combination of observational methods that allowed us screening of available parasites and identification of females with eggs by microCT in a first step and more detailed morphological analysis of the eggs in the selected parasites by FESEM in a second step.

Methods: Individual parasites were carefully removed from the intestinal wall of the olm and fixed in 4% formaldehyde in 0,1M phosphate buffer. After washing, specimens were gradually transferred to 70% ethanol and contrasted overnight in 0,3% phosphotungstic acid (PTA) in 70% ethanol before scanning with a Neoscan N80 microtomograph at 50 kV, 80 mA at 1,8 μm resolution, 0,2° rotation step and averaging of 4 scans. Virtual cross sections were reconstructed from 989 X-ray projections covering the entire size of the parasites. Between 2665 and 3025 sections were used for 3D modelling and segmentation analysis in Dragonfly software (ORS Inc.). Samples for FESEM observation were gradually transfer to HMDS via ethanol series of increased concentration, air-dried at room temperature [2] and mounted to sample holders using carbon disks. Dried samples were opened with dissecting needles to expose the body cavity and sputter coated with 7 nm of platinum prior to observation with the JSM 7500F field emission scanning electron microscope.

Results: MicroCT analysis of the parasites contrasted with PTA provided a non-destructive insight into their internal anatomy. Based on the presence and distribution of eggs in their body cavity, individual female specimens were selected for FESEM analysis. Morphological analysis of the eggs in the body cavity using FESEM revealed predominantly immature, oval-shaped eggs and occasionally also fully matured eggs, characterized by their elongated morphology.

Discussion and conclusions: The combination of microCT and FESEM used in our study allowed non-destructive screening of the parasites for the presence of eggs prior to their detailed morphological analysis by FESEM. Although not conventionally applied, the chosen combination of methods proved efficient in here presented morphological analysis and foremost minimized the number of samples required to confirm the potential of the olm as the final host of A. anguillae. The results support the first case of complete developmental cycle of a multi-host parasite in a subterranean environment and provide

new insights into the potential threats to the welfare of this highly endangered cave animal by parasites in its natural environment.

Acknowledgements: The work was supported by Slovenian Research and Innovation Agency funding to research program "Integrative zoology and speleobiology" (grant number P1-0184) and by the infrastructural center "Microscopy of biological samples", (MRIC UL, I0-0022-0481-08) located at the University of Ljubljana, Biotechnical faculty.

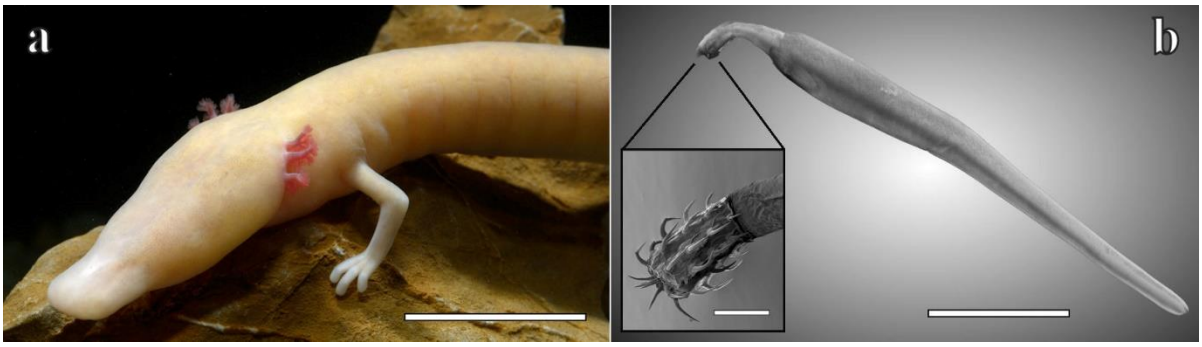


Figure 1: Olm or proteus (*Proteus anguinus*), an endangered cave salamander (bar = 2 cm) (a) and microCT reconstruction of its parasite *Acantocephallus anguillae* (bar = 2mm) with distinctive attachment hooks in its frontal part shown by FESEM (inset, bar = 100 µm).

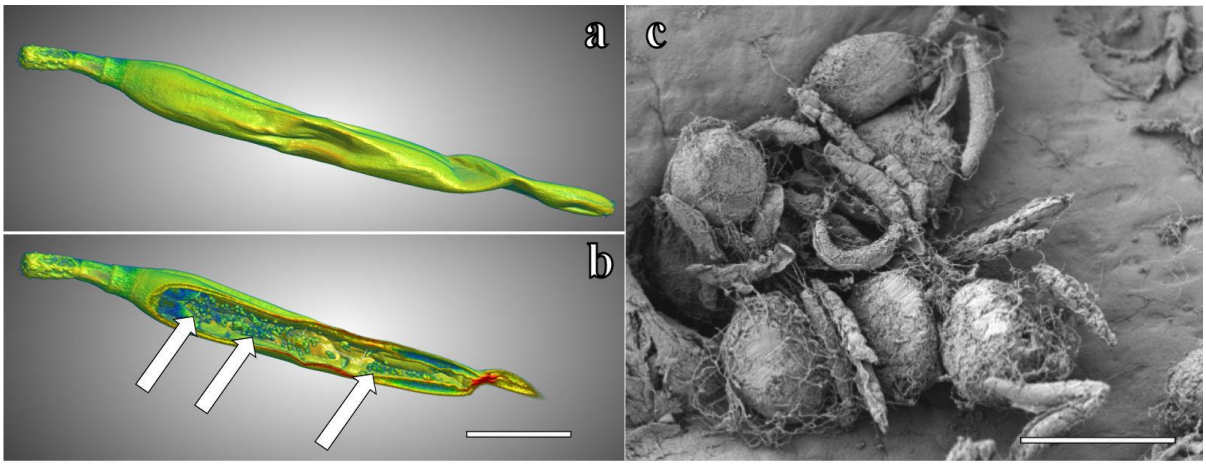


Figure 2. MicroCT-generated view of outer surface (a) and virtual cross-section (b) of the parasite revealing the eggs (arrows) in its body cavity (scale bar = 1mm) (a) and FESEM micrograph of the cluster of exposed eggs in the parasite revealing two different egg morphotypes (bar = 50 µm) (c).

References:

1. Amin OM, Heckmann RA, Fišer Ž, Zakšek V, Herlyn H, Kostanjšek R. *Folia Parasitologica*, **2019**, 66: 1-13. doi: 10.14411/fp.2019.015.
2. Černoša A, Gotinčar C., Holcar M, Kostanjšek R, Lenassi M, Gunde-Cimerman N. *Scientific reports*, **2025**, *15*, 1413, doi: 10.1038/s41598-024-84189-3

Type of presentation: Poster

LS6-P-5 Safe-by-Design Characterization of TiO_2 Nanoparticles in a Cell Model: An Integrated Experimental Workflow

Jummi Laishram[a], Maria Eugênia Fortes Brollo[b], Jessica Ponti[c], Camilla Abrahamsson[d], Julia Linell[d], Christina Isaxon[d], Alexander Suarez[e], Hiram Castillo Michel[e], Regina Ciancio[a]

[a]*Area Science Park, (Trieste), Italy*

[b]*CNR-IOM, (Trieste), Italy*

[c]*European Commission Joint Research Centre, (Ispra), Italy*

[d]*Lund University, (Lund), Sweden*

[e]*European Synchrotron Radiation Facility, (Grenoble), France*

Contact email: jummi.laishram@areasciencepark.it

Introduction: The advancement of nanotechnology requires the development of reliable and safe strategies for the characterization of nanomaterials, particularly in the context of their biological interactions, across complementary techniques. This experimental study aims to demonstrate the applicability of a safe-by-design characterization workflow by demonstrating the feasibility of using a combination of various advanced imaging techniques and fine analysis for the characterization of a selected nanomaterial in a cellular model.

Methods: In our work, to mimic exposure of lung tissue to airborne nanoparticles, Titanium dioxide nanoparticles (TiO_2 NPs) have been chosen as the model nanomaterial, while human bronchial epithelial cells BEAS-2B - CRL-3588™ serve as the exposure model. Cells were exposed to aerosolized TiO_2 NPs for 3 hours, fixed after 24 and 48 hours of exposure, cryosectioned, and mounted on 3 mm Cu grids for further investigation using scanning electron microscopy (SEM) in Scanning Transmission Electron Microscopy (STEM) mode.

Results: To enable correlative studies, we developed a precise method to register the location of individual cells containing nanoparticles, allowing their targeted analysis using synchrotron-based techniques. In particular, once identified using STEM, the cells were further analyzed with X-ray Fluorescence (XRF) at X-ray Microscopy Beamline ID21 at ESRF in order to determine NPs uptake and localization in the cells. X-ray absorption spectroscopy (XANES) measurements were done to determine if NPs underwent chemical transformations in the cells.

Discussion and conclusions: Our approach bridges high-resolution electron microscopy with synchrotron-based spectroscopic techniques, offering a powerful strategy for studying nanoparticle-cell interactions. This methodology enhances our understanding of cellular responses to nanomaterials, paving the way for more advanced multidisciplinary investigations.

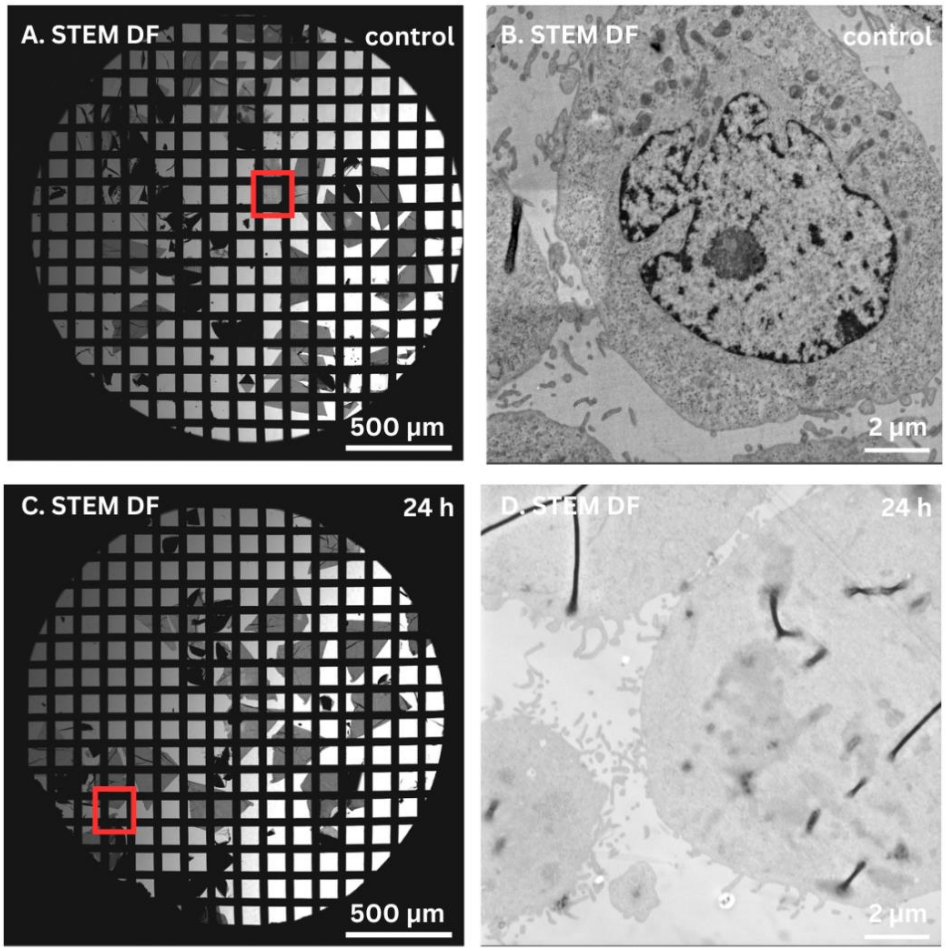


Figure 1: Identification and localisation of cells using Dark Field STEM imaging: the cell of interest is first identified and its location in the full grid is registered at low and high magnification. A and B: Control cells not exposed to nanoparticles fixed at time point 48 hours. C and D: Images of cells after 3 hours exposure to TiO_2 nanoparticles fixed at time point 24 hours. Position of cells of interest were registered using the same procedure.

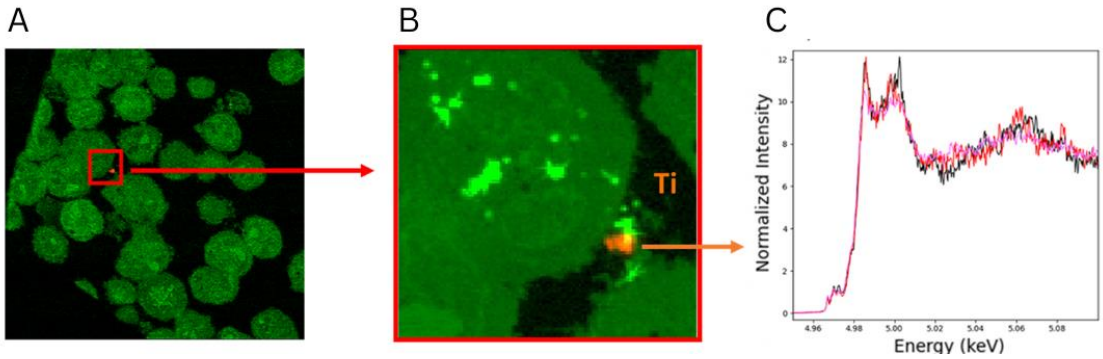


Figure 2. µ-XRF maps and µ-XANES point analyses of human bronchial epithelial cells (BEAS-2B - CRL-3588™) exposed to TiO_2. A: Os (green) and Ti (red) distribution over an 80 × 80 µm² area. B: Zoom-in on the region of interest (16 × 16 µm²). C: Ti K-edge XANES spectra acquired on the Ti-enriched region.

Type of presentation: Poster

LS6-P-6 Ciliate Community in Podutik Reservoir, Slovenia: assessment of species diversity improved by the diversity of microscopic techniques

Dren Dolničar[a], Mihael Jožef Toman[a], Polona Mrak[a]

[a]*University of Ljubljana, Biotechnical Faculty, Department of Biology, Ljubljana, Slovenia*

Contact email: polona.mrak@bf.uni-lj.si

Ciliates are a diverse group of unicellular eukaryotes that vary widely in size, shape, body plan, and ecological niche and are ciliated in various patterns. They are an important link in aquatic ecosystems because they are primary consumers of bacteria and algae and play a key role in nutrient cycling. They regulate microbial populations and contribute to the decomposition of organic matter, thereby influencing the overall productivity of the ecosystem [1]. They are therefore good bioindicators, as has been clearly demonstrated by numerous review studies [2, 3] and practical research [4, 5]. By analysing species composition and density of the ciliate community, we can assess water quality and the wastewater treatment process [6, 7]. Accordingly, it is necessary to identify the species of ciliates, which can be achieved using ciliate identification keys and morphological observation of ciliates by adequate microscopic methods such as stereomicroscopy, light microscopy with different modes (bright field, differential interference contrast (DIC), fluorescence) and different staining techniques. In general, there is not much research available on ciliate communities in nature and the methods for species identification are not well developed. In Slovenia, the data on ciliate communities in different water bodies are very rare and incomplete. The aim of our research was to assess the species diversity and examine the species composition of the ciliate community in the Podutik reservoir in Ljubljana. The study was conducted in several phases, which included field sampling, laboratory analyses of chemical and physical parameters of water and species identification using different light microscopy methods.

After concentrating the ciliates in our water samples, we have prepared fresh samples of living organisms for the light microscope observation. Using DIC technique, we determined the ciliate species according to "A user-friendly guide to the ciliates (Protozoa, Ciliophora) commonly used by hydrobiologists as bioindicators in rivers, lakes, and waste waters, with notes on their ecology" [6]. Next, we have evaluated different preparation of semi-permanent and permanent microscope mounts using two different fixatives: 1.85% formaldehyde solution in 0.1M phosphate buffer and Lugol's iodine. We have tested different staining procedures, including methyl green-pyronin and fluorescent dye Flutax-2. The samples were imaged with a Zeiss AxioImager Z.1 light microscope equipped with cameras HRc and MRm Axiocam. Flutax-2 labeling was imaged in fluorescence mode using Filter set 09 (FITC) and structured illumination ApoTome to produce 3D images of ciliates.

Using the above-described imaging methods and identification key, we managed to determine a total of 54 taxa of ciliates at 10 sampling sites, of which we were able to identify 40 to species level, seven to species complexes, six to genus level and one to subclass level. The taxa we recorded belong to 31 families, 19 orders and 7 classes of the Ciliophora phylum.

To identify the species, observing living ciliates using the DIC technique has proved to be the most appropriate method, which enables us to observe the intact (unfixed and unstained) specimens. In testing the two fixatives, the problem of species recognition arose with both fixation methods due to deformation of ciliate body to some degree. Lugol's iodine proved to be more suitable as it preserved the shape of the ciliate cells better. Ciliates fixed with formalin were more likely to disintegrate or deform. Particularly problematic are larger species (especially scl. Hypotrichia), whose cells are more fragile and disintegrate quickly, and contractile species, which are severely deformed by formalin fixation and are no longer recognizable (e.g., scl. Peritrichia). Specialized staining procedures, as described in Foissner [7], reveal the characteristics useful in identifying the species, but they are quite

demanding and time-consuming, and are therefore rarely used in routine ecological studies. In our study, the methyl green-pyronin staining method was valuable to reveal the number and shape of the nuclei, one of the important identifying characteristics of ciliates. We have used the fluorescent dye Flutax-2 (Oregon Green™ 488 Taxol), which is one of the dyes in recent use as a simpler alternative to the silver staining procedures [8]. Flutax (7-O-[N-(4-fluoresceincarbonyl)-L-alanyl] taxol) is a fluorescent derivative of taxol (Paclitaxel) that binds specifically to microtubules. Staining with Flutax-2 revealed ciliate characteristics that are useful for species identification, such as main ciliature patterns and location of structures important for the taxonomic identification of ciliates. It can also be used as a vital stain, as it does not always require prior fixation or permeabilization, although our evaluation showed that the permeabilization process provides better results. After exposure to excitation light, the fluorescence of Flutax-2 quickly fades, so it's not possible to make permanent preparations, which is the main drawback of this technique. Next, our results demonstrated that dehydration steps can cause significant body shape deformation, even in fixed samples, thus the semi-permanent samples are better choice for repeated observation of stained specimens.

Our results are the first data on the ciliate species in this area and contribute to the knowledge of ciliates in inland aquatic ecosystems and thus provide an important basis for further research on ciliates in Slovenia. With the evaluation of different microscopic methods for providing ciliates morphology and species identification, our study exposes that no single method works equally well for all groups of ciliates, so a combination of diverse microscopic techniques may be necessary for successful species identification.

References:

1. K. G. Porter, M. L. Pace, J. F. Battey, *Nature*. **1979**, 277, 563–565.
2. O. M. S. Mostafa, N. A. A. A. El-Hady, A. M. H. Nigm, *Egypt. J. Aquatic Biol. Fish.* **2023**, 27, 6, 805–813.
3. J. A. Vilas-Boas, M. V. X. Senra, R. J. P. Dias, *Acta Limnol. Bras*. **2020,** 32.
4. R. J. P. Dias, P. M. de Souza, M. F. Rossi, A. H. Wieloch, I. D. da Silva-Neto, M D'Agosto, *Environ Pollut*. **2021,** 268.
5. V. Gulin Beljak, B. Vlaičević, M. Sertić Perić, R. Matoničkin Kepčija, *Knowl. Manag. Aquat. Ecosyst*. **2023**, 424: 1–14.
6. W. Foissner, H. Berger, *Freshw. Biol*. **1996**, 35(2), 375-482.
7. W. Foissner, *Eur. J. Protistol*. **2016** 55, 75–94.
8. W. Foissner, *Int. J. Syst. Evol. Microbiol*. **2014**, 64, 271-292.
9. J. S. Abraham, S. Sripoorna, S. Maurya, S. Makhija, R. Gupta, R. Toteja, *Int. J. Syst. Evol. Microbiol*. **2019**, 69(4), 877-894.

Type of presentation: Poster

LS6-P-7 Multiscale 3D imaging of digestive system morphogenesis during arthropod development

Polona Mrak[a], Katja Kunčič[a], Urban Bogataj[a], Jiří Týč[b], František Kitzberger[b,c], Marie Vancová[b, c], Nada Žnidaršič[a]

[a]*University of Ljubljana, Biotechnical Faculty, Department of Biology, Ljubljana, Slovenia*

[b] *Institute of Parasitology, Biology Centre of the Czech Academy of Sciences, Česke Budejovice, Czech Republic*

[c] *Faculty of Sciences, University of South Bohemia, České Budějovice, Czech Republic*

Contact email: polona.mrak@bf.uni-lj.si

Morphogenetic processes involved in organism development are deeply conserved within the animal kingdom. The advancement of understanding of tissue and organ morphogenesis and the application of these concepts in various fields of bioscience is achieved through the multidisciplinary investigations of animal embryonic and postembryonic development. Imaging of embryos and larvae by complementary methods is one of the key tools, which allows us to study the developmental processes in the physiological environment and in the context of multiple organization levels, from cells to the whole organism. Morphogenesis of epithelia is a fundamental part of organism development, crucial for the shaping of organs and for establishment of organs' vital functions. Epithelia, as the key tissue type of multicellular organisms, function as barriers between different compartments in the organism. Cell junctions, connecting epithelial cells, enable the integrity of the tissue and the regulation of the paracellular transport. Cell junctions are dynamic complexes and their formation and remodelling in conjunction with cytoskeletal elements are crucial for cell shape changes during epithelial morphogenesis. In the context of comparative studies of arthropod development, we aim to investigate morphogenesis of the digestive system in selected arthropod species, including the species important from the perspective of crop protection. Our study addressed cell shape modifications and ultrastructural differentiation of cell junctions. Imaging of whole animals and isolated organs was applied at different levels of biological organization, from subcellular to whole organism, and focused to their 3D structure.

The combined use of complementary imaging techniques was performed in this study: micro-computed tomography (micro-CT), histology, transmission electron microscopy (TEM) and array tomography (AT) (Fig. 1). The samples of crustaceans (*Porcellio scaber*) and insects (*Drosophila suzukii*) were analysed, including distinct embryonic and postembryonic stages and adults. For micro-CT imaging whole animals were chemically fixed, dehydrated and HMDS-dried, after imaging the segmentation of the digestive system was performed. Histological and ultrastructural analysis were performed on semithin and ultrathin sections, respectively, prepared from chemically fixed, dehydrated and resin-embedded samples of whole organisms or isolated organs. Morphometric analysis was performed using Fiji/Image J software, including evaluation of the cell shapes and circularity of the nuclei. Next, several measurements of the selected ultrastructural characteristics of adherens and septate junctions were used to unveil the differentiation of cell junctions.

We show here the 3D anatomy of the digestive system in whole organisms of distinct developmental stages and adults as revealed by micro-CT. In embryos of *P. scaber* we have characterized the elongation of invaginated foregut and hindgut, their fusion into a single digestive tube (Fig. 2a) and the gradual incorporation of yolk into the developing digestive glands, originating from the midgut. The differentiation of the distinct gut regions was clearly visible in postembryonic stages. In hindgut and digestive glands of mid- and late-stage embryos the epithelial cells are columnar or flattened (Fig. 2b), respectively, and in early postembryonic development they acquire a specific dome-shaped morphology in accordance to those in adults. The processes of cell junction differentiation were characterised by transmission electron microscopy, supplemented with AT for the 3D context of the cell junctions. The ultrastructure of subapical adherens junctions (AJs), providing the mechanical stability, was similar in all developmental stages analysed, whereas the ultrastructure of the septate junctions (SJs) varied

according to the function of the epithelium. The SJs in hindgut change gradually from shorter (Fig. 2c) to longer arrays of septa and are intensively remodelled during molting. The SJs in digestive glands are already ultrastructurally differentiated at the mid-embryonic stage and during the development of the organism mainly elongate. As shown by the 3D reconstruction of *D. suzukii* larva imaged by micro-CT, the midgut is the longest part of the alimentary canal and is highly convoluted, occupying a large part of larva body volume. The SJs in *D. suzukii* midgut epithelium are extensive and convoluted, showing more resemblance to the SJs observed in the *P. scaber* hindgut than to those in the *P. scaber* digestive glands.

The advantage of our approach is the ability to study biogenesis and remodelling of cell junctions in accordance with changes in tissue architecture and processes at the whole organism level during development, including accompanying physiological processes, like molting in arthropods. Therefore, we were able to assess the progression of ultrastructural differentiation of cell junctions in relation to the key events in the digestive system morphogenesis during *P. scaber* development. With the new findings on the ultrastructure of septate junctions in *D. suzukii* midgut epithelium, we have provided new knowledge on the structure of the digestive system of this pest species. This is important with regard to the development of new strategies for crop protection, particularly for the assessment of potential biopesticides targeting the insect midgut.

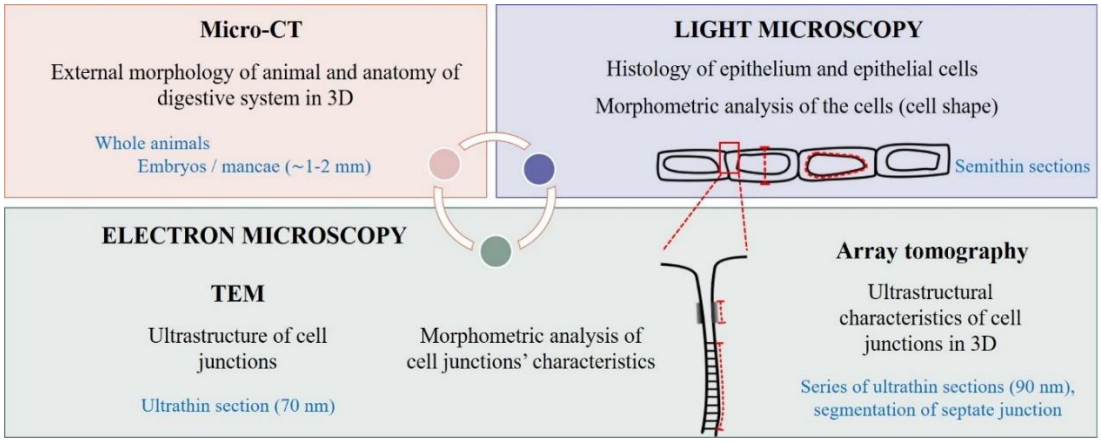


Figure 1: The combination of complementary imaging techniques used in the study. For each individual technique the morphological characteristics investigated are identified and the type of samples is specified

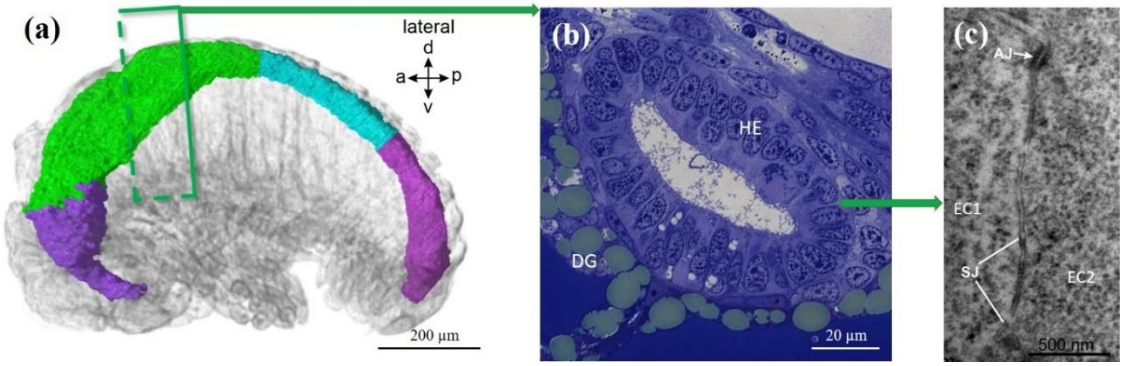


Figure 2: Imaging of gut morphogenesis in *P. scaber* late embryo from whole animal level to ultrastructural level. (a) Micro-CT of whole animal with segmented gut regions, from anterior (a) to posterior (p): foregut, anterior chamber, papillate region, rectum. (b) Cross section of hindgut shows morphology of hindgut epithelial cells (HE). Digestive glands (DG) filled with yolk are visible ventrally to the gut. (c) Ultrastructure of adherens junction (AJ) and septate junction (SJ) between two neighbouring epithelial cells (EC1, EC2) in the hindgut of late embryo is discernable.

Type of presentation: Poster

LS6-P-8 Intestinal stem cells of Colorado potato beetle – imaging from the morphology of the digestive tract in the whole animal to the cell ultrastructure

Nada Žnidaršič[a], Urban Bogataj[a], Polona Mrak[a], Katja Jenko[a,b]

[a]*University of Ljubljana, Biotechnical Faculty, Department of Biology, Ljubljana, Slovenia*

[b] *University of Ljubljana, Faculty of Education, Ljubljana, Slovenia*

Contact email: nada.znidarsic@bf.uni-lj.si

Intestinal stem cells are essential for the structural integrity, adequate function and renewal of the intestine. They are well characterized in mammals, including their location in the crypts of Liberkühn in the small intestine and their ability to self-renew and produce progenitor cells that differentiate into distinct intestinal cell types. Data on non-mammalian stem cells is very incomplete, detailed analyses are available mainly for traditional model organisms, e.g. the insect common fruit fly (*Drosophila melanogaster*). The intestinal stem cells in the larvae and adults of the fruit fly reside at the basal side of the midgut epithelium. The insect midgut epithelium plays a central role in digestion and absorption of nutrients and in protection against toxins and pathogens. An additional level of complexity is represented by the diversity of cells in different regions of the midgut, exhibiting specific morphological and physiological characteristics, which is well known in the fruit fly but has not yet been studied in detail in other species. The insect digestive tract consists of three main anatomical and functional regions in general: the foregut and hindgut, which form from the ectoderm during embryonic development, and the midgut, which develops from the endoderm. The epithelium of the digestive tract is the boundary between the external and internal environment and is crucial for regulating the transport of substances and protecting the organism. Proliferation of stem cells is increased in the midgut of *Drosophila* after various types of damage, including the infection and might play an important role also in the response to xenobiotics.

The aim of our study is the characterization of stem cells in the midgut epithelium of Colorado potato beetle (*Leptinotarsa decemlineata*) (CPB) to upgrade the knowledge on the non-mammalian intestinal stem cells and to support new strategies for crop plants protection, as stem cells are crucial for gut homeostasis and are a potential target of xenobiotics in food. CPB is primarily known as a major defoliator of potatoes and feeding damage can result in significant yield loss, but data on its digestive tract morphology, midgut epithelium architecture and stem cells structure are lacking.

To get a comprehensive insight into the architecture of CPB digestive tract, midgut epithelium organization and ultrastructure of the intestinal stem cells, we have applied imaging by transmission electron microscopy, light microscopy and micro-computed tomography (micro-CT) in combination. Micro-CT imaging is a non-destructive technique and it was performed on chemically fixed whole animals that were contrasted with iodine solution in absolute ethanol. Imaging was followed by data processing and segmentation using Dragonfly software (Comet) to obtain the data on 3D internal anatomy, focused to reveal the morphology of the digestive tract in the context of the whole organism. Dissected gut samples of adult CPB and larvae were fixed in aldehydes and embedded in Agar 100 resin. Serial semithin sections were used to reconstruct the 3D architecture of the selected midgut segments at the level of the tissue and cells, images were registered and aligned into a 3D stack in the open-source software FIJI with TrakEM2 plugin, followed by segmentation and 3D reconstruction in the Dragonfly software (Comet). TEM imaging was applied for the ultrastructural characterization of distinct cell types in the midgut, with emphasis on the stem cells and progenitor cells.

The digestive tract in adult CPB consists of a short and narrow foregut, followed by a dilated anterior part of the midgut, which transitions into a narrow and convoluted posterior part (Fig. 1A). The midgut is followed by a hindgut, which is narrow and convoluted anteriorly and terminates with a dilated

rectum. The midgut epithelium of CPB is composed of several cell types, including the principal absorptive cells - columnar enterocytes and numerous undifferentiated stem and progenitor cells. In the midgut of CPB larvae columnar enterocytes with dense apical microvilli prevail and stem cells reside in clusters in the basal part of the gut epithelium. Stem cells do not form septate junctions with neighboring cells, while enterocytes display abundant intercellular junctions. Midgut architecture in adult CPB is even more complex, comprising epithelium invaginations, in which stem and progenitor cells are located (Fig. 1B, 1C). The complementary imaging modalities applied in our study provided an integrative view of the 3D architecture and ultrastructure of the gut in CPB and proved to be indispensable for the characterization of insects from a whole organism to subcellular scale.

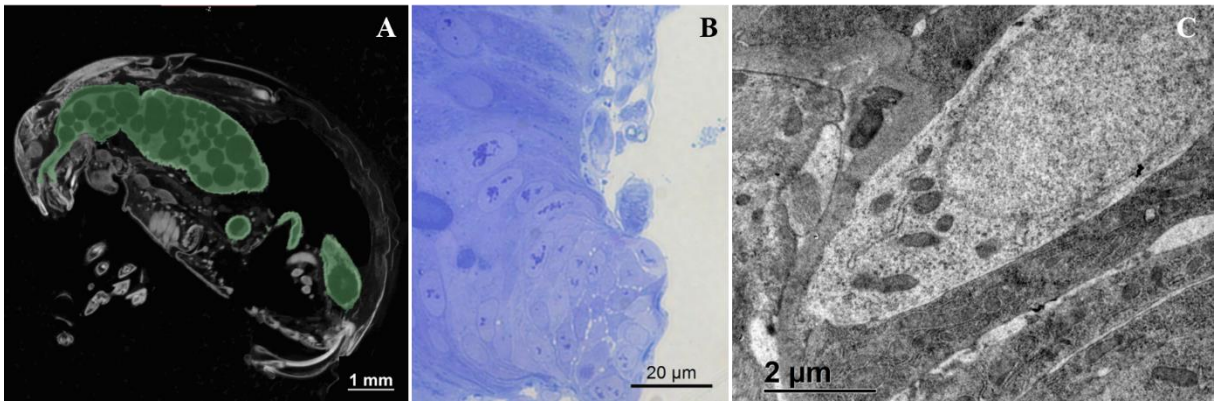


Figure 1: Anatomy of the digestive tract in adult Colorado potato beetle (A); midgut epithelium architecture and a cluster of stem and progenitor cells in the epithelium invagination (B); ultrastructure of the cells forming the epithelium invagination (C).

This study was supported by the Slovenian Research and Innovation Agency Grants P1-0184 and J4-2543, the equipment of Infrastructure Centre ‘Microscopy of biological samples’ of the Biotechnical Faculty, University of Ljubljana (https://www.bf.uni-lj.si/en/research/infrastructure-centres/108/ic-mikroskopija-bioloskih-vzorcev) was used in this study.

LS7 Advances in sample preparation in biomedical research and beyond

Type of presentation: Invited

LS7-IN-1 Adapting Inpainting and non-Raster scanning for cryo Volume Electron Microscopy (cvEM) using the JEOL JIB 4700F cryo Focus Ion Beam Scanning Electron Microscope

Maryna Kobylynska[a], Daniel Nicholls[b], Jack Wells[b], Zoe Broad[c], Damien McGrouther[d], Nigel Browning[c], Roland Fleck[a]

[a]*King's College London, United Kingdom*

[b]*SenseAI Innovations Ltd. United Kingdom*

[c]*University of Liverpool, United Kingdom*

[d]*JEOL (UK) Ltd., United Kingdom*

Contact email: roland.fleck@kcl.ac.uk

Cryo vEM employs a processs of sequential sectioning and imaging in a cryoFIBSEM at high resolution. This is limted by beam sensitivity of the vitrified samples and significant challenges to the generation of sufficient signal to noise. Using an external beam scan and software we have used "random" line hop and interleaved scanning strategies to assist in managing charge and beam induced damage. In addition, we have integrated SenseAI compressive sensing to further help with charge dissipation and reduce beam induced damage and data collection times. We have shown that the workflow can be successfully extended to multicellular volumes and that compressive sensing and post-sampling tools help overcome the limits of multiple frame integrations and significantly increase acquition speed providing opportunities to acquire larger data volumes up to 16k x 16k.

INTRODUCTION

Using a novel cryo vEM (cvEM) approach following a processs of sequential sectioning and imaging in a cryoFIBSEM at high resolution we have been able to observe the microalgae Euglena gracilis, Chlorella vulgaris and nematode Caenorhabditis elegans close to their biological native state. By successfully overcoming the beam sensitivity of the vitrified samples and significant challenges to the generation of sufficient signal to noise it has been possible define the ultrastructural details of the model systems. This allows the generation of larger 3D volumes than possible with cryo TEM tomograohy (cryoET).

Commercially available SEM's scan the electron beam in a Raster scanning mode, in lines across the surface of the sample, building up charge and may inducing beam damage. This challenge has restricted the visualization produced by cvEM, due to the beam sensitivity of vitreous samples and difficulty in balancing charge whilst generating sufficient contrast to noise. We have employed an external beam scan controller (Quantum Detectors Scan Engine) and software (JEOL U.K. UHD Imaging) and have developed custom "random" line hop and interleaved scanning strategies to assist in managing charge and beam induced damage. Together with this, we have integrated SenseAI compressive sensing technique, which further helps with charge dissipation/ accumulation through reducing the delivered electron dose. This provides additional benefits of reducing beam induced damage and reducing data collection times.

CONCLUSION

It has been possible to demonstrate the potential of cvEM as a complementary approach to cryoET capable of generating larger volumes (e.g., an entire cell), and at the same time retain resolution able to define ultrastructural details at the length scale of the membrane bilayer. We have shown that the workflow can be successfully extended to multicellular volumes by increasing vitrification depth with high pressure freezing. Compressive sensing and post-sampling tools help overcome the limits of multiple frame integrations giving a 4 to 5 times improvement in acquition speed providing opportunities to acquire larger data volumes up to 16k x 16k.

Type of presentation: Invited

LS7-IN-2 Sample Preparation Strategies for Biological Electron Microscopy: Challenges and Innovations

Marie Vancová[a,b], Martin Strnad[a], František Kitzberger[a,b], Jiří Týč[a], Jana Kopecká[a], Rego Ryan[a,b] , Nebesářová, Jana[a,b]

[a]*Institute of Parasitology, Biology Centre of the CAS, České Budějovice, Czech Republic*

[b]*Faculty of Science, University of South Bohemia, České Budějovice, Czech Republic*

Contact email: vancova@paru.cas.cz

Electron microscopy is an indispensable tool for visualizing the details of organelles, cells, tissues, and small organisms at the nanoscale. Recent advances in electron microscopy now enable high-resolution, 3D imaging and imaging of samples in their near-native state. However, data quality, image resolution, and the reliability of biological interpretations are strongly influenced by sample preparation, which must be tailored to specific sample types. In my presentation, I will outline strategies for preparing a range of biological samples (e.g., unicellular organisms, biofilms, plant and animal tissues, and extremophiles adapted to high-salt environments) for EM analysis. Special attention will be given to the challenges of handling large sample volumes, selecting appropriate embedding resins, and applying high-pressure freezing and substitution techniques to enhance contrast. Recent developments in ultramicrotomy workflows will also be discussed, including targeted trimming, "pick-up" strategies, and staining compounds, including alternatives to uranyl acetate.

Type of presentation: Oral

LS7-O-1 Unique structural features of the human Kir2.1 channel in two different conformational states unveiled by cryo-electron microscopy

Andreas Zoumpoulakis[a], Carlos Fernandes[b], Rafael Ferreira Veloso[a], Tahar Bouceba[c], Catherine Vénien-Bryan[a]

aSorbonne University, Institute of Mineralogy, Materials Physics and Cosmochemistry (IMPMC), France

bSão Paulo State University, Institute of Biosciences, Department of Biophysics and Pharmacology, Brazil

cSorbonne University, CNRS, Institut de Biologie Paris-Seine (IBPS), Protein Engineering Platform, Molecular Interaction Service

Contact email: andreas.zoumpoulakis@sorbonne-universite.fr

Kir2.1 belongs to a family of inward rectifier potassium (K+) channels that selectively control the permeation of K+ at the cell membrane of a variety of tissues. Expressed especially in cardiomyocytes, Kir2.1 contributes to the establishment and maintenance of the resting membrane potential and action potential plateau.

Although Kir channels are constitutively active, their gating is modulated by intracellular ligands, such as divalent cations and polyamines, but mainly by the membrane lipid phosphatidylinositol 4,5-bisphosphate (PIP2), that binds directly to the channel and allows for its electrical activity. Recently, an endogenous cardiac miRNA (miR1) was discovered by our collaborators as a physiological regulator that physically binds to Kir2.1 and suppresses K^+ current (Yang et al., *Circulation* 2021). However, how the channel gates in response to modulators is only beginning to be understood.

Having solved the first structure of the human Kir2.1 channel (Fernandes et al., *Science* Advances 2022), here we present the two complex structures solved by cryo-EM; in the activatory PIP2-bound state (3.26 Å) and the inhibited miR1-bound state (2.75 Å). Our results reveal unique structural differences between the two conformations. Given that both ligands have distnict binding sites, our surface plasmon resonance interestingly demonstrate a competition between the two modulators, indicating a preferential binding to a specific conformational state.

These findings shed light on the so far obscure gating molecular mechanism of human Kir channels and the effect of modulators, such as PIP2 and miR1, on the associated conformational rearrangements that are vital for the regulation of the cardiac action potential.

Type of presentation: Oral

LS7-O-2 Ultrastructural Analysis of *Azotobacter vinelandii* Encapsulated in Alginate Hydrogel Using Cryogenic Preparation and Electron Microscopy Techniques

Anna Havlíčková[a, b], Kateřina Mrázová[a, b], Kamila Hrubanová[a], Martin Súkeník[b], Petr Sedláček[b], Vladislav Krzyžánek[a]

[a]*Institute of Scientific Instruments of the CAS, Brno, Czech Republic*

[b]*Faculty of Chemistry BUT, Brno, Czech Republic*

Contact email: annahav@isibrno.cz

One of the key aspects of sustainable agriculture is the development of novel biofertilizers, which often rely on plant growth-promoting microorganisms (PGPMs), including a subgroup of rhizobacteria (PGPRs). These rhizobacteria colonize plant roots and support growth through both direct and indirect mechanisms [1]. One example of such a bacterium is *Azotobacter vinelandii*, a gram-negative bacterium capable of producing intracellular poly-3-hydroxybutyrate granules (PHB) and extracellular alginate, which helps retain water around plant roots [2, 3, 4]. In its vegetative state, *A. vinelandii* has a rod-shaped morphology, but under unfavourable conditions, encystation occurs. This process is characterized by the gradual rounding of central body and the formation of a protective capsule around it. This capsule consists of two layers: the outer layer is an electron-dense exine, beneath which lies an electron-transparent intine (using traditional contrast-enhancing techniques) [5, 6, 7].

In this research, alginate produced by the bacteria was crosslinked with selected agents ($CaCl_2$, malic acid, glucono-δ-lactone (GDL) and GDL in a mixture with $CaCO_3$), resulting in the encapsulation of the bacteria. The encapsulated bacteria in alginate were then prepared for cryogenic scanning electron microscopy (cryo-SEM) and low-voltage scanning transmission electron microscopy (LV-STEM). The preparation for cryo-SEM included high-pressure freezing (HPF), freeze fracturing, and freeze etching. The samples were examined using cryo-SEM, at −120 °C, with electron beam energy of 2 kV and probe current of 6.3 A. The preparation for LV-STEM also started with HPF, followed by freeze substitution, epoxy embedding, ultrathin sectioning, and contrasting of sections [8]. The samples were observed in a SEM equipped with a STEM detector, using an electron beam energy of 20 kV and a probe current 6.3 A.

Cryo-SEM enabled rapid imaging of the samples while preserving their near-native state, without the need for sputter-coating. In contrast, LV-STEM provided high-resolution ultrastructural analysis while avoiding structural alterations associated with chemical fixation. The ultrastructure of *A. vinelandii* bacteria was observed in the encystation phase and in the mature cyst state. Apart from shape, the key difference between these states was the formation of an inner layer of the capsule, called intine, which forms later in the encystment process than the exine. Furthermore, vesicles surrounded by a bilayer membrane were also observed outside the bacteria central body, where they were fusing. Regarding the surrounding hydrogel, changes in its structure were observed depending on the crosslinking agent used. Samples crosslinked with $CaCl_2$ and malic acid showed similar structures, but the hydrogel was significantly denser in the samples with GDL, and even denser in the sample with GDL in a mixture with $CaCO_3$.

These findings demonstrate the potential of cryogenic preparation and electron microscopy techniques for ultrastructural analysis of biological samples, advancing methodologies for studying encapsulated bacteria and similar complex systems. Further detailed investigations are ongoing to expand our understanding of these structural features and their implications. This research is part of a broader study focused on the development of sustainable biological fertilizers.

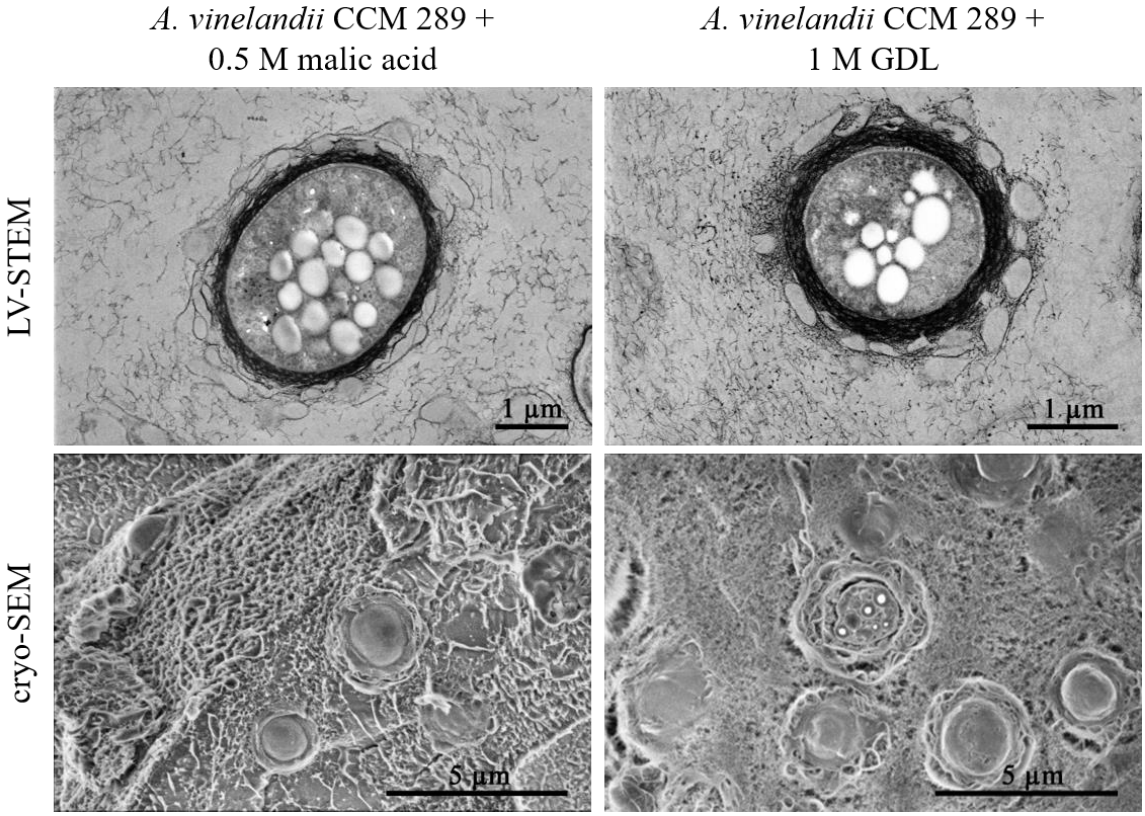


Figure 11: LV-STEM and cryo-SEM images of Azotobacter vinelandii CCM 289 encapsulated in an alginate hydrogel crosslinked with either 0.5 M malic acid or 1 M GDL. The scale bars are 1 µm for LV-STEM images and 5 µm for cryo-SEM images.

Acknowledgements This research was supported by the projects GA23-06757S provided by The Czech Science Foundation (GACR) and TN02000020 (TACR). We also acknowledge the Core Facility Electron Microscopy and Raman Spectroscopy, supported by the Czech-BioImaging large RI project (LM2023050 funded by MEYS CR).

References:
1. D. Goswami, J. N. Thakker, et al., *Cogent Food Agric.*, **2016**, *2*(1), 1127500.
2. T. Castilo, A. García, et al., *J. Biotech.*, **2020**, 48, 36-45.
3. B. M. Barney, *Trends Microbiol.*, **2024**, 32(10), 1034-1035.
4. H. Naseem, M. Ahsan, et al., *J. Basic Microbiol.*, **2018**, 58(12), 1009-1022.
5. H. L. Sadoff, *Bacteriol. Rev.*, **1975**, 39(4), 516-539.
6. O. Wyss, M. G. Neumann, et al., *J. Cell Biol.*, **1961**, 10(4), 555-565.
7. V. M. Hitchins, H. L. Sadoff, *J. Bacteriol.*, **1970**, 104(1), 492-498.
8. K. Mrázová, J. Bačovský, et al., *Microorganisms*, **2023**, 11(4), 888.

Type of presentation: Oral

LS7-O-3 Serial Block-Face Scanning Electron Microscopy (SBEM): Comparative Analysis of Protocols for Enhancing Contrast and Reducing Charging in Mouse Brain Tissue Samples

Nebesářová, Jana[a,b], Kitzberger, František[a,b,d], Krzyžánek Vladislav[c], Skoupý Radim[e], Týč Jiří[a]

[a]*Biology Centre CAS, Branisovska 31, 37005 Ceske Budejovice, Czech Republic*

[b]*Faculty of Science, Charles University, Prague, Czech Republic*

[c]*Institute of Scientific Intruments CAS, Kralovopolska 147, 612 00 Brno, Czech Republic*

[d]*Faculty of Science, University of South Bohemia, České Budějovice, Czech Republic*

[e]*Biozentrum, University of Basel, Basel, Switzerland*

Contact email: nebe@paru.cas.cz

Serial block-face scanning electron microscopy (SBEM) is a state-of-the-art method for 3D reconstruction of biological specimens with a volume capacity of up to several cubic millimetres. The technique involves cutting ultrathin sections from a sample using a small ultramicrotome located inside the microscope. After each section is cut, the newly exposed surface is imaged using back-scattered electron (BSE) mode.

Sample preparation for SBEM is based on protocols developed for transmission electron microscopy. It typically begins with chemical fixation, followed by dehydration and en bloc staining, and concludes with embedding the sample in a hard epoxy resin. However, charging and insufficient contrast often limit the quality of visualization, making sample preparation a crucial step in SBEM analysis.

We compared four SBEM sample preparation protocols (Deerinck [1], Hua [2], Katsumoto [3], and Genaud [4]), focusing on the distribution of heavy metals used as staining agents to enhance contrast and reduce charging. Mouse brain tissue samples were prepared according to these protocols, and the resulting blocks were analyzed using light microscopy, high-resolution SEM with BSE imaging, and energy-dispersive X-ray (EDX) analysis.

Our findings demonstrated that the widely used Deerinck protocol results in incomplete contrast, with adequate staining limited to the outermost ~100 μm of the sample surface. In contrast, the Katsumoto protocol produced a well-osmified layer twice as deep beneath the surface. This deeper staining increases the likelihood that an SBEM-prepared sample will exhibit good contrast and reduced charging during primary electron irradiation.

This work was supported by TACR (TN02000020) and MEYS CR (Czech BioImaging LM2018129).

References:
[1] Deerinck, T. J. et al.: Microscopy, 6–8 (2010).
[2] Hua, Y. et al.: *Nature Communications*, *6*(1), 7923 (2015)
[3] Katsumoto T. et al.: *J. Electron Microscopy*, *30*(3), 177-182 (1981)
[4] Genoud, C. et al.: *Frontiers in Neuroanatomy*, *12*, 1–8 (2018)

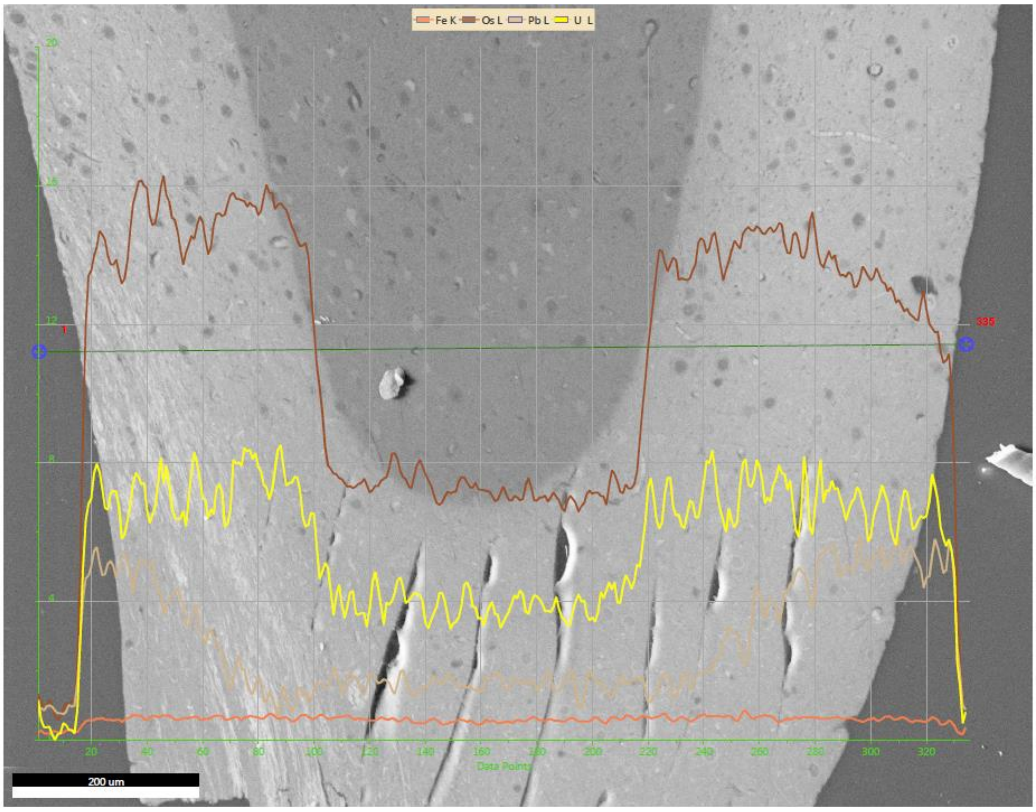


Fig 1: The distribution of heavy atoms in the mouse brain tissue prepared for SBEM according to Hua protocol. Fe (orange), Os (brown), Pb (beige), U (yellow)

Type of presentation: Oral

LS7-O-4 Sample Preparation for Electron Microscopy

Bruno M. Humbel[a]

[a]*Optical Neuro Imaging, Okinawa Institute of Science and Technology, Tancha, Okinawa, Japan*

Contact email: b.humbel@oist.jp

Since the beginning of biological electron microscopy, sample preparation is a crucial point. Every step we perform leads to changes of the original biological structure. To date the best preparation method is based on cryo-fixation and cryo-imaging in a cryoTEM or cryoSEM. But mostly we ignore the changes due to sample pre-preparation: extraction of organ; excision from tissue; cell culture cells, which are an artificial system; but also the isolation of molecules for atomic resolution analysis. Further, most biological relevant systems are too large for cryo-fixation. In addition volume microscopy to establish large connection networks cannot be done without chemical fixation.

In contrast to my PhD time, I think chemical fixation is still an acceptable and more regrettably not avoidable method. To justify and make good use of its application we need to establish the artefacts that can be induced and reduce the level of our interpretation on the 'chemical' resolution of our preparation protocols. In this short presentation I will try show what I learnt about the influence of the commonly used fixatives, dehydration methods and embedding. I also would like to introduce a new light microscope to build into an SEM that together with a new generation of fluorochromes should help to facilitate correlative light and electron microscopy.

References

1. Kiernan JA. 2000. *Microscopy Today*, **8**, 8.
2. Peters K, Richards FM. 1977. *Annu Rev Biochem*, **46**, 523.
3. Behrman EJ. 1983. *In* The Science of Biological Specimen Preparation 1983. Revel JP Barnard T and Haggis GH, eds. SEM Inc., AMF O'Hare, 1.
4. Plumel M. 1948. *Bul Soc Chim Biol*, **30**, 129.
5. Causton BE. 1986. In *The Science of Biological Specimen Preparation 1985*, Müller M, Becker RP, Boyde A, Wolosewick JJ. eds. SEM Inc.: AMF O'Hare; 209
6. Von Hase J, etal. 2021. Patent submitted 7th January 2021.

Type of presentation: Poster

LS7-P-1 Structural Stabilization of Alginate for Imaging Hydrogel-encapsulated Bacterial Cells Using LV-STEM

Katerina Mrazova[a,b], Anna Havlickova[a,b], Diana Cernayova[b], Petr Sedlacek[b], Vladislav Krzyzanek[a]

[a]*Institute of Scientific Instruments of the Czech Academy of Sciences, v.v.i., Brno, Czech Republic*

[b] *Faculty of Chemistry, Brno University of Technology, Brno, Czech Republic*

Contact email: mrazova@isibrno.cz

Introduction

Hydrogels are polymer-based materials capable of binding large amounts of water, making them valuable in various applications, including medicine or agriculture. While some hydrogels are synthetically produced, others occur naturally [1]. A notable example is the biopolymer alginate, synthesized by the bacterium *Azotobacter vinelandii*, a plant growth-promoting microorganism (PGPR). Alginate production allows *A. vinelandii* to form a protective polysaccharide capsule around its cells, protecting them from drying out and other environmental stress conditions [2]. To better understand the properties and behaviour of alginate hydrogels it is valuable to have detailed information on the structure of the polymer net. The imaging of hydrogel samples, let alone complex samples such as hydrogel-encapsulated cells, is highly challenging for electron microscopy. There are several studies relying on the various combinations of sample preparation approaches (such as lyophilisation) and different scanning electron microscopy techniques (e.g., ESEM, cryo-SEM) [3,4]. However, to observe also the intracellular ultrastructure of the studied cells, it is necessary to employ transmission electron microscopy techniques. In our study, we focused on the development of a sample preparation protocol suitable for alginate-encapsulated *A. vinelandii* cells imaged using low-voltage scanning transmission electron microscopy (LV-STEM).

Methods

Samples of *A. vinelandii* cells were encapsulated in alginate hydrogel by adding the equivalent volume of cell suspension to a 2% solution of $CaCl_2$. The formed hydrogel was cut using a scalpel to approx. $1mm^3$ cubes and submerged in the fixative solution of 2,5% glutaraldehyde and 2% formaldehyde. After fixation, a crosslinking agent in 1% concentration was added to the following steps to stabilize the fine structure of the hydrogel net. Samples were washed and postfixed by 1% OsO_4 with 1% $K_3[Fe(CN)]_6$, followed by staining using UA-zero, a commercial uranium-free staining reagent. Methanol was chosen as the dehydrating agent because of its high volatility and good solubility of $CaCl_2$. To compare the effect of the presence of the crosslinking agent during the preparation on the ultrastructure of the cells, pure unencapsulated cultures of *A. vinelandii* were prepared using the same protocol, but without the addition of $CaCl_2$. Subsequently, the samples were embedded in Spurr's resin and cured for 48h at 62 °C. Ultrathin sections were briefly contrasted with Reynold's lead citrate and subsequently imaged in the scanning electron microscope (Magellan 400/L, FEI) equipped with a STEM3+ detector, using a 20 keV electron beam.

Results

In the images of the encapsulated samples, a clearly distinguishable polymeric net is visible surrounding the cells, but in contrast to the control unencapsulated cells, it extends to greater distances from the cells. In detail, it is also possible to notice the difference between the fine fibres of free alginate in pure cultures and the clearly defined cross-linked fibres in $CaCl_2$-treated samples. The study of cell ultrastructure further revealed a polymeric capsule surrounding the cells. This capsule consists of two parts, intine and exine, with a fibrous structure predominantly observed in the exine part. In addition to the polymeric capsule of the cell, vesicles were also imaged. These structures were found both in close proximity to the cell wall as well as gradually permeating through the polymeric layers into the intercellular space. Moreover, PHA storage granules were also identified inside the cells as electron-transparent regions.

Discussion and conclusions

In our work, the addition of a crosslinking agent to the individual steps of chemical sample preparation for (scanning) transmission electron microscopy was shown to help stabilize the fine structure of the hydrogel network. It has been previously described that when an alginate hydrogel is placed in an environment with different ionic strengths, bivalent Ca^{2+} can be substituted for monovalent ions (e.g. Na^{+}), resulting in changes in the gel structure and its destabilization [5]. If we also focus on preserving the ultrastructure of the cells, it is important that the first step of the preparation, fixation, is carried out without the presence of an additional crosslinking agent. An increased concentration of $CaCl_2$ in the medium without prior cell fixation could osmotically damage the cells. Our presented results suggest that it is relevant to continue further experiments on the optimisation of the preparation protocol of such complex samples, focusing for example on the influence concentration of $CaCl_2$ used for hydrogel net stabilization.

Acknowledgement

This work was supported by TACR (project TN02000020). Microscopic analysis was provided by CF ISI EM which is supported by the Czech-BioImaging large RI project (LM2023050 funded by MEYS CR).

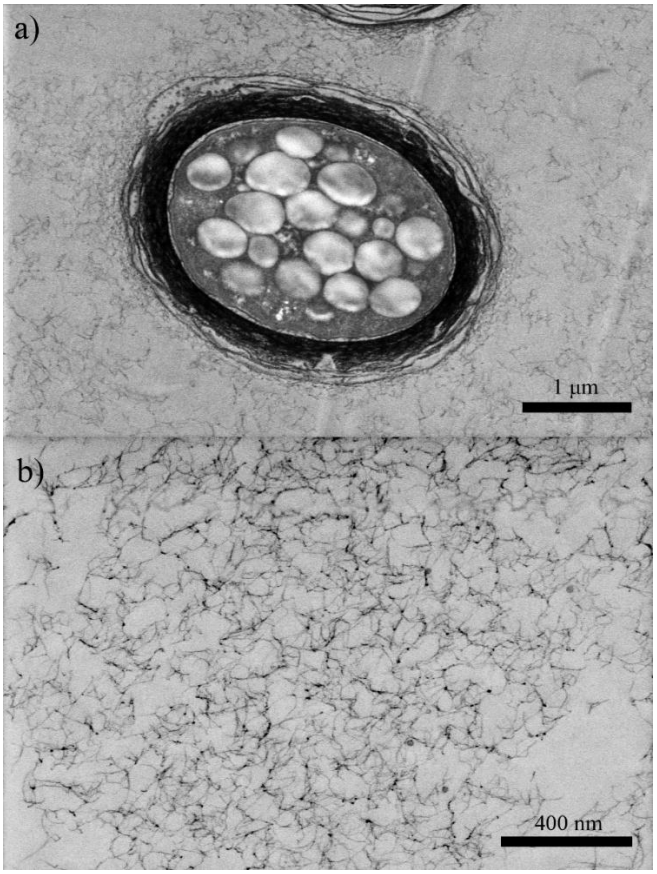


Figure 1: LV-STEM images of a) *A. vinelandii* cells encapsulated in alginate-based hydrogel, b) detail of crosslinked alginate polymer net.

References:

1. E.M. Ahmed, *J Adv Res*. **2015**, 6, 105-121.
2. J. D. Noar, J. M., Bruno-Bárcena, *Microbiology* **2018**, 164, 421-436.
3. Z. Kaberova, E. Karpushkin, et al., *Polymers* **2020**, 12, 578.
4. M. Trudicova, J. Smilek, et al., *Polymers* **2020**, 12, 2561.
5. K. Y. Lee, D. J. Mooney, *Prog. Polym. Sci.* **2012**, 37, 106-126.

Type of presentation: Poster

LS7-P-2 Red blood cells morphological alterations during preparation for electron microscopy imaging

Elizaveta Pavlova[a], Marija Kostić[a], Zorana Budakov-Obradović[b,c], Jasmina Grujić[b,c], Marko Radenković[a]

[a]*BioSense Institute - Research and Development Institute for Information Technologies in Biosystems, University of Novi Sad, Novi Sad, Serbia*

[b]*Blood Transfusion Institute Vojvodina, Novi Sad, Serbia*

[c]*Faculty of Medicine, University of Novi Sad, Novi Sad, Serbia*

Contact email: elizaveta.pavlova@biosense.rs

Introduction:
Red blood cells (RBCs) exhibit distinct morphological characteristics that are crucial for their proper function in oxygen transport. Nevertheless, they are highly sensitive to their microenvironment. Classical preparation of RBCs for SEM includes glutaraldehyde (GA) fixation, adhesion cells to coverslip, multistep dehydration and incubation with hexamethyldisilazane (HMDS) or critical point drying (CPD). Thus, the process of preparing RBCs for SEM can induce alterations in their morphology, particularly echinocytosis, which may affect the accuracy of imaging and analysis [1]. This study aims to simplify the preparation procedure and investigate the impact of different preparation surfaces (aluminium, copper, silicon wafers and glass coverslips) on RBCs morphology.

Methods:
In this study, two procedures were used for the preparation of red blood cells (RBCs) for scanning electron microscopy (SEM).
Long procedure: A 2% suspension of RBCs, isolated from healthy donors (blood type B), was prepared in 10 mM phosphate-buffered saline (PBS). This suspension (500 µl) was mixed with an equal volume of 1% GA in 10 mM PBS and incubated overnight at 4°C for fixation. Following fixation, small droplets (2 µl) of the RBCs suspension were carefully placed onto clean surfaces (aluminium, copper, silicon and glass) and allowed to adhere for 2 minutes. Then the surfaces were washed three times with PBS. For dehydration, a graded ethanol–water series was used: 10%, 20%, 30%, 40%, 50%, 60%, 70%, 70%, 80%, 90%, 96%, and 96%. Each step involved a 3-minute incubation to ensure gradual dehydration of the samples. After dehydration, the samples were treated with a 1:1 mixture of HMDS and ethanol for 3 minutes, followed by three additional incubations in 100% HMDS. The last incubation in pure HMDS continued until all HMDS had completely evaporated. To remove any residual salts, the surfaces were rinsed three times with deionized water and allowed to dry completely.
The short procedure followed the same steps as the long one but omitted the dehydration and HMDS steps. This simplified approach was used to evaluate the impact of these steps on RBCs morphology.
RBCs were characterized without any additional metal coating using an Apreo 2C HRSEM (Thermo Fisher Scientific, USA) at low accelerating voltage (1 kV) and probe current (0.1 nA) on an Everhardt-Thornley detector (EDT). In order to statistically evaluate the percentage of echinocytes, images with the horizontal field width (HFW) of 127 µm were analysed, the total cell count for each sample was approximately 800.

Results:
No significant differences in RBCs morphology were observed between the two sample preparation methods. However, the short procedure offered a faster preparation time and resulted in a lower percentage of echinocytes compared to the long procedure. Among the surfaces tested, glass proved to be the most effective in minimizing the percentage of echinocytes (~15%), particularly at their terminal stage (<1%, Figure 1).

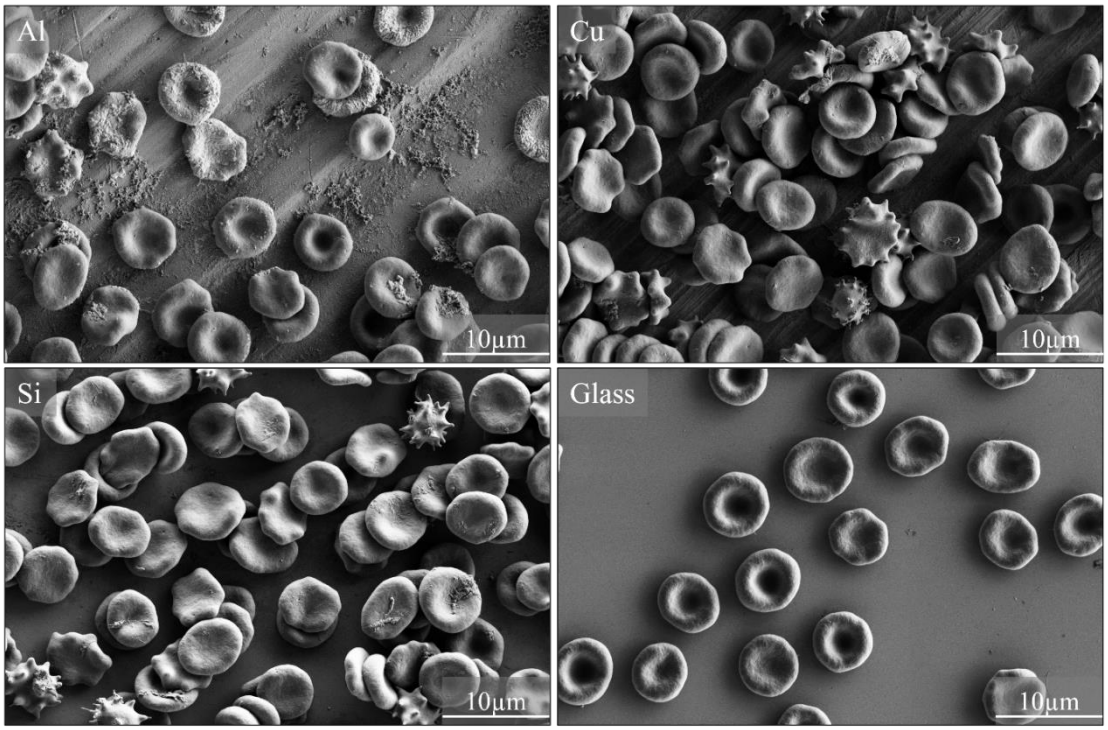


Figure 1: SEM images of RBCs on different surfaces (aluminium, copper, silicon wafer and glass coverslip).

Discussion and Conclusions:

This study demonstrates that surface properties impact RBCs morphology during electron microscopy preparation, with hydrophilic glass providing the best preservation of RBCs integrity. The findings underscore the importance of optimizing surface interactions to minimize artifacts and ensure accurate imaging.

Acknowledgements:

The authors gratefully acknowledge the financial support of the Ministry of Science, Technological Development, and Innovation of the Republic of Serbia (Grants No. 451-03-66/2025–03/200358).

References:

1. N. M. Geekiyanage, M. A. Balanant, E. Sauret, S. Saha, R. Flower, C. T. Lim, et al, *PLoS ONE*, **2019**, *14(4)*

Type of presentation: Poster

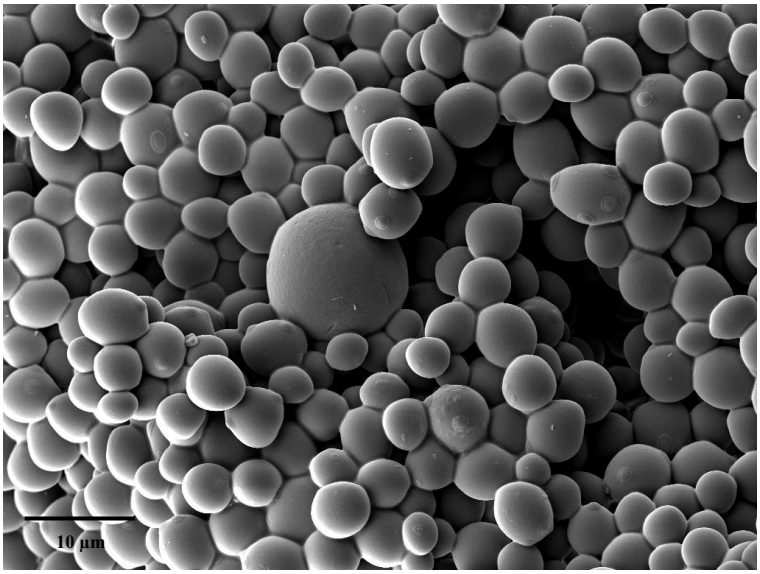
LS7-P-3 Fast and Frozen: Visualising a wide spectrum of specimens using Cryo-SEM combined with an on-site freeze fracture system

Dominique Pernitsch[a], Kerstin Hingerl[a], Melisa Malovcic[a], Dagmar Kolb[a,b]

[a]*Core Facility Ultrastructure Analysis, Center for Medical Research, Medical University of Graz, Graz, Austria*
[b]*Division of Cell Biology, Histology and Embryology, Gottfried Schatz Research Center, Medical University of Graz, Graz, Austria*
Contact email: dominique.pernitsch@medunigraz.at

The main goal in the electron microscopic field of life sciences remains preserving the ultrastructure from biological samples as native as possible. A crucial technique against this issue proved to be cryogenic fixation, which is growing in significance in research communities over the years. This boom is primarily focused on samples suitable for TEM microscopes. Yet, how should someone proceed if their research question demands SEM procedures?
We, the team of the Core Facility Ultrastructure Analysis at the Medical University of Graz, would like to present the various range of applications of our Quorum PP3010T Cryo-SEM Preparation System, which is attached to our Zeiss Sigma 500.

The Cryo-SEM system comprises of two dewars for cooling, a preparation desk containing a slusher pot for the freezing process, a transfer device and a prep chamber, which is connected with the microscope chamber. Thus, we have the potential to plunge freeze, transfer the frozen samples under cold vacuum conditions into the preparation chamber, freeze fracture, sublime and sputter coat samples on location. Having such a fast and simple freeze fracture device beside our SEM makes investigating the samples simple and supports the effort of preparing them close to their natural state.
As a result, the spectrum of applications for our Cryo-SEM is remarkable and encompasses human, animal, plant and food samples as well as microorganisms. Moreover, one of the Cryo-SEM's biggest advantages is the ability to prepare even samples that cannot be processed using room temperature SEM methods so far. Saliva, gels or foams are finally viable for examining in an electron microscope. Armed with the above insights and perspectives, it is obvious how the Quorum PP3010T Cryo-SEM Preparation System has become a core component of our methodological portfolio.



Cryo-SEM image of Saccharomyces cerevisiae

LS8 3D functional imaging of materials and biological samples

Type of presentation: Invited

LS8-IN-1 Advanced multimodal and multiscale imaging for material characterization

Lucia Mancini[a]

[a]*Slovenian National Building and Civil Engineering Institute (ZAG), Ljubljana*

Contact email: lucia.mancini@zag.si

The recent advances in the complementary use of X-ray and neutron 3D imaging techniques, coupled with computational modelling, can offer a deeper understanding of how the morpho-textural properties of materials influence fluid dynamics.
In particular, the properties of pore networks, including pore size distribution, shape, connectivity, and tortuosity, play a crucial role in the migration of fluids within geo-materials as well materials employed for energy supply and storage solutions. An accurate estimation of the fluid transport properties is essential to decipher the performances of the investigated materials for their final application.
In this talk some results obtained in the characterization of materials relevant for the energy sector will be presented together with the perspectives these methods can open in other applications based on non-destructive imaging techniques.

Bio:
Lucia Mancini graduated in Physics at the University of L'Aquila (Italy) and in 1998 obtained a PhD at the University J. Fourier (Grenoble, France) working at the European Synchrotron Radiation Facility. There she contributed to the early development of propagation-based phase-contrast (PB PC) methods applied to quasicrystals introducing, for the first time, the simultaneous acquisition of X-ray diffraction topography and PB PC images. She moved to the Italian Elettra synchrotron in Trieste where, from 2001 to 2022, she coordinated the hard X-ray imaging activity in material science, also leading a laboratory equipped with fully customized μCT stations exploiting PB PC imaging. Since 2010, she has been performing a pioneering work in the application of ultrafast synchrotron X-ray μCT to geomaterials at PSI (Switzerland), then pursuing the activity on dynamic μCT at Elettra. She coordinated the implementation of the Pore3D software library for the extraction of quantitative parameters from CT data. Lucia is actually co-leading the scientific activity of the 3D X-ray Imaging center at the Slovenian National Building and Civil Engineering Institute (ZAG) in Ljubljana.

Type of presentation: Invited

LS8-IN-2 Synaptic basis of feature selectivity in hippocampal neurons

Kevin Gonzalez[a]

[a]*Columbia University, United States of America*

Contact email: kg2685@cumc.columbia.edu

A central question in neuroscience is how synaptic plasticity shapes the feature selectivity of neurons in behaving animals. Hippocampal CA1 pyramidal neurons display one of the most striking forms of feature selectivity by forming spatially and contextually selective receptive fields called place fields, which serve as a model for studying the synaptic basis of learning and memory. Various forms of synaptic plasticity have been proposed as cellular substrates for the emergence of place fields. However, despite decades of work, our understanding of how synaptic plasticity underlies place-field formation and memory encoding remains limited, largely due to a shortage of tools and technical challenges associated with the visualization of synaptic plasticity at the single-neuron resolution in awake behaving animals. To address this, we developed an all-optical approach to monitor the spatiotemporal tuning and synaptic weight changes of dendritic spines before and after the induction of a place field in single CA1 pyramidal neurons during spatial navigation. We identified a temporally asymmetric synaptic plasticity kernel resulting from bidirectional modifications of synaptic weights around the induction of a place field. Our work identified compartment-specific differences in the magnitude and temporal expression of synaptic plasticity between basal dendrites and oblique dendrites. Our results provide experimental evidence linking synaptic plasticity to the rapid emergence of spatial selectivity in hippocampal neurons, a critical prerequisite for episodic memory.

Type of presentation: Oral

LS8-O-1 Structural recognition and stabilization of tyrosine hydroxylase by the J-domain protein DNAJC12

Mary Dayne S. Tai[a,b], Lissette Ochoa[c], Marte I. Flydal[a,d], Lorea Velasco-Carneros[e], Jimena Muntaner[c], César Santiago[c], Kunwar Jung-KC[a,b,f], Fernando Moro[e], Gloria Gamiz-Arco[a,b], David Gil-Cantero[c], Miguel Marcilla[c], Juha P. Kallio[a], Arturo Muga[e], José María Valpuesta[c,g], Jorge Cuéllar[c], Aurora Martinez[a,b,f]

[a]*Department of Biomedicine, University of Bergen, Bergen, Norway.*

[b]*Neuro-SysMed Center, Department of Neurology, Haukeland University Hospital, Bergen, Norway.*

[c]*Centro Nacional de Biotecnología (CNB-CSIC), Madrid, Spain.*

[d]*Department of Medical Genetics, Haukeland University Hospital, 5021, Bergen, Norway.*

[e]*Instituto Biofisika (UPV/EHU, CSIC), Universidad del País Vasco, (UPV/EHU), and Departamento de Bioquímica y Biología Molecular, Facultad de Ciencia y Tecnología, Universidad del País Vasco, (UPV/EHU), Barrio Sarriena, 48940 Leioa, Spain.*

[f]*K.G Jebsen Center for Translational Research in Parkinson's Disease, University of Bergen, Bergen, Norway.*

[g]*Unidad de Nanobiotecnología, CNB-CSIC-IMDEA Nanociencia Associated Unit, 28049 Madrid, Spain*

Contact email: jmv@cnb.csic.es

Pathogenic variants of the molecular chaperone DNAJC12 cause parkinsonism, which is associated with a defective interaction of DNAJC12 with the enzyme tyrosine hydroxylase (TH), the rate-limiting enzyme in dopamine (DA) biosynthesis. Here, we report the purification and biophysical characterization of full-length DNAJC12 and the structural characterization of its complex with TH (1). DNAJC12 was purified as a monomer with a mostly unstructured C-terminal region that binds with high affinity to TH. We have characterized the interaction between TH and DNAJC12, showing that DNAJC12 binding stabilizes TH and the TH deficiency (THD) associated variant TH-p.R202H, and delays their time-dependent aggregation in an Hsp70-independent manner, while maintaining TH activity and regulatory inhibition by DA. DNAJC12 alone barely activates Hsc70, but synergistically stimulates Hsc70 ATPase activity when complexed with TH or with the THD variant. Cryoelectron microscopy (Figure 1) supported by crosslinking-mass spectroscopy (XL-MS) reveals two DNAJC12 monomers bound per TH tetramer, each embracing one of the two regulatory domain dimers, leaving the active sites available for substrate and feed-back inhibitory DA interaction. Our results reveal the key role of the C-terminal region of DNAJC12 in TH binding, explaining the pathogenic mechanism of the DNAJC12 disease variant p.W175Ter.

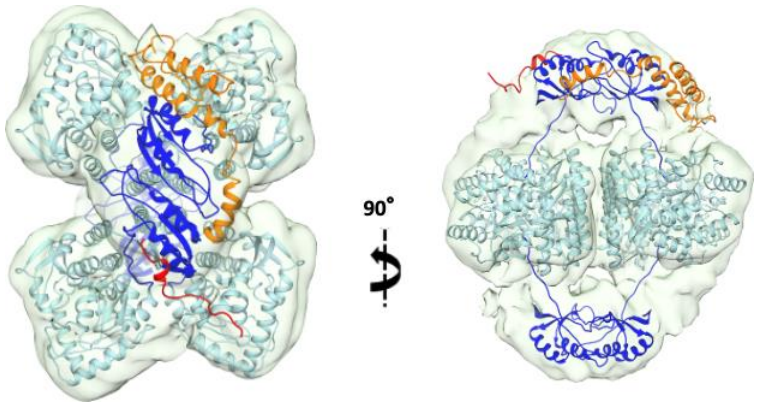


Figure 1. Two orthogonal views of the 3Dreconstruction by cryoelectron microscopy of the TH:DNAJC12 complex

References:

1. MDS Tai, L Ochoa, MI Flydal, L Velasco-Carneros, J Muntaner, C Santiago, G Gamiz-Arco, F Moro, J Jung-KC, D Gil-Cantero, M Marcilla, JP Kallio, A Muga, JM Valpuesta, J Cuéllar, A Martínez. **Nat. Commun** (in press)

Type of presentation: Oral

LS8-O-2 Spatiotemporal acquisition of genetically encoded biosensors in intact plant leaves reveals hormonal crosstalk in response to wounding

Valentina Levak[a,b], Tjaša Mahkovec Povalej[a], Karmen Pogačar[a,b], Katja Stare[a], Maja Zagorščak[a], Tim Hawkins[c], Joanne Robson[c], David Dobnik[a], Tjaša Lukan[a], Kristina Gruden[a]

[a]*Department of Biotechnology and Systems Biology, National Institute of Slovenia (Ljubljana) Slovenia*

[b]*Jožef Stefan International Postgraduate School (Ljubljana) Slovenia*

[c]*Department of Biosciences, Durham University (Durham) UK*

Contact email: valentina.levak@nib.si

Introduction: Understanding molecular background of plant defence response is key in the development of resilient plants. Plant defence relies on coordination of various processes, balancing the trade-off between growth and costly defence response. This coordination is achieved through crosstalk of different signalling pathways. For example, plant's response to wounding is known to be predominantly orchestrated by phytohormone jasmonic acid (JA). The activation of distinct signalling pathway in individual cells or tissue can be followed live in intact samples by using genetically encoded biosensors. Those that employ fluorescent proteins as reporters can be followed using spatiotemporal confocal imaging.

Methods: confocal microscopy, qPCR.

Results: To follow wounding response in potato plants, we generated two biosensor potato lines, each following a certain step of JA signalling cascade. One biosensor detects degradation of transcriptional repressors of JA-dependent genes while the other detects subsequent event: actual expression of JA-dependent gene. Biosensors' fluorescence was followed through time with confocal microscopy in nondetached potato leaves in response to herbivore and mechanical wounding. Both biosensors revealed that JA signalling occurred in a restricted area around the wound. Interestingly, JA-dependent gene expression was inhibited in the cells close to the wound, while transcriptional repressor of JA-dependent gene expression was degraded confluently from the wound outwards. In search of the mechanisms of this response, we showed that salicylic acid (SA) is accumulating in the cells close to the wound using SA reporter. Additionally, we introduced JA-dependent gene expression sensor in SA-depleted NahG plants, which showed uniform spread of the sensor's expression and thus confirmed the role of SA in attenuation of JA response close to the wound.

Discussion and conclusions: Recent reports showed that antagonism between JA and SA was involved in plant's response to various infections of plants. Our results indicate that the dynamic JA-SA crosstalk is involved also in response to herbivore and mechanical wounding. Our work now continues to find the key players behind the observed dynamic JA-SA crosstalk.

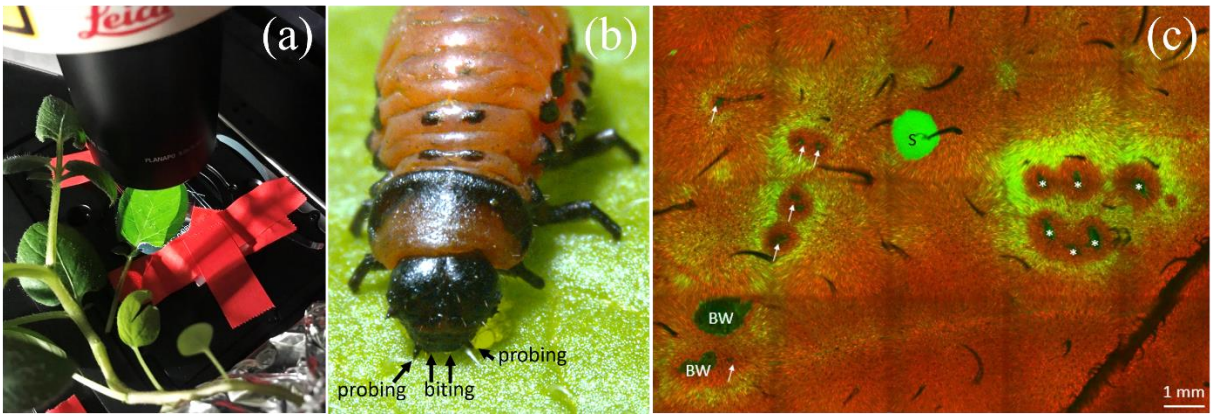


Figure 1: Spatiotemporal confocal imaging of plant's response to wounding. (a) Wounded leaf was placed under confocal macroscope for in vivo imaging of biosensor's response. Leaf was still attached to the plant during > 20 h of imaging. (b) Colorado potato beetle larvae exhibited different types of wounding based on the used part of mouth apparatus: probing with maxillary palpi and biting using labrum. (c) Response of the biosensor of JA-dependent gene expression in potato leaf as seen at 20 h after wounding. Different types of wounding were applied: mechanical woundings with needle (asterisks) and herbivore woundings caused by biting (BW) or probing (arrows). Additionally, a drop of herbivore's saliva was applied, which did not trigger biosensor's response but strong autofluorescence in biosensor's channel. Biosensor's activity (green) is shown on background chlorophyll fluorescence (red) and it shows localized response, comparable among different types of wounds.

Type of presentation: Oral

LS8-O-3 The exopolysaccharide EpsA-O has a decisive role in 3D microstructure formation of *Bacillus subtilis* biofilm

Iztok Dogsa[a], Paola Cescutti[b], Barbara Bellich[c], Mojca Blaznik[a], Cristina Lagatolla[b], Neil Ravenscroft[d], David Stopar[a]

[a]*Department of Microbiology, Biotechnical faculty,University of Ljubljana, Slovenia*

[b]*Department of Life Sciences, University of Trieste, Italy*

[c] *Institute for Maternal and Child Health - IRCCS "Burlo Garofolo" – Trieste, Italy*

[d]*Department of Chemistry, University of Cape Town, South Africa*

Contact email: iztok.dogsa@bf.uni-lj.si

Biofilms represent the predominant mode of bacterial life, consisting of microbial consortia embedded in a self-produced exopolymeric matrix. *Bacillus subtilis* is one of the best-studied Gram-positive biofilm model organisms. Although significant progress has been made in characterizing the *B. subtilis* biofilm[1] and its matrix, the structure and function of crucial exopolysaccharide, EpsA-O, remain poorly understood. In our recent study[2] we investigated the EpsA-O role, by designing 3D-printed slides that allowed us to visualize *B. subtilis* biofilms in their native, undisturbed state using confocal laser scanning microscopy (CLSM). 3D image reconstruction revealed distinct microstructures forming exclusively in wild-type (WT) biofilms, whereas EpsA-O-deficient mutants (*Δeps*) produced flat, featureless biofilms. Supplementing *Δeps* biofilms with purified EpsA-O restored the 3D biofilm phenotype, confirming EpsA-O as a key structural determinant. To localize EpsA-O within the intercellular space, we tested several fluorescent dyes for CLSM imaging. Concanavalin A and wheat germ agglutinin lacked specificity for EpsA-O, consistent with their known affinity for teichoic acids in *B. subtilis* cell walls. Calcofluor White produced only weak, nonspecific fluorescence, prompting us to apply wide-field microscopy. Using India ink staining and differential interference contrast (DIC) microscopy, we demonstrated that EpsA-O fills the intercellular space, promoting cell-cell aggregation. In parallel, we characterized EpsA-O's molecular properties. We determined its primary structure by NMR, its molecular weight using HPLC-SEC combined with intrinsic viscosity, and its viscoelastic properties via rotational rheometry. Integrating these data, we applied the String-of-Beads model to visualize EpsA-O in 3D solution space, providing molecular-level insights into its adhesive function in biofilm formation.

Our findings establish EpsA-O as a crucial component driving 3D biofilm architecture and offer new insights into the molecular mechanisms underlying biofilm stability and resilience.

Acknowledgements:
The work was supported by the Slovenian Research and Innovation Agency (ARIS) J1-3021, P4-0116 and Infrastructural Centre Microscopy of Biological Samples (MRIC UL, I0-0022-0481-08).

References:

1. Krajnc, M., Stefanic, P., Kostanjšek, R. et al. Systems view of Bacillus subtilis pellicle development. npj Biofilms Microbiomes 8, 25 (2022).
2. Dogsa, I., Bellich, B., Blaznik, M. et al. Bacillus subtilis EpsA-O: A novel exopolysaccharide structure acting as an efficient adhesive in biofilms. npj Biofilms Microbiomes 10, 98 (2024).

Type of presentation: Oral

LS8-O-4 XCT state-of-the-art scanning modality for the characterization of 3D-printed flat panels

Lidija Korat Bensa[a], Uroš Bohinc[a], Rok Rudolf[a], Rožle Repič[a]

[a]*Slovenian National Building and Civil Engineering Institute, Dimičeva 12, 1000 Ljubljana, Slovenia*

Contact email: lidija.korat@zag.si

Recent advances in microscopy and computer analysis have made detailed 3D visualisation possible, especially for samples with a specific shape. Non-destructive methods such as X-ray microtomography can be used to evaluate the 3D information of such customised materials. The flexible hardware and software of the new XCT devices allows working with state-of-the-art scanning modalities such as hellicoil, stack and laminography modes.

Therefore, the characterization of 3D-printed planar objects (panels) with X-ray microlaminography is proposed in this work, which proves to be a promising tool for non-destructive 3D analysis, especially when the same sample needs to be characterised multiple times. Prior to the experiments, the panels were fabricated using the binder jetting process (Zprinter 310, Z Corporation, Burlington, USA), which allows the fabrication of highly complex geometries with customised porous and cellular structures. The panels were then scanned with X-ray tomograph EasyTOM XL Ultra (RX Solutions) equipped with a cone beam open source using the laminography mode (XAct software). With this technique, the three-dimensional structure of the laterally extended flat panel can be visualised, which is normally difficult to observe with conventional X-ray tomography due to its large dimensions and small thickness. In this study, the near-surface structure and the inner structure (shape of the openings) were examined in detail.

This study demonstrates the potential of microtomography for developing a knowledge base for 3D printed samples. It has also shown that this technique is suitable for determining the architecture of 3D printed samples and for verifying print resolution and quality control. For conducting such experiments on large flat samples, as shown here, laminography is essential to ensure accurate measurements and detailed information.

Acknowledgements: The authors gratefully acknowledge the financial support of the Slovenian Research and Innovation Agency (research core funding No. P2-0273 and No. I0-0032).

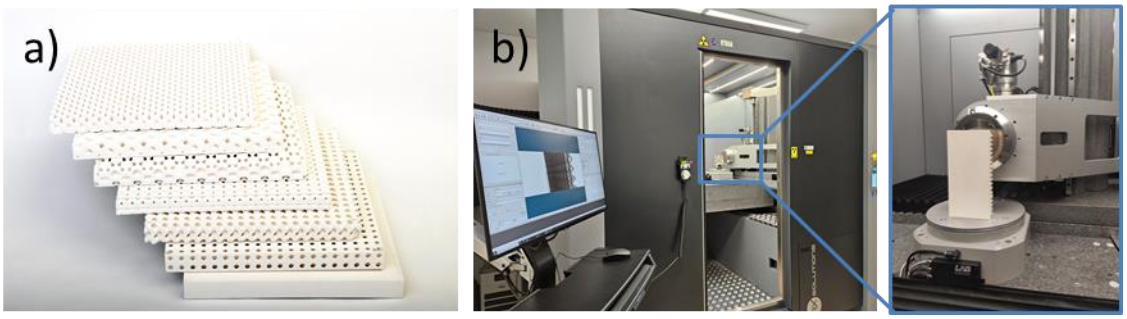


Figure 1: 3D printed flat panels. Various examples of panels with different geometries (a), RX Solutions EasyTOM XL Ultra with sample (b).

Type of presentation: Poster

LS8-P-1 Micro-CT analysis of femoral bone structure in ovariectomized rats following treatment with alendronate, hop extract and their combination

Edi Rođak[a,b], Robert Grgac[a], Rok Kostanjšek[c], Nada Oršolić[d], Tatjana Belovari[a], Nikola Bijelić[a]

[a]*Department for Histology and Embryology, Faculty of Medicine Osijek, University of Osijek, J. Huttlera 4, 31000 Osijek, Croatia*

[b]*UCONN Health, 263 Farmington Ave., Farmington, CT 06030, USA*

[c]*Department of Biology, Biotechnical Faculty, University of Ljubljana, Večna pot 111, 1000 Ljubljana, Slovenia*

[d]*Department of Animal Physiology, Faculty of Science Zagreb, University of Zagreb, Rooseveltov trg 6, Zagreb, Croatia*

Contact email: nbijelic@mefos.hr

Introduction. Ovariectomized rats are a widely used model for osteoporosis, replicating bone architecture changes caused by decreased estrogen levels in postmenopausal women. Alendronate, a member of the bisphosphonate group, is one of the most common medications used to treat osteoporosis. Phytoestrogens gained increasing attention in osteoporosis research in recent decades. One of the most potent phytoestrogens, 8-prenylnaringenin, is found in hop extracts. We evaluated the effect of alendronate, hop extract, and their combination on bone structure in ovariectomized rats.

Methods. The study protocol involved 70 female Wistar rats (6 months old) divided into 7 groups of 10. A sham operation was performed on one of the groups, and bilateral ovariectomy on all others. Ovariectomized rats were further divided into six groups: one untreated group and five treatment groups receiving low-dose alendronate, high-dose alendronate, hop extract, low-dose alendronate + hop extract or high-dose alendronate + hop extract. Animals were euthanized and femurs were carefully isolated and preserved in 4% paraformaldehyde. The distal epiphyses of bones were scanned using a Neoscan N80 Micro-CT device at 50 kV, 200 µA, and 10 µm resolution. A 1-cm segment of the distal epiphysis was scanned, images were processed and exported as 2D projections, which were then used to generate 3D models in Dragonfly software for segmentation and analysis. Bone models were denoised, and the bone analysis plugin in Dragonfly software was used to determine regions of interest, which were then analyzed. Bone parameters for analysis were determined as per Bouxsein et al. [1].

Results. Comparison of sham-operated and ovariectomized controls confirmed the successful development of an ovariectomy-induced osteoporosis model. Significant changes were noted in the following parameters: bone volume, bone volume fraction, endocortical perimeter, endocortical surface, cortical bone area, cortical area fraction, average cortical thickness, and trabecular thickness. Overall, bone quality was significantly improved in animals treated with high-dose alendronate, hop extract, and low-dose alendronate + hop extract. Bone quality parameters of these three groups were similar to non-ovariectomized controls. High-dose alendronate + hop extract group exhibited significantly lower bone quality than the three groups and the controls.

Discussion and conclusions. Hop extract alone or in combination with low-dose alendronate significantly improved the bone quality of ovariectomized rats. Probably due to the effects of 8-prenylnaringenin, hop extract is a putative candidate for osteoporosis therapy, alone or in combination with lower doses of alendronate, since the latter has certain side effects. Reasons for the somewhat surprising effect found in high-dose alendronate + hop extract group should be further investigated.

Acknowledgments. The authors would like to acknowledge the help of Hopsteiner company by generously donating hop extract XanthoFlav™ for research purposes, and the support of Slovenian

Research Agency to “Infrastructural Center Microscopy of Biological Samples” (MRIC UL, I0-0022-0481-08), which enabled the micro-CT analysis at Biotechnical Faculty, University of Ljubljana, Slovenia.

References:
1. Bouxsein ML, Boyd SK, Christiansen BA, Guldberg RE, Jepsen KJ, Müller R. Guidelines for assessment of bone microstructure in rodents using micro-computed tomography. Journal of bone and mineral research : the official journal of the American Society for Bone and Mineral Research. 2010 Jul 7;25(7):1468–86.

Type of presentation: Poster

LS8-P-2 3D Atlas of Arthropods

Urban Bogataj[a], Gregor Bračko[a], Teo Delić[a], Žiga Fišer[a], Rudi Verovnik[a], Miloš Vittori[a], Valerija Zakšek[a], Cene Fišer[a], Rok Kostanjšek[a]

[a]*University of Ljubljana, Biotechnical faculty, Department of biology, (Ljubljana), Slovenia*

Contact email: urban.bogataj@bf.uni-lj.si

Introduction: The project 3D Atlas of Arthropods aims to advance the digitalization in education at the University of Ljubljana. Within the project, we want to approach the biodiversity of arthropods to students of natural sciences, biology teachers, high school students and nature enthusiasts. Arthropods represent vast majority of currently known animal species, thriving in all ecosystems around the globe, and comprising an impressive diversity in functional morphologies. Visualization of the selected arthropod species will expectedly improve student's understanding of how arthropod taxa differ from each other but also elucidate the associations between the form and function.

Methods: The main visualization technique used in the 3D Atlas of Arthropods was an X-ray microtomography. The selected species were acquired from our collection, either fixed in ethanol or dry, and from additional collections in the field, preserved in ethanol. The specimens were contrasted with 1% I_2 solution in 100% ethanol and scanned with a Neoscan N80 (Neoscan) microtomograph. In a microtomograph, a sequence of two-dimensional X-ray projection images of a selected specimen were recorded at multiple angles. This series of images was then used to reconstruct the animal's 3D structure with filtered backprojection, which is the reconstruction algorithm used by the Neoscan N80 system. The obtained 3D reconstruction is a stack of detailed cross-section images in successive planes along the body of the scanned specimen (Fig. 1A). A series of such cross-section images can be rendered as a 3D model of the scanned arthropod. The obtained 3D stack of images was then processed using Dragonfly software (Comet Technologies). In the 3D dataset the body of the specimen was first segmented from the background (Fig. 1B). This subset of voxels representing the entire body of the animal was then segmented into the main body regions (Fig. 1C). For each body region a 3D mesh of its surface was prepared (Fig. 1D). In the open-source Blender software, these meshes were then stitched into a 3D model of a whole animal with body regions displayed in different colours.

Results: We scanned specimens of 50 arthropod species from all four arthropod subphyla (Chelicerata, Myriapoda, Crustacea and Hexapoda). 3D models with labelled body regions have been uploaded to the project's website (http://3datlas.si) and supplied with descriptions of their external anatomy and biology, as well as with detailed photographs. At the website, the models are displayed in a 3D viewer, in which they can be freely rotated in all three spatial axes, zoomed in or out and thus observed from different angles at high resolution.

Discussion and future prospects: Although the online 3D atlas of arthropod external morphology serves primarily as a digital teaching aid in courses of invertebrate biology, the idea behind the atlas is also improvement of awareness on arthropod biodiversity in general public and promotion of scientific activity at the University of Ljubljana. We foresee two future directions of the development. Firstly, we plan to expand the set of scanned species with additional representatives, to more exhaustively cover the arthropod diversity. Additionally, we aim for an in-depth analyses of arthropod body plan, with additional segmentation of the appendages, mouthparts and visualization of internal organ systems.

Acknowledgements: The project is funded under the development framework of University of Ljubljana. The purchase of the Neoscan N80 microtomograph was co-financed by the Republic of Slovenia, Ministry of Education, Science, and Sport and the European Union from the European Regional Development Fund. The microtomograph, sample preparation laboratory, and supporting computer equipment are part of the infrastructure center "IC Microscopy of Biological Samples" at the Faculty of Biotechnology (MRIC UL, I0-0022-0481-08), which is part of the University of Ljubljana's

Network of Infrastructure Centers. We thank the students Vito Ham, Vesna Jurjevič, Gaj Kušar and Adrijan Samuel Stell Pičman who participated in the project.

Author contributions: UB performed X-ray microtomography scans of arthropods, 3D data processing and generation of 3D models. GB, TD, ŽF, RV, MV and VZ provided descriptions and photographs of included arthropod species. CF and RK are the project leaders.

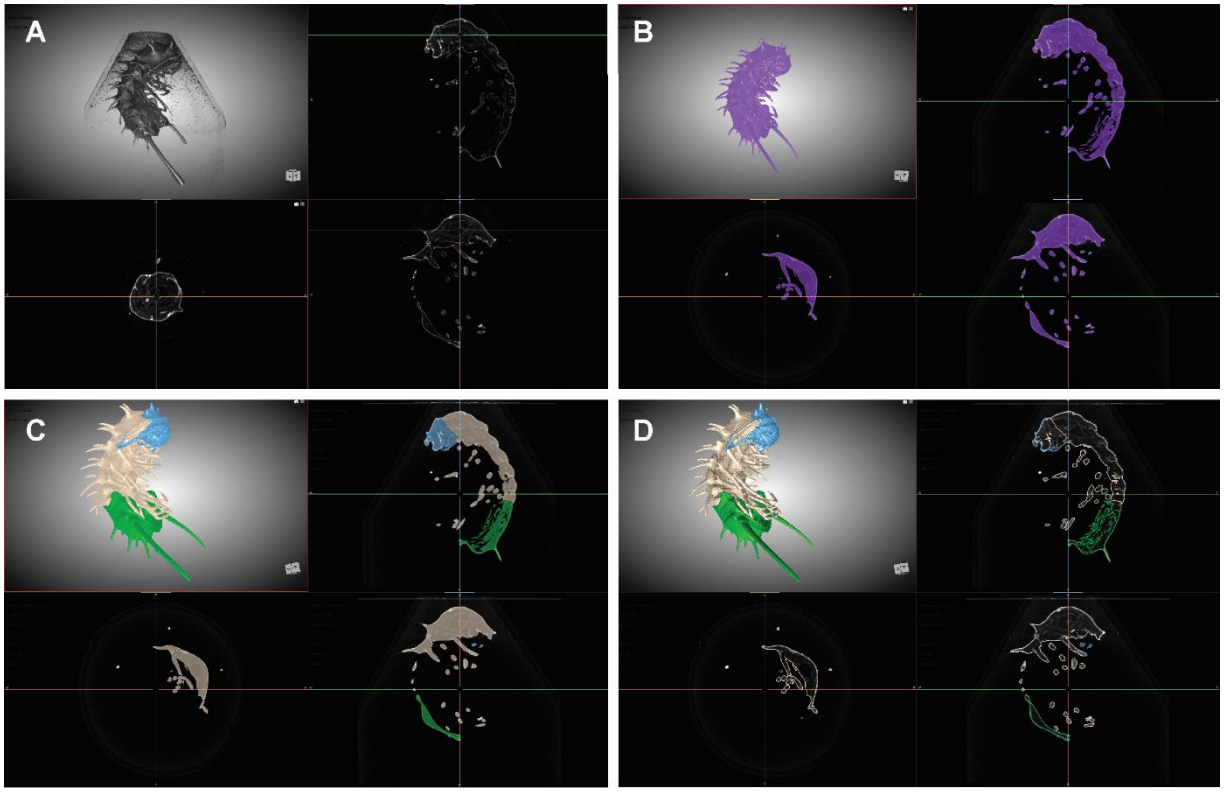


Figure 1: Processing of the 3D dataset. 3D dataset reconstructed from X-ray projection images (A), segmentation of the full body (B), segmentation of body regions (C), generation of 3D surface meshes used in the representation of the specimen in the 3D Atlas (D).

Type of presentation: Poster

LS8-P-3 Resolution Limitations in Cryo-EM Analysis of SUMO-Anchored Ferritin

Zdenko Gardian[a], Ondrej Hajdusek[a]

[a]*Biology Centre CAS, Ceske Budejovice, Czech Republic*

Contact email: gardian@prf.jcu.cz

Ferritin is a well-characterized iron-storage protein that can be structurally resolved at atomic resolution. In this study, we employed cryo-electron microscopy (cryo-EM) to determine the structures of native ferritin and a modified ferritin construct containing a SUMO anchor, aiming to achieve near-atomic resolution and investigate potential structural differences.

Samples were vitrified using plunge-freezing, and data were collected on a high-end cryo-EM system equipped with a direct electron detector. Image processing and 3D reconstruction were performed using standard single-particle analysis workflows. The resolution of native ferritin was determined to be better than 4 Å, allowing for precise atomic modeling. However, under identical experimental conditions, the SUMO-anchored ferritin could not be resolved beyond ~10 Å.

This significant difference in achievable resolution suggests that the SUMO modification introduces structural heterogeneity, flexibility, or preferred orientation effects, negatively impacting high-resolution reconstruction. Understanding these limitations is essential for optimizing the structural characterization of engineered protein assemblies. Future work will focus on improving sample preparation and data collection strategies to overcome these challenges.

Type of presentation: Poster

LS8-P-4 3D visualisation of wood: 3D X-ray microtomography and 3D printing

Rožle Repič[a], Lidija Korat Bensa[a], Daša Krapež[b], Maks Merela[b]

[a]*Slovenian National Building and Civil Engineering Institute, Department of Materials, (Ljubljana), Slovenia,*

[b]*University of Ljubljana, Biotechnical Faculty, Department of Wood Science and Technology, (Ljubljana), Slovenia*

Contact email: rozle.repic@zag.si

Introduction: Current research on wood is carried out on fresh or technological wood, as well as on old or archaeological wood. In the case of old or archaeological wood, X-ray computed microtomography has proved to be an essential method, as the sample does not need to be specially prepared for imaging. This means that the material can be observed in exactly the same condition as it is in nature (non-destructive, without cutting, sanding, sputtering, etc...). In the case of wooden artefacts, not destroying the sample is the most important thing, additionally microtomography is precise enough to analyse the structure of such samples in detail (Figure 1).

Methods: The structure of different wood species and filaments were scanned at submicron resolution using Xradia µCT-400 tomograph (Xradia, USA) or EasyTOM XL Ultra system (RX Solutions, France). At least 1601 projections were taken during 360° rotation of the sample and the reconstruction was made using XAct software or XRM Reconstructor software. The advanced software Avizio Fire (Thermo Fisher Scientific, USA) was used for image filtering, segmentation and 3D model preparation. After data processing, 3D models of the wood structure were printed at a 1:500 scale.

Results: After reconstruction, the 3D image can be processed in any direction and histological sections can be digitally created at the desired direction and location, allowing for further analyses, such as wood identification or dendrochronological studies. Additionally, a 3D image can be exported as a 3D object and printed using a 3D printer (Figure 1). This opens up new possibilities for studying details and transferring knowledge to younger generations or interested public [1].

Discussion and conclusions: When observing/examining the microstructure of wood, it is important to keep the sample as small as feasible, as this contributes to the best quality images. Whenever possible, we need to pay attention to the dimensions of the samples and the desired image quality/magnification when designing the experiments or sampling itself. Acquired images can be processed with advanced computer programmes and studied in detail with accurate measurements in 3D space. 3D models of microstructure of wood are a state-of-art tool for studying the anatomical structure of wood, among others. As the models are relatively cheap, accurate and quickly reproducible, 3D-printed educational tools open up new possibilities for studying details and transferring knowledge with hands-on learning [1].

The development of alternative materials for 3D printing is on the rise. The incorporation of wood particles in 3D printing filament to a certain proportion is an established practice, but it has its challenges. 3D microtomography has been used to analyse the structure of 3D printing filaments with incorporated wood particles [2] (Figure 2).

Acknowledgements: The authors gratefully acknowledge the financial support of the Slovenian Research and Innovation Agency (research core funding No. P2-0273, P4-0015, J4-50131, J7-50226 and I0-0032).

References:

1. Merela, M., Krapež, D., Balzano, A., Repič, R., Straže, A., Krže, L., Žigon, J. Innovative Educational Tools: Integrating X-ray Computed Tomography and 3D Printing for Enhanced Learning, International Symposium on Wood Science and Technology 2025 (ISWST2025), March 17-19, Sendai, Japan.
2. Krapež, D., Schwarzkopf, M., Repič, R. et al. 2024. Eur. J. Wood Prod. 82, 403–416. https://doi.org/10.1007/s00107-023-02018-2.

3. Sketchfab – Wood microstructure collection. https://skfb.ly/p8ost.

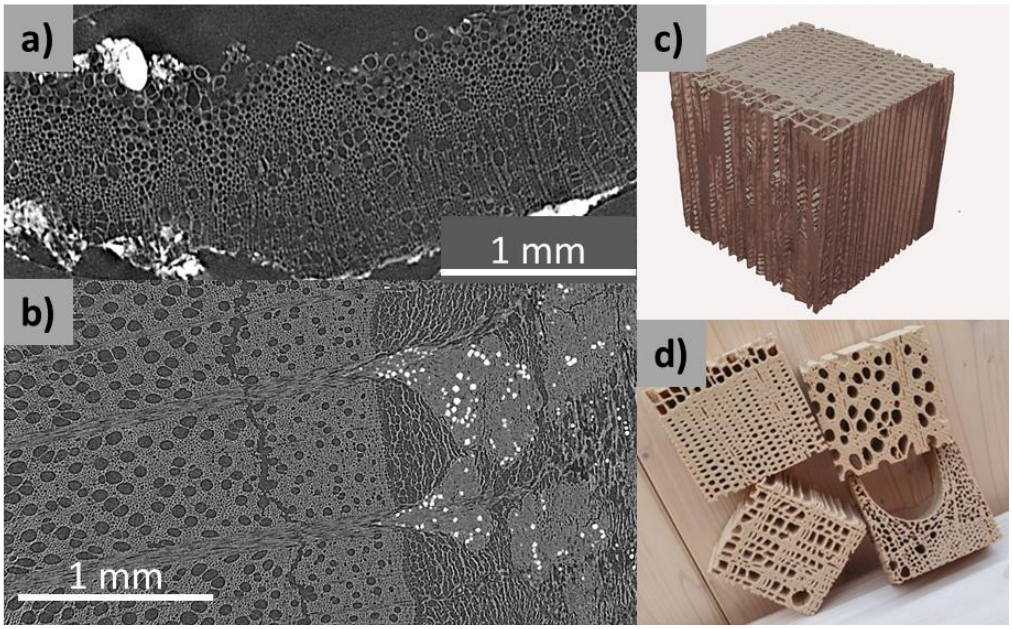


Figure 12: Cros-section of a microstructure of an archaeological wood (a); Cros-section of a microstructure of a recent wood (b); Virtual 3D model of wood derived from a CT scan [3] (c); 3D printed models of wood [3].

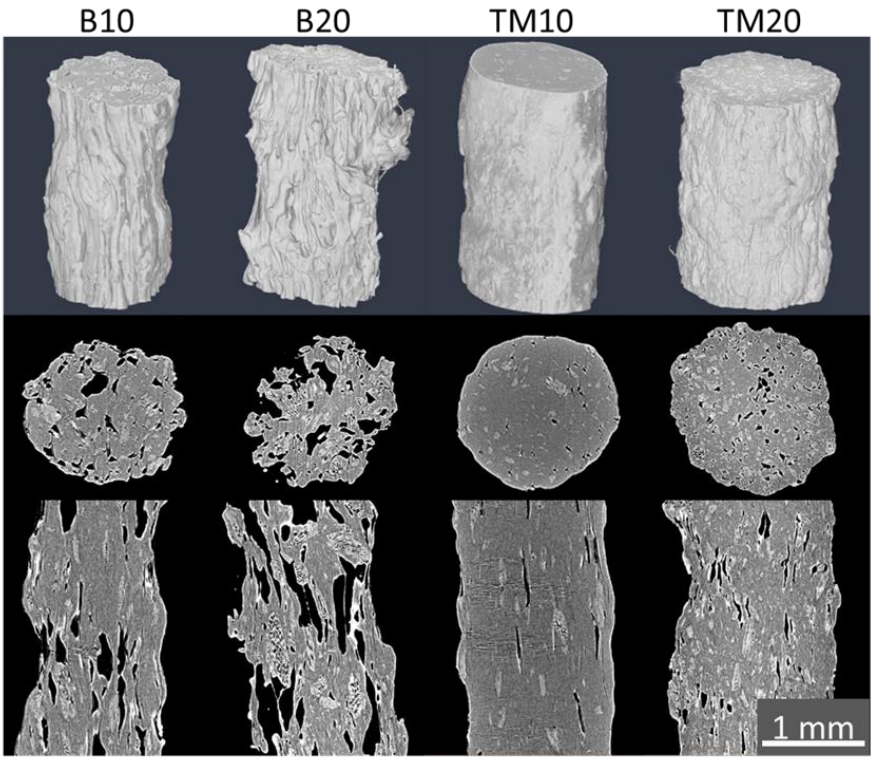


Figure 13: 3D analysis of different 3D printing filaments with added wood particles [2].

Type of presentation: Poster

LS8-P-5 Origami roly poly: arthropods fold their exoskeletons as they roll into a ball

Miloš Vittori[a]

[a]*University of Ljubljana, Biotechnical Faculty, Department of Biology, Ljubljana, Slovenia*

Contact email: milos.vittori@bf.uni-lj.si

Numerous arthropods can roll into a ball. This ability, which likely protects them from predators, characterizes several lineages of terrestrial isopod crustaceans, the so called pill bugs or roly polies (Schmalfuss, 2008; Tuf and Ďurajková, 2022).

When an animal with a rigid exoskeleton rolls into a ball, this change of shape compresses the ventral body wall. In addition, the appendages must fit into the resulting sphere despite the compression of the ventral surface. While certain morphological adaptations that allow the exoskeletons of rolling crustaceans to fit together into an almost perfect sphere have been described, the mechanics of shifting between extended and rolled states has not been well understood. In particular, how different components of the exoskeleton rotate relative to each other and the ways in which the ventral skeletal plates and legs fit into the ball that is formed by the body have remained largely speculative.

We performed a comparative imaging of extended and rolled isopods using micro-computed X-ray tomography (micro-CT) of rapidly frozen individuals, aiming to explain how the repositioning of different skeletal elements of isopods enables their fitting into a tight sphere and how this is accomplished mechanically. The major challenge in this work was the immobilization of isopods in relevant poses. We used flash freezing in liquid nitrogen to preserve the fully extended and fully rolled body positions. Micro-CT scans were obtained using a Neoscan 80 X-ray microtomograph. The frozen specimens were mounted on a TS2103 thermal stage (Neoscan) and scanned at -10 °C. Image segmentation and 3-D reconstruction were performed using Dragonfly software (Object Research Systems).

Our results show that the points of rotation between consecutive body segments are positioned dorsolaterally and are not fixed joints. Instead, ridges at the edges of consecutive dorsal plates (tergites) lean against each other, allowing consecutive body segments to rotate. Terrestrial isopods capable of rolling into a ball have shorter sternal plates than non-rollers. The sternal plates overlap in rolled isopods (Figure 1), jointly forming furrows that accommodate the walking legs. Furthermore, the sternal plates are able to bend along a flexible suture at their midline, allowing them to fold inwards during rolling. Anterior lateral plates of the exoskeleton have furrows that accommodate the more posteriorly positioned lateral plates.

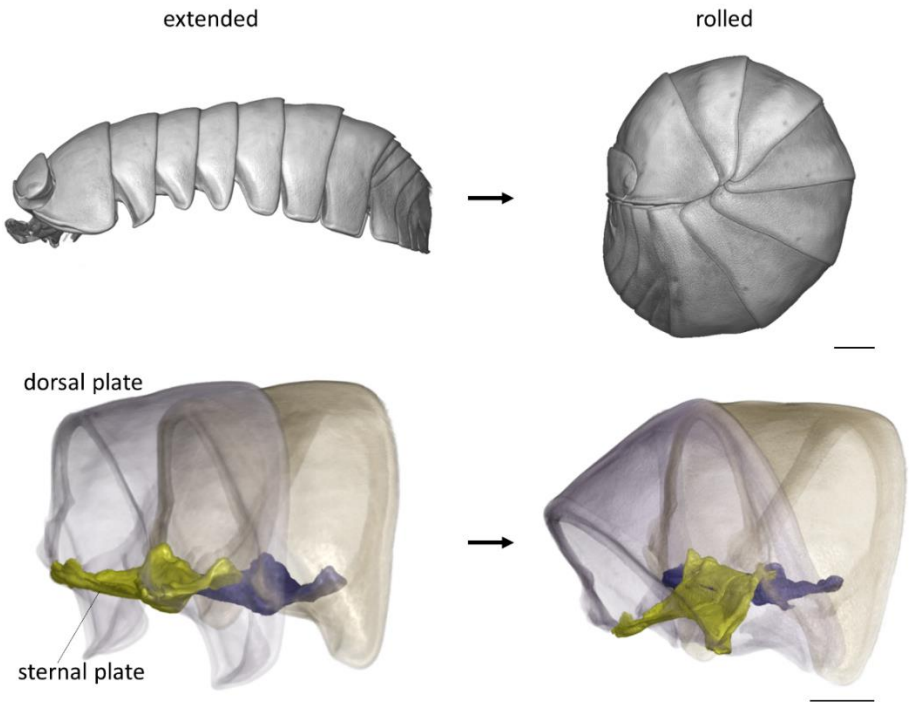


Figure 1: Micro-CT reconstructions of the terrestrial isopod *Armadillo officinalis* while extended (left) and rolled into a ball (right). The sternal plates are brought to overlap and they folds inwards along their midline. Scale bars: 1 mm.

Acknowledgements
This work was supported by the University Infrastructural Center "Microscopy of Biological Samples" at the Biotechnical Faculty, University of Ljubljana, and the project "Development of research infrastructure (RI) for the international competitiveness of the development of Slovenian RI space – RI-SI-LifeWatch". The operation is co-financed by the Republic of Slovenia, Ministry of Education, Science and Sport and the European Union from the European Regional Development Fund.

References
1. Schmalfuss, H., 2008. Stuttg. Beitr. Naturk. A New. Ser. 1, 143–151.
2. Tuf, I.H., Ďurajková, B., 2022. ZooKeys 1101, 109–129.

MS1 Ceramics, ceramic composites and geological materials

Type of presentation: Invited

MS1-IN-1 Studying the crystallization of inorganic materials using correlated transmission electron microscopy

Rik Brydson[a], Martha Ilett[a], Stephanie Foster[a], Zabeada Aslam[a], Maryam Afzali[a], Joanna Galloway[b], Fiona Meldrum[b]

[a]*School of Chemical and Process Engineering, University of Leeds, Leeds LS2 9JT, UK*

[b]*School of Chemistry, University of Leeds, Leeds LS2 9JT, UK*

Contact email: mtlrmdb@leeds.ac.uk

Complex, electron-beam sensitive systems include organic crystals, polymers, hybrid organic-inorganic materials, some inorganic materials such as hydrates, as well as multiphase solid/liquid and solid/gas systems. Arguably they constitute the majority of systems of current interest across a wide range of scientific and engineering disciplines. We review the use of analytical transmission electron microscopy (TEM) for the characterisation of such beam-sensitive materials and complex, multiphase systems *in-situ* or close to their native state. Such materials are prone to damage by radiolysis which cannot be eliminated or switched off, requiring TEM analysis to be done within an electron dose budget so as to achieve an optimum dose-limited resolution and reliable, artefact-free results. We highlight the importance of determining the damage sensitivity of a particular system in terms of characteristic changes that occur on irradiation under both an electron fluence and flux. We discuss the choice of electron beam accelerating voltage and detectors for optimizing resolution and outline the different strategies employed for low-dose microscopy in relation to the damage processes in operation. In particular, we discuss the use of scanning TEM (STEM) for maximizing information content from high-resolution imaging and spectroscopy of materials and the use of cryogenic sample preservation techniques.

As an example of the analysis of a complex electron-beam sensitive system, we describe studies of the early stages of the aqueous crystallization process in both the calcium sulfate and calcium carbonate systems using a correlated approach: a combination of in-situ liquid cell TEM (LCTEM), in-situ Raman spectroscopy and cryogenic TEM (cryo-TEM). These findings are compared to conventional TEM studies using a range of differing preparation methods to arrest the crystallization reaction and dry the sample for analysis in the microscope vacuum.

Recent studies have suggested that the calcium sulfate polymorph gypsum ($CaSO_4.2H_2O$) can form in aqueous solution via a bassanite ($CaSO_4.0.5H_2O$) intermediate. Hence, initially we studied the transformation of bassanite nanorods to gypsum in an undersaturated aqueous solution of calcium sulfate. When coupled with Raman spectroscopy, the real-time data generated by LCTEM, and structural data obtained from time resolved cryo-TEM (i.e. crystallising solution samples vitrified at various time points) showed that bassanite can transform to gypsum via multiple pathways, the predominant one being dissolution/reprecipitation as opposed to the oriented attachment of nanorods and subsequent solid state transformation. Comparisons between LCTEM and cryo-TEM also showed significantly reduced kinetics within the confined liquid cell as compared with bulk solution, however the electron beam induced radiolysis of water (so lowering the local pH) can accelerate the transformation process. Further studies focused on the direct formation of gypsum from aqueous solution using a range of different sample preparation methods: drop casting of solutions and drying, vacuum filtration, chemical quenching and drop casting, time-resolved cryogenic freezing, as well as LCTEM. Similar studies were undertaken on the crystallization of equimolar calcium carbonate solutions at varying levels of supersaturation. Analysis of both inorganic systems suggests that the observed crystallization pathway can be highly dependent on the degree of supersaturation experienced during the sample preparation method, which may lead to highly erroneous observations.

This work emphasises the need to consider carefully both sample radiolysis by the electron beam and confinement effects during in-situ LCTEM studies, as well as electron microscopy sample preparation

for conventional TEM, when designing experiments to study early stages of chemical reactions such as crystallization, in order to avoid any artefacts and determine true reaction mechanisms. Overall we strongly recommend the use of cryogenic quenching of crystallising solutions and the examination of vitrified samples using cryo-TEM or cryo-SEM.

Keywords
Crystallisation, sample preparation, radiolysis, in situ TEM

References:
1. M. Ilett et al., Phil. Trans. R. Soc. A 378: 20190601 (2020). doi:10.1098/rsta.2019.0601.
2. M. Ilett et al., J. Microscopy 2022, 288 : 155-168. doi: 10.1111/jmi.1310
3. M. Ilett et al., J. Microscopy 2024 : 295: 215-299, doi.org/10.1111/jmi.13300

Type of presentation: Invited

MS1-IN-2 The Past and Future of Electron Backscattered Diffraction (EBSD) in Earth Sciences

José Alberto Padrón-Navarta[a], Marco A. Sanchez-Lopez[a]

[a]*Instituto Andaluz de Ciencias de la Tierra (IACT-CSIC), Av. Palmeras 4, 18100 Armilla, Granada, Spain*

Contact email: alberto.padron@csic.es

The microscopic investigation of minerals in rocks using plane-polarised light with early petrographic microscopes laid the foundations of Mineralogy and Petrology in the mid-19th century [1], establishing essential tools for the emerging science of Geology. Further developments in optical instrumentation—particularly the development of the universal stage (U-stage) with multiple rotation axes in the early 20th century—enabled the investigation of the three-dimensional orientation of optical properties in minerals, allowing a quantitative description of mineral fabrics in rocks. This innovation enabled pioneers such as B. Sanders to link crystal-preferred orientations (CPOs) to plastic deformation and kinematics in rocks ([2], and references therein). Later, studies of CPOs in both natural and experimental mantle samples confirmed the connection between plastic deformation and seismic anisotropy [3], expanding mineral fabric analysis into the realm of geophysics of Earth's interior. Since then, Earth scientists have sought to quantify mineral fabrics across scales, from mantle convection to dislocation-driven deformation at the atomic level.

The labour-intensive nature of U-stage measurements was overcome with the development of Electron Backscattered Diffraction (EBSD) in the 1980s and early 1990s [4]. Automated orientation mapping with EBSD at the whole thin-section scale advanced our understanding of deformation mechanisms in both crustal and mantle rocks. Today, major improvements in acquisition speed, spatial resolution, and data analysis, especially through open-source tools such as the MTEX toolbox [5], have transformed EBSD into a central method in structural geology, petrology and mineral physics. In this context, we will present recent case studies that illustrate new applications of EBSD to mineral reactions and replacement processes, and will offer perspectives on potential future developments in this evolving field.

References

1. J. W. J., "The Evolution of the Petrographical Microscope", *Nature*, vol. 94, no. 2351, pp. 314–315, 1914. doi:10.1038/094314a0.
2. Wenk, H.-R. (Ed.), 1985. Preferred orientation in deformed metals and rocks: an introduction to modern texture analysis. Academic Press, Orlando.
3. A. Nicolas and N. I. Christensen, "Formation of Anisotropy in Upper Mantle Peridotites – A Review", in *Composition, Structure and Dynamics of the Lithosphere-Asthenosphere System*, AGU, 1987, pp. 111–123. doi:10.1029/GD016p0111.
4. D. J. Prior, E. Mariani, and J. Wheeler, "EBSD in the Earth Sciences: Applications, Common Practice, and Challenges", in *Electron Backscatter Diffraction in Materials Science*, Springer US, 2009, pp. 345–360. doi:10.1007/978-0-387-88136-2_26.
5. R. Hielscher and H. Schaeben, "A novel pole figure inversion method: specification of the MTEX algorithm", *J. Appl. Cryst.*, vol. 41, pp. 1024–1037, 2008. doi:10.1107/S0021889808030112.

Type of presentation: Oral

MS1-O-1 Direct observation of phase transformations during dehydration of cementitious phases at high temperatures

Sorour Semsari Parapari[a], Francisco Ruiz-Zepeda[b], Mehmet Ali Gulgun[c], Saso Sturm[a,d]

a Jozef Stefan Institute, Ljubljana, Slovenia

b National Institute of Chemistry, Ljubljana, Slovenia

c Sabanci University, Istanbul, Turkey

d Jožef Stefan International Postgraduate School, Ljubljana, Slovenia

Contact email: sorour.semsari.parapari@ijs.si

Introduction

Cement has been a primary binding material in the construction industry since the 19th century, valued for its exceptional performance. However, its production significantly impacts the environment, depleting natural resources and generating substantial carbon dioxide emissions. Meanwhile, the amount of cement construction and demolition waste is increasing constantly raising the problem of waste disposal and landfilling. Recycling of cement can potentially alleviate such problems. Recently it has been shown that the hydrated cement phases, namely calcium silicate hydrates (CSH) and calcium hydroxide (CH), which are accounted for the properties of hardened cement paste, can be reactivated at elevated temperatures [1]. The phase transformation of CSH and CH to unhydrated cement phases can facilitate their rehydration process and ease the recycling of cement. Until now, various thermal, chemical and phase analysis methods have been used to investigate the hydrated cement phases after the thermal activation process, but generally they have yielded controversial, sometimes contradicting results. In-situ heating Transmission Electron Microscopy (TEM) can unveil the details about the structural, chemical and morphological changes during the dehydration at elevated temperatures. In this work, for the first time, the phase transformation of hydrated cement phases has been investigated using the in-situ heating TEM technique.

Methods

For this work, an ordinary Portland cement paste which was hydrated and aged for over 1 year was used. The cement paste was ground prior to the TEM experiments. The in-situ heating experiments were performed using a Cs-probe corrected JEOL-JEM ARM200CF operated at a 200 kV accelerating voltage. An Aduro Protochips Inc holder with a heating stage was used for in-situ heating of the hydrated cement powder. In this in-situ system, disposable MEMS-based E-Chips with silicon nitride membranes as sample supports are used. The ground powder is drop-casted on the carbon-coated E-Chip membranes with electron-transparent windows using a mask chip. The heating temperature on the specimen area was accurately controlled by an electrical signal on two electrodes using an external power supply.

Results

The sample was heated up from room temperature to 900 °C with 1 °C/s heating rate. The heating was stopped at various intervals and the phases were evaluated by electron diffraction and by microstructure imaging to analyze the structural and morphological changes, respectively. The results unfold important details about the nature of the thermal activation of the cementitious CH phase. The crystalline CH plate-like particles go through several stages of decomposition. Such phase transformation occurs from crystalline to crystalline phases, without an apparent transforming to an amorphous phase. A single particle changes into several smaller crystallites and then sinter back to form a single particle during the heating process, as could be observed from the diffraction patterns as well as the particle morphology. The transformation to the anhydrous CaO phase starts around 400 °C, but this phase itself alters at higher temperatures.

Discussion and conclusions

The findings in this study help with gaining insight into the reactivation mechanisms of cementitious phases. Understanding these processes is of utmost importance for the recycling of cement waste into useful materials, which will ensure a sustainable use and production of cement and concrete.

Acknowledgments

We acknowledge the ERA-MIN2 project RECEMENT (Re-generating (raw) materials and end-of-life products for re-use in Cement/Concrete) with grant agreement No c3330-20-252003.

References

1. Zhang, Q., Ye, G, J Therm Anal Calorim **2012** 110, 153–158.

Type of presentation: Oral

MS1-O-2 Impact of clay construction components on indoor aerosols: what can automated SEM-EDX and Raman reveal?

Manfred Nachtnebel[a], Harald Fitzek[a], Stefan Mitsche[a,b], Nadine Egger[c], Maria Fötsch[c], Martin Steiner[c], Ute Muñoz-Czerny[d]

[a]*Graz Centre for Electron Microscopy (ZFE), (Graz), Austria*

[a]*Institute of Electron Microscopy and Nanoanalysis (FELMI) (Graz), Austria*

[c]*Graz University of Technology, (Graz), Austria*

[d]*Österreichisches Institut für Bauen und Ökologie GmbH (IBO), (Vienna), Austria*

Contact email: manfred.nachtnebel@felmi-zfe.at

Introduction: The construction of buildings is responsible for about 10% of the total greenhouse gas emissions worldwide [1]. The majority of this is generated in the production of building materials, like cement-, steel- and glass manufacturing. Substituting one of the materials with a natural source, thus will lead to a reduction of the environmental impact of this sector. In the "RE-FORM earth" project, various solutions are being developed for the integration of clay in the construction industry [2]. This is because this traditionally used material has not yet been standardised for modern construction work. One of the project subtasks is to analyse the impact of clay construction components on the indoor air quality, especially in terms of their contribution to dust particles. Therefore, automated particle analysis of indoor aerosols was performed to obtain information about its origin.

Methods: Collecting aerosols is a critical task, particularly for the subsequent used spectroscopic methods. In this study mainly SEM-EDX (Scanning Electron Microscopy, Energy Dispersive X-ray spectroscopy) with a Zeiss Sigma 300 VP combined with an Oxford XmaxN 80 (Aztec vers. 3.4) was used to automatically collect at least 25.000 particle spectra per measurement. Additionally, Raman analysis, with a Horiba LabRam HR 800, is used, supported by XRD (X-Ray Diffraction, Siemens D5005) measurements. Aerosol particles were collected indoors, at a household where clay is used as internal plaster with white clay paint as the topmost layer, using a particle sampler PS 30 (Holbach). As automated particle analysis was performed, ten thousand of spectra were collected during every measurement. In order to handle the large amount of data, classification was performed by a custom Python component analysis program (scikit-learn library). Here the UMAP (Uniform Manifold APproximation & transform) dimension reduction and subsequently the HDBSCAN (Hierarchical Density-Based Spatial Clustering of Applications with Noise) for clustering was used to assign every particle to a specific cluster.

Results: To obtain fundamental information about the target substances, clay and the white clay paint, they were characterized by XRD (crystalline part). For clay the major component was quartz, followed by other silicate minerals like Muscovite and Kaolinite and the iron mineral Goethite. The white clay painting consists mainly of calcium carbonate, followed by Rutile, Kaolinite, quartz and Muscovite. All these minerals are very common materials in the earth´s crust [3].

The classical sampler substrate has a sticky tape on top of a glass substrate, which turned out to be incompatible for the subsequent analyses, thus new substrates were fabricated. Glass slides sputtered with approx. 100 nm gold and classical C-tape attached to glass slides proven to be best for Raman and SEM-EDX analysis respectively.

First automated particle investigation where performed with the SEM-EDX system. For the particle localisation, BSE imaging with subsequent grey-value thresholding was sufficient, due to the high contrast between the mineral particles and the C-tape substrate, see Figure 1 (a) and (b). The system software was then used to semi-quantify the obtained spectra, resulting in a particle list, containing morphological as well as elemental information for each particle. As stated above, the build in classification wasn't adequate enough to cluster the particles into the containing classes, the list was processed by a customized Python script. The result can be seen in Figure 1 (c). Here C & O is omitted, to get a better overview of the residual elements. Class 2 only contains C & O, thus is not visible. Because of the elemental composition, the majority of the particles can be assigned to the mineral group

of Feldspar. About 56% are counted in this phase, followed by organic compounds (25% consist of only C & O), Zeolite group, salts and further silicates. In summary, it can be said, that most of the particles in the collected aerosol are agglomerates of different phases. This can already be seen at the shown BSE image in Figure 1 (a): The bigger particle on the top right side contains a bright region incapsulated into a less bright particle.
To obtain the mineral information about the aerosols, in addition to the elemental one, also automated Raman particle analysis was performed. Here the gold sputtered glass slides are used as substrate. The particle-substrate adhesive interactions where sufficient enough, to keep them on place. Therewith the raw materials as well as the collected aerosol was analysed. The analysis of the raw materials resulting in the same outcome, as the previous XRD measurement, as expected. During initial measurements of the collected aerosol, it become clear that the automated routing used for the raw materials, was not applicable. Because lower a laser power has to be used, longer accumulation times per particle are necessary to obtain a suitable Raman spectrum. This leads to missing the particles possibly due to drift issues during the automation process. Thus, manual measurements were performed, to obtain initial information about the present materials. The evaluation of these dataset show, that only a small fraction of less than 1% of can potentially be assigned to the clay or its painting.

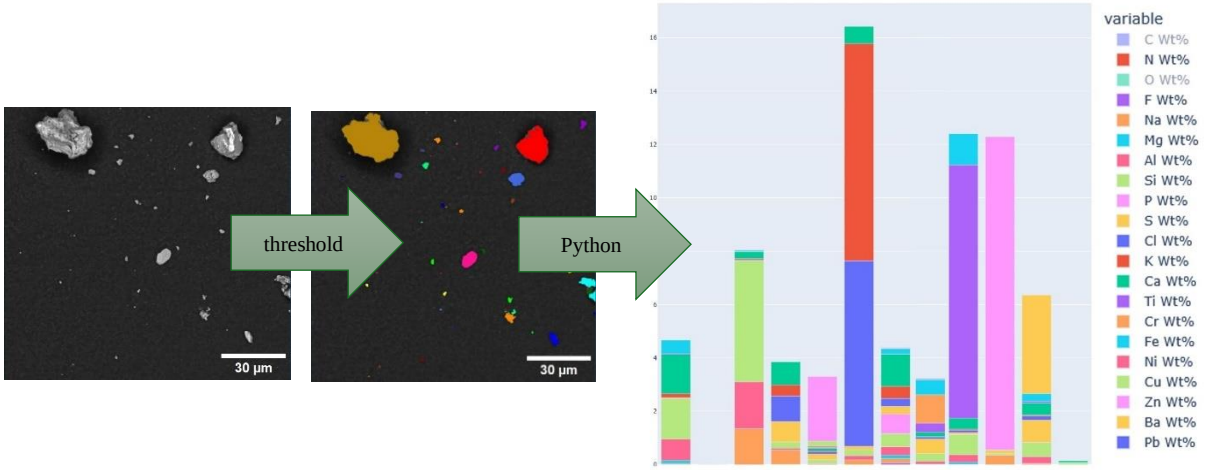


Figure 1: BSE image of particles on C-tape (a), is sufficient for subsequent segmentation via grey-value segmentation (b), and the resulting clusters after classification of the EDX data by a customized Python script (c) [C & O are omitted, to have a better overview].

Discussion and Conclusion: XRD measurements give a good overview of the major containing components, which also helps identifying the phases found during the automated SEM-EDX particle analysis. This is mainly due to the fact that most of the aerosol particles are present as agglomerates. To be able to cluster these agglomerates into its major components, specially adapted evaluation routines by Python scripting are necessary, as the system software does not provide suitable results. Automated Raman analysis, on the other hand, already yield into the containing mineral phases. By optimizing the automated recording routine, it should be possible to obtain statistically more stable results. Initial results of both automated spectroscopic methods show, that they are feasible for the detection of clay components in indoor aerosols. However, more work needs to be done to separate the background dust and the dust originate from the clay construction. This is mainly due to the fact, that clay is one of the main components of the earth´s crust, thus naturally can be found everywhere.
Acknowledgement: This project has received funding from the circular economy and production technologies call. Circular economy and production technologies is a research, technology and innovation funding programme of the Republic of Austria, Ministry for Climate Action, Environment, Energy, Mobility, Innovation and Technology (BMK). The Austrian Research Promotion Agency (FFG) has been authorised for the operational management.

References:

1. Global Status Report for Buildings and Construction, **2020**, UN environment programme
2. https://www.ibo.at/en/research/reference-projects/data/re-form-earth, **2024**
3. S. Ulrich, *Gesteinskunde*, **2022**, 5th ed., Springer Spektrum, 221 p.

Type of presentation: Oral

MS1-O-3 Sulfidic inclusions in the Muong Nong tektites from Laos

Mariana Klementová[a], Lukáš Palatinus[a], Jan Maňák[a], Šárka Křížová[b], Roman Skála[b]

[a] *FZU – Institute of Physics of the Czech Academy of Sciences, Prague, Czech Republic*

[b] *Institute of Geology of the Czech Academy of Sciences, Prague, Czech Republic*

Contact email: klemari@fzu.cz

Instruction: Tektites (from the Greek *tēktos* = molten) are natural glasses found in geographically defined areas called strewn fields. Currently, five such fields are documented in the literature [1], with ages ranging from 35 million to 780,000 years. It is generally agreed that these glasses result from hypervelocity impacts of extraterrestrial bodies on Earth's sedimentary or weathered surface sequences [2,3]. Based on appearance and internal structure, tektites are classified into splashform, ablated/aerodynamically shaped, and Muong Nong types (sometimes called layered, abbreviated MNT). The last type is named after Muong Nong in southern Laos, where they were first described [4]. Tektites up to 2 mm in diameter are called microtektites and are usually splashform. Other key characteristics include high SiO2 content (over 70% except for some microtektites), a lack of crystalline phases, low meteorite content, water content up to a few hundred ppm, and the presence of lechatelierite (quartz glass) particles. Tektites can contain crystalline inclusions which can help us to deduce their origin.

Methods: Small, up to 20 microns in size, inclusions were studied by SEM and several TEM techniques, such as 4D STEM (ACOM), EDS, 3D ED to identify the phases present and their mutual relationship.

Results: Two types of sulfidic inclusions were observed (Fig. 1): (A) with Fe- and (Fe,Ni)-sulfide domains and irregular edges bordered by Mg and Fe silicates, with stoichiometry resembling pyroxene-group minerals, and (B) with small worm-like Fe and Ni sulfides in a matrix of FeS. Type (A) inclusions have complex mineralogy, with pentlandite and pyrrhotite identified as main constituents. These inclusions typically feature a pyroxene-group mineral rim 100-150 nm thick, chemically identified as ferrosilite. The structural phases include both monoclinic (P21/c) and rhombohedral (Pbca) forms. The monoclinic phase also contains low concentrations of Ca, Mn, and Al. A layer of chalcopyrite, up to 100 nm thick, is often present between the rim and the sulfide phase, with rare hercynite domains (Fig. 2). Another spinel mineral, magnetite, is found as domains up to 500 nm within pentlandite. Hercynite additionally contains low levels of Ti, Cr, and Zn, while magnetite contains chromium. Type (B) inclusions mainly consist of pyrrhotite, with pentlandite and chalcopyrite also present. Unlike type (A) inclusions, magnetite in type (B) inclusions is pure, without other elements. Native copper is also found in these inclusions.

Discussion and Conclusions: The presence of these sulfidic inclusions seems more consistent with the inclusion of (ultra)mafic magmatic rocks or their weathered products into tektite melt, rather than extraterrestrial material, supporting their similarity to sulfide inclusions found in terrestrial magmatic rocks [5, 6].

Acknowledgement: The study was carried out thanks to the support of the Czech Science Foundation project number GAČR 22-28249S. CzechNanoLab project LM2023051 funded by MEYS CR is gratefully acknowledged for the financial support of the measurements at LNSM Research Infrastructure.

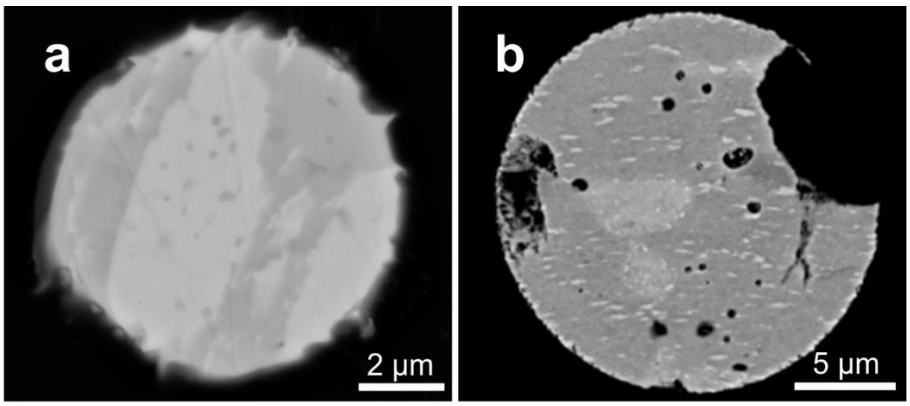


Figure 1: SEM micrographs of the sulfidic inclusions in the Muong Nong tektites.

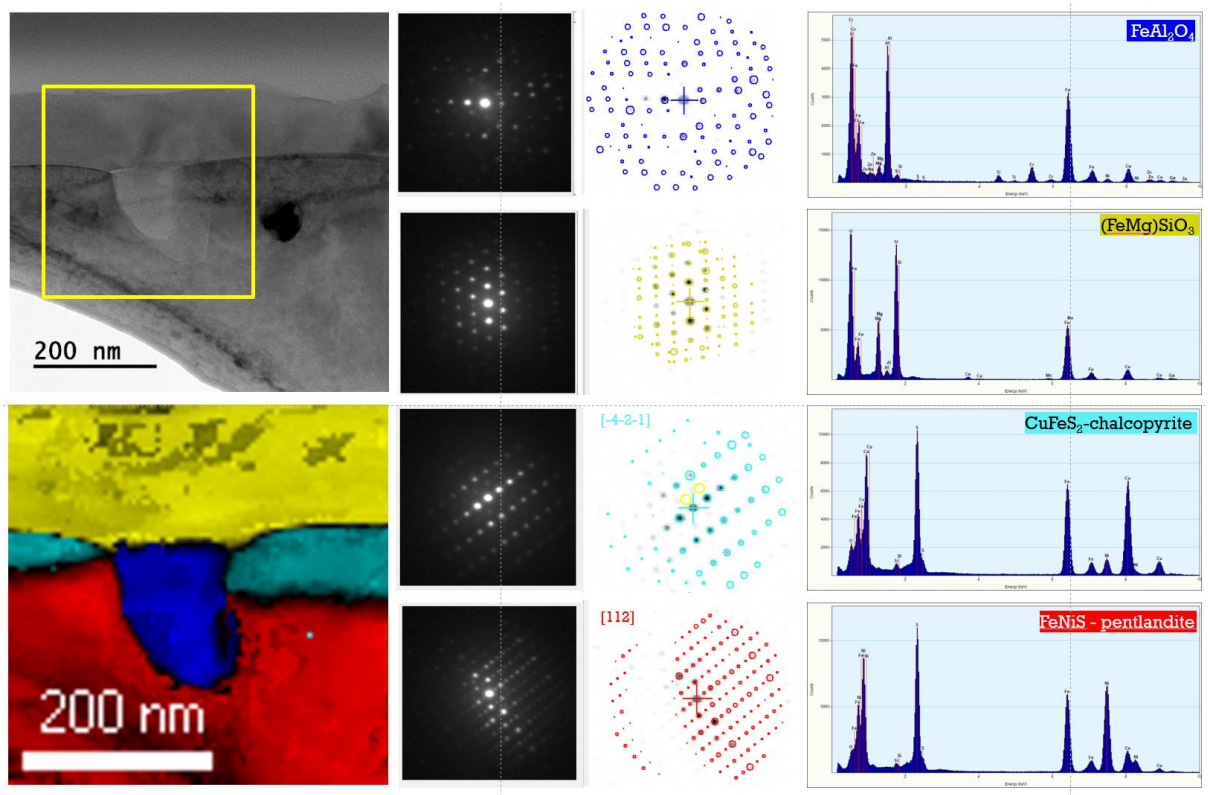


Figure 2: Phases present in the A-type inclusion determined by ACOM and EDX mapping..

References:

1. Rochette P. et al.: *Commun. Earth Environ.* **2021**, *2*, 94.
2. Koeberl C.: *Geological Society of America Special Paper* **1994**, *293*, 133-151.
3. Koeberl C. in *Treatise on Geochemistry*, eds. H. D. Holland & K. K. Turekian, **2014**, 133-151.
4. Lacroix A.: *Compt. Rend. Acad. Sci. Paris* **1935**, *200*, 2129.
5. Zelenski M. et al.: *Lithos* **2018** *318-319*, 14.
6. Georgatou M. et al.: *Solid Earth* **2020**, *11*, 1.

Type of presentation: Oral

MS1-O-4 Oxygen vacancy distribution in different regions of $La_{1-x}Sr_xGa_{1-y}Mg_yO_{3-\delta}$

Sergej Ražnjević[a,b], Sandra Drev[b], Vinko Sršan[b], Matthäus Siebenhofer[c], Christin Böhme[c], Sašo Šturm[b], Miran Čeh[b], Markus Kubicek[c], Zaoli Zhang[a]

[a]*Erich Schmid Institute of Materials Science, Austria*

[b]*Jožef Stefan Institute, Slovenia*

[c]*Institute of Chemical Technologies and Analytics, Austria*

Contact email: Sergej.Raznjevic@ijs.si

Solid Oxide Fuel Cells are an efficient energy conversion technology with a reduced environmental impact compared to fossil fuels. However, their high operating temperatures (approximately 1000 °C) present challenges, including material degradation and elevated costs. To overcome these issues, operating temperatures must be lowered to the intermediate range (500 to 800 °C), necessitating the development of suitable electrolyte materials. Among these, lanthanum gallate with strontium and magnesium doping (LSGM) has shown promise due to its high ionic conductivity. However, excessive doping can cause vacancy clustering, which impairs oxygen ion transport, especially at lower temperatures.

In this study, we analyze the structure of LSGM single crystals using X-ray diffraction and transmission electron microscopy. X-ray diffraction results indicate the presence of multiple domains with varying lattice parameters. High-resolution transmission electron microscopy and integrated differential phase contrast imaging reveal two distinct regions: one exhibiting 90° symmetry and another with non-90° symmetry. Moreover, oxygen vacancies appear ordered in the non-90° region, whereas they are randomly distributed in the 90° region. Energy-dispersive X-ray spectroscopy confirms that doping level variations between these regions remain within detectability limits. However, electron energy loss near-edge structure analysis reveals noticeable differences in bonding characteristics.

Type of presentation: Poster

MS1-P-1 Understanding the formation mechanism of growth-type planar defects in natural and synthesized perovskites based on STEM analyses

Nina Daneu[a], Petruša Borštnar[a], Marjeta Maček Kržmanc[a]

[a]*Department for Advanced Materials, Jožef Stefan Institute, Jamova 39, 1000 Ljubljana, Slovenia*

Contact email: nina.daneu@ijs.si

Perovskites occur as natural minerals in a wide variety of parageneses with complex chemical composition, and are even more important as functional materials with a wide range of interesting properties. Their crystal structure based on the ABO_3 formula is flexible and can be modified by changing the A:B ion size ratio and doping. Besides, the formation of crystallographic planar (2D) defects inside the perovskite matrix is common. One of the most interesting are defects that form during crystal growth (growth-type defects) like Ruddlesden-Popper (RP)-type defects and twin boundaries. They have significant influence on crystal growth, crystal morphology and consequently the properties of functional materials. They are characterised by different local structure and chemical composition in comparison to the matrix phase. In this contribution we will show that the knowledge about the local atomic structure and chemical composition of the planar defects resolved by scanning transmission electron microscopy imaging and spectroscopy techniques is important for understanding the formation mechanism.

The first example are **chemically-induced RP-type defects** in $Li_{3x}La_{2/3-x}TiO_3$ (LLTO) based ceramics with high ionic conductivity. Their formation is triggered by small excess addition of Li and La. This shifts the phase balance slightly towards the $Li_2La_2Ti_3O_{10}$ phase with layered structure. As a consequence, planar defects with the crystal structure related to this phase form inside the matrix LTO grains In the beginning of crystal growth, which accelerate the growth of the matrix perovskite grains and as a result, ceramics with coarse-grained microstructure is formed.[1] Quantitative STEM of the defects at different stages of the recrystallization process was used to understand their formation mechanism and influence on microstructure development and functional properties of the LLTO-based ceramics.[2]

The second example that will be presented are **recrystallization-type single atomic layers** in $SrTiO_3$ (STO) platelets prepared by topochemical recrystallization from $Bi_4Ti_3O_{12}$ (BIT) precursors during hydrothermal synthesis. The recrystallized STO platelets contain a single atomic Bi-rich layers running along the central part of the platelets parallel to their longer sides. The formation of these Bi-rich layers was reconstructed based on STEM analyses of the STO-BIT composite crystals at different stages of recrystallization.

The third example are **nucleation-type twin boundaries** in interpenetration twins of loparite-Ce, a naturally occurring perovskite with complex chemical composition. STEM analyses of twin boundary contacts along the primary (111) plane and secondary {120} planes are characterised by the presence of subnanometer thin amorphous Si-layer and resemble general grain boundaries. Based on this, we concluded that the interpenetration twin formed during the nucleation stage.

References:

1 Borštnar et al. *J.Eur.Ceram.Soc.* (2023) 43,1017-1027.

2 Borštnar et al. *ACS Nano* (2024) 18, 10850-10862.

3. Maček Kržmanc et al. *ACS Appl. Mater. Interfaces* (2021) 13, 370−3814.

4. Čontala et al. Nanoscale Adv. (2023) 5, 3005.

Acknowledgement: Funding by Slovenian research and innovation agency within fundamental research project J1-3025 and by M-ERA.NET project HetCat is gratefully acknowledged.

Type of presentation: Poster

MS1-P-2 Enhanced Analysis of Relative Thickness on TEM Samples

Drev Sandra[a], Tara Gudžulić[a], Čeh Miran[a,b]

[a]*Center for Electron Microscopy and Microanalysis, Ljubljana, Slovenia*

[b]*Department for Nanostructured Materials, Jožef Stefan Institute, Ljubljana, Slovenia & Jožef Stefan International Postgraduate School, Ljubljana, Slovenia*

Contact email: sandra.drev@ijs.si

Introduction: Sample preparation methods are crucial in transmission electron microscopy (TEM). The emergence of new materials, such as ceramics, thin films, and composites, introduces unique properties that require precise treatment and often post-treatment. This presents ongoing challenges, necessitating continuous adjustments and improvements in advanced TEM preparation techniques like focused ion beam (FIB) sample preparation and conventional sample preparation.
Methods: In this comparison, we examine the most common TEM sample preparation techniques to date: conventional and focused ion beam sample preparation. The sample for the analysis was a dissimilar Al alloy produced by single-pass friction stir welding (FSW). To achieve optimal results for further advanced STEM analysis, samples prepared with both techniques were subsequently treated using the NanoMill® (model 1040, Fischione Instruments, Inc.). Finally, the sample quality was controlled with an EELS relative thickness map and STEM analysis using Spectra 300 Cs S-CORR probe corrected scanning electron microscope at the Center for Electro Microscopy and Microanalysis (JSI, Ljubljana, Slovenia).
Results: The first TEM sample (Al1_fib) was prepared using the FEI Helios NanoLab dual-beam Focused Ion Beam (FIB) system. This sample underwent final treatment (thinning and cleaning) with the NanoMill under specific conditions convenient for FIB-prepared samples. The next TEM sample (Al1_con) was prepared conventionally. The sample was thinned and dimpled down to a transparent thickness using a Dimple Grinder (Gatan Inc.) and then ion-milled with a Precision Ion Polishing System (PIPS, Gatan Inc.) to achieve perforation. The sample was finally treated with the NanoMill under specific conditions convenient for conventional sample preparation.
Conclusion: We aim to emphasize the significance of selecting the appropriate technique and conditions for TEM sample preparation.

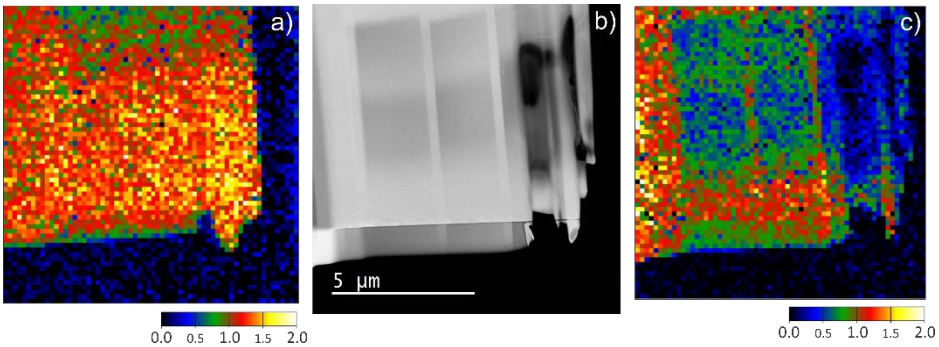


Figure 1: (a) Untreated and (b,c) treated FIB sample using NanoMill. *Scale bar indicating the thickness of the sample from 0-200nm.*

Reference:
1. R. Seidl, Specimen Preparation for Transmission Electron Microscopy by Focused Ion Beam: Refinement of Post-Treatment using Focused Low Energy Argon Ion Milling, Master's thesis, 2016.

Type of presentation: Poster

MS1-P-3 Crystal structure of wulfenite crystals from Mežica analysed by SEM-FIB and TEM

Gračanin Nik[a,b], Podlogar Matejka[b], Semsari Parapari Sorour[b], Ruiz-Zepeda Francisco[c], Šturm Sašo[b], Rogan Šmuc Nastja[a]

[a]*University of Ljubljana, Faculty for Natural Sciences and Engineering, (Ljubljana), Slovenia*

[b]*Institute Jožef Stefan, (Ljubljana), Slovenia*

[c]*National Institute of Chemistry, (Ljubljana), Slovenia*

Contact email: nik.gracanin@ijs.si

Introduction

Wulfenite ($PbMoO_4$) is a tetragonal scheelite-type mineral known for its varied external morphology, particularly bipyramidal {101} and tabular {001} crystal forms observed in specimens from Mežica lead-zinc mine[1]. This variation may indicate internal defects, such as twinning or ion substitutions[2]. The study focused on characterizing microscopic inclusions in wulfenite crystals through SEM-EDS and identifying lattice defects and chemical composition at atomic resolution via FIB-SEM for subsequent TEM analysis to propose a model of wulfenite crystal growth in Mežica mine.

Methods

Bipyramidal and tabular specimens were indexed based on external morphology for SEM-EDS and TEM analysis along the zone axis (image 1 (a)). Each specimen was cross-sectioned, embedded in epoxy resin, and coated with a 3 nm carbon layer prior to analysis with a Thermo Fisher Quanta 650 ESEM and Oxford Ultim Max SSD 40 mm² EDS system. Two lamellae, one from each crystal type, were prepared using standard SEM-FIB techniques and analyzed via JEOL JEM-ARM 200CF with STEM-EDS and HAADF techniques.

Results

Cross-sectional analysis revealed numerous inclusions, primarily carbonate minerals, distributed in layers or clusters, especially in the central regions of bipyramidal crystals (image 1 (b)). STEM-EDS analysis indicated uniform distribution of Mo, Pb, and O, with no detected impurities or substitutions. High and low magnification HAADF STEM images displayed an atomic model and associated lattice spacing (image 1 (c)).

Discussion and Conclusions

SEM-EDXS confirmed multiple carbonate inclusions in layered or clustered arrangements. TEM analyses showed no lattice defects, twinning, or substitutions in either crystal mprhology, suggesting that the internal structure does not account for the differing external crystal morphologies of Mežica wulfenites. The presence of carbonate inclusions, which form layers or bands indicates a potential abrupt change in chemical composition during wulfenite precipitation, thereby influencing crystal morphology.

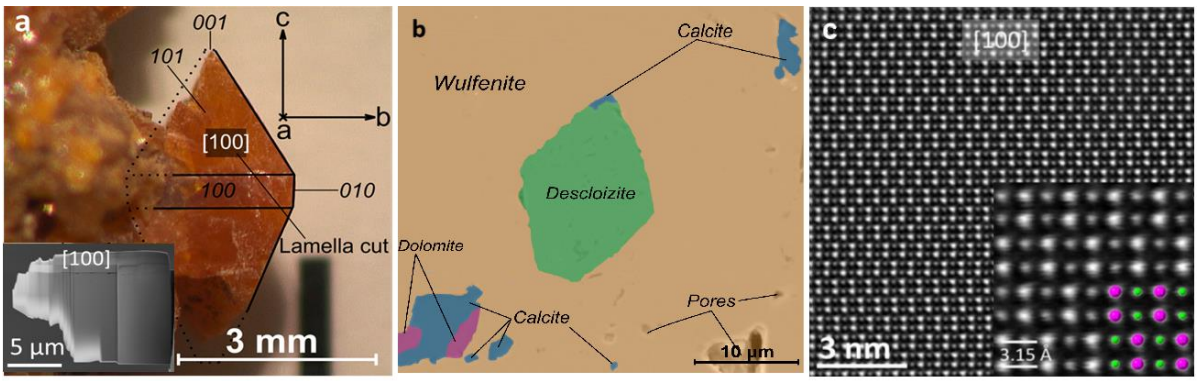


Figure 1: (a) Bipyramidal crystal with indexed surfaces, showing lamella cut area. SEM micrograph on the lamella in the bottom left. (b) Color-coded SEM image of wulfenite inclusions made with data from EDS. Vanadium-rich mineral descloisite is in the center, which is also seldomly present as inclusion in the wulfenites of Mežica. (c) HAADF-STEM Z-contrast image [100] together higher resolution image in the bottom right corner with superimposed atomic model and lattice spacing.

References:

1. I. Cora, M. Czugler, I. Dódony, A. Rečnik, *Acta Crystallographica Section C: Crystal Structure Communications.* **2011**, *67*, 33-35.
2. A. Rečnik, J. Zavašnik, S. Fajmut-Štrucl, *The Mežica mine, Koroška (Slovenia).* **2014**, Mineralogical record.

Type of presentation: Poster

MS1-P-4 Effect of pretreatment and organic fibre reinforcement on the mechanical and microstructural properties of microwave irradiated alkali-activated radioactive fly ash

Barbara Horvat[a], Nadja Železnik[a], Lara Petrič[b], Sara Tominc[c]

[a]*Milan Vidmar Electric Power Research Institute, (Ljubljana), Slovenia*

[b]*Biotechnical Faculty, University of Ljubljana, (Ljubljana), Slovenia*

[c]*Slovenian National Building and Civil Engineering Institute, (Ljubljana), Slovenia*

Contact email: barbara.horvat@eimv.si

Introduction: Conventional building and civil engineering materials (Figure 1) exert a significant strain on the environment: (i) they account for more than 40% of human-made carbon footprint, (ii) the annual consumption of the raw materials can be approximated by 2/3 of Mount Everest, (iii) the embodied energy of inorganic building materials is higher than for consumer goods because of the substantial energy required for their production (temperatures exceeding 1000 °C) and the large quantities needed for construction. Alternatives that would decrease the negative impact of the building materials available on the market are usually weaker in performance, not long-term tested in real life, or have even other drawbacks: availability and chemical consistency of the material is not permanent, and the presence of hazardous and even radioactive elements is concerning.

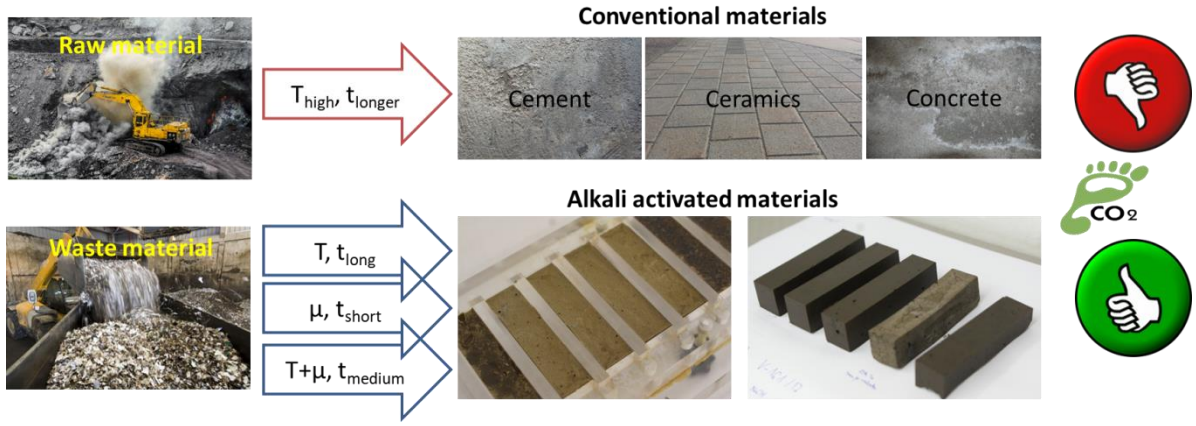


Figure 1: Alkali-activated materials are a potential replacement for the traditional building industry materials, but should not represent health or environmental issues, and should have acceptable mechanical properties.

One of the alternative materials for building industry products is alkali activated materials (AAMs). They do not require natural raw materials as an ingredient, but can be made by using solely secondary raw materials that contain enough Si and Al in an amorphous state, which dissolve and react with alkali in liquid media at temperatures below 100 °C. One of the sources can be ash, also fly ash (FA), which contains a significant amount of cellulose due to the incomplete combustion. As cellulose naturally degrades over time, this can also lead to the deterioration of the entire product in the building industry product.

Methods: FA (Figure 2) was therefore pretreated either (i) by sieving, (ii) by milling and sieving, or (iii) by exposure to elevated temperatures, before mixing with alkali silicate solution to form AAM. FA (as received and pretreated) was chemically analysed to gain insight into the presence of hazardous and radioactive materials to avoid problems with the AAM before it was even made. With the desire to gain as high compressive strength as possible, freshly mixed and moulded ingredients were additionally exposed to low-power microwave irradiation and compared to their non-irradiated counterparts to evaluate the benefits of the irradiation. With the aim of increasing bending strength, organic fibres were

added to the FA, the dry mixture was thoroughly homogenised and then activated with a Na-silicate solution. The organic fibres were hollow winter dog coat hairs (without split ends or other vertical splits of the hair), genetically analysed and collected from intact animals during their natural coat shedding. The selected breeds, (i) Chesapeake Bay Retriever (CBR, Figure 2), (ii) Curly Coated Retriever (CCR), and (iii) Nova Scotia Duck Tolling Retriever (NSDTR), were chosen for their natural waterwork-functionality coats. The quality of embedment of fibres in the AAM (Figure 2) was evaluated using a scanning electron microscope (SEM, Jeol JSM-IT500) under low-vacuum conditions at an accelerating voltage of 20 kV, examining cross-sections in the undamaged regions of the samples after destructive mechanical strength testing.

Results: After removing the cellulose from the FA, either by sieving below 200 µm or by heat treatment at 550 °C, the compressive strength was highest among the samples (above 60 MPa, which is 20% more than AAM from intact FA), and the sieved radionuclide-free sample behaved as if it was transparent to microwave irradiation, as no effect on compressive strength was observed. While the bending and compressive strength increased with the addition of 1 mass percentage of organic fibres to milled and sieved FA below 125 µm (above 65 MPa when fibre was from the CBR), a clear increase in compressive strength occurred after microwave irradiation (especially in the case of the CCR and NSDTR fibres, where the CCR fibre almost reached the value of the non-irradiated CBR fibre). While SEM analysis of the pretreated FA exposed the samples with present/removed cellulose (smaller fractions were cellulose-free, as well as FA treated at 550 °C or higher), a strong bond between the organic fibre and the aluminosilicate network of AAM was indicated by sharp longitudinal and vertical splitting of the fibres after mechanical testing: it was easier to split the dog hair in half than to break the bond between dog hair and the aluminosilicate network.

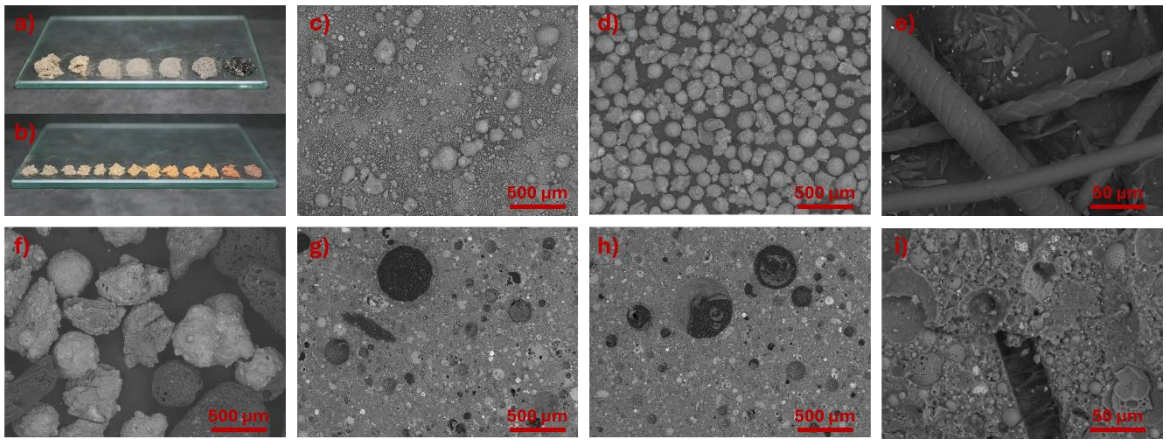


Figure 2: Photograph of a) fractions of sieved FA (smaller to bigger) and b) thermally treated FA (from lower to higher T). Micrographs of: c) intact FA, d) FA fraction below 125 µm, e) CBR fibres, f) FA fraction above 400 µm, g) AAM from intact FA, h) AAM from FA sieved below 125 µm, i) CBR fibre in AAM after mechanical strength measurement.

Discussion and conclusions: While the separation of radionuclides in the naturally occurring radioactive materials (FA) has to be additionally evaluated and proven, stronger adhesion between organic fibres and the aluminosilicate network compared to the fibre's own internal cohesion was not expected. The stronger compressive strength after irradiation in the case of the fibre-reinforced samples is attributed to the natural oils on the hair surface, which are not transparent to microwaves. As a result, these oils absorb microwave energy, which leads to localised heating that enhances dissolution and subsequent matrix formation in their vicinity. During the "gelation" process, the fibre-matrix bond is strengthened, which contributes to the improved mechanical properties.

Acknowledgments: This study is part of Dr. Barbara Horvat's ARIS project and was financially supported by the Slovenian Research Agency under Grant No. J2-3035. The present study was performed at the Slovenian National Building and Civil Engineering Institute while Dr Horvat was still employed there, for which Dr. Horvat is thankful.

Type of presentation: Poster

MS1-P-5 Microwave-irradiated alkali-activated extraterrestrial simulants

Barbara Horvat[a], Sara Tominc[b]

[a]*Milan Vidmar Electric Power Research Institute, (Ljubljana), Slovenia*

[b]*Slovenian National Building and Civil Engineering Institute, (Ljubljana), Slovenia*

Contact email: barbara.horvat@eimv.si

Introduction: With increasing interest in space travel, not only for exploration but also for resource extraction, to address Earth's growing consumption of (critical) raw materials, and to relocate environmentally demanding industries off-planet, sustainable construction on extraterrestrial surfaces will be crucial. With the aim of reducing dependence on Earth-based resources and supporting the long-term space exploration and habitation, alkali activation of regoliths enables in-situ resource utilisation (ISRU). In addition, alkali-activated materials have the potential for enhanced radiation shielding, high mechanical performance, lower energy requirements for production, minimised water consumption, and adaptability to various extraterrestrial regolith types, making them a promising solution for future space infrastructure.

Methods: For a preliminary assessment of the potential of regolith to be successfully "geopolymerised", Martian, Lunar, and Asteroidal planetary simulants were milled and sieved below 250 μm before being subjected to alkali activation. The extraterrestrial simulants acquired from Space Resource Technologies were "Carbonaceous chondrite (CM-E) High-Fidelity Asteroid Simulant" (*labelled A-2*), "Mars Global Hydrated Clay (MGS-1C) Martian Dirt Simulant" (*labelled M-2*), and "Lunar Mare (LMS-1) High-Fidelity Moon Dirt Simulant" (*labelled L-2*). A sodium silicate solution was used as the activator in the experimentally determined ratio to the pulverised material to ensure a slurry consistency that was neither too liquid, which could lead to buoyancy and settling of the particles, nor too stiff, which would hinder workability and shaping. The final mass ratios between solid and liquid were chosen as follows: 100:60 for A-2, 100:70 for M-2, and 100:30 for L-2. The ingredients were mixed for 1 minute at up to 1000 rpm, moulded in silicone-rubber moulds, and immediately (i) irradiated with microwaves at 100 W for 2 minutes before being treated at 80 °C for 20 hours, or immediately (ii) treated at 80 °C for 20 hours. After heat treatment, samples were cooled down at room temperature for 4 hours.
The physicochemical transformation of the planetary simulants into "geopolymeric" materials was evaluated by monitoring the curing time together with the behaviour of the slurry. The mechanical strength of the 24-hour-old cured samples was measured to assess the material's durability. Additionally, the microstructure of the original powders and cross-sections in the undamaged regions of the alkali-activated samples was analysed after the destructive mechanical strength test. For the microscopic analysis, the samples were not coated, as the scanning electron microscope (SEM, Jeol JSM-IT500) was used under low-vacuum conditions at an accelerating voltage of 20 kV.

Results: While the compressive strength of simulants A-2 and M-2 increased by more than 100% when the slurry was irradiated with microwaves, the effect was the opposite for L-2. Among all the samples, only M-2 behaved like it is not-from-this-planet, because after mixing M-2 with sodium silicate solution, the semi-liquid slurry completely hardened in 2-3 minutes at room conditions. While many alkali-activated materials dissolve in water, the hardened M-2 "geopolymer" did not. The reaction was so rapid and permanent that removing alkali-activated M-2 from the beaker was impossible.
While the alkali-activated asteroidal regolith simulant A-2 exhibited larger cracks (Figure 1) that negatively impacted mechanical strength, the alkali-activated Martian regolith simulant M-2 had smaller, shapeless pores caused by the rapid reaction that did not allow dissolution of the slowly dissolving parts of M-2 and resulted in an incomplete bonding of the material throughout the entire volume, leading to weaker overall structural integrity. In contrast to A-2 and M-2, the alkali-activated Lunar regolith simulant L-2 had fewer pores but had large areas of excessive sodium content, which can lead to efflorescence and deterioration of the materials.

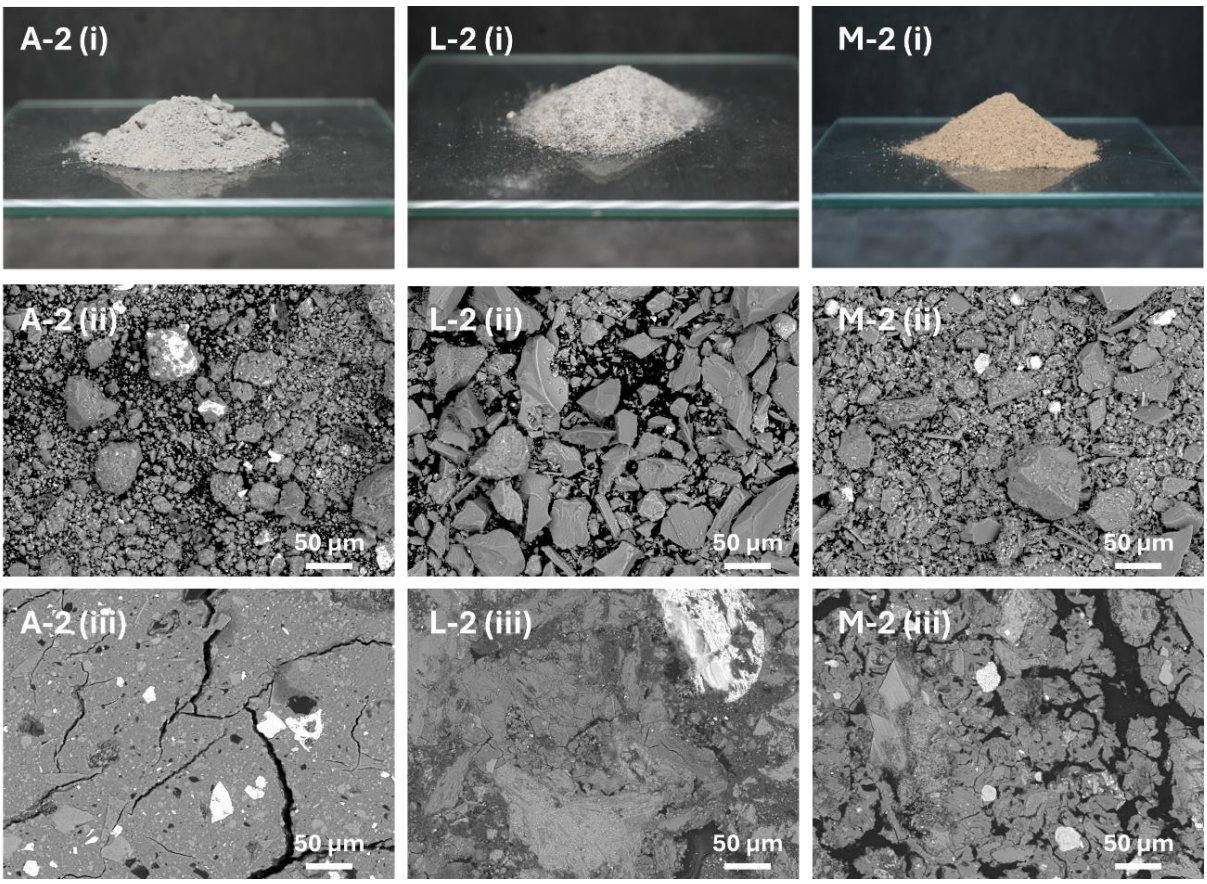


Figure 1: (i) Photograph and (ii) SEM micrograph of regolith simulants A-2, L-2 and M-2, and their (iii) alkali-activated counterparts.

Discussion and conclusions: All three extraterrestrial regolith simulants exhibited unique advantages, with the Martian simulant standing out due to its extremely rapid reaction at room conditions. However, a combination of different materials will be necessary, with each contributing its beneficial properties while also helping to compensate for the limitations of other materials in the mixture.

Acknowledgments: This study is part of Dr. Barbara Horvat's ARIS project and was financially supported by the Slovenian Research Agency under Grant No. J2-3035. The present study was performed at the Slovenian National Building and Civil Engineering Institute while Dr Horvat was still employed there, for which Dr. Horvat is thankful. Dr Horvat also thanks the Milan Vidmar Electric Power Research Institute for offering peer review, proofreading, and evaluation of the work by the committee.

Type of presentation: Poster

MS1-P-6 Transmission electron microscopy of hypomineralized enamel apatite nanocrystals

Viktória K. Kis[a], Máté Hegedűs[b], Lívia Vásárhelyi[c], Ákos Kukovecz[c], Levente Illés[a], Noémi Szász[a], Éva Mlinkó[d], Noémi Katinka Rózsa[d], Zsolt Kovács[b]

[a]*HUN-REN Centre for Energy Research, Budapest, Hungary*

[b]*Department of Materials Physics, Eötvös Loránd University, Budapest,*

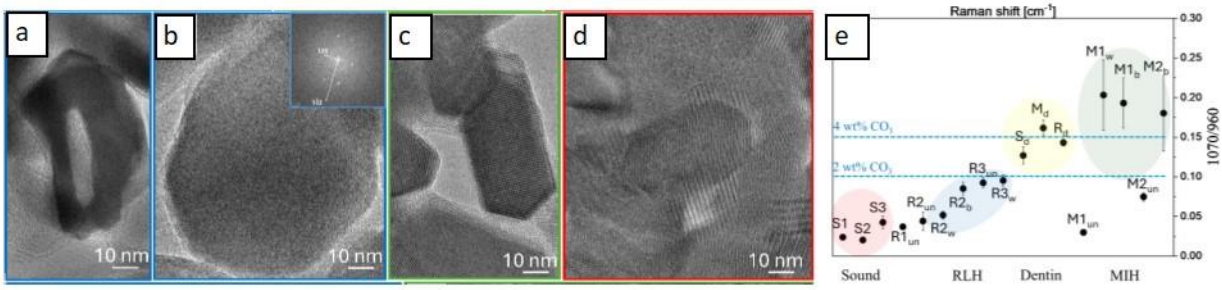
[c]*Hungary Interdisciplinary Excellence Centre, Department of Applied and Environmental Chemistry, University of Szeged, Szeged, Hungary*

[d]*Department of Pedodontics and Orthodontics, Faculty of Dentistry, Semmelweis University, Budapest, Hungary*

Contact email: kis.viktoria@ek.hun-ren.hu

Human dental enamel is a uniquely hard and tough biological structure build up by inherently brittle apatite nanocrystals. In sound enamel, mechanical properties are organically fine-tuned by nanoscale changes of enamel apatite crystal chemistry as function of anatomical position. However, developmental disorders – such as hypomineralization - often lead to severe enamel alterations resulting in weaker mechanical performance and shorter lifetime as in case of molar-incisor hypomineralization (MIH) which has a global prevalence of 13.5 %. Background of the development of hypomineralization disorder is still not completely understood and it is an intensively investigated research topic. Recently we have reported a new form of dental hypomineralization for the first time [1]. Structural and chemical alterations of dental enamel exhibiting this special ribbon-like hypomineralization (RLH) are compared to the characteristics of sound and MIH-affected teeth. Microporosity, mineral density and characteristic 3D macroscopic shape of the RLH affected volumes were captured by micro-CT analysis. These RLH specific features are coupled with a particular chemical fingerprint in Raman spectroscopy, which allows its clear separation from MIH affected and sound enamel. In this contribution, we present a comparative transmission electron microscopy study of enamel apatite nanocrystals from hypomineralized enamel samples showing markedly different Raman spectra (Figure 1). Based on these nanostructural features we conclude different failure mechanisms in the biochemical control during crystallization of the RLH and MIH enamel.

[1] Hegedűs, M, Kovács, Zs., Vásárhelyi, L., Kukovecz, Á., Illés, L., Szász, N., Mlinkó, É., Rózsa, N.K., Kis, V.K.: Ribbon-like hypomineralization in human dental enamel. Acta Biomaterialia 196 (2025) 281–292. https://doi.org/10.1016/j.actbio.2025.02.064.



Type of presentation: Poster

MS1-P-7 Ex-situ differential individual particle analysis of various Pb, Zn and Fe ore minerals after periodical leaching in soil column experiments

Saša Kos[a], Nina Zupančič[b,c], Miloš Miler[d]

[a]*"Jožef Stefan" Institute, (Ljubljana), Slovenia*

[b]*Faculty of natural sciences and technology, University of Ljubljana, (Ljubljana), Slovenia*

[c]*Ivan Rakovec Institute for Palaeontology, (Ljubljana), Slovenia*

[d]*Geological survey of Slovenia, (Ljubljana), Slovenia*

Contact email: sasa.kos@ijs.si

The ex-situ differential individual particle analysis [1] was used to understand the microchemical and micromorphological changes of several Pb minerals (PbS, $PbSO_4$ and PbO_2) along with Zn and Fe sulfides (ZnS, FeS_2) in soils under laboratory conditions. Soil column experiments were performed with the aim of understanding the migration and transformation behaviour of minerals in semi-natural conditions.

Naturally occurring and uncontaminated soils were used for experiments. Soils were characterized using pedological parameters, XRD, ICP-MS and SEM/EDS. Ore minerals (PbS, ZnS, and FeS_2) and synthetic materials ($PbSO_4$ and PbO_2) were prepared mechanically via grinding and sieving under 32 μm. Initial material characteristics were determined before the experiment using ICP-MS, XRD, SEM/EDS and laser granulometry. Materials were then exposed in soil columns, which were leached weekly with ultrapure water over a period of one year and the physico-chemical parameters of the leachates were measured simultaneously. After completing the experiment, the exposed particles were collected from soil by gravity separation with bromoform and prepared for individual particle analysis by SEM/EDS. The microchemical and micromorphological characteristics of the exposed minerals were determined.

Compared to primary characteristics of mineral particles, PbS and $PbSO_4$ underwent the most intense morphological changes due to oxidation and consequent dissolution of particles throughout the soil column. Meanwhile, PbO_2 remained mostly unchanged under oxidizing and alkaline conditions. Secondary Pb carbonate crystals (hydrocerussite) were found in oxidized zones and formed due to PbO_2 reaction to soil pCO_2. Exposure of ZnS and FeS_2 showed negligible chemical and morphological changes in soil. Reducing conditions in soils affected the partial dissolution of PbO_2 and secondary Pb carbonate. Secondary nanocrystalline PbS coatings were also found in reduced zones of soils. The formation was facilitated by local low oxygen levels, neutral to alkaline pH, presence of sufficient sulphate and Pb ions in soil pore water and naturally present sulfate-reducing bacteria.

The microchemical and morphological transformations of selected materials found in laboratory experiments showed similarities to minerals in natural conditions in environment. However, oxidation processes of sulfides show, galena was most consumed during the experiment, which is in contrast to oxidation processes in natural environments where pyrite shows highest oxidation rates. Further investigation of surface transformations of particles using different microanalytical tools should be done for more comprehensive understanding of microchemical characteristics of particles.

References:

1. A. Hunt, D.L. Johnson, *J. Environ. Qual.* **2011**, 40(3), 742-750.

Type of presentation: Poster

MS1-P-8 Multidisciplinary Application of Scanning Electron Microscopy (SEM) in Heritage Research, Conservation and Presentation at the Croatian Natural History Museum

Snježana Mikulčić Pavlaković[a], Iva Mihoci[a], Tatjana Vlahović[a], Marin Šoufek[a]

[a]*Croatian Natural History Museum, (Zagreb), Croatia*

Contact email: snjezana.mikulcic@hpm.hr

Introduction

Scanning Electron Microscopy (SEM) has emerged as a pivotal tool in heritage research, offering unparalleled insights into the microstructural and compositional characteristics of natural history specimens. This presentation explores the multidisciplinary application of SEM in the study and preservation of geological and biological collections within the Croatian Natural History Museum. By leveraging SEM's high and low vacuum imaging and energy-dispersive X-ray spectroscopy (EDS), we can uncover intricate details about the composition, structure and morphology of minerals, fossils and biological specimens.

Methods

Specimens were studied using Tescan Vega GMU Scanning Electron Microscope (SEM) (Fig. 1), equipped with Energy Dispersive X-ray spectrometer (EDS) suitable for imaging and analysis of biological and geological materials. Some non-conductive samples were coated with gold.

Results

Several geological samples were analysed revealing their micromorphology and stability of mineral phases. Sulphide minerals from Trepča/Stari Trg mine (Kosovo), especially pyrite (FeS_2) often showed products of oxidation on the mineral surface indicating early signs of decay, important for evaluation of conservation treatments and preservation of the specimen. Perfectly developed galena (PbS) crystals (Fig. 2a) showed their pseudotetragonal symmetry, uncommon, considering it is a cubic mineral. A recent study suggested that the oriented growth of boulangerite needles with galena (Fig.2b) contributes to the unusual galena crystal morphology [1]. Conodont fauna (Fig. 2c) indicated Middle Triassic age (Anisian-Ladinian boundary interval) of the marine reptile discovered in limestone of Žumberak Mt. (Vlašić brdo) in Croatia [2]. SEM imaging of biological samples such as insects' body parts, lepidopteran wing scales or antennae (Fig 2d, e) and lycopodium spores (Fig 2f) revealed amazing details in their microstructure.

Discussion and conclusions

This research underscores the importance of SEM in advancing our understanding of natural history heritage and enhancing conservation practices, specifically in the realms of mineralogy/petrography, palaeontology, zoology and botany, within the unique context of the Croatian Natural History Museum. An important aspect of this research is its integration into museum exhibitions, which not only showcase cutting-edge research but also underscore the importance of preserving our planet's biological and geological heritage for future generations.

Acknowledgments

SEM was cofinanced by the European Regional Development Fund and the City of Zagreb within the project "Guardian of Heritage as a Catalyst for Development, Research, and Learning – new Croatian Natural History Museum"

References
1. V. Zebec, Trepča/Stari Trg – monography, *Croatian Natural History Museum & University of Zagreb*, **2012.**
2. F. Vidaković, Master thesis, *Faculty of Science, University of Zagreb*, **2024.**



Figure 1. SEM equipped with EDS detector at the laboratory of the Croatian Natural History Museum.

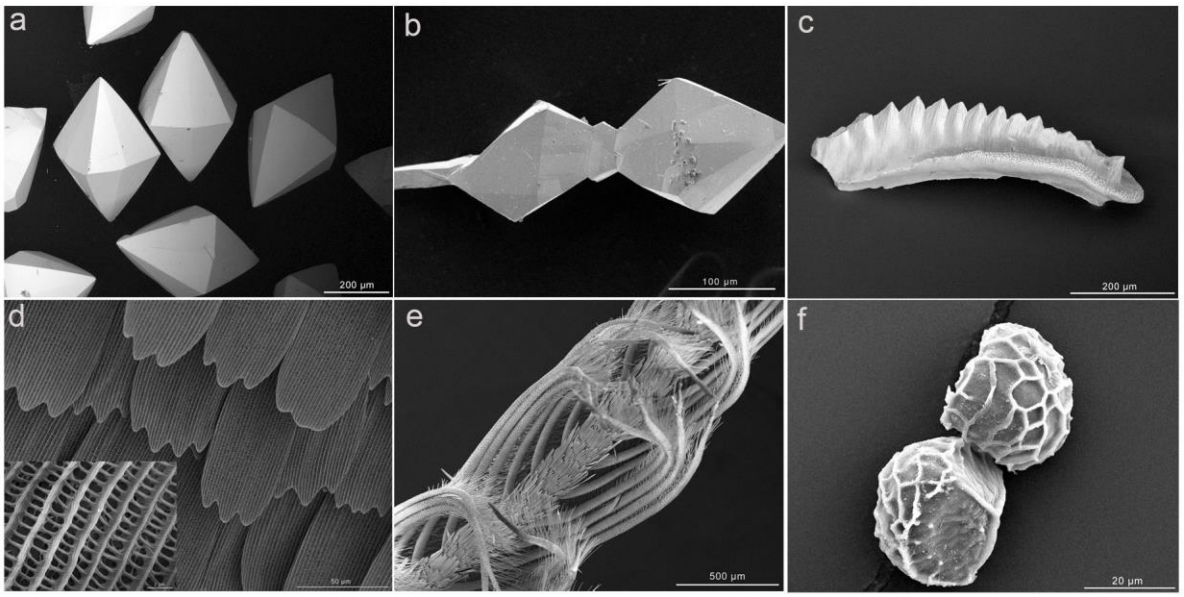


Figure 2. SEM-SE images of geological and biological samples. Pseudotetragonal galena crystals (a), oriented growth of galena and boulangerite needle (b), conodont fossil remains (c), lepidopteran wing scales (the large white *Pieris brassicae* (Linnaeus, 1758)) (d), geometrid moth's antennae (e), *Lycopodium annotinum* L. (f).

Type of presentation: Poster

MS1-P-9 Comprehensive study of Inversion Boundaries in ZnO

Vesna Ribić[a], Matej Komelj[a], Anton Kokalj[a], Zorica Branković[b], Goran Dražić[c], Matejka Podlogar[a], Goran Branković[b], Aleksander Rečnik[a]

[a] *Jožef Stefan Institute (Ljubljana), Slovenia*

[b] *Institute for Multidisciplinary Research (Belgrade), Serbia*

[c] *National Institute of Chemistry (Ljubljana), Slovenia*

Contact email: vesna.ribic@ijs.si

Introduction: Inversion boundaries (IBs) as chemically-induced planar defects, have drawn a lot of interest for their role as a crucial structural component in electron transport, phonon scattering and many other physical properties, which derive from their quantum-well structure. IBs in ZnO are currently known to be generated by the addition of certain dopants with higher oxidation states than Zn^{2+}, such as In^{3+}, Fe^{3+}, Mn^{3+}, Ga^{3+}, Si^{4+}, Sn^{4+}, Ti^{4+} and Sb^{5+}. The polar c-axis can be oriented head-to-head (h-h) or tail-to-tail (t-t) across the plane of inversion. They are mostly found as primary growth defects in basal planes (b-IBs) or as secondary defects in pyramidal planes (p-IBs), compensating t-t inversions in case of multiple parallel h-h b-IBs. Head-to-head *b*-IBs are the most frequent type of IBs, with IB-plane octahedral layer and an in-plane dopant distribution that follows the 3+ charge rule. With a broad range of dopants and variety translations, IBs in ZnO present an ideal model system for studying the formation mechanisms and stability of growth defects in crystals. Here, focus will be on IBs in Sb_2O_3- and SnO_2-doped ZnO, which exhibit unusual structural features that are associated with optoelectronic properties, phonon scattering, and electron transport. On the other hand, these two dopants represent the only two dopants that form h-h b-IBs in ZnO that have higher oxidation state than 3+, which is leading to partially occupied IB-layers in conjunction with octahedrally coordinated Zn^{2+}, which generates yet unexplored electronic states in the IB plane. The reported p-type and n-type conductivity of Sb_2O_3-doped and SnO_2-doped ZnO materials is highly promising for the production of p-n homojunctions. To fully understand the role of IBs in related physical phenomena, there are few structural issues that have to be resolved. These include identification of IB-translation state and local cation ordering.

Methods: Structure and chemistry of basal-plane IBs in Sb_2O_3-doped and SnO_2-doped ZnO ceramics were investigated by means of high-resolution transmission electron microscopy (HRTEM), high-angle annular dark-filed (HAADF) and annular bright filed (ABF) STEM methods to study the local structure, and energy dispersive X-ray spectroscopy (EDS) to determine the chemical composition of the IB-plane (Jeol 2010F and ARM). Experimental studies were complemented by structure modeling and density functional theory (DFT) calculations to identify low energy translation states and cation distributions in the IB-layer. DFT optimized structures were crosschecked by image simulations and matching.

Results: Quantitative HRTEM and DFT calculations were combined to solve local structures of IBs in Sb_2O_3-doped [1] and SnO_2-doped [2] ZnO. From observed stacking sequences in the originating wurtzite structure 5 hypothetical IB translations were derived, one of which, with Aβ−Bα−AβC−γA−αC (IB_2)

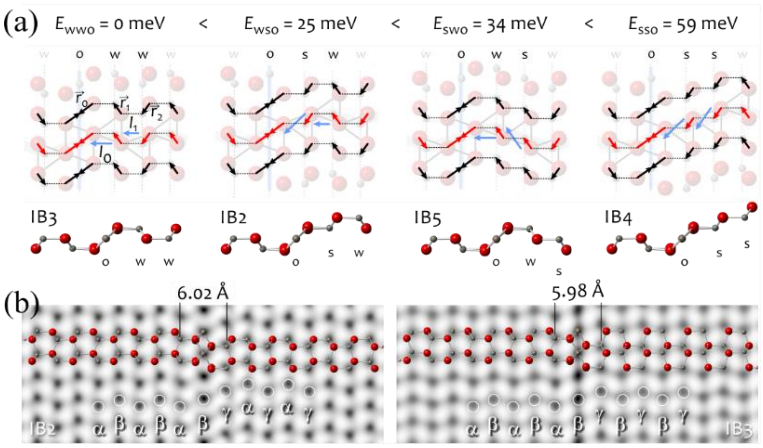


Fig. 1. Comparison of lowest energy IB models through structure vectors: (**a**) models with least cubic bonds are most stable. (**b**) Experimental HRTEM images of two types of IBs in Sb_2O_3-doped ZnO [1] with overlaid models IB_2 and IB_3.

Jeol 2010F

sequence, was previously reported for Sb-rich IB in ZnO, and as such it was expected to have the lowest total energy. Contrary to expectations, first principles calculations based on DFT, suggested that another model with Aβ−Bα−AβC−γB−βC (IB_3) sequence should be the most stable model for Sb-doped ZnO (Fig. 1). Unexpected outcome in calculations was also experimentally verified and it has been confirmed that the IB_3 structure is even more common than the reported IB_2. In addition to structure type, lattice expansions and local relaxations were accurately predicted by DFT. Combined theoretical/experimental approach has been shown to yield better than 1 pm accuracy in structure determination [1].

In Sn-rich IBs, on the other hand, only one translation state of was identified and that corresponds to the Aβ−Bα−AβC−γB−βC (IB_3) sequence, which is likely the only stable IB structure in SnO_2-doped ZnO. O atomic columns, that are readily resolved by ABF-STEM, confirm a head-to-head inversion mode and a stochastic distribution of Sn atoms in the IB-plane (Fig. 2) according to the Zn:Sn = 1:1 distribution of cations, as determined by EDS. Atomic-scale study of IBs in Sn-doped ZnO, showed a very unusual in-plane distribution of atoms that defies the logic of crystal structures; instead of striving for a perfect order, cations in the IB-plane seek to find a maximum disorder! This fascinating phenomenon is driven by two conditions that are enforced in this 2D confined geometry: the 6-fold in-plane symmetry of the octahedral close-packed layer and the local charge balance that must be maintained. As a result, Sn^{4+} and Zn^{2+} cations are randomly distributed to maximize the in-plane entropy [2].

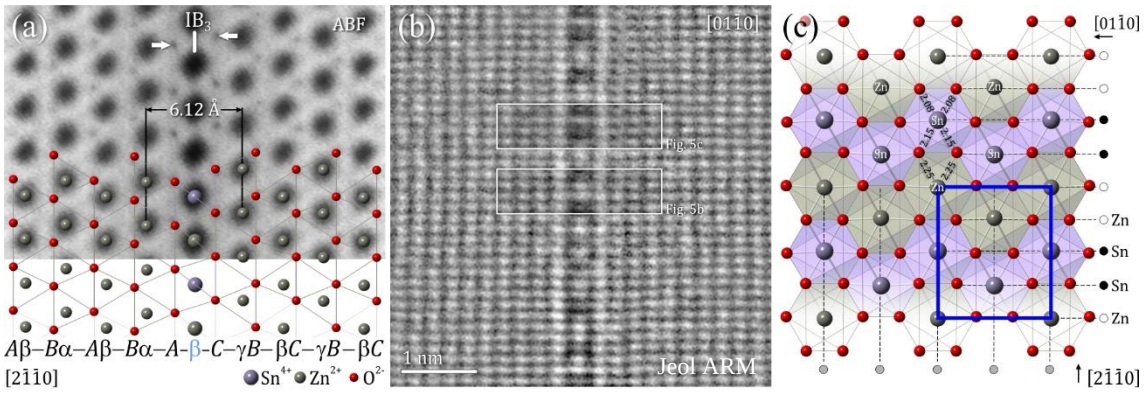


Fig. 2: Atomic structure of Sn-rich IBs in ZnO. (**a**) High-resolution ABF-STEM image of IB translation in [2$\bar{1}\bar{1}$0] projection with resolved O atoms (small black dots) enabling to determine coordination of cations, polarity and stacking. (**b**) IB cation distribution in [01$\bar{1}$0] projection suggesting different short-range ordering modes due to the Sn:Zn ratio of 1:1 fixed by charge balance. (**c**) Zigzag distribution of Sn and Zn atoms in IB-plane [2].

Discussion and conclusions: Combined theoretical and experimental methodology demonstrated in this study shows that the quantum-mechanical modeling of materials can be leveraged with the atomic-scale electron microscopy methods to retrieve fine structural details directly from the interfaces. Prediction of a new type of IBs in Sb-doped ZnO by DFT, that was subsequently experimentally confirmed, gives a

full credit to quantum chemical methods to forecast interface structures to better than ~1 pm accuracy. Determining atomistic structures with such a high confidence has a great potential of solving series of open questions related to their structural and physical properties, preferences why specific dopants form IBs and others do not, and what are the possible mechanisms of their formation.

Funding: This research was supported by ARIS postdoctoral project No. Z2-50056.

References:

1. V. Ribić, A. Rečnik, M. Komelj, A. Kokalj, Z. Branković, M. Zlatović, G. Branković, *Acta Materialia*, **2020**, 199, 633-648. DOI: 10.1016/j.actamat.2020.08.035
2. V. Ribić, A. Rečnik, G. Dražić, M. Podlogar, Z. Branković, G. Branković, *Science of Sintering*, **2021**, 53/2, 237-252. DOI: 10.2298/SOS2102237R

Type of presentation: Poster

MS1-P-10 Effects of Ti Doping on Structure, Microstructure and Mechanical Properties of $(K_{0.5}Na_{0.5})NbO_3$

Janina Roknić[a,b], Katarina Žiberna[a,b], Andraž Bradeško[a], Aljaž Drnovšek[c], Maja Koblar[a], Brigita Kmet[a], Silvo Drnovšek[a], Barbara Malič[a,b], Goran Dražić[d], Andreja Benčan Golob[a,b]

[a]*Electronic Ceramics Department, Jožef Stefan Institute, Ljubljana, Slovenia*

[b]*Jožef Stefan International Postgraduate School, Ljubljana, Slovenia*

[c]*Department of Thin Films and Surfaces, Jožef Stefan Institute, Ljubljana, Slovenia*

[d]*Department of Materials Chemistry, National Institute of Chemistry, Ljubljana, Slovenia*

Contact email: janina.roknic@ijs.si

The functional properties of potassium sodium niobate–based piezoelectrics $(K_{0.5}Na_{0.5})NbO_3$ - KNN, lead-free alternatives to traditional lead-based piezoelectrics, can be tuned through chemical doping, enabling broad application versatility. For example, the incorporation of acceptor dopants (such as Zr^{4+} and Ti^{4+}) induces hardening effects, as evidenced by a decrease in dielectric loss and an increase in the mechanical quality factor [1]. It also enhances densification, though observed grain refinement may arise from microstructural effects rather than doping itself. While studies provide valuable insights into the functional properties of acceptor-doped KNN ceramics, a comprehensive understanding of their microstructure, local structural features, defects and domain morphology remains limited. Additionally, the mechanical properties of these materials are not yet well understood. Therefore, the aim of this work is to investigate in detail the influence of TiO_2, as an acceptor dopant, on the microstructural and structural characteristics of KNN, along with mechanical property measurements.

KNN powders with 0.1-1 mole % of TiO_2 were prepared by conventional solid-state synthesis. The powder compacts were isostatically pressed and sintered at 1120 °C (KNN) and 1100 °C (Ti-doped KNN) for 2 hours in air. For scanning electron microscopy (SEM) analysis and nanoindentation, the samples were prepared by grinding, polishing, and final polishing with colloidal silica (OPS). For scanning transmission electron microscopy (STEM) analysis, the samples were prepared by grinding, polishing, dimpling, and Ar ion milling, followed by carbon coating.

SEM was performed using a JEOL 7600 microscope. A probe aberration-corrected X-FEG/Monochromator STEM (Thermo Fisher Spectra 300) was used to study composition and structure of Ti-doped KNN. Mechanical properties, such as hardness and elastic modulus, were measured using the nanoindentation method (Hysitron TS 77, Bruker). In the presentation, the structural characteristics of Ti-doped KNN ceramics will be discussed, with special attention given to the distribution of Ti within the KNN matrix and its local effect on unit cell distortion. The mechanical properties will also be correlated with microstructural and structural observations.

References:

1. X. Vendrell, J. E. García, X. Bril, D. A. Ochoa, L. Mestres, G. Dezanneau, *J. Eur. Ceram.* **2015**, *35*(1), 125–130.

Type of presentation: Poster

MS1-P-11 Advanced quantitative EPMA-WDS approach for accurate compositional analysis of cerium-doped barium titanate ceramics

Zoran Samardžija[a]

[a]*Department for Nanostructured Materials, Jožef Stefan Institute, Ljubljana, Slovenia*

Contact email: zoran.samardzija@ijs.si

Introduction: The elemental composition of cerium-doped barium titanate ($BaTiO_3$) ceramics was analysed employing a detailed optimization of the EPMA-WDS procedure. The inherent peak-overlap of the Ce-Lα_1 and Ba-L$\beta_{1,4}$ spectral lines was present also when using the WDS. This problem of peak-overlap was solved by introducing three dedicated methods following by off-line quantification using refined $\Phi(\rho z)$-ZAF matrix-correction algorithm in order to achieve reliable and highly accurate quantitative results and to determine exact solubility of cerium in the $BaTiO_3$.

Methods: Electron-probe microanalysis (EPMA) with wavelength-dispersive X-ray spectroscopy (WDS) was applied for a quantitative elemental analysis of cerium-doped $BaTiO_3$ ceramics. Within the optimization of the WDS measurements a careful inspection of wavelength spectra of analytical lines revealed that the Ce-Lα_1 line interferes/overlaps with both the Ba-Lβ_1 and Ba-Lβ_4 lines, as shown in figure 1. Consequently a systematic error is present in the quantification of the relatively low i.e. minor mass fractions of Ce-dopant in the $BaTiO_3$ [1]. To obtain correct and reliable quantitative analysis with highest accuracy we have proposed three methods to solve this problem due to Ba-Ce spectral interference:

1. The correction of the Ce-Lα_1 - Ba-L$\beta_{1,4}$ peak overlap using the method based on relative spectral line intensities. Here we assume that the ratio between the Ba-Lα_1 intensity and the intensity of the Ba-L$\beta_{1,4}$ measured at the Ce-Lα_1 position is the same in the $BaTiO_3$ standard (BT) and in the Ce-doped $BaTiO_3$ sample (BTC). The true Ce-Lα_1 intensity (I^*) corrected for the contribution of the Ba-L$\beta_{1,4}$ is then calculated by

$$I^{*\,BTC}_{CeL\alpha1} = I^{BTC/measured}_{CeL\alpha1} - \left[I^{BT}_{BaL\beta1,4\ at\ CeL\alpha1\ position} \times \left(I^{BTC}_{BaL\alpha1} / I^{BT}_{BaL\alpha1}\right)\right] \quad (1)$$

2. The correction of Ce-Ba overlap using the calibration curve method. Here we assume that the Ba-L$\beta_{1,4}$ intensity measured at the Ce-Lα_1 peak position increases linearly with the increase of the Ba concentration. The intensity of Ba-L$\beta_{1,4}$ was then measured versus the Ba-Lα_1 intensity in three Ba-Ti-O compounds (without Ce) and a linear calibration curve was obtained, as shown in figure 2. The slope of calibration curve gave a correction factor that was used to determine the contribution of the Ba-L$\beta_{1,4}$ to the Ce-Lα_1 in the Ce-doped $BaTiO_3$ matrix (BTC). The true, corrected Ce-Lα_1 intensity (I^*) is then calculated by

$$I^{*\,BTC}_{CeL\alpha1} = I^{BTC/measured}_{CeL\alpha1} - 0.066 \times I^{BTC}_{BaL\alpha1} \quad (2)$$

3. An analysis using an alternative analytical spectral line for Ce, namely the Ce-Lβ_1 line.

The WDS measurements were carried out in a JEOL JXA 8600 Superprobe at 20 kV, 40 nA and 40° take-off angle using the LiF crystal for the measurements of Ba-Lα_1, Ba-L$\beta_{1,4}$, Ti-Kα_1, Ce-Lα_1 and Ce-Lβ_1 intensities. The standards were pure ceramics $BaTiO_3$ and CeO_2. The measured k-ratios for Ce-Lα_1 were firstly corrected off-line by subtracting the contribution of the interfering Ba-L$\beta_{1,4}$ line according to formulae (1) and (2). The quantification was performed off-line using $\Phi(\rho z)$-PROZA matrix correction and oxygen content was calculated by stoichiometry to nominal cation valency [2]. A high analytical precision was achieved applying sufficient counting times in order to ensure standard counting deviations σ_c below 1% relative thus being ≤ 0.4 % for Ba and Ti and ≤ 0.8 % for Ce.

Results and Discussion: A summary of quantitative WDS results for a representative cerium-doped $BaTiO_3$ sample is given in table 1 showing the comparison between different methods of analysis, where 1, 2, and 3 refer to above-described methods and 4 refers to the analysis performed by measuring the Ce-Lα_1 line without the use of a peak-overlap correction.

Both methods for the correction of the Ce-Ba spectral overlap, 1 and 2, gave similar quantitative results, which perfectly fit to the perovskite solid solution formula given by $Ba_{0.923}Ce_{0.077}Ti_{0.981}(V_{Ti})_{0.019}O_3$ or in general form

by $Ba_{1-x}Ce_xTi_{1-x/4}(V_{Ti})_{x/4}O_3$ where x = 0.08 and V_{Ti} are vacancies at the Ti-sites. This result directly confirms that in the selected sample Ce incorporates into the $BaTiO_3$ as donor Ce^{3+} at the Ba^{2+} sites. In this case excess donor charge is compensated with ionized vacancies at the Ti-sites V_{Ti}. Direct evidence for this mechanism of charge compensation is that the deficit at the Ti-sites, attributed to $[V_{Ti}]$, is equal to $[Ce^{3+}]/4$.

Table 1. Results of EPMA-WDS quantitative analysis of cerium-doped $BaTiO_3$

Method	Mass Fractions (%)					Atomic Fractions (%)			
	Ba	Ti	Ce	O	Total*	Ba	Ti	Ce	O
1	54.38	20.13	4.63	20.64	99.78	18.54	19.69	1.55	60.23
2	54.37	20.13	4.73	20.64	99.87	18.52	19.67	1.58	60.23
3	54.69	20.16	4.39	20.63	99.88	18.62	19.69	1.47	60.22
4	*54.16*	*20.13*	*7.22*	*20.49*	*102.00*	*18.10*	*19.30*	*2.36*	*60.24*

* Non-normalized analytical total

The non-normalized analytical totals close to ideal 100 % (methods 1, 2 and 3) and the perfect fit of the results to the perovskite ABO_3 type formula verify the correctness of the applied analytical approach and the accuracy of the quantitative WDS analysis.

When analysing the Ce-Lβ_1 line (method 3) the elemental concentration of Ce was slightly underestimated mainly due to an inaccurate absorption correction caused by uncertainty of the mass absorption coefficient value and due to poorer counting statistics for the Lβ line. The analysis performed by measuring the Ce-Lα_1 line without peak overlap correction (method 4) is obviously erroneous, with a significantly overestimated cerium concentration.

Conclusions: Advanced approach with quantitative WDS compositional analysis of the cerium-doped barium titanate ceramics was applied and successfully performed by introducing two methods for the correction of the peak overlap which is present between the Ce-Lα_1 and Ba-L$\beta_{1,4}$ spectral lines. The obtained quantitative results allowed us to accurately determine the exact solid solubility of cerium in the $BaTiO_3$, to describe the perovskite solid solution formula and to define the mode of incorporation of cerium and the charge compensation mechanism as well.

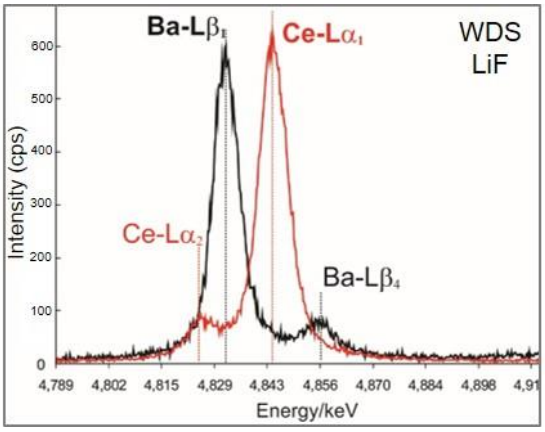


Figure 1: WDS spectral overlap of the Ba-Lβ_1 and Ba-Lβ_4 lines with the Ce-Lα_1 line.

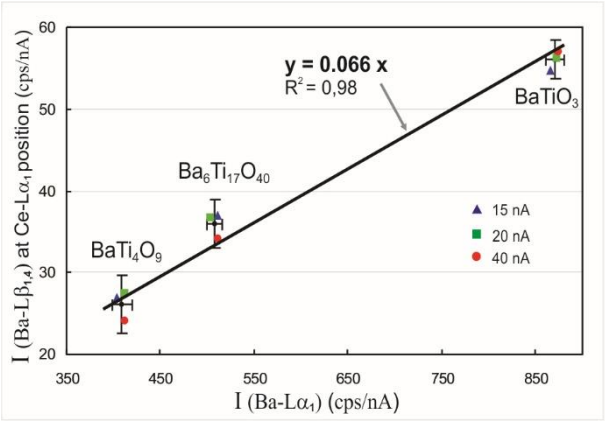


Figure 2: Calibration curve used for the evaluation of Ba-L$\beta_{1,4}$ contribution to the Ce-Lα_1 intensity.

References:

1. Z. Samardžija, M. Čeh, D. Makovec, D. Kolar, *Mikrochim. Acta* **1996**, *13*, 517-523.
2. J.T. Armstrong, J. Donovan, P. Carpenter, *Microsc. Microanal.* **2013**, *19*, 812-813.

Type of presentation: Poster

MS1-P-12 Complex polycrystalline clusters of diamond and graphite from metamorphic rocks

Tim Sotelšek [a], Sorour Semsari Parapari [b], Nik Gračanin [b], Sašo Šturm [a, b], Marian Janák [c], Mirijam Vrabec [a]

[a]*Department of Geology, Faculty of Natural Sciences and Engineering, University of Ljubljana, (Ljubljana), Slovenia*

[b]*Department for Nanostructured Materials, Jožef Stefan Institute, (Ljubljana), Slovenia*

[c]*Earth Science Institute, Slovak Academy of Sciences, (Bratislava), Slovak Republic*

Contact email: tim.sotelsek@ntf.uni-lj.si

Introduction

The Pohorje Mountains consist of a central igneous intrusion surrounded by metamorphic rocks, including micaschists, phyllites, marbles, metaquartzites, and gneisses. In the southeastern region, numerous eclogite bodies and metamorphosed ultramafic rocks are present. The peak pressure-temperature (P-T) conditions of these metamorphic rocks were in the ultrahigh-pressure (UHP) metamorphism zone, close to or within the diamond stability field [1, 2 and references therein].

Among these rocks, metapelitic gneiss hosts garnet porphyroblasts containing numerous inclusions, including diamonds and complex grains comprised of diamond and graphite domains. To better understand their nature and conditions of their formation, we characterized their occurrence and internal structures at the atomic scale using transmission electron microscopy (TEM).

Methods

Thin sections were prepared from rock samples collected in the field. A focused ion beam/scanning electron microscope (FIB/SEM) was used to prepare a lamella of a diamond-bearing inclusion. The Thermo Fisher Scientific Helios NanoLab 600i Dual Beam System was employed for FIB-SEM sample preparation, and subsequent analyses were conducted using a JEOL JEM-ARM 200CF microscope.

To achieve atomic-scale resolution, high-resolution (scanning) transmission electron microscopy (HR(S)TEM) techniques were applied. These included high-angle annular dark-field scanning transmission electron microscopy (HAADF-STEM), combined with energy-dispersive X-ray spectroscopy (EDS) and electron energy loss spectroscopy (EELS).

Results

The cross-section of the inclusion revealed three carbonaceous grains (Figure 1a), confirmed through EELS and EDS analyses. Selected area electron diffraction (SAED) patterns indicated that one grain is monocrystalline diamond, while the others are polycrystalline clusters of diamond and graphite (Figure 1b). Polycrystalline grains exhibit a preferential orientation of nanocrystallites. However, diffraction spots of diamond and graphite are very close together and hard to distinguish from each other, hindering the complex nature of polycrystalline clusters. Therefore, further high-resolution imaging was conducted. Imaging at the atomic scale revealed that the polycrystalline grains consist of numerous crystallites ranging from 5 to several tens of nanometres in size (Figure 1c). Some nanocrystals exhibit an undisturbed internal structure, while others display imperfections such as stacking faults, twinning, and lattice dislocations. Additionally, EELS analysis confirmed the presence of carbon domains in the form of graphite within the polycrystalline diamonds. Carbonaceous grains are intimately intergrown with the host garnet but show no crystallographic relationship. In some regions between the polycrystalline clusters and the garnet, an amorphous layer with a composition similar to garnet was identified.

Discussion and Conclusions

The coexistence of both monocrystalline and polycrystalline grains within a single inclusion raises questions about their crystallization conditions. We hypothesize that pressure and temperature variations during metamorphism may have influenced the formation of grains with different structures. Previous analyzes of the walls of inclusions have revealed compositional banding, suggesting that chemical conditions have changed over time, presumably in response to changing P-T conditions. We hypothesize that the growth of monocrystalline diamond occurred under more stable tectonic conditions, whereas polycrystalline clusters precipitated under decreasing P-T metamorphic conditions. Precipitation probably started when the rock was still in the stability range of diamond and continued when conditions decreased to the stability field of graphite. Therefore, we can now observe complex internal structures of intergrown diamond and graphite domains. Further studies are needed to refine these interpretations and to fully understand the mechanisms driving the crystallization of the different carbon allotropes in UHPM environments.

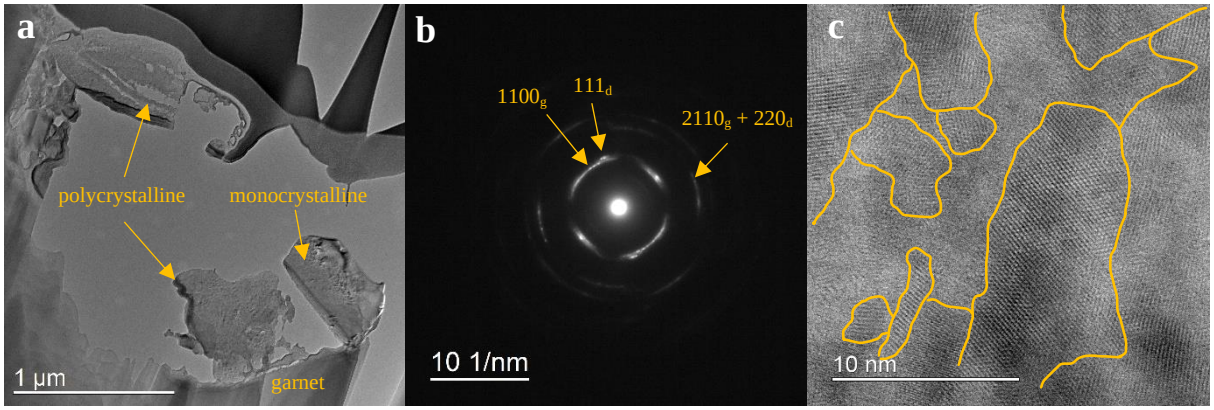


Figure 1: TEM images of analysed carbon-bearing inclusion. (a) STEM image of lamella, showing positions of three grains within the inclusion. Two are polycrystalline clusters composed of diamond and graphite domains. One is monocrystalline diamond. (b) SAED of the lower polycrystalline grain shown in (a). Diffraction spots of 1100 graphite and 111 diamond can be distinguished, while 2110 graphite and 220 diamond and further spots are difficult to distinguish. (c) HRSTEM image of the same polycrystalline grain showing nanocrystallites.

References:

1. M. Vrabec, M. Janák, N. Froitzheim, C. J. De Hoog, *Lithos*, **2012**, *144*, 40–55.

2. M. Janák, N. Froitzheim, K. Yoshida, V. Sasinkova, M. Nosko, T. Kobayashi, T. Hirajima, M. Vrabec, *J. Metamorph. Geol.*, **2015**, *33*, 495– 512.

Type of presentation: Poster

MS1-P-13 Exploring High-Baroque Stucco: Microscopy of Materials and Techniques at Kroměříž Chateau

Sylwia Svorová Pawełkowicz[a], Jan Válek[a], Petr Kozlovcev[a], Kristýna Kotková[a], Dita Frankeová[a]

[a]*Institute of Theoretical and Applied Mechanics, Czech Academy of Science, (Prague), Czech Republic*

Contact email: svorova_pawelkowicz@itam.cas.cz

This study examines the materials and techniques employed in the high-baroque stucco decorations of the Sala Terrena at Kroměříž Chateau, Czech Republic, executed by renowned Baldassare Fontana and his workshop. During the early modern period, artists and craftsmen from the Lake Lugano region and the surrounding areas along the present-day Italian-Swiss border—encompassing Canton of Ticino and Lombardy—developed a remarkable expertise in stucco decoration. These skilled artisans travelled across Central and Eastern Europe, completing prestigious commissions to adorn noblemen's palaces.

Employing advanced methods such as a combination of thin section microscopy, scanning electron microscopy with energy dispersive spectroscopy (SEM-EDS), thermal analysis (TA), and X-ray diffraction (XRD), the study provides insights into the stratigraphy and composition of the stucco layers. It also sheds light on how artisans adapted their techniques to local materials while maintaining high artistic standards.

The findings revealed a multilayered stucco structure comprising core modelling mortars and finishing layers. Thin-section microscopy highlighted the microstructure of lime and gypsum binders, aggregates, and binder-related particles (BRPs) indicative of material preparation techniques. SEM-EDS confirmed the predominant use of highly calcitic lime as the main binder, noted for its purity and low content of impurities, such as magnesium and silicate compounds. Gypsum emerges as a secondary binder, prominently used in structural mortars for rapid setting, with unprocessed gypsum fragments indicating low-temperature burning practices.

Thermal analysis quantified the proportions of lime and gypsum in the mortars, revealing consistent mixing ratios across samples. XRD further characterized the crystalline phases, confirming the predominance of calcite in finishing layers and gypsum in reinforcement mortars. The analysis of aggregates showed variability in size and composition, with siliciclastic sand as the primary aggregate in core mortars. As exception to the rule, in some samples crushed marble was introduced in select finishing layers probably to achieve a smoother, more reflective surface. This deliberate adjustment suggests technological innovations aimed at enhancing aesthetic quality. Crushed marble appears selectively in finishing layers, likely to enhance surface smoothness and reflectivity, reflecting technological innovation. The presence of distinct mortar types—one using siliciclastic sand and another with crushed marble—may suggest a shift in technique or the involvement of different workshops.

The coatings applied to the surface layers were examined in detail, revealing up to eight successive limewashes and paint applications. Elemental mapping identified zinc-based pigments in secondary layers, dating repainting phases to the 18th century or, more likely, the second half of the 19th century. Surface morphology and adhesion studies demonstrated differences between original and secondary coatings, emphasizing the stratigraphic complexity and historical interventions.

The findings highlight the adaptability and expertise of traveling artisans, who demonstrated remarkable flexibility in utilizing local materials while maintaining the artistic integrity of their work. These results contribute significantly to understanding the craftsmanship and technological advancements of baroque stucco-making, while providing critical data for informed conservation strategies.



Figure 1: (a), West hall of Sala Terrena at Kroměříž Chateau; sample 20 extracted from wall decoration frames. (b), cross-section of the sample 20

Acknowledgment:
This research was carried out within the Erasmus+ project STUDEC (Stucco Decoration Across Europe) – grant project number, 2022-1-CZ01-KA220-HED-000085652.

Type of presentation: Poster

MS1-P-14 Study of vanadinite as a painting pigment

Sylwia Svorová Pawełkowicz[a,b], BarbaraWagner[a], Bożena Gołebiowska[c], Petr Svora[d], Jan Fábry[d]

[a]*Biological and Chemical Research Centre, Faculty of Chemistry, University of Warsaw, (Warsaw), Poland*

[b]*Institute of Theoretical and Applied Mechanics, Czech Academy of Science, (Prague), Czech Republic*

[c]*Department of Mineralogy, Petrography and Geochemistry, AGH University of Science and Technology, (Cracow), Poland*

[d]*Institute of Physics of the Czech Academy of Sciences (Prague), Czech Republic*

Contact email: s.svorova-pawelkowicz@uw.edu.pl

Modern analytical techniques have revolutionized the study of historical paintings, enabling the identification of minerals used as pigments, including those previously unrecognized. In the early 16th-century decoration of the chancel vault in the Nativity of the Blessed Virgin Mary filial church in Chotków (Lubuskie Voivodeship, Żagań County, Brzeźnica Municipality), vanadinite, $Pb_5(VO_4)_3Cl$ – lead (II) chloroorthovanadate (V), has been identified in the yellow foliage motifs. This discovery marks the first documented occurrence of vanadinite in Polish artworks.

Vanadinite, belongs to the apatite mineral group and is isostructural with mimetite $Pb_5(AsO_4)_3Cl$, pyromorphite $Pb_5(PO_4)_3Cl$ and wulfenite $Pb_5(MoO_4)_3Cl$. It is often found alongside barite $BaSO_4$, calcite $CaCO_3$, quartz SiO_2 and mottramite $PbCu(VO_4)(OH)$ [1] in deposits.

Vanadinite is rarely recognized as a pigment in artworks, with only six examples documented so far. Known examples include Iranian paintings from 224-651 AD [2], Roman murals from the 1st century BC to the 2nd century AD in Israel [3], tomb decoration from the Western Han Dynasty period (206 BC - 9 BC) in Xi'an, China [4], medieval paintings in the church of St. Susanna in Quirinal [5] and in the Minorite church in Copra, Slovenia, in a painting dated to the 15th century [6]. Vanadinite was also identified together with isomorphic mimetite in the decoration of Greek stelae from the Louvre collection [7] – in this case, the painting has degraded and the parts where vanadinite was identified are now black.

The discovery at Chotków raises intriguing questions: was vanadinite intentionally chosen for its yellow hue, or did it form from the degradation of other minerals? If intentional, its use deviates from the expected green pigment for foliage, suggesting either material limitations or a deliberate artistic choice. Alternatively, if vanadinite resulted from chemical transformation, understanding the environmental factors and original precursors becomes critical.

This research aims to determine whether vanadinite was deliberately applied or unintentionally formed. It also explores whether the mineral was naturally sourced or synthetically produced. Understanding the degradation behaviour of vanadinite—whether natural or artificial—will provide vital information for preserving artworks containing this pigment. The study employs advanced techniques, including optical and electron microscopy (SEM) with an energy-dispersive X-ray spectrometry (EDS) and a wavelength-dispersive X-ray spectrometry (WDS), transmission electron microscopy (TEM) with selected area electron diffraction (SAED), laser ablation inductively coupled plasma ionisation mass spectrometry (LA-ICP-MS), X-ray powder diffractometry (XRD), infrared and Raman spectroscopy, to analyse the pigment palette and trace supply routes, artistic practices, and workshop methodologies of the period.

In the project's initial phase, we will synthesize vanadinite and subject it to degradation conditions such as humidity, UV radiation, salinity, and biological by-products like oxalic acid. Mock samples, combining vanadinite with different painting binders, will be produced to simulate its stability under typical wall painting conditions. These tests aim to replicate aging processes and evaluate long-term

behaviour. By understanding whether vanadinite's presence reflects intentional artistic decisions or chemical transformations, the research provides insights into historical material usage.

By increasing awareness of vanadium-based minerals in art and their degradation processes, this project enhances conservation science. The findings will assist conservators in developing tailored strategies for preserving cultural heritage works containing vanadinite. Additionally, the study contributes to a broader understanding of vanadium compounds in art and fosters interdisciplinary collaboration in conservation chemistry.



Figure 1: Extraction site of the sample and the cross-section of the sample.

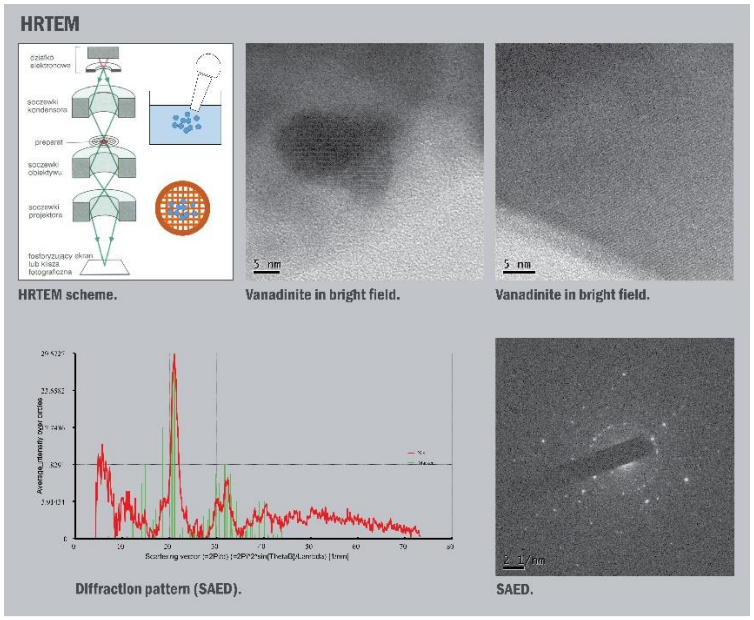


Figure 2: HRTEM and SAED analysis of the vanadinite pigment from Chotków .

References:

1. mindat. org
2. Holakooei P, Karimy AH, Hassanpour A, Oudbashi O (2016) *Spectrochimica Acta Part A: Molecular and Biomolecular Spectroscopy*, v. 169, 169–174.
3. Piovesan R, Maritan L, Amatucci M, Nodari L, Neguer J (2016). *European Journal of Mineralogy*, v. 28, no. 2, 435–448.
4. Blaendsorf C, Yin Xia (2006) *"Testing and optimising conservation technologies for the preservation of cultural heritage of the Shaanxi Province, PR China*", Report, 87–98.
5. Marabelli M, Santopadre P, Bianchetti P (2006) *Bollettino ICR*, N. 13, 64–73.
6. Levstik MG, Mladenovič A, Križnar A, Kramar S (2019) *Periodico di Mineralogia*, 88(1):95–104.
7. Rouveret A, Walter P (1998). *Revue Archéologique*, 1:216–220.

Type of presentation: Poster

MS1-P-15 FIB-SEM characterization of various types of materials

Tina Radošević[a], Nik Gračanin[a], Klara L. Konda[a], Damjan Vengust[a], Nina Daneu[a], Sašo Šturm[a], Matejka Podlogar[a]

[a]*Jožef Stefan Institute, Ljubljana, Slovenia*

Contact email: tina.radosevic@ijs.si

In this study, we demonstrate the versatility of Focused Ion Beam (FIB) techniques across a wide range of materials. This powerful and increasingly common method enables site-specific deposition, milling, cutting, imaging, and sample preparation at the micro- and nanoscale. FIB operates with a finely focused beam of ions, most often gallium. A typical FIB system features a dual-beam setup, integrating both a scanning electron microscope (SEM) and FIB columns. This allows for complementary imaging and processing of the same region of interest. Depending on the application, FIB can operate at low ion currents for high-resolution imaging or at higher currents for efficient and precise material removal. These features make it ideal for applications such as cross-sectioning, defect analysis, and lamella preparation for transmission electron microscopy (TEM).

For the ZnO nanorod arrays grown on a glass substrate, FIB enabled the precise preparation of site-specific regions for high-resolution TEM. This provided valuable insights into crystal growth and film formation processes. In contrast to samples mechanically detached and subsequently observed via TEM, samples prepared by FIB allowed us to trace the growth process of the ZnO nanorods from the seed layer through their length and up to the top. The empty spaces between the nanorods were filled with electron- and ion-deposited platinum to stabilize the structure during milling and lift-out.
Powdered samples present a challenge for TEM investigations, as individual particles are often thicker than the electron-transparent limit. TiO_2 powder, which was initially too thick for structural analysis with TEM, was thinned to enable detailed morphological and structural examination. This additional thinning of selected particles allowed for high-resolution imaging and more accurate structural characterization that would otherwise not be achievable.

Plastic microfibers subjected to photocatalytic degradation and a piece of spruce wood, two non-conductive organic materials, were also examined, revealing increased surface roughness and internal changes. When surface analysis alone was insufficient, cross-sectional samples were prepared, enabling a more detailed investigation of bulk morphology, pore dimensions, and interfacial contacts.
In addition, we investigated beam-sensitive samples such as magnetic NdFeB, where strong magnetization can distort electron trajectories and degrade image quality in electron microscopy. We show that in FIB-prepared samples of extremely small dimensions, these effects are significantly reduced.

Overall, these examples highlight the precision and versatility of FIB, making it an essential tool for site-specific sample preparation and high-resolution structural characterization across diverse materials.

MS2 Polymers, soft, and organic materials

Type of presentation: Invited

MS2-IN-1 Multimodal *in vitro* and *in vivo* tissue imaging: Design, synthesis and surface engineering of nanoprobes

Daniel Horák[a], Oleksandr Shapoval[a]

[a]*Institute of Macromolecular Chemistry CAS, Prague, Czech Republic*

Contact email: horak@imc.cas.cz

Introduction: Effective diagnosis and treatment of many serious diseases requires multifunctional all-in-one nanolabels that can be imaged simultaneously by several techniques. Among the labels, bioconjugated upconversion nanoparticles (UCNPs) have the advantage of a low optical background enabling the design of ultrasensitive immunoassays as well as high contrast and deep tissue imaging. In addition, UCNPs are bright markers exhibiting several narrow emission lines. In this presentation, we will therefore focus on UCNPs or magnetic nanoparticles that are targeted and internalized by cells and subsequently imaged.

Methods: UCNPs based on $NaYF_4$:(Gd)Yb,Er(Tm) or Gd(Tb)F_3:Tb(Gd),Yb,Nd cores, optionally with NaY(Gd)F_4:(Nd) shells, were obtained by high-temperature coprecipitation or thermal decomposition of lanthanide precursors. The protective coatings then included diverse polymers such as phosphonic acid-terminated polyglucopyranose (PMG-P) derivative, PEG-neridronate, poly(4-styrenesulfonic acid-*co*-maleic acid) (PSSMA), poly(*N*,*N*-dimethylacrylamide-*N*-acryloylglycine methyl ester)-alendronate [P(DMA-AGME)-Ale], poly(*N*,*N*-dimethylacrylamide-*co*-2-aminoethyl acrylate)-alendronate [P(DMA-AEA)-Ale], ^{125}I-radiolabeled PEG-neridronate, azidopentanoyl-RGDS-NH_2 and TAT-NH_2 peptide reacting with alkyne-silica, or neat silica. The particles were characterized by transmission electron microscopy (TEM) combined with energy-dispersive X-ray spectroscopy, X-ray diffraction analysis and dynamic light scattering, while the coatings were analyzed by atomic absorption and ATR-FTIR spectroscopy and thermogravimetric analysis. Cell imaging modalities involved optical microscopy, TEM, magnetic resonance imaging (MRI) and single-photon emission computed tomography (SPECT).

Results: First, PMG–P@Fe_3O_4 nanoparticles were developed that had high relaxivity as confirmed by MR relaxometry but rather low cellular uptake. Nevertheless, the labeled cells still provided visible contrast enhancement in the MRI. In addition, the cell viability was not compromised by the nanoparticles. RGDS and TAT peptide-conjugated $NaYF_4$:Yb,Er@SiO_2 UCNPs supported both extra- and intracellular nanoparticle uptake by human cervix carcinoma HeLa cells, enabling targeting and optical imaging of the specific tumor phenotypes. ^{125}I-radiolabeled upconversion $NaYF_4$:Yb,Er@PEG nanoparticles were useful for *in vivo* bimodal tissue imaging, in particular SPECT/CT monitoring of nanoparticle biodistribution in the body, and near-infrared photothermal/photodynamic cancer theranostics. The magnetic upconversion $NaGdF_4$:Yb,Er(Tm)@PEG, $NaGdF_4$:Yb,Tb,Nd@PSSMA, GdF_3:Eu(Tb)@PSSMA or Gd(Tb)F_3:Tb(Gd),Yb,Nd@Ale-P(DMA-AGME) nanoparticles with multimodal bioimaging involving down- and upconversion luminescence, MRI, SPECT and X-ray CT (Figure 1) have been shown to be well internalized by live cells, monitoring biodistribution in mouse organs, pancreatic β-cells and Langerhans islets. Moreover, temoporfin and/or hypericin conjugation to P(DMA-AEA)-Ale surface-modified core $NaYF_4$:Yb,Er,Fe and core-shell $NaYF_4$:Yb,Er@$NaYF_4$:Nd UCNPs increased their bioavailability for multimodal imaging (bright-field imaging, upconversion luminescence and Raman microspectroscopy) and enabled effective photodynamic therapy.

Discussion and conclusions: The nanoscale and uniform size of UCNPs enables their dispersibility in biological environments, respectively ensures reproducibility of the results and is critical for consistent physical and biological characteristics. As bioconjugated UCNPs can be detected without interfering optical background and with very low nonspecific binding, the list of applications in biomedical diagnostics and imaging modalities merged in all in one system is continuously expanding. UCNPs are thus suited for super-resolution multimodal imaging of diseased tissues and as theranostic nanoprobe for experimental and regenerative medicine, drug delivery and/or photodynamic therapy.

Acknowledgments. Support of the Czech Science Foundation (No. 25-16155S) is acknowledged.

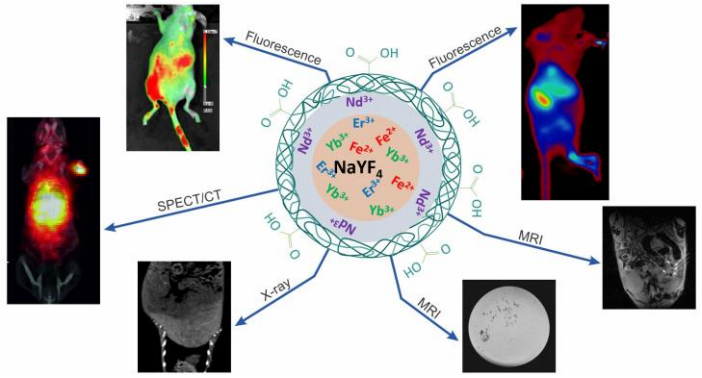


Figure 1: Schematic view of different imaging modalities of UCNPs.

Type of presentation: Invited

MS2-IN-2 Study of the electron-induced damage of polymer based materials during STEM-EELS measurements

Maria de la Mata[a], Luisa Maria Valencia-Liñan[a], Miriam Herrera[a], Sergio I. Molina[a]

[a]*Universidad de Cadiz, IMEYMAT, Spain*

Contact email: maria.delamata@uca.es

Polymer nanocomposites render a rich playground for the development of novel lightweight materials with appealing 3D printing processing capabilities, which have drawn the attention of researchers and industry over the last years. Unfortunately, some polymer-based materials are easily damaged under the experimental STEM conditions, which restricts the application of certain characterization techniques and the attainable information. Thus, being aware of the degradation processes during the measurements becomes key in order to optimize the experimental procedures, as well as assisting the interpretation of the obtained results.

Within this context, we have studied how does different polymer matrices commonly employed in 3D printing approaches degrade under 200kV STEM conditions. In particular, we cover acrylic resin (AR)[1], polylactic acid (PLA), polycaprolactone (PCL), acrylonitrile butadiene styrene (ABS) and acrylonitrile styrene acrylate (ASA)[2]. The EEL spectral evolution with the accumulated electron dose points differentiated losing rates of the chemical constituents (i.e., C, O and N), and allows estimating the critical electron dose and likely degradation pathways of every analyzed material. The kinetics of the monitored processes (namely, the mass losing) allows distinguishing the underlying phenomena driving the degradation, since knock-on damage results in material thinning proportional to the electron dose, whereas the radiolysis decomposition follows a first-order equation. Importantly, both phenomena may contribute until different extend to the degradation of polymer. The atomic structure of the polymer chains also plays a critical role on their tolerance to the electron doses, particularly depending on the presence of aromatic or aliphatic groups. The results point the higher critical electron doses of polymers containing aromatic groups in contrast to those containing aliphatic groups.

Moreover, we provide the STEM characterization of different polymer nanocomposites, rendering comprehensive insights on their formation and performance, focusing on 3D-printable tailored nanocomposites. The studies include the development of functionalized resins containing either inorganic nanoparticles, and suitable for stereolithography (SLA). The nanostructures allow for tuning the electrical conductivity[3] as well as the optical behavior of the hosting matrices[4], which can be further studied by (S)TEM related techniques (i.e., low-loss EELS).

References:
[1] Polymer Degradation and Stability 203 (2022) 110044
[2] Polymer Degradation and Stability 230 (2024) 111030
[3] Polymers 14 (2022) 5238
[4] ACS Materials Au 4 (2024) 424−435

Type of presentation: Oral

MS2-O-1 Advanced Nanoscale Characterization of Organic Photovoltaic Materials

Philipp Christ[a], Julia Hönigsberger[b], Georg Haberfehlner[a], Claudia Mayerhofer[a], Sebastian Rauch[a], Gerald Kothleitner[a], Thomas Rath[b], Gregor Trimmel[b] and Daniel Knez[a]

[a]*Institute of Electron Microscopy and Nanoanalysis (FELMI), Graz University of Technology & Graz Centre for Electron Microscopy (ZFE), Steyrergasse 17, 8010 Graz, Austria*

[b]*Institute for Chemistry and Technology of Materials (ICTM), NAWI Graz, Graz University of Technology, Stremayrgasse 9, 8010, Graz, Austria*

Contact email: philipp.christ@felmi-zfe.at

In order to explore the full potential of organic photovoltaics (OPV), there are a number of scientific challenges regarding material properties, ageing effects, and their integration into device architecture to be overcome.

Figure 1a shows the layered structure of these OPV cells recorded by scanning transmission electron microscopy (STEM) and uses suitable spectroscopy methods such as electron energy loss spectroscopy (EELS) and energy dispersive X-ray spectrometry (EDX) to determine the chemical elements of this layer structure and possible degradation effects at the interfaces of the active layer (AL). The active layer consists of a donor and an acceptor (PM6 & Y6), which can be distinguished by their chemical composition using EELS elemental mapping, as shown in Figure 1b. To assess the effects of sun ageing or degradation, we analyse the change in absorption characteristics [2]. A method based on STEM EELS and Kramers-Kronig Analysis (KKA) is developed to determine the optical properties of OPV materials at the nanoscale [1].

To this end, we evaluated the optical range (3.1eV to 1.24eV) of monochromated EEL spectra by means of machine learning assisted processing steps. By employing Richardson-Lucy deconvolution (RLD), and subtracting the zero loss peak (ZLP) via vacuum EELS data, the scattering distribution (SD) is obtained. This distribution is further processed using KKA and a full spectrum image (SI) is computed for the absorption with the mean absorbance in Figure 1c, which can directly be compared with the outcome of UV-Vis measurements.

We plan to take retardation effects into account and apply a surface plasmon correction for the SD, this should bring the results from the KKA closer to the UV-Vis measurements [1]. Furthermore, the absorption spectra will further be analysed using cluster analysis to distinguish PM6 and Y6 by identifying the corresponding absorption peak and compare the results with the EELS elemental map. Finally, sun ageing effects and the absorption spectra of the individual components of the active layer will be identified and localized.

Financial support of the Austrian Science Fund (FWF) [P 34815-N] is gratefully acknowledged.

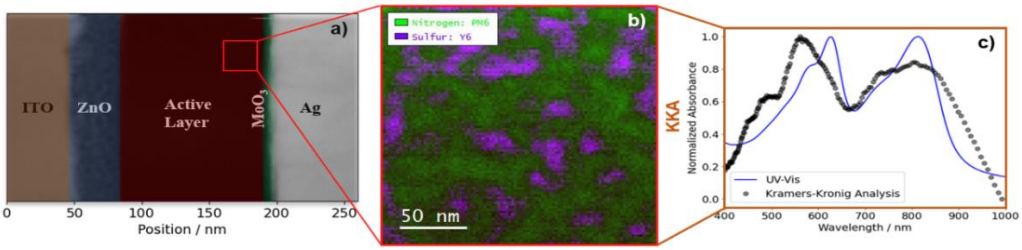


Figure 14: The absorption analyse for the active layer of an OPV cell with a) the layer structure of the cell, b) an elemental map generated via STEM EELS and c) the corresponding absorption spectra after the KKA compared with the UV-Vis outcome.

References:

1. R. F. Egerton, *Springer US*, **2011**, *3*, 231-255
2. T. Haoran and et al, *Advanced materials Deerfield Beach, Fla.*, **2023**, *36*, 1-6.

Type of presentation: Oral

MS2-O-2 Nanocellulose-based functional composite materials

Domagoj Belić[a], Mislav Mustapić[a], Denis Stanić[a], Nikola Španić[b], Judit Budai[c], Lázár Tóth[c], Zsuzsanna Márton[c]

[a]*Department of Physics, Josip Juraj Strossmayer University of Osijek, Croatia*

[b]*Faculty of Forestry and Wood Technology, University of Zagreb, Croatia*

[c]*ELI-ALPS, ELI-HU Non-Profit Ltd., Szeged, Hungary*

Contact email: dbelic@fizika.unios.hr

Cellulose, an abundant and renewable natural polymer, offers extensive opportunities for diverse applications in materials science due to its favorable properties. In this context, nanocomposite materials combining cellulose or its derivatives with metal or metal-oxide nanoparticles, such as Au or Fe_3O_4, emerge as versatile platforms for sensor development.
The main objective of our study is to create ultrathin flexible nanocomposite materials specialized for sensing humidity and volatile organic compounds (VOCs), exploiting the synergistic effects of percolating networks of nanoparticles within the matrices of fibrillated nanocellulose or cellulose acetate. Additionally, we investigate the thermoresponsive properties of such nanocomposite materials, produced entirely from abundant biocompatible resources.

Firstly, we outline approaches for synthesizing fibrillated nanocellulose, cellulose acetate, nanoparticles of Au and Fe_3O_4, as well as the related composite nanomaterials, with the objective to integrate nanoparticles into/onto thin flexible cellulose matrices. Next, advanced electron microscopy techniques including conventional and low-dose Transmission Electron Microscopy (TEM), high- and low-vacuum Scanning Electron Microscopy (SEM), Focused Ion Beam (FIB) sectioning and Energy-Dispersive X-ray Spectroscopy (EDX) mapping are employed for precise characterization of nanocomposite morphology, structure and nanoparticle distribution. Finally, we present results of *I–t* measurements on these nanocomposites in varying environmental conditions (humidity, VOC, and temperature) in the custom-built sensing system, aiming to evaluate their performance as sensors.

The findings underscore the potential of these multifunctional nanocomposites for diverse applications in thin, flexible sensor platforms, paving the way for next-generation sensing technologies.

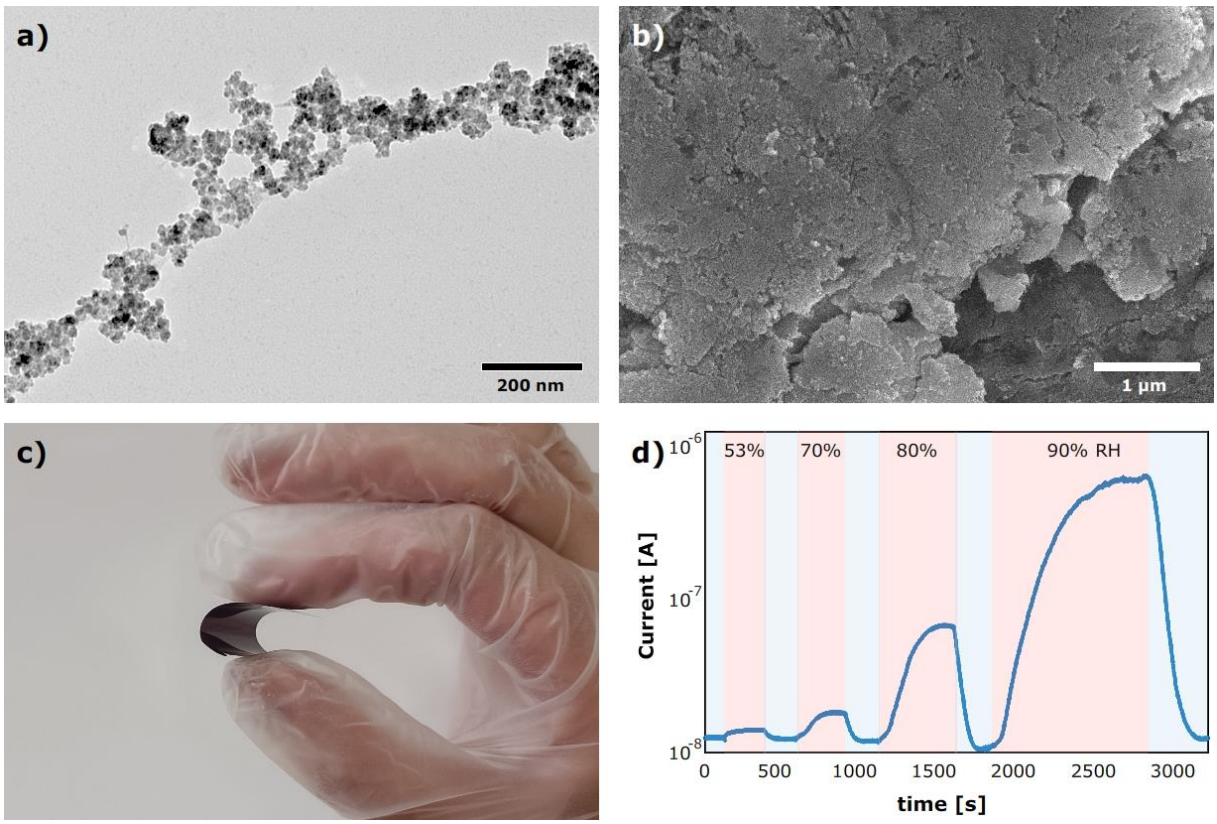


Figure 1. Structural characterization and sensing performance evaluation of nanocomposite material comprising cellulose nanofibers and Fe_3O_4 nanoparticles: a) a TEM image of individual fibrous structure; b) an SEM image of a thin, bulk sample; c) Photograph of a thin, bulk sample, demonstrating its flexibility; d) I-t measurements performed under varying levels of relative humidity, showcasing its potential for application as a humidity sensor.

Type of presentation: Oral

MS2-O-3 4D-STEM of Soft Matter: Structural Characterisation of Beam-Sensitive Polymers and Molecular Crystals Using Fast Precession and a Direct Electron Detector on a Tescan Tensor

Natalia Koniuch[a], Sang Pham[a], Zabeada Aslam[a], Emily Wynne[a], Rik Drummond-Brydson[a], Sean M Collins[a,b], Andy Brown[a]

[a]*Bragg Centre for Materials Research & School of Chemical and Process Engineering, University of Leeds, (Leeds), UK*

[b]*School of Chemistry, University of Leeds, (Leeds), UK*

Contact email: n.a.koniuch@leeds.ac.uk

Structural characterisation of organic and polymeric materials by transmission electron microscopy remains challenging due to their sensitivity to electron beam-induced damage and the low elastic scattering cross-sections associated with low-Z elements [1]. Conventional high-resolution imaging and diffraction techniques frequently exceed the critical electron dose required to preserve crystallinity and molecular order, leading to irreversible structural damage before meaningful data can be acquired. To address these limitations, we apply a low-dose four-dimensional scanning transmission electron microscopy (4D-STEM) approach, combining fast beam precession (72 kHz), low probe current (~10 pA), and a direct electron detector on a Tescan Tensor dedicated STEM. This configuration enables the acquisition of spatially resolved nanodiffraction patterns from highly beam-sensitive systems at total exposures below 10 $e^{-}Å^{-2}$, allowing crystallographic analysis while preserving structural integrity.

We demonstrate this methodology on long-chain molecular crystals (*n*-alkane and *n*-alkanol, with n = 30 - 31, respectively), where the recorded diffraction patterns at each probe position reveal dislocations, lamellar domains, and variations in molecular orientation [2, 3]. The approach is further extended to a range of polymeric materials, including pristine and recycled elastomers, uniaxially drawn poly(ethylene terephthalate), shape-memory PET/PMMA blends, and selected small-molecule organic compounds.

These results demonstrate that low-dose 4D-STEM opens up a new approach for the analysis of rich crystallographic details from beam-sensitive soft matter. The technique enables direct investigation of polymer morphology, molecular ordering, and dislocations in materials relevant to advanced manufacturing, sustainable elastomers, and pharmaceutical formulations. These advances offer new opportunities for correlating structure and properties across these materials technologies.

References:

1. Ilett et al., *Phil Trans A*, **2020**, 378 (2186), 20190601.
2. Pham et al., *Nature Materials*, **2025**, 24, 682–687.
3. Wynne et al., *Crystal Growth and Design*, **2024**, 24, 10127-10142.

Type of presentation: Oral

MS2-O-4 SEM Image contrast analysis for polymers with optimized imaging conditions

Markus Boese[a], Kirill Atlasov[a]

[a]ZEISS microscopy GmbH,

Contact email: markus.boese@zeiss.com

For polymer characterization usually various signals can be used in the SEM. In this study we will focus on the contrast of materials containing polymers using BSE and SE detection.
The Gemini column was originally developed to gain a good resolution at low voltages. This is achieved by using in-column beam deceleration, without immersing the sample in strong electric or magnetic fields. While decelerating the primary beam, the detectable electrons are accelerated towards the lens. This design also gave unique imaging contrast to the inlens detectors for SE and BSE (secondary and backscattered electrons) as well as controlling the ratio of SE and BSE to avoid charging artefacts.

These intentional properties of the detection system can be used to gain material contrast. For different combinations of materials there are sweet spots, which can be used to image with a good contrast and a high signal to noise ratio. There are many examples shown in Literature, which use the detection pattern of the Gemini detection lens. Some examples, dealing with different materials, are described in this study.

For serial block face imaging (SBF-SEM) overcoming the charging issues is the biggest challenge. In this study we used a combination of a sensitive backscatter detector together with focal charge compensation to achieve a 3D volume reconstructed from an ultrafiltration membrane (Figure 1).

The mapping of imaging conditions can be used to optimize material contrast to enable sweet spot imaging. Depending on the material combination investigated the detection system can be tuned. The energy selectivity of the detection system can be used to gain materials contrast which act as a unique and valuable tool for microstructural characterization.

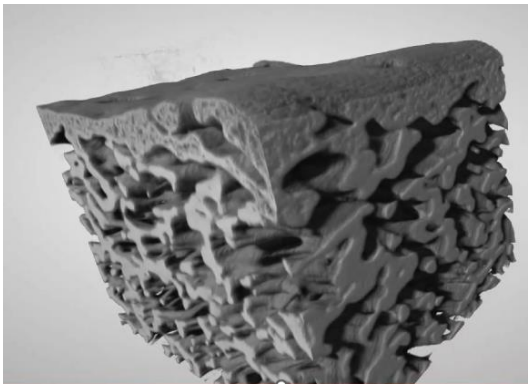


Figure 1. Polymer ultrafiltration membrane imaged with serial block face imaging utilizing focal charge compensation (1µm section of reconstructed volume)

Type of presentation: Poster

MS2-P-1 Correlation Between Adhesion and Swimming Activity in Developing Zebrafish Exposed to Polystyrene and Polyethylene Micro- and Nanoplastics

Valentina Perc[a], Victor Wepener[b], Urban Dajčman[c], Matej Hočevar[d], Damjana Drobne[a], Sara Novak[a]

[a]*University of Ljubljana, Biotechnical faculty, Ljubljana, Slovenia*

[b]*Water Research Group, Unit for Environmental Sciences and Management, North-West University, 11 Hoffman St, Potchefstroom, 2520, South Africa*

[c] *Department of Organisms and Ecosystem Research, National Institute of Biology, Slovenia*

[d]*Institute of Metals and Technology (IMT), Ljubljana, Slovenia*

Contact email: valentina.perc@bf.uni-lj.si

Introduction: Microplastics (MPs) and nanoplastics (NPs) are widespread environmental contaminants that originate from the degradation of plastic waste and are found in various aquatic ecosystems. Due to their small size, these particles have the potential to bioaccumulate in organisms and exert toxic effects, raising concerns about their impact on aquatic life. While studies have extensively examined the uptake, biodistribution, and physiological effects of MPs and NPs, their direct adhesion to biological surfaces remains an underexplored factor in toxicity assessments. This aspect is particularly relevant in early-life stages of fish, where surface interactions may influence development and behaviour. Zebrafish (*Danio rerio*) are a widely used model for evaluating the effects of environmental pollutants due to their genetic similarity to other vertebrates, rapid development, and transparent embryos, which allow real-time observation of physiological changes. Previous research has demonstrated that polystyrene (PS) and polyethylene (PE) MPs can impair zebrafish development, alter swimming behaviour, and induce cardiovascular dysfunction. However, limited data are available on how PE NPs, in particular, adhere to larval surfaces and influence locomotor activity. This study investigates the differential toxicity of PS and PE particles based on size (100nm, 5µm), shape (spherical, irregular), and origin (primary, secondary). We assess the correlation between material adhesion to the chorion, external adherence to larvae, and their impact on swimming activity in zebrafish, aiming to bridge knowledge gaps in plastic particle interactions with the early-life stages of fish.

Methods: Zebrafish embryos were exposed to PS and PE MPs and NPs until 96 hours post-fertilization (hpf). Swimming behaviour (distance travelled) was analyzed using the DanioVision system and EthoVision XT software. Following exposure, embryos and larvae were chemically fixed, dehydrated in an ethanol series, and dried using hexamethyldisilazane (HMDS) before being examined via Field emission scanning electron microscopy (FE-SEM) (Thermo Scientific Apreo 2) to assess material adherence.

Results: NPs adhered to the larval surface more extensively than MPs, with secondary PE MPs of irregular shape adhering less frequently or not at all compared to spherical PS MPs. MPs aggregated and adhered in random clusters, whereas PS and PE NPs covered larger body surface areas. Adhesion appeared to be associated with changes in larval swimming behaviour. While MPs adhered randomly and to a lesser extent, their impact on swimming activity was stochastic and not concentration-dependent. In contrast, PE NPs exhibited the highest degree of adhesion and caused a statistically significant reduction in swimming distance, even at very low, environmentally relevant concentrations.

Conclusions: These findings suggest that particle size, shape, and polymer type play a crucial role in adhesion and behavioural effects in zebrafish larvae. The high adhesion and toxic impact of PE NPs highlight their potential ecological risks, emphasizing the need for further research on long-term biological effects and trophic transfer. This study enhances our understanding of MP and NP interactions with aquatic organisms, providing valuable insights for regulatory frameworks and environmental risk assessments.

Type of presentation: Poster

MS2-P-2 Plastic-Degrading or Just Settling? First TEM insights into microbial-plastic interactions in a Cold-Climate Ecosystem

Emely Weissenbach[a], Sophia Mützel[b,c], Birgit Sattler[b,c] Magdalena Knapp[a], Anna Seybold[a]

[a]*Department of Zoology, University of Innsbruck, Innsbruck, Austria*

[b]*Department of Ecology, University of Innsbruck, Innsbruck, Austria*

[c]*Austrian Polar Research Institute, Vienna, Austria*

Contact email: anna.seybold@uibk.ac.at

Plastic pollution has reached remote cryospheric ecosystems, which are already stressed by climate change and biodiversity loss. In these cold habitats, biofilms play a key role in geochemical cycling and food web dynamics. Plastics introduce novel substrates for colonization, potentially disrupting ecological functions. However, how these biofilm microbial communities are influenced by different polymer types are unknown. Here we studied the formation of microbial biofilms on polyethylene (PE), polypropylene (PP), and polyethylene terephthalate (PET) over ten weeks during the ablation season in a proglacial lake in the Austrian Alps. Combining 16S rRNA gene amplicon sequencing with Light, Scanning (SEM), and, for the first time in this context, Transmission Electron Microscopy (TEM), we visualized microbial colonization and examined community composition. PET showed the densest coverage, while PE exhibited sparse attachment. TEM revealed close associations between cells and surface topography, with roughness and concavities facilitating adhesion. Early-stage communities differed significantly between polymers and were dominated by Betaproteobacteria, with diversity increasing over time. Potential plastic-degrading taxa were identified across all substrates, especially PE; however, whether these bacteria actively degrade polymers remains unresolved. Our results highlight how plastisphere communities in cold ecosystems are shaped by surface properties and temporal dynamics, and provide the first TEM ultrastructural insight into microbial-plastic interactions in cryospheric environments.

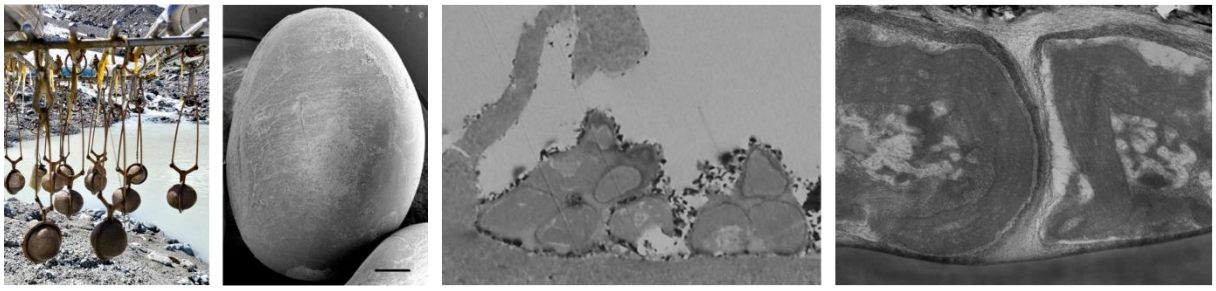


Figure 1: Plastic-associated biofilm formation: Plastic-pellet incubation in a proglacial lake (a), LM of PE, PP and PET pellets (b), TEM of the microbial-plastic interaction (c,d). Scale bar:

References:

Mützel et al. *Polymer Matters*. Early stage of plastic-associated biofilms reveals substrate-specific and polymer-degrading microbial communities during glacier melt [Manuscript submitted for publication].

MS3 Metals and alloys

Type of presentation: Invited

MS3-IN-1 Microstructural characterization of beta-Sn to alpha-Sn phase transformation

Alena Michalcová[a], Dominika Fink[a], Šárka Msallamová[a], Martin Friák[b]

[a]*University of Chemistry and Technology, Prague, Department of Metals and Corrosion Engineering, Technická 5, 166 28 Prague 6, Czech Republic*

[b]*Institute of Physics of Materials, v.v.i., Czech Academy of Sciences, Žižkova 22, Brno, 61662, Czech Republic*

Contact email: michalca@vscht.cz

The so-called tin pest is a degradation process of tin and tin rich alloys that is based on change of modification from white tin to grey tin at temperatures lower than 13 °C. It is well known that the process is influenced by temperature, inoculation, and composition of the alloy, although the effect of individual components is not clear.

The importance of low-temperature phase transformation in tin occurred due to utilization of lead-free solders that are endangered by the tin pest. The lead-free soldier materials have similar or very close composition of tin rich historical alloys. By description the degradation mechanism in historical materials, we can avoid the influence of errors caused by artificial ageing of the materials.

The tin pest can be artificially induced by presence of pink salt $(NH_4)_2SnCl_6$, which is a tin-based compound that occurs naturally in volcano ashes. This process will be also described and documented by SEM and TEM.

The authors acknowledge the Czech Science Foundation for the financial support received under the Project No. 22-05801S.

Type of presentation: Invited

MS3-IN-2 The Microstructure and Mechanical Properties of LPBF Produced Nickel-based Alloy IN718 Influenced by Laser Beam Shape and Post Heat-Treatment

Črtomir Donik[a], Matjaž Godec[a], Narges Mirzabeigi[b,c], Danijela A. Skobir Balantič[a], Simon Malej[a], Irena Paulin[a], Bojan Podgornik[a], Jonas Grünewald[b], Tobias Novotny[c], Florian Bayer[c], Katrin Wudy[b]

[a]*Institute of Metals and Technology, Ljubljana, Slovenia*

[b]*Technical University of Munich, Munich, Germany*

[c]*EOS GmbH Electro Optical Systems, Munich, Germany*

Contact email: crtomir.donik@imt.si

The study investigates how Gaussian and ring-shaped laser beam profiles influence the microstructural development and mechanical properties of LPBF-processed nickel-based alloy Inconel 718 in both as-built and post-heat-treated states. Beam shaping was employed to increase the build rate without sacrificing material quality. One goal was to optimise heat treatment parameters for the beam-shaped profile. The post-heat-treatment process involved four separate solution annealing temperatures (954 °C, 984 °C, 1034 °C, and 1154 °C), followed by a two-step standard IN718 ageing process. Microstructural changes were analysed using scanning electron microscopy (SEM) equipped with energy-dispersive X-ray spectroscopy (EDS) and Electron Backscatter Diffraction (EBSD). Using a Gaussian laser beam yields a fine-grained microstructure with no prominent columnar structure. In contrast, the ring beam profile produces a distinct columnar structure with larger nanodendritic grains and dislocation cells. Temperatures above 1034 °C cause recrystallisation, grain growth, and the formation of carbonitrides, which reduce mechanical properties. Based on the findings, the recommended optimal heat-treatment temperature for both laser beam shapes is 984 °C. At this temperature, tensile strength becomes similar in both horizontal and vertical build directions, while yield strength improves, benefiting most applications.

Keywords: PBF-LB/M, beam shaping, IN718, heat treatment, mechanical properties

Type of presentation: Oral

MS3-O-1 Influence of Al_3Zr dispersoids on the Young's Modulus of Al matrix in Al 2195 Alloy: Insights from Analytical Electron Microscopy and DFT Calculations

Mohamed E. Daoud[a], Muna S. Khushaim[b] Naga Venkateswara Rao Nulakani[a] and Dalaver H. Anjum[a]

[a]*Department of Physics, Khalifa University, P.O. Box 127788, Abu Dhabi, United Arab Emirates*

[b]*Department of Physics, Faculty of Science, Taibah University, P.O. Box 30002, Al-Madina 41447, Saudi Arabia*

Contact email: 100061429@ku.ac.ae

Introduction:

The Al2195-T8 alloy represents a significant advancement in the materials engineering domain, particularly within the aerospace industry. This high-strength aluminium-lithium (Al-Li) alloy is renowned for its exceptional combination of properties, including lower density, high stiffness, and excellent damage tolerance for creating components [1]. The addition of alloying elements leads to the formation of diverse precipitation strengthening phases in the third-generation Al–Cu–Li alloys, including the plate-like T1 (Al_2CuLi), platelet θ' (Al_2Cu), lath S' (Al_2CuMg), lenticular δ' (Al_3Li), and spherical β (Al_3Zr)[2-3]. Zirconium (Zr) is added to aluminum alloys to form fine Al_3Zr dispersoids, critical in enhancing mechanical properties and inhibiting recrystallization[4]. These dispersoids effectively pin grain boundaries, subgrain boundaries, and dislocation motion, stabilizing the microstructure. Elastic constants, such as Young's modulus (Y_M), are fundamental parameters that describe a material's response to mechanical stress, quantifying stiffness and originating from atomic-scale interactions. These properties arise from interatomic bonds, where external forces alter atomic separations, increasing potential energy and invoking restoring forces that drive atoms back to equilibrium, defining elasticity. Howe et al.[5] have established strong correlations between bulk plasmon energy (E_p) and elastic properties, hardness, and cohesive energy, using models like the free-electron theory and universal binding energy relationship (UBER). These relationships, validated via energy-filtering transmission electron microscopy (EF-TEM) and valence electron energy-loss spectroscopy (VEELS), enable the prediction of elastic properties, with Young's modulus for metals expressed as $Y_M = 0.08\ E_p^{2.25}$**.** This study investigates how Al_3Zr phase precipitates in Al2196-T8 alloy influence $Y_M$in the aluminum matrix. Using scanning transmission electron microscopy combined with electron energy loss spectroscopy (STEM-EELS), we probe nanoscale elasticity changes near precipitates. In parallel, density functional theory (DFT) is utilized to predict elastic constants of the created Al-Al_3Zr heterostructure model. By comparing experimental STEM-EELS data with DFT calculations, we aim to elucidate the atomic-scale mechanisms governing elasticity in aluminum alloys, advancing our understanding of how microstructural features impact macroscopic mechanical properties.

Materials and Methods:

A commercially available alloy AA2195 in T8 temper has been used as a case study. The nominal chemical composition of this alloy is as follows: 4 wt.% Cu, 1 wt.% Li, 0.36 wt.% Mg, 0.28 wt.% Ag, 0.14 wt.% Zr, and 94.22 wt.% Al. Samples on the T8 condition were solutions treated for 1 hr to 783 K, quenched, stretched to 3%, and subsequently aged to 423 K for 30 hrs. Aberration-corrected scanning transmission electron microscopy (AC-STEM) was utilized in this work. TEM investigations were conducted on electron-transparent foils of AA2195 alloy, prepared by mechanically grinding 3 mm diameter discs to ~150 μm thickness, followed by twin-jet electropolishing using a solution of 20 vol.% nitric acid in methanol at −20°C. AC-STEM experiments were performed using a probe-corrected Titan 80–300 ST instrument operated at 300 kV. A high-angle annular dark-field (HAADF) detector was employed to acquire conventional DF-STEM and aberration-corrected HR-STEM images, enabling detailed microstructural analysis of the alloy. Young's modulus map was produced from low-loss EELS data acquired in microscope DF-STEM mode, with a pixel size of 1 nm and 30 meV eV/channel dispersion. STEM-EELS spectrum-imaging datasets were analyzed using the non-linear least square

method to generate plasmon energy (E_p) maps, indicating shifts in E_p values per pixel. The value of Y_M at each pixel was determined from the measured E_p by using the following equation: $Y_M = 0.08\ E_P^{2.5}$.

Results:
Fig.1(a) shows a DF-STEM image of AA2195 in a T8 temper alloy sample. The image showcases the presence of the primary α-Al matrix and the β dispersoids in the sample. The β dispersoids have spherical shapes, as seen in Fig .1(a).

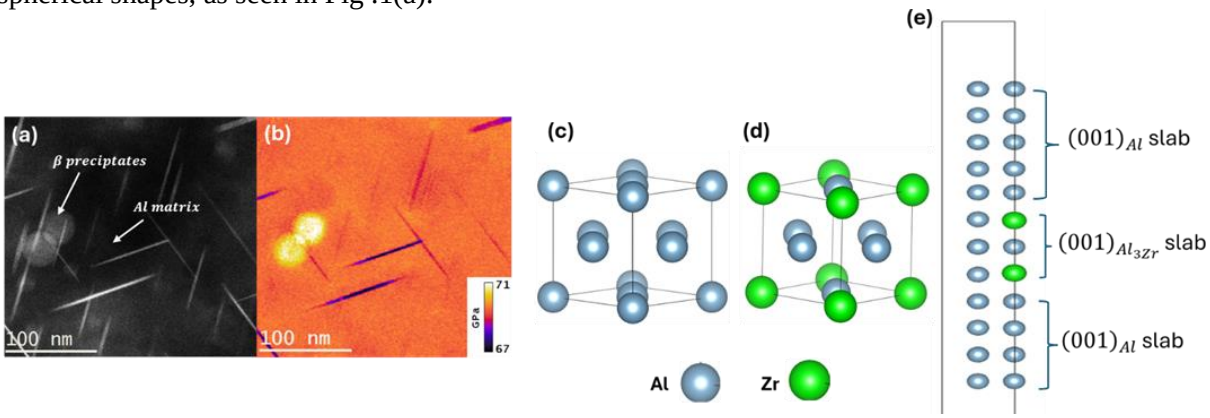


Figure1. (a) DF-STEM image. (b) STEM-EELS generated Young's modulus map in [110] direction. (c) Al unit cell model,(d) Al3Zr until cell model, and (e) The created Al-β heterostructure used in the DFT cautions.

The STEM-EELS analysis of the alloy sample was carried out to generate Young's modulus (Y_M) map as shown in Fig.1. (b),. The specimen was tilted along the $[110]_{Al}$ zone axis. In this way, penetrating electron beam generated bulk plasmons acting as longitudinal oscillators at a specific energy (E_p), also along the $[110]_{Al}$ direction. In this way, the energy of bulk plasmons (E_p), can be determined by recording the EELS spectra in the low-loss range while acquiring STEM-EELS datasets. The performed STEM-EELS analysis enabled determining the E_p values of bulk plasmons of Al at each image-pixel and were then utilized to calculate the corresponding value of the Y_M under the equation $Y_M = 0.08\ E_p^{2.25}$. The color code in Fig.1(b) indicates the range of Young modulus from 67 to 71 GPa. The values of Y_M at the β dispersoids, with an average of 71.6 GPa, are higher compared to Al matrix regions, with an average of 70.3 GPa. It can be noted the Y_M of the Al increased in the presence of the beta dispersoids; this is due to the introduction of Zr into the Al matrix, which altered the Al-Al bonds and made stronger bonds, hence higher values of Y_M. The next step was utilizing DFT to mimic the experimental observation by creating an Al-beta heterostructure and calculating the Youngs modules of the model. According to literature, the β dispersoids of the Al_3Zr precipitates tend to grow along the {100} planes of the Al matrix. This is because the {100} planes in the Al matrix and the Al_3Zr precipitate have similar atomic arrangements and lattice parameters, facilitating coherent or semi-coherent growth. So with DFT, the Youngs modulus of the Al(001) slab was calculated and compared to the Al-β heterostructure. The calculation showed that the Young's modulus of the Al(001) slab was 82 GPa, and the for the heterostructure was 94 GPa. This shows a trend of increase similar to the external observations obtained by STEM-EELS.

Conclusion:
The study conclusively demonstrates that STEM-EELS analyses provide an accurate method for determining Young modules at the nanoscale. It showed an increase in Y_M value at the β dispersoids compared to the Al matrix. DFT was also utilized to complete the experimental observation. The calculation also showed a trend in the increase of Y_M of Al-β compared to the Al slab.

Acknowledgements

The authors would like to thank Electron Microscopy Facilities at King Abdullah University of Science & Technology (KAUST) and Khalifa University (KU) for providing access to the experiments.

References:

1. L. Xia, Y. Li, M. Huang, J. Liu, and P. Hu, "Improved corrosion resistance of 2195 Al-Cu-Li alloy through T6I6 interrupted aging," Journal of Alloys and Compounds, vol. 956, p. 170055, 2023
2. C. Dwyer, M. Weyland, L.-Y. Chang, and B. Muddle, "Combined electron beam imaging and ab initio modeling of T1 precipitates in Al–Li–Cu alloys," Applied Physics Letters, vol. 98, no. 20, 2011
3. S. Zhang et al., "Effect of aging treatment on high temperature mechanical properties of a cast Al–Li–Cu alloy," Materials Science and Engineering: A, vol. 896, p. 146300, 2024.
4. Liu Q, Fan G, Tan Z, Li Z, Zhang D, Wang J, Zhang H. Precipitation of Al3Zr by two-step homogenization and its effect on the recrystallization and mechanical property in 2195 Al–Cu–Li alloys. Materials Science and Engineering: A. 2021 Jul 21;821:141637.
5. J. M. Howe and V. P. Oleshko, "Application of valence electron energy-loss spectroscopy and plasmon energy mapping for determining material properties at the nanoscale," Microscopy, vol. 53, no. 4, pp. 339-351, 2004.

Type of presentation: Oral

MS3-O-2 Atomic-resolution electron microscopy analysis of oxygen-mediated Ti nanocrystalline synthesized by high-pressure torsion

Qiulin Qu[a], Yong Huang[a], Zhuo Chen[a], Maxim N. Popov[b], Georg Haberfehlner[c], Gerald Kothleitner[c], Zaoli Zhang[a]

[a]*Erich Schmid Institute of Materials Science, Austrian Academy of Sciences, 8700 Leoben, Austria*

[b]*Materials Center Leoben Forschung GmbH, 8700 Leoben, Austria;*

[c]*Institute of Electron Microscopy and Nanoanalysis, 8010 Graz, Austria*

Contact email: qiulin.qu@oeaw.ac.at

Introduction

It is known that oxygen incorporation can enhance the strength of titanium (Ti) alloys but also result in a loss of ductility. However, the face-centered cubic (*fcc*) Ti with multiple slip systems has recently attracted significant attention as a potential solution. In this study, high-pressure torsion (HPT) was employed to produce a hexagonal close-packed (*hcp*) Ti matrix with intergranular *fcc*-Ti lamellae and randomly distributed simple hexagonal structure omega phase (ω-Ti). By applying atomic-resolution electron microscopy, complemented by theoretical calculations, we investigate the nucleation mechanism and location of the *fcc*-Ti phase, the role of oxygen in the phase transformation, and their influence on the mechanical properties.

Experimental Methods

Bulk oxygen (O)-mediated Ti was prepared using arc-melting. High-pressure torsion was used to synthesize oxygen-mediated Ti nanocrystalline. The X-ray diffraction (Bruker D2 Phaser) was used to characterize the crystallographic structure. The TEM samples were prepared by grinding, mechanical polishing, dimpling, and electropolishing. Two transmission electron microscopes (image-side spherical aberration corrected JEOL JEM-2100F, probe-corrected FEI Titan^3 G2) were utilized to analyze the microstructure and chemistry. The Vickers hardness and tensile tests were performed to determine the O-mediated nanocrystalline's hardness and tensile strength. The tensile fracture surfaces were closely examined using the scanning electron microscope (Zeiss Leo 1525). DFT calculations were performed in the VASP code using PBEsol exchange-correlation functional, plane-wave cut-off of 400 eV, and Brillouin zone integration over a uniform grid with resolution of 0.1 Å^{-1}.

Results

TEM analysis shows that as the oxygen content increases, the average grain size significantly decreases while the relative content of ω-Ti diminishes and the relative content of *fcc*-Ti rises. Using high-resolution transmission electron microscopy (HRTEM), the *fcc*-Ti lamellae at grain boundaries and the *hcp*/*fcc* interfaces orientated as $\{0002\}_{hcp}\|\{11\text{-}1\}_{fcc}$ and $\{0002\}_{hcp}\|\{002\}_{fcc}$ are observed, while the special ω/*fcc* interfaces orientated as $\{03\text{-}30\}_{\omega}\|\{220\}_{fcc}$ are also observed for the first time. Combined with electron energy-loss spectroscopy (EELS) and density functional theory calculations, we found that oxygen atoms preferentially distribute in *fcc*-Ti due to their lower solution energy at octahedral interstitial sites. The mechanical tests indicate that O-mediated Ti exhibits high strength (1210 MPa) and reasonable ductility (2.2%).

Discussion and conclusions

Deformation-induced dislocation accumulation at grain boundaries provides numerous *fcc*-Ti nucleation sites. Accompanied by oxygen incorporation, these locations eventually facilitate the prominent growth of the intergranular *fcc*-Ti phase. Energetically, O atoms are located in the octahedral interstitial sites in *fcc*-Ti, leading to significantly lower dissolution enthalpy. Such a way drives more oxygen to diffuse into the *fcc*-Ti, reducing the system's energy. Structurally, the interstitial oxygen increases the lattice parameter of *fcc*-Ti and reduces the interface misfits, thus enhancing the structural stability and inhibiting the reverse transformation to *hcp*-Ti. Due to the superior mechanical properties of *fcc*-Ti, this oxygen-mediated intergranular *fcc*-Ti can primarily enhance strength while maintaining good ductility

of nanocrystalline Ti. This also offers a novel mechanism for stabilizing *fcc*-Ti at grain boundaries via combinatorial O incorporation and deformation.

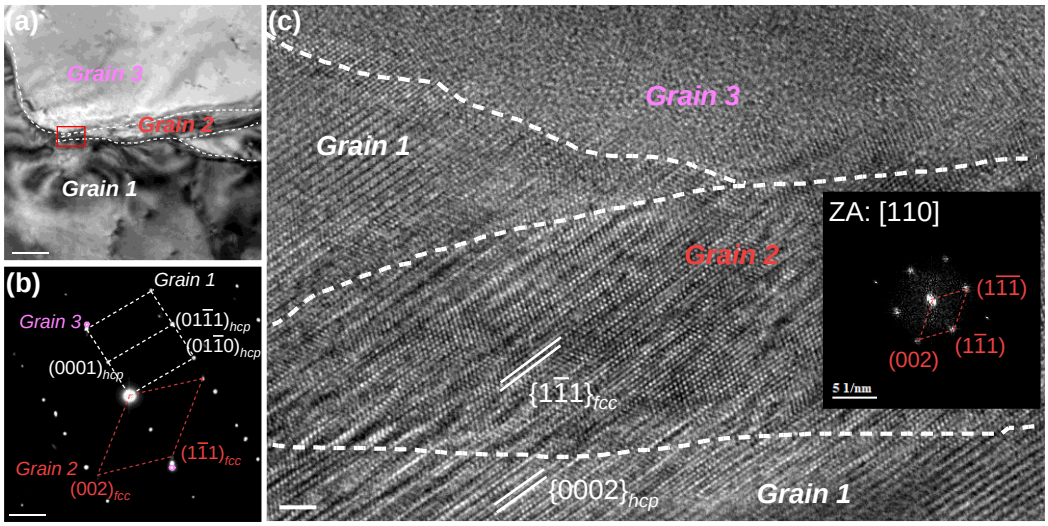


Figure 1: The TEM images of the 0.14 wt.% O specimen: (a) bright-field image of lamellar grain boundaries, (b) the selected area electron diffraction (SAED) pattern of (a), (c) HRTEM image of the red box in (a) inset with fast Fourier transform (FFT) pattern in Grain 2, exhibiting the *fcc*-Ti phase.

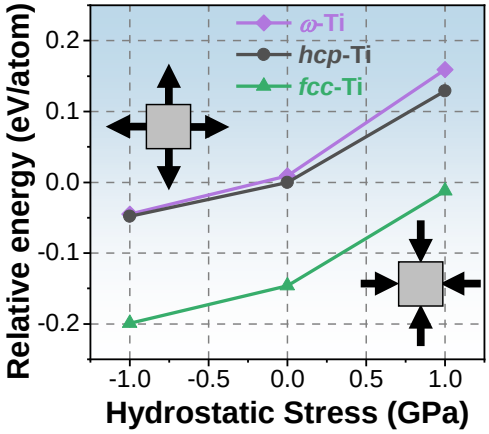


Figure 2: The relative solution enthalpy of oxygen at octahedral interstitial sites in *hcp*, *ω*, and *fcc* Ti lattices under varying hydrostatic pressures, calculated by density functional theory (DFT).

Acknowledgment: This work is financially supported by the Austrian Science Fund (FWF036581). The authors thank Prof. Yanmin Zhang (Henan University of Science and Technology, China) for delivering bulk Ti materials. We acknowledge access to the FEI Titan³ G2 at the Graz Centre for Electron Microscopy including a K2 camera funded by the "Zukunftsfond Steiermark". M.N.P. gratefully acknowledges the financial support under the scope of the COMET program within the K2 Center "Integrated Computational Material, Process and Product Engineering (IC-MPPE)" (Project No 886385).

Type of presentation: Oral

MS3-O-3 (S)TEM study of the WTaVCr alloy for fusion application

Andreja Gajović[a], Sandra Drev[b], Kristina Tomić Luketić[a], Toni Dunatov[a], Mario Matić[a], Vedran Kojić[a], Krunoslav Juraić[a], Jasminka Popović[a], Željko Skoko[c], Tonči Tadić[a], Miran Čeh[b]

[a]*Ruđer Bošković Institute, (Zagreb), Croatia*

[b]*Jožef Stefan Institute, (Ljubljana), Slovenia*

[c]*University of Zagreb, Faculty of Science, Department of Physics, (Zagreb), Croatia*

Contact email: Andreja.Gajovic@irb.hr

Introduction: Development of fusion-based power plants (FPPs) is of paramount importance for the European Green Deal initiative of lowering carbon emissions, since FPPs do not generate CO_2 or other substance harmful to the atmosphere. In the context of achieving FPP reliability, one of the important points is the effect of high energy fusion neutrons (MeV range) on the component materials of the fusion reactor. Therefore, the engineering and design of materials for fusion reactors are of key importance [1]. The two processes that are the most relevant when testing a material for fusion environments are its response to (1) displacement damage and (2) transmutation reactions [2]. That processes can be mirrored by ion beam irradiation since effects can be introduced into the material much more simply and quickly then by neutrons generated in fission reactors due to low or no radioactivity and the larger cross-sections of ion beams. Displacement damage can be emulated by heavy ion irradiation, while nuclear transmutation reactions can be mimicked by helium implantation. This is most impactful when these two types of ion irradiation are applied simultaneously, e.g. in the dual-beam irradiation setup, like the Dual-Beam Ion Irradiation Facility for Fusion Materials (DiFU) at Ruđer Bošković Institute [3], which is one of only a dozen worldwide [4].

For fusion application, the tungsten and tungsten-based alloys, especially refractory high entropy alloys (RHEA), are defined as high heat flux (about 10 MW/m^2) materials for plasma facing components e.g. first wall and diverter [5]. Quaternary W-based alloy WTaVCr is declared as highly resistant upon irradiation [6]. So, to verify our capabilities of depositing RHEA, WTaVCr was prepared and its structural properties as well as chemical composition are evaluated before and after irradiation in DiFU.

Methods: We deposited 1 μm thick film of WTaVCr on silicon substrate by RF magnetron sputtering. WTaVCr film was irradiated in DiFU with 8 MeV Cu^{3+} and 200 keV He^+ to dose 1 dpa (1.9 x 10^{15} ions/cm^2). Then it was characterized by XRD, SEM, EDS and (S)TEM before and after irradiation.

Results: As-deposited WTaVCr film dominantly contains body-centered cubic structure with a unit-cell parameter a=3.191(2) Å with interplanar distances d_{011}=2.25 Å and d_{022}=1.13 Å (Figure 1a). Additionally, a second, minority body-centered cubic phase with unit-cell parameter a=3.126(3) Å (with interplanar distance of d_{011}=2.21 Å) is also observed. While the appearance of the second phase indicates a possible phase segregation of lighter element (V or Cr), this assumption has been disproved by EDS mapping. EDS measurements in SEM as well as STEM imaging in combination with EDS mapping show that all the elements (W, Ta, V and Cr) are homogenously distributed in all the crystal grains. These results led to the conclusion that both *bcc* phases are actually the high entropy alloys lattices containing all four metals.

After irradiation in DiFU, high entropy alloy with a unit-cell parameter a=3.126 Å becomes dominant crystalline phase, although the presence of HEA structure with a=3.191 Å can still be observed. Irradiated sample has also been investigated by atomic resolution STEM imaging in combination with EDS mapping and confirmed that all the elements are homogenously distributed (Fig. 2), while the measured atomic ratio of elements observed in crystal lattice of as-deposited sample in comparison to their ratio after irradiation was similar, within statistical deviation. From the atomic ratio of elements, the thermodynamic parameters were calculated by phenomenological approach [7] and the results

indicate stable single-phase system, while electronic composition of the valence electrons (VEC) predicts the appearance of a single BCC phase.

Discussion and conclusions: In the course of Rietveld refinements, the line broadening analysis has also been conducted. It was found that line profiles of HEA structure with larger unit-cell (present in as-deposited sample) are broader compared to those of HEA structure with smaller unit-cell obtained after the irradiation. Such broadening is caused by the presence of significant distortions within the crystal lattice of as-prepared sample due to the different atomic radii occupying the same crystallographic position yielding the micro-strain value ε that is significantly larger compared to the micro-strain present in the irradiated HEA having smaller unit-cell. Observed decrease in micro-strain indicates that the irradiation causes the significant reduction in number of distortions and the relaxation of deformations originally present within the as-prepared crystal lattice finally also leading to the observed decrease of unit-cell parameters. These results put the studied multicomponent alloy in the forefront as highly resistant to intense irradiation.

Acknowledgment
This work is financed by European union NextGenerationEU within RBI program KP3-24.

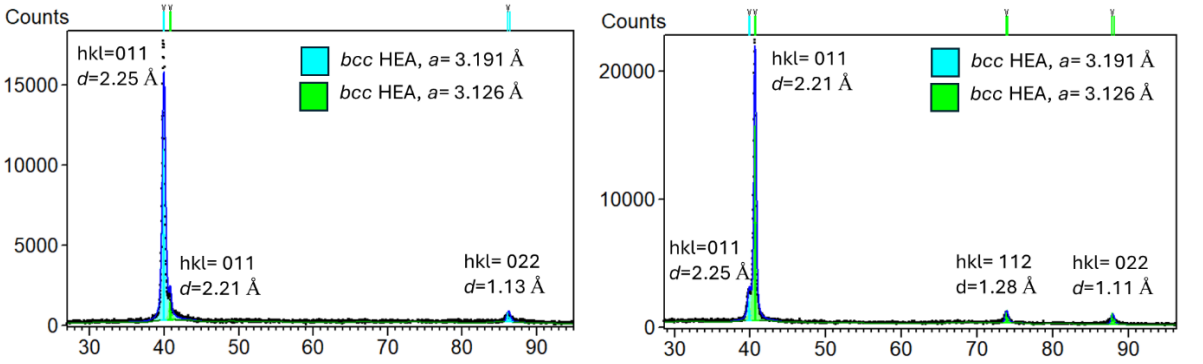


Figure 1: X-ray diffraction pattern of WTaVCr film (a) as deposited, (b) after irradiation in DiFU.

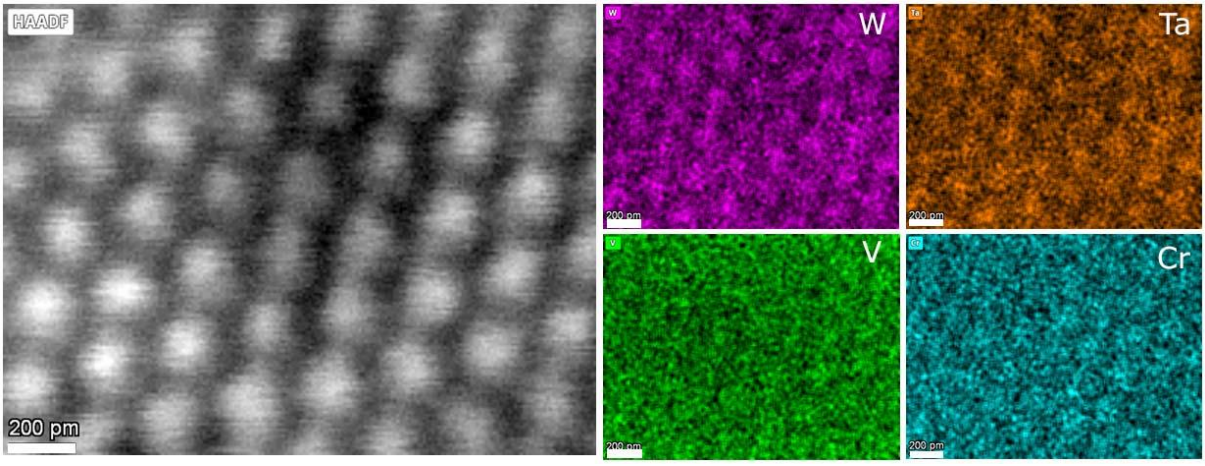


Figure 2: HAADF and EDS maps of WTaVCr film after irradiation in DiFU. Scale bars are 200 pm.

References:
1. M. Gorley, E. Diegele, s. Dudarev, G. Pintsuk, *Fusion Engineering and Design* **2018**, *136*, 298–303.
2. Was, G. S. Fundamentals of radiation materials science: metals and alloys, Springer, **2007**.
3. T. Tadić, T. Dunatov, S. Fazinić, D. D. Cosic, M. Jakšić, Z. Siketić, M. Vićentijević, W. Kada, C. D. Hardie, *Materials* **2023**, *16* (3), 1144.
4. R. Vila, The role of IFMIF-DONES in the fusion material challenge, Xcitech DONES – School for science and technology, Granada, April 26th **2024**.
5. G. Pintsuk, G. Aiello, S. L. Dudarev, M. Gorley, J. Henry, M. Richou, M. Rieth, D. Terentyev, R. Vila, *Fusion Engineering and Design* **2022**, *174*, 112994.

6. O. El-Atwani, N. Li, M. Li, A. Devaraj, J. K. S. Baldwin, M. M. Schneider, D. Sobieraj, J. S. Wróbel, D. Nguyen-Manh, S. A. Maloy, E. Martinez, *Sci. Adv.* **2019**, *5* (3), eaav2002.
7. O. El Atwani, H. T. Vo, M. A. Tunes, C. Lee, A. Alvarado, N. Krienke, J. D. Poplawsky, A. A. Kohnert, J. Gigax, W.-Y. Chen, M. Li, Y. Q. Wang, J. S. Wróbel, D. Nguyen-Manh, J. K. S. Baldwin, O. U. Tukac, E. Aydogan, S. Fensin, E. A. Martinez, *Nat Commun* **2023**, *14* (1), 2516.

Type of presentation: Oral

MS3-O-4 Correlative Transmission Electron Microscopy for Nanophase Identification in Galvannealed Advanced High-Strength Steel

Alexey Minenkov[a], Aleksander Brozyniak[a], Heiko Groiss[a]

[a]*Christian Doppler Laboratory for Nanoscale Phase Transformations, Center for Surface and Nanoanalytics, Johannes Kepler University Linz, Altenberger Straße 69, Linz, 4040, Austria*

Contact email: oleksii.minienkov@jku.at

Designing cutting-edge Advanced High-Strength Steel (AHSS) that meets the demands of modern automotive production calls for dependable investigation methods. To ensure safety and durability, modern AHSS products need effective corrosion protection, which is routinely achieved by applying Zn-based coating through a carefully controlled galvannealing process. Alloying elements, such as Mn and Si, enhance the mechanical properties of AHSS but dramatically alter the desired interaction between Fe and Zn [1-3]. Due to low Si solubility in Zn-Fe phases, its presence destabilizes these compounds, resulting in the formation of numerous Si-rich nanoprecipitates (NPs) [1,2]. To make further advancements in material development, it is essential to have detailed structural and chemical insights into the achieved phase configuration.

The unambiguous identification of nanoscaled phases, especially those embedded in a matrix, is an extensively challenging task, which stretches conventional analytical methods to the limit. In this contribution, we present a correlative transmission electron microscopy approach based on the synergy of HRTEM, STEM EDX, PED, and TKD [1]. The method efficiency was verified using Fe-Si-Al NPs (20 – 50 nm in diameter) embedded in a Zn-Fe matrix of similar structure in a galvannealed steel coating. Given the dimensions of the entities under study, dependable and high-quality thin TEM sample preparation plays a decisive role. We achieved this by employing a PFIB operated with Xe and performing the final thinning step at a temperature as low as −50°C to suppress beam-induced effects in Zn-Fe phases. This workflow is a logical advancement of our previously presented approach [3].
As a result, the phases of NPs and the matrix were refined as DO_3-type structured $AlFe_2Si$ and Γ_1 Zn-Fe intermetallic compound, respectively [1]. The best-fitted candidates of the phases in question were first revealed using complementary STEM EDX and HRTEM. This result formed the basis for the next step - confirming the structure with PED using a sample tilt series workflow. To facilitate the analysis of broad regions containing multiple NPs, we tested the TKD technique augmented with post-processing and phase identification by the AZtecCrystal MapSweeper solution, showing its prominent potential. We believe that the flexibility and robustness of our approach can be highly relevant for the advanced characterization of nanostructured materials, such as those formed by additive manufacturing or representing high-entropy alloys.

Acknowledgements: We gratefully acknowledge the financial support by the Austrian Federal Ministry of Labour and Economy, the National Foundation for Research, Technology and Development and the Christian Doppler Research Association.

[1] A. Minenkov, A. Brozyniak, H. Groiss, Nanophase identification via correlative transmission electron microscopy: A case study of galvannealed advanced high-strength steel, Materials & Design, 2025, 251, 113696. https://doi.org/10.1016/j.matdes.2025.113696
[2] A. Minenkov, et al., Interaction and evolution of phases at the coating/substrate interface in galvannealed 3rd Gen AHSS with high Si content, Materials & Design, 2024, 237, 112597. https://doi.org/10.1016/j.matdes.2023.112597
[3] A. Minenkov, et al., Towards a dependable TEM characterization of hot-dip galvanized steels with low and high Si content, Materials & Design, 2023, 227, 111684. https://doi.org/10.1016/j.matdes.2023.111684

Type of presentation: Poster

MS3-P-1 Corrosion at Home: Microscopy's Role in Understanding Everyday Material Failures

Tanja Antić[a], Mirjam Bajt Leban[a], Tadeja Kosec[a]

[a]*Slovenian National Building and Civil Engineering Institute, Laboratory for Metals, Corrosion and Anticorrosion protection (Ljubljana), Dimičeva 12, Slovenia*

Contact email: tanja.antic@zag.si

Introduction: In our daily lives, we encounter various forms of corrosion affecting household objects and infrastructure. The severity of corrosion damage ranges from minor aesthetic issues to hazards that threaten safety or cause significant financial loss—such as leaks in internal water distribution systems. This paper highlights three case studies of household corrosion failures. The first examines leaks in galvanized pipes used for cold drinking water distribution. The second explores the catastrophic failure of an Italian-style coffee maker and the underlying cause. The third focuses on a unique form of corrosion affecting aluminium handlebars on a road bicycle.

Methods: Samples from each case study were prepared regarding to the mode of failure and the required analytical techniques to identify the causes of failure.
In the case of the galvanized cold drinking water distribution system, the affected pipe section was first examined through visual inspection. The pipe was then cut into two segments to prepare metallographic specimens for analyzing corrosion deposits and the remaining Zn protective layer on the inner pipe wall. Investigations included metallography, scanning electron microscopy (SEM), X-ray mapping, and Raman spectroscopy to characterize the corrosion morphology and elemental composition.
For the Italian-style coffee maker failure, a metallographic cross-section was prepared near the observed crack at the upper edge of the lower container. The microstructure of different stainless steel components was revealed using the aqua regia etchant. Optical emission spectroscopy (OES) was performed to verify the chemical composition of the stainless steel alloys involved.
In the case of the aluminum bicycle handlebars, initial surface examination was conducted using optical microscopy to assess the extent of corrosion damage. A metallographic cross-section was prepared from the area showing the most severe corrosion. The corrosion products and microstructural features were further analyzed using SEM coupled with energy-dispersive X-ray spectroscopy (EDS).

Results and discussion: The analysis of the 40-year-old cold water distribution pipe revealed that the leakage was caused by extensive localized corrosion. A significant accumulation of corrosion products was observed around the pinhole, where the wall thickness was substantially reduced. This localized thinning resulted from the continuous formation and subsequent flushing of corrosion products away, leading to progressive material loss. Notably, at the bottom section of the pipe, the zinc protective layer was completely absent, exposing the underlying steel to further corrosion.
The Italian-style coffee maker experienced catastrophic failure during operation, resulting in a high-pressure rupture that propelled the device across the room. Detailed analysis indicated that the failure was due to the combination of incompatible materials and a defective weld. Variations in hardness across the heat-affected zone (HAZ) of the weld led to mechanical weakness. This structural inconsistency, combined with thermal and mechanical stresses during coffee preparation, ultimately caused the weld to fracture under pressure.
Corrosion of the aluminum handlebars occurred beneath the fine grip insulation. Human sweat, which contains water, lactates, and urea, creates a highly corrosive environment. Chloride ions, present in concentrations ranging from 0.7 to 1.2 g/L, further accelerate the corrosion process. The insulated region also limits oxygen availability, promoting crevice corrosion. This aggressive localized attack weakened the aluminum structure, leading to the failure of the handlebars.
Conclusions: In the presented case studies, a variety of microscopic and spectroscopic techniques were employed to investigate the underlying causes of failures in household appliances, ranging from those used for drinking water distribution, coffee preparation, to daily bicycle training.

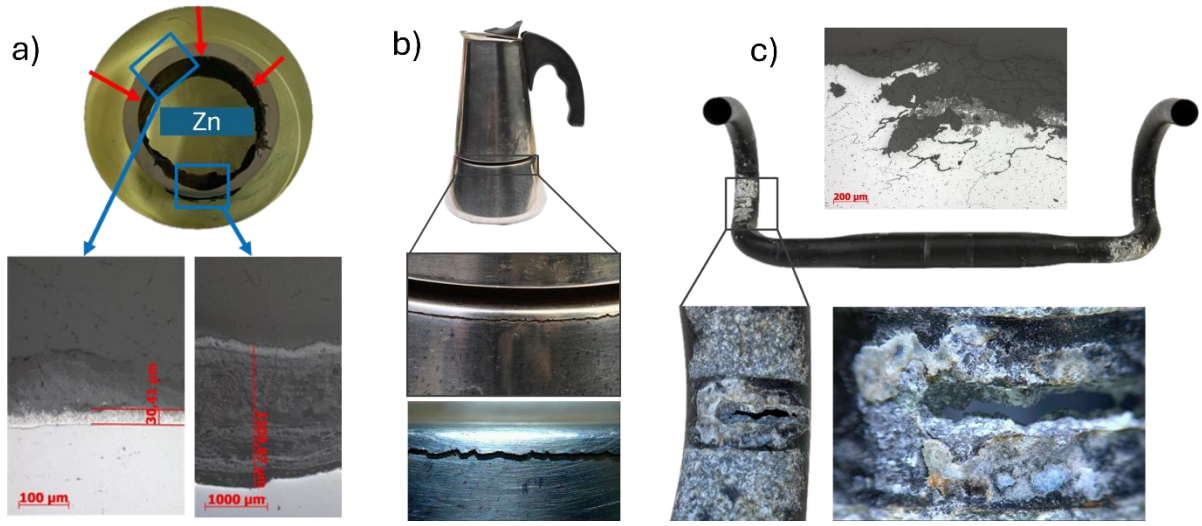


Figure 1: Three different case studies to study failure due to corrosion or material characteristics: galvanized steel pipe for drinking water distribution (a), failure of Italian style coffee maker (b) and corrosion failure of aluminium bicycle handle bar (c).

Type of presentation: Poster

MS3-P-2 Plastic deformation in the Magnesium alloy AZ80 - an EBSD study of the effects of cavitation peening

Bor Arah[a], Iztok Naglič[b], Boštjan Markoli[b], Sebastjan Žagar[c], Roman Šturm[c], Hitoshi Soyama[d]

[a]*Center for Electron Microscopy and Microanalysis, Jožef Stefan Institute, Jamova cesta 39, 1000 Ljubljana, Slovenia*

[b]*Faculty of Natural Sciences and Engineering, Aškerčeva 12, 1000 Ljubljana, Slovenia*

[c]*Faculty of Mechanical Engineering, Aškerčeva 6, 1000 Ljubljana, Slovenia*

[d]*Department of Finemechanics, Tohoku University, Sendai 980-8579, Japan*

Contact email: bor.arah@ijs.si

Magnesium alloys have applications in aviation, aerospace, electronics, and automotive industries due to their light weight and specific strength. However, their poor ductility, weak corrosion resistance and low thermal conductivity represent significant drawbacks, limiting their use. The mechanical properties and corrosion resistance of these alloys are dependent on grain size, texture, residual stress, second phase distribution, and alloying additions [1] and can be modified using several methods. While the effects of cavitation peening on AZ80A were previously studied by Žagar *et al.* [2], the suitability of cavitation peening for the purpose of hardening of Mg-Al-Zn alloy surfaces was further evaluated in this study by comparing the microstructure of a cavitation peened region with an untreated region of the AZ80.

The aim of this study was to compare the microstructure of AZ80 just below the cavitation peened surface, at a depth of approximately 400 μm, with the microstructure at an approximate depth of 5 mm. The presence of twins in the shallow region was previously confirmed via optical microscopy techniques, however, with EBSD the twinning could be further characterized. It was expected that the majority of the twins occurring due to the plastic deformation would be extension twins {10-12}, with a grain boundary misorientation angle of 86°, rather than contraction twins {10-11}, which have an angle of 56° [3].

It was necessary to expend significant effort in optimizing the sample preparation technique, as the alloy contains homogenously dispersed inclusions of an intermetallic phase, rendering chemical etching unsuitable - it resulted in the dissolution of only the matrix, while the inclusions remained. The sample was finally prepared by gentle manual grinding on SiC paper followed by polishing. This proved challenging due to the poor corrosion resistance of the alloy, which was readily etched by the colloidal silica suspension. EBSD maps with a step size of 0.5 μm were recorded on a Thermo Fisher Scientific Apreo 2S SEM coupled with an Oxford Instruments C-Swift+ EBSD detector.

[1] V. Beura *et al.*, Enhanced mechanical behavior and corrosion resistance of AZ31 magnesium alloy through a novel solid-phase processing, *Corrosion Science* 197 (**2022**) 110074;
[2] S. Žagar *et al.*, Surface integrity of heat treatable magnesium alloy AZ80A after cavitation peening, Journal of materials research and technology 17 (**2022**) 2098;
[3] J.F. Nie *et al.*, Microstructure, Deformation, and Property of Wrought Magnesium Alloys, Metall Mater Trans A 51 (**2020**) 6045.

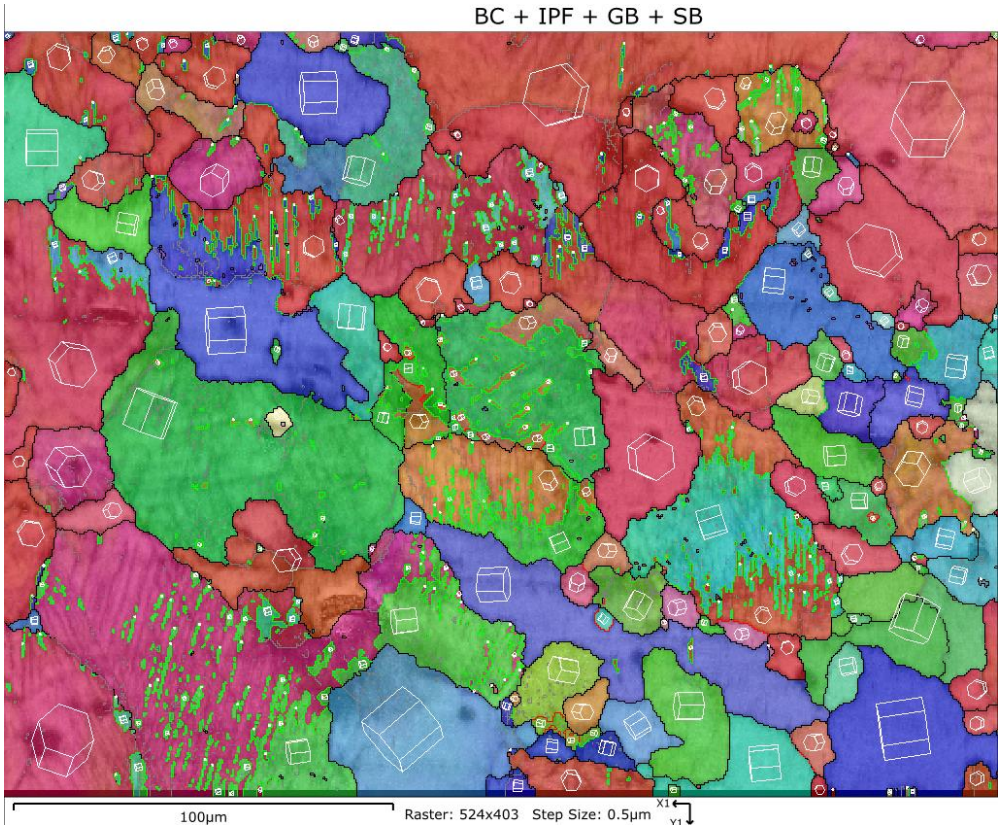


Figure 15: EBSD map of the shallow sub-surface region of the cavitation-peened sample.

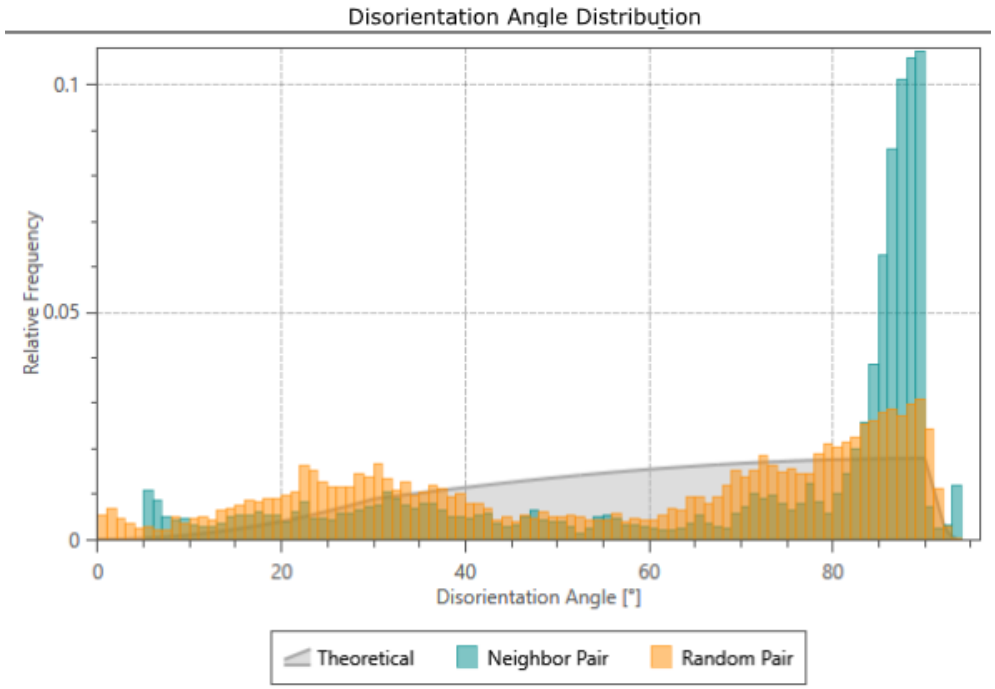


Figure 16: *Disorientation angle distribution between neighbouring and random pairs in the region presented in Figure 1, compared to the theoretical distribution.*

Type of presentation: Poster

MS3-P-3 Precession Electron Diffraction in modern steel systems

Aleksander Brozyniak[a], Alexey Minenkov[a], Martin Krenn[a], Philipp Kürnsteiner[a], Heiko Groiss[a]

[a]*Christian Doppler Laboratory for Nanoscale Phase Transformations, Center for Surface and Nanoanalytics, Johannes Kepler University Linz, Altenberger Str. 69, 4040 Linz, Austria*

Contact email:aleksander.brozyniak@jku.at

Precession electron diffraction (PED) is a powerful tool for the analysis of modern steel-based systems, improving phase identification at the micro- and nanoscale. Its key advantages include a highly localized electron beam (≈ 1 nm in diameter), the generation of quasi-kinematic diffraction patterns, an increased number of reflexes, and reduced sensitivity to zone axis misorientations. The combination of PED with energy-filtered transmission electron microscopy (EFTEM) further improves the signal-to-noise ratio and enhances pattern clarity. These features enable more accurate lattice determination and phase identification than conventional diffraction techniques such as selected area electron diffraction (SAED).

In materials exhibiting large phase grains, PED facilitates the accurate identification of complex phases, such as Fe-Zn intermetallic compounds, and provides deeper insight into phase and orientation relationships [1]. By acquiring a series of diffraction patterns from the same area of the sample tilted at different angles (multi-tilt approach), PED allows for reliable phase identification by comparing the experimental tilting angles with theoretical interzonal ones. This capability is particularly valuable for complementing other techniques such as energy-dispersive X-ray spectroscopy (EDX), which may struggle to distinguish phases with similar composition but different structure.

PED is particularly useful for the study of nanostructures (10-50 nm in at least one dimension) embedded in a matrix. Compared to SAED, where the amount of diffraction information generated by such nanostructures is small compared to the surrounding matrix, PED provides high quality diffraction patterns due to its highly localized beam. In quenched and partitioned (Q&P) steels, we show the results of a multi-tilt approach where PED allowed unambiguous identification of cementite (θ-Fe_3C) and transition carbides (ε-Fe_3C and η-Fe_2C), as well as a full orientation relationship with the surrounding martensite matrix. Similarly, the reliable identification of DO_3-structured $AlFe_2Si$ nanoprecipitates, surrounded by a Γ_1 matrix, in high-Si galvannealed advanced high-strength steels (AHSS) could be achieved [2]. The review of PED applications for modern steels is complemented by an outlook on the possibilities of 4D-STEM mapping.

1. A. Minenkov *et al.*, “Interaction and evolution of phases at the coating/substrate interface in galvannealed 3rd Gen AHSS with high Si content,” *Mater Des*, vol. 237, p. 112597, 2024.
2. A. Minenkov, A. Brozyniak, and H. Groiss, “Nanophase Identification via Correlative Transmission Electron Microscopy: A Case Study of Galvannealed Advanced High-Strength Steel,” *Mater Des*, p. 113696, 2025.

Type of presentation: Poster

MS3-P-4 TEM Analysis of Maraging Steel

Jan Duchon[a], Drahomír Dvorský[a], Petr Svora[a],

[a]*Institute of Physics, Czech Academy of Science, Na Slovance 1999/2, Praha 8, 182 21 Prague, Czech Republic*

Contact email: duchon@fzu.cz

Transmission Electron Microscopy (TEM) plays a pivotal role in analyzing powder metallurgy materials, including maraging steel. TEM enables high-resolution imaging of microstructures, such as grain boundaries, dislocations, and precipitates, which are critical for understanding the mechanical properties of the material. In the context of powder pre-treatment, TEM can reveal the effects of thermal treatments on the distribution and morphology of precipitates, as well as the interaction between different phases in self-composite materials. This detailed analysis helps in optimizing the pre-treatment processes to achieve desired strength and ductility in engineering applications.

The Mg-Y-Zn magnesium alloy system is well-known for its exceptional balance of high strength and ductility, achieved with only small amounts of alloying elements. This impressive performance stems from its distinctive microstructure, which features Long-Period Stacking Ordered (LPSO) phases or the Mille-Feuille structure (MFS), a unique microstructure derived from the LPSO phase. The properties of such a system, before will be investigated using TEM.

Acknowledgement
CzechNanoLab project LM2023051 funded by MEYS CR is gratefully acknowledged for the financial support of the measurements/sample fabrication at LNSM Research Infrastructure.

Type of presentation: Poster

MS3-P-5 Microstructure Analysis of Carbonyl Iron Powder (CIP)

Tara Gudžulić[a], Aleksander Učakar[a,b,c] and Miran Čeh[a,b,c]

[a]*Center for Microscopy and Microanalysis, Jožef Stefan Institute, 1000 Ljubljana, Slovenia*

[b]*Department for Nanostructured Materials, Jožef Stefan Institute, 1000 Ljubljana, Slovenia*

[c]*Jožef Stefan International Postgraduate School, 1000 Ljubljana, Slovenia*

Contact email: tara.gudzulic@ijs.si

Carbonyl Iron Powder (CIP) is a fine powder of iron that is produced by carbonylation, which involves the reaction of iron with carbon monoxide at high temperatures and pressures. The result is a very pure and fine form of iron with a high surface area. Carbonyl Iron Powder features excellent absorption of radar and microwaves, high purity, outstanding quality and consistency. It can also be easily incorporated in plastic, elastomeric, or varnish matrices to provide efficient shielding of electronic equipment from electromagnetic interference and minimize reflection of objects exposed to radiation in the radar and microwave frequency bands [1]. It is used in powder metallurgy (PM)/powder applications, in basic research material, metal injection mouldings, chemical and in the electronic industries. Due to its fineness and sphericity Carbonyl Iron power was at the beginning used as a "model powder" for investigating the behaviour of Iron powder especially during the sintering process [2]. Carbonyl Iron Powder appearance is usually a grey powder, composed of spherical particles. Carbonyl Iron particles, typically 20 - 40 %, are suspended in 60 - 80 % carrier fluid [3].

In this study a series of samples were prepared. Comparative study was made between raw air atomized Carbonyl Iron Powder with its contour part that has been embedded in polymer. We focused on morphological differences between raw and embedded particles and particle density and destitution in polymer samples. Particle size distribution (PSD) played an important role on the end microstructure. Sample differences in cover layer were one polymer sample with embedded particles was shielded only from one side and the other one from both sides. For both samples cross section was prepared, samples were then carbon coated.
To better understand the differences between the samples, we examined them using SEM and SEM - EDS analysis. The SEM analysis technique has revealed that there are no major differences between the two samples. In both cases we have a roughly homogeneous particle distribution where smaller particles stick to the larger ones in the form of clusters. Additionally, secondary morphological variation of Iron embedded particles was observed, that was vermicular shaped. Using SEM Energy Dispersive Spectroscopy (SEM-EDS) we confirmed that the chemical composition of Carbonyl Iron Powder embedded in polymer was the same in both samples.

Key words: SEM, SEM-EDS, Carbonyl Iron Powder, microstructure, polymer.

Acknowledgement: Infrastructure Center for Electronic Microscopy and Microanalysis, Jožef Stefan Institute, Ljubljana, Slovenia (PR-05722).

Reference

1. Carbonyl Iron Powder (CIP), BASF (2024)
2. D. I. Bloemacher, Carbonyl Iron Powders: Its Production and New Developments (1990)
3. CIP Brochure General BASF, 100 years of innovation (2021)

Type of presentation: Poster

MS3-P-6 Laser Surface Functionalization of 316L Stainless Steel Under Ambient and Inert Argon Atmospheres

Matej Hočevar[1], Barbara Šetina Batič[1], Damjana Drobne[2], Veno Kononenko[2], Peter Gregorčič[3]

[1]*Institute of Metals and Technology, Lepi pot 11, 1000 Ljubljana*

[2]*Biotechnical Faculty, University of Ljubljana, Jamnikarjeva ulica 101, 1000 Ljubljana, Slovenia*

[3]*University of Ljubljana, Faculty of Mechanical Engineering, Aškerčeva 6, 1000 Ljubljana, Slovenia*

E-mail: matej.hocevar@imt.si

Stainless steel is one of the most widely used metallic biomaterials, valued for its mechanical strength, affordability, and durability [1–3]. Its surface can be functionalized through various techniques to enhance biocompatibility without altering its bulk properties. Surface modifications that affect morphology, chemistry, and wettability play a key role in modulating biological responses at the material–cell interface [4–7]. Laser texturing stands out as a versatile, single-step method for creating precise multiscale features without the use of chemical treatments.
In this study, nanosecond laser texturing was applied to 316L stainless steel surfaces in both ambient and argon environments to explore the effects of laser parameters and processing atmosphere on surface properties and biocompatibility. Laser surface engineering facilitates precise micro- and nanoscale surface modifications, driven by factors such as pulse fluence, duration, wavelength, polarization, and the processing environment.

A nanosecond Nd:YAG laser (1064 nm, 95 ns pulse duration) was used for direct laser texturing at fluences above the laser ablation threshold (DLT-HF). Laser topographies were generated by moving the laser beam alternately left and right, creating lines and grooves with varying spacing by adjusting laser parameters such as hatch distance, pulse fluence, and scanning pattern.
Samples were characterized using scanning electron microscopy (SEM), X-ray photoelectron spectroscopy (XPS), surface roughness, and wettability measurements. They were then exposed to *in vitro* biocompatibility testing using the MG63 cell line. Cellular responses, including viability, morphological changes, and adhesion distribution patterns, were analyzed through fluorescence microscopy, cytotoxicity assays, and SEM.

Laser processing enhanced the surface roughness and altered both the surface chemistry and wettability of 316L samples. Notably, the processing environment was crucial in determining surface chemistry, with ambient conditions resulting in higher concentrations of toxic hexavalent chromium oxide (CrO_3) compared to surfaces processed in an argon atmosphere. *In vitro* tests with MG63 osteoblast cells showed that surface topography and chemical composition, especially Cr oxide levels, influenced cell adhesion, viability, and cytotoxicity. On polished control surfaces, cells exhibited strong adhesion and polygonal morphology, while laser-textured surfaces altered cell morphology and induced mechanical strain.

Surfaces processed under ambient conditions exhibited cytotoxicity after 24 hours, likely due to the presence of chromium oxides. In contrast, laser texturing in an argon environment reduced the formation of these toxic oxides, thereby enhancing cell adhesion and maintaining biocompatibility for up to seven days (Figure 1). This improvement was most pronounced on the D sample topography, which was subjected to the highest laser power.
Biocompatibility assays confirmed enhanced cell responses, highlighting the potential of laser functionalization to improve the biocompatibility of metallic biomaterials.

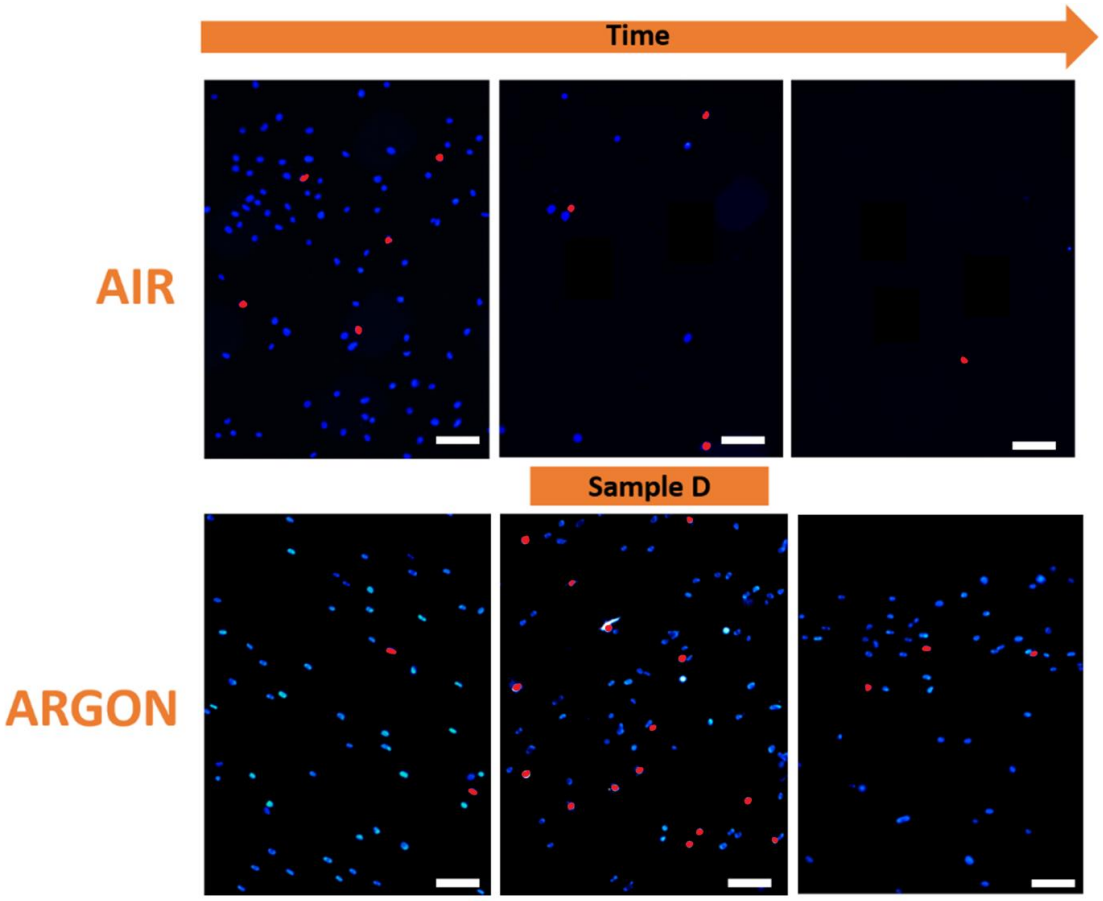


Figure 1: Cell adhesion to sample D (processed in air and argon) after 24 h, 72 h, and 168 h of incubation. Fluorescence microscopy (differential nuclear staining – nuclei of live cells are stained blue and nuclei of dead cells are stained red) was used to count viable and damaged adhered cells. Scale bar = 100 µm.

Acknowledgement: The authors acknowledge the financial support from the Slovenian Research and Innovations Agency project No. J2-60051. This work was also supported by the infrastructural center "Microscopy of biological samples" (MRIC UL, I0–0022–0481–08), located at the Biotechnical faculty, University of Ljubljana.

References:

1. Y. Su et al., Bioinspired surface functionalization of metallic biomaterials, J. Mech. Behav. Biomed. Mater. 77 (2018) 90–105.
2. A. Bekmurzayeva et al., Surface modification of stainless steel for biomedical applications: Revisiting a century-old material, Mater. Sci. Eng. C. 93 (2018) 1073–1089.
3. R.M. Pilliar, Metallic Biomaterials, in: R. Narayan (Ed.), Biomed. Mater., Springer US, Boston, MA, 2009: pp. 41–81.
4. D. Waugh et al., Surface Treatments to Modulate Bioadhesion: A Critical Review, Rev. Adhes. Adhes. 4 (2016) 69–103.
5. M. Rizwan, et al., Chapter 27 - Cell–Substrate Interactions, in: A. Atala, R. Lanza, A.G. Mikos, R.B.T.-P. of R.M. (Eds.), Academic Press, Boston, 2019: pp. 437–468.
6. R. Agarwal, A.J. García, Chapter 37 - Surface Modification of Biomaterials, in: A. Atala, R. Lanza, A.G. Mikos, R.B.T.-P. of R.M. (Eds.), Academic Press, Boston, 2019: pp. 651–660.
7. K. Munir, A. Biesiekierski, C. Wen, Y. Li, 12 - Surface modifications of metallic biomaterials, C.B.T.-M.B.P. and M.D.M. Wen (Ed.), Woodhead Publishing, 2020: pp. 387–424.

Type of presentation: Poster

MS3-P-7 Nano- and micro-structural configurations of functional complex metallic alloys

Andreja Jelen[a], Samo Kralj[a,b], Janez Dolinšek[a,c]

[a]*J. Stefan Institute, Ljubljana, Slovenia*

[b]*Faculty of Natural Sciences and Mathematics, University of Maribor, Slovenia*

[c]*Faculty of Mathematics and Physics, University of Ljubljana, Slovenia*

Contact email: andreja.jelen@ijs.si

Introduction

Being a microscopist and spending a lot of time observing different specimens, sometimes we observe the shapes of our investigated material that can easily be associated with the know objects in our everyday life [1]. In this contribution, I will present three different complex metallic materials – two of them are high-entropy alloys [2,3] and one is intermetallic compound [4]. They are designed for different purposes, having various physical properties, but all of them exhibiting the shape of the heart.

High-entropy alloys (HEAs) represent novel metals-based materials with complicated microstructures, where at least five different chemical elements, all in majority concentrations, are mixed on a simple crystal lattice. Likewise, the materials are usually comprised of more than one phase on different microscopic levels, ranging from a few nm to 1 mm.

Intermetallic compounds were proven to be attractive alternatives to pure and alloyed metals as catalyst materials in heterogeneous catalysis because of their increased selectivity to specific reactions and better long-term stability.

Methods

The materials were synthesized via arc-melting [3, 2] or Czochralski technique [4].

In order to interpret the physical properties as accurately as possible, the microstructure has to be known at different orders of magnitude (multi-spatial-scale), using different types of electron microscopes (correlative microscopy) that enable such magnifications. For complete microstructural investigation of HEAs, the following electron microscopes with corresponding techniques were used: Scanning Electron Microscope (SE and BSE imaging, EDS, EBSD), Transmission Electron Microscope (HAADF, EDS) and Focused Ion Beam (channelling contrast).

Magnetic measurements were conducted on a Quantum Design MPMS3 SQUID magnetometer equipped with a 7-T magnet, operating at temperatures between 1.8 and 400 K.

Results

The scandium-containing Sc-Hf-Nb-Ta-Ti-Zr system is a superconducting refractory high-entropy alloy [2]. The addition of Sc produces a two-phase structure in the Sc-Hf-Nb-Ta-Ti-Zr alloys, with one phase being bcc and the other hexagonal close-packed (hcp). The hcp phase absorbs practically all Sc, whereas the Sc-poor bcc phase is identical to the bcc phase in the Hf-Nb-Ta-Ti-Zr parent system. Upon the Sc addition, the microstructure becomes very inhomogeneous. Large bcc dendrites (10–100 μm) are homogeneous in the central parts, but become a fine dispersion of sub-micron precipitates of the bcc and hcp phases close to the edges. The interdendritic regions are also fine dispersion of the two phases. Superconductivity of the Sc-Hf-Nb-Ta-Ti-Zr alloys originates from the bcc phase fraction, which demonstrates identical superconducting parameters as the bcc Hf-Nb-Ta-Ti-Zr parent alloys, while the Sc-containing hcp phase fraction is non-superconducting.

In another attempt to incorporate tin (Sn) into high-entropy alloys composed of refractory metals Hf, Nb, Ti and Zr with the addition of 3d transition metals Cu, Fe, and Ni, we synthesized a series of alloys in the system HfTiZrSnM (M = Cu, Fe, Nb, Ni) [2]. All Sn-containing alloys are multi-phase mixtures of intermetallic compounds (in most cases four). A common feature of the alloys is a microstructure of large crystalline grains of a hexagonal $(Hf,Ti,Zr)_5Sn_3$ partially ordered phase embedded in a matrix that also contains many small inclusions. In the HfTiZrSnCu alloy, some Cu is also incorporated into the

grains. Based on the electrical resistivity, specific heat, and magnetization measurements, a superconducting (SC) state was observed in the HfTiZr, HfTiZrSn, HfTiZrSnNi, and HfTiZrSnNb alloys. The HfTiZrSnFe alloy shows a partial SC transition, whereas the HfTiZrSnCu alloy is non-superconducting. All SC alloys are type II superconductors and belong to the Anderson class of "dirty" superconductors.

In a routine handling of a catalyst material, exposure to air can usually not be avoided. For noble metal catalysts [4] that are resistant to oxidation, this is not an issue, but becomes important for intermetallic catalysts composed of two or more non-noble chemical elements that possess much different standard enthalpies of the oxide formation. The element with higher affinity to oxygen concentrates on the surface in the oxide form, whereas the element with lower affinity sinks into the subsurface region. This changes the number of active sites and the catalytic performance of the catalyst. We have investigated the instability of the surface composition to oxidation of the Ga_3Ni_2 noble metal-free intermetallic compound, a new catalyst for the CO_2 reduction to CO, CH_4 and methanol.
Ga_3Ni_2 and other Ga–Ni intermetallic compounds are good examples of binary intermetallic catalysts, whose catalytic performance is strongly affected by exposure to the air.

Discussion and conclusion

The complex atomic and phase structure, together with the choice of the elements and their concentrations, determine the physical properties (magnetic, electric and thermal) of the HEAs, which are usually not just a compositional average of physical properties of the constituent phases. Beside its functionality, it can also have an aesthetic value.

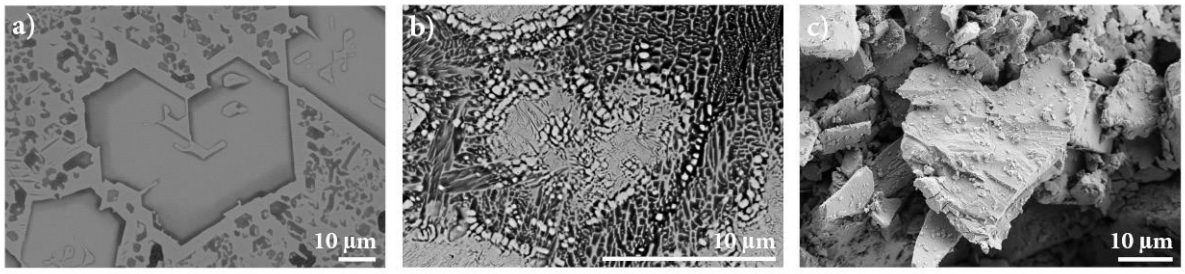


Figure 1: SEM secondary electron images of new complex metallic materials, all of them exhibiting the shapes of the heart [1]: (a) TiZrHfSnFe superconducting high-entropy alloy [3], (b) ScTiHfTa refractory high-entropy alloy [2] and (c) Ga_3Ni_2 intermetallic compound for catalysis [4].

References:

1. A. Jelen et al., *J Mol. Liq*. **2024**, 415, 126275.
2. M. Krnel, A. Jelen et al. *Materials* **2022**, 15, 1122.
3. D. Gačnik, A. Jelen et al. *Alloys. Materials* **2021**, 14, 3953.
4. M. Wencka et al. *J Analyt. Sci. Tech.* **2018**, 9, 12.

Type of presentation: Poster

MS3-P-8 Composition and microstructure of wrought and additively manufactured DED-LB of Ti-6Al-4V alloy

Barbara Kapun[a], Bor Arah[b], Peter Rodič[a] and Ingrid Milošev[a]

Jožef Stefan Institute, [a]Department of Physical and Organic Chemistry, [b]Center for Electron Microscopy and Microanalysis, Jamova c. 39, SI-1000 Ljubljana, Slovenia

Contact email: ingrid.milosev@ijs.si

Ti-6Al-4V, also known as titanium grade 5, is a commonly used alpha-beta titanium alloy composed of 90 wt.% titanium, 6 wt.% aluminum, and 4 wt.% vanadium. The alloy is valued for its excellent mechanical properties, corrosion resistance, and biocompatibility.[1] Nowadays, novel manufacturing methods such as additive manufacturing (AM), particularly directed energy deposition using a laser beam (DED-LB), offer significant advantages over conventional methods, including design flexibility, reduced material waste, and fabricating complex geometries.

This study aims to compare the composition and microstructure of wrought and directed energy deposition by a laser beam (DED-LB) manufactured Ti-6Al-4V, highlighting the differences in grain structure and phase distribution. Sample preparation included chemo-mechanical pre-treatment to obtain an appropriate surface for accurate microstructural analysis.[2] Surface characterization was performed using focused ion beam scanning electron microscopy (FIB-SEM) coupled with energy-dispersive X-ray spectroscopy (EDX) and electron backscatter diffraction (EBSD) to examine grain morphology, phase composition, and texture.

Microstructural analysis revealed significant differences between the wrought Ti-6Al-4V and DED-LB titanium alloy, Figure 1. The wrought alloy exhibited an equiaxed α+β microstructure with refined grains due to thermomechanical processing. In contrast, the DED-LB alloy displayed a columnar structure with mainly α lamellae, resulting from the rapid solidification and thermal cycling inherent to the additive manufacturing process.

These findings highlight the potential of DED-LB as a viable alternative to conventional manufacturing, offering advantages in design complexity and material utilization.

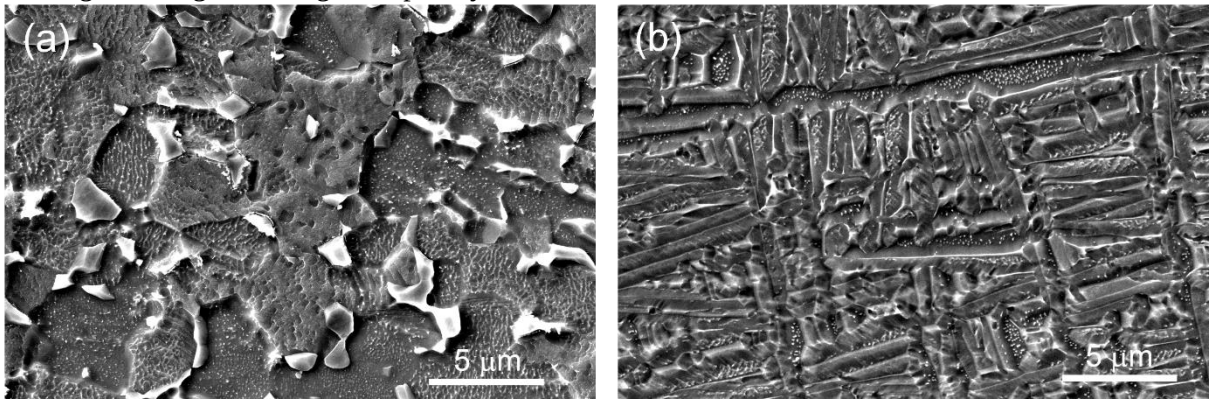


Figure 1: SEM images of surface morphology for a) wrought and b) DED-LB manufactured Ti-6Al-4V

References:

1. Leo Kumar, S.P.; Avinash, D. *Mater. Manuf. Process.* **2020**, 35, 869–892
2. Ingrid Milošev, Denis Sačer, Barbara Kapun and Peter Rodič, *J. Electrochem. Soc.* **2024**, 171, 111503

Acknowledgements:

The authors acknowledge the Slovenian Research and Innovation Agency (ARIS) for the funding of the project »Antibacterial alloys: Development by additive 3D manufacturing, characterisation and clinical applications«, acronym BIOAD, https://bioad.ijs.si/ (grant No. J7-4639). The authors also acknowledge Centre of Excellence in Nanoscience and Nanotechnology-Nanocenter, Ljubljana, Slovenia and Center for electron microscopy and microanalysis (CEMM) of the Jožef Stefan Institute for the use of the scientific equipment SEM/EDXS/EBSD.

Type of presentation: Poster

MS3-P-9 Effect of recycled powder on microstructure and chemical composition of additively manufactured AlSi7Mg alloy

Piotr Ledwig[a], Krystian Zyguła[a], Amelia Zięba[a], Kamila Gryner[a], Beata Dubiel[a]

[a]*AGH University of Krakow, Faculty of Metals Engineering and Industrial Computer Science, Krakow, Poland*

Contact email: pledwig@agh.edu.pl

Introduction

Recycling of waste materials, such as machining chips, has a high potential to reduce costs through a circular economy approach and reduce the primary production of materials. Unfortunately, chips are often oxidised and contaminated with coolant and other materials [1]. Metal chips are recycled by compaction and melting, but could also be used to produce fine powder by gas or ultrasound atomisation [2] or mechanical milling [3].

Potentially, atomised powder from metal chips might be used as feedstock material for additive manufacturing processes such as laser powder bed fusion (LPBF). The porosity and microstructure of LPBFed materials are very sensitive in terms of powder morphology, chemical composition and oxygen content [1].

In our study, the microstructure and chemical composition of recycled powder obtained from cold compressed AlSi7Mg chips was examined by scanning electron microscopy (SEM). The microstructure and chemical composition of the samples additively manufactured from the recycled powder using the laser powder bed fusion process (LPBF) were characterised by SEM and scanning transmission electron microscopy(STEM).

Methods

The feedstock AlSi7Mg chips were cleaned in isopropyl alcohol and cold-pressed, and subsequently arc melted, and ultrasound atomised using Ato Lab+ (3D LAB) equipped with a 35 KHz generator and tungsten tip sonotrode.

The LPBF process was performed using an AYAS 120 ML 3D printer (Inntec.pl). A set of 20 samples was prepared to determine the process window from commercial gas atomised AlSi7Mg powder and a mixture containing the addition of 30% recycled powder from the powder from chips. The powder morphology, microstructure, and chemical composition, as well as the microstructure and chemical composition of the LPBF samples, were investigated using the FEI SEM Inspect S50 equipped with EDS and EBSD. TEM, STEM and EDS analyses using the JEM-ARM200F NEOARMex microscope of JEOL were performed for further microstructure characterization, determination of phase composition by selected area electron diffraction, and quantitative EDS mapping of chemical composition. The size distribution of the powders and the volume fraction of the oxides were determined with the use of ImageJ software.

Results and Discussion

Figures 1 a and c show the morphology of gas-atomised AlSi7Mg (GA) powder and ultrasound atomised powder achieved from AlSi7Mg chips (UA). GA powder is characterised by numerous satellites and splat caps defects, with the d50 of the equivalent circular diameter (ECD) equal to 38.6 μm. Otherwise, the UA powder particles are highly spherical with d50 equal to 65.4 μm with rare morphological defects. On the surface of the UA powder, a thick film of process condensate with a high amount of oxygen was observed.

The chemical composition of the UA powder was different from that of the chips. EDS microanalysis showed that the content of Si and Fe was significantly higher, while Mg was on a similar level. Some of the particles were also characterised by a high content of Cu. The increase in Si and Fe content is

most likely due to the selective evaporation of Al and Mg during the process and the formation of aluminium oxides. However, Cu probably appeared in the powder as a result of contamination from the atomisation platform.

The porosity analysis of the LPBFed samples indicated that for the GA powder the optimal volumetric energy density was in the range of 30 – 40 J / mm^3, resulting in small porosity < 0.5%. The addition of 30% UA powder to the mixture provides the necessary increase in the volumetric energy density in LPBF process to a value greater than 50 J/mm^3 to achieve similar results to that for GA powder.

The microstructure of the AlSi7Mg samples obtained from the GA powder (Figure 1b) is typical for the LPBFed Al-Si alloys and characterized by the bimodal grain size with smaller grains in the melt pool interior. The grains exhibit the cellular microstructure with segregation of Si to the cell walls. Submicrometric Si-rich precipitates formed at the rapid cooling conditions of melt pools are observed in the whole volume of the investigated materials [4].

In the case of the addition of the UA powder, the microstructures after LPBF was less homogeneous according to the impurities of Cu and oxides in the powder (Figure 1d). The Cu segregation in the material was randomly observed in different regions of samples in the form of small submicrometric Cu particles and enrichment in Cu along the cell walls. The introduction of Cu in larger amounts is not advisable due to the possibility of hot cracking of LPBFed Al-Si alloys. It is similar to the behavior of Al-Cu alloys, in which the segregation of Cu in increases the possibility of cracking along grain boundaries where the eutectic is located [5].

The thin film of oxides on the surface of UA powders might be the cause of the formation of spherical inclusions of Al_2O_3 in the Al alloy matrix. In the whole volume of LPBFed samples in Al_2O_3 inclusions with diameters from several dozen nanometres to 5 μm were observed.

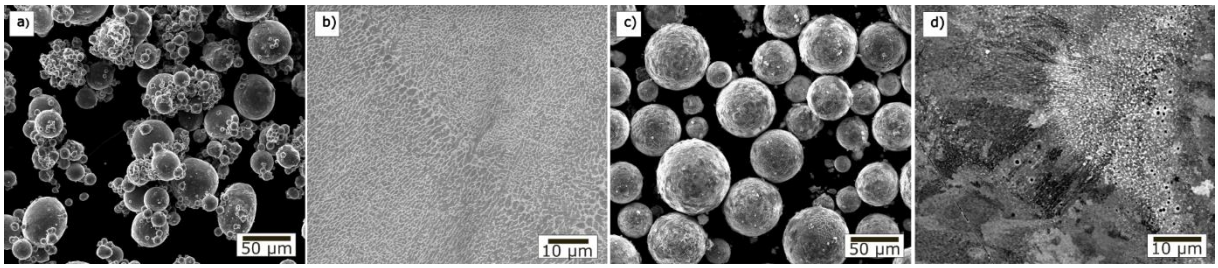


Figure 17 Powder morphology and corresponding microstructure of LPBF additively manufactured samples for a,b) gas-atomised AlSi7Mg powder and c, d) ultrasound-atomised powder from AlSi7Mg chips.

Conclusions

The direct ultrasound atomisation of cold-pressed chips provides a way to obtain powder with high oxide content and Cu contamination. These impurities affect the stability of the LPBF process, requiring a significant increase in VED to achieve porosity levels to commercially used powders.

Microstructural analysis showed that LPBF samples obtained from the powder with the addition of 30% recycled powder were less homogeneous due to oxide inclusions and Cu-rich precipitates. The presence of Al_2O_3 inclusions, ranging from nanometers to micrometers, suggests that they can originate from the oxide film on the recycled powder.

Direct atomisation of chips, using arc melting and ultrasonic atomisation, are the low efficient methods of producing powder for additive manufacturing, so prior removal of impurities by metallurgical processes is recommended.

References:

1. B. Denkena, M.A. Dittrich, V. Suntharakumaran, and S. Kettelmann: *CIRP Annals*, 2024, vol. 73, pp. 73–76, https://doi.org/10.1016/j.cirp.2024.04.046
2. A. Łagoda, A. Pawlak, A. Kurek, K. Moj, and S. Lis: *International Journal of Precision Engineering and Manufacturing - Green Technology*, 2025,https://doi.org/10.1007/s40684-024-00681-1

3. L.K. Wei, S.Z. Abd Rahim, M.M. Al Bakri Abdullah, A.T.M. Yin, M.F. Ghazali, M.F. Omar, O. Nemeș, A.V. Sandu, P. Vizureanu, and A.E. hadj Abdellah: *Materials*, 2023, vol. 16,https://doi.org/10.3390/ma16134635
4. H. Qin, Q. Dong, V. Fallah, and M.R. Daymond: *Metall Mater Trans A Phys Metall Mater Sci*, 2020, vol. 51, pp. 448–466, https://doi.org/10.1007/s11661-019-05505-5
5. J. Gao, L. Yan, J. Wan, J. Li, and B. Chen: *Mater Charact*, 2024, vol. 215,https://doi.org/10.1016/j.matchar.2024.114139

Type of presentation: Poster

MS3-P-10 SEM and EDS characterization of 316L Stainless Steel exposed to Different Bacteria

Aleksander Lesar[a], Mojca Blaznik[b], David Stopar[b], Barbara Šetina[a], Matej Hočevar[a]

[a]*Institute of Metals and Technology, Ljubljana, Slovenia*

[b]*Biotechnical faculty, University of Ljubljana, Ljubljana, Slovenia*

Contact email: aleksander.lesar@imt.si

Microbial Induced Corrosion (MIC) refers to the degradation of metals and other materials caused by metabolic activities of microorganisms such as bacteria, fungi, and algae. These microbes form biofilms on surfaces and produce metabolic byproducts — such as acids, sulfides, and ammonia, which accelerate corrosion. MIC poses a major challenge in various industries, including oil and gas industries, water treatment, and marine engineering [1].

Samples of 316L stainless steel were polished to a smoothness of 1200 grit and placed in Petri dishes containing various culture media, each inoculated with a different bacterial species. The tested bacteria included *M. luteus, S. marcescens, E. coli, S. aureus, S. pseudointerm, P. putida, B. subtilis, P. aeruginosa, P. fluorescens*, as well as mixed bacterial cultures obtained from metal corroded key, corroded stainless steel cooking pan, and from different hydropower plants along the Sava River, where MIC related issues had been reported previously. All samples were incubated at 37 °C for 20 days in rich growth media. Following incubation, they were ultrasonically cleaned in distilled water for 5 seconds to remove weakly attached bacteria and analysed using Scanning Electron Microscopy (SEM) coupled with Energy Dispersive X-ray Spectroscopy (EDS).

After 3 months of incubation, no visible signs of corrosion were observed on the 316L stainless steel samples, indicating its strong resistance to microbiologically influenced corrosion. Bacterial adhesion and the presence of organic material were observed on the metal surface shown in Figure 1, suggesting the initial formation of biofilms. However, a longer exposure period may be necessary to fully assess MIC development, particularly when using steels with higher corrosion resistance.

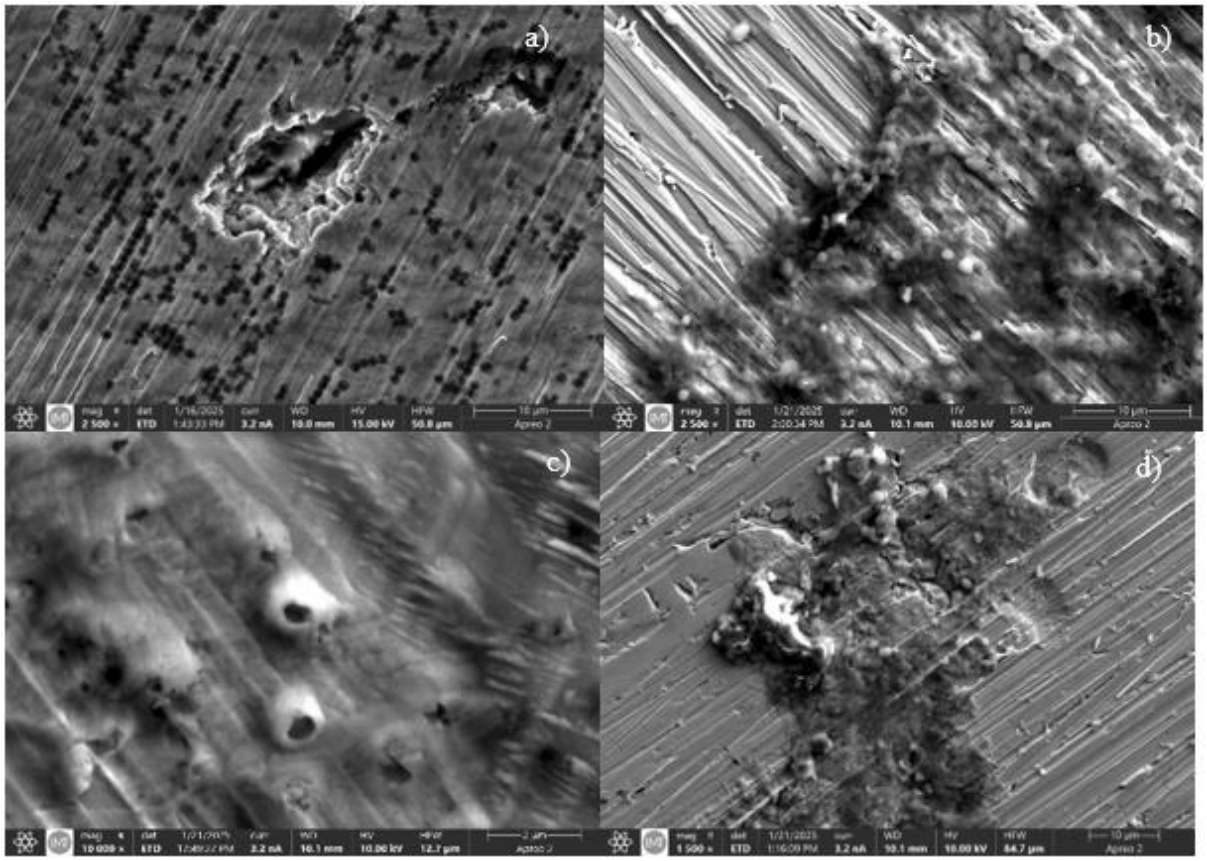


Figure 1. (a) *Staphylococcus aureus* cells located near mechanical damage on the material surface. (b) Biofilm containing bacteria from a sample incubated in LB medium alongside scraped corroded particles from metal key. (c) Organic structures produced by *Pseudomonas fluorescens*. d) Bacterial cells and organic material from water sampled at hydropower plant Krško.

Acknowledgement: The authors acknowledge the financial support from the Slovenian Research Agency (research core funding No. P2-0132 and grant numbers J2-60051 and L2-50060).

References:

1. J. Knisz, R. Eckert, A. Koerdt, J. S. Lee, E. R. Silva, T. I. Skovhus, B. A. An Stepec, S. A. Wade, FEMS Microbiology Reviews, **2023**, 47, 1-33

Type of presentation: Poster

MS3-P-11 Sublayer structure in fire gilding layer on medieval jewellery

Jan Maňák[a], Jan Duchoň[a], Estelle Ottenwelter[b]

[a]*Institute of Physics of the Czech Academy of Sciences (Prague), Czech Republic*

[b]*Institute of Archaeology of the Czech Academy of Sciences (Prague), Czech Republic*

Contact email: manak@fzu.cz

Fire gilding was a frequently used decorative method in the manufacture of medieval jewellery. Standard metallographic preparation of gilded samples often results in the deformation of the soft gilded layer, resulting in an altered microstructure. For that reason, focused ion beam (FIB) milling is particularly well adapted, since it allows obtaining damage-free cross section cuts to analyse the fragile gilded layer, as demonstrated by previous studies on hollow spherical pendants known as *gombiky* from the 10th century [1]. To compare the skills of craftsmen in fire gilding in terms of thickness and porosity on other *gombiky*, more specimens from the same archaeological context were investigated. Characterisation of the gilding layer was also performed to determine the sublayer structure observed in previous studies [1] and to distinguish the different metallic phases present in the gilding layer.

Microstructure was examined by scanning electron microscopy (SEM). Energy dispersive spectroscopy (EDS) and electron backscatter diffraction (EBSD) were used to determine the chemical composition and crystallographic structure of gilded layers. Samples were then further investigated in more detail by transmission electron microscopy (TEM). Automated crystal orientation mapping (ACOM) and EDS were used for thorough examination of the sublayers.

The analysis revealed that the gilded layers consist of several Au-Hg-Cu phases and silver precipitates. Furthermore, it is shown that a sublayer of copper is formed at the interface between the gilded layer and the copper substrate. This sublayer is also visible around voids in the gilded layer, which are created by the evaporation of mercury during the fire gilding process. Various oxidation states of the substrate were observed in each *gombiky*, along with impurities and silver precipitates.

The precise characterisation of gilding layers revealed differences in the quality of the layers; thereby, confirming different levels of skill and knowledge among craftsmen in fire gilding. The two-layer structure of the fire gilding layer was observed in all cases. Further information concerning the metallic phases present in the gilding was evidenced.

References:

1. E. Ottenwelter, C. Josse, A. Proietti, L. Robbiola, Fire gilding investigation on early medieval copper-based jewellery by focused ion beam (FIB) on FEG-SEM, *J. Archaeol. Sci. Rep.* **2022**, 46, 103602.

Type of presentation: Poster

MS3-P-12 The impact of high hydrostatic pressure annealing on microstructure evolution

Krzysztof Sielicki[a], Michael Kerber[b], Witold Chromiński[a], Małgorzata Lewandowska[a], Erhard Schafler[b], Agnieszka T. Krawczyńska[a]

[a]*Warsaw University of Technology, Faculty of Materials Science and Engineering (Warsaw), Poland*

[b]*University of Vienna, Faculty of Physics, (Vienna), Austria*

Contact email: krzysztof.sielicki.wim@pw.edu.pl

Introduction

Nickel and its alloys are commonly employed in applications demanding superior mechanical strength, corrosion resistance, and thermal stability. However, preserving their nanostructured grain size under thermal conditions presents a significant challenge due to processes such as recovery and grain growth. High-pressure torsion (HPT) is recognized as an effective method for generating nanostructured nickel [1–4]. Yet, materials produced this way often suffer from thermal instability resulting from a high density of grain boundaries, dislocations, and vacancies. To address this, high hydrostatic pressure annealing (HPA) has been introduced as a potential solution for stabilizing the microstructure by mitigating abnormal grain growth and reducing defect density [5,6]. This research explores the combined impact of HPT followed by HPA on the thermal stability of nanostructured nickel, with a focus on evaluating whether HPA can effectively maintain the fine-grained structure at elevated temperatures.

Methods

Nickel samples of 99.99% purity were processed using HPT under 6 GPa pressure with five revolutions at a rotation speed of 0.2 rpm. Following HPT, the samples underwent HPA at 0.4 Tm for 60 minutes under pressures of 2 GPa (HPT_HPA2) and 6 GPa (HPT_HPA6). Conventional annealing (CA) was performed at 220°C for 1h. The microstructure and mechanical properties were characterized using transmission electron microscopy (TEM), scanning electron microscopy (SEM), electron backscatter diffraction (EBSD) and microhardness testing.

Results

Firstly, TEM and SEM analysis were conducted for HPT-processed samples to investigate the microstructure. The mean value of grain size was approximately 220 nm with coefficient of variation (CV) of 43%. Then, the samples after HPA were examined in the same way. HPT_HPA6 samples exhibited slightly higher grain size of mean diameter 230 nm with CV equal to 32%, which proves that the microstructure is more uniform than the HPT_HPA2 with mean diameter of 260 nm and CV equal to 36%. Therefore, the question arises of how the nickel materials will behave after annealing. To investigate that, the conventional annealing was performed at atmospheric pressure (220°C, 1h). Interestingly, for HPT and HPT_HPA2, abnormal grain growth occurs, with the dominance of the grains >500 nm. Contrary to that, in the HPT_HPA6, the grain growth is partially inhibited as presented on the SEM images in **Figure 1.**

Discussion and conclusions

The results indicate that HPA significantly affects microstructural evolution and thermal stability of nanostructured nickel. HPT_HPA6 led to a more uniform grain size distribution than observed in the case of HPT and HPT_HPA2 processed samples. Probably, a more uniform grain size distribution combined with a reduced dislocation density increased the thermal stability of the HPT_HPA6 compared with the HPT and HPT_HPA2-processes samples. These findings contribute to a better understanding of the mechanisms behind grain boundary movement under high hydrostatic pressure annealing and suggest the potential of HPA for enhancing the thermal stability of nanostructured metals.

Acknowledgments

This research was financially supported by National Science Centre (NCN) (POLAND, project no. 2021/03/Y/ST5/00253) and by Austrian Science Funds (FWF) (AUSTRIA, project no. I-6082).

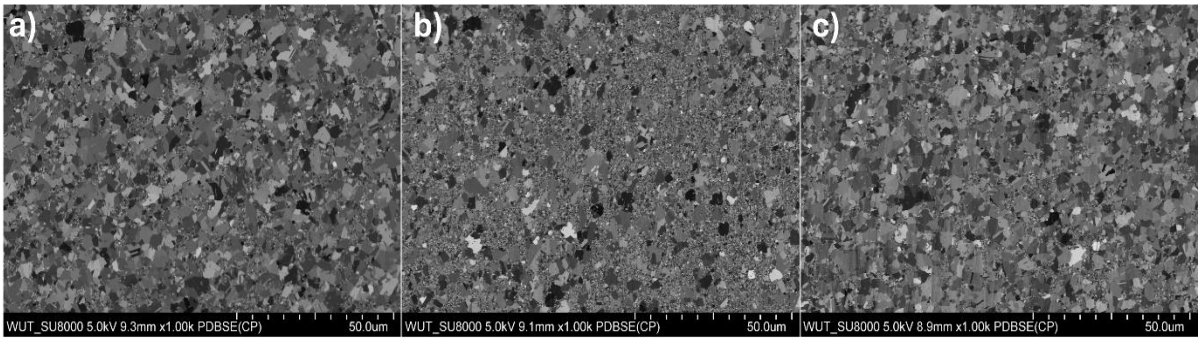


Figure 18. SEM images of grain microstructure of nickel samples after annealing at 220°C for 1h: HPT(a), HPT_HPA6 (b) and HPT_HPA2 (c).

References:

1. A. Zhilyaev, Microstructural Characteristics of Ultrafine-Grained Nickel, Nanostructured Materials by High-Pressure Severe Plastic Deformation (2006) 83–88.
2. N. Krasilnikov, W. Lojkowski, Z. Pakiela, R. Valiev, Tensile strength and ductility of ultra-fine-grained nickel processed by severe plastic deformation, Materials Science and Engineering: A 397 (2005)
3. A.P. Zhilyaev, T.G. Langdon, Using high-pressure torsion for metal processing: Fundamentals and applications, Prog Mater Sci 53 (2008) 893–979.
4. P. Cengeri, M.B. Kerber, E. Schafler, M.J. Zehetbauer, D. Setman, Strengthening during heat treatment of HPT processed copper and nickel, Materials Science and Engineering: A 742 (2019) 124–131
5. A.T. Krawczynska, M. Kerber, P. Suchecki, B. Romelczyk-Baishya, M. Lewandowska, D. Setman, The impact of the stacking fault energy of nanostructured metals on phenomena during annealing at the high hydrostatic pressure, Materials Science and Engineering: A 808 (2021) 140913
6. A.T. Krawczynska, M. Kerber, P. Suchecki, B. Romelczyk-Baishya, M.O. Liedke, M. Butterling, E. Hirschmann, A. Wagner, M. Lewandowska, D. Setman, The impact of high hydrostatic pressure maintenance after high-pressure torsion on phenomena during high hydrostatic pressure annealing, Materials Science and Engineering: A 840 (2022) 142874

MS4 0D, 1D and 2D materials

Type of presentation: Invited

MS4-IN-1 Dynamic Atomic Behaviour in 2D Heterostructures and Nanocatalysts

Sarah J Haigh[a], Matthew Lindley[a], Nick Clark[a], Sam Sullivan-Allsop[a], Rui Zhang[a], Gareth Tainton[a], Yi-Chi Wang [a], Thomas Slater[b], Pedro H. C. Camargo[c], Roman Gorbachev[a]

[a]*University of Manchester, (Manchester), U.K.*

[b]*Cardiff University, (Cardiff), U.K.*

[c]*University of Helsinki, (Helsinki), Finland.*

Contact email: sarah.haigh@manchester.ac.uk

Introduction: Transmission electron microscopy (TEM) and scanning transmission electron microscopy (STEM) can directly image reveal the local elemental composition and atomic structure for a wide range of nanomaterials, including atomically thin 2D materials, single atom catalysts and nanoparticle catalysts [1,2]. Yet conventional imaging has limitations in that the systems are typically observed when exposed to the vacuum of the TEM, and the images are generally 2D projections of the 3D structure. Yet, many catalyst systems have complex 3D structures, and the vacuum environment can induce changes to the surface compared to the operando conditions. Both limitations can lead to the potential for artefacts that impede determination of structure-property relationships. Tomographic methods enable 3D structure visualisation while in situ or operando TEM techniques enable retaining a liquid or gas environment around the sample while studying dynamic behaviour, yet all these methods usually compromise the spatial resolution and spectral sensitivity of the TEM.

Methods: In this talk I present our recent work illustrating our efforts to retain the performance of STEM imaging and spectroscopy for 2D heterostructures and nanocatalysts while performing in situ or tomographic analysis. We combine in situ TEM holders, clean room fabrication of advanced 2D heterostructure environmental cells and machine learning data analysis to study the surfaces and interfaces of these nanomaterials.

Results and Discussion: Specifically, I will report the use of scanning electron microscopy (SEM) and STEM to study reconstruction domains in twisted transition metal dichalcogenide (TMDs) heterostructures, even for buried interfaces and in the presence of a bulk substrate [3]. Ptychographic reconstruction from 4D-STEM data on suspended samples is then shown to reveal the 3D atomic positions within the reconstructed buried interface as a function of TMD thickness.

I will also report experiments using our graphene liquid cells, which allow atomic resolution imaging of isolated metal species surrounded by liquids. Our 2D heterostructure graphene liquid cell design enables functionality such as liquid-liquid mixing [4] and the study of atomic scale dynamics at a solid-liquid interfaces [5], most recently revealing quantitative understanding of atomic behaviour for single atom catalysts in different solvent conditions.

I will show elemental spectroscopy to study the distribution alloy puddles on nanoparticle surfaces at low doping concentrations (<1at%), resulting in charge distribution which enhances photocatalysis [1,2]. I will report in-situ gas cell STEM to investigate how the catalyst morphology evolves during catalyst activation dependent on the presence of Mn promotor in Fischer Tropsch catalysts [6]. Finally, I will discuss approaches using machine learning denoising for in situ data and progress towards gaining time-resolved 3D compositional information for dynamic systems under operando conditions and single particle reconstruction (SPR) [7,8].

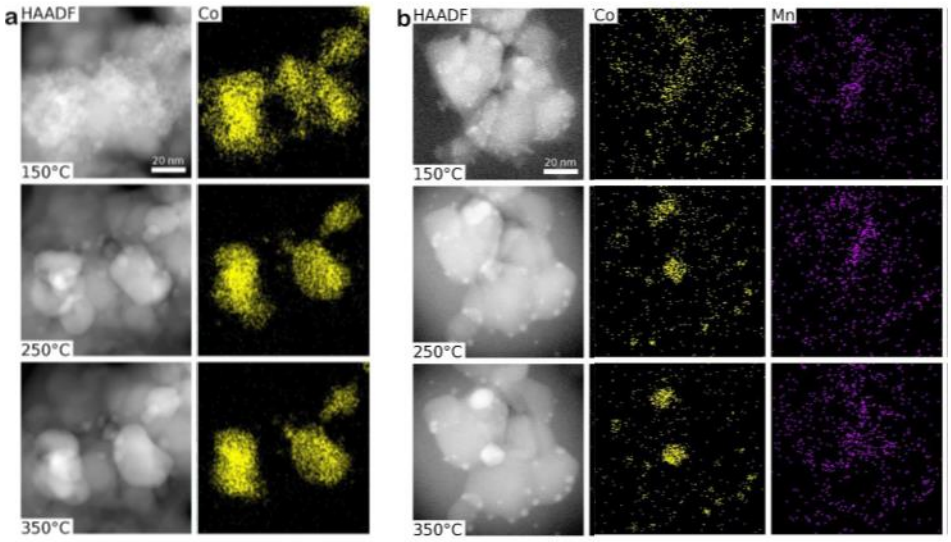


Figure 1: In situ gas cell structural and chemical characterisation of changes to the Co dispersion during activation in 1 bar hydrogen at elevated temperature with and without Mn promotor. The cobalt is initially an oxide on the TiO_2 support after wet impregnation synthesis but changes to the catalytically active metallic nanoparticles after the activation treatment. High angle annular dark field STEM imaging and energy dispersive X-ray spectroscopy elemental maps are compared for the Co/TiO_2 catalyst (a) without 5wt% Mn promotor and (b) with Mn promotor.

Acknowledgments: Funding is acknowledged from EPSRC grants EP/M010619/1 and EP/P009050/1, BP through the BP-International Centre for Advanced Materials (ICAM53 project), the European Research Council (ERC) under the European Union's Horizon 2020 research and innovation programme (grant ERC-2016-STG-EvoluTEM-715502) and Henry Royce Institute for Advanced Materials, funded through EPSRC grants EP/R00661*X*/1, EP/S019367/1, EP/P025021/1, and EP/P025498/1.

References:

1. KN da Silva, S Shetty, S Sullivan−Allsop, *et al ACS Nano*, **2024**, 18, 24391–24403.
2. LS Bezerra, P Brasseur, S Sullivan–Allsop, *et al*, *Angewandte Chemie*, **2024**, 136, e202405459.
3. E Tillotson JG McHugh, J Howarth, T Hashimoto, NJ Clark, A Weston, V Enaldiev, S Sullivan-Allsop, W. Thornley, W. Wang, M Lindley, AJ Pollard, VI Fal'ko, RV Gorbachev, SJ Haigh *ACS Nano*, **2024**, 18, 50, 34023–34033
4. DJ Kelly, N Clark, M Zhou, D Gebauer, RV Gorbachev, SJ Haigh, *Advanced Materials*, **2021**, 33, 2100668.
5. N Clark, DJ Kelly, M Zhou, YC Zou, CW Myung, DG Hopkinson, C Schran, A Michaelides, R Gorbachev, SJ Haigh, *Nature*, **2022**, 609, 942–947.
6. M Lindley, P Stishenko, JWM Crawley, F Tinkamanyire, M Smith, J Paterson, M Peacock, Z Xu, C Hardacre, AS Walton, AJ Logsdail, SJ Haigh, *ACS Catalysis*, **2024**,14, 10648-10657.
7. YC Wang, TJA Slater, GM Leteba, CI Lang, Z Lin Wang, SJ Haigh, *Small*, **2024**, 20 (10), 2302426.
8. GM Leteba, YC Wang, TJA Slater, R Cai, C Byrne, CP Race, DRG Mitchell, PBJ Levecque, NP Young, SM Holmes, A Walton, AI Kirkland, SJ Haigh, CI Lang, *Nano Letters*, **2021,** 21, 3989-3996.

Type of presentation: Invited

MS4-IN-2 From Structure to Dynamics: Exploring Nanoparticle Behavior with In-Situ and Aberration Corrected TEM/STEM.

Paulo Ferreira[a,b]

[a]*INL - International Iberian Nanotechnology Laboratory, Av. Mestre José Veiga, 4715-330, Braga, Portugal*

[b]*Mechanical Engineering Department and IDMEC, Instituto Superior Técnico, Av. Rovisco Pais 1, 1049-001, Lisboa, Portugal*

Contact email: paulo.ferreira@inl.int

A thorough knowledge of the atomic structure, composition and dynamics of nanoparticles is paramount to the development of advanced materials. In this talk, we first investigate the thermal stability and sintering of silver NPs by in situ TEM. Sublimation kinetics from isothermal experiments enabled assessment of local beam-induced heating. Smaller NPs exhibited discrete sublimation events and faceting, in contrast to the continuous behavior observed in larger NPs. Sintering initiated via particle or atomic diffusion, with neck growth governed by surface diffusion. Secondly, the dynamic behavior of Pt and Pt-alloy catalysts nanoparticles under voltage cycling is also investigated. Pt-based catalyst NPs supported on carbon nanotubes and carbon black are analyzed before and after cycling using a novel combination of 2D and 3D identical location (IL) TEM/STEM. Together, these studies demonstrate the power of advanced TEM techniques in revealing atomic-scale mechanisms governing nanoparticle behavior under real-world conditions.

Type of presentation: Oral

MS4-O-1 Insights into the degradation of metallic core-shell nanoparticles under fuel cell conditions by 3D identical location STEM

Alba Garzón Manjón[a], Miquel Vega Paredes[b], Raquel Aymerich Armengol[b], Daniel Arenas-Esteban[c], Sara Bals[c], Christina Scheu[b]

[a]*Institut Catala de Nanociència i Nanotecnologia, Bellaterra, Spain*

[b]*Max Planck Institut for Sustainable Materials, Düsseldorf, Germany*

[c]*Electron Microscopy for Materials Science (EMAT), Belgium*

Contact email: alba.garzon@icn2.cat

Proton exchange membrane fuel cells (PEMFCs) are electrochemical devices capable of generating electricity by oxidizing H2, reformate (H2 rich gas with carbon monoxide (CO) impurities) or other fuels. In recent times, metallic core-shell nanoparticles (NPs) (M@Pt, M=Ru, Rh…) have attracted a big interest as anode catalysts of reformate fed PEMFCs [1]. The high catalytic activity of Pt towards the HOR, together with the CO poisoning tolerance introduced by the accompanying metal make them ideal for heavy-duty applications. Furthermore, since in M@Pt NPs the less stable metal (Rh or Ru) is not directly exposed to the electrolyte, their stability is expected to be higher than in the corresponding alloyed NPs, which commonly suffer from dissolution and dealloying [2]. However, M@Pt can still suffer from degradation under fuel cell conditions by processes that are yet not fully understood, which hinders the design of more stable and durable catalysts.

We investigated the degradation behavior of Rh@Pt NPs by means of identical location-scanning transmission electron microscopy (IL-STEM). This quasi in-situ technique allows to overcome the limitations of the ex-situ techniques, in which only statistical general insights are possible, since in IL-STEM the changes of individual particles are tracked between potential cycles. In particular, we characterized the Rh@Pt NPs after 0, 1000, 4000 and 10000 potential cycles (0.06-0.8V, 0.1V/s). Furthermore, since many of the degradation phenomena take place in 3D (e.g., particle migration and corresponding aggregation), selected regions were reconstructed in 3D by means of electron tomography.

We observed particle migration on the carbon support in all the stages of the potential cycling. However, no widespread particle aggregation was observed, even after 10000 potential cycles. A slight Rh dissolution (up to 5 at.%) during the cycles was detected, which decreased as the number of cycles increased. Even though some small particles dissolved during the first 1000 cycles, the main degradation mechanism responsible for the loss of electrochemically active surface area was found to be particle detachment.

Our results indicate that the investigated Rh@Pt NPs present a remarkable stability, and show how IL-STEM can be used for studying the degradation of catalyst NPs.

References:

1. Garzón Manjón, A§.; et al. (2022). *Nanoscale. 14,* 18060-18069.
2. Vega Paredes, M.; Aymerich Armengol, R.; Arenas Esteban, D.; Martí Sánchez, S.; Bals, S.; Scheu, C.; Garzón Manjón, A§. (2023) *ACS Nano. 17,* 17, 16943–16951.

Type of presentation: Oral

MS4-O-2 Atomic-resolution investigation of 2D hematene

Jana Dzíbelová[a], Jan Filip[b], Jani Kotakoski[a]

[a]*Faculty of Physics, University of Vienna, (Vienna), Austria*

[b]*Czech Advanced Research and Technology Institute, Palacký University, (Olomouc), Czechia*

Contact email: jana.dzibelova@univie.ac.at

2D materials have attracted scientific interest for decades, since they possess distinct physico-chemical properties compared to their 3D counterparts due to quantum confinement. These atomically thin structures such as graphene, hBN, etc. are typically based on so-called van der Waals systems. These 3D counterparts are defined by strong bonds oriented in-plane and merely weak interlayer bonding.

However, 2D materials can also be created from a parent material with strong bonding interactions in all three directions, the so called non-van der Waals (n-vdW) materials. Cleaving them into individual layers is significantly more complex, however, atomically thin sheets of these n-vdW materials could offer a playground to explore the changes in properties induced by dimensionality restriction. Recently, a new member of the n-vdW 2D materials has been introduced: hematene, the 2D form of α-Fe2O3 [1]. Hematene is interesting not only for fundamental research but also shows potential for energy storage applications, e. g. it is photocatalytically active for ammonia decomposition induced by visible-light irradiation [2].

The dimensional confinement of the hematene structure is expected to introduce changes to the lattice [3]. This distortion of atomic positions affects electronic configuration and therefore the magnetic, electronic and optical behavior of the system [4]. In other words, the properties of the material are expected to vary with the thickness of the sheets, i. e. number of hematene layers. Here, we employ (scanning) transmission electron microscopy to investigate the atomic structure and distortions of the lattice in thin hematene sheets with the aim to quantify the lattice distortions and facilitate the physical description of the material.

References:

1. Puthirath Balan, A., et al., *Nature Nanotech.*, **2018**, 13 ,602
2. Dzíbelová, J., et. al. *Appl. Mater. Today*, **2023**, 34, 101881
3. Friedrich, R. et al., *Nano Lett.*, **2022**, 22, 989
4. S. Maiti, K. et al., *Energy Environ. Sci.*, **2021**, 14, 3717

Type of presentation: Oral

MS4-O-3 High-Entropy Oxide Nanoparticles as Stable and Efficient Catalysts for the Oxygen Evolution Reaction

David Llorens Rauret[a], Hui Chen[a], Alejandro G. Roca[a], Alba Garzón Manjón[a], Josep Nogués[a,b], Jordi Arbiol[a,b]

[a]*ICN2, CSIC and BIST (Barcelona), Spain*

[b]*ICREA, (Barcelona), Spain*

Contact email: david.llorens@icn2.cat

Amid the current global energy crisis, the oxygen evolution reaction (OER) has become a critical process for sustainable energy generation, conversion, and storage. As the anodic half-reaction in water electrolysis, OER is essential for green H_2 production. However, its sluggish 4-electron transfer mechanism requires exceptionally high activity levels, currently only achieved by scarce and expensive noble metals such as Ir [1,2]. This constraint limits the widespread adoption of OER technologies, hindering advancements in green energy solutions. High-entropy oxides (HEOs) have recently emerged as promising OER catalysts, offering superior activity, remarkable stability, and tunable properties. By incorporating multiple cations, HEOs exhibit complex crystal structures that enable diverse OER pathways [3]. Their strong metal-oxygen bonds and entropy-stabilized phases enhance durability, preventing structural degradation under harsh electrochemical conditions, making them attractive candidates for next-generation electrocatalysts.

In this study, earth-abundant CrMnFeCoNi-based HEO nanoparticles were synthesized via a green, low-temperature liquid-phase process [4]. A multimodal characterization approach was employed to establish correlations between catalyst structure and performance, combining the high spatial resolution of scanning transmission electron microscopy (STEM) with chemical and coordination information from X-ray absorption spectroscopy (XAS) and X-ray photoelectron spectroscopy (XPS). Moreover, by using a loaded TEM grid as the working electrode, identical location (IL)-STEM was employed to assess the changes of the same particles after catalysis, providing stronger insights into the stability of the HEOs.

STEM analysis confirmed that the as-synthesized oxides crystallize in a spinel structure, which remains stable even after prolonged OER operation. Electrochemical tests demonstrated promising OER activity, with performance comparable to benchmark Ir black. IL-STEM showed similar trends to the electrochemical tests and revealed the degradation mechanisms occurring on the catalyst during reaction. XPS provided insights into the oxidation states of the constituent elements, while XANES and EXAFS further revealed the material's electronic and structural evolution. These spectroscopic techniques revealed the oxidation states of the HEO elements, identifying Mn^{2+}, Co^{2+} and Ni^{2+} as 2+ cations, while Cr^{3+} and Fe^{3+} were present as 3+ cations.

The results from (IL)-STEM investigations revealed that the catalyst maintained its spinel crystal structure during OER, demonstrating high structural and compositional stability. Minimal changes were observed in elemental distribution, confirming the resilience of the HEO under operating conditions. Electrochemical tests showed promising OER activity for noble-metal-free anodes [5], comparable to benchmark Ir black, with prolonged stability in harsh acidic environments. Moreover, our findings suggest that Cr and Mn play key roles in enhancing the electrochemical performance of these oxides. Notably, the spinel structure features distinct cation sites, with tetrahedral (M) positions predominantly occupied by 2+ oxidation state cations and octahedral (N) positions by 3+ oxidation state cations. The coexistence of multiple oxidation states among transition metals introduces structural flexibility, allowing for tunable electronic, magnetic, and electrochemical properties. Future operando characterization, combined with advanced theoretical calculations, is anticipated to further elucidate the role of each metal during OER.

In summary, this study establishes CrMnFeCoNi-based HEOs as promising active and durable OER catalysts, providing a viable alternative to noble-metal-based materials. Understanding the structure-property relationship of these oxides is crucial for the rational design of next-generation catalysts. By leveraging the inherent stability and tunability of HEOs, this work paves the way for the development of more efficient, scalable, and cost-effective solutions for sustainable H_2 production.

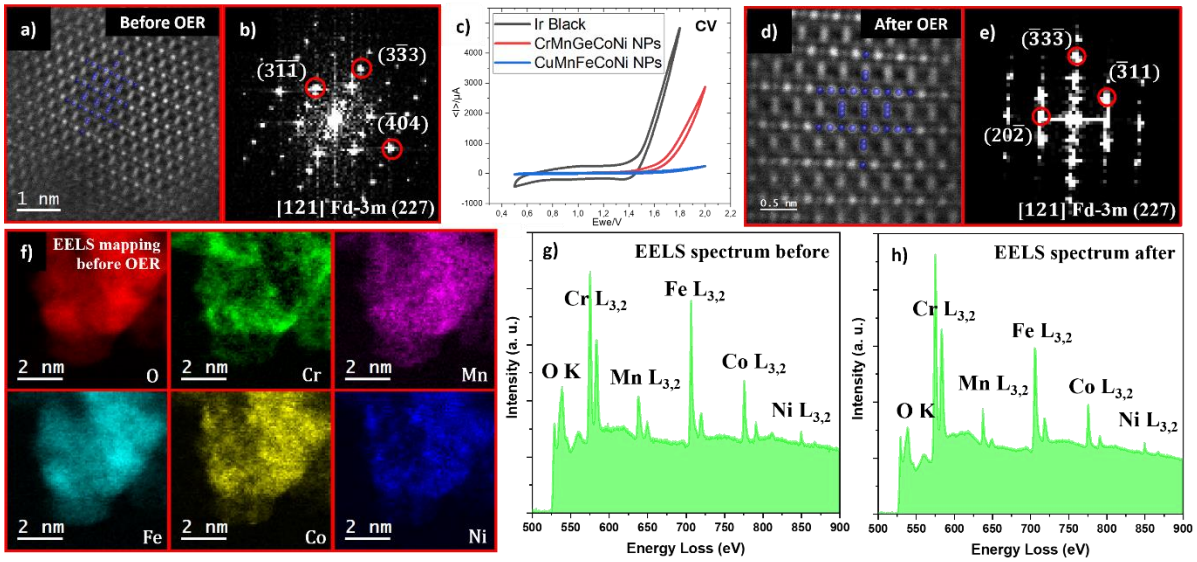


Figure 1: STEM characterization of CrMnFeCoNi oxide before and after the OER and cyclic voltammetry measurement of different HEOs and Ir catalysts.

References:

1. J. Suntivich, et al., *Nat. Energy* **2024**, *9*, 1191-1198.
2. R. Ram, et al., *Science* **2024**, *384*, 1373-1380.
3. Y. Sun, et al., *Sci. Adv.* **2021**, *7* (20), eabg1600.
4. D. Wang, et al., *Sustain. Energy Fuels* **2022**, *6* (6), 1479–1488.
5. Z. Wang, et al., *Green Chem.* **2024**, *26* (18), 9569-9598.

Type of presentation: Oral

MS4-O-4 Metallene synthesis by ion irradiation: Growth of two-dimensional gold by vacancy-induced nucleation on defect-engineered graphene

Wael Joudi[a,b], Sadegh Ghaderzadeh[d], Alberto Trentino[a,b], Kenichiro Mizohata[c], Kimmo Mustonen[a], Elena Besley[d], Jani Kotakoski[a], E. Harriet Åhlgren[a,c]

[a]*University of Vienna, Faculty of Physics, Boltzmanngasse 5, 1090 Vienna, Austria*

[b]*University of Vienna, Vienna Doctoral School in Physics, Boltzmanngasse 5, 1090 Vienna, Austria*

[c]*University of Helsinki, Department of Physics, Pietari Kalmin katu 2, 00560 Helsinki, Finland*

[d]*University of Nottingham, School of Chemistry, NG7 2RD, Nottingham, UK*

Contact email: wael.joudi@univie.ac.at

We present a route for the creation of one-atom-thick two-dimensional gold (goldene) on defective graphene via a two-step ion implantation process. In the first step, monolayer graphene is irradiated by Au ions with a kinetic energy of 200 eV, creating vacancies in the material. In the subsequent step the Goldene flake growth is initiated by ultra-low energy (25 eV) irradiation. At these ultra-low energies, the energy transfer is insufficient for creating new vacancies. As a result, the adsorbed Au atoms migrate thermally on the surface until they encounter a trapping site in the form of a vacancy. This gold fills the vacancy taking a substitutional site and acts as a nucleation site for the 2D gold growth. We find a large number of flat gold clusters with varying thicknesses, depending on the implantation dose, down to a single atomic layer (Fig. 1a) that have been imaged at atomic resolution via scanning transmission electron microscopy (STEM). The elemental composition of these gold flakes is determined via electron energy loss spectroscopy (EELS). The EEL spectrum shows the minor O_2 and O_3 edge at 54 eV and 72 eV, respectively, providing evidence for the Au content. Furthermore, the EELS indicates no traces of Fe or Cu, which both are common in CVD-grown graphene as a result of the manufacturing process. The absence of the major L_2 and L_3 edges in Fe (721 eV and 703 eV, respectively) and Cu (951 eV and 931 eV, respectively) suggest no such presence within the goldene flakes. Considering one-atom-thick goldene flakes, we observe an electron-beam-induced reversible transformation into an amorphous spherical structure. Additionally, the crucial role of the vacancy for the gold formation as well as the stability of the flat structure is revealed via *ab-initio*-based atomistic simulations. When comparing a spherical configuration with the energetically less favourable flat configuration, a single vacancy reduces the energy penalty from +2.34 eV to only +0.25 eV, permitting the formation of the goldene flakes. Lastly, dynamic simulations demonstrate the goldene formation by gold atoms impinging on defective graphene with a kinetic energy of 25 eV. The impact energy is dissipated across the graphene membrane, leaving the Au atom migrating across the surface until it is trapped by a vacancy. Subsequent Au atom impacts permit the growth of a goldene flake at the nucleation site as shown in Fig. 1b, c.

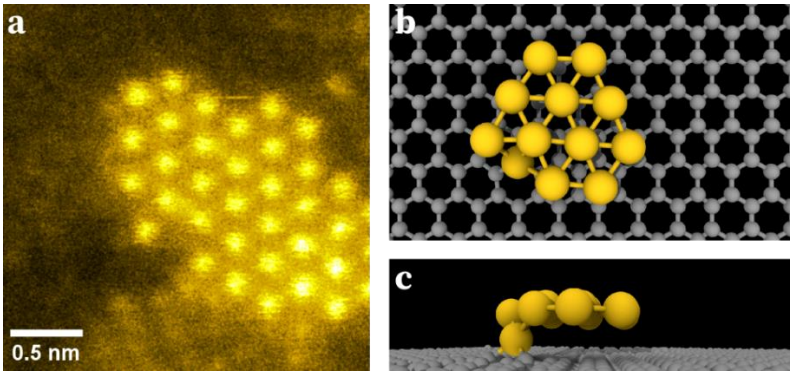


Figure 19: (a) Atomic resolution STEM image of goldene supported by monolayer defective graphene (with a Gaussian blur of 1 px), (b) snapshot from dynamic simulation showing the goldene flake anchored to the graphene substrate through the single vacancy and (c) side view of the flake shown in (b).

Type of presentation: Poster

MS4-P-1 Investigation of Boron-Based Nanosheets, Nanoscrolls and Nanotubes by TEM Analyses

Ahmet Eymen Akşener[a], Mehmet Ali Gülgün[b], Melike Nur Önder[b]

[a]*Sabancı University Nanotechnology Research and Application Center, Istanbul, Turkey*

[b]*Sabancı University, Faculty of Engineering and Natural Sciences, Istanbul, Turkey*

Contact email: eymen.aksener@sabanciuniv.edu

Introduction: Since the first report of carbon nanotubes (CNTs), formidable efforts have been devoted to the synthesis of nanoscale tubular one-dimensional structures. Interest is due to their future applications, such as nanoelectronics, optoelectronic and biochemical sensing devices. Despite their outstanding mechanical and electrical properties, CNT's success fueled the interest in alternative one-dimensional materials that can be mass-produced with high purity. Boron, positioned adjacent to carbon on the left side of the periodic table, exhibits a diverse chemistry comparable only to that of carbon [1-2]. Because of electron-deficient nature of elemental boron, the BNTs can be identified as promising candidate materials [3]. Recent experiments demonstrating the synthesis of boron nanotubes have heightened interest and expectations regarding their potential applications in various fields [4]. The aim of our study is to investigate the nanosheets, nanoscrolls and nanotubes obtained by ultrasonication-assisted production method by TEM analysis.

Methods: All the chemicals were purchased and applied as received without further purification. The experimental materials used in this work were boron powder (purity ≥95%), acetone and isopropanol (purity ≥99,5%). The boron powder precursor was first mixed in solvents. The mixture sonicated with a prope-type sonicator at 400 W under nitrogen atmosphere for 4 h, followed by centrifugation at 4750 rpm for 40 min. The supernatant was collected and thermally treated at 150˚C in the autoclave with a PTFE container for 12 h. Then 0.05 mL of this sample was dropped on a TEM grid, and the solvent was evaporated prior to transmission electron microscopy (TEM) analysis. The TEM results were obtained using the JEOL JEM-ARM200CFEG UHR-TEM (equipped with STEM, Cs corrected STEM, EDS, Gatan Quantum GIF and Digital CCD Camera) at 200 keV.

Results: When the TEM image at low magnification is examined, the presence of round-shaped amorphous particles with diameters ranging between approximately 50nm and 150 nm is observed (Fig1-A). In figure 1-B the tubes like structures can be seen with a length of approximately 200nm and a diameter of 40nm. The hallow-like structure can be clearly discerned from the TEM observation (Fig1-C).

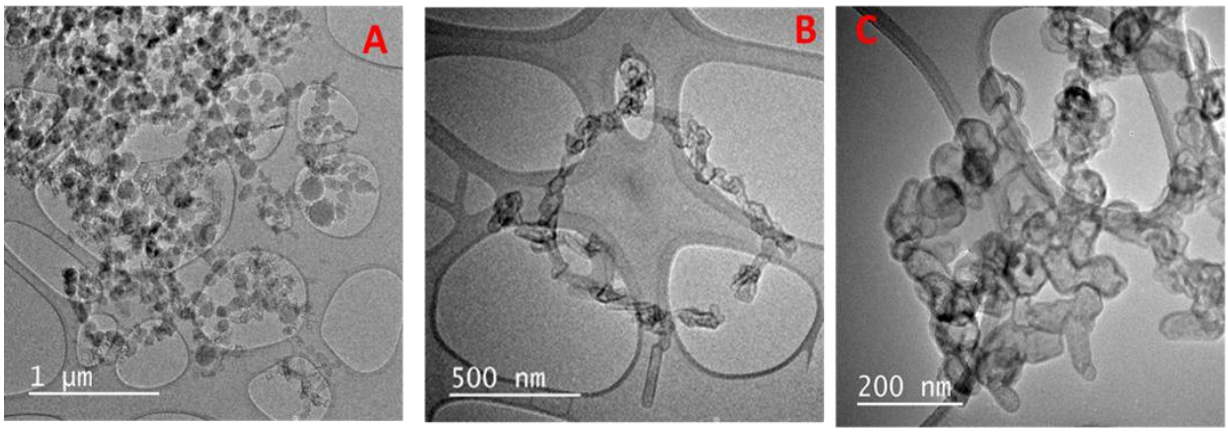


Figure 1: TEM images at different magnifications.

EDS analysis of selected regions shows that the nanosheets (marked with red arrows) are composed of boron with some other impurities (Fig 2-A).

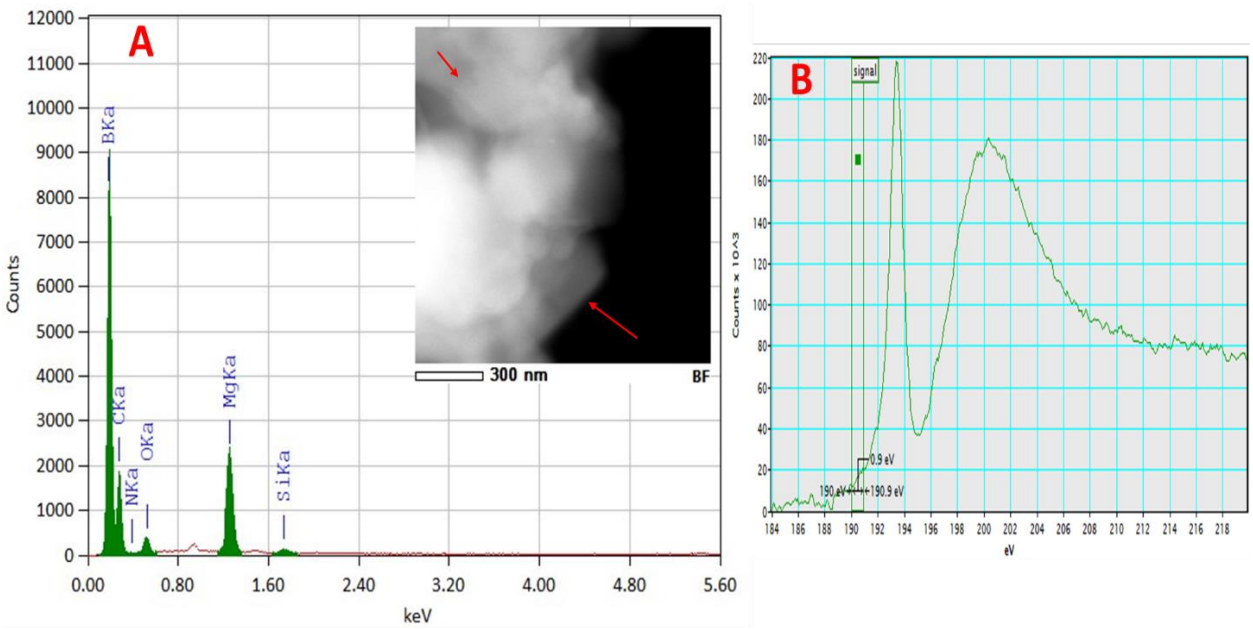


Figure 2: EDS analyse on the selected regions (A) and ELNES result (B).

Discussion and conclusions: We believe that all these different structures showed in figure-1 are formed due to the exfoliation by sonication process and the separation of different shapes / structures in reaction vessels and by centrifugation after the production process. We think that the magnesium clearly seen in the EDS can be a contamination from the raw material remaining of magnesothermic reactions during elemental boron production. The carbon may be due to the fact that the EDS area is close to the grid /Carbon-lacey. When the ELNES shared in figure 2-B is examined, it is seen that the results in terms of boron coincide with the EDS data, suggesting that boron is oxidized. The measured near edge structure for B_2O_3 is characterized by sharp peak at 194eV associated with transitions to non-bonding $\pi^*(P_z)$ orbitals and a broad feature at ~203eV originated from σ^* orbitals [5]. We are continuing our experiments and trying to understand the factors that affect the formation or transformation of different boron structures, especially boron nanotubes. For this purpose, we are investigating what the resulting structures depend on by establishing a relationship between controlled parameter changes and TEM analyses in follow-up experiments.

References:

1. Wu, S., Yang, Z., Guo, A., Ouyang, F., Electron Transport Along Boron Nanotubes Rolled From β12-Borophene: A First-Principles Study,Physica E: Low-dimensional Systems and Nanostructures,Volume 126,2021

2. Wang, J., Liu, Y. and Li, Y.-C., A New Class of Boron Nanotube. ChemPhysChem, 10: 3119-3121, 2009

3. Lau, K.C., Pandey, R., Pati, R., Karna, S., P.; Theoretical Study Of Electron Transport In Boron Nanotubes. Appl. Phys. Lett.; 88 (21): 212111, 2006

4. Wu, Y,. Yifan, C., Hou, S., Zuxin, W., Na, Q., Jingyu, Li., Hui, B., Xiufang, L.,. Growth of Single-Crystalline Boron Nanotubes in Cu Alloy, CrystEngComm, 2017

5. G. Mountjoy, A. Corrias, P.H. Gaskell, An electron energy loss spectroscopy study of Ni60B40 alloys prepared by chemical reduction and melt spinning, Journal of Non-Crystalline Solids 192 & 193 (1995) 616-619.

Type of presentation: Poster

MS4-P-2 Complex Electron Microscopy Analysis of Nanoscale Epitaxial Heterostructures Involving Metal Halides

Cara Bradsher[a], Giorgio Divitini[a], Liberato Manna[a]

[a]*Istituto Italiano di Tecnologia, (Genova), Italy*

Contact email: cara.bradsher@iit.it

Introduction:
The development of nanocrystal heterostructures by building epitaxial interfaces between two materials that match each other with atomic precision is the key to controlling the flow of electrons in many technological devices, spanning electronics, optics, and catalysis. Nanocrystal heterostructures are crystals consisting of two or more distinct domains and are synthesized to either combine the properties of multiple materials into one single nanostructure or obtain new properties not belonging to its individual components. The ability to build epitaxial interfaces between two materials has been realized in systems such as core/shell quantum dots, to control their optical properties, and noble metal nanocrystals, to influence their plasmonic properties. However, synthesizing nano-heterostructures involving metal halides, such as perovskites, has proven to be more complex due to their high reactivity and the difficulty of coupling highly structurally mismatched materials. Since metal halides comprise a diverse range of materials, many applications would greatly benefit from the ability to grow heterostructures involving these nanocrystals. Therefore, by utilizing the intrinsic reactivity of metal halides alongside our recent discovery that these heterostructures can form when there is continuity in their ionic sublattices, I will synthesize novel nano-heterostructures and develop complex analytical techniques to understand their formation.

Methods:
Bright-field TEM images of the samples were acquired with a JEOL-1400Plus transmission electron microscope operating at an acceleration voltage of 100 kV. STEM-HAADF images were acquired with a JEOL-2200FS analytical image-aberration-corrected (scanning) transmission electron microscope. Elemental analysis and mapping was performed by energy-dispersive X-ray spectroscopy (EDS) with a 30 mm^2 silicon drift detector in the JEOL-2200FS. Samples were prepared by drop casting from diluted nanocrystal solutions onto ultrathin holey carbon-film-coated 200 mesh copper grids.

Results:
Within the Nanoscale Epitaxial Heterostructures Involving Metal Halides project of the Manna group at the Italian Institute of Technology, we have synthesized several novel nano-heterostructures. I have developed techniques for imaging of several new nano-heterostructure materials, including perovskite-metal selenide, perovskite-metal bromide, chalcogenide-metal sulfide, and new perovskite-chalcogenide heterostructures, for qualitative and quantitative elemental analysis. These samples have varying types and levels of beam-sensitivity and therefore require different imaging methods, such as cryo-electron microscopy, adjusting beam current, and post-deposition grid treatment. Even while implementing these techniques, there are still several limitations in quantitative elemental analysis.

Discussion and Conclusions:
The Manna group has continued to generate new nano-heterostructures through several synthetic methods that are not yet published. While implementing conventional techniques for analysis of these new, often beam-sensitive materials, there are still several limitations in quantitative elemental analysis. In order to further improve quantitative analysis of these beam-sensitive materials, I will extend the analysis of the nano-heterostructures to multidimensional methods, such as 4D-STEM and iDPC. Our ability to develop numerous new synthetic pathways, alongside complex electron microscopy analysis using multidimensional methods and advanced diffraction studies, will result in a deep understanding of the formation and optimization of nano-heterostructures for a broad range of applications.

Type of presentation: Poster

MS4-P-3 RIANA: Research Infrastructure Access in Nanoscience & Nanotechnology

Jummi Laishram[a], Maria Eugênia Fortes Brollo[a,b], Regina Ciancio[a,b]

[a]*Area Science Park, (Trieste), Italy*

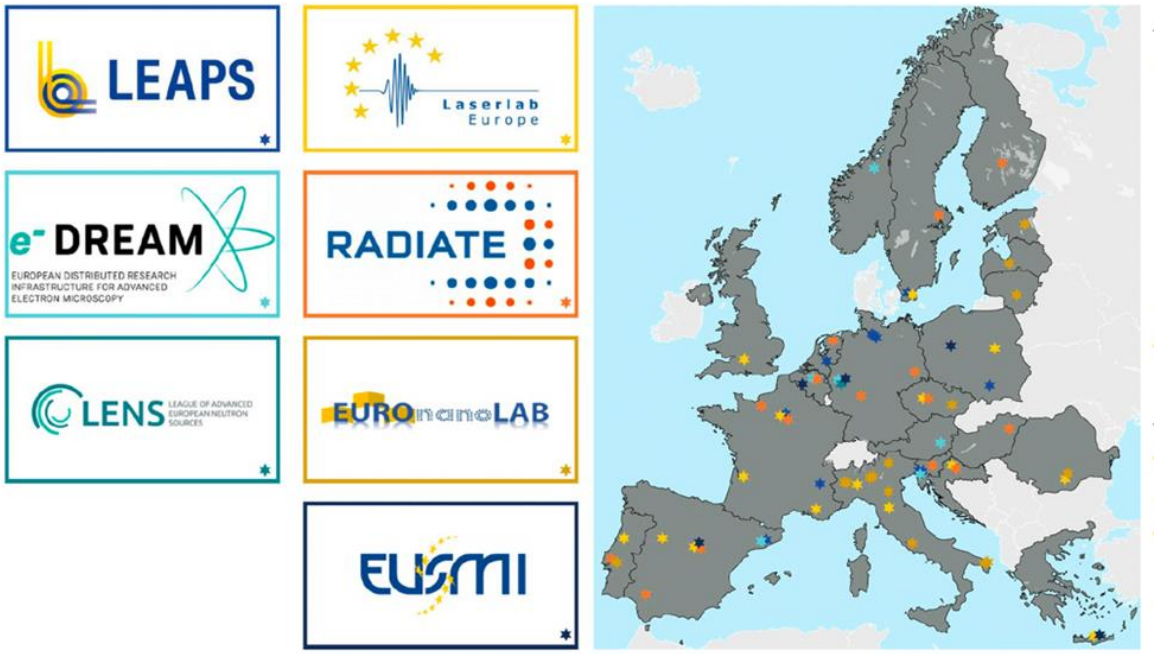
[b]*CNR-IOM, (Trieste), Italy*

Contact email: jummi.laishram@areasciencepark.it

The RIANA (Research Infrastructure Access for Nanoscience Advancement) project is a Horizon Europe initiative that provides transnational access to world-class research infrastructures supporting nanoscale science and technology. Through a coordinated, multidisciplinary platform, RIANA offers free access to cutting-edge techniques, such as electron microscopy, surface analysis, synchrotron radiation, and nanofabrication, across 69 facilities in 22 European countries.

RIANA serves both academic and industrial users, enabling high-impact research on nanomaterials, devices, and processes. A cornerstone of the project is its network of Junior Scientists: early-career researchers who provide dedicated, one-on-one scientific support throughout the proposal, experimental, and analysis stages. Their expertise is particularly valuable for newcomers to advanced methods like electron microscopy, offering guidance on sample preparation, measurement strategies, and data interpretation.

The project welcomes applications through a rolling call and is particularly committed to supporting interdisciplinary research. By enabling access to complementary techniques and fostering collaborative networks, RIANA empowers researchers to address key challenges in nanoscience and technology, while enhancing the impact and visibility of Europe's leading analytical and nanotechnology infrastructures. As part of the e-DREAM network, Area Science Park contributes to the initiative by offering access to advanced electron microscopy techniques and expert support.



Type of presentation: Poster

MS4-P-4 Hematene lattice parameter variation as a function of thickness

Maximilian Melchior[a], Jana Dzibelova[a], Anastasiia Nihei[b], Rico Friedrich[b], Jani Kotakoski[a]

[a]*University of Vienna, (Vienna), Austria*

[b]*TU Dresden, (Dresden), Germany*

Contact email: maximilian.melchior@univie.ac.at

Hematene (α-Fe_2O_3) is a relatively new two-dimensional non-van der Waals material, first exfoliated successfully in 2018 [1]. Contrary to its bulk counterpart, this iron oxide exhibits photocatalytic activity in its low-dimensional state making it interesting for various applications [1, 2]. However, the so-far-reported magnetic and electronic properties of hematene differ in both theory and experiment. The change in properties can be attributed to the modification of the electronic structure which is related to the lattice parameters. First principle calculations have shown an alteration of the lattice constant from bulk to monolayer due to the accommodation of dangling bonds [3]. This contribution utilizes multiple microscopic techniques to experimentally investigate the correlation of the lattice parameters and the thickness of hematene in the regime of few atomic layers.

Specifically, thickness measurements are performed using four-dimensional scanning transmission electron microscopy (4D-STEM). Position averaged convergent electron beam diffraction (PACBED) is sensitive to material thickness. The collected PACBED patterns are matched with data of known thickness simulated with *ab*TEM [4, 6]. Another technique utilized is the Log-Ratio model based on electron energy loss spectroscopy (EELS) [5]. The custom-made SiN grids (Silson Ltd) used in STEM are compatible with atomic force microscopy (AFM) which is also available in the University of Vienna CANVAS system [7]. Future work will make use of this setup in an effort to cross correlate thickness measurements of all techniques.

References:

1. A. Puthirath Balan, S.Radhakrishnan, C.F. Woellner *et al., Nature Nanotech* **2018**,13, 602–609
2. J. Dzíbelová, *et al., Applied Materials Today* **2023**, 34, 101881
3. R. Friedrich, *et al*., *Nano Letters* **2022**, *22*, 989-997
4. C. Ophus, *et al., Appl. Phys. Lett.* **2017**, 110, 063102
5. K. Iakoubovskii, *et al., Microsc. Res. Tech.* **2008**, 71, 626-631
6. J.Madsen, T.Susi, *Open Research Europe* **2021**, 1:24
7. C Mangler, *et al*., *Microscopy and Microanalysis* **2022**, 28 (S1), 2940–2942

Type of presentation: Poster

MS4-P-5 Stability of gold nanorods under tunable ps-pulsed laser illumination: an in-situ TEM study

Loriane Monin[a], Wiebke Albrecht[a]

[a]*AMOLF, Amsterdam, The Netherlands*

Contact email: l.monin@amolf.nl

Dynamic and resonant plasmonic photocatalysis is a new and exciting field that could overcome the classic Sabatier limit in catalysis. In fact, by delivering short laser pulses, fast heating and cooling of the plasmonic particles can be achieved. This could pave the road towards controlling chemical reactions both spatially and temporally. However, gold NPs have been shown to reshape at temperatures below the bulk melting temperature of gold which limits their use in a novel type of chemical reactors [1,2]. In this project, the structural stability of gold nanorods (GNRs) under tunable ps laser excitation is investigated.

This research is conducted in an aberration corrected TEM equipped with the IDES light in-coupling unit (Figure 1a). This allows us to directly use any fibre coupled laser into the TEM column. By spatially overlapping the electron and the laser beam, we can study the structural changes that GNRs undergo when illuminated. For this set of experiments, we couple a tunable ps laser enabling us to select the wavelength, the repetition rate and the fluence used during the experiment.

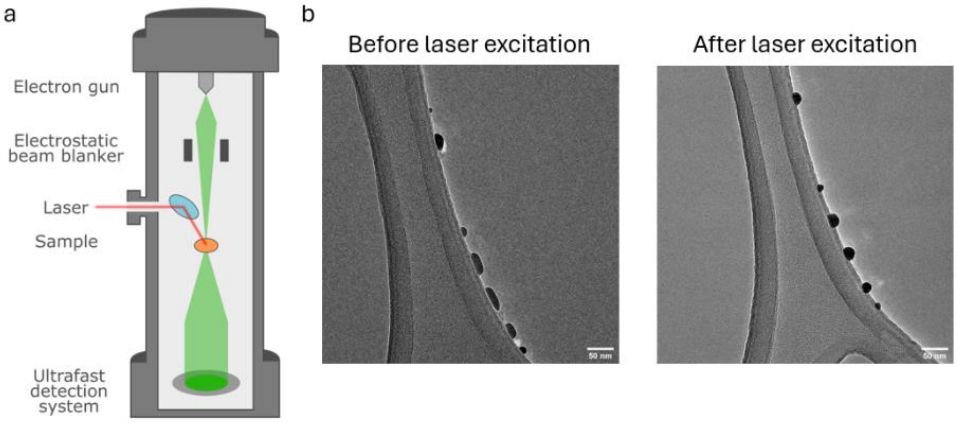


Figure 1. (a) Scheme of the TEM with the fiber coupled laser through the column. (b) demonstration of the structural changes of gold nanorods on a lacey carbon grid before (left) and after (right) laser excitation at resonance. The GNPs were illuminated at a wavelength of 680nm with a fluence of $2.1 \times 10^{-3}\ mJ\ cm^{-2}$.

In this work, we demonstrate that the laser excitation scheme plays a crucial role for the structural stability of GNPs (Figure 1b). Varying the fluence and the cooling time between the heating cycles provides insights about the kinetics of the reshaping of GNPs. We observe that heating of the substrate is the main contributor to the morphological instability of the GNRs under study. Finally, the temperature reached by the particles during the experiment is estimated with heat simulations.
In conclusion, coupling light directly into the electron column allows us to observe how catalytic GNPs behave in real conditions. This research paves the road for the design of GNPs that would be stable under dynamic and resonant catalytic conditions. Future steps include the use of a holder equipped with a small reactor allowing to mimic the operational conditions of a light driven catalytic reactor.

References:
[1] Albrecht et al., Adv. Mater. 33, 2100972 (2021)
[2] González-Rubio et al., Science 358, 640–644 (2017)

Type of presentation: Poster

MS4-P-6 Assessing the morphology and fractal properties of aggregated nanoparticles in 2 and 3 dimensions by transmission electron microscopy

Noa Olluyn[a,b], Evgenii Vlasov[b], Charlotte Wouters[a], Jan Mast[a], Sara Bals[b], Eveline Verleysen[a]

[a]*Sciensano (Brussels), Belgium*

[b]*EMAT, University of Antwerp (Antwerp), Belgium*

Contact email: noa.olluyn@sciensano.be

Characterisation of materials that contain a fraction of nanoparticles includes measurement of the size and shape distributions of the constituent particles. The material properties can be further influenced by extrinsic properties, such as aggregate morphology and agglomeration behaviour under specific experimental conditions. Transmission electron microscopy (TEM) is often applied to determine the particle size and shape properties, covering the full nanosize range (1 – 100 nm) and beyond in a quantitative manner. The interpretation of 2D images taken from 3D objects is, however, not always unambiguous, especially for aggregated or agglomerated particles. Multiple approaches exist to further extend 2D measurement and quantification of particle morphology [1-3]. To describe the aggregate structure, the fractal dimension can be determined, either using a power law calculated from the number of particles, the particle size, and the radius of gyration, or using the box counting method [2]. However, since the aggregates are complex 3D structures, 2D projections can be misleading or cause problems during image analysis, due to overlapping particles. Electron tomography (ET) is therefore employed to obtain information in three dimensions, but the acquisition of conventional ET tilt series is a time- and labour intensive process when a statistically relevant number of particles has to be investigated. The acquisition of surface-specific information through the mapping of the secondary electron e-beam induced current (SEEBIC) in the sample can help to overcome limitations in image analysis caused by overlapping particles. This recently developed SEEBIC technique provides valuable surface information at high resolution, and at much lower acquisition times than conventional ET [1].

This study evaluates above described TEM based approaches, and a combination thereof, to characterise the morphology of the aggregates present in two synthetic amorphous silica representative test materials that form fractal-like aggregates (JRCNM10404a and JRCNM02000a). A certified reference material (ERM-FD100 colloidal silica) is applied as a control for size and shape measurements. The morphology and fractal dimensions of the aggregates in the materials are determined based on 2D TEM and high angle annular dark field scanning electron microscopy (HAADF-STEM) imaging, and it is evaluated whether the combination of SEEBIC and HAADF-STEM can complement the assessment of the aggregate structure when employing 2D projection imaging methods (Figure 1A-B). Electron tomography is performed to determine the size and position of the constituent particles, and the fractal dimension of the aggregates/agglomerates in 3D (Figure 1C). The different imaging and image analysis methods are subjected to an in-depth analysis, highlighting the validity of the results and the strengths and weaknesses of each approach.

The methodology presented in this study is applicable to a larger variety of aggregated and agglomerated particulate materials and can be applied, for example, to study agglomeration behaviour under different environmental conditions.

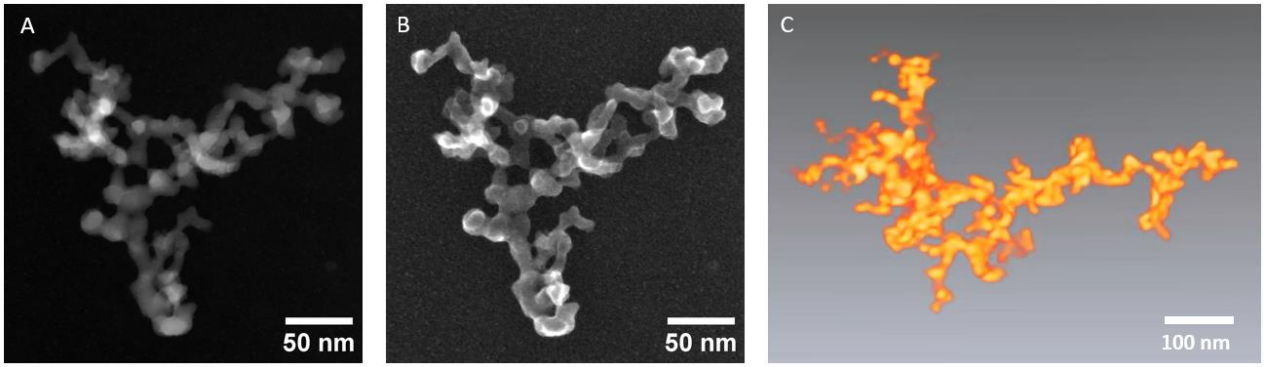


Figure 1: Images of fractal-like aggregate obtained with various imaging techniques. A) HAADF-STEM image of a fractal-like aggregate, B) SEEBIC image of the same aggregate as presented in A, C) Volume rendering of an electron tomogram of a fractal-like aggregate.

References:

1. Vlasov, E.; Skorikov, A.; Sánchez-Iglesias, A.; Liz-Marzán, L. M.; Verbeeck, J.; Bals, S. Secondary Electron Induced Current in Scanning Transmission Electron Microscopy: An Alternative Way to Visualize the Morphology of Nanoparticles. *ACS Mater. Lett.* **2023**, *5* (7), 1916–1921. https://doi.org/10.1021/acsmaterialslett.3c00323.
2. Wang, R.; Singh, A. K.; Kolan, S. R.; Tsotsas, E. Fractal Analysis of Aggregates: Correlation between the 2D and 3D Box-Counting Fractal Dimension and Power Law Fractal Dimension. *Chaos Solitons Fractals* **2022**, *160*, 112246. https://doi.org/10.1016/j.chaos.2022.112246.
3. Weyland, M.; Midgley, P. A. Electron Tomography. *Mater. Today* **2004**, *7* (12), 32–40. https://doi.org/10.1016/S1369-7021(04)00569-3.

Type of presentation: Poster

MS4-P-7 Atomic-scale Investigation of FEL-Induced Structural Modifications in Pyrolytic Graphite via TEM Analysis

Sara Passuti[a], Claudia Fasolato[b,c], Elena Stellino[b], Caterina Petrillo[a,b], Francesco Sacchetti[b,d], Regina Ciancio[a]

[a]*AREA Science Park, Padriciano 99, I-34149 (Trieste), Italy*

[b]*Dipartimento di Fisica e Geologia, Università di Perugia (Perugia), Italy*

[c]*Istituto dei Sistemi Complessi, Consiglio Nazionale delle Ricerche (CNRISC), Roma I-00185, Italy*

[d]*Officina dei Materiali, Consiglio Nazionale delle Ricerche (CNR-IOM), (Perugia), Italy*

Contact email: sara.passuti@areasciencepark.it

Introduction

High-order pyrolytic graphite (HOPG) has been the subject of intense investigation due to its unique structural and electronic properties, making it an ideal candidate for studies involving intense photon-matter interactions. One such approach, using Free Electron Laser (FEL) irradiation, has recently been explored to examine ultrafast processes and structural modifications in graphite under extreme conditions. A prior study on Thomson scattering of coherent soft X-ray pulses around the carbon K-edge revealed a superradiant scattering process that is intrinsically linked to vibrational collective modes [1]. These observations indicated significant changes in the absorption coefficient following femtosecond-scale irradiation, suggesting a transformation in the graphite structure.

Despite the absence of macroscopic material removal, optical microscopy hinted at mild structural alterations, while superradiant scattering measurements provided evidence of substantial modifications in the phonon dynamics, including a decrease in the velocity of longitudinal acoustic phonons and energy shifts in longitudinal optical phonons. Such changes strongly suggested the presence of a modified structural phase post-irradiation, warranting further high-resolution investigation.

This work focuses on the microscopical characterization of the sample subjected to FEL radiation, with the objective of determining the nature of the observed changes in its physical properties.

Methods

Transmission Electron Microscopy (TEM) was employed to elucidate the microscopic morphological and crystallographic changes induced by FEL irradiation. By comparing pristine HOPG samples with those subjected to FEL irradiation, we aimed to characterize nanoscale modifications, defect formations, and potential phase transitions. A JEOL F200 cFEG TEM working at 200 kV was used for the characterization. For the acquisition of diffraction patterns and High Resolution (HR) images, the front CCD camera and a Dectris ELA hybrid pixelated detector were used. For TEM analysis, the samples have been prepared both as lamellae with a FIB-SEM system and thinned by PIPS (Precision Ion Polishing System). 3D Electron Diffraction (3D ED) acquired on the pristine sample were processed using the software PEST2 and Jana2020.

Results

3D Electron Diffraction (3D ED) performed on the pristine sample allowed to solve *ab initio* the crystal structure of graphite, confirming the quality and composition of the specimen before FEL irradiation. TEM imaging of the sample irradiated with FEL reveals a dense nanocrystallites composition, with an average size of 10-15 nm (Fig.1a), in opposition to the pristine sample, which showed a uniform appearance. This provides hints of a possible re-crystallization process following the FEL irradiation.

To assess the structure of the crystallites, ring Diffraction Patterns were collected on large areas containing hundreds of nanocrystallites (Fig.1b), from which a 1D diffraction profile was extracted and compared to the theoretical pattern computed for graphite. From the comparison, the presence of non-indexed peaks emerged, notably around the 0002 peak of graphite (Fig.1c). This suggests a variation in the crystal structure of graphite upon FEL irradiation.

Closer inspection of the crystallites was performed by High Resolution TEM (HRTEM). A Bright field TEM image of a representative ensemble of crystallites is shown in Fig 2. The FFT computed on the

individual crystallites (a representative one is displayed in the inset) exhibits the typical fingerprint of the crystalline graphite structure along with the presence of additional peaks at d* = 5.5 nm^{-1}, close to the indexed ones at d* = 4.8 nm^{-1}.These findings suggest the occurrence of twins or superstructures in the newly formed crystals, thus supporting the hypothesis of a modification in the graphite crystal structure.

Discussion and conclusions

Our TEM investigations provide critical insights into the evolution of graphite's microstructure under FEL irradiation. These findings contribute to a deeper understanding of the FEL-induced structural dynamics in graphite and open perspectives towards the crystallization of new phases in other related compounds.

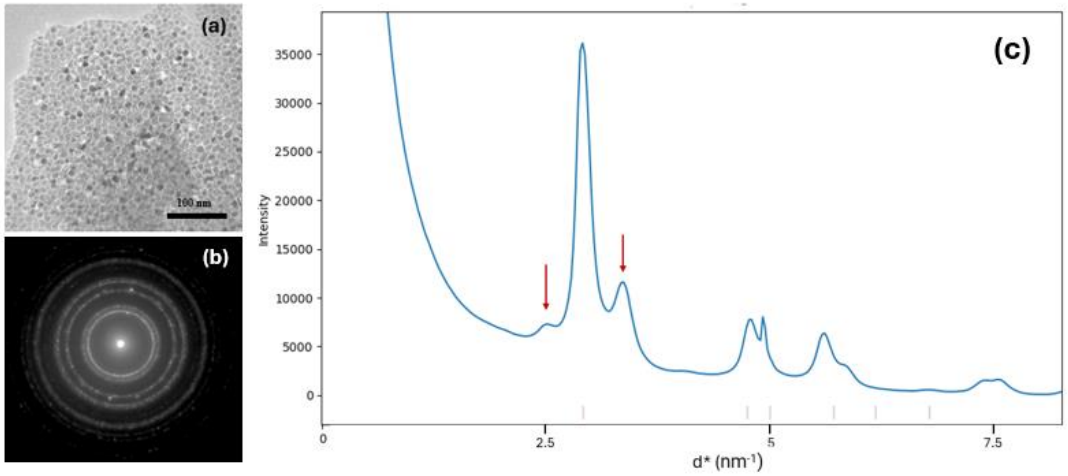


Figure 1: (a) TEM image of an area of the graphite sample irradiated with FEL showing the presence of nanocrystallites, (b) ring electron diffraction pattern acquired with the Dectris ELA hybrid pixelated detector, (c) 1D diffraction profile obtained from (b).

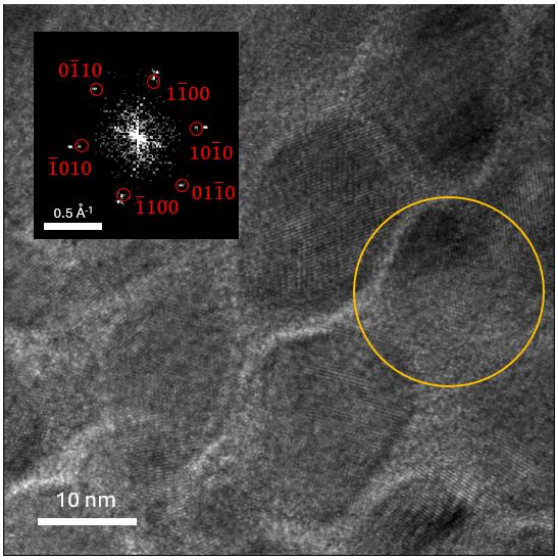


Figure 2: HRTEM image of the nanocrystallites acquired with the Dectris ELA hybrid pixelated detector. Inset: processed FFT computed from the area circled in yellow.

References:

1. Fasolato, Claudia, et al. "Superradiant Thomson scattering from graphite in the extreme ultraviolet." Proceedings of the National Academy of Sciences 121.4 (2024): e2221293121.

Type of presentation: Poster

MS4-P-8 Ab initio Study of Angle-Resolved Spectroscopy of Few-Layer Graphene

Aleš Paták[a], Martin Zouhar[a], Ivo Konvalina[a], Eliška Materna Mikmeková[a], Lukáš Průcha[a], Ilona Müllerová[a], Anna Charvátová Campbell[b], Miroslav Valtr[b], Michal Horák[c], Vlastimil Křápek[c], Eugene Krasovskii[d]

[a]*Institute of Scientific Instruments of the Czech Academy of Sciences, (Brno), Czech Republic*

[b]*Czech Metrology Institute, (Brno), Czech Republic*

[c]*Brno University of Technology, (Brno), Czech Republic*

[d]*Departamento de Polímeros y Materiales Avanzados: Física, Química y Tecnología, Universidad del Pais Vasco/Euskal Herriko Unibertsitatea, (Donostia/San Sebastián), Basque Country, Spain; Donostia International Physics Center (DIPC), (Donostia/San Sebastián), Basque Country, Spain; and IKERBASQUE, Basque Foundation for Science, (Bilbao), Basque Country, Spain*

Contact email: patak@isibrno.cz

Introduction: Graphene, a two-dimensional material with extraordinary electronic properties, has attracted significant interest for its potential applications in nanoelectronics. The characterization of few-layer graphene (FLG) remains a challenge, particularly in determining the number of layers, stacking type, and moiré patterns. Angle-resolved reflected-electron spectroscopy (ARRES) offers a non-destructive method for FLG characterization. In this work, we present an **ab initio** theoretical study of ARRES for FLG, including inelastic effects via an optical potential derived from electron energy-loss spectra (EELS) simulations.

Methods: The electronic structure and reflection spectra of FLG were calculated using density functional theory – via QUANTUM ESPRESSO (QE) [1] and the APW method [2], and many-body perturbation theory [3,4]. The inelastic effects were incorporated through an optical potential derived from simulated EELS data. The reflectivity spectra were computed for different incidence angles, graphene thickness and stacking order. Experimental data were used to validate the theoretical model. The experimental ARRES data published in Ref. [5] were kindly provided by the Leiden University group. Our own experimental EELS data were measured using the TEM FEI Titan equipped with a GIF Quantum spectrometer operated at 60 keV. Further details, including addressing the spurious interaction of artificial copies of FLG due to the supercell approach in the calculations, see Fig. 1(a), are provided in Ref. [6].

Results: A comparison of the simulated EELS data with our experimental results has been made, and a reasonable degree of agreement has been found, providing a verification of the optical potential obtained from the calculated data. The simulations of reflectivities reveal distinct features corresponding to different FLG configurations. Inelastic effects lead to attenuation of spectral contrast, yet the key features remain observable, enabling layer number determination and stacking order differentiation. The agreement between theoretical predictions and experimental results confirms the validity of the presented approach, see Figs. 1(b) , 1(c), Ref. [5], and Ref. [6].

Discussion and Conclusions: Our findings demonstrate that ARRES, supplemented by theoretical modeling, provides a powerful tool for FLG characterization. The method is capable of distinguishing stacking types in twisted bilayer graphene and detecting moiré patterns. The results support the application of ARRES in quality control for graphene-based electronic devices, offering high spatial resolution and sensitivity to structural variations.

Acknowledgments: This research was supported by the Czech Science Foundation (Grant No. GA22–34286S), the Technology Agency of the Czech Republic (Grant No. TN02000020), MEYS CR (Project No. LM2023051), Brno University of Technology (Project No. FSI-S-23-8336), the Ministry of Industry and Trade of the Czech Republic and the Spanish Ministry of Science and Innovation (Grants No. PID2022-139230NB-I00 and No. PID2022-138750NB-C22). The authors thank S. J. van der Molen and

P. Neu from Leiden University for providing the experimental ARRES data and acknowledge discussions with experts in the field.

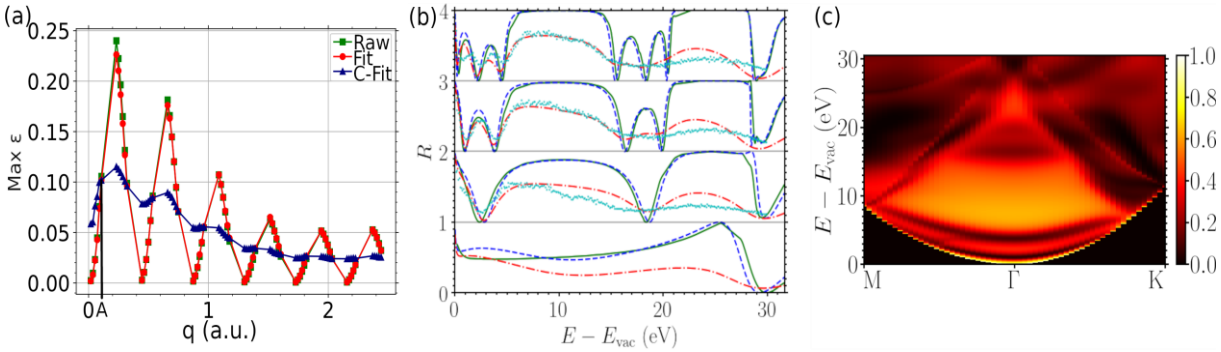


Figure 1: (a) Unphysical oscillations of the amplitude of the calculated (utilizing the truncated electrostatic potential) dielectric function ε of graphene (maxima of its imaginary part within the interval [11.0, 15.3] eV) with momentum transfer q along the ΓA direction: raw data (green squares), maxima extracted after fitting ε using an appropriate finite set of basis functions (red dots), and an attempt to correct the fit (blue triangles); (b) Normal incidence FLG electron reflectivity R spectra for 1 to 4 layers, bottom to top, as a function of landing energy featuring characteristic oscillations allowing to determine the thickness. We show data calculated without inelastic effects using QE (green solid lines) and the APW method (blue dashed lines), with included inelastic effects using the APW method (red dotted-dashed lines). Cyan symbols correspond to experimental reflectivities from Ref. [5]; (c) Simulated (with inelastic effects using the APW method) ARRES of freestanding 3-layer graphene for incident electron beams with in-plane wave vectors along MΓK.

References

1. P. Giannozzi *et al.*, *J. Phys.: Condens. Matter*, **2009**, 21, 395502.
2. E. E. Krasovskii, *Phys. Rev. B*, **2004**, 70, 245322.
3. A. Marini, C. Hogan, M. Grüning, and D. Varsano, *Comput. Phys. Commun.*, **2009**, 180, 1392.
4. I. Timrov, N. Vast, R. Gebauer, and S. Baroni, *Comput. Phys. Commun.*, **2015**, 196, 460.
5. J. Jobst, J. Kautz, D. Geelen, R. M. Tromp, and S. J. van der Molen, *Nat. Commun.*, **2015**, 6, 8926.
6. A. Paták, M. Zouhar, I. Konvalina, E. Materna Mikmeková, L. Průcha, I. Müllerová, A. Charvátová Campbell, M. Valtr, M. Horák, V. Křápek, E. Krasovskii, *Phys. Rev. B*, **2025**, 111, 125113.

Type of presentation: Poster

MS4-P-9 Thermal and Chemical Stability of High-Entropy-Alloy Nanoparticles Synthesized via Laser Ablation in Organic Liquid

Felix Pohl[a], Robert Struckert[b], Oleg Prymak[c], Ulrich Schürmann[a], Christoph Rehbock[b], Stephan Barcikowski[b], Lorenz Kienle[a]

[a]*Institute for Material Science, Faculty of Engineering, Kiel University, Kaiserstraße 2, 24143 Kiel, Germany*

[b]*Technical Chemistry I and Center for Nanointegration Duisburg-Essen (CENIDE), University of Duisburg-Essen, Universitaetsstr. 7, 45141 Essen, Germany*

[c]*Inorganic Chemistry and Center for Nanointegration Duisburg-Essen (CENIDE), University of Duisburg-Essen, Universitaetsstraße 7, 45141 Essen, Germany*

Contact email: usc@tf.uni-kiel.de

Introduction

High-entropy alloy nanoparticles (HEA NPs) synthesized by laser ablation in liquid (LAL) are of extraordinary interest, since they form a simple solid solution structure despite their high chemical complexity [1,2]. In LAL a HEA bulk target immersed in a liquid is irradiated with a pulsed laser yielding colloidal HEA NPs. As part of this work a noble metal (NM) HEA system made from CuPdAgPtAu was investigated. While an equimolar composition (NM-Eq) of elements in the bulk target leads to a single fcc solid solution structure in both target and LAL fabricated NPs, an excess of one element could result in phase segregation. Therefore, a target with an excess (50 at%) of Cu (NM-Cu) or Ag (NM-Ag) were prepared and used in LAL Here phase segregation and the formation of two fcc structures with different lattice constants were observed in the target but notably the nanoparticles showed no elemental segregation and were characterized by a single fcc structure. This opens up the possibility to enforce an elemental segregation via thermal or chemical treatment of the NPs. In addition, selective etching into porous structures can be investigated, since Cu and Ag are less noble than the other three elements. NPs are already interesting for catalysis due to their high surface-to-volume ratio. With porous structures this can be enhanced while thermal and chemical treatment can influence the formation of suitable reactive sites on their surface.

Methods

The nanoparticles were synthesized by LAL in a circulating organic solvent with NIR-laser pulses and characterized with aberration corrected (S)TEM. For chemical analysis methods like Z-contrast imaging and nanoprobe elemental mapping were applied, while the structural analysis was performed using TEM -high-resolution imaging (-HR imaging) and selected area electron diffraction (SAED). To investigate thermal phase stability *in situ* and *ex situ* heating X-ray diffraction, SAED and nanoprobe elemental mapping experiments were performed. In order to survey the chemical stability identical location (ILTEM) experiments were performed where nanoparticles are investigated in STEM before and after etching with acetic, nitric or hydrochloric acid. Furthermore, the surface of these nanoparticles was investigated using secondary electron (SE)-STEM, enabling to correlate morphological and chemical changes in the NPs.

Results

As already mentioned above, NPs with an excess of Cu or Ag show no elemental segregation and were characterized by a single fcc. For this reason, heating experiments of these NPs are conducted resulting in an elemental segregation between Ag and Cu inside the NPs. Structural information obtained by SAED and HRTEM proved the formation of the previously found second phase in the bulk target.

Preliminary etching experiments using nitric acid reduced the Au content in the NM-Eq NPs which is unlikely due to the high redox potential of Au which should lead to high acid resistance of Au compared to the other elements in the NPs. Recent ILTEM results on the other hand show a reduction of Ag, Cu and Pd as well as surface oxidation for the NM-Eq system. So far, no selective etching process leading to porous structures was observed. Clusters of Pd-Ag-N-O were observed while these clusters lack Cu, Pt and Au. Similar experiments are planned for the other two compositions.

Discussion and Conclusion

As the excess of Cu or Ag exceeds the solid solubility of the HEA fcc phase a second phase enriched with the excess element is most likely formed in the target due to slow cooling under thermodynamic control. In addition, the lack of solubility of Cu with Ag might be the driving force behind segregation [3]. Since the NPs are synthesized from the same material the segregation must be hindered in some way during NP synthesis, probably because the target is atomized in the ablation plume and particles form from this plume at high cooling rates freezing metastable structures with statistical atom distributions. These structures are reverted to their thermodynamically more stable state by slow heating exceeding the activation energy for phase segregation. While the etching of the NPs only resulted in loss of material but no definitive elemental surface segregation, it was shown that identical location TEM is possible even with using acids and solvents on TEM grids. This opens up a promising area for analyzing different environmental effects on those nanoparticles.

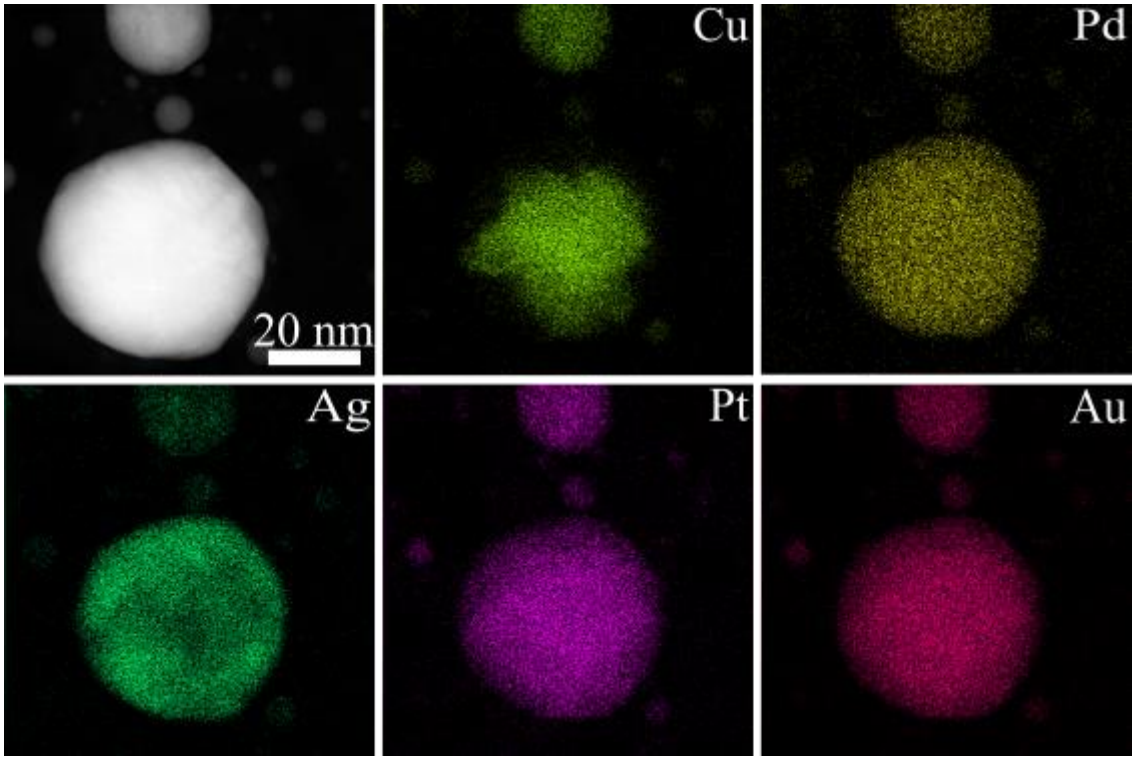


Figure 20: EDX- Map of NM-Cu NP heated up to 550 °C showing segregation of Cu and Ag.

Reference:

[1] F. Waag, Y. Li, A. R. Ziefuss, E. Bertin, M. Kamp, V. Duppel, G. Marzun, L. Kienle, S. Barcikowski and B. Gökce, Rsc Advances 2019, 9, 18547-18558.

[2] J. Johny, Y. Li, M. Kamp, O. Prymak, S. X. Liang, T. Krekeler, M. Ritter, L. Kienle, C. Rehbock, S. Barcikowski and S. Reichenberger, Nano Research 2022, 15, 4807-4819.

[3] SUBRAMANIAN, P. R.; PEREPEZKO, J. H. The Ag-Cu (silver-copper) system. Journal of Phase Equilibria, 1993, 14. Jg., S. 62-75.

Type of presentation: Poster

MS4-P-10 Physicochemical characterization of copper oxides applied as feed additives and plant protection products

Sevenants Linde[a,b,c], Siciliani Lisa[a], Scholz Sophie[d], Sieg Holger[d], Cubadda Francesco[e], Cappoen Davie[b], Verleysen Eveline[a], Mertens Birgit[b], Vanhaecke Tamara[c], Mast Jan[a]

[a]*Trace Elements and Nanomaterials Unit - Sciensano (Brussels), Belgium*

[b]*Risk and Health Impact Assessment Unit – Sciensano (Brussels), Belgium*

[c]*In Vitro Toxicology and Dermato-Cosmetology research group - Vrije Universiteit Brussel (Brussels), Belgium*

[d]*German Federal Institute for Risk Assessment - BfR (Berlin), Germany*

[e]*Italian National Institute of Health – ISS (Rome), Italy*

Contact email: linde.sevenants@vub.be

The human population can be exposed to copper oxides due to their use as plant protection products and feed additives. Cupric oxide (CuO) is authorised as pesticide, while both cupric oxide and cuprous oxide (Cu_2O) are authorised as feed additive [1-3]. They are commercially available as powders or formulations and are broadly used. However, limited information on their particle size is available, which in turn can influence other physicochemical properties/endpoints such as dissolution and surface reactivity. For particulate materials applied in food and feed, the EFSA Guidance on Particle-Technical Requirements requires measuring the particle size distribution to assess whether a nano-specific risk assessment should be performed [4]. In this work, the properties of copper oxide particles applied as feed additive and/or as plant protection product were determined using electron microscopy-based methods. Sample preparation, on grid sampling, imaging and image analysis methods were optimised and combined for particle size measurement.

A total of 20 copper oxide materials, including five feed additives (one Cu_2O and four CuO), one pesticide (Cu_2O), and 14 benchmark materials (seven Cu_2O and seven CuO materials, including four labelled as "micrometer-sized particles"), were sourced from the European market. The properties of the copper oxide particles, including size, shape, agglomeration state, and elemental composition, were determined using (scanning) transmission electron microscopy ((S)TEM) and energy-dispersive X-ray spectroscopy (EDX). Three marketed copper oxide materials were selected for further testing: two feed additives (F_CuO_a and F_Cu_2O) and one pesticide (P_Cu_2O). Crystallographic phase analysis using selected area electron diffraction (SAED) was performed to confirm the identity of the materials by their crystal structure. Zeta potential curves in aqueous medium were determined across a pH range of pH 2-12 to assess the condition where a stable dispersion can be obtained. To prepare dispersions for quantitative size measurement of the constituent particles of the selected copper oxide materials by (S)TEM, the conditions proposed in the generic Nanogenotox protocol were evaluated [5]. Descriptive EM analysis was performed to assess whether notable differences in the agglomerate size and number of particles per grid surface existed between ethanol pre-treated and non pre-treated samples. In addition, the effects of increasing sonication energies on dispersions prepared in a distilled water containing 0.05%BSA solution were investigated. It was assessed if notable changes in agglomeration, as well as constituent particle size and morphology, occur. To sample a broad size range, from nano to micro-sized particles, on the EM-grid in a representative manner, several EM-specimen preparation methods were evaluated, including grid-on-drop, (air-dried) drop-on-grid, and on-grid centrifugation methods. The particle size distributions of the selected copper oxides were measured by (S)TEM applying counting rule 4 [6,7]. Normalized number-based distributions and descriptive statistics were determined for minimum and maximum Feret diameters and for the aspect ratio. For a representative test material, a validation study is conducted to estimate the measurement uncertainties associated to these particle size measurement.

The obtained results are a first step in addressing some of the current data gaps identified in the physicochemical characterization needed for hazard assessment of copper oxides applied in the food chain. The results will be complemented by an assessment of the transformations of the particles in *in vitro* test media, simulating the gastrointestinal tract (GIT) of livestock and humans.

This research is performed under the NAMS4NANO action via funding from the European Union through a grant of the European Food Safety Authority (agreement GP/EFSA/MESE/2022/01). This communication reflects only the author's view and EFSA is not responsible for any use that may be made of the information it contains.

1. EFSA SCIENTIFIC COMMITTEE 2013. Guidance on the renewal of the authorisation of feed additives. EFSA Journal, 11.
2. EFSA SCIENTIFIC COMMITTEE 2016. Panel on Additives, Products or Substances used in Animal Feed; Safety and efficacy of dicopper oxide as feed additive for all animal species. EFSA Journal, 14.
3. EFSA SCIENTIFIC COMMITTEE 2018. Peer review of the pesticide risk assessment of the active substance copper compounds copper (I), copper (II) variants namely copper hydroxide, copper oxychloride, tribasic copper sulfate, copper (I) oxide, Bordeaux mixture. EFSA Journal, 16.
4. EFSA SCIENTIFIC COMMITTEE 2021. Guidance on technical requirements for regulated food and feed product applications to establish the presence of small particles including nanoparticles. EFSA Journal, 19.
5. K. A. Jensen et al., The Generic NANOGENOTOX Dispersion Protocol, in Standard Operation Procedures (SOP) and Background Documentation: Final Protocol for Producing Suitable Manufactured Nanomaterial Exposure Media., edited by K. A. Jensen and N. Thieret (2011).
6. Bresch, H., Hodoroaba, V.-D., Schmidt, A., Rasmussen, K., Rauscher, H., 2022. Counting Small Particles in Electron Microscopy Images—Proposal for Rules and Their Application in Practice. Nanomaterials 12, 2238.
7. EFSA SCIENTIFIC COMMITTEE 2021. Guidance on risk assessment of nanomaterials to be applied in the food and feed chain: human and animal health. EFSA Journal, 19.

Type of presentation: Poster

MS4-P-11 Investigation of Electrodeposition and Electrodissolution Mechanisms of Silver Nanoparticles Using Electrochemical Liquid Cell Transmission Electron Microscopy

Layrton José Souza da Silva[a,b], Sorour Semsari Parapari[a], Monica Parpal Giménez[c], Mohamed El Marini[c], Jon Ustarroz[c,d], Sašo Sturm[a,b,e]

[a]*Department for Nanostructured Materials, Jožef Stefan Institute, Ljubljana, Slovenia*

[b]*Jožef Stefan International Postgraduate School, Ljubljana, Slovenia*

[c]*ChemSIN – Chemistry of Surfaces, Interfaces and Nanomaterials, Universit´e libre de Bruxelles Brussels, Belgium*

[d]*SURF – Research Group Electrochemical and Surface Engineering, Vrije Universiteit Brussel, Brussels, Belgium*

[e]*Department of Geology, Faculty of Natural Sciences and Engineering, University of Ljubljana, Ljubljana, Slovenia*

Contact email: layrton.jose.souza.dasilva@ijs.si

Silver nanoparticles are a versatile group of nanoparticles that have been thoroughly studied due to their tunable shapes, structures, and properties. Different methods to produce nanoparticles with various shapes – nanocubes, nanospheres, nanorods – have been described in the literature [1,2]. Among all the possible techniques, the electrochemical synthesis of nanoparticles allows the proper tuning of nanoparticle properties by varying solution concentration, potential bias, or applied current. However, precise control over the final conditions of the synthesis process is intrinsically connected to the knowledge of the synthesis mechanisms. This gap in mechanistic knowledge can be bridged by using *in-situ* microscopy techniques to access real-time reactions directly. *In-situ* Liquid-Cell Transmission Electron Microscopy (*in-situ* LCTEM) is a technique that can be used to directly visualize nanoscale chemical and electrochemical reactions with good spatial and temporal resolution in an aqueous phase. This study employs a miniaturized electrochemical cell setup to investigate silver nanoparticles' electrochemical deposition and dissolution dynamics, providing direct mechanistic insights into the electrochemical growth and dissolution processes.

The electrodeposition and electrodissolution of silver were studied by *in-situ* LCTEM technique. The experiments were done with a JEOL JEM 2100 TEM (JEOL, Japan) at 200 kV acceleration voltage. The liquid cell holder is a Protochips Poseidon holder (Protochips Inc., USA). The Liquid cell consisted of two E-Chips, a big and a small E-Chip, which were sandwiched against one another. Both E-Chips have a 50 nm thick silicon nitride electron transparent window, allowing the visualization of the electrodeposited particles in a liquid environment. Finally, the big E-Chip has three electrodes patterned onto it, allowing for the measurement and application of electrochemical signals. The electrochemical bias was controlled using a Gamry Potentiostat Reference 600 (Gamry Company, USA). The cyclic voltammetry (CV) technique was used to obtain the characteristic curve for the electrolyte/electrode deposition system, potential window between -300 mV to 200 mV vs. Pt. The electrolyte solution containing 2 mM $AgNO_3$ and 50 mM KNO_3 in ultrapure deionized water was used for the electrodeposition experiments. The electron beam dose was estimated to be around 978 $e^-/Å^2 \cdot s$.

With the CV technique, the oxidative peak was recorded at +48 mV vs. Pt, and the deposition peaks were measured at -150 mV and -50 mV vs. Pt for the redeposition of silver; these values are comparable with the silver dissolution in a macroscopic electrochemical cell, with Pt pseudoreference electrode. During the anodic (oxidative) part of the cycle, incomplete dissolution of silver occurred; the external part of the particle remained, a shell of the original particles. The redeposition in the following cathodic part of the CV happened in the regions where the shells were left behind. These spots displayed more

affinity to the redeposition of silver when compared with the glassy carbon surface. The formation of faceted particles and small islands was also probed during the cathodic electrodeposition.

Using LCTEM, it was possible to directly observe and measure complex dynamic processes at the nanoscale. This approach reveals mechanisms and intermediary steps that cannot be directly observed using classical electrochemical and microscopy techniques, such the initial stages of deposition, facet formation, and the initial stages of nanoparticle dissolution.

Acknowledgments:

The Slovenian Research Agency has financially supported this work through the national program P2-0084, ARIS projects number PR-12334 (Young Researcher Program), Z2-50057, J7-4636, and J2-4433, and the ARRS-FWO bilateral project N1-0196.

References:

1. N.P.U. Nguyen, N.T. Dang, L. Doan, T.T.H. Nguyen, Synthesis of Silver Nanoparticles: From Conventional to 'Modern' Methods—A Review, Processes. 11 (2023) 2617. https://doi.org/10.3390/pr11092617.
2. A.A. Yaqoob, K. Umar, M.N.M. Ibrahim, Silver nanoparticles: various methods of synthesis, size affecting factors and their potential applications–a review, Appl. Nanosci. 10 (2020) 1369–1378. https://doi.org/10.1007/s13204-020-01318-w.

MS5 Magnetic, ferroelectric, and spintronic materials

Type of presentation: Invited

MS5-IN-1 Insight into Defects and Polarization in Lead-Free Ferroelectrics by Advanced STEM Techniques

Andreja Benčan Golob[a], Katarina Žiberna[a], Janina Roknić[a], Maja Koblar[a], Meryem Lachhab[a], Mojca Otoničar[a], Matic Poberžnik[b], Anton Kokalj[b], Marjan Stoimchev[c], Matej Martinc[c], Sašo Džeroski[c], Goran Dražić[d]

[1]*Electronic Ceramics Department, Jožef Stefan Institute, Ljubljana, Slovenia*

[2]*Physical and Organic Chemistry Department, Jožef Stefan Institute, Ljubljana, Slovenia*

[3]*Knowledge Technologies Department, Jožef Stefan Institute, Ljubljana, Slovenia*

[4]*Department of Materials Chemistry, National Institute of Chemistry, 1000 Ljubljana, Slovenia*

Contact email: andreja.bencan@ijs.si

Ferroelectrics are a class of materials characterized by spontaneous polarization that can be reversed by an external electric field. Understanding and controlling this polarization, along with its connection to domain morphology and domain walls, is essential for optimizing their properties. Additionally, the behavior of ferroelectric materials is significantly influenced by structural defects, which can arise during synthesis or develop under external stimuli such as mechanical stress or electric fields. These defects, spanning various length scales, including point defects and dislocations, play a crucial role in determining the material's functional properties.

In this talk, I will present structural studies of environmentally friendly perovskite ferroelectrics, such as potassium sodium niobate and bismuth ferrite, in bulk form using a probe Cs-corrected ARM 200 CF microscope (JEOL, Tokyo, Japan) and a Spectra 300 microscope (Thermo Fisher Scientific, Waltham, USA). I will highlight how various types and distributions of defects influence local materials properties, including strain fields and charge distributions. A part of the talk will focus on the identification of structural defects using new pixelated detectors (4D STEM), demonstrating how, by simulating 4D STEM diffraction patterns and integrating first-principles calculations with machine-learning models, we aim to detect polarization directions and investigate the influence of point defects, such as oxygen vacancies, on local polarization distribution.

This work was supported by the Slovenian Research and Innovation Agency (P2-0105 and J7-4637).

Type of presentation: Invited

MS5-IN-2 Next generation spintronic devices and 3D curved magnets examined by Lorentz microscopy

Trevor P. Almeida[a], Kayla Fallon[a], Danian A. Dugato[b], Wesley B. F. Jalil[b], András Kovács[c], David Cooper[d], Flavio Garcia[b], Thomas Moore[e], Christopher H. Marrows[e], Rafal E. Dunin-Borkowski[c], Stephen McVitie[a]

[a]*SUPA, School of Physics and Astronomy, University of Glasgow, Glasgow G12 8QQ, UK.*

[b]*Centro Brasileiro de Pesquisas Físicas (CBPF), Rua Dr Xavier Sigaud 150, Urca, 22290-180, Rio de Janeiro-RJ, Brazil.*

[c]*Ernst Ruska-Centre for Microscopy and Spectroscopy with Electrons (ER-C), 52425 Jülich, Germany.*

[d]*Univ Grenoble Alpes, CEA, LETI, Minatec campus F-38054, Grenoble, France.*

[e]*School of Physics and Astronomy, University of Leeds, Leeds LS2 9JT, United Kingdom*

Contact email: trevor.almeida@glasgow.ac.uk

To better understand the functional performance of modern spintronic devices, it is often necessary to investigate the underlying processes on the nanoscale. Lorentz transmission electron microscopy (TEM) techniques such as electron holography or differential phase contrast (DPC) imaging allows for the imaging of magnetic configurations in nanostructures with spatial resolution ≤ 1 nm. Adding the influence of external stimuli, e.g., biasing, heating, etc., through innovative *in-situ* TEM holders can further elucidate their dynamic magnetic behavior on the localized-scale operando conditions. In this context, several examples of the use of Lorentz TEM and *in-situ* experiments will be presented.

Equiatomic iron-rhodium (FeRh) has attracted much interest due to its magnetostructural transition from its antiferromagnetic (AF) to ferromagnetic (FM) phase and is considered desirable for potential application in a new generation of novel nanomagnetic or spintronic devices. Several scanning TEM techniques are performed to visualize the localized chemical, structural and magnetic properties of a series of cross-sectional and planar FeRh thin films [1-3]. Fig. 1a presents a cross-section of an Ir / Pd gradient-doped FeRh thin film, where DPC images show the AF / FM phase boundary (PB) motion with temperature when heating from 50°C to 200°C. Fig. 1b shows a planar FeRh sample in a FM state at 150°C with well-resolved DWs, which are then driven in an upwards direction by the application of 500μs current pulses (CPs) (Fig. 1c, arrowed). Hence, Figure 1 has shown that PB motion in FeRh cross-sections can be controlled using Ir-gradient doping and application of CPs allows for current-driven DW motion in planar FeRh thin films.

Perpendicular shape anisotropy (PSA) offers practical solutions to downscale spin-transfer torque magnetic random-access memory (STT-MRAM) beyond 20 nm technology nodes [4,5]. However, as these modern devices become smaller and three-dimensionally (3D) complex, our understanding of their magnetic behavior often relies on magnetoresistance measurements and micromagnetic modeling. Here, we present the stacking of electron holograms to improve phase sensitivity and allows the imaging of the thermal stability of <20 nm PSA-STT-MRAM nano-pillars and subtle variations in induced by annealing. The high-angle annular dark-field (HAADF) scanning TEM (STEM) image (Fig. 2a) reveals the general morphology of a NiFe-based nanopillar, whilst the combined EDX / magnetic induction map (Fig. 2b) demonstrates the magnetization lies along the elongated axis of the NiFe section (~ 20 diameter, ~ 60 nm height), as indicated by the white arrow. Subsequent magnetic induction maps acquired during *in-situ* heating to 250°C (Fig. 2c-e) demonstrate the nano-pillar to retain this direction of magnetization and confirms that the high-aspect-ratio NiFe section provides out-of-plane PSA that is resistant to thermal variations during operation [4].

Magnetic textures in self-supported nanostructures, such as vortex or skyrmion states, are promising for magnetic hyperthermia therapy and spintronics due to their low remanent state and topological protection. This work presents the use of colloidal lithography to fabricate curved nanocaps (Fig. 3a)

[6] with unique magnetic properties. Electron holography of single-layer permalloy ($Ni_{80}Fe_{20}$) nanocaps experimentally confirmed that nanocaps with diameter of 500 nm and thicknesses of 10 nm, 20 nm and 50 nm (Fig. 3b,c), all exhibited a vortex magnetic configuration as the ground state. Multi-layered [Pt(1 nm)/Co(t)/Pt(1 nm)]×10 nanocaps with varying Co thickness (t) were simulated using micromagnetic modelling to show the ground state in relation to effective radial anisotropy constant (K_{radial}) and interfacial Dzyaloshinskii-Moriya interaction (iDMI). The K_{radial} resulting in skyrmionic states corresponded to 2 nm thick Co layers and was examined experimentally using electron holography. The phase image (Fig. 3d) and magnetic induction map (Fig. 3e) confirms the presence of a single Néel-type skyrmion (labelled 'sk') and is consistent with that observed from Néel skyrmions in thin films [3,4]. This works provides fundamental insight into the impact of geometric curvature on controlling ground states and iDMI, allowing effective engineering of vortex and skyrmionic configurations without the need to apply fields at room temperature.

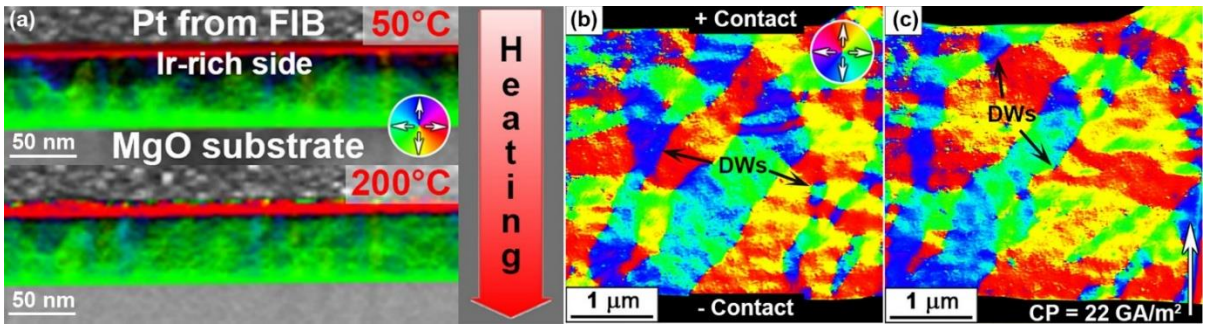


Fig. 1. (a) DPC imaging of the Ir/Pd gradient-doped FeRh film as a function of increasing temperature, displaying the upward PB motion to the Ir-rich side. (b,c) DPC imaging of a planar FeRh thin film showing DWs in a planar FeRh thin film heated to (b) 150ºC; and (c) after application of 500µs CPs with a current density of ~ 2.2×10^{10} A/m^2 in the arrowed direction. The direction of magnetization in is depicted in the color wheels (inset).

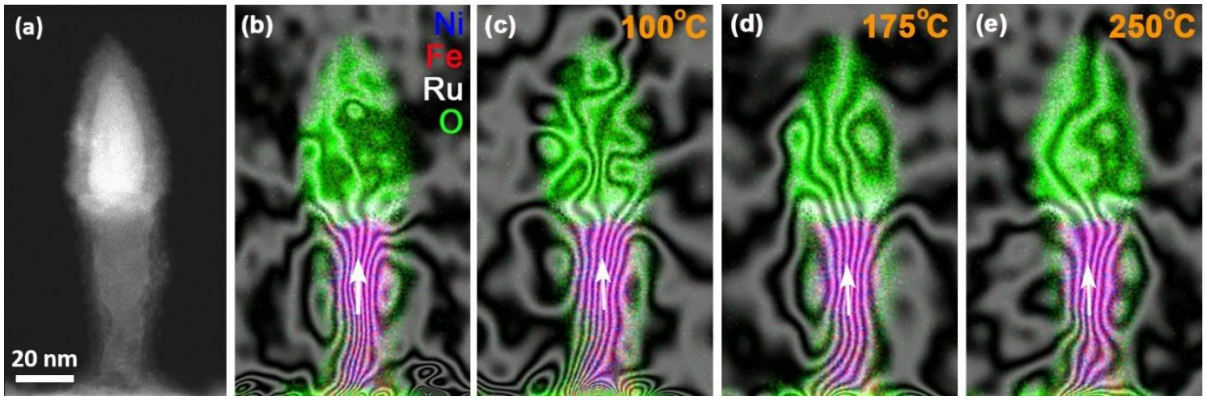


Fig. 2. (a) HAADF STEM image of a PSA nanopillar with a diameter of ~ 20nm; and (b) combined EDX / magnetic induction map showing the magnetization oriented along the long axis of the NiFe section at 20°C and during *in situ* heating to (c) 100, (d) 175°C and (e) 250 °C. The contour spacing is 0.042 rad (cosine of 150 times ϕm), and the field direction is indicated by arrows.

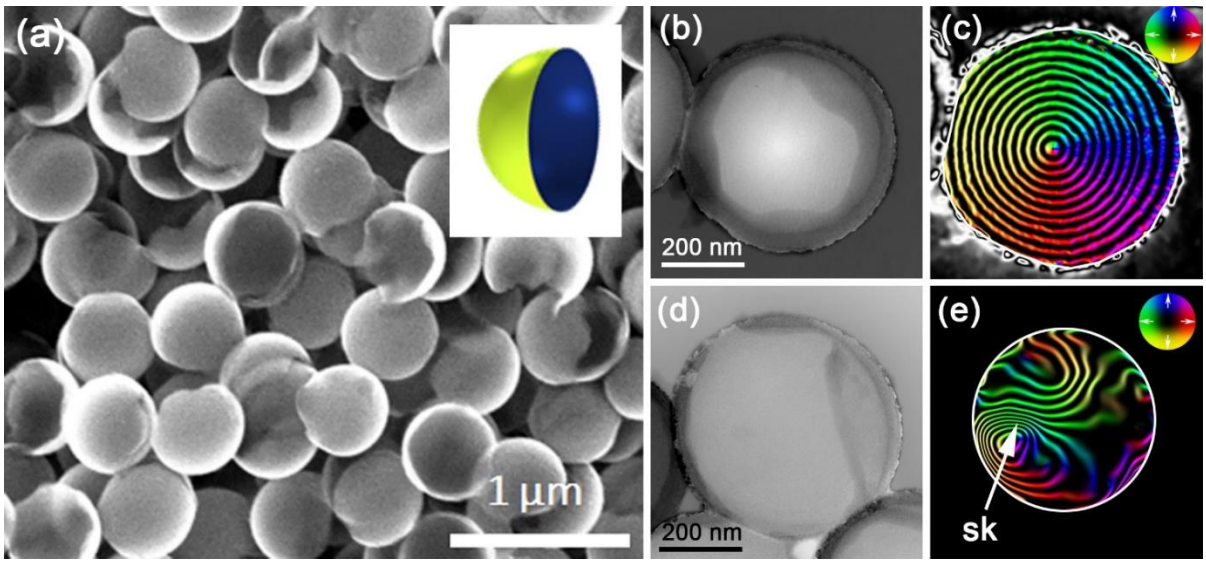


Fig. 3. (a) SEM image of nanocaps (d = 500 nm) produced by colloidal lithography and schematic of their idealized geometry (inset). (b) Electron holography phase image and (c) associated reconstructed magnetic induction map of a permalloy nanocap showing its vortex configuration. (d) Phase image and (e) associated reconstructed magnetic induction map of a multi-layered [Pt(1 nm)/Co(2 nm)/Pt(1nm)]×10 nanocap confirming the presence of a single Néel-type skyrmion (labelled 'sk'). The contour spacings are (c) 1.26 rad and (e) 0.157 rad, and the direction of magnetic induction is indicated by the color wheel (inset).

References:

1. Almeida, T. P. *et al.* Scientific Reports (2017) **7**, 17835. https://doi.org/10.1038/s41598-017-18194-0
2. Temple, R. C. *et al.* Applied Physics Letters (2021) **118**, 122403. https://doi.org/10.1063/5.0038950
3. Almeida, T. P. *et al.* Physical Review Materials (2020) **4(3)**, 034410. https://doi.org/10.1103/PhysRevMaterials.4.034410
4. Almeida, T. P. *et al.* Nano Letters (2022) **22**, 4000–4005. https://doi.org/10.1021/acs.nanolett.2c00597
5. Almeida, T. P. *et al.* APL Materials (2022) **10**, 061104 https://doi.org/10.1063/5.0096761
6. Jalil, W. B. F. *et al* Journal of Physics D: Applied Physics (2023) **56**, 385001. https://doi.org/10.1088/1361-6463/acdaa8

Type of presentation: Oral

MS5-O-1 The magnetic microstructure in FeCo alloys and its interaction with non-magnetic inclusions

Hannah Cole[a], James Loudon[a], Thomas Selby[b], Howard Stone[a] and Paul Midgley[a]

[a]Department of Materials Science and Metallurgy University of Cambridge 27 Charles Babbage Road, Cambridge, CB3 0FS, United Kingdom

[b]Department of Chemical Engineering and Biotechnology, University of Cambridge, Philippa Fawcett Dr, Cambridge CB3 0AS.United Kingdom

Contact email: hcc72@cam.ac.uk

Introduction:
FeCo alloys are considered essential for the manufacture of the high power density motors required for the electrification of civil aviation. In particular, equiatomic FeCo is a preferred candidate for the soft magnetic components as it offers a combination of high saturation magnetisation, low coercivity, high Curie temperatures, and good mechanical properties. Commercial FeCo alloys contain other elements including V and Nb [1] that are thought to help control the ordering reaction that occurs in these alloys. However these elements may also form oxides and carbides that can lead to the formation of (non-ferromagnetic) inclusions. Such inclusions may interact with the magnetic microstructure in these alloys, for example by acting as pinning sites for the domain walls resulting in an increase in coercivity. Here, we study how the magnetic microstructure interacts with these inclusions of various sizes, using a combination of Lorentz TEM imaging and corresponding GPU-accelerated Mumax3 simulations [2].

Methods:
Vacodur-49 alloy (49Co-49Fe-2V + Nb) samples were received in a cold-rolled state and annealed to optimise the magnetic properties. These samples were electropolished using a Struers Tenupol twin-jet electropolishing unit in order to produce electron-transparent regions. A FEI Tecnai F20 was operated in field-free mode, with the objective lens current set to zero, to image the magnetic structure around inclusions initially without any applied field. We used a form of phase contrast imaging (Fresnel imaging) in order to convert phase information (sensitive to the local B-field) to amplitude information. A 'through-focal' series of images (using positive and negative defocus) was acquired from regions of interest to enable the application of the Transport of Intensity Equation (TIE) analysis. This TIE analysis was based on python scripting, including the use of AntsPy [3] a state-of-the-art image registration package to carefully align the through focal series. An external field could be applied to the sample by slightly exciting the objective lens (c.a. 1% current/0.022T) and tilting the sample to enable the applied field (from the lens) to generate an in-plane component. In-situ videos were recorded using a Gatan Oneview camera to capture the dynamic interaction of domain walls with the inclusions. To support this, a Zeiss Gemini SEM was used to investigate the chemical nature of the inclusions using EDX. This was supplemented by GPU accelerated Mumax3 simulations [2], which allowed the simulation of the minimised energy state for a given geometry and material. Ubermag python package [4] was then used to calculate the Fresnel micrographs expected from the magnetisation in these minimised energy states.

Results:
Fresnel imaging has shown that in these materials there is the formation of Néel spikes around non-ferromagnetic inclusions. Néel's inclusion theory [5] proposes at the surface of non-ferromagnetic inclusions there will be free poles associated with magnetostatic energy (which will be particularly large in FeCo alloys due to high magnetisation saturation). To reduce the concentration of these poles they spread out along spikes whose length is limited by the domain wall energy cost. Many of the spike domains observed consist of two spikes instead of four [6] (the latter was the configuration originally suggested by Néel). Both the TEM (Fig.1a) and simulation data (Fig.1c) seem to indicate that the most stable spike structure for this sample geometry and material is 4-spike formation instead of the more typical 2-spike. The magnetic B-field maps around these inclusions have been determined using TIE analysis (Fig.1b) and this corresponds well with what is seen in the simulation data (Fig.1c) using a 'silhouette' of the inclusions (the in-focus shape) and a 40 nm sample thickness. The simulated Fresnel image (Fig.1d) corresponds strongly to what is seen in the experimental data (Fig.1a). The formation of

the spike domains around these inclusions firstly confirms that they are non-ferromagnetic and from EDX analysis it is known that these inclusions are rich in V and, compared to the bulk, rich also in Nb.

Another way these inclusions can interact is by forming subsidiary domains when larger inclusions intercept a domain wall (Fig.2a). Fig 2b and c then show the configuration after a magnetic field has been applied and the domain wall has been partially unpinned from the inclusions but still has two out of four spikes attached. Additionally, in the top of Fig 2b there is a small inclusion pinning the domain wall, but the wall is unpinned in Fig 2c; the time difference between the two frames is 0.02 seconds, giving an upper bound to the true de-pinning time.

Discussion and conclusions:

In conclusion the as-received commercial FeCo alloys contain inclusions present of various sizes, rich in V and to some extent Nb, present due to the addition of these elements in the manufacture process. These micro alloy elements are needed in these alloys to improve ductility and control the rate of the ordering reaction, however there are inclusions forming as a result which interact with the magnetic microstructure. One of the key ways this occurs is through the formation of 4-spike domains around these inclusions. Using Fresnel imaging and matching magnetic simulations, we find that the smallest inclusions appear to have minimal interaction with domain walls, medium sized inclusions can lead to spike domains being formed and / or weakly pin domain walls, and the presence of large sized inclusions can lead to subsidiary domains which interact strongly with the domain wall and pin it. The pinning of domain wall increases the coercivity of these soft magnetic alloys. It therefore suggests that in order to further decrease the coercivity of these alloys it would be important to control the size and distribution of these non-ferromagnetic inclusions. The structures that are seen in these data are all consistent with what is predicted by Néel's inclusion theory including the original 4-spike domain formation [5].

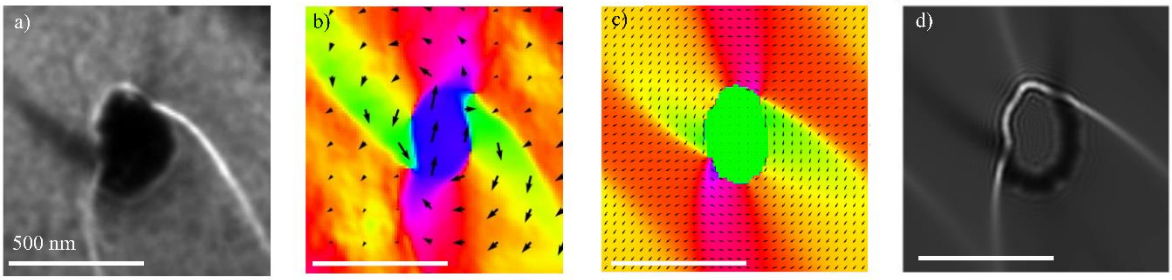


Figure 1 a) Fresnel image showing magnetic structure around non-magnetic inclusions. b) In-plane B-field direction determined by TIE analysis. c) Micromagnetic simulation of the central slice of the in-plane magnetisation around the inclusion. d) Simulation of a Fresnel image from the structure shown in c).

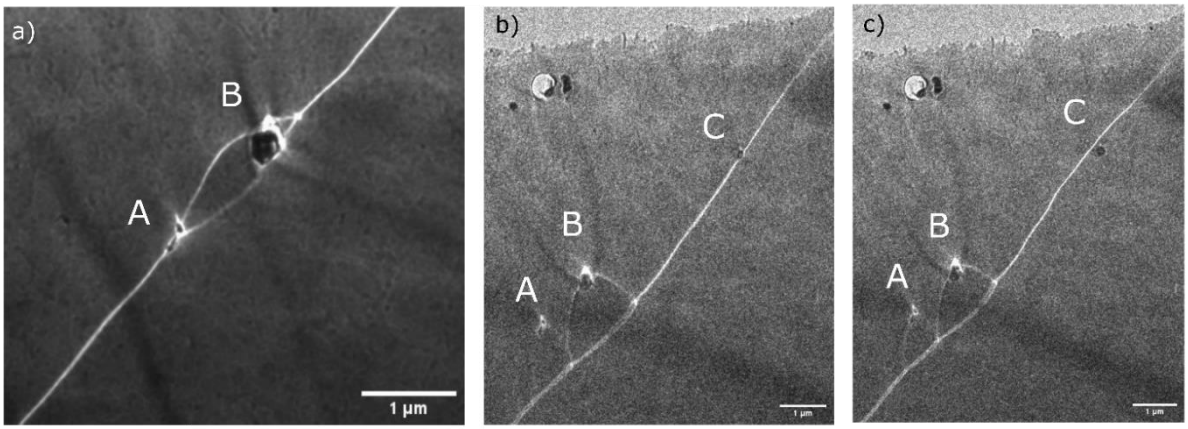


Figure 2 a) Fresnel image showing the pinning of a domain wall on inclusions 'A' and 'B' with subsidiary domains forming. b) A single frame extracted from a movie recorded with the sample under an applied magnetic field, showing the partial unpinning from the inclusions 'A' and 'B' shown in a) and the pinning by inclusion 'C'. c) A frame extracted 0.02 seconds later than b) showing the domain wall unpinning from inclusion 'C'.

References and Acknowledgments:

1. T. Sourmail, *Prog. Mater. Sci.* **2005**, *50:7*, 816-880.
2. A.Vanstennkiste et al, *AIP Adv*. **2014,** 4:10.

3. N. Tustison et al, *Sci. Rep.* **2021**, 11, 9098.
4. M. Beg et al, *IEEE Trans.* **2022,** *Magn.*, 58:2, 1-5.
5. L.Néel *Cah.. Phys.* **1944**, 25, 21-44.
6. H.J.Williams, *Phys. Rev.* **1947**, 71, 646.

Acknowledgement to Rolls-Royce PLC and the EPSRC ICase voucher number (220040) for the funding of this project. PAM thanks the EPSRC for funding under grant numbers EP/V007785/1 and EP/R008779/

Type of presentation: Oral

MS5-O-2 Investigating Local Structure in NBT-BT system Using (S)TEM Techniques

Beatriz Vargas[a], Pranjal Nandi[a], Sergi Plana-Ruiz[a,b], Lluís Yedra[a], Angélica M. Benitez-Castro[c,d], Juan Muñoz-Saldaña[d], Bernat Mundet[e], Sonia Estradé[a], Lluís López-Conesa[a,f], Francesca Peiró[a]

[a]*LENS, Department of Electronics and Biomedical Engineering and Institute of Nanoscience and Nanotechnology (IN2UB), University of Barcelona (UB) (Barcelona) Spain.*

[b]*Servei de Recursos Científics i Tècnics, Universitat Rovira i Virgili (Tarragona) Spain.*

[c]*Institute of Glass and Ceramics, Department of Materials Science and Engineering, Friedeich-Alexander-Universitä Erlangen-Nürnberg (Erlangen) Germany.*

[d]*Centro de Investigación y de Estudios Avanzados del IPN (Querétaro) Mexico.*

[e]*Catalan Institute of Nanoscience and Nanotechnology (ICN2), CSIC and BIST, Campus UAB, (Bellaterra) Spain.*

[f]*TEM MAT Laboratory - Scientific and Technological Centers of the University of Barcelona (CCiTUB) (Barcelona) Spain.*

Contact email: francesca.peiro@ub.edu

Introduction

Perovskite relaxor ferroelectric materials are very interesting for a variety of applications due to their extraordinary piezoelectric properties. However, understanding the complicated local order/disorder phenomena within these materials is crucial for optimizing their performance. Transmission Electron Microscopy (TEM) and Scanning Transmission Electron Microscopy (STEM) techniques were employed to study the local order/disorder phenomena in (1-x)$Na_{1/2}Bi_{1/2}TiO_3$-x$BaTiO_3$ (NBT-BT) compositions with varying $BaTiO_3$ concentration (x = 2.5, 7.5, and 15% mol).

Methods

The samples with mol fractions of 0.025, 0.075, and 0.15 were prepared using conventional synthesis methods for mixed oxides. High-purity powders of Bi_2O_3, Ti_2O, Na_2CO_3, $BaCO_3$ and K_2CO_3 were combined in stoichiometric ratios, then milled in a planetary mill at 250 RPM for 2 hours. After drying, the mixture was calcined three times at 920°C for 5 hours to ensure formation and purity of the perovskite-type phase. The resulting powder was ground again and passed through a 100 μm sieve. Afterwards, the powders were compacted uniaxially and isostatically at 180 Mpa pressure into discs, then sintered at 1080°C for 10 hours in a powder bed of the same composition to minimize element volatilization. Cross-sectional samples were prepared using the ThermoFischer Scios 2 DualBeam in the Scientific and Technical Resources Service of the Universitat Rovira i Virgili.

Our research was aimed at understanding the chemical composition, domain configurations, and structural evolution of these materials. The crystalline structure was analysed by selected area diffraction (SAED); local changes in lattice parameters were monitored using HAADF-STEM and the presence of polar nanodomains (PNRs) was assessed by iDPC imaging techniques. The samples were observed in a ThermoFisher SPECTRA (S)TEM 300 at 300 kV (ALBA synchrotron), in a JEOL 2010F TEM and in a JEOL 2100 TEM, both working at 200 kV (Scientific and Technological Centers of the Universitat de Barcelona).

Results

Our findings showed the presence of various phases within the samples. For lower x value, *R3c* symmetry coexisted with *Pm-3m*, but higher $BaTiO_3$ ratios resulted in a transition from *Pm-3m* to *P4bm* symmetry. For the sample with x = 0.15 mol, only *P4bm* symmetry was observed. Conversely, for x = 0.025 mol, *R3c* and *Pm-3m* symmetries were detected, and for x = 0.075 mol, all three symmetries were observed in distinct grains. The analysis of the lattice parameters through HAADF and iDPC images also showed the transition from a rhombohedral phase for x = 0.025, to cubic phase for x = 0.075, and

to the tetragonal phase for x = 0.15 mol. Polarization maps form iDPC technique will highlight the presence of PNRs. Electron Energy Loss Spectroscopy (EELS) also exhibited particular features in the spectra when increasing BaTiO3 ratio. Low-loss energy loss spectroscopy was also conducted to observe variations in the optical response.

Conclusions

This study explores the general panorama of domain configurations and structural complexities in these materials, as well as the spectroscopic properties observed, including the dielectric function and ELF, as the $BaTiO_3$ ratio is incrementally increased.

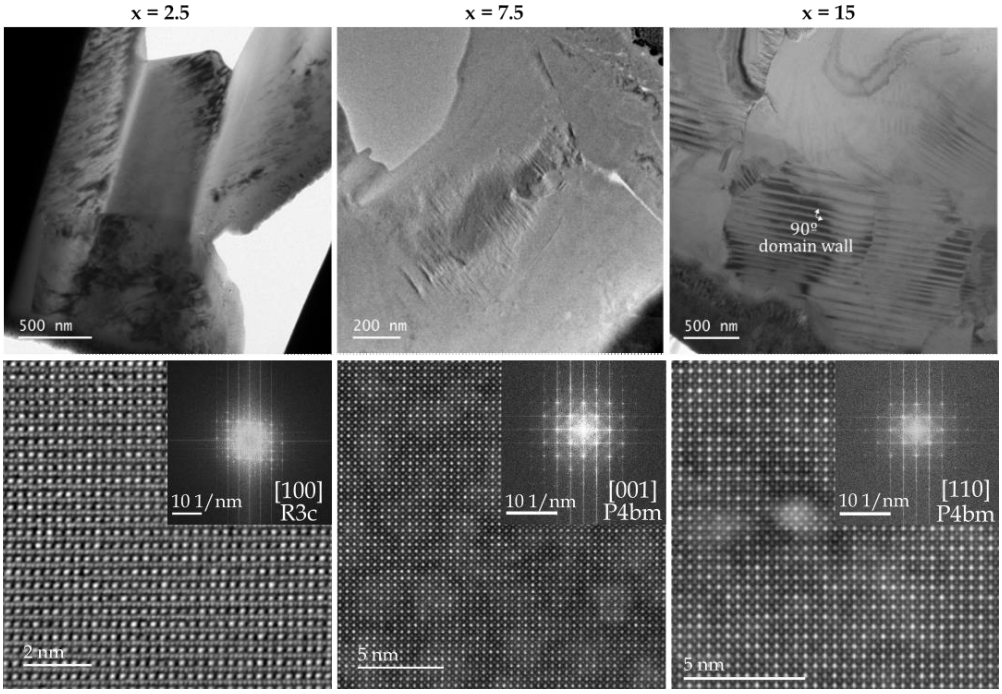


Figure 21: BF-TEM and high-resolution STEM images for all three sample.

References:

1. Physical Review Materials 6, 064409 (2022). DOI: 10.1103/PhysRevMaterials.6.064409.
2. Adv Struct Chem Imag 3, 9 (2017). DOI: 10.1186/s40679-017-0042-5.
3. (2021). PinkShnack/TEMUL: (Version 0.1.3). Zenodo. DOI: 10.5281/zenodo.4543963.
4. ACS Appl. Mater. Interfaces 14, 5525−5536 (2022). DOI: 10.1021/acsami.1c17383.

Type of presentation: Oral

MS5-O-3 3D Nano-Printing of Complex Metal Structures via Focused Electron Beam Induced Deposition

Sameh Okasha[a], Trevor P. Almeida[a]

[a]*School of Physics and Astronomy, University of Glasgow, Glasgow, G12 8QQ, United Kingdom*

Contact email: sameh.okasha@glasgow.ac.uk, trevor.almeida@glasgow.ac.uk

The transition from two-dimensional to three-dimensional nanostructures represents a transformative shift not only in nanomagnetism but across the broader landscape of nanotechnology. [1,2] Fields such as nanoelectronics [3], nanophotonics [4], and data storage stand to benefit from this evolution, driving the development of more efficient, multifunctional, and sustainable technologies. Recent advances in bottom-up lithography, high-resolution microscopy, and computational modeling have brought these innovations closer to reality. Focused electron beam-induced deposition (FEBID) has emerged as a versatile, direct-write nanofabrication technique, enabling precise control over material deposition at the nanoscale. When combined with other technologies[5–7], the unique magnetic behavior of nanomaterials, FEBID holds particular promise for next-generation magnetic memory devices like racetrack memory. Considerable efforts have therefore focused on refining fabrication methods and characterizing magnetic nanoelements composed of various metal deposits. For 3D nanoprinting, the high vapor pressure of precursors such as Pt and Co proves advantageous under electron-limited conditions, where enhanced precursor flux supports more efficient growth. However, Fe-based structures, essential for magnetic applications, pose a significant challenge due to the lower vapor pressure of their precursors. While increasing the precursor pressure has been explored as a potential workaround, it paradoxically impedes 3D nanoprinting performance. This highlights the need for novel strategies to enable high-fidelity Fe nanostructures, driving further innovation in material design and deposition processes. In our work, Fe-based nanostructures have been fabricated precisely using iron pentacarbonyl ($Fe(CO)_5$) as a precursor. These structures include nanowires, Bipod, 5-µm bridge, rings, tetrapods, spirals and flower-like nanostructures as shown in figure (1). The deposition parameters, including electron beam dwell time, beam current, and precursor flux, have been further refined, have been further refined, enabling the precise fabrication of complex geometries.

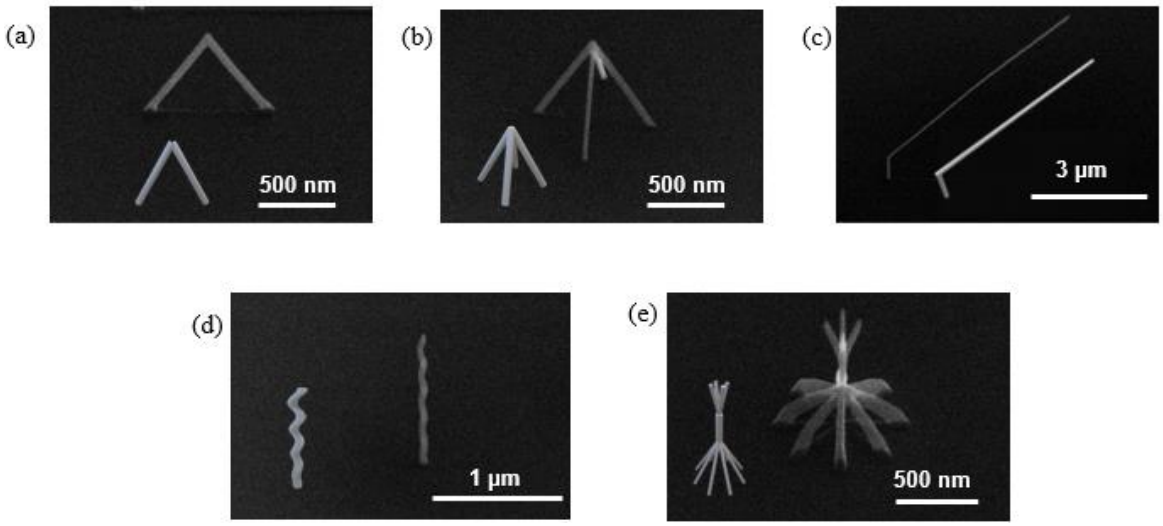


Figure 1. SEM images of various structures fabricated by FEBID using a 3D nanoprinting model and the approach of extended calibration method (a) Bipod, (b) tetrapod, (c) 5µm-bridge, (d) spiral, and (e) flower-like structure.

References:
1. Winkler R, Fowlkes JD, Rack PD, Plank H. 3D nanoprinting via focused electron beams. J Appl Phys 2019;125:210901. https://doi.org/10.1063/1.5092372/957930.
2. Reisecker V, Winkler R, Plank H. A Review on Direct-Write Nanoprinting of Functional 3D Structures with Focused Electron Beams. Adv Funct Mater 2024;34:2407567. https://doi.org/10.1002/ADFM.202407567.
3. Piasecki T, Kwoka K, Gacka E, Kunicki P, Gotszalk T. Electrical, thermal and noise properties of platinum-carbon free-standing nanowires designed as nanoscale resistive thermal devices. Nanotechnology 2023;35:115502. https://doi.org/10.1088/1361-6528/AD13C0.
4. Reisecker V, Kuhness D, Haberfehlner G, Brugger-Hatzl M, Winkler R, Weitzer A, Loibner D, Dienstleder M, Kothleitner G, Plank H. Spectral Tuning of Plasmonic Activity in 3D Nanostructures via High-Precision Nano-Printing. Adv Funct Mater 2024;34:2310110. https://doi.org/10.1002/ADFM.202310110.
5. Okasha S, Munson D, Yoshikawa J. N2/H2 Plasma-Enhanced Atomic Layer Deposition for SiO2 Gap Filling: Implications for Nanoelectronics in Semiconductor Manufacturing. ACS Appl Nano Mater 2025;8:5347–54. https://doi.org/10.1021/ACSANM.4C06844.
6. Okasha S, Almeida TP. Characterization of alane (AlH3) thin films grown by atomic layer deposition for hydrogen storage applications. Appl Surf Sci 2024;672:160840. https://doi.org/10.1016/J.APSUSC.2024.160840.
7. Okasha S, Sekine Y, Sasaki S, Harada Y. Atomic layer deposition of aluminum (111) thin film by dimethylethylaminealane precursor. Thin Solid Films 2021;732. https://doi.org/10.1016/J.TSF.2021.138784.

Type of presentation: Oral

MS5-O-4 Characterization of hierarchically structured nanocomposite catalyst based on Ru nanoparticles deposited on ceria supports with embedded magnetic nanoparticles

Nina Križaj Kosi[a,b], Darko Makovec[a,b]

[a]*Department for Materials Synthesis, Jožef Stefan Institute, Ljubljana, Slovenia*

[b]*Jožef Stefan International Postgraduate School, Ljubljana, Slovenia*

Contact email: nina.kosi@ijs.si

Introduction: Heterogeneous catalysis is widely used in a plethora of industrial applications. Noble metals (e.g., Ru, Pt, Pd, Ir) in the form of small nanoparticles are the most common catalysts. To prevent degradation due to aggregation and sintering, the catalytic nanoparticles are usually deposited on inert, refractory support with a high specific surface area (e.g., alumina (Al_2O_3), ceria (CeO_2), zirconia (ZrO_2), and carbon). Energy needed to drive catalytic reactions can be provided by magnetic heating enabled by incorporation of magnetic nanoparticles into the catalyst support. When exposed to a high-frequency magnetic field the magnetic nanoparticles selectively heat the catalyst. The so-called "magnetic" catalyst is therefore a composite material that consists of small catalytic nanoparticles (e.g., Ru, Co, Ni) deposited on a support with embedded magnetic nanoparticles. Properties of the catalyst (e.g., catalytic activity, heating ability) crucially depend on its nanostructure [1,2].

Methods In this work, Ru-ceria magnetic catalysts for potential use in valorisation of used biomass by magnetically-heated catalysis were characterized using transmission (TEM) and scanning transmission (STEM) electron microscopy. TEM Jeol JEM-2100 was operated at 200 kV. For atomic-resolution imaging and EDXS analysis C_S-probe-corrected STEMs, Jeol ARM 200FC, operated at 80 kV, and Thermo Fisher Scientific Spectra 300, operated at 200 kV, were used. The catalysts were synthesized by subsequent deposition of different nanomaterials onto the magnetic iron-oxide nanoparticles. First, the nanoparticles were coated with inner shell of nanostructured silica or alumina (γ-Al_2O_3) to increase the effective surface area of the catalyst support. Second, outer shell of monocrystalline ceria (CeO_2) was deposited onto the inner shell for the improved catalytic properties. Finally, small catalytic nanoparticles (Ru, CoNi) were deposited onto the surfaces of magnetic supports. Characterization of these hierarchically structured composite was quite challenging. In particular, it was difficult to image small (few nanometres) catalytic nanoparticles when deposited onto a heavy support, such as ceria. In addition, the nanoparticles were sensitive to the electron beam.

Results: The magnetic catalysts exhibited hierarchically structured globular composite nanoparticles approximately 50 nm in size, with globular maghemite (γ-Fe_2O_3) nanoparticles (~19 nm in size), coated with inner shell of thin (2-4 nm thick) silica layer. The silica -coated maghemite nanoparticles were covered with an outer shell of nanocrystalline ceria that was composed of globular crystallites, 3-5 nm in size (Figure 1 (c) and (d)). On the composite surfaces, Ru catalytic particles were homogeneously distributed as determined using EDXS mapping in STEM (Figure 1 (f)). Atomic-resolution STEM imaging that Ru particles were in form of small nanoparticles, 1-2 nm in size (Figure 1 (e)).

The results showed that the nanostructuring of individual materials can be influenced by changing the synthesis parameters and conditions. For example, instead of the relatively-smooth ceria shell composed of globular ceria nanocrystallites, the coarser shell can be deposited. In this case, the shell was composed of larger (~ 10 nm) nanocrystallites with the shape of truncated octahedra. To further increase an effective surface area of the magnetic catalyst, mesoporose silica or nanostructured alumina can be deposited onto the maghemite nanoparticles prior to the ceria deposition. The nanostructured inner shell strongly improves the roughness of surfaces, thus improving the surface area of the composite.

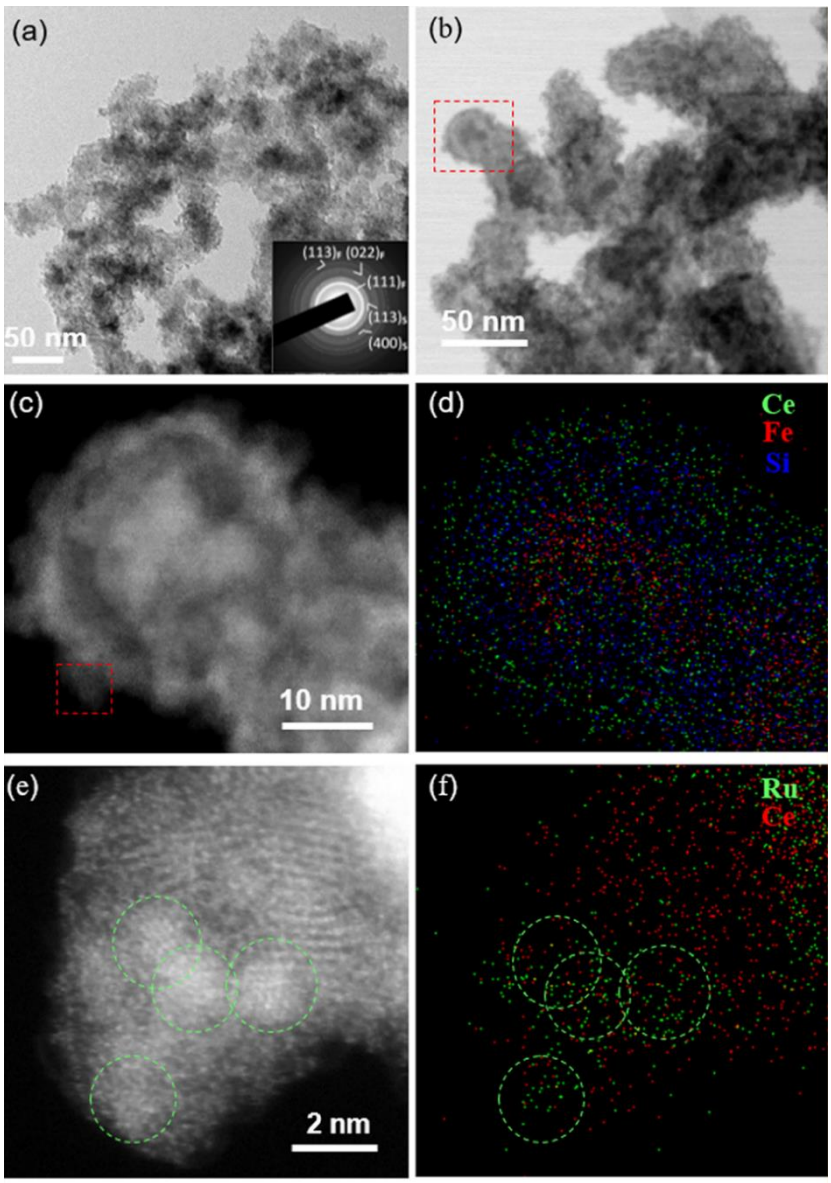


Figure 22: Hierarchically structured composite catalyst composed of silica-coated iron-oxide nanoparticles with shell of nanocrystalline ceria and with Ru nanoparticles deposited on the surfaces: (a) TEM image (inset shows a corresponding electron diffraction pattern indexed according to the fluorite (F) structure of ceria and spinel (S) structure of iron oxide). (b) BF STEM image, (c) HAADF STEM image of enlarged area marked with red square on Figure (b) with a corresponding EDXS elemental maps (d) showing distribution of Ce (green), Si (blue) and Fe (red). (e) HAADF STEM image of enlarged area marked with red square on Figure (c) with a corresponding EDXS elemental maps (f) for Ce (red) and Ru (green) shows small Ru nanoparticles deposited on the ceria.

Acknowledgements: The authors acknowledge the financial support from the Slovenian Research Agency (ARRS) for research core funding No. P2-0089.

References:

[1] M. Bowker, *Oxford University Press Inc.* **1998**.
[2] S. Gyergyek, M. Grilc, B. Likozar, D. Makovec, *Green Chem.* **2022**, 24, 2788–2794.

Type of presentation: Poster

MS5-P-1 Probing Magnons with High-Energy Electrons: Theoretical Insights into Spin and Charge Scattering in STEM-EELS

Julio do Nascimento[a], Fabrizio Cossu[b,d], Adam Kerrigan[b], Daniel Cheshire[a], Phil Hasnip[a], Stuart Cavill[a], Demie Kepaptsoglou[a,c], Quentin Ramasse[c,e], Vlado Lazarov[a,b]

[a]*University of York*

[b]*York Jeol Nanocentre*

[c]*SuperSTEM*

[d]*University of Aberdeen*

[e]*University of Leeds*

Contact email: julio.nascimento@york.ac.uk

The utilisation of magnons in device applications requires the characterisation of their properties with high resolution across both energy and spatial scales, for nanometre-sized samples. Techniques such as inelastic neutron scattering (INS), time-resolved Kerr microscopy and Brillouin light scattering provide high energy resolution but have limited spatial resolution.

In contrast, advancements in monocromation and detection of electron beams in scanning transmission electron microscopy (STEM) have opened the possibility of studying such quasi-particles at the nanometre scale. The signature of phonons in STEM-EELS has been demonstrated and is currently being investigated for magnons, despite their weaker interaction with electrons [1]. Theoretical predictions support this notion, suggesting potential STEM-EELS signals arising from thermal magnons [2,3].

Experimental applications of meV-resolution STEM-EELS for the direct probing of magnons have already been reported [4], alongside its utilisation in detecting magnon-phonon coupling [5]. This technique offers the ability to merge high spatial resolution with energy resolution comparable to INS, all while significantly reducing acquisition time. This capacity paves the way for the exploration of spin structures at surfaces and interfaces, as well as topological spin textures, at the nanometer scale.

We investigate the inelastic scattering of high-energy electrons interacting with a magnetic system, as observed in electron energy-loss spectroscopy (EELS). The developed methodology provides a numerical approach to simulate the interaction of the electron beam in a STEM EELS experiment, concentrating specifically on the local vector potential generated by a magnetic lattice. Besides the interaction between the electron's spin and the material's vector potential, dubbed spin-based interaction, reminiscent of neutron scattering experiments, we also explore the vector potential's effect on the electron's canonical momentum, i.e. the interaction due to the electron's charge. This interaction results in a strong scattering vector dependence (q^{-2}) and a near-square dependence on the electron probe's momentum. We also investigate the intensity dependence on the relative orientation between the probe wavevector and the local magnetic moments of the solid, which displays a pronounced dependence, indicating the potential for locally probing the orientation of these local magnetic moments. The insights gained from our calculations offer a valuable approach to enhancing the magnon signal in STEM-EELS experiments.

References

1. O.L. Krivanek, et al.; Nature, 2014, 514(7521), 209–212.
2. J.C. Loudon; Physical Review Letters, 2012, 109, 267204.
3. K. Lyon, et al.; Physical Review Letters, 2021, 104, 214418.
4. D. Kepaptsoglou, et al.; arXiv, 2024, arXiv:2410.02908.
5. A. Reifsnyder, et al.; Microscopy and Microanalysis, 2024, 30(Supplement_1).

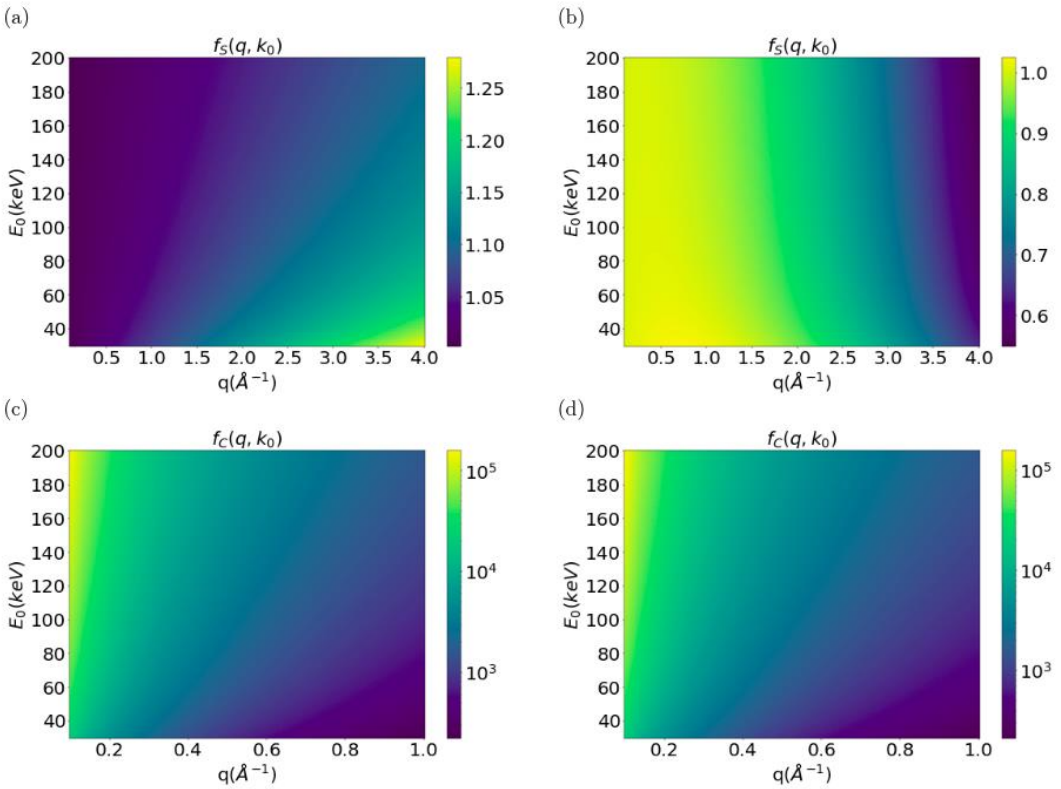


Fig. 1 Cross-section dependence with the scattering vector q and incoming electron beam energy E_0 is shown for (a) spin-based interaction, (b) spin-based interaction taking the magnetic form factor for Fe^{+3} into account, (c) charge-based interaction and (d) charge-based interaction taking the magnetic form factor for Fe^{+3} into account.

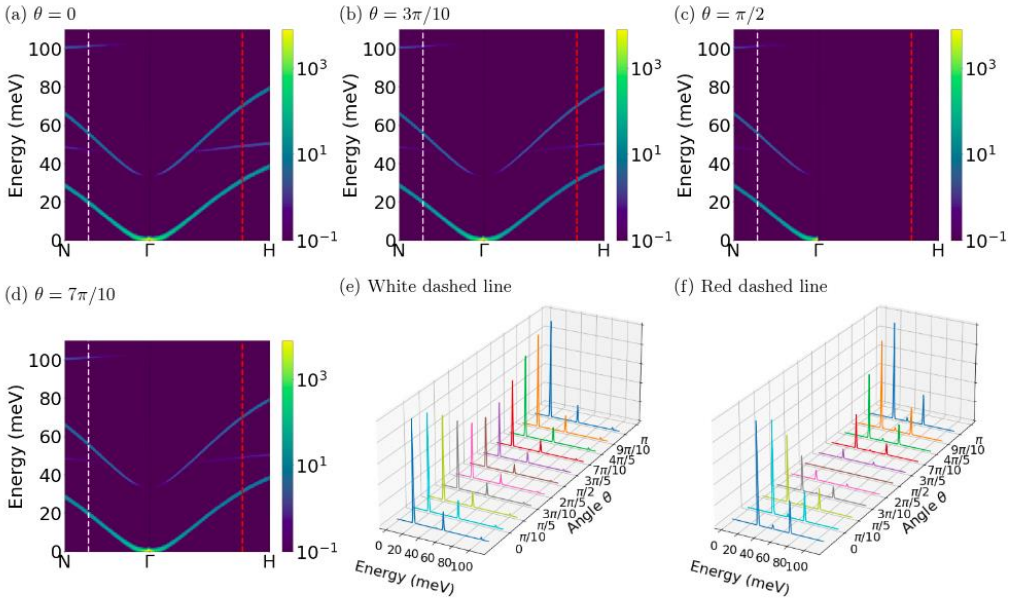


Fig. 2) Charge-related EELS in YIG, for varying relative angles θ between the probe's wave vector and the Nèel vector. e-f) Angle-dependent intensity for a particular point in momentum space, showing a strong angle dependence on the point represented by the red dashed line (f), but not on the point represented by the white dashed line (e).

Type of presentation: Poster

MS5-P-2 Are we observing channelling or magnetic contrast?

Petr Svora[a], Jan Maňák[a], Karel Jurek[a]

[a]*FZU-Institute of Physics of the Czech Academy of Sciences*

Contact email: svora@fzu.cz

Introduction: Channeling and magnetic contrast in scanning electron microscopy (SEM) are advanced imaging techniques that provide insights into the crystallographic and magnetic microstructures of materials. Electron channeling contrast arises from the interaction of energetic electrons with crystalline materials, enabling visualization of grain boundaries, orientation patterns, and microstructural features. Magnetic contrast, on the other hand, leverages the deflection and polarization of electrons by internal and external magnetic fields to reveal domain structures and magnetization vectors. Together, these methods offer powerful tools for non-destructive analysis of material properties, aiding research in fields such as materials science and condensed matter physics [1], [2].

A misinterpretation, where channeling contrast in SEM images was mistaken for magnetic contrast, prompted us to delve deeper into this field of study. In this work, we outline the errors that led to the incorrect interpretation of our results and demonstrate how such mistakes can be avoided by combining SE, BSE, and EBSD techniques effectively [3].

This refined approach is particularly valuable when studying NiMnGa alloys, which exhibit unique ferromagnetic shape memory properties. The channeling contrast provides insights into the crystallographic twin structures critical to their shape memory behaviour, while magnetic contrast uncovers the magnetic domain interactions driving their field-induced strain effects. Together, these SEM imaging techniques and alloy studies highlight how understanding and overcoming interpretational challenges can lead to improved methodologies and a deeper comprehension of advanced functional materials [4].

Acknowledgments: CzechNanoLab project LM2023051 funded by MEYS CR is gratefully acknowledged for the financial support of the measurements/sample fabrication at LNSM Research Infrastructure. Thanks to Dr. Ross H. Colman from the Faculty of Mathematics and Physics, Charles University, Prague, for providing the NiMnGa sample, which was vital for this work.

Reference

1. Goldstein, J. I., Newbury, D. E., Michael, J. R., Ritchie, N. W. M., Scott, J. H. J., & Joy, D. C. (2007). Scanning Electron Microscopy and X-Ray Microanalysis (4th ed.). Springer.
2. Reimer, L. (1998). Scanning Electron Microscopy: Physics of Image Formation and Microanalysis (2nd ed.). Springer.
3. Hulínský, V., Jurek, K. (1982). Zkoumání látek elektronovým paprskem (1st ed.). Státní nakladatelství technické literatury.
4. Heczko, O., Jurek, K., Ullakko, K. (2001). Magnetic properties and domain structure of magnetic shape memory Ni–Mn–Ga alloy. *Journal of Magnetism and Magnetic Materials*, vol. 226-230, p. 996-998.

Type of presentation: Poster

MS5-P-3 EBSD analysis of Sr-hexaferrite sintered in different atmospheres

Aleksander Učakar[a,b,c], Andraž Kocjan[b,c], Petra Jenuš Belec[b]

[a]*Jožef Stefan Institute, Center for Microscopy and Microanalysis, 1000 Ljubljana, Slovenia*

[b]*Jožef Stefan Institute, Department for Nanostructured Materials, 1000 Ljubljana, Slovenia*

[c]*Jožef Stefan International Postgraduate School, 1000 Ljubljana, Slovenia*

Contact emaill: aleksander.ucakar@ijs.si

Permanent magnets are a core component in modern devices and enabling technologies as they allow delivering, converting and storing energy [1]. By volume, Ba- and Sr-ferrites are one of the world's most-used permanent magnetic materials [2]. Although rare-earth magnets exhibit overwhelming superiority in performance, the harmful environmental impact of their production, the uneven distribution of raw materials and increasingly questionable supply chain force us to look for alternatives. One such solutions can be found in the group of hexagonal ferrites [3], which do not contain critical raw materials.

Aim of this study was to investigate the influence of the atmosphere during sintering on the microstructure of the material. To achieve this, Sr-hexaferrite samples were sintered in different atmospheres (air, Ar, N_2 and vacuum). The difference in partial pressure of oxygen in the immediate surroundings of the sample played an important role on the final microstructure. In samples that were not sintered in air, segregation of the material into Sr-rich and Sr-depleted phases occurred. Samples sintered in air atmosphere differentiated significantly from the peers sintered in vacuum and protective atmosphere, which underwent phase transformation. The composition and microstructure of sintered samples were comprehensively investigated using electron backscatter diffraction (EBSD) analysis.

Several different phases in the samples were observed and analysed with SEM-EBSD. A rough estimate of phase changes across the microstructure was observed. In samples sintered in vacuum as well as protective atmospheres the results indicate segregation of the material, into strontium-rich and strontium-depleted Sr-Fe oxide phases.

Reference

1. J. Cui et al., "Manufacturing Processes for Permanent Magnets: Part I—Sintering and Casting," *Jom*, vol. 74, no. 4, pp. 1279–1295, 2022, doi: 10.1007/s11837-022-05156-9.
2. Global market insights: Permanent magnet market size to exceed USD 50 Bn by 2024. (2019). Available at: https://www.gminsights.com/pressrelease/permanent-magnet-market. (Accessed: 9th January 2021)
3. Riba J-R, López-Torres C, Romeral L and Garcia A 2016 *Renewable Sustainable Energy Rev.* **57**, 367-379

Acknowledgements: Slovenian Research Agency is acknowledged for funding the research programs (P2-0405, P2-0087-2) and Infrastructure Center for Electronic Microscopy and Microanalysis, Jožef Stefan Institute, Ljubljana, Slovenia (PR-05722).

Type of presentation: Poster

MS5-P-4 Synthesis Strategies for Effective Doping of Barlowite

Polona Umek[a], Tina Arh[a,b], Matej Pregelj[a,b], Matjaž Gomilšek[a,b], Zvonko Jagličić[c,d], Andrej Zorko[a,b]

[a]*Jožef Stefan Institute, Ljubljana, Slovenia*

[b]*Faculty of Mathematics and Physics, University of Ljubljana, Ljubljana, Slovenia*

[c]*Faculty of Civil and Geodetic Engineering, University of Ljubljana, Ljubljana, Slovenia*

[d]*Institute of Mathematics, Physics and Mechanics, Ljubljana, Slovenia*

Contact email: Polona.Umek@ijs.si

Quantum spin liquid (QSL) materials have an exotic magnetic ground state characterised by the spins evading conventional magnetic long-range order down to T= 0 K and possessing long-range quantum entanglement [1,2]. One of the best experimental realizations of QSLs is the metal oxyhalide mineral herbertsmithite, $Cu_3Zn(OH)_6Cl_2$ [3,4]. The mineral barlowite, $Cu_4(OH)_6FBr$, is another rare example of a material with undistorted S=1/2 kagomé lattice (Figure 1). However, it also contains Cu^{2+} ions on its interlayer site, presumably causing it to order magnetically at 15 K [5]. Barlowite, therefore, is not a QSL material, however, DFT calculations show that substituting the interlayer site with nonmagnetic Zn^{2+} or Mg^{2+} should suppress the long-range magnetic order and lead to a QSL state [6].

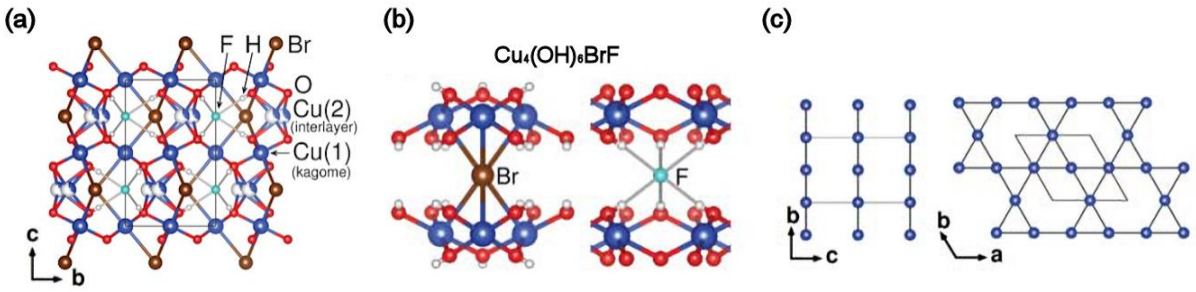


Figure 1: Crystal structure of barlowite – $Cu_4(OH)_6FBr$ (*P* 63*/mmc* space group). Note that the Cu(2) site with Wyckoff position 12*j* is 1⁄3 filled (a). Bromide and fluoride environments of barlowite (b) and the preference of Br for covalent bonding and of F for hydrogen bonding lead to perfect alignment of kagome layers in $Cu_4(OH)_6FBr$ (only Cu(1) sites are shown here) (c)

Therefore, a promising route to the discovery of new QSL candidates is the synthesis of compounds structurally similar to herbertsmithite. In this work, we have explored various synthesis approaches to doping barlowite with Zn^{2+}, Mg^{2+}, Cd^{2+} and Hg^{2+}. The aim was to replace Cu^{2+} on the interlayer site ($Cu_3A(OH)_6FBr$, A = Zn^{2+}, Mg^{2+}, Cd^{2+} and Hg^{2+}). In a typical reaction, a copper precursor was basic copper carbonate ($Cu(OH)_2$ $CuCO_3$), while a source of dopant ions was a suitable bromide and/or fluoride salts, which were also sources of fluoride and bromide ions. The synthesis was carried out under hydrothermal conditions between 120 and 180 °C.

The morphology and chemical composition of the synthesized barlowite samples, particularly the molar ratio of Cu^{2+} to A^{2+}, were determined using a field-emission scanning electron microscope (SEM) equipped with an energy-dispersive X-ray (EDX) elemental analysis system. SEM images show that Zn- and Mg-doped barlowite crystallizes into micro-crystals with hexagonal symmetry, as shown in Figure 2. Our findings show that the presence of dopant ions influenced both the particle size and particle shape (Figure 2). Incorporating Zn^{2+} and Mg^{2+} into the crystalline framework was successful; however, increasing the reaction temperature and slowly cooling the reaction mixture to room temperature

improved the amounts of incorporated ions. On the other hand, Cd^{2+} and Hg^{2+} did not replace Cu^{2+} in its interlayer positions.

The crystal structure and phase purity of the barlowite samples were determined via powder X-ray diffraction. Our structural refinement by XRD reveals P63/mmc symmetry of the unit cell and is in line with previous reports [7, 8] and shows the presence of two minor impurity phases, unreacted basic copper carbonate and, in the case of Zn-doped barlowite zinc hydroxy fluoride (Zn(OH)F).

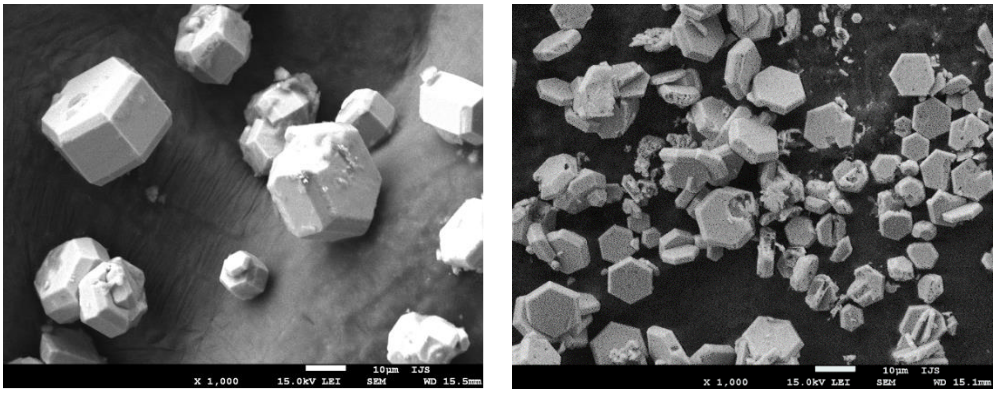


Figure 2: SEM images of Mg^{2+} (left) and Zn^{2+} -doped (right) barlowite samples synthesised at 140 °C. Both images were captured at the same magnification.

Reference:

1. P. W. Anderson, *Science* **1987**, 235, 1196.
2. A. Kitaev and J. Preskill, *Phys. Rev. Lett.* **2006**, 96, 110404.
3. M. P. Shores, E. A. Nytko, B. M. Bartlett and D. G. Nocera, *J. Am. Chem. Soc.* **2005**, 127, 13462.
4. T.-H. Han, J. S. Helton, S. Chu, D. G. Nocera, J. A. Rodrigues-Rivera, C. Broholm, and Y. S. Lee, *Nature* **2012**, 492, 406.
5. H. O. Jeschke, F. Salvat-Pujol, and R. Valenti, Phys. Rev. B **2015**, 92, 094417.
6. Z. Feng, Z. Li, X. Meng, W. Yi, Y. Wei, J. Zhang, Y.-C. Wang, W. Jiang, Z. Liu, S. Li, F. Liu, J. Luo, S. Li, G.-Q. Zheng, Z. Y. Meng, J.-W. Mei, and Y. Shi, *Chin. Phys. Let.* **2017**, 34.
7. R. W. Smaha, W. He, J. M. Jiang, J. Wen, Y.-F. Jiang, J. P. Sheckelton, C. J. Titus, S. G. Wang, Y.-S. Chen, S. J. Teat, A. A. Aczel, Y. Zhao, G. Xu, J. W. Lynn, H.- C. Jiang, and Y. S. Lee, *npj Quantum Mater.* 2020, **5**, 1.

Type of presentation: Poster

MS5-P-5 Electron magnetic circular dichroism with atomic plane resolution

Qi Wang[a,b,c], Xiaoyan Zhong[a,b,c]

[a]*TRACE EM Unit and Department of Materials Science and Engineering, City University of Hong Kong,*

Kowloon, Hong Kong SAR, People's Republic of China.

[b]*City University of Hong Kong Matter Science Research Institute (Futian, Shenzhen), 518048, Shenzhen,*

People's Republic of China.

[c]*Nanomanufacturing Laboratory (NML), City University of Hong Kong Shenzhen Research Institute, 518048, Shenzhen, People's Republic of China.*

Contact email: qwang422@cityu.edu.hk

Understanding the local spin configuration of magnetic materials at the atomic level is crucial for controlling their physical properties. However, experimentally characterizing these magnetic properties with atomic-scale spatial resolution is a significant challenge. Electron Magnetic Circular Dichroism (EMCD)[1], also known as electron energy-loss magnetic chiral dichroism, offers a promising solution. Similar to X-ray Magnetic Circular Dichroism (XMCD), EMCD leverages the transfer of angular momentum during inelastic electron scattering to selectively excite atomic magnetic sublevels. The use of structured electron beams, which possess orbital angular momentum, and the ease of focusing electron beams enable probing magnetism at the atomic scale, surpassing the spatial resolution of XMCD.

Previous work has demonstrated a strong EMCD signal in transition metal oxides, allowing for site-specific identification of Fe atom spin states using standing wave methods. [2] EMCD, in principle, provides higher spatial resolution and greater depth sensitivity due to the short de Broglie wavelength and deep penetration of high-energy electrons. Recent advancements using EMCD in conjunction with achromatic electron microscopy have achieved magnetic circular dichroism measurements with atomic plane resolution. This technique, when combined with aberration-corrected transmission electron microscopy, allows for the simultaneous acquisition of magnetic polarization, atomic configurations, and chemical states from the exact same sample region. This abstract will showcase examples in complex oxides like Sr_2FeMoO_6, [3] nanocomposite $Sr_2Fe_{1+x}Re_{1-x}O_6$, and at the antiphase boundary of $NiFe_2O_4$, demonstrating how atomic-scale magnetic, chemical, and structural information can be obtained.[4]

Reference

1. Schattschneider, P., Rubino, S., Hébert, C. et al, Detection of magnetic circular dichroism using a transmission electron microscope, Nature 441, 486–488 (2006).
2. Wang, Z., Zhong, X., Yu, R. et al, Quantitative experimental determination of site-specific magnetic structures by transmitted electrons, Nat Commun 4, 1395 (2013).
3. Wang, Z., Tavabi, A.H., Jin, L. et al, Atomic scale imaging of magnetic circular dichroism by achromatic electron microscopy, Nature Mater 17, 221–225 (2018).
4. This work was financially supported by NSFC (52171014), GuangDong Basic and Applied Basic Research Foundation (2024A1515012303), Sino-German Center for Research Promotion (M-0265), RGC (C1013-23EF, C1018-22E, CityU 11309822), European Research Council (856538, “3D MAGiC”), and CityU (9610484, 9680291, 9678288, 9610607).

MS6 Thin films, heterostructures, coatings, surfaces and interface

Type of presentation: Invited

MS6-IN-1 Automated analysis of STEM data of semiconductor heterostructures for quantum computing

Marc Botifoll[a], Ivan Pinto-Huguet[a], Enzo Rotunno[b], Thomas Galvani[a], Catalina Coll[a], Yann-Michel Niquet[c], Sara Martí-Sánchez[a], Georgios Katsaros[d], Giordano Scappucci[e], Peter Krogstrup[f], Giovanni Isella[g], Maria Chiara Spadaro[a], Stephan Roche[a,h], Pablo Ordejón[a], Vincenzo Grillo[b], Jordi Arbiol[a,h]

[a]*ICN2, CSIC and BIST, Barcelona, Spain*

[b]*CNR-IMEM, Parma, Italy*

[c]*Univ. Grenoble Alpes, CEA, IRIG-MEM-L Sim, Grenoble, France*

[d]*Institute of Science and Technology Austria, Klosterneuburg, Austria*

[e]*QuTech and Kavli Institute of Nanoscience, Delft TU, Delft, The Netherlands*

[f]*10NNF Quantum Computing Programme, NBI, University of Copenhagen, Denmark*

[g]*Politecnico di Milano, Como, Italy*

[h]*ICREA, Barcelona, Catalonia, Spain*

Contact email: marc.botifoll@icn2.cat

Background and aims

The process of discovering and refining new materials, as well as enhancing existing ones for a variety of uses, including quantum applications, is a complex and multifaceted endeavour. This involves identifying needs, reviewing existing literature, proposing materials, engineering devices, characterizing materials, and testing applications. However, the process can be hindered by its time-intensive and costly nature, especially when precision at the atomic level is necessary to comprehend the functionality of materials and heterostructured devices.

In this digital age and with quantum supremacy in the horizon, semiconductor heterostructures within a chip have become indispensable and ubiquitous, propelling significant industrial value chains. They facilitate progress in both emerging sectors like quantum applications and established ones. For that, the trend of miniaturization, which is now reaching nanoscale dimensions and nearing the atomic limit, is a key driver of progress which demands special characterisation needs. [1,2] To answer to these needs, in this work, we present a revolutionary analytical framework aimed at the comprehensive characterization of device heterostructures, with a particular focus on quantum devices and their materials.

Methods

The characterisation that must answer these demands is high-resolution Transmission Electron Microscopy (TEM), as the most optimal way to access structural information at the atomic level. We propose a workflow capable of processing both parallel illumination TEM and Scanning TEM (STEM) data, although it is specially designed for the latter. In addition, it can extract compositional information from Electron Energy Loss Spectroscopy (EELS), which is used to make the characterisation an exhaustive and complete process. Importantly, the workflow we suggest, combines traditional algorithmics, with unsupervised and supervised machine learning algorithms. This way, we ensure that model-based computing and artificial intelligence work hand by hand to provide the comprehensive and material-independent solution we seek for. [3]

Results

Our pioneering workflow autonomously determines material composition, crystallographic phase, and spatial orientation across various regions of analysed (S)TEM-based images or image datasets through detailed model comparison. It is completed with automated strain analysis, enabling a comprehensive characterization of the device's structural properties. Eventually, we incorporate the extracted knowledge to automate the creation of models that facilitate simulations and provide vital physical and chemical insights necessary for understanding the device's performance in practical applications. [3]

Conclusions

Although the method is highly versatile, we focus on quantum computing devices to autonomously optimize their functional properties. In particular, we prove it with SiGe quantum well heterostructures that proved outstanding quantum performance for spin qubits generation. [1,2] However, the main advantage placing our workflow beyond state of the art is its generalisation capabilities. It works for any material configuration and not only does it answer the pressing automation need, but unlocks getting physical models and simulations of complex devices with unprecedented accuracy. [3]

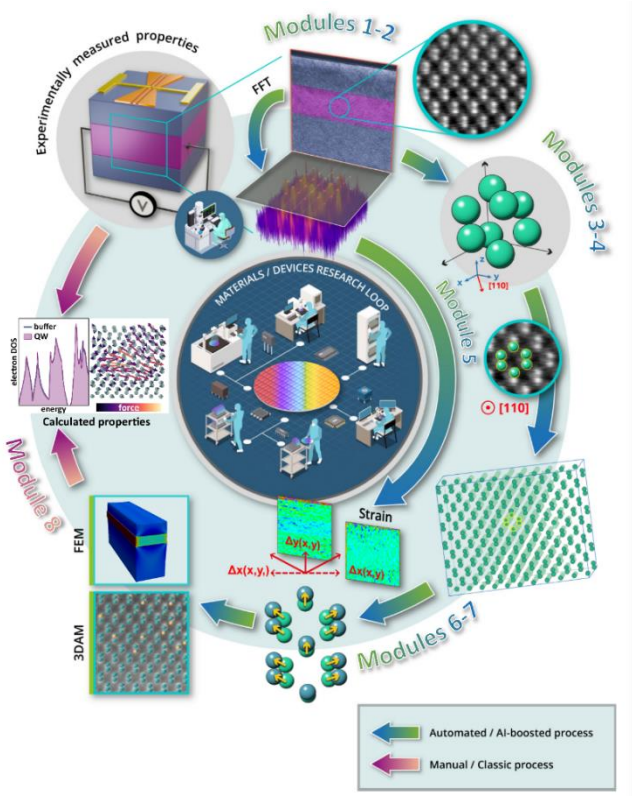


Figure 1: Automated workflow pipeline for the autonomous unveiling of physical knowledge.

References

1. Jirovec, D. et al. Nature Materials, (2021) doi.org/10.1038/s41563-021-01022-2
2. Paquelet, B. et al Nat. Commun. 14, 1385 (2023)
3. Botifoll, M. et al, (2024) Submitted, https://doi.org/10.48550/arXiv.2411.01024

Type of presentation: Invited

MS6-IN-2 Advanced low dose electron microscopy of metal halide perovskites

Nadine J. Schrenker[a], Irina Skvortsova[a], Tom Braeckevelt[b], Annick De Backer[a], Nikolaos Livakas[c], Stefano Toso[c], Bapi Pradhan[d], Johan Hofkens[d], Maarten Roeffaers[e], Veronique Van Speybroeck[b], Liberato Manna[c], Johan Verbeeck[a], Sandra Van Aert[a], Sara Bals[a]

[a]*Electron Microscopy for Materials Science (EMAT) and NANOlab Center of Excellence, University of Antwerp, Antwerp, Belgiumn,*

[b]*Center for Molecular Modeling (CMM), Ghent University,Ghent , Belgium*

[c]*Department of Nanochemistry, Istituto Italiano di Tecnologia (IIT), Genova, Italy*

[d]*Department of Chemistry, KU Leuven, 3001 Leuven, Belgium*

[e]*cMACS, Department of Microbial and Molecular Systems, KU Leuven, Leuven, Belgium*

Contact email: nadine.schrenker@uantwerpen.be

Metal halide perovskites (MHP) are promising semiconductors for the next generation of optoelectronic devices. Due to their tunable bandgap, they fulfil the requirement for various applications, including solar cells, light-emitting diodes, lasers and photodetectors. Unfortunately, MHPs still lack of long-term stability which hampers their commercial application. Degradation occurs due to their instability under environmental triggers, such as moisture and oxygen. Thus, the combination of *in situ* and ex situ TEM techniques can provide valuable insights about the underlying degradation mechanisms to extend the working lifetime of perovskites. Another challenge for TEM investigations of MHPs is their high electron beam sensitivity. Therefore, we develop low-dose protocols using 4D STEM. Hence, we are able to investigate the MHP without degradation due to Pb-cluster formation or amorphization and quantitatively interpret the STEM images using statistical parameter estimation theory.

Via low-dose 4D STEM measurements we investigated $FAPbBr_3$ nanocrystals (NCs), which are of great interest for green light-emitting diodes. To retrieve phase contrast imaging from 4D STEM datasets, we utilize the capacity of machine learning (see Figure 1). In the phase contrast reconstructions, the different atomic columns in the perovskite structure could be detected, and it was also possible to clearly distinguish the light FA cations and the Br atomic columns from the image intensity. Furthermore, we quantified the observed elongation of the projections of the Br atomic columns, suggesting an alternation in the position of the Br atoms perpendicular to the Pb−Br−Pb bonds. Together with molecular dynamics simulations, these results remarkably reveal local distortions in an on-average cubic structure [1,2].

Additionally, we investigated $CsPbI_3$, whose photoactive phases spontaneously convert into a non-photoactive yellow orthorhombic δ-phase under ambient conditions. This transformation results in a significant increase in bandgap and a loss of photoactive functionality. We studied the impact of Zn^{2+} and Cd^{2+} dopants on the phase stability of $CsPbI_3$ NCs, emphasizing the formation of Ruddlesden–Popper (RP) planar defects. Via TEM we followed the temporal evolution of the phase transformation, where black-phase NCs agglomerate and form elongated microtubes with a yellow-phase crystal structure. Our observations demonstrate that doped samples are significantly more stable, while the dopants are key factors in the formation of the RP-like defects with specific atomic arrangements [3].

For heterostructures, consisting of perovskite nano cubes and a chalcohalide, we applied the described low-dose STEM techniques to study the interface nature. Interestingly, the cationic subnetwork of Pb and Cs is maintained through the interface, which results in an epitaxial relationship. We also found that the perovskite can be used as disposable epitaxial template for the phase-selective synthesis of lead sulfochloride nanocrystals [4]. Additionally, we explored novel $CsPbX_3$/chalcohalide heterostructures, investigating a direct $Cl^- \rightarrow I^-$ halide exchange process that induces a striking transformation in optical properties. These discoveries highlight the unique adaptability of these heterostructures, offering new design of tunable halide-exchanged materials with novel optoelectronic properties.

Acknowledgement:
The authors acknowledge financial support from the Research Foundation-Flanders (FWO) through a postdoctoral fellowship to N.J.S. (FWO Grants 1238622N and 12AAO25N).

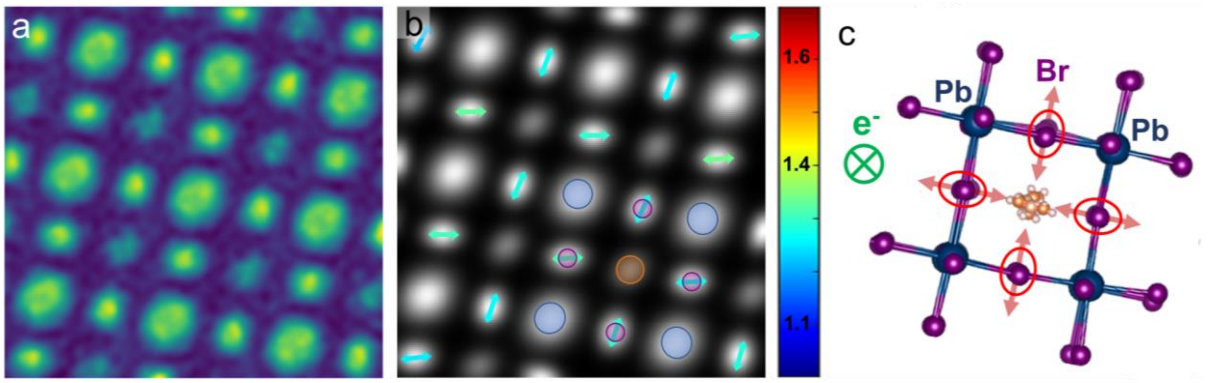


Figure 1: Octahedral network in $FAPbBr_3$ NCs [1]. (a) Phase contrast reconstruction from 4D STEM of a $FAPbBr_3$ NC. (b) The obtained model after fitting elliptical Gaussian peaks to the atomic columns in the phase contrast reconstruction of (a). The color bar represents the ellipticity ratio of the projections of the Br atomic columns. The overlay indicates the different atomic columns (Br = purple, Pb–Br = blue, FA = orange). (c) Schematic illustration of a $FAPbBr_3$ structure, where the Br anions contain a small displacement perpendicular to the Pb–Br–Pb bond, as indicated by the red arrows. The red ellipses show the exemplary position of the Br atomic columns that are analysed in (b).

References:

1. N.J. Schrenker et al., *Nano Lett.* **2024**, 24, 10936−10942
2. T. Friedrich et al., *Microscopy and Microanalysis*, **2023**, 29, 395–407
3. I. Skvortsova et al., *ACS Nano*, **2025**, 19, 17698−17708
4. S. Toso et al., *Nature Communication*, ***2022***, 13, 3976

Type of presentation: Oral

MS6-O-1 Indium segregation at stacking faults in zincblende InGaN epilayers

Petr Vacek[a], Martin Frentrup[a], Menno J. Kappers[a], David J. Wallis[a,b], Rachel A. Oliver[a]

[a]*Dept. of Materials Science and Metallurgy, University of Cambridge, Cambridge, United Kingdom*

[b]*Centre for High Frequency Engineering, Cardiff, United Kingdom*

Contact email: pv305@cam.ac.uk

GaN in the hexagonal wurtzite (wz) phase is a widely used material for electronic and optoelectronic applications. Unfortunately, strong spontaneous polarization and piezoelectric fields across the active region of wz InGaN-based green LEDs lead to a significant efficiency drop, known as the green gap problem. In contrast, (001) InGaN in the cubic zincblende (zb) phase does not exhibit these effects, which, together with its smaller bandgap compared to its wz counterpart, makes zb InGaN a promising material for optoelectronic devices emitting in green part of a visible spectrum.

However, zb InGaN and GaN epilayers are metastable and hence often exhibit a high density of {111} stacking faults (SFs) and unwanted wurtzite inclusions as the predominant crystal defects. These defects leads to significant inhomogeneities in the alloy distribution as Indium (In) tends to segregate in the vicinity of defects [1]. This inhomogeneity significantly impacts the optical and structural properties of the layer.

In order to understand the effects leading to the In segregation in zb InGaN epitaxial layers, we have performed a detailed scanning transmission electron microscopy (STEM) study. The investigated samples were grown by metalorganic vapour-phase epitaxy on 3C-SiC/Si templates and consisted of a 600nm-thick zb GaN buffer layer and an approximately 40 nm-thick InGaN layer. The templates had a 4° miscut, which suppressed the formation of antiphase domains. To investigate the influence of the crystallographic in-plane orientation of the In segregation at SFs, two different sets of TEM specimen were prepared, one with the zone axis (ZA) parallel to the miscut and one with the ZA perpendicular to the miscut. A previous microscopy study showed that the {111} planes visible along those zones axes have Ga- and N-polarity, respectively [2].

Indium segregation near SFs was previously reported for InGaN quantum wells in the ZA perpendicular to the miscut [1]. We observe a similar behaviour in 40 nm-thick InGaN epilayers, which show a clear segregation of In adjacent to, rather than directly on, SFs and wz inclusions. However, the In segregation behaves differently for the orientation where the ZA is parallel to the miscut. There, In tends to segregate directly on the stacking faults and wurtzite inclusions. This behaviour was observed using high-resolution STEM imaging and further confirmed by energy-dispersive x-ray spectroscopy (EDX) mapping, which can be seen in Figure 1.

We suggest that the difference in the In segregation near SFs for the two in-plane orientations is due to a different Ga- or N-polar bonding configuration at the surface step terminating a {111} SF during the epilayer growth. Alternatively, the presence of small {111}-like facets on the growth surface may affect the In incorporation for the orientation perpendicular to the miscut, while these facets may not be present for the orientation parallel to the miscut. Additionally, miscut causes a small tilt of the major crystal axes, which introduce a different strain state in the zone perpendicular to the miscut. This strain field can then affect In distribution near stacking faults. Understanding of In segregation mechanism in zb InGaN epilayers is an important step towards optoelectronic devices emitting in green part of a visible spectrum.

We acknowledge financial support from EPSRC project – Segregation of alloy and dopant atoms at defects in nitride materials (EP/Y00423X/1).

Reference

1. B. Ding, M. Frentrup, S.M. Fairclough, M.J. Kappers, M. Jain, A. Kovács, D.J. Wallis, R.A. Oliver, Alloy segregation at stacking faults in zincblende GaN heterostructures, *J. Appl. Phys.* **128** (2020) 145703. https://doi.org/10.1063/5.0015157.

2. H. Xiu, S.M. Fairclough, A. Gundimeda, M.J. Kappers, D.J. Wallis, R.A. Oliver, M. Frentrup, Polarity determination of crystal defects in zincblende GaN by aberration-corrected electron microscopy, *J. Appl. Phys.* **133** (2023) 105302. https://doi.org/10.1063/5.0138478.

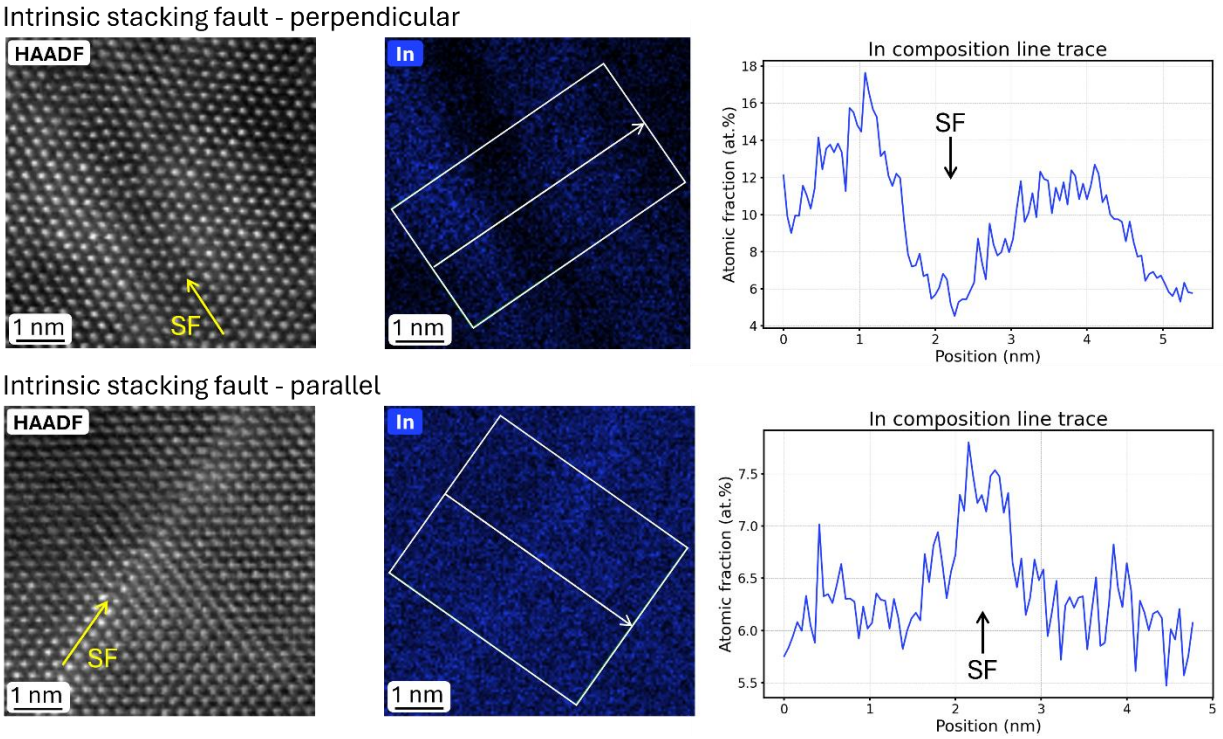


Figure 1: High-angle annular dark field (HAADF) images (left), In intensity signal images (middle), and In composition line trace integrated from an area indicated in the In Intensity image (right) of an intrinsic stacking fault perpendicular (top) and parallel (bottom) to the miscut. In the zone perpendicular to the miscut In segregates away from the {111} N-polar stacking fault position. However, in the zone parallel to the miscut the In segregates onto the {111} Ga-polar stacking fault.

Type of presentation: Oral

MS6-O-2 Mechanical properties enhancement in ceramics through vacancy-mediated unit cell disturbance

Zhuo Chen[a], Yong Huang[a], Zaoli Zhang[a]

[a]*Erich Schmid Institute of Materials Science, Austrian Academy of Sciences, 8700 Leoben, Austria*

Contact email: zhuo.chen@oeaw.ac.at

Introduction

Tailoring vacancies is a feasible way to improve the mechanical properties of ceramics. However, high concentrations of vacancies usually compromise the strength (or hardness). In this work[1], We show that a high elasticity and flexural strength could be achieved simultaneously using a nitride superlattice architecture with disordered anion vacancies up to 50%. Enhanced mechanical properties primarily result from a distinctive deformation mechanism in superlattice ceramics, i.e., unit-cell disturbances. Such a disturbance substantially relieves local high-stress concentration, thus enhancing deformability. No dislocation activity involved also rationalizes its high strength. The work renders a unique understanding of the deformation and strengthening/toughening mechanism in nitride ceramics.

Experimental Methods

All superlattice and monolithic TiN were synthesized via unbalanced DC reactive using an AJA International Orion 5 magnetron sputtering deposition system. The bending strain/stress of WN_x/TiN thin films was unveiled by performing single cantilever bending experiments of freestanding coating material. A 200 kV field emission TEM (JEOL 2100F) equipped with an image-side C_S-corrector was used in the high-resolution TEM (HRTEM) study, which demonstrates a resolution of 1.2 Å at 200 kV.

Results

In this work, by exploiting the superlattice (SL) architecture, we stabilized the metastable cubic (fcc) WNx with high concentration (up to ~50%) of disordered anion vacancies through the template effect from highly structurally stable and perfectly lattice-matched fcc phase of TiN. Due to the significant vacancy content in WN_x ($x = 0.5$), the SL layers exhibited severe local distortions. Microcantilever experiments confirmed that such ceramic's high strength (~9 GPa) and bending strain (~2.8%). Employing spherical aberration (Cs)-corrected transmission electron microscopy (TEM) and atomic-scale simulations, we demonstrate that the mechanical response of WN_x is dominated by a unit-cell disturbance (which implies that further unit-cell distortions occur during deformation), which acts as a deformation carrier and simultaneously prevents high stress concentrations.

Discussion and conclusions

The enhanced mechanical properties of WN_x/TiN SL can be attributed to effects induced by the ultra-high concentration of vacancies: unit-cell disturbances that absorb deformation energy, increased valence electron concentration, and hindered dislocation nucleation/motion. Our study underscores the importance of rational vacancy structure design, i.e., characterized by high vacancy concentration and disordered distribution, which can improve the deformation ability and strength of ceramics.

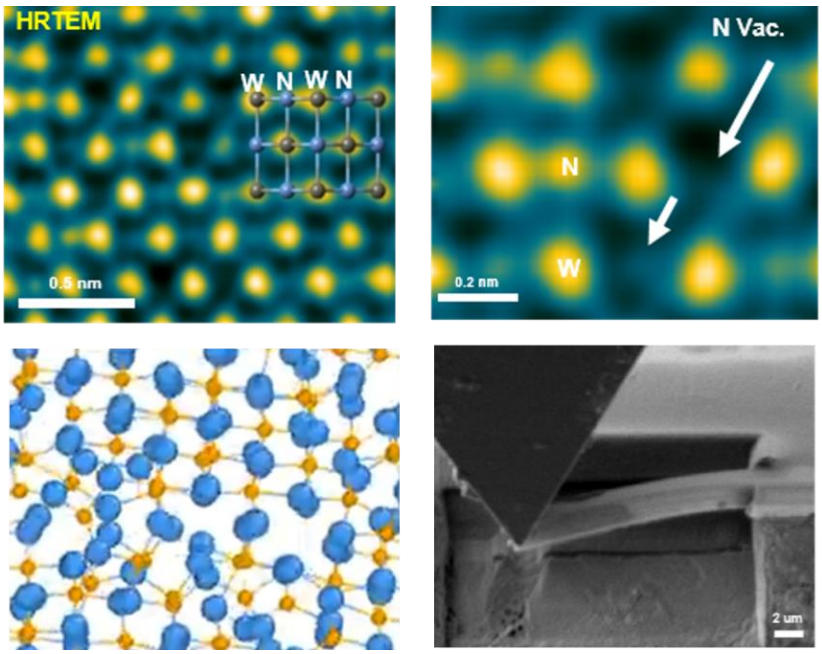


Figure 1, The unit cell disturbance caused by vacancies, leading to improved toughness.

Reference
1. Zhuo Chen et al. Nature communications (2023)14:8387.

Acknowledgment:
The authors thank Dr. Georg Haberfehlner and Prof. Gerald Kothleitner for their STEM-EELS characterization, Prof. Paul H. Mayrhofer for thin film synthesis, and Nikola Koutná and Dr. Davide G. Sangiovanni for AIMD simulation. This work is financially supported by FWF P 33696 (Z.C., Y.H., Z.Z.).

Type of presentation: Oral

MS6-O-3 Multi-modal Microscopy Analysis of Co-doped InAs/GaAs Quantum Dot Lasers

Eve Burgess[a], Samuel Shutts[a], Mingchu Tang[b], Huiyun Liu[b], Thomas Rodgers[c], Peter M Smowton[a], Juan Pereiro Viterbo[a] and Naresh Gunasekar[a]

[a]*Department of Physics and Astronomy, Cardiff University, (Cardiff), UK*

[b]*Department of Electrical Engineering, University College London, (London), UK*

[c]*Carl Zeiss Microscopy GmbH, (Oberkochen), Germany*

Contact email: burgesser@cardiff.ac.uk

III-V quantum dot (QD) lasers are a promising candidate for use as light sources in photonic integrated circuits (PICs). However, these devices must operate efficiently over a wide temperature range with minimal operating currents for commercial viability. To address this, a co-doping approach - combining p-type modulation doping and direct n-type doping - has been shown to reduce threshold current density across a broad temperature range [1]. Despite this progress, the reliability and failure mechanisms of QD lasers, particularly co-doped QD lasers, remain largely unexplored.

This work employs advanced electron microscopy techniques to investigate how co-doping influences material quality and device degradation. Electron channelling contrast imaging (ECCI) is used to assesses threading dislocation density (TDD), while passive voltage contrast (PVC) and electron beam induced current (EBIC) imaging are used to analyse pn-junction shifts in degraded devices. Transmission electron microscopy (TEM) provides nanoscale insight into defect formation and propagation. By correlating microscopy findings with device performance, this study advances the understanding of QD laser reliability.

The co-doped epitaxial structure was grown on [001] GaAs substrates via molecular beam epitaxy (MBE), as shown in Figure 1a, and broad-area laser test structures were fabricated. Before failure analysis, the epitaxial material was characterised to establish baseline properties. Atomic force microscopy (AFM) revealed distinct differences in surface morphology between the un-doped and co-doped samples. Electron channelling contrast imaging (ECCI) was employed to determine the threading dislocation density (TDD). The un-doped material exhibited a TDD on the order of 10^6 cm^{-2}, whereas the co-doped material demonstrated an order-of-magnitude reduction to approximately 10^5 cm^{-2}. Understanding the initial state of the material is crucial for reliability studies, as a higher TDD in the undoped sample could contribute to accelerated degradation compared to the co-doped counterpart.

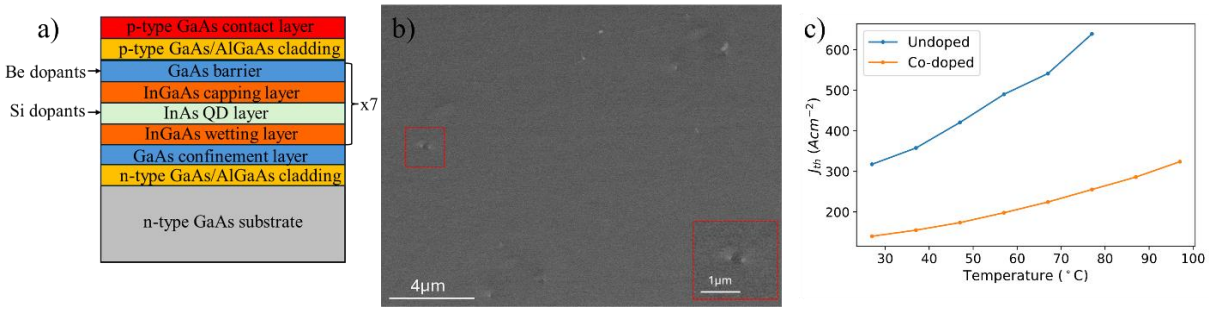


Figure 1a) shows the epitaxial structure of the co-doped QD laser, grown via MBE, b) shows an example ECCI image of the epitaxial material, used to determine TDD, the inset is a zoomed-in region showing two dislocations and c) shows the variation of threshold current density (J_{th}) with temperature (27°C to 97°C) for the unintentionally doped and co-doped regimes.

Passive voltage contrast (PVC) also known as secondary electron (SE) dopant contrast, a technique commonly used in failure analysis, was here used as a prerequisite to electron beam induced current (EBIC) imaging to locate the approximate position of the pn-junction in the co-doped laser material, as

shown in Figure 2a. EBIC was then performed on unaged and degraded devices to assess potential changes in device behaviour. Samples were prepared with cleaved cross-sections, eliminating the need for complex focused ion beam (FIB) cross-sectioning. Key degradation indicators include shifts in the pn-junction position due to dopant diffusion, variations in EBIC signal intensity, and changes in minority carrier lifetime. Preliminary EBIC results from a degraded device, overlaid on the corresponding SE image, are shown in Figure 2b. These preliminary results show an approximately 20nm shift in the pn-junction towards the p-side in the degraded device. In other degraded GaAs/AlGaAs-based laser diodes, a pn-junction shift towards the n-side is observed [2], which is attributed to the diffusion of p-dopants into the active region during operation. Therefore, the shift towards the p-side suggests that adding n-dopants into the active region has a more significant effect than the diffusion of the p-dopants. Detailed high resolution transmission electron microscopy work is underway to validate this claim.

Our work demonstrates the importance of the multi-microscopy workflow in understanding the failure mechanisms in QD lasers, particularly co-doped QD lasers which have shown lower threshold currents and reduced sensitivity to temperature than their unintentionally doped counterparts. They are likely candidates for use as active components in Si-based PICs.

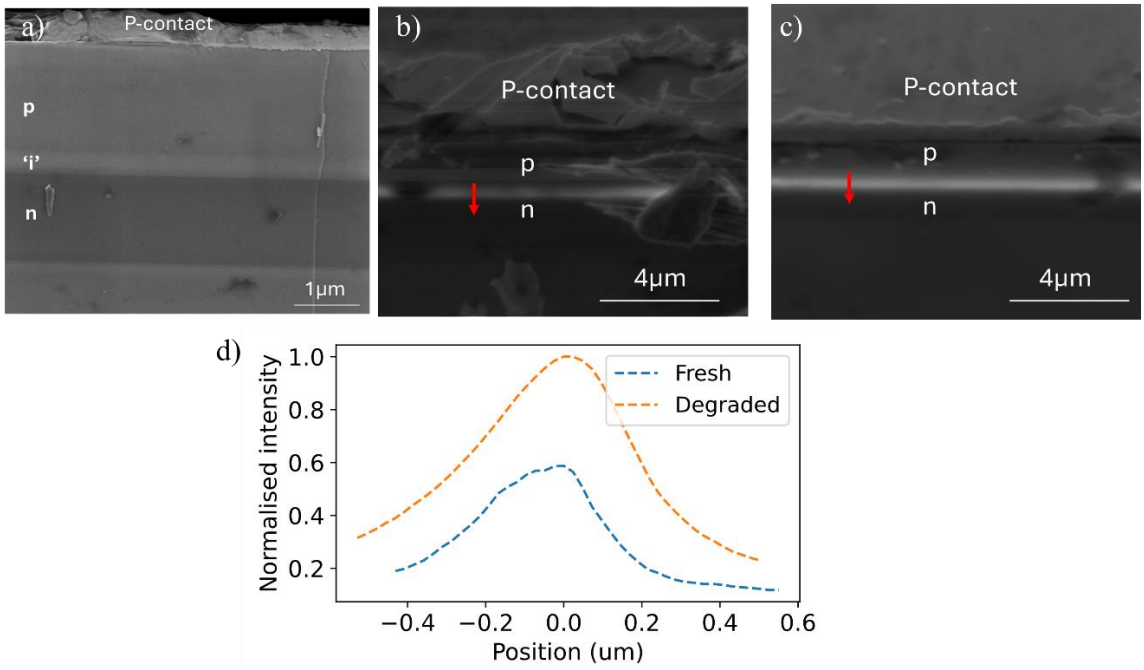


Figure 2a) is a PVC image of a co-doped device at the facet b) is the EBIC image overlayed on the SE image of a fresh device (showing considerable contamination) and (c) of a degraded device and d) shows the profile across the junction. Profiles are extracted using ImageJ and the location and direction they are taken from is indicated by the red arrow in b) and c).

Acknowledgements:
Thanks to Dr Paul Edwards and Prof. Robert Martin at the University of Strathclyde for performing EBIC measurements and to Greg Johnson at Carl Zeiss Microscopy GmbH for invaluable advice about PVC and EBIC.

References:

1. H. Deng *et al.*, '1.3 µm InAs/GaAs Quantum-Dot Lasers with p-Type, n-Type, and Co-Doped Modulation', *Adv. Phys. Res.*, vol. 3, no. 10, p. 2400045, 2024, doi: 10.1002/apxr.202400045.

2. A. Jakubowicz and A. Oosenbrug, 'SEM/EBIC characterization of degradation at mirrors of GaAs/AlGaAs laser diodes', *Microelectron. Eng.*, vol. 24, no. 1, pp. 189–194, Mar. 1994, doi: 10.1016/0167-9317(94)90070-1.

Type of presentation: Oral

MS6-O-4 Structural characterization of phase transformations in gallium oxide by transmission electron microscopy

Ildikó Cora[a], Zsolt Fogarassy[a], Matteo Bosi[b], András Kovács[c], Roberto Fornari[b,d], Alaxander Azarov[e], Andrej Kuznetsov[e], Béla Pécz[a], György Sáfrán[a]

[1]HUN-REN Centre for Energy Research, Institute of Technical Physics and Materials Science, Budapest 1121, Hungary

[2]IMEM-CNR, Viale delle Scienze 37/A, 43124 Parma, Italy.

[3]Ernst Ruska-Centre for Microscopy and Spectroscopy with Electrons, Forschungszentrum Jülich, Jülich 52425, Germany

[4]Department of Mathematical, Physical and Computer Sciences, University of Parma, Viale delle Scienze 7/A, 43124 Parma, Italy

[5]University of Oslo, Department of Physics, Centre for Materials Science and Nanotechnology, PO Box 1048 Blindern, N-0316 Oslo, Norway

Contact email: cora.ildiko@ek.hun-ren.hu

The intrinsic properties of Ga_2O_3 make it a promising candidate for high power electronics, suitable for the fabrication of solar-blind detectors for UV-C radiation.

Besides the stable monoclinic β, other polymorphs (α, γ, κ(ε), δ) are relevant candidates for applications. The most important step in device development is the structural characterization of the polymorphs: understanding their detailed crystal structure, growth mechanism, thermal stability and phase transformations up to 900°C, and the structural relationship between polymorphs at the atomic scale. Atomic scale studies can be achieved by conventional and scanning transmission electron microscopy (TEM) combined with elemental mapping and image simulation. Moreover, *in situ* TEM annealing is particularly a suitable method to study transformations directly.

In this work we present five polymorph transformations that have been studied using *ex situ* and *in situ* TEM heating experiments. The κ → β transformation was crystallographically described *in situ* in the microscope under vacuum, and by differential scanning calorimetry. The κ→γ transformation was also studied with *ex situ* heating measurements on a κ-Ga-oxide thin film, where the role of the O_2 fugacity of the heating measurements on the transformation of the κ structure was discovered and the interfaces between κ /β and κ /γ were modelled. Our second set of TEM experiments was carried out on the radiation induced phase transformation of β-Ga_2O_3. First, the β → γ phase transformation was crystallographically described. Later, the structural and textural development of the γ→ β transformation was monitored by *ex situ* heating using series of samples at different temperatures from RT up to 1100°C, and *in situ* TEM annealing experiments. The experimental data were supported by simulations using JEMS software, which uses a multislice approach to TEM image simulations.

Type of presentation: Oral

MS6-O-5 Advanced TEM characterization of 2D compound semiconductors

Bela Pecz[a], Antal Koós[a], Anelia Kakanakova[b], Salvatore Ethan Panasci[c], Gianfranco Sfuncia[c], Giuseppe Nicotra[c], Fabrizio Roccaforte[c], and Filippo Giannazzo[c]

[a]*HUN-REN Centre for Energy Research, Institute of Technical Physics and Materials Science, Budapest, Hungary*

[b]*Department of Physics, Chemistry and Biology (IFM), Linköping University, 581 83 Linköping, Sweden*

[c]*Consiglio Nazionale delle Ricerche – Istituto per la Microelettronica e Microsistemi (CNR-IMM), Z.I. VIII Strada 5, 95121 Catania, Italy*

Contact email: pecz.bela@ek.hun-ren.hu

Introduction: Group-III Nitride semiconductors (i.e., GaN, InN, AlN, and their alloys) are strategic materials for optoelectronics, high power and high frequency electronics. In their bulk form, they exhibit a wurzite structure. However, it has been theoretically predicted that ultrathin films of these materials can be stable in the 2D hexagonal buckled structure. From the experimental viewpoint, 2D Nitrides are difficult to obtain by conventional epitaxial growth, since ultra-thin films preferentially grow in the 3D island mode. The first experimental demonstration of 2D nitrides was the growth of GaN structure with rhombohedral symmetry obtained by Al Balushi et al. [1] by the confinement epitaxy at Epi-Gr/SiC interface using metal organic chemical vapor deposition (MOCVD). That inspired our work as well on 2D GaN [2] and also on 2D InN.
Recently, the growth of transition metal dichalcogenides (TMDs), such as MoS_2, on GaN has attracted increasing interest for heterojunction diodes and UV photodetectors applications. MoS_2 is a known 2D material which changes properties dramatically when we step down to a single layer, while the bandgap of a few layer MoS_2 is indirect and is about 1.3 eV, at a single layer thickness that is changed for direct bandgap 1.9 eV large. Therefore, our goal was to synthetise and characterise a single layer MoS2 on GaN. The substrate used was a Ga polar bulk GaN, while the two-step method developed in the group was used to prepare 2D MoS_2 [3].

Methods: Epitaxial graphene on nominally on-axis 4H-SiC (0001) substrates were used for the intercalation of InN at 700ºC in a horizontal-type hot-wall MOCVD reactor (GR508GFR Aixtron) [4]. The 2D MoS_2 on Ga-polar bulk GaN was obtained by a two-steps CVD approach. Namely first an about 1.5 nm thick MoOx was deposited on GaN by magnetron sputtering, then it was annealed in a two zone CVD furnace, where the sample was placed at 700 ºC, while in another zone Sulphur powder was heated at 150 °C.
The TEM lamellas were cut by focused ion beam (FIB) using a dual beam FEI SCIOS2 equipment in which the energy of Ga ions was reduced to 2 keV and initial observations were carried out using an FEI THEMIS 200 microscope equipped with an image corrector at 200 keV. Scanning transmission electron microscopy (S/TEM) was carried out in a probe corrected JEOL ARM 200F microscope.

Results and Discussion: The MOCVD growth resulted in a 2D layer, which however is composed from two layers of gallium oxide on the top and a single GaN layer on SiC as it is shown in Fig.1.
Similar experiments on 2D InN resulted in a bilayer of InN [4]. Occasionally some 3D regions with 6-7 layers of InN were also observed still covered by the bilayer of graphene. Scanning Tunnelling Spectroscopy was used to take I-V curves and to determine the forbidden bandgap of bilayer InN for what 2 eV was obtained showing a remarkable higher value than the 0.7 eV of bulk InN. STEM images will be shown in which the indium and nitrogen atoms could be distinguished.

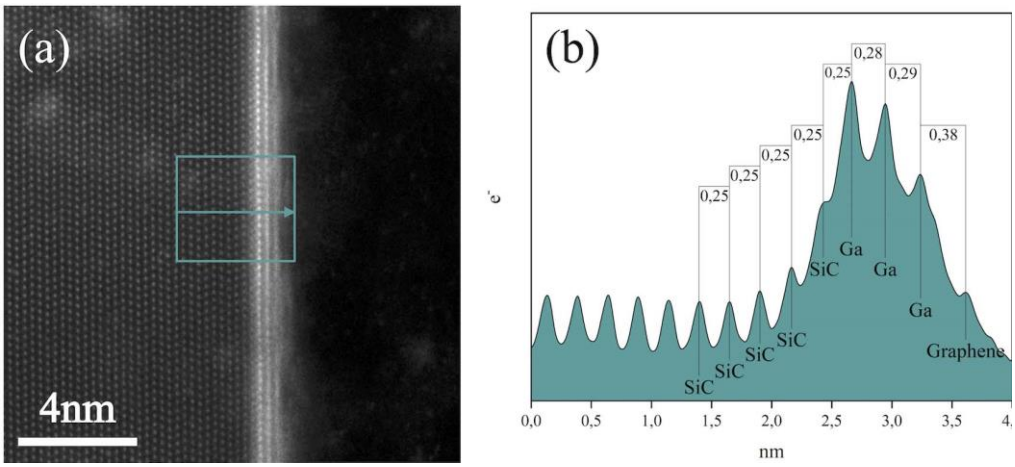


Figure 1: 2D GaN and oxide in the confined space of graphene and SiC grown by MOCVD. a) HAADF image with Z contrast, b) lattice spacings.

Atomic resolution structural and compositional analyses by aberration-corrected electron microscopy revealed a nearly-ideal van der Waals interface between MoS2 and the Ga-terminated GaN crystal, where only the topmost Ga atoms are affected by oxidation [5].

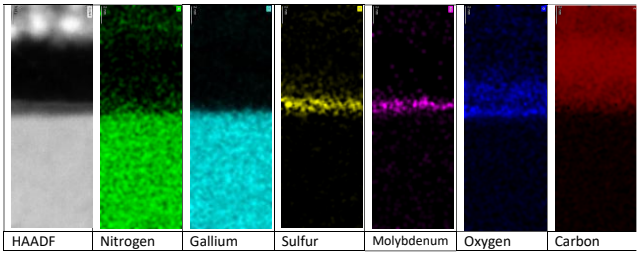


Figure 2: Single layer of MoS_2 on GaN with elemental maps taken by EDS.

Fig.2 shows the EDS elemental maps (also an HAADF image) of the layer. Note that sulphur map is clearly wider than molybdenum, as the Mo sheet is situated among two sulphur sheets. Raman spectroscopy confirmed the formation of a single layer MoS2 and indicated the p-type doped nature of the layer. Electrical characterization had shown a Schottky diode type behaviour with a Von=1.7 V in a good agreement with the expected value between GaN and p-type doped single MoS2 layer [5].

Conclusions: Several 2D nitrides can be grown by MOCVD via intercalation through epitaxial graphene on SiC. Also, there are several examples for growing 2D MoS_2 onto sapphire SiC and GaN. However, the single layer of MoS2 is rarely realised on wide bandgap semiconductors. In both subjects the control of the process needs TEM investigations due to the very small dimensions.

Acknowledgments: B.P acknowledges funding from the national project TKP2021-NKTA-05. The authors from CNR acknowledge Next Generation EU funding through the MUR - PRIN2022 project "2DIntegratE" (2022RHRZN2) and the MUR - PNRR project "SAMOTHRACE" (ECS00000022). Funding from travelling from the CNR/HAS 2023-25 bilateral project "GHOST III" is also acknowledged.

References:

1. Al Balushi, Z.L. et al., Nat. Mater. **2016**, 15, 1166.
2. Sfuncia G., et al., CRYSTENGCOMM, **2023**, 5180-5187.
3. Panasci, S.E.; et al., MICROELECTRONIC ENGINEERING, **2023**, 274, 111967.
4. Pecz B. et al., Adv.Mater. **2021**, 33, 2006660.
5. Giannazzo, F.; et al., APPLIED SURFACE SCIENCE, **2023**, 631, 157513

Type of presentation: Poster

MS6-P-1 Effects of processing gas on the growth of $SrTiO_3$ Thin Films: a TEM study

Maria Eugenia Fortes Brollo[a], Sandeep Kumar Chaluvadi[a], Shyni Punathum Chalil[a], Sara Passuti[b], Pasquale Orgiani[a], Regina Ciancio[b]

[a]*CNR-IOM Istituto Officina dei Materiali, I-34139 Trieste, Italy*

[b]*AREA Science Park, 34149 Trieste, Italy*

Contact email: brollo@iom.cnr.it

Strontium titanate $SrTiO_3$ (STO) thin films are widely used in the oxide thin films community, particularly in high-k dielectric applications. However, structural defects can significantly degrade film performance by inducing leakage currents and reducing the dielectric constant. Therefore, precise control over thin film growth and defect minimization are crucial for optimizing functional properties. In this study, we investigate the impact of processing gas on the atomic structure and internal stress of STO thin films grown on LSAT substrates using pulsed laser deposition (PLD). Films were deposited under different environments—namely, in ultra-high vacuum (UHV) or with neon (Ne), argon (Ar) and oxygen (O_2) as processing gas. High resolution transmission electron microscopy (HRTEM) was performed in cross-sectional geometry to analyze the atomic structure and the nanostructural evolution of the films. The aim was to assess how different growth conditions influence defect formation and strain at the atomic level.

HRTEM investigation reveals variations in the out-of-plane lattice parameter across different processing gases, indicating possible differences in strain and defect distribution. Representative bright field TEM images of the STO/LSAT heterostructure, produced under UHV and 10^{-3} mbar of $Ne/Ar/O_2$ processing gases in the [001] direction are shown in Figure 1. STO films grown under UHV conditions are characterized by potential defects in the crystal structure which can correlated to the high-speed of ablated species impinging the film surface during the deposition [ACS Nano 2020, 14, 3896−3906]. On the other hand, higher structural order is observed in thin films grown in presence of a process gas. These findings are in fully agreement with X-ray diffraction characterization (reported Figure 1) and it can be tentatively correlated to the reduced velocity of the ablated species impinging onto the film surface. Additionally, Energy-Dispersive X-ray Spectroscopy (EDS) and Electron Energy Loss Spectroscopy (EELS) analyses are in progress to provide insights into elemental composition, chemical bonding, and oxidation states, shedding light on the influence of deposition atmospheres on film properties.

Our study provides insights into optimizing STO thin film processing and characterization for a wide range of advanced materials.

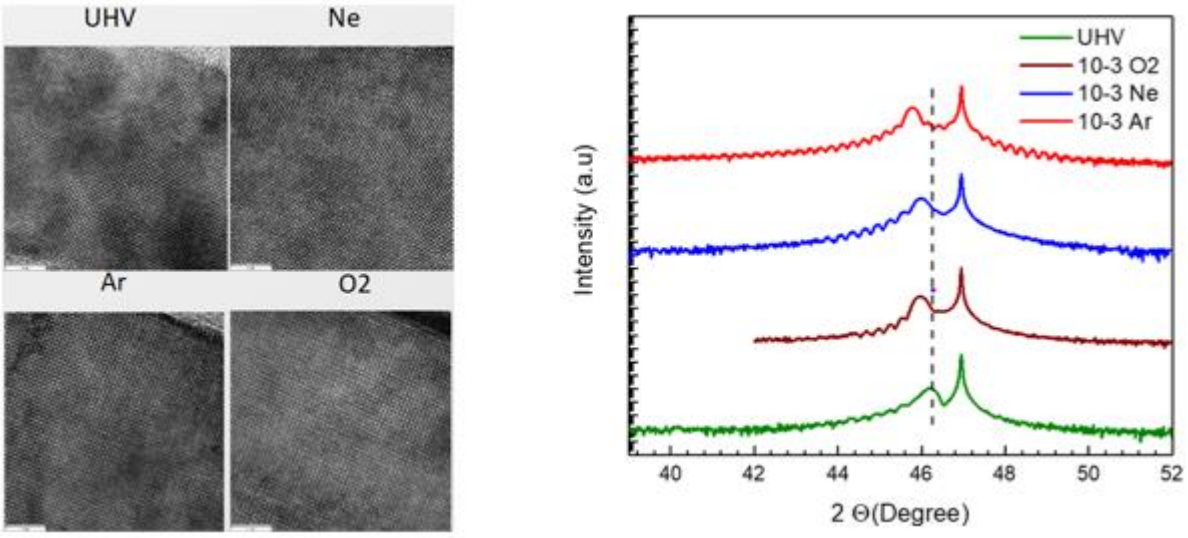


Figure 1: (left) Cross-sectional HRTEM images of STO/LSAT prepared under UHV and 10^{-3} mbar of Ne, Ar an O_2 process gases. (right) XRD θ–2θ symmetrical scans of STO films grown in the same conditions.

Type of presentation: Poster

MS6-P-2 Microstructure and selected properties of multicomponent wear-resistant and low-friction coatings on titanium alloy substrates

Aleksandra Fiołek[a], Sławomir Zimowski[b], Tomasz Moskalewicz[a]

[a]*AGH University of Krakow, Faculty of Metals Engineering and Industrial Computer Science, Poland*

[b]*AGH University of Krakow, Faculty of Mechanical Engineering and Robotics, Poland*

Contact email: kruka@agh.edu.pl

Introduction

More than half of commercial applications of titanium alloys are attributed to the Ti-6Al-4V alloy. This is due to two main reasons, firstly, its favorable mechanical properties, and secondly, it is currently the most studied alloy [1]. Unfortunately, poor tribological properties prevent its use in friction nodes. Therefore, surface treatment, including the deposition of a protective coating, is necessary for applications exposed to wear and friction [2]. Electrophoretic deposition (EPD) combined with heat treatment has significant potential in the field of coatings for mechanical engineering applications, especially for composite coatings based on thermoplastic polymers. By incorporating second phase particles into the polymer matrix, these coatings acquire unique properties that cannot be achieved through other methods. However, research indicates that adding a single type of reinforcing phase particle to the matrix often improves only one specific property [3,4]. Therefore, the use of more than one type of particle could be a better approach, leading to the development of multicomponent coatings with a broader range of enhanced properties. Nevertheless, EPD of multicomponent coatings poses challenges. Surfactants are often necessary to stabilize the suspension used for deposition, allowing different types of particles to be co-deposited on the same electrode [5]. The aim of this study was to establish the impact of EPD conditions on the morphology and microstructure of multicomponent TiN/PTFE/PEEK coatings on the Ti-6Al-4V alloy. The key properties of coated alloy, such as adhesion strength, scratch resistance, friction coefficient and wear resistance, were also investigated.

Methods

To deposit the coatings, three ethanol-based mixtures were prepared, in which three different surfactants, chitosan polyelectrolyte, sodium alginate and PAZO, were used at the same concentration of 0.5 g/l. PEEK 708 (30 g/l) and PTFE (2 g/l) powders as well as TiN (0.4 g/l) nanopowder were added to the mixtures. The suspensions were prepared by mixing PTFE with ethanol, then adding water with the appropriate surfactant, and finally the remaining powders. The coatings were deposited on a Ti-6Al-4V alloy substrate in the voltage range of 10 - 150 V (in steps of 10 V) for 90 s. All coating components, suspensions used for deposition and coatings after heat treatment were examined using the FEI Inspect S50 SEM and Tecnai TF 20 XTWIN (FEI) TEM. The cross-sectional lamella was cut by a focused ion beam (FIB) using a FEI QUANTA 3D 200i device. The adhesion of the coatings to the substrates was investigated using the cross-cut tape test method in accordance with the ASTM D3359 standard (test method B). The scratch test was performed on a Micro-Combi-Tester using a Rockwell C diamond, a maximum load of 30 N at a measuring length of 5 mm and an indenter speed of 5 mm/min. Friction and wear tests were carried out in the ball-on-disc test with an Al_2O_3 ball at the following parameters: load 5 N, speed 0.04 m/s, friction radius 3 mm and sliding distance 2000 m. The surface of the samples after the adhesion and friction tests was examined using SEM.

Results

Investigation of coating components showed that PEEK and PTFE particles revealed a similar globular shape, with a size in the range of 2 – 15 μm for PEEK particles and 1 – 10 μm for PTFE particles. TiN nanoparticles (NPs) had a spherical and irregular morphology with a diameter in the range of 2 to 75 nm. The observations of suspensions containing various additives, sodium alginate, PAZO, or chitosan polyelectrolyte, showed the presence of PTFE and PEEK particles as well as TiN NPs or their small agglomerates, which were closely surrounded by surfactants adsorbed on their surfaces. SEM observations of the heat-treated coatings showed that there were no voids or discontinuities in the

coating deposited with chitosan. A network of microcracks that covered the entire coating surface was observed, but they occurred only in the near-surface layer of the coating and did not extend to the substrate. Lighter and darker areas were also visible in the microstructure of the coating. The results of chemical composition microanalysis revealed that the brighter areas of the coating were enriched in fluorine, which means that they contained PTFE agglomerates. The coating deposited with sodium alginate was not compact and inhomogeneous because of the presence of many open pores that may be related to the degradation of the surfactant. The coating deposited with PAZO was also inhomogeneous and discontinuous due to the very large shrinkage of the polymers in the coating, which caused the formation of many large and deep microcracks. TEM investigation of the coating deposited with chitosan performed on its cross-section showed that the coating was relatively homogeneous, with single TiN NPs and their agglomerates, and the presence of pores could also be observed. The coatings deposited with alginate and PAZO were characterized by very poor adhesion strength and poor scratch resistance. Microscopic observations showed complete removal of the coatings and exposure of the substrate. On the contrary, the coating obtained using suspension with chitosan had a high adhesion strength. The friction coefficient in cooperation with the Al_2O_3 ball of the alloy with coating deposited with chitosan or alginate was 0.10 and 0.18/0.19, respectively. SEM observations of the wear tracks indicated the abrasive wear mechanism of the coatings. The coating obtained with PAZO had very low wear resistance and was completely destroyed during tests.

Discussion and conclusions

All surfactants provided electrosteric stabilization of suspensions and enabled the co-deposition of all types of particles (PEEK, PTFE and TiN) on one electrode (substrate materials), forming a multicomponent coating. The EPD mechanism involved the adsorption of the surfactant on the particles and imparting a positive charge (chitosan) or a negative charge (PAZO, sodium alginate). Heat treatment performed above the melting point of PEEK (374 °C) and PTFE (326.8 °C) resulted in compact and homogeneous composite coatings that relatively uniformly covered the titanium alloy substrates. Heat-treated coatings deposited with chitosan contained a network of surface microcracks, but they were homogeneous. The coatings obtained from the alginate suspension were porous as a result of surfactant degradation, whereas those achieved from the suspension with PAZO contained large and deep cracks. The coatings deposited with chitosan, unlike other ones, showed high adhesion strength and scratch resistance. Microscopical observations showed that the wear of coatings obtained with the addition of chitosan and alginate was of an abrasive nature, as evidenced by numerous scratches and grooves in the wear track arranged in the direction of sliding. Additionally, the formation of a thin tribofilm was observed on the surfaces of the Al_2O_3 balls. The research results confirmed the validity of the introduction of hard TiN NPs and solid PTFE lubricant particles into the PEEK matrix, resulting in a reduction in both the friction coefficient and the wear rate in the case of coatings obtained from chitosan and alginate suspensions.

Acknowledgments

The study was supported by AGH-UST (project no. 16.16.110.663). The authors appreciate the valuable contribution of M. Gajewska (AGH University of Krakow) for help with the TEM investigation.

References:

[1] X. Ye, L. Wang, Z. T. H. Tse, G. Tang, G. Song, *Mater. Sci. Eng. C.* **2015**, 49, 851-860.
[2] Q. L. Niu, X. H. Zheng, W. W. Ming, M. Chen, *Tribol. Trans.* **2013**, 56, 101-108.
[3] A. Fiołek, S. Zimowski, A. Kopia, M. Sitarz, T. Moskalewicz, *Metall. Mater. Trans. A.* **2020**, 51, 4786-4798.
[4] T. Moskalewicz, M. Warcaba, S. Zimowski, A. Łukaszczyk, *Metall. Mater. Trans. A.* **2019**, 50, 5914-5924.
[5] L. Besra, M. Liu, *Prog. Mater. Sci.* **2007**, 52, 1-61.

Type of presentation: Poster

MS6-P-3 Multi-scale investigation of superior mechnical properties in nitride ceramics with negative stacking fault energy

Yong Huang[a], Zhuo Chen[a], Zaoli Zhang[a]

[a]*Erich Schmid Institute of Materials Science, Austrian Academy of Sciences, Jahnstraße 12, Leoben, A-8700, Austria*

Contact email: yong.huang@oeaw.ac,at

Introduction:
Ceramics are widely used in various structural and functional applications; however, their intrinsic brittleness at room temperature remains a critical challenge, often leading to early-stage catastrophic failures. This brittleness arises primarily due to the high critical-resolved shear stress required to initiate dislocation movement and the limited number of operational slip systems. Addressing this limitation is crucial for the development of ceramics with improved mechanical properties. This study aims to develop a novel strategy for enhancing the deformability of ceramics by leveraging negative stacking fault energy (SFE). The approach seeks to reduce the energetic barriers to dislocation motion and expand the number of available slip systems, ultimately improving room-temperature plasticity while maintaining high strength and toughness.

Materials & Methods:
A TiN/TaN superlattice was fabricated and subjected to in-situ micro-mechanical testing to evaluate its mechanical response. Post-mortem transmission electron microscopy (TEM) was employed to analyze deformation mechanisms at the atomic scale, providing insights into the role of negative SFE in promoting dislocation activity, atomic plane faulting, and twinning.

Results:
The TiN/TaN superlattice exhibited remarkable room-temperature compressive plasticity (~43%), attributed to extensive atomic plane faulting and twinning facilitated by negative SFE. This behavior enabled an exceptional combination of plasticity, strength, and toughness, demonstrating the feasibility of overcoming the brittleness barrier in ceramics.

Conclusion:
This study successfully demonstrates a new paradigm for designing intrinsically ductile ceramics through negative SFE engineering. The findings provide a fundamental framework for the development of advanced ceramic materials with enhanced mechanical performance, paving the way for broader structural applications requiring both strength and deformability.

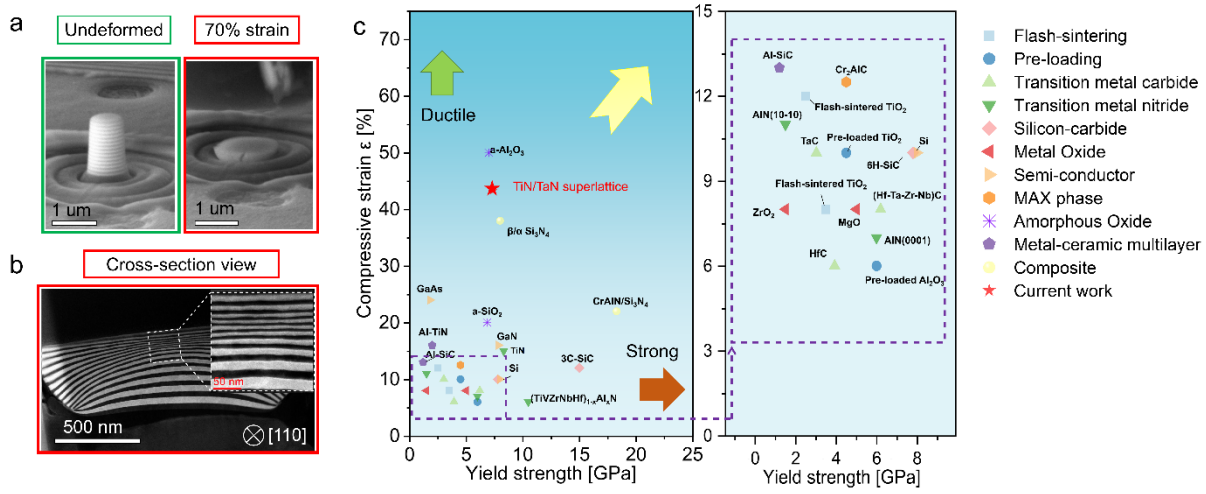


Fig.1 (a) Scanning electron microscopy images of an undeformed pillar and its post-compression state with $\varepsilon_c \approx 70\%$. (b) Cross-section view high-angle annular dark field scanning TEM image of the compressed pillar with $\varepsilon_c \approx 70\%$ (c) Recently reported maximum strain without cracking and yield strength of ceramics and semiconductor materials measured by micropillar compression at room temperature.

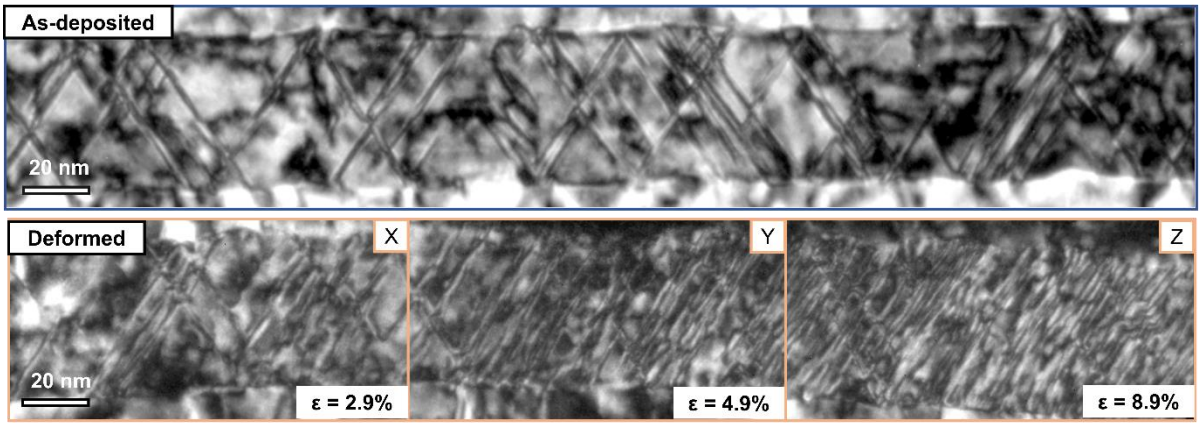


Fig. 2. Bright field TEM images of as-deposited TaN and deformed TaN along [110] zone axis.

References:

1. Huang, Y., et al. (2025). "Harvesting superior intrinsic plasticity in nitride ceramics with negative stacking fault energy." Acta Materialia: 120774.

Acknowledgement:

The authors would like to thank Dr. Christian Mitterer, Velislava Terziyska (Montanuniversität Leoben) for the film deposition. We sincerely thank Rainer Hahn and Helmut Riedl (TU Wien) for their invaluable assistance with the micropillar compression tests. We also appreciate Verena Maier-Kiener (Montanuniversität Leoben) for her support with the nanoindentation tests and Michael Meindlhumer (Montanuniversität Leoben) for his help with the microcantilever bending tests. Additionally, we acknowledge David Holec, Thomas Leiner, and Lukas Hatzenbichler (Montanuniversität Leoben)for their contributions to the DFT calculations. Also, thanks to Zequn Zhang (ESI) and Yonghui Zheng for their help with microscopy. The financial support (Y.H., Z.C., and Z.L.Z.) by the Austrian Science Fund (PAT 1946623) is highly acknowledged.

Type of presentation: Poster

MS6-P-4 Spray-Coated Metallosurfactant-Alginate Coatings: Dual Antimicrobial Action

Ana Ivančić[a], Krunoslav Bojanić[a], Zhenxue Zhang[b], Hyoungwon Park[c], Íris Soares[d], Silke Christiansen[c,d], Maja Dutour Sikirić[a], Darija Domazet Jurašin[a]

[a]*Ruđer Bošković Institute, 10000 Zagreb, Croatia*

[b]*University of Birmingham, Birmingham, B15 2TT, United Kingdom*

[c]*Fraunhofer Institute for Ceramic Technologies and Systems IKTS, Forchheim, Germany*

[d]*Institute for Nanothechnology and Correlative Microscopy, Forchheim, Germany*

Contact email: djurasin@irb.hr

Surfactants are amphiphilic compounds containing a hydrophilic moiety and one or multiple hydrophobic chains [1]. Among surfactants, cationic quaternary ammonium salts are widely used, especially for their antimicrobial properties [2]. The combination of quaternary ammonium surfactants and metal ions creates unique compounds, metallosurfactants, with both surfactant and metal properties. Additionally, metals such as copper, which are known to have antibacterial properties [3], can be used. This can yield compounds with enhanced properties due to dual antimicrobial action through different mechanisms. The cationic quaternary ammonium surfactant mode of action involves binding to the bacterial cell membrane and disrupting its function through destabilization and permeabilization, ultimately leading to lysis and cell death. The antimicrobial activity of copper ions also lies in the electrostatic interactions with the microbe's outer membrane, causing the membrane to rupture, while also forming reactive oxygen species that cause further cell damage. A compound that combines these multiple modes of action is less likely to promote the development of antibacterial resistance.

In this work, the dimeric metallosurfactant bis(*N*,*N*-dimethyl-*N*-dodecyl)ethylene-1,2-diammonium tetrabromocuprate (II), denoted (12-2-12)[$CuBr_4$], was synthetized [4]. Unlike conventional single-chain surfactants, dimeric surfactants are made up of two amphiphilic moieties covalently linked by a spacer group. Consequently, such compounds exhibit enhanced physico-chemical properties compared to their monomeric counterparts [5].

To obtain antibacterial coatings with multimodal action, a concentrated (12-2-12)[$CuBr_4$] solution was spray-coated onto stainless steel plates using an airbrush. Airbrushing was used as a highly efficient large-area deposition method for spray-coating. To enhance antibacterial action, (12-2-12)[$CuBr_4$] suspensions with CuO or TiO_2 nanoparticles were also spray-coated and tested. To ensure better mechanical properties and durability of the coatings, alginate was airbrushed as a top coating. Both sprayed components were applied in two layers to guarantee satisfactory surface coverage.

Scanning electron microscopy (SEM) was used for surface characterization of the prepared coatings. SEM images show that the coatings have island-like structures on the surface, confirming that the surface is not fully covered (Figure 1), which is consistent with the spray coating. Peel-off and scratch tests were also conducted to evaluate the adhesion and cohesion of the coatings in the context of potential application as antimicrobial coatings on frequently touched surfaces. Peel-off test results indicate that the coatings are well adhered to the substrate surface. In contrast, scratch test results reveal that the coatings can withstand a continuous increasing load of up to 20 mN. While the island-like structure of the coatings was easy to cut, they were not completely removed after scratch test.

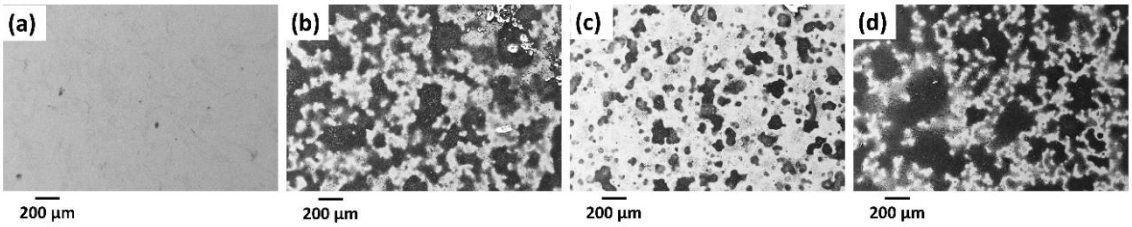


Figure 1. Scanning electron micrographs (Crossbeam 550, ZEISS) of stainless steel substrate: (a) without coating, and airbrushed with (b) (12-2-12)[$CuBr_4$] and alginate, (c) (12-2-12)[$CuBr_4$] with TiO_2 nanoparticles and alginate and (d) (12-2-12)[$CuBr_4$] with CuO nanoparticles and alginate.

Finally, biofilm growth experiments were done with Gram-positive *Staphylococcus aureus* and Gram-negative *Pseudomonas aeruginosa* bacteria using crystal violet staining. By measuring optical density, planktonic growth and biofilm growth studies were done. Nevertheless, results of antibacterial activity assays showed good antibacterial properties and inhibition of biofilm formation in all prepared coatings. After biofilm growth experiments, the samples were characterized by SEM to confirm the previous findings (Figure 2). The obtained micrographs match the optical density values collected previously.

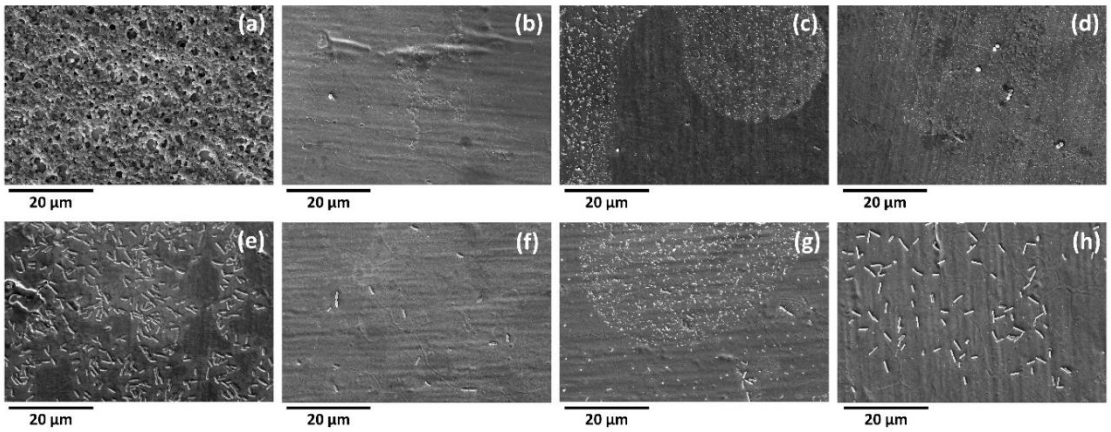


Figure 2. Scanning electron micrographs (Axia ChemiSEM, Thermo Fisher Scientific) of stainless steel substrate after biofilm growth experiments with Staphylococcus aureus (in the first row) and Pseudomonas aeruginosa (in the second row): (a), (e) without coating; (b), (f) airbrushed with (12-2-12)[$CuBr_4$] and alginate; (c), (d) (12-2-12)[$CuBr_4$] with TiO_2 nanoparticles and alginate; and (d) (12-2-12)[$CuBr_4$] with CuO nanoparticles and alginate.

Using the dimeric (12-2-12)[$CuBr_4$] metallosurfactant results in highly effective antibiofilm-forming coatings, despite only partial surface coverage (Figure 1). The addition of nanoparticles showed no clear difference in inhibiting biofilm formation, indicating that the surfactant itself was sufficient to prevent the formation of a strong biofilm. The next step in this research involves testing a different coating method, such as spin-coating, as well as varying metallosurfactant concentrations.

Acknowledgments:
This work was financially supported by the European Union's Horizon-RIA project, Surface Transfer of Pathogens (STOP), Grant agreement ID: 101057961 and Croatian Science Foundation project IP-2024-05-3668, MSurf-*n*-SWIM.

References:

1. S. Kumari, M. Nehra, S. Jain, N. Dilbaghi, G. R. Chaudhary, K. Kim, S. Kumar, *Adv. Colloid Interface Sci.* **2024**, *323*, 103065, https://doi.org/10.1016/j.cis.2023.103065
2. M. N. Nadagouda, P. Vijayasarathy, A. Sin, H. Nam, S. Khan, J. B. M. Parambath, A. A. Mohamed, C. Han, *Med. Chem. Res.* **2022**, *31*, 1663 – 1678, https://doi.org/10.1007/s00044-022-02924-9
3. I. Salah, I. P. Parkin, E Allan, *RSC Adv.* **2021**, *11*, 181179, https://doi.org/10.1039/d1ra02149d
4. M. Rubčić, M. Herak, L. Zagorec, D. Domazet Jurašin, *Inorg. Chem.* **2024**, *63*, 12218–12230, https://doi.org/10.1021/acs.inorgchem.4c01550
5. R. Sharma, A. Kamal, M. Abdinejad, R.K. Mahajan, H.-B. Kraatz, *Adv. Colloid Interface Sci.* **2017**, *248*, 35–68. https://doi.org/10.1016/j.cis.2017.07.032

Type of presentation: Poster

MS6-P-5 Photocatalytic activity of thin ZnO films deposited at room temperature by plasma-enhanced atomic layer deposition

Daria Jardas Babić[a,b], Robert Peter[a,b], Krešimir Salamon[c], Marko Perčić[b,d], Damjan Vengust[e], Tina Radošević[e], Matejka Podlogar[e], Ivna Kavre Piltaver[a,b], Aleš Omerzu[a,b]

[a]*University of Rijeka, Faculty of Physics, (Rijeka), Croatia*

[b]*University of Rijeka, Centre for Micro- and Nanosciences and Technologies, (Rijeka), Croatia*

[c]*Ruđer Boskovic Institute, (Zagreb), Croatia*

[d]*University of Rijeka, Faculty of Engineering, (Rijeka), Croatia*

[e]*Jožef Stefan Institute, (Ljubljana), Slovenia*

Contact email: daria.jardas@uniri.hr

Introduction

Plasma-enhanced atomic layer deposition (PEALD) enables the deposition of ZnO thin films at low temperatures by increasing the reactivity of the precursors through plasma activation. This is particularly advantageous for applications on temperature-sensitive substrates and for reducing energy consumption. Recent studies have shown that the deposition of ZnO at room temperature is possible with PEALD, where the reactor configuration and plasma parameters play a crucial role in determining the film properties [1, 2]. This work investigates the effects of RF power on properties of ZnO thin films deposited at room temperature, focussing on their structural properties and photocatalytic performance.

Methods

Thin ZnO films were deposited at room temperature using PEALD with diethylzinc (DEZ) as precursor and O_2 plasma as oxidising agent. A capacitively coupled plasma (CCP) configuration was used and the RF power was systematically varied. The film structure was characterised by high-resolution transmission electron microscopy (HR-TEM), atomic force microscopy (AFM) and X-ray diffraction (XRD). The chemical composition was analysed using X-ray photoelectron spectroscopy (XPS), while the optical properties were investigated using UV-Vis spectroscopy. The photocatalytic activity was evaluated by monitoring the degradation of methylene blue (MB) in aqueous solution under UV illumination.

Results

The structural analysis revealed that the PEALD grown ZnO films deposited at room temperature are predominantly amorphous. The films deposited with an RF power of more than 200 W show a slightly improved crystallinity. Photocatalytic tests showed that ZnO films synthesised with RF power above 200 W exhibited significantly higher MB degradation efficiency compared to films deposited with lower RF power.

Discussion and Conclusions

These results indicate that PEALD enables the deposition of ZnO films with tunable properties at room temperature without the need for additional thermal energy. The observed correlation between the RF power and the photocatalytic performance emphasises the potential of PEALD grown ZnO at low temperature for future applications.

Acknowledgments

The research leading to these results has received funding from the core fundings NPOO.C3.2.R2-I1.06.0083 supported by the European Union NextGenerationEU, the Croatian Science Foundation

through grant no. MOBDOK-2023-9307 supported by European Union NextGenerationEU, and projects No. 23-190 and 23-4 supported by the University of Rijeka.

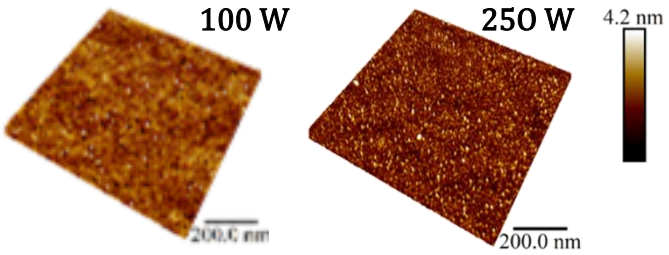


Figure 1: AFM micrographs of thin PEALD ZnO films deposited at room temperature using 100 W and 250 W RF power.

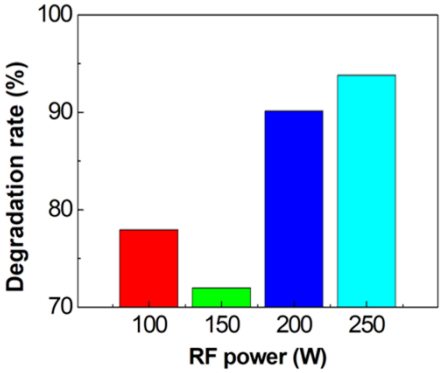


Figure 2: Photodegradation rate of thin ZnO films deposited by PEALD at room temperature as a function of RF power.

References:

1. M. Napari, M. Lahtinen, A. Veselov, J. Julin, E. Østreng, *Surf. Coat. Technol.* **2017**, 326, 281–290.
2. J. Pilz, A. Perrotta, P. Christian, M. Tazreiter, R. Resel, G. Leising, T. Griesser, A. M. Coclite, *J. Vac. Sci. Technol. A: Vac. Surf. Films* **2018**, 36, 01A109.

Type of presentation: Poster

MS6-P-6 Electron microscopy investigation of Cu-TiO_2 nanocomposites for solar-driven photocatalysis

Ivana Jelovica Badovinac[a,b], Ivna Kavre Piltaver [a,b], Lucija Črep[a], Daria Jardas Babić[a,b], Iva Šarić Janković[a,b], Krešimir Salamon[c], Martina Kocijan[a], Matejka Podlogar[d], Robert Peter[a,b]

[a]*University of Rijeka, Faculty of Physics, Rijeka, Croatia*

[b]*University of Rijeka, Center for Micro- and Nanosciences and Technologies, Rijeka, Croatia*

[c]*Ruder Boskovic Institute, Zagreb, Croatia*

[d]*Jozef Stefan Institute, Ljubljana, Slovenia*

Contact email: ijelov@phy.uniri.hr

Introduction: Various structural modifications of TiO_2-based photocatalysts have been used to improve the photocatalytic efficiency of TiO_2. These include doping the material with different transition metal and nonmetal elements, dye photosensitization of TiO_2 surfaces, or the formation of heterojunctions with suitable low bandgap semiconductors [1,2]. One approach has attracted special attention - the formation of TiO_2-metal composites in which metallic nanoparticles (NPs) are deposited on the surface of the TiO_2 photocatalyst or incorporated into its matrix [3,4]. It has been shown that the formation of TiO_2-Cu composites can significantly improve the photocatalytic properties of TiO_2 materials. In our study, we synthesized TiO_2-Cu composites in the form of thin polycrystalline films by atomic layer deposition (ALD). We investigated the photocatalytic efficiency of the samples [5,6] with Cu NPs directly incorporated into the TiO_2 matrix by monitoring the degradation of methylene blue (MB) in an aqueous solution irradiated with a sunlight-simulated lamp. Here we will pay special attention to the contribution of electron microscopy to the research results.

Methods: The ALD syntheses were carried out in a Beneq TFS 200 system at a deposition temperature of 250 °C on Si(100), quartz(100) or amorphous glass substrates. For the growth of TiO_2-Cu composites with different copper content, copper(II) acetate (Cu(OAc)2) was introduced into the reaction chamber during the growth of the TiO_2 films. The surface morphology, elemental composition, crystalline and electronic structure, conductivity and optical absorption of the pure TiO_2 thin film and three Cu-TiO_2 composite films with different copper content, labelled TiO_2–Cu25, TiO_2–Cu75 and TiO_2–Cu200, were investigated by a series of analytical techniques: X-ray diffraction (XRD), X-ray photoelectron spectroscopy (XPS), scanning electron microscopy (SEM), energy dispersive X-ray spectroscopy (EDS), transmission electron microscopy (TEM), UV-Vis spectroscopy, photoconductivity and photocatalytic efficiency measurements.

Results: Our samples exhibit polycrystalline structure, with the anatase TiO_2 and metallic Cu phases mixed in the ALD-grown composites. Figure 1 shows a set of SEM images taken from ALD-synthesized films at two different magnifications: 20000x (top row) and 100000x (bottom row). SEM and TEM measurements show that metallic Cu is present in the ALD-grown composite films in the form of NPs, which are incorporated in the TiO_2 matrices.

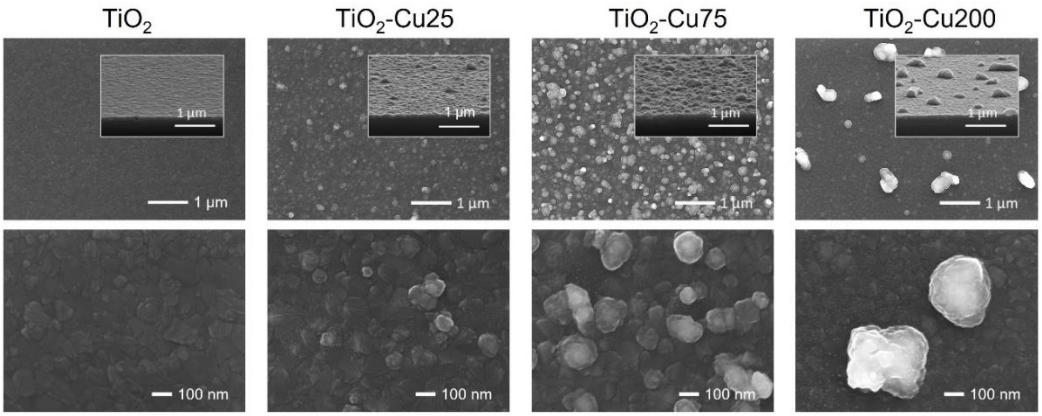


Figure 1: SEM images of a pure TiO_2 sample and TiO_2-Cu composite films, obtained by collecting secondary electrons at working distance of 3 mm, with an acceleration voltage of 10 kV. Images were taken at two different magnifications: 20000x (top row) and 100000x (bottom row). Insets show SEM images of corresponding films tilted for 10° and recorded at working distance of 10 mm.

Discussion and conclusion: We have shown that the incorporation of Cu-NPs into the TiO_2 matrix has a significant effect on the optical absorption of the ALD-grown films. As for the photocatalysis, the pure TiO_2 sample degrades about 75% of the MB when exposed to light for 7 hours. On the other hand, the sample with the lowest Cu content, TiO_2-Cu25, shows the best photocatalytic efficiency and degrades about 95% of the MB. The photocatalytic process of these samples is divided into two distinct phases. These ALD-grown TiO_2-Cu composites exhibit excellent photocatalytic properties compared to similar compounds. To explain the results of the photocatalytic activity of our samples, further analysis is currently being carried out.

Acknowledgments: The research leading to these results has received funding from the core fundings NPOO.C3.2.R2-I1.06.0083 supported by the European Union NextGenerationEU and project numbers 23-190 and 23-4 supported by the University of Rijeka.

References:

1. Q. Guo, C. Zhou, Z. Ma, X. Yang, *Adv. Mater*. **2019**, 31, 1901997.
2. C. Karthikeyan, P. Arunachalam, K. Ramachandran, A. M. Al-Mayouf, S. Karuppuchamy, *J. Alloys Compd.* **2020**, 828, 154281.
3. L. Gomathi Devi, R. Kavitha, *Appl. Surf. Sci*. **2016**, 360, 601–622.
4. A. Kumar, P. Choudhary, A. Kumar, P. H. C. Camargo, V. Krishnan, *Small*, **2022**, 18, 2101638.
5. I. Jelovica Badovinac, R. Peter, A. Omerzu, K. Salamon, I. Šarić, A. Samaržija, M. Perčić, I. Kavre Piltaver, G. Ambrožić, M. Petravić, *Thin Solid Films*, **2020**, 709, 138215.
6. R. Peter, A. Omerzu, I. Kavre Piltaver, R. Speranza, K. Salamon, M. Podlogar, K. Veličan, M. Perčić, M. Petravić, *Ceram. Int*. **2023**, 49 (22), 35229-35238.

Type of presentation: Poster

MS6-P-7 Intense Pulsed Light Processing for Rapid Crystallization of Titania Nanotube Thin Films

Krunoslav Juraić[a], Vedran Kojić[a], Mario Bohač[a], Marko Zubak[b], Petar Kassal[b]

[a]*Ruđer Bošković Institute, Zagreb, Croatia*

[b]*University of Zagreb, Faculty of Chemical Engineering and Technology, Zagreb, Croatia*

Contact email: kjuraic@irb.hr

Instruction:
Titania (TiO_2) nanotube thin films have gained significant attention due to their high surface area, photocatalytic activity, and optical transparency, making them promising for applications in photovoltaics, sensors, and self-cleaning coatings. In particular, the development of TiO_2 nanotubes on flexible substrates is crucial for next-generation flexible solar cells, which require lightweight, bendable, and efficient photoanodes. However, one of the main challenges in their fabrication is the high-temperature annealing required to obtain the anatase phase, which restricts the choice of substrates and increases processing time and energy consumption. The goal of this study is to develop a low-temperature, rapid, and scalable method for synthesizing transparent anatase TiO_2 nanotube thin films suitable for flexible devices.the corresponding author should be underlined and will be the contact person for the organizers. At least one of the authors needs to be registered for 17th Multinational Conference on Microscopy (17MCM). The corresponding author is responsible for ensuring that all co-authors agree with the content of the submitted abstract.

Methods:
We present a modified approach for the synthesis of TiO_2 nanotube thin films, based on our established magnetron sputtering and electrochemical anodization process [1, 2, 3]. A titanium thin film was deposited onto a transparent conducting oxide (TCO)-coated glass substrate via magnetron sputtering, followed by anodization in a two-electrode reactor to form the nanotube structures. Instead of conventional high-temperature tube furnace annealing, we employed intense pulsed light (IPL) processing for crystallization. IPL processing utilizes high-intensity xenon flash lamps to deliver rapid, millisecond-scale energy pulses, enabling phase transformation without prolonged high-temperature exposure. The influence of IPL processing parameters, including the number and energy of light pulses, was systematically analyzed. Optical properties were examined using ultraviolet-visible (UV-Vis) transmittance spectroscopy, while structural characterization was performed using X-ray diffraction (XRD). Surface morphology was analyzed using scanning electron microscopy (SEM).

a) b)

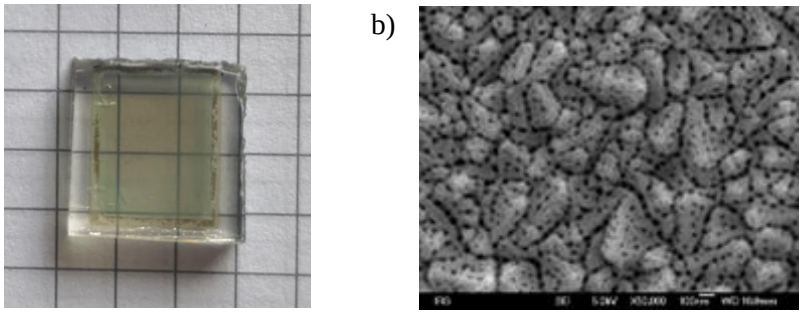


Figure 1 Photo of titania nanotube thin film sample after IPL processing (a) and SEM image of sample surface (b)

Results:
Transparent anatase TiO_2 nanotube thin films were successfully synthesized on both TCO-coated glass and flexible substrates. The structural integrity of the nanotube layer was preserved, and the films exhibited high optical transparency (Figure 1a). XRD analysis confirmed the formation of the anatase phase (Figure 2), while SEM imaging showed well-defined porous structure (Figure 1b). UV-Vis

transmittance measurements indicated excellent transparency, making the films suitable for optoelectronic applications.

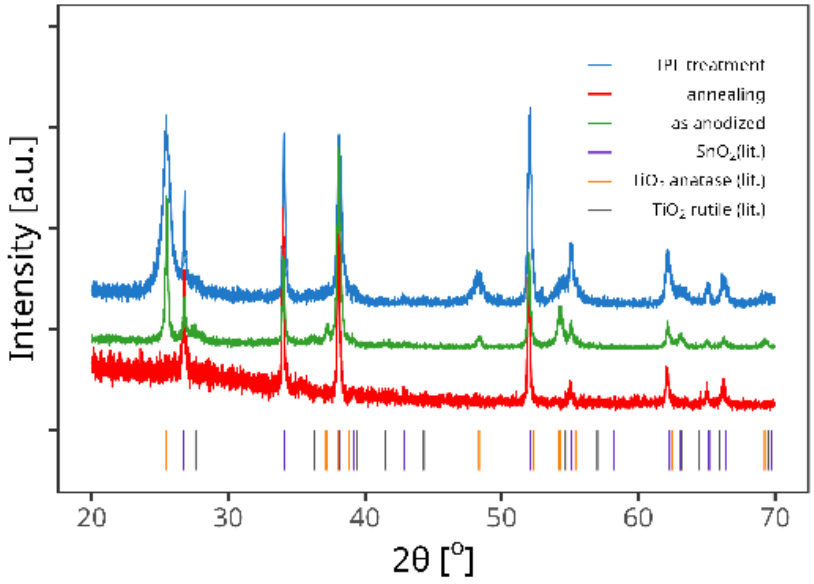


Figure 2 GIXRD of TNT samples: IPL treated, annealed in tube furnace and as anodized. Position of diffraction peaks characteristic for SnO_2, TiO_2 anantase and TiO_2 rutile phase taken from literature are marked below difractograms.

Discussion and Conclusions:

Our findings indicate that the number of pulses and energy must be carefully optimized to prevent damage to the nanotube layer due to excessive pulse energy. Specifically, during the initial stage of IPL processing, a lower pulse energy should be applied, gradually increasing throughout the process. This is essential because the absorption of the nanotube layer is highest at the beginning of the process and continuously decreases as the sample crystallizes. By optimizing the pulse parameters, we achieved controlled crystallization while maintaining the structural integrity of the nanotubes. This method provides a rapid, energy-efficient, and scalable alternative to conventional high-temperature annealing, enabling the fabrication of flexible TiO_2 nanotube-based photoanodes for next-generation flexible solar cells and other optoelectronic applications. Future work will focus on enhancing the functional properties of these films and integrating them into prototype flexible photovoltaic devices.

Acknowledgement:

This research was supported by The Ministry of Science, Education and Youth Croatia, project Novel perovskite solar cells with enhanced performance based on hybrid halide perovskite/transition-metal disulfides nanocomposites (Sol-HP-TMD-NanoComp) and by European Union – NextGenerationEU (KP3-2025).

References:

[1] Bohač M, Čižmar T, Kojić V, Marčec J, Juraić K, Grčić I, et al. Novel, simple and low-cost preparation of Ba-modified TiO2 nanotubes for diclofenac degradation under UV/Vis radiation. Nanomaterials. 2021 Oct 1;11(10).

[2] Mandić V, Plodinec M, Kereković I, Juraić K, Janicki V, Gracin D, et al. Tailoring anatase nanotubes for the photovoltaic device by the anodization process on behalf of microstructural features of titanium thin film. Solar Energy Materials and Solar Cells. 2017 Aug 1;168:136–45.

[3] Juraić K, Plodinec M, Kereković I, Meljanac D, Mandić V, Gracin D, et al. Modelling of simultaneously obtained small and wide angle synchrotron-radiation scattering depth profiles of ordered titania nanotube thin films. Mater Chem Phys. 2020 Jan 15;240.

Type of presentation: Poster

MS6-P-8 Optimizing Photocatalytic Degradation of Pollutants Using Cu-Doped ZnO and TiO_2 Films Grown by ALD

Ivna Kavre Piltaver[a,b], Daria Jardas Babić[a,b], Matejka Podlogar[c], Nik Gračanin[c], Rafaela Radičić[d], Karlo Veličan[a,b], Robert Peter[a,b],

[a]*University of Rijek, Faculty of Physics (Rijeka) Croatia*

[b]*University of Rijeka, Center for Micro- and Nanosciences and Technologies (Rijeka) Croatia*

[c]*Jožef Stefan Institute (Ljubljana) Slovenia*

[d]*Institute for Physics (Zagreb) Croatia*

Contact email: ivna.kavre@uniri.hr

Introduction

Industrial development has significantly contributed to environmental pollution, particularly through the release of organic pollutants into water systems. This has highlighted the urgent need for effective wastewater recycling solutions on a global scale [1]. One promising approach to address this issue is the photocatalytic degradation of pollutants. Photocatalysis involves the use of light energy and semiconductor materials to break down harmful organic pollutants into less toxic by-products, such as carbon dioxide and water [2]. The process begins with light absorption by a semiconductor, which generates free electrons and holes. These excited particles then react with oxygen and water on the surface of the semiconductor, producing highly reactive species like hydroxyl and superoxide radicals. These radicals can effectively oxidize a wide range of pollutants, transforming them into environmentally safe compounds [2]-[3].

Zinc oxide (ZnO) and titanium dioxide (TiO_2) are wide bandgap semiconductor photocatalysts that facilitate photocatalysis under UV light exposure. Current research focuses on modifying the energy bandgap and enhancing visible light absorption, often achieved by doping these semiconductors with transition metal atoms, such as copper [4]. To optimize the photocatalytic activity of Cu-doped thin ZnO and TiO_2 films under visible light, various fabrication techniques have been explored. Among these, atomic layer deposition (ALD) stands out as a promising method for growing semiconductors or insulating thin films, offering precise control over film thickness and deposition on different substrates [5]. The goal of our research is to identify a photocatalyst that exhibits enhanced photocatalytic activity under UV and simulated sunlight irradiation.

Methods

In this study, we employed the atomic layer deposition (ALD) technique to synthesize thin ZnO, TiO_2, and Cu-doped ZnO and TiO_2 films on flat silicon substrates. All films were grown in a Beneq TSF 200 system. Pure ZnO films were deposited at 200°C using diethylzinc (DEZ, $Zn(C_2H_5)_2$) and distilled water (H_2O) as the zinc and oxygen precursors, respectively. Similarly, pure TiO_2 films were grown at 250°C using titanium tetrachloride ($TiCl_4$) and distilled water as the titanium and oxygen precursors. For the Cu-doped ZnO and TiO_2 films, copper (II) acetate ($Cu(OAc)_2$) was used as the copper source, evaporated at 185°C from a hot source into the reaction chamber with nitrogen as the carrier gas.

The influence of Cu dopants on the surface morphology of the samples was investigated using scanning electron microscopy (SEM) and transmission electron microscopy (TEM). Crystallinity was analyzed by grazing incidence X-ray diffraction (GIXRD), while X-ray photoelectron spectroscopy (XPS) was used to determine the chemical state of the Cu atoms. Optical properties were assessed through photoluminescence (PL) measurements, and the electrical properties of the samples were characterized by Hall effect measurements. Finally, the photocatalytic activity was evaluated by measuring the degradation rate of methylene blue (MB) in an aqueous solution under UV and simulated sunlight irradiation.

Results

The ALD synthesis of ZnO and TiO_2 films, employing DEZ, $TiCl_4$, and H_2O as precursors, typically results in polycrystalline films. The size, shape, and crystal orientation of the ZnO and TiO_2 grains are

influenced by various deposition parameters, including temperature, pulsing and purging times of the precursors, and the type of substrate used. Our analysis begins with scanning electron microscopy (SEM) images of undoped and Cu-doped ZnO and TiO_2 films on flat substrates (Fig. 1). The pure ZnO and TiO_2 films exhibit a uniformly covered surface with grains, while the doped films show island-like structures on the surface of the ZnO and TiO_2 films. These islands, as confirmed by transmission electron microscopy (TEM) and energy-dispersive X-ray spectroscopy (EDS) analysis, contain a core of metallic copper, upon which the ZnO or TiO_2 films are deposited. The presence of the metallic copper greatly influences the optical, electrical, and photocatalytic properties of the Cu-doped samples.

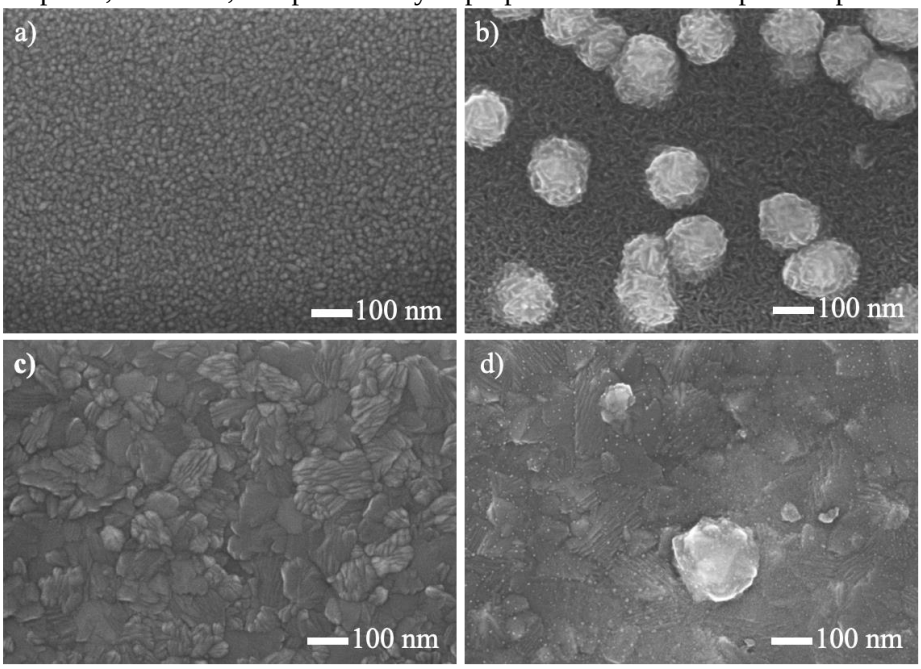


Figure 1: SEM images of ALD grown films: pure ZnO (a), Cu-doped ZnO (b), pure TiO_2 (c) and Cu-doped TiO_2 (d).

Discussion and Conclusion

In summary, we investigated the structural, optical, electrical, and photocatalytic properties of pure ZnO and TiO_2 films, as well as Cu-doped ZnO and TiO_2 films synthesized on flat substrates by ALD. Our results show that Cu-doped ZnO and TiO_2 films exhibit improved optical, electrical, and photocatalytic performance. Specifically, these films demonstrate greater photocatalytic activity under both UV and simulated solar light irradiation compared to pure ZnO and TiO_2 films.

Acknowledgements

The research leading to these results has received funding from the core fundings NPOO.C3.2.R2-I1.06.0083 supported by the European Union NextGenerationEU and project number 23-190 and 23-4 supported by the University of Rijeka.

References:

1. L. Schweityer, J. Noblet, *Green Chem. An Incl. Approach.* **2018**, 261-290.
2. I. Ahmad, Y. Zou, J. Yan, Y. Liu, S. Shukrullah, M. Y. Naz, H. Hussain, W. Q. Khan, N. R. Khalid, *Adv. Colloid Interface Sci*. **2023**, 311, 102830.
3. H. Kisch, Semiconductor Photocatalysis: Principles and Applications, *Wiley-VCH: Weinheim* **2015**.
4. R. Peter, A. Omerzu, I. Kavre Piltaver, R. Speranza, K. Salamon, M. Podlogar, K. Velican, M. Percic, M. Petravic, *Ceram. Int.* **2023**, 49 35229-35238.
5. M. Knez, K. Nielsch, L. Niinisto, *Adv. Mater*. **2007**, 19, 3425–3438.

Type of presentation: Poster

MS6-P-9 Atomic layer deposition of nitrogen-doped TiO_2 thin films for photocatalytic applications

Martina Kocijan[a], Robert Peter[a,b], Iva Šarić Jankovič[a,b], Karlo Veličan[a,b], Ivna Kavre Piltaver[a,b]

[a]*Faculty of Physics, University of Rijeka, Radmile Matejčić 2, 51 000 Rijeka, Croatia*

[b]*Center for Micro- and Nanosciences and Technologies, University of Rijeka, Radmile Matejčić 2, 51000 Rijeka, Croatia*

Contact email: martina.kocijan@uniri.hr

Introduction: The scarcity of freshwater resources represents a critical global challenge. In recent decades, the presence of emerging pollutants, including pharmaceuticals, personal care products, microplastics, and dyes, has raised significant concerns due to their potential risks to both human health and environmental systems. These contaminants are highly harmful due to their high chemical and physical stability, which makes conventional water treatment processes ineffective in their removal. Consequently, their accumulation in aquatic environments continues to increase, highlighting the urgent need for innovative and sustainable remediation strategies. As a promising alternative, photocatalysis has emerged as a highly efficient and sustainable method for the degradation of synthetic dyes and other persistent organic pollutants. Its ability to harness light energy for pollutant breakdown makes it a compelling approach for advanced wastewater treatment and environmental remediation [1].
Titanium dioxide (TiO_2) is widely utilised in photocatalysis applications for wastewater treatment. Investigations have demonstrated that the structure of titanium dioxide significantly contributes to improving micropollutant degradation efficiency. However, pure TiO_2 mainly absorbs UV light, which limits its efficiency under solar irradiation. To extend its photoresponse into the visible light region, various strategies have been explored, including doping with metals or non-metals and coupling with other semiconductors [2]. Non-metal doping, using elements such as carbon, sulphur, phosphorus, and nitrogen, has been shown to suppress the recombination of photogenerated electron-hole pairs, thereby enhancing photocatalytic efficiency. Nitrogen doping is known to induce a red shift in the TiO_2 band gap, enabling visible light absorption and expanding its applicability under solar irradiation.
Indeed, pollutant degradation rates are enhanced when using photocatalysts with highly ordered structures and a high specific surface area, such as thin films prepared by atomic layer deposition (ALD). ALD is a highly effective technique for the controlled synthesis of photocatalysts, allowing for the fabrication of thin films with excellent uniformity, conformality, and atomic-scale precision [3].

Methods: Pure TiO_2 and nitrogen-doped TiO_2 thin films were deposited by ALD on flat silicon wafers. In the thermal ALD process, TiO_2 thin films were deposited using titanium isopropoxide (TTIP) as the metal precursor and water vapour as the co-reactant. For nitrogen doping, ammonia (NH_3) gas was introduced as the nitrogen source during the ALD cycle. Furthermore, all prepared ALD thin films were calcinated at 550 °C. This study examines the impact of synthesis parameters, including substrate temperature and calcination temperature, on the structural, morphological, and photocatalytic properties of nitrogen-doped TiO_2 films. Scanning electron microscopy (SEM) was used to analyse surface morphology, while X-ray photoelectron spectroscopy (XPS) provided insights into the chemical states. The photocatalytic performance was evaluated using methylene blue (MB) as a model pollutant in an aqueous solution under simulated solar irradiation (Ultra Vitalux, 300 W, Osram) in a cylindrical reactor. The photocatalytic activity was monitored by UV-vis spectroscopy.

Results: The XPS spectra provide information on the chemical states of titanium, oxygen, and nitrogen. XPS results confirm the polycrystalline nature of the ALD-grown and calcined pure TiO_2 and nitrogen-doped TiO_2 films. The surface morphology of the pure TiO_2 film and nitrogen-doped TiO_2 film is shown in Fig. 1(a) and (b), respectively. The SEM micrographs indicate that the TiO_2 grains in Fig. 1(b) (nitrogen-doped) are larger than those in the pure TiO_2 film. In contrast, the pure TiO_2 film exhibits smaller and more uniformly distributed grains. This suggests that nitrogen doping influences grain

growth, resulting in a less uniform grain size distribution. Obtained results confirmed incorporation of nitrogen into the TiO_2 lattice, aiming to narrow the band gap and enhance visible-light absorption leading faster degradation of MB from water.

Discussion and conclusions: Comparing the photocatalytic activity of undoped TiO_2 thin films with nitrogen-doped TiO_2 thin films prepared by ALD reveals that nitrogen doping leads to the formation of a well-structured catalyst with significantly higher degradation efficiency, especially after calcination of the thin films. These research findings enhance the degradation efficiency of organic pollutants from water, making N-doped TiO_2 a more effective and sustainable photocatalyst for solar-driven wastewater treatment compared to undoped TiO_2.

Acknowledgment
The research leading to these results has received funding from the core funding NPOO.C3.2.R2-I1.06.0083 supported by the European Union NextGenerationEU.

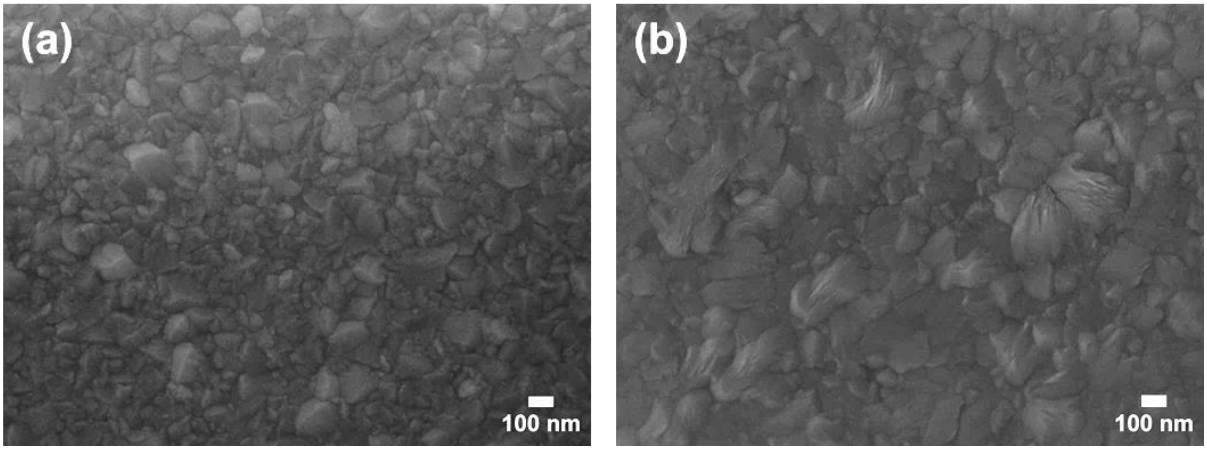


Figure 1: SEM micrographs of (a) pure TiO_2 and (b) nitrogen doped TiO_2 film surfaces.

References:

1. X. Li, *Ecotox. Environ. Safe.* **2024** *278*, 116420.
2. S. Sayegh, et al., *Colloids Surf. A: Physicochem. Eng. Asp.*, **2022**, *655*, 130213.
3. N. K. R. Eswar, et. al., *Mater. Chem. A*, **2019**, *7*, 17703-17734.

Type of presentation: Poster

MS6-P-10 The impact of solvents on the morphology and optical properties of organo-metal thin films

Vedran Kojić[a], Rafaela Kovačević[b], Stjepan Dolić[a], Vlasta Mohaček Grošev[a], Tihana Čižmar[a], Andreja Gajović[a]

[a]*Ruđer Bošković Institute, Zagreb, Croatia*

[b]*Faculty of Chemical Engineering and Technology, Zagreb, Croatia*

Contact email: vkojic@irb.hr

Introduction:
In the last 15 years, the research on organo-metal lead and tin halide perovskites has become a large and fruitful field of photovoltaic research in regards to performance and device stability. The reports of state-of-the-art devices have clocked at 27% efficient perovskite cells [1], while the device stability is still elusive to garner investors in the commercialization of the technology. Although the device efficiencies have shown a steady progress, there is still a significant gap regarding the chemistry of the behaviour of perovskite thin film crystallization in regards to the choice of perovskite anion composition, the choice of solvents and anti-solvents as well as the use of the deposition methods [2]. In the majority of the literature reports, solvent choice is moreover constant while perovskite composition is varied to create the optimal absorber layer thin film. The chemistry of the film crystallization is approached mostly phenomenologically rather than with the full understanding of the influence of above mentioned parameters. Research based on the solvent crystallization characteristics can further improve the knowledge needed to engineer the optimal thin film manufacturing strategy. The purpose of this research is to study the crystallization of methylammonium lead iodide thin films from various concentrations of precursor solutions and solvents and to investigate its impact on the morphology and optical properties of the obtained films.

Methods:
In this work organo-metal lead halide perovskite based on the composition of methylammonium lead iodide thin films were prepared from different pure solvent (DMF or DMSO) with variable perovskite solute concentrations (0.1 M, 0.5 M and 1 M). The films were prepared via dissolving MAI precursor in 1:1 molar ratio inside the PbI_2 solution of the chosen solvent in the above mentioned concentrations, and prepared by spin coating the solution on substrates followed by annealing the obtained films at 150 ^{o}C. Obtained samples were analysed by the means of UV-Vis spectroscopy, profilometry SEM and AFM in order to observe the impact of the pure solvent on the formation of thin films with XRD analysis to confirm the structure.

Results:
The results have shown that thin films prepared from the DMF solvent exhibit a general trend of lower optical transmittance through the concentration ranges and thicker films in comparison to the films prepared from DMSO. DMF films have shown neglectable reflectance while DMSO thin film exhibit an impactful amount of both specular and diffractive reflectance of the incident light. SEM and AFM analysis has shown how the chemistry of the crystal growth results in differently shaped grain sizes of the polycrystalline thin films. Grain size obtained from the DMF solvent results in lager grain size alongside coarser morphology in comparison to films prepared from the DMSO solvent

Discussion and conclusions:
The literature has shown how DMSO can form complex solvent interactions with the perovskite precursors, mainly PbI_2. The formation of the stable intermediary soluble phase then impacts the rate of nucleation and crystallization, delaying the formation of the critical radius in the precipitation phase of the crystallization. Perovskite prepared from DMF, a solvent with lower total solubility of the perovskite precursors, tend to form smaller crystal nuclei earlier than DMSO. However, larger grain size leads to dead space in between grains which increases the amount of defects of the film resulting in high recombination rates of the photo-generated charge carriers. This information can be useful in the

optimization of the choice of perovskite solvents for the thin film preparation enabling cost-effective scalability as well as the method to control the surface of the perovskite morphology for the inevitable passivation strategy for prolonging the stability of the phtotovoltaic devices.

Acknowledgment:
The presented results were obtained within the framework of cooperation between the Government of the Republic of Croatia and the Government of the State of Israel with co-financing from the The Ministry of Science, Education and Youth Croatia, project Novel perovskite solar cells with enhanced performance based on hybrid halide perovskite/transition-metal disulfides nanocomposites (Sol-HP-TMD-NanoComp). The SEM pictures were obtained on the Tescan Vega3 LMU at the Institute of Physics, Zagreb, which is a part of Center of Excellence for Advanced Materials and Sensing Devices, Research unit - Science of Graphene and Related 2D Structures.

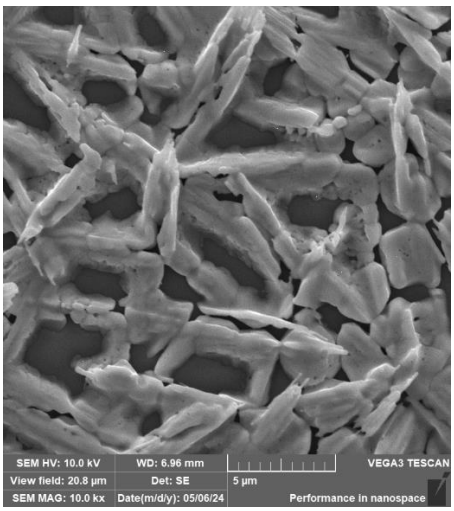


Figure 1: SEM image of the $MAPbI_3$ prepared from the 1M solution in DMF

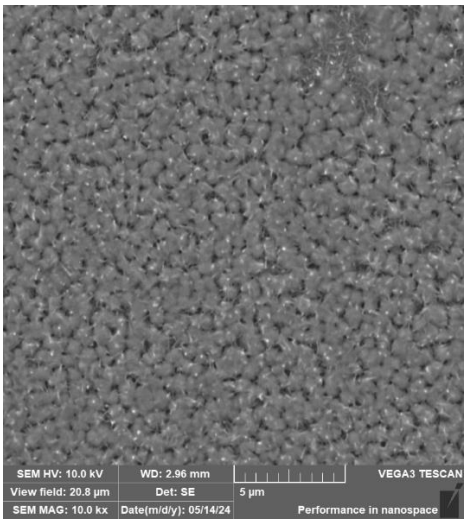


Figure 2: SEM image of the $MAPbI_3$ prepared from the 1M solution in DMSO

References:

1. https://www.nrel.gov/pv/cell-efficiency.html (accessed on 10th of May 2025.)
2. M. Jung, S. Ji, G. Kim, S. Seok, *Chem. Soc. Rev.* **2019**, 48, 2011

Type of presentation: Poster

MS6-P-11 New Genesis XPS Spectrometer at the Jožef Stefan Institute for advanced surface and thin film characterization

Janez Kovač[a], Alenka Vesel[a], Miran Mozetič[a], Rok Zaplotnik[a], Gregor Primc[a], Domen Paul[a], Tatjana Filipič[a], Ingrid Milošev[a], Peter Rodič[a], Ana Kraš[a], Miha Čekada[a]

[a]*Jožef Stefan Institute, Jamova cesta 39, Ljubljana, Slovenia*

Contact email: janez.kovac@ijs.si

Introduction

X-ray Photoelectron Spectroscopy (XPS) is a widely used and well-established technique for surface and thin film analysis. The XPS method provides data on the quantitative elemental chemical composition, identification of chemical and oxidation state, and bonding of elements at surfaces in thin films and multilayered structures. XPS method is based on the photo effect, i.e., the irradiation of the specimen surface by a monochromatic X-ray beam from an anode and subsequent analysis of the photoelectrons emitted from the surface in an ultra-high vacuum.

XPS Genesis spectrometer

At our laboratory, XPS was introduced for the first time in Slovenia in 2005. Due to the growing demand for XPS analysis over the past decade, a new XPS spectrometer was installed in October 2024 at the Jožef Stefan Institute. The new instrument, model Genesis, was manufactured by Physical Electronics, a division of ULVAC-PHI. The acquisition of the new spectrometer was made possible with the support of the Slovenian Research and Innovation Agency (ARIS), as well as the Department of Surface Technology – F4, the Department of Thin Films and Surfaces – F3, and the Department of Physical and Organic Chemistry – K3, all affiliated with the Jožef Stefan Institute.

The Genesis XPS spectrometer is a state-of-the-art scanning X-ray instrument that enables high-resolution XPS analysis with a small analysis spot of 5 microns and an excellent energy resolution of 0.48 eV [1]. It is equipped with a monochromatic Al Kα X-ray source, a 32-channel energy analyzer for photoelectrons, and a monoatomic Ar^+ ion gun for sputtering inorganic materials. For organic materials, it features an Ar-cluster gas cluster ion beam (GCIB) source. Additional capabilities include a Zalar rotation module for high-depth-resolution profiling, an ultraviolet (UV) source for detailed valence band analysis using Ultraviolet Photoelectron Spectroscopy (UPS), angular resolved analyses (AR-XPS), and Low Energy Inverse Photoelectron Spectroscopy (LEIPS). An integrated heating module allows for in situ sample annealing. The system supports automated operation, enabling high-throughput analysis of multiple samples. The primary applications of the XPS spectrometer include surface chemical composition analysis, scanning X-ray imaging - SXI, identification of oxidation states, and depth profiling of elements in thin films. The instrument has a possibility to be upgraded by Cr X-ray source in order to analyse deeper subsurface region of thickness 20 nm in the HAXPES mode.

Applications of Genesis spectrometer

The capabilities of the new instrument will be demonstrated through representative examples, such as the analysis of oxide films, plasma-treated polymers, cellulose, multilayer thin film structures, and corrosion-resistant coatings.

Conclusions

The new research equipment will improve existing analysis methods in Slovenia. It will enable further development of the field of surface and thin film analysis, in which we have a long tradition. The new spectrometer will enable the development of new technologies and materials, and the implementation of basic and applied research.

Acknowledgments

Slovenian Research and Innovation Agency – ARIS co-financed acquisition of the new Genesis instrument through the program "Paket 21" in 2022

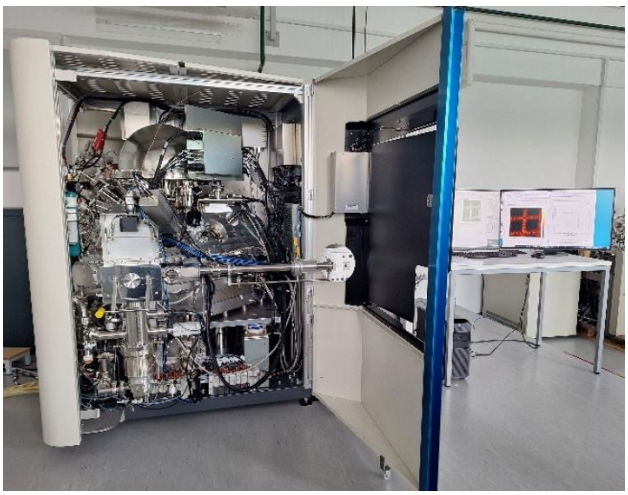


Figure 1: New Genesis XPS spectrometer at Jožef Stefan Institute in Ljubljana, Slovenia

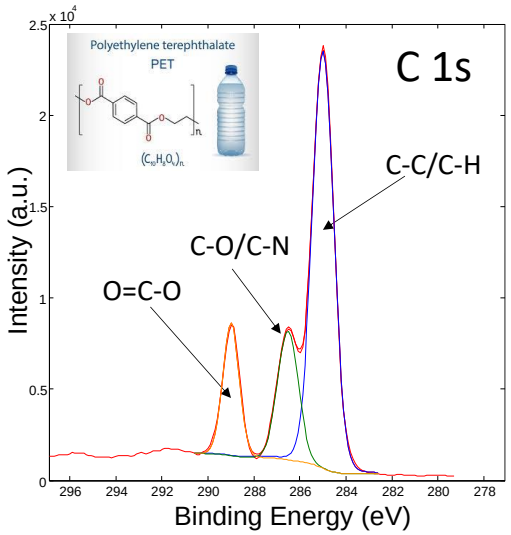


Figure 2: Identification of C-bonds in XPS spectrum C 1s from Poly-ethylene-teraphthalate PET foil

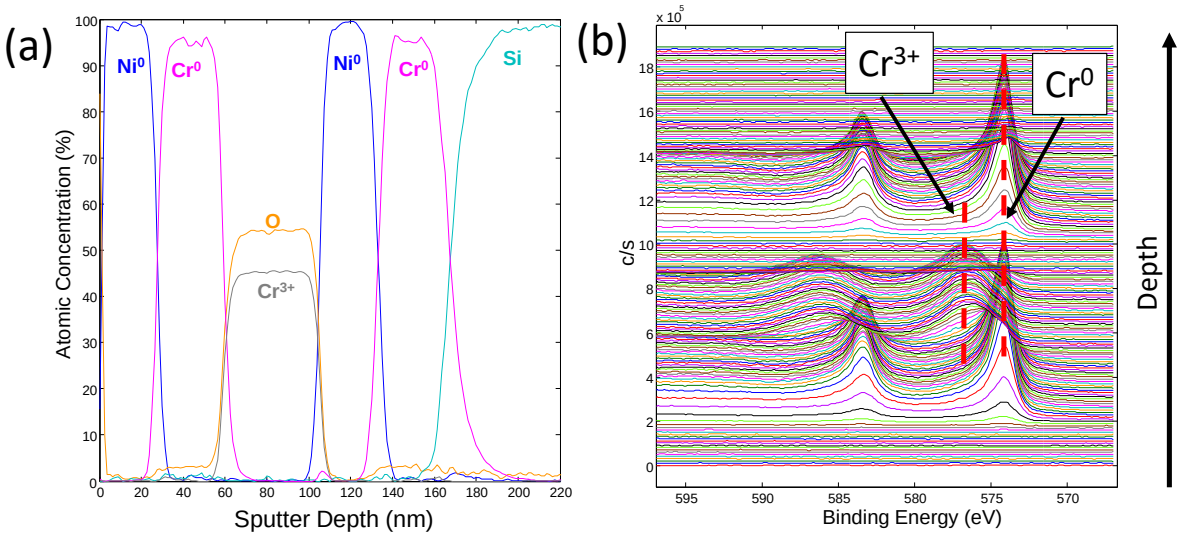


Figure 3: XPS depth profile of multilayer Ni/Cr/Cr_2O_3/Ni/Cr/Si applying Zalar rotation to improve depth resolution at interfaces.

References:

1. https://www.phi.com/surface-analysis-equipment/genesis.html

Type of presentation: Poster

MS6-P-12 In situ TEM dynamics of Au and Au/zirconia clusters in nanostructured thin films: a quantitative analysis

Mattia Lizzano[a], Alberto Casu[b], Filippo Profumo[b], Francesca Borghi[b], Paolo Milani[b], Andrea Falqui[b], Giorgio Divitini[a]

[a]*Istituto Italiano di Tecnologia, (Genova), Italy*

[b]*Università degli Studi di Milano, (Milano), Italy*

Contact email: Mattia.lizzano@iit.it

Introduction

Au clusters can be assembled in thin films with a high density of nano-junctions and grain boundaries that exhibit electrical properties analogous to biological systems (neuromorphic) and thus have a potential to enable next generation computation [1]. While in previous work we demonstrated that *in situ* biasing and heating TEM can be used to observe the rearrangement of the Au clusters directly, here [2] we demonstrate how the addiction of zirconium oxide, co-deposited with Au (Au 85%, Zr 15%) (Figure 1), allows us to tune the properties of the film, and apply a custom-built analysis toolkit developed in python to extract quantitative descriptors and their evolution as a function of temperature.

Methods

Pure gold and gold/zirconia nanostructured thin films were fabricated using Supersonic Cluster Beam Deposition (SCBD) combined with a Pulsed Microplasma Cluster Source (PMCS) and deposited onto a silicon nitride membrane (Protochips Fusion MEMS chip). *In situ* heating TEM was carried out in a Thermo Fisher Spectra 300, equipped with a highly dose-efficient Gatan K3 camera, to maximise temporal resolution while minimising beam-induced effects on the sample. Quantitative data analysis was performed using a custom-developed Python script (https://github.com/Nomeutente1/ClusterSpacingAnalysis)

Results

Changes in thin films include rearrangement of grain/grain interfaces and networked clusters retracting their branches during electrical or thermal stimuli. *In situ* TEM was employed to study the coalescence, or de-percolation, process at the nanoscale. In both films, the initial highly branched and interconnected structure evolves under thermal stimulus by retracting its branches and uncovering the silicon nitride membrane, resulting in a structure with isolated grains (Figure 1).

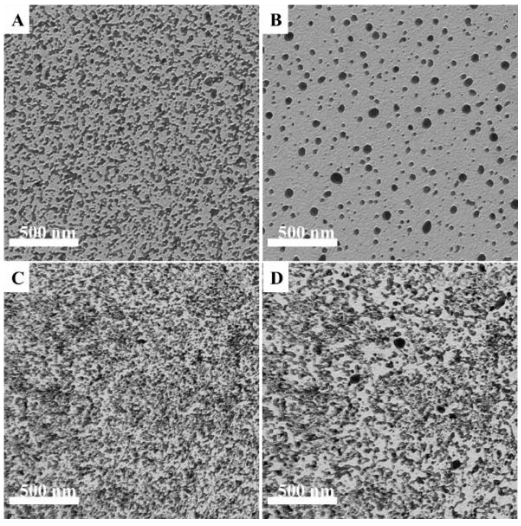


Figure 23: A) Pure gold film at 250 °C. B) Pure gold film at 1000 °C. C) gold/zirconia film at 250 °C and D) gold/zirconia film at 1000 °C.

We developed a python script that processes the TEM time series by extracting four representative frames, corresponding to specific temperatures, binarises them, and calculates the distance between different clusters using two methods: Euclidean Distance (ED) and Nearest Neighbour (NN). The binarisation process is not straightforward due to sample drift induced by the heating of the membrane and the presence of zirconia, which reduces the contrast between the gold clusters and SiN substrate. The first method calculates the ED map of the interstices, then extracts the ridge map and calculates the distribution of the distances thus obtained. The results provide information about how the voids are distributed along the image, which serves as a complementary counterpart to the information about cluster separation. The second method finds the contour of each cluster and calculates the nearest distance between one cluster at a time and its first nearest neighbours (Figure 2).

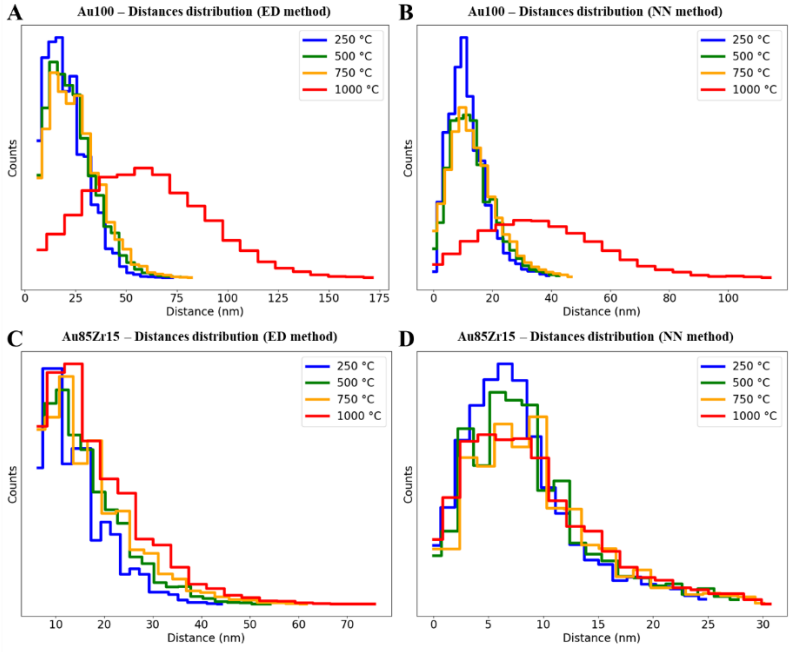


Figure 24: Top: distances distribution for the pure gold film obtained with: A) ED method and B) NN method. Bottom: distances distribution for the gold/zirconia film obtained with: C) ED method and D) NN method.

Regardless of the method used, the results show that gold/zirconia films systematically have a smaller characteristics distance compared to the pure gold films, indicating that zirconia could be used to stabilise the films and delay de-percolation.

Conclusions

Using a specifically built Python script, we were able to estimate the mean distance between the clusters in both the film containing pure gold and the one containing a gold/zirconia composite, as well as their time evolution. The results demonstrated how the distance between clusters changes as a function of temperature. As expected, the clusters uncover the underlying substrate and tend to coalesce, increasing their respective distance. Moreover, the presence of zirconia suggests that it could be used to stabilise the films by impeding the coalescence process, paving a way to finely tuned devices for neuromorphic computation.

References:

1. M. Mirigliano, F. Borghi, A. Podestà, A. Antidormi, L. Colombo, and P. Milani, *Nanoscale Advances*, **2019**, DOI: 10.1039/C9NA00256A
2. A. Casu, C. Melis, G. Divitini, F. Profumo, M. Lizzano, F. Borghi, Y. P. Ivanov, R. Dettori, L. Colombo, P. Milani, and A. Falqui, *ACS Applied Nano Materials* **2025**, DOI: 10.1021/acsanm.4c05993

Type of presentation: Poster

MS6-P-13 Etching and printing of daguerreotypes: experimental reconstruction and microscopic analysis of first photomechanical reproduction processes

Zuzana Šupolová[a,b], Soňa Borovská[a,b], Valentina Ljubic Tobisch[a], Janka Blaško Križanová[b], Wolfgang Kautek[c]

[a]*TU Wien, X-Ray Center, Vienna, Austria*

[b]*Academy of Fine Arts and Design in Bratislava, Department of Conservation and Restoration, Bratislava, Slovakia*

[c]*University of Vienna, Department of Physical Chemistry, Vienna, Austria*

Contact email: valentina.tobisch@tuwien.ac.at

Keyword: Daguerreotype etching, Ag-Hg nanoparticles, photomechanical reproduction, SEM/EDX, light microscopy

Introduction:
Two pioneering techniques emerged in the late 1830s that profoundly shaped the development of graphic arts and image reproduction: electrotyping, invented by Moritz Hermann von Jacobi in 1838 [1], and photography, introduced by Louis Jacques Mandé Daguerre in 1839 [2]. Their combination enabled the advent of photomechanical and photochemical reproduction processes, revolutionising photography and mass image production [3–5]. In Vienna, Joseph Berres and his contemporaries were among the first to investigate the use of daguerreotypes as printing plates. By the early 1840s, they succeeded in producing prints either through direct etching or via galvanoplastic replication [5].
This study investigates the material and structural aspects of chemically etched daguerreotype plates used in these early photomechanical reproduction techniques. Through the reconstruction of 19th-century processes, we aim to better understand how daguerreotypes were transformed into printing matrices and how surface morphology influenced print quality and durability.

Methods:
Contemporary daguerreotype plates were fabricated using historically accurate materials and methods. Chemical etching was applied under controlled conditions to create intaglio surfaces. These etched plates were analysed using optical microscopy, digital 3D microscopy, and scanning electron microscopy (SEM) combined with energy-dispersive X-ray spectroscopy (EDX), in order to assess etching depth, surface topography, and nanoparticle distribution. The resulting prints were examined under magnification to correlate surface characteristics with print quality.

Results:
Microscopy revealed that Ag-Hg amalgam nanoparticles, primarily concentrated in highlight areas, provided surface protection and hindered etching. In contrast, midtone and shadow regions, where such particles were sparse or absent, underwent significant etching. SEM and 3D imaging confirmed the formation of microcavities in etched areas capable of ink retention. The morphology of these cavities was directly influenced by the type and concentration of the etching media.

Discussion and conclusions:
This study demonstrates the significant influence of image-forming nanoparticles on the etching behaviour of daguerreotype plates. The protective Ag-Hg layer in highlight zones accounts for selective etching patterns and the tonal gradation observed in the resulting prints. Microscopic analysis proved essential for evaluating the functional transformation of daguerreotypes into printable matrices. These insights contribute to a more precise identification and understanding of early photomechanical prints derived from etched daguerreotypes.

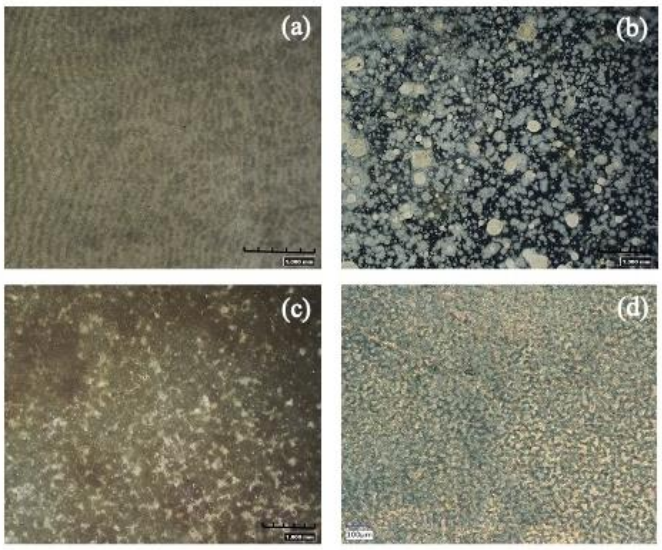


Figure 25: Optical micrographs of the etched plates. (a) Optical micrograph of the etched plate using concentrated nitric acid, (b) Optical micrograph of the etched plate using vapors of nitric acid, (c) Optical micrograph of the etched plate using 20% nitric acid (d) Optical micrograph of the historical etched daguerreotype plate "Venice as it was", Vienna, 1844, by J. Berres, J. Axmann and F. Theyer.

Acknowledgements:
The research was conducted within the Heritage Science Austria project *PHELETYPIA* [6], supported by TU Wien in collaboration with Academy of Fine Arts and Design in Bratislava and University of Vienna. Special thanks to all institutions and partners involved in the experimental work and scientific imaging.

References:
1. M. H. von Jacobi, *Die Galvanoplastik : oder das Verfahren cohärentes Kupfer in Platten oder nach sonst gegebenen Formen, unmittelbar aus Kupferauflösungen, auf galvanischem Wege zu produciren ; nach dem auf Befehl des Gouvernements in russischer Sprache bekannt gemachten Originale*, Petersburg, **1840**.
2. L. J. M. Daguerre, *Historique et Description des Procedes du Daguerreotype et du Diormama*, Paris, **1839**.
3. P. Trnkova, The Unbearable (and Irresistible) Charm of "Duplicates.", *Photo-Objects Mater. Photogr. Photo Arch*, Berlin, **2019**.
4. M. Jürgens, I. Vasallos, L. Fernandes, *The Rijksmuseum Bulletin.* **2018**, *66*, 144–169.
5. V. Ljubić Tobisch & W. Kautek, *ChemPlusChem*, **2019**, *84*, 1730–1738.
6. Project PHELETYPIA, "The impact of early photography and electrotyping media on the creation of images and contemporary art", Heritage 2020-060 PHELETYPIA, Heritage Science Austria grant program of the Austrian Academy of Sciences.

Type of presentation: Poster

MS6-P-14 Nanoscale investigation of degradation processes in historical daguerreotype plates

Soňa Borovská[a,b], Zuzana Šupolová[a,b], Valentina Ljubic Tobisch[a], Janka Blaško Križanová[b], Wolfgang Kautek[c]

[a]*TU Wien, X-Ray Center, Vienna, Austria*

[b]*Academy of Fine Arts and Design in Bratislava, Department of Conservation and Restoration, Bratislava, Slovakia*

[c]*University of Vienna, Department of Physical Chemistry, Vienna, Austria*

Contact email: valentina.tobisch@tuwien.ac.at

Keyword: Daguerreotype degradation, corrosion mapping, SEM-EDX, photographic conservation, Ag-Hg nanoparticles

Introduction:
The daguerreotype, introduced by Louis Jacques Mandé Daguerre in 1839, was the first commercially successful photographic process and represents a major cultural and technological achievement [1]. Daguerreotypes are unique images formed on silver-plated copper plates sensitized with halogens, producing Ag-Hg amalgam nanoparticles. Over time, these delicate surfaces undergo various degradation phenomena that affect both structural integrity and visual quality [2–4]. Understanding these processes at the nanoscale is essential for developing effective conservation strategies [5–6]. This study investigates degradation features on historical daguerreotype plates from diverse provenances and conservation histories.

Methods:
During this study, multiple historical daguerreotype plates were analysed. The daguerreotypes exhibited diverse stated of degradation, including corrosion, nanoparticle alternation, delamination and effects from previous cleaning interventions. The plates originated from different environments and were housed under varying conditions. Analytical techniques included scanning electron microscopy (SEM) with energy-dispersive X-ray spectroscopy (EDX), micro X-ray fluorescence (μXRF) and optical microscopy, allowing detailed characterization of surface morphology, elemental composition, and corrosion products.

Results:
SEM and μXRF analyses revealed heterogeneous corrosion patterns, including localized degradation caused by leaching from deteriorated cover glasses. Plates that had undergone previous cleaning showed altered surface chemistry and increased vulnerability to further degradation. Comparison between housed and unhoused specimens demonstrated the protective role of original framing. Elemental mapping also showed migration and redistribution of Ag and Hg nanoparticles, with delamination observed in severely degraded zones.

Discussion and conclusions:
Nanoscale insights from multimodal microscopy highlight the complex interaction between original material composition, environmental exposure, and past conservation interventions. These findings stress the importance of conservation approaches that account for both original manufacturing techniques and subsequent handling. Future research will focus on non-invasive diagnostic tools and refined preservation strategies based on a deeper understanding of daguerreotype degradation mechanisms.

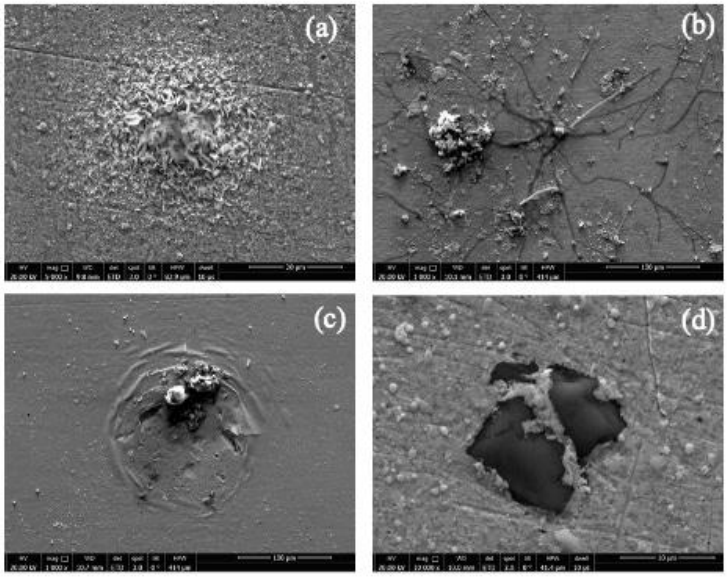


Figure 26: SEM micrographs of degradation features on the daguerreotype surface. (a) SEM micrograph of "Daguerreian measle", degradation product related to previous cleaning attempts, (b) SEM micrograph of mold growth on the surface, (c) SEM micrograph of the degradation inducted by glass corrosion droplet, (d) SEM micrograph of the residue from the polishing process.

Acknowledgements:
The research was conducted within the Heritage Science Austria project *PHELETYPIA* [5], supported by TU Wien in collaboration with Academy of Fine Arts and Design in Bratislava and University of Vienna. Special thanks to all institutions and partners involved in the experimental work and scientific imaging.

References:
1. L. J. M. Daguerre, *Historique et Description des Procedes du Daguerreotype et du Diormama*,Paris, **1839**.
2. A. E. Schlather, P. Gieri, M. Robinson, S. A. Centeno, and A. Manjavacas, "Nineteenth-century nanotechnology: The plasmonic properties of daguerreotypes," *Proc Natl Acad Sci U S A*, **2019**, *116*, 13791–13798.
3. D. Q. Balbas, B. Cattaneo, R. Fontana, J. Striova, A. Cagnini, P. Belluzzo, S. Rossi, *Sensors*, **2023**, *23*, 1-15.
4. V. Ljubić Tobisch, K. Hradil, K. Whitmore, C. Streli, P. Wobrauschek, W. Kautek, *J. Cult. Herit.*, **2024**, *70*, 223–230.
5. P. Ravines, R. Wiegandt, C. M. Wichern, *Surface Engineering*, **2007**, *24*, 138-146.
6. E. Da Silva, M. Robinson, C. Evans, A. Pejović-Milić, D. V. Heyd, *J. Anal. At. Spectrom.*, **2010**, *25*, 654–661.
6. Project PHELETYPIA, "The impact of early photography and electrotyping media on the creation of images and contemporary art", Heritage 2020-060 PHELETYPIA, Heritage Science Austria grant program of the Austrian Academy of Sciences.

Type of presentation: Poster

MS6-P-15 Microstructural characterisation of sodium alginate coatings with addition of essential oils for antimicrobial protection of steel

Tomasz Moskalewicz[a], Tomasz Cudak[a], Aleksandra Fiołek[a]

[a]*AGH University of Krakow, Faculty of Metals Engineering and Industrial Computer Science, Poland*

Contact email: tmoskale@agh.edu.pl

Introduction

Austenitic stainless steel is the biomaterial of choice for temporary bone implants in orthopedic. One of the main disadvantages of steel is its susceptibility to the formation of bacterial biofilm on the surface of the implant and associated peri-implant infections [1]. The inhibition of biofilm formation can be achieved by antimicrobial coatings. Sodium alginate, a polysaccharide derived from brown algae, is one of the most promising polymers for the natural antimicrobial coating matrix. Essential oils (EOs), including thyme and cinnamon oils, are very promising coating components of natural origin with outstanding antimicrobial properties [2]. In this work, sodium alginate coatings with the addition of various essential oils were developed by electrophoretic deposition (EPD) on chemically treated stainless steel substrates. The aim of the work was to investigate the EPD route to obtain composite costings with high adhesion to the steel substrate as well as to characterize their morphology and microstructure.

Methods

Sodium alginate, thyme essential oil (TEO), cinnamon leaf (CLEO) and cinnamon bark (CBEO) essential oils, and hydrophilic non-ionic surfactant Tween 80 were used as coating components. The alginate solution and the chemical treatment of the substrates were prepared according to the procedure described in our previous work [3]. A specific EO (2 ml/l) alone and with Tween 80 (ratio 1:1) was added to the sodium alginate solution and homogenized at 20000 rpm for 6 minutes. Single-layer EO/sodium alginate coatings and double-layer coatings, consisting of an inner sodium alginate layer and an outer sodium alginate layer incorporated in the EO, were deposited on AISI 316L austenitic stainless steel substrates by EPD at a constant current voltage of 5 V during 1 and 2 minutes, respectively. The surface morphology of the coatings was investigated using FEI Inspect S50 and FEI Nova NanoSEM 450 scanning electron microscopes (SEM). The coating microstructure was investigated using a JEOL JEM-ARM200F NEOARMex transmission electron microscope (TEM). The lamellae from the cross-section of coatings for TEM investigations were prepared by the focused ion beam (FIB) technique using a Quanta 3D 200i FIB/SEM dual beam microscope. The adhesion strength of the coatings was investigated using the tape test method in accordance with ASTM D3359-23 (method B). The surface of the samples after testing was investigated using SEM.

Results

All single-layer EO/sodium alginate coatings and double-layer coatings were deposited similarly on chemically etched steel substrates, with the same EPD parameters including the deposition of an intermediate sodium alginate layer and an outer oil-enriched sodium alginate layer. They were macroscopically homogeneous and had a similar appearance. The relatively uniform distribution of oil droplets with size up to 5 μm embedded in sodium alginate occurred on the surface of the coatings. However, the oil droplets were better visible on the surface of the single-layer coatings. For example, in the coating containing CLEO obtained from the mixture without Tween 80 its size was up to 8 μm. TEM investigations of the coatings with CLEO and CBEO in the cross section showed that smaller droplets with a size of about 100 nm also occurred in the sodium alginate matrix. The addition of Tween 80 to the emulsion used for EPD contributed to the fragmentation of droplets and developed a nanoemulsion. Much smaller oil droplets with nanometric size were observed in the double-layer coatings containing CLEO and CBEO obtained from the nanoemulsion. Coatings with thickness up to 1 μm containing oil droplets distributed throughout the cross section, although the inner sodium alginate

layer was first deposited. This may be the result of the diffusion and gravitational movement of oil droplets in sodium alginate, which are characterized by a lower density. In the investigated area of the coating, droplets with a size of about 200 nm and less than 100 nm were present in the near surface area and in the area of the coating adjacent to the substrate (Fig. 1). In the middle of the coatings, holes were observed. They were probably the result of droplets falling or degradation of the polymer during FIB preparation.

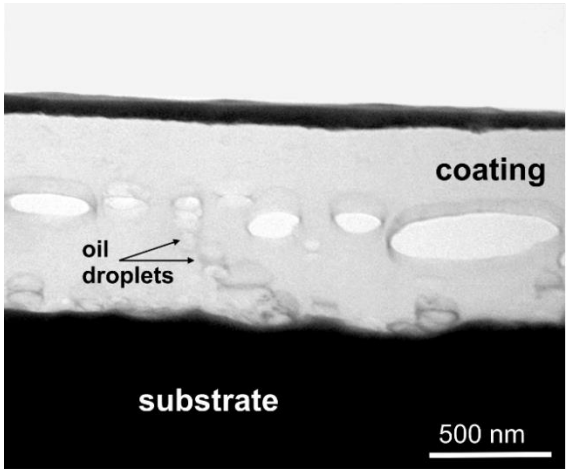


Figure 1: Annular bright field (ABF) STEM micrograph of the nCBEO/SA//SA coating obtained during two-stage EPD on an etched steel substrate

All double-layer coatings were detected to have high adhesion (class 4B) to chemically treated steel substrates, much higher than single-layer coatings. The SEM investigation of the coated steel surface after tape tests did not show any delamination of the double-layer coatings.

Discussion and conclusions

A hybrid approach that combines chemical treatment of steel and the deposition of composite coatings in a two-stage EPD process allowed the obtaining of robust coatings with high adhesion to the substrates. The adhesion strength of the double-layer coatings was enhanced by eliminating direct contact between droplets and the surface of the substrate. In addition, the addition of Tween 80 surfactant to the emulsions used for EPD resulted in the fragmentation of oil droplets and further increased their adhesion strength. The microstructure of the coatings consisted of oil droplets embedded in a sodium alginate matrix. As a result of the gravitational fall of the oil in the polymer matrix, the droplets occurred on the entire cross-section of the coatings. The introduction of Tween 80 into the emulsion used for deposition reduced the size of oil droplets in the coatings.

The coatings are important for the development of antimicrobial protection of stainless steel used for temporary bone implants. Further characterization of the electrochemical corrosion resistance, antibacterial properties and cytotoxicity of biomaterials is in progress.

Acknowledgments

This research was funded in whole by the National Science Centre, Poland [DEC-2022/45/B/ST5/00242].

References:

1. L. Kadirvelu, S.S. Sivaramalingam, D. Jothivel, D.D. Chithiraiselvan, D.K. Govindarajan, K. Kandaswamy, *Curr. Res. Microb. Sci.*, **2024**, 6, 100231.
2. C. Shu, L. Ge, Z. Li, B. Chen, S. Liao, L. Lu, Q. Wu, X. Jiang, Y. An, Z. Wang, M. Qu, *Front. Pharmacol.* **2024**, 15, 1378434.
3. T. Moskalewicz, M. Warcaba, Ł. Cieniek, M. Sitarz, M. Gajewska, A.R. Boccaccini, *Appl. Surf. Sci.* **2021**, 540, 148353.

Type of presentation: Poster

MS6-P-16 Microscopical study of 19th century photomechanical prints: in-situ investigations in museum collections

Valentina Ljubic Tobisch[a], Leon Ploszczanski[b], Wolfgang Kautek[c]

[a] *TU Wien, X-Ray Center, Vienna, Austria*

[b] *BOKU University, Institute of Physics and Materials Science, Vienna, Austria*

[c] *University of Vienna, Department of Physical Chemistry, Vienna, Austria*

Contact email: leon.ploszczanski@boku.ac.at

Introduction:
Shortly after the announcement of the photographic process in 1839, Viennese anatomy professor Joseph Berres (1796-1844) and engraver Josef Axmann (1793-1873) developed one of the first photomechanical printing techniques, later known as the Viennese method[1]. Although these prints mark a key moment in the transition from photography to print reproduction, their identification remains a challenge due to the lack of technical documentation and surface analysis[2]. This study aims to raise awareness of the need for reliable identification and preservation strategies for these historically significant objects.

Methods:
Photomechanical prints attributed to Berres[3] and Axmann from the early 1840s were examined in situ in two institutions: the Moravian Gallery in Brno and the Albertina in Vienna. Due to the fragility and value of the originals, samples could not be removed from the collections. Surface characterisation was carried out using a Keyence VHX-5000 digital microscope under varying magnifications and lighting conditions. No sample preparation was performed to preserve the original condition of the prints.

Results:
Microscopical imaging revealed fine etched structures and irregular ink distribution patterns characteristic of early photomechanical processes. Distinct morphological features, such as partially visible etching lines and tonal gradations produced by varying ink depth, were identified. Historically, Berres is considered the inventor of the etching technique for Daguerreotypes, yet his etched plates proved to be technically insufficient: the etching depth was too shallow, and the detail resolution too low. Moreover, the original photographic images often lacked depth of field and sharp outlines, which further reduced the effectiveness of the etching process. As a result, Axmann had to undertake extensive manual retouching of the plates to achieve printable quality. Given the extremely high standards of 19th-century printmaking, both aimed to deliver visually refined results — but never revealed the exact technical details of their process.

Discussion and conclusions:
This study presents the first detailed microscopical documentation of prints made using the Viennese method. The findings not only contribute to the technical understanding of early photomechanical printing but also provide a foundation for the development of identification criteria for similar prints in other collections. Future work will aim to compare these results with other early photomechanical techniques and to further develop non-invasive methods for analysing photographic heritage materials.

Acknowledgments:
This research was funded by the Heritage Science Austria funding programme of the Austrian Academy of Sciences as part of the PHELETYPIA project[4] and supported by the BOKU University of Vienna.

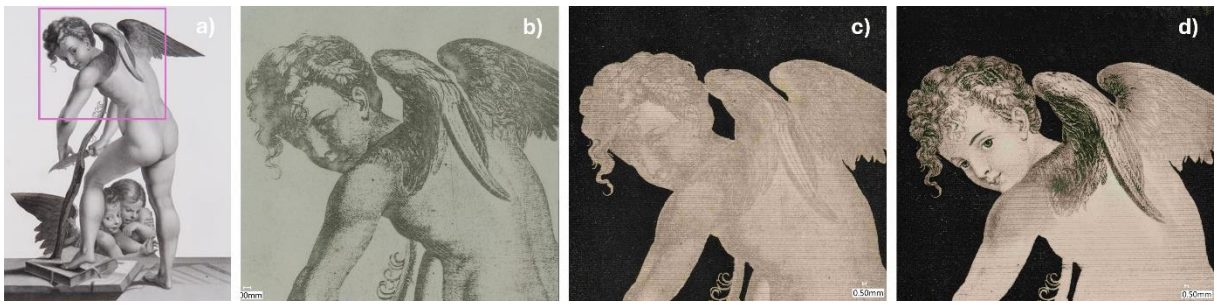


Figure 1: Cupid carving a bow. a) Engraving after the painting by Parmigianino in the Kunsthistorisches Museum by Paul Gleditsch, Moravian Gallery in Brno (MM 649); b) Print from etched daguerreotype by Joseph Berres, Albertina, Vienna, 1840 (FotoGLV2000/1718); c) print of etched daguerreotype by Josef Axmann, Moravian Gallery in Brno, (C 2486); d) print of daguerreotype, by Josef Axmann, print of etched daguerreotype, Moravian Gallery in Brno, (C 2485).

References:

1. V. Ljubić Tobisch and W. Kautek, Chempluschem **84**, 1730 (2019).
2. P. Trnkova, in *Photo-Objects Mater. Photogr. Photo Arch.*, edited by J. Bärnighausen, C. Caraffa, S. Klamm, F. Schneider, and P. Wodtke (Berlin, 2019), pp. 245–250.
3. M. Jürgens, I. Vasallos, and L. Fernandes, Rijksmus. Bull. **66**, 144 (2018).
4. V. Ljubic Tobisch, A. Artaker, and W. Kautek, Proj. PHELETYPIA “The Impact Early Photogr. Electrotyping Media Creat. Images Contemp. Art" (Heritage 2020-060 PHELETYPIA) by Herit. Sci. Austria Grant Progr. Austrian Acad. Sci. (2023).

Type of presentation: Poster

MS6-P-17 Microscopic Identification of Daguerreotypes Through Hallmark Analysis

Soňa Borovská[a,b], Zuzana Šupolová[a,b], Leon Ploszczanski[d], Janka Blaško Križanová[b], Wolfgang Kautek[c], Valentina Ljubic Tobisch[a]

[a]*TU Wien, X-Ray Center, Vienna, Austria*

[b]*Academy of Fine Arts and Design in Bratislava, Department of Conservation and Restoration, Bratislava, Slovakia*

[c]*University of Vienna, Department of Physical Chemistry, Vienna, Austria*

[d]*Boku University, Institute of Physics and Materials Science, Vienna, Austria*

Contact email: leon.ploszczanski@boku.ac.at

Keyword: Daguerreotypes, hallmark, optical microscopy, profilometry, photography

Introduction:
Daguerreotypes are historically significant photographic objects characterized by their unique image-forming process on silver-plated copper plates. [1] Daguerreotype plates often bear small hallmarks stamped into the metal surface, typically indicating information about the manufacturer, silver purity, or origin. [2] Their identification can be challenging, often overlooked and undocumented due to their microscopic scale, corrosion-related degradation, abrasion, or incomplete impressions. [3-4] This study explores the possibilities of non-invasive imaging techniques, especially optical microscopy and surface profilometry, for locating, documenting and analysing hallmarks on historical daguerreotype plates.

Methods:
A selection of historical daguerreotypes from various European collections was examined. Plates varied in format, condition and geographical origin. Optical microscopy using a Keyence VHX-5000 digital microscope, combined with various lighting techniques, was used to locate and enhance the visibility of hallmarks, particularly those in a deterioration condition. 3D surface profilometry was then applied to map the depth and surface deformation of selected imprints. Identified marks were compared against hallmark reference databases to support attribution and dating.

Results:
Optical microscopy enabled the identification of multiple hallmarks, including heavily worn or partially present silver standard marks and pictograms. By employing high-resolution surface profilometry, it was possible to generate detailed topographic maps of the imprints. This made it possible to distinguish between mechanically struck hallmarks and those that had been either lightly impressed or eroded over time. These analyses offered valuable insights into the objects' manufacturing techniques and historical trajectories, but it is also placing the findings within a wider international context of research into hallmarking practices tracing the provenance of silver artifacts beyond their current locations.

Discussion and conclusions:
The integration of optical microscopy and profilometry offers a non-invasive and useful approach to the study of daguerreotype hallmarks. These techniques revealed previously undocumented or overlooked features and supported object-level attribution through material and typological analysis. By recovering obscured or partial marks, the method enabled more accurate identification and enhanced curatorial documentation. Beyond its immediate application, this research contributes to international efforts in the preservation and interpretation of photographic heritage, offering valuable insights for fields of conservation science, art history and museum practice.

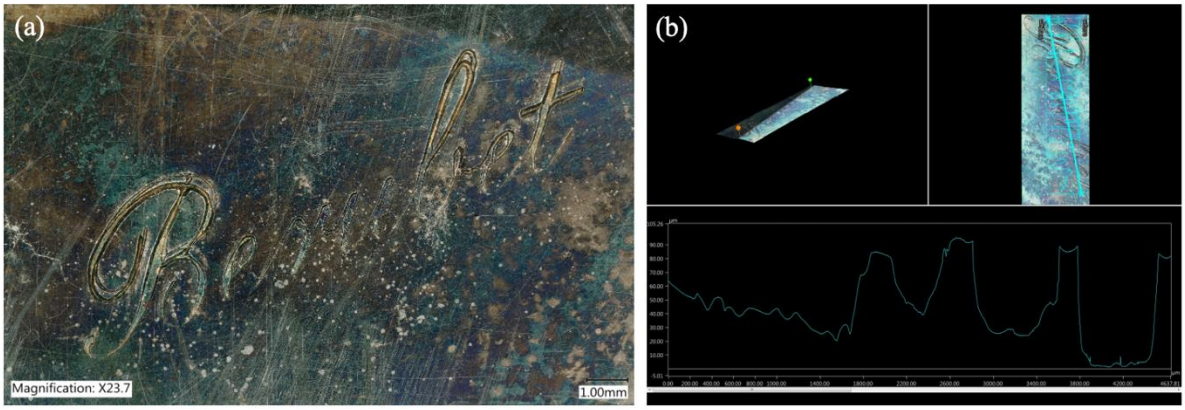


Figure 1: Hallmark on the historical daguerreotype plate. (a) Optical microscopy image showing a hallmark attributed to a French daguerreotypist, (b) 3D surface profilometry revealing the depth profile and topographical structure of the hallmark.

Acknowledgements:
The research was conducted within the Heritage Science Austria project *PHELETYPIA* [5], supported by TU Wien in collaboration with Academy of Fine Arts and Design in Bratislava and University of Vienna. Special thanks to all institutions and partners involved in the experimental work and scientific imaging.

References:

1. L. J. M. Daguerre, *Historique et Description des Procedes du Daguerreotype et du Diormama*,Paris, **1839**.
2. V. Ljubić Tobisch, K. Hradil, K. Whitmore, C. Streli, P. Wobrauschek, W. Kautek, *J. Cult. Heritage*, **2024**, 70, 223-230
3. G. Chiesa, P. Gosio, *Daguerreotype hallmarks*, **2020**, 1-112
4. S. Barrio, L. Alba, C. M. Prieto, *Journal of Cultural Heritage*, **2024**, *66*, 1-38.
5. Project PHELETYPIA, "The impact of early photography and electrotyping media on the creation of images and contemporary art". Heritage 2020-060 PHELETYPIA, Heritage Science Austria grant program of the Austrian Academy of Sciences.

Type of presentation: Poster

MS6-P-18 Characterization of ZnO Films Prepared via FIB-SEM

Klara Laura Konda[a], Tina Radošević[a], Nik Gračanin[a], Damjan Vengust[a], Matejka Podlogar[a]

[1] *Jožef Stefan Institute, Ljubljana, Slovenia*

Contact email: matejka.podlogar@ijs.si

Zinc oxide (ZnO) typically crystallizes in the stable wurtzite phase; however, at the nanoscale, a coexistence of wurtzite and zinc blende structures is often reported. We synthesized ZnO nanorod arrays via hydrothermal growth at 90 °C from aqueous solution of zinc nitrate, producing vertically aligned nanorods on glass substrates. X-ray diffraction and Raman spectroscopy confirmed a dominant wurtzite structure. Interestingly, post-synthesis annealing, which is supposed to improve the stability and crystallinity of ZnO, revealed, through local structural analysis, a coexistence of the cubic zinc blende polymorph, which increased in content with higher annealing temperatures. Notably, the samples containing mixed phases exhibited enhanced photocatalytic activity in degrading a model water pollutant, namely caffeine, compared to pure wurtzite.

For detailed structural characterization of such sample using transmission electron microscopy (TEM), conventional sample preparation proved challenging due to the nanorods' variable thickness. To overcome this, we employed focused ion beam (FIB) milling to extract and thin selected regions of the ZnO nanorod arrays for TEM analysis. We pinpointed the region of interest, covered the in-between nanorod empty space with electronic and ionic platinum, and extracted arrays from a 2x10 μm area for further etching. The thin enough sample was subsequently characterized with TEM. Complementary SEM, XRD, and Raman studies further elucidated the role of polytypism in tailoring ZnO nanostructures for photocatalytic applications.

Type of presentation: Poster

MS6-P-19 Compositionally Graded Kesterite Nanostructured Film for Photovoltaic Applications

Bogdan Stefan Vasile[a,b,c], Iulian Boerasu[a,c], Adrian Vasile Surdu[d], Roxana Doina Trusca[c], Ovidiu Cristian Oprea[b,c]

[a]*Advanced Research Center for Innovative Materials, Products and Processes, National Polytechnic University of Science and Technology of Bucharest, Romania*

[b]*Romanian Academy of Scientists, Bucharest, Romania*

[c]*National Research Center for Micro and Nanomaterials, Faculty of Applied Chemistry and Materials Science, National Polytechnic University of Science and Technology of Bucharest, Romania*

[d]*Department of Materials Science, Faculty of Materials Science and Engineering, Transilvania University of Brasov, Romania*

Contact email: boogdan.vasile@upb.ro

Introduction. Due to the high production cost per watt of crystalline Si photovoltaics, it is essential to explore stable, cost-efficient, and environmentally friendly alternatives such as CZTS kesterite-based solar cells. The purpose of this research is to enhance the optical and photoelectrical properties of high-quality Cu_2ZnSnS_4 (CZTS) absorbers by adjusting the Cu/(Zn+Sn) ratio through implying a continuously compositional gradient (CCG) across the layer thickness. The targeted main feature of this approach consist into engineering the absorber's energy bandgap to achieve a graded bandgap solar cell.

Methods. X-ray diffraction (XRD) was used to determine the crystalline phase, while scanning electron microscopy (SEM) examined the top and cross-section morphology of the samples. UV-VIS spectroscopy analyzed optical absorption properties, and Rietveld refinement was applied to evaluate crystallinity and crystallite size. Three CZTS compositions were synthesized using an environmentally friendly technique: C0 (stoichiometric), C1 (Zn/Sn = 0.9), and C2 (Zn/Sn = 0.8). The CCG structure was obtained by sequentially depositing three layers of each composition onto Mo-coated soda-lime glass (Mo-SLG) substrates. The solution was spin-coated at 3000 rpm for 30s, followed by two-step pyrolysis in air at 160°C and 400°C. The final structure was crystallized by thermal annealing at 400°C in an Ar atmosphere.

Results. XRD confirmed the presence of a pure kesterite phase. Rietveld refinement showed that crystallinity increased as the concentration gradient decreased, while the average crystallite diameter was nearly halved compared to the stoichiometric sample. SEM (Figure 1) images indicated uniform, fully covering layers with no pinholes or cracks, and a final CCG structure thickness of 542 nm. Cross-sectional SEM analysis showed an increase in film thickness from 359 nm to 542 nm as the Cu/(Zn+Sn) ratio decreased. UV-VIS spectroscopy revealed strong visible-range absorbance, with a weaker band around 260 nm in the UV range. The extended absorption beyond 800 nm suggested the potential for infrared radiation absorption, with applications in low-energy-consumption windows and solar energy devices.

Discussion and Conclusions. The study demonstrated that a CZTS absorber with a compositional gradient can be successfully fabricated, influencing structural, morphological, and optical properties. As the Cu/(Zn+Sn) ratio decreased, crystallinity improved, and crystallite size reduced. The uniform layer coverage, strong absorption in the visible range, and extended infrared absorption suggest CZTS as a promising material for solar energy applications. This research supports the feasibility of bandgap engineering in CZTS absorbers, contributing to the development of cost-effective, high-efficiency photovoltaic technologies. Future work will focus on optimizing deposition parameters to enhance solar cell performance.

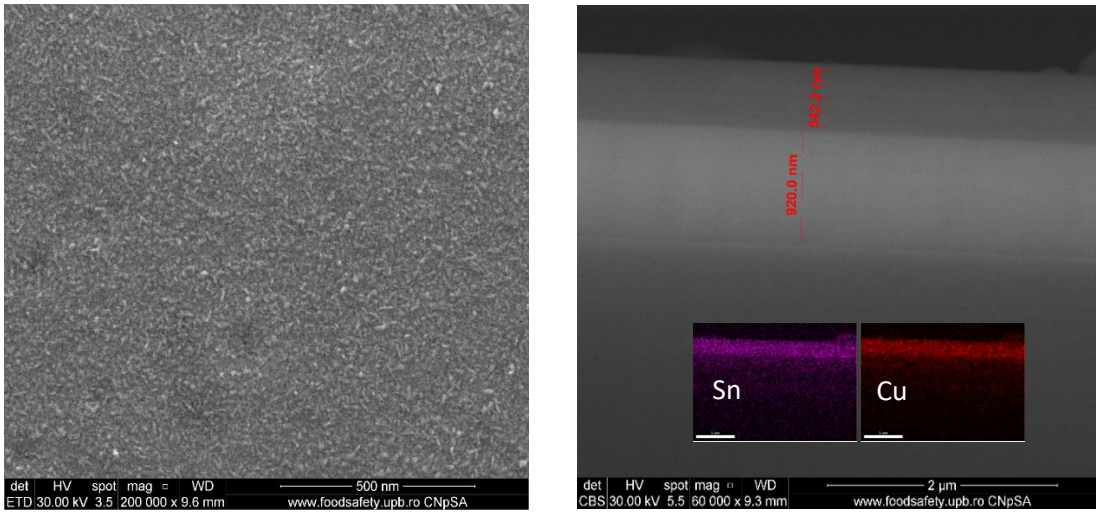


Figure 1: SEM Images (surface, cross-section and elemental mapping) on kesterite sample

References:

1. I. Boerasu, B.S. Vasile, *Materials*, **2022**, *15(23), 8427*

MS7 Advanced materials for energy storage and conversion

Type of presentation: Invited

MS7-IN-1 Atomic-to-Microscale Insights into Electrocatalyst Stability via Identical-Location Electron Microscopy

Nejc Hodnik[a,b]

[a]*National Institute of Chemistry, Hajdrihova 19, 1000 Ljubljana, Slovenia*

[b]*Institute of Metals and Technology, Lepi pot 11, 1000 Ljubljana, Slovenia*

Contact email: nejc.hodnik@ki.si

Electrochemical energy conversion depends on high-surface-area, conductive nanomaterials—particularly metal-based electrocatalysts, for driving key reactions. While structure, activity relationships have guided catalyst design, long-term durability demands a shift toward understanding structure–stability relationships.[1] Traditional methods often overlook critical multiscale features, such as dislocations, twin boundaries, grain orientation, voids, and cracks, that govern degradation, much like in metallurgy.

In this talk, I will present recent advances in identical-location electron microscopy (IL-EM) and 4D-STEM, which allow atomic-scale tracking of individual nanoparticles during electrochemical cycling. [2]Combined with unsupervised machine learning, these methods reveal degradation pathways, phase transformations, and structural motifs responsible for catalyst stability in Pt-alloy and Ir-based systems. We observe key processes, including disordering, twin-boundary migration, and local amorphization, that directly impact longevity.
Additionally, I will introduce Nano Lab, a next-generation platform integrating high-resolution microscopy with electrochemistry.[3] This setup enables tracking of atomic rearrangements in oxygen evolution catalysts and reveals how metal–support interactions and single-atom stabilization strategies enhance resilience.

By combining imaging, data science, and operando methods, we move toward predictive design of more stable electrocatalysts, offering a framework for accelerating the development of future energy materials.

References:
1. L.J. Moriau, A. Hrnjić, A. Pavlišič, A.R. Kamšek, U. Petek, F. Ruiz-Zepeda, M. Šala, L. Pavko, V.S. Šelih, M. Bele, P. Jovanovič, M. Gatalo, N. Hodnik, Resolving the nanoparticles' structure-property relationships at the atomic level: a study of Pt-based electrocatalysts, IScience 24 (2021). https://doi.org/10.1016/j.isci.2021.102102.
2. A.R. Kamšek, F. Ruiz-Zepeda, M. Bele, A. Logar, G. Dražić, N. Hodnik, Structure–Stability Relationships in Pt-Alloy Nanoparticles Using Identical-Location Four-Dimensional Scanning Transmission Electron Microscopy and Unsupervised Machine Learning, ACS Nano (2025). https://doi.org/10.1021/acsnano.4c12528.
3. M. Bele, G.K. Podboršek, A. Lončar, P. Jovanovič, A. Hrnjić, Ž. Marinko, J. Kovač, A.K. Surca, A.R. Kamšek, G. Dražić, N. Hodnik, L. Suhadolnik, "Nano Lab" Advanced Characterization Platform for Studying Electrocatalytic Iridium Nanoparticles Dispersed on TiOxNy Supports Prepared on Ti Transmission Electron Microscopy Grids, ACS Appl Nano Mater 6 (2023) 10421–10430. https://doi.org/10.1021/acsanm.3c01368.

Type of presentation: Oral

MS7-O-1 Charge density distribution in single-atom-on-substrate catalysts

Dražić Goran[a], Marjan Bele[a], Matic Poberžnik[b], Anton Kokalj[b], Nejc Hodnik[a]

[a]*National Institute of Chemistry, Ljubljana, Slovenia*

[b]*Jožef Stefan Institute, Ljubljana, Slovenia*

Contact email: goran.drazic@ki.si

In single-atom catalysts, where isolated atoms are attached on a support material, the spatial arrangement of electron density and atomic-level electric fields are crucial factors of performance. These parameters directly govern the catalytic activity and durability of the single atom sites. The substrate acts not only as a structural support but also dynamically shapes the electronic configuration of the anchored atoms. Charge transfer processes between the atom and support can alter the oxidation states of the active sites, modulating their chemical reactivity. Additionally, localized electric fields generated by the substrate may induce polarization in reactant molecules and modify their energy levels, thereby steering reaction pathways toward desired products while lowering activation barriers. Therefore, understanding and controlling these interactions at the atomic level is essential for the engineering of high-performance single-atom catalysts, with potential applications in sustainable chemical processes and renewable energy systems [1].

These insights are further advanced by computational tools such as density functional theory (DFT), which calculate charge density distributions and electric field profiles at the atomic level. With DFT, we can predict how specific single atom-substrate combinations influence electronic states and field interactions, enabling the rational design of catalysts with optimized charge transfer behaviour and tailored electric field environments. This predictive modelling bridges the gap between theoretical understanding and practical catalyst engineering, allowing for systematic adjustments in material composition, binding geometries, and electronic properties to enhance catalytic efficiency and selectivity.

Complementing these computational advances, experimental techniques like Four-Dimensional Scanning Transmission Electron Microscopy (4D-STEM) provide direct, high-resolution measurements of charge density and electrostatic field distributions in catalytic materials. In 4D-STEM, a two-dimensional diffraction pattern is captured at each scan position within a sample, generating a four-dimensional dataset. Analysis of these patterns enables precise mapping of charge density and electrostatic fields at nanometer-scale resolution. Techniques such as differential phase contrast and centre-of-mass imaging quantify phase shifts in electron beams induced by electric fields, visualizing internal field variations [2].

These capabilities make 4D-STEM indispensable for studying materials in applications like Proton Exchange Membrane (PEM) fuel cells, where electrostatic interactions at catalyst surfaces dictate proton transport and reaction kinetics. By correlating 4D-STEM-derived charge and field maps with catalytic performance, we can refine nanostructural designs such as optimizing single-atom anchoring sites or tailoring substrate-induced electric fields to enhance activity and durability [3].

We conducted a 4D-STEM study of two catalytic systems: iron (Fe) single-atom catalysts on a nitrogen-doped carbon substrate (Fe/C) for the oxygen reduction reaction (ORR) and iridium (Ir) single-atom catalysts on a titanium oxynitride substrate (Ir/TiON) for the oxygen evolution reaction (OER). Using a Jeol ARM 200 probe Cs-corrected STEM equipped with a Merlin 4DSTEM pixelated detector (Quantum Detectors, Oxford, UK), we collected 4D-STEM datasets from both Fe/C and Ir/TiON materials. From these datasets, atomic-resolution differential charge density maps and electric field

maps were constructed, revealing localized charge transfer dynamics and substrate-induced field gradients.

The experimental maps were directly correlated with DFT calculated charge density and field distributions for various structural models of Fe/C and Ir/TiON systems. For instance, DFT simulations predicted how specific binding geometries (e.g., Fe-N_4 coordination in Fe/C or Ir-O-Ti configurations in Ir/TiON) influence charge polarization and electric field magnitudes. By comparing experimental and computational maps, we evaluated the accuracy of these models in replicating real-world electronic environments. The results highlight how subtle differences in atomic arrangement such as substrate defects or interfacial bonding symmetry alter charge redistribution and field strengths, ultimately dictating catalytic activity and stability.

Acknowledgement:
This work was supported by the Slovenian Research and Innovation Agency (N2-0248, J7-4637, J1-50218, P2-0421, P2-0393)

References:
1. Wang, C.S., Wang, H., Wu, R. and Ragan, R., Evaluating the stability of single-atom catalysts with high chemical activity. *The Journal of Physical Chemistry C*, **2018,** 122(38), pp.21919-21926.
2. Ophus, C., Four-dimensional scanning transmission electron microscopy (4D-STEM): From scanning nano diffraction to ptychography and beyond. *Microscopy and Microan*alysis, **2019**, 25(3), pp.563-582.
3. Wang, Y., Chu, F., Zeng, J., Wang, Q., Naren, T., Li, Y., Cheng, Y., Lei, Y. and Wu, F. Single atom catalysts for fuel cells and rechargeable batteries: principles, advances, and opportunities, ACS nano, 2021, 15(1), pp.210-239

Type of presentation: Oral

MS7-O-2 Pore characterization of hard carbon anodes for sodium storage in sodium ion batteries by 2D and 3D TEM.

Georg Haberfehlner[a], Tatiana Kormilina[b], Daniel Knez[a], Harald Fitzek[b], Olzhas Kaupbay[c], Ilie Hanzu[c]

[a]*Institute of Electron Microscopy and Nanoanalysis, Graz University of Technology, (Graz), Austria*

[b]*Graz Centre for Electron Microscopy, (Graz), Austria*

[c]*Institute for Chemistry and Technology of Materials, Graz University of Technology, (Graz), Austria*

Contact email: georg.haberfehlner@felmi-zfe.at

Introduction

Sodium ion batteries have the potential of providing a cost-effective and sustainable energy storage solution [1]. With cathode materials based on widely available transition metals, such as Fe or Mn, a main candidate for the anode side are hard carbons, ideally stemming from renewable (bio-based) sources [2]. The general model for sodium storage in hard carbons distinguishes between adsorption of Na^+-ions, intercalation and pore filling, all of which are affecting the charge/discharge behaviour. Transmission electron microscopy can shed light on the nanoscale morphology of hard carbons with respect to the arrangement of graphitic layers and nanoscale porosity.

Methods

Hard carbon powders, which were also characterized in terms of their electrochemical cycling behaviour, were investigated in a probe aberration-corrected FEI Titan³ 60-300 microscope in STEM mode. 2D investigations were performed at both 300 kV and 80 kV, as beam damage can be significantly reduced by lowering the high tension. In particular, integrated differential phase contrast (iDPC) clearly reveals the graphitic layering within the hard carbons, while in combination with annular dark field (ADF) images also the presence of pores can be analysed. Electron tomography using different STEM detectors (ADF, bright-field, BF) was performed at 80 kV in order to limit beam damage during tilt series acquisition. Tomographic reconstruction employed conventional (SIRT) reconstruction methods, as well as total (generalized) variation (TV/TGV) minimization in order to facilitate interpretation and analysis of the tomographic reconstructions [3].

Results

iDPC STEM clearly reveals graphitic layers in hard carbons (Fig. 1a). In addition to the graphitic layer spacing (d_{002}), also d_{100} and d_{110} distances can be measured, which can serve as an internal calibration reference. As expected for hard carbons the measured d_{002} spacing is larger than for graphite, in the range of 0.39 nm. Imaging at 80 kV mostly eliminates beam damage, which is of particular importance for imaging nanopores in the hard carbon, as the focused electron beam can also introduce artificial holes in the sample. Nanopores in the sample can be identified in iDPC images, and confirmed by simultaneous ADF imaging (Fig. 1b), which shows a lower mass-thickness in pore positions. As TEM images only provide information integrated over the sample thickness, electron tomography can provide means to localize and measure pores inside the sample in 3D. Fig. 2 shows 3D reconstructions of a hard carbon particle reconstructed from an ADF STEM tilt series. By using a standard reconstruction algorithm (SIRT) large pores can be identified (Fig. 2a), while the presence of smaller pores only becomes more evident in a TV minimization reconstruction (Fig. 2b).

Discussion and conclusions

Porosity of hard carbon materials can be accessed by 2D and 3D STEM imaging and can potentially be correlated with the charging/discharging behaviour of sodium ion batteries, even though quantification of pore sizes and distribution is challenging. These investigations can also form the basis for TEM imaging of sodium stored within the hard carbon.

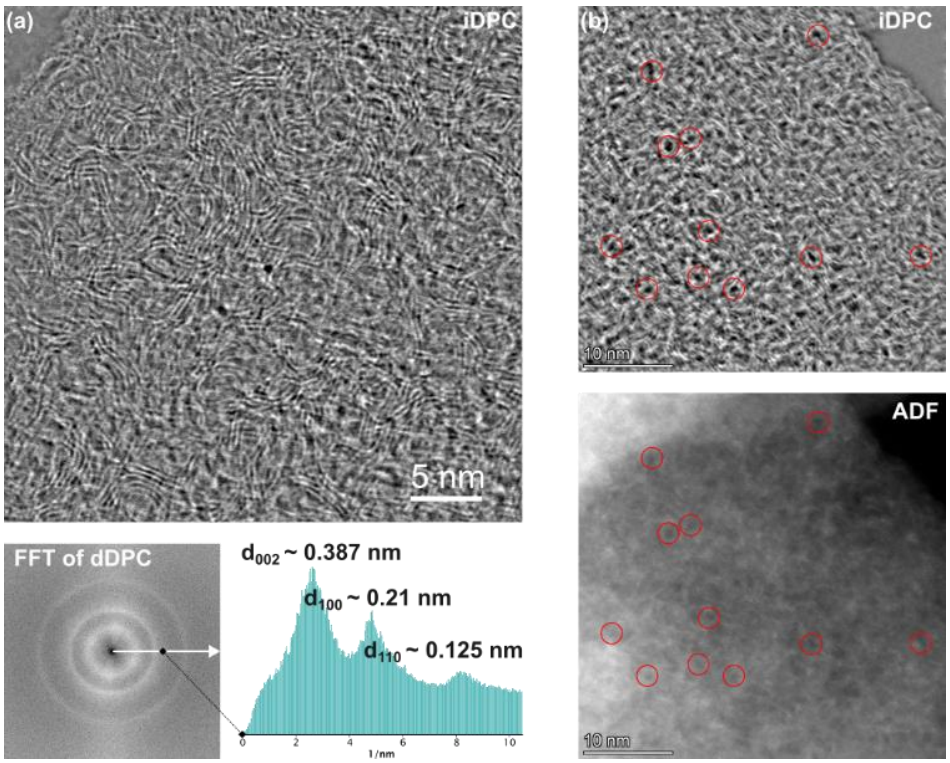


Figure 1: STEM images of hard carbon samples. (a), iDPC image along with FFT showing graphitic layer spacing (d_{002}). (b), iDPC and ADF images with locations of some nanopores indicated in the images.

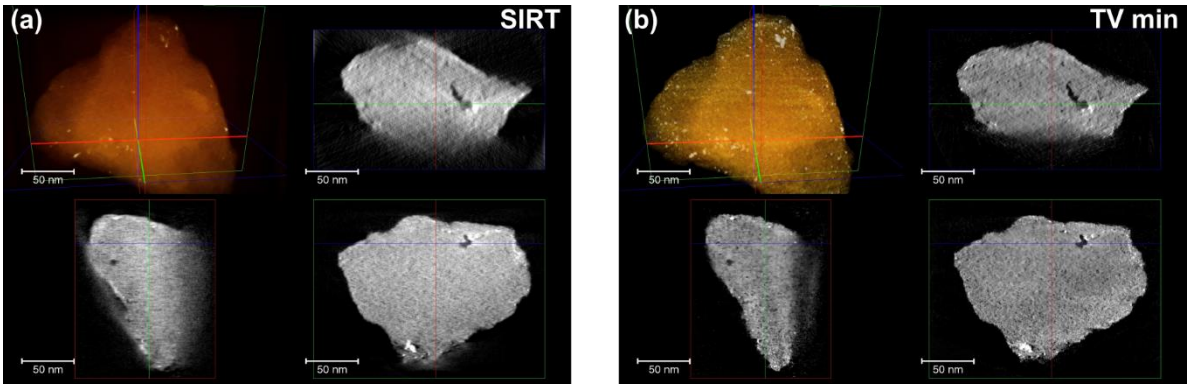


Figure 2: Tomographic reconstruction of a hard carbon particle, volume rendering and three orthogonal slices. (a), Conventional SIRT reconstruction (b), TV minimization reconstruction, where small pores become visible within the sample.

Acknowledgments
The authors thank Corina Taeubert, Rudolf Grasberger and Klaus Höll from Schunk Carbon Technology GmbH for providing hard carbon samples and FFG Austria for funding under the SAM4SIB project (FFG-BRIDGE; project number: 903691).

References:

1. Yu, T., *et al. Journal of Alloys and Compounds* **2023**, *958*, 170486
2. D. Saurel, et al, *Advanced Energy Materials* **2018**, *8*, 1703268.
2. R. Huber, et al., *Nanoscale.* **2019**, 11, 5618-5632.

Type of presentation: Oral

MS7-O-3 Real Time Imaging of Lithium-Ion Transport in Solid-State Batteries: An *Operando* FIB-SIMS approach

Sayantan Sharma[a,b], Tom Wirtz[a], Santhana Eswara[a]

[a]*Advanced Instrumentation for Nano-Analytics (AINA), Luxembourg Institute of Science and Technology (LIST), Belvaux, Luxembourg*

[b]*University of Luxembourg, 2 Avenue de l'Université, Esch-sur-Alzette L-4365, Luxembourg*

Contact email: sayantan.sharma@list.lu

Solid-state lithium-ion batteries have gained significant attention in recent years due to their enhanced safety compared to the conventional lithium-ion batteries with liquid electrolyte. However, their widespread commercialization remains challenging due to limitations in overall electrochemical performance. So, efforts are now focused on enhancing the key electrochemical parameters of the solid-state batteries, such as cycling life, capacity, and charge transport properties. Achieving these improvements requires a thorough understanding of the degradation mechanisms within these batteries, particularly how the degradation processes affect the lithium-ion transport during operation. This, in turn, demands high-resolution *operando* characterization techniques capable of correlating microstructural and chemical evolution of the batteries with its electrochemical performance. In this context, *operando* electron microscopy techniques have gained a lot of popularity as they provide excellent spatial resolution for microstructural imaging. But, utilizing electron microscopy to simultaneously obtain microstructural and chemical information is challenging. Conventional chemical analysis methods in electron microscopes, such as energy-dispersive X-ray spectroscopy (EDX) and electron energy loss spectroscopy (EELS), face limitations in detecting lithium. These challenges arise due to the low characteristic transition energy and low fluorescence yield of lithium in case of EDX and the stringent sample requirements for EELS. Secondary ion mass spectrometry (SIMS) can be a great alternative as it is capable of detecting lithium even at very low concentration and is even capable of distinguishing different isotopes of an element.

In this contribution, we report on the development of an *operando* methodology for microstructural and chemical imaging of solid-state batteries with nano-scale spatial resolution using a prototype dual-beam focused ion beam (FIB)-SIMS platform developed at Luxembourg Institute of Science and Technology [1]. Our approach integrates the use of a specially designed electrochemical cycling setup and a sample holder, enabling simultaneous SIMS analysis and cell operation. This addresses the limitation of previously reported quasi-*operando* SIMS methods [2,3] by allowing SIMS imaging without interruption of the electrochemical processes inside the cell.

As a proof-of-concept of this methodology, we imaged the lithium-ion transport in an all-solid-state battery with lithium metal as both the working and counter electrode. A foil of ^{6}Li, the less abundant isotope of Li in nature, was used as a working electrode. A chronopotentiometry (CP) sequence was performed by applying a positive constant electronic current in the working electrode, causing migration of the ^{6}Li ions from this electrode into the electrolyte (Figure:1). SIMS imaging was done at different stages of the CP sequence to understand the charge transport via tracking the ^{6}Li enrichment of the electrolyte which initially had the Li isotopic ratio close to the natural abundance (Figure:2).

The methodology reported here can be highly useful for studying lithium migration through different phases of the composite materials that are now emerging as electrodes and electrolytes for solid-sate batteries.

The authors acknowledge funding from the European Union's Horizon Europe research and innovation program under Grant Agreement No. 101104032 (OPINCHARGE).

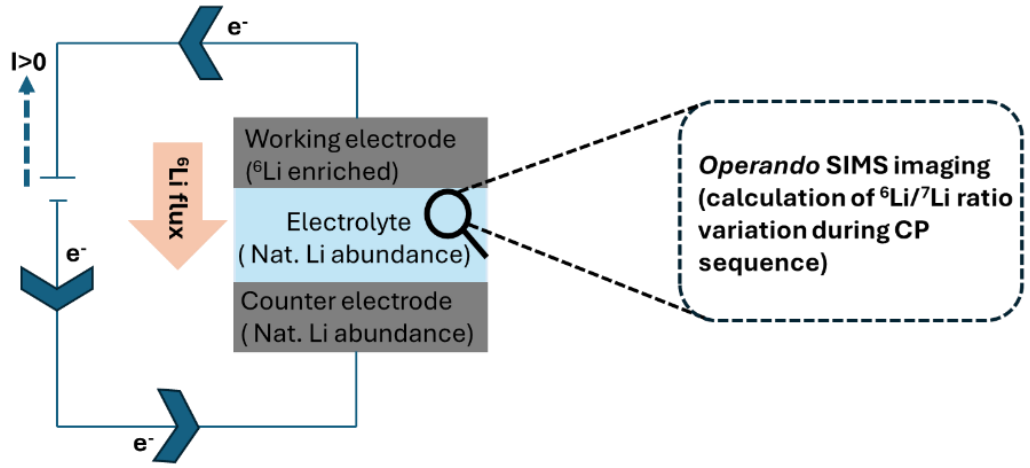


Figure 1: Schematic describing the proof-of-concept experiment for validation of the *operando* SIMS methodology.

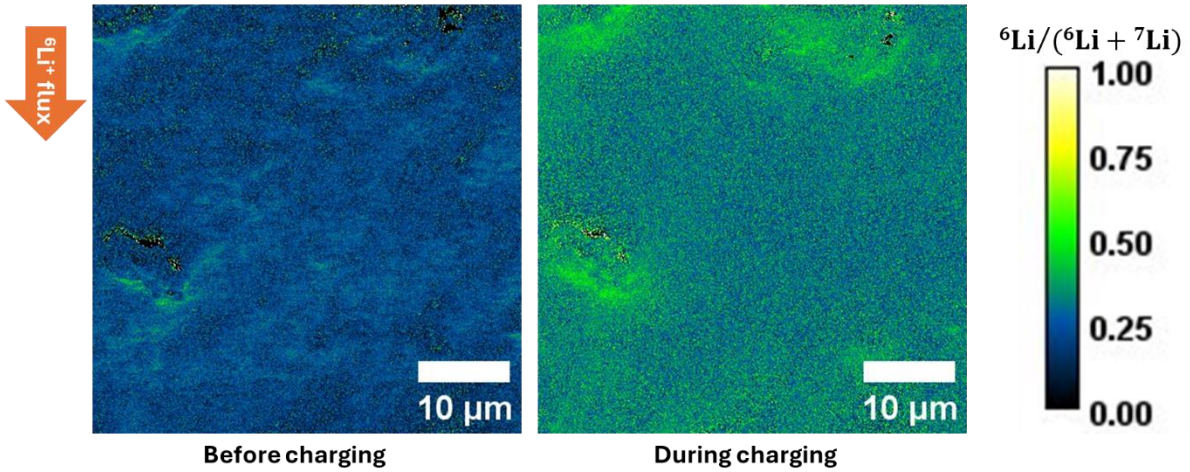


Figure 2: SIMS ratio maps of both lithium isotopes calculated via pixel-by-pixel division of ^{6}Li secondary ion counts by the sum of the secondary ion counts for both isotopes. The colour bar represents the value of ^{6}Li fraction in the imaged region. The mean ^{6}Li fraction in the imaged region before charging was 0.191±0.004 and during charging it increased to 0.299±0.005. The increase in ^{6}Li fraction during charging is attributed to the incoming ionic flux from the working electrode.

References:

[1] O. De Castro et al., Analytical Chemistry 94 (2022).
[2] H. Masuda et al., Journal of Power Sources 400 (2018).
[3] L. Cressa et al., Analytical Chemistry 95 (2023).

Type of presentation: Oral

MS7-O-4 Understanding local crystallography in solar cells materials with scanning electron diffraction using unsupervised machine learning

Andrea Griesi[a], Yurii P. Ivanov[a], Arivazhagan Valluvar Oli[b], Simon Fairclough[c], Paola De Padova[d], Carlo Ottaviani[d], Udari Wijesinghe[f], Giulia Longo[e,f], Oliver S. Hutter[f], Aldo Di Carlo[d], Yucheng Hu[c], Gunnar Kusch[c], Rachel A Oliver[c], Susanne Siebentritt[b], Giorgio Divitini[a],

[a]*Electron Spectroscopy and Nanoscopy, Istituto Italiano di Tecnologia, Genova, Italy*

[b]*Laboratory for Photovoltaics, Department of Physics and Materials Science Research Unit, University of Luxembourg.*

[c]*Department of Materials Science and Metallurgy, Cambridge University, Cambridge, United Kingdom*

[d]*Consiglio Nazionale delle Ricerche - Istituto di Struttura della Materia, Roma, Italy.*

[e]*Instituto de Diseño y Fabricación, Universitat Politécnica de Valencia, Camí de Vera s/n, 46022, Valencia, Spain,*

[f]*Department of Mathematics, Physics and Electrical Engineering, Northumbria University, Newcastle United Kingdom.*

Contact email: andrea.griesi@iit.it

Introduction

The performance and reliability of photovoltaic devices are intrinsically linked to their grain structure and local crystallographic properties, which play a pivotal role in enabling high power conversion efficiency and ensuring stable long-term operation. Defects, grain boundaries, and spurious phases often arise due to compositional heterogeneities or specific synthesis conditions, requiring in-depth investigation and precise control to optimise device performance. Understanding the crystallographic characteristics of complex systems with multiple phases requires advanced characterisation techniques capable of resolving nanoscale features with high spatial resolution, and remains challenging, primarily due to the technical and computational complexity involved. In this study, we focus on three advanced photovoltaic materials: Cu(In,Ga)S_2 (CIGS), halide perovskites ($CsPbBr_3$), and antimony selenide (Sb_2Se_3), each representing archetypical systems for next generation solar cells and presenting distinct challenges in engineering at grain scale. CIGS features complex stoichiometry, phase coexistence, and intricate grain structures. Halide perovskites are highly sensitive to electron beam exposure, complicating direct structural characterisation. Sb_2Se_3, in contrast, exhibits dense grain structures and unique crystallographic orientations, offering intrinsic advantages such as benign grain boundaries that minimise recombination losses.

Methods

To address these challenges, we employ 4D Scanning Transmission Electron Microscopy (4D-STEM) on cross-sectional samples prepared using Focused Ion Beam (FIB). This method records diffraction patterns at each probe position, generating four-dimensional datasets that link real-space coordinates with reciprocal-space information. This allows for the comprehensive mapping of crystallographic properties at the nanoscale, including grain orientation, phase distribution, and defect density. An aberration-corrected scanning transmission electron microscope (Thermo Fisher Scientific, Spectra 300) was used at an acceleration voltage of 300 kV. The diffraction patterns for the 4DSTEM data were acquired using a scintillator-based camera on a Continuum energy filter. Using a camera length of 38 mm (for $CsPbBr_3$) and 81 mm (Sb_2Se_3) with an exposure time of 0.01s and pixel size in diffraction patterns less than 0.1 nm^{-1}. The analysis of 4D-STEM datasets, often exceeding 15 GB per scan, requires advanced computational techniques to extract meaningful insights. We leverage unsupervised machine learning approaches, including dimensionality reduction techniques such as Non-Negative Matrix

Factorization (NMF) and clustering algorithms like K-Means and Mini Batch K-Means. These methods allow us to uncover key features in the data, facilitating a detailed understanding of the relationship between microstructural properties and device performance.

Discussion

In the case of CIGS, our analysis reveals the critical role of compositional tuning in optimising photovoltaic performance. Adjustments to the [Ga/(Ga+In)] ratio enhance grain size, reduce defect density, and improve carrier lifetime[1]. By applying NMF, we identify irregular domains within the chalcopyrite layer, while diffraction pattern indexing highlights distinct crystal orientations. These findings underscore the importance of tailoring both composition and structure to achieve high-efficiency devices.

For halide perovskites, particularly $CsPbBr_3$, the use of ultra-high vacuum molecular beam epitaxy (UHV-MBE) enabled the growth of highly crystalline films directly on Si(111) substrates[2]. This synthesis method eliminates compositional gradients, resulting in films with compelling crystallographic coherence and minimal interfacial defects. These characteristics are crucial for efficient charge transport in heterojunction devices. Despite challenges associated with the sensitivity of perovskites to electron beams, machine learning methods effectively classified diffraction patterns into eight distinct crystallographic zones, providing valuable insights into the structural integrity and orientation of the material.

Our analysis on Sb_2Se_3 focusses on the unique alignment of $[Sb_4Se_6]_n$ atomic chains, which determine intrinsic "benign grain boundaries", reducing recombination losses compared to conventional absorbers[3]. The application of Flash Lamp Annealing (FLA) introduces a gradient in crystallinity, with larger grain domains observed near the TiO_2 substrate. Mini Batch K-Means clustering efficiently identifies distinct zones within the Sb_2Se_3 layer, while Automated Crystal Orientation Mapping (ACOM) provides a higher-resolution understanding of crystallographic orientation. Notably, the Sb_2Se_3 layer exhibits a predominant [010] direction near the substrate, a growth orientation that minimises non-radiative recombination and enhances photovoltaic efficiency.

Conclusion

This study highlights the transformative potential of integrating 4D-STEM with advanced computational methods for analysing photovoltaic materials. By adhering to FAIR (**F**indability, **A**ccessibility, **I**nteroperability, and **R**euse) principles and utilising open-source tools such as Pyxem and py4DSTEM, we ensure that our methodologies are transparent, reproducible, and accessible to the broader scientific community. Additionally, we address critical considerations in experimental reliability, discussing strategies to mitigate potential artefacts arising during sample preparation, data acquisition, or analysis. The insights gained from this work advance our understanding of material behaviour at the nanoscale and establish a robust framework for addressing key challenges in optoelectronic and microelectronic device design.

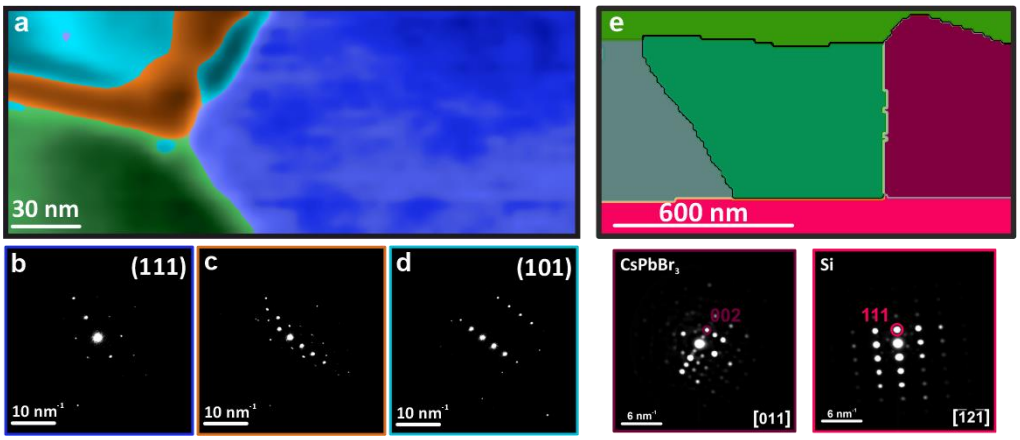


Figure 1: NMF decomposition results for a small area of 4DSTEM from a CIGS cross-section (a: loadings, b-d: representative diffraction patterns corresponding to the spatial components in a). (e) Result of the clustering algorithm on $CsPbBr_3$ 4DSTEM data.

References:

1. A. Thomere, N. Barreau, *et al. Solar Energy Materials and Solar Cells* **2022**, *237*, 111563.
2. P. De Padova, C. Ottaviani, *et al. Sci Rep* **2024,** 14, 23618.
3. U. Wijesinghe, G. Longo, *Energy Advances* **2023**, *2* (1), 12–33.

Type of presentation: Poster

MS7-P-1 Observation of defects in Li rich oxides as a product of temperature and chelating agent during synthesis

Rabail Badar Abbasi[a,b,c], Giuliana Aquilanti[d], Jasper Plasier [d], Anton Meden[b], Marjan Bele[a], Elena Tchernychova[a], Robert Dominko[a,b,c]

[a]*Department of Materials Chemistry, National Institute of Chemistry, Hajdrihova 19, 1000 Ljubljana, Slovenia*

[b]*Faculty of chemistry and chemical technology, University of Ljubljana, Slovenia*

[c]*ALISTORE-European Research Institute, Amiens, France*

[d]*Elettra-Sincrotrone Trieste S.C.p.A., s.s. 14 km 163.5, 34149 Basovizza, Trieste, Italy*

Contact email: rabail.badar.abbasi@ki.si

Li-rich layered oxides (LROs) are regarded as some of the most promising high-voltage cathode materials for enhancing the efficiency of Li-ion batteries (LIBs) due to their low toxicity and cost-effectiveness. LROs have demonstrated the ability to achieve capacities exceeding that of commercial cathode materials, such as $LiCoO_2$. However, they encounter challenges, including low initial coulombic efficiency, voltage decay, and limited high-rate performance. These issues are difficult to resolve and fully understand because of the inherent complexity of their structure[1,2].
In this study, we synthesize LROs using sol-gel synthesis, exploring the effects of various synthesis parameters on the resulting structure. A specific composition of $Li_{1.2}Mn_{0.54}Co_{0.13}Ni_{0.13}O_2$ was synthesized with different chelating agents (citric and oxalic acid) and calcination temperatures (850˚C and 900˚C).

We tracked the structural evolution of the oxalic and citric acid derived samples, by XRD analysis. We were able to note that due to oxalic-acid being a poorer chelating agent (compared to citric acid), it creates an inhomogeneous amorphous matrix which leads to higher degree of disorder for the oxalic-acid derived samples, by the presence of stacking faults and oxygen vacancies. Local structural analysis through EELS analysis at Mn $L_{2,3}$ edge, showed that for oxalic acid samples, there is a higher signal for Mn^{2+} species, which could be present due to higher concentration of oxygen vacancies. Furthermore, the electrochemical performance of the oxalic acid-derived LROs was found to be superior to that of the citric acid-derived samples, at both temperatures. XRD operando measurements for the first cycle of the samples, showed that the oxalic acid derived samples end up with a larger unit cell volume at the end of discharge, which would enable more stable cycling as it would limit Li/Ni intermixing and prevent the growth of the spinel phase.

Our findings indicate that the presence of defects plays a crucial role in enhancing the long-term cycling stability of LROs. These defects can be systematically introduced by carefully adjusting synthesis parameters, allowing for better control over the material's structural and electrochemical properties. By demonstrating how defect engineering influences cycling performance, this study offers valuable insights into optimizing LRO synthesis strategies to maximize their potential for energy storage applications.

References:

1. Xie, Y., Jin, Y., & Xiang, L. (2022). Li-rich layered oxides: Structure, capacity and voltage fading mechanisms and solving strategies. Particuology, 61, 1-10. https://doi.org/10.1016/j.partic.2021.05.011
2. Liu, T., Liu, J., Li, L. *et al.* Origin of structural degradation in Li-rich layered oxide cathode. *Nature* **606**, 305–312 (2022). https://doi.org/10.1038/s41586-022-04689-y

Type of presentation: Poster

MS7-P-2 Utilizing SEM thin-film measurements to deepen the understanding of perovskite solar cell performance

Stjepan Dolić[a], Vedran Kojić[a], Krunoslav Juraić[a], Andreja Gajović[a]

[a]*Ruđer Bošković Institute, (Zagreb), Croatia*

Contact email: sdolic@irb.hr

Perovskite solar cells (PSCs) have emerged as a promising photovoltaic technology due to their high power conversion efficiency and cost-effectiveness. However, their performance is often hindered by morphological defects, interfacial inconsistencies, and degradation mechanisms. Scanning Electron Microscopy (SEM) provides crucial insights into these factors, enabling targeted improvements in device fabrication and stability. This study explores the application of SEM techniques for the characterization of PSCs, focusing on morphology, grain size distribution, layer uniformity, and defect analysis. Specifically, we analysed SEM images of tin dioxide and perovskite layers prepared by different methods to evaluate their impact on device performance.

A series of PSCs were fabricated using a solution-processed perovskite layer, sandwiched between electron and hole transport layers. The imaging conditions were optimized to minimize beam-induced damage while maximizing contrast. Energy-dispersive X-ray spectroscopy (EDS) was employed for elemental mapping. Image processing software was used to quantify grain size distribution and interface roughness. SEM images of tin dioxide and perovskite layers prepared using different deposition methods were analysed to determine the influence of fabrication techniques on film morphology and device efficiency.

SEM imaging revealed that grain size distribution and surface coverage of photoactive and charge-transporting layers plays a crucial role in PSC efficiency. Larger multicrystaline perovskite material grains are correlated with reduced grain boundaries and lower charge recombination, leading to improved performance (Figure 1. (a)).[1] Also, better tin dioxide thin-film surface coverage ensures excellent charge separation and mitigates circuit shorting (Figure 1. (b)). [2] This is a crucial factor when analysing the quality of tin dioxide thin-film preparation. EDS analysis confirmed homogeneous elemental distribution in perovskite thin films, except for areas exhibiting degradation, where lead iodide (PbI_2) accumulation was observed (Figure 1. (a)). Furthermore, SEM analysis of tin dioxide and perovskite layers prepared by different methods revealed significant variations in film quality. Layers deposited via different methods exhibited smoother surfaces and better coverage, while others showed increased roughness and defect density, impacting overall device efficiency.

The findings underscore the importance of SEM in optimizing PSC morphology for enhanced performance. Grain boundary reduction and film uniformity are critical parameters that can be controlled through processing techniques, as revealed by SEM analysis. Furthermore, defect identification via SEM aids in the development of strategies to mitigate degradation. The analysis of tin dioxide and perovskite layers prepared by different methods highlights the impact of fabrication techniques on material quality and device stability. Future work will focus on in-situ SEM studies to monitor real-time degradation mechanisms and improve long-term stability. These insights contribute to the advancement of PSC technology towards commercial viability.

References:

1. M. Kim et. al., *Joule* **2019**, *3*, 2179−2192.
2. J. J. Yoo et. al., *Nature* **2021**, *590*, 587−593.

AGNOWLEDGMENTS: The presented results were obtained within the framework of cooperation between the Government of the Republic of Croatia and the Government of the State of Israel with co-financing from the The Ministry of Science, Education and Youth Croatia, project Novel perovskite solar cells with enhanced performance based on hybrid halide perovskite/transition-metal disulfides

nanocomposites (Sol-HP-TMD-NanoComp). We would also like to thank the work of Marija Mirosavljević whose expertise in SEM measurements has made this research possible.

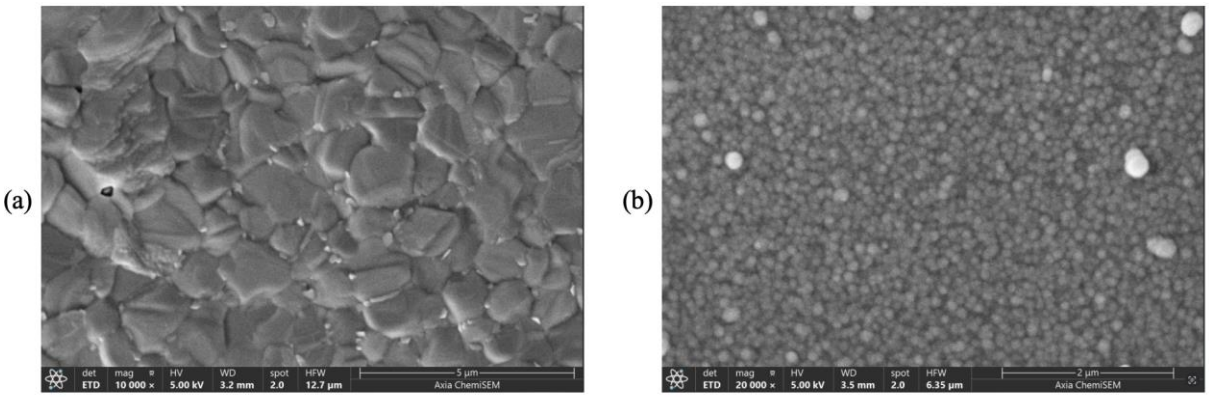


Figure 1. Top-view SEM images of (a) $FAPbI_3$ and (b) SnO_2 thin films.

Type of presentation: Poster

MS7-P-3 Microstructural analysis of the copper matrix composites for electrodes of plasma torches

Izabela Kalemba-Rec[a], Piotr Ledwig[a], Agnieszka Kopia[a], Laura Ząbek[a], Ronny Schimpke[b], Victoriia Kison[b] and Beata Dubiel[a]

[a]*AGH University of Krakow, Faculty of Metals Engineering and Industrial Computer Science, Krakow, Poland*

[b]*Technical University Bergakademie Freiberg, Institute of Energy Process Engineering and Chemical Engineering, Germany*

Contact email: bdubiel@agh.edu.pl

Introduction

High-performance materials with tailored characteristics are needed to extend the lifetime of plasma torch electrodes applied in the plasma gasification process adapted to convert wastes into hydrogen-containing syngas. Due to its high electrical and thermal conductivity combined with mechanical strength and corrosion resistance, copper is used for arc plasma electrodes protected by inert gases [1]. However, using pure steam in plasma-assisted waste gasification to produce syngas dramatically reduces the lifetime of copper electrodes, mainly due to the influence of reactive gases [2]. The promising materials for electrodes of plasma torches with improved corrosion and erosion resistance are copper matrix composites strengthened by oxide particles. In addition, oxide dispersion strengthened composites exhibit microstructural stability at high temperature because of the resistance to grain growth and thus capability to maintain strength [3].

In our study the microstructure of four copper matrix composites reinforced by Al_2O_3 particles, fabricated by mechanical alloying and reaction milling, followed by forming through extrusion were examined by scanning and scanning transmission electron microscopy and X-ray diffraction. The most important microstructural features characteristic for the composites in as-received condition are described.

Methods

The copper matrix composites examined, called CEP DISCUP®, were delivered by CEP – Compound Extrusion Products GmbH, Germany in the form of round bars fabricated by mechanical alloying (C3/30, C3/60 and C3/80) and reaction milling (C3/11-M) followed by extrusion. The microstructure was studied by SEM using the Nova NanoSEM 450 microscope of FEI equipped with EDS and EBSD, as well by STEM using JEM-ARM200F NEOARMex microscope of JEOL. For microanalysis of chemical composition quantitative EDS maps were recorded in STEM. The phase composition was analyzed using X-ray diffraction using Empyrean DY 1061 Malvern PANalytical diffractometer and selected area electron diffraction in TEM. The grain size and crystallographic orientation were determined by EBSD. The size distribution and volume fraction of reinforcing oxide particles were determined using image analysis performed by ImageJ software. The hardness measurements were carried out using the Duramin-40 hardness tester of Struers.

Results and discussion

Figure 1 shows the microstructure of the copper matrix composites reinforced by Al_2O_3 particles. SEM microstructural analysis indicates that the composites are almost free from pores. The copper matrix in composites is characterized by the non-uniform grain size. In the longitudinal sections of the bars the bands of larger and smaller grains are visible. Grain size inhomogeneity is related to the distribution of Al_2O_3 reinforcing particles, which are arranged in bands parallel to the direction of processing. The inhomogeneity in grain size and distribution of Al_2O_3 particles is more pronounced in C3/11-M composite fabricated by reaction milling than in mechanically alloyed composites. The diameters of oxide particles range from several nanometers up to a few tenths of a micrometer. STEM-EDS analysis shows that the nanosized oxide particles tend to form agglomerates. The volume fraction of oxide particles varies in particular composites from 1.8% to 3.6%. An increase in the fraction of Al_2O_3 and decrease in grain size corresponds with increasing in hardness in the range from 137 HV to 188 HV.

Crystallographic orientation maps in the longitudinal and transverse planes versus fabrication direction show random grain orientation.
The X-ray diffraction analysis indicates that Cu peaks are slightly shifted out of the ideal positions to higher angles (Fig. 1d). It can be caused by the change of Cu lattice parameter due to addition of even a small amount of alloying elements or residual stress. Moreover, the asymmetry of the Cu (111) peak at $2\Theta=43.2°$ is due to its overlapping with the Al_2O_3 (113) peak at $2\Theta=43.8°$.

Conclusions
Copper matrix composites reinforced by Al_2O_3 particles fabricated by mechanical alloying or reaction milling are dense and free of pores. Their microstructure is characterized by inhomogeneity in grain size and distribution of oxide particles. The pinning of grain boundaries by oxide particles shows that these composites could maintain microstructural stability under plasma conditions. Further investigations are needed to confirm their potential as promising materials for electrodes of plasma torches.

Acknowledgments
The study was performed within the M-ERA.NET project ArcAMAT. The research was funded by the National Science Centre, Poland, grant no DEC-2023/05/Y/ST11/00236. The help of Hubert Pasiowiec (AGH) in sample preparation is gratefully acknowledged.

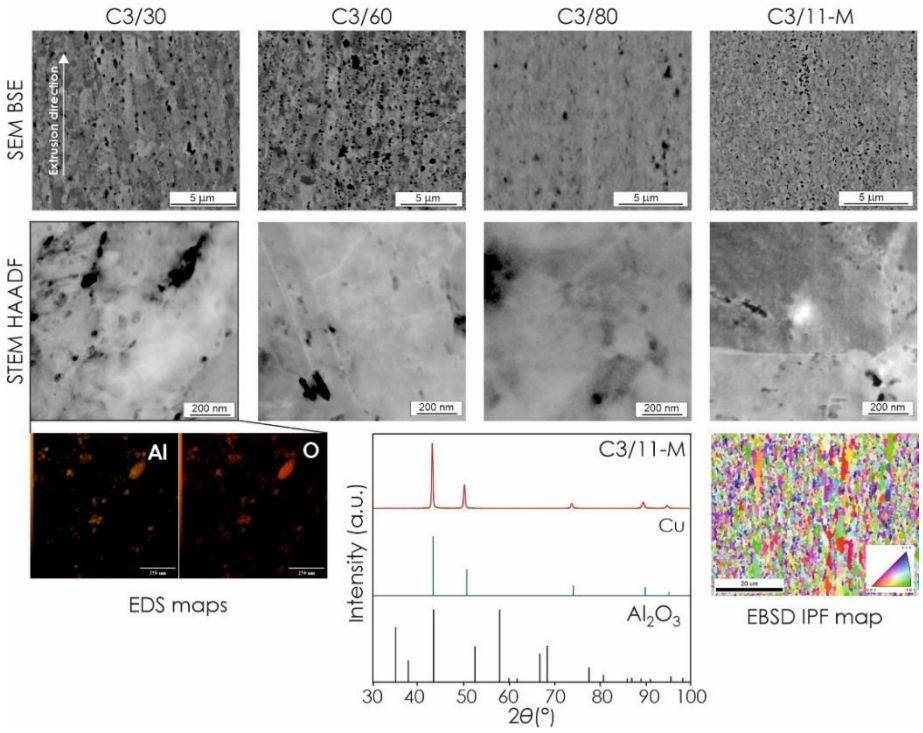


Figure 1: SEM and STEM images of the microstructure of four copper matrix composites reinforced by Al_2O_3 particles showing the inhomogeneity in grain size and distribution of oxide particles, with exemplary EDS maps for C3/30, as well as XRD spectrum and EBSD inverse pole figure (IPF) map for C3/11-M.

References:

1. A.S. Anshakov, P.V. Domarov, V.A. Faleev, *J. Engin. Thermophys.* **2023**, *32*, 596–602.
2. E. Gomez, D. Amutha Rani, C.R. Cheeseman, D. Deegan, M. Wise, A.R. Boccaccini, *Journal of Hazardous Waste*. **2009**, *161*, 614–626.
3. A. Jamwal, P. Mittal, R. Agrawal, et al. *Journal of Composite Materials*. **2020**, 54, 2635-2649.

Type of presentation: Poster

MS7-P-4 Characterization of hard carbons for Na-ion battery electrodes by a combination of electron microscopy and vibrational spectroscopy

Harald Fitzek[a], Olzhas Kaupbay[b], Daniel Knez[c], Tatiana Kormilina[a], Georg Haberfehlner[c], Ilie Hanzu[b]

[a]*Graz Centre for Electron Microscopy, (Graz), Austria*

[b]*Institute for Chemistry and Technology of Materials, Graz University of Technology, (Graz), Austria*

[c]*Institute of Electron Microscopy and Nanoanalysis, Graz University of Technology, (Graz), Austria*

Contact email: harald.fitzek@felmi-zfe.at

Introduction

The development of cost-effective and sustainable stationary energy storage is a key requirement for the full transition to renewable energy sources. Sodium-ion batteries are a prime candidate for this application, as they can be constructed from broadly available raw materials. Typical cathode materials consist of transition metals such as Fe or Ni, whereas on the anode side the most promising material from a sustainability point of view are hard carbons [1]. Here we focus on the analysis of hard carbon anodes relative to their performance in electrochemical cycling by applying a multi-technique approach using a combination of electron microscopy and vibrational spectroscopy.

Methods

Before electrochemical cycling we employ both FTIR-ATR (Bruker Tensor 27/Hyperion 3000) and Raman microscopy (LabRAM HR 800) on powdered samples, for the characterization of the surface chemistry/impurities and the bulk carbon structure, respectively. This is supplemented by SEM-EDS (Zeiss Sigma 300/Oxford X-Max) analysis on the cross-section of assembled electrodes for morphological and elemental analysis. The cross-section preparation is done by embedding in epoxy resin and grinding/polishing. After electrochemical cycling, irreversible changes to the carbon material are again investigated by the combination of FTIR-ATR, Raman microscopy and SEM-EDS on the cross-section of the electrodes.

Results

Raman spectroscopy is well suited for the analysis of the bulk material of hard carbons, as it has a high sensitivity for sp^2-bonds, as well as the crystallinity of carbon materials [2]. Conveniently, FTIR-ATR is highly insensitive to sp^2-carbon and thus reveals the complimentary information about impurities and surface groups that is lacking from Raman spectroscopy [3]. Figure 1 shows an example of both applied to the same sample.

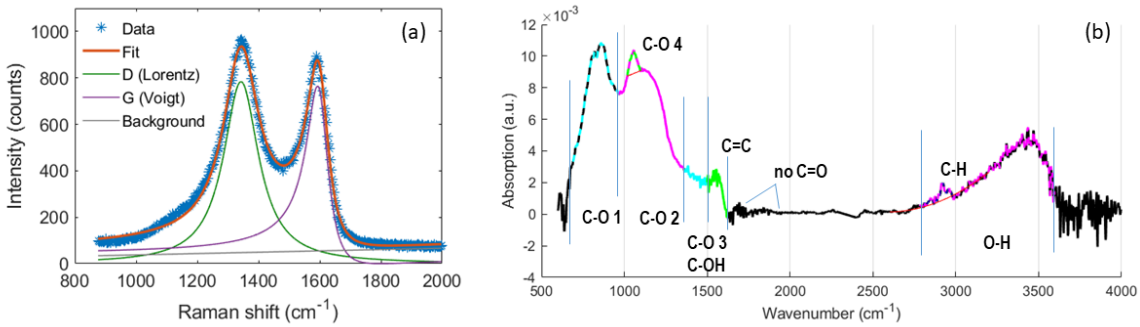


Figure 1: Example of a combined Raman and FTIR-ATR(Ge) analysis on a powdered hard carbon sample. *(a)* Main Raman bands of the hard carbon structure (D-&G-band) with a band fit. The fit parameters give us insights into the crystallinity and sp^2-network of the carbon [2]; *(b)* FTIR-ATR spectrum with the indication of the main bonds from surface groups and impurities contributing to the signal [3].

At the same time the morphology, especially the size distribution, and density of hard carbon particles is crucial to the cell performance and not accessible by vibrational spectroscopy. Exactly this information is accessible by SEM at a cross-section of the sample. In addition, EDS-analysis can provide further information about impurities and the distribution of the Na throughout the electrode. Figure 2 shows an example of both.

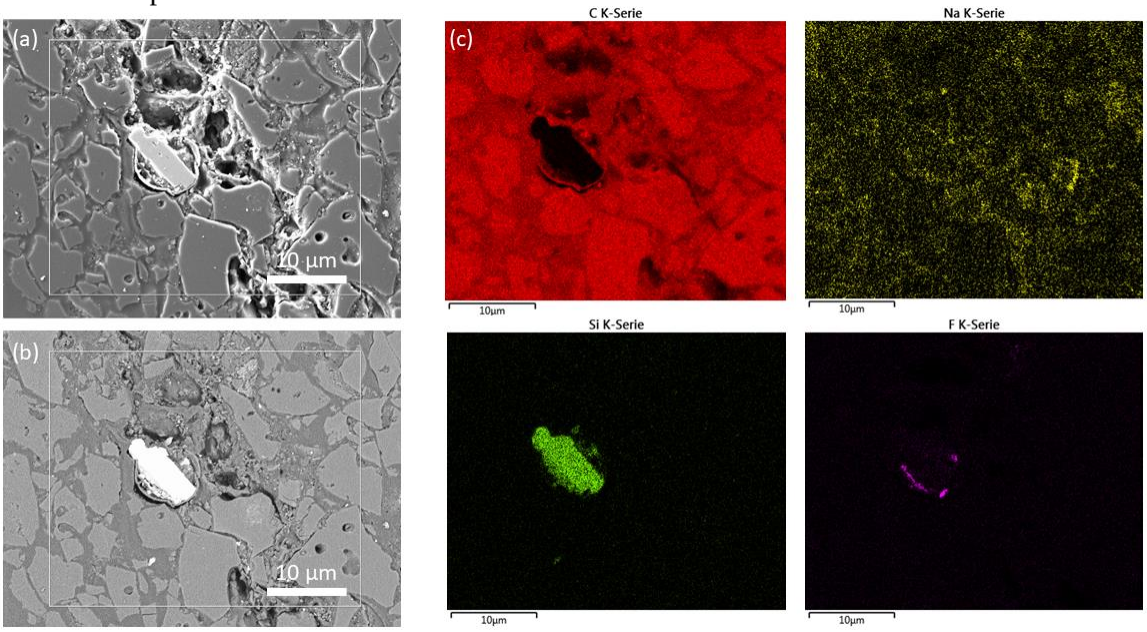


Figure 2: Example of a SEM-EDS-analysis on the cross-section of a hard-carbon electrode, both the main hard carbon material and a contamination particle that was embedded in the electrode are shown. *(a)* SE-image, clearly showing the contamination and holes in the electrode next to it; *(b)* BSE-image, the size distribution of the hard carbon particles around the inclusion is nicely visible; *(c)* EDS-mappings of selected elements.

Discussion and conclusions

A routine for the combined application of Raman microscopy, FTIR-ATR and SEM-EDS on hard carbon electrodes was established. It reveals different parameters that are influencing the electrochemical performance. We are currently correlating these results, as shown in the examples above, with electrochemical measurements to reveal the key parameters to be optimized in cell design. Furthermore, we will attempt *insitu* Raman spectroscopy on selected samples of the hard carbons to directly observe the dynamics of Na-adsorption/intercalation in the sample.

Acknowledgments

Authors thank Corina Taeubert, Rudolf Grasberger and Klaus Höll from Schunk Carbon Technology GmbH for providing hard carbon samples and FFG Austria for funding under the SAM4SIB project (FFG-BRIDGE; project number: 903691).

References:

1. Yu, T., Li, G., Duan, Y., Wu, Y., Zhang, T., Zhao, X., ... & Liu, Y. (2023). The research and industrialization progress and prospects of sodium ion battery. *Journal of Alloys and Compounds, 958*, 170486
2. Ferrari, A. C., & Robertson, J. (2004). Raman spectroscopy of amorphous, nanostructured, diamond–like carbon, and nanodiamond. *Philosophical Transactions of the Royal Society of London. Series A: Mathematical, Physical and Engineering Sciences*, 362(1824), 2477-2512.
3. Ţucureanu, V., Matei, A., & Avram, A. M. (2016). FTIR spectroscopy for carbon family study. *Critical reviews in analytical chemistry*, 46(6), 502-520.

Type of presentation: Poster

MS7-P-5 Atomic-scale insights into Solid-State Batteries via in situ TEM

Gregor Kapun[a,b,c], Blaž Jaklič[d], Jan Žuntar[d], Petruša Borštnar[d], Matjaž Spreitzer[d], Goran Dražić[a,d], Robert Dominko[a,b]

[a]*National Institute of Chemistry, Ljubljana, Slovenia*

[b]*Faculty of Chemistry and Chemical Technology University of Ljubljana, Ljubljana, Slovenia*

[c]*Center of Excellence on Nanoscience and Nanotechnology – Nanocenter, Ljubljana, Slovenia*

[d]*Jožef Stefan Institute, Ljubljana, Slovenia*

Contact email: gregor.kapun@ki.si

Solid-state lithium-ion batteries (SSBs) are gaining attention as a next-generation energy storage technology due to their high energy density and improved safety compared to conventional lithium-ion systems. A fundamental challenge in SSB research is understanding the electrochemical processes at the interface between the electrode and electrolyte, which is buried beneath the surface and difficult to characterize in its native state [1]. While conventional electrochemical techniques such as cyclic voltammetry (CV) and electrochemical impedance spectroscopy (EIS) provide valuable macroscopic insights, they lack spatial resolution and elemental specificity, limiting their ability to study interfacial dynamics and degradation mechanisms.

The advent of microelectromechanical systems (MEMS) based on E-chips has made in situ transmission electron microscopy (TEM) a powerful tool for direct observation of these processes at high spatial resolution. This technique enables real-time observations of dynamic electrochemical processes and structural evolution in SSBs and provides important insights into phase boundaries and material transformations [2].

In this study, we employ in situ TEM technique to investigate the electrochemical and structural properties of an epitaxially grown thin-film solid-state battery (TSSB) with an NMC//LLTO//LTO architecture. The battery was fabricated by pulsed laser deposition (PLD), sequentially depositing $Li_4Ti_5O_{12}$ (LTO) as the anode, $Li_2La_2Ti_3O_{10}$ (LLTO) as the solid electrolyte and $LiNi_{0.33}Mn_{0.33}Co_{0.33}O_2$ (NMC111) as the cathode on a conductive Nb-doped $SrTiO_3$ (STO:Nb) substrate. Two variants of the full-stack battery were fabricated using STO:Nb substrates with the orientations <111> and <110>. Initial macroscopic electrochemical tests were performed in a coffee bag configuration, where CV and EIS measurements confirmed the battery's functionality.

For in situ TEM characterization, we developed an optimized focused ion beam (FIB) technique to fabricate SSB lamellae directly on a four-electrode E-chip without breaking the vacuum at any step of the fabrication process. This method includes: Lifting the rough lamella perpendicular to the FIB column and landing parallel to the E-chip contacts, precisely contacting the positive and negative poles of the SSB lamella with the Pt contacts of the E-chip, and thinning/polishing the SSB lamella in the final step. The prepared E-chip was mounted on an in situ TEM holder and the electrical terminals were connected to a high-sensitivity battery measurement system.

Atomically resolved TEM/STEM images as well as STEM-EDS and STEM-EELS analysis, revealed the epitaxial growth of all three layers while maintaining crystallographic symmetry from the substrate upwards. Structural defects and secondary phases were observed at the interfaces, which could affect the electrochemical performance. We successfully performed open circuit voltage (OCV) measurements and monitored the electrochemical response during in situ charging of the SSB lamella, although this part needs further investigation and optimization.

Our results demonstrate that in situ TEM is a highly effective multimodal tool to study electrochemical and electromechanical phenomena in SSBs. This approach provides unprecedented insights into electrode reactions, the evolution of phase boundaries and degradation mechanisms, and advances the fundamental understanding of solid-state battery behavior at the atomic-scale.

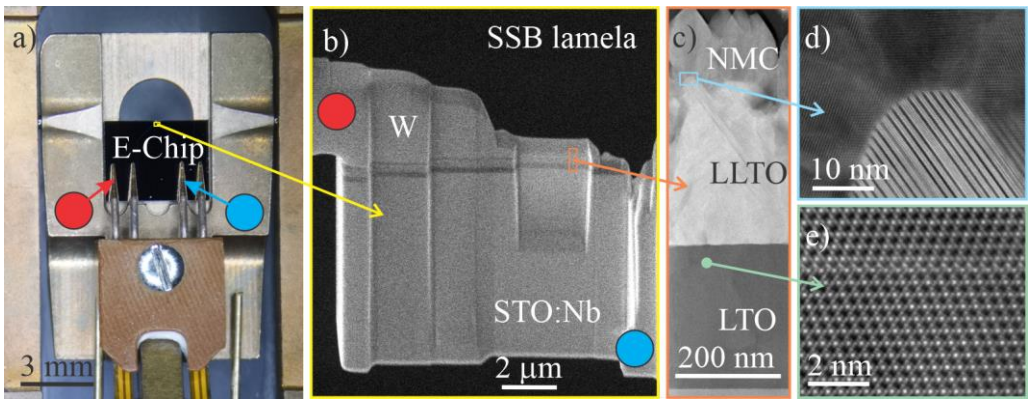


Figure 1. In situ TEM holder with E-chip (a), FIB-prepared SSB lamella (b), STEM image of SSB layers (c), "Ruddlesden-Popper" type sequence in LLTO (d), example of structural defect in LTO (e)

References:

1. Boaretto N. *et al*, Journal of Power Sources, 502 (2021), p. 229919.
2. Sun, Z. *et al*, eTransportation 14 (2022), p. 100203.

Type of presentation: Poster

MS7-P-6 Microscopic Insights into Catalyst Layer of PEMFC: IL-SEM Study of Electrochemical Effects

Mitja Kostelec[a,b], Miha Hotko[a,b], Matija Gatalo[b,c], Nejc Hodnik[a,b]

[a]*University of Nova Gorica, (Vipavska 13, SI-5000 Nova Gorica), Slovenia*

[b]*National Institute of Chemistry, (Hajdrihova ulica 19, 1000 Ljubljana), Slovenia*

[c]*ReCatalyst d.o.o., (Hajdrihova ulica 19, 1001 Ljubljana), Slovenia*

Contact email: mitja.kostelec@ki.si

Introduction: Proton exchange membrane fuel cells (PEMFCs) rely on high-performance electrocatalysts to ensure efficient and durable energy conversion. Understanding the structural and morphological evolution of catalyst layers during electrochemical operation is essential for optimizing their performance and longevity.[1] Identical location scanning electron microscopy (IL-SEM) provides a powerful tool for tracking nanoscale changes in catalyst layers, offering direct insights into structural modifications and degradation mechanisms. In this study, IL-SEM is applied to investigate the electrochemical effects on PEMFC catalyst layers, utilizing a gas diffusion electrode (GDE) half-cell setup for controlled sample conditioning.[2]

Methods: Catalyst layers were prepared on GDEs using commercially available electrocatalyst. The samples underwent electrochemical conditioning in a GDE half-cell setup, mimicking fuel cell environments. Identical locations on the samples were imaged before and after electrochemical treatment using a high-resolution field emission scanning electron microscopy (FE-SEM) Apreo 2 S (Thermo Fisher Scientific, Netherlands) and energy dispersive spectrometer (EDS) Ultim Max 100 (Oxford, UK). Image processing and particle size distribution analyses were conducted to quantify morphological changes. Additional characterization techniques, such as energy-dispersive X-ray spectroscopy (EDS), were employed to assess elemental redistribution and potential degradation pathways.[3.4]

Results: IL-SEM imaging revealed changes in catalyst layer morphology following electrochemical conditioning. Notable observations included nanoparticle aggregation, ionomer redistribution, and porosity variations. Quantitative image analysis showed an increase in average particle size, suggesting either agglomeration or Ostwald ripening and particle coalescence as key degradation pathways. EDS mapping further indicated local elemental rearrangements, providing insights into catalyst stability under operating conditions.

Discussion and Conclusions: The results highlight the effectiveness of IL-SEM in tracking structural and compositional changes in PEMFC catalyst layers, offering valuable insights into mechanisms occurring during conditioning. The combination of IL-SEM with electrochemical conditioning in a GDE setup enables a realistic yet well-controlled platform for studying catalyst evolution under operationally relevant conditions. Future work will focus on expanding the methodology to include additional characterization techniques, such as IL-XPS and IL-XRD, to further elucidate surface chemistry and crystallographic transformations. Establishing IL-SEM as a standardized tool for PEMFC research will contribute to the development of more durable and efficient fuel cell materials.[1,3]

Keywords: Gas diffusion electrode (GDE) half cell setup, Proton-exchange membrane fuel cell (PEMFC), Identical location scanning electron microscopy (IL-SEM), Electrocatalyst,

References:

1. M. Kostelec, M. Gatalo, N. Hodnik, Chem. Rec. **2024**, 24.
2. K. Ehelebe, N. Schmitt, G. Sievers, A. W. Jensen, A. Hrnjić, P. Collantes Jiménez, P. Kaiser, M. Geuß, Y.-P. Ku, P. Jovanovič, K. J. J. Mayrhofer, B. Etzold, N. Hodnik, M. Escudero-Escribano, M. Arenz, S. Cherevko, ACS Energy Lett. **2022**, 7, 816–826.
3. N. Hodnik, S. Cherevko, Curr. Opin. Electrochem. **2019**, 15, 73–82.
4. J. Bals, M. Epple, RSC Adv. **2023**, 13, 2795–2802.

Type of presentation: Poster

MS7-P-7 Identifying and studying open Li-ion channels along a preferred crystallographic axis in battery electrodes via scanning electron diffraction

Amoghavarsha Mahadevegowda[a,b], Caterina Ducati[a,b]

[a]*Department of Materials Science and Metallurgy, University of Cambridge, Cambridge, UK*

[b]*Faraday Institution, Quad One, Harwell Science and Innovation Campus, Didcot, UK*

Contact email: am2729@cam.ac.uk

Nb-based oxides are increasingly being investigated for their electrochemical attributes, which have shown to significantly improve battery performance [1-2]. These oxides offer stability at high cycling rates coupled with high specific capacities that make them desirable as anodes for Li-ion batteries [1-2]. The source of this relatively high cycling capacity is suggested to originate from an open framework-based structure that facilitates Li-ion diffusion within the Nb-based oxides [3]. These structures are currently being studied by X-ray and neutron diffraction-based techniques. However, such techniques do not offer a view of the local structure within the domain of a crystal that is usually studded with defects, which can only be visualised along a specific crystallographic axis. Moreover, the range over which the local arrangement of atoms stays consistent and essentially demarcates the domain boundaries also varies with composition, which affects Li-diffusion rates within the crystal [1,4-5].

High-resolution transmission electron microscopy can be employed to overcome the shortcomings inherent in X-ray based characterisation techniques. However, the morphology of the oxides - spheres of bundled-up primary particles - make it extremely difficult to image the primary particles and reports are limited to the surface or near-edge of the particles [6-7]. We have used scanning electron diffraction to navigate the entire cross-section of such a sphere, and analysed the patterns using an in-house developed code to identify and image the primary particles. These selected particles were then studied to obtain high-resolution transmission electron microscopy images that revealed the arrangement of cations and defects at a nanoscale, especially in and around the open channels in Nb-based oxides. In addition to the study of Li-diffusion channels, we have also been able to probe the inter-connections between particles within the sphere and their amorphous-crystalline nature, which might offer a 'non-rigid' link between the individual crystals to allow expansion and contraction of the structure during cycling. Our diffraction-based technique has the potential for automation, especially in the new generation of electron microscopes that allow running of python scripts, and hence can enable the study of battery materials at an atomic scale to uncover the underpinning principles of high stability anodes.

References:

1. T Li et al., Mater. Sci. Eng. R Rep. **2025**, 162, 100887
2. X Zhu et al., ACS Appl. Mater. Interfaces **2018**, 10, 23711−23720.
3. G Li et al., J. Mater. Chem. A, **2013**, 1, 12409.
4. N Takami et al., J. Power Sources **2018**, 396, 429–436.
5. C Kocer et al., Chem. Mater. **2020**, 32, 9, 3980–3989.
6. J Hu, Electrochim. Acta, 331, **2020**, 135364.
7. R Li, Ceram. Int., 45, 9, **2019**, 12211-12217.

Type of presentation: Poster

MS7-P-8 Microstructure and stability of carbon wrapped Cu@Cu_2O nanowires

Francisco Ruiz-Zepeda[a], Mohammed Azeezulla Nazrulla[a], Lazar Bijelic[a], Marjan Bele[a], Nejc Hodnik[a]

[a]*National Institute of Chemistry, Slovenia*

Contact email: francisco.ruizzepeda@ki.si

In this study, we investigated the microstructure and stability of carbon-wrapped core-shell Cu@Cu_2O nanowires for their potential applications in CO_2 reduction, utilizing advanced electron microscopy techniques. The nanowires were characterized using Scanning and Transmission Electron Microscopy ((S)TEM), alongside other analytical methods such as Electron Energy Loss Spectroscopy (EELS) and electron diffraction, to gain deeper insights into their microstructure, morphology, and composition. Our observations revealed that the nanowires consist of three distinct components: a Cu core, a Cu_2O shell and a carbon wrap surrounding the structure. Furthermore, the system was analyzed after undergoing an electrochemical process to identify any changes occurring at the nanoscale level. This allowed us to explore the nanostructure's evolution and its relationship with the catalytic activity, selectivity, and stability of the material during electrolysis. These findings contribute to a better understanding of how the nanostructure influences the performance of the catalyst, which is critical for improving CO_2 reduction processes.

Acknowledgments
Authors would like to thank the European Research Council (ERC) Starting Grant 123STABLE (Grant agreement ID: 852208) and the funding for Marie Skłodowska-Curie Actions, Individual Fellowships Project CO2-CAT-ALOG (grant reference no. 897866) the EU commission for Horizon 2020 Framework Program.

Type of presentation: Poster

MS7-P-9 Impact of $La_{0.07}Ba_{0.93}SnO_3$ interlayer on epitaxial growth of $Li_4Ti_5O_{12}$ thin film anodes for all-solid-state Li-ion batteries

Elena Tchernychova[a], Jan Žuntar[b], Blaž Jaklič[b], Gregor Kapun[a], Matjaž Spreitzer[b], Robert Dominko[a,c,d],

[a]*National Institute of Chemistry (Ljubljana), Slovenia*

[b]*Jožef Stefan Institute (Ljubljana), Slovenia*

[c]*Faculty of chemistry and chemical technology, University of Ljubljana (Ljubljana), Slovenia*

[d]*ALISTORE-European Research Institute (Amiens), France*

Contact email: elena.tchernychova@ki.si

Introduction: Due to its excellent cycling stability and low volume change (cca. 0.2 %) or »zero-strain« behavior during Li insertion/extraction, spinel lithium titanate (LTO, $Li_4Ti_5O_{12}$) continues to be one of the most widely studied insertion-type anode materials for lithium-ion batteries [1]. LTO has recently gained much attention as an anode material candidate for all-solid-state thin-film batteries. However, in a number of cases the pulsed laser deposition (PLD) fabricated LTO thin films grown on Nb:$SrTiO_3$ substrates exhibited the presence of a secondary phase, most commonly an anatase TiO_2 phase [2], but also a β-Li_2TiO_3 phase [3] or a $Li_{0.74}Ti_3O_6$ phase [4]. Among the approaches, one can try to improve the quality of PLD-grown epitaxial LTO thin films by changing the substrate material and first depositing a thin epitaxially grown conductive interlayer. The latter shall possess a proper lattice mismatch in between the LTO and Nb:STO on top of the Nb:STO substrate and be electronically conductive. One of such candidates is a La-doped $BaSnO_3$ (LBSO), a cubic perovskite oxide which has received a lot of research attention as a transparent conductor for thin-film optoelectronic devices [5,6]. In addition, epitaxial growth of LBSO on $SrTiO_3$ single-crystal substrates by pulsed laser deposition has already been demonstrated in literature. In this work, we systematically studied the structural and electrochemical properties of LTO thin films grown by pulsed laser deposition on Nb:STO single-crystal substrates with (100), (110) and (111) out-of-plane orientations with and without LBSO interlayer. The study aimed to suppress secondary phase formation in LTO and to evaluate the LBSO interlayer impact on structural and electrochemical properties.

Methods: Epitaxial LTO thin films, with and without LBSO interlayers (~50 nm thick), were synthesized on (100), (110), and (111)-oriented Nb:STO single-crystal substrates using PLD at 700°C. Structural characterization employed in-situ reflective high-energy electron diffraction (RHEED), atomic force microscopy (AFM), high-resolution X-ray diffraction (HR-XRD) including out-of-plane/in-plane scans, rocking curves, and reciprocal space mapping (RSM). Post-cycling microstructure was analyzed using scanning transmission electron microscopy (STEM). Electrochemical properties were assessed in liquid electrolyte (1M $LiPF_6$ in EC/DEC) pouch cells versus Li metal, cycling between 1.45 V and 2.5 V vs. Li/Li^+ at rates from C/20 to 12C.

Results: XRD analysis confirmed significant suppression of secondary phases (e.g., anatase TiO_2, β-Li_2TiO_3) in LTO films grown on LBSO interlayers across all orientations compared to LTO grown directly on Nb:STO. AFM revealed preserved orientation-dependent morphologies (truncated pyramids for (100), ridges for (110), triangular facets for (111)) but with reduced facet size on LBSO. RSM and rocking curves indicated reduced mosaicity specifically for (100)-oriented LTO on LBSO. Electrochemically, (111)-oriented LTO (with or without LBSO) showed poor rate capability and stability. In contrast, (100) and (110) oriented LTO on LBSO exhibited the best performance, achieving stable discharge capacities near ~140 mAh g^{-1} at 3C and retaining ~93% capacity after 200 cycles (LTO+LBSO (110)). STEM analysis of cycled LTO+LBSO (110) confirmed a well-preserved morphology and Ti-O sublattice with no detectable interfacial degradation layer.

Discussion and Conclusions: LBSO interlayers effectively suppress secondary phase formation in epitaxial LTO thin films without altering their fundamental growth mode or orientation-dependent

morphology, while even reducing facet size and improving mosaicity for (100). The poor performance of (111) orientations is attributed to intrinsically hindered Li^+ transport in this densely packed plane. Critically, the LBSO interlayer enhances the structural quality without compromising the electrochemical performance of (100) and (110) oriented films, with LTO+LBSO (110) demonstrating excellent long-term stability. The absence of a degradation layer at the interface after cycling, confirmed by TEM, supports the robustness of the modified structure. This work demonstrates LBSO interlayers as a promising strategy for improving the phase purity and structural quality of epitaxial LTO anodes for advanced thin-film batteries. Future work will focus on integrating these anodes into full all-solid-state thin-film battery configurations.

Acknowledgements: This work has received funding from the Slovenian Research Agency ARIS through core program funding P2-0423 and projects J2-3050, J7-4637 and JV-4637.

References:
1. G.-N. Zhu et al., *Energy Environ. Sci.*, **2012**, *5*, 6652-6667
2. K. Kim et al., Electrochemistry, **2012** *80*, 800-803
3. D. M. Kunha et al, ACS Appl. Energy Mater., **2019**, *2*, 3410−3418
4. T. Hitosugi et al., Proceedings of SPIE - The International Society for Optical Engineering, **8987**, 89870U
5. a. V. Sanchela et al., J. Mater. Chem. C, **2019**, *7*, 5797
6. H. J. Kim et al., Applied Physics Express, **2012,** *5*, 061102

Type of presentation: Poster

MS7-P-10 How to Perform Identical Location Scanning Electron Microscopy: Workflow, Advantages, Challenges, and Applications

Blaž Tomc[a,b], Marjan Bele[a], Ana Rebeka Kamšek[a,c], Milena Martins[a], Aleš Marsel[a], Miha Hotko[a,b], Stefan Popović[a], Gregor Kapun[a,c], Črtomir Donik[d], Matjaž Godec[d], Nejc Hodnik[a,b,d], Luka Suhadolnik[a]

[a]*Department of Materials Chemistry, National Institute of Chemistry, Hajdrihova 19, 1000 Ljubljana, Slovenia*

[b]*University of Nova Gorica, 5000 Nova Gorica, Slovenia*

[c]*Faculty of Chemistry and Chemical Technology, University of Ljubljana, 1000 Ljubljana*

[d]*Institute of Metals and Technology, 1000 Ljubljana, Slovenia*

Contact email: blaz.tomc@ki.si

Introduction: Understanding and controlling material transformations at the nano- and microscale is essential for advancing technologies that rely on precisely engineered materials, such as in catalysis, energy storage, and functional nanomaterials. Conventional scanning electron microscopy (SEM) often falls short in tracking subtle changes, as it captures randomly selected locations. Identical location SEM (IL-SEM) overcomes this limitation by enabling precise revisits to the same nano-location, ensuring an unambiguous transformation history.[1,2]
Despite its simplicity and unique capability for revealing material dynamics, IL-SEM remains underutilized. When applied following a well-defined protocol, it provides unparalleled insights into morphology, microstructure, and local composition—insights often inaccessible with standard SEM approaches. This state-of-the-art technique enables precise monitoring of degradation, structural evolution, and surface modifications with exceptional accuracy. IL-SEM is particularly valuable for studying surface-sensitive phenomena where localized changes directly influence material performance.[3]

Method: The IL-SEM workflow[4] typically consists of five straightforward steps, requiring no significant adjustments or advanced optimization (Figure 1):
1.1 Sample insertion and location selection: Insert the sample into the SEM and identify a nano-location on the material where changes will be tracked.
1.2 Image recording: Capture SEM images, starting from the highest magnification and progressing to lower magnifications, moving from the nano- to the micro- to the macro-scale.
2. Sample treatment: Retract the sample from the SEM, perform the desired treatment, and reinsert the sample into the SEM.
3. Relocating the IL position: Use the recorded images from the first session as a guide to navigate from the macro- to micro- to nano-scale and locate the identical position.
4. Image comparison: Capture new images at the IL position and compare them with the before-treatment images to analyze changes.

Discussion: In this presentation, we offer a comprehensive guide to IL-SEM, outlining its advantages, addressing key challenges, and providing practical solutions. Through case studies and an optimized workflow with actionable recommendations, we demonstrate how IL-SEM can significantly enhance materials research, unlocking previously hidden insights and accelerating innovation across multiple disciplines.

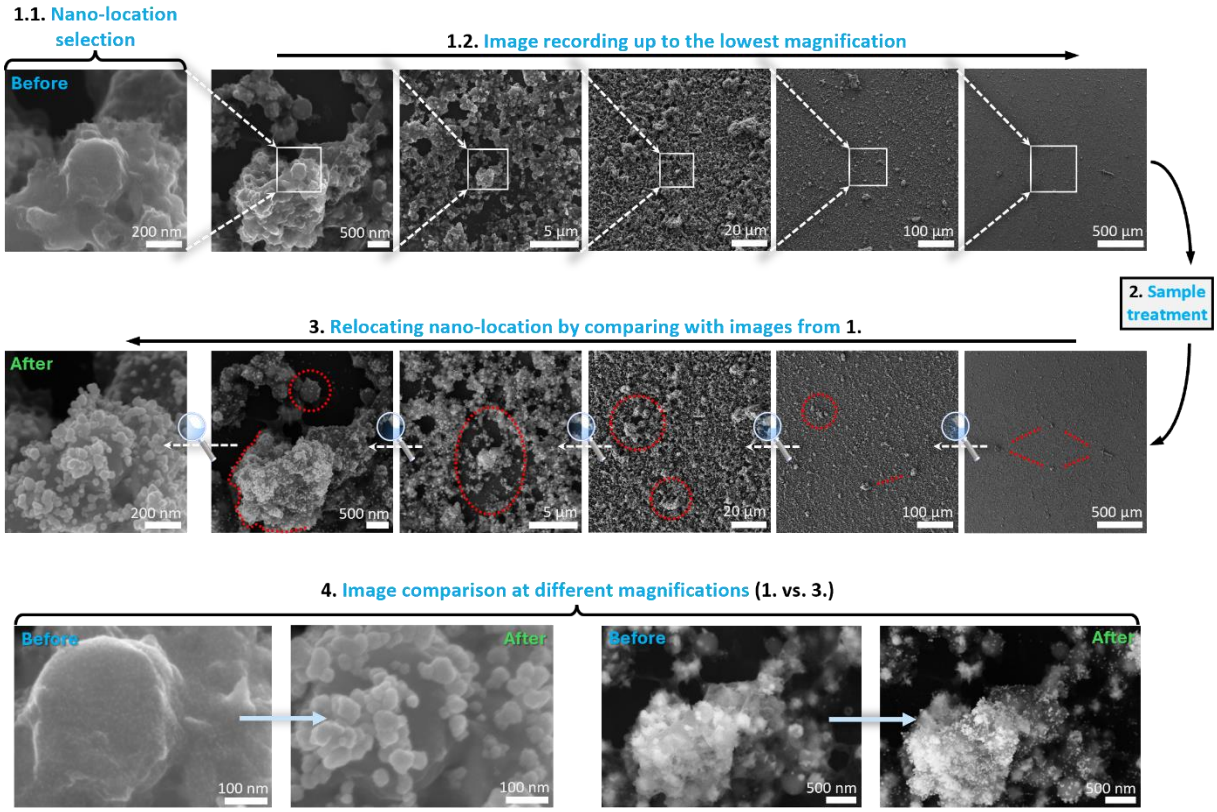


Figure 1: Typical IL-SEM workflow consisting of five steps, as described in the text. This case study illustrates copper nanostructured material embedded in carbon, analyzed before and after CO_2RR. In step 1, a nano-location was selected (1.1), and images were recorded at decreasing magnifications (200,000x to 100x, 1.2). The sample was then retracted, mounted in an electrochemical cell, and CO_2RR was conducted at -0.93 V vs. RHE (step 2). Upon re-insertion, the macro-location was relocated by comparing images at 100x magnification, using a distinctive 4-particle pattern (highlighted in red) as a reference. Gradually increasing the magnification enabled precise identification of the nano-location through distinct features (step 3). Finally, comparing images at various magnifications (step 4) revealed that the macro- and micro-structures remained stable, while the nano-structure showed significant alterations, including the disappearance of sub-5 nm copper nanoparticles. These findings underscore IL-SEM's ability to capture material evolution, as further elaborated by Tomc et al.[3].

References:

1. N. Hodnik, M. Zorko, M. Bele, S. Hočevar, M. Gaberšček, J. Phys. Chem. C **2012**, 116, 21326–21333.
2. M. Zorko, B. Jozinović, M. Bele, N. Hodnik, M. Gaberšček, Ultramicroscopy **2014**, 140, 44–50.
3. B. Tomc, M. Bele, M. A. Nazrulla, P. Šket, M. Finšgar, A. K. Surca, A. R. Kamšek, M. Šala, J. Š. Hudokli, M. Huš, B. Likozar, N. Hodnik, J. Mater. Chem. A **2025**, 13, 4119–4128.
4. B. Tomc, M. Bele, Ana Rebeka Kamšek, Milena Martins, Aleš Marsel, Miha Hotko, Stefan Popović, Gregor Kapun, Črtomir Donik, Matjaž Godecd, N. Hodnik, L. Suhadolnik: How to Perform Identical Location Scanning Electron Microscopy: Workflow, Advantages, Challenges, and Applications, **Submitted paper**.

MS8 Advanced functional materials

Type of presentation: Invited

MS8-IN-1 Adaptive 3d nanoprinting via focused electron beams: precision, functionality, and beyond

Harald Plank[a]

[a]*Institute of Electron Microscopy and Nanoanalysis, Graz University of Technology*

Graz Centre of Electron Microscopy

Steyrergasse 17, 8010 Graz, Austria

Contact email: harald.plank@felmi-zfe.at

Over the past decade, additive direct-write manufacturing has emerged as a transformative approach, now occupying a pivotal role in research and development due to its distinctive capabilities. While methods have progressed impressively down to the microscale and even found application in industrial settings, the challenges intensify as we venture into the meso- and nanoscale realms, where demands for resolution, spatial precision, predictability, and reliability escalate significantly. Among the limited pool of additive direct-write technologies suitable for nanoscale fabrication, focused electron beam induced deposition (**FEBID**) has witnessed remarkable strides in recent years. This technology bases on the precise, localized synthesis of nanostructures induced by a particle beam, utilizing surface-adsorbed precursor molecules introduced into the vacuum chamber via gas injection systems. Consequently, FEBID imposes minimal constraints on substrate materials (in terms of vacuum-/ beam-compatibility) and surface morphologies, rendering it into a true additive direct-write technology. One of FEBID's distinguishing features is its capability to fabricate intricate, freestanding 3D nanostructures through controlled movement of the electron beam combined with defined pulse durations. This enables the attainment of individual feature sizes down to the sub-10 nm range in a predictable and reproducible manner unlike other methods. Moreover, with an expanding repertoire of precursor materials and enhanced software packages facilitating robust upfront design, 3D FEBID has ascended to the status of true 3D nano-printer, poised to spearhead advancements in direct-write additive manufacturing at the cutting edge.

In this talk, we embark on a journey through the most important fundamental principles of FEBID-based 3D Nanoprinting, delving into recent advancements while placing particular emphasis on the current state of fabrication techniques and tuning capabilities within 3D-space. We explore the intricacies of meshed, closed, and mixed 3D designs and highlighting their challenges during fabrication with the ambition to push the boundaries of this technology. Additionally, we scrutinize the technical and physical constraints that govern 3D FEBID, offering insights into the various application pathways through an examination of both direct and multi-stage procedures. This discussion is complemented by an exploration of materials, dissecting their structural and chemical compositions to illustrate how their properties can be tailored to suit specific requirements. Moreover, we briefly showcase a range of examples spanning diverse fields such as nano-optics, electronics, magnetics, advanced scanning nanoprobes, and sensing applications, illustrating the wide-ranging applicability of 3D FEBID. Finally, we give a view towards the horizon, offering a glimpse into the future of this technology, identifying nascent avenues in materials, research areas, and technological developments that are poised to shape the landscape in unprecedented ways.

Type of presentation: Oral

MS8-O-1 Low-dose 4DSTEM analysis of local strain in 2D perovskite lateral heterostructures

Sirous Khabbaz Abkenar[a], Alexander Schleusener[b], Mehrdad Faraji[b,c], Roman Krahne[b], Giorgio Divitini[a]

[a]*Electron Spectroscopy and Nanoscopy, Istituto Italiano di Tecnologia, (Genova), Italy*

[b]*Optoelectronics, Istituto Italiano di Tecnologia, (Genova), Italy*

[c]*Dipartimento di Chimica e Chimica Industriale, Università degli Studi di Genova, Via Dodecaneso, 31, 16146 Genova, Italy*

Contact email: giorgio.divitini@iit.it

Introduction

Lead halide perovskites are a popular class of emerging semiconductors and feature a wide compositional and structural tunability. The structural arrangement is conventionally classified according to how octahedra are locally arranged, distinguishing between the most heavily studied 3D structure, where a 3D network is formed, and the so-called 2D structure, where the octahedra form sheets separated by organic spacers. This specific configuration has in-built anisotropy and has a strong potential for optoelectronic applications [1]. Furthermore, their inherently soft crystal lattice is tolerant to lattice mismatch, making them promising for heterostructure formation [2]. Our group has demonstrated the ability to thus grow 2D heterostructures, as well as probing their local optoelectronic properties using cathodoluminescence [3]. To understand the interplay between optoelectronic and structural properties, a thorough understanding of the local crystallography is needed. Therefore, we applied low-dose scanning electron diffraction (4DSTEM) to observe local crystallographic features and strain on triple halide core-frame heterostructures featuring a sequence of chloride, bromide and iodide phases.

Objectives

The main objective of this work is determining local crystallography and lattice parameters in 2D perovskite lateral heterostructures built with a sequence of different halide ions. We combine crystallographic insight with compositional mapping using Scanning Transmission Electron Microscopy / Energy-Dispersed X-ray spectroscopy (STEM-EDX). The outcomes of this study will enable new optoelectronic devices for lighting, as well as model systems for the study of physical phenomena such as polaritons. For correlative measurements, low-dose 4DSTEM measurements were carried out first.

Materials & Methods

A solution-based process was used to produce lateral heterostructures. Anion exchange in microcrystalline phenethylammonium (PEA) lead-halide 2DLPs led to PEA_2PbCl_4–PEA_2PbBr_4–PEA_2PbI_4 core-frame microcrystals. 4DSTEM datasets were acquired in a ThermoFisher Spectra 300 S/TEM, operated at 300 kV in microprobe mode. The semi-convergence angle was set to 0.5 mrad; the diffraction patterns were recorded on a post-filter Gatan Continuum camera. Strain analysis was done within Gatan Digital Micrograph**.** The EDX signal was collected on a Dual-X setup of 2 detectors with a total acquisition solid angle of 1.7 sr.

Results

Using EDX, we determined the bromide phase of the heterostructure to have the expected stoichiometry. A degree of intermixing was found in the other two phases (chloride-rich core and iodide-rich shell). The bromide/iodide interface was found to be relatively sharp, with limited intermixing and a transition over <100 nm, while the chloride/bromide interface presents an extended gradient with intermediate composition (Fig 1a-b).

4D-STEM measurements of the local crystallinity highlighted a uniform crystal phase through the entire heterostructure, with a visible change in lattice parameters at the interfaces (Fig 1c-e). The measured change in lattice spacing was smaller than what anticipated from the relaxed structures, suggesting that selective alloying mediates the lattice mismatch and enables a good interface between the phases in the heterostructure.

Conclusion

Our approach yielded representative, robust crystallographic information from beam-sensitive materials using a low-dose 4DSTEM approach with an electron dose <1 e/A^2. Anisotropy of the strain, combined with the compositional information, indicates a potential interplay between composition and crystallography in accommodating different soft perovskite phases and enabling lattice continuity through the heterostructures, demonstrating these perovskites as a promising optoelectronic platform.

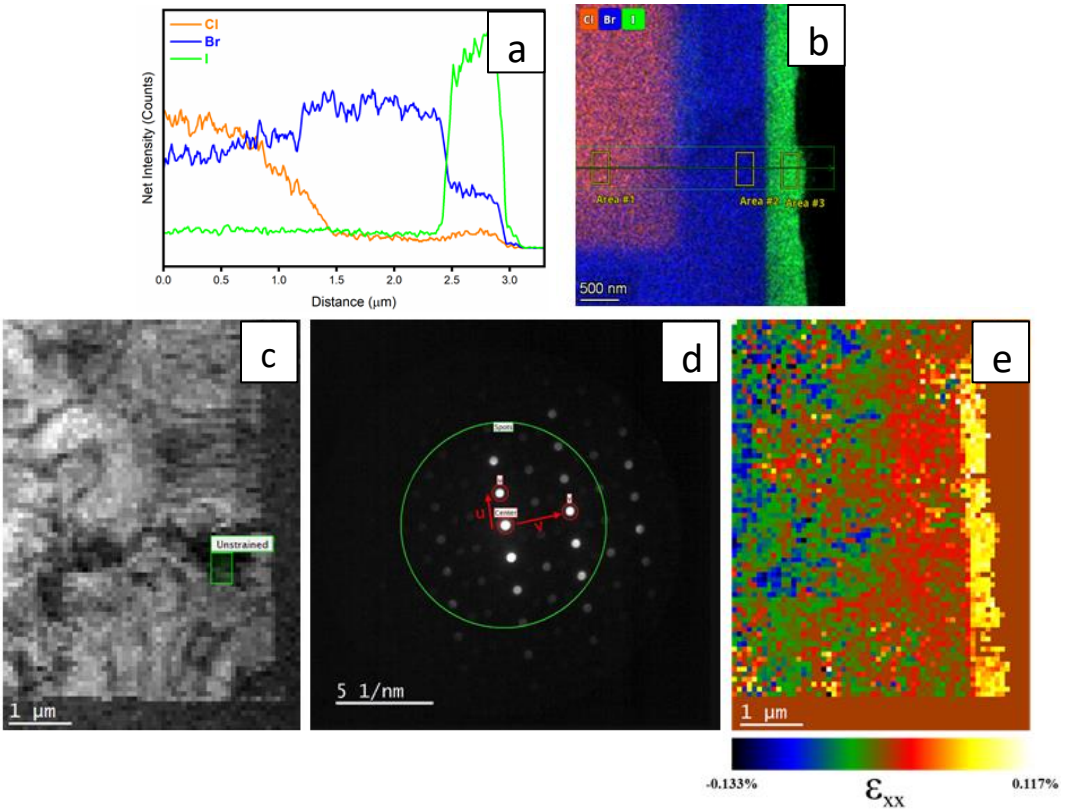


Figure 1. a) EDX compositional profile and b) map of a 2D perovskite lateral heterostructure; the three areas indicate representative regions for each phase and the green band is the area the profile was extracted from. c) Virtual dark field reference for the 4DSTEM dataset. d) Reference diffraction pattern from a relaxed bromide area (labelled "unstrained" in panel c)). e) Lattice parameter variation along the interface.

References

1. A. Schleusener et al., Heterostructures via a Solution-Based Anion Exchange in Microcrystalline 2D Layered Metal-Halide Perovskites. Advanced Materials, 2024. 36(31).
2. E. Shi et al., Two-dimensional halide perovskite lateral epitaxial heterostructures. Nature, 2020. 580: p. 614-620.
3. A. Griesi et al., Mapping emission heterogeneity in layered halide perovskites using cathodoluminescence. Nanotechnology, 2024, 35 105204

Type of presentation: Oral

MS8-O-2 Revealing atomic-level plasticity of ceramic materials through advanced electron microscopy

Zaoli Zhang[a], Zhuo Chen[a], Yong Huang[a]

[a]*Erich Schmid Institute of Materials Science, Austrian Academy of Sciences, Jahnstraße 12, Leoben, A-8700, Austria*

Contact email: zaoli.zhang@oeaw.ac.at

Atomic-level plasticity includes partial dislocation emission from GBs/interfaces, lattice distortion, local phase transitions, and dislocation creations and defects (point, line, and planar defects) generations. How do these relate to the macroscopic properties of materials? Usually, metals and alloys exhibit good plasticity because of dislocation migration. Thus, dislocation behaviors are strongly related to the observed mechanical properties. However, ceramic materials are usually very brittle and hard to exhibit prominent plasticity due to the limited slip system and high critical resolved slip stress (CRSS) required to initiate the dislocation migration. As a technical ceramic, transition metal nitrides (TMNs) have found widespread applications in the cutting- and machining-tool industry due to their extreme hardness, thermal stability, and corrosion resistance. The increasing demand for these nitrides requires an in-depth understanding of their structures at the atomic level. The local plasticity in these ceramics could be unveiled using spherical aberration-corrected TEM and associated techniques. With the help of advanced electron microscopy methods, our understanding of the structure and property relationship of TMNs has been significantly advanced [1-5].

Objective:
1) the paper intends to reveal and evaluate the local atomic level plasticity in TMN ceramics; 2) to elucidate the relation of the atomic level plasticity and macroscopic mechanical properties.
Materials and methods
The film used in this study was prepared by direct current magnetron sputtering using a custom-made lab-scale magnetron sputter deposition system. The film was grown on MgO(001) or Si substrate at 700 ℃, and the potential was kept floating during the deposition. Specific deposition conditions for different films are slightly different.
Nanoindentation and in-situ micro-mechanical testing were used to evaluate mechanical response. Post-mortem transmission electron microscopy (TEM) was employed to analyze the atomic scale's local structure and deformation mechanisms. Quantitative analysis on atom displacements and local strains was also carried out. Electron energy loss spectroscopy was also used to analyze the changes in the local electronic structure. All these provide atomic insights into the plasticity of ceramics, revealing the role of different defects, such as dislocation activity, stacking fault, and twins.
For high-resolution TEM (HRTEM) characterization, JEOL 2100F and FEI Titan Themis 60-300 cubed TEM equipped with an image-side Cs-corrector were adopted. The scanning TEM (STEM) images and energy-dispersive X-ray spectroscopy (EDXS) were acquired by a 300 kV field emission TEM (JEOL ARM300F) equipped with double Cs-correctors. Two windowless detectors, each with an active area of 100 mm^2, are equipped on the microscope.

Results
(a). Partial dislocations emitted from interfaces are found to be involved in the local plasticity of TaN/TiN multilayer by detailed HRTEM observations and quantitative analysis.[1] (b) By evaluating the atomic planar spacings, local strains, and simulations, we further demonstrated the local phase transformation of AlN in the CrN/AlN small-bilayer multilayer originating from the strain variations. This primarily affects the local bulk modulus. The findings were corroborated by theoretical calculations [2]. (c)We observed an atomic-scale intermixing phenomenon in the nanoscale TiN/AlN multilayer by coupling the cross-sectional FIB cutting with detailed atomic resolution electron microscopy analyses [3]. A new phase was created during nanoindentation, which could be unambiguously shown by mapping the electronic structure differences (i.e., using Ti-$L_{2,3}$ edge). This raises concerns about using

the nanoindentation method to understand experimentally measured hardness values in multilayers. (d) Via the quantitative HRETM analysis, we recently found that vacancy–mediated unit-cell distortions could achieve local plasticity in ceramics. Such observation is also well validated by theoretical calculation [6].

Conclusions

Advanced electron microscopy methods help understand the atomic-level plasticity in ceramics. The changes in atomic and electronic structure induced by local plasticity allow a correlation with properties at the atomic scale and lead to potential new findings.

References:

[1] Yong Huang et al., *Acta Materialia* 255 (2023) 119027
[2] Zaoli Zhang et al., *Acta Materialia*, 194(2020) 343
[3] Zhuo Chen et al., *Acta Materialia*, 214(2021)117004.
[4] Zhuo Chen et al., *Acta Materialia*,234(2022) 118008
[5] Zaoli Zhang et al., *Materials & Design*, 207(2021)109844.
[6] Zhuo Chen et al., *Nature Communications*, (2023)

Acknowledgment: This work is financially supported by the Austrian Science Fund (FWF P33696-N). The authors would like to thank Prof. Christian Mitterer, David Holec (Montanuniversität Leoben), and Paul Heinz Mayrhofer (Technische Universitaet Wien) for delivering the samples, performing DFT calculations and for very fruitful discussions.

Type of presentation: Oral

MS8-O-3 Structural modulations in antiferroelectric $NaNbO_3$-based ceramics investigated by STEM

Mojca Otoničar[a,b], Aadil Abass Shah[a], Meryem Lachhab[a,b], Elena Buixaderas[c], Barbara Malič[a,b]

[1] *Electronic ceramics department, Jožef Stefan Institute, Jamova 39, Ljubljana, Slovenia*

[2] *Jožef Stefan International Postgraduate School, Jamova 39, Ljubljana, Slovenia*

[3] *Department of Dielectrics, Institute of Physics, Czech Academy of Sciences, Na Slovance 2, 18200 Prague 8, Czechia*

Contact email: mojca.otonicar@ijs.si

Antiferroelectric materials hold great promise for electrical energy storage components due to their high storage density compared to conventional dielectric capacitors and short discharge times compared to batteries of SOFCs. While most efficient antiferroelectric materials out there are lead-based, environmental concerns push us to find lead-free alternatives. So far, the most promising lead-free antiferroelectric material is considered to be $NaNbO_3$ with ABO_3 perovskite structure. However, while this material shows the Pbcm symmetry with antiparallel cation ordering, which is a fingerprint of antiferroelectrics, electrical measurements show a single polarization-electric field (P-E) hysteresis loop and high remanent polarization, typical for ferroelectrics. With irreversible conversion to ferroelectric, the capacity to store charge is lost.

To better understand the local crystal and domain structure of NaNbO3 that should exhibit the antiferroelectric behaviour, we synthesized pure $NaNbO_3$ and $SrSnO_3$-modified and $BiMnO_3$-modified $NaNbO_3$ solid solutions, where the latter two actually exhibit a double hysteresis P-E loop, typical for antiferroelectrics. We investigate the structures of all three compositions in detail by X-ray diffraction, transmission electron microscopy and electron diffraction, as well as by scanning transmission electron microscopy (annular bright field and integrated differential phase contrast imaging) and X-ray energy dispersive spectroscopy. Our goal is to find major structural differences between these compositions, which contribute to a significantly different responses to electric field despite similar macroscopically observed structures.

In this contribution, we will present the key atomic-scale structural modulations and periodicities in the pure $NaNbO_3$, and $SrSnO_3$-modified and $BiMnO_3$-modified $NaNbO_3$, marking major differences that contribute to phase stability with temperature and applied external fields, linking the structure and functional properties of the studied antiferroelectric materials.

Type of presentation: Oral

MS8-O-4 Correlative Imaging and Surface Analysis workflow

Yahya Zakaria[a], Christopher Deeks[a], Tim Nunney[a], Paul Mack[a], Robin Simpson[a]

[a]*Thermo Fisher Scientific, United Kingdom*

Contact email: yahya.zakaria@thermofisher.com

Materials science field has seen tremendous progress in the last decades due mainly to technological developments related to materials synthesis, characterization and applications. Ultra-thin films, 2D, and functionalized materials exhibit usually complex chemistry, which requires a thorough characterization involving multiple analytical methods. To assure confidence in the results from imaging and surface analysis, it is advantageous to be able to perform measurements in the same position.

Correlative imaging and surface analysis is a comprehensive approach that combines multiple analytical techniques to provide a detailed understanding of the surface properties and composition of materials. This method is particularly useful in materials science, nanotechnology, and other fields where detailed surface characterization is crucial. This process is based on dataset alignment, where point-of-interest correlations can be established between XPS and SEM using precise positioning. This can guarantee the accuracy of the correlation and merge seamlessly with the datasets.

In addition, Raman spectroscopy can be combined with XPS to offer a complementary chemical characterization, particularly for identifying the quality of 2D materials. This combination is more useful when the focal points of XPS and Raman spectroscopy are aligned, allowing their respective data to be acquired from the point simultaneously.

Furthermore, there are other complementary techniques that can be used as XPS accessories. For instance, Low Energy Ion Scattering (LEIS or ISS) offers more surface-sensitive elemental composition information than XPS alone. Auger Electron Spectroscopy (AES) provides surface sensitive composition at higher spatial resolution than XPS can offer.

Combining these techniques enables a more comprehensive understanding of advanced materials, such as 2D and functionalized materials. In this presentation, we will discuss the advantages of combining XPS with MAGCIS and Raman spectroscopy, along with examples from various applications.

Type of presentation: Poster

MS8-P-1 Focused e-Beam Heating for local Material Modification: Melting, Patterning, and Band Gap tuning

Shahzeb Ahmad[a], Mattia Fanetti[a]

[a]*Materials Research Laboratory, University of Nova Gorica, Vipavska 13c, Ajdovščina 5270, Slovenia*

Contact email: ahmad.shahzeb@ung.si

Introduction: In the domain of nano-fabrication, lithography plays a significant role, encompassing the precise patterning and surface modification at the micro or nanoscale level. It allows for alterations in precise regions while leaving the surrounding areas unaffected [1]. In the wide variety of lithographic techniques, mask-less techniques don't require for a pre-patterned mask, i.e. the pattern is customizable every time, which makes them suitable for research and prototype fabrication. Among mask-less techniques, laser lithography (LL) is one of the fastest, but limited to a resolution of $\simeq 1$ μm [2], while Electron Beam Lithography (EBL), which can reach < 10 nm resolution, has disadvantage of expensive dedicated equipment. Moreover, both LL and EBL require resist deposition, development and removal, which brings multistep complex procedure and possible surface contamination. On the other hand, Focused ion beam (FIB) lithography allows for mask-less and resist-less patterning with a resolution down to 5 nm, but its application is restricted to etching [1]. In this contribution a novel approach to local modifications is investigated, associated with the phenomenon of local heating, which is produced by e-beams on the surface of materials. The proposed idea is to develop a technology that enables localized heating of materials by means of controlled irradiation with an incident e-beam, allowing for precise modifications of the materials with high lateral resolution. In comparison with the lithographic techniques previously mentioned, e-beam heating is a particularly intriguing process due to its capacity for direct utilisation in the annealing and fabrication of nano-materials, obviating the necessity for masks and resist. Another advantage of this approach is that we can use the e-beam generated in a Scanning Electron Microscope (SEM), an instrument which is commonly available almost at every materials research institutes.

Methods: In order to perform the thermal modifications by the e-beam, we used a field emission SEM (JEOL JSM 7100F TTL) available at the Materials Research Laboratory of University of Nova Gorica. The experiments were conducted to investigate the effects of local e-beam heating on indium (In), bismuth selenide (Bi_2Se_3), vanadium pentoxide (V_2O_5), and glass. In order to estimate the temperature rise at the surface of selected substrates, calculations were performed according to the Reimer's model for heat dissipation in SEM described in [3]. A focused e-beam was employed to locally heat the samples, with exposure conditions (beam energy, current and irradiating time) carefully controlled to reach the target modification temperature. A 40 nm thin film of In was deposited on SiO_2 (100 nm) on top of Si wafer by e-beam sputtering, while Bi_2Se_3 flakes were mechanically exfoliated from a Bi_2Se_3 crystal and V_2O_5 pellets were prepared via hydraulic pressing. Glass substrates were used as-is. The effects of localized e-beam heating were investigated on these materials to analyze structural and thermal responses. Prior to irradiation, the samples were characterized by using SEM (In, Bi_2Se_3 and glass) and in-situ cathodoluminescence (V_2O_5) to confirm their response as an effect of e-beam heating.

Results: The experiments revealed distinct effects of localized electron beam heating on the materials under study. The deposited In develops three dimensional islands with size of few hundred of nm. Figure 1(a) shows the three different irradiated areas indicated by the arrows, whereas, figure 1(b,c, and d) show the magnified images of those irradiated spots. It can be seen that by irradiating a single island under appropriate conditions, melting can be observed due to localized heating induced by the e-beam. The melted area is confined within few 100s of nm. The effect of local e-beam heating on Bi_2Se_3 was a local etching and creation of holes. Also the glass surface exhibited potential for electron beam-assisted patterning, highlighting its utility for microfabrication. Finally, cathodoluminescence analysis of locally irradiated V_2O_5 indicated a reduction in the band gap, in agreement with a thermal-triggered semiconductor-to-metal transition. The evaluated local temperature raising (according to Reimer's model [3]) is consistent with the transition temperature reported in literature [4].

By demonstrating the ability to induce controlled melting, patterning, and electronic property changes in above mentioned materials, the study opens new avenues for advanced manufacturing and device fabrication at the micro- and nanoscale.

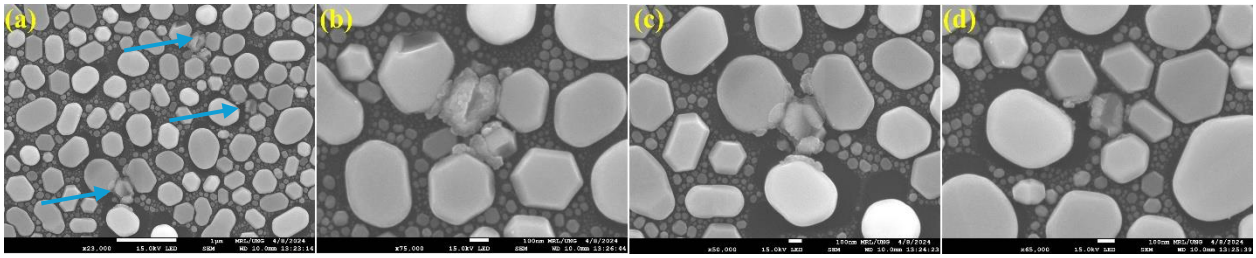


Figure 1(a,b,c, and d): SEM images exhibiting the surface morphology of e-beam irradiated In surface.

References:

1. K. Karimi, A. Fardoost, N. Mhatre, J. Rajan, D. Boisvert,M. Javanmard, Micromachines. **2024**, 1510, 1274.
2. H. Park, H. Park, M. Suleman, M. Kim, S. Kumar,Y. Seo, Microelectronic Engineering. **2024**, 295, 112275.
3. L. Reimer, Scanning electron microscopy: physics of image formation and microanalysis. 2nd ed. **1995**, Springer Series in Optical Sciences, vol.45, 57-134.
4. A.K. Kumawat, R. Nathawat, S.S. Rathore,A.K. Mukhopadhyay, Mater. Today: Proceedings. **2021**, 43, 2939-2943.

Type of presentation: Poster

MS8-P-2 Influence of La, Er, and Sm Doping on the Structural and Morphological Properties of ZnO for EMI Shielding

Oana Brincoveanu[a,d], Cosmin Romanitan[a], Petronela Pascariu[a], Lucian Barbu[b], Mirela Suchea[a,c], Emmanouel Koudoumas[a,c]

1: National Institute for Research and Development in Microtechnologies – IMT Bucharest, 126A, Erou Iancu Nicolae Street, 077190, Voluntari- Bucharest, ROMANIA

2: Electron Microscopy Integrated Laboratory, National Institute for Research and Development of Isotopic and Molecular Technologies, 67-103 Donath Str., Cluj-Napoca, Cluj County, 400293, Romania

3: Center of Materials Technology and Photonics, School of Engineering, Hellenic Mediterranean University, 71410 Heraklion, Crete, Greece

4: Research Institute of the University of Bucharest (ICUB), University of Bucharest, 060023, Bucharest

Contact email: oana.brincoveanu@imt.ro

The morphological and structural properties of metal oxide-based materials are critical to their performance in electromagnetic interference (EMI) shielding applications. In this study, zinc oxide (ZnO) doped with 1% lanthanum (La), erbium (Er), and samarium (Sm) was synthesized via the electrospinning–calcination method and characterized using X-ray diffraction (XRD), scanning electron microscopy (SEM), transmission electron microscopy (TEM), and energy-dispersive X-ray spectroscopy (EDX). XRD patterns of all samples revealed sharp and distinct diffraction peaks corresponding to the hexagonal wurtzite structure of ZnO. For Er- and Sm-doped ZnO, additional peaks were observed corresponding to cubic Er_2O_3 and Sm_2O_3 phases, respectively, indicating secondary phase formation. In contrast, no secondary phases were detected in La-doped ZnO. SEM and TEM analyses revealed that all samples consisted of a mixture of nanoparticles and nanorods, with dopant-specific variations in size and morphology. Interplanar distances calculated from TEM images and EDX results confirmed successful rare-earth incorporation into the ZnO matrix. The observed correlation between doping type and morphological variation suggests that rare-earth dopants significantly influence particle growth and nanorod formation. These findings enhance the understanding of doped ZnO's structural evolution and support its potential for improved dielectric properties and enhanced EMI shielding effectiveness.

Acknowledgements: PN 2307 – µNanoEl Contract No. 8N/03.01.2023, "Advanced research in micro-nano electronic and photonic devices, sensors and microsystems for societal applications" µNanoEl within PNCDI IV (2022–2027) and by PNRR/2022/C9/MCID/I8 CF23/14 11 2022 contract 760101/23.05.2023 financed by the Ministry of Research, Innovation and Digitalization in "Development of a program to attract highly specialized human resources from abroad in research, development, and innovation activities" within the – PNRR-IIIC9-2022 - I8 PNRR/2022/Component 9/investment 8.

Type of presentation: Poster

MS8-P-3 Y(Eu, Tb) frameworks with thiazolothiazoledicarboxylate: structural investigation by electron microscopy and diffraction techniques

Eduardo H. Lago Falcao[a,b], Sean M. Collins[b], Karolyne Santos da Silva[a], Fanny N. Costa[b], Leonis L. da Luz[a], Severino Alves Junior[a], Ana C. Vaz de Araújo[b,c], Emanoel L. T. França[a], Robert C. Carroll[b], Zabeada Aslam[b]

[a]*Universidade Federal de Pernambuco, Recife, Brazil*

[b]*University of Leeds, Leeds, United Kingdom*

[c]*Universidade Federal Rural de Pernambuco, Cabo de Santo Agostinho, Brazil*

Contact email: eduardo.lfalcao@ufpe.br

The rare earths (RE) are a group of metallic elements comprising Sc, Y, and the lanthanides (La through Lu). These elements are crucial for technologies such as lasers, lighting, communications, and magnets. Relatively recent research has focused on using RE ions for synthesising coordination polymers (CPs). The aim is to combine the photophysical, magnetic and chemical properties of RE with the structural versatility stemming from the choice of ligand and reaction conditions.

The 2,5-thiazolo[5,4-*d*]thiazoledicarboxylate ($C_6N_2S_2O_4^{2-}$, Thz^{2-}) has been used to produce CPs with cations of alkaline-earths [1], transition metals [2] and lanthanides [3]. The thiazolothiazole heteroaromatic ring features interesting properties [4] and presents additional coordination possibilities via the nitrogen atoms, which may lead to greater structural diversity. In the case of CPs of Thz^{2-} with lanthanides [3], a slow crystallization approach was utilized in order to produce crystals with the general formula $[Ln_2(Thz)_3(H_2O)_8]\cdot 4H_2O$ (Ln = La, Ce, Nd, Sm, Eu, and Gd). Their structure consisted of 2-D networks in which the lanthanide occupied two different crystallographic sites. All compounds were isostructural (P-1 triclinic space group). Initial attempts to obtain a similar CP with Tb(III) and later lanthanides were unsuccessful, which was attributed to their smaller ionic radii. Still, synthesising compounds combining two or more luminescent lanthanides may lead to applications in color generation and thermometry. In many cases, the active ion is incorporated in small quantities, substituting the site occupied by a similar ion, such as La(III) or Y(III).

In this work, we have used the hydrothermal route to prepare CPs with Thz^{2-} and Y(III), Eu(III) and Tb(III). Initial results suggest that these compounds are isostructural with the ones previously reported [3], although a secondary phase was sometimes present. We have also prepared compounds in which a small amount of Eu or Tb is incorporated into the Y framework. Techniques such as powder X-ray diffraction (XRD), electron microscopy with EDS and electron diffraction (ED) are then being used to better understand the formation, structure and properties of these materials.

The CPs were synthesized by the hydrothermal method. First, aqueous solutions of the desired RE^{3+} chloride(s) (RE = Y, Eu, Tb) and the Thz^{2-} ligand were transferred to a Teflon reaction flask, which was then sealed and kept at 60 °C for 6 days. The resulting crystals were filtered and dried at room temperature. According to the relative amounts of RE^{3+} included in the reaction mixtures, the compounds were designated YTb_X-Thz and YEu_X-Thz (X = 01 for the mixture 99% Y and 1% Tb or Eu; X = 10 for the mixture 90% Y and 10% Tb or Eu). Frameworks containing only one metal ion were named Y-Thz, Tb-Thz and Eu-Thz.

SEM/EDS and STEM/EDS analyses were performed on a Tescan Vega3 (10-25 kV) and on a FEI Titan Themis (300 kV) microscopes, respectively. XRD data were collected on a Rigaku Smartlab and on a PANalytical Empyrean diffractometer (copper Kα radiation, 1.541 Å). The photoluminescent measurements were performed in a Horiba Jobin Yvon Fluorolog-3 spectrofluorometer on ground solid samples, with an excitation wavelength of 340 nm.

Figure 1(a) shows the XRD patterns for for Y-Thz, YEu_{01}-Thz and YTb_{01}-Thz, along with the pattern calculated from Eu-Thz CIF [3]. Rietveld refinement of the data indicates that the compounds are isostructural with the series previously synthesised by open/gel crystallization. The hydrothermal method, therefore, proved effective in producing pure Y-Thz, Y-Thz with varying amounts of Eu(III)

and Tb(III) and the Tb-Thz compound. Nevertheless, a secondary phase was observed in the Y-Thz and Tb-Thz by XRD – but not in samples of YTb_{01}-Thz and YEu_{01}-Thz. EDS maps for a crystal of YTb_{01}-Thz are shown in Figure 1(b-e). The homogeneous distribution of the elements, especially Tb, suggest that within this crystal a single phase with both metals is present.

The room temperature emission spectra of Eu-Thz and YEu_{10}-Thz have both shown intraconfigurational 4f-4f transitions $^5D_0 \rightarrow {}^7F_J$ (J = 0, 1, 2, 3, and 4) in the 570-720 nm region (Figure 1(f)). The absence of ligand fluorescence in the emission spectra of Eu-Thz is due to the high sensitization efficiency of Thz on Eu luminescence. On the other hand, the emission spectra of YEu_{10}-Thz shows Thz fluorescence in the 370-450 nm region, which is associated with Y-Thz centers. The emission spectra of Tb-Thz and YTb_{10}-Thz only show emission bands related to the ligand (Figure 1(f)). The absence of Tb^{3+} emission bands in YTb_{10}-Thz excludes the possibility of deactivation by concentration quenching. The most probable deactivation pathway is through the triplet state, with an energy $E(T_1)$ = 17,390 cm^{-1}, below the emission state energy of Tb^{3+} ($^5D_4 \rightarrow {}^7F_5$; 18,416 cm^{-1}).

Additional XRD, TEM and ED experiments are currently being planned in order to determine (a) the crystallographic site preference for Eu(III) and Tb(III) and (b) the actual stoichiometry for the mixed compounds, (c) the secondary phase present in some of the compounds, and (d) which synthetic parameters might favor each phase. Another goal of this work is to demonstrate the potential of electron microscopy, particularly advanced electron diffraction experiments, to elucidate structural features in materials not suitable to be studied by more conventional techniques.

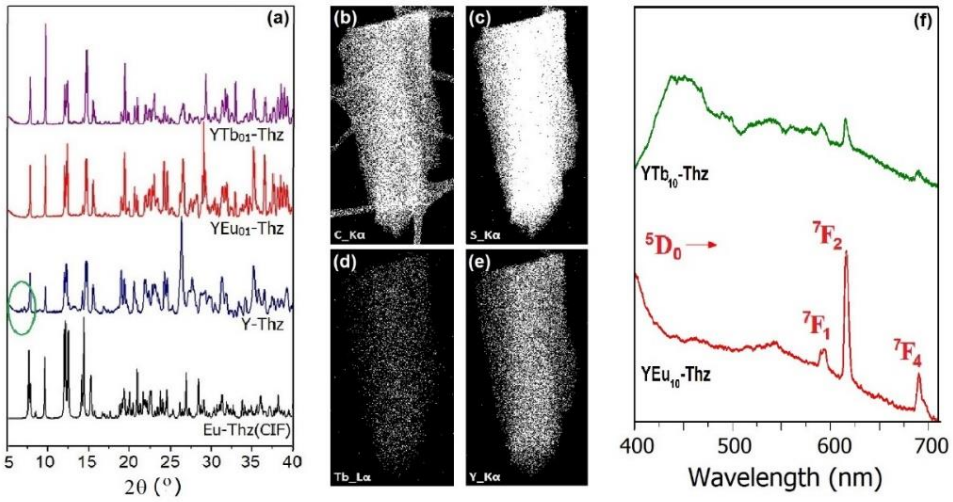


Figure 1: Experimental XRD patterns for Y-Thz, YEu_{01}-Thz and YTb_{01}-Thz, along with the pattern calculated from Eu-Thz CIF (a), C Ka (b), S Ka (c), Tb La (d) and Y Ka (e) EDS maps of a YTb_{01}-Thz crystal, and emission spectra (excitation 340 nm) for YEu_{10}-Thz and YTb_{10}-Thz (f).

Acknowledgments

Financial support from CNPq (Proc. 442937/2023-7), FACEPE (APQ-1105-1.06/24, APQ-0742-1.06/15), CAPES, UK Research and Innovation (EP/Y024583/1, project AMICI selected by the European Research Council) and the Engineering and Physical Sciences Research Council (EP/V028855/1) is gratefully acknowledged. This work has benefitted from the use of the XRD Facility and the LEMAS Facility in the Bragg Centre for Materials Research at Leeds.

References:

1. E.H.L. Falcao, Naraso, R.K. Feller, G. Wu, F. Wudl, A.K. Cheetham, *Inorg. Chem.* **2008**, 47, 8336-8342.
2. A. Aprea, V. Colombo, S. Galli, N. Masciocchi, A. Maspero, G. Palmisano, *Solid State Sci.* **2010**, 12, 795-802.
3. R.F.P. Clementino, A.B. de Souza Santos, O.J.B.J. Marques, D.R. Ratkovski, C.C. Gatto, I. Malvestiti, F.L.A. Machado, E.H.L. Falcao, *J. Solid State Chem.* **2018**, 268, 94-101.
4. X.-C. Huang, J.-J. Kong, *CrystEngComm* **2025**, Advance Article.

Type of presentation: Poster

MS8-P-4 SEM insights into crystallization behavior of oxide glass-ceramics

Marija Mirosavljević[a], Sara Marijan[a], Teodoro Klaser[a], Željko Skoko[b], Luka Pavić[a]

[a]*Division of Materials Chemistry, Ruđer Bošković Institute, Bijenička cesta 54, Zagreb, Croatia*

[b]*Department of Physics, Faculty of Science, University of Zagreb, Bijenička cesta 32, Zagreb, Croatia*

Contact email: mmirosav@irb.hr

Phosphate-based glasses and glass-ceramics are known for their exceptional properties and are widely used in optics, laser technology, nuclear waste immobilization, electronics and biomedicine. Alkali phosphate-based ones, in particular, show potential as solid-state electrolytes due to their unique electrical transport properties which arise from incorporation of alkali oxides into their network. Additionaly, the introduction of transition metal oxides(TMOs) such as Nb_2O_5, V_2O_5, and/or intermediates (Al_2O_3, ZnO) significantly influences their structure, enhancing conductivity.

In this study, various phospate-based glass-ceramics with incorporated oxides (Nb_2O_5, V_2O_5, and/or Al_2O_3) were prepared by spontaneous/controlled crystallization during melt-quenching from compositions near the glass-forming region. Their micro(structural) properties were investigated, and obtained results are correlated with electrical properties assessed using impedance spectroscopy (IS). The PXRD analysis confirmed the presence of crystalline phases embedded in the amorphous matrix, while SEM-EDS provided detailed information on the micro- and nano-scale features of the samples. The Axia ChemiSEM Microscope System was employed, utilizing various setups and detectors, including the ETD (Everhart-Thornley SE detector), CBS (Circular Backscatter detector) with beam deceleration (BD) mode, and energy dispersive X-ray spectroscopy (EDS) for elemental distribution mapping.

The results offer valuable insights into the crystallization process and the formation of crystalline phases within the amorphous matrix. Understanding the structure-property relationships of these materials enhances their potential for use in advanced technological applications.

ACKNOWLEDGMENTS

This work is supported by the Croatian Science Foundation, projects IP-2018--2018-01-5425 and DOK-2021-02-9665. The authors acknowledge the use of SEM Thermo Fisher Scientific model Axia™ ChemiSEM™ at the Ruđer Bošković Institute delivered by the project O-ZIP (Grant No. KK.01.1.1.11.0001) co-financed by the European Union through the European Regional Development Fund and the support of project CeNIKS (Grant No. KK.01.1.1.02.0013), co-financed by the Croatian government and the European Union through the European Regional Development Fund, Competitiveness and Cohesion Operational Programme.

Type of presentation: Poster

MS8-P-5 Probing beam-sensitive MOF mesocrystals at the nanoscale using 4D-STEM scanning nanodiffraction

Karen C. Bustillo[a], Alexis T. Bell[b,c], Darinka Primc[b,d]

[a]*National Center for Electron Microscopy, Molecular Foundry, Lawrence Berkeley National Laboratory, Berkeley, CA 94720, USA*

[b]*Department of Chemical and Biomolecular Engineering, University of California Berkeley, Berkeley, California 94720, USA*

[c]*Chemical Sciences Division, Lawrence Berkeley National Laboratory, Berkeley, CA 94720, USA*

[d]*Advanced Materials Department, Jozef Stefan Institut, Ljubljana, Slovenia*

Contact email: darinka.primc@ijs.si, dprimc@lbl.gov

Metal–organic frameworks (MOFs) are highly porous, crystalline materials formed by the coordination of metal ions and organic linkers, offering tunable structures for diverse applications such as gas storage, separation, and catalysis. Spontaneous self-assembly of nanoscale MOF particles holds great promise for enhanced functionality; however, most conventional synthesis methods predominantly yield larger, micron-sized particles. In this study, we report the controlled synthesis of Zeolitic Imidazolate Framework-8 (ZIF-8) cube-like nanoparticles that spontaneously self-assemble with cube-corners into chains and mesocrystalline superstructures, demonstrating a bottom-up strategy for hierarchical MOF organization.

Conventionally, mesocrystalline morphology—characterized by superstructures of mutually aligned nanoparticles—is identified using selected-area electron diffraction (SAED) and fast Fourier transforms (FFT) of real-space images in the TEM. However, due to the beam sensitivity of MOFs, we employed four-dimensional scanning transmission electron microscopy (4D-STEM) in low-dose mode, enabling high-resolution structural characterization while preserving the integrity of the nanostructures. Scanning nanodiffraction (4D-STEM) provided a low-dose approach to acquire diffraction data from nanoparticle clusters, and due to the air and moisture sensitivity of the samples, freshly prepared specimens were promptly transferred into the microscope column within a few hours.
To minimize beam damage, 4D-STEM was performed in low-dose mode with 3 nm probe spacing, gently sampling each region multiple times. As MOFs are highly beam-sensitive, only brief low-magnification scans were used to locate suitable areas, which were then imaged without further exposure . Survey and pre-scan doses were kept minimal (0.03 and 0.1 $e^{-}/Å^{2}$), while the full dataset was acquired at 100 $e^{-}/Å^{2}$. All measurements were conducted at room temperature on freshly prepared samples. We revealed that the self-assembled ZIF-8 chains and mesocrystals exhibit a predominant crystallographic alignment among neighbouring nanoparticles, confirming their monocrystalline nature.

Future work will focus on investigating the early stages of the reaction using 4D-STEM to pinpoint when nanoparticles first nucleate, become crystalline, and begin to self-assemble. This time-resolved approach will provide deeper insights into the mechanisms behind hierarchical MOF organization and guide strategies to control self-assembly pathways.

Type of presentation: Poster

MS8-P-6 Quantum chemical simulation of spontaneous water dissociation on 110 || 110 rutile TiO_2 interfaces

Vesna Ribić[a], Vanja Jordan[a], Sandra Drev[a], Janez Kovač[a], Goran Dražić[b], Aleksander Rečnik[a]

[a]*Jožef Stefan Institute (Ljubljana), Slovenia*

[b]*National Institute of Chemistry (Ljubljana), Slovenia*

Contact email: vesna.ribic@ijs.si

Introduction. In the world's growing demand for clean energy, hydrogen is one of the cleanest sources that releases large amounts of energy on combustion with the reaction product being pure water. One way to produce hydrogen is water splitting, which is the reverse chemical reaction where water is split into hydrogen and oxygen. Thermal splitting of water is an energy–demanding process that occurs at temperatures above 2000 degrees Celsius, which is uneconomic for production. On the other hand, we all know the natural process of photosynthesis, where the high–energy O–H bonds are easily split at ambient conditions. This raises a question that scientists have been facing for over 50 years, namely, can we discover an as efficient water–splitting process whose product would be hydrogen?

Methods. Fibrous rutile TiO_2 was studied in terms of interface translation, atomic structure, and surface chemistry in the presence of water, by means of advanced electron microscopy (HADDF–STEM) and spectroscopy (EELS, XPS) methods combined with atomistic modeling and quantum chemical (DFT) calculations. Resulting structures were crosschecked by image simulations and matching.

Results. During a routine study of hydrothermal growth of rutile twins, we discovered that under specific processing conditions rutile forms acicular fibrous terminations. Electron microscopy study of the so–formed forest of rutile fibers showed that they are homoepitaxially grown on preexisting rutile crystals. The fibers are interconnected through long, atomically flat 110 || 110 interfaces, that stay habitually separated for a fraction of a nanometer throughout the growth process. Besides the separation, the fibers were shown to be systematically shifted for a half–a–unit–cell along the crystallographic c–axis, suggesting an alternating harmonic compression/stretching mode of so–organized crystals [1].

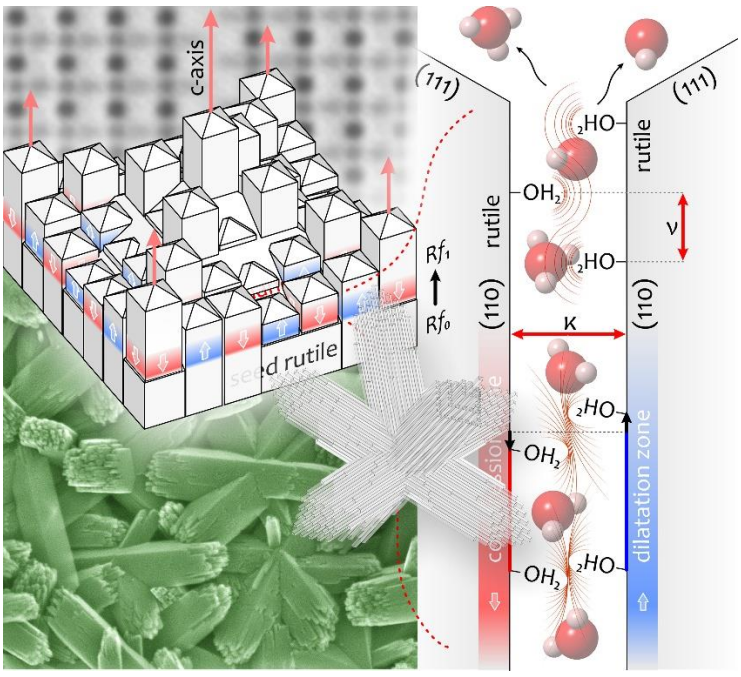


Fig. 1. Fibrous rutile TiO_2 grown on twinned rutile seeds exhibits specific structural registry driven by surface mineral–water interactions that hold them in stable separation during their growth. The adjacent fibers are successively compressed/stretched to accommodate highly charged aqueous species on their surface. In turn, this particular interface structure has the ability to crack up to 25% of neutral water into its dissociates.

Rigid–block translations and interface contrast features were used to reconstruct a hypercell of rutile–fiber network. Supercells including a pair of 110 interfaces across three adjacent fibers were used as a model system for ab–initio calculations. It was shown that the fibers while staying in stable separation

during their growth, adopt a specific crystallographic registry that is controlled by repulsion forces between fully hydroxylated and protonated 110 surfaces (Fig. 1). During interface structure relaxation, a turbulent proton transfer and cracking of O–H bonds is observed, generating a strong acidic character via proton jump from the bridge –OH^b to terminal –OH^t groups, and spontaneous dissociation of interfacial water via a transient protonation of the –OH^t groups. It has been shown that interface without the observed shifts does not dissociate interfacial water, whereas the interface with the observed shifts dissociates interfacial water proving the fascinating effect of quantum–confined structures (Fig. 2).

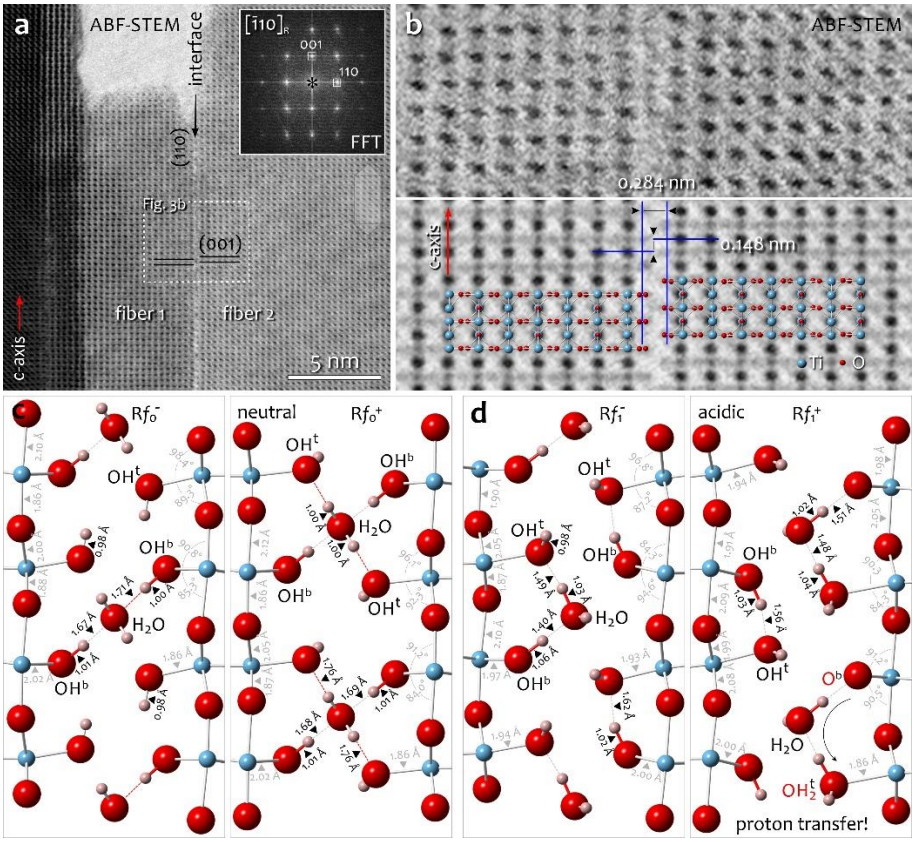


Fig. 2. STEM study of rutile fibers. (**a**) the interface is sharp and well defined. (**b**) experimental ABF–STEM image of rutile–rutile interface displaying systematic lateral and vertical displacements. These features are used to construct the starting Rf_1 interface model, superimposed on processed STEM image (below). During DFT optimization (**c**) Hydroxylated Rf_0 interface H_2O forms H bonds with –OH groups on rutile surface, O–H bonds are stretched. No distortions are transferred into the TiO_2 lattice. (**d**) In the Rf_1 structure, that involves the observed shifts, the equilibrium state shows highly dissociated species. O–H bonds are constantly stretched and broken to generate dissociation products H_3O^+ and OH^- in the medium with protonated –OH_2^t and deprotonated –O^b groups on the surface.

Discussion. For the first time a mineral–water interface capable of inducing an acidic response in the initially neutral medium when re–immersed was identified. Our discovery has opened up new avenues to explore in research of catalyst water splitting and poses a significant step in clean energy pursuits.

Funding. This research was supported by ARIS postdoctoral project No. Z2-50056.

Reference:

1. V. Ribić, V. Jordan, S. Drev, J. Kovač, G. Dražić, A. Rečnik, *Adv. Mater.* **2024**, *36*, 2308027. DOI: 10.1002/adma.202308027

Type of presentation: Poster

MS8-P-7 Structural study of a Magnetic Graphitic Nanocomposite

Ana Claudia Vaz de Araujo[a,b], Walyson K. Lins da Silva[a], Eduardo H. Lago Falcao[c,d], Fanny Nascimento Costa[e], Zabeada Aslam[e], Timothy Moorsom[b], Rik Drummond-Brydson[b].

[a]*Universidade Federal Rural de Pernambuco, Cabo de Santo Agostinho, Brazil*

[b]*University of Leeds, School of Chemical and Process Engineering, Leeds, United Kingdom*

[c]*University of Leeds, School of Chemistry, Leeds, United Kingdom*

[d]*Universidade Federal de Pernambuco, Departamento de Química Fundamental, Recife, Brazil*

[e]*University of Leeds, Bragg Centre for Materials Research, Leeds, United Kingdom*

Contact email: claudia.vaz@ufrpe.br; a.c.vazdearaujo@leeds.ac.uk

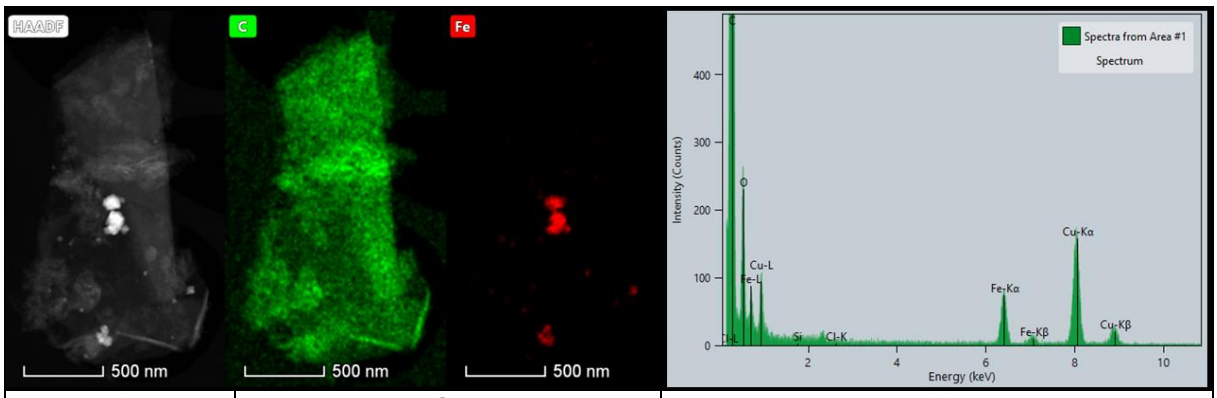
The combination of graphitic and magnetic materials has shown promise as adsorbents and catalysts, due to properties such as high specific surface area, ease of preparation, low cost, and magnetism. These features work together to improve the interaction with the target (pollutants, for example) and to facilitate the removal and recovery processes [1,2,3,4]. The formation and interaction mechanisms of magnetic iron oxide nanoparticles/graphite nanocomposites for the efficient removal of pollutants were investigated by electron microscopy and diffraction techniques as well as batch experiments.

The iron oxide nanoparticles (NPs) were synthesized by co-precipitation according to the following procedure: 50 mL of an aqueous solution of NH_4OH (1.0 mol L^{-1}) was added continuously to an aqueous solution of $FeSO_4 \cdot 7H_2O$ (0.1 mol L^{-1}, 50 mL) via ultrasound at 50°C. The particles were washed with HCl solution (0.01 mol L^{-1}) and water, and centrifuged. The powders were dried at 60°C for 24 h. The magnetic graphite nanocomposite (MGN) was synthesized by the hydrothermal method: 0.02 g of the NP and 0.02 g of graphite were dispersed in 15 mL of deionized water in a Teflon tube. A NH_4OH solution was dropped into the dispersion to adjust the pH to 8. The mixture was sealed and kept at 200°C for 24 h, and the resulting black powder was collected. The synthesized materials were characterized by XRD + Rietveld, magnetometry, and TEM, EDS.

The diffractogram of NPs exhibits narrow, well-defined peaks, indicating a crystalline sample. The diffraction pattern was indexed to the magnetite (Fe_3O_4) cubic phase with lattice parameter a = 8.3780 Å (COD no. 96-900-5840, *Fd-3m* space group). Similarly, the diffractogram obtained for MGN confirms the presence of magnetite's characteristic peaks. Additionally, peaks associated with graphite were observed, including a prominent reflection at $2\theta = 26.5°$, two less intense peaks in the 2θ range of 50–55°, and a weak peak between 75–80°. A Rietveld refinement was performed, confirming the cell parameters and the symmetry of the material.

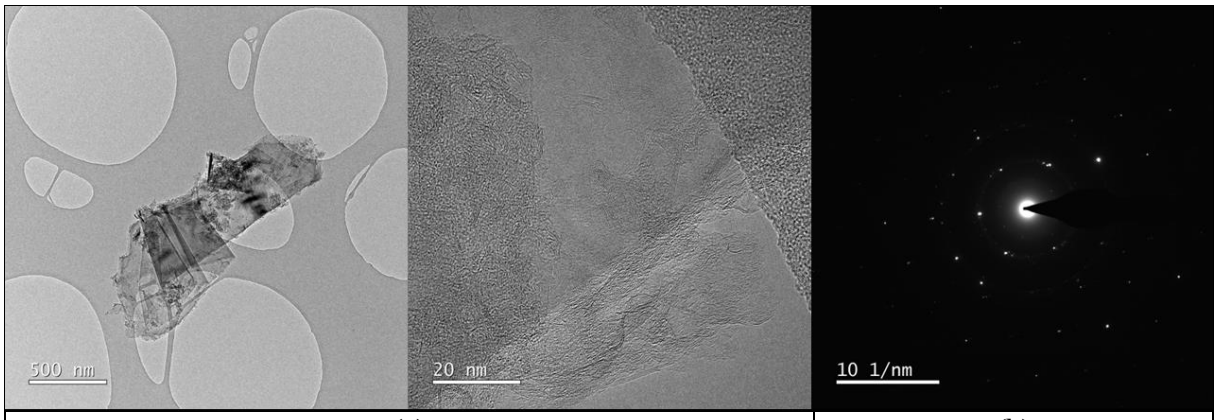
Zero-field-cooled/field-cooled measurements have been used to analyse the magnetic behaviour of the particles and estimate their size distribution. This analysis shows the particles are ferrimagnetic with a Curie temperature well above room temperature.

Transmission Electron Microscopy was carried using the Titan Themis Cubed operated at 300 K and fitted with a Monochromator. To reduce beam damage, a beam current of 1 nA was used for imaging. Bright-field TEM images were collected on the Gatan OneView 16 Megapixel CMOS digital camera. It is equipped with the Super-X EDX system with windowless 4-detector design and 0.7 srad solid angle for EDS analysis. EDS maps were collected with a probe current of 100 pA. Figure 1(a) presents the HAADF STEM image of a graphene flake decorated with iron oxide nanoparticles and Figure 1(b) shows the EDS maps of graphite (C – green) and iron oxide nanoparticles (Fe – red). Figure 1(c) presents the EDS spectrum that shows the presence of C, Fe and O, Cu and Si peaks are from the Cu TEM grid. Figure 2(a) presents the Bright-Field TEM images of a graphite flake at different magnifications, and Fig. 2(b) shows a diffraction pattern featuring the hexagonal arrangement of spots associated with graphite.



(a) (b) (c)

Fig. 1: (a) HAADF STEM image of a graphene flake decorated with iron oxide nanoparticles, (b) EDS maps of graphite and iron oxide nanoparticles, and (c) EDS spectrum for the MGN nanocomposite.



(a) (b)

Fig. 2: (a) Bright-Field TEM images of a graphite flake at different magnifications, and (b) diffraction pattern of the MGN nanocomposite.

Additional analyses are being performed with the aim of better understanding the interactions between the NPs and graphite, their surface and magnetic properties, and the way they interact with certain pollutants. Our results may lead to more efficient purification systems and open venues for new, additional applications.

Acknowledgments

We gratefully acknowledge the financial support from Brazilian agencies Fundação de Amparo à Ciência e Tecnologia do Estado de Pernambuco (FACEPE, APQ-0787-3.03/24), and Conselho Nacional de Desenvolvimento Científico e Tecnológico (CNPq, UNIVERSAL: 407723.2023-4, PD: 201239/2024-8). This work has benefitted from the use of the XRD Facility in the Bragg Centre for Materials Research at Leeds.

References:

1. B. S. Damasceno, A. F. V. da Silva, A. C. V. de Araújo, *J. Environ. Chem. Eng.* **2020**, *8*, 103994.
2. R. K. do Nascimento, B. S. Damasceno, A. N. de Melo, P. H. M. de Farias, J. V. F. L. Cavalcanti, D. C. S. Sales, E. H. L. Falcão, A. C. V. de Araújo, *Cellulose*, **2023**, *30*, 2483-2501.
3. M. A. O. Porangaba, R. A. A. Silva, D. F. Gomes, A. C. V. de Araújo, M. G. Ghislandi, *Chem. Eng. Res. Design*, **2023**, *193*, 222-230.
4. B. S. Damasceno, V. C. da Silva, A. R. Rodrigues, E. H. L. Falcão, A. C. V. de Araújo, *J. Alloys Comp.*, **2024**, *1005*, 175907.

Exhibitor presentations

Type of presentation: Oral

Bruker EMA, Unique Range of Analytical Tools for Electron Microscopes

Cristian Vailati[a]

[a]*Bruker Nano GmbH*

Contact email: cristian.vailati@bruker.com

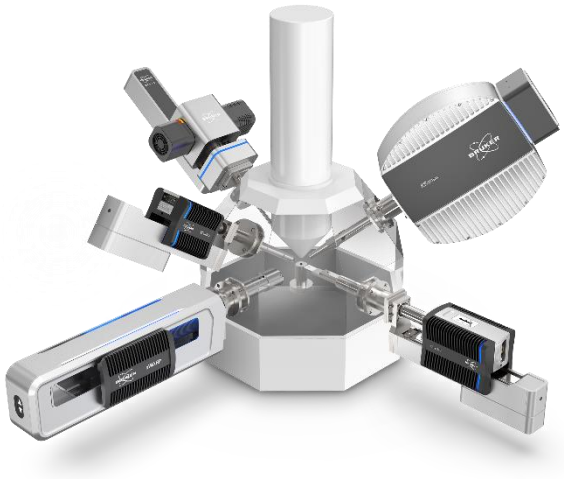
Bruker's electron microscope analyzers EDS, EBSD, WDS and Micro-XRF on SEM offer the most comprehensive compositional and structural analysis of materials available today. The full integration of all these techniques into the ESPRIT software allows you to easily combine data obtained by these complementary methods for the best results.

Bruker's latest generation of QUANTAX EDS features the XFlash® 7 detector series, which provides the largest solid angle for X-ray collection (also called collection angle) and the highest throughput.

eWARP is the first ever EBSD detector powered by a pixelated sensor that was designed from scratch with EBSD in mind. This, alongside the sensors wide area pixels and CMOS technology, makes eWARP the fastest and most signal efficient detector available.

The QUANTAX WDS for SEM consists of the XSense wavelength dispersive spectrometer yielding the best resolution among all parallel-beam WDS systems. The large solid angle, due to the parallel-beam design, results in a much higher signal intensity for low-energy X-rays

Micro-X-ray Fluorescence (micro- XRF) spectroscopy is a non-destructive analytical technique that can be used alongside conventional Energy Dispersive Spectroscopy (EDS) on a Scanning Electron Microscope (SEM). Micro-XRF on SEM, also known as SEM XRF, delivers the SEM with a range of new capabilities such as the ability to measure and map trace elements, the analysis of layered samples, and more.



Type of presentation: Oral

Comprehensive and intuitive analysis with Apreo ChemiSEM™, ChemiPhase™ and TruePix EBSD™"

Daniel Phifer[a], Chris Stephens[b]

[a]*Thermo Fisher Scientific, Eindhoven, The Netherlands*

[b]*Thermo Fisher Scientific, Eindhoven, The Netherlands*

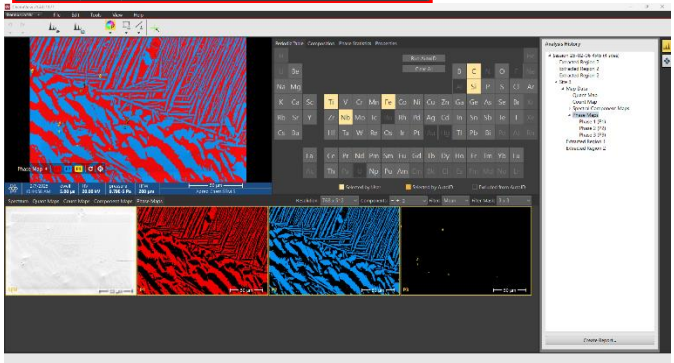
Contact email: daniel.phifer@thermofisher.com

Introduction:
Ti-Nb-Fe alloys are a class of titanium-based materials known for their biocompatibility, mechanical strength, and corrosion resistance. Their low elastic modulus and biocompatibility make them ideal for orthopedic and dental implants, reducing stress shielding effects. These alloys also offer lightweight yet strong properties, making them suitable for high-performance structural components in aircrafts and vehicles. While primarily used for hydrogen storage, their mechanical stability allows integration into structural frameworks for energy applications, including battery electrodes. The presence of iron in the alloy contributes to high-temperature performance, stabilizing certain phases, making these alloys more resistant to creep and oxidation and improving weldability over other titanium alloys.

Methods:
Better understanding the structure-property relationship within materials is a critical step in in improving overall material performance: linking structure, property and chemistry related questions enables better control over production processes. SEM imaging enables understanding into surface morphology and topography, energy dispersive spectroscopy identifies elements, their distribution and their concentration, electron backscatter diffraction provides microstructural information on phases, orientation and strain, while correlative analysis links all these modalities together. Uniquely, Apreo ChemiSEM integrates all of these techniques within a simplified platform, providing a simplified analysis workflow and a greater configurability for real-world applications.

Results:
As with most SEM analysis workflows, locating regions of interest within the Apreo ChemiSEM workflow is usually performed with an optical navigation camera and then SEM SE and BSE imaging. After this step EDS analysis is used to identify elements in the sample, most typically using X-ray point mode and X-ray quantitative mapping. However, within this alloy there are two chemically similar phases where the difference in composition is relatively small, making it difficult to differentiate these regions based on standard elemental X-ray mapping approaches alone within a reasonably timeframe. Using a multivariate statistical analysis approach, we were able to clearly differentiate these phases from a very low number of X-rays per pixel (<10) enabling the analysis to be performed real time (figure 1).

Element	Line	At. %	Wt. %	Net Counts
Ti	K	88.1 %	81.6 %	71 413 097
Fe	K	4.1 %	4.5 %	2 363 488
Nb	L	7.8 %	13.9 %	13 750 261

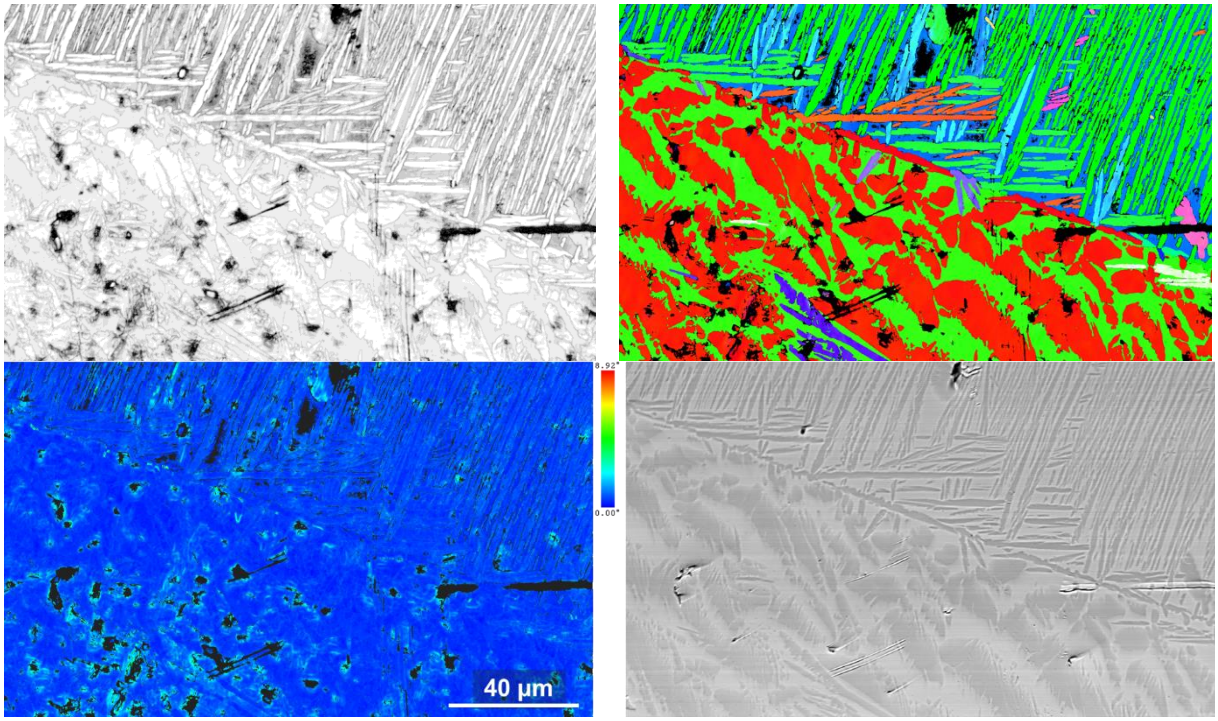


Element	Line	At. %	Wt. %	Net Counts
Ti	K	93.4 %	88.9 %	64 561 420
Fe	K	1.6 %	1.8 %	763 666
Nb	L	5.0 %	9.3 %	7 557 474

Name	Color	Area (µm²)	Area (px)	Area %
Phase 1 (P1)		14658.0	216 444	55.04 %
Phase 2 (P2)		11952.1	176 487	44.88 %
Phase 3 (P3)		19.3	285	0.07 %

Figure 27: ChemiPhase enables the discovery of material phases through advanced statistical analysis. The chart gives area distribution and composition of the phases. Acquired at 15 kV, 3.2 nA, 35 seconds acquisition time

The phases present in TiNbFe alloys are influenced by the relative proportions of titanium (Ti), niobium (Nb), and iron (Fe), and the processing temperature. Overall, the composition is extremely complicated which makes the quantification of possible gradients and chemical variations more difficult. For Structural analysis, the TruePix EBSD is based on a direct electron detection technology, enabling exceptional performance at low kV. Figure 2 shows the results of this analysis for one area of interest. First, the pattern quality map reveals the grain structure and some small surface damage, second the IPX (x) orientation map reveals a strong overall texture, third localised misorientation highlights regions of deformity around the surface damaged regions, finally, median electron counts, a unique electron counting mode shows the regions of contrast owing to different element compositions and electron channelling based on orientation.



Discussion:
ChemiPhase determines the material phases in less than a minute, since it uses a multi-variate analysis it is able to correctly separate regions from very sparse data. With such an approach, the algorithm looks at the EDS spectrum associated with each pixel and clusters spectra based on a statistical similarity. ChemiPhase makes it possible to separate phases real-time, using this as a basis for further analysis with EBSD. The EBSD highlights phase, orientation and misorientation within the specimen, providing greater insight. By maintaining performance at lower beam energy due to the direct-electron technology, Apreo ChemiSEM maintains good spatial resolution.

Conclusion:
The automation in ChemiSEM, ChemiPhase and TruePix EBSD avoid much of the need for prior knowledge of the sample and eliminates user bias in analysis. This new instrument will make it faster and easier to perform such routine investigations by newer and less experienced SEM operators as well as take lower the knowledge hurdle for experienced users.

Type of presentation: Oral

From Slices to Structure: Volume EM in Life Sciences

Meltem Sezen Ozkoc[a]

[a]*Thermo Fisher Scientific, Eindhoven, Netherlands*

Contact email: meltem.sezenozkoc@thermofisher.com

Introduction:
The primary objective of this research is to explore the advancements and applications of volume electron microscopy (vEM) in life sciences. Volume EM, recognized as one of Nature's Technologies to Watch in 2023, encompasses a range of imaging techniques that utilize electron microscopy to investigate cellular ultrastructure, tissues, and small organisms in three dimensions at nanometer resolutions. This emerging field aims to provide deeper insights into biological structures and processes by capturing detailed 3D images.

Methods:
Various vEM techniques were employed, including serial block-face imaging, array tomography, serial FIB/PFIB imaging, and TEM tomography. Samples were prepared using methods such as resin embedding, cryogenic preservation, and high-pressure tissue freezing. Serial block-face scanning electron microscopy (SBF-SEM) and plasma focused ion beam scanning electron microscopy (PFIB-SEM) were used to collect sequential 2D images, which were then reconstructed into 3D representations. TEM tomography involved collecting 2D images at different angles to create a 3D reconstruction. Advanced software, including Maps Software and Amira Software, facilitated the alignment, recombination, and visualization of these images.

Results:
The study demonstrated the capability of vEM to produce high-resolution 3D images of biological specimens. Serial block-face imaging and serial FIB/PFIB imaging provided detailed views of tissue and cellular structures, revealing intricate details at the nanoscale. Array tomography enabled the reconstruction of complex subcellular components, while TEM tomography offered high-resolution 3D data of electron-thin samples. The integration of cryogenic techniques preserved the native state of samples, enhancing the accuracy and reliability of the observations.

Discussion and Conclusions:
The findings underscore the significance of vEM in providing comprehensive insights into biological processes at the nanoscale. The ability to visualize tissues, cells, and organelles in their native context is crucial for understanding disease mechanisms and developing targeted treatments. Volume EM bridges the gap between large-scale 3D analysis and detailed structural characterization, offering critical insights into the physiological context of biomolecules. Future prospects include further refinement of vEM techniques, increased automation, and broader application in biomedical research, potentially leading to groundbreaking discoveries in cellular and molecular biology. The continued development of vEM technology promises to enhance our understanding of complex biological systems and drive advancements in medical science.

Type of presentation: Oral

Ion Milling System : ArBlade 5000

Sajjad Tollabimazraehno[a]

[a]*Videko GmbH, Austria*

Contact email: sajjad.tollabimazraehno@videko.at

The ArBlade 5000 is Hitachi's flagship ion milling system, engineered to meet the evolving demands of high-precision sample preparation for electron microscopy and materials analysis. Featuring the advanced PLUS-II ion gun, the system achieves a significantly enhanced milling rate up to 1 mm/hour making it ideal for processing hard materials with minimal thermal or structural damage. Its hybrid design supports both cross-section and flat milling, including wide-area milling capabilities, and integrates seamlessly with Hitachi SEM systems for efficient, high-resolution observation. A user-friendly LCD touch interface, automatic second milling function, and optional cooling temperature control expand its utility across a wide range of specimen types from metals and semiconductors to composite materials and fossils. With superior precision, versatility, and throughput, the ArBlade 5000 sets a new benchmark in ion beam milling technology for scientific and industrial applications.

Type of presentation: Oral

Momentum Microscopy: A complementary tool for imaging

Saumya Mukherjee[a], Stefan Böttcher[a], Michael Meyer[a], Sven Mähl[a], Thorsten Kampen[a], Oliver Schaff[a]

[a]SPECS Surface Nano Analysis GmbH, Voltastrasse 5, 13355 Berlin, Germany

Contact email: Saumya.Mukherjee@specs.com

Complementary to conventional electron microscopes operating at high energy, one of the key developments in the field of imaging appeared in the form of low energy new generation electron spectrometers. A solution was developed by combining hemispherical analyzers and PEEM lens system to provide high energy and lateral resolution in both momentum and real space imaging. Such a system was coined as momentum microscope (MM) which operates at relatively lower energy and allows aperture based selective area imaging and band dispersion analysis. Together with advancement in deflector and aperture technology it provides scanning and zooming ability, similar to the standard electron microscopes, but with added functionality to perform such functions not only in real space but also in momentum space. This provides an alternative opportunity to the scientific community to perform multifunctional operations within the same instrument such PEEM-like imaging and ARPES-like band dispersion. In addition to low operational kinetic energy of electrons, these systems benefit from easy-to-handle sample preparation and can host a wide variety of materials. The fundamental operation is based on photoemission spectroscopy and due to growing demands of multifunctionality our microscopes are also adapted to host spin-resolved imaging and time-resolved spectroscopy studies.

In this talk, I will introduce our product portfolio on MM-systems and provide a clear overview on functionality and attempt to establish MM as a complementary tool to standard electron microscopes. We will demonstrate recent results achieved across multiple in-labs to synchrotron-based end stations. Thereby, a detailed overview of these new developments for MM technology at SPECS will be presented.

Type of presentation: Oral

Oxford instruments – solution for materials characterization at the nanometre scale

Tomas Bartak[a]

[a]*Oxford Instruments GmbH, Germany*

Contact email: tomas.bartak@oxinst.com

Oxford Instruments provides market-leading scientific technology, tools and expertise that enable materials characterisation and sample manipulation at the nanometre scale. Used on electron microscopes (SEM and TEM) and ion-beam systems (FIB), our instruments are used for R&D across a wide range of academic and industrial applications including semiconductors, renewable energy, mining, metallurgy, and forensics. Oxford Instruments EDS, EBSD, BEX, Raman and in-situ analysis systems are leading-edge analytical solutions based on innovation as the driving force behind our growth and success.

Recent advances in hardware technology for EDS have improved detection capability and sensitivity in many areas. The new Ultim Max ∞ range of EDS detectors for SEMs and FIBs unlocks the infinite potential of EDS analysis in the SEM for nano-characterisation and light element detection.

The Unity detector from Oxford Instruments is the world's first BEX imaging detector that combines Backscattered Electron and X-ray (BEX) imaging in a single technique, simultaneously. It seamlessly combines BEX signals to deliver colour imaging embedded with elemental information as you navigate around your sample. This new analytical technique will accelerate your time to scientific discovery, delivering more reliable and complete information about your sample compared to traditional imaging. The Symmetry S3 electron backscatter diffraction (EBSD) detector combines unparalleled analysis speeds and sensitivity with all the unique features that ensure leading-edge performance without any compromise. Empowered by Aztec Crystal EBSD data processing software including unique Aztec MapSweeper technology the AZTEC HKL EBSD system represents the solution for the new era of high-speed EBSD detectors and ever-expanding EBSD applications.

Type of presentation: Oral

Specion Microscopy HUB

Martin Bačík[a]

[a]*SPECION, s.r.o., Květnového vítězství 332/31, 149 00 Praha 4 – Chodov, Czech Republic*

Contact email: bacik@specion.cz

Explanation of light and electron microscopy portfolio, services and support in regions. Through the synergy of market-leading technologies and local expertise, we deliver high-quality tools that enable innovation, accelerate progress and create healthier and more sustainable future.

Type of presentation: Oral

Technological Advances for Temperature Dependent Liquid-Phase and Electrochemical Studies Using *In Situ* TEM

Zayna King[a], Katherine Stephens[a], Patrick Wellborn[a], Franklin S. Walden[a], III, Jennifer McConnell[a], John Damiano[a]

[a]*Protochips, Inc.*

Contact email: Zayna.King@protochips.com

Transmission electron microscopy (TEM) is a powerful technique used to characterize materials at the nano- and atomic scale. No other method achieves the same level of structural and chemical resolution, making TEM indispensable for understanding the atomic and chemical makeup that governs material behavior. However, because TEM operates in a high-vacuum environment, observing materials in their native state is theorectically impossible. This challenge has been addressed with *in situ* TEM holders, which create a sealed environment within the TEM, isolating samples from vacuum while allowing the controlled introduction of liquids, gases, and external stimuli such as temperature, voltage, and pressure. With this capability, researchers can now directly observe nanoscale phenomena, including electrocatalytic surface area loss[1], corrosion propagation in steel[2], nucleation and growth of nanomaterials[3], and battery shorting[4,5].

For materials subjected to electrochemical stress during operation, temperature also plays a crucial role in overall performance. However, until now, no *in situ* TEM system has provided the broad temperature range needed for most applications. A breakthrough in temperature-controlled liquid systems for *in situ* TEM now enables experiments from -50°C to 300°C, simultaneous with electrochemical testing. This advancement allows researchers to replicate real-world conditions experienced by fuel cell catalysts and electric vehicle batteries, as well as achieve the high temperatures required for nanomaterial synthesis, such as high-entropy alloys. Additionally, these temperature capabilities can accelerate slow reactions, decelerate fast ones, and reduce dose damage—making it possible to visualize otherwise challenging processes and materials.

In this presentation, examples of how the temperature, both below and above room temperature, affect the kinetics of electrochemical reactions as well as the morphological structures of the maerials will be showcased (Figure 1). In addition, examples of temperature-dependent phenomena, such as the crystallization of water to ice and the nucleation and growth of gold (Figure 2) will be discussed, with diffraction, energy-dispersive X-ray spectroscopy (EDX), and electron energy loss spectroscopy (EELS) analyses as a complement.

Temperature has a major impact on material behavior and, until now, it has been impossible to study materials at more extreme yet realistic temperatures *in situ* in a liquid environment within the TEM. Now, it is possible to study temperature dependence on batteries that will operate in cold climates, electrocatalysts at elevated temperatures, and the formation of different nanomaterials that at high temperatures.

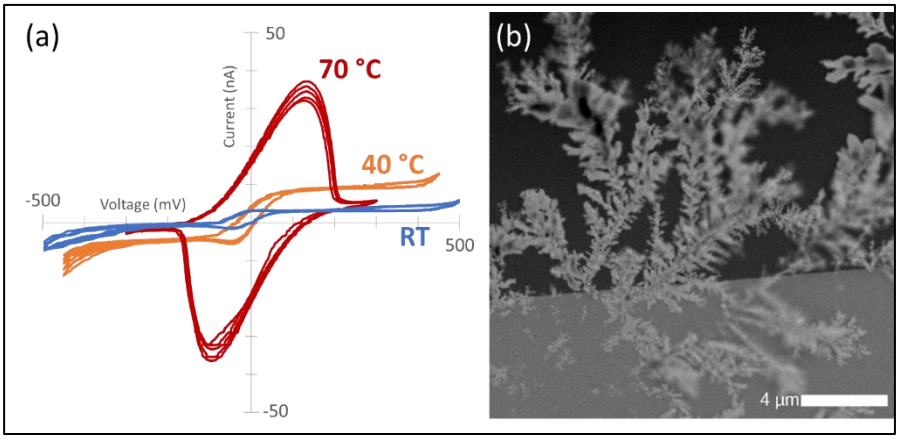


Figure 1. (a) Chemical redox cycling of 50 mM ferric and 50 mM ferrous chloride at room temperature (blue), 40 °C (orange) and 70 °C (red) within a closed-cell TEM system (b) TEM micrograph of silver dendrites formed in real time on the platinum working electrode by chronoamperometry.

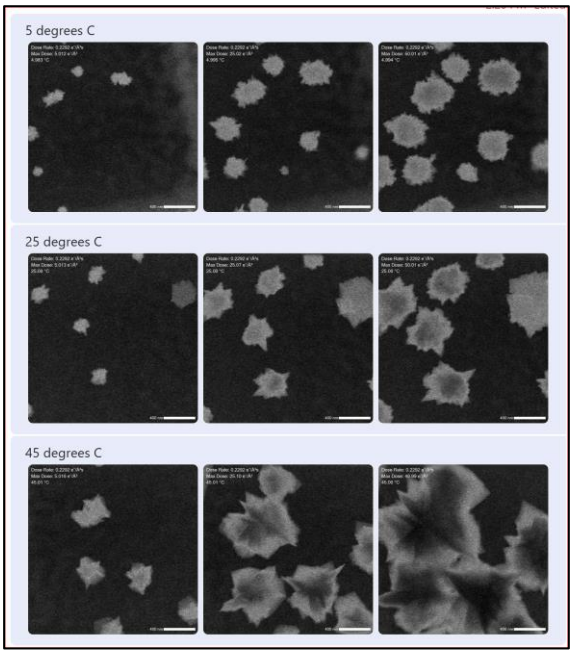


Figure 2. Demonstrating the effect of temperature while holding total dose constant on morphology as gold nucleates and grows in a solution of gold chloride.

[1] A. Impagnatiello, et al., ACS Appl. Energy Mater. 2020, 3, 3, 2360–2371
[2] D. Kovalov, et al., Corrosion Science 2022, 199, 110184
[3] K.A. Vailonis, et al., J. Am. Chem. Soc. 2019, 141, 10177−10182
[4] J. Poulizac, et. al., Microscopy and Microanalysis, 2023, 29, 105–117
[5] W. Dachraoui, et al., ACS Nano, 2023, 17(20), 20434-20444

Type of presentation: Oral

Precession enhanced Electron Diffraction applications in TEM for nano crystals

Athanassios S. Galanis[a]

[a]*NanoMEGAS SPRL Rue Emile Claus 49 bte9, B-1050 Brussels Belgium*

Contact email: tgalanis@nanomegas.com

NanoMEGAS [1] is the pioneer offering the first precession [2] generator in TEM since early 2000s. In parallel, NanoMEGAS introduced the first Scanning Precession Electron Diffraction (4D-SPED) full and robust application in TEM (ASTAR) in the late 2000s, even before the introduction of the 4D-STEM terminology introduced after the development of the pixelated detectors in the 2010s.
Nowadays, NanoMEGAS has expanded the arsenal of 4D-SPED applications, offering full packages of automated and robust acquisition and data processing h/w and s/w.
Orientation & Phase mapping: Automated data acquisition and analysis of a variety of materials (metals, semiconductors, oxides etc.) by TEM using 4D-SPED technique consists of a successful application based on PED, called ASTAR [3]. The major benefit of the technique is the high spatial resolution that can be down to 1-3 nm resolution (in case of FEG-TEM).
Strain mapping: The 4D-SPED acquisition method can also be applied to obtain strain mapping analysis (TopSPIN strain) of semiconductor materials at 1-4 nm resolution (sensitivity 0.02%), based on comparison of PED- patterns of strained areas with a reference (non-strained) area.
Electric Field: Detailed characterization of local Electric Fields and built-in potentials in functional materials is NanoMEGAS' recent application, combining 4D-SPED acquisition together with dedicated data processing software. Beam Precession is essential to get rid of dynamical effects which prevent accurate determination of the COM (Centre of Mass) and obtain ED patterns with less noise leading to enhanced results [5].
Precession enhanced 3DED: PED was first applied in electron crystallography, which in combination with 3D diffraction tomography (or 3D-ED, MicroED) in TEM, has become a critical method for structure determination of various nanocrystals, from minerals and alloys to complex zeolites, MOFs, organic compounds and proteins. Acquired data are automatically processed by specific software (ADT-3D) [6,7].
ePair Distribution Function (static): PED in TEM is reported to provide high quality data for analysis of amorphous or nanocrystalline materials [8]. Typical total scattering patterns are acquired in TEM in a few seconds, a speed only matched by synchrotron radiation (lab X-ray acquisition is a much more time-consuming approach for such materials (2-20 hours). The total scattering data are processed by specific software (ePDF) using the well know Pair Distribution Function method. Amorphous and/or nanocrystalline materials can be characterized through the interatomic distances from the PDF diagram.
ePair Distribution Function mapping: The latest (introduced spring 2025) software expands the basic ePDF version to analyze 4D-SPED data, obtaining ePDF maps, which is particularly useful for studying amorphous, nanocrystalline, and disordered systems, with applications in semiconductor materials, amorphous glass, amorphous solid dispersions and polymers [9].

References:

[1] NanoMEGAS: www.nanomegas.com
[2] R. Vincent and P. Midgley, *Ultramicroscopy* **53** (1994) p. 271
[3] E.F. Rauch, J. Portillo, S. Nicolopoulos, D. Bultreys, S. Rouvimov and P. Moeck: *Zeitschrift für Kristallographie* **225** (2010) p. 103.
[4] E.F. Rauch and M. J. Veron: *Mater. Sci. Eng. Tech*. **36** (2005) p. 552
[5] V. S. Chejarla, S. Ahmed, J. Belz, J. Scheunert, A. Beyer, K. *Small Methods* (2023) 2300453
[6] . Mugnaioli, T. Gorelik and U. Kolb: *Ultramicroscopy* **109** (2009) p. 758.
[7] U. Kolb, T. Gorelik, C. Kübel, M.T. Otten and D. Hubert: *Ultramicroscopy*. **107** (2007) p. 507.
[8] AM Abeykoon, Ch. D Malliakas, P. Juhás, E. S Bozin, M. G Kanatzidis, S. JL Billinge: *Zeitschrift für Kristallographie Crystalline Materials* **227** (2012) p. 248
[9] Y. Rakita et al. Acta Materialia, Volume **242** (2023) 118426

Type of presentation: Oral

Empowering Innovation in Science with Tescan Solutions

Martin Suchanek[a]

[a]*TESCAN GROUP, a.s., Libušina třída 21, 623 00 Brno, Czech Republic*

Type of presentation: Oral

ZEISS Volutome: The Next Generation of Serial Block-Face Imaging

Kirill A. Atlasov[a]

[a]*Carl Zeiss microscopy GmbH*

Contact email: kirill.atlasov@zeiss.com

In this presentation we will describe the fully ZEISS-proprietary solution for high-resolution Serial Block Face (SBF) imaging – ZEISS Volutome. This solution is based on the GEMINI electron optics that was originally developed for high-resolution imaging at low accelerating voltages and for the largest versatility of sample materials and system add-ons. This, in particular, is achieved by using in-column beam deceleration, without immersing the sample in strong electric or magnetic fields. While decelerating the primary beam within the column, the detectable electrons are at the same time accelerated back towards the inLens detectors. This design thus also gives unique imaging contrast to the inlens detectors for SE and BSE (secondary and backscattered electrons) as well as controlling the ratio of SE and BSE to avoid charging artefacts and capture the finest details of sample surface.

For the SBF imaging overcoming the charging issues is the biggest challenge. In this presentation we will illustrate a unique implementation in the ZEISS Volutome solution of the combination of the dedicated low-kV sensitive backscatter detector Volume BSD together with ZEISS focal charge compensation to achieve clear reliable high-resolution 3D volumes of data from most challenging beam sensitive materials.

https://www.zeiss.com/microscopy/en/products/sem-fib-sem/sem/volutome.html



IMPRESS Special session

Type of presentation: Poster

IMPRESS 1 End-to-end Autonomous Unveiling of Physical Knowledge of Quantum Devices through Electron Microscopy Data

Marc Botifoll Moral[a,b], Ivan Pinto-Huguet[b], Enzo Rotunno[c], Thomas Galvani[b], Catalina Coll[b], Yann-Michel Niquet[d], Sara Martí-Sánchez[b], Georgios Katsaros[e], Giordano Scappucci[f], Peter Krogstrup[g], Giovanni Isella[h], Maria Chiara Spadaro[b], Stephan Roche[b,i], Pablo Ordejón[b], Vincenzo Grillo[c], Jordi Arbiol[b,i]

[a]*Forschungszentrum Jülich, Germany*

[b]*ICN2, CSIC and BIST, Barcelona, Spain*

[c]*CNR-IMEM, Parma, Italy*

[d]*Univ. Grenoble Alpes, CEA, IRIG-MEM-L Sim, Grenoble, France*

[e]*Institute of Science and Technology Austria, Klosterneuburg, Austria*

[f]*QuTech and Kavli Institute of Nanoscience, Delft TU, Delft, The Netherlands*

[g]*0NNF Quantum Computing Programme, NBI, University of Copenhagen, Denmark*

[h]*Politecnico di Milano, Como, Italy*

[i]*ICREA, Barcelona, Catalonia, Spain*

Contact email: m.botifoll@fz-juelich.de

BACKGROUND AND AIMS

The process of discovering and refining new materials, as well as enhancing existing ones for a variety of uses, including quantum applications, is a complex and multifaceted endeavour. This involves identifying needs, reviewing existing literature, proposing materials, engineering devices, characterizing materials, and testing applications. However, the process can be hindered by its time-intensive and costly nature, especially when precision at the atomic level is necessary to comprehend the functionality of materials and heterostructured devices.

In this digital age and with quantum supremacy in the horizon, semiconductor heterostructures within a chip have become indispensable and ubiquitous, propelling significant industrial value chains. They facilitate progress in both emerging sectors like quantum applications and established ones. For that, the trend of miniaturization, which is now reaching nanoscale dimensions and nearing the atomic limit, is a key driver of progress which demands special characterisation needs. [1,2] To answer to these needs, in this work, we present a revolutionary analytical framework aimed at the comprehensive characterization of device heterostructures, with a particular focus on quantum devices and their materials.

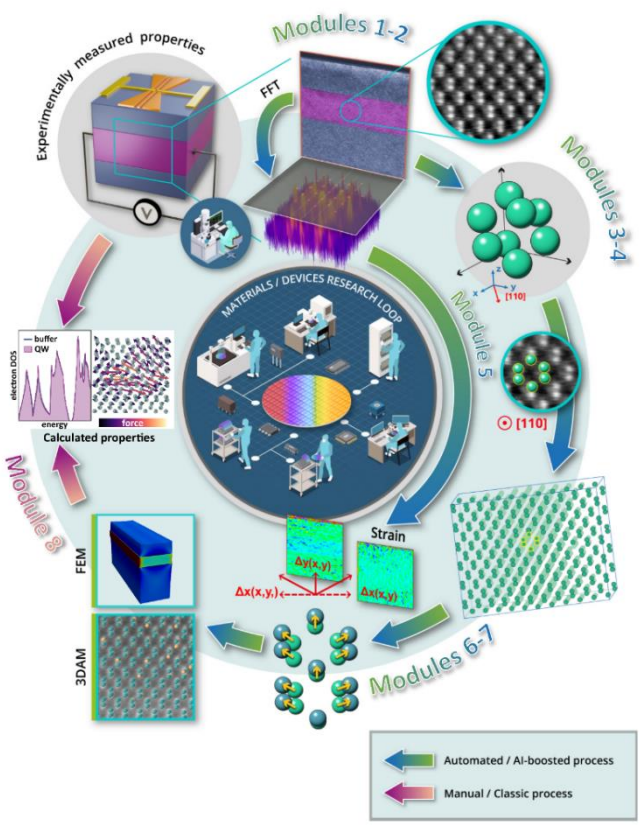
METHODS

The characterisation that must answer these demands is high-resolution Transmission Electron Microscopy (TEM), as the most optimal way to access structural information at the atomic level. We propose a workflow capable of processing both parallel illumination TEM and Scanning TEM (STEM) data, although it is specially designed for the latter. In addition, it can extract compositional information from Electron Energy Loss Spectroscopy (EELS), which is used to make the characterisation an exhaustive and complete process. Importantly, the workflow we suggest, combines traditional algorithmics, with unsupervised and supervised machine learning algorithms. This way, we ensure that model-based computing and artificial intelligence work hand by hand to provide the comprehensive and material-independent solution we seek for. [3]

RESULTS

Our pioneering workflow autonomously determines material composition, crystallographic phase, and spatial orientation across various regions of analysed (S)TEM-based images or image datasets through detailed model comparison. It is completed with automated strain analysis, enabling a comprehensive characterization of the device's structural properties. Eventually, we incorporate the extracted

knowledge to automate the creation of models that facilitate simulations and provide vital physical and chemical insights necessary for understanding the device's performance in practical applications. [3]



CONCLUSIONS

Although the method is highly versatile, we focus on quantum computing devices to autonomously optimize their functional properties. In particular, we prove it with SiGe quantum well heterostructures that proved outstanding quantum performance for spin qubits generation. [1,2] However, the main advantage placing our workflow beyond state of the art is its generalisation capabilities. It works for any material configuration and not only does it answer the pressing automation need, but unlocks getting physical models and simulations of complex devices with unprecedented accuracy. [3]

Reference

[1] Jirovec, D. et al. Nature Materials, (2021) doi.org/10.1038/s41563-021-01022-2
[2] Paquelet, B. et al Nat. Commun. 14, 1385 (2023)
[3] Botifoll, M. et al, (2024) Submitted, https://doi.org/10.48550/arXiv.2411.01024

Type of presentation: Poster

IMPRESS 2 The IMPRESS Project: Developing an Innovative Interoperable Platform for Next-Generation Transmission Electron Microscopy

Regina Ciancio[a], Rafal E. Dunin-Borkowski[b], Riccardo Brancaleon[c], Amir H. Tavabi[b]

[a]*AREA Science Park & CNR-IOM, (Trieste), Italy*

[b] *Forschungszentrum Jülich (Jülich), Germany.*

[c] *Promoscience srl (Trieste), Italy*

Contact email: brancaleon@promoscience.com

Introduction

Transmission electron microscopy (TEM) is a powerful technique for the high-resolution structural and chemical analysis of materials. However, its broader use in advanced research is often limited by a lack of adaptability for the implementation of specialized approaches, in particular for *in situ*, operando and correlative studies of materials. The EU-funded project "IMPRESS" (Interoperable electron Microscopy Platform for advanced RESearch and Services) aims to overcome this limitation by developing a modular, flexible and interoperable next-generation TEM ecosystem. With 19 partners, comprising leading academic and industrial experts and five of Europe's leading Research Infrastructures, IMPRESS ensures scientific excellence and user-focused innovation.

At the heart of the project is the introduction of a comprehensive platform built around an "e-CAT" (Correlative Adaptable and Transferable) cartridge concept. Standardized cartridges will be designed to integrate with TEM specimen holders, aperture rods and a broad range of complementary tools, including sample preparation systems, surface analysis equipment microfocus X-ray tomography and synchrotron beamlines. The e-CAT system is intended to enable secure, controlled transfer of samples across instruments under different environmental conditions (*e.g.*, cryogenic, elevated temperature, vacuum and inert gas), in order to ensure seamless, contamination-free experimental workflows.

IMPRESS ultimately aims to deliver TEM technologies that are based on open standards to promote interoperability, ease of customization and long-term sustainability. This approach will enhance TEM's role in integrated, multimodal research and broaden its impact across diverse scientific fields.

Methods

The project is structured in seven Work Packages (WPs), four of which are technically focused and form the foundation of the platform's development.

WP3 concentrates on the design of advanced electron sources, with the goal of improving beam quality and versatility. Research efforts are directed toward reducing electron optical aberrations, enhancing brightness, lowering energy spread and enabling rapid beam modulation, all of which are critical for high-performance imaging and spectroscopy.

WP4 is focused on advancing the optical and detection capabilities of TEM systems. It includes the development of adaptive electron optics based on programmable phase plates and next-generation event-driven detectors. These innovations are intended to improve contrast, spatial and temporal resolution and data acquisition efficiency, thereby enabling new imaging and spectroscopic modalities.

WP5 is dedicated to the development of multifunctional chips and sample environments that are tailored for *in situ* and correlative experiments. The chips are designed in close collaboration with end users to ensure compatibility with a wide range of experimental conditions and requirements. Environmental control capabilities are integrated directly into the chip design, allowing researchers to observe and manipulate material behavior in real time under carefully maintained conditions.

In WP6, software tools are developed to support automation of experimental workflows, instrument alignment, control and data acquisition. The tools are designed to provide intuitive interfaces and robust functionality for planning, executing and analyzing complex experiments, while ensuring interoperability with hardware components, which are developed in parallel.

Results

Since its launch in 2023, the IMPRESS project, which is scheduled to end in 2028, has reached several important milestones. A major achievement in the initial phase has been the completion of the functional specifications for the e-CAT cartridges. These specifications define the core requirements for the system's modular architecture and will guide the detailed design and implementation work in the next stages.

In the area of electron source development, initial conceptual models have demonstrated the feasibility of achieving improved beam brightness and coherence. These advancements also provide opportunities for fast temporal modulation of the electron beam, thereby extending the operational flexibility of TEMs for both static and time-resolved experiments.

Research into adaptive optics has provided promising preliminary outcomes, for example in the testing of programmable phase plates. These devices bring new opportunities for shaping electron wavefronts, enhancing phase contrast and enabling low-dose imaging, which is particularly valuable for the study of electron-beam-sensitive materials [1].

The prototyping of multifunctional sample environments is actively underway, with designs informed by continuous dialogue with end users. These environments are being developed to support a wide range of experimental conditions, including precise control of temperature and atmosphere, enabling *in situ* and *operando* investigations of materials under realistic working conditions.

Progress in software development includes the initial deployment of alignment and control tools in simulated environments [2] [3]. The tools are designed to simplify instrument setup, improve usability and support experimental planning, providing a critical software backbone for future integration with hardware systems.

Alongside these technical developments, the project has initiated a training programme, which includes interactive workshops focused on collaborative advancements in TEM, as well as a five-day School on *Operando* and Correlative Experiments hosted by the ALBA Synchrotron in Spain.

Discussion and Conclusions

The IMPRESS project introduces a comprehensive and integrated approach for advancing the state of the art in transmission electron microscopy. By addressing challenges in hardware, software and user training, the project is laying the groundwork for a new generation of interoperable TEM platforms, which are capable of supporting complex, multidisciplinary research.

The modular philosophy that underpins the platform design – particularly through the e-CAT cartridge system – aims to ensure that the solutions that are developed are not only technically robust but also adaptable to diverse experimental contexts. This approach is intended to maximize the platform's utility across a wide spectrum of scientific investigations, ranging from materials science and nanotechnology to catalysis, energy storage and biomedical research.

While technical challenges remain, particularly in harmonizing mechanical and electronic interfaces and ensuring reliable integration across different systems, the collaborative framework of the project provides a strong basis for overcoming these obstacles. The involvement of a network of academic institutions, research infrastructures and innovative industry partners ensures that these developments will remain closely aligned with scientific needs and technological feasibility.

As the project continues, its emphasis will shift from design and conceptual development to testing, integration and community engagement. Increased involvement by the broader microscopy and materials science communities will be essential to ensure that the platform not only meets current requirements but also anticipates the future demands of high-resolution and *in situ* electron microscopy and correlative techniques.

With its emphasis on modularity, interoperability and open standards, the IMPRESS project represents a significant step forward in the evolution of TEM and sets the stage for a more flexible, accessible and scientifically productive microscopy landscape across Europe and beyond.

Acknowledgments

The IMPRESS project has received funding from the HORIZON EUROPE framework program for research and innovation under grant agreement number 101094299.

References

1. C. Yu, F. Vega Ibañez, A. Béché, J. Verbeeck, *SciPost Physics*. **2023**, *15*, 223.
2. A. Annys, D. Jannis, J. Verbeeck, *Scientific Reports*. **2023**, *13*, 13724.
3. L. Grossetête, C. Marcelot, C. Gatel, S. Pauchet, M. Hytch, *Ultramicroscopy*. **2024**, *267*, 114047.

Type of presentation: Poster

IMPRESS 3 Characterization of electric and magnetic fields at interfaces in manganese-containing heterostructures using correlative TEM techniques

Qianqian Lan[a], Michael Schnedler[a], Philipp Ebert[a], Rafal E. Dunin-Borkowski[a]

[a]*Ernst Ruska-Centre for Microscopy and Spectroscopy with Electrons, Forschungszentrum Jülich GmbH, 52425 Jülich, Germany*

Contact email: r.dunin-borkowski@fz-juelich.de

As a result of symmetry breaking and discontinuities at interfaces or surfaces, materials can host phenomena that are not found in the bulk, including two-dimensional electron/ hole gases, magnetoelectric coupling, chiral magnetic domains, novel spin transport and emergent electromagnetic fields.

However, probing magnetism at interfaces remains challenging. First, magnetic phenomena are often confined to only a few nm or even just a few atomic layers. The resulting magnetic signals can be extremely weak - often below the detection limits of conventional bulk characterization techniques. Second, real interfaces deviate from ideal models. They can exhibit chemical intermixing, cation diffusion, strain gradients and defects, all of which can modify intrinsic magnetic behavior and complicate interpretation. Third, even at structurally perfect interfaces, the mechanisms behind interfacial magnetism are inherently complex. They typically arise from multiple overlapping effects, including electrostatics, orbital reconstruction, spin-lattice-charge coupling and even topological contributions. This complexity presents a significant challenge for quantitative analysis and data interpretation. Finally, additional challenges stem from sample preparation and experimental measurement constraints. Given these difficulties, correlative techniques are essential - offering high spatial resolution, strong magnetic sensitivity, depth resolution and the potential for quantitative analysis.

In this work, interfacial magnetism and its electrostatic origin are investigated quantitatively by applying correlative transmission electron microscopy (TEM) techniques to a 200-nm-thick $La_{0.7}Sr_{0.3}MnO_3$ (LSMO) film grown on a $SrTiO_3$ (STO) substrate. As shown in Fig. 1, we introduce a workflow for the implementation of the chosen correlative techniques, which include off-axis electron holography combined with model-based iterative magnetization reconstruction, electron energy-loss spectroscopy (EELS) and self-consistent electrostatic simulations of interfacial electrostatic fields and charge distributions. These measurements are further correlated with atomic-resolution structural, chemical and strain characterization using scanning-TEM-based techniques to obtain a comprehensive picture of the interfacial environment.

Surprisingly, our results reveal a long-range magnetic transition region at a ferromagnetic/ ferromagnetic (FM/ FM) interface, which is driven by electrostatics and characterized by a modulation in magnetization magnitude without a change in direction [1]. We also observe a long-range proximity effect at a FM/ paramagnetic (FM/PM) interface and a hole-concentration-dependent FM/PM phase boundary [2]. These results underscore the critical role of charge–spin coupling at complex oxide interfaces and represent a significant advancement in nanoscale magnetic characterization of correlated systems.

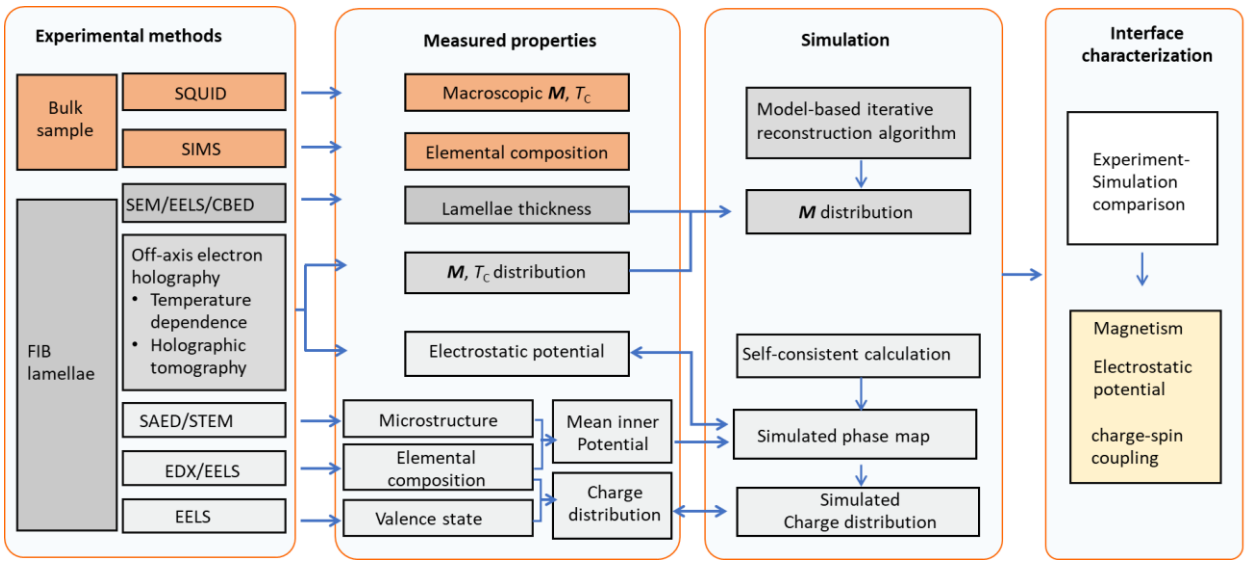


Figure 1: Workflow for interface magnetic and electric field characterization in perovskite oxide heterostructures using correlative TEM-based techniques combined with simulations.

References:

[1] Q. Lan, M. Schnedler, L. Freter, C. Wang, K. Fischer, P. Ebert, R. E. Dunin-Borkowski. Electrostatic extension of magnetic proximity effect in $La_{0.7}Sr_{0.3}MnO_3$, Phys. Rev. B, 2023, 108 (18), L180410.

[2]. Q. Lan, C. Wang, L. Jin, M. Schnedler, L. Freter, K. Fischer, J. Caron, X. Wei, T. Denneulin, A. Kovács, P. Ebert, X. Zhong, R. E. Dunin-Borkowski. Electrostatic shaping of magnetic transition regions in $La_{0.7}Sr_{0.3}MnO_3$, Phys. Rev. Lett. 2022, 129, 057201.

Type of presentation: Poster

IMPRESS 4 Electrostatic potential measurement at liquid helium temperature using off-axis electron holography

Yan Lu[a], Peng-Han Lu[a], Denys Sutter[b], Dominik Biscette[b], Johan Chang[b], Giulio Pozzi[a,c], Rafal E. Dunin-Borkowski[a]

[a]*Ernst Ruska-Centre for Microscopy and Spectroscopy with Electrons, Forschungszentrum Jülich GmbH, 52428 Jülich, Germany*

[b]*condenZero AG, Hagenholzstrasse 85, 8050 Zürich, Switzerland*

[c]*Department FIM, University of Modena and Reggio Emilia, via G. Campi 213/a, 41125 Modena, Italy*

Contact email: r.dunin-borkowski@fz-juelich.de

Local variations in electrostatic potential in materials, which can include contributions from both the intrinsic mean inner potential (MIP) and additional charge redistribution, can have a significant influence on chemical reactions and dielectric properties. The MIP is defined as the volume-averaged electrostatic potential of a material with respect to a distant vacuum reference. MIPs of many materials have been measured at room temperature in the transmission electron microscope (TEM) using phase contrast techniques such as off-axis electron holography [1]. However, few low temperature measurements have been performed, even though low sample temperatures can have profound effects on mass density and atomic bounding, leading to significant changes in electrostatic potential, and even though cryogenic cooling of samples using liquid nitrogen in the TEM is now widely utilized in both materials science and biology [2].

Off-axis electron holography is a powerful TEM technique that can be used to map local variations in electron optical phase shift, which are in turn sensitive to projected electrostatic potentials and magnetic fields within and around materials. In the phase object approximation, in the absence of magnetic contributions to the phase shift, the recorded phase is proportional to the projected electrostatic potential. Here, we record off-axis electron holograms using a recently developed liquid-helium-cooled specimen holder that can reach a sample temperature of 5.3 K within one minute. Electron holograms were recorded at 300 kV on an FEI Titan G2 TEM equipped with a 4K Gatan K2 camera. Each hologram was acquired by using a total exposure time of 6 s sub-divided into 30 frames of 0.2 s. Phase reconstruction was performed using HoloWorks software.

We studied polystyrene latex beads, which are of interest for use as immunodiagnostic reagents. Temperature-dependent measurements of MIP and electron-beam-induced charging of the latex beads, which had diameters of between 230 and 600 nm, were recorded between room temperature and 5.3 K. By using a model-independent approach to quantify the spatially-dependent projected charge density from the recorded phase images [3, 4], the amount of positive charge on each sphere was determined. After subtracting the contribution to the electrostatic potential from electron-beam-induced charging, an unexpected linear increase in MIP with decreasing sample temperature was revealed, with a measured increase in MIP of 16.8% at 5.3 K when compared to that at room temperature. This study highlights the importance of studying new material properties at cryogenic temperature.

References:

1. M. Yesibolati, S. Laganà, H. Sun et al., *Phys. Rev. Lett.* **2018**, 124, 065502.
2. Y. Li, W. Huang, Y. Li, W. Chiu, Y. Cui, *ACS Nano* **2020**, 14, 9263-9276.
3. M. Beleggia, T. Kasama, R. E. Dunin-Borkowski, S. Hofmann, G. Pozzi, *Appl. Phys. Lett.* **2011**, 98, 243101.
4. C. Gatel, A. Lubk, G. Pozzi, E. Snoeck, M. J. Hÿtch, *Phys. Rev. Lett.* **2013**, 111, 025501.

Type of presentation: Poster

IMPRESS 5 Quantifying carbon site switching dynamics in GaN by off-axis electron holography

Keyan Ji,[a], Michael Schnedler[a], Qianqian Lan[a], Rafal E Dunin-Borkowski[a], Philipp Ebert[a]

[a]*Ernst Ruska-Centre for Microscopy and Spectroscopy with Electrons, Forschungszentrum Jülich GmbH, 52425 Jülich, Germany*

Contact email: r.dunin-borkowski@fz-juelich.de

Understanding the role of carbon (C) in the electronic properties and long-term stability of group-III nitride devices remains a major challenge. On one hand, carbon is believed to play a central role in the degradation of devices such as laser diodes. On the other, it is intentionally introduced to achieve semi-insulating layers, which reduce drain leakage and enhance breakdown voltages in high-electron-mobility transistors. However, information about dynamic processes and point defect reactions of C is scarce, although being of paramount importance to understand degradation as well as explore paths towards extended durability of group-III nitride devices.

In this study, we investigate Si-doped GaN lamellas prepared by focused ion beam (FIB) using a correlative approach combining off-axis electron holography (EH) in a transmission electron microscope (TEM), secondary ion mass spectrometry (SIMS), and self-consistent electrostatic simulations. FIB preparation unavoidably induces a nm-thick amorphous surface layer, under which a crystalline but point-defect-rich region forms. This defect-rich region causes Fermi-level pinning and strong upward band bending, which is screened toward the core of the lamella.

Among the various intrinsic and extrinsic defects likely present, only C substitutional defects on nitrogen sites (C_N) exhibit a (-/0) charge transition level in the lower half of the bandgap - capable of producing the observed upward band bending. The experimentally determined pinning level at ~ 0.7 eV above the valence band edge (E_V) matches well with this charge transition level of C_N in GaN, confirming its presence and electrostatic dominance in the defect-rich layer.

The upward band bending leads to a pronounced enhancement of the electron-optical phase contrast at n-n^+ doping interfaces; a surface effect that largely determines the observed contrast in EH. By studying the temperature and time dependence of this contrast upon annealing, we probe the dynamics of Fermi-level pinning and its underlying defect reactions. Annealing below 500 °C leads to an irreversible reduction in phase contrast, indicating the (partial) lifting of the Fermi level pinning. Systematic experiments across multiple lamellas show that this process accelerates with temperature, consistent with a diffusion-driven process with an activation energy of 2.27 ± 0.26 eV and a diffusion length on the order of a lattice constant.

These findings suggest a thermally activated site-switching of carbon from substitutional to interstitial positions, accompanied by a charge state reversal, as the mechanism behind the lifting of the Fermi level pinning. Our work establishes electron holography in TEM as a powerful technique to study charged point defect dynamics in GaN, and provides new insights into the thermal processes that govern the long-term stability of nitride-based semiconductor devices. Furthermore, our findings emphasize the importance of combining complementary techniques, as only their integration enables a comprehensive understanding of the structural and electronic phenomena at play.[1]

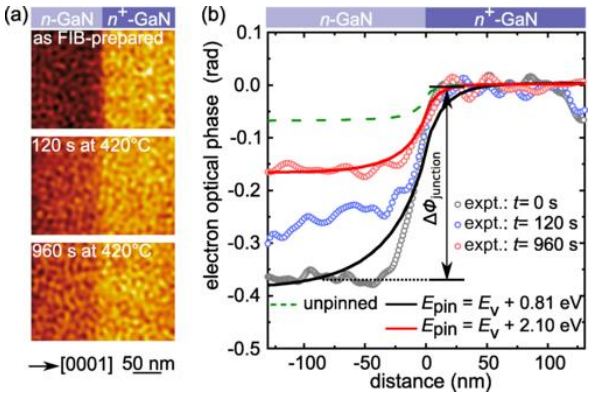


Figure 1: (a) Electron optical phase maps of the n-n$^+$ GaN junction measured by electron holography. The top image shows the as-FIB-prepared lamella; the middle and bottom images were taken after annealing at 420 °C for 120 s and 960 s, respectively. (b) Corresponding line profiles showing changes in the electron optical phase across the junction (interface at 0 nm). Open symbols represent experimental data after annealing; lines indicate simulated phase profiles for varying surface pinning levels.

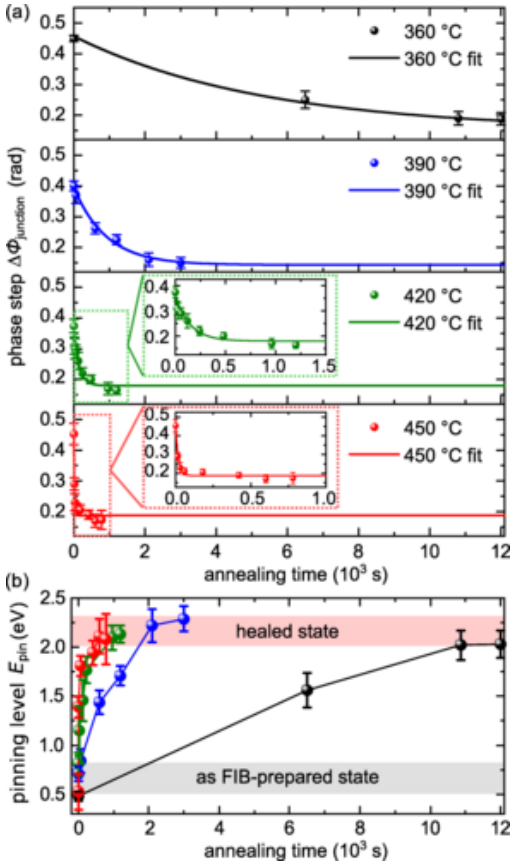


Figure 2: (a) Time evolution of the phase step $\Delta\phi_{junction}$ across the n-n$^+$ GaN junction at different annealing temperatures. (b) Extracted Fermi-level pinning positions vs. annealing time. The data show a shift from $E_V + (0.57 \pm 0.13)$ eV in the as-FIB-prepared state (attributed to C_N defects) to $E_V + (2.14 \pm 0.09)$ eV in the healed state (associated with states at the amorphous outer shell).

References:

1. K. Ji *et al.*, Phys. Rev. Research **2025**, *7*, 013200

Type of presentation: Poster

IMPRESS 6 NanoMi: An open-source electron microscope

Darren Homeniuk[a], Marek Malac[a,b], Mark Salomons[a], Jesus Alejandro Marin Calzada[b], Makoto Schreiber[b], Sam Ruttiman[b], Martin Cloutier[a], Patrick Price[a], Xuanhao Wang[b], Mohammad Kamal[b], Olivier Adkin-Kaya[b], Sophia Cockram[c], Ka Wing Kwan[c], Misa Hayashida[a], Ray Egerton[b], Ken Harada[d]

[a]*National Research Council. Quantum and Nanotechnologies Research Center, (Edmonton), Canada*

[b]*University of Alberta, (Edmonton), Canada*

[c]*University of British Columbia, (Vancouver), Canada*

[d]*RIKEN Center for Emergent Matter Science, (Hatoyama), Japan*

Contact email: darren.homeniuk@nrc-cnrc.gc.ca

Many fields of science rely on electron microscopes (EM) for measurement and visualization of various physical phenomena. Three EM modes are scanning (SEM), transmission (TEM), and scanning transmission (STEM), each of which has benefits and drawbacks depending on the user's goals and sample type. In our modern age, EMs have approached usability similar to modern computers, where you simply turn the unit on and press a button to acquire an image. Our group however argues that while a user does not need to understand how a computer works to effectively use a web browser, EMs are different. A user needs to grasp how images are formed and get a feel for the various settings to ensure that their data is representing the sample properly. Commercially purchased EMs often mask settings behind proprietary code, and so users may struggle to comprehend what is actually happening in the column. In addition to this gap, the cost of recent commercial EMs prohibits access for many potential users. These factors limit the usefulness and spread of this otherwise useful tool.

With this in mind, we present our work on NanoMi[1][2], an open-source electron microscope. The goal of the project is to develop and build a community of users who share blueprints, schematics, ideas and technical support for a modular EM that they build and maintain. Components like electrostatic lenses, deflectors, stigmators, apertures and samples are placed onto a physical breadboard inside the column such that SEM, TEM or STEM are made possible by adding, removing, or moving components on the breadboard and adjusting the modular code. An individual or group can pay for the cost of components at a small fraction of the cost of a commercial EM, and with some time and learning, build their own microscope. Users will then have more ability to understand the inner workings of the column, as every setting is at their fingertips. An added bonus is that if a user designs a new vacuum-compatible component for novel purposes, it can easily be incorporated into NanoMi, whereas this would not normally be possible with commercial microscopes.

NanoMi was designed to be as modular as possible. Conflat™ flanges are used to assemble the ultra-high vacuum column, which allows for simple interfacing with electrical cables and viewing of components. Piezoelectric movers based on slipstick motion are available to shift apertures and sample stages around using electronic control. The movers provide motion with nanometer resolution while offering range on the order of millimeters. Electrostatic lenses, deflectors and stigmators minimize the need for cooling and to also allow ion beam control. Operating voltages for the lenses and electron gun are limited to 50 kV at this time, which limits the imaging resolution to on the order of 10's of nanometers. Electronics for control of the deflectors, stigmators and piezoelectric movers are available as part of the blueprint package, and we also plan to make pre-manufactured electronics available for purchase. A scanning unit we refer to as ScanOMi has also been created and validated for SEM and STEM modes. ScanOMi generates two beam-placement analog signals with 16-bit resolution, and can read in up to 8 non-multiplexed 14-bit signals back from the column. This allows for precise beam placement on the sample, and for any combination of detectors (secondary electron detector, transmitted electron detector, segmented annular array, and more) to be used simultaneously. A volatile memory RAM is on-board as well to store data until it can be transmitted to a computer via standard USB

communication. Software for all of NanoMi is written in python and is also modular, such that if a new component is created, a user interface template script file is modified, renamed, and on next start-up a button will appear with the new component code integrated.

Two versions of NanoMi have been built, as shown in Figure 1. Validation of SEM and TEM modes are complete on the first version, with STEM in progress. As an example of novel device integration, the second version of NanoMi was created with interfacing to a terahertz laser source in mind, with the goal of attempting to stimulate the electron beam emission via laser-source interactions and acquire time resolved measurements[3]. Also shown are electronics that drive the piezoelectric movers via a remote control and the blue circuit board, as well as electronics that operate the alignment deflectors in green.

Some results from NanoMi hardware are shown in Figure 2. SEM was proven via the image of dandelion parachutes acquired from NanoMi version 1 using ScanOMi. TEM was proven via the diffraction pattern of single-layer gold. To validate the ScanOMi outside of any other sources of error in NanoMi, it was connected to a Hitachi S5500 SEM such that it could drive the beam and read back intensity data to acquire an image of multi-walled carbon nanotubes. A comparison image of the same nanotubes from the S5500 is also shown at the same scale, but acquired with the S5500 scan generator.

To conclude, our group is developing a public license open-source electron microscope platform that we refer to as NanoMi. The goal of this project is to build a community that supports anyone being able to build and maintain their own electron microscope while minimizing the financial cost. NanoMi as a platform can see use cases in training students on the use of electron microscopy, doing research, and prototyping new conceptual hardware. Interested parties can check the references below and join the community in whatever role they desire.

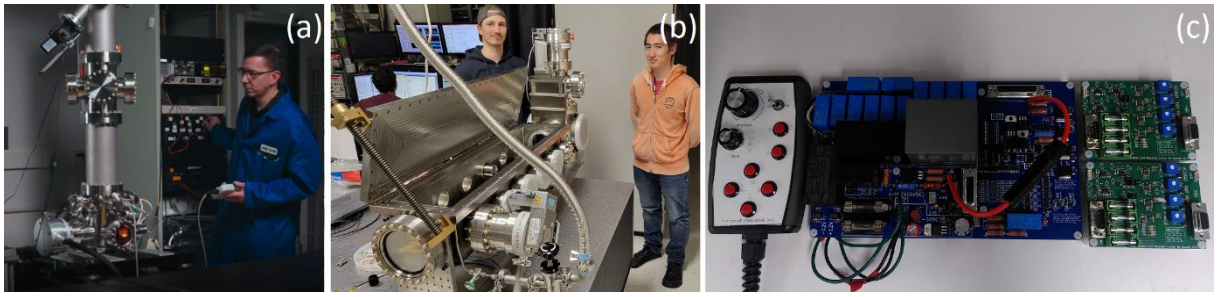


Figure 1: Two versions of NanoMi have been created thus far. (a) NanoMi version 1, (b) NanoMi version 2, (c) electronics for control of deflectors/stigmators in green and piezoelectric movers in blue.

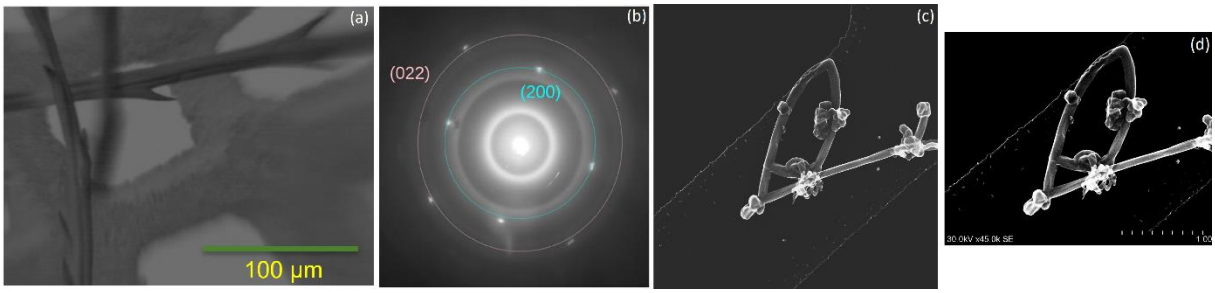


Figure 2: Images acquired using NanoMi hardware (a) NanoMi version 1 SEM image of carbon coated dandelion parachute on a 200 mesh copper grid, (b) NanoMi version 1 diffraction pattern in TEM mode of single-layer gold, (c) Image of multi-walled carbon nanotubes on a carbon grid, acquired on a Hitachi S5500 SEM column using ScanOMi to drive and sample, (d) Comparison image of the same multi-walled carbon nanotubes on a carbon grid at the same scale using the Hitachi S5500 SEM as purchased.

References:

1. nanomi.org and https://github.com/NRC-NANOmi/NanoMi
2. M. Malac et. al, NanoMi : An open source electron microscope hardware and software platform, *Micron*, **2022**, 163, 103362.
3. S. Ruttiman et. al, NanoMi : A modular platform for terahertz-integrated UTEM, *2023 48th International Conference on Infrared, Millimeter and Terahertz Waves (IRMMW-THz)*, **2023**, DOI: 10.1109/IRMMW-THz57677.2023.10298919

Type of presentation: Poster

IMPRESS 7 EFLY – a Fast Versatile Charge Particle Optics Code

Axel Lubk[a,b], Zhi Li[a], Florent Houdellier[c], Heiko Müller[d], Stephan Uhlemann[d]

[a]*Leibniz Institute for Solid State and Materials Research Dresden, Dresden, Germany*

[b]*Institute of Solid State and Materials Physics of TU Dresden, Dresden, Germany*

[c]*CEMES (CNRS), Toulouse, France*

[d]*CEOS GmbH, Heidelberg, Germany*

Contact email: a.lubk@ifw-dresden.de

Introduction:

Advanced charge particle optics (CPO) requires fast and accurate computational tools for calculating (relativistic) particle trajectories including aberrations that, ideally, handle both arbitrary electrics and magnetic field sources leading to arbitrarily bend optical axis, allow incorporation of symmetries (e.g., rotational or mirror), incorporate optimization of design parameters, such as pole piece diameter or pole distances. The CPO software development described in this contribution intends to address that need.

Methods:

Here we report on the development of an open source computational CPO framework incorporating the following principles to allow for an accurate, fast and flexible trajectory calculation: (A) The boundary element method (BEM) is used for the computation of electric and magnetic fields, yielding smooth and accurate potentials, fields and higher-order derivatives (up to 5th order) at optical axis at arbitrary sampling, while reducing the meshing effort to surfaces (e.g., electrodes and pole pieces) of the CPO device. Herein, single layer representations of both electric and magnetic scalar potential are most efficient. (B) A semianalytical hierarchical solution of perturbation series of Hamiltonian equations of motion around an optical axis[1] is employed in order to provide computationally effective, fast and accurate built-up of aberrations along (bend) optical axes. (C) The fast field and particle trajectory computation is combined with non-linear optimization routines facilitating automatic optimization of design parameters (e.g., pole piece gap) with respect to certain target functionalities. (D) A graphic user interface provides easy access to the functionalities of the code for standard CPO computations. This tool chain is written in Python and makes use of advanced open source libraries (OpenCascade for CAD, gmsh for meshing, BEMPP for BEM field computation, sympy for semianalytic Hamiltonian mechanics perturbation expansion including automatic code generation, scipy for solving equations of motion and geometry optimization) in a modular way. Notably, BEMPP was extended by parallel just-in-time compiled numba and opencl kernels for field derivative computations on optical axis as required for fast CPO computations.

Discussion and conclusions:

We demonstrate and discuss the above tool chain with the help several electrostatic and magnetostatic CPO / building blocks of CPO, notably electrostatic Einzellens, magnetic lens and half sphere analyzator, touching implementation (e.g., CAD import, defining boundary conditions, vector potential gauge), numerical (e.g., mesh size, precision of paraxial solution) and CPO (e.g., chromatic and geometric aberrations) aspects.

Acknowledgments:

The authors acknowledge funding from the HORIZON EUROPE framework program for research and innovation under grant agreement n. 101094299.

References:

[1] Kern, F., Krehl, J., Thampi, A., Lubk, A. “A Hamiltonian mechanics framework for charge particle optics in straight and curved systems”, *Optik,* 2021, 242, 167242

Type of presentation: Poster

IMPRESS 8 Multi-purpose MEMS devices for correlative operando experiments in battery research

Paolo Ronchese[a], Simone Dal Zilio[b], Benedetta Marmiroli[c], Alberto Roncaglia[d], Payam Habibzadeh Kavkanir[e], Albert Eichel[f,g,h], Vettorio Morandi[d], Amir Hossein Tavabi[i], Shibrabata Basak[f], Regina Ciancio[a]

[a]*AREA Science Park, (SS 14 km 163.5, 34149 Basovizza, Trieste), Italy*

[b]*CNR-IOM, (SS 14 km 163.5, 34149 Basovizza, Trieste), Italy*

[c]*Institut für Anorganische Chemie, TU Graz, (8010 Graz, Stremayrgasse 9/IV), Austria*

[d]*CNR-ISMN, (Via P. Gobetti 101, 40129 Bologna), Italy*

[e]*Dipartimento di Scienze Fisiche, Informatiche, Matematiche, Università di Modena e Reggio Emilia, (Via Campi 213/A, 41125 Modena), Italy*

[f]*Institute of Energy Technologies, Fundamental Electrochemistry (IET-1), Forschungszentrum Jülich, (D-52425 Jülich), Germany*

[g]*Institute of Physical Chemistry, RWTH Aachen University, (D-52074 Aachen), Germany*

[h]*Faculty of Mechanical Engineering, RWTH Aachen University, (D-52074 Aachen), Germany*

[i]*Physik Nanoskaliger Systeme (ER-C-1), Ernst Ruska-Centrum für Mikroskopie und Spektroskopie mit Elektronen, Forschungszentrum Jülich, (D-52425 Jülich), Germany*

Contact email: paolo.ronchese@areasciencepark.it

Introduction

The ever-growing demand for energy storage systems has stimulated substantial advancements in battery technologies. Understanding the fundamental properties and mechanisms governing battery performance and degradation requires direct observation of morphological, structural, and chemical changes at the nanoscale under electrochemical operating conditions. Transmission Electron Microscopy (TEM) provides combination of unparallel spatial and temporal resolution for investigating these processes, but its inherent limitations, such as the need for high-vacuum environment and electron-beam induced degradation, pose challenges for direct in situ/in operando battery studies. [1,2,3]

Correlative approaches that integrate TEM with complementary techniques, facilitated by portable microreactors, provide a powerful solution to overcome these limitations. [4,5]

Within the IMPRESS project, we are addressing the challenge by developing two innovative devices for correlative experiments, in both TEMs and synchrotron beamlines to study batteries under operando conditions. The first device (Figure 1, A) is designed for the battery chemistry with liquid electrolytes – the closed-cell configuration allows the direct observation of key electrochemical processes in different battery systems. The second device (Figure 1, B and C) is tailored for operando experiments using solid-state battery lamellae, operating under realistic current density.

Methods

All the chips have been thought to be produced from silicon wafers covered with a thin layer of silicon nitride: the wafers are etched to accommodate various elements, such as the electrical traces and the O-ring grooves.

Chips designs have been developed with Autodesk Fusion and validated by means of simulations run on COMSOL Multiphysics®.

The fabrication protocol of the chips composing the devices is based on multiple aligned optical lithography steps. The engraved features were produced by combining dry and wet etching processes: dry etching by inductively coupled plasma was employed for producing the O-ring groove, Reactive Ion Etching to selectively remove silicon nitride and wet etching protocols in KOH were exploited to remove silicon. Moreover, sputtering and evaporation steps are needed to create the electrodes, the insulating layer and the spacers. The fabrication sequence is set and optimized for every single chip, depending on the final feature to by produced.

Results

Figure 1 displays the chips designs. The electrochemical cell for studying batteries with liquid electrolytes (panel A) relies on a bottom chip and a top chip to ensure the confinement of the liquid environment inside the cell. The cell is designed to allow liquid to flow inside a designated area by depositing and patterning on the chip surface a thick layer of SiO_2 spacer, forming a channel. The bottom chip houses all the electrical contacts. Among the seven electrodes present, two are for heating and the rest for biasing. The heating strip has been designed to heat the entire chip assembly uniformly from the outer edges. The five biasing electrodes, one working, two reference and two counter, are all located inside the flow path. The design allows dynamic distance change, while O-ring between them prevents the system from leakage.

The operando cell for solid-state batteries experiments is based on a top chip that hosts four electrodes on the side of the silicon nitride window and the heating element (panel B), and a bottom chip (panel C) containing a cantilever tip that can work as a 3D-moving reference electrode.

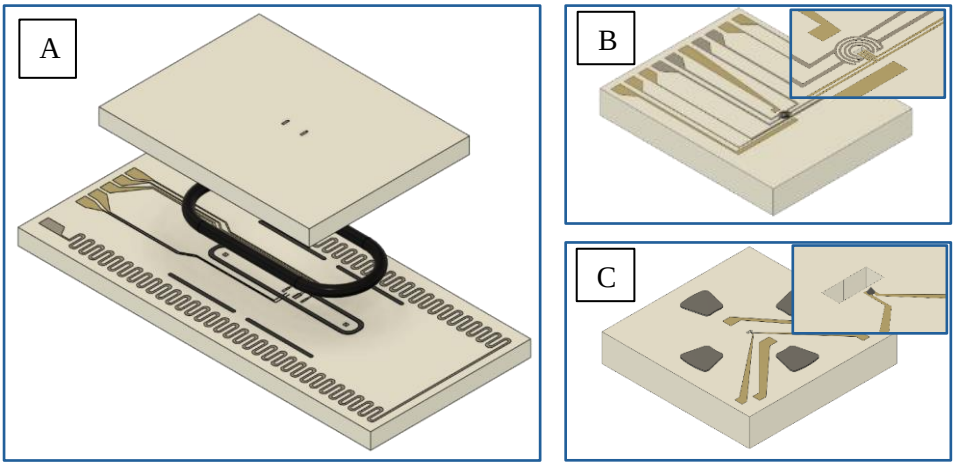


Figure 1. Lateral view of the electrochemical cell for studying batteries with liquid electrolytes at operando conditions (A), lateral view the chips composing the operando cell for solid-state batteries experiments. In the insets, a closer view of the imaging windows area of both chips is reported (B and C).

The early prototypes of the cells are currently under development aiming at validating the operational functionalities of the devices. Based on the results, the design and fabrication process can be changed following an iterative process in order to optimize the performances of the systems.

Discussion and conclusions

Both devices have been designed to be compatible with advanced analytical TEM techniques, like low dose 4DSTEM and spectroscopic techniques such as electron energy-loss and energy-dispersive X-ray spectroscopy, as well as beam line analytics such as X-ray absorption spectroscopy.

This integrated approach provides multi-dimensional insights into both static properties and dynamic processes in batteries, including fundamental advancements on the development of electrode structure, chemistry and shape. Furthermore, these devices have been conceptualized to thoroughly investigate electrolyte stability and local ionic distribution, as well as to map electric fields and current-density distribution during electrochemical operations as, for example, charge/discharge cycles.

By bridging the gap between atomic-scale imaging and macroscopic battery performance, these innovations significantly enhance our ability to develop next-generation energy storage materials.

References

[1] Sun et al., *Adv. Energy Mater*., **2024**, *14*, 2303165.
[2] Zhang et al., *Adv. Mater*., **2019**, 1904094.
[3] Yuan et al., *Joule*, **2019**, *3*, 471–484.
[4] Sharma and Yang, *Microscopy*, **2024**, *73(2)*, 79–100.
[5] Zhao et al., *ChemCatChem*, **2015**, *7*, 3683 – 3691.

Type of presentation: Poster

IMPRESS 9 Artificial Intelligence for TEM: Real-Time Automation and Predictive Analysis in In Situ Experiments

Enzo Rotunno[a], Marc Botifoll[b], Daniel Knez[c], Amir H. Tavabi[d], Paolo Rosi[a], Gerald Kothleitner[c], Jordi Arbiol[b], Vincenzo Grillo[a], Rafal Dunin Borkowski[d]

[a]*Instituto Nanoscienze CNR, (Modena), Italy*

[b]*Catalan Institute of Nanoscience and Nanotechnology, CSIC and BIST, (Barcelona), Spain*

[c]*Graz University of Technology, (Graz), Austria*

[d] *Ernst Ruska-Centre for Microscopy and Spectroscopy with Electrons Forschungszentrum Jülich, (Jülich), Germany*

Contact email: enzo.rotunno@cnr.it

Introduction

The unprecedented volume and complexity of data generated by Transmission Electron Microscopy (TEM) experiments present significant challenges for real-time analysis and experimental control. We develop and implement Artificial Intelligence (AI) tools, primarily Artificial Neural Networks (ANNs), to automate TEM workflows, enhance data interpretation, and optimize experimental efficiency. These solutions are particularly valuable for in situ, in operando, and correlative microscopy, where real-time decision-making is crucial.

Methods

We leverage machine learning to automate TEM alignment, data acquisition, and analysis, reducing the need for manual intervention. Deep learning models assist in identifying spectral features [1], crystallographic structures, and nanoscale dynamics, enabling real-time decision-making. Additionally, AI-driven optimization techniques adjust imaging parameters on the fly, improving both data quality and experimental efficiency.

Results

As TEM experiments push the boundaries of resolution and data complexity, AI is becoming an essential partner in both automation and discovery. In our work, we have transformed microscope operation by implementing an AI-driven auto-alignment system able to continuously corrects alignment parameters with human-level precision [2]. This technology significantly reduces the effort required for manual alignment, ensuring long-term stability even in prolonged in situ and operando experiments.

A major breakthrough has been in structural characterization, where we have leveraged deep learning models to analyze atomic-resolution images and accurately determine zone axes from diffraction patterns (Fig. 1a). This tool streamlines the traditionally time-intensive process of crystallographic indexing, making complex structure determination more accessible to the broader research community.

AI also enhances thickness estimation, where our ANN-based position average convergent beam electron diffraction (PACBED) analysis enables fast and reliable determination of sample thickness (Fig. 1b). By leveraging deep learning models, we have improved the accuracy and consistency of thickness measurements, reducing dependency on manual interpretation and ensuring more robust quantification of sample properties.

Perhaps one of the most visually impactful advancements is our development of a real-time segmentation framework for tracking magnetic quasiparticles in dynamic TEM experiments (Fig. 1b). Integrated with augmented reality visualization, this system overlays analytical insights directly onto the live microscope feed, allowing researchers to interact with data in ways never before possible. By offering immediate feedback, this AI-driven augmentation enhances decision-making during experiments, ensuring that critical moments are captured and analyzed in real time.

Beyond automation, AI is proving to be a powerful tool for optimization, where predictive models dynamically adjust imaging parameters based on early experimental feedback. This adaptive AI system not only refines image acquisition settings in real time but also reduces beam exposure, preserving beam-

sensitive materials while maximizing data quality. By guiding experimental trajectories based on evolving conditions, AI is shifting TEM workflows from reactive adjustments to proactive control.

Discussion and Conclusions

Our findings demonstrate that AI-driven automation significantly enhances TEM efficiency, accuracy, and accessibility. By eliminating the need for manual intervention in alignment, data interpretation, and workflow control, these tools reduce experimental overhead and democratize advanced microscopy techniques. Future work will focus on further integrating AI with digital twin models, expanding real-time automation capabilities, and developing open-source AI frameworks for the TEM community.

Acknowledgments: This work is supported by the IMPRESS project, funded by the HORIZON EUROPE program (Grant No. 101094299).

References:

1. A. Annys et al, *Scientific Reports*, **2023**, 13, 13724.
2. L. Grossetete et al., *Ultramicroscopy*,**2024**, 114047.

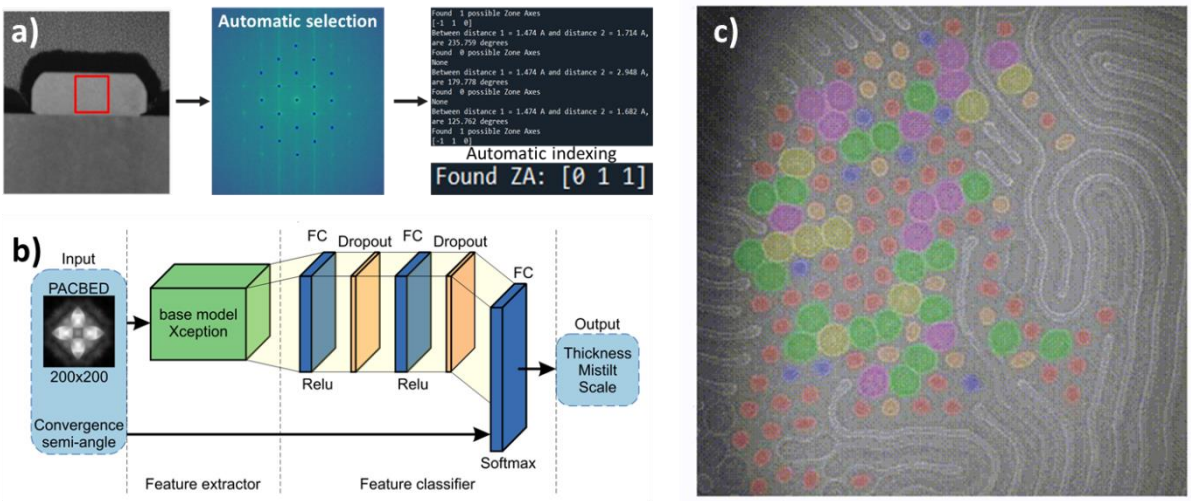


Figure 1: (a) example of automatic zone axis indexing, (b) layer structure of the artificial neural network used for determining sample thickness in automated PACBED experiments, and (c) automatic identification of magnetic quasi-particles.

Type of presentation: Poster

IMPRESS 10 Applications Support for Complex TEM Workflows

Daniel G. Stroppa[a,b]

[a]*DSTL GmbH, Switzerland*

[b]*DECTRIS AG, Switzerland*

Corresponding author: daniel.stroppa@dstl.ch

Transmission electron microscopy (TEM) instrumentation has received consistent updates over the last few years, including novel electron sources, more flexible electron optics, fast and efficient direct electron detectors, and hardware that supports in situ experiments. These features enable increasingly sophisticated characterization workflows, including correlative modalities, and support the high-impact advances on materials characterization.

A grand technical and operational challenge is to integrate these technologies into cohesive, scientifically productive workflows. The main reason is that they often provided by different vendors with proprietary interfaces and software environments. In addition, the resulting complexity requires users to have deeper instrument knowledge and workflow-level expertise to exploit the full potential of such setups.

To address the onboarding of new users and support a broad use of the latest TEM technologies, there is need for applications support able to bridge the many instrumental resources and guide their use towards to specific scientific goals. Such support must extend beyond routine training, and offer flexible, vendor-agnostic guidance that adapts to local infrastructure, research objectives, and evolving experimental requirements.

This contribution discusses a model for delivering customized applications support fit to TEM instruments with high-degree of customization. It is based on a modular structure developed together with the local scientists and new users, followed by tailored hands-on experimental sessions and data processing sessions. With the diversity of instrumentation and experiments interests, the co-development of optimized workflows is proposed as a collaborative approach in tandem with manufacturers and counting with continued applications support.

Type of presentation: Poster

IMPRESS 11 Mechanical strain and light-induced control of magnetic states in Fe_3Sn_2 *in situ* in the TEM

András Kovács[a], Dely Kong[b], Michalis Charilaou[c], Jonathan T. Weber[d], Amir H. Tavabi[a], István Kézsmárki[e], Sascha Schäfer[d], Rafal E. Dunin-Borkowski[a]

[a]*Ernst Ruska-Centre for Microscopy and Spectroscopy with Electrons, Forschungszentrum Jülich, (Jülich), Germany*

[b]*Southern University of Science and Technology, (Shenzhen), China*

[c]*University of Louisiana at Lafayette, (Lafayette), USA*

[d]*University of Regensburg, (Regensburg), Germany*

[e]*University of Augsburg, (Augsburg), Germany*

Contact email: a.tavabi@fz-juelich.de

The ability to control magnetism and magnetic properties of materials on the nanoscale using external stimuli has the potential to broaden the scope of applications of spin degrees of freedom in data storage, spintronics and quantum computing. Transmission electron microscopy (TEM) is attractive for the direct observation of such processes, as it offers powerful *in situ* techniques for quantitative magnetic imaging of nanoscale samples. Here, we report the application of MEMS-based mechanical straining and ultrafast light pulse modulation to the study of the dynamics of magnetic properties of topological materials *in situ* in the TEM.

Focused ion beam sputtering with Ga in a dual beam scanning electron microscope (TFS Helios Nanolab 460F1) was used to prepare TEM specimens from an Fe_3Sn_2 single crystal that had been grown by a chemical transport method. A standard lift-off procedure was used to produce lamellae on Cu Omniprobe grids or MEMS chips (Fig. 1a). The strain level in the TEM was controlled by using a piezo activator for displacement control (Bestron ST). Fresnel defocus images and off-axis electron holograms of magnetic domains were recorded in magnetic-field-free conditions using an aberration corrected FEI Titan 60-300 TEM equipped with a direct electron counting detector (Gatan K2). Light-induced experiments were carried out at 200 kV in a modified JEOL JEM-F200 TEM, which was equipped with a cold FEG and connected to a home-built laser system (RUN Regensburg). Optical pumping was performed using an amplified Yb-doped KGW femtosecond laser system operated at 400 kHz. For positioning the optical focus, a focusing lens mounted on a 3D piezo actuator was placed on a home-built light-in coupling unit.

Kagome-type Fe_3Sn_2 has a high Curie temperature and exhibits a wide range of intriguing magnetic properties. Competing uniaxial and shape anisotropies can lead to the formation of diverse topological spin textures, such as dipolar skyrmions (Fig. 1b). Tensile strain (rather than electric current or external magnetic field) was used to control the magnetic textures of Fe_3Sn_2 samples and their transitions were followed *in situ* in the TEM. Strain control revealed: (i) the formation of a regular vertical stripe pattern by the gradual elimination and merging of dipolar skyrmions up to a strain of 1%; (ii) the formation of large domains with in-plane magnetization separated by straight domain walls (1−1.7%); (iii) recovery of the vertical stripe pattern upon strain release (Fig. 1c). Micromagnetic modelling supported the experimental findings, revealing a hysteretic behaviour resulting from configurational anisotropy and a competition between magnetocrystalline and strain-induced anisotropies [1].

A different Fe_3Sn_2 lamella was exposed to a series of femtosecond light pulses. Fresnel defocus images were subsequently recorded at magnetic remanence. After each light pulse, contrast variations were observed at the centres of the dipolar skyrmions. These variations were attributed to light-induced switching of the helicities of Néel caps, while the core Bloch domain walls maintained their configurations (Fig. 1d). In the images, bright contrast corresponds to counterclockwise field rotation

on both the top and the bottom of the dipolar skyrmions (ccw state); dark contrast corresponds to clockwise field rotation (cw state); no contrast is associated with opposite helicities (mixed state), which cancel out in projection. Statistical analysis (Fig. 1e) revealed that the dipolar skyrmions adopted a mixed state for approximately 50% of the events and that changes occurred randomly. These findings demonstrate that all-optical stochastic switching of Néel cap helicity occurs in dipolar skyrmions in Fe_3Sn_2 at room temperature and magnetic remanence [2].

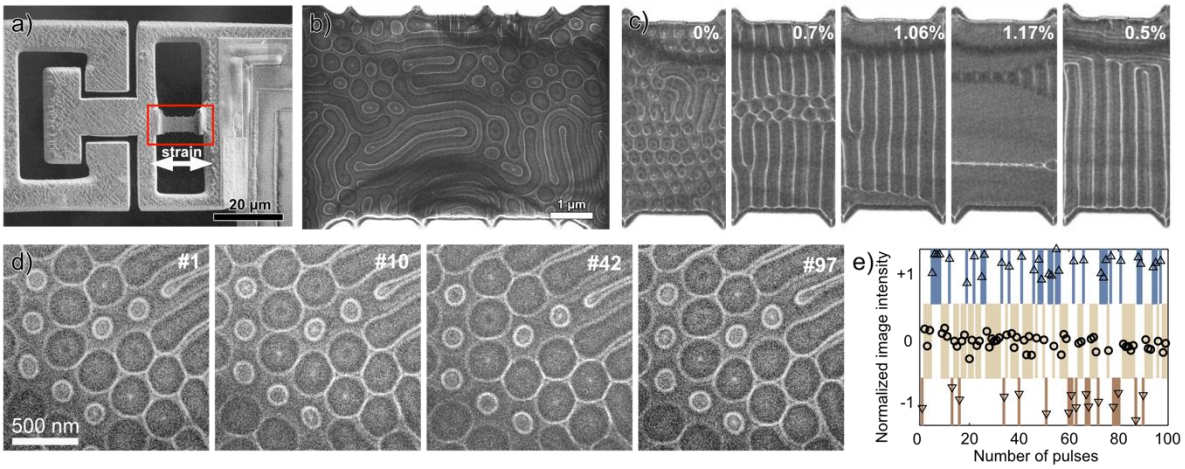


Figure 1: (a) Secondary electron image recorded in a scanning electron microscope of an Fe_3Sn_2 lamella mounted in a mechanical straining device. (b) Fresnel defocus image showing stripe domains and dipolar skyrmions. (c) Fresnel defocus images of part of the lamella recorded during *in situ* tensile straining and releasing. The strain levels are indicated. (d) Magnified regions of Fresnel defocus images recorded after applying a 169 fs light pulse (n#) for 100x. Note the contrast variations at the centres of the dipolar skyrmions. (e) Statistical analysis of the switching states, with +1, 0 and -1 indicating counterclockwise, mixed and clockwise rotation senses.

In summary, a MEMS-based mechanical straining nanodevice, which also allows for heating and/ or electrical biasing, provides new opportunities for the study of functional properties of materials with high precision and stability during *in situ* TEM experiments. In addition, by using ultrafast light illumination in the TEM, insight could be obtained into the dynamics of topological magnetisation textures. Further advances are required to improve the temporal resolution of *in situ* TEM experiments of ultrafast processes.

The authors are grateful for funding from the European Union under grant agreements No. 101094299 ("IMPRESS") and No. 856538 ("3D MAGiC"). The authors express their gratitude to L. Prodan, V. Tsurkan, A. Schröder, N. S. Kiselev, D. Meier and X. Han for contributions and discussions.

References:

1. D. Kong et al., *ACS Nano* **2025**, *19*, 8142.
2. J.T. Weber et al., arXiv 2503.05660, **2025**

Type of presentation: Poster

IMPRESS 12 A laser-free approach to ultra-fast transmission electron microscopy

Govind Ummethala[a], Benjamin Zingsem[a], Eric Montgomery[b], Ryan Gnabasik[b], Martin Linck[c], Heiko Müller[c], Rafal E. Dunin-Borkowski[a], Amir H. Tavabi[a]

[a]*Ernst Ruska-Centre for Microscopy and Spectroscopy with Electrons, Forschungszentrum Jülich, Jülich, Germany*

[b]*Euclid Techlabs LLC, Maryland, USA*

[c]*CEOS GmbH, Heidelberg, Germany*

Contact email: b.zingsem@fz-juelich.de

In the transmission electron microscope (TEM), high temporal resolution can be achieved using short electron pulses, typically in a pump-probe stroboscopic scheme. Temporal resolution can be described in terms of a convolution of pump and probe pulses, in addition to jitter arising from random phase shifts in their arrival times. The primary methods for generating short electron pulses in the TEM are photoemission and beam blanking. In photoemission, a short (fs to μs) ultraviolet laser pulse strikes a photocathode in the electron gun, resulting in electron emission through either the photoelectric effect or laser-triggered field emission. The use of fs lasers is often costly, requiring complex instrument modifications, and beam instability can result from laser pointing fluctuations on the cathode. In beam blanking, the electron gun remains unchanged, while a continuous electron beam is chopped into short pulses by sweeping it rapidly over a narrow slit placed before the sample. Even a "fast" electrostatic beam blanker is limited by the capacitive response of the electrostatic elements, which constrains the temporal resolution to nanoseconds or longer [1, 2].

Here, we show how a travelling wave radiofrequency (RF) deflection cavity combined with a small aperture can be used to chop a continuous electron beam to generate short electron pulses. In this approach, the constant beam is swept across the aperture, producing a pulsed beam. A second correcting RF cavity is operated to zero out the time-dependent transverse momenta introduced by the first deflecting RF cavity, in a way that maintains the original peak brightness and energy spread. This approach does not require the use of fs lasers or invasive modifications to the electron source. Such an RF-driven electron beam pulser can generate short electron pulses with a tunable repetition rate up to 12 GHz [3, 4]. This pulser is a next-generation design involving substantial RF and optical upgrades, automation-compatible software, and improved control of pulsed spot size and shape.

The second-generation Ultra-Fast Pulser (UFP) unit from Euclid Techlabs LLC, with optics from CEOS GmbH, was installed on a FEI Titan G2 60-300 TEM, in order to allow time-resolved experiments to be performed when combined with an ultrafast pump, in any standard operating mode of imaging, diffraction or spectroscopy without the need for and several orders of magnitude faster than state-of-the-art time-resolved detectors. The unit, which can achieve electron beam pulses as short as 20 ps (sub-ps with a smaller aperture), is placed at the gun exit to maintain the original TEM modalities when no RF signal is applied. Once activated, it can be operated in RF (2 to 6 GHz) or Pulse Picker mode.

Figure 1(a) shows a schematic diagram of the internal elements of the Pulser, which comprises three principal components: an electron beam modulator (K1)/ demodulator (K2), beam chopping aperture (A), quadrupole magnets (Q1 through Q3, new for the second generation UFP) and a CL0 lens (to accommodate for the longer distance to the gun crossover). A continuous microwave signal is used to dynamically deflect the electron beam at frequencies of up to 6 GHz (limited by the bandwidth of the RF structure) using K1 and correct the beam in K2. The beam travels through an aperture twice during every deflection cycle, resulting in a tuneable repetition rate of up to 12 GHz. The size of the aperture, the RF power, and the frequency determine the pulse width as it is swept across the aperture. In this way, ps (or with small apertures and control of the C0 crossover, sub-picosecond) electron beam pulses can be generated, enabling dynamics to be monitored at frequencies of up to 12 GHz with appropriate

pumping schemes. A microwave signal can be used as a trigger to synchronise the UFP's RF pulsetrain with a given sample excitation. By precisely tuning the phase delay between the pump excitation signal and the probing UFP signal, we can scan and record sample excitation dynamics with picosecond resolution.

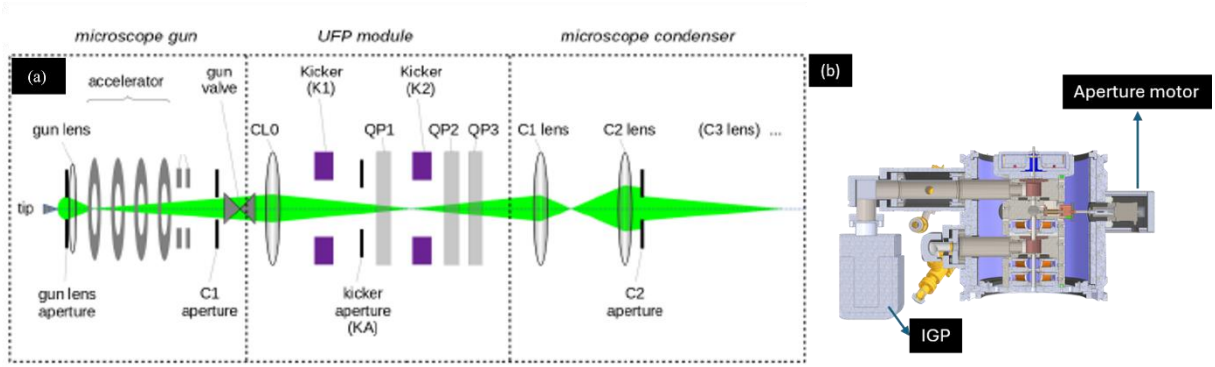


Figure 1: (a) Overview of 2nd generation UFP optics module. The ray path from left to right corresponds to the top-to-bottom orientation in the microscope. (b) Cross-sectional sketch of the UFP unit showing the internal optics, additional ion getter pump (IGP) and aperture of the UFP module.

Figure 2 shows an image of an Au cross grating sample recorded using a 100-ps pulsed beam. The corresponding Fourier transform shows that a resolution close to that of the unmodified microscope can be achieved when operating in pulsed beam mode.

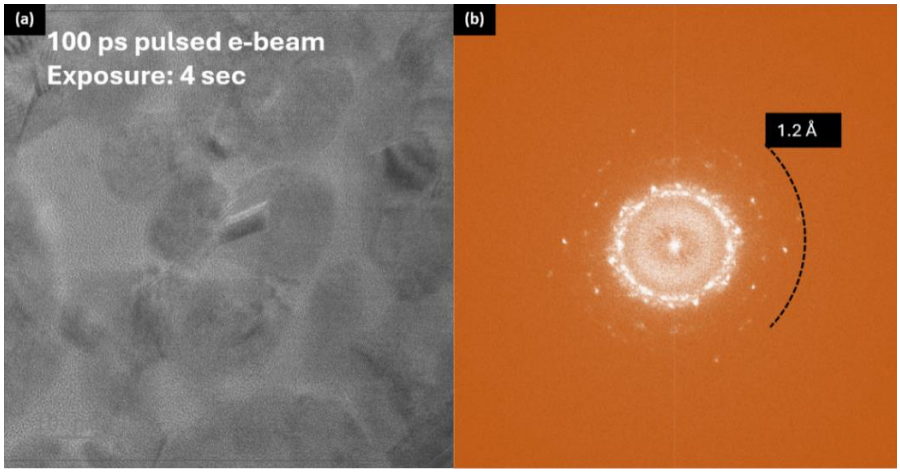


Figure 2: (a) Image of Au grating and (b) corresponding Fourier transform recorded using a pulsed electron beam.

The ability to pulse an electron beam with a wide range of frequencies provides the opportunity to study numerous ultrafast phenomena (*e.g.*, in phase change and magnetic materials) based on the use of external stimuli and specific sample environments, ideally combined with a workflow that allows experiments to be transferred to complementary techniques such as those at synchrotron X-ray beamlines to enable correlative time-resolved studies. Different high repetition rate lasers and microwave-enabled sample holders are available in the Ernst Ruska-Centre in Forschungszentrum Jülich for performing stroboscopic time-resolved studies, with a focus on studies of (i) nucleation and transformations of topological magnetic textures such as skyrmions using surface acoustic waves; and (ii) laser-induced phase transformations in materials that are used as ultrafast photoconductive switches.

References

1. Ultramicroscopy 176, 2017, 63-73.
2. Ultramicroscopy 184, 2018, 8-17.
3. Ultramicroscopy 235, 2022, 113497.
4. Sci. Adv. 6, 2020, eabc3456.

Type of presentation: Poster

IMPRESS 13 Time-resolved imaging of dynamic and resonant spin phenomena in situ in the TEM

Benjamin W. Zingsem[a], Joseph Vimal Vas[a], Alexander Clausen[a], Govind Ummethala[a], Amir H. Tavabi[a], Michael Schaaf[b], Michael Farle[c], Rafal E. Dunin-Borkowski[a]

[a]*Forschungszentrum Jülich GmbH, Ernst Ruska-Centre for Microscopy and Spectroscopy with Electrons, Germany*

[b]*Forschungszentrum Jülich GmbH, Institute of Technology and Engineering, Germany*

[c]*University Duisburg-Essen, AG-Farle, Germany*

Contact email: b.zingsem@fz-juelich.de

We present direct transmission electron microscopy imaging results of thermal phase transitions of topological spin textures, spin waves, electron spin resonance and spin Hall scattering in magnetic skyrmions and collinear ferromagnets. By applying a combination of bright field imaging, time-resolved imaging using a beam pulser and recording using a delay line detector, magnetic domain wall motion and vortex gyration can be imaged. Both the ground state and higher harmonics can be mapped in ferromagnetic resonance spectroscopy of individual magnetic nanodots and micron sized chiral magnets. By monitoring the beam deflection in defocused bright-field and diffraction images, cavitronic coupling of spin resonance eigenstates in electron spin resonance of paramagnetic diphenyl-pikryl-hydrazyl (DPPH) and ferromagnetic magnetite (Fe3O4). By using an electron beam pulser, the time-dependent behavior of a magnetic skyrmion phase transition in FeGe can be monitored.

Lunch workshops

Type of presentation: Oral

Advanced microscopy solutions from Leica-Microsystems

Martin Kopecký[a]

[a]*SPECION*

Contact email: bacik@specion.cz

Advances in spatial biology rely on cutting-edge imaging technologies that allow researchers to explore biological systems with unprecedented precision, resolution, and context thanks to dedicated Electron and Light Microscopy workflows. Leica Microsystems provides an integrated portfolio of microscopy solutions tailored to these needs. The Leica STELLARIS confocal platform extends detection sensitivity, spectral flexibility, and photon efficiency, enabling deeper insights into molecular interactions and cellular dynamics. For super-resolution applications, Leica STED microscopy breaks the diffraction limit, allowing nanoscale visualization of biomolecular processes in living cells. Complementing these systems, Leica CryoCLEM integrates cryogenic sample preparation with correlative light and electron microscopy, bridging structural biology and functional imaging. Leica EM ICE with advanced cryo fixation capabilities. Together, these technologies form a comprehensive toolkit for spatial biology, empowering researchers to map molecular architecture, cellular context, and tissue organization with clarity and depth.

Type of presentation: Oral

Hydra Bio plasma FIB: pushing the boundaries to larger 3D volumes

Itziar Serna Martin[a], Cveta Tomova[b]

[a]*Thermo Fisher Scientific, Eindhoven, The Netherlands*

[b]*Thermo Fisher Scientific, Brno, Czech Republic*

Contact email: itziarserna.martin@thermofisher.com

Cryo-electron microscopy has revolutionised structural biology and our ability to explain with molecular precision how many macromolecules function. However, it is being increasingly recognised that studying these structures in isolation—away from the context of their native cell, tissue, and organism—leaves significant gaps in our understanding. This has reinforced the need to develop techniques that are capable of handling larger samples and bigger volumes, bridging cellular biology and structural biology.

The introduction of the latest generation of the Hydra Bio plasma FIB to biological sciences has opened the door to the imaging of cells and tissues through Slice & View (serial FIB SEM) both at room and cryo temperatures in a way that achieves optimal quality and resolution. Further combining volumetric imaging approaches with cryo-ET allows insight to be gained across orders of magnitude of scale.

This workshop will explore the latest advancements in the applications of plasma FIBs, highlighting their pivotal role in volume imaging and sample preparation for cryo-electron tomography (cryo-ET). Additionally, we will introduce the latest features which are set to further enhance the precision and efficiency of 3D volume data acquisition: AI driven adaptive scanning and dynamic auto functions. These significantly improve both the total size and the speed with which data can be acquired, opening avenues to automated analysis of extensive biological volumes while maintaining nanoscale resolution and transforming our ability to study cellular processes in their native context.

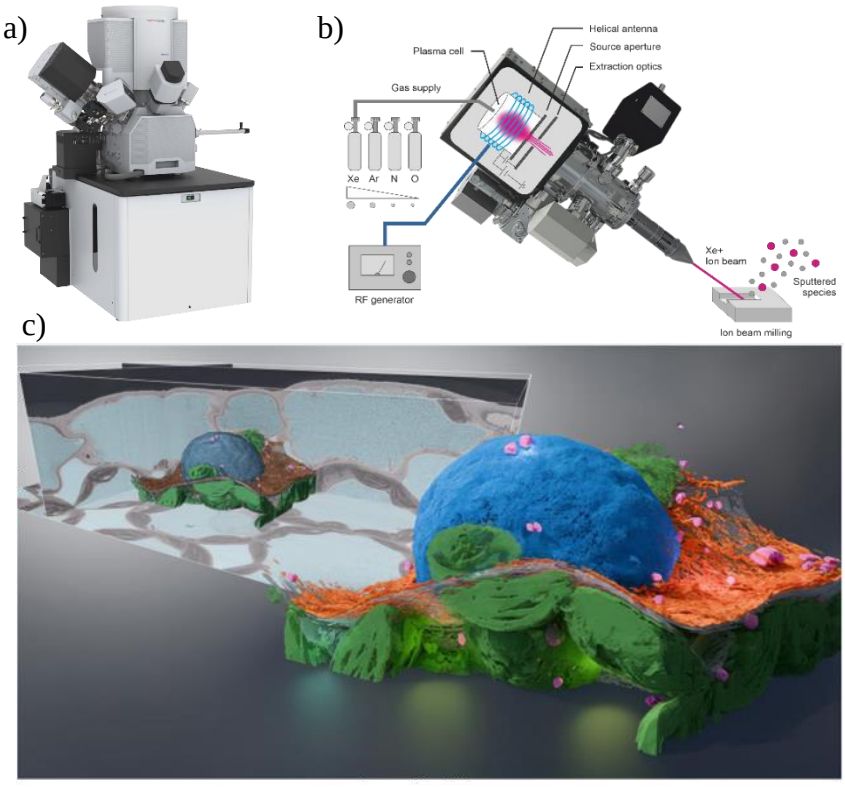


Figure 1: (a), Thermo Fisher Scientific Hydra Bio plasma FIB SEM (b), Schematic of plasma cell ion beam source with four different gases with unique milling properties (c). segmented volume EM dataset of tobacco plant tissue showing vacuoles (cyan) automatically identified for faster, lower resolution scanning through AI driven adaptive scanning resulting in a 49% time saving in volume acquisition.

Type of presentation: Oral

New solutions for advanced multimodal characterization of materials at the nanoscale

Martin Suchanek[a]

TESCAN GROUP, a.s., Libušina třída 21, 623 00 Brno, Czech Republic

Contact email: lucie.brnkova@tescan.com

Continuing demand for new and improved materials in metallurgy, automotive industry, energy research and other fields of Materials Science necessitates the utilization of advanced and accessible solutions for multimodal characterization of a broad range of samples. Recent advances in electron diffraction techniques provide new insights into the underlying structural and compositional characteristics that determine the macroscopic properties, such as strength, corrosion resistivity, thermal stability, fatigue and deformation properties. However, these techniques of scanning transmission electron microscopy (STEM) have been traditionally reserved only for highly skilled operators and scientists. The introduction of the newly developed analytical STEM platform, Tescan TENSOR, with fully automated alignments is game changing for both Academic research and Industry applications. This new microscope was designed for high-throughput analysis that leverages guided workflows, fast electron beam precession, and on-the-fly data processing to interactively provide meaningful and interpretable results during the microscope session. This ensures that even non-expert operators can produce high-quality analytical STEM and 4D-STEM data and results without extensive post-processing steps. Moreover, the deep hardware and software integration in TENSOR provides the ability to collect fully synchronized datasets with simultaneous STEM, precession diffraction, and EDX data collected in the same scan, allowing for multimodal analysis. Simple and rapid access to industry standard strain, or crystal orientation analysis is facilitated by the advanced system automation, which enables precession 4D-STEM experiments to be performed in mere minutes, while relying only on the analyzed specimen and not on the operator for success of the analysis.

Keywords: electron microscopy; analytical; multimodal; diffraction; 4D-STEM; precession; grain distribution; boundaries; 3D structure

Type of presentation: Oral

JEOL: cutting edge products for time resolved microscopy and TEM evolutions

Guillaume Brunetti[a]

[a]*JEOL (EUROPE) SAS*

Contact email: brunetti@jeol.fr

Since 1949, JEOL's legacy has been one of the most remarkable innovations in the development of instruments used to advance scientific research and technology. JEOL has 75 years of expertise in the field of electron. This presentation will be focused on the cutting-edge developments based on ultrafast shutter and laser injection inside the TEM column. Recently JEOL acquire IDES company and started to incorporate their technologies in the transmission electron microscopes. IDES is a leader and pioneer in the field of Ultrafast and Dynamic TEM, specializing in pulsed lasers and high-speed electrostatic beam blanking and deflection technologies. These products add time resolution to the TEM's exceptional spatial resolution enabling new applications and the exploration of the dynamics of specimens across a range of very fast time scales. Here is a non-exhaustive list of the innovations we will present: EDM Basic (Electrostatic Dose Modulator) / Programmable STEM with EDM Synchrony / Luminary Micro Compact Specimen Photoexcitation System (Fig. 1 & 2). In the second part of this presentation, we're going to talk about the development paths envisaged by JEOL for the coming generation of highest performance TEM (Fig. 3).

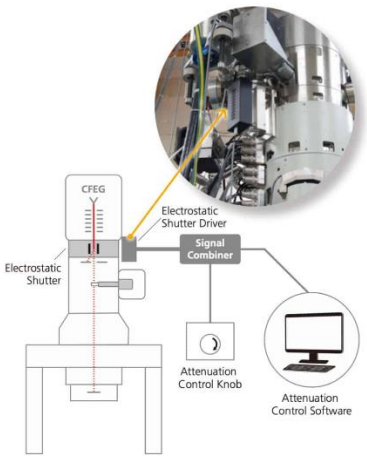


Figure 1. EDM: Electron Dose Modulator.



Figure 2. Luminary Micro: Compact Specimen Photoexcitation System



Figure 3. Magnetic field-free electron microscope

Type of presentation: Oral

Iliad, the new (S)TEM platform: Expand and simplifies electron energy loss analytics

Reza Zamani[a]

[a]*Thermo Fisher Scientific, Eindhoven, The Netherlands*

Contact email: reza.zamani@thermofisher.com

Introduction:
The Thermo Scientific™ Iliad™ (S)TEM is a next-generation, fully integrated transmission electron microscope platform that combines advanced electron energy-loss spectroscopy (EELS) with the NanoPulser™ ultrafast electrostatic beam blanker, the dedicated Zebra™ EELS detector, and the Velox™ software ecosystem. This integration extends to the optical design of the EELS spectrometer and energy filter, delivering enhanced mechanical and thermal stability, precise alignment, and optimized performance for multimodal workflows such as simultaneous EELS and energy-dispersive X-ray spectroscopy (EDS). Full Python access through Thermo Scientific™ Autoscript™ enables the creation of customized workflows and AI-driven acquisition and processing strategies, making sophisticated techniques accessible to both expert and novice users.

Methods:
EELS is a powerful technique for probing structure, chemistry, and electronic properties down to the atomic scale, but its effectiveness depends on accurately coordinated control of TEM and spectrometer optics. A broad range of electron energies must be simultaneously transferred through the microscope and the spectrometer, from the specimen down to the detector, without introducing chromatic blur or chromatic distortions. The Iliad platform's deep integration eliminates these common challenges by enabling the seamless transfer of a broad range of electron energies through the microscope and spectrometer. The so-called Always-in-Focus technology will be presented and several practical examples covering the broad range of applications enabled by the new Iliad STEM platform will be shown. The new Zebra detector provides fast, high-sensitivity data collection, allowing for the application of the MultiEELSTM mode while the unified Velox software environment simplifies operation, improves reproducibility, and supports efficient electron dose optimization strategies.

Results:
Example EEL spectra of $DyScO_3$ clearly show the improved performance within the <2keV range, where the – commonly present – spectral defocus is eliminated.

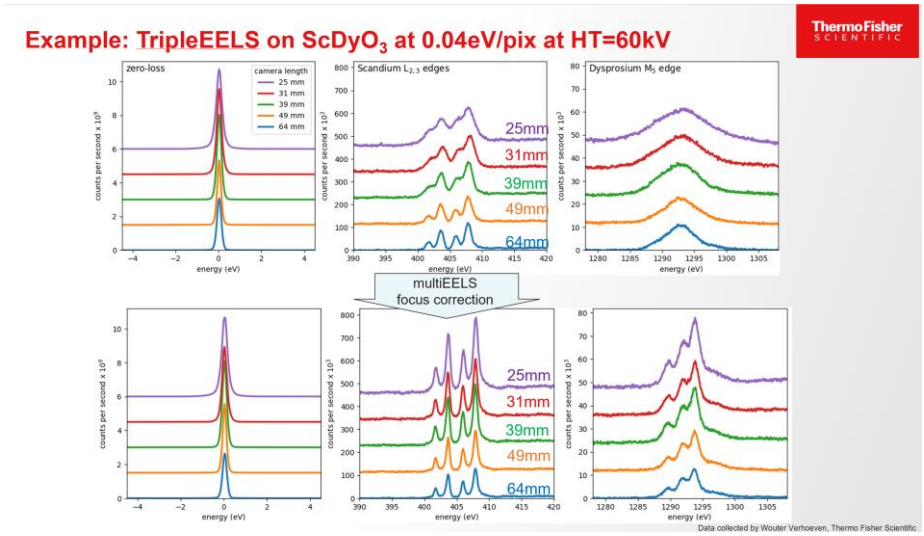


Figure 28: Eliminated spectral defocus enabled through deep integration of filter and TEM.

Moving on to higher energy ranges of 9keV (Cu K) clearly shows the superior performance of the Iliad EELS system. This enables the direct interpretation of EELS data by X-ray synchrotron software and the extraction of coordination information at sub-micrometer scale as depicted in Figure 27.

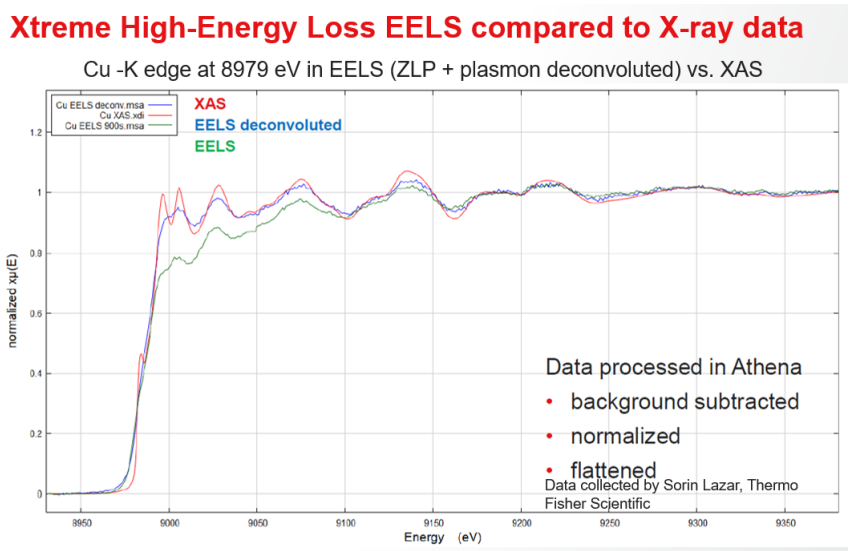


Figure 29: Interpretation of high-loss EELS data via Athena software package.

Reference:

S. Lazar, P. Tiemeijer, C. S. Schnohr, M. Meledina, C. Patzig, T. Höche, P. Longo, B. Freitag, *PHYSICAL REVIEW APPLIED* **2025** 23, 054095

Type of presentation: Oral

Global JEOL workflow for air & beam sensitive samples from micro to nano scale

Nicolas Ravier[a]

[a]*JEOL (EUROPE) SAS*

Contact email: ravier@jeol.fr

Since 1949, JEOL's legacy has been one of the most remarkable innovations in the development of instruments used to advance scientific research and technology. JEOL has 75 years of expertise in the field of electron.

In response to the challenges posed by research on new materials such as 2D materials or solid-state batteries, JEOL offers a set of complementary and interconnected instruments to enable the preparation, imaging, and analysis of these materials while keeping them protected from air at every stage.

a)  b)  c) 

Fig.1: the different instruments used during the workflow for air & beam sensitive samples: FEG SEM IT810 (a), FIB PS500i (b) and for the sample preparation the Cryo Cross Polisher (c)

Index of Authors

Aballe, Lucía	IM2-O-3 Investigating Magnetic Domain Wall Pinning in Nanowires via Correlative X-ray and Electron Transmission Microscopy IM7-P-1 InCAEM: A Singular Infrastructure for Advanced Energy Materials Research
Abbasgholi-NA, Behnaz	IM8-O-2 Optimization of SEM Instrumental Parameters for Enhanced Imaging Applying Machine Learning
Abbasi, Rabail Badar	MS7-P-1 Observation of defects in Li rich oxides as a product of temperature and chelating agent during synthesis
Abdelrahman, Abdelaziz Mohamed	IM8-O-1 ViFoSe, an user-friendly open-source post-processing tool for foreground segmentation in time-lapse videos.
Abhrajyoti, Chakrabarti	LS1-O-1 Immersive Virtual Reality System for Mice Combined with 3D-Targeted Photostimulation as a Prototype for Visual Restoration
Abkenar, Sirous Khabbaz	MS8-O-1 Low-dose 4DSTEM analysis of local strain in 2D perovskite lateral heterostructures
Abrahams, Jan Pieter	LS1-P-1 Quantifying Electron Radiation Damage in Biological Samples: Insights from Fluorescence Analysis
Aćić, Svetlana	LS6-P-1 Morphological features of Himantoglossum calcaratum (Beck) Schltr. subsp. calcaratum (Orchidaceae) pollinarium
Acikel Elmas, Merve	LS3-P-1 Protective effect of ferulic acid in monosodium glutamate-induced kidney injury: a light and transmission electron microscopical study
Adkin-Kaya, Olivier	IMPRESS 6 NanoMi: An open-source electron microscope
Afshar, Erfan	IM3-P-8 Surface and sub-surface defect analysis in semiconductors by Secondary Electron Emission Spectroscopy and local charge transport mapping IM1-P-7 Quantum state secondary electron emission spectroscopy in low voltage scanning electron microscope for probing Valence band
Afzali, Maryam	MS1-IN-1 Studying the crystallization of inorganic materials using correlated transmission electron microscopy
Åhlgren, E. Harriet	MS4-O-4 Metallene synthesis by ion irradiation: Growth of two-dimensional gold by vacancy-induced nucleation on defect-engineered graphene IM8-IN-1 Convolutional neural networks for scanning transmission electron microscopy image analysis: Towards automated analysis of large volume datasets
Ahmad, Shahzeb	MS8-P-1 Focused e-Beam Heating for local Material Modification: Melting, Patterning, and Band Gap tuning
Aksener, Eymen	MS4-P-1 Investigation of Boron-Based Nanosheets, Nanoscrolls and Nanotubes by TEM Analyses
Albrecht, Wiebke	MS4-P-5 Stability of gold nanorods under tunable ps-pulsed laser illumination: an in-situ TEM study
Alessi, Antonino	IM1-P-3 Irradiation-induced point defects in optical fibers investigated by cathodoluminescence microscopy and spectroscopy.
Almeida, Trevor	MS5-IN-2 Next Generation Spintronic Devices And 3D Curved Magnets examined by Lorentz microscopy MS5-O-3 3D Nano-Printing of Complex Metal Structures via Focused Electron Beam Induced Deposition
Álvaro-Gómez, Laura	IM2-O-3 Investigating Magnetic Domain Wall Pinning in Nanowires via Correlative X-ray and Electron Transmission Microscopy

Alves Junior, Severino	MS8-P-3 Y(Eu, Tb) frameworks with thiazolothiazoledicarboxylate: structural investigation by electron microscopy and diffraction techniques
Ametrano, Claudio	LS3-P-10 Optimization of Sample Preparation and Scanning Electron Microscopy Imaging for the Investigation of Trebouxia Flagellate Cells
Anderluh, Gregor	IM4-O-2 A closer look at the protein-lipid complex of actinoporin pores
Andosch, Ancuela	LS2-O-1 Beyond Apoptosis: Unravelling Thapsigargin-Induced Non-Apoptotic Cell Death Pathways in Immune- and Cancer Cells
Andrius, Plauska	LS1-O-1 Immersive Virtual Reality System for Mice Combined with 3D-Targeted Photostimulation as a Prototype for Visual Restoration
Antić, Tanja	MS3-P-1 Corrosion at Home: Microscopy's Role in Understanding Everyday Material Failures
Arah, Bor	MS3-P-8 Composition and microstructure of wrought and additively manufactured DED-LB of Ti-6Al-4V alloy MS3-P-2 Plastic deformation in the Magnesium alloy AZ80 - an EBSD study of the effects of cavitation peening
Arbak, Serap	LS3-P-1 Protective effect of ferulic acid in monosodium glutamate-induced kidney injury: a light and transmission electron microscopical study
Arbiol, Jordi	MS6-IN-1 Automated analysis of STEM data of semiconductor heterostructures for quantum computing MS4-O-3 High-Entropy Oxide Nanoparticles as Stable and Efficient Catalysts for the Oxygen Evolution Reaction IMPRESS 9 Artificial Intelligence for TEM: Real-Time Automation and Predictive Analysis in In Situ Experiments IM7-P-1 InCAEM: A Singular Infrastructure for Advanced Energy Materials Research IMPRESS 1 End-to-end Autonomous Unveiling of Physical Knowledge of Quantum Devices through Electron Microscopy Data
Arché-Núñez, Ana	IM2-O-3 Investigating Magnetic Domain Wall Pinning in Nanowires via Correlative X-ray and Electron Transmission Microscopy IM7-P-1 InCAEM: A Singular Infrastructure for Advanced Energy Materials Research
Arenal, Raul	IM1-P-2 Low-energy Core-loss EELS as a Dose-effective Approach for Elemental and Oxidation State Mapping
Arenas Esteban, Daniel	MS4-O-1 3D Identical Location STEM Insights into the Degradation of Metallic Core-Shell Nanoparticles under Fuel Cell Conditions
Arh, Tina	MS5-P-4 Synthesis Strategies for Effective Doping of Barlowite
Arikawa, Kentaro	LS2-P-1 The sexually dimorphic retina of a butterfly, from microspectrophotometry to connectomics
Arilla del Caño, Rodrigo	IM7-P-1 InCAEM: A Singular Infrastructure for Advanced Energy Materials Research
Ashnar, Erfan	IM1-O-3 Perspectives of ultrafast hyperspectral imaging in Scanning Electron Microscopy

Aslam, Zabeada	MS8-P-7 Structural study of a Magnetic Graphitic Nanocomposite MS8-P-3 Y(Eu, Tb) frameworks with thiazolothiazoledicarboxylate: structural investigation by electron microscopy and diffraction techniques MS2-O-3 4D-STEM of Soft Matter: Structural Characterisation of Beam-Sensitive Polymers and Molecular Crystals Using Fast Precession and a Direct Electron Detector on a Tescan Tensor MS1-IN-1 Studying the crystallization of inorganic materials using correlated transmission electron microscopy
Aslan, Said Bahadir	LS4-P-14 Human Serum Albumin Nanoparticles as a Drug Delivery System to Enhance Temozolomide Efficacy in Glioblastoma Cell Line LS4-P-1 Investigation of the Therapeutic Effects of Allium cepa Extract on Ovaries and Uterus in Chronically Administered DHEA Rats by Apoptotic Pathways
Atlasov, Kirill	MS2-O-4 SEM Image contrast analysis for polymers with optimized imaging conditions ZEISS Volutome: The Next Generation of Serial Block-Face Imaging
Auad, Yves	IM1-IN-2 Recent advances in STEM spectroscopy using synchronized electron and photon beams
Audinot, Jean-Nicolas	IM2-O-2 Multimodal cryo-FIB-SIMS imaging on frozen-hydrated lamella of biological tissues
Aydemir, Duygu	LS3-P-4 Investigating the Effects of Vitamin D on Non-Alcoholic Fatty Pancreas Disease in an Experimental Metabolic Syndrome Rat Model
Aymerich Armengol, Raquel	MS4-O-1 3D Identical Location STEM Insights into the Degradation of Metallic Core-Shell Nanoparticles under Fuel Cell Conditions
Azarov, Alexander	MS6-O-4 Structural characterization of phase transformations in gallium oxide by transmission electron microscopy
Azeezulla Nazrulla, Mohammed	MS7-P-8 Microstructure and stability of carbon wrapped Cu@Cu2O nanowires
Bačík, Martin	Specion Microscopy HUB SPECION lunch workshop
Bačnik, Katarina	LS4-P-2 Virome of the invasive signal crayfish and its correlation with histopathological changes of the hepatopancreas
Bagués, Núria	IM2-O-3 Investigating Magnetic Domain Wall Pinning in Nanowires via Correlative X-ray and Electron Transmission Microscopy IM7-P-1 InCAEM: A Singular Infrastructure for Advanced Energy Materials Research
Baj, Gabriele	IM2-P-1 All-Micro (ALLiance to boost cross-border innovation through MICROscopy): an ITA-SLO cross-border Network for Sustainable Microscopy
Bajt Leban, Mirjam	MS3-P-1 Corrosion at Home: Microscopy's Role in Understanding Everyday Material Failures
Balen, Biljana	LS3-P-6 Visualizing the algal response on polystyrene particles: A focus on EPS production
Balogh, Virág	LS3-IN-1 Fruit fly nephrocytes: Versatile tools to study the endolysosomal system.
Bals, Sara	MS4-O-1 3D Identical Location STEM Insights into the Degradation of Metallic Core-Shell Nanoparticles under Fuel Cell Conditions MS4-P-6 Assessing the morphology and fractal properties of aggregated nanoparticles in 2 and 3 dimensions by transmission electron microscopy MS6-IN-2 Advanced low dose electron microscopy of metal halide perovskites

Balzano, Angela	LS1-O-3 Optimizing Microscopy Methodologies for Xylogenesis: Advances and Challenges in Wood and Phloem Formation Analysis
Banavath, Parimala	IM5-IN-2 The combination of high-resolution diffraction techniques in the scanning electron microscope for statistical relevant description of crystal defects and resulting properties in metals and alloys
Bannykh, Katherine S.	LS4-P-3 Molecular switch from Laminin beta 2 to Laminin beta 1 chain in brain microvasculature supports endothelial sprouting and is associated with increased blood brain barrier permeability
Bannykh, Serguei I.	LS4-P-3 Molecular switch from Laminin beta 2 to Laminin beta 1 chain in brain microvasculature supports endothelial sprouting and is associated with increased blood brain barrier permeability
Barbu, Lucian	MS8-P-2 Influence of La, Er, and Sm Doping on the Structural and Morphological Properties of ZnO for EMI Shielding
Barcikowski, Stephan	MS4-P-9 Thermal and Chemical Stability of High-Entropy-Alloy Nanoparticles Synthesized via Laser Ablation in Organic Liquid
Bárkai, Tünde	LS3-O-1 Recognition of a new exctracellular vesicle release mechanism
Barlen, Peer	IM8-P-1 Dimensional calibration of high resolution instrumentation at nanoscale
Barral, Duarte	LS2-IN-1 Shedding Light on the Molecular Mechanisms of Skin Pigmentation
Barrena, Esther	IM7-P-1 InCAEM: A Singular Infrastructure for Advanced Energy Materials Research
Bartak, Tomas	OXFORD INSTRUMENTS – SOLUTION FOR MATERIALS CHARACTERIZATION AT THE NANOMETRE SCALE
Basak, Shibrabata	IMPRESS 8 Multi-purpose MEMS devices for correlative operando experiments in battery research
Bayer, Florian	MS3-IN-2 The Microstructure and Mechanical Properties of LPBF Produced Nickel-based Alloy IN718 Influenced by Laser Beam Shape and Post Heat-Treatment
Bayrak Komurcu, Evrim	LS3-P-4 Investigating the Effects of Vitamin D on Non-Alcoholic Fatty Pancreas Disease in an Experimental Metabolic Syndrome Rat Model
Bayram Gurel, Cigdem	LS3-P-4 Investigating the Effects of Vitamin D on Non-Alcoholic Fatty Pancreas Disease in an Experimental Metabolic Syndrome Rat Model
Bayramova, Nargiz	LS3-P-4 Investigating the Effects of Vitamin D on Non-Alcoholic Fatty Pancreas Disease in an Experimental Metabolic Syndrome Rat Model
Bedina Zavec, Apolonija	LS3-O-2 Nanoalgosomes as observed by scanning and cryogenic transmission electron microscopes
Bele, Marjan	MS7-P-10 How to Perform Identical Location Scanning Electron Microscopy: Workflow, Advantages, Challenges, and Applications MS7-O-1 Charge density distribution in single-atom-on-substrate catalysts MS7-P-8 Microstructure and stability of carbon wrapped Cu@Cu2O nanowires
Belec, Blaž	IM1-P-1 Cathodoluminescence spectroscopy study of plasmonic emissions in different Bi2Se3 systems
Beleggia, Marco	IM6-O-3 Electron Beam Shaping with a MEMS Phase Plate via Current-Controlled Electrostatic Potential
Belić, Domagoj	MS2-O-2 Nanocellulose-based Functional Nanocomposite Materials
Belko Parkel, Kaja	LS5-IN-2 Noradrenaline and Cannabinoid Regulation of Astrocyte Energy Metabolism Revealed by FRET Nanosensors

Belkorissat, Redouane	IM7-O-3 Electron beam enlargement modelling in the environmental scanning electron microscope at the low gas temperature.
Bell, Alexis T.	MS8-P-5 Probing beam-sensitive MOF mesocrystals at the nanoscale using 4D-STEM scanning nanodiffraction
Bellich, Barbara	LS8-O-3 The exopolysaccharide EpsA-O has a decisive role in 3D microstructure formation of Bacillus subtilis biofilm
Belovari, Tatjana	LS8-P-1 Micro-CT analysis of femoral bone structure in ovariectomized rats following treatment with alendronate, hop extract and their combination LS4-P-7 Adiposoft-based analysis of visceral adipose tissue in ovariectomized rats treated with alendronate, hop extract, and their combination, stained with picrosirius red
Belsito, Luca	IM1-O-1 First demonstration of angular-momentum-resolved electron energy-loss spectroscopy
Belušič, Gregor	LS2-P-1 The sexually dimorphic retina of a butterfly, from microspectrophotometry to connectomics
Ben Meriem, Amatassalam	LS1-P-1 Quantifying Electron Radiation Damage in Biological Samples: Insights from Fluorescence Analysis
Benčan Golob, Andreja	MS5-IN-1 Insight into Defects and Polarization in Lead-Free Ferroelectrics by Advanced STEM Techniques MS1-P-10 Effects of Ti Doping on Structure, Microstructure and Mechanical Properties of (K0.5Na0.5)NbO3
Benitez-Castro, Angélica	MS5-O-2 Investigating Local Structure in NBT-BT system Using (S)TEM Techniques
Benko, Grega	LS6-P-4 Internal anatomy of parasitic acantocephalans in endangered underground amphibian analyzed by a combination of microCT and FESEM
Bernatová, Silvie	IM1-P-6 Raman tweezers for the analysis of secondary microplastics generated by degradation of surgical masks in water
Berro, Zahraa	IM2-O-2 Multimodal cryo-FIB-SIMS imaging on frozen-hydrated lamella of biological tissues
Bertoni, Giovanni	IM1-O-1 First demonstration of angular-momentum-resolved electron energy-loss spectroscopy
Besley, Elena	MS4-O-4 Metallene synthesis by ion irradiation: Growth of two-dimensional gold by vacancy-induced nucleation on defect-engineered graphene
Betancort, Pepe	IM7-P-2 Ecosystemic Transformation of Water Mining – RE-VESTIC INSPIRE PepePolymers®
Bezard, Malo	IM1-IN-2 Recent advances in STEM spectroscopy using synchronized electron and photon beams
Beznusenko, Galina	IM2-IN-1 Applications of Correlative Light Electron Microscopy (CLEM) and Volume Electron Microscopy in Cancer Biology
Bibes, Manuel	IM3-O-2 Electric Field and Pair Distribution Function mapping by Precession Scanning Electron Diffraction (4D-SPED) in TEM
Biela, Artur	IM4-O-1 From MDa to kDa - across the scale cryoEM SPA analysis of biological molecules. IM4-P-3 Optimization of macromolecules imaging in Cryo EM method
Bielen, Ana	LS4-P-2 Virome of the invasive signal crayfish and its correlation with histopathological changes of the hepatopancreas
Biesemeier, Antje Kristina	IM2-O-2 Multimodal cryo-FIB-SIMS imaging on frozen-hydrated lamella of biological tissues

Bijelic, Lazar	MS7-P-8 Microstructure and stability of carbon wrapped Cu@Cu2O nanowires
Bijelić, Nikola	LS8-P-1 Micro-CT analysis of femoral bone structure in ovariectomized rats following treatment with alendronate, hop extract and their combination LS4-P-7 Adiposoft-based analysis of visceral adipose tissue in ovariectomized rats treated with alendronate, hop extract, and their combination, stained with picrosirius red
Bilgili, Mustafa Gokhan	Improving Bone Regeneration through Estrogen-Loaded Cement in a Modified Masquelet Approach
Biscari, Caterina	IM7-P-1 InCAEM: A Singular Infrastructure for Advanced Energy Materials Research
Biscette, Dominik	IMPRESS 4 Electrostatic potential measurement at liquid helium temperature using off-axis electron holography
Bischof, Johanna	LS6-IN-3 Open Access to Imaging Excellence and Opportunities for Imaging Core Facility Staff – Updates from Euro-BioImaging and Global BioImaging
Blaby-Haas, Crysten	LS6-O-1 Volume Electron Microscopy Methods for Investigating Nitrogen Handling and Cellular Vision in Microscopic Algae
Blanco-Portals, Javier	IM8-O-5 Enhanced Low-Loss EELS Analysis through Hybrid Unsupervised and Supervised Machine Learning
Blaško Križanová, Janka	MS6-P-13 Etching and printing of daguerreotypes: experimental reconstruction and microscopic analysis of first photomechanical reproduction processes MS6-P-14 Nanoscale investigation of degradation processes in historical daguerreotype plates MS6-P-17 Microscopic Identification of Daguerreotypes Through Hallmark Analysis
Blazit, Jean-Denis	IM1-IN-2 Recent advances in STEM spectroscopy using synchronized electron and photon beams
Blaznik, Mojca	LS8-O-3 The exopolysaccharide EpsA-O has a decisive role in 3D microstructure formation of Bacillus subtilis biofilm MS3-P-10 SEM and EDS characterization of 316L Stainless Steel exposed to Different Bacteria
Bleker, Carissa Robyn	LS3-P-8 Light and Transmission Electron Microscopy Complement Functional Genomics Screening in Chlamydomonas reinhardtii to Reveal Novel Mechanisms of Susceptibility to Herbicide Paraquat
Boc, Eva	Microscopy-based analysis of biomimetic 2D and 3D in vitro models for preclinical studies
Boccato, Enrico	LS3-P-10 Optimization of Sample Preparation and Scanning Electron Microscopy Imaging for the Investigation of Trebouxia Flagellate Cells
Bocher, Laura	IM8-O-5 Enhanced Low-Loss EELS Analysis through Hybrid Unsupervised and Supervised Machine Learning
Bočina, Ivana	LS3-P-2 Ultrastructural changes of the injured renal tissues in the cage-reared rainbow trout Oncorhynchus mykiss (Walbaum, 1792)
Bodor, Iván	LS3-IN-1 Fruit fly nephrocytes: Versatile tools to study the endolysosomal system.
Boerasu, Iulian	MS6-P-19 Compositionally Graded Kesterite Nanostructured Film for Photovoltaic Applications
Boese, Markus	MS2-O-4 SEM Image contrast analysis for polymers with optimized imaging conditions

Bogataj, Urban	LS4-P-6 Chemotherapy-induced metabolic changes in glioblastoma stem and differentiated cells in a context of the tumor microenvironment LS8-P-2 3D Atlas of Arthropods IM5-P-3 Micro-computerized tomography for evaluation of dental stud attachment wear LS6-P-8 Intestinal stem cells of Colorado potato beetle – imaging from the morphology of the digestive tract in the whole animal to the cell ultrastructure LS6-P-7 Multiscale 3D imaging of digestive system morphogenesis during arthropod development
Bohač, Mario	MS6-P-7 Intense Pulsed Light Processing for Rapid Crystallization of Titania Nanotube Thin Films
Bohak, Ciril	LS2-O-2 Membrane Segmentation in Volumetric Electron Microscopy Data LS2-O-3 Volume electron microscopy of intracellular compartments in the urinary bladder epithelium
Bohinc, Uroš	LS8-O-4 XCT state-of-the-art scanning modality for the characterization of 3D-printed flat panels
Böhme, Christin	MS1-O-4 Oxygen vacancy distribution in different regions of La1−xSrxGa1−yMgyO3−δ
Bojanić, Krunoslav	MS6-P-4 Spray-Coated Metallosurfactant-Alginate Coatings: Dual Antimicrobial Action
Borghi, Francesca	MS6-P-12 In situ TEM dynamics of Au and Au/zirconia clusters in nanostructured thin films: a quantitative analysis
Borovská, Soňa	MS6-P-13 Etching and printing of daguerreotypes: experimental reconstruction and microscopic analysis of first photomechanical reproduction processes MS6-P-14 Nanoscale investigation of degradation processes in historical daguerreotype plates MS6-P-17 Microscopic Identification of Daguerreotypes Through Hallmark Analysis
Borštnar, Petruša	MS7-P-5 Atomic-scale insights into Solid-State Batteries via in situ TEM MS1-P-1 Understanding the formation mechanism of growth-type planar defects in natural and synthesized perovskites based on STEM analyses
Bosi, Matteo	MS6-O-4 Structural characterization of phase transformations in gallium oxide by transmission electron microscopy
Botifoll Moral, Marc	MS6-IN-1 Automated analysis of STEM data of semiconductor heterostructures for quantum computing IMPRESS 1 End-to-end Autonomous Unveiling of Physical Knowledge of Quantum Devices through Electron Microscopy Data IMPRESS 9 Artificial Intelligence for TEM: Real-Time Automation and Predictive Analysis in In Situ Experiments
Botrè, Francesco	LS3-P-14 Characterization of red blood cells changes during storage by atomic force microscope
Bottauscio, Niccolò	IM7-P-3 Novel Nano Channel Chip for In Situ TEM Liquid Cell Analysis and Particle Trapping Without Manual Preassembly of Chip
Bouceba, Tahar	LS7-O-1 Unique structural features of the human Kir2.1 channel in two different conformational states unveiled by cryo-electron microscopy
Bouton, Olivier	IM8-O-3 Mitigating beam damage during FIB-SIMS imaging: a new methodology using alternative FIB scans

Bozzuto, Giuseppina	LS4-P-16 Microscopy techniques to evaluate the cytotoxic effect induced by copper complexes on glioblastoma cells
Bračko, Gregor	LS8-P-2 3D Atlas of Arthropods
Bradeško, Andraž	MS1-P-10 Effects of Ti Doping on Structure, Microstructure and Mechanical Properties of (K0.5Na0.5)NbO3
Bradsher, Cara	MS4-P-2 Complex Electron Microscopy Analysis of Nanoscale Epitaxial Heterostructures Involving Metal Halides
Braeckevelt, Tom	MS6-IN-2 Advanced low dose electron microscopy of metal halide perovskites
Brancaleon, Riccardo	IMPRESS 2 The IMPRESS Project: Developing an Innovative Interoperable Platform for Next-Generation Transmission Electron Microscopy
Branković, Goran	MS1-P-9 Comprehensive study of Inversion Boundaries in ZnO
Branković, Zorica	MS1-P-9 Comprehensive study of Inversion Boundaries in ZnO
Breunig, Joshua J.	LS4-P-3 Molecular switch from Laminin beta 2 to Laminin beta 1 chain in brain microvasculature supports endothelial sprouting and is associated with increased blood brain barrier permeability
Breznik, Barbara	LS4-P-6 Chemotherapy-induced metabolic changes in glioblastoma stem and differentiated cells in a context of the tumor microenvironment
Brincoveanu, Oana	MS8-P-2 Influence of La, Er, and Sm Doping on the Structural and Morphological Properties of ZnO for EMI Shielding
Broad, Zoe	LS7-IN-1 Adapting Inpainting and non-Raster scanning for cryo Volume Electron Microscopy (cvEM) using the JEOL JIB 4700F cryo Focus Ion Beam Scanning Electron Microscope.
Brollo, Maria Eugenia Fortes	MS4-P-3 RIANA: Research Infrastructure Access in Nanoscience & Nanotechnology MS6-P-1 Effects of processing gas on the growth of SrTiO3 Thin Films: a TEM study
Brown, Andy	MS2-O-3 4D-STEM of Soft Matter: Structural Characterisation of Beam-Sensitive Polymers and Molecular Crystals Using Fast Precession and a Direct Electron Detector on a Tescan Tensor
Browning, Nigel	LS7-IN-1 Adapting Inpainting and non-Raster scanning for cryo Volume Electron Microscopy (cvEM) using the JEOL JIB 4700F cryo Focus Ion Beam Scanning Electron Microscope.
Brozyniak, Aleksander	MS3-O-4 Correlative Transmission Electron Microscopy for Nanophase Identification in Galvannealed Advanced High-Strength Steel MS3-P-3 Precession Electron Diffraction in modern steel systems
Brunetti, Guillaume	JEOL: cutting edge products for time resolved microscopy and TEM evolutions
Brunner, Philipp	IM3-O-1 Advanced STEM of Point Defect Clusters in Doped STO
Bryk, Jaroslaw	LS4-O-1 Navigating the Human Protein Atlas to map the composition of extracellular matrix proteins in normal and cancer tissues
Buchner, Julia	LS6-P-2 Bridging Flourescence and Electron Microscopy: R221 Resin for CLEM in Microbes and Plants
Budai, Judit	MS2-O-2 Nanocellulose-based Functional Nanocomposite Materials

Budakov-Obradović, Zorana	LS7-P-2 Red blood cells morphological alterations during preparation for electron microscopy imaging
Buixaderas, Elena	MS8-O-3 Structural modulations in antiferroelectric NaNbO3-based ceramics investigated by STEM
Burden, Jemima	LS2-IN-2 Array Tomography: A flexible and accessible approach to volume electron microscopy
Burgess, Eve	MS6-O-3 Multi-modal Microscopy Analysis of Co-doped InAs/GaAs Quantum Dot Lasers
Busch, Ingo	IM8-P-1 Dimensional calibration of high resolution instrumentation at nanoscale
Bustillo, Karen C.	MS8-P-5 Probing beam-sensitive MOF mesocrystals at the nanoscale using 4D-STEM scanning nanodiffraction
Bustos, Karol Y.	IM7-P-1 InCAEM: A Singular Infrastructure for Advanced Energy Materials Research
Buzás, Edit I	LS3-O-1 Recognition of a new exctracellular vesicle release mechanism
Bzowska, Monika	IM4-P-1 Targeted liposomes loaded with monoclonal antibodies for drug delivery - structure and function
Calcabrini, Annarica	LS4-P-16 Microscopy techniques to evaluate the cytotoxic effect induced by copper complexes on glioblastoma cells
Calzada, Jesus	IMPRESS 6 NanoMi: An open-source electron microscope
Camargo, Pedro	MS4-IN-1 Dynamic Atomic Behaviour in 2D Heterostructures and Nanocatalysts
Campbell, Anna Charvátová	MS4-P-8 Ab initio Study of Angle-Resolved Spectroscopy of Few-Layer Graphene
Can, Anil	LS3-P-1 Protective effect of ferulic acid in monosodium glutamate-induced kidney injury: a light and transmission electron microscopical study
Candottto Carniel, Fabio	LS3-P-10 Optimization of Sample Preparation and Scanning Electron Microscopy Imaging for the Investigation of Trebouxia Flagellate Cells
Çanıllıoğlu, Yasemin Ersoy	LS4-P-1 Investigation of the Therapeutic Effects of Allium cepa Extract on Ovaries and Uterus in Chronically Administered DHEA Rats by Apoptotic Pathways
Cao, Wenzheng	IM3-P-8 Surface and sub-surface defect analysis in semiconductors by Secondary Electron Emission Spectroscopy and local charge transport mapping IM1-P-7 Quantum state secondary electron emission spectroscopy in low voltage scanning electron microscope for probing Valence band IM1-O-3 Perspectives of ultrafast hyperspectral imaging in Scanning Electron Microscopy
Capo, Ivan	LS4-IN-2 Expression of GABA-A receptors in brain tumors
Cappoen, Davie	MS4-P-10 Physicochemical characterization of copper oxides applied as feed additives and plant protection products
Carroll, Robert C	MS8-P-3 Y(Eu, Tb) frameworks with thiazolothiazoledicarboxylate: structural investigation by electron microscopy and diffraction techniques
Casas, Joan	IM7-P-1 InCAEM: A Singular Infrastructure for Advanced Energy Materials Research

Castellani, Gastone	IM8-O-1 ViFoSe, an user-friendly open-source post-processing tool for foreground segmentation in time-lapse videos. LS1-O-2 Micropipette-Based Single-Cell Isolation from Live Spheroids.
Castioni, Florian	IM1-IN-2 Recent advances in STEM spectroscopy using synchronized electron and photon beams
Casu, Alberto	MS6-P-12 In situ TEM dynamics of Au and Au/zirconia clusters in nanostructured thin films: a quantitative analysis
Caviglia, Miriam	LS4-P-16 Microscopy techniques to evaluate the cytotoxic effect induced by copper complexes on glioblastoma cells
Cavill, Stuart	MS5-P-1 Probing Magnons with High-Energy Electrons: Theoretical Insights into Spin and Charge Scattering in STEM-EELS
Cazorla, Alba	IM7-P-1 InCAEM: A Singular Infrastructure for Advanced Energy Materials Research
Cebi, Ceren	LS4-O-2 The First Identification of Telocyte Cells in the Human Ovarian Stroma: Morphological and Immunophenotypical Characterization
Cebi, Sait Sukru	LS4-O-2 The First Identification of Telocyte Cells in the Human Ovarian Stroma: Morphological and Immunophenotypical Characterization
Čeh, Miran	MS1-P-2 Enhanced Analysis of Relative Thickness on TEM Samples MS3-P-5 Microstructure Analysis of Carbonyl Iron Powder (CIP) MS1-O-4 Oxygen vacancy distribution in different regions of La1−xSrxGa1−yMgyO3−δ MS3-O-3 (S)TEM study of the WTaVCr alloy for fusion application
Čekada, Miha	MS6-P-11 New Genesis XPS Spectrometer at the Jožef Stefan Institute for advanced surface and thin film characterization
Cepni, İsmail	LS4-P-13 Effect of endometrial environment on chromatin abnormalities of sperm LS3-P-13 The Adaptation of Mitochondrial Dynamics to Hormonal Changes in the Endometrium and Placenta LS4-O-2 The First Identification of Telocyte Cells in the Human Ovarian Stroma: Morphological and Immunophenotypical Characterization
Cerkvenik, Uroš	LS2-P-1 The sexually dimorphic retina of a butterfly, from microspectrophotometry to connectomics Microscopy-based analysis of biomimetic 2D and 3D in vitro models for preclinical studies
Černayová, Diana	LS7-P-1 Structural Stabilization of Alginate for Imaging Hydrogel-encapsulated Bacterial Cells Using LV-STEM
Cescutti, Paola	LS8-O-3 The exopolysaccharide EpsA-O has a decisive role in 3D microstructure formation of Bacillus subtilis biofilm
Chalil, Shyni Punathum	MS6-P-1 Effects of processing gas on the growth of SrTiO3 Thin Films: a TEM study
Chaluvadi, Sandeep Kumar	MS6-P-1 Effects of processing gas on the growth of SrTiO3 Thin Films: a TEM study
Chang, Johan	IMPRESS 4 Electrostatic potential measurement at liquid helium temperature using off-axis electron holography
Charilaou, Michalis	IMPRESS 11 Mechanical strain and light-induced control of magnetic states in Fe3Sn2 in situ in the TEM
Chávex-Ángel, Emigdio	IM7-P-1 InCAEM: A Singular Infrastructure for Advanced Energy Materials Research

Chen, Hui	MS4-O-3 High-Entropy Oxide Nanoparticles as Stable and Efficient Catalysts for the Oxygen Evolution Reaction IM7-P-1 InCAEM: A Singular Infrastructure for Advanced Energy Materials Research
Chen, Zhuo	MS6-P-3 Multi-scale investigation of superior mechanical properties in nitride ceramics with negative stacking fault energy MS6-O-2 Mechanical properties enhancement in ceramics through vacancy-mediated unit cell disturbance MS3-O-2 Atomic-resolution electron microscopy analysis of oxygen-mediated Ti nanocrystalline synthesized by high-pressure torsion MS8-O-2 Revealing atomic-level plasticity of ceramic materials through advanced electron microscopy
Cheradil, Andrea Elizabeth Babu Dominic	LS6-P-2 Bridging Flourescence and Electron Microscopy: R221 Resin for CLEM in Microbes and Plants
Chersicola, Marko	LS2-P-2 Ultrastructure and gene expression in tomato flower pedicel abscission zone
Cheshire, Daniel	MS5-P-1 Probing Magnons with High-Energy Electrons: Theoretical Insights into Spin and Charge Scattering in STEM-EELS
Chevalier Kwon, Min	IM3-P-1 Evaluating Electron Radiation Damage Mitigation in Graphene Liquid Cell
Chokappa, Shrirang	IM3-P-2 Selective defect creation in 2D hexagonal boron nitride via low-energy Ar+ irradiation
Christ, Philipp	MS2-O-1 Advanced Nanoscale Characterization of Organic Photovoltaic Materials
Christiansen, Silke	MS6-P-4 Spray-Coated Metallosurfactant-Alginate Coatings: Dual Antimicrobial Action
Chromiński, Wtiold	MS3-P-12 The impact of high hydrostatic pressure annealing on microstructure evolution
Ciancio, Regina	MS6-P-1 Effects of processing gas on the growth of SrTiO3 Thin Films: a TEM study MS4-P-7 Atomic-scale Investigation of FEL-Induced Structural Modifications in Pyrolytic Graphite via TEM Analysis IMPRESS 8 Multi-purpose MEMS devices for correlative operando experiments in battery research MS4-P-3 RIANA: Research Infrastructure Access in Nanoscience & Nanotechnology IMPRESS: A Gateway to New TEM Frontiers Round table discussion with panellists IMPRESS 2 The IMPRESS Project: Developing an Innovative Interoperable Platform for Next-Generation Transmission Electron Microscopy
Cicconardi, Andrea	IM8-P-2 Convolutional neural network for machine vision in electron and optical microscopy for correlative analysis
Ciftci, Mehmet Utku	Improving Bone Regeneration through Estrogen-Loaded Cement in a Modified Masquelet Approach
Čizmar, Anja	LS5-IN-1 Dictyostelium discoideum IQGAP proteins IqgC and IqgD - siblings or distant relatives
Čižmar, Tihana	MS6-P-10 The impact of solvents on the morphology and optical properties of organo-metal thin films
Clark, Nick	MS4-IN-1 Dynamic Atomic Behaviour in 2D Heterostructures and Nanocatalysts

Clausen, Alexander	IM8-O-4 Automated Thickness Determination from 4D-STEM Data by CNNs IMPRESS 13 Time-resolved imaging of dynamic and resonant spin phenomena in situ in the TEM
Cloutier, Martin	IMPRESS 6 NanoMi: An open-source electron microscope
Cockram, Sophia	IMPRESS 6 NanoMi: An open-source electron microscope
Cocks, Erin	LS2-O-4 Some neurons are better connected than others in a locust's network of visual interneurons
Colbea, Claudiu	IM7-O-1 Atomic-Scale Dynamics of Ni Catalysts Revealed by Operando TEM in Dry Reforming of Methane
Cole, Hannah	MS5-O-1 The magnetic microstructure in FeCo alloys and its interaction with non-magnetic inclusions
Coll, Catalina	MS6-IN-1 Automated analysis of STEM data of semiconductor heterostructures for quantum computing IM8-O-5 Enhanced Low-Loss EELS Analysis through Hybrid Unsupervised and Supervised Machine Learning IMPRESS 1 End-to-end Autonomous Unveiling of Physical Knowledge of Quantum Devices through Electron Microscopy Data
Collins, Sean M	MS8-P-3 Y(Eu, Tb) frameworks with thiazolothiazoledicarboxylate: structural investigation by electron microscopy and diffraction techniques MS2-O-3 4D-STEM of Soft Matter: Structural Characterisation of Beam-Sensitive Polymers and Molecular Crystals Using Fast Precession and a Direct Electron Detector on a Tescan Tensor
Colone, Marisa	LS4-P-16 Microscopy techniques to evaluate the cytotoxic effect induced by copper complexes on glioblastoma cells
Cooper, David	MS5-IN-2 Next Generation Spintronic Devices And 3D Curved Magnets examined by Lorentz microscopy
Cora, Ildikó	IM5-P-5 High throughput micro-combinatorial study of microstructure and materials properties of binary and ternary layer systems MS6-O-4 Structural characterization of phase transformations in gallium oxide by transmission electron microscopy
Cossu, Fabrizio	MS5-P-1 Probing Magnons with High-Energy Electrons: Theoretical Insights into Spin and Charge Scattering in STEM-EELS
Costa-Ledesma, Vanessa	IM8-O-5 Enhanced Low-Loss EELS Analysis through Hybrid Unsupervised and Supervised Machine Learning
Costa, Fanny N	MS8-P-3 Y(Eu, Tb) frameworks with thiazolothiazoledicarboxylate: structural investigation by electron microscopy and diffraction techniques
Črep, Lucija	MS6-P-6 Electron microscopy investigation of Cu-TiO2 nanocomposites for solar-driven photocatalysis
Crnković, Ana	IM4-O-2 A closer look at the protein-lipid complex of actinoporin pores
Cserép, Csaba	LS3-O-1 Recognition of a new exctracellular vesicle release mechanism
Cubadda, Francesco	MS4-P-10 Physicochemical characterization of copper oxides applied as feed additives and plant protection products
Cudak, Tomasz	MS6-P-15 Microstructural characterisation of sodium alginate coatings with addition of essential oils for antimicrobial protection of steel

Ćurić, Valentina	LS3-P-7 Insight into the particle-based nature of mucilage as a response of Chlorella sorokiniana cell to manganese excess
Cuxart, Marc G.	IM7-P-1 InCAEM: A Singular Infrastructure for Advanced Energy Materials Research
da Luz, Leonis L	MS8-P-3 Y(Eu, Tb) frameworks with thiazolothiazoledicarboxylate: structural investigation by electron microscopy and diffraction techniques
Da Silva, José Antonio	IM7-P-2 Ecosystemic Transformation of Water Mining – RE-VESTIC INSPIRE PepePolymers®
Dajčman, Urban	MS2-P-1 Correlation Between Adhesion and Swimming Activity in Developing Zebrafish Exposed to Polystyrene and Polyethylene Micro- and Nanoplastics
Dal Zilio, Simone	IM8-O-2 Optimization of SEM Instrumental Parameters for Enhanced Imaging Applying Machine Learning IM2-P-1 All-Micro (ALLiance to boost cross-border innovation through MICROscopy): an ITA-SLO cross-border Network for Sustainable Microscopy IMPRESS 8 Multi-purpose MEMS devices for correlative operando experiments in battery research
Daneu, Nina	MS1-P-1 Understanding the formation mechanism of growth-type planar defects in natural and synthesized perovskites based on STEM analyses MS1-P-15 FIB-SEM characterization of various types of materials
Danilović Luković, Jelena	LS3-O-2 Nanoalgosomes as observed by scanning and cryogenic transmission electron microscopes LS3-P-7 Insight into the particle-based nature of mucilage as a response of Chlorella sorokiniana cell to manganese excess
Daoud, Mohamed	MS3-O-1 Influence of Al3Zr dispersoids on the Young's Modulus of Al matrix in Al 2195 Alloy: Insights from Analytical Electron Microscopy and DFT Calculations
Das, Partha Pratim	IM3-O-2 Electric Field and Pair Distribution Function mapping by Precession Scanning Electron Diffraction (4D-SPED) in TEM
Daul, Lars	IM8-P-1 Dimensional calibration of high resolution instrumentation at nanoscale
de Araujo, Ana C V	MS8-P-3 Y(Eu, Tb) frameworks with thiazolothiazoledicarboxylate: structural investigation by electron microscopy and diffraction techniques
De Backer, Annick	MS6-IN-2 Advanced low dose electron microscopy of metal halide perovskites
De Castro, Olivier	IM8-O-3 Mitigating beam damage during FIB-SIMS imaging: a new methodology using alternative FIB scans
de la Mata, Maria	MS2-IN-2 Study of the electron-induced damage of polymer based materials during STEM-EELS measurements
de la Peña, Francisco	IM1-P-2 Low-energy Core-loss EELS as a Dose-effective Approach for Elemental and Oxidation State Mapping
De La Torre, Xavier	LS3-P-14 Characterization of red blood cells changes during storage by atomic force microscope
De Padova, Paola	MS7-O-4 Understanding local crystallography in solar cells materials with scanning electron diffraction using unsupervised machine learning
Deeks, Christopher	MS8-O-4 Correlative Imaging and Surface Analysis workflow
Del Gobbo, Jo'	LS4-P-16 Microscopy techniques to evaluate the cytotoxic effect induced by copper complexes on glioblastoma cells

del-Pozo-Bueno, Daniel	IM8-O-5 Enhanced Low-Loss EELS Analysis through Hybrid Unsupervised and Supervised Machine Learning IM1-P-2 Low-energy Core-loss EELS as a Dose-effective Approach for Elemental and Oxidation State Mapping
Delić, Teo	LS8-P-2 3D Atlas of Arthropods
Demirdag, Cetin	LS4-P-13 Effect of endometrial environment on chromatin abnormalities of sperm
Dénes, Ádám	LS3-O-1 Recognition of a new exctracellular vesicle release mechanism
Dermastia, Marina	LS2-P-2 Ultrastructure and gene expression in tomato flower pedicel abscission zone
Deutsch, Maja	LS3-O-3 Immunolocalisation of mechanosensory proteins PIEZO and TRPV4 in the urinary bladder urothelium: which method to believe?
Di Carlo, Aldo	MS7-O-4 Understanding local crystallography in solar cells materials with scanning electron diffraction using unsupervised machine learning
Di Felice, Sara	IM8-P-6 Fractal modelling and fracture mechanics of urban particle populations in biological tissues
Dimitrov, Nino	LS3-P-6 Visualizing the algal response on polystyrene particles: A focus on EPS production
Diosdi, Akos	LS1-O-2 Micropipette-Based Single-Cell Isolation from Live Spheroids.
Divitini, Giorgio	MS6-P-12 In situ TEM dynamics of Au and Au/zirconia clusters in nanostructured thin films: a quantitative analysis IM8-P-2 Convolutional neural network for machine vision in electron and optical microscopy for correlative analysis MS4-P-2 Complex Electron Microscopy Analysis of Nanoscale Epitaxial Heterostructures Involving Metal Halides MS7-O-4 Understanding local crystallography in solar cells materials with scanning electron diffraction using unsupervised machine learning MS8-O-1 Low-dose 4DSTEM analysis of local strain in 2D perovskite lateral heterostructures IM3-P-9 Sub-Angstrom Resolution at below 40 e-/Å2 with Electron Ptychography
Djordjević, Vladan	LS6-P-1 Morphological features of Himantoglossum calcaratum (Beck) Schltr. subsp. calcaratum (Orchidaceae) pollinarium
Dkhil, Brahim	IM3-O-3 Exploring perovskites at the atomic level by 4DSTEM: Experimental & Simulation
do Nascimento, Julio	MS5-P-1 Probing Magnons with High-Energy Electrons: Theoretical Insights into Spin and Charge Scattering in STEM-EELS
Dobnik, David	LS8-O-2 Spatiotemporal acquisition of genetically encoded biosensors in intact plant leaves reveals hormonal crosstalk in response to wounding
Dobos, Gergely	LS1-O-1 Immersive Virtual Reality System for Mice Combined with 3D-Targeted Photostimulation as a Prototype for Visual Restoration
Dobričić, Aleksandra	LS3-P-3 Histopathology of the gills of farmed common carp (Cyprinus carpio): a bioindication method
Dodony, Erzsébet	IM5-P-1 EDIC; A new method to enhance reliability of structure determination, using electron diffraction data correction
Dódony, István	IM5-P-1 EDIC; A new method to enhance reliability of structure determination, using electron diffraction data correction

Dogsa, Iztok	LS8-O-3 The exopolysaccharide EpsA-O has a decisive role in 3D microstructure formation of Bacillus subtilis biofilm
Dolić, Stjepan	MS7-P-2 Utilizing SEM thin-film measurements to deepen the understanding of perovskite solar cell performance MS6-P-10 The impact of solvents on the morphology and optical properties of organo-metal thin films
Dolinšek, Janez	MS3-P-7 Nano- and micro-structural configurations of functional complex metallic alloys
Dolničar, Dren	LS6-P-6 Ciliate Community in Podutik Reservoir, Slovenia: assessment of species diversity improved by the diversity of microscopic techniques
Domazet Jurašin, Darija	MS6-P-4 Spray-Coated Metallosurfactant-Alginate Coatings: Dual Antimicrobial Action
Dominko, Robert	MS7-P-5 Atomic-scale insights into Solid-State Batteries via in situ TEM MS7-P-9 Impact of La0.07Ba0.93SnO3 interlayer on epitaxial growth of Li4Ti5O12 thin film anodes for all-solid-state Li-ion batteries
Donati, Francesco	LS3-P-14 Characterization of red blood cells changes during storage by atomic force microscope
Donato, Maria G.	IM1-P-6 Raman tweezers for the analysis of secondary microplastics generated by degradation of surgical masks in water
Donik, Črtomir	MS7-P-10 How to Perform Identical Location Scanning Electron Microscopy: Workflow, Advantages, Challenges, and Applications MS3-IN-2 The Microstructure and Mechanical Properties of LPBF Produced Nickel-based Alloy IN718 Influenced by Laser Beam Shape and Post Heat-Treatment
Doolin, Alexander	LS3-P-9 Cytotoxicity Assessment of Functionalized Graphene-Based Composites
dos Reis, Roberto	IM3-P-7 Contrast Optimization Aided by Machine Learning Applied to Virtual 4D-STEM Images
Dragin Jerman, Urška	Microscopy-based analysis of biomimetic 2D and 3D in vitro models for preclinical studies
Drav, Sandra	MS3-O-3 (S)TEM study of the WTaVCr alloy for fusion application
Dražić, Goran	MS1-P-9 Comprehensive study of Inversion Boundaries in ZnO MS8-P-6 Quantum chemical simulation of spontaneous water dissociation on 110 || 110 rutile TiO2 interfaces MS5-IN-1 Insight into Defects and Polarization in Lead-Free Ferroelectrics by Advanced STEM Techniques IM3-O-3 Exploring perovskites at the atomic level by 4DSTEM: Experimental & Simulation MS7-O-1 Charge density distribution in single-atom-on-substrate catalysts MS1-P-10 Effects of Ti Doping on Structure, Microstructure and Mechanical Properties of (K0.5Na0.5)NbO3 MS7-P-5 Atomic-scale insights into Solid-State Batteries via in situ TEM
Drev, Sandra	MS1-P-2 Enhanced Analysis of Relative Thickness on TEM Samples MS8-P-6 Quantum chemical simulation of spontaneous water dissociation on 110 || 110 rutile TiO2 interfaces Atomistic structure of interfaces: Where theory and experiment meet MS1-O-4 Oxygen vacancy distribution in different regions of La1−xSrxGa1−yMgyO3−δ

Drljaca Lero, Jovana	LS4-IN-2 Expression of GABA-A receptors in brain tumors
Drnovšek, Aljaž	MS1-P-10 Effects of Ti Doping on Structure, Microstructure and Mechanical Properties of (K0.5Na0.5)NbO3
Drnovšek, Silvo	MS1-P-10 Effects of Ti Doping on Structure, Microstructure and Mechanical Properties of (K0.5Na0.5)NbO3
Drobne, Damjana	MS2-P-1 Correlation Between Adhesion and Swimming Activity in Developing Zebrafish Exposed to Polystyrene and Polyethylene Micro- and Nanoplastics MS3-P-6 Laser Surface Functionalization of 316L Stainless Steel Under Ambient and Inert Argon Atmospheres LS3-P-9 Cytotoxicity Assessment of Functionalized Graphene-Based Composites IM5-P-2 The Power of FIB-SEM for Visualizing the Internalization of 2D Materials In Vitro
Drummond-Brydson, Rik	MS8-P-7 Structural study of a Magnetic Graphitic Nanocomposite MS2-O-3 4D-STEM of Soft Matter: Structural Characterisation of Beam-Sensitive Polymers and Molecular Crystals Using Fast Precession and a Direct Electron Detector on a Tescan Tensor MS1-IN-1 Studying the crystallization of inorganic materials using correlated transmission electron microscopy
Dubiel, Beata	MS7-P-3 Microstructural analysis of the copper matrix composites for electrodes of plasma torches MS3-P-9 Effect of recycled powder on microstructure and chemical composition of additively manufactured AlSi7Mg alloy
Ducati, Caterina	MS7-P-7 Identifying and studying open Li-ion channels along a preferred crystallographic axis in battery electrodes via scanning electron diffraction
Duchoň, Jan	MS3-P-11 Sublayer structure in fire gilding layer on medieval jewellery MS3-P-4 TEM Analysis of Maraging Steel
Dudás, István	LS3-O-1 Recognition of a new exctracellular vesicle release mechanism
Dugato, Danian	MS5-IN-2 Next Generation Spintronic Devices And 3D Curved Magnets examined by Lorentz microscopy
Dunatov, Toni	MS3-O-3 (S)TEM study of the WTaVCr alloy for fusion application

Dunin-Borkowski, Rafal	MS5-IN-2 Next Generation Spintronic Devices And 3D Curved Magnets examined by Lorentz microscopy IM1-O-1 First demonstration of angular-momentum-resolved electron energy-loss spectroscopy IMPRESS 4 Electrostatic potential measurement at liquid helium temperature using off-axis electron holography IMPRESS 5 Quantifying carbon site switching dynamics in GaN by off-axis electron holography IMPRESS 3 Characterization of electric and magnetic fields at interfaces in manganese-containing heterostructures using correlative TEM techniques IM8-O-4 Automated Thickness Determination from 4D-STEM Data by CNNs IMPRESS 2 The IMPRESS Project: Developing an Innovative Interoperable Platform for Next-Generation Transmission Electron Microscopy IMPRESS 13 Time-resolved imaging of dynamic and resonant spin phenomena in situ in the TEM IMPRESS 11 Mechanical strain and light-induced control of magnetic states in Fe3Sn2 in situ in the TEM IMPRESS 9 Artificial Intelligence for TEM: Real-Time Automation and Predictive Analysis in In Situ Experiments IMPRESS 12 A laser-free approach to ultra-fast transmission electron microscopy
Dupuis, Maria Luisa	LS4-P-16 Microscopy techniques to evaluate the cytotoxic effect induced by copper complexes on glioblastoma cells
Durinova, Eva	LS6-O-1 Volume Electron Microscopy Methods for Investigating Nitrogen Handling and Cellular Vision in Microscopic Algae
Durmaz, Goksan Inci	LS3-P-4 Investigating the Effects of Vitamin D on Non-Alcoholic Fatty Pancreas Disease in an Experimental Metabolic Syndrome Rat Model
Duruksu, Gokhan	LS4-P-5 Brain Decellularization Process in Transgenic Alzheimer Rat Model
Dutour Sikirić, Maja	MS6-P-4 Spray-Coated Metallosurfactant-Alginate Coatings: Dual Antimicrobial Action
Dvorský, Drahomír	MS3-P-4 TEM Analysis of Maraging Steel
Džeroski, Sašo	MS5-IN-1 Insight into Defects and Polarization in Lead-Free Ferroelectrics by Advanced STEM Techniques IM8-P-4 A Deep Learning Approach to Drift Correction in Atomic-Scale STEM Imaging
Dzibelova, Jana Dzibelova, Jana	MS4-O-2 Atomic-resolution investigation of 2D hematene MS4-P-4 Hematene lattice parameter variation as a function of thickness
Ebert, Philipp	IMPRESS 5 Quantifying carbon site switching dynamics in GaN by off-axis electron holography IMPRESS 3 Characterization of electric and magnetic fields at interfaces in manganese-containing heterostructures using correlative TEM techniques
Edwards, Katarina	LS3-O-2 Nanoalgosomes as observed by scanning and cryogenic transmission electron microscopes
Egerton, Ray	IMPRESS 6 NanoMi: An open-source electron microscope

Egger, Nadine	MS1-O-2 Impact of clay construction components on indoor aerosols: what can automated SEM-EDX and Raman reveal?
Eichel, Rüdiger-Albert	IMPRESS 8 Multi-purpose MEMS devices for correlative operando experiments in battery research
Ekici, Oguzhan	LS4-P-4 The Effects of Amylin on Aggression in Wistar Rats Exposed to the Resident-Intruder Paradigm
El Marini, Mohamed	MS4-P-11 Investigation of Electrodeposition and Electrodissolution Mechanisms of Silver Nanoparticles Using Electrochemical Liquid Cell Transmission Electron Microscopy
Elbaum, Michael	IM3-IN-2 Low-Dose 4D STEM for Cross-Disciplinary Materials Characterisation
Eleršek, Tina	LS3-P-8 Light and Transmission Electron Microscopy Complement Functional Genomics Screening in Chlamydomonas reinhardtii to Reveal Novel Mechanisms of Susceptibility to Herbicide Paraquat
Emik, Serkan	LS4-P-14 Human Serum Albumin Nanoparticles as a Drug Delivery System to Enhance Temozolomide Efficacy in Glioblastoma Cell Line
Enderlein, Jörg	LS1-IN-1 Advancing Super-Resolution Imaging: Integrating Fluorescence Lifetime, Scanning Microscopy, and Energy Transfer Techniques for Isotropic Nanoscale Bioimaging
Ercius, Peter	LS6-O-1 Volume Electron Microscopy Methods for Investigating Nitrogen Handling and Cellular Vision in Microscopic Algae
Erdani Kreft, Mateja	LS1-O-4 High-throughput automated quantitative fluorescence microscopy and image feature analysis for in vitro detection of adverse effects LS4-P-17 Revealing Disparities in Macropinocytosis Between Bladder Cancer and Normal Urothelial Cells: Implications for Targeted Therapy LS3-P-11 Unveiling tunnelling nanotubes in urothelial spheroids and bladder cancer biopsy samples LS4-O-4 Periodontal and bone regeneration with magnesium barrier membranes: an in vitro study
Eriksen, Martin Børstad	IM7-P-1 InCAEM: A Singular Infrastructure for Advanced Energy Materials Research
Eriksson, Matias	IM6-P-1 Towards spatially coherent low-energy electron and ion beams
Erkanli Senturk, Gozde	LS4-P-4 The Effects of Amylin on Aggression in Wistar Rats Exposed to the Resident-Intruder Paradigm
Erman, Andreja	LS3-P-5 In search of specific markers of telocytes in mouse urinary bladder by fluorescence microscopy and transmission electron microscopy LS3-O-3 Immunolocalisation of mechanosensory proteins PIEZO and TRPV4 in the urinary bladder urothelium: which method to believe? Microscopy-based analysis of biomimetic 2D and 3D in vitro models for preclinical studies
Estradé, Sonia	MS5-O-2 Investigating Local Structure in NBT-BT system Using (S)TEM Techniques IM8-O-5 Enhanced Low-Loss EELS Analysis through Hybrid Unsupervised and Supervised Machine Learning IM1-P-2 Low-energy Core-loss EELS as a Dose-effective Approach for Elemental and Oxidation State Mapping
Estrader, Marta	IM1-P-2 Low-energy Core-loss EELS as a Dose-effective Approach for Elemental and Oxidation State Mapping

Eswara, Santhana	MS7-O-3 Real Time Imaging of Lithium-Ion Transport in Solid-State Batteries: An Operando FIB-SIMS approach IM8-O-3 Mitigating beam damage during FIB-SIMS imaging: a new methodology using alternative FIB scans
Fabri, Emiliana	IM3-P-5 Electron ptychography experiment design with PtychoScopy
Fabry, Jan	MS1-P-14 Study of vanadinite as painting pigment
Fairclough, Simon	MS7-O-4 Understanding local crystallography in solar cells materials with scanning electron diffraction using unsupervised machine learning
Faix, Jan	LS5-IN-1 Dictyostelium discoideum IQGAP proteins IqgC and IqgD - siblings or distant relatives
Falcao, Eduardo H L	MS8-P-3 Y(Eu, Tb) frameworks with thiazolothiazoledicarboxylate: structural investigation by electron microscopy and diffraction techniques
Fallon, Kayla	MS5-IN-2 Next Generation Spintronic Devices And 3D Curved Magnets examined by Lorentz microscopy
Falqui, Andrea	MS6-P-12 In situ TEM dynamics of Au and Au/zirconia clusters in nanostructured thin films: a quantitative analysis
Fanetti, Mattia	IM1-P-1 Cathodoluminescence spectroscopy study of plasmonic emissions in different Bi2Se3 systems IM2-P-1 All-Micro (ALLiance to boost cross-border innovation through MICROscopy): an ITA-SLO cross-border Network for Sustainable Microscopy IM1-P-3 Irradiation-induced point defects in optical fibers investigated by cathodoluminescence microscopy and spectroscopy. MS8-P-1 Focused e-Beam Heating for local Material Modification: Melting, Patterning, and Band Gap tuning
Faraji, Mehrdad	MS8-O-1 Low-dose 4DSTEM analysis of local strain in 2D perovskite lateral heterostructures
Farle, Michael	IMPRESS 13 Time-resolved imaging of dynamic and resonant spin phenomena in situ in the TEM
Fasolato, Claudia	MS4-P-7 Atomic-scale Investigation of FEL-Induced Structural Modifications in Pyrolytic Graphite via TEM Analysis
Feher, Andras	LS1-O-1 Immersive Virtual Reality System for Mice Combined with 3D-Targeted Photostimulation as a Prototype for Visual Restoration
Feizpour, Darja	LS3-P-7 Insight into the particle-based nature of mucilage as a response of Chlorella sorokiniana cell to manganese excess
Fernandes, Carlos	LS7-O-1 Unique structural features of the human Kir2.1 channel in two different conformational states unveiled by cryo-electron microscopy
Fernandez Godoy, Maria	LS3-P-2 Ultrastructural changes of the injured renal tissues in the cage-reared rainbow trout Oncorhynchus mykiss (Walbaum, 1792)
Fernandez Scarioni, Michelle	IM8-P-1 Dimensional calibration of high resolution instrumentation at nanoscale
Fernandez-Gonzaleza, Claudia	IM2-O-3 Investigating Magnetic Domain Wall Pinning in Nanowires via Correlative X-ray and Electron Transmission Microscopy
Ferreira Veloso, Rafael	LS7-O-1 Unique structural features of the human Kir2.1 channel in two different conformational states unveiled by cryo-electron microscopy
Ferreira, Paulo	MS4-IN-2 From Structure to Dynamics: Exploring Nanoparticle Behavior with In-Situ and Aberration Corrected TEM/STEM

Fickler, Robert	IM6-P-1 Towards spatially coherent low-energy electron and ion beams
Fidler, Aleš	LS4-P-10 Antiviral Efficacy of Electrolysed Saline (EOS) Against Both Enveloped and Non-Enveloped Viruses: A TEM Study
Filić, Vedrana	LS5-IN-1 Dictyostelium discoideum IQGAP proteins IqgC and IqgD - siblings or distant relatives
Filip, Jan	MS4-O-2 Atomic-resolution investigation of 2D hematene
Filipič, Tatjana	MS6-P-11 New Genesis XPS Spectrometer at the Jožef Stefan Institute for advanced surface and thin film characterization
Filipovic, Lado	IM8-IN-1 Convolutional neural networks for scanning transmission electron microscopy image analysis: Towards automated analysis of large volume datasets
Filipovic, Milos	LS4-P-15 Therapeutic effects of H_2S donors on ferroptosis-mediated liver damage in C57BL/6 mice – a microscopic study
Fink, Dominika	MS3-IN-1 Microstructural characterization of beta-Sn to alpha-Sn phase transformation
Fink, Jörg	IM6-IN-2 Electron Optics and Beam Shaping with a Special View on EELS
Fink, Katja	LS5-P-1 Live Imaging of Calcium and Hormonal Crosstalk in Potato: Insights into Endophyte-Mediated Immune Enhancement LS5-IN-2 Noradrenaline and Cannabinoid Regulation of Astrocyte Energy Metabolism Revealed by FRET Nanosensors
Fiołek, Aleksandra	MS6-P-15 Microstructural characterisation of sodium alginate coatings with addition of essential oils for antimicrobial protection of steel MS6-P-2 Microstructure and selected properties of multicomponent wear-resistant and low-friction coatings on titanium alloy substrates
Fišer, Cene	LS8-P-2 3D Atlas of Arthropods
Fišer, Žiga	LS8-P-2 3D Atlas of Arthropods
Fitzek, Harald	MS1-O-2 Impact of clay construction components on indoor aerosols: what can automated SEM-EDX and Raman reveal? MS7-O-2 Pore characterization of hard carbon anodes for sodium storage in sodium ion batteries by 2D and 3D TEM MS7-P-4 Characterization of hard carbons for Na-ion battery electrodes by a combination of electron microscopy and vibrational spectroscopy
Fleck, Roland	LS7-IN-1 Adapting Inpainting and non-Raster scanning for cryo Volume Electron Microscopy (cvEM) using the JEOL JIB 4700F cryo Focus Ion Beam Scanning Electron Microscope.
Fletcher, Kelsey	LS3-O-1 Recognition of a new exctracellular vesicle release mechanism
Flöter, Sarah Charlotte Eva	IM3-IN-1 Developments in 4D-STEM and Ptychography: From Series Registration to Live Compression
Fogarassy, Zsolt	MS6-O-4 Structural characterization of phase transformations in gallium oxide by transmission electron microscopy
Folco, Luigi	IM3-P-3 Combining 3D electron diffraction and nanotexture analysis for the characterization of meteorite's impact ejecta
Fon Tacer, Klementina	LS4-P-6 Chemotherapy-induced metabolic changes in glioblastoma stem and differentiated cells in a context of the tumor microenvironment

Fornari, Roberto	MS6-O-4 Structural characterization of phase transformations in gallium oxide by transmission electron microscopy
Fořt, Tomáš	IM1-O-2 Investigation of Electron Scattering in Ultrathin Films Using Time-of-Flight Spectroscopy
Foster, Stephanie	MS1-IN-1 Studying the crystallization of inorganic materials using correlated transmission electron microscopy
Foti, Antonino	IM1-P-6 Raman tweezers for the analysis of secondary microplastics generated by degradation of surgical masks in water
Fötsch, Maria	MS1-O-2 Impact of clay construction components on indoor aerosols: what can automated SEM-EDX and Raman reveal?
Frabboni, Stefano	IM1-O-1 First demonstration of angular-momentum-resolved electron energy-loss spectroscopy
França, Emanoel L T	MS8-P-3 Y(Eu, Tb) frameworks with thiazolothiazoledicarboxylate: structural investigation by electron microscopy and diffraction techniques
Frankeová, Dita	MS1-P-13 Exploring High-Baroque Stucco: Microscopy of Materials and Techniques at Kroměříž Chateau
Fransen, Martijn	IM3-O-2 Electric Field and Pair Distribution Function mapping by Precession Scanning Electron Diffraction (4D-SPED) in TEM
Frentrup, Martin	MS6-O-1 Indium segregation at stacking faults in zincblende InGaN epilayers
Friák, Martin	MS3-IN-1 Microstructural characterization of beta-Sn to alpha-Sn phase transformation
Friedrich, Rico	MS4-P-4 Hematene lattice parameter variation as a function of thickness
Fuentes-Fayos, Antonio C.	LS4-P-3 Molecular switch from Laminin beta 2 to Laminin beta 1 chain in brain microvasculature supports endothelial sprouting and is associated with increased blood brain barrier permeability
Furat, Selenay	LS4-P-5 Brain Decellularization Process in Transgenic Alzheimer Rat Model
Furlani, Borut	LS6-IN-1 Advanced Microscopy Approaches Unveil Plectin as a Key Regulator of Focal Adhesions in Astrocytes
G. Roca, Alejandro	MS4-O-3 High-Entropy Oxide Nanoparticles as Stable and Efficient Catalysts for the Oxygen Evolution Reaction
Gagliardi, Alessio	IM8-P-2 Convolutional neural network for machine vision in electron and optical microscopy for correlative analysis
Gajović, Andreja	MS7-P-2 Utilizing SEM thin-film measurements to deepen the understanding of perovskite solar cell performance MS6-P-10 The impact of solvents on the morphology and optical properties of organo-metal thin films MS3-O-3 (S)TEM study of the WTaVCr alloy for fusion application
Galanis, Athanassios S	Precession enhanced Electron Diffraction applications in TEM for nano crystals. IM3-O-2 Electric Field and Pair Distribution Function mapping by Precession Scanning Electron Diffraction (4D-SPED) in TEM
Galloway, Johanna	MS1-IN-1 Studying the crystallization of inorganic materials using correlated transmission electron microscopy
Galun, Simona Katrin	LS4-P-6 Chemotherapy-induced metabolic changes in glioblastoma stem and differentiated cells in a context of the tumor microenvironment

Galvani, Thomas	MS6-IN-1 Automated analysis of STEM data of semiconductor heterostructures for quantum computing IMPRESS 1 End-to-end Autonomous Unveiling of Physical Knowledge of Quantum Devices through Electron Microscopy Data
Garcia de Herreros, Antoni	IM7-P-1 InCAEM: A Singular Infrastructure for Advanced Energy Materials Research
Garcia, Flavio	MS5-IN-2 Next Generation Spintronic Devices And 3D Curved Magnets examined by Lorentz microscopy
Gardian, Zdenko	LS8-P-3 Resolution Limitations in Cryo-EM Analysis of SUMO-Anchored Ferritin
Gardonio, Sandra	IM1-P-1 Cathodoluminescence spectroscopy study of plasmonic emissions in different Bi2Se3 systems
Garzon Manjon, Alba	MS4-O-1 3D Identical Location STEM Insights into the Degradation of Metallic Core-Shell Nanoparticles under Fuel Cell Conditions MS4-O-3 High-Entropy Oxide Nanoparticles as Stable and Efficient Catalysts for the Oxygen Evolution Reaction IM7-P-1 InCAEM: A Singular Infrastructure for Advanced Energy Materials Research
Gašperšič, Rok	LS4-P-10 Antiviral Efficacy of Electrolysed Saline (EOS) Against Both Enveloped and Non-Enveloped Viruses: A TEM Study
Gašpirc, Boris	LS4-O-4 Periodontal and bone regeneration with magnesium barrier membranes: an in vitro study
Gatalo, Matija	MS7-P-6 Microscopic Insights into Catalyst Layer of PEMFC: IL-SEM Study of Electrochemical Effects
Gázquez-Alabart, Jaume	IM3-O-2 Electric Field and Pair Distribution Function mapping by Precession Scanning Electron Diffraction (4D-SPED) in TEM
Gazzadi, Gian Carlo	IM1-O-1 First demonstration of angular-momentum-resolved electron energy-loss spectroscopy
Gedda, Lars	LS3-O-2 Nanoalgosomes as observed by scanning and cryogenic transmission electron microscopes
Gemmi, Mauro	IM3-P-3 Combining 3D electron diffraction and nanotexture analysis for the characterization of meteorite's impact ejecta
Ghaderzadeh, Sadegh	MS4-O-4 Metallene synthesis by ion irradiation: Growth of two-dimensional gold by vacancy-induced nucleation on defect-engineered graphene
Giani, Raffaele	IM3-P-8 Surface and sub-surface defect analysis in semiconductors by Secondary Electron Emission Spectroscopy and local charge transport mapping
Giannazzo, Filippo	MS6-O-5 Advanced TEM characterization of 2D compound semiconductors
Giménez, Monica Parpal	MS4-P-11 Investigation of Electrodeposition and Electrodissolution Mechanisms of Silver Nanoparticles Using Electrochemical Liquid Cell Transmission Electron Microscopy
Girard, Sylvain	IM1-P-3 Irradiation-induced point defects in optical fibers investigated by cathodoluminescence microscopy and spectroscopy.
Gladyshev, Anton	IM3-IN-1 Developments in 4D-STEM and Ptychography: From Series Registration to Live Compression
Glatt, Sebastian	IM4-P-3 Optimization of macromolecules imaging in Cryo EM method
Gnabasik, Ryan	IMPRESS 12 A laser-free approach to ultra-fast transmission electron microscopy

Göbel, Christoph	IM1-P-5 Advanced EELS techniques in catalyst analysis
Godec, Matjaž	MS7-P-10 How to Perform Identical Location Scanning Electron Microscopy: Workflow, Advantages, Challenges, and Applications MS3-IN-2 The Microstructure and Mechanical Properties of LPBF Produced Nickel-based Alloy IN718 Influenced by Laser Beam Shape and Post Heat-Treatment
Godec, Tim	LS3-P-8 Light and Transmission Electron Microscopy Complement Functional Genomics Screening in Chlamydomonas reinhardtii to Reveal Novel Mechanisms of Susceptibility to Herbicide Paraquat
Goessler, Walter	LS4-P-11 Post mortem degradation of ferritin and its significance for determining the iron content of the human brain
Golebiowska, Bozena	MS1-P-14 Study of vanadinite as painting pigment
Gómez-Cruz, Lucía	IM2-O-3 Investigating Magnetic Domain Wall Pinning in Nanowires via Correlative X-ray and Electron Transmission Microscopy
Gomez-Perez, Alejandro	IM3-O-2 Electric Field and Pair Distribution Function mapping by Precession Scanning Electron Diffraction (4D-SPED) in TEM
Gomilšek, Matjaž	MS5-P-4 Synthesis Strategies for Effective Doping of Barlowite
Gonzalez, Kevin	LS8-IN-2 Synaptic basis of feature selectivity in hippocampal neurons
Gorbachev, Roman	MS4-IN-1 Dynamic Atomic Behaviour in 2D Heterostructures and Nanocatalysts
Gračanin, Nik	MS6-P-8 Optimizing Photocatalytic Degradation of Pollutants Using Cu-Doped ZnO and TiO2 Films Grown by ALD MS1-P-12 Complex polycrystalline clusters of diamond and graphite from metamorphic rocks MS1-P-3 Crystal structure of wulfenite crystals from Mežica analysed by SEM-FIB and TEM MS6-P-18 Characterization of ZnO Films Prepared via FIB-SEM MS1-P-15 FIB-SEM characterization of various types of materials
Gregorčič, Peter	MS3-P-6 Laser Surface Functionalization of 316L Stainless Steel Under Ambient and Inert Argon Atmospheres
Grgac, Robert	LS8-P-1 Micro-CT analysis of femoral bone structure in ovariectomized rats following treatment with alendronate, hop extract and their combination LS4-P-7 Adiposoft-based analysis of visceral adipose tissue in ovariectomized rats treated with alendronate, hop extract, and their combination, stained with picrosirius red
Gribbon, Anna	IM7-P-1 InCAEM: A Singular Infrastructure for Advanced Energy Materials Research
Griesi, Andrea	MS7-O-4 Understanding local crystallography in solar cells materials with scanning electron diffraction using unsupervised machine learning
Grigorov, Ilijana	LS4-P-15 Therapeutic effects of H_2S donors on ferroptosis-mediated liver damage in C57BL/6 mice – a microscopic study

Grillo, Vincenzo	MS6-IN-1 Automated analysis of STEM data of semiconductor heterostructures for quantum computing IM1-O-1 First demonstration of angular-momentum-resolved electron energy-loss spectroscopy IMPRESS 9 Artificial Intelligence for TEM: Real-Time Automation and Predictive Analysis in In Situ Experiments IM6-O-3 Electron Beam Shaping with a MEMS Phase Plate via Current-Controlled Electrostatic Potential IMPRESS 1 End-to-end Autonomous Unveiling of Physical Knowledge of Quantum Devices through Electron Microscopy Data Electron wave shaping and its applications from ghost imaging and ptychography to quantum state tomography
Grivas, Evangelos	IM3-O-2 Electric Field and Pair Distribution Function mapping by Precession Scanning Electron Diffraction (4D-SPED) in TEM
Grm, Mark	Microscopy-based analysis of biomimetic 2D and 3D in vitro models for preclinical studies
Grogger, Nikolaus	IM1-P-4 EDXS Quantification in the TEM: How Can Ray Tracing Help?
Grogger, Werner	IM1-P-4 EDXS Quantification in the TEM: How Can Ray Tracing Help?
Groiss, Heiko	MS3-O-4 Correlative Transmission Electron Microscopy for Nanophase Identification in Galvannealed Advanced High-Strength Steel MS3-P-3 Precession Electron Diffraction in modern steel systems
Gruden, Kristina	LS8-O-2 Spatiotemporal acquisition of genetically encoded biosensors in intact plant leaves reveals hormonal crosstalk in response to wounding LS5-P-1 Live Imaging of Calcium and Hormonal Crosstalk in Potato: Insights into Endophyte-Mediated Immune Enhancement
Grujić, Jasmina	LS7-P-2 Red blood cells morphological alterations during preparation for electron microscopy imaging
Grünewald, Jonas	MS3-IN-2 The Microstructure and Mechanical Properties of LPBF Produced Nickel-based Alloy IN718 Influenced by Laser Beam Shape and Post Heat-Treatment
Gryner, Kamila	MS3-P-9 Effect of recycled powder on microstructure and chemical composition of additively manufactured AlSi7Mg alloy
Gucciardi, Pietro G.	IM1-P-6 Raman tweezers for the analysis of secondary microplastics generated by degradation of surgical masks in water
Guckelhorn, Janine	IM3-O-2 Electric Field and Pair Distribution Function mapping by Precession Scanning Electron Diffraction (4D-SPED) in TEM
Gudelj, Andjelija S.	LS4-P-15 Therapeutic effects of H_2S donors on ferroptosis-mediated liver damage in C57BL/6 mice – a microscopic study LS4-P-12 Proferroptotic response to nutrient deprivation and sorafenib treatment in hepatocellular carcinoma cells – a microscopic study
Gudžulić, Tara	MS1-P-2 Enhanced Analysis of Relative Thickness on TEM Samples MS3-P-5 Microstructure Analysis of Carbonyl Iron Powder (CIP)
Guella, Graziano	LS3-P-8 Light and Transmission Electron Microscopy Complement Functional Genomics Screening in Chlamydomonas reinhardtii to Reveal Novel Mechanisms of Susceptibility to Herbicide Paraquat
Guizar-Sicairos, Manuel	IM3-P-5 Electron ptychography experiment design with PtychoScopy
Gul, Burcu	LS3-P-4 Investigating the Effects of Vitamin D on Non-Alcoholic Fatty Pancreas Disease in an Experimental Metabolic Syndrome Rat Model

Gülgün, Mehmet Ali	MS1-O-1 Direct observation of phase transformations during dehydration of cementitious phases at high temperatures MS4-P-1 Investigation of Boron-Based Nanosheets, Nanoscrolls and Nanotubes by TEM Analyses
Gunasekar, Naresh	MS6-O-3 Multi-modal Microscopy Analysis of Co-doped InAs/GaAs Quantum Dot Lasers
Guo, Jinming	IM7-IN-1 Atomic-Scale High-Entropy Design for Superior Capacitive Energy Storage Performance in Lead-Free Ceramics
Gurdag, Gulten	LS4-P-14 Human Serum Albumin Nanoparticles as a Drug Delivery System to Enhance Temozolomide Efficacy in Glioblastoma Cell Line
Guvenir Seven, Sila	LS4-P-4 The Effects of Amylin on Aggression in Wistar Rats Exposed to the Resident-Intruder Paradigm
Guzel Meydanli, Elif	LS4-P-13 Effect of endometrial environment on chromatin abnormalities of sperm LS3-P-13 The Adaptation of Mitochondrial Dynamics to Hormonal Changes in the Endometrium and Placenta LS3-P-12 Does endoplasmic reticulum stress contribute to the damage of trophoblast cells caused by bisphenol A?
Guzinatti, Giulio	IM6-IN-2 Electron Optics and Beam Shaping with a Special View on EELS
Guzman, Roger	IM3-O-2 Electric Field and Pair Distribution Function mapping by Precession Scanning Electron Diffraction (4D-SPED) in TEM
H. Tavabi, Amir	IMPRESS 12 A laser-free approach to ultra-fast transmission electron microscopy
Haas, Benedikt	IM3-IN-1 Developments in 4D-STEM and Ptychography: From Series Registration to Live Compression
Haberfehlner, Georg	MS3-O-2 Atomic-resolution electron microscopy analysis of oxygen-mediated Ti nanocrystalline synthesized by high-pressure torsion MS7-O-2 Pore characterization of hard carbon anodes for sodium storage in sodium ion batteries by 2D and 3D TEM MS7-P-4 Characterization of hard carbons for Na-ion battery electrodes by a combination of electron microscopy and vibrational spectroscopy IM1-P-4 EDXS Quantification in the TEM: How Can Ray Tracing Help?
Habibzadeh Kavkani, Payam	IM6-O-3 Electron Beam Shaping with a MEMS Phase Plate via Current-Controlled Electrostatic Potential
Habler, Gerlinde	IM8-IN-1 Convolutional neural networks for scanning transmission electron microscopy image analysis: Towards automated analysis of large volume datasets
Haigh, Sarah	MS4-IN-1 Dynamic Atomic Behaviour in 2D Heterostructures and Nanocatalysts
Hajdusek, Ondrej	LS8-P-3 Resolution Limitations in Cryo-EM Analysis of SUMO-Anchored Ferritin
Halbutogullari, Seda	LS4-P-5 Brain Decellularization Process in Transgenic Alzheimer Rat Model
Hansen, Luka	IM7-O-2 Advancements in Plasma Microcell Integration for in situ TEM Experiments
Hanzu, Ilie	MS7-O-2 Pore characterization of hard carbon anodes for sodium storage in sodium ion batteries by 2D and 3D TEM MS7-P-4 Characterization of hard carbons for Na-ion battery electrodes by a combination of electron microscopy and vibrational spectroscopy

Harada, Ken	IMPRESS 6 NanoMi: An open-source electron microscope
Hargitai, Dávid	LS3-IN-1 Fruit fly nephrocytes: Versatile tools to study the endolysosomal system.
Harmati, Maria	LS1-O-2 Micropipette-Based Single-Cell Isolation from Live Spheroids.
Haslinger, Philipp	IM1-O-4 Spin Resonance Spectroscopy meets Transmission Electron Microscopy IM6-O-1 Entanglement in Bragg Scattering
Hasnip, Phil	MS5-P-1 Probing Magnons with High-Energy Electrons: Theoretical Insights into Spin and Charge Scattering in STEM-EELS
Havlíčková, Anna	LS7-O-2 Ultrastructural Analysis of Azotobacter vinelandii Encapsulated in Alginate Hydrogel Using Cryogenic Preparation and Electron Microscopy Techniques LS7-P-1 Structural Stabilization of Alginate for Imaging Hydrogel-encapsulated Bacterial Cells Using LV-STEM
Hawkins, Tim	LS8-O-2 Spatiotemporal acquisition of genetically encoded biosensors in intact plant leaves reveals hormonal crosstalk in response to wounding
Hayashida, Misa	IMPRESS 6 NanoMi: An open-source electron microscope
Hegedűs, Máté	MS1-P-6 Transmission electron microscopy of hypomineralized enamel apatite nanocrystals
Herak Bosnar, Maja	LS5-P-2 Unraveling the Noncanonical Mitochondrial Import Signals of NME6 – a Member of the NME/NDPK Family
Herranz, Gervasi	IM3-O-2 Electric Field and Pair Distribution Function mapping by Precession Scanning Electron Diffraction (4D-SPED) in TEM
Herrera, Miriam	MS2-IN-2 Study of the electron-induced damage of polymer based materials during STEM-EELS measurements
Herzog, Max	IM6-O-2 Miniaturized Magnetic Multipoles for Ultrafast Beam Shaping in the Transmission Electron Microscope
Hetaba, Walid	IM1-P-5 Advanced EELS techniques in catalyst analysis
Heumann, Saskia	IM1-P-5 Advanced EELS techniques in catalyst analysis
Hingerl, Kerstin	IM2-P-2 Fast and Frozen: Visualising a wide spectrum of specimens using Cryo-SEM combined with an on-site freeze fracture system
Hingerl, Kerstin	LS7-P-3 Fast and Frozen: Visualising a wide spectrum of specimens using Cryo-SEM combined with an on-site freeze fracture system
Hinz, Alicja	IM4-P-1 Targeted liposomes loaded with monoclonal antibodies for drug delivery - structure and function
Hočevar, Matej	LS3-O-2 Nanoalgosomes as observed by scanning and cryogenic transmission electron microscopes MS2-P-1 Correlation Between Adhesion and Swimming Activity in Developing Zebrafish Exposed to Polystyrene and Polyethylene Micro- and Nanoplastics MS3-P-10 SEM and EDS characterization of 316L Stainless Steel exposed to Different Bacteria MS3-P-6 Laser Surface Functionalization of 316L Stainless Steel Under Ambient and Inert Argon Atmospheres LS3-P-9 Cytotoxicity Assessment of Functionalized Graphene-Based Composites

Hodnik, Nejc	MS7-P-10 How to Perform Identical Location Scanning Electron Microscopy: Workflow, Advantages, Challenges, and Applications MS7-P-6 Microscopic Insights into Catalyst Layer of PEMFC: IL-SEM Study of Electrochemical Effects MS7-O-1 Charge density distribution in single-atom-on-substrate catalysts MS7-P-8 Microstructure and stability of carbon wrapped Cu@Cu2O nanowires MS7-IN-1 Atomic-to-Microscale Insights into Electrocatalyst Stability via Identical-Location Electron Microscopy
Hofer, Ferdinand	IM3-O-1 Advanced STEM of Point Defect Clusters in Doped STO
Hofkens, Johan	MS6-IN-2 Advanced low dose electron microscopy of metal halide perovskites
Homeniuk, Darren	IMPRESS 6 NanoMi: An open-source electron microscope
Horák, Daniel	MS2-IN-1 Multimodal in vitro and in vivo tissue imaging: Design, synthesis and surface engineering of nanoprobes
Horák, Michal	MS4-P-8 Ab initio Study of Angle-Resolved Spectroscopy of Few-Layer Graphene
Horký, Pavel	IM1-P-6 Raman tweezers for the analysis of secondary microplastics generated by degradation of surgical masks in water
Horne, Aidan	IM3-O-4 Multidimensional and Multimodal 4D STEM and Electron Ptychography
Horvat, Barbara	MS1-P-4 Effect of pretreatment and organic fibre reinforcement on the mechanical and microstructural properties of microwave irradiated alkali-activated radioactive fly ash MS1-P-5 Microwave-irradiated alkali-activated extraterrestrial simulants
Horvat, Milena	LS3-P-8 Light and Transmission Electron Microscopy Complement Functional Genomics Screening in Chlamydomonas reinhardtii to Reveal Novel Mechanisms of Susceptibility to Herbicide Paraquat
Horvath, Peter	LS1-O-2 Micropipette-Based Single-Cell Isolation from Live Spheroids.
Hotko, Miha	MS7-P-10 How to Perform Identical Location Scanning Electron Microscopy: Workflow, Advantages, Challenges, and Applications MS7-P-6 Microscopic Insights into Catalyst Layer of PEMFC: IL-SEM Study of Electrochemical Effects
Houben, Lothar	IM3-IN-2 Low-Dose 4D STEM for Cross-Disciplinary Materials Characterisation
Houdellier, Florent	IMPRESS 7 EFLY – a Fast Versatile Charge Particle Optics Code
Hozak, Pavel	LS6-P-3 Czech-BioImaging - a national imaging platform available to all
Hrabar, Jerko	LS3-P-2 Ultrastructural changes of the injured renal tissues in the cage-reared rainbow trout Oncorhynchus mykiss (Walbaum, 1792)
Hrubanová, Kamila	LS7-O-2 Ultrastructural Analysis of Azotobacter vinelandii Encapsulated in Alginate Hydrogel Using Cryogenic Preparation and Electron Microscopy Techniques
Hu, Yucheng	MS7-O-4 Understanding local crystallography in solar cells materials with scanning electron diffraction using unsupervised machine learning

Huang, Yong	MS6-P-3 Multi-scale investigation of superior mechanical properties in nitride ceramics with negative stacking fault energy MS6-O-2 Mechanical properties enhancement in ceramics through vacancy-mediated unit cell disturbance MS3-O-2 Atomic-resolution electron microscopy analysis of oxygen-mediated Ti nanocrystalline synthesized by high-pressure torsion MS8-O-2 Revealing atomic-level plasticity of ceramic materials through advanced electron microscopy
Hudek, Lucija	LS4-P-7 Adiposoft-based analysis of visceral adipose tissue in ovariectomized rats treated with alendronate, hop extract, and their combination, stained with picrosirius red
Hudina, Sandra	LS4-P-2 Virome of the invasive signal crayfish and its correlation with histopathological changes of the hepatopancreas
Hudoklin, Samo	LS2-O-2 Membrane Segmentation in Volumetric Electron Microscopy Data LS2-O-3 Volume electron microscopy of intracellular compartments in the urinary bladder epithelium LS3-P-15 Distribution of Golgi matrix proteins GRASP65 and GRASP55 during early urothelial regeneration Microscopy-based analysis of biomimetic 2D and 3D in vitro models for preclinical studies
Humbel, Bruno M.	LS2-O-3 Volume electron microscopy of intracellular compartments in the urinary bladder epithelium LS7-O-4 Sample Preparation for Electron Microscopy
Hutter, Oliver S.	MS7-O-4 Understanding local crystallography in solar cells materials with scanning electron diffraction using unsupervised machine learning
Iglič, Aleš	LS3-O-2 Nanoalgosomes as observed by scanning and cryogenic transmission electron microscopes LS3-P-7 Insight into the particle-based nature of mucilage as a response of Chlorella sorokiniana cell to manganese excess
Ilett, Martha	MS1-IN-1 Studying the crystallization of inorganic materials using correlated transmission electron microscopy
Ilić, Marko	LS2-P-1 The sexually dimorphic retina of a butterfly, from microspectrophotometry to connectomics
Illés, Levente	MS1-P-6 Transmission electron microscopy of hypomineralized enamel apatite nanocrystals
Ilvan, Sennur	LS4-O-2 The First Identification of Telocyte Cells in the Human Ovarian Stroma: Morphological and Immunophenotypical Characterization
Indyka, Paulina	IM4-P-1 Targeted liposomes loaded with monoclonal antibodies for drug delivery - structure and function
Isella, Giovanni	MS6-IN-1 Automated analysis of STEM data of semiconductor heterostructures for quantum computing IM3-P-8 Surface and sub-surface defect analysis in semiconductors by Secondary Electron Emission Spectroscopy and local charge transport mapping IMPRESS 1 End-to-end Autonomous Unveiling of Physical Knowledge of Quantum Devices through Electron Microscopy Data
Isildar, Basak	LS4-P-8 Investigating the antitumor effects of quercetin on human colorectal adenocarcinoma cells: An in vitro study
Ivančić, Ana	MS6-P-4 Spray-Coated Metallosurfactant-Alginate Coatings: Dual Antimicrobial Action

Ivanov, Yurii P	MS7-O-4 Understanding local crystallography in solar cells materials with scanning electron diffraction using unsupervised machine learning
Jagličić, Zvonko	MS5-P-4 Synthesis Strategies for Effective Doping of Barlowite
Jaklič, Blaž	MS7-P-5 Atomic-scale insights into Solid-State Batteries via in situ TEM MS7-P-9 Impact of La0.07Ba0.93SnO3 interlayer on epitaxial growth of Li4Ti5O12 thin film anodes for all-solid-state Li-ion batteries
Jalil, Wesley	MS5-IN-2 Next Generation Spintronic Devices And 3D Curved Magnets examined by Lorentz microscopy
Jampani, Venkata SR	LS3-O-2 Nanoalgosomes as observed by scanning and cryogenic transmission electron microscopes
Janák, Marian	MS1-P-12 Complex polycrystalline clusters of diamond and graphite from metamorphic rocks
Janc, Mojca	LS4-P-9 The Effect of a Novel SARS-CoV E Protein Inhibitor on Ultrastructure of Murine Hepatitis Virus-Infected L-929 Cells
Janev, Aleksandar	LS1-O-4 High-throughput automated quantitative fluorescence microscopy and image feature analysis for in vitro detection of adverse effects LS4-P-17 Revealing Disparities in Macropinocytosis Between Bladder Cancer and Normal Urothelial Cells: Implications for Targeted Therapy LS4-O-4 Periodontal and bone regeneration with magnesium barrier membranes: an in vitro study LS3-P-15 Distribution of Golgi matrix proteins GRASP65 and GRASP55 during early urothelial regeneration Microscopy-based analysis of biomimetic 2D and 3D in vitro models for preclinical studies
Jankovics, Hajnalka	IM5-P-4 Effects of different preparation methods and detector use on SEM imaging of bacterial flagella
Jardas Babić, Daria	MS6-P-8 Optimizing Photocatalytic Degradation of Pollutants Using Cu-Doped ZnO and TiO2 Films Grown by ALD MS6-P-5 Photocatalytic activity of thin ZnO films deposited at room temperature by plasma-enhanced atomic layer deposition MS6-P-6 Electron microscopy investigation of Cu-TiO2 nanocomposites for solar-driven photocatalysis
Jazvinšćak Jembrek, Maja	LS5-P-2 Unraveling the Noncanonical Mitochondrial Import Signals of NME6 – a Member of the NME/NDPK Family
Jelen, Andreja	MS3-P-7 Nano- and micro-structural configurations of functional complex metallic alloys
Jelovica Badovinac, Ivana	MS6-P-6 Electron microscopy investigation of Cu-TiO2 nanocomposites for solar-driven photocatalysis
Jenko, Katja	LS6-P-8 Intestinal stem cells of Colorado potato beetle – imaging from the morphology of the digestive tract in the whole animal to the cell ultrastructure
Jensen, Emil Christian Stillhoff	IM7-P-3 Novel Nano Channel Chip for In Situ TEM Liquid Cell Analysis and Particle Trapping Without Manual Preassembly of Chip
Jenuš Belec, Petra	MS5-P-3 EBSD analysis of Sr-hexaferrite sintered in different atmospheres
Jernejc, Manca	LS3-P-5 In search of specific markers of telocytes in mouse urinary bladder by fluorescence microscopy and transmission electron microscopy

Jeruc, Jera	LS4-P-18 Revealing LRAT and NeuroD1 Colocalization in human urothelial cancer cells in vivo using proximity ligation assay LS3-P-11 Unveiling tunnelling nanotubes in urothelial spheroids and bladder cancer biopsy samples
Jevnikar, Peter	IM5-P-3 MICRO-COMPUTERIZED TOMOGRAPHY FOR EVALUATION OF DENTAL STUD ATTACHMENT WEAR
Ježek, Jan	IM1-P-6 Raman tweezers for the analysis of secondary microplastics generated by degradation of surgical masks in water
Ji, Keyan	IMPRESS 5 Quantifying carbon site switching dynamics in GaN by off-axis electron holography
Jones, Rhys	IM3-O-4 Multidimensional and Multimodal 4D STEM and Electron Ptychography
Jordan, Vanja	MS8-P-6 Quantum chemical simulation of spontaneous water dissociation on 110 || 110 rutile TiO2 interfaces Atomistic structure of interfaces: Where theory and experiment meet
Jorgačevski, Jernej	LS5-O-1 Exploring Plectin's Function in Migration of Astrocytes and Glioblastoma Through Confocal Microscopy LS6-IN-1 Advanced Microscopy Approaches Unveil Plectin as a Key Regulator of Focal Adhesions in Astrocytes
Joudi, Wael	IM2-O-1 Correlative microscopy: Uncovering the role of vacancies and contamination on the mechanical stiffness of defect-engineered graphene. MS4-O-4 Metallene synthesis by ion irradiation: Growth of two-dimensional gold by vacancy-induced nucleation on defect-engineered graphene IM8-IN-1 Convolutional neural networks for scanning transmission electron microscopy image analysis: Towards automated analysis of large volume datasets
Jožef Toman, Mihael	LS6-P-6 Ciliate Community in Podutik Reservoir, Slovenia: assessment of species diversity improved by the diversity of microscopic techniques
Judak, Linda	LS1-O-1 Immersive Virtual Reality System for Mice Combined with 3D-Targeted Photostimulation as a Prototype for Visual Restoration
Juffmann, Thomas	IM6-IN-1 Optical Near-field Electron Microscopy
Juhasz, Gabor	LS1-O-1 Immersive Virtual Reality System for Mice Combined with 3D-Targeted Photostimulation as a Prototype for Visual Restoration
Juraić, Krunoslav	MS6-P-7 Intense Pulsed Light Processing for Rapid Crystallization of Titania Nanotube Thin Films MS7-P-2 Utilizing SEM thin-film measurements to deepen the understanding of perovskite solar cell performance MS3-O-3 (S)TEM study of the WTaVCr alloy for fusion application
Jurek, Karel	MS5-P-2 Are we observing channeling or magnetic contrast?
K. Kis, Viktoria	MS1-P-6 Transmission electron microscopy of hypomineralized enamel apatite nanocrystals
Kakanakova, Anelia	MS6-O-5 Advanced TEM characterization of 2D compound semiconductors
Kalemba-Rec, Izabela	MS7-P-3 Microstructural analysis of the copper matrix composites for electrodes of plasma torches
Kamal, Mohammad	IMPRESS 6 NanoMi: An open-source electron microscope

Kamšek, Ana Rebeka	MS7-P-10 How to Perform Identical Location Scanning Electron Microscopy: Workflow, Advantages, Challenges, and Applications
Kanduti, Domen	LS4-O-4 Periodontal and bone regeneration with magnesium barrier membranes: an in vitro study
Kappers, Menno J.	MS6-O-1 Indium segregation at stacking faults in zincblende InGaN epilayers
Kapun, Barbara	MS3-P-8 Composition and microstructure of wrought and additively manufactured DED-LB of Ti-6Al-4V alloy
Kapun, Gregor	MS7-P-10 How to Perform Identical Location Scanning Electron Microscopy: Workflow, Advantages, Challenges, and Applications IM2-P-1 All-Micro (ALLiance to boost cross-border innovation through MICROscopy): an ITA-SLO cross-border Network for Sustainable Microscopy MS7-P-5 Atomic-scale insights into Solid-State Batteries via in situ TEM MS7-P-9 Impact of La0.07Ba0.93SnO3 interlayer on epitaxial growth of Li4Ti5O12 thin film anodes for all-solid-state Li-ion batteries
Karahuseyinoglu, Sercin	LS4-P-13 Effect of endometrial environment on chromatin abnormalities of sperm
Karimi, Ebrahim	IM1-O-1 First demonstration of angular-momentum-resolved electron energy-loss spectroscopy
Kassal, Petar	MS6-P-7 Intense Pulsed Light Processing for Rapid Crystallization of Titania Nanotube Thin Films
Katsaros, Georgios	MS6-IN-1 Automated analysis of STEM data of semiconductor heterostructures for quantum computing IMPRESS 1 End-to-end Autonomous Unveiling of Physical Knowledge of Quantum Devices through Electron Microscopy Data
Kaupbay, Olzhas	MS7-O-2 Pore characterization of hard carbon anodes for sodium storage in sodium ion batteries by 2D and 3D TEM MS7-P-4 Characterization of hard carbons for Na-ion battery electrodes by a combination of electron microscopy and vibrational spectroscopy
Kautek, Wolfgang	MS6-P-13 Etching and printing of daguerreotypes: experimental reconstruction and microscopic analysis of first photomechanical reproduction processes MS6-P-14 Nanoscale investigation of degradation processes in historical daguerreotype plates MS6-P-16 Microscopical study of 19th century photomechanical prints: in-situ investigations in museum collections MS6-P-17 Microscopic Identification of Daguerreotypes Through Hallmark Analysis
Kavkani, Payam Habibzadeh	IMPRESS 8 Multi-purpose MEMS devices for correlative operando experiments in battery research
Kavre Piltaver, Ivna	MS6-P-8 Optimizing Photocatalytic Degradation of Pollutants Using Cu-Doped ZnO and TiO2 Films Grown by ALD MS6-P-5 Photocatalytic activity of thin ZnO films deposited at room temperature by plasma-enhanced atomic layer deposition MS6-P-6 Electron microscopy investigation of Cu-TiO2 nanocomposites for solar-driven photocatalysis MS6-P-9 Atomic layer deposition of nitrogen-doped TiO2 thin films for photocatalytic applications
Kaya Dagistanli, Fatma	LS3-P-4 Investigating the Effects of Vitamin D on Non-Alcoholic Fatty Pancreas Disease in an Experimental Metabolic Syndrome Rat Model

Kayisli, A. Umit	LS3-P-13 The Adaptation of Mitochondrial Dynamics to Hormonal Changes in the Endometrium and Placenta
Kenar, Halime	LS5-P-3 EFFECT OF DECELLULARIZED PLACENTA-DERIVED ECM MOLECULES ON IN VITRO ANGIOGENESIS
Kepaptsoglou, Demie	IM1-IN-1 Beyond phonon spectroscopy: progress in high-resolution STEM-EELS MS5-P-1 Probing Magnons with High-Energy Electrons: Theoretical Insights into Spin and Charge Scattering in STEM-EELS
Kerber, Michael	MS3-P-12 The impact of high hydrostatic pressure annealing on microstructure evolution
Kerenčič, Maruša	LS3-P-8 Light and Transmission Electron Microscopy Complement Functional Genomics Screening in Chlamydomonas reinhardtii to Reveal Novel Mechanisms of Susceptibility to Herbicide Paraquat
Kerrigan, Adam	MS5-P-1 Probing Magnons with High-Energy Electrons: Theoretical Insights into Spin and Charge Scattering in STEM-EELS
Kerschbaum, Hubert	LS2-O-1 Beyond Apoptosis: Unravelling Thapsigargin-Induced Non-Apoptotic Cell Death Pathways in Immune- and Cancer Cells
Kersten, Holger	IM7-O-2 Advancements in Plasma Microcell Integration for in situ TEM Experiments
Kević, Nives	LS3-P-2 Ultrastructural changes of the injured renal tissues in the cage-reared rainbow trout Oncorhynchus mykiss (Walbaum, 1792)
Kézsmárki, István	IMPRESS 11 Mechanical strain and light-induced control of magnetic states in Fe3Sn2 in situ in the TEM
Khaliq, Muhammad Waqas	IM7-P-1 InCAEM: A Singular Infrastructure for Advanced Energy Materials Research
Khaliq, Waqas	IM2-O-3 Investigating Magnetic Domain Wall Pinning in Nanowires via Correlative X-ray and Electron Transmission Microscopy
Khan, Madiha	IM3-P-8 Surface and sub-surface defect analysis in semiconductors by Secondary Electron Emission Spectroscopy and local charge transport mapping IM1-P-7 Quantum state secondary electron emission spectroscopy in low voltage scanning electron microscope for probing Valence band IM1-O-3 Perspectives of ultrafast hyperspectral imaging in Scanning Electron Microscopy
Khursheed, Anjam	IM3-P-8 Surface and sub-surface defect analysis in semiconductors by Secondary Electron Emission Spectroscopy and local charge transport mapping IM1-P-7 Quantum state secondary electron emission spectroscopy in low voltage scanning electron microscope for probing Valence band IM1-O-3 Perspectives of ultrafast hyperspectral imaging in Scanning Electron Microscopy
Kienle, Lorenz	IM7-O-2 Advancements in Plasma Microcell Integration for in situ TEM Experiments MS4-P-9 Thermal and Chemical Stability of High-Entropy-Alloy Nanoparticles Synthesized via Laser Ablation in Organic Liquid
Kilic, Can	LS4-P-5 Brain Decellularization Process in Transgenic Alzheimer Rat Model
King, Zayna	Technological Advances for Temperature Dependent Liquid-Phase and Electrochemical Studies Using In Situ TEM
Kison, Victoriia	MS7-P-3 Microstructural analysis of the copper matrix composites for electrodes of plasma torches

Kisovec, Matic	LS3-O-2 Nanoalgosomes as observed by scanning and cryogenic transmission electron microscopes IM4-P-2 Activities of the cryo-EM facility at the National Institute of Chemistry, Slovenia
Kitzberger, František	LS6-O-2 Semi-automated Classification of Nanoparticle Signals from Opposite Surfaces of Ultrathin Sections in Low-Voltage STEM LS7-O-3 Serial Block-Face Scanning Electron Microscopy (SBEM): Comparative Analysis of Protocols for Enhancing Contrast and Reducing Charging in Mouse Brain Tissue Samples LS7-IN-2 Sample Preparation Strategies for Biological Electron Microscopy: Challenges and Innovations LS6-P-7 Multiscale 3D imaging of digestive system morphogenesis during arthropod development
Kizovský, Martin	IM1-P-6 Raman tweezers for the analysis of secondary microplastics generated by degradation of surgical masks in water
Kladnik, Aleš	LS2-P-2 Ultrastructure and gene expression in tomato flower pedicel abscission zone
Klaser, Teodoro	MS8-P-4 SEM insights into crystallization behavior of oxide glass-ceramics
Klementová, Mariana	MS1-O-3 Sulfidic inclusions in the Muong Nong tektites from Laos
Klingl, Andreas	LS6-P-2 Bridging Flourescence and Electron Microscopy: R221 Resin for CLEM in Microbes and Plants
Klumperman, Judith	Bridging structure and function: Advancing CLEM workflows for organelle-level imaging
Kmet, Brigita	MS1-P-10 Effects of Ti Doping on Structure, Microstructure and Mechanical Properties of (K0.5Na0.5)NbO3
Knapp, Magdalena	MS2-P-2 Plastic-Degrading or Just Settling? First TEM insights into microbial-plastic interactions in a Cold-Climate Ecosystem
Knez, Daniel	IM3-O-1 Advanced STEM of Point Defect Clusters in Doped STO IM8-O-4 Automated Thickness Determination from 4D-STEM Data by CNNs MS7-O-2 Pore characterization of hard carbon anodes for sodium storage in sodium ion batteries by 2D and 3D TEM MS7-P-4 Characterization of hard carbons for Na-ion battery electrodes by a combination of electron microscopy and vibrational spectroscopy IMPRESS 9 Artificial Intelligence for TEM: Real-Time Automation and Predictive Analysis in In Situ Experiments IM1-P-4 EDXS Quantification in the TEM: How Can Ray Tracing Help?
Kobe, Nina	LS4-P-9 The Effect of a Novel SARS-CoV E Protein Inhibitor on Ultrastructure of Murine Hepatitis Virus-Infected L-929 Cells
Koblar, Maja	MS5-IN-1 Insight into Defects and Polarization in Lead-Free Ferroelectrics by Advanced STEM Techniques MS1-P-10 Effects of Ti Doping on Structure, Microstructure and Mechanical Properties of (K0.5Na0.5)NbO3
Kobylynska, Maryna	LS7-IN-1 Adapting Inpainting and non-Raster scanning for cryo Volume Electron Microscopy (cvEM) using the JEOL JIB 4700F cryo Focus Ion Beam Scanning Electron Microscope.
Kocev, Dragi	IM8-P-4 A Deep Learning Approach to Drift Correction in Atomic-Scale STEM Imaging

Koch, Christoph Tobias	IM3-IN-1 Developments in 4D-STEM and Ptychography: From Series Registration to Live Compression
Kociak, Mathieu	IM8-O-5 Enhanced Low-Loss EELS Analysis through Hybrid Unsupervised and Supervised Machine Learning IM1-IN-2 Recent advances in STEM spectroscopy using synchronized electron and photon beams
Kocijan, Martina	MS6-P-6 Electron microscopy investigation of Cu-TiO2 nanocomposites for solar-driven photocatalysis MS6-P-9 Atomic layer deposition of nitrogen-doped TiO2 thin films for photocatalytic applications
Kocjan, Andraž	MS5-P-3 EBSD analysis of Sr-hexaferrite sintered in different atmospheres
Kofler, Clara	IM8-IN-1 Convolutional neural networks for scanning transmission electron microscopy image analysis: Towards automated analysis of large volume datasets
Kogovšek, Polona	LS4-P-9 The Effect of a Novel SARS-CoV E Protein Inhibitor on Ultrastructure of Murine Hepatitis Virus-Infected L-929 Cells
Kohlmann, Niklas	IM7-O-2 Advancements in Plasma Microcell Integration for in situ TEM Experiments
Kojić, Vedran	MS6-P-7 Intense Pulsed Light Processing for Rapid Crystallization of Titania Nanotube Thin Films MS7-P-2 Utilizing SEM thin-film measurements to deepen the understanding of perovskite solar cell performance MS6-P-10 The impact of solvents on the morphology and optical properties of organo-metal thin films MS3-O-3 (S)TEM study of the WTaVCr alloy for fusion application
Kokalj, Anton	MS1-P-9 Comprehensive study of Inversion Boundaries in ZnO MS5-IN-1 Insight into Defects and Polarization in Lead-Free Ferroelectrics by Advanced STEM Techniques MS7-O-1 Charge density distribution in single-atom-on-substrate catalysts
Kolb, Dagmar	IM2-P-2 Fast and Frozen: Visualising a wide spectrum of specimens using Cryo-SEM combined with an on-site freeze fracture system LS7-P-3 Fast and Frozen: Visualising a wide spectrum of specimens using Cryo-SEM combined with an on-site freeze fracture system
Kolenc, Marko	LS4-P-10 Antiviral Efficacy of Electrolysed Saline (EOS) Against Both Enveloped and Non-Enveloped Viruses: A TEM Study
Komazec, Bruno	LS3-P-6 Visualizing the algal response on polystyrene particles: A focus on EPS production
Komelj, Matej	MS1-P-9 Comprehensive study of Inversion Boundaries in ZnO Atomistic structure of interfaces: Where theory and experiment meet
Konda, Klara L.	MS1-P-15 FIB-SEM characterization of various types of materials
Konda, Klara Laura	MS6-P-18 Characterization of ZnO Films Prepared via FIB-SEM
Kong, Dely	IMPRESS 11 Mechanical strain and light-induced control of magnetic states in Fe3Sn2 in situ in the TEM
Konijnenberg, Peter	IM5-IN-2 The combination of high-resolution diffraction techniques in the scanning electron microscope for statistical relevant description of crystal defects and resulting properties in metals and alloys

Koniuch, Natalia	MS2-O-3 4D-STEM of Soft Matter: Structural Characterisation of Beam-Sensitive Polymers and Molecular Crystals Using Fast Precession and a Direct Electron Detector on a Tescan Tensor
Kononenko, Veno	MS3-P-6 Laser Surface Functionalization of 316L Stainless Steel Under Ambient and Inert Argon Atmospheres LS3-P-9 Cytotoxicity Assessment of Functionalized Graphene-Based Composites
Konvalina, Ivo	MS4-P-8 Ab initio Study of Angle-Resolved Spectroscopy of Few-Layer Graphene IM1-O-2 Investigation of Electron Scattering in Ultrathin Films Using Time-of-Flight Spectroscopy
Koos, Antal	MS6-O-5 Advanced TEM characterization of 2D compound semiconductors
Kopecká, Jana	LS7-IN-2 Sample Preparation Strategies for Biological Electron Microscopy: Challenges and Innovations
Kopia, Agnieszka	MS7-P-3 Microstructural analysis of the copper matrix composites for electrodes of plasma torches
Korat Bensa, Lidija	LS8-O-4 XCT state-of-the-art scanning modality for the characterization of 3D-printed flat panels LS8-P-4 3D visualisation of wood: 3D X-ray microtomography and 3D printing
Kormilina, Tatiana	MS7-O-2 Pore characterization of hard carbon anodes for sodium storage in sodium ion batteries by 2D and 3D TEM MS7-P-4 Characterization of hard carbons for Na-ion battery electrodes by a combination of electron microscopy and vibrational spectroscopy
Kos, Monika	LS2-P-1 The sexually dimorphic retina of a butterfly, from microspectrophotometry to connectomics
Kos, Saša	MS1-P-7 Ex-situ differential individual particle analysis of various Pb, Zn and Fe ore minerals after periodical leaching in soil column experiments
Kosari Mehr, Abbas	IM3-P-8 Surface and sub-surface defect analysis in semiconductors by Secondary Electron Emission Spectroscopy and local charge transport mapping IM1-P-7 Quantum state secondary electron emission spectroscopy in low voltage scanning electron microscope for probing Valence band IM1-O-3 Perspectives of ultrafast hyperspectral imaging in Scanning Electron Microscopy
Kosec, Tadeja	MS3-P-1 Corrosion at Home: Microscopy's Role in Understanding Everyday Material Failures
Kosjek, Tina	LS3-P-8 Light and Transmission Electron Microscopy Complement Functional Genomics Screening in Chlamydomonas reinhardtii to Reveal Novel Mechanisms of Susceptibility to Herbicide Paraquat
Kostanjšek, Rok	LS6-P-4 Internal anatomy of parasitic acantocephalans in endangered underground amphibian analyzed by a combination of microCT and FESEM LS8-P-2 3D Atlas of Arthropods IM5-P-3 Micro-computerized tomography for evaluation of dental stud attachment wear LS8-P-1 Micro-CT analysis of femoral bone structure in ovariectomized rats following treatment with alendronate, hop extract and their combination
Kostelec, Mitja	MS7-P-6 Microscopic Insights into Catalyst Layer of PEMFC: IL-SEM Study of Electrochemical Effects

Kostić, Marija	LS7-P-2 Red blood cells morphological alterations during preparation for electron microscopy imaging
Kotakoski, Jani	IM2-O-1 Correlative microscopy: Uncovering the role of vacancies and contamination on the mechanical stiffness of defect-engineered graphene. MS4-O-2 Atomic-resolution investigation of 2D hematene MS4-O-4 Metallene synthesis by ion irradiation: Growth of two-dimensional gold by vacancy-induced nucleation on defect-engineered graphene MS4-P-4 Hematene lattice parameter variation as a function of thickness IM8-IN-1 Convolutional neural networks for scanning transmission electron microscopy image analysis: Towards automated analysis of large volume datasets
Kothleitner, Gerald	MS3-O-2 Atomic-resolution electron microscopy analysis of oxygen-mediated Ti nanocrystalline synthesized by high-pressure torsion IM3-O-1 Advanced STEM of Point Defect Clusters in Doped STO IM8-O-4 Automated Thickness Determination from 4D-STEM Data by CNNs IMPRESS 9 Artificial Intelligence for TEM: Real-Time Automation and Predictive Analysis in In Situ Experiments IM1-P-4 EDXS Quantification in the TEM: How Can Ray Tracing Help?
Kotková, Kristýna	MS1-P-13 Exploring High-Baroque Stucco: Microscopy of Materials and Techniques at Kroměříž Chateau
Koudoumas, Emmanouel	MS8-P-2 Influence of La, Er, and Sm Doping on the Structural and Morphological Properties of ZnO for EMI Shielding
Koundinya, NTBN	IM5-IN-2 The combination of high-resolution diffraction techniques in the scanning electron microscope for statistical relevant description of crystal defects and resulting properties in metals and alloys
Kovač, Janez	MS8-P-6 Quantum chemical simulation of spontaneous water dissociation on 110 || 110 rutile TiO2 interfaces MS6-P-11 New Genesis XPS Spectrometer at the Jožef Stefan Institute for advanced surface and thin film characterization
Kovačević, Rafaela	MS6-P-10 The impact of solvents on the morphology and optical properties of organo-metal thin films
Kovács, András	MS5-IN-2 Next Generation Spintronic Devices And 3D Curved Magnets examined by Lorentz microscopy MS6-O-4 Structural characterization of phase transformations in gallium oxide by transmission electron microscopy IMPRESS 11 Mechanical strain and light-induced control of magnetic states in Fe3Sn2 in situ in the TEM
Kovács, Zsolt	MS1-P-6 Transmission electron microscopy of hypomineralized enamel apatite nanocrystals
Kozlovcev, Petr	MS1-P-13 Exploring High-Baroque Stucco: Microscopy of Materials and Techniques at Kroměříž Chateau
Krahne, Roman	MS8-O-1 Low-dose 4DSTEM analysis of local strain in 2D perovskite lateral heterostructures
Kralj-Iglič, Veronika	LS3-O-2 Nanoalgosomes as observed by scanning and cryogenic transmission electron microscopes LS3-P-7 Insight into the particle-based nature of mucilage as a response of Chlorella sorokiniana cell to manganese excess
Kralj, Samo	MS3-P-7 Nano- and micro-structural configurations of functional complex metallic alloys

Křápek, Vlastimil	MS4-P-8 Ab initio Study of Angle-Resolved Spectroscopy of Few-Layer Graphene
Krapež, Daša	LS8-P-4 3D visualisation of wood: 3D X-ray microtomography and 3D printing
Krasovskii, Eugene	MS4-P-8 Ab initio Study of Angle-Resolved Spectroscopy of Few-Layer Graphene
Krawczyńska, Agnieszka T.	MS3-P-12 The impact of high hydrostatic pressure annealing on microstructure evolution
Kreft, Marko	LS5-IN-2 Noradrenaline and Cannabinoid Regulation of Astrocyte Energy Metabolism Revealed by FRET Nanosensors
Kreft, Mateja Erdani	Microscopy-based analysis of biomimetic 2D and 3D in vitro models for preclinical studies
Krenn, Martin	MS3-P-3 Precession Electron Diffraction in modern steel systems
Križaj Kosi, Nina	MS5-O-4 Characterization of hierarchically structured nanocomposite catalysts based on Ru nanoparticles deposited on ceria supports with embedded magnetic nanoparticles
Křížová, Šárka	MS1-O-3 Sulfidic inclusions in the Muong Nong tektites from Laos
Krogstrup, Peter	MS6-IN-1 Automated analysis of STEM data of semiconductor heterostructures for quantum computing IMPRESS 1 End-to-end Autonomous Unveiling of Physical Knowledge of Quantum Devices through Electron Microscopy Data
Krstić, Jelena S.	LS4-P-12 Proferroptotic response to nutrient deprivation and sorafenib treatment in hepatocellular carcinoma cells – a microscopic study
Krže, Luka	LS1-O-3 Optimizing Microscopy Methodologies for Xylogenesis: Advances and Challenges in Wood and Phloem Formation Analysis
Krzyzanek, Vladislav	IM3-P-6 4D-STEM/PNBD: A semi-automated powder electron diffraction in SEM microscopes IM3-P-4 Automated processing of powder electron diffraction patterns LS7-O-2 Ultrastructural Analysis of Azotobacter vinelandii Encapsulated in Alginate Hydrogel Using Cryogenic Preparation and Electron Microscopy Techniques LS7-P-1 Structural Stabilization of Alginate for Imaging Hydrogel-encapsulated Bacterial Cells Using LV-STEM LS7-O-3 Serial Block-Face Scanning Electron Microscopy (SBEM): Comparative Analysis of Protocols for Enhancing Contrast and Reducing Charging in Mouse Brain Tissue Samples IM5-IN-1 Novel embedding resins for volume EM with enhanced resistance to e-beam damage
Ku, Bosung	IM8-O-1 ViFoSe, an user-friendly open-source post-processing tool for foreground segmentation in time-lapse videos.
Kubicek, Markus	MS1-O-4 Oxygen vacancy distribution in different regions of La1−xSrxGa1−yMgyO3−δ
Kukovecz, Ákos	MS1-P-6 Transmission electron microscopy of hypomineralized enamel apatite nanocrystals
Kunčič, Katja	LS6-P-7 Multiscale 3D imaging of digestive system morphogenesis during arthropod development
Kuret, Tadeja	Microscopy-based analysis of biomimetic 2D and 3D in vitro models for preclinical studies
Kürnsteiner, Philipp	MS3-P-3 Precession Electron Diffraction in modern steel systems

Kusch, Gunnar	MS7-O-4 Understanding local crystallography in solar cells materials with scanning electron diffraction using unsupervised machine learning
Kutnjak, Denis	LS4-P-2 Virome of the invasive signal crayfish and its correlation with histopathological changes of the hepatopancreas
Kuwahara, Makoto	IM8-P-3 EELS spectrum analysis using Bayesian estimation
Kuznetsov, Andrej	MS6-O-4 Structural characterization of phase transformations in gallium oxide by transmission electron microscopy
Kwak, Bongseop	IM8-O-1 ViFoSe, an user-friendly open-source post-processing tool for foreground segmentation in time-lapse videos.
Kwan, Ka Wing	IMPRESS 6 NanoMi: An open-source electron microscope
Lachhab, Meryem	MS5-IN-1 Insight into Defects and Polarization in Lead-Free Ferroelectrics by Advanced STEM Techniques IM3-O-3 Exploring perovskites at the atomic level by 4DSTEM: Experimental & Simulation MS8-O-3 Structural modulations in antiferroelectric NaNbO3-based ceramics investigated by STEM
Lagatolla, Cristina	LS8-O-3 The exopolysaccharide EpsA-O has a decisive role in 3D microstructure formation of Bacillus subtilis biofilm
Lago Falcao, Eduardo H.	MS8-P-7 Structural study of a Magnetic Graphitic Nanocomposite
Laishram, Jummi	LS6-P-5 Safe-by-Design Characterization of TiO2 Nanoparticles in a Cell Model: An Integrated Experimental Workflow MS4-P-3 RIANA: Research Infrastructure Access in Nanoscience & Nanotechnology
Lam, Yun Wah	LS4-O-1 Navigating the Human Protein Atlas to map the composition of extracellular matrix proteins in normal and cancer tissues
Lammer, Judith	IM1-P-4 EDXS Quantification in the TEM: How Can Ray Tracing Help?
Lamprecht, David	IM8-IN-1 Convolutional neural networks for scanning transmission electron microscopy image analysis: Towards automated analysis of large volume datasets
Lan, Qianqian	IMPRESS 5 Quantifying carbon site switching dynamics in GaN by off-axis electron holography IMPRESS 3 Characterization of electric and magnetic fields at interfaces in manganese-containing heterostructures using correlative TEM techniques
Längle, Manuel	IM8-IN-1 Convolutional neural networks for scanning transmission electron microscopy image analysis: Towards automated analysis of large volume datasets
Lankovics, Lilla	LS3-O-1 Recognition of a new exctracellular vesicle release mechanism
Lazarov, Vlado	MS5-P-1 Probing Magnons with High-Energy Electrons: Theoretical Insights into Spin and Charge Scattering in STEM-EELS
Ledwig, Piotr	MS7-P-3 Microstructural analysis of the copper matrix composites for electrodes of plasma torches MS3-P-9 Effect of recycled powder on microstructure and chemical composition of additively manufactured AlSi7Mg alloy
Lee, Misu	IM8-O-1 ViFoSe, an user-friendly open-source post-processing tool for foreground segmentation in time-lapse videos.

Lei, Yu	IM3-O-4 Multidimensional and Multimodal 4D STEM and Electron Ptychography
Leitinger, Gerd	LS4-P-11 Post mortem degradation of ferritin and its significance for determining the iron content of the human brain LS2-O-4 Some neurons are better connected than others in a locust's network of visual interneurons
Lengar, Živa	LS4-P-9 The Effect of a Novel SARS-CoV E Protein Inhibitor on Ultrastructure of Murine Hepatitis Virus-Infected L-929 Cells
Lenzinger, Dorina	LS3-O-1 Recognition of a new exctracellular vesicle release mechanism
Leopold, Klemen	IM5-P-3 Micro-computerized tomography for evaluation of dental stud attachment wear
Leroux, Hugues	IM1-P-2 Low-energy Core-loss EELS as a Dose-effective Approach for Elemental and Oxidation State Mapping
Lesar, Aleksander	MS3-P-10 SEM and EDS characterization of 316L Stainless Steel exposed to Different Bacteria
Levak, Valentina	LS8-O-2 Spatiotemporal acquisition of genetically encoded biosensors in intact plant leaves reveals hormonal crosstalk in response to wounding LS4-P-9 The Effect of a Novel SARS-CoV E Protein Inhibitor on Ultrastructure of Murine Hepatitis Virus-Infected L-929 Cells LS3-P-8 Light and Transmission Electron Microscopy Complement Functional Genomics Screening in Chlamydomonas reinhardtii to Reveal Novel Mechanisms of Susceptibility to Herbicide Paraquat LS5-P-1 Live Imaging of Calcium and Hormonal Crosstalk in Potato: Insights into Endophyte-Mediated Immune Enhancement
Lewandowska-Łańcucka, Joanna	IM4-P-1 Targeted liposomes loaded with monoclonal antibodies for drug delivery - structure and function
Lewandowska, Małgorzata	MS3-P-12 The impact of high hydrostatic pressure annealing on microstructure evolution
LI, Xiaoyan	IM1-IN-2 Recent advances in STEM spectroscopy using synchronized electron and photon beams
Li, Zhi	IMPRESS 7 EFLY – a Fast Versatile Charge Particle Optics Code
Liang, Feng-Xia {Alice}	LS2-O-3 Volume electron microscopy of intracellular compartments in the urinary bladder epithelium
Libisch, Florian	IM2-O-1 Correlative microscopy: Uncovering the role of vacancies and contamination on the mechanical stiffness of defect-engineered graphene.
Lichtenegger, Helga C.	LS4-O-3 Morphological and Mechanical Characterization of Major Ampullate Spider Silk Fibers in Liquid Environments: Insights from SEM and Single-Fiber Tensile Testing
Linck, Martin	IMPRESS 12 A laser-free approach to ultra-fast transmission electron microscopy
Lindley, Matthew	MS4-IN-1 Dynamic Atomic Behaviour in 2D Heterostructures and Nanocatalysts
Lins da Silva, Walyson K.	MS8-P-7 Structural study of a Magnetic Graphitic Nanocomposite
Liu, Huiyun	MS6-O-3 Multi-modal Microscopy Analysis of Co-doped InAs/GaAs Quantum Dot Lasers
Liu, Xu	IM6-P-2 Development and Application of an Aberration Calculation Program for Electron Lenses Based on Differential Algebra

Liu, Zhicheng	IM6-P-2 Development and Application of an Aberration Calculation Program for Electron Lenses Based on Differential Algebra
Livakas, Nikolaos	MS6-IN-2 Advanced low dose electron microscopy of metal halide perovskites
Lizzano, Mattia	MS6-P-12 In situ TEM dynamics of Au and Au/zirconia clusters in nanostructured thin films: a quantitative analysis
Ljubić Tobisch, Valentina	MS6-P-13 Etching and printing of daguerreotypes: experimental reconstruction and microscopic analysis of first photomechanical reproduction processes MS6-P-14 Nanoscale investigation of degradation processes in historical daguerreotype plates MS6-P-16 Microscopical study of 19th century photomechanical prints: in-situ investigations in museum collections MS6-P-17 Microscopic Identification of Daguerreotypes Through Hallmark Analysis
Llorens Rauret, David	MS4-O-3 High-Entropy Oxide Nanoparticles as Stable and Efficient Catalysts for the Oxygen Evolution Reaction IM7-P-1 InCAEM: A Singular Infrastructure for Advanced Energy Materials Research
Löffler, Stefan	IM6-O-1 Entanglement in Bragg Scattering
Longo, Giulia	MS7-O-4 Understanding local crystallography in solar cells materials with scanning electron diffraction using unsupervised machine learning
López-Conesa, Lluís	MS5-O-2 Investigating Local Structure in NBT-BT system Using (S)TEM Techniques
Lopez-Sanchez, Marco A.	MS1-IN-2 The Past and Future of Electron Backscattered Diffraction (EBSD) in Earth Sciences
Lőrincz, Péter	LS3-O-1 Recognition of a new exctracellular vesicle release mechanism LS3-IN-1 Fruit fly nephrocytes: Versatile tools to study the endolysosomal system.
Loudon, James	MS5-O-1 The magnetic microstructure in FeCo alloys and its interaction with non-magnetic inclusions
Lu, Peng-Han	IMPRESS 4 Electrostatic potential measurement at liquid helium temperature using off-axis electron holography
Lu, Yan	IMPRESS 4 Electrostatic potential measurement at liquid helium temperature using off-axis electron holography
Lubk, Axel	IM6-O-2 Miniaturized Magnetic Multipoles for Ultrafast Beam Shaping in the Transmission Electron Microscope IMPRESS 7 EFLY – a Fast Versatile Charge Particle Optics Code Next-Generation Electron Source Optics IM6-IN-2 Electron Optics and Beam Shaping with a Special View on EELS
Lukan, Tjaša	LS8-O-2 Spatiotemporal acquisition of genetically encoded biosensors in intact plant leaves reveals hormonal crosstalk in response to wounding LS3-P-8 Light and Transmission Electron Microscopy Complement Functional Genomics Screening in Chlamydomonas reinhardtii to Reveal Novel Mechanisms of Susceptibility to Herbicide Paraquat LS5-P-1 Live Imaging of Calcium and Hormonal Crosstalk in Potato: Insights into Endophyte-Mediated Immune Enhancement
Maak, Pal	LS1-O-1 Immersive Virtual Reality System for Mice Combined with 3D-Targeted Photostimulation as a Prototype for Visual Restoration

Maček Kržmanc, Marjeta	MS1-P-1 Understanding the formation mechanism of growth-type planar defects in natural and synthesized perovskites based on STEM analyses
Mack, Paul	MS8-O-4 Correlative Imaging and Surface Analysis workflow
Mačukanović-Jocić, Marina	LS6-P-1 Morphological features of Himantoglossum calcaratum (Beck) Schltr. subsp. calcaratum (Orchidaceae) pollinarium
Madlmayr, Anna	LS2-O-1 Beyond Apoptosis: Unravelling Thapsigargin-Induced Non-Apoptotic Cell Death Pathways in Immune- and Cancer Cells
Madsen, Jacob	IM2-O-1 Correlative microscopy: Uncovering the role of vacancies and contamination on the mechanical stiffness of defect-engineered graphene. IM8-IN-1 Convolutional neural networks for scanning transmission electron microscopy image analysis: Towards automated analysis of large volume datasets
Magazzù, Alessandro	IM1-P-6 Raman tweezers for the analysis of secondary microplastics generated by degradation of surgical masks in water
Mahadevegowda, Amoghavarsha	MS7-P-7 Identifying and studying open Li-ion channels along a preferred crystallographic axis in battery electrodes via scanning electron diffraction
Mahkovec Povalej, Tjaša	LS5-P-1 Live Imaging of Calcium and Hormonal Crosstalk in Potato: Insights into Endophyte-Mediated Immune Enhancement LS8-O-2 Spatiotemporal acquisition of genetically encoded biosensors in intact plant leaves reveals hormonal crosstalk in response to wounding
Majkowska, Natalia	IM4-P-1 Targeted liposomes loaded with monoclonal antibodies for drug delivery - structure and function
Majumder, Prosenjit	IM6-P-1 Towards spatially coherent low-energy electron and ion beams
Makovec, Darko	MS5-O-4 Characterization of hierarchically structured nanocomposite catalysts based on Ru nanoparticles deposited on ceria supports with embedded magnetic nanoparticles
Malac, Marek	IMPRESS 6 NanoMi: An open-source electron microscope
Malej, Simon	MS3-IN-2 The Microstructure and Mechanical Properties of LPBF Produced Nickel-based Alloy IN718 Influenced by Laser Beam Shape and Post Heat-Treatment
Malgaj, Tine	IM5-P-3 MICRO-COMPUTERIZED TOMOGRAPHY FOR EVALUATION OF DENTAL STUD ATTACHMENT WEAR
Malič, Barbara	MS1-P-10 Effects of Ti Doping on Structure, Microstructure and Mechanical Properties of (K0.5Na0.5)NbO3 MS8-O-3 Structural modulations in antiferroelectric NaNbO3-based ceramics investigated by STEM
Malovcic, Melisa	IM2-P-2 Fast and Frozen: Visualising a wide spectrum of specimens using Cryo-SEM combined with an on-site freeze fracture system LS7-P-3 Fast and Frozen: Visualising a wide spectrum of specimens using Cryo-SEM combined with an on-site freeze fracture system
Maňák, Jan	MS3-P-11 Sublayer structure in fire gilding layer on medieval jewellery MS5-P-2 Are we observing channeling or magnetic contrast? MS1-O-3 Sulfidic inclusions in the Muong Nong tektites from Laos
Mancini, Lucia	LS8-IN-1 Advanced multimodal and multiscale imaging for material characterization

Mangler, Clemens	IM2-O-1 Correlative microscopy: Uncovering the role of vacancies and contamination on the mechanical stiffness of defect-engineered graphene. IM8-IN-1 Convolutional neural networks for scanning transmission electron microscopy image analysis: Towards automated analysis of large volume datasets
Manna, Liberato	MS4-P-2 Complex Electron Microscopy Analysis of Nanoscale Epitaxial Heterostructures Involving Metal Halides MS6-IN-2 Advanced low dose electron microscopy of metal halide perovskites
Mao, Wei	IM3-O-4 Multidimensional and Multimodal 4D STEM and Electron Ptychography
Maragò, Onofrio M.	IM1-P-6 Raman tweezers for the analysis of secondary microplastics generated by degradation of surgical masks in water
Marijan, Sara	MS8-P-4 SEM insights into crystallization behavior of oxide glass-ceramics
Marinova, Maya	IM1-P-2 Low-energy Core-loss EELS as a Dose-effective Approach for Elemental and Oxidation State Mapping
Marinović, Maja	LS5-IN-1 Dictyostelium discoideum IQGAP proteins IqgC and IqgD - siblings or distant relatives
Markelić, Milica B.	LS4-P-15 Therapeutic effects of H_2S donors on ferroptosis-mediated liver damage in C57BL/6 mice – a microscopic study LS4-P-12 Proferroptotic response to nutrient deprivation and sorafenib treatment in hepatocellular carcinoma cells – a microscopic study
Markoli, Boštjan	MS3-P-2 Plastic deformation in the Magnesium alloy AZ80 - an EBSD study of the effects of cavitation peening
Markovič, Gaja	Microscopy-based analysis of biomimetic 2D and 3D in vitro models for preclinical studies
Marković, Zoran	LS3-P-3 Histopathology of the gills of farmed common carp (Cyprinus carpio): a bioindication method
Marmiroli, Benedetta	IMPRESS 8 Multi-purpose MEMS devices for correlative operando experiments in battery research
Marolt, Matija	LS2-O-2 Membrane Segmentation in Volumetric Electron Microscopy Data LS2-O-3 Volume electron microscopy of intracellular compartments in the urinary bladder epithelium
Marrows, Christopher	MS5-IN-2 Next Generation Spintronic Devices And 3D Curved Magnets examined by Lorentz microscopy
Marsel, Aleš	MS7-P-10 How to Perform Identical Location Scanning Electron Microscopy: Workflow, Advantages, Challenges, and Applications
Martí-Sánchez, Sara	MS6-IN-1 Automated analysis of STEM data of semiconductor heterostructures for quantum computing IMPRESS 1 End-to-end Autonomous Unveiling of Physical Knowledge of Quantum Devices through Electron Microscopy Data
Martín-Jiménez, Daniel	IM7-P-1 InCAEM: A Singular Infrastructure for Advanced Energy Materials Research
Martin, Itziar Serna	Hydra Bio plasma FIB: pushing the boundaries to larger 3D volumes.
Martinc, Matej	MS5-IN-1 Insight into Defects and Polarization in Lead-Free Ferroelectrics by Advanced STEM Techniques
Martínez, Ana Belén	IM7-P-1 InCAEM: A Singular Infrastructure for Advanced Energy Materials Research

Martinovic, Vesna	LS4-P-15 Therapeutic effects of H_2S donors on ferroptosis-mediated liver damage in C57BL/6 mice – a microscopic study
Martins, Milena	MS7-P-10 How to Perform Identical Location Scanning Electron Microscopy: Workflow, Advantages, Challenges, and Applications
Márton, Zsuzsanna	MS2-O-2 Nanocellulose-based Functional Nanocomposite Materials
Mast, Jan	MS4-P-10 Physicochemical characterization of copper oxides applied as feed additives and plant protection products MS4-P-6 Assessing the morphology and fractal properties of aggregated nanoparticles in 2 and 3 dimensions by transmission electron microscopy
Materna Mikmeková, Eliška	IM1-O-2 Investigation of Electron Scattering in Ultrathin Films Using Time-of-Flight Spectroscopy
Matić, Mario	MS3-O-3 (S)TEM study of the WTaVCr alloy for fusion application
Mayer, Barbara M.	IM8-IN-1 Convolutional neural networks for scanning transmission electron microscopy image analysis: Towards automated analysis of large volume datasets
McGrouther, Damien	LS7-IN-1 Adapting Inpainting and non-Raster scanning for cryo Volume Electron Microscopy (cvEM) using the JEOL JIB 4700F cryo Focus Ion Beam Scanning Electron Microscope.
McVitie, Stephen	MS5-IN-2 Next Generation Spintronic Devices And 3D Curved Magnets examined by Lorentz microscopy
Meglič, Andrej	LS2-P-1 The sexually dimorphic retina of a butterfly, from microspectrophotometry to connectomics
Melchior, Maximilian	MS4-P-4 Hematene lattice parameter variation as a function of thickness
Meldrum, Fiona	MS1-IN-1 Studying the crystallization of inorganic materials using correlated transmission electron microscopy
Melek, Korollus	LS2-O-1 Beyond Apoptosis: Unravelling Thapsigargin-Induced Non-Apoptotic Cell Death Pathways in Immune- and Cancer Cells
Merela, Maks	LS1-O-3 Optimizing Microscopy Methodologies for Xylogenesis: Advances and Challenges in Wood and Phloem Formation Analysis LS8-P-4 3D visualisation of wood: 3D X-ray microtomography and 3D printing
Merino, Gonzalo	IM7-P-1 InCAEM: A Singular Infrastructure for Advanced Energy Materials Research
Mertens, Birgit	MS4-P-10 Physicochemical characterization of copper oxides applied as feed additives and plant protection products
Michalcová, Alena	MS3-IN-1 Microstructural characterization of beta-Sn to alpha-Sn phase transformation
Midgley, Paul	MS5-O-1 The magnetic microstructure in FeCo alloys and its interaction with non-magnetic inclusions
Migani, Sofia	LS4-P-16 Microscopy techniques to evaluate the cytotoxic effect induced by copper complexes on glioblastoma cells
Mihoci, Iva	MS1-P-8 Multidisciplinary Application of Scanning Electron Microscopy (SEM) in Heritage Research, Conservation and Presentation at the Croatian Natural History Museum
Mijanović, Lucija	LS5-IN-1 Dictyostelium discoideum IQGAP proteins IqgC and IqgD - siblings or distant relatives
Mikmeková, Eliška Materna	MS4-P-8 Ab initio Study of Angle-Resolved Spectroscopy of Few-Layer Graphene

Miksatko, Jiri	LS6-O-1 Volume Electron Microscopy Methods for Investigating Nitrogen Handling and Cellular Vision in Microscopic Algae
Mikulčić Pavlaković, Snježana	MS1-P-8 Multidisciplinary Application of Scanning Electron Microscopy (SEM) in Heritage Research, Conservation and Presentation at the Croatian Natural History Museum
Mikuletič, Tina	LS4-P-10 Antiviral Efficacy of Electrolysed Saline (EOS) Against Both Enveloped and Non-Enveloped Viruses: A TEM Study
Milani, Paolo	MS6-P-12 In situ TEM dynamics of Au and Au/zirconia clusters in nanostructured thin films: a quantitative analysis
Milenkovic, Aleksandar	LS4-IN-2 Expression of GABA-A receptors in brain tumors
Milenkovic, Ivan	LS4-IN-2 Expression of GABA-A receptors in brain tumors
Miler, Marko	LS4-P-15 Therapeutic effects of H_2S donors on ferroptosis-mediated liver damage in C57BL/6 mice – a microscopic study
Miler, Miloš	MS1-P-7 Ex-situ differential individual particle analysis of various Pb, Zn and Fe ore minerals after periodical leaching in soil column experiments
Milošev, Ingrid	MS3-P-8 Composition and microstructure of wrought and additively manufactured DED-LB of Ti-6Al-4V alloy MS6-P-11 New Genesis XPS Spectrometer at the Jožef Stefan Institute for advanced surface and thin film characterization
Miloševic, Ivana	IM5-P-4 Effects of different preparation methods and detector use on SEM imaging of bacterial flagella
Minenkov, Alexey	MS3-O-4 Correlative Transmission Electron Microscopy for Nanophase Identification in Galvannealed Advanced High-Strength Steel MS3-P-3 Precession Electron Diffraction in modern steel systems
Miranda Martínez, Andrés	IM8-O-3 Mitigating beam damage during FIB-SIMS imaging: a new methodology using alternative FIB scans
Mironov, Alexander	IM2-IN-1 Applications of Correlative Light Electron Microscopy (CLEM) and Volume Electron Microscopy in Cancer Biology LS2-O-2 Membrane Segmentation in Volumetric Electron Microscopy Data
Mirosavljevic, Marija	MS8-P-4 SEM insights into crystallization behavior of oxide glass-ceramics
Mirt, Tadej	IM5-P-3 MICRO-COMPUTERIZED TOMOGRAPHY FOR EVALUATION OF DENTAL STUD ATTACHMENT WEAR
Mirzabeigi, Narges	MS3-IN-2 The Microstructure and Mechanical Properties of LPBF Produced Nickel-based Alloy IN718 Influenced by Laser Beam Shape and Post Heat-Treatment
Mišić Radić, Tea	LS3-IN-2 Insights into the surface properties of microalgae using atomic force microscopy (AFM)
Mišmaš Zrimšek, Maruša	LS4-P-18 Revealing LRAT and NeuroD1 Colocalization in human urothelial cancer cells in vivo using proximity ligation assay
Mitsche, Stefan	MS1-O-2 Impact of clay construction components on indoor aerosols: what can automated SEM-EDX and Raman reveal?
Mizohata, Kenichiro	MS4-O-4 Metallene synthesis by ion irradiation: Growth of two-dimensional gold by vacancy-induced nucleation on defect-engineered graphene
Mlinkó, Éva	MS1-P-6 Transmission electron microscopy of hypomineralized enamel apatite nanocrystals

Mohaček Grošev, Vlasta	MS6-P-10 The impact of solvents on the morphology and optical properties of organo-metal thin films
Mojzes, Peter	LS6-O-1 Volume Electron Microscopy Methods for Investigating Nitrogen Handling and Cellular Vision in Microscopic Algae
Molina, Sergio I.	MS2-IN-2 Study of the electron-induced damage of polymer based materials during STEM-EELS measurements
Monin, Loriane	MS4-P-5 Stability of gold nanorods under tunable ps-pulsed laser illumination: an in-situ TEM study
Montgomery, Eric	IMPRESS 12 A laser-free approach to ultra-fast transmission electron microscopy
Moore, Thomas	MS5-IN-2 Next Generation Spintronic Devices And 3D Curved Magnets examined by Lorentz microscopy
Moorsom, Timothy	MS8-P-7 Structural study of a Magnetic Graphitic Nanocomposite
Mora, Matilde	IM2-O-4 Urban particulate matter and human health: correlative microscopy methods and simulated tissues modeling.
Morandi, Vittorio	IMPRESS 8 Multi-purpose MEMS devices for correlative operando experiments in battery research New Direction in Operando and Correlative TEM
Morelli, Maria Beatrice	LS4-P-16 Microscopy techniques to evaluate the cytotoxic effect induced by copper complexes on glioblastoma cells
Moskalewicz, Tomasz	MS6-P-15 Microstructural characterisation of sodium alginate coatings with addition of essential oils for antimicrobial protection of steel MS6-P-2 Microstructure and selected properties of multicomponent wear-resistant and low-friction coatings on titanium alloy substrates
Mozetič, Miran	MS6-P-11 New Genesis XPS Spectrometer at the Jožef Stefan Institute for advanced surface and thin film characterization
Mrak, Polona	LS4-P-9 The Effect of a Novel SARS-CoV E Protein Inhibitor on Ultrastructure of Murine Hepatitis Virus-Infected L-929 Cells LS6-P-8 Intestinal stem cells of Colorado potato beetle – imaging from the morphology of the digestive tract in the whole animal to the cell ultrastructure LS6-P-6 Ciliate Community in Podutik Reservoir, Slovenia: assessment of species diversity improved by the diversity of microscopic techniques LS6-P-7 Multiscale 3D imaging of digestive system morphogenesis during arthropod development
Mrázová, Kateřina	LS7-O-2 Ultrastructural Analysis of Azotobacter vinelandii Encapsulated in Alginate Hydrogel Using Cryogenic Preparation and Electron Microscopy Techniques LS7-P-1 Structural Stabilization of Alginate for Imaging Hydrogel-encapsulated Bacterial Cells Using LV-STEM
Msallamová, Šárka	MS3-IN-1 Microstructural characterization of beta-Sn to alpha-Sn phase transformation
Mugarza, Aitor	IM7-P-1 InCAEM: A Singular Infrastructure for Advanced Energy Materials Research
Mugnaioli, Enrico	IM3-P-3 Combining 3D electron diffraction and nanotexture analysis for the characterization of meteorite's impact ejecta
Mukherjee, Saumya	Momentum Microscopy: A complementary tool for imaging
Muller, Elisabeth	IM3-P-5 Electron ptychography experiment design with PtychoScopy

Müller, Heiko	IMPRESS 7 EFLY – a Fast Versatile Charge Particle Optics Code IMPRESS 12 A laser-free approach to ultra-fast transmission electron microscopy
Müllerová, Ilona	MS4-P-8 Ab initio Study of Angle-Resolved Spectroscopy of Few-Layer Graphene IM1-O-2 Investigation of Electron Scattering in Ultrathin Films Using Time-of-Flight Spectroscopy
Mundet, Bernat	MS5-O-2 Investigating Local Structure in NBT-BT system Using (S)TEM Techniques
Munjaković, Haris	LS4-P-10 Antiviral Efficacy of Electrolysed Saline (EOS) Against Both Enveloped and Non-Enveloped Viruses: A TEM Study
Muñoz-Czerny, Ute	MS1-O-2 Impact of clay construction components on indoor aerosols: what can automated SEM-EDX and Raman reveal?
Muñoz-Saldaña, Juan	MS5-O-2 Investigating Local Structure in NBT-BT system Using (S)TEM Techniques
Mustapić, Mislav	MS2-O-2 Nanocellulose-based Functional Nanocomposite Materials
Mustonen, Kimmo	IM2-O-1 Correlative microscopy: Uncovering the role of vacancies and contamination on the mechanical stiffness of defect-engineered graphene. MS4-O-4 Metallene synthesis by ion irradiation: Growth of two-dimensional gold by vacancy-induced nucleation on defect-engineered graphene
Mützel, Sophia	MS2-P-2 Plastic-Degrading or Just Settling? First TEM insights into microbial-plastic interactions in a Cold-Climate Ecosystem
Nachtnebel, Manfred	MS1-O-2 Impact of clay construction components on indoor aerosols: what can automated SEM-EDX and Raman reveal?
Naghilou, Aida	LS4-O-3 Morphological and Mechanical Characterization of Major Ampullate Spider Silk Fibers in Liquid Environments: Insights from SEM and Single-Fiber Tensile Testing
Naglič, Iztok	MS3-P-2 Plastic deformation in the Magnesium alloy AZ80 - an EBSD study of the effects of cavitation peening
Nagy, Anikó	LS3-IN-1 Fruit fly nephrocytes: Versatile tools to study the endolysosomal system.
Nandi, Pranjal	MS5-O-2 Investigating Local Structure in NBT-BT system Using (S)TEM Techniques
Nascimento Costa, Fanny	MS8-P-7 Structural study of a Magnetic Graphitic Nanocomposite
Nebesarova, Jana	LS7-O-3 Serial Block-Face Scanning Electron Microscopy (SBEM): Comparative Analysis of Protocols for Enhancing Contrast and Reducing Charging in Mouse Brain Tissue Samples IM5-IN-1 Novel embedding resins for volume EM with enhanced resistance to e-beam damage LS7-IN-2 Sample Preparation Strategies for Biological Electron Microscopy: Challenges and Innovations
Neccar, Duygu	LS4-P-13 Effect of endometrial environment on chromatin abnormalities of sperm LS4-P-4 The Effects of Amylin on Aggression in Wistar Rats Exposed to the Resident-Intruder Paradigm
Nerl, Hannah C.	IM7-O-1 Atomic-Scale Dynamics of Ni Catalysts Revealed by Operando TEM in Dry Reforming of Methane

Nicholls, Daniel	LS7-IN-1 Adapting Inpainting and non-Raster scanning for cryo Volume Electron Microscopy (cvEM) using the JEOL JIB 4700F cryo Focus Ion Beam Scanning Electron Microscope.
Nicolás, Josep	IM7-P-1 InCAEM: A Singular Infrastructure for Advanced Energy Materials Research
Nicolas, Ravier	Global JEOL workflow for air & beam sensitive samples from micro to nano scale
Nicolopoulos, Stavros	IM3-O-2 Electric Field and Pair Distribution Function mapping by Precession Scanning Electron Diffraction (4D-SPED) in TEM
Nicotra, Giuseppe	MS6-O-5 Advanced TEM characterization of 2D compound semiconductors
Nihei, Anastasiia	MS4-P-4 Hematene lattice parameter variation as a function of thickness
Nimmrichter, Stefan	IM6-O-1 Entanglement in Bragg Scattering
Niquet, Yann-Michel	MS6-IN-1 Automated analysis of STEM data of semiconductor heterostructures for quantum computing IMPRESS 1 End-to-end Autonomous Unveiling of Physical Knowledge of Quantum Devices through Electron Microscopy Data
Nogués, Josep	MS4-O-3 High-Entropy Oxide Nanoparticles as Stable and Efficient Catalysts for the Oxygen Evolution Reaction IM8-O-5 Enhanced Low-Loss EELS Analysis through Hybrid Unsupervised and Supervised Machine Learning
Normanno, Nicola	IM8-O-1 ViFoSe, an user-friendly open-source post-processing tool for foreground segmentation in time-lapse videos. LS1-O-2 Micropipette-Based Single-Cell Isolation from Live Spheroids.
Novak, Metka	LS4-P-6 Chemotherapy-induced metabolic changes in glioblastoma stem and differentiated cells in a context of the tumor microenvironment
Novak, Sara	MS2-P-1 Correlation Between Adhesion and Swimming Activity in Developing Zebrafish Exposed to Polystyrene and Polyethylene Micro- and Nanoplastics LS3-P-9 Cytotoxicity Assessment of Functionalized Graphene-Based Composites IM5-P-2 The Power of FIB-SEM for Visualizing the Internalization of 2D Materials In Vitro
Novotny, Tobias	MS3-IN-2 The Microstructure and Mechanical Properties of LPBF Produced Nickel-based Alloy IN718 Influenced by Laser Beam Shape and Post Heat-Treatment
Nunney, Tim	MS8-O-4 Correlative Imaging and Surface Analysis workflow
Oberaigner, Michael	IM8-O-4 Automated Thickness Determination from 4D-STEM Data by CNNs IM1-P-4 EDXS Quantification in the TEM: How Can Ray Tracing Help?
Ocal, Carmen	IM7-P-1 InCAEM: A Singular Infrastructure for Advanced Energy Materials Research
Ocsai, Katalin	LS1-O-1 Immersive Virtual Reality System for Mice Combined with 3D-Targeted Photostimulation as a Prototype for Visual Restoration
Ogawa, Satoshi	IM8-P-3 EELS spectrum analysis using Bayesian estimation

Okasha, Sameh	MS5-O-3 3D Nano-Printing of Complex Metal Structures via Focused Electron Beam Induced Deposition
Olasz, Daniel	IM5-P-5 High throughput micro-combinatorial study of microstructure and materials properties of binary and ternary layer systems
Olib, Arivazhagan V.	MS7-O-4 Understanding local crystallography in solar cells materials with scanning electron diffraction using unsupervised machine learning
Oliver, Rachel A.	MS6-O-1 Indium segregation at stacking faults in zincblende InGaN epilayers MS7-O-4 Understanding local crystallography in solar cells materials with scanning electron diffraction using unsupervised machine learning
Olluyn, Noa	MS4-P-6 Assessing the morphology and fractal properties of aggregated nanoparticles in 2 and 3 dimensions by transmission electron microscopy
Omerzu, Aleš	MS6-P-5 Photocatalytic activity of thin ZnO films deposited at room temperature by plasma-enhanced atomic layer deposition
Önder, Melike Nur	MS4-P-1 Investigation of Boron-Based Nanosheets, Nanoscrolls and Nanotubes by TEM Analyses
Opelka, Jakub	LS6-O-2 Semi-automated Classification of Nanoparticle Signals from Opposite Surfaces of Ultrathin Sections in Low-Voltage STEM
Oprea, Ovidiu Cristian	MS6-P-19 Compositionally Graded Kesterite Nanostructured Film for Photovoltaic Applications
Ordejón, Pablo	MS6-IN-1 Automated analysis of STEM data of semiconductor heterostructures for quantum computing IMPRESS 1 End-to-end Autonomous Unveiling of Physical Knowledge of Quantum Devices through Electron Microscopy Data
Orgiani, Pasquale	MS6-P-1 Effects of processing gas on the growth of SrTiO3 Thin Films: a TEM study
Oršolić, Nada	LS8-P-1 Micro-CT analysis of femoral bone structure in ovariectomized rats following treatment with alendronate, hop extract and their combination LS4-P-7 Adiposoft-based analysis of visceral adipose tissue in ovariectomized rats treated with alendronate, hop extract, and their combination, stained with picrosirius red
Ostatnicky, Tomas	LS6-O-1 Volume Electron Microscopy Methods for Investigating Nitrogen Handling and Cellular Vision in Microscopic Algae
Ostermeier, Matthias	LS6-P-2 Bridging Flourescence and Electron Microscopy: R221 Resin for CLEM in Microbes and Plants
Otašević, Vesna M.	LS4-P-15 Therapeutic effects of H_2S donors on ferroptosis-mediated liver damage in C57BL/6 mice – a microscopic study LS4-P-12 Proferroptotic response to nutrient deprivation and sorafenib treatment in hepatocellular carcinoma cells – a microscopic study
Otón, Joaquín	IM7-P-1 InCAEM: A Singular Infrastructure for Advanced Energy Materials Research
Otoničar, Mojca	MS5-IN-1 Insight into Defects and Polarization in Lead-Free Ferroelectrics by Advanced STEM Techniques IM3-O-3 Exploring perovskites at the atomic level by 4DSTEM: Experimental & Simulation MS8-O-3 Structural modulations in antiferroelectric NaNbO3-based ceramics investigated by STEM
Ottaviani, Carlo	MS7-O-4 Understanding local crystallography in solar cells materials with scanning electron diffraction using unsupervised machine learning

Ottenwelter, Estelle	MS3-P-11 Sublayer structure in fire gilding layer on medieval jewellery
Ozgun, Gokcen	LS3-P-1 Protective effect of ferulic acid in monosodium glutamate-induced kidney injury: a light and transmission electron microscopical study
Ozonder, Furkan	Improving Bone Regeneration through Estrogen-Loaded Cement in a Modified Masquelet Approach
Ozturk, Ahmet	LS4-P-5 Brain Decellularization Process in Transgenic Alzheimer Rat Model
Ozturk, Canan	LS4-P-5 Brain Decellularization Process in Transgenic Alzheimer Rat Model
Padrón-Navarta, José Alberto	MS1-IN-2 The Past and Future of Electron Backscattered Diffraction (EBSD) in Earth Sciences
Paillard, Charles	IM3-O-3 Exploring perovskites at the atomic level by 4DSTEM: Experimental & Simulation
Pal, Viktor	LS1-O-2 Micropipette-Based Single-Cell Isolation from Live Spheroids.
Palacios-Rivera, Rogger	IM7-P-1 InCAEM: A Singular Infrastructure for Advanced Energy Materials Research
Palatinus, Lukáš	MS1-O-3 Sulfidic inclusions in the Muong Nong tektites from Laos
Panahi, Seyedeh Leila	IM7-P-1 InCAEM: A Singular Infrastructure for Advanced Energy Materials Research
Panasci, Salvatore Ethan	MS6-O-5 Advanced TEM characterization of 2D compound semiconductors
Panizon, Emanuele	IM8-O-2 Optimization of SEM Instrumental Parameters for Enhanced Imaging Applying Machine Learning
Parapari, Sorour Semsari	MS4-P-11 Investigation of Electrodeposition and Electrodissolution Mechanisms of Silver Nanoparticles Using Electrochemical Liquid Cell Transmission Electron Microscopy
Park, Hyoungwon	MS6-P-4 Spray-Coated Metallosurfactant-Alginate Coatings: Dual Antimicrobial Action
Parlanti, Paola	IM3-P-3 Combining 3D electron diffraction and nanotexture analysis for the characterization of meteorite's impact ejecta
Pascariu, Petronela	MS8-P-2 Influence of La, Er, and Sm Doping on the Structural and Morphological Properties of ZnO for EMI Shielding
Passarella, Alessandra	IM8-P-6 Fractal modelling and fracture mechanics of urban particle populations in biological tissues IM2-O-4 Urban particulate matter and human health: correlative microscopy methods and simulated tissues modeling.
Passuti, Sara	MS6-P-1 Effects of processing gas on the growth of SrTiO3 Thin Films: a TEM study MS4-P-7 Atomic-scale Investigation of FEL-Induced Structural Modifications in Pyrolytic Graphite via TEM Analysis
Paták, Aleš	MS4-P-8 Ab initio Study of Angle-Resolved Spectroscopy of Few-Layer Graphene IM1-O-2 Investigation of Electron Scattering in Ultrathin Films Using Time-of-Flight Spectroscopy
Pattison, Alexander	LS6-O-1 Volume Electron Microscopy Methods for Investigating Nitrogen Handling and Cellular Vision in Microscopic Algae

Paul, Domen	MS6-P-11 New Genesis XPS Spectrometer at the Jožef Stefan Institute for advanced surface and thin film characterization
Paulin, Irena	MS3-IN-2 The Microstructure and Mechanical Properties of LPBF Produced Nickel-based Alloy IN718 Influenced by Laser Beam Shape and Post Heat-Treatment
Pavić, Luka	MS8-P-4 SEM insights into crystallization behavior of oxide glass-ceramics
Pavlova, Elizaveta	LS7-P-2 Red blood cells morphological alterations during preparation for electron microscopy imaging IM5-P-4 Effects of different preparation methods and detector use on SEM imaging of bacterial flagella
Pavlova, Ewa	IM3-P-6 4D-STEM/PNBD: A semi-automated powder electron diffraction in SEM microscopes IM3-P-4 Automated processing of powder electron diffraction patterns IM5-IN-1 Novel embedding resins for volume EM with enhanced resistance to e-beam damage
Pécz, Béla	MS6-O-5 Advanced TEM characterization of 2D compound semiconductors MS6-O-4 Structural characterization of phase transformations in gallium oxide by transmission electron microscopy
Peharec Štefanić, Petra	LS3-P-6 Visualizing the algal response on polystyrene particles: A focus on EPS production
Peiró, Francesca	MS5-O-2 Investigating Local Structure in NBT-BT system Using (S)TEM Techniques IM8-O-5 Enhanced Low-Loss EELS Analysis through Hybrid Unsupervised and Supervised Machine Learning IM1-P-2 Low-energy Core-loss EELS as a Dose-effective Approach for Elemental and Oxidation State Mapping
Pelaez-Fernandez, Mario	IM1-P-2 Low-energy Core-loss EELS as a Dose-effective Approach for Elemental and Oxidation State Mapping
Pellei, Maura	LS4-P-16 Microscopy techniques to evaluate the cytotoxic effect induced by copper complexes on glioblastoma cells
Pennycook, Timothy J..	IM3-P-9 Sub-Angstrom Resolution at below 40 e-/Å2 with Electron Ptychography IM3-P-5 Electron ptychography experiment design with PtychoScopy
Perc, Valentina	MS2-P-1 Correlation Between Adhesion and Swimming Activity in Developing Zebrafish Exposed to Polystyrene and Polyethylene Micro- and Nanoplastics
Perčić, Marko	MS6-P-5 Photocatalytic activity of thin ZnO films deposited at room temperature by plasma-enhanced atomic layer deposition
Perez, Lucas	IM2-O-3 Investigating Magnetic Domain Wall Pinning in Nanowires via Correlative X-ray and Electron Transmission Microscopy
Pernitsch, Dominique	IM2-P-2 Fast and Frozen: Visualising a wide spectrum of specimens using Cryo-SEM combined with an on-site freeze fracture system LS7-P-3 Fast and Frozen: Visualising a wide spectrum of specimens using Cryo-SEM combined with an on-site freeze fracture system
Perrotta, Ida Daniela	LS4-IN-1 An ultrastructural perspective on cell death with a focus on atherosclerosis
Peskar, Dominika	LS3-O-3 Immunolocalisation of mechanosensory proteins PIEZO and TRPV4 in the urinary bladder urothelium: which method to believe?
Peter, Karolina	LS4-O-3 Morphological and Mechanical Characterization of Major Ampullate Spider Silk Fibers in Liquid Environments: Insights from SEM and Single-Fiber Tensile Testing

Peter, Robert	MS6-P-8 Optimizing Photocatalytic Degradation of Pollutants Using Cu-Doped ZnO and TiO2 Films Grown by ALD MS6-P-5 Photocatalytic activity of thin ZnO films deposited at room temperature by plasma-enhanced atomic layer deposition MS6-P-6 Electron microscopy investigation of Cu-TiO2 nanocomposites for solar-driven photocatalysis MS6-P-9 Atomic layer deposition of nitrogen-doped TiO2 thin films for photocatalytic applications
Petrič, Lara	MS1-P-4 Effect of pretreatment and organic fibre reinforcement on the mechanical and microstructural properties of microwave irradiated alkali-activated radioactive fly ash
Petrillo, Caterina	MS4-P-7 Atomic-scale Investigation of FEL-Induced Structural Modifications in Pyrolytic Graphite via TEM Analysis
Pham, Sang	MS2-O-3 4D-STEM of Soft Matter: Structural Characterisation of Beam-Sensitive Polymers and Molecular Crystals Using Fast Precession and a Direct Electron Detector on a Tescan Tensor
Phifer, Daniel	Comprehensive and intuitive analysis with Apreo ChemiSEM™, ChemiPhase™ and TruePix EBSD™"
Piccinini, Filippo	IM8-O-1 ViFoSe, an user-friendly open-source post-processing tool for foreground segmentation in time-lapse videos. LS1-O-2 Micropipette-Based Single-Cell Isolation from Live Spheroids.
Pietralunga, Silvia Maria	IM3-P-8 Surface and sub-surface defect analysis in semiconductors by Secondary Electron Emission Spectroscopy and local charge transport mapping IM1-P-7 Quantum state secondary electron emission spectroscopy in low voltage scanning electron microscope for probing Valence band IM1-O-3 Perspectives of ultrafast hyperspectral imaging in Scanning Electron Microscopy
Pilát, Zdeněk	IM1-P-6 Raman tweezers for the analysis of secondary microplastics generated by degradation of surgical masks in water
Pilatova, Jana	LS6-O-1 Volume Electron Microscopy Methods for Investigating Nitrogen Handling and Cellular Vision in Microscopic Algae
Piňos, Jakub	IM1-O-2 Investigation of Electron Scattering in Ultrathin Films Using Time-of-Flight Spectroscopy
Pinto-Huguet, Ivan	MS6-IN-1 Automated analysis of STEM data of semiconductor heterostructures for quantum computing IMPRESS 1 End-to-end Autonomous Unveiling of Physical Knowledge of Quantum Devices through Electron Microscopy Data
Pirih, Primož	LS2-P-1 The sexually dimorphic retina of a butterfly, from microspectrophotometry to connectomics
Plana-Ruiz, Sergi	MS5-O-2 Investigating Local Structure in NBT-BT system Using (S)TEM Techniques IM3-O-2 Electric Field and Pair Distribution Function mapping by Precession Scanning Electron Diffraction (4D-SPED) in TEM
Plank, Harald	MS8-IN-1 Adaptive 3D Nanoprinting via Focused Electron Beams: Precision, Functionality, and Beyond
Plevka, Pavel	Enterovirus genome release and delivery
Plodinec, Milivoj	IM7-O-1 Atomic-Scale Dynamics of Ni Catalysts Revealed by Operando TEM in Dry Reforming of Methane

Ploszczanski, Leon	LS4-O-3 Morphological and Mechanical Characterization of Major Ampullate Spider Silk Fibers in Liquid Environments: Insights from SEM and Single-Fiber Tensile Testing MS6-P-16 Microscopical study of 19th century photomechanical prints: in-situ investigations in museum collections MS6-P-17 Microscopic Identification of Daguerreotypes Through Hallmark Analysis
Poberžnik, Matic	MS5-IN-1 Insight into Defects and Polarization in Lead-Free Ferroelectrics by Advanced STEM Techniques MS7-O-1 Charge density distribution in single-atom-on-substrate catalysts
Podgornik, Bojan	MS3-IN-2 The Microstructure and Mechanical Properties of LPBF Produced Nickel-based Alloy IN718 Influenced by Laser Beam Shape and Post Heat-Treatment
Podlogar, Matejka	MS6-P-8 Optimizing Photocatalytic Degradation of Pollutants Using Cu-Doped ZnO and TiO2 Films Grown by ALD MS1-P-9 Comprehensive study of Inversion Boundaries in ZnO MS6-P-5 Photocatalytic activity of thin ZnO films deposited at room temperature by plasma-enhanced atomic layer deposition MS6-P-6 Electron microscopy investigation of Cu-TiO2 nanocomposites for solar-driven photocatalysis MS1-P-3 Crystal structure of wulfenite crystals from Mežica analysed by SEM-FIB and TEM MS6-P-18 Characterization of ZnO Films Prepared via FIB-SEM MS1-P-15 FIB-SEM characterization of various types of materials
Podobnik, Marjetka	IM4-P-2 Activities of the cryo-EM facility at the National Institute of Chemistry, Slovenia IM4-O-2 A closer look at the protein-lipid complex of actinoporin pores IM4-IN-1 Use of cryo-EM to study filamentous plant viruses and their virus-like particles
Pogačar, Karmen	LS8-O-2 Spatiotemporal acquisition of genetically encoded biosensors in intact plant leaves reveals hormonal crosstalk in response to wounding
Poghosyan, Emiliya	IM3-P-5 Electron ptychography experiment design with PtychoScopy
Pohl, Felix	MS4-P-9 Thermal and Chemical Stability of High-Entropy-Alloy Nanoparticles Synthesized via Laser Ablation in Organic Liquid
Polishchuk, Roman	IM2-IN-2 Correlative Light-Electron Microscopy: A Precision Tool for Unraveling Complex Cellular Processes in Health and Disease
Pompe Novak, Maruša	LS4-P-9 The Effect of a Novel SARS-CoV E Protein Inhibitor on Ultrastructure of Murine Hepatitis Virus-Infected L-929 Cells LS2-P-2 Ultrastructure and gene expression in tomato flower pedicel abscission zone
Popov, Maxim N.	MS3-O-2 Atomic-resolution electron microscopy analysis of oxygen-mediated Ti nanocrystalline synthesized by high-pressure torsion
Popovic, Aleksandra	LS4-IN-2 Expression of GABA-A receptors in brain tumors
Popović, Jasminka	MS3-O-3 (S)TEM study of the WTaVCr alloy for fusion application
Popović, Stefan	MS7-P-10 How to Perform Identical Location Scanning Electron Microscopy: Workflow, Advantages, Challenges, and Applications

Porrelli, Davide	LS3-P-10 Optimization of Sample Preparation and Scanning Electron Microscopy Imaging for the Investigation of Trebouxia Flagellate Cells
Portillo, Joaquim	IM3-O-2 Electric Field and Pair Distribution Function mapping by Precession Scanning Electron Diffraction (4D-SPED) in TEM
Poschmann, Michael	IM1-P-5 Advanced EELS techniques in catalyst analysis
Potokar, Maja	LS5-O-1 Exploring Plectin's Function in Migration of Astrocytes and Glioblastoma Through Confocal Microscopy LS6-IN-1 Advanced Microscopy Approaches Unveil Plectin as a Key Regulator of Focal Adhesions in Astrocytes
Pozzi, Giulio	IMPRESS 4 Electrostatic potential measurement at liquid helium temperature using off-axis electron holography
Pradhan, Bapi	MS6-IN-2 Advanced low dose electron microscopy of metal halide perovskites
Predojević, Luka	Microscopy-based analysis of biomimetic 2D and 3D in vitro models for preclinical studies
Pregelj, Matej	MS5-P-4 Synthesis Strategies for Effective Doping of Barlowite
Pren, Tin	LS2-O-2 Membrane Segmentation in Volumetric Electron Microscopy Data
Prenassi, Marco	IM8-O-2 Optimization of SEM Instrumental Parameters for Enhanced Imaging Applying Machine Learning
Pretto, Tobia	LS4-P-2 Virome of the invasive signal crayfish and its correlation with histopathological changes of the hepatopancreas
Price, Patrick	IMPRESS 6 NanoMi: An open-source electron microscope
Primc, Darinka	MS8-P-5 Probing beam-sensitive MOF mesocrystals at the nanoscale using 4D-STEM scanning nanodiffraction
Primc, Gregor	MS6-P-11 New Genesis XPS Spectrometer at the Jožef Stefan Institute for advanced surface and thin film characterization
Profumo, Filippo	MS6-P-12 In situ TEM dynamics of Au and Au/zirconia clusters in nanostructured thin films: a quantitative analysis
Propst, Diana	IM2-O-1 Correlative microscopy: Uncovering the role of vacancies and contamination on the mechanical stiffness of defect-engineered graphene. IM8-IN-1 Convolutional neural networks for scanning transmission electron microscopy image analysis: Towards automated analysis of large volume datasets
Proust, Bastien	LS5-P-2 Unraveling the Noncanonical Mitochondrial Import Signals of NME6 – a Member of the NME/NDPK Family
Průcha, Lukáš	MS4-P-8 Ab initio Study of Angle-Resolved Spectroscopy of Few-Layer Graphene IM1-O-2 Investigation of Electron Scattering in Ultrathin Films Using Time-of-Flight Spectroscopy
Prymak, Oleg	MS4-P-9 Thermal and Chemical Stability of High-Entropy-Alloy Nanoparticles Synthesized via Laser Ablation in Organic Liquid
Punčuh, Alen	Microscopy-based analysis of biomimetic 2D and 3D in vitro models for preclinical studies

Purelku, Merjem	Improving Bone Regeneration through Estrogen-Loaded Cement in a Modified Masquelet Approach LS4-O-2 The First Identification of Telocyte Cells in the Human Ovarian Stroma: Morphological and Immunophenotypical Characterization
Putar, Darija	LS5-IN-1 Dictyostelium discoideum IQGAP proteins IqgC and IqgD - siblings or distant relatives
Pyun, Jae-Chul	IM8-O-1 ViFoSe, an user-friendly open-source post-processing tool for foreground segmentation in time-lapse videos.
Qin, Bin	IM6-P-2 Development and Application of an Aberration Calculation Program for Electron Lenses Based on Differential Algebra
Qu, Qiulin	MS3-O-2 Atomic-resolution electron microscopy analysis of oxygen-mediated Ti nanocrystalline synthesized by high-pressure torsion
Radenković, Marko	LS7-P-2 Red blood cells morphological alterations during preparation for electron microscopy imaging IM5-P-4 Effects of different preparation methods and detector use on SEM imaging of bacterial flagella
Radičić, Rafaela	MS6-P-8 Optimizing Photocatalytic Degradation of Pollutants Using Cu-Doped ZnO and TiO2 Films Grown by ALD
Radošević, Tina	MS6-P-5 Photocatalytic activity of thin ZnO films deposited at room temperature by plasma-enhanced atomic layer deposition MS6-P-18 Characterization of ZnO Films Prepared via FIB-SEM MS1-P-15 FIB-SEM characterization of various types of materials
Radtke, Christine	LS4-O-3 Morphological and Mechanical Characterization of Major Ampullate Spider Silk Fibers in Liquid Environments: Insights from SEM and Single-Fiber Tensile Testing
Radulovic, Snjezana	LS4-P-11 Post mortem degradation of ferritin and its significance for determining the iron content of the human brain LS2-O-4 Some neurons are better connected than others in a locust's network of visual interneurons
Rakici, Gafur	LS4-P-4 The Effects of Amylin on Aggression in Wistar Rats Exposed to the Resident-Intruder Paradigm
Ramadan, Mervan	IM7-P-3 Novel Nano Channel Chip for In Situ TEM Liquid Cell Analysis and Particle Trapping Without Manual Preassembly of Chip
Ramasse, Quentin	IM1-IN-1 Beyond phonon spectroscopy: progress in high-resolution STEM-EELS MS5-P-1 Probing Magnons with High-Energy Electrons: Theoretical Insights into Spin and Charge Scattering in STEM-EELS
Ramermann, Daniela	IM1-P-5 Advanced EELS techniques in catalyst analysis
Ramšak, Živa	LS2-P-2 Ultrastructure and gene expression in tomato flower pedicel abscission zone
Rašković, Božidar	LS3-P-3 Histopathology of the gills of farmed common carp (Cyprinus carpio): a bioindication method
Rätzel, Dennis	IM6-O-1 Entanglement in Bragg Scattering
Ravenscroft, Neil	LS8-O-3 The exopolysaccharide EpsA-O has a decisive role in 3D microstructure formation of Bacillus subtilis biofilm
Raventós, Marc	IM7-P-1 InCAEM: A Singular Infrastructure for Advanced Energy Materials Research
Rawski, Michał	IM4-P-3 Optimization of macromolecules imaging in Cryo EM method

Ražnjević, Sergej	MS1-O-4 Oxygen vacancy distribution in different regions of La1−xSrxGa1−yMgyO3−δ
Rečnik, Aleksander	MS1-P-9 Comprehensive study of Inversion Boundaries in ZnO MS8-P-6 Quantum chemical simulation of spontaneous water dissociation on 110 || 110 rutile TiO2 interfaces Atomistic structure of interfaces: Where theory and experiment meet
Reghioua, Imène	IM1-P-3 Irradiation-induced point defects in optical fibers investigated by cathodoluminescence microscopy and spectroscopy.
Rehbock, Christoph	MS4-P-9 Thermal and Chemical Stability of High-Entropy-Alloy Nanoparticles Synthesized via Laser Ablation in Organic Liquid
Reimer, Robert	LS2-O-4 Some neurons are better connected than others in a locust's network of visual interneurons
Remondini, Daniel	LS1-O-2 Micropipette-Based Single-Cell Isolation from Live Spheroids.
Repič, Rožle	LS8-O-4 XCT state-of-the-art scanning modality for the characterization of 3D-printed flat panels LS8-P-4 3D visualisation of wood: 3D X-ray microtomography and 3D printing
Resnik, Nataša	LS4-P-18 Revealing LRAT and NeuroD1 Colocalization in human urothelial cancer cells in vivo using proximity ligation assay LS4-P-17 Revealing Disparities in Macropinocytosis Between Bladder Cancer and Normal Urothelial Cells: Implications for Targeted Therapy LS3-P-11 Unveiling tunnelling nanotubes in urothelial spheroids and bladder cancer biopsy samples LS4-O-4 Periodontal and bone regeneration with magnesium barrier membranes: an in vitro study Microscopy-based analysis of biomimetic 2D and 3D in vitro models for preclinical studies
Restović, Ivana	LS3-P-2 Ultrastructural changes of the injured renal tissues in the cage-reared rainbow trout Oncorhynchus mykiss (Walbaum, 1792)
Režonja, Blaž	LS1-O-4 High-throughput automated quantitative fluorescence microscopy and image feature analysis for in vitro detection of adverse effects
Ribić, Vesna	MS1-P-9 Comprehensive study of Inversion Boundaries in ZnO MS8-P-6 Quantum chemical simulation of spontaneous water dissociation on 110 || 110 rutile TiO2 interfaces Atomistic structure of interfaces: Where theory and experiment meet
Rinaldi, Luca	IM8-O-1 ViFoSe, an user-friendly open-source post-processing tool for foreground segmentation in time-lapse videos.
Rind, F. Claire	LS2-O-4 Some neurons are better connected than others in a locust's network of visual interneurons
Robson, Joanne	LS8-O-2 Spatiotemporal acquisition of genetically encoded biosensors in intact plant leaves reveals hormonal crosstalk in response to wounding
Rocaglia, Alberto	IM1-O-1 First demonstration of angular-momentum-resolved electron energy-loss spectroscopy
Roccaforte, Fabrizio	MS6-O-5 Advanced TEM characterization of 2D compound semiconductors
Roche, Stephan	MS6-IN-1 Automated analysis of STEM data of semiconductor heterostructures for quantum computing IMPRESS 1 End-to-end Autonomous Unveiling of Physical Knowledge of Quantum Devices through Electron Microscopy Data

Rodani, Tommaso	IM8-O-2 Optimization of SEM Instrumental Parameters for Enhanced Imaging Applying Machine Learning
Rodgers, Thomas	MS6-O-3 Multi-modal Microscopy Analysis of Co-doped InAs/GaAs Quantum Dot Lasers
Rodič, Peter	MS3-P-8 Composition and microstructure of wrought and additively manufactured DED-LB of Ti-6Al-4V alloy MS6-P-11 New Genesis XPS Spectrometer at the Jožef Stefan Institute for advanced surface and thin film characterization
Rođak, Edi	LS8-P-1 Micro-CT analysis of femoral bone structure in ovariectomized rats following treatment with alendronate, hop extract and their combination LS4-P-7 Adiposoft-based analysis of visceral adipose tissue in ovariectomized rats treated with alendronate, hop extract, and their combination, stained with picrosirius red
Roeffaers, Maarten	MS6-IN-2 Advanced low dose electron microscopy of metal halide perovskites
Rogan Šmuc, Nastja	MS1-P-3 Crystal structure of wulfenite crystals from Mežica analysed by SEM-FIB and TEM
Roknič, Janina	MS5-IN-1 Insight into Defects and Polarization in Lead-Free Ferroelectrics by Advanced STEM Techniques MS1-P-10 Effects of Ti Doping on Structure, Microstructure and Mechanical Properties of (K0.5Na0.5)NbO3
Romanitan, Cosmin	MS8-P-2 Influence of La, Er, and Sm Doping on the Structural and Morphological Properties of ZnO for EMI Shielding
Romih, Rok	LS2-O-2 Membrane Segmentation in Volumetric Electron Microscopy Data LS3-O-3 Immunolocalisation of mechanosensory proteins PIEZO and TRPV4 in the urinary bladder urothelium: which method to believe? LS2-O-3 Volume electron microscopy of intracellular compartments in the urinary bladder epithelium LS3-P-15 Distribution of Golgi matrix proteins GRASP65 and GRASP55 during early urothelial regeneration Microscopy-based analysis of biomimetic 2D and 3D in vitro models for preclinical studies
Romolo, Anna	LS3-O-2 Nanoalgosomes as observed by scanning and cryogenic transmission electron microscopes LS3-P-7 Insight into the particle-based nature of mucilage as a response of Chlorella sorokiniana cell to manganese excess
Roncaglia, Alberto	IMPRESS 8 Multi-purpose MEMS devices for correlative operando experiments in battery research
Ronchese, Paolo	IMPRESS 8 Multi-purpose MEMS devices for correlative operando experiments in battery research
Ropele, Stefan	LS4-P-11 Post mortem degradation of ferritin and its significance for determining the iron content of the human brain
Rosas, Gemma	IM7-P-1 InCAEM: A Singular Infrastructure for Advanced Energy Materials Research
Rosi, Paolo	IM1-O-1 First demonstration of angular-momentum-resolved electron energy-loss spectroscopy IMPRESS 9 Artificial Intelligence for TEM: Real-Time Automation and Predictive Analysis in In Situ Experiments IM6-O-3 Electron Beam Shaping with a MEMS Phase Plate via Current-Controlled Electrostatic Potential

Rotunno, Enzo	MS6-IN-1 Automated analysis of STEM data of semiconductor heterostructures for quantum computing IM1-O-1 First demonstration of angular-momentum-resolved electron energy-loss spectroscopy IMPRESS 9 Artificial Intelligence for TEM: Real-Time Automation and Predictive Analysis in In Situ Experiments AI-Driven Automation and Data-Centric Workflows in TEM IMPRESS 1 End-to-end Autonomous Unveiling of Physical Knowledge of Quantum Devices through Electron Microscopy Data
Rozman, Špela	LS1-O-4 High-throughput automated quantitative fluorescence microscopy and image feature analysis for in vitro detection of adverse effects
Rozsa, Balazs	LS1-O-1 Immersive Virtual Reality System for Mice Combined with 3D-Targeted Photostimulation as a Prototype for Visual Restoration
Rózsa, Noémi Katinka	MS1-P-6 Transmission electron microscopy of hypomineralized enamel apatite nanocrystals
Rudolf, Rok	LS8-O-4 XCT state-of-the-art scanning modality for the characterization of 3D-printed flat panels
Ruiz-Gómez, Sandra	IM2-O-3 Investigating Magnetic Domain Wall Pinning in Nanowires via Correlative X-ray and Electron Transmission Microscopy IM7-P-1 InCAEM: A Singular Infrastructure for Advanced Energy Materials Research
Ruiz-Zepeda, Francisco	MS1-O-1 Direct observation of phase transformations during dehydration of cementitious phases at high temperatures MS7-P-8 Microstructure and stability of carbon wrapped Cu@Cu2O nanowires MS1-P-3 Crystal structure of wulfenite crystals from Mežica analysed by SEM-FIB and TEM
Ruland, Holger	IM1-P-5 Advanced EELS techniques in catalyst analysis
Ruttiman, Sam	IMPRESS 6 NanoMi: An open-source electron microscope
Ryan, Rego	LS7-IN-2 Sample Preparation Strategies for Biological Electron Microscopy: Challenges and Innovations
Sacchetti, Francesco	MS4-P-7 Atomic-scale Investigation of FEL-Induced Structural Modifications in Pyrolytic Graphite via TEM Analysis
Saeki, Hayato	IM8-P-3 EELS spectrum analysis using Bayesian estimation
Sáfrán, György Gyula	MS6-O-4 Structural characterization of phase transformations in gallium oxide by transmission electron microscopy IM5-P-1 EDIC; A new method to enhance reliability of structure determination, using electron diffraction data correction IM5-P-5 High throughput micro-combinatorial study of microstructure and materials properties of binary and ternary layer systems
Sag, Fatma Beyza	LS3-P-12 Does endoplasmic reticulum stress contribute to the damage of trophoblast cells caused by bisphenol A?
Saha, Ambarneil	LS6-O-1 Volume Electron Microscopy Methods for Investigating Nitrogen Handling and Cellular Vision in Microscopic Algae
Şahin, Hakan	LS4-P-14 Human Serum Albumin Nanoparticles as a Drug Delivery System to Enhance Temozolomide Efficacy in Glioblastoma Cell Line LS4-P-1 Investigation of the Therapeutic Effects of Allium cepa Extract on Ovaries and Uterus in Chronically Administered DHEA Rats by Apoptotic Pathways

Sahin, Simal Yaren	LS5-P-3 EFFECT OF DECELLULARIZED PLACENTA-DERIVED ECM MOLECULES ON IN VITRO ANGIOGENESIS
Saje, Špela	LS3-P-9 Cytotoxicity Assessment of Functionalized Graphene-Based Composites IM5-P-2 The Power of FIB-SEM for Visualizing the Internalization of 2D Materials In Vitro
Saksida, Tamara A.	LS4-P-12 Proferroptotic response to nutrient deprivation and sorafenib treatment in hepatocellular carcinoma cells – a microscopic study
Salamon, Krešimir	MS6-P-5 Photocatalytic activity of thin ZnO films deposited at room temperature by plasma-enhanced atomic layer deposition MS6-P-6 Electron microscopy investigation of Cu-TiO2 nanocomposites for solar-driven photocatalysis
Salazar-Alvarez, Germán	IM1-P-2 Low-energy Core-loss EELS as a Dose-effective Approach for Elemental and Oxidation State Mapping
Salomons, Mark	IMPRESS 6 NanoMi: An open-source electron microscope
Samardžija, Zoran	MS1-P-11 Advanced quantitative EPMA-WDS approach for accurate compositional analysis of cerium-doped barium titanate ceramics
Samek, Ota	IM1-P-6 Raman tweezers for the analysis of secondary microplastics generated by degradation of surgical masks in water
Santini, Carlo	LS4-P-16 Microscopy techniques to evaluate the cytotoxic effect induced by copper complexes on glioblastoma cells
Santrač, Isidora	LS3-P-7 Insight into the particle-based nature of mucilage as a response of Chlorella sorokiniana cell to manganese excess
Sardoč, Žiga	Microscopy-based analysis of biomimetic 2D and 3D in vitro models for preclinical studies
Šarić Janković, Iva	MS6-P-6 Electron microscopy investigation of Cu-TiO2 nanocomposites for solar-driven photocatalysis MS6-P-9 Atomic layer deposition of nitrogen-doped TiO2 thin films for photocatalytic applications
Sarneri, Michele	IM8-O-1 ViFoSe, an user-friendly open-source post-processing tool for foreground segmentation in time-lapse videos.
Sattler, Birgit	MS2-P-2 Plastic-Degrading or Just Settling? First TEM insights into microbial-plastic interactions in a Cold-Climate Ecosystem
Savić, Nevena N.	LS4-P-15 Therapeutic effects of H_2S donors on ferroptosis-mediated liver damage in C57BL/6 mice – a microscopic study LS4-P-12 Proferroptotic response to nutrient deprivation and sorafenib treatment in hepatocellular carcinoma cells – a microscopic study
Scappucci, Giordano	MS6-IN-1 Automated analysis of STEM data of semiconductor heterostructures for quantum computing IMPRESS 1 End-to-end Autonomous Unveiling of Physical Knowledge of Quantum Devices through Electron Microscopy Data
Schaaf, Michael	IMPRESS 13 Time-resolved imaging of dynamic and resonant spin phenomena in situ in the TEM
Schäfer, Sascha	IMPRESS 11 Mechanical strain and light-induced control of magnetic states in Fe3Sn2 in situ in the TEM
Schafler, Erhard	MS3-P-12 The impact of high hydrostatic pressure annealing on microstructure evolution
Schattschneider, Peter	IM6-O-1 Entanglement in Bragg Scattering

Scheu, Christina	MS4-O-1 3D Identical Location STEM Insights into the Degradation of Metallic Core-Shell Nanoparticles under Fuel Cell Conditions
Schimpke, Ronny	MS7-P-3 Microstructural analysis of the copper matrix composites for electrodes of plasma torches
Schleusener, Alexander	MS8-O-1 Low-dose 4DSTEM analysis of local strain in 2D perovskite lateral heterostructures
Schloz, Marcel	IM3-IN-1 Developments in 4D-STEM and Ptychography: From Series Registration to Live Compression
Schmid, Luca	LS4-P-11 Post mortem degradation of ferritin and its significance for determining the iron content of the human brain
Schnedler, Michael	IMPRESS 5 Quantifying carbon site switching dynamics in GaN by off-axis electron holography IMPRESS 3 Characterization of electric and magnetic fields at interfaces in manganese-containing heterostructures using correlative TEM techniques
Scholz, Sophie	MS4-P-10 Physicochemical characterization of copper oxides applied as feed additives and plant protection products
Schreiber, Makoto	IMPRESS 6 NanoMi: An open-source electron microscope
Schrenker, Nadine Julia	MS6-IN-2 Advanced low dose electron microscopy of metal halide perovskites
Schultz, Johannes	IM6-O-2 Miniaturized Magnetic Multipoles for Ultrafast Beam Shaping in the Transmission Electron Microscope IM6-IN-2 Electron Optics and Beam Shaping with a Special View on EELS
Schürmann, Ulrich	IM7-O-2 Advancements in Plasma Microcell Integration for in situ TEM Experiments MS4-P-9 Thermal and Chemical Stability of High-Entropy-Alloy Nanoparticles Synthesized via Laser Ablation in Organic Liquid
Sculean, Anton	LS4-O-4 Periodontal and bone regeneration with magnesium barrier membranes: an in vitro study
Sedláček, Petr	LS7-O-2 Ultrastructural Analysis of Azotobacter vinelandii Encapsulated in Alginate Hydrogel Using Cryogenic Preparation and Electron Microscopy Techniques LS7-P-1 Structural Stabilization of Alginate for Imaging Hydrogel-encapsulated Bacterial Cells Using LV-STEM
Seifer, Shahar	IM3-IN-2 Low-Dose 4D STEM for Cross-Disciplinary Materials Characterisation
Selby, Thomas	MS5-O-1 The magnetic microstructure in FeCo alloys and its interaction with non-magnetic inclusions
Seme, Katja	LS4-P-10 Antiviral Efficacy of Electrolysed Saline (EOS) Against Both Enveloped and Non-Enveloped Viruses: A TEM Study
Semsari Parapari, Sorour	MS1-P-12 Complex polycrystalline clusters of diamond and graphite from metamorphic rocks MS1-O-1 Direct observation of phase transformations during dehydration of cementitious phases at high temperatures MS1-P-3 Crystal structure of wulfenite crystals from Mežica analysed by SEM-FIB and TEM

Şentürk, Gözde Erkanlı	LS4-P-14 Human Serum Albumin Nanoparticles as a Drug Delivery System to Enhance Temozolomide Efficacy in Glioblastoma Cell Line LS4-P-1 Investigation of the Therapeutic Effects of Allium cepa Extract on Ovaries and Uterus in Chronically Administered DHEA Rats by Apoptotic Pathways
Sepčić, Kristina	LS3-P-8 Light and Transmission Electron Microscopy Complement Functional Genomics Screening in Chlamydomonas reinhardtii to Reveal Novel Mechanisms of Susceptibility to Herbicide Paraquat
Sepúlveda, Borja	IM8-O-5 Enhanced Low-Loss EELS Analysis through Hybrid Unsupervised and Supervised Machine Learning
Serényi, Miklós	IM5-P-5 High throughput micro-combinatorial study of microstructure and materials properties of binary and ternary layer systems
Servetto, Giulia Pia	IM8-P-6 Fractal modelling and fracture mechanics of urban particle populations in biological tissues IM2-O-4 Urban particulate matter and human health: correlative microscopy methods and simulated tissues modeling.
Šest, Irena	LS4-P-10 Antiviral Efficacy of Electrolysed Saline (EOS) Against Both Enveloped and Non-Enveloped Viruses: A TEM Study
Šetina Batič, Barbara	MS3-P-6 Laser Surface Functionalization of 316L Stainless Steel Under Ambient and Inert Argon Atmospheres MS3-P-10 SEM and EDS characterization of 316L Stainless Steel exposed to Different Bacteria
Sevenants, Linde	MS4-P-10 Physicochemical characterization of copper oxides applied as feed additives and plant protection products
Seybold, Anna	MS2-P-2 Plastic-Degrading or Just Settling? First TEM insights into microbial-plastic interactions in a Cold-Climate Ecosystem
Sezen Ozkoc, Meltem	From Slices to Structure: Volume EM in Life Sciences
Sezer, Seda	LS3-P-1 Protective effect of ferulic acid in monosodium glutamate-induced kidney injury: a light and transmission electron microscopical study
Sezer, Zehra	LS4-P-13 Effect of endometrial environment on chromatin abnormalities of sperm LS3-P-13 The Adaptation of Mitochondrial Dynamics to Hormonal Changes in the Endometrium and Placenta LS3-P-12 Does endoplasmic reticulum stress contribute to the damage of trophoblast cells caused by bisphenol A?
Sfuncia, Gianfranco	MS6-O-5 Advanced TEM characterization of 2D compound semiconductors
Shah, Aadil Abass	MS8-O-3 Structural modulations in antiferroelectric NaNbO3-based ceramics investigated by STEM
Shaikh, Talha Mehtab	IM7-P-1 InCAEM: A Singular Infrastructure for Advanced Energy Materials Research
Sháněl, Ondřej	IM6-P-3 Aberration correctors and their benefits in SEM
Shapoval, Oleksandr	MS2-IN-1 Multimodal in vitro and in vivo tissue imaging: Design, synthesis and surface engineering of nanoprobes
Sharma, Sayantan	MS7-O-3 Real Time Imaging of Lithium-Ion Transport in Solid-State Batteries: An Operando FIB-SIMS approach IM8-O-3 Mitigating beam damage during FIB-SIMS imaging: a new methodology using alternative FIB scans

Shutts, Samuel	MS6-O-3 Multi-modal Microscopy Analysis of Co-doped InAs/GaAs Quantum Dot Lasers
Siciliani, Lisa	MS4-P-10 Physicochemical characterization of copper oxides applied as feed additives and plant protection products
Siebenhofer, Matthäus	MS1-O-4 Oxygen vacancy distribution in different regions of La1−xSrxGa1−yMgyO3−δ
Siebentritt, Susanne	MS7-O-4 Understanding local crystallography in solar cells materials with scanning electron diffraction using unsupervised machine learning
Sieg, Holger	MS4-P-10 Physicochemical characterization of copper oxides applied as feed additives and plant protection products
Sielicki, Krzysztof	MS3-P-12 The impact of high hydrostatic pressure annealing on microstructure evolution
Sikorová, Pavlína	IM3-P-6 4D-STEM/PNBD: A semi-automated powder electron diffraction in SEM microscopes LS6-O-2 Semi-automated Classification of Nanoparticle Signals from Opposite Surfaces of Ultrathin Sections in Low-Voltage STEM IM3-P-4 Automated processing of powder electron diffraction patterns
Šiler, Martin	IM1-P-6 Raman tweezers for the analysis of secondary microplastics generated by degradation of surgical masks in water
Silva, Karolyne S	MS8-P-3 Y(Eu, Tb) frameworks with thiazolothiazoledicarboxylate: structural investigation by electron microscopy and diffraction techniques
Simpson, Robin	MS8-O-4 Correlative Imaging and Surface Analysis workflow
Simsek, Gonul	LS4-P-4 The Effects of Amylin on Aggression in Wistar Rats Exposed to the Resident-Intruder Paradigm
Singh, Gyanendra	IM3-O-2 Electric Field and Pair Distribution Function mapping by Precession Scanning Electron Diffraction (4D-SPED) in TEM
Sinn, Gerhard	LS4-O-3 Morphological and Mechanical Characterization of Major Ampullate Spider Silk Fibers in Liquid Environments: Insights from SEM and Single-Fiber Tensile Testing
Skakalova, Viera	IM8-IN-1 Convolutional neural networks for scanning transmission electron microscopy image analysis: Towards automated analysis of large volume datasets
Skála, Roman	MS1-O-3 Sulfidic inclusions in the Muong Nong tektites from Laos
Skobir Balantič, Danijela A.	MS3-IN-2 The Microstructure and Mechanical Properties of LPBF Produced Nickel-based Alloy IN718 Influenced by Laser Beam Shape and Post Heat-Treatment
Skoko, Željko	MS8-P-4 SEM insights into crystallization behavior of oxide glass-ceramics MS3-O-3 (S)TEM study of the WTaVCr alloy for fusion application
Skoupý, Radim	IM3-P-4 Automated processing of powder electron diffraction patterns LS7-O-3 Serial Block-Face Scanning Electron Microscopy (SBEM): Comparative Analysis of Protocols for Enhancing Contrast and Reducing Charging in Mouse Brain Tissue Samples IM3-P-5 Electron ptychography experiment design with PtychoScopy
Škrobot Vidaček, Nikolina	LS5-P-2 Unraveling the Noncanonical Mitochondrial Import Signals of NME6 – a Member of the NME/NDPK Family
Skvortsova, Irina	MS6-IN-2 Advanced low dose electron microscopy of metal halide perovskites

Slater, Thomas	MS4-IN-1 Dynamic Atomic Behaviour in 2D Heterostructures and Nanocatalysts
Šlouf, Miroslav	IM3-P-6 4D-STEM/PNBD: A semi-automated powder electron diffraction in SEM microscopes LS6-O-2 Semi-automated Classification of Nanoparticle Signals from Opposite Surfaces of Ultrathin Sections in Low-Voltage STEM IM3-P-4 Automated processing of powder electron diffraction patterns IM5-IN-1 Novel embedding resins for volume EM with enhanced resistance to e-beam damage
Smowton, Peter M	MS6-O-3 Multi-modal Microscopy Analysis of Co-doped InAs/GaAs Quantum Dot Lasers
Soares, Íris	MS6-P-4 Spray-Coated Metallosurfactant-Alginate Coatings: Dual Antimicrobial Action
Šolinc, Gašper	IM4-O-2 A closer look at the protein-lipid complex of actinoporin pores
Šoštarić, Ivan	LS6-P-1 Morphological features of Himantoglossum calcaratum (Beck) Schltr. subsp. calcaratum (Orchidaceae) pollinarium
Sotelšek, Tim	MS1-P-12 Complex polycrystalline clusters of diamond and graphite from metamorphic rocks
Šoufek, Marin	MS1-P-8 Multidisciplinary Application of Scanning Electron Microscopy (SEM) in Heritage Research, Conservation and Presentation at the Croatian Natural History Museum
Souza da Silva, Layrton José	MS4-P-11 Investigation of Electrodeposition and Electrodissolution Mechanisms of Silver Nanoparticles Using Electrochemical Liquid Cell Transmission Electron Microscopy
Soyama, Hitoshi	MS3-P-2 Plastic deformation in the Magnesium alloy AZ80 - an EBSD study of the effects of cavitation peening
Spadaro, Maria Chiara	MS6-IN-1 Automated analysis of STEM data of semiconductor heterostructures for quantum computing IMPRESS 1 End-to-end Autonomous Unveiling of Physical Knowledge of Quantum Devices through Electron Microscopy Data
Španić, Nikola	MS2-O-2 Nanocellulose-based Functional Nanocomposite Materials
Spreitzer, Matjaž	MS7-P-5 Atomic-scale insights into Solid-State Batteries via in situ TEM MS7-P-9 Impact of La0.07Ba0.93SnO3 interlayer on epitaxial growth of Li4Ti5O12 thin film anodes for all-solid-state Li-ion batteries
Sprengel, Wolfgang	IM3-O-1 Advanced STEM of Point Defect Clusters in Doped STO
Srnko, Marija	IM4-O-2 A closer look at the protein-lipid complex of actinoporin pores
Sršan, Vinko	MS1-O-4 Oxygen vacancy distribution in different regions of La1−xSrxGa1−yMgyO3−δ IM8-P-4 A Deep Learning Approach to Drift Correction in Atomic-Scale STEM Imaging
Stadlmayr, Sarah	LS4-O-3 Morphological and Mechanical Characterization of Major Ampullate Spider Silk Fibers in Liquid Environments: Insights from SEM and Single-Fiber Tensile Testing
Štampar, Martina	LS1-O-4 High-throughput automated quantitative fluorescence microscopy and image feature analysis for in vitro detection of adverse effects

Stančić, Ana T.	LS4-P-15 Therapeutic effects of H_2S donors on ferroptosis-mediated liver damage in C57BL/6 mice – a microscopic study LS4-P-12 Proferroptotic response to nutrient deprivation and sorafenib treatment in hepatocellular carcinoma cells – a microscopic study
Stanić, Denis	MS2-O-2 Nanocellulose-based Functional Nanocomposite Materials
Starčič Erjavec, Marjanca	Microscopy-based analysis of biomimetic 2D and 3D in vitro models for preclinical studies
Stare, Katja	LS8-O-2 Spatiotemporal acquisition of genetically encoded biosensors in intact plant leaves reveals hormonal crosstalk in response to wounding LS2-P-2 Ultrastructure and gene expression in tomato flower pedicel abscission zone LS3-P-8 Light and Transmission Electron Microscopy Complement Functional Genomics Screening in Chlamydomonas reinhardtii to Reveal Novel Mechanisms of Susceptibility to Herbicide Paraquat
Steiner, Martin	MS1-O-2 Impact of clay construction components on indoor aerosols: what can automated SEM-EDX and Raman reveal?
Steiner, Philip	LS2-O-1 Beyond Apoptosis: Unravelling Thapsigargin-Induced Non-Apoptotic Cell Death Pathways in Immune- and Cancer Cells
Stellato, Mariachiara	LS1-O-2 Micropipette-Based Single-Cell Isolation from Live Spheroids.
Stellino, Elena	MS4-P-7 Atomic-scale Investigation of FEL-Induced Structural Modifications in Pyrolytic Graphite via TEM Analysis
Stephan, Odile	IM1-IN-2 Recent advances in STEM spectroscopy using synchronized electron and photon beams
Štern, Alja	LS1-O-4 High-throughput automated quantitative fluorescence microscopy and image feature analysis for in vitro detection of adverse effects
Steyer, Andrej	LS4-P-10 Antiviral Efficacy of Electrolysed Saline (EOS) Against Both Enveloped and Non-Enveloped Viruses: A TEM Study
Štimac, Valentina	LS5-P-2 Unraveling the Noncanonical Mitochondrial Import Signals of NME6 – a Member of the NME/NDPK Family
Stöger-Pollach, Michael	LS4-P-11 Post mortem degradation of ferritin and its significance for determining the iron content of the human brain
Stoimchev, Marjan	MS5-IN-1 Insight into Defects and Polarization in Lead-Free Ferroelectrics by Advanced STEM Techniques IM8-P-4 A Deep Learning Approach to Drift Correction in Atomic-Scale STEM Imaging
Stone, Howard	MS5-O-1 The magnetic microstructure in FeCo alloys and its interaction with non-magnetic inclusions
Stopar, David	LS8-O-3 The exopolysaccharide EpsA-O has a decisive role in 3D microstructure formation of Bacillus subtilis biofilm MS3-P-10 SEM and EDS characterization of 316L Stainless Steel exposed to Different Bacteria
Strachota, Adam	IM5-IN-1 Novel embedding resins for volume EM with enhanced resistance to e-beam damage
Strachota, Beata	IM5-IN-1 Novel embedding resins for volume EM with enhanced resistance to e-beam damage
Stringaro, Annarita	LS4-P-16 Microscopy techniques to evaluate the cytotoxic effect induced by copper complexes on glioblastoma cells

Strnad, Martin	LS7-IN-2 Sample Preparation Strategies for Biological Electron Microscopy: Challenges and Innovations
Stroppa, Daniel	IM3-P-7 Contrast Optimization Aided by Machine Learning Applied to Virtual 4D-STEM Images IMPRESS 10 Applications Support for Complex TEM Workflows
Struckert, Robert	MS4-P-9 Thermal and Chemical Stability of High-Entropy-Alloy Nanoparticles Synthesized via Laser Ablation in Organic Liquid
Štulpa, Michal	IM1-O-2 Investigation of Electron Scattering in Ultrathin Films Using Time-of-Flight Spectroscopy
Šturm, Roman	MS3-P-2 Plastic deformation in the Magnesium alloy AZ80 - an EBSD study of the effects of cavitation peening
Šturm, Sašo	MS4-P-11 Investigation of Electrodeposition and Electrodissolution Mechanisms of Silver Nanoparticles Using Electrochemical Liquid Cell Transmission Electron Microscopy MS1-P-12 Complex polycrystalline clusters of diamond and graphite from metamorphic rocks MS1-O-1 Direct observation of phase transformations during dehydration of cementitious phases at high temperatures MS1-O-4 Oxygen vacancy distribution in different regions of La1−xSrxGa1−yMgyO3−δ IM8-P-4 A Deep Learning Approach to Drift Correction in Atomic-Scale STEM Imaging MS1-P-3 Crystal structure of wulfenite crystals from Mežica analysed by SEM-FIB and TEM MS1-P-15 FIB-SEM characterization of various types of materials
Suchanek, Martin	TESCAN lunch workshop: New solutions for advanced multimodal characterization of materials at the nanoscale Empowering Innovation in Science with Tescan Solutions
Suchea, Mirela	MS8-P-2 Influence of La, Er, and Sm Doping on the Structural and Morphological Properties of ZnO for EMI Shielding
Suhadolnik, Luka	MS7-P-10 How to Perform Identical Location Scanning Electron Microscopy: Workflow, Advantages, Challenges, and Applications
Súkeník, Martin	LS7-O-2 Ultrastructural Analysis of Azotobacter vinelandii Encapsulated in Alginate Hydrogel Using Cryogenic Preparation and Electron Microscopy Techniques
Sullivan-Allsop, Sam	MS4-IN-1 Dynamic Atomic Behaviour in 2D Heterostructures and Nanocatalysts
Sunkara, Sowmya	LS4-P-11 Post mortem degradation of ferritin and its significance for determining the iron content of the human brain
Šupolová, Zuzana	MS6-P-13 Etching and printing of daguerreotypes: experimental reconstruction and microscopic analysis of first photomechanical reproduction processes MS6-P-14 Nanoscale investigation of degradation processes in historical daguerreotype plates MS6-P-17 Microscopic Identification of Daguerreotypes Through Hallmark Analysis
Surdu, Adrian Vasile	MS6-P-19 Compositionally Graded Kesterite Nanostructured Film for Photovoltaic Applications

Susi, Toma	IM2-O-1 Correlative microscopy: Uncovering the role of vacancies and contamination on the mechanical stiffness of defect-engineered graphene. IM8-IN-1 Convolutional neural networks for scanning transmission electron microscopy image analysis: Towards automated analysis of large volume datasets
Šutić, Maja	LS5-P-2 Unraveling the Noncanonical Mitochondrial Import Signals of NME6 – a Member of the NME/NDPK Family
Sutter, Denys	IMPRESS 4 Electrostatic potential measurement at liquid helium temperature using off-axis electron holography
Svora, Petr	MS1-P-14 Study of vanadinite as painting pigment MS5-P-2 Are we observing channeling or magnetic contrast? MS3-P-4 TEM Analysis of Maraging Steel
Svorová Pawełkowicz, Sylwia	MS1-P-14 Study of vanadinite as painting pigment MS1-P-13 Exploring High-Baroque Stucco: Microscopy of Materials and Techniques at Kroměříž Chateau
Szalay, Gergely	LS1-O-1 Immersive Virtual Reality System for Mice Combined with 3D-Targeted Photostimulation as a Prototype for Visual Restoration
Szász, Noémi	MS1-P-6 Transmission electron microscopy of hypomineralized enamel apatite nanocrystals
Szebik, Huba	LS1-O-1 Immersive Virtual Reality System for Mice Combined with 3D-Targeted Photostimulation as a Prototype for Visual Restoration
Szepesi, Aron	LS1-O-1 Immersive Virtual Reality System for Mice Combined with 3D-Targeted Photostimulation as a Prototype for Visual Restoration
Tadić, Tonči	MS3-O-3 (S)TEM study of the WTaVCr alloy for fusion application
Tagliaferri, Alberto	IM3-P-8 Surface and sub-surface defect analysis in semiconductors by Secondary Electron Emission Spectroscopy and local charge transport mapping IM1-P-7 Quantum state secondary electron emission spectroscopy in low voltage scanning electron microscope for probing Valence band IM1-O-3 Perspectives of ultrafast hyperspectral imaging in Scanning Electron Microscopy
Tainton, Gareth	MS4-IN-1 Dynamic Atomic Behaviour in 2D Heterostructures and Nanocatalysts
Tang, Mingchu	MS6-O-3 Multi-modal Microscopy Analysis of Co-doped InAs/GaAs Quantum Dot Lasers
Tanriverdi, Bulent	Improving Bone Regeneration through Estrogen-Loaded Cement in a Modified Masquelet Approach
Tanriverdi, Gamze	LS4-P-14 Human Serum Albumin Nanoparticles as a Drug Delivery System to Enhance Temozolomide Efficacy in Glioblastoma Cell Line Improving Bone Regeneration through Estrogen-Loaded Cement in a Modified Masquelet Approach LS4-O-2 The First Identification of Telocyte Cells in the Human Ovarian Stroma: Morphological and Immunophenotypical Characterization

Tanwar, Ritik	IM3-P-8 Surface and sub-surface defect analysis in semiconductors by Secondary Electron Emission Spectroscopy and local charge transport mapping IM1-P-7 Quantum state secondary electron emission spectroscopy in low voltage scanning electron microscope for probing Valence band IM1-O-3 Perspectives of ultrafast hyperspectral imaging in Scanning Electron Microscopy
Tarjan, Balazs	LS1-O-1 Immersive Virtual Reality System for Mice Combined with 3D-Targeted Photostimulation as a Prototype for Visual Restoration
Tatti, Francesco	IM5-P-2 The Power of FIB-SEM for Visualizing the Internalization of 2D Materials In Vitro
Taubitz, Tatjana	IM2-O-2 Multimodal cryo-FIB-SIMS imaging on frozen-hydrated lamella of biological tissues
Tavabi, Amir Hossein	IMPRESS 9 Artificial Intelligence for TEM: Real-Time Automation and Predictive Analysis in In Situ Experiments A Bold Vision for Co-Developing the Future of TEM IMPRESS 2 The IMPRESS Project: Developing an Innovative Interoperable Platform for Next-Generation Transmission Electron Microscopy IMPRESS 13 Time-resolved imaging of dynamic and resonant spin phenomena in situ in the TEM IMPRESS 11 Mechanical strain and light-induced control of magnetic states in Fe3Sn2 in situ in the TEM IM1-O-1 First demonstration of angular-momentum-resolved electron energy-loss spectroscopy IMPRESS 8 Multi-purpose MEMS devices for correlative operando experiments in battery research
Tchernychova, Elena	MS7-P-9 Impact of La0.07Ba0.93SnO3 interlayer on epitaxial growth of Li4Ti5O12 thin film anodes for all-solid-state Li-ion batteries
Terracciano, Francesca	LS3-P-14 Characterization of red blood cells changes during storage by atomic force microscope
Teurtrie, Adrien	IM1-P-2 Low-energy Core-loss EELS as a Dose-effective Approach for Elemental and Oxidation State Mapping
Thajudeen, Thanveer	IM1-P-1 Cathodoluminescence spectroscopy study of plasmonic emissions in different Bi2Se3 systems
Tiemeijer, Peter	IM1-O-1 First demonstration of angular-momentum-resolved electron energy-loss spectroscopy
Timuroglu, Timucin	LS3-P-13 The Adaptation of Mitochondrial Dynamics to Hormonal Changes in the Endometrium and Placenta
Tizei, Luiz	Adaptive Optics and New Electron Detectors for Innovative TEM experiments IM1-IN-2 Recent advances in STEM spectroscopy using synchronized electron and photon beams
Tolić, Iva Marija	LS5-P-2 Unraveling the Noncanonical Mitochondrial Import Signals of NME6 – a Member of the NME/NDPK Family
Tollabimazraehno, Sajjad	Ion Milling System : ArBlade 5000
Tomc, Blaž	MS7-P-10 How to Perform Identical Location Scanning Electron Microscopy: Workflow, Advantages, Challenges, and Applications
Tomić Luketić, Kristina	MS3-O-3 (S)TEM study of the WTaVCr alloy for fusion application

Tominc, Sara	MS1-P-4 Effect of pretreatment and organic fibre reinforcement on the mechanical and microstructural properties of microwave irradiated alkali-activated radioactive fly ash MS1-P-5 Microwave-irradiated alkali-activated extraterrestrial simulants
Tomova, Cveta	Hydra Bio plasma FIB: pushing the boundaries to larger 3D volumes.
Toso, Stefano	MS6-IN-2 Advanced low dose electron microscopy of metal halide perovskites
Tóth, Éva	IM5-P-4 Effects of different preparation methods and detector use on SEM imaging of bacterial flagella
Tóth, Lázár	MS2-O-2 Nanocellulose-based Functional Nanocomposite Materials
Tratnjek, Larisa	LS4-P-17 Revealing Disparities in Macropinocytosis Between Bladder Cancer and Normal Urothelial Cells: Implications for Targeted Therapy LS3-P-11 Unveiling tunnelling nanotubes in urothelial spheroids and bladder cancer biopsy samples Microscopy-based analysis of biomimetic 2D and 3D in vitro models for preclinical studies
Travailleur, Allan	IM1-P-3 Irradiation-induced point defects in optical fibers investigated by cathodoluminescence microscopy and spectroscopy.
Trenti, Francesco	LS3-P-8 Light and Transmission Electron Microscopy Complement Functional Genomics Screening in Chlamydomonas reinhardtii to Reveal Novel Mechanisms of Susceptibility to Herbicide Paraquat
Trentino, Alberto	IM2-O-1 Correlative microscopy: Uncovering the role of vacancies and contamination on the mechanical stiffness of defect-engineered graphene. MS4-O-4 Metallene synthesis by ion irradiation: Growth of two-dimensional gold by vacancy-induced nucleation on defect-engineered graphene
Tretiach, Mauro	LS3-P-10 Optimization of Sample Preparation and Scanning Electron Microscopy Imaging for the Investigation of Trebouxia Flagellate Cells
Triglav, Tina	LS4-P-10 Antiviral Efficacy of Electrolysed Saline (EOS) Against Both Enveloped and Non-Enveloped Viruses: A TEM Study
Trusca, Roxana Doina	MS6-P-19 Compositionally Graded Kesterite Nanostructured Film for Photovoltaic Applications
Tsai, Shao-Pu	IM5-IN-2 The combination of high-resolution diffraction techniques in the scanning electron microscope for statistical relevant description of crystal defects and resulting properties in metals and alloys
Tušek Žnidarič, Magda	LS4-P-9 The Effect of a Novel SARS-CoV E Protein Inhibitor on Ultrastructure of Murine Hepatitis Virus-Infected L-929 Cells LS2-P-2 Ultrastructure and gene expression in tomato flower pedicel abscission zone LS3-P-8 Light and Transmission Electron Microscopy Complement Functional Genomics Screening in Chlamydomonas reinhardtii to Reveal Novel Mechanisms of Susceptibility to Herbicide Paraquat

Týč, Jiří	LS7-O-3 Serial Block-Face Scanning Electron Microscopy (SBEM): Comparative Analysis of Protocols for Enhancing Contrast and Reducing Charging in Mouse Brain Tissue Samples LS7-IN-2 Sample Preparation Strategies for Biological Electron Microscopy: Challenges and Innovations LS6-IN-2 Merging Electrons with Other Modalities LS6-P-7 Multiscale 3D imaging of digestive system morphogenesis during arthropod development
Učakar, Aleksander	MS3-P-5 Microstructure Analysis of Carbonyl Iron Powder (CIP) MS5-P-3 EBSD analysis of Sr-hexaferrite sintered in different atmospheres
Ugrin, Marina	LS3-P-2 Ultrastructural changes of the injured renal tissues in the cage-reared rainbow trout Oncorhynchus mykiss (Walbaum, 1792)
Uhlemann, Stephan	IMPRESS 7 EFLY – a Fast Versatile Charge Particle Optics Code
Ulusu, Nuray	LS3-P-4 Investigating the Effects of Vitamin D on Non-Alcoholic Fatty Pancreas Disease in an Experimental Metabolic Syndrome Rat Model
Umek, Polona	MS5-P-4 Synthesis Strategies for Effective Doping of Barlowite
Ummethala, Govind	IMPRESS 13 Time-resolved imaging of dynamic and resonant spin phenomena in situ in the TEM IMPRESS 12 A laser-free approach to ultra-fast transmission electron microscopy
Unterleutner, Elena	IM3-O-1 Advanced STEM of Point Defect Clusters in Doped STO
Ustarroz, Jon	MS4-P-11 Investigation of Electrodeposition and Electrodissolution Mechanisms of Silver Nanoparticles Using Electrochemical Liquid Cell Transmission Electron Microscopy
V Vukman, Krisztina	LS3-O-1 Recognition of a new exctracellular vesicle release mechanism
Vacek, Petr	MS6-O-1 Indium segregation at stacking faults in zincblende InGaN epilayers
Vailati, Cristian	Bruker EMA, Unique Range of Analytical Tools for Electron Microscopes
Valant, Matjaž	IM1-P-1 Cathodoluminescence spectroscopy study of plasmonic emissions in different Bi2Se3 systems
Valcz, Gábor	LS3-O-1 Recognition of a new exctracellular vesicle release mechanism
Válek, Jan	MS1-P-13 Exploring High-Baroque Stucco: Microscopy of Materials and Techniques at Kroměříž Chateau
Valencia-Liñan, Luisa Maria	MS2-IN-2 Study of the electron-induced damage of polymer based materials during STEM-EELS measurements
Vallet, Maxime	IM3-O-3 Exploring perovskites at the atomic level by 4DSTEM: Experimental & Simulation
Valpuesta, José M.	LS8-O-1 Structural recognition and stabilization of tyrosine hydroxylase by the J-domain protein DNAJC12
Valtr, Miroslav	MS4-P-8 Ab initio Study of Angle-Resolved Spectroscopy of Few-Layer Graphene
Van Aert, Sandra	MS6-IN-2 Advanced low dose electron microscopy of metal halide perovskites

van Midden, Katarina Petra	LS3-P-8 Light and Transmission Electron Microscopy Complement Functional Genomics Screening in Chlamydomonas reinhardtii to Reveal Novel Mechanisms of Susceptibility to Herbicide Paraquat
Van Noorden, Cornelis J.F.	LS4-P-6 Chemotherapy-induced metabolic changes in glioblastoma stem and differentiated cells in a context of the tumor microenvironment
Van Speybroeck, Veronique	MS6-IN-2 Advanced low dose electron microscopy of metal halide perovskites
Vancová, Marie	LS7-IN-2 Sample Preparation Strategies for Biological Electron Microscopy: Challenges and Innovations LS6-P-7 Multiscale 3D imaging of digestive system morphogenesis during arthropod development
Vanhaecke, Tamara	MS4-P-10 Physicochemical characterization of copper oxides applied as feed additives and plant protection products
Varambhia, Aakash	IM8-P-5 Delivering state of the art imaging data science to aid research and development at Johnson Matthey
Vardjan, Nina	LS5-IN-2 Noradrenaline and Cannabinoid Regulation of Astrocyte Energy Metabolism Revealed by FRET Nanosensors
Vargas, Beatriz	MS5-O-2 Investigating Local Structure in NBT-BT system Using (S)TEM Techniques
Vas, Joseph Vimal	IMPRESS 13 Time-resolved imaging of dynamic and resonant spin phenomena in situ in the TEM
Vásárhelyi, Lívia	MS1-P-6 Transmission electron microscopy of hypomineralized enamel apatite nanocrystals
Vasile, Bogdan Stefan	MS6-P-19 Compositionally Graded Kesterite Nanostructured Film for Photovoltaic Applications
Vašina, Radovan	IM6-P-3 Aberration correctors and their benefits in SEM
Vaz de Araujo, Ana Claudia	MS8-P-7 Structural study of a Magnetic Graphitic Nanocomposite
Vega Paredes, Miquel	MS4-O-1 3D Identical Location STEM Insights into the Degradation of Metallic Core-Shell Nanoparticles under Fuel Cell Conditions
Veličan, Karlo	MS6-P-8 Optimizing Photocatalytic Degradation of Pollutants Using Cu-Doped ZnO and TiO2 Films Grown by ALD MS6-P-9 Atomic layer deposition of nitrogen-doped TiO2 thin films for photocatalytic applications
Veličković, Ksenija D.	LS4-P-15 Therapeutic effects of H_2S donors on ferroptosis-mediated liver damage in C57BL/6 mice – a microscopic study LS4-P-12 Proferroptotic response to nutrient deprivation and sorafenib treatment in hepatocellular carcinoma cells – a microscopic study
Vengust, Damjan	MS6-P-5 Photocatalytic activity of thin ZnO films deposited at room temperature by plasma-enhanced atomic layer deposition MS6-P-18 Characterization of ZnO Films Prepared via FIB-SEM MS1-P-15 FIB-SEM characterization of various types of materials
Vénien-Bryan, Catherine	LS7-O-1 Unique structural features of the human Kir2.1 channel in two different conformational states unveiled by cryo-electron microscopy
Veranič, Peter	LS3-P-11 Unveiling tunnelling nanotubes in urothelial spheroids and bladder cancer biopsy samples LS4-O-4 Periodontal and bone regeneration with magnesium barrier membranes: an in vitro study Microscopy-based analysis of biomimetic 2D and 3D in vitro models for preclinical studies

Verbeeck, Johan	MS6-IN-2 Advanced low dose electron microscopy of metal halide perovskites
Veres, Mate	LS1-O-1 Immersive Virtual Reality System for Mice Combined with 3D-Targeted Photostimulation as a Prototype for Visual Restoration
Verleysen, Eveline	MS4-P-10 Physicochemical characterization of copper oxides applied as feed additives and plant protection products MS4-P-6 Assessing the morphology and fractal properties of aggregated nanoparticles in 2 and 3 dimensions by transmission electron microscopy
Véron, Muriel	IM3-P-3 Combining 3D electron diffraction and nanotexture analysis for the characterization of meteorite's impact ejecta
Verovnik, Rudi	LS8-P-2 3D Atlas of Arthropods
Vesel, Alenka	MS6-P-11 New Genesis XPS Spectrometer at the Jožef Stefan Institute for advanced surface and thin film characterization
Vicente, Sergio	IM7-P-1 InCAEM: A Singular Infrastructure for Advanced Energy Materials Research
Vigliaturo, Ruggero	IM8-P-6 Fractal modelling and fracture mechanics of urban particle populations in biological tissues IM2-O-4 Urban particulate matter and human health: correlative microscopy methods and simulated tissues modeling.
Višnjar, Tanja	Microscopy-based analysis of biomimetic 2D and 3D in vitro models for preclinical studies
Visnovitz, Tamás	LS3-O-1 Recognition of a new exctracellular vesicle release mechanism
Viterbo, Juan Pereiro	MS6-O-3 Multi-modal Microscopy Analysis of Co-doped InAs/GaAs Quantum Dot Lasers
Vittori, Miloš	LS4-P-6 Chemotherapy-induced metabolic changes in glioblastoma stem and differentiated cells in a context of the tumor microenvironment LS3-O-4 Mysteries of crustacean armour: a combined approach to scale formation LS8-P-5 Origami roly poly: arthropods fold their exoskeletons as they roll into a ball LS8-P-2 3D Atlas of Arthropods
Vlahović, Tatjana	MS1-P-8 Multidisciplinary Application of Scanning Electron Microscopy (SEM) in Heritage Research, Conservation and Presentation at the Croatian Natural History Museum
Vlasov, Evgenii	MS4-P-6 Assessing the morphology and fractal properties of aggregated nanoparticles in 2 and 3 dimensions by transmission electron microscopy
Vodička, Martin	IM6-P-3 Aberration correctors and their benefits in SEM
Vrabec, Mirijam	MS1-P-12 Complex polycrystalline clusters of diamond and graphite from metamorphic rocks
Vrbančić, Lea	LS5-P-2 Unraveling the Noncanonical Mitochondrial Import Signals of NME6 – a Member of the NME/NDPK Family
Wagner, Barbara	MS1-P-14 Study of vanadinite as painting pigment
Wallis, David J.	MS6-O-1 Indium segregation at stacking faults in zincblende InGaN epilayers

Wan, Wenchao	IM1-P-5 Advanced EELS techniques in catalyst analysis
Wang, Heyu	IM1-IN-2 Recent advances in STEM spectroscopy using synchronized electron and photon beams
Wang, Peng	IM3-O-4 Multidimensional and Multimodal 4D STEM and Electron Ptychography
Wang, Qi	MS5-P-5 Electron magnetic circular dichroism with atomic plane resolution
Wang, Xuanhao	IMPRESS 6 NanoMi: An open-source electron microscope
Wang, Yi-Chi	MS4-IN-1 Dynamic Atomic Behaviour in 2D Heterostructures and Nanocatalysts
Wang, Zeyu	IM3-P-9 Sub-Angstrom Resolution at below 40 e-/Å2 with Electron Ptychography
Ważny, Grzegorz	IM4-P-3 Optimization of macromolecules imaging in Cryo EM method
Weber, Dieter	IM8-O-4 Automated Thickness Determination from 4D-STEM Data by CNNs
Weber, Igor	LS5-IN-1 Dictyostelium discoideum IQGAP proteins IqgC and IqgD - siblings or distant relatives
Weber, Jonathan T.	IMPRESS 11 Mechanical strain and light-induced control of magnetic states in Fe3Sn2 in situ in the TEM
Wechtersbach, Karmen	LS4-P-18 Revealing LRAT and NeuroD1 Colocalization in human urothelial cancer cells in vivo using proximity ligation assay LS3-P-11 Unveiling tunnelling nanotubes in urothelial spheroids and bladder cancer biopsy samples
Weidler, Lukas	IM7-P-4 Characterization of Carbon Black Produced via Methane Pyrolysis Using Environmental TEM
Weissenbach, Emely	MS2-P-2 Plastic-Degrading or Just Settling? First TEM insights into microbial-plastic interactions in a Cold-Climate Ecosystem
Wells, Jack	LS7-IN-1 Adapting Inpainting and non-Raster scanning for cryo Volume Electron Microscopy (cvEM) using the JEOL JIB 4700F cryo Focus Ion Beam Scanning Electron Microscope.
Wepener, Victor Wepener	MS2-P-1 Correlation Between Adhesion and Swimming Activity in Developing Zebrafish Exposed to Polystyrene and Polyethylene Micro- and Nanoplastics
Wiesbauer, Lena	LS2-O-1 Beyond Apoptosis: Unravelling Thapsigargin-Induced Non-Apoptotic Cell Death Pathways in Immune- and Cancer Cells
Wijesinghe, Udari	MS7-O-4 Understanding local crystallography in solar cells materials with scanning electron diffraction using unsupervised machine learning
Windisch, Rika Saskia	IM2-O-1 Correlative microscopy: Uncovering the role of vacancies and contamination on the mechanical stiffness of defect-engineered graphene.
Wirtz, Tom	MS7-O-3 Real Time Imaging of Lithium-Ion Transport in Solid-State Batteries: An Operando FIB-SIMS approach IM8-O-3 Mitigating beam damage during FIB-SIMS imaging: a new methodology using alternative FIB scans
Wolf, Elisabeth H.	IM1-P-5 Advanced EELS techniques in catalyst analysis
Wouters, Charlotte	MS4-P-6 Assessing the morphology and fractal properties of aggregated nanoparticles in 2 and 3 dimensions by transmission electron microscopy

Wu, Sean	IM3-O-4 Multidimensional and Multimodal 4D STEM and Electron Ptychography
Wu, Xiaoyan	IM3-P-9 Sub-Angstrom Resolution at below 40 e-/Å2 with Electron Ptychography
Wudy, Katrin	MS3-IN-2 The Microstructure and Mechanical Properties of LPBF Produced Nickel-based Alloy IN718 Influenced by Laser Beam Shape and Post Heat-Treatment
Wynne, Emily	MS2-O-3 4D-STEM of Soft Matter: Structural Characterisation of Beam-Sensitive Polymers and Molecular Crystals Using Fast Precession and a Direct Electron Detector on a Tescan Tensor
Yazir, Yusufhan	LS4-P-5 Brain Decellularization Process in Transgenic Alzheimer Rat Model
Yedra, Lluís	MS5-O-2 Investigating Local Structure in NBT-BT system Using (S)TEM Techniques
Yesibolati, Murat Nulati	IM7-P-3 Novel Nano Channel Chip for In Situ TEM Liquid Cell Analysis and Particle Trapping Without Manual Preassembly of Chip
Yildirim, Eren	LS4-P-14 Human Serum Albumin Nanoparticles as a Drug Delivery System to Enhance Temozolomide Efficacy in Glioblastoma Cell Line
Yuan, Biao	IM3-P-9 Sub-Angstrom Resolution at below 40 e-/Å2 with Electron Ptychography
Yucel, Oguz	LS4-P-14 Human Serum Albumin Nanoparticles as a Drug Delivery System to Enhance Temozolomide Efficacy in Glioblastoma Cell Line
Ząbek, Laura	MS7-P-3 Microstructural analysis of the copper matrix composites for electrodes of plasma torches
Zaefferer, Stefan	IM5-IN-2 The combination of high-resolution diffraction techniques in the scanning electron microscope for statistical relevant description of crystal defects and resulting properties in metals and alloys
Žagar, Sebastjan	MS3-P-2 Plastic deformation in the Magnesium alloy AZ80 - an EBSD study of the effects of cavitation peening
Zaghloul, Mohamed	IM1-P-7 Quantum state secondary electron emission spectroscopy in low voltage scanning electron microscope for probing Valence band IM1-O-3 Perspectives of ultrafast hyperspectral imaging in Scanning Electron Microscopy
Zagorščak, Maja	LS8-O-2 Spatiotemporal acquisition of genetically encoded biosensors in intact plant leaves reveals hormonal crosstalk in response to wounding LS2-P-2 Ultrastructure and gene expression in tomato flower pedicel abscission zone
Zakaria, Yahya	MS8-O-4 Correlative Imaging and Surface Analysis workflow
Zakšek, Valerija	LS8-P-2 3D Atlas of Arthropods
Zamani, Reza	Iliad, the new (S)TEM platform: Expand and simplifies energy loss analytics
Zaplotnik, Rok	MS6-P-11 New Genesis XPS Spectrometer at the Jožef Stefan Institute for advanced surface and thin film characterization
Zaveršek, Tim	LS2-O-3 Volume electron microscopy of intracellular compartments in the urinary bladder epithelium LS3-P-15 Distribution of Golgi matrix proteins GRASP65 and GRASP55 during early urothelial regeneration

Žegura, Bojana	LS1-O-4 High-throughput automated quantitative fluorescence microscopy and image feature analysis for in vitro detection of adverse effects
Železnik Ramuta, Taja	Microscopy-based analysis of biomimetic 2D and 3D in vitro models for preclinical studies
Železnik, Nadja	MS1-P-4 Effect of pretreatment and organic fibre reinforcement on the mechanical and microstructural properties of microwave irradiated alkali-activated radioactive fly ash
Zemánek, Pavel	IM1-P-6 Raman tweezers for the analysis of secondary microplastics generated by degradation of surgical masks in water
Žerovnik Mekuč, Manca	LS2-O-2 Membrane Segmentation in Volumetric Electron Microscopy Data LS2-O-3 Volume electron microscopy of intracellular compartments in the urinary bladder epithelium
Zhang, Rui	MS4-IN-1 Dynamic Atomic Behaviour in 2D Heterostructures and Nanocatalysts
Zhang, Yongchao	IM7-P-1 InCAEM: A Singular Infrastructure for Advanced Energy Materials Research
Zhang, Zaoli	MS6-P-3 Multi-scale investigation of superior mechanical properties in nitride ceramics with negative stacking fault energy MS6-O-2 Mechanical properties enhancement in ceramics through vacancy-mediated unit cell disturbance MS3-O-2 Atomic-resolution electron microscopy analysis of oxygen-mediated Ti nanocrystalline synthesized by high-pressure torsion MS1-O-4 Oxygen vacancy distribution in different regions of La1−xSrxGa1−yMgyO3−δ MS8-O-2 Revealing atomic-level plasticity of ceramic materials through advanced electron microscopy
Zhang, Zhenxue	MS6-P-4 Spray-Coated Metallosurfactant-Alginate Coatings: Dual Antimicrobial Action
Zhong, Xiaoyan	MS5-P-5 Electron magnetic circular dichroism with atomic plane resolution
Zhu, Shikai	IM6-P-2 Development and Application of an Aberration Calculation Program for Electron Lenses Based on Differential Algebra
Žiberna, Katarina	MS5-IN-1 Insight into Defects and Polarization in Lead-Free Ferroelectrics by Advanced STEM Techniques MS1-P-10 Effects of Ti Doping on Structure, Microstructure and Mechanical Properties of (K0.5Na0.5)NbO3
Zięba, Amelia	MS3-P-9 Effect of recycled powder on microstructure and chemical composition of additively manufactured AlSi7Mg alloy
Zierler, Susanna	LS2-O-1 Beyond Apoptosis: Unravelling Thapsigargin-Induced Non-Apoptotic Cell Death Pathways in Immune- and Cancer Cells
Zimowski, Sławomir	MS6-P-2 Microstructure and selected properties of multicomponent wear-resistant and low-friction coatings on titanium alloy substrates
Zingsem, Benjamin W.	IMPRESS 12 A laser-free approach to ultra-fast transmission electron microscopy IMPRESS 13 Time-resolved imaging of dynamic and resonant spin phenomena in situ in the TEM
Ziroglu, Nezih	Improving Bone Regeneration through Estrogen-Loaded Cement in a Modified Masquelet Approach

Žnidaršič, Nada	LS6-P-8 Intestinal stem cells of Colorado potato beetle – imaging from the morphology of the digestive tract in the whole animal to the cell ultrastructure LS6-P-7 Multiscale 3D imaging of digestive system morphogenesis during arthropod development
Zorec, Robert	LS5-O-1 Exploring Plectin's Function in Migration of Astrocytes and Glioblastoma Through Confocal Microscopy LS6-IN-1 Advanced Microscopy Approaches Unveil Plectin as a Key Regulator of Focal Adhesions in Astrocytes LS5-IN-2 Noradrenaline and Cannabinoid Regulation of Astrocyte Energy Metabolism Revealed by FRET Nanosensors
Zorkaya, Betul	LS3-P-4 Investigating the Effects of Vitamin D on Non-Alcoholic Fatty Pancreas Disease in an Experimental Metabolic Syndrome Rat Model
Zorko, Andrej	MS5-P-4 Synthesis Strategies for Effective Doping of Barlowite
Zouhar, Martin	MS4-P-8 Ab initio Study of Angle-Resolved Spectroscopy of Few-Layer Graphene
Zoumpoulakis, Andreas	LS7-O-1 Unique structural features of the human Kir2.1 channel in two different conformational states unveiled by cryo-electron microscopy
Zubak, Marko	MS6-P-7 Intense Pulsed Light Processing for Rapid Crystallization of Titania Nanotube Thin Films
Žugec, Maja	LS5-O-1 Exploring Plectin's Function in Migration of Astrocytes and Glioblastoma Through Confocal Microscopy
Žuntar, Jan	MS7-P-5 Atomic-scale insights into Solid-State Batteries via in situ TEM MS7-P-9 Impact of La0.07Ba0.93SnO3 interlayer on epitaxial growth of Li4Ti5O12 thin film anodes for all-solid-state Li-ion batteries
Zupančič, Daša	LS4-P-18 Revealing LRAT and NeuroD1 Colocalization in human urothelial cancer cells in vivo using proximity ligation assay LS3-P-11 Unveiling tunnelling nanotubes in urothelial spheroids and bladder cancer biopsy samples Microscopy-based analysis of biomimetic 2D and 3D in vitro models for preclinical studies
Zupančič, Nina	MS1-P-7 Ex-situ differential individual particle analysis of various Pb, Zn and Fe ore minerals after periodical leaching in soil column experiments
Županič, Anže	LS3-P-8 Light and Transmission Electron Microscopy Complement Functional Genomics Screening in Chlamydomonas reinhardtii to Reveal Novel Mechanisms of Susceptibility to Herbicide Paraquat
Žuran, Ana	LS3-O-4 Mysteries of crustacean armour: a combined approach to scale formation
Zyguła, Krystian	MS3-P-9 Effect of recycled powder on microstructure and chemical composition of additively manufactured AlSi7Mg alloy

Tescan

Join us at
17th Multinational
Congress on Microscopy

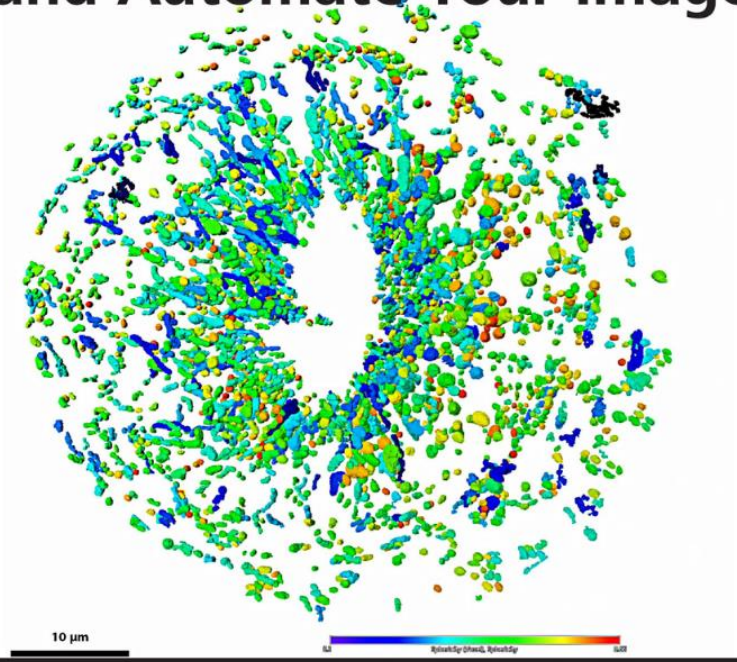
TESCAN MIRA XR

From Routine to Remarkable

Ultra-High-Resolution
SEM-EDS Solution

Connect with us to hear our fresh
perspective on electron microscopy —
streamlined, connected, collaborative.

Scale up and Automate Your Image Analysis



ZEISS arivis Software
Your Complete Image Analysis Solution
for Material & Life Sciences

zeiss.com/microscopy

ZEISS



SCIENCE SERVICES – Your Partner for Microscopy and Lab Supplies

Since 1976, **SCIENCE** SERVICES has been a trusted partner for laboratories around the world, providing **high-quality solutions** for sample preparation in **microscopy** and **ultracentrifugation**. Our customers in research and industry value our expertise and long-term collaborations.

Our portfolio comprises **over 20.000 products** from carefully selected specialist manufacturers with whom we maintain long-standing partnerships. We focus on delivering solutions for materials and life sciences, particularly in the areas of **TEM**, **SEM**, **cryo-EM**, and **CLEM**.

Our interdisciplinary team of scientists, technicians, and application experts provides in-depth consultation and dependable support tailored to **your needs**.

SCIENCE SERVICES

Your Partner for Microscopy and Lab Supplies

WE HAVE IT

Info@ScienceServices.eu
www.ScienceServices.eu